Hans-Eckhardt Schaefer

Nanoscience

The Science of the Small in Physics, Engineering, Chemistry, Biology and Medicine

Springer

Nanoscience

Hans-Eckhardt Schaefer

Nanoscience

The Science of the Small in Physics, Engineering, Chemistry, Biology and Medicine

Springer

Prof. Dr. Hans-Eckhardt Schaefer
Universität Stuttgart
Fak. Mathematik und Physik
Institut für Theoretische und
Angewandte Physik
Pfaffenwaldring 57
70569 Stuttgart
Germany
hans-eckhardt.schaefer@itap.uni-stuttgart.de

ISBN 978-3-642-10558-6 e-ISBN 978-3-642-10559-3
DOI 10.1007/978-3-642-10559-3
Springer Heidelberg Dordrecht London New York

Library of Congress Control Number: 2010928839

Cover design: eStudio Calamar S.L.

Printed on acid-free paper

Springer is part of Springer Science+Business Media (www.springer.com)

For Bettina

Preface

Nanoscience is an interdisciplinary field of science which has its early beginnings in the 1980s. At small dimensions of a few nanometers (billionths of a meter) new physical properties emerge, often due to quantum mechanical effects. During the last decades, additionally novel microscopical techniques have been developed in order to observe, measure, and manipulate objects at the nanoscale. It rapidly turned out that nanosized features not only play a role in physics and materials sciences but also are most relevant in chemistry, biology, and medicine, giving rise to new fenestrations between these disciplines and wide application prospects.

The early precursors to this book on *Nanoscience* date back to the 1990s when the author initiated a course on Nanoscience and Nanotechnology at Stuttgart University, Germany, based on his early studies of nanostructured solids which were performed due to most stimulating discussions in the early 1980s with Herbert Gleiter and the late Arno Holz, at that time at Saarbrücken University.

Together with the growing interdisciplinarity of the field, the author's research and teaching activities in nanoscience were extended at Stuttgart University and at research laboratories in South America, Japan, China, and Russia. During these research and teaching activities it became clear that a comprehensive yet concise text which comprises the current literature on nanoscience from physics to materials science, chemistry, biology, and medicine would be highly desirable. Such a textbook or monograph should be a valuable source of information for students and teachers in academia and for scientists and engineers in industry who are involved in the many different fields of nanoscience.

In the present book, the state of the art of nanoscience is presented, emphasizing in addition to the width and interdisciplinarity of the field the rapid progress in experimental techniques and theoretical studies. The text which focuses to the fundamental aspects of the field in 12 chapters is supported by more than 600 figures and a bibliography of nearly 2000 references which may be useful for more detailed studies and for looking at historical developments and which cover with their own references the wealth of the literature. A number of textbooks and review articles are quoted as introductory literature to the various fields.

The book starts in Chap. 1 with some general comments, physical principles, and a number of nanoscale measuring methods with the subsequent Chap. 2 on microscopy techniques for investigating nanostructures. Chapter 3 is devoted to

the synthesis of nanosystems whereas Chap. 4 surveys dimensionality effects with Chap. 5 focusing to carbon nanostructures and Chap. 6 to bulk nanocrystalline materials. In the Chaps. 7 and 8 the topics of nanomechanics, nanophotonics, nanofluidics, and nanomagnetism are raised before in Chap. 9 nanotechnology for computers and data storage devices are overviewed. The text is concluded with Chap. 10 on nanochemistry and Chap. 11 on nanobiology with finally an extended section on nanomedicine in Chap. 12.

These 12 chapters are closely linked and intertwined as demonstrated by many cross-references between the chapters. Although a particular chapter is dedicated, e.g., to synthesis (Chap. 3), some synthesis aspects reappear in other chapters. The same is true for nanomagnetism. In addition to the particular chapter on this topic (Chap. 8), nanomagnetic features appear in the introductory chapter, in the chapters on nanocrystalline materials (Chap. 6), on nanotechnology for computers and data storage (Chap. 9), on nanobiology (Chap. 11), or nanomedicine (Chap. 12). The Subject Index may additionally help the reader to find the appropriate information in his field of interest quickly.

The wide application prospects of nanoscience are discussed in the various chapters. The importance of risk assessment strategies and toxicity studies in nanotechnology is emphasized in Sect. 12.11.

Stuttgart, Germany Hans-Eckhardt Schaefer
December 7, 2009

Acknowledgments

The author is indebted to highly competent colleagues for critically reading single chapters of the present book: W. Sprengel, Graz Technical University, Austria; B. Fultz, California Institute of Technology, Pasadena, USA; H. Strunk, Stuttgart University, Germany; L. Ley, Erlangen University, Germany; H. Krenn, Graz University, Austria; R. Würschum, Graz Technical University, Austria; H. Schaefer, retired from Nycomed GmbH, Konstanz, Germany; and R. Ghosh, Stuttgart University, Germany.

The financial support of the author's research projects by Deutsche Forschungsgemeinschaft, by the European Union, Alexander von Humboldt Foundation, Deutscher Akademischer Austauschdienst, Baden-Württemberg Stiftung, and NATO is highly appreciated.

Parts of the book have been designed during research and teaching periods of the author abroad, kindly hosted by P. Vargas, Universidad Técnica Federico Santa Maria, Valparaiso, Chile; by K. Lu, Institute of Metal Research, Chinese Academy of Sciences, Shenyang, China; by Y. Shirai, Kyoto University; by T. Kakeshita and H. Araki, Osaka University, Japan; and by A. A. Rempel, Institute of Solid State Chemistry, Russian Academy of Sciences, Ekaterinburg, Russia. Continuous support by C. Ascheron, Springer Verlag, Heidelberg, Germany, is gratefully acknowledged.

The efficient help by S. Heldele, M. Jakob, P. C. Li, Y. Rong, and H. Schatz and the financial support by H. Strunk, Stuttgart University, Germany, were crucial for the technical preparation of the manuscript. Thanks are due to S. Blümlein, P. Brommer, U. Mergenthaler, J. Roth, and H. R. Trebin, Stuttgart University, Germany, for most valuable technical and organizational help.

Furthermore, thanks are due to many publishing houses, scientific societies, governments, companies, and individuals for kindly granting the copyright permissions for a large number of figures: Advanced Study Center St. Petersburg, Agentur-Focus, American Association for the Advancement of Sciences (AAAS), American Association of Cancer Research, American Association of Physics Teachers, American Cancer Society, American Chemical Society, American Dental Association, American Institute of Physics, American Physical Society, American

Scientific Publishers, Annual Reviews, Baden-Württemberg Stiftung, Biophysical Society, Cambridge University Press, Chinese Society of Metals, Congress of Neurological Surgeons, Elsevier, European Molecular Biology Association, Gerhard Glück, German Academy of Sciences Leopoldina, German Federal Ministry of Education and Research, Institute of Electrical and Electronic Engineers (IEEE), Institute of Physics, Intel Corp., Japanese Society of Applied Physics, Karlsruhe Institute of Technology, Korean Chemical Society, Lippincott Williams and Wilkins, Massachusetts Medical Society, Materials Research Society, Max-Planck Society, National Academy of Sciences of the USA, Nature Publishing Group, Oldenbourg Publ., Optical Society of America, Orthopaedic Research Society, Photonik, Radiological Society of North America, Royal Society of Chemistry, SAGE, Scientific American, Sigma-Aldrich, Space Channel, Spektrum der Wissenschaft, Society of Nuclear Medicine, Springer Publ., Taylor and Francis, Techscience Press, VDI Technologiezentrum, Wiley Interscience, Wiley-VCH, World Federation of Ultrasound in Medicine and Biology, and World Scientific.

Contents

1 Introduction and Some Physical Principles 1
1.1 Introduction 1
1.2 Thermal Properties of Nanostructures 7
1.2.1 Violation of the Second Law of Thermodynamics for Small Systems and Short Timescales 7
1.2.2 Surface Energy 8
1.2.3 Thermal Conductance 9
1.2.4 Melting of Nanoparticles 11
1.2.5 Lattice Parameter 12
1.2.6 Phase Transitions 13
1.3 Electronic Properties 14
1.3.1 Electron States in Dependence of Size and Dimensionality 14
1.3.2 The Electron Density of States D(E) 16
1.3.3 Luttinger Liquid Behavior of Electrons in 1D Metals . 17
1.3.4 Superconductivity 17
1.4 Giant Magnetoresistance (GMR) and Spintronics 19
1.4.1 Giant Magnetoresistance (GMR) and Tunneling Magnetoresistance (TMR) 21
1.4.2 Spintronics in Semiconductors 23
1.4.3 Spin Hall Effect 26
1.5 Self-Assembly 27
1.5.1 Self-Assembly of Ni Nanoclusters on Rh (111) via Friedel Oscillations 28
1.5.2 Self-Assembly of Fe Nanoparticles by Strain Patterns 29
1.5.3 Chiral Kagomé Lattice from Molecular Bricks 29
1.5.4 Self-Assembled Monolayers (SAMs) 30
1.5.5 Magnetic Assembly of Colloidal Superstructures . . . 31
1.5.6 Self-Assembly via DNA or Proteins 33
1.6 Casimir Forces 33
1.7 Nanoscale Measuring Techniques 35
1.7.1 Displacement Sensing 35

1.7.2 Mass Sensing 35
1.7.3 Sensing of Weak Magnetic Fields at the Nanoscale . . 36
1.7.4 Nuclear Magnetic Resonance Imaging (MRI) at the Nanoscale 37
1.7.5 Probing Superconductivity at the Nanoscale by Scanning Tunneling Microscopy (STM) 39
1.7.6 Raman Spectroscopy on the Nanometric Scale 40
1.7.7 "Nanosized Voltmeter" for Mapping of Electric Fields in Cells 40
1.7.8 Detection of Calcium at the Nanometer Scale 41
1.8 Summary 43
References 44

2 Microscopy – Nanoscopy 49
2.1 Scanning Tunneling Microscopy (STM) 49
2.1.1 Scanning Units, Electronics, Software 50
2.1.2 Constant Current Imaging (CCI) 51
2.1.3 Constant-Height Imaging (CHI) 53
2.1.4 Synchrotron Radiation Assisted STM (SRSTM) for Nanoscale Chemical Imaging 54
2.1.5 Studying Bulk Properties and Volume Atomic Defects by STM 54
2.1.6 Radiofrequency STM 56
2.2 Atomic Force Microscopy (AFM) 56
2.2.1 Topographic Imaging by AFM in Contact Mode . . . 57
2.2.2 Frictional Force Microscopy 59
2.2.3 Non-contact Force Microscopy 59
2.2.4 Chemical Identification of Individual Surface Atoms by AFM 60
2.2.5 AFM in Bionanotechnology 61
2.3 Scanning Near-Field Optical Microscopy (SNOM) 61
2.3.1 Scanning Near-Field Optical Microscopy (SNOM) 63
2.3.2 Near-Field Scanning Interferometric Apertureless Microscopy (SIAM) 64
2.3.3 Mapping Vector Fields in Nanoscale Near-Field Imaging 65
2.3.4 Terahertz Near-Field Nanoscopy of Mobile Carriers in Semiconductor Nanodevices 66
2.4 Far-Field Optical Microscopy Beyond the Diffraction Limit . . 67
2.4.1 Stimulated Emission Depletion (STED) Optical Microscopy 68
2.4.2 Stochastic Optical Reconstruction Microscopy (2D-STORM) 69
2.4.3 Three-Dimensional Far-Field Optical Nanoimaging of Cells 70

2.4.4 Video-Rate Far-Field Nanooptical Observation of Synaptic Vesicle Movement 73
2.5 Magnetic Scanning Probe Techniques 74
2.5.1 Magnetic Force Microscopy (MFM) 74
2.5.2 Spin-Polarized Scanning Tunneling Microscopy (SP-STM) 75
2.6 Progress in Electron Microscopy 76
2.6.1 Aberration-Corrected Electron Microscopy 76
2.6.2 TEM Nanotomography and Holography 81
2.6.3 Cryoelectron Microscopy and Tomography 81
2.7 X-Ray Microscopy 84
2.7.1 Lens-Based X-Ray Microscopy 85
2.7.2 X-Ray Nanotomography 87
2.7.3 Lens-Less Coherent X-Ray Diffraction Imaging . . . 89
2.7.4 Upcoming X-Ray Free-Electron Lasers (XFEL) and Single Biomolecule Imaging 89
2.8 Three-Dimensional Atom Probes (3DAPs) 91
2.9 Summary 95
References 95

3 Synthesis 99
3.1 Nanocrystals and Clusters 99
3.1.1 From Supersaturated Vapors 99
3.1.2 Particle Synthesis by Chemical Routes 101
3.1.3 Semiconductor Nanocrystals (Quantum Dots) 104
3.1.4 Doping of Nanocrystals 104
3.1.5 Magnetic Nanoparticles 105
3.2 Superlattices of Nanocrystals in Two (2D) and Three (3D) Dimensions 107
3.2.1 Free-Standing Nanoparticle Superlattice Sheets 107
3.2.2 3D Superlattices of Binary Nanoparticles 109
3.3 Nanowires and Nanofibers 111
3.3.1 Vapor–Liquid–Solid (VLS) Growth of Nanowires . . 113
3.3.2 Pine Tree Nanowires with Eshelby Twist 116
3.3.3 Ultrathin Nanowires 117
3.3.4 Electrospinning of Nanofibers 120
3.3.5 Bio-Quantum-Wires 121
3.3.6 Formation of Arsenic Sulfide Nanotubes by the Bacterium Shewanella sp. Strain HN-41 122
3.4 Nanolayers and Multilayered Systems 123
3.4.1 Layered Oxide Heterostructures by Molecular Beam Epitaxy (MBE) 127
3.4.2 Atomic Layer Deposition (ALD) 128
3.5 Shape Control of Nanoparticles 132
3.6 Nanostructures with Complex Shapes 134

3.7 Nanostructures by Ball Milling or Strong Plastic Deformation . . . 136
3.8 Carbon Nanostructures . . . 137
3.8.1 Fullerenes . . . 137
3.8.2 Single-Walled Carbon Nanotubes (SWNTs) – Synthesis and Characterization . . . 139
3.8.3 Graphene . . . 143
3.9 Nanoporous Materials . . . 145
3.9.1 Zeolites and Mesoporous Metal Oxides . . . 145
3.9.2 Nanostructured Germanium . . . 150
3.9.3 Nanoporous Metals . . . 150
3.9.4 Single Nanopores – Potentials for DNA Sequencing . . . 152
3.10 Lithography . . . 154
3.10.1 UV Optical Lithography . . . 155
3.10.2 Electron Beam Lithography . . . 157
3.10.3 Proton-Beam Writing . . . 157
3.10.4 Nanoimprint Lithography (NIL) . . . 158
3.10.5 Dip-Pen Nanolithography (DPN) . . . 158
3.10.6 Block Copolymer Lithography . . . 159
3.10.7 Protein Nanolithography . . . 162
3.10.8 Fabrication of Nanostructures in Supercritical Fluids . . . 163
3.10.9 Two-Photon Lithography for Microfabrication . . . 164
3.11 Summary . . . 165
References . . . 165

4 Nanocrystals – Nanowires – Nanolayers . . . 169
4.1 Nanocrystals . . . 169
4.1.1 Synthesis of Nanocrystals . . . 169
4.1.2 Metal Nanocrystallites – Structure and Properties . . . 172
4.1.3 Semiconductor Quantum Dots . . . 174
4.1.4 Colorful Nanoparticles . . . 178
4.1.5 Double Quantum Dots for Operating Single-Electron Spins as Qubits for Quantum Computing . . . 181
4.1.6 Quantum Dot Data Storage Devices . . . 183
4.2 Nanowires and Metamaterials . . . 183
4.2.1 Metallic Nanowires . . . 183
4.2.2 Negative-Index Materials (Metamaterials) with Nanostructures . . . 184
4.2.3 Semiconductor Nanowires . . . 186
4.2.4 Molecular Nanowires . . . 192
4.2.5 Conduction Through Individual Rows of Atoms and Single-Atom Contacts . . . 193
4.3 Nanolayers and Multilayers . . . 195
4.3.1 2D Quantum Wells . . . 195

4.3.2 2D Quantum Wells in High Magnetic Fields 196
4.3.3 The Integral Quantum Hall Effect (IQHE) 196
4.3.4 The Fractional Quantum Hall Effect (FQHE) 198
4.3.5 2D Electron Gases (2DEG) at Oxide Interfaces 199
4.3.6 Multilayer EUV and X-Ray Mirrors with High Reflectivity 201
4.4 Summary 205
References 205

5 Carbon Nanostructures – Tubes, Graphene, Fullerenes, Wave-Particle Duality 209
5.1 Nanotubes 209
5.1.1 Synthesis of Carbon Nanotubes 209
5.1.2 Structure of Carbon Nanotubes 212
5.1.3 Electronic Properties of Carbon Nanotubes 214
5.1.4 Heteronanocontacts Between Carbon Nanotubes and Metals 219
5.1.5 Optoelectronic Properties of Carbon Nanotubes . . . 219
5.1.6 Thermal Properties of Carbon Nanotubes 220
5.1.7 Mechanical Properties of Carbon Nanotubes 220
5.1.8 Carbon Nanotubes as Nanoprobes and Nanotweezers in Physics, Chemistry, and Biology . . 224
5.1.9 Other Tubular 1D Carbon Nanostructures 227
5.1.10 Filling and Functionalizing Carbon Nanotubes 230
5.1.11 Nanotubes from Materials Other than Pure Carbon . . 235
5.1.12 Application of Carbon Nanotubes 236
5.2 Graphene 245
5.2.1 Imaging of Graphene, Defects, and Atomic Dynamics 246
5.2.2 Electronic Structure of Graphene, Massless Relativistic Dirac Fermions, and Chirality 248
5.2.3 Quantum Hall Effect 250
5.2.4 Anomalous QHE in Bilayer Graphene 251
5.2.5 Absence of Localization 252
5.2.6 From Graphene to Graphane 252
5.2.7 Graphene Devices 252
5.3 Fullerenes, Large Carbon Molecules, and Hollow Cages of Other Materials 253
5.3.1 Fullerenes 253
5.3.2 Fullerene Compounds 254
5.3.3 Superheating and Supercooling of Metals Encapsulated in Fullerene-Like Shells 255
5.3.4 Large Carbon Molecules 257
5.3.5 Hollow Cages of Other Materials 258
5.4 Fullerenes and the Wave-Particle Duality 259
5.5 Summary 261
References 262

6 Nanocrystalline Materials 267
6.1 Molecular Dynamics Simulation of the Structure of Grain Boundaries and of the Plastic Deformation of Nanocrystalline Materials 267
6.2 Grain Boundary Structure 268
6.3 Plasticity and Hall–Petch Behavior of Nanocrystalline Materials 271
6.4 Plasticity Studies by Nanoindentation 276
6.5 Ultrastrength Nanomaterials 279
6.6 Enhancement of Both Strength and Ductility 282
6.7 Superplasticity 285
6.8 Fatigue 288
6.9 Nanocomposites 290
6.9.1 Metallic Nanocomposites 290
6.9.2 Ceramic/Metal Nanocomposites with Diamond-Like Hardening 292
6.9.3 Oxide/Dye/Polymer Nanocomposites – Optical Properties 293
6.9.4 Polymer Nanocomposites 294
6.10 Nanocrystalline Ceramics 300
6.10.1 Low Thermal Expansion Nanocrystallite-Glass Ceramics 301
6.11 Atomic Diffusion in Nanocrystalline Materials 303
6.12 Surface-Controlled Actuation and Manipulation of the Properties of Nanostructures 306
6.12.1 Charge-Induced Reversible Strain in Nanocrystalline Metals 307
6.12.2 Artificial Muscles Made of Carbon Nanotubes 308
6.12.3 Electric Field-Controlled Magnetism in Nanostructured Metals 308
6.12.4 Surface Chemistry-Driven Actuation in Nanoporous Gold 310
6.13 Summary 310
References 310

7 Nanomechanics – Nanophotonics – Nanofluidics 315
7.1 Nanoelectromechanical Systems (NEMS) 315
7.1.1 High-Frequency Resonators 316
7.1.2 Nanoelectromechanical Switches 316
7.2 Putting Mechanics into Quantum Mechanics – Cooling by Laser Irradiation 319
7.3 Nanoadhesion: From Geckos to Materials 323
7.3.1 Materials with Bioinspired Adhesion 324
7.3.2 Climbing Robots and Spiderman Suit 324

7.4 Single-Photon and Entangled-Photon Sources and Photon Detectors, Based on Quantum Dots 325
7.4.1 Single-Photon Sources 325
7.4.2 Entangled-Photon Sources 327
7.4.3 Single-Photon Detection 328
7.5 Quantum Dot Lasers 329
7.6 Plasmonics 331
7.6.1 Plasmon-Controlled Synthesis of Metallic Nanoparticles 334
7.6.2 Extinction Behavior of Nanoparticles and Arrays . . . 335
7.6.3 Plasmonic Nanocavities 337
7.6.4 Surface-Enhanced Raman Spectroscopy (SERS) and Fluorescence 338
7.6.5 Receiver–Transmitter Nanoantenna Pairs 341
7.6.6 Electro-optical Nanotraps for Neutral Atoms 341
7.6.7 Unifying Nanophotonics and Nanomechanics 342
7.6.8 Integration of Optical Manipulation and Nanofluidics 342
7.6.9 Single-Photon Transistor 343
7.6.10 Application Prospects of Plasmonics 343
7.7 2D-Confinement of Fluids, Wetting, and Spreading 346
7.7.1 Phase Transitions Induced by Nanoconfinement of Liquid Water 347
7.7.2 Fluid Flow and Wetting 348
7.7.3 Superhydrophobic Surfaces 348
7.7.4 Liquid Spreading Under Nanoscale Confinement . . . 349
7.8 Fast Transport of Liquids and Gases Through Carbon Nanotubes 351
7.8.1 Limits of Continuum Hydrodynamics at the Nanoscale 351
7.8.2 Water Transport in CNTs 351
7.8.3 Gas Transport in CNTs 353
7.9 Nanodroplets 353
7.9.1 Dynamics of Nanoscopic Water in Micelles 353
7.9.2 Nanoscale Double Emulsions 354
7.9.3 Zeptoliter Liquid Alloy Droplets and Surface-Induced Crystallization 354
7.9.4 Superfluid Helium Nanodroplets 356
7.10 Nanobubbles 358
7.10.1 Stable Surface Nanobubbles 358
7.10.2 Polygonal Nanopatterning of Stable Microbubbles . . 358
7.10.3 Bubbles for Tracking the Trajectory of an Individual Electron Immersed in Liquid Helium . . . 359
7.11 Summary 360
References 361

8 Nanomagnetism 365
8.1 Magnetic Imaging 365
8.1.1 Magnetic Force Microscopy (MFM) and Magnetic Exchange Force Microscopy (MEx FM) . . 366
8.1.2 Spin-Polarized Scanning Tunneling Microscopy (SP-STM) and Manipulation 370
8.1.3 Electron Microscopy 376
8.1.4 X-Ray Magnetic Circular Dichroism (XMCD) 381
8.2 Size and Dimensionality Effects in Nanomagnetism – Single Atoms, Clusters (0D), Wires (1D), Films (2D) 383
8.2.1 Single Atoms 384
8.2.2 Finite-Size Atomic Clusters 386
8.2.3 Ferromagnetic Nanowires 388
8.2.4 Magnetic Films (2D) 393
8.2.5 Curie Temperature T_C in Dependence of Size, Dimensionality, and Charging 396
8.3 Soft-Magnetic Materials 397
8.4 Nanostructured Hard Magnets 399
8.5 Antiferromagnetic and Complex Magnetic Nanostructures . . 401
8.5.1 Spin Structure of Antiferromagnetic Domain Walls . . 403
8.5.2 Antiferromagnetic Monatomic Chains 403
8.5.3 Antiferromagnetic Nanoparticles 403
8.5.4 Complex Magnetic Structure of an Iron Monolayer on Ir (111) 407
8.6 Ferromagnetic Nanorings 407
8.7 Current-Induced Domain Wall Motion in Magnetic Nanostructures 410
8.8 Single Molecule Magnets 412
8.9 Multiferroic Nanostructures 412
8.10 Magnetically Tunable Photonic Crystals of Superparamagnetic Colloids 416
8.11 Nanomagnets in Bacteria 417
8.11.1 In Vivo Doping of Magnetosomes 418
8.11.2 Magnetosomes for Highly Sensitive Biomarker Detection 419
8.12 Summary 420
References 420

9 Nanotechnology for Computers, Memories, and Hard Disks 425
9.1 Transistors and Integrated Circuits 426
9.2 Extreme Ultraviolet (EUV) Lithography – The Future Technology of Chip Fabrication 431
9.3 Flash Memory 434
9.4 Emerging Solid State Memory Technologies 436
9.4.1 Phase-Change Memory Technology 437

9.4.2 Magnetoresistive Random-Access Memories (MRAM) 441
9.4.3 Ferroelectric Random-Access Memories (FeRAM) . . 446
9.4.4 Resistance Random Access Memories (ReRAMs) . . 447
9.4.5 Carbon-Nanotube (CNT)-Based Data Storage Devices (NRAM) 448
9.4.6 Magnetic Domain Wall Racetrack Memories (RM) . . 450
9.4.7 Single-Molecule Magnets 452
9.4.8 10 Terabit/Inch^2 Block Copolymer (BCP) Storage Media 452
9.5 Magnetic Hard Disks and Write/Read Heads 454
9.5.1 Extensions to Hard Disk Magnetic Recording 456
9.5.2 Magnetic Write Head and Read Back Head 457
9.6 Optical Hard Disks 462
9.6.1 Principles and Materials Considerations 463
9.6.2 Magneto-Optical Recording 466
9.6.3 Multilayer Recording 467
9.6.4 Holographic Data Storage 468
9.7 High-*k* Dielectrics for Replacing SiO_2 Insulation in Memory and Logic Devices 470
9.8 Low-*k* Materials as Interlayer Dielectrics (ILD) 471
9.9 Summary 474
References 474

10 Nanochemistry – From Supramolecular Chemistry to Chemistry on the Nanoscale, Catalysis, Renewable Energy, Batteries, and Environmental Protection 477
10.1 Supramolecular Chemistry 477
10.1.1 Architecture in Supramolecular Chemistry 478
10.1.2 Supramolecular Materials 480
10.1.3 Molecular Recognition, Reactivity, Catalysis, and Transport 484
10.1.4 Molecular Photonics and Electronics 486
10.1.5 Molecular Recognition and Self-Organization 489
10.1.6 DNA Self-Assembled Nanostructures 493
10.1.7 Supramolecular DNA Polyhedra 493
10.2 Large Inorganic Hollow Clusters 495
10.2.1 Nano-hedgehogs Shaped from Molybdenum Oxide Building Blocks 495
10.2.2 Vesicle-Like Structures with a Diameter of 90 nm . . 495
10.2.3 Nitride–Phosphate Clathrate 497
10.3 Chemistry on the Nanoscale 498
10.3.1 Nano Test Tubes 498
10.3.2 Dynamics in Water Nanodroplets 499
10.3.3 Targeted Delivery and Reaction of Single Molecules . 500

10.4 Catalysis . . . 502
10.4.1 Au Nanocrystals . . . 502
10.4.2 Pt Nanocatalysts . . . 505
10.4.3 Pd Nanocatalysts . . . 506
10.4.4 MoS_2 Nanocatalysts as Model Catalysts for Hydrodesulfurization (HDS) . . . 507
10.4.5 In Situ Phase Analysis of a Catalyst . . . 509
10.5 Renewable Energy . . . 510
10.6 Solar Energy – Photovoltaics . . . 510
10.6.1 Nitrogen-Doped Nanocrystalline TiO_2 Films Sensitized by CdSe Quantum Dots . . . 511
10.6.2 Polymer-Based Solar Cells . . . 512
10.6.3 Silicon Nanostructures . . . 512
10.7 Solar Energy – Thermal Conversion . . . 514
10.8 Antireflection (AR) Coating . . . 515
10.9 Conversion of Mechanical Energy into Electricity . . . 516
10.10 Hydrogen Storage and Fuel Cells . . . 516
10.11 Lithium Ion Batteries and Supercapacitors . . . 519
10.11.1 Carbon Nanotube Cathodes . . . 519
10.11.2 Tin-Based Anodes . . . 519
10.11.3 $LiFePO_4$ Cathodes . . . 520
10.11.4 Supercapacitors . . . 522
10.12 Environmental Nanotechnology . . . 522
10.13 Summary . . . 524
References . . . 524

11 Biology on the Nanoscale . . . 527
11.1 The Cell – Nanosized Components, Mechanics, and Diseases . 528
11.1.1 Cell Structure . . . 529
11.1.2 Mechanics, Motion, and Deformation of Cells . . . 532
11.1.3 Cell Adhesion . . . 533
11.1.4 Disease-Induced Alterations of the Mechanical Properties of Single Living Cells . . . 534
11.1.5 Control of Cell Functions by the Size of Nanoparticles Alone . . . 536
11.2 Nanoparticles for Bioanalysis . . . 537
11.2.1 Various Materials of Nanoparticles . . . 537
11.2.2 Surface Functionalization of Nanoparticles . . . 540
11.2.3 Examples for Labeling Biosystems by Nanoparticles . 540
11.2.4 In Vivo and Deep Tissue Imaging . . . 543
11.2.5 Nanoparticle-DNA Interaction . . . 546
11.2.6 Nanoparticle-Protein Interaction . . . 552
11.2.7 Biodistribution of Nanoparticles . . . 556
11.3 Nanomechanics of DNA, Proteins, and Cells . . . 557
11.3.1 DNA Elasticity . . . 557

11.3.2 From Elasticity to Enzymology . . . 557
11.3.3 Unzipping of DNA . . . 559
11.3.4 Protein Mechanics . . . 560
11.4 Molecular Motors and Machines . . . 563
11.4.1 Myosin . . . 564
11.4.2 Kinesin . . . 567
11.4.3 Motor–Cargo Linkage and Regulation . . . 568
11.4.4 Diseases . . . 569
11.4.5 ATP Synthase (ATPase) . . . 569
11.5 Membrane Channels . . . 571
11.5.1 The K^+ Channel . . . 571
11.5.2 The Ca^{2+} Channel . . . 573
11.5.3 The Chloride (Cl^-) Channel . . . 575
11.5.4 The Aquaporin Water Channel . . . 575
11.5.5 Protein Channels . . . 576
11.5.6 Pentameric Ligand-Gated Ion Channels . . . 579
11.5.7 Nuclear Pores . . . 579
11.6 Biomimetics . . . 580
11.6.1 Energy Conversion . . . 580
11.6.2 Sensing . . . 582
11.6.3 Signaling . . . 583
11.6.4 Molecular Motors . . . 583
11.6.5 Materials . . . 585
11.6.6 Artificial Cells – Prospects for Biotechnology . . . 590
11.7 Bone and Teeth . . . 593
11.7.1 Bone . . . 594
11.7.2 Tooth Structure and Restoration . . . 596
11.8 Photonic Bionanostructures – Colors of Butterflies and Beetles . . . 597
11.8.1 Structures . . . 598
11.8.2 Formation Processes of Photonic Bionanostructures . . . 601
11.9 Lotus Leaf Effect – Hydrophobicity and Self-Cleaning . . . 601
11.10 Food Nanostructures . . . 604
11.11 Cosmetics . . . 605
11.11.1 Skin Care . . . 606
11.11.2 Encapsulating a Fragrance in Nanocapsules . . . 608
11.11.3 PbS Nanocrystals in Ancient Hair Dyeing . . . 609
11.12 Summary . . . 610
References . . . 610

12 Nanomedicine . . . 615
12.1 Introduction . . . 615
12.2 Diagnostic Imaging and Molecular Detection Techniques . . . 618
12.2.1 Magnetic Resonance Imaging (MRI) . . . 618
12.2.2 CT Contrast Enhancement . . . 630

12.2.3 Contrast-Enhanced Ultrasound Techniques 632
12.2.4 Positron Emission Tomography (PET) 635
12.2.5 Raman Spectroscopy Imaging 637
12.2.6 Photoacoustic Tomography 637
12.2.7 Biomolecular Detection for Medical Diagnostics . . . 637
12.3 Nanoarrays and Nanofluidics for Diagnosis and Therapy . . . 650
12.3.1 Lab-on-a-Chip 651
12.3.2 Microarrays and Nanoarrays 652
12.3.3 Microfluidics and Nanofluidics 653
12.3.4 Integration of Nanodevices in Medical Diagnostics . . 656
12.3.5 Implanted Chips 656
12.4 Targeted Drug Delivery by Nanoparticles 658
12.4.1 Porous Silica Nanoparticles for Targeting Cancer Cells 659
12.4.2 Gene Therapy and Drug Delivery for Cancer Treatment 662
12.4.3 Liposomes and Micelles as Nanocarriers for Diagnosis and Drug Delivery 667
12.4.4 Drug Delivery by Magnetic Nanoparticles 670
12.4.5 Nanoshells for Thermal Drug Delivery 672
12.4.6 Photodynamic Therapy 672
12.5 Brain Cancer Diagnosis and Therapy with Nanoplatforms . . . 672
12.5.1 General Comments 674
12.5.2 MRI Contrast Enhancement with Magnetic Nanoparticles 674
12.5.3 Nanoparticles for Chemotherapy 675
12.5.4 Targeted Multifunctional Polyacrylamide (PAA) Nanoparticles for Photodynamic Therapy (PDT) and Magnetic Resonance Imaging (MRI) 676
12.6 Hyperthermia Treatment of Tumors by Using Targeted Nanoparticles 678
12.6.1 Alternating Magnetic Fields for Heating Magnetic Nanoparticles 679
12.6.2 Radiofrequency Heating of Carbon Nanotubes 682
12.6.3 Light-Induced Heating of Nanoshells 684
12.7 Nanoplatforms in Other Diseases and Medical Fields 686
12.7.1 Heart Diseases 686
12.7.2 Diabetes 688
12.7.3 Lung Therapy – Targeted Delivery of Magnetic Nanoparticles and Drug Delivery 689
12.7.4 Alzheimer's Disease (AD) 691
12.7.5 Ophthalmology 696
12.7.6 Viral and Bacterial Diseases 701

12.8 Nanobiomaterials for Artificial Tissues 704
12.8.1 Enhancement of Osteoblast Function by Carbon Nanotubes on Titanium Implants 705
12.8.2 Nanostructured Bioceramics for Bone Restoration . . 706
12.8.3 Fibrous Nanobiomaterials as Bone Tissue Engineering Scaffolds 707
12.8.4 Tissue Engineering of Skin 708
12.8.5 Angiogenesis 708
12.8.6 Promoting Neuron Adhesion and Growth 708
12.8.7 Spinal Cord In Vitro Surrogate 710
12.8.8 Efforts for Synthesizing Chromosomes 712
12.9 Nanosurgery – Present Efforts and Future Prospects 712
12.9.1 Femtosecond Laser Surgery 712
12.9.2 Sentinel Lymph Node Surgery Making Use of Quantum Dots 713
12.9.3 Progress Toward Nanoneurosurgery 713
12.9.4 Future Directions in Neurosurgery 714
12.10 Nanodentistry 717
12.10.1 Nanocomposites in Dental Restoration 718
12.10.2 Nanoleakage of Adhesive Interfaces 719
12.10.3 Nanostructured Bioceramics for Maxillofacial Applications 720
12.10.4 Release of Ca–PO_4 from Nanocomposites for Remineralization of Tooth Lesions and Inhibition of Caries 721
12.10.5 Growing Replacement Bioteeth 722
12.11 Risk Assessment Strategies and Toxicity Considerations 723
12.11.1 Risk Assessment and Biohazard Detection 724
12.11.2 Cytotoxicity Studies on Carbon, Metal, Metal Oxide, and Semiconductor-Based Nanoparticles . . . 725
12.12 Summary 728
References 728

Name Index 737

Subject Index 753

Chapter 1
Introduction and Some Physical Principles

1.1 Introduction

Nanoscience, a field of science which has emerged during the last three decades, nowadays comprises many different [1.1] fields and starts to play an important role as key technology in application and business.

The term *nano*, derived from the Greek word *nanos* which means dwarf, designates a billionth fraction of a unit, e.g., of a meter. Thus the science of nanostructures is often defined as dealing with objects on a size scale of 1–100 nm.

Nanostructures may be compared [1.2] to a human hair which is ∼50,000 nm thick whereas the diameters of nanostructures are ∼0.3 nm for a water molecule, 1.2 nm for a single-wall carbon nanotube, and 20 nm for a small transistor. DNA molecules are 2.5 nm wide, proteins about 10 nm, and an ATPase biochemical motor about 10 nm. This is the ultimate manufacturing length scale at present with building blocks of atoms, molecules, and supramolecules as well as integration along several length scales. In addition, living systems work at the nanoscale.

The investigation of nanostructures and the development of nanoscience started around 1980 when the scanning tunneling microscope (STM) was invented [1.3] and the concept of nanostructured solids was suggested [1.4]. More than 20 years earlier R. Feynman had emphasized that "... there is plenty of room at the bottom ... in the science of ultra-small structures" [1.5] (see Fig. 1.1).

Clearly, nanostructures were available much earlier. Albert Einstein calculated in his doctoral dissertation from the experimental diffusion data of sugar in water the size of a single sugar molecule to about 1 nm (see [1.7]). Michael Faraday remarked during a lecture on the optical properties of gold in 1857 that "... a mere variation in the size of the (nano) particles gave rise to a variety of resultant colors" [1.8]. In fact, nanostructures already existed in the early solar nebula or in the presolar dust (4.5 billion years ago) as deduced from the detection of nanosized C_{60} molecules in the Allende meteorite [1.9].

From its early infancy the field of nanoscience has more and more grown up (see Fig. 1.2) and enjoys worldwide scientific popularity and importance. For the characterization of this research field the notations "Nanostructured Science" or "Nanotechnology" were coined by K.E. Drexler [1.11].

H.-E. Schaefer, *Nanoscience*, DOI 10.1007/978-3-642-10559-3_1,

Fig. 1.1 R. Feynman in a 1974 photograph. (Reprinted with permission from [1.6]. © 2010 agentur-focus)

Fig. 1.2 Small things are absolutely fascinating. (Reprinted with permission from [1.10]. © 1999 Gerhard Glück)

A huge variety of approaches are available for synthesizing nanostructures (see Chap. 3). In the *top-down* techniques bulk material is chiseled out of or added to surfaces. Microchips or better nanochips with line widths of about 30 nm at present are the most notable examples. In contrast, *bottom-up* manufacturers use self-assembly processes [1.12] to put together larger structures – atoms or molecules or clusters of many atoms – that make ordered arrangements spontaneously.

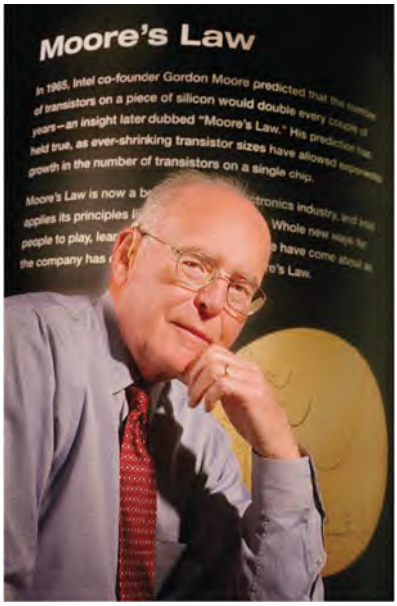

Fig. 1.3 Gordon Moore postulated in 1965 [1.13, 1.14] that the computer power will double every 18–24 months. This prediction is still valid nowadays. (© Courtesy Intel Corp)

Novel properties are inherent to nanosized systems due to a reduction in dimensionality, or when the size of nanoparticles decreases below intrinsic length scales as the Fermi wavelength of electrons, the ferromagnetic exchange length, etc. In addition, when the particle size decreases, the volume fraction of atoms at surfaces or in interfaces increases. This gives rise to a modification of the thermal, electronic, optical, magnetic properties, etc., of nanostructured materials compared to their coarse-grained counterparts and strongly affects materials research in general.

Nanoscience will be central to the next epoch of the information age. According to Moore's law (see Fig. 1.3, [1.13, 1.14]) the sizes of transistors and data storage components will exponentially shrink by a factor of 2 approximately every 18 months and within the next 10 years the top-down processes for miniaturization of electronic components to the nanoscale (see Sect. 9.1) will presumably approach physical limits. From the top ten advances in materials science [1.15] at least five are directly related to nanoscience. Some people think that nanoscience is likely to revolutionize many areas of human activity, such as materials science, information processing, biotechnology, and medicine [1.16].

In chemistry nanotechnology tools such as scanning tunneling microscopy (STM) enable the study and manipulation of chemical reactions on the atomic scale, nanocatalytical processes can be initiated, and the bottom-up synthesis of organic as well as inorganic supramolecular structures for, e.g., molecular devices is revitalized.

In biological systems nanosized structures play an important role from proteins to deoxyribonucleic acid (DNA) carrying the genetic code, ribonucleic acid (RNA, see Fig. 1.4), or molecular motors. Nanostructures are fundamental for the properties

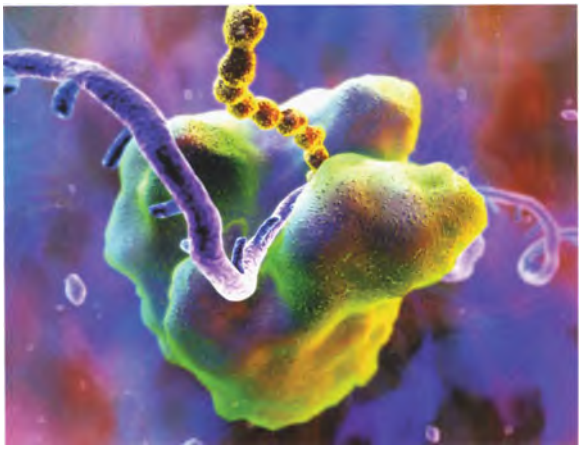

Fig. 1.4 Schematic of a ribosome reading the information from an RNA strand (*violet*) and how to synthesize a protein (*golden*) from amino acid building blocks. (Reprinted with permission from [1.17]. © 2010 agentur-focus)

of bone and teeth. In medical applications nanosized particles will play a role in diagnosis, therapy (Fig. 1.5), and drug delivery.

Food products from milk, cereals, or meat are based on colloidal, i.e., nanoscopic, structures such as gels, emulsions, foams, or combinations thereof. As an example, electron microscopical techniques are employed in order to study liposomes (see Fig. 1.6) as a substantial nanoscopic component of food emulsions.

Much progress in nanotechnology stems from the emergence of high-resolution scanning probe microscopy tools and their many specific variants (see Chap. 2). The rapid development of electron microscopy [1.20] and x-ray microscopy [1.21] also contributes to the exploration of nanotechnologies (see Chap. 2).

From this brief outline it is evident that nanoscience is a most interdisciplinary approach [1.22–1.24] because all disciplines and areas converge at the nanoscale to the same basic principles and the same basic tools so that the frontiers between the disciplines even seem to disappear. It is well recognized that for the exploitation of

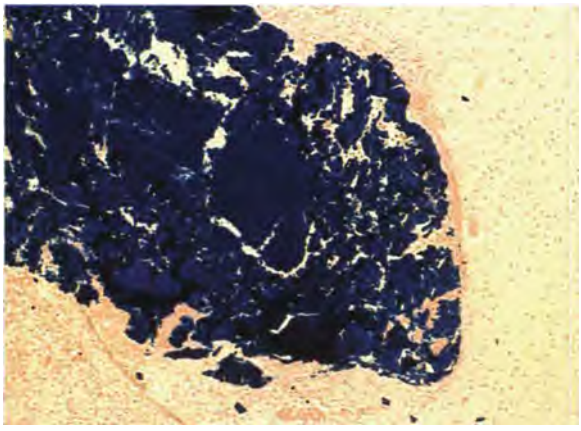

Fig. 1.5 Brain tumor cells (*dark*) decorated by coated magnetite nanoparticles. The tumor is sensitized for therapy by slight heating of the nanoparticles by means of an alternating magnetic field. (Reprinted with permission from [1.18]. © 2008 A. Jordan)

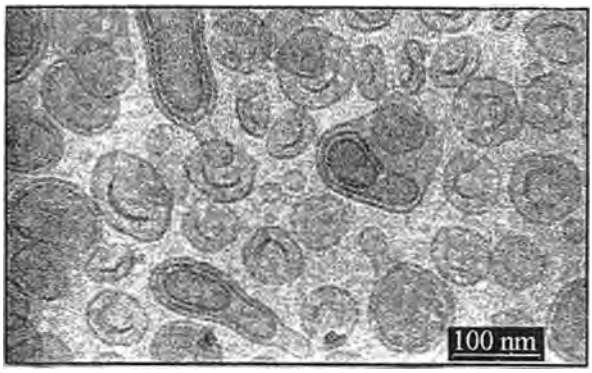

Fig. 1.6 Cryo TEM of liposomes. (Reprinted with permission from [1.19]. © 2000 Materials Research Society)

nanoscience and nanotechnology one must understand the physics and chemistry of the nanoscale and one must learn how to make materials and functional devices [1.25]. This scenario centers to bring together researchers from many disciplines to provide the tools to do nanoscale research, from work to understand the economical and societal benefits and perils of this new field of development, and finally from workforce, education, and training.

A large number of nanoscience research centers [1.26] and nanoscience competence centers have been established worldwide. Many universities in Europe now offer master courses in nanotechnology [1.27]. Some of the world's largest universities undergo dramatic departmental restructuring to foster interdisciplinary and nanoscience research [1.28].

The role of nanotechnology in industry is rapidly growing. Over 600 products in the consumer market alone use nanomaterials with a further 1500 patented [1.29]. Nanotechnology is found in applications as diverse as self-cleaning windows, high-performance paints, anti-aging products, and sunscreen (see Sect. 11.11). Nanofilled resins are used to manufacture large-scale composite panels for production cars (see Sect. 6.9). Other products include a scratch-resistant topcoat used on car bodies, as well as coatings for alloy wheels and polycarbonate headlight covers. Resin-filled carbon nanotubes (CNTs) have been used in high-performance composites in rackets, baseball bats, and ice hockey sticks [1.29]. Energy storage is an area of great activity where the high surface area of nanomaterials provides an instant benefit with a stream of new materials being developed for high charge rate batteries (see Sect. 10.11) and supercapacitors, and solid-state hydrogen storage. Also of interest is the generation of hydrogen by photocatalysis of water and the development of improved membranes for fuel cells [1.29]. Nanotechnology solutions are also to meet environmental challenges such as water purification and remediation, air purification, and clean processing [1.29].

In 2006, an estimated US $50 billion in products worldwide incorporated nanotechnology. This figure has been projected by some to reach US $1–2.6 trillion

until 2011–2016 [1.30, 1.31]. About 10 million nano-related jobs are expected to be created until 2014 [1.32]. It is projected that the production of nanoparticles will increase from the estimated 2,300 tons today to 58,000 tons by 2020 [1.33].

By the visions of Eric Drexler [1.11] (Fig. 1.7), who brought the term nanotechnology into vogue, a discussion about the risks and benefits of this development was initiated. Drexler envisioned an era in which factory production lines are replaced by self-replicating nanoscale assemblers which fabricate nanoscale medical devices (Fig. 1.8), computers, etc., from atoms and molecules.

The Drexlarian visions of nanotechnology gave rise to morose concern of Bill Joy [1.35], the chief scientist of Sun Microsystems, who worried about the implications of intelligent nanorobots that could multiply uncontrollably and that one should consider a moratorium for nanotechnology. This has been criticized because of the enormous difficulties to create robots at the nanoscale [1.7, 1.36], because

Fig. 1.7 The nanovisionary K.E. Drexler propagates the idea of molecular machinery. The atomic structure of such a machine is shown in the background. (Reprinted with permission from [1.34]. © 2010 agentur-focus)

Fig. 1.8 A medical nanorobot (*top left*) swims in a blood vessel and repairs a vessel closure by cutting the deposits. This tiny submarine is hardly larger than the disk-like erythrocytes. Future applications of this type of devices are expected by K.E. Drexler. (Reprinted with permission from [1.34]. © 2010 agentur-focus)

of incompatibilities with the laws of thermodynamics [1.37], because it belongs squarely in the realm of science fiction [1.38], or because this concern is rejected as Frankenstein nonsense on the nanoscale [1.39].

Others recommend a sober and unemotional assessment and searches for ways out of perceptible or suspected risks [1.40] or anticipate that the concerns about malevolent nanoassemblers will be replaced by excitement over the field's scientific and economic potentials [1.41].

Many scientists think that nanotechnology will eventually affect how people work, what they eat, how they communicate, and how long they live. It will change their medical care, energy sources, water, and environment [1.42]. Therefore, evaluating the risks and benefits of nanotechnology, the health and environment impact of nanotech products should be considered over their full life cycle, including the development, manufacture, transport, and disposal. Appropriate internationally applied regulations should be developed to mitigate risks without stifling innovation [1.43]. Considering the interplay with other emerging technologies, new global oversight mechanisms may be required that can handle the complex convergence of nanotechnology, biotechnology, and information and cognitive science [1.42].

In the following, some physical principles of nanoscience will be discussed within this chapter, including thermal and electronic properties of nanostructures, giant magnetoresistance (GMR) and spintronics, self-assembly, Casimir forces, and nanoscale measuring techniques. In the subsequent sections, the wider fields of microscopy, synthesis of nanostructures, nanocrystals–nanowires–nanolayers, carbon nanostructures, bulk nanomaterials, nanomechanics–nanophotonics–nanofluidics, nanomagnetism, nanotechnology for computers–memories–hard disks, nanochemistry, biology on the nanoscale, and nanomedicine will be presented.

1.2 Thermal Properties of Nanostructures

1.2.1 Violation of the Second Law of Thermodynamics for Small Systems and Short Timescales

The second law of thermodynamics states that for large systems and over long times the entropy production rate is necessarily positive. However, the fluctuation theorem predicts [1.44] measurable violations of the second law for small systems over short timescales. This has been shown experimentally by following the trajectory of a colloidal particle in an optical trap. An optical trap is formed when the micron-sized particle with a refraction index higher than that of the surrounding medium is located within a focused laser beam; the refracted rays eventually exert a force on the particle which can be resolved to 2×10^{-15} N. From observing the particle's position and the optical forces acting on the particle, the entropy production rate Σ can be determined [1.45]. It turns out that entropy consuming, i.e., second-law-defying events, can be discerned for micron-sized particles on the timescales of

seconds. This is particularly important to applications of nanomachines and molecular motors. As these nanomachines become smaller, the probability that they will run thermodynamically in reverse inescapably increases [1.45].

1.2.2 Surface Energy

The surface energy of nanoparticles has been measured to be higher than that of bulk solids. This is essential for processes such as melting and evaporation. This effect depends on whether the particles are free or deposited on a substrate (see Table 1.1; Fig. 1.9).

The surface energy γ can, e.g., be determined according to the Kelvin equation

$$p_s/p_{s_0} = \exp[4\gamma M/(\rho_p R T_{on} d_M)]$$

by measuring the onset temperature T_{on} of evaporation in dependence of the particle size d_M (see Fig. 1.9) where M is the molecular weight, ρ_p the particle mass density, R the gas constant, p_s the vapor pressure of the nanoparticle, and p_{s_0} the vapor pressure of a plane surface. The increase of γ with decreasing d_M, which is supported

Table 1.1 Surface energies of nanoparticles

	Surface energy γ(J/m^2)			
Material	Free nanoparticle	Particle on substrate	Bulk	Reference
Ag	7.2		1.0–1.5	[1.46]
Pd		6.0	1.8	[1.47]
CdS	2.5	1.7	0.75	[1.48]
		1.13	0.75	[1.49]
Ar	0.042		0.23	[1.50]

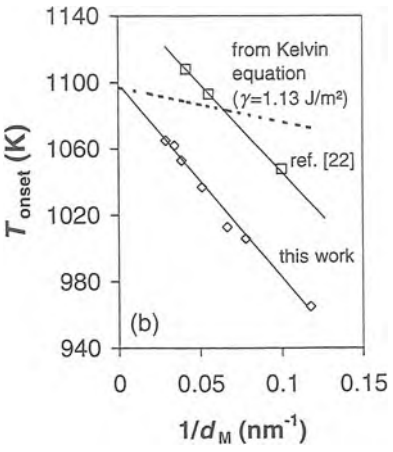

Fig. 1.9 Onset temperature T_{on} of the evaporation from Ag nanoparticles in dependence of the particle size d_M. (Reprinted with permission from [1.46]. © 2003 American Physical Society)

by molecular dynamics studies [1.50] and which is attributed to a weak dilatation of the nanoparticle surface, is discussed in a simple model in terms of a net increase of the inward cohesive force which is reduced in a particle on a substrate or in a matrix giving rise to a reduction of γ (see Table 1.1).

1.2.3 Thermal Conductance

In nanosystems the classical picture of a diffusive heat flow mechanism is often not applicable because the phonons or electrons that carry heat have mean free paths similar to or larger than the nanoscale feature size. This is a challenge for heat removal in microelectronic devices which already involve features with sizes of the order of the mean free path.

The thermal conductance $\kappa(V_g)$ of electrons in a semiconductor quantum wire at low temperatures shows a quantized behavior in dependence of a gate voltage V_g (Fig. 1.10). This originates from the plateaus in the electrical conductance $G(V_g)$ quantized in units of $G_O = 2e^2/h$ [1.51]. In the case that charge and energy are transported by electrons the Wiedemann–Franz relation

$$\kappa/GT = \pi^2 k_B^2/3e^2 = L_o$$

applies with L_O the Lorenz number. From this relation it is expected that the electrical conductance plateaus in units of G_O are matched by a thermal conductance

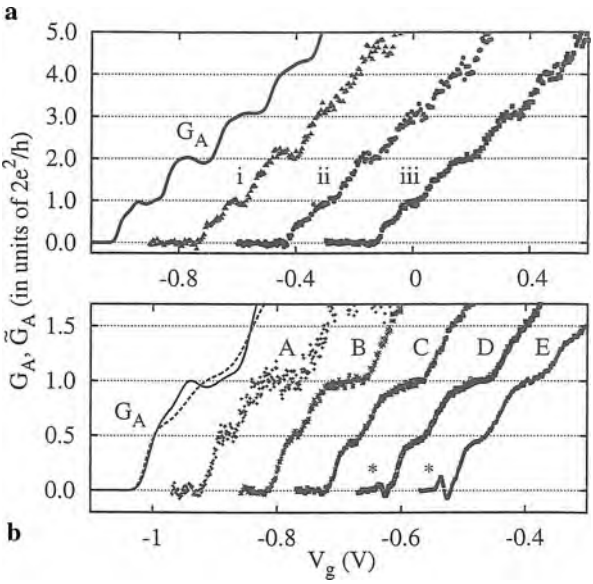

Fig. 1.10 (**a**) Quantized step-like behavior of the thermal conductance $\tilde{G}_A(i, ii, iii)$ and of the electrical conductance G_A of a semiconductor quantum wire at 0.27 K obeying the Wiedemann–Franz relation. (**b**) Close-up of (a) with a half plateau $\kappa = L_O T(G_O/2)$ for $G < G_O$. (Reprinted with permission from [1.51]. © 2006 American Physical Society)

quantized in units of $L_O T G_O = \pi^2 k_B^2 2T/3h = \left(1.89 \cdot 10^{-12} W/k^2\right) T$. This is in agreement with the data in Fig. 1.10 for $G > G_O$.

The temperature dependence of the phonon thermal conductivity $K(T)$ has been measured for individual multiwalled carbon nanotubes (MWNTs) [1.52] with a high value of over 3000 W/K m at room temperature (Fig. 1.11) in the range of theoretical expectations of 3000–6000 W/K m [1.53] or of diamond or graphite (2000 W/K m [1.54])

In a simple model the phonon thermal conductivity $\kappa = \sum_p c_p v_p l_p$ is given by the specific heat c_p, the group velocity v_p, and the mean free path l_p of the phonon mode p. The phonon mean free path consists of two contributions: $l^{-1} = l_{st}^{-1} + l_{um}^{-1}$ where l_{st} and l_{um} are the static and umklapp scattering lengths, respectively. At low temperatures, the umklapp freezes out, $l = l_{st}$, and therefore the κ of the MWNT follows the temperature dependence of c_p with $k \propto T^{2.5}$ similar to that of 3D graphite [1.55] and which therefore indicates the 3D features of MWNTs.

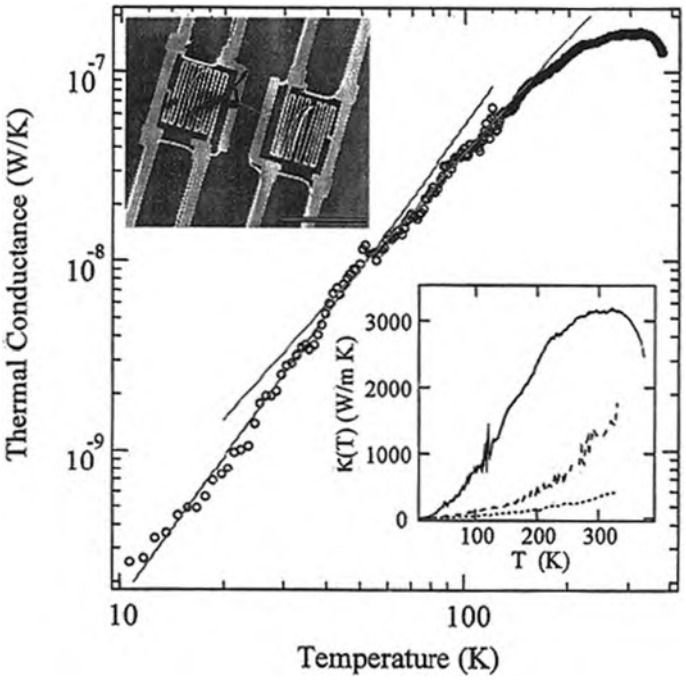

Fig. 1.11 The thermal conductance of an individual multiwalled carbon nanotube (MWNT) of a diameter of 14 nm. The *solid lines* represent linear fits of the data in a logarithmic scale at different temperatures with the slopes 2.50 and 2.01. *Lower inset*: the *solid line* represents κ(T) of an individual MWNT ($d = 14$ nm). *Broken* and *dotted lines* represent small ($d = 80$ nm) and large bundles ($d = 200$ nm) of MWNTs, respectively. *Upper inset*: SEM image of suspended islands with an individual MWNT. Scale bar: 10 μm. (Reprinted with permission from [1.52]. © 2001 American Physical Society)

For 50 K < T < 150 K, a $\kappa \propto T^2$ behavior is found (Fig. 1.11) and at higher temperatures κ decreases due to the onset of phonon umklapp processes and a rapidly decreasing l_{um}. From the peak value of $\kappa(T)$ where $l_{\mathrm{st}} \sim l_{\mathrm{um}}$ a T-independent value $l_{\mathrm{st}} \sim 500$ nm for MWNTs can be estimated. This means that below room temperature phonon transport in the 2.5 μm long MWNT is nearly ballistic with only a few scattering events. The ratio of the thermal conductances $\kappa_{\mathrm{el}}/\kappa_{\mathrm{phon}}$ of electrons and phonons increases rapidly when the temperature is lowered [1.56].

The thermoelectric power of MWNTs [1.52] is found to be linearly increasing with T which indicates a hole-like major carrier.

What happens, however, to the thermal conductivity of systems that are effectively one dimensional, such as a single-wall carbon nanotube (SWNT), a nanowire, or a DNA molecule [1.57, 1.58]? By analytical calculations it is estimated that the thermal conductivity diverges with a one-third power law as the length of a 1D system increases. This would be a very promising feature to use in the application of SWNTs, such as the design of components that dissipate heat efficiently in nanocircuits.

It should be mentioned here that for the investigation of heat conductivity in confined dimensions extremely sensitive calorimeters are developed [1.59] with a low-temperature heat capacity of $c \approx 10^3 k_{\mathrm{B}}$ [1.59]. This may lead to an energy sensitivity sufficient to count individual thermal phonons at 10–100 mK and observe the particle nature of phonons [1.59].

1.2.4 Melting of Nanoparticles

According to simple theories for spherical nanoparticles the bulk melting temperature T_{b} is decreased in terms of the Gibbs–Thompson equation by

$$\Delta T_{\mathrm{m}} = 4\gamma v_0 T_{\mathrm{b}}/Ld$$

with d the particle diameter, γ the surface energy of the solid, L the latent heat of fusion, and v_0 the molar volume of the solid [1.60]. This qualitatively applies to nanoparticles embedded in matrices or deposited on substrates (see Table 1.2 and Fig. 1.12). However, the melting behavior of embedded particles may be strongly affected by the characteristics of the embedding material.

For free Na clusters, T_{m} is found to be lower than the bulk T_{b} (see Table 1.2) but roughly independent of cluster size (Fig. 1.13).

For free Ga clusters and free Sn clusters an increase of T_{m} compared to the bulk materials is observed (see Table 1.2) which is attributed to more covalent bonding in the cluster in contrast to covalent-metallic bonding of the bulk material [1.61].

The latent heat of fusion (0.012 eV/atom) as well as the entropy of fusion (0.5 k_{B}) of Na clusters is lower than the bulk values (0.025 eV/atom; 0.85 k_{B}) [1.62]. The evaporation of atoms from nanoparticles is facilitated when the particle size

Table 1.2 Melting temperatures T_m of free nanoparticles, of particles in matrices or on substrates, and of the bulk materials

	T_m (K)			
Material, size	Free	In matrix, on substrate	Bulk	References
Na, 2–3 nm	230–290		371	[1.62]
Ga, 1.2 nm	550		303	[1.64]
Sn, 1.0 nm	555		505	[1.65]
Sn, 5.0 nm		410	505	[1.66]
In, 5.0 nm		418	430	[1.67]
In, 5.0 nm		383	430	[1.68]
Hg, 7 nm		∼190	234	[1.60]
Hg, 7 nm		∼200	234	[1.69]
Au, 5 nm		1100	1338	[1.70]
H_2O, 4 nm		262	273	[1.71]

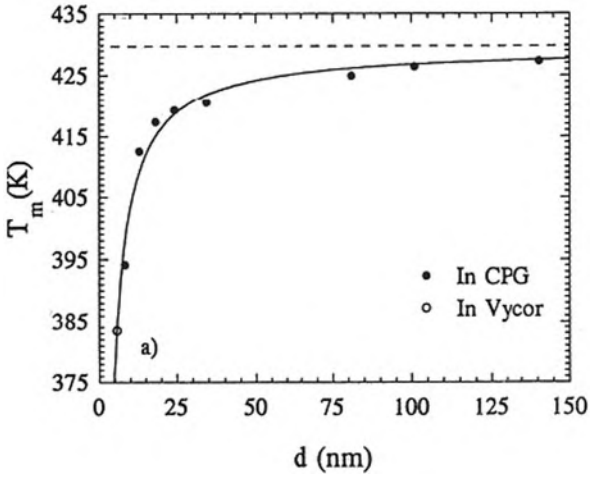

Fig. 1.12 Melting temperatures of In particles in CPG glass or Vycor glass matrices as a function of particle size *d*. (Reprinted with permission from [1.68]. © 1993 American Physical Society)

decreases. This is concluded from the observation that the temperature at which free PbS nanoparticles start to evaporate decreases with decreasing particle size [1.63].

1.2.5 Lattice Parameter

The lattice parameter of Pd nanoparticles in a polymer matrix decreases by about 3% when the particle size decreases from 10 to 1.4 nm [1.72]. A similar behavior is observed for Ag nanoparticles [1.73].

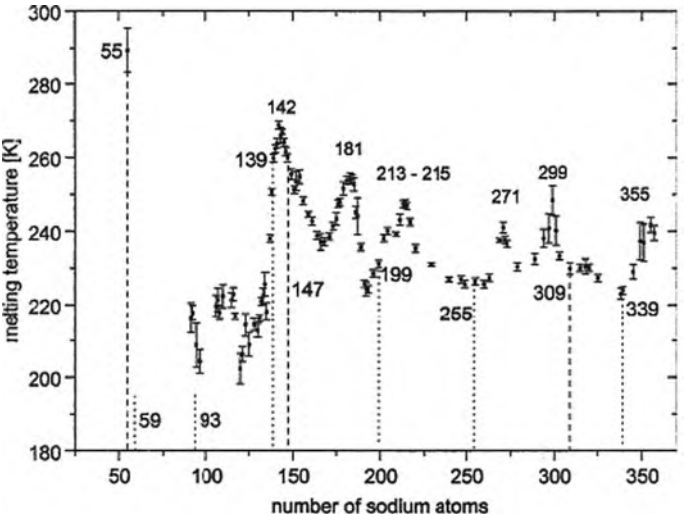

Fig. 1.13 Melting temperatures of Na^+ clusters versus the cluster size. The oscillations do not correlate with electronic (*dotted lines*) or geometric (*dashed lines*) shell closings. The smallest cluster Na_{55}^+ which has an icosahedral structure exhibits the highest melting temperature $T_m = 290$ K where the bulk melting temperature is 371 K. (Reprinted with permission from [1.62]. © 2002 Elsevier)

1.2.6 Phase Transitions

Phase transitions in confined systems differ, as shown in the case of the melting transition above, from those of bulk materials and strongly depend on particle size, wetting, as well as the interaction of a nanoscale system with a matrix or a substrate [1.60]. Phase transitions in nanosized systems have been investigated for superfluidity where the critical behavior of superfluid He in an aerogel deviates from that of bulk He [1.74]. In superconductivity the superconducting transition temperatures of Ga [1.75] or In nanoparticles [1.76] in vycor glass are shifted to values higher than in the bulk materials. The Curie temperature T_C of ferromagnetic nanolayers decreases with decreasing layer thickness [1.77]. Liquefaction [1.78] in nanopores or order–disorder phase transitions near surfaces [1.79] was also found to differ from that of bulk systems. Two examples of solid–solid phase transitions on the nanoscale will be sketched in the following.

Under elevated pressures PbS undergoes a B1-to-orthorhombic structural phase transition. For PbS nanoparticles in a NaCl matrix, the transition is shifted to higher pressures when the particle size is reduced [1.80].

The stability of crystal structures at ambient conditions depends on the size of ZrO_2 nanocrystals which exhibit a tetragonal structure for small sizes and the bulk orthorhombic structure for larger sizes [1.81, 1.82]. In this oxide, the lattice strain varies with the grain sizes giving rise to a variation of the Landau free energy so that for small grain sizes the tetragonal phase is stabilized whereas for grain sizes $d > 54$ nm the bulk orthorhombic phase appears.

1.3 Electronic Properties

1.3.1 Electron States in Dependence of Size and Dimensionality

Standard quantum mechanical texts show (see [1.83]) that for an electron in an infinitely deep square potential well of width a in one dimension, the coordinate x has the range values $-\frac{1}{2}a \leq x \leq \frac{1}{2}a$ inside the well, and the energies are given by

$$E_n = \frac{\pi^2\hbar^2}{2ma^2}n^2 = E_0 n^2$$

where $E_0 = \pi^2\hbar^2/2ma^2$ is the ground-state energy and the quantum number n assumes the values $n = 1, 2, 3, \ldots$ This shows that, when the free electrons in a solid are confined to particle sizes smaller the Fermi wavelength (quantum confinement), the electron energy shifts to higher values (blue shift) with shrinking size a of the well which is of importance for many electronic or optical properties of nanostructures.

In addition to quantum confinement effects, quantization effects appear in nanoparticles because the charge of the electron is quantized in units of e [1.84, 1.85]. When the electron with the quantized charge tunnels to an island with the capacitance C (see Fig. 1.14a) the electrostatic potential of the island changes by discrete values of the charging energy $E_c = e^2/C$. This can be detected at low temperatures when the energies fluctuations

$$k_B T << e^2/C$$

are small, and when the resistance R_t of the tunneling barriers is sufficiently high. From the charging time $\Delta t = R_t \cdot C$ of the island and the Heisenberg uncertainty principle $\Delta E \cdot \Delta t = (e^2/C)R_t C > h$ it can be estimated that

$$R_t >> h/e^2$$

should be much higher than the resistance quantum $h/e^2 = 25.813\text{k}\Omega$.

These conditions can be met by small dots with low C values and weak tunneling coupling. For a quantum dot sphere with a 1 μm diameter the value $E_c \cong 3\,\text{meV}$ is found [1.84] which can be easily resolved at low temperatures. If a voltage V_g is applied to the gate capacitor c_g (Fig. 1.14a) a charge is induced on the island which leads to the so-called *Coulomb oscillations* of the source-drain conductance as a function of V_g at a fixed source-drain voltage V_{sd} (Fig. 1.14b). In the valleys between the oscillations, the number of electrons on the dots is fixed to the integer N with zero conductance (*Coulomb blockade*). Between the two stable configurations N and N+1 a "charge degeneracy" (see Fig. 1.14b) appears where the number of electrons can alternate between N an N+1. This produces a current flow and results in the observed current peaks.

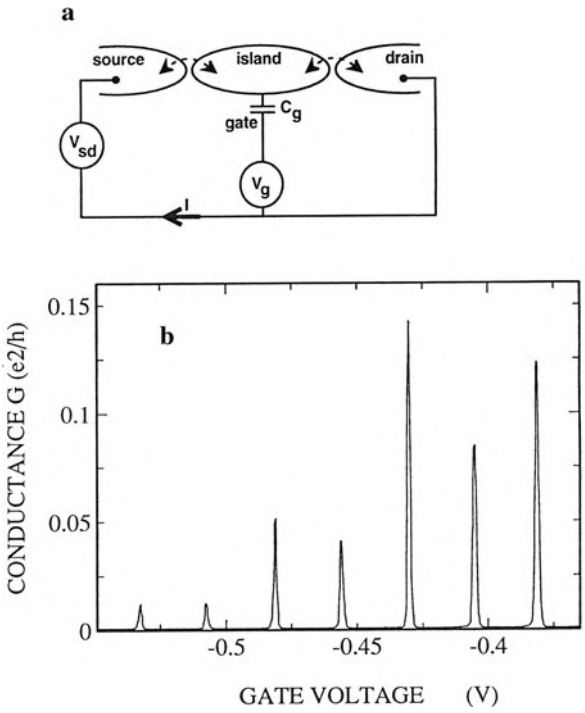

Fig. 1.14 (**a**) Schematics of a quantum dot (island) connected to three terminals: source, drain, and gate. The terminals and the island are separated by thin insulating layers. (**b**) Coulomb oscillations for illustrating the effect of single electronic charges on the macroscopic conductance I/V_{sd}. The period in the gate voltage is about e/C_g. (Reprinted with permission from [1.84]. © 1999 Springer Verlag)

An alternative measurement with fixed gate voltage V_g and varying source-drain voltage shows nonlinear current–voltage characteristics exhibiting a *Coulomb staircase* (see Fig. 1.15). A new current step occurs at a threshold voltage e^2/C at which an extra electron is energetically allowed to enter the island. This threshold voltage is periodic in the gate voltage (see Fig. 1.15) in accordance with the Coulomb oscillations of Fig. 1.14(b).

Quantum confinement with spacing ΔE between the energy levels and effects of charge quantization can be observed simultaneously. Electrons in a semiconductor hetero-interface quantum dot [1.84] with a diameter of 100 nm yield a level spacing of ~0.03 mV which can be detected at dilution refrigeration temperatures. The change of the gate voltage ΔV_g (see Fig. 1.14a) between current oscillations in a quantum dot is given by

$$\Delta V_g = \frac{C}{eC_g}\left[\Delta E + \frac{e^2}{C}\right]$$

where C_g is the gate capacitance (Fig. 1.14a). By sweeping V_g, a peak structure in the current is observed for $k_B T << \Delta E << e^2/C$ (see Fig. 1.16) where the peak-to-peak distance is ascribed to the addition energy $e^2/C + \Delta E$ and the separation of the minipeaks to the level spacing ΔE.

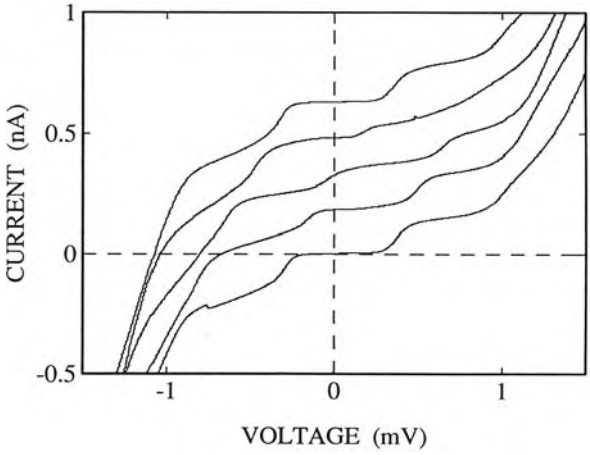

Fig. 1.15 Coulomb staircases in the $I - V_{sd}$ characteristics of a GaAs/AlGaAs hetero-structure. The different curves which are shifted vertically for clarity ($I = 0$ occurs at $V_{sd} = 0$) are taken for five different gate voltages to illustrate the periodicity in accordance with the oscillations in Fig. 1.14(b). (Reprinted with permission from [1.84]. © 1999 Springer Verlag)

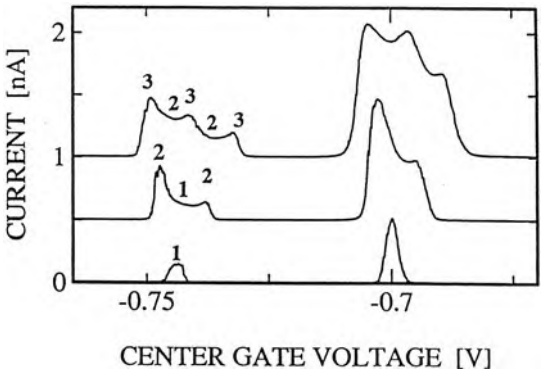

Fig. 1.16 Coulomb peaks at $B = 4T$ measured at different $V_{sd} = 0.1$, 0.4, and 0.7 mV from bottom to top. The peak-to-peak distance corresponds to the addition energy, the distance between the shoulders within a peak to the excitation energy ΔE (level spacing) for a constant number of electrons on a dot. (Reprinted with permission from [1.84]. © 1999 Springer Verlag)

1.3.2 The Electron Density of States D(E)

The electron density of states D(E) depends dramatically on the dimensionality of nanostructures (see Fig. 1.17). Whereas for bulk systems a square-root dependence of energy prevails, a staircase behavior is characteristic for 2D-quantum well structures, spikes are found in 1D quantum wires, and discrete features appear in 0D quantum dots. Since many solid-state properties are dominated by the electron density of states, these properties, such as the electronic specific heat C_{el}, the Pauli conduction electron magnetic susceptibility χ_{el}, the thermopower, the superconducting energy gap, etc., are sensitive to dimensional changes.

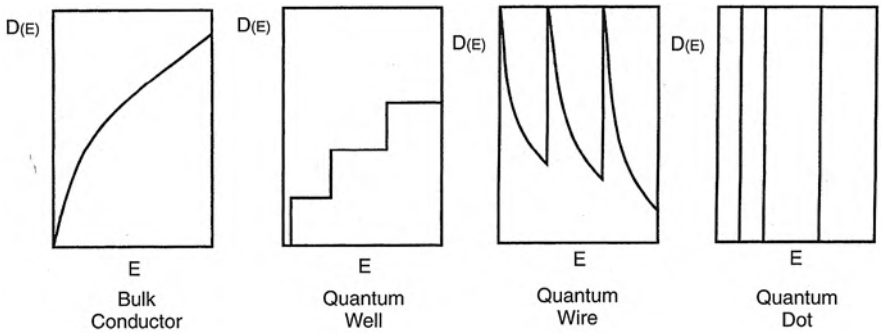

Fig. 1.17 Electron density of states $D(E)$ for conductors in dependence of dimensionality. (Reprinted with permission from [1.83]. © 2003 Wiley Interscience)

1.3.3 Luttinger Liquid Behavior of Electrons in 1D Metals

In 3D metals the conduction electrons are well described by the Fermi liquid theory of non-interacting quasi-particles, owing to the fact that the Pauli exclusion principle strongly quenches the electron–electron interaction (see [1.86]). In contrast to that, the electron system in 1D metals (quantum wires) is strongly affected by electron–electron interaction, essentially because the electrons cannot avoid each other (see [1.87]). These correlated electrons are better described by the Luttinger liquid (LL) theory [1.86, 1.88–1.90]. The correlation gives rise to enhanced backscattering of electrons leading to zero conductance at low temperatures [1.91].

The main consequences of the LL theory are (1) the spin and charge degrees of freedom of electrons are separated, (2) the charge velocity (v_c) is higher than the Fermi velocity (v_F), while the spin velocity is close to v_F, and (3) the density of states is expected to exhibit a power law suppression $N(\omega) \sim |\omega|^{\alpha}$ near the Fermi level [1.92] where $\alpha = \left(2 + g + g^{-1}\right)/8$ with g the Luttinger parameter [1.93]. Efforts have been made to investigate the short-range physics determining the Luttinger liquid by calculating the ground state energy density $\varepsilon(n)$ of 1D wires [1.94].

Several experimental observations of Luttinger liquid behavior have been reported: (1) power laws of the current–voltage and the conductance–temperature characteristics of the edge tunneling in the fractional quantum Hall regime [1.94, 1.95], (2) momentum-resolved electron tunneling between two nanowires [1.96], or (3) power-law dependence of the electronic density of states of carbon nanotubes [1.97] (see Fig. 1.18).

1.3.4 Superconductivity

In superconducting solids the conduction electrons condense at low temperatures into Cooper pairs with the characteristic size given by the coherence length ξ. This macroscopically coherent quantum mechanical state is described by a single wave

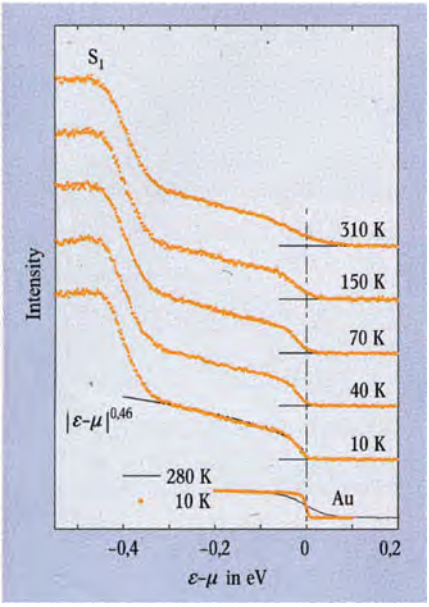

Fig. 1.18 Photo-emission spectra of bulk Au and of carbon nanotube bundles at different temperatures. The Au spectra show at the chemical potential $\varepsilon = \mu$ the Fermi function behavior characteristic for a Fermi liquid in 3D metals. The carbon nanotubes at low temperatures exhibit, however, at energies close to μ a power-law behavior with a 0.46 power as characteristic for a Tomonaga–Luttinger liquid behavior. (Reprinted with permission from [1.97]. © 2004 Wiley-VCH)

function $\psi = |\psi| e^{i\rho}$ where the magnitude $|\psi|$can change on scales larger than ξ and the phase ρ is related to the supercurrent density $j \sim \nabla\rho$.

In a superconducting 1D wire with transverse dimensions $d < \xi$ there is always a finite probability of thermal fluctuations driving instantly a fraction of the wire into a normal state. This process can be described as a thermally activated jump of the system from on local potential minimum into a neighboring one separated by $\pm 2\pi$ in the ρ space (so called phase slip) in analogy to a "classical" jump of a particle over an energy barrier ΔF provoked by the thermal energy $k_B T$. However, taking into account the quantum mechanical nature of the superconducting system an alternative mechanism has been suggested where tunneling through the barrier occurs [1.98, 1.99]. The phase difference between two remote points of the system might change in time due to quantum phase fluctuations. This purely quantum mechanical phenomenon of phase tunneling, also called quantum phase slip (QPS), should provide an additional channel of energy dissipation and increase of the resistance in a current-carrying system [1.100].

Superconductivity in quantum wires depends on whether the normal resistance R_N of the wire is lower (superconducting) or higher (normal conducting) than the quantum resistance $R_q = h/(2e)^2 \approx 6.5/k\Omega$ for Cooper pairs. This has been demonstrated for MoGe quantum wires of diameters of ~15 nm and lengths of ~150 nm [1.101] with a coherence length (size of Cooper pairs) $\xi = 8$ nm, where the normal resistance R_N increases with decreasing diameter so that superconductivity disappears at diameters below 14 nm (see Fig. 1.19). This normal conducting behavior at small diameters is ascribed to quantum phase slip tunneling [1.102]. A non-zero low-temperature resistance has also been observed for an 11 nm diameter wire ($R_N = 9k\Omega$) of Al which is a bulk superconductor [1.100].

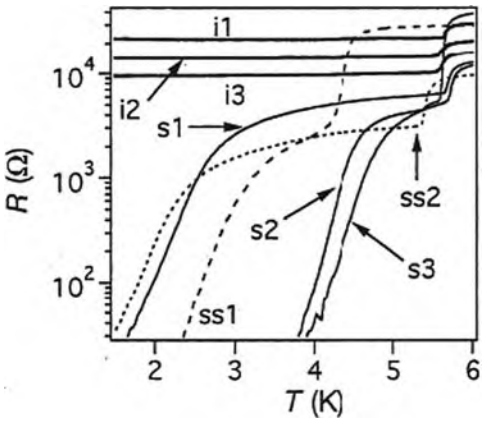

Fig. 1.19 Temperature dependence of the resistance of Mo–Ge quantum wires with the diameters and resistances in brackets: i1 (11 nm, 22.6 kΩ), i2 (11.4 nm, 14.79 kΩ), i3 (13.2 nm, 10.34 kΩ), s1 (18 nm, 6.4 kΩ), s2 (21 nm, 4.5 kΩ), and s3 (16.2 nm, 5.66 kΩ). The thin wires i1–i3 exhibit normal conductance, whereas the wires s1–s3 are superconducting at low temperatures. (Reprinted with permission from [1.101]. © 2000 Nature Publishing Group)

Magnetic hardening of thin films of the soft bulk superconductor Pb, i.e., an increase of the critical current density J_c (see Fig. 1.20a) to high values $J_c = 4 \cdot 10^{10}\mathrm{Am}^{-2}$ is observed when the film thickness is reduced to a few monolayers [1.103]. This is attributed to a strong trapping (trapping energy of ∼0.05 eV) of vortices to the voids in the Pb film (see Fig. 1.20b). The coherence length $\xi_0 = 9.1$ nm of bulk Pb is reduced to 2.3 nm in a 2.6 nm Pb film which is ascribed to a reduction of the electronic mean free path in the films. In addition, the critical temperature T_c decreases with decreasing d (see Fig. 1.20c) which can be understood by a surface energy term included in the Ginzburg–Landau free energy of the superconductor, and superconductivity only disappears for $d \leq 0.43$ nm [1.104]. A complete destabilization of superconducting order is only expected when the system size is so small that the electronic energy level spacing becomes larger than the bulk superconducting energy gap Δ. Thus, the so-called Anderson criterion [1.105] suggests that superconductivity may persist at length scales much below ξ. In Nb the decrease of T_c and of the gap energy Δ with particle size d is ascribed to a change of the electron density of states (DOS) due to discretization of the energy bands [1.106] and not to changes in the electron–phonon coupling as suggested earlier.

1.4 Giant Magnetoresistance (GMR) and Spintronics

Electrons have a charge and a spin, but conventionally charges and spins have been considered separately. In conventional electronics, the charges are manipulated by electric fields but the spins are ignored. Other classical technologies, magnetic recording, for example, are using the spin but only through its macroscopic

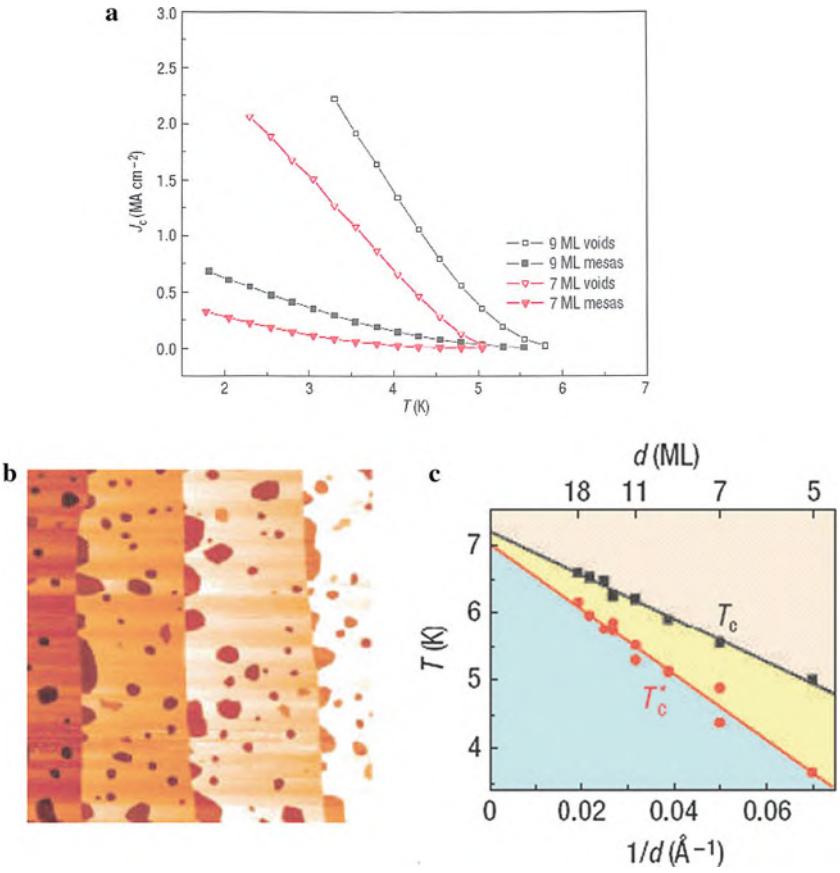

Fig. 1.20 (**a**) Temperature dependence of the critical current density J_c of 7 and 9 monolayer (ML) thick Pb films. *Open symbols* refer to films with nanovoids, *filled symbols* to films with nanoscale mesas. (**b**) Scanning tunneling microscopy (STM) images (700×700 nm^2) of a 9 ML Pb film with nanovoids (dark dots). (**c**) Critical temperatures T_c derived from the onset of magnetic screening and T_c^* from the extra-polated $H_{c2}(T)$ data. For $d \to \infty$, T_c^* extrapolates to a value close to the bulk $T_{co} = 7.2\,K$. (Reprinted with permission from [1.103]. © 2006 Nature Publishing Group)

manifestation, the magnetization of a ferromagnet. This picture started to change when the discovery [1.107, 1.108] of the giant magnetoresistance (GMR) of magnetic multilayers – for which A. Fert and P. Grünberg were awarded the 2007 Nobel prize in physics [1.109, 1.110] – opened the way to an efficient control of the motion of electrons by acting on their spin through the orientation of the magnetization. To employ this spin degree of freedom – i.e., that the spin can assume two different values – for faster switching of electronic components with reduced energy consumption could lead to the next step in electronics and initiate the age of spin electronics or spintronics [1.111–1.114]. The progress toward understanding and

implementing spintronics in metallic multilayers and in semiconductors is gaining momentum and spintronic read head sensors are already impacting a multibillion dollar industry.

To incorporate spins into existing semiconductor technology, one has to resolve technical issues such as efficient spin injection, transport control and manipulation, and detection of spin polarization as well as spin-polarized currents. There are visions that the merging of electronics, photonics, and magnetics will ultimately lead to spin-based multifunctional devices, optical switches operating at terahertz frequencies, or quantum bits (qubits) for quantum computation and communication.

1.4.1 Giant Magnetoresistance (GMR) and Tunneling Magnetoresistance (TMR)

GMR (see [1.109, 1.110]) is a quantum mechanical effect observed in layered magnetic thin film structures that are composed of alternating layers of ferromagnetic and non-magnetic metallic films (Fig. 1.21a). In zero magnetic field the ferromagnetic layers are antialigned (Fig. 1.23a) with maximum spin-dependent scattering of the electrons (maximum resistance, see Fig. 1.22). When in an external magnetic field the ferromagnetic layers are aligned in parallel (Fig. 1.23b), the spin-dependent scattering is minimized (low resistance, Fig. 1.22). For the zero-field antialigned coupling of the two ferromagnetic layers a long-range RKKY-type (Ruderman–Kittel–Kasuya–Yosida) magnetic coupling of electrons is assumed.

A spin valve (Fig. 1.21a) is a GMR-based device with two ferromagnetic layers (e.g., Fe, Ni, Co) separated by a thin non-magnetic conductor layer (e.g., Cu) where one of the ferromagnetic layers is "pinned" to an antiferromagnetic layer, i.e., its magnetization cannot be changed by moderate magnetic fields. The magnetization of the other ferromagnetic layer can be changed easily by a magnetic field giving rise to a resistance change of 5–10% in a relatively small magnetic field. Commercial GMR read heads use the spin-valve format for hard drives and magnetic field sensors.

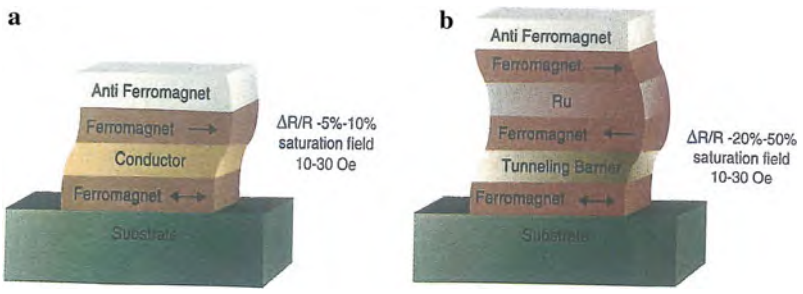

Fig. 1.21 Spin-dependent transport structures. (**a**) Spin valve. (**b**) Magnetic tunneling junction. (Reprinted with permission from [1.112]. © 2001 American Association for the Advancement of Science (AAAS))

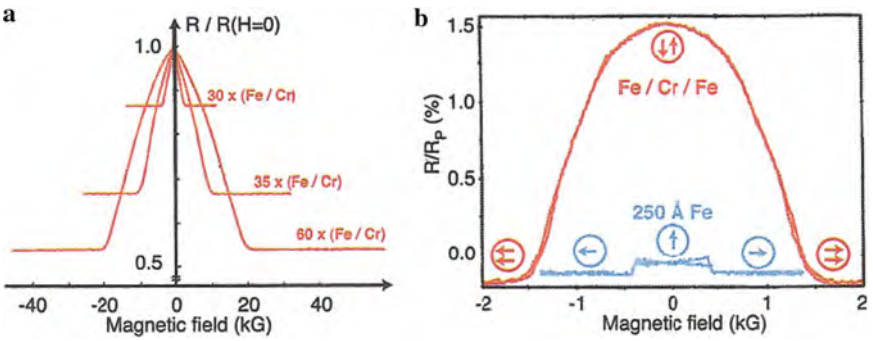

Fig. 1.22 First observations of giant magnetoresistance (GMR) in (**a**) a multilayer [1.107] and (**b**) a double layer [1.108] of Fe interspaced by Cr. In (**b**), the earlier found anisotropic magnetoresistance (AMR) effect of a Fe film is shown for comparison. (Reprinted with permission from [1.110]. © 2008 American Physical Society)

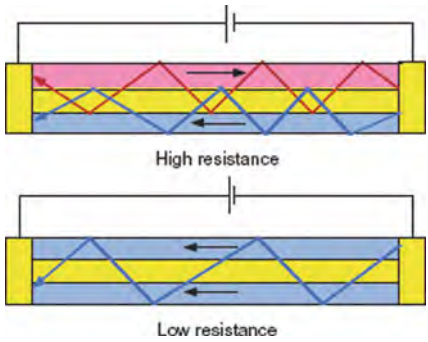

Fig. 1.23 Schematics of electron transport parallel to the plane of a layered metallic structure with ferromagnetic (*arrows*) and non-magnetic layers with aligned (low resistance) and antialigned (high resistance) magnetization. (Reprinted with permission from [1.111]. © 1998 AAAS)

A magnetic tunneling junction (MTJ) is a device (Fig. 1.21b) in which a pinned ferromagnetic layer and a free ferromagnetic layer are separated by a very thin insulating layer (e.g., Al_2O_3, MgO) [1.115, 1.116]. The electron tunneling phenomenon arises from the wave nature of the electrons while the resulting junction electrical conductance is determined by the evanescent state of the electron wave function within the tunneling barrier. The tunneling magnetoresistance (TMR) arises from the difference in the electronic density of states (DOS) at the Fermi level E_F between spin-up $N_\uparrow(E_F)$ and spin-down $N_\downarrow(E_F)$ electrons. Since electrons preserve their spin orientation during the tunneling process, electrons can only tunnel into the subbands of the same spin orientation, thus, in the case of the same spin orientation of the two electrodes, the tunneling conductance is proportional to the product of the Fermi level DOS values of the two electrodes. A change from a parallel magnetization to an antiparallel magnetization of the two electrodes will result in an exchange between the two spin sub-bands of one of the electrodes for the tunneling process with a decrease of the conductance, provided that the Fermi level DOS

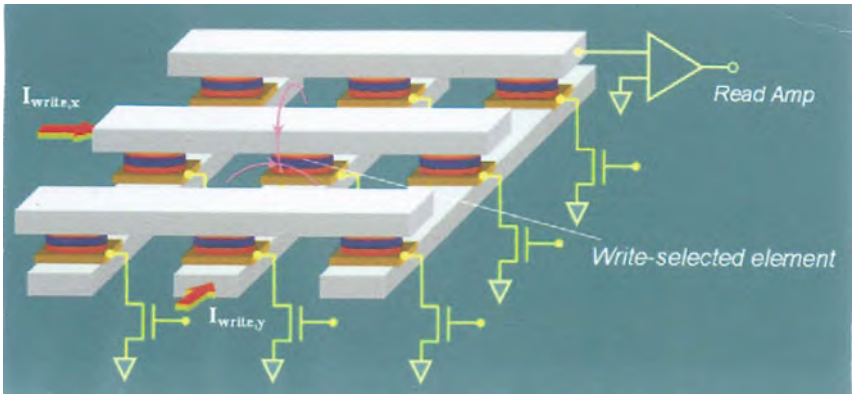

Fig. 1.24 Schematics of magnetic random access memory (MRAM) array with magnetic tunneling junction (MTJ) memory elements. For the toggle MRAM, the long axis of the eliptically shaped element (magnetic shape anisotropy) is oriented diagonally with respect to the *x*–*y* grid of write lines. Each element is connected to a transistor performing the read selection. (Reprinted with permission from [1.115]. © 2006 Elsevier)

values are different for the two spin sub-bands [1.115]. High TMR values are found for Co(001)/MgO(001)/Co(001) tunneling junctions [1.116].

GMR sensors in the spin-valve format as originally proposed by IBM [1.117] or MTJ sensors [1.118] have been used as read heads in hard disk drives (HDD; see Sect. 9.5) with data rates exceeding 1 Gbit/s [1.115].

Magnetoresistive devices such as MTJs can be employed as components of a magnetic random access memory (MRAM) which may be the "dream memory" because this is capable of the speed of the semiconductor SRAM (static random access memory), the density of a DRAM (dynamic random access memory), and the non-volatility of an HDD for integration of a computer system on a single chip. To date, Freescale's toggle MRAM (see Sect. 9.5) with a 4 Mbit chip of MTJ elements is in production (see Fig. 1.24). The storage layer of the memory elements is a synthetic antiferromagnet (SAF) as, e.g., CoFe (2.5 nm)/Ru(0.8 nm)/CoFe(2.5 nm), oriented at 45° to the orthogonally arranged current lines. Two current pulses on the two write lines effectuate a 180° rotation of the magnetic moment of the SAF storage layer of the selected element. Calculations based on the so-called spin-torque switching [1.115] suggest that such a design may enable MRAMs to reach a storage capacity of many Gbits per chip with low operating power.

1.4.2 Spintronics in Semiconductors

Recently, efforts have been made to exploit electron spin degrees of freedom in semiconductors, where the spin orientation can be actively controlled [1.113]. In a spin transistor the current of the spin-polarized electrons can be controlled by a gate

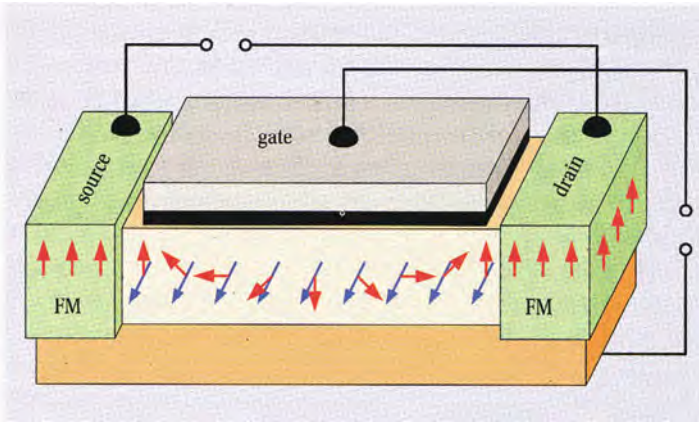

Fig. 1.25 In a spin transistor [1.119] spin-polarized electrons (*red arrows*) are injected from a ferromagnetic source contact into a semiconductor channel where they migrate to a spin selective drain contact. A voltage perpendicular to the current gives rise to a spin–orbit coupling corresponding to an effective magnetic field (*blue arrows*) perpendicular to the directions of current and electrical field which effectuates a spin precession. Only when the electron spins arriving at the drain are parallel to the spins there, then the electrons can leave via the drain and a current flows in the transistor. (Reprinted with permission from [1.113]. © 2004 Wiley-VCH)

voltage via spin–orbit coupling (see Fig. 1.25). Another example is a spin-controlled semiconductor laser where the intensity and the polarization of the emission can be manipulated by the spin orientation without changing the electron density [1.113]. In addition, spintronics is correlated to quantum information processing where entangled quantum mechanical states are employed for designing new computer architectures and safe quantum communication systems.

For spintronics, first spin-polarized electrons must be injected into the semiconductor by optical or electrical procedures. By optical excitation the angular momentum of a circularly polarized photon can be used to transfer exclusively electrons of a particular spin orientation from the valence band to the conduction band in order to generate an effective electron spin polarization. By electrical methods spin-polarized electrons can be transferred from ferromagnetic contacts into a semiconductor with degrees of polarization of 30% [1.120].

The spin polarization of charge carriers injected from magnetic layers as, e.g., *n*-ZnBeMgSe into a semiconductor can be detected optically by the polarization of the luminescence in a light-emitting diode (LED; see Fig. 1.26) – a direct inversion of the optical generation of spin-polarized charge carriers. Considerable progress in electron spin polarization in semiconductors has been achieved by the discovery of ferromagnetism in strongly Mn-doped GaAs [1.121] or in $Zn_{0.8}Cr_{0.2}Te$ films [1.122]. In these dilute magnetic semiconductors (DMS, see [1.123]), owing to the short-range character of the direct exchange interaction between the tightly localized magnetic orbitals of the magnetic dopants, the coupling between the *d* spins proceeds *indirectly* (superexchange) via *sp* bands in the tetrahedrally coordinated

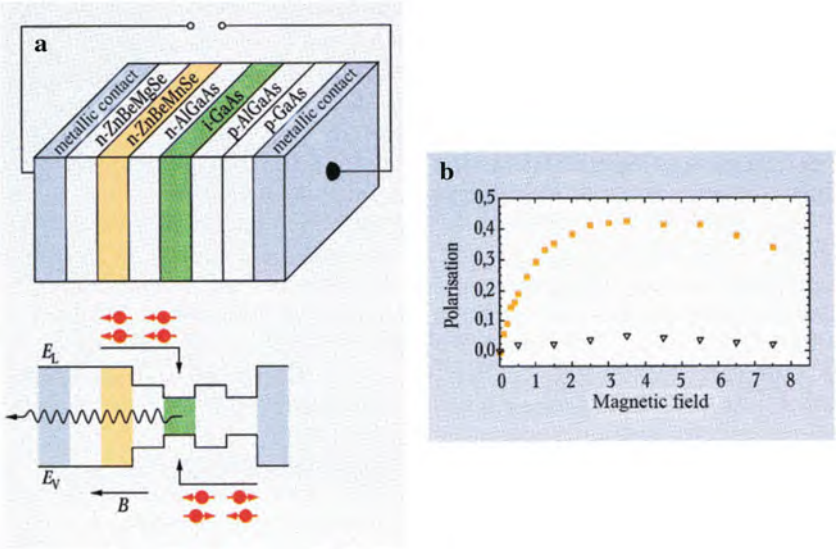

Fig. 1.26 (**a**) Layer sequence of a AlGaAs light-emitting diode (LED) (*green*) with an Mn-doped contact (*orange*) for spin polarization. The lower part shows the position-dependent conduction band edge (E_L) and the valence band (E_v). By an electric field the spin-polarized electrons (*red*) are transported from the ZnBeMnSe layer into the non-magnetic AlGaAs and GaAs layers forming the LED which – according to the spin polarization – emits circularly polarized light. (**b**) Degree of polarization of the light emitted from the LED in dependence of the external magnetic field ***B*** for a diode with a paramagnetic ZnBeMnSe layer (□□□) and with a non-magnetic ZnBeMgSe (▽▽▽) layer. [1.125]. (Reprinted with permission from [1.113]. © 2004 Wiley-VCH)

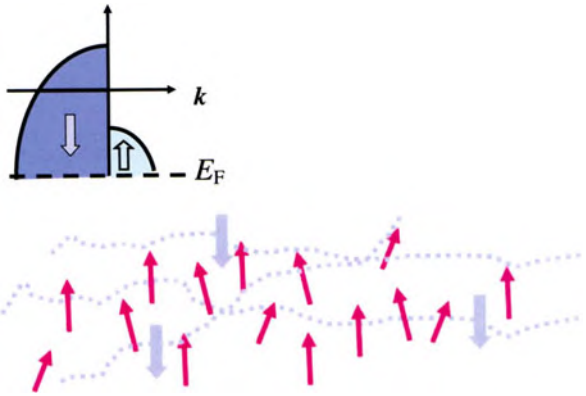

Fig. 1.27 Schematics of carrier-mediated ferromagnetism in ***p***-type dilute magnetic semiconductors (DMS). Owing to the ***p–d*** exchange interaction, ferromagnetic ordering of localized spins (*red arrows*) leads to spin splitting of the ***sp*** valence band. The redistribution of the carriers between the spin sub-bands lowers the energy of the holes which can overcompensate an increase of the free energy associated with a decrease in Mn entropy. (Reprinted with permission from [1.123]. © 2006 Elsevier)

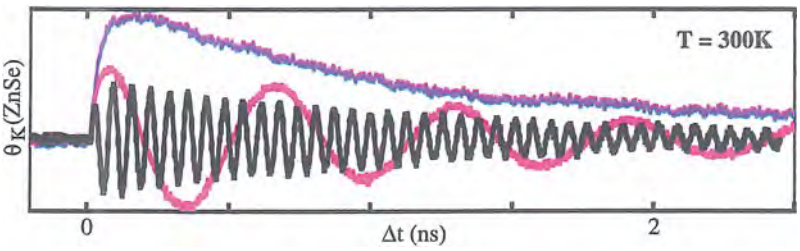

Fig. 1.28 Spin transport across a GaAs/ZnSe junction at ambient temperature. Kerr rotation detects coherent spins in ZnSe generated in GaAs and transferred to the ZnSe layer. The spin precession is observed in a magnetic field $B = 0$T (*purple*), 0.025T (*pink*), and 0.25T (*black*)). (Reprinted with permission from [1.126]. © 2001 AAAS)

DMS (see Fig. 1.27). A more detailed quantum mechanical treatment indicates that the sign of the interaction between the localized spins oscillates with their distance according to the Ruderman–Kittel–Kasuya–Yosida (RKKY) model.

For the development of semiconductor-based spintronics the understanding of spin transport and spin relaxation times is of importance. For information storage purposes spin polarization should be maintained over long times whereas rapid spin relaxation may be advantageous for fast switching [1.124]. Spin relaxation times can be at present manipulated from picoseconds to many milliseconds [1.113]. Long-time spin polarization can be experimentally observed by the spin precession in a magnetic field (see Fig. 1.28).

For application of dilute magnetic semiconductors ferromagnetic behavior at ambient temperature is desirable. In the case of (Zn, Cr) Te, ferromagnetism persists up to 300 K [1.122] whereas in (Ga, Mn) As, Mn-rich (Mn, Ga) As nanocrystals [1.127] account for the high apparent T_c of 360 K. In quantum wires of Mn-doped GaN with a diameter down to 40 nm and lengths of 20 μm, ferromagnetic behavior has been shown at ambient temperature [1.128].

1.4.3 Spin Hall Effect

In the spin Hall effect, which was postulated more than 30 years ago (see [1.129]), a voltage on a specimen – as in the normal Hall effect – gives not only rise to a current in field direction but also to a spin current $j_s = \sigma_{sH} E$ transverse to the field direction (see Fig. 1.29) where σ_{sH} is the spin Hall conductivity. In contrast to the normal Hall effect this is not due to an external magnetic field but rather due to spin–orbit scattering. Therefore, the spin Hall current is a pure spin current where no charge is transported. The spin Hall effect was demonstrated experimentally in ZnSe [1.130] by making use of a Kerr rotation microscope with a spatial resolution of 1 μm scanning the spin polarization profile over a distance of 100 μm. Due to the large ZnSe band gap and the long spin coherence time the effect can also be detected at ambient temperature.

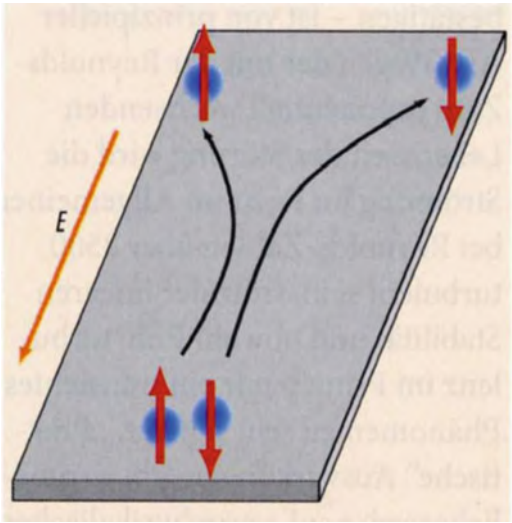

Fig. 1.29 In the extrinsic spin Hall effect (spin-dependent electron scattering at defects) electrons with differing spin polarization are scattered asymmetrically which gives rise to an unbalance perpendicular to the charge current and thereby to a spin polarization at the specimen fringes. (Reprinted with permission from [1.129]. © 2006 Wiley-VCH)

1.5 Self-Assembly

On a atomic or molecular scale, the application of interatomic or intermolecular forces can lead to new and previously unachievable nanostructures. This is why molecular self-assembly is a highly topical and promising field of research in nanoscience [1.131]. The term self-assembly implies spontaneity, a structure builds itself from modular construction units, an ordered pattern forms from a disordered state. The self that drives the assembly is the interaction among building blocks rather than the generally stronger bonding force within them [1.132]. The forces governing self-assembly include hydrogen bonding, electrostatic and magnetic interaction, hydrophobic interaction, and van der Waals forces (see [1.131]). To self-assemble building blocks into well-organized constructs depends on the ability to control their size, shape, surface properties precisely (e.g., charge, hydrophobicity, hydrophilicity, functionality, see also Sect. 3.2). A prime goal, therefore, is to gain control over the attractive and repulsive forces between the building blocks to allow them to assemble spontaneously over multiple length scales [1.133] to create an integrated chemical, physical, or biological system with new functionality.

In the absence of external influences, building block static self-assembly is driven by energy minimization to form static equilibrium structures. Under outside influences, a dynamically self-assembling system may prevail that can adjust to the surrounding environment, by residing on an energetic minimum which is caused by the influx of energy into the system – once the energy flow stops, the minimum disappears, and the system disassembles. Any living organism is a perfect example of dynamic self-assembly. It reduces entropy by absorbing energy from

the environment (see [1.132]). Once that flux ceases, the organism disassembles. Self-assembly forms the basis for many natural processes including protein folding, DNA transcribing and hybridization, and the formation of cell membranes (see [1.131]).

In the following a few examples of static self-assembly will be discussed, including self-assembly via Friedel oscillations [1.134], via strains [1.135] and via molecular interaction for the formation of a Kagomé lattice [1.136] or of self-assembled monolayers (SAMs) [1.131]. In addition, self-assembly gives rise to colloidal superstructures in a magnetic field [1.137] or to complex nanostructures making use of DNA [1.138, 1.139].

1.5.1 Self-Assembly of Ni Nanoclusters on Rh (111) via Friedel Oscillations

When a Rh (111) substrate is covered by 0.8 monolayers (ML) of Ni, hollow crystallographic Ni nanoclusters with predominantly 12 atoms (see Fig. 1.30a) are formed on the Ni adislands. Surface Friedel oscillations of electrons can generate standing waves (SWs) which modify the electron local density of states (LDOS) at the surface and can be imaged by scanning tunneling microscopy (STM). Friedel oscillations modify the adsorption properties of the surface. A maximum in the variation ΔLDOS of the LDOS due to the Friedel oscillations is a potential well and a suitable atomic adsorption site. The map of the ΔLDOS (Fig. 1.30b) calculated by a simple model [1.134] for a 12-atom cluster can be directly compared with the STM image in Fig. 1.30a and suggests that the Friedel oscillations are responsible for the formation of the triangular clusters. A model for the likely sites of adsorption for a cluster of 12 atoms is shown in Fig. 1.30c.

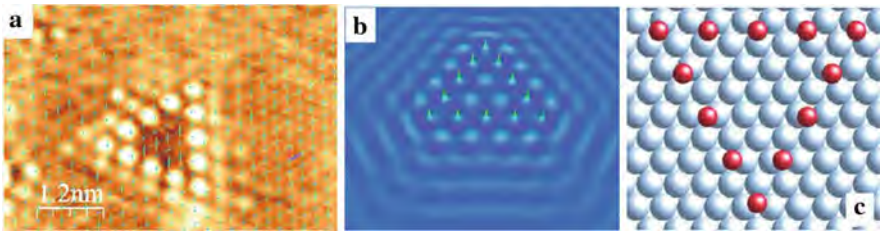

Fig. 1.30 (**a**) Scanning tunneling micrograph (STM) of a hollow Ni nanocluster with 12 atoms on a Ni adisland deposited on a Rh (111) substrate. (**b**) Variation ΔLDOS map of the electron local density of states (LDOS) obtained by linear combination of the single patterns produced by each interfering adatom. (**c**) Model of the likely sites of adsorption for a cluster of 12 atoms. *Light blue* corresponds to the Ni adisland layer while *red* represents the adatoms of the cluster. (Reprinted with permission from [1.134]. © 2008 American Physical Society)

1.5.2 Self-Assembly of Fe Nanoparticles by Strain Patterns

Self-assembly of nanoparticles can be induced by strain fields [1.135]. In bilayers of two thin films of metals as, e.g., Cu/Pt (111), with different lattice parameters, the lattice misfit is compensated by a regular network of surface-near dislocations, which can be detected by STM due to their strain fields. The strain fields are repulsive toward diffusing Fe adatoms so that the Fe atoms regularly agglomerate between the dislocations with exactly one island or agglomerate per network unit cell (Fig. 1.31). The islands exhibit a narrow size distribution.

Fig. 1.31 Scanning tunneling micrograph (STM) of a periodic array of Fe islands nucleated on a dislocation network of a Cu/Pt (111) bilayer at 250 K. (Reprinted with permission from [1.135]. © 1998 Nature Publishing Group)

1.5.3 Chiral Kagomé Lattice from Molecular Bricks

Long-range periodic nanonetworks can be formed on a surface atomic lattice using simple linear molecular bricks. Making use of, e.g., dicarbonitrile-pentaphenyl NC-Ph_5-CN (Fig. 1.32a) a uniform tiling forms (Fig. 1.32b) where two triangles and two hexagons join each vertex, which is known in natural science as "Kagomé" lattice (see [1.136]). The molecular networks are commensurate with the underlying Ag (111) surface, with the terminal benzonitrile group of the NC-Ph_5-CN molecule showing a rotation of 20° around the molecular axis (Fig. 1.32c–f) as determined by near-edge x-ray absorption fine structure spectroscopy (NEXAFS; see [1.136]) and supported by extended Hückel theory calculations. This suggests that the terminal Ph–CN groups are rotated to form a CN π-bond instead of a CN–H linkage, demonstrating the interplay between substrate epitaxial fit, non-covalent lateral interactions, and the molecules' conformational flexibility.

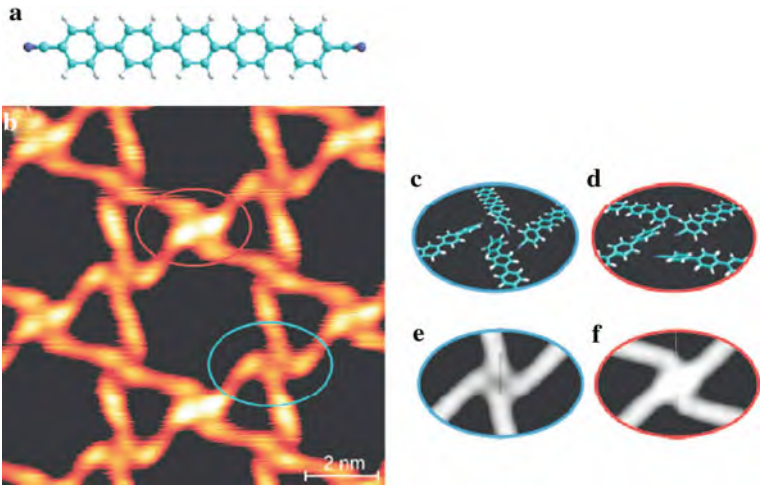

Fig. 1.32 Kagomé lattice formed by dicarbonitrile–pentaphenyl NC–Ph_5–CN molecules self-assembled on a Ag (111) surface. (**a**) Structure model of the NC–Ph_5–CN building block. (**b**) High-resolution scanning tunneling micrograph identifying two different types of nodes in the Kagomé lattice. (**c**, **d**) 3D representations of structural models of two specific non-planar nodal geometries associated with molecular flexure. (**e**, **f**) The corresponding charge density contour plots mimic the main features of the experimental data. (Reprinted with permission from [1.136]. © 2008 American Chemical Society)

1.5.4 Self-Assembled Monolayers (SAMs)

For SAMs, synthetic chemistry is used only to construct the constituent molecules, such as thiols and silanes, and weaker van der Waals interactions are involved in arranging and binding the constituents together into a structure. The weak bonding makes solution, and hence reversible processing of SAMs, possible. A typical alkanethiol (Fig. 1.33) monolayer forms a $(\sqrt{3} \times \sqrt{3})$ R 30° structure (see [1.131])

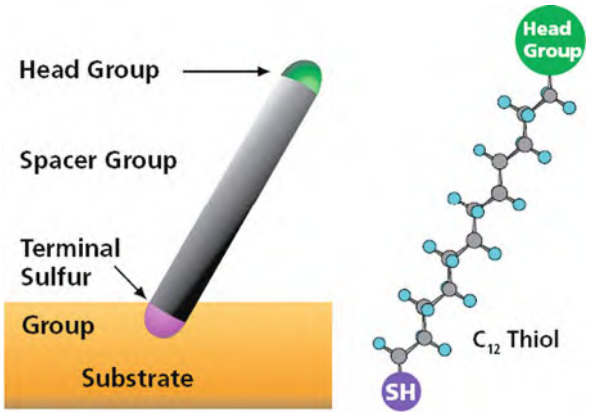

Fig. 1.33 Schematic diagram of a thiol molecule for building a self-assembled monolayer. The sulfur group links the molecule to the gold surface. The head group can be designed to provide virtually any surface chemistry or binding capacity. (Reprinted with permission from [1.131]. © 2006 Sigma-Aldrich)

on gold with the thiol chains tilted approximately 30° from the surface normal. The sulfur–gold interaction is about 45 kcal/mol and, therefore, weaker than the C–C bond strength of ~83 kcal/mol (see [1.131]). By simply changing the head group, a surface can be created that is hydrophobic (methyl head group), hydrophilic (hydroxyl or carboxyl head group), or allows chemical binding (azide, carboxyl, amine head groups). This enables the researcher to custom design a surface to serve any desired function (see [1.131]).

1.5.5 Magnetic Assembly of Colloidal Superstructures

By self-assembly in a magnetic field a diverse set of colloidal particles can be organized, making use of the magnetostatic dipole–dipole interaction between effectively diamagnetic (susceptibility χ_{NM}) and paramagnetic (χ_{PM}) particles within a magnetized ferrofluid of 10 nm Fe_3O_4 nanoparticles in water (χ_f) [1.137]. For the non-magnetic particle ($\chi_{NM} < \chi_f$) the potential energy is strictly positive, which causes the particle to move toward regions of minimum magnetic field. Paramagnetic particles ($\chi_{PM} > \chi_f$) have a strictly negative potential energy, causing them to move to regions of maximum field. Hence, in mixed suspensions of non-magnetic and paramagnetic particles, the magnetic force drives the non-magnetic particle toward the "equator" of the paramagnetic particle, where the dipolar field of the paramagnetic particle subtracts from the external field. Likewise, the paramagnetic particles move toward the equator of the non-magnetic particles, where the dipolar field of the non-magnetic particle adds to the external field. Two-tone structures (with two different colors, Fig. 1.34) are assembles in a mixture of 2.7 μm

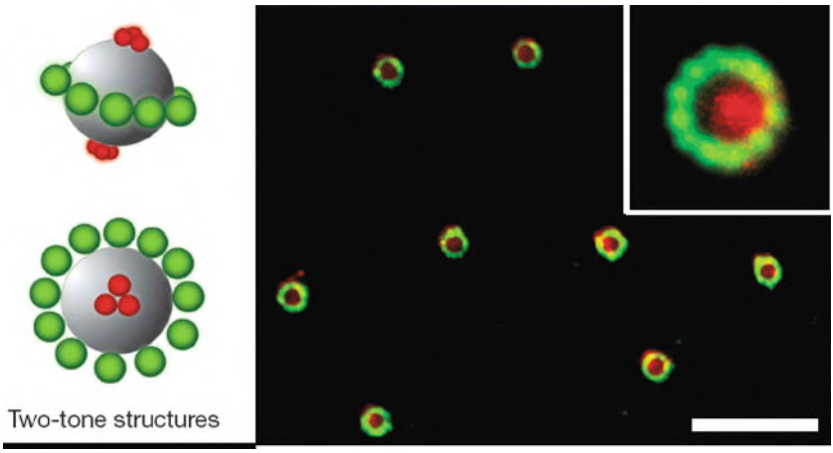

Fig. 1.34 Demonstration of multicomponent particle assembly in a magnetic field. Fluorescent images of structure formation in four-component colloidal-particle aqueous suspensions consisting of ferrofluid (magnetic susceptibility $\chi_f = 0.24$), 0.21 μm (*red*) non-magnetic particles, 1.0 μm (*green*) non-magnetic particles, and 2.7 μm paramagnetic core particles. The panel includes a sketch of the assembled structure and a view of one of the assembled structures (inset). Scale bar, 20 μm. (Reprinted with permission from [1.137]. © 2009 Nature Publishing Group)

diameter paramagnetic particles, 1.0 μm (green) non-magnetic particles, 0.21 μm (red) non-magnetic particles, and a ferrofluid at an appropriate dilution ($\chi_f = 0.2$). In these conditions, the smaller non-magnetic particles acquire positive magnetization with respect to the ferrofluid, whereas the larger non-magnetic particles acquire negative magnetization with respect to the ferrofluid. Hence, the smaller particles are attracted to the poles of the paramagnetic particle, whereas the larger particles are attracted to the equator of the same paramagnetic particle [1.137].

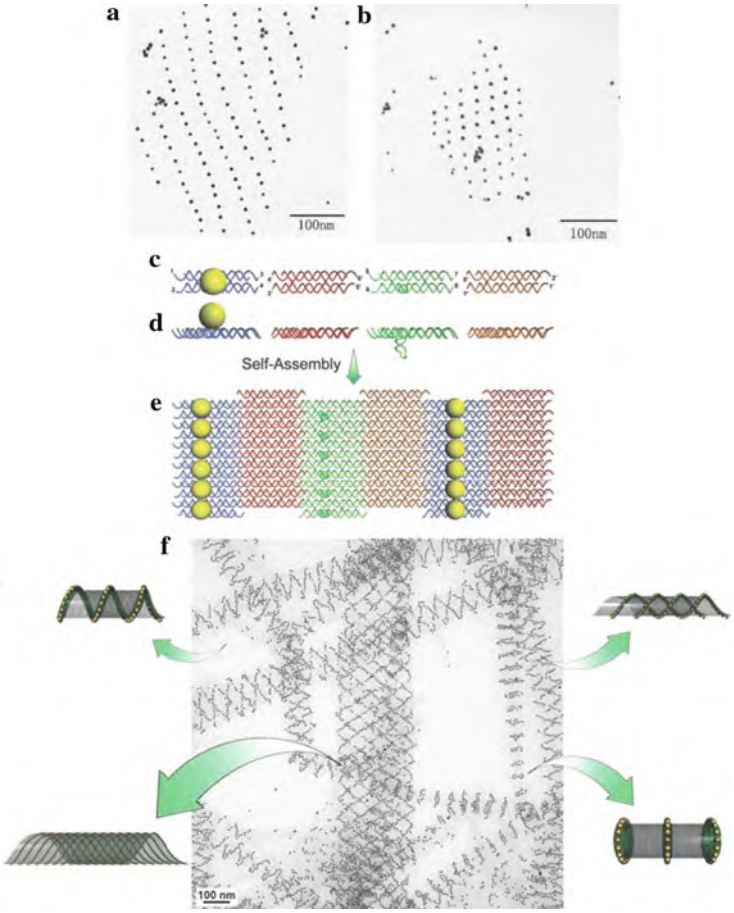

Fig. 1.35 2D and 3D organization of gold nanoparticles using self-assembling DNA templates. Transmission electron micrographs (TEM) of 2D arrays of (**a**) 5 nm gold nanoparticles and (**b**) alternating 5 and 10 nm gold nanoparticles. The DNA tiles are invisible [1.142]. (**c–d**) Top and side view of four DNA tiles for the formation of tubular structures decorated by 5 nm Au nanoparticles (A tile, *blue*; B tile, *red*; C tile, *green*; and D tile, *brown*). The A tile carries a 5 nm Au nanoparticle on top of the tile. The C tile carries a DNA stem loop pointing downward. (**f**) The different tube conformations indicated in the adjacent model structures are observed in a single transmission electron micrograph (TEM). (Reprinted with permission from [1.138]. © 2009 AAAS)

1.5.6 Self-Assembly via DNA or Proteins

The stable deoxyribonucleic acid (DNA) building blocks (tiles), and the ability to combine them with sticky-ended cohesion, makes possible a wide variety of structures using self-assembly, such as 2D lattices (see [1.139]) or 3D nanostructures [1.138, 1.140, 1.141]. In 2D DNA structures, the control of the interparticle spacing can be demonstrated through variation of the DNA-tile dimensions. A periodic pattern can be achieved by attaching gold nanoparticles to strands in two different building blocks to produce a 2D array of alternating 5 and 10 nm Au nanoparticles (Fig. 1.35a, b). 3D nanoparticle assemblies can be synthesized through self-assembly of multihelix DNA bundles or the rolling of DNA sheets (Fig. 1.35c–e) to produce a variety of Au nanoparticle architectures including single, double, and nested spirals (Fig. 1.35f). Interestingly, the nanoparticles were found to influence the conformations of the DNA nanotubes through size-dependent steric repulsion effects.

1.6 Casimir Forces

Casimir forces [1.143] are caused by quantum fluctuations in the nanometer space between surfaces and are critically dependent on their nanometer-scale shape [1.144]. Two reflecting plates facing each other in vacuum attract with the force (see [1.145])

$$F = -\frac{A\hbar c\pi}{240d^4}$$

where, besides the plate surface, A, and the plate distance, d, only the velocity of light, c, and Planck's constant, $\hbar$, appear. The Casimir effect is a quantum mechanical effect that arises because the vacuum is filled with fluctuations of the electromagnetic field, imposed by the Heisenberg uncertainty principle, and imbuing the vacuum with a non-zero energy (see [1.146]). The reflecting plates provide boundaries between which only some electromagnetic fluctuations can exist compared with those in the unrestricted vacuum outside the plates (see Fig. 1.36). The

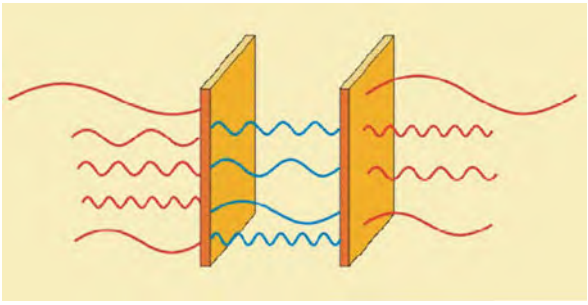

Fig. 1.36 Two parallel plane mirrors act on the quantum electrodynamical vacuum fluctuations like a resonator which amplifies resonant oscillation modes and suppresses non-resonant modes. (Reprinted with permission from [1.145]. © 2005 Wiley-VCH)

vacuum energy between the plates is thus different from outside, resulting in the Casimir "force", which scales with the fourth power of the inverse distance between the plates (see above). For example, two mirrors with an area of 1 cm^2 in a distance of 1 μm exert between each other an attractive force of 10^{-7} N [1.145] which is equivalent to the weight of a water droplet with a diameter of 0.3 mm. Although this may be small, the Casimir force is the dominating force between neutral objects at distances in the nanometer range where it is, however, somehow smaller than predicted by the above relationship [1.145].

Repulsive long-range Casimir forces can be measured below 100 nm distances between solids (1, 2) separated by a fluid (3) with the dielectric response functions ε_1, ε_2, and ε_3 [1.147]. The interaction of the materials 1 and 2 across medium 3 goes as a summation of terms with differences in material permittivities $-(\varepsilon_1 - \varepsilon_3)(\varepsilon_2 - \varepsilon_3)$. Between two like materials, $\varepsilon_1 = \varepsilon_2$, these terms are negative and correspond to attraction. However, for $\varepsilon_1 > \varepsilon_2 > \varepsilon_3$, the $-(\varepsilon_1 - \varepsilon_3)(\varepsilon_2 - \varepsilon_3)$ terms are positive; the force is repulsive. Measurements have been performed between a plate and a 39.8 μm diameter polystyrene sphere coated with a 100 nm thick gold film, which is attached to a cantilever and mounted on an atomic force microscope (AFM) (Fig. 1.37a) with a cell filled with liquid bromobenzene. The

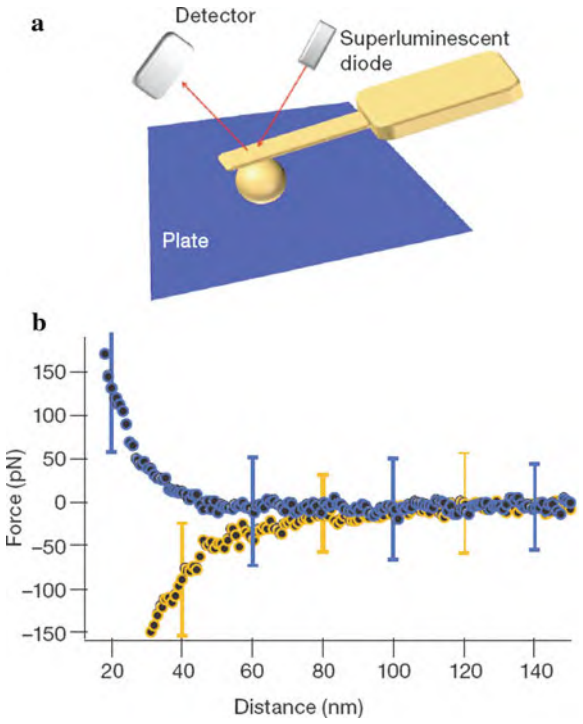

Fig. 1.37 (**a**) Experimental set-up for measuring the repulsive and the attractive Casimir force. A sphere is attached to an atomic force microscope (AFM) cantilever, which is enclosed within a bromobenzene filled cell for force measurements. (**b**) Data for the repulsive and attractive Casimir force measurements. *Blue* (*orange*) circles represent the data sets for the force between a gold sphere and a silica (gold) plate in bromobenzene. (Reprinted with permission from [1.147]. © 2009 Nature Publishing Group)

force is changed from attractive to repulsive by replacing a gold plate with a silica plate (Fig. 1.37b). This shows that long-range quantum electrodynamic forces between solid bodies on nanoscale distances can become repulsive when the optical properties of the materials are properly chosen. With such materials, quantum levitation of one surface above another in a fluid should be possible and could lead to ultra-low friction devices [1.147].

The precise nanoscale shape of the plates also has an effect as demonstrated by measuring the Casimir force between a gold-covered sphere and a nanostructured silicon surface [1.144].

A force between two plates, which is not quantum electrodynamic in origin but rather a result of classical thermodynamic fluctuations [1.148], is the "critical" Casimir force. This temperature-dependent force increases to values of 0.6 pN [1.149] when a critical temperature is approached, in agreement with theoretical studies [1.149].

1.7 Nanoscale Measuring Techniques

Microscopy imaging techniques such as scanning probe microscopy, far-field sub-diffraction-limit light microscopy, electron microscopy, x-ray microscopy, or atom probes (see Chap. 2) are of fundamental importance in nanoscience. However, other nanoscale measuring techniques for, e.g., displacement, mass, magnetic fields, and magnetic resonance imaging (MRI), superconductivity, Raman spectroscopy, voltage, or ion concentration are of growing importance in physics, materials science, biology, and medicine and will be discussed in the following.

1.7.1 Displacement Sensing

The motion of a nanomechanical resonator (see Sect. 7.1) can be detected with picometer (pm) sensitivity [1.150] by coupling to a single-electron transistor (SET). The SET consists of a conducting islands (see Sect. 1.3) separated from leads by low-capacitance, high resistance tunnel junctions where the current through the SET is modulated by the charge induced on its gate electrode.

1.7.2 Mass Sensing

The state-of-the-art mass sensing is approaching 100 Da $= 0.17 \times 10^{-21}$ g $= 0.17$ zeptogram by making use of nanoelectromechanical systems (NEMS; see Sect. 7.1) in vacuum (see [1.151]) and a NEMS mass sensitivity below a single proton (< 1 Da) is theoretically anticipated [1.152]. Single bacterial cells and proteins can be weighed in water [1.153] with sub-femtogram (< 1 fg $= 10^{-15}$ g) resolution by

Fig. 1.38 (**a**) Electron micrograph of a suspended microchannel resonator. The 200 µm × 33 µm × 7 µm (length × width × thickness) microcantilever containing a 3 µm × 8 µm (height × width) channel is suspended in a vacuum cavity. The cantilever has been intentionally etched open to visualize the fluidic conduit inside. (Reprinted with permission from [1.153]. © 2007 Nature Publishing Group)

placing the solution inside a hollow microresonator that is surrounded by vacuum (Fig. 1.38). Single-molecule mass-spectrometry (MS) employing NEMS techniques has been used to study the protein bovine serum albumin (BSA; 66 kDa), and BSA monomers, trimers, and pentamers can be resolved [1.151]. With this MS technique, which measures the mass directly rather than the mass-to-charge ratio in conventional MS techniques, a future accuracy of 100 ppm (parts per million) for 10 kDa molecules is expected [1.151].

1.7.3 Sensing of Weak Magnetic Fields at the Nanoscale

The detection of weak magnetic fields at small length-scales is a long-standing challenge in physics. A good figure of merit for a nanoscale magnetic sensor is its magnetic moment sensitivity [1.154] which is basically the smallest number of spins it can detect. Because a magnetic field of a dipole, like an electron spin, drops off roughly as r^{-3}, where r is the distance, a good sensor has to be small and must be brought very close to the sample. The issue is even more challenging for detection and manipulation of the much weaker nuclear magnetism which is fundamental for magnetic resonance imaging (MRI). The development of nanotesla magnetic field sensors and of nanoscale MRI will be briefly discussed in the following.

A sensor with exceptional properties appears to be the nitrogen-vacancy defect center in diamond, which is an extra nitrogen atom next to a vacant lattice site. The electron spin of the nitrogen-vacancy center is very sensitive to its magnetic environment and slight changes in the magnetic field, which will lead to a shift in the spin resonance frequency that can be detected by optical techniques. This sensitivity is due to the fact that the smallest measurable frequency shift is set by

the inverse of the spin coherence time which can be many seconds (see [1.155]) in high purity diamond, depleted of the ^{13}C isotope with a non-zero nuclear spin which with its magnetic field decreases the electron spin coherence time. In highly pure diamonds a spin coherence time of ∼0.5 ms is achieved [1.156] promising a ∼10 nm lateral resolution and a ∼1 nT magnetic field sensitivity. With the synthesis of high-purity diamonds with a ^{13}C isotope content depleted to 0.3% [1.155] a spin coherence time of 1.8 ms was measured with a sensitivity improvement of an order of magnitude compared with earlier experiments [1.156]. This diamond magnetometer can be considered for future use to detect magnetic fields associated with the ion flow through membrane channels in cells. An array of nitrogen-vacancy centers could be used as a room-temperature quantum device for quantum computing applications [1.155].

1.7.4 Nuclear Magnetic Resonance Imaging (MRI) at the Nanoscale

Magnetic resonance imaging (MRI) is well known in medicine and in neuroscience as a powerful tool for acquiring 3D morphological and functional information with resolution in the millimeter to sub-millimeter range. A resolution of 4 nm can be achieved by the combination of ultrasensitive magnetic resonance force microscopy (MRFM) with 3D image reconstruction [1.157]. Nanoscale MRI, with its capacity for 3D subsurface imaging, its potential for generating contrast by selective isotopic labeling and its non-destructive nature, can be a welcome contrast to other microscopy techniques (see Chap. 2). The key to pushing MRI to the nanoscale is detection sensitivity. This can be achieved by the generation of magnetic field gradients as high as 4 million Tesla (T) per meter, detailed understanding of the MFRM detection geometry (point-spread function) and the application of an image-reconstruction technique capable of converting magnetic force measurements into a 3D map of proton density. MRFM is based on mechanical measurements of ultrasmall (10 attonewton $= 10^{-17}$ N) magnetic forces between nuclear spins in a sample and a nearby magnetic tip (see Fig. 1.39a–c). The tobacco mosaic virus (TMV; diameter 18 nm and length ∼300 nm) test samples, with ∼95% of the virus mass consisting of proteins, are deposited on the flat end of an ultrasensitive silicon cantilever. The end of the cantilever is positioned close to a 200 nm diameter magnetic tip that produces a strong and very inhomogeneous magnetic field in combination with the field from an external superconducting magnet. The magnetic tip sits on a copper "microwire" that serves to efficiently generate a radiofrequency (rf) magnetic field that excites nuclear magnetic resonance (NMR) [1.157] with a periodic inversion of the ^{1}H spins in the sample, resulting in a periodic force that drives the mechanical resonance of the cantilever. Monitoring the cantilever oscillation amplitude while mechanically scanning the magnetic tip with respect to the sample in three dimensions provides data that allow the reconstruction of the ^{1}H density. The imaging is performed in vacuum at low temperatures ($T = 0.3$ K). The MRI of

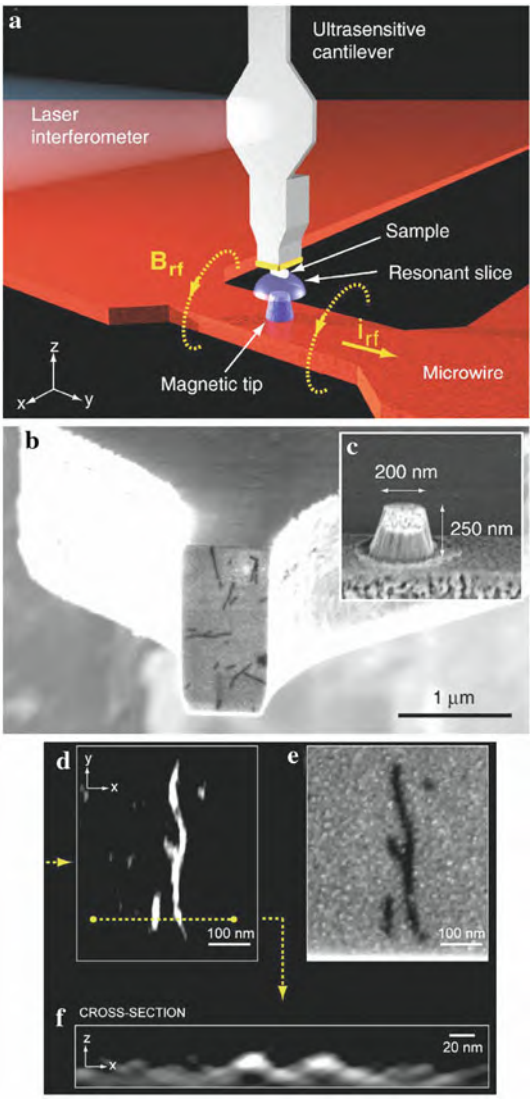

Fig. 1.39 (**a**), (**b**) Configuration of the magnetic resonance force microscope (MRFM). (**a**) Tobacco mosaic virus (TMV) particles (sample), attached to the end of an ultrasensitive Si cantilever, are positioned close to a magnetic tip. A radiofrequency (fr) current i_{rf} passing through a Cu microwire generates an alternating magnetic field B_{rf} that induces magnetic resonances in the 1H spins of the virus particles. The resonant slice represents those points in space where the field from the magnetic tip (plus the external field) matches the condition for magnetic resonance. 3D scanning of the tip with respect to the cantilever, followed by image reconstruction is used to generate a 3D image of the spin density in the virus sample. (**b**) Scanning electron micrograph of the end of a cantilever. Individual tobacco mosaic virus particles as long dark rods on the 0.8 μm × 1.3 μm sized sample platform. (**c**) Detail of the magnetic tip. (**d**) Horizontal slice of the reconstructed 3D 1H spin density of the viruses. (**e**) Scanning electron micrograph of the same region. (**f**) Cross-sectional MRFM showing two viruses. (Reprinted with permission from [1.157]. © 2009 National Academy of Sciences U.S.A)

the TMV is shown in Fig. 1.39d with a cross-section in Fig. 1.39 f. For comparison, the TMV of Fig. 1.39d is imaged by scanning electron microscopy (SEM) in Fig. 1.39e.

1.7.5 Probing Superconductivity at the Nanoscale by Scanning Tunneling Microscopy (STM)

In superconductors, a detailed knowledge of the Fermi surface is essential for an understanding of their physical properties. However, most techniques for measuring the Fermi surface of superconductors only produce spatially averaged data, rather than information on how the surface changes on nanometer length scales [1.158]. Studies of the surface of bismuth-based cuprate superconductors at the nanoscale can be performed by scanning tunneling microscopy (STM; see Sect. 2.1) in order to measure the local density of states of electrons – which is related to conductance – as a function of energy and position in two dimensions [1.159]. By Fourier transformation of these maps, changes of the Fermi surface at the nanoscale are observed, as shown by the images of an inhomogeneous conductance (Fig. 1.40a) with maxima as red dots and of the inhomogeneous superconductivity gap map of the same area (Fig. 1.40b) with gap sizes between 20 mV (red) and 85 mV (blue). Inhomogeneity of doping or charge is common in many materials and leads naturally to the idea of nanoscale Fermi surface (FS) variation [1.159]. However, the question is raised of whether an FS, typically thought of as a bulk property, can be meaningfully defined inside nanometer-sized domains and at what point a *k*-space description as this stops being useful [1.159].

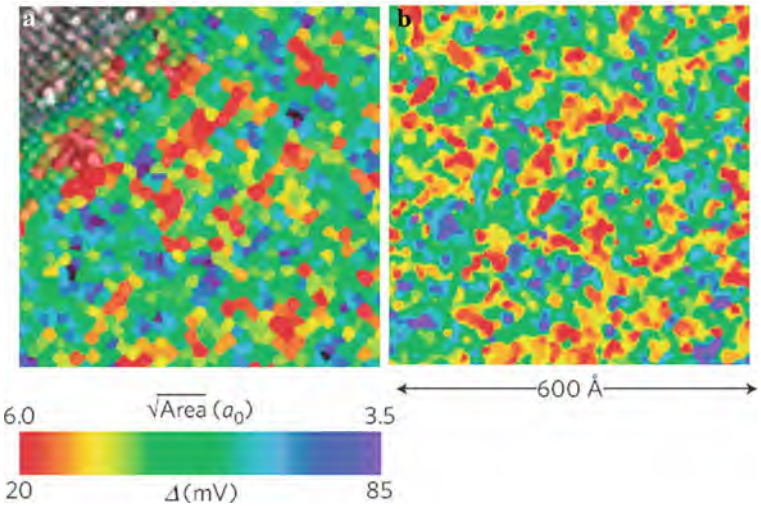

Fig. 1.40 (**a**) Conductance map of $T_c = 32$ K underdoped $Bi_2Sr_2CuO_{6+x}$(Bi - 2201), showing a spatially varying modulation with maxima (*red dots*). (**b**) Gap map of the same area showing variations of the gap size Δ from 20 mV (*red*) to 85 mV (*blue*). (Reprinted with permission from [1.159]. © 2009 Nature Publishing Group)

1.7.6 Raman Spectroscopy on the Nanometric Scale

Near-field tip-enhanced Raman scattering (TERS) spectroscopy can overcome the diffraction limit of light. This is attributed to the highly confined evanescent field at the laser-illuminated apex of a metal-coated nanotip probe (see Fig. 1.41a). TERS experiments with extremely high accuracy can be performed [1.160] by making use of the oscillating tip under the tapping-mode operation of an atomic force microscope (AFM; see Sect. 2.2) with selectively illuminating the tip only when it is positioned at a particular distance from the sample. The dominant interaction between the tip and the sample is electromagnetism with an interaction length of the order of a few nanometers. As shown in Fig. 1.41b, the intensity of the characteristic Raman mode (*G* band) of a single-walled carbon nanotube drastically increases as the tip-nanotube distance decreases, which reflects the near-field enhancement in TERS. A spatial resolution of TERS of at least 3 nm can be achieved [1.160].

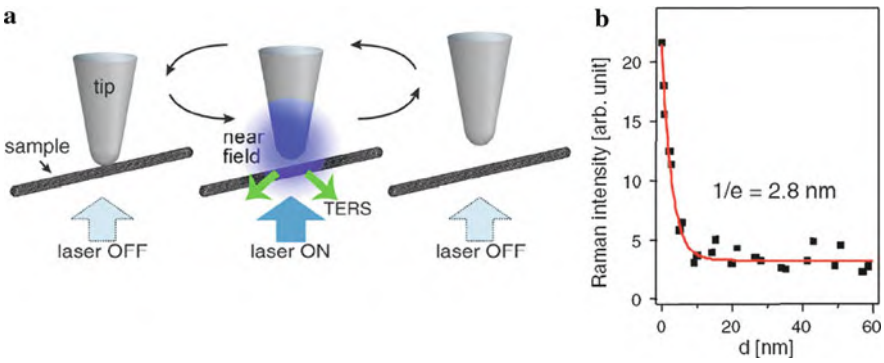

Fig. 1.41 (**a**) In tip-enhanced Raman scattering (TERS) the tip-sample arrangement is selectively illuminated only for a predecided tip-sample distance. (**b**) Plot of the integrated Raman intensity of the *G*-band of a single-walled carbon nanotube versus tip-sample distance *d*. The *solid curve* represents a profile obtained from simulation. (Reprinted with permission from [1.160]. © 2009 American Physical Society)

1.7.7 "Nanosized Voltmeter" for Mapping of Electric Fields in Cells

Electric fields (*E* fields) are found in every living cell and are critical for proper functioning of biological processes. These *E* fields preserve the energy-dependent non-equilibrium chemical steady state of the cell or the cell-to-cell signaling fields in complex organisms (see [1.161]). Changes in *E* fields can indicate perturbations

in biological function, such as observed in Alzheimer's disease (see [1.161]) or cell death. Three-dimensional (3D) *E* field profiling throughout the volume of the living cell can be performed by a "photonic voltmeter", 30 nm in size – a nanoparticle (E-PEBBLEs; Fig. 1.42a) that contains the voltage-sensitive dye di-4-ANEPPS [1.162]. These particles are illuminated at 488 nm and the emission, collected at 600 and 700 nm, depends on the applied *E* field. The chromophore is believed to undergo a large electronic charge shift as a result of optical excitation from the ground state to the excited state and this underlies the electrochromic mechanism for the sensitivity of these dyes to *E* fields [1.162].

For measuring intracellular *E* fields$_1$ rat astrocytes (star-shaped celles) with autofluorescent mitochondria (organelles in the cytoplasma, important for cell metabolism; see Sect. 11.1; see Fig. 1.42b, c) were incubated with E-PEBBLEs. The regions of interest (4.5 μm wide) in Fig. 1.42c contain both mitochondrial regions (regions 5–10) and cytosolic regions (regions 1–4). The *E* field (Fig. 1.42d) determined from the emission intensity of the E-PEBBLEs [1.161] drops significantly (regions 1–2) with distance from the mitochondrial membrane (region 5) and is still measurable several microns away from the mitochondria, much farther than the 10 nm expected from calculations (see [1.161]). This may be due to the structure of the cytoplasm which may be gel-like rather than a simple solution (see [1.161]).

1.7.8 Detection of Calcium at the Nanometer Scale

By transport through membrane channels, cells funnel bursts of calcium ions to specific locations, where the ions selectively activate a wide variety of physiological functions. Because of the importance of localization for controlling the effects of calcium signals, it is desirable to detect calcium signals at the nanometer scale [1.163].

For this purpose, a small molecular sensor, known as Calcium Green FlAsH (CaGF; see Fig. 1.43a), has been developed [1.164]. This molecule comprises a receptor that binds selectively to calcium, a fluorescent reporter that responds to calcium binding, and two arsenic groups that label proteins only at specially incorporated peptide sequences that consist of four cystein amino acids. The CaGF can be targeted to calcium channels (see Sect. 11.5) that control the flow of calcium ions into cells (Fig. 1.43b). The results [1.164] suggest that bursts of calcium signals exist that are only a few nanometers wide, and that calcium channels cluster together for signaling.

This concept [1.164] could also be exploited to visualize protein regions by using methods other than fluorescence, such as electron microscopy, magnetic resonance imaging, positron-emission tomography, and ultrasound [1.163] and is a step toward the ambitious goal of developing chemical probes that can visualize specific features of living systems with molecular resolution.

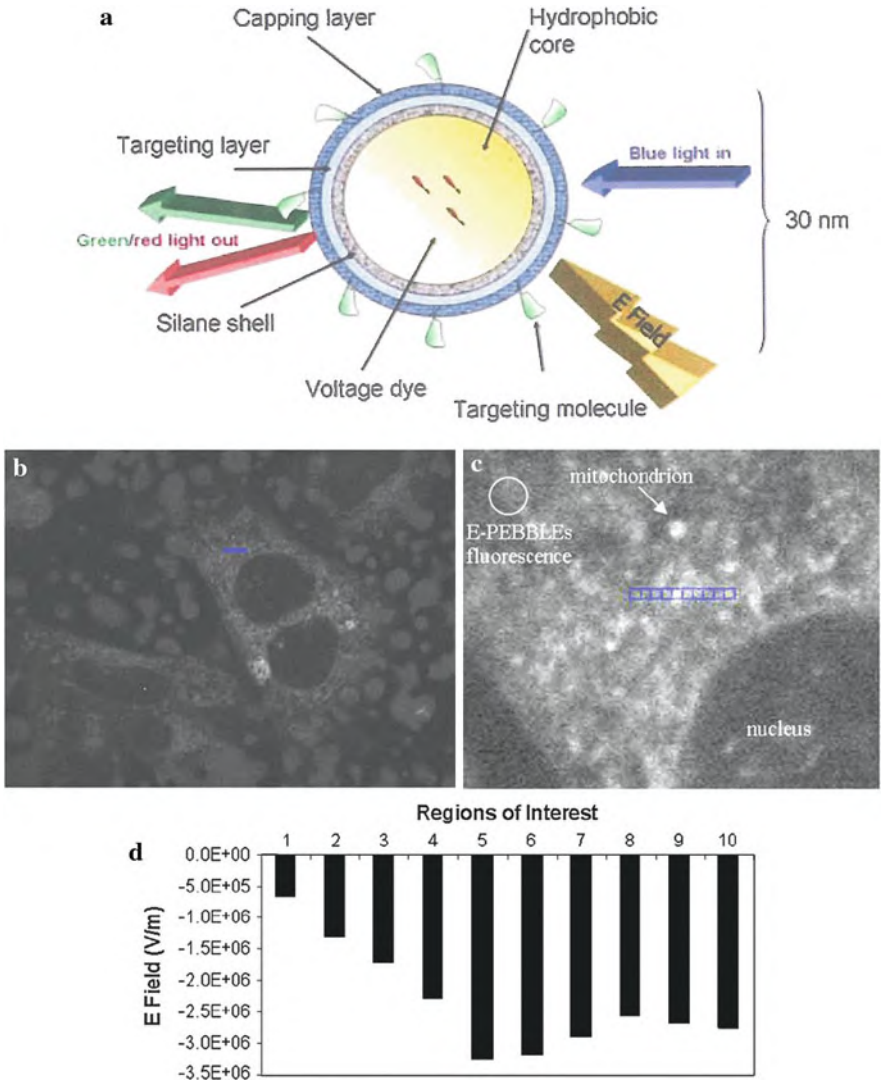

Fig. 1.42 (**a**) Schematic of fluorescent nanoparticles for electric field mapping (E-PEBBLEs). The voltage-sensitive dye is encapsulated in a silane-capped micelle. The fluorescence-voltage relationship can be calibrated before delivery to cells. (**b–d**) E-PEBBLEs can measure *E* fields both in cytosolic and membrane regions of cells. (**b**) Astrocytes incubated with E-PEBBLES. The middle cell contains the region analyzed (*blue line*, 4.5 μm). (**c**) Enlarged region of the cellular region. An *arrow* points out a representative mitochondrion. The *blue line* (4.5 μm) contains the regions analyzed, numbered 1–10 from *left* to *right*. Region 5 contains a mitochondrion, whereas regions 6–10 cross over other mitochondrial regions. (**d**) In the graph of the *E* field for the region of interest, the highest *E* field is seen in region 5 where a mitochondrion is located. (Reprinted with permission from [1.161]. © 2007 Elsevier)

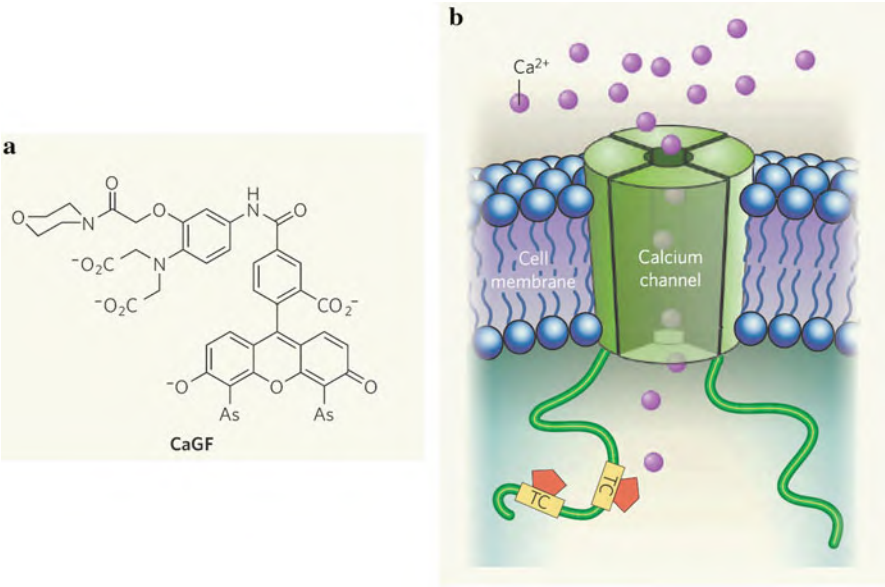

Fig. 1.43 Detecting calcium in living systems at nanometer scale. (**a**) Ca^{2+} sensor, known as Calcium Green FlAsH (CaGF), that recognizes specific peptide sequences called tetracysteines (TCs). (**b**) CaGF molecules (red pentagons) bind to TCs that have been attached to the protein chain of a calcium channel in a cell membrane. Calcium ions entering the cell through the channel are trapped by CaGF which becomes fluorescent and can be detected by fluorescence microscopy for monitoring [1.164] the calcium ion fluctuations in living systems in real time. (Reprinted with permission from [1.163]. © 2007 Nature Publishing Group)

1.8 Summary

Nanoscience will in the future be of interdisciplinary importance to physics, engineering, information science, chemistry, biology, and medicine. Some US$ 1–2 trillion in products worldwide are projected until 2015. The novel properties of nanostructures are due to quantum mechanical effects and to surface and interface effects. Changes in the thermal properties may give rise to a decrease of the melting temperature with decreasing particle size, strongly depending on the substrate. The electronic properties are governed by quantum confinement effects and charge quantization (Coulomb blockade). The electronic density of states strongly varies with the dimensionality of the nanostructure. The Fermi liquid behavior of electrons in bulk systems changes to a Luttinger behavior of interacting electrons in metallic nanowires. In nanomultilayers of ferromagnetic and non-magnetic metals the GMR effect or in systems of ferromagnetic and insulating nanolayers the TMR effect appear which are of enormous technical importance. Self-assembly may lead to new and previously unachievable nanostructures. Attractive or repulsive Casimir forces may play an important role on the nanoscale. High-resolution mass sensing, measurements of weak magnetic fields, magnetic resonance imaging, measurements

of voltages, and ion concentrations can be performed in the nanorealm, whereas the microscopic imaging techniques with capabilities down to sub-atomic resolution are discussed in Chap. 2.

References

1.1 P. Rodgers (ed.), *Nanoscience and Technology – A Collection of Reviews from Nature Journals* (World Scientific, 2009)
1.2 M.C. Roco, J. Nanoparticles Res. **1**, 435 (1999)
1.3 G. Binnig et al., Phys. Rev. Lett. **49**, 57 (1982)
1.4 H. Gleiter, in *Deformation of Polycrystals: Mechanisms and Microstructures*, eds. N. Hansen et al. (Risø Nat. Lab., Roskilde, 1981), p. 15
1.5 R. Feynmann, "There is plenty of room at the bottom", talk given on Dec. 29th 1959 at the annual meeting of the American Physical Society at the California Institute of Technology (Caltech); published in Caltech's Engineering and Science, Feb. 1960. (see also: http://www.zyvex.com/nanotech/feynman.html)
1.6 M. Roukes, Sci. Am., Sept. 2001, p. 42
1.7 G. Stix, Sci. Am., Sept. 2001, p. 26
1.8 M. Faraday, Philos. Trans. Royal Soc. **147**, 145 (1857)
1.9 L. Becker et al., Nature **400**, 227 (1999)
1.10 Neue Zürcher Zeitung, Folio, Feb. 1999, p. 65
1.11 K.E. Drexler, *Engines of creation: The coming era of nanotechnology*, (Oxford University Press, Oxford, 1986); K.E. Drexler, C. Terson, G. Pergamit, *Unbounding the Future: The Nanotechnology Revolution* (Morrow, New York, 1991); K.E. Drexler, *Nanosystems: Molecular Machinery, Manufacturing, and Computation*, (Wiley, New York, 1992)
1.12 J. Aizenberg et al., Nature **398**, 495 (1999)
1.13 G. Moore, Electronics **38**, 8 (1965)
1.14 G.E. Moore, ISSCC Dig. Tech. Pap. 20 (2003)
1.15 J. Wood, Materials today **11**, Jan-Feb 2008, p. 40
1.16 O. Bourgeois et al., Phys. Rev. Lett. **94**, 057007 (2005)
1.17 G.M. Whitesides, Sci. Am., Sept. 2001, p. 70
1.18 Nanotechnologie, German Federal Ministry of Education and Research, May 2004, p. 35
1.19 A.M. Hermansson et al., MRS Bull., Dec. 2000, p. 30
1.20 C.L. Jia, K. Urban, Science **303**, 2001 (2004)
1.21 D. Attwood, Nature **442**, 642 (2006)
1.22 M. di Ventra et al. (eds.), *Introduction to Nanoscale Science and Technology* (Springer, New York, 2004)
1.23 E.L. Wolf, *Nanophysics and Nanotechnology* (Wiley-VCH, Weinheim, 2006)
1.24 G.L. Hornyak et al., *Introduction to Nanoscience and Nanotechnology* (Taylor and Francis Group, Boca Raton, 2009)
1.25 I. Thomas, P. Dehmer, MRS Bull., October 2001, p. 761
1.26 C. Macilwain, Nature **405**, 730 (2000)
1.27 http://www.nano.org.uk/nanomasters (2009)
1.28 Whitfield, Nature **451**, 872 (2008)
1.29 M. Kemp, Materials today **12**, May 2009, p. 55
1.30 C.G. Li et al., J. Mol. Cell Biol. **1**, (2009), doi: 10.1093/jmcb/mjp002
1.31 J. Kerry, US Senator, Press Release May 7, 2008
1.32 Commission of the European Union, see Stuttgarter Nachrichten June 17, 2008
1.33 N. Lewinski et al., Small **4**, No. 1, 26 (2008)
1.34 K.E. Drexler, Spektrum der Wissenschaft, Spezial 2, 2001, p. 64
1.35 B. Joy, Wired, April 2000; Frankfurter Allgemeine Zeitung June 6, 2001

1.36 R.E. Smalley, Sci Am, Sept. 2001, p. 68
1.37 G.M. Whitesides, Sci Am, Sept. 2001, p. 70
1.38 A.P. Alivisatos, Sci Am, Sept. 2001, p. 59
1.39 H. Störmer, Wirtschaftswoche, December 21, 2000
1.40 H. Markl, Frankfurter Allgemeine Zeitung, January 13, 2001
1.41 H. Rohrer, Neue Züricher Zeitung, August 22, 2001
1.42 J.A. Moore, Nature **442**, 747 (2006)
1.43 T. Shelley, *Nanotechnology: New Promises, New Dangers*, (Zed Books, London, 2006)
1.44 D.J. Evans et al., Phys. Rev. Lett. **71**, 2401 (1993)
1.45 G.M. Wang et al., Phys. Rev. Lett. **89**, 050601 (2002)
1.46 K.K. Nanda et al., Phys. Rev. Lett. **91**, 106102 (2003)
1.47 R. Lamber et al., Phys Rev. B **51**, 1096B (1995)
1.48 A.N. Goldstein et al., Science **256**, 1425 (1992)
1.49 M. Blackman et al., Nature **217**, 1245 (1968)
1.50 A. Rytkönen et al., J. Chem. Phys. **106**, 1888 (1997)
1.51 O. Chiatti et al., Phys. Rev. Lett. **97**, 056601 (2006)
1.52 P. Kim et al., Phys. Rev. Lett. **87**, 215502 (2001)
1.53 S. Berber et al., Phys. Rev. Lett. **84**, 4613 (2000)
1.54 D.R. Lide, *CRC Handbook of Chemistry and Physics*, (CRC Press, New York, 1998)
1.55 B.T. Kelley, *Physics of Graphite* (Applied Science Publishers, London, 1981)
1.56 T. Yamamoto et al., Phys. Rev. Lett. **92**, 075502 (2004)
1.57 O. Narayan, S. Ramaswamy, Phys. Rev. Lett. **89**, 200601 (2002)
1.58 R. Livi and S. Lepri, Nature **421**, 327 (2003)
1.59 K. Schwab et al., Nature **404**, 974 (2000)
1.60 B.F. Borisov et al., Phys. Rev. B **58**, 5329 (1998)
1.61 S. Chacko et al., Phys. Rev. Lett. **92**, 135506 (2004)
1.62 M. Schmidt, H. Haberland, C.R. Physique 3, 327 (2002)
1.63 K.K. Nanda et al., Phys. Rev. Lett. **89**, 256103 (2002)
1.64 G.A. Breaux et al., Phys. Rev. Lett. **91**, 215508 (2003)
1.65 A.A. Shvartsburg, M.F. Jarrold, Phys. Rev. Lett. **85**, 2530 (2002)
1.66 C.E. Bottani et al., Phys. Rev. B **59**, R15601 (1999)
1.67 M. Dippel et al., Phys. Rev. Lett. **87**, 095505 (2001)
1.68 K.M. Unruh et al., Phys. Rev. B **48**, 9021 (1993)
1.69 Yu. A. Kumzerov et al., Phys. Rev. B **52**, 4772 (1995)
1.70 M.S. El-Shall, A.S. Edelstein, in *Nanomaterials*, eds. by A.S. Edelstein, R.C. Cammerata, 10 P, (Bristol, 1996) p. 13
1.71 E. Tombari et al., J. Chem. Phys. **122**, 104712 (2005)
1.72 R. Lamber et al., Phys. Rev. B **51**, 10968 (1995)
1.73 H. Hofmeister et al., Appl. Phys. Lett. **70**, 1694 (1997)
1.74 M. Larson et al., Phys. Rev. Lett. **68**, 3896 (1992)
1.75 C. Tien et al., Phys. Rev. B **54**, 11880 (1996)
1.76 M. J. Graf et al., Phys. Rev. B **45**, 3133 (1992)
1.77 X.Y. Lang et al., Phys. Rev. B **73**, 224444 (2006)
1.78 J.A. Duffy et al., J. Phys. Condens. Matte. **7**, 27L (1995)
1.79 H. Reichert et al., Phys. Rev. Lett. **78**, 3475 (1997)
1.80 S.B. Quadri et al., Phys. Rev. Lett. **69**, 2205 (1996)
1.81 R. Garvie, J. Phys. Chem. **69**, 1238 (1965)
1.82 G. Baldinozzi et al., Phys. Rev. Lett. **90**, 216103 (2003)
1.83 C.P. Poole, F.J. Owens, *Introduction to Nanotechnology*, (Wiley-Interscience, Hoboken, 2003)
1.84 L.P. Kouwenhoven, P.L. McEuen, in *Nanotechnology*, ed. G.L. Timp, (Springer, New York, 1999), p. 471
1.85 M. Tinkham, Phil. Mag. **B79**, 1267 (1999)

1.86 J.-C. Charlier et al., Rev. Mod. Phys. **79**, 677 (2007)
1.87 Z. Ristivojevic, T. Nattermann, Phys. Rev. Lett. **101**, 016405 (2008)
1.88 J.M. Luttinger, Phys. Rev. **119**, 1153 (1960)
1.89 R. Egger et al., Phys. Rev. Lett. **79**, 5082 (1997)
1.90 C.L. Kane et al., Phys. Rev. Lett. **79**, 5086 (1997)
1.91 C.L. Kane, M.P.A. Fischer, Phys. Rev. B **46**, 15233 (1992)
1.92 J. Voit, Rep. Prog. Phys. **58**, 977 (1995)
1.93 S. Eggert, Phys. Rev. Lett. **84**, 4413 (2000)
1.94 M.M. Fogler, Phys. Rev. Lett. **94**, 056405 (2005)
1.95 A.M. Chang et al., Phys. Rev. Lett. **77**, 2538 (1996)
1.96 O.M. Auslaender et al., Science **295**, 825 (2002)
1.97 H. Ishii et al., Nature **426**, 540 (2003); V. Meden, R. Claessen, Physik J. **3**(2), 16 (2004)
1.98 N. Giordano, Physica B **203**, 460 (1994)
1.99 G. Schön, Nature **404**, 948 (2000)
1.100 M. Zgirski et al., Nano Lett. **5**, 1029 (2005)
1.101 A. Bezryadin et al., Nature **404**, 971 (2000)
1.102 A.D. Zaikin et al., Phys. Rev. Let. **78**, 1552 (1997)
1.103 M.M. Özer et al., Nature Physics **2**, 173 (2006)
1.104 S.Y. Qin et al., Science **324**, 1314 (2009)
1.105 P.W. Anderson, J. Phys. Chem. Solid. **11**, 26 (1959)
1.106 S. Bose et al., Phys. Rev. Lett. **95**, 147003 (2005)
1.107 M.N. Baibich et al., Phys. Rev. Lett. **61**, 2472 (1988)
1.108 G. Binasch et al., Phys. Rev. B **39**, 4828 (1989)
1.109 A. Fert, Rev. Mod. Phys. **80**, 1517 (2008)
1.110 P.A. Grünberg, Rev. Mod. Phys. **80**, 1531 (2008)
1.111 G.A. Prinz, Science **282**, 1660 (1998)
1.112 S.A. Wolf et al., Science **294**, 1488 (2001)
1.113 R. Winkler, M. Oestreich, Phys. J. **3**(11), 39 (2004)
1.114 Žutić et al., Rev. Mod. Phys. **76**, 323 (2004)
1.115 J.G. Zhu, C. Park, Materials today **9**, November 2006, p.36
1.116 S. Ynasa et al., Appl. Phys. Lett. **89**, 042505 (2006)
1.117 C. Tsang et al., IEEE Trans. Magn. **30**, 3801 (1994)
1.118 M.K. Ho et al., IEEE Trans. Magn. **37**, 1691 (2001)
1.119 S. Datta, B. Das, Appl. Phys. Lett. **56**, 665 (1990)
1.120 B.T. Jonker, Proc. IEE. **91**, 727 (2003)
1.121 H. Akinaga, H. Ohno, IEEE T. Nanotechnol. **1**, 19 (2002)
1.122 H. Saito et al., Phys. Rev. Lett. **90**, 207202 (2003)
1.123 T. Dietl, H. Ohno, Materials today **9**(11), 18 (2006)
1.124 M. Oestreich et al., Semicond. Sci. Technol. **17**, 285 (2002)
1.125 R. Fiederling et al, Nature **402**, 787 (1999)
1.126 J.M. Kikkawa et al., Physica E **9**, 194 (2001)
1.127 M. Yokoyama et al., J. Appl. Phys. **97**, 10 317 (2005)
1.128 D.S. Han et al., Appl. Phys. Lett. **86**, 032506 (2005)
1.129 P. Schwab, Phys. J. **5** (11), 20 (2006)
1.130 N.P. Stern et al., Phys. Rev. Lett. **97**, 126603 (2006)
1.131 M. Boeckl, D. Graham, Mater. Matt. (Sigma-Aldrich. **1**, 3 (2006)
1.132 G.A. Ozin et al., Materials today **12**, May 2009, p. 12
1.133 G.M. Whitesides, B. Grzybowski, Science **295**, 2418 (2002)
1.134 G. Manai et al., Phys. Rev. Lett. **101**, 165701 (2008)
1.135 H. Brune et al., Nature **394**, 451 (1998)
1.136 U. Schlickum et al., J. Am. Chem. Soc. **130**, 11778 (2008)
1.137 R.M. Erb et al., Nature **457**, 999 (2009)
1.138 J. Sharma et al., Science **323**, 112 (2009)

1.139 H. Li et al., Materials today **12**, May 2009, p. 24
1.140 E.S. Andersen et al., Nature **459**, 73 (2009)
1.141 S.M. Douglas et al., Nature **459**, 414 (2009)
1.142 J.W. Zheng et al., NanoLett. **6**, 1502 (2006)
1.143 H.B.G. Casimir, Proc. K. Ned. Akad. Wet. **51**, 793 (1948)
1.144 H.B. Chan et al., Phys. Rev. Lett. **101**, 030401 (2008)
1.145 A. Lambrecht, Phys. Unserer Zeit **36**(2), 85 (2005)
1.146 A. Lambrecht, Nature **454**, 836 (2008)
1.147 J.N. Munday et al., Nature **457**, 170 (2009)
1.148 M.E. Fisher, P.-G. De Gennes, Acad. Sci. Paris B **287**, 207 (1978)
1.149 C. Hertlein et al., Nature **451**, 172 (2008)
1.150 R.G. Knobel, A.N. Cleland, Nature **424**, 291 (2003)
1.151 A.K. Naik et al., Nat. Nanotechnol. **4**, 445 (2009)
1.152 K.L. Eknici et al., J. Appl. Phys. **95**, 2682 (2004)
1.153 T.P. Burg et al., Nature **446**, 1066 (2007)
1.154 C. Degen, Nat. Nanotechnol. **3**, 643 (2008)
1.155 G. Balasubramanian et al., Nat. Mater. **8**, 383 (2009)
1.156 J.R. Maze et al., Nature **455**, 644 (2008)
1.157 C.L. Degen et al., Proc. Natl. Acad. Sci. USA **106**, 1313 (2009)
1.158 A. Sandhu, Nat. Nanotech. **4**, 142 (2009)
1.159 W.D. Wise et al., Nat. Phys. **5**, 213 (2009)
1.160 T. Ichimura et al., Phys. Rev. Lett. **102**, 186101 (2009)
1.161 K.M. Tyner et al., Biophys. J. **93**, 1163 (2007)
1.162 L.M. Loew, Pure Appl. Chem. **68**, 1405 (1996)
1.163 C.J. Chang, Nature **448**, 654 (2007)
1.164 O. Tour et al., Nat. Chem. Biol. **3**, 423 (2007)

Chapter 2
Microscopy – Nanoscopy

Microscopy – or literally nanoscopy – is of pivotal importance for the atomic-scale characterization of the structure, composition or bonding of nanosystems, for the understanding of electronic, optical, or magnetic properties of nanostructures, or for the elucidation of the dynamics of chemical and physiological nanoscale phenomena. The invention of the scanning probe techniques, such as the scanning tunneling microscope (STM) [2.1], the atomic force microscope (AFM) [2.2], or the scanning near-field optical microscope (SNOM) [2.3] with all their variants enormously stimulated the early development of nanoscience and surface microscopy [2.4–2.6]. Novel approaches emerged to overcome the diffraction (Abbé) limit of far-field optical microscopy [2.7, 2.8], which is of particular interest for nanoscale studies in life science [2.9]. A number of scanning probe techniques are available for magnetic imaging [2.10] (see also Sect. 8.1). In electron microscopy, which has been invented nearly 80 years ago [2.11], substantial progress toward subatomic resolution and accuracy has been achieved by aberration correction designs [2.12–2.14]. The rapid development of x-ray microscopy [2.15] was initiated with the advent of powerful synchrotron x-ray sources and the intense x-rays from upcoming free-electron lasers [2.16] promise even the imaging of free single molecules [2.17]. The 3D atom probe [2.18] with its atomic-scale structural and compositional resolution capabilities has been developed starting from the field-ion microscope [2.19] by which a single atom has been "seen" for the first time.

In the following, some recent developments of these microscopy techniques with relevance to nanoscience will be outlined.

2.1 Scanning Tunneling Microscopy (STM)

In the cases of STM or AFM, atomic resolution has been achieved and manipulation on the atomic or molecular scale has been made possible. The atomic resolution capability in real space has important consequences:

(i) Surface structures, either given by nature or artificially created, can be monitored and controlled on an atomic scale.
(ii) The tip can be positioned with atomic accuracy above a preselected atomic site and a local experiment can be performed.

H.-E. Schaefer, *Nanoscience*, DOI 10.1007/978-3-642-10559-3_2,

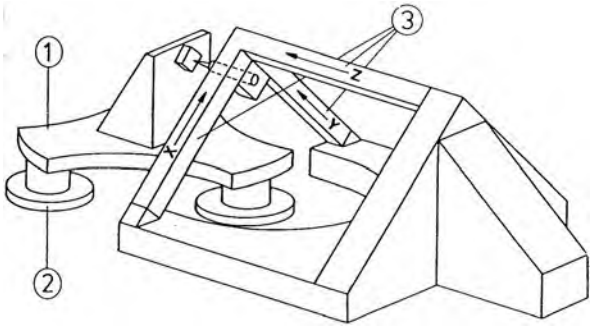

Fig. 2.1 Device with a piezoelectric base plate (*1*) and three feet (*2*) allowing the sample to be approached toward the tip which is mounted on a piezoelectric tripod scanner (*3*). (Reprinted with permission from [2.20]. © 1994 Cambridge University Press)

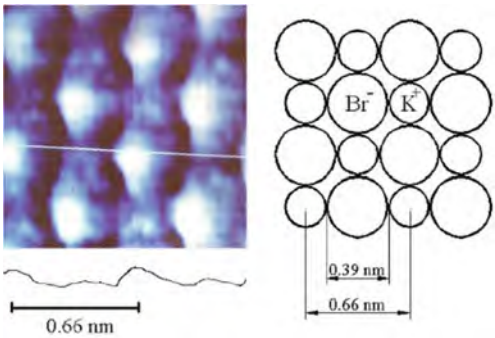

Fig. 2.2 Atomically resolved image of KBr(001) in contact AFM mode. The small and large protrusions are attributed to K+ and Br^- ions, respectively. (Reprinted with permission from [2.21]. © 2003 American Physical Society)

(iii) Atomic resolution together with atomic positioning of the tip leads to the controlled manipulation on the atomic level and the prospects of creating atomic-scale devices.

Scanning probe microscopes are operated after the following common principles: A very fine, nanosized probe tip interacts with a specimen surface and is scanned line by line over this surface. Commonly, the relative movement between tip and specimen surface is effectuated by piezodrives (see Fig. 2.1). The data registered by the tip in dependence of the lateral and normal movements are stored in a computer and displayed in a color code on a monitor (see Fig. 2.2). With the scanning probe microscopy techniques presently available, a wide field of applications in nanotechnology emerges.

2.1.1 Scanning Units, Electronics, Software

For atomic resolution of a surface, isolation of the microscope against vibrations is required. Piezoelectric drives can be used for the scanning units operating the 3D tip

motion (see Fig. 2.1). The bars or tubes with high stiffness offer high resonance frequencies making video scan rates possible without exciting vibrations. This enables the study of dynamic processes as, e.g., atomic surface diffusion. Furthermore, high sensitivity, large scan areas, and low thermal drifts are of importance.

By the electronics set-up, a tip bias voltage is supplied giving rise to a tunneling current which is compared to a preset current level in order to feed the difference signal into feedback amplifiers in the constant current imaging mode (see below). The experiments are equipped with computer control and data visualization.

The sensor tip, the most critical component of an STM, should have a small tip radius and a high-aspect ratio. Sharp tips can be prepared by electrolytical etching and ion milling [2.20]. Metallic tips can be magnetically modified for high-resolution magnetic sensing [2.10]. For chemical sensing on a nanometer scale carbon nanotube tips have been specifically modified (see Chap. 5.1).

2.1.2 Constant Current Imaging (CCI)

This is a widely used STM mode (see Fig. 2.3). As described earlier [2.20] a feedback loop adjusts the height of the tip during scanning so that the tunneling current flowing between tip and specimen is constant. Therefore, the recorded signal $U_z\left(U_x, U_y\right)$ can be translated into a "topography" $z\,(x, y)$, provided that the sensitivities of the three piezoelectric drives are known.

In a theoretical treatment of STM the tunneling probability of a 1D contact can be dealt with in a perturbative time-dependent approach (Bardeen's transfer Hamiltonian, see [2.20]). Within Bardeen's formalism, the tunneling current I can be evaluated in a first-order time-dependent perturbation theory according to

$$I = \frac{2\pi e}{\hbar} \sum_{\mu,\nu} \left\{ f\left(E_\mu\right)\left[1 - f\left(E_\nu + eU\right)\right] - f\left(E_\nu + eU\right)\left[1 - f\left(E_\mu\right)\right] \right\} \times \left|M_{\mu\nu}\right|^2 \delta\left(E_\nu - E_\mu\right)$$

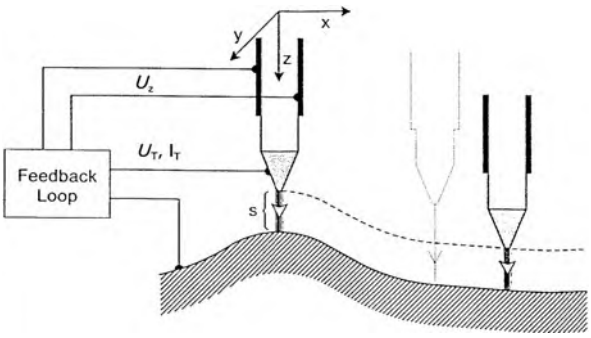

Fig. 2.3 Schematics of the constant current mode of STM operation. (Reprinted with permission from [2.20]. © 1994 Cambridge University Press)

where $f(E)$ is the Fermi function, U is the applied sample bias voltage, $M_{\mu\nu}$ is the tunneling matrix element between the unperturbed electronic states ψ_μ of the tip, and ψ_ν of the sample surface, E_μ (E_ν) is the energy of the state ψ_μ (ψ_ν) in the absence of tunneling, and the delta function describes the conservation of energy for the case of elastic tunneling. The essential issue is the calculation of the tunneling matrix element $M_{\mu\nu}$ [2.22] which requires explicit expressions for the wave functions ψ_μ and ψ_ν of the tip and of the sample surface, respectively. In the simplest model, an s-type tip wave function [2.23] is assumed. Then, the STM images obtained at low bias voltage in the constant current mode represent contour maps of constant surface local densities of states (LDOS) at the Fermi energy E_F of the sample surface, provided the s-wave approximation for the tip is justified. In this model the tunneling current

$$I \propto \exp(-2\kappa s)$$

is an exponential function of the distance s between tip and substrate with the decay rate κ. It should be mentioned that modifications of this model are necessary for the widely used W or Pt–Ir tips in STM studies because for these materials the density of states at the Fermi level is dominated by electronic d states rather than s states.

A direct comparison between an experimental constant current scan and a calculated contour of constant local density of states at the Fermi level using the adatom-on-jellium model was made for the case of xenon atoms adsorbed on a Ni(110) surface [2.24]. A reasonable agreement appears in Fig. 2.4 because Xe binds at relatively large distances from metal surfaces with a relatively large size of the Xe 6s orbital extending further out into the vacuum than the base-surface wave function.

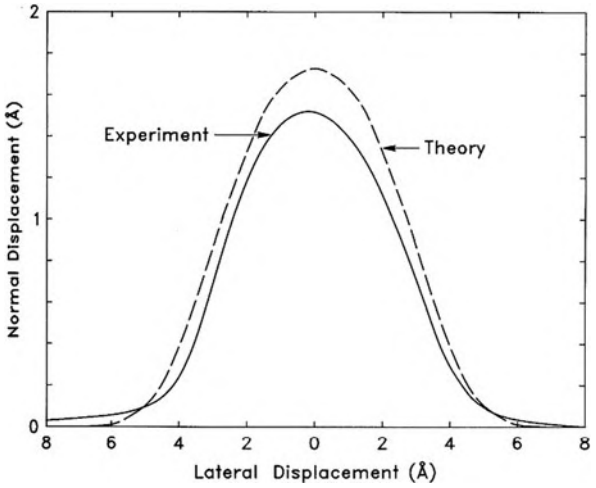

Fig. 2.4 A comparison of theoretical and experimental normal tip displacement versus lateral tip displacement for a Xe atom absorbed on a metal surface. (Reprinted with permission from [2.24]. © 1991 American Physical Society)

The lateral resolution in constant current STM is given by (see [2.20])

$$L_{\text{eff}} = \left[(R+s)/\kappa\right]^{1/2}$$

with the geometrical quantities R (tip radius) and s (distance between sample surface and front end of the tip) rather than by the wavelength of the tunneling electrons. This is the typical situation of the so-called near-field microscopes which are operated at distances (1.2–12 nm) between probe and sample that are not so large compared to the electron wavelength (0.3–1.0 nm). STM facilities are operated under UHV conditions not only at low temperatures but also at elevated pressures and temperatures [2.25].

2.1.3 Constant-Height Imaging (CHI)

In constant current imaging the data acquisition rate is limited by the time-consuming feedback loop. This feedback is switched off in the constant-height imaging (CHI) mode. In this mode the modulation of the tunneling current with the full sensitivity of the exponential current dependence on the tip-surface spacing reflects the atomic-scale topography (see Fig. 2.5). In this mode STM images can be collected at video rates for the observation of dynamic surface processes such as

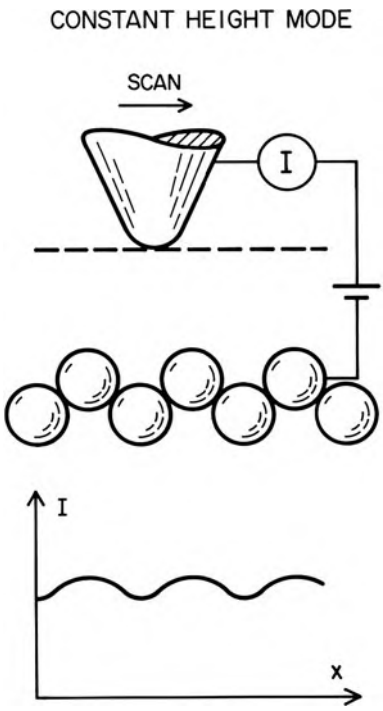

Fig. 2.5 Schematic of the constant-height mode of STM. (Reprinted with permission from [2.27]. © 1987 American Institute of Physics)

diffusion [2.26]. However, the CHI mode is preferably used for zooming to selected smaller surface areas of sufficient flatness.

2.1.4 Synchrotron Radiation Assisted STM (SRSTM) for Nanoscale Chemical Imaging

With STM, which conventionally is sensitive to conduction electrons, chemical information on the composition of a surface can be gained by photo-induced secondary electrons that are produced by core–electron excitation under synchrotron radiation [2.4]. Since the intensity of the secondary electrons emitted from the surface is proportional to the x-ray absorption probability of core–electrons, one can obtain the chemical "fingerprint" of an element by measuring with the STM the secondary electron intensities below and above the characteristic x-ray L absorption edge of, e.g., Ni or Fe (see Fig. 2.6). By this technique, checkerboard-patterned samples of Fe and Ni stripes on a thick Au film formed on Si (001) can be specifically detected (Fig. 2.6b, c) with a lateral resolution of $\sim$ 10 nm.

2.1.5 Studying Bulk Properties and Volume Atomic Defects by STM

The surface-sensitive STM technique can be used to study bulk properties of a crystal by exploiting the wave nature of electrons, e.g., in copper and study their interference patterns on the surface caused by scattering centers in the bulk of the material [2.28, 2.31]. Most solid-state properties can be characterized by the structure of the Fermi surface – the dividing line between the states occupied by an

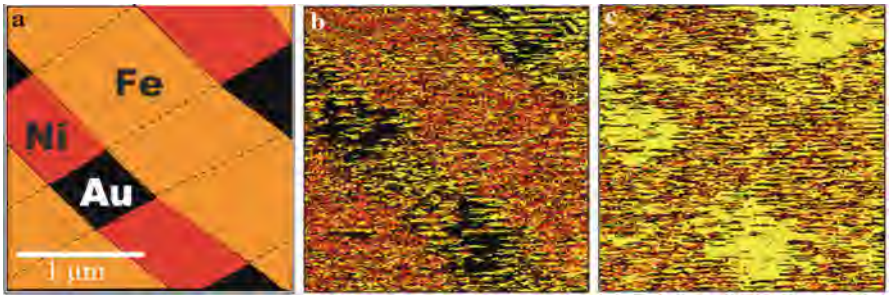

Fig. 2.6 (**a**) Schematic of an Fe and Ni checkerboard pattern as observed by synchrotron radiation assisted scanning tunneling microscopy (SRSTM). (**b**) Element-specific image of Fe obtained by dividing a photo-current image taken at the top of the Fe L_3 absorption edge ($h\nu = 706$ eV) by that at the bottom of the edge (698 eV). (**c**) Element-specific image of Ni obtained around the Ni L_3 absorption edge ($h\nu = 852$ and 843 eV). (Reprinted with permission from [2.4]. © 2009 American Physical Society)

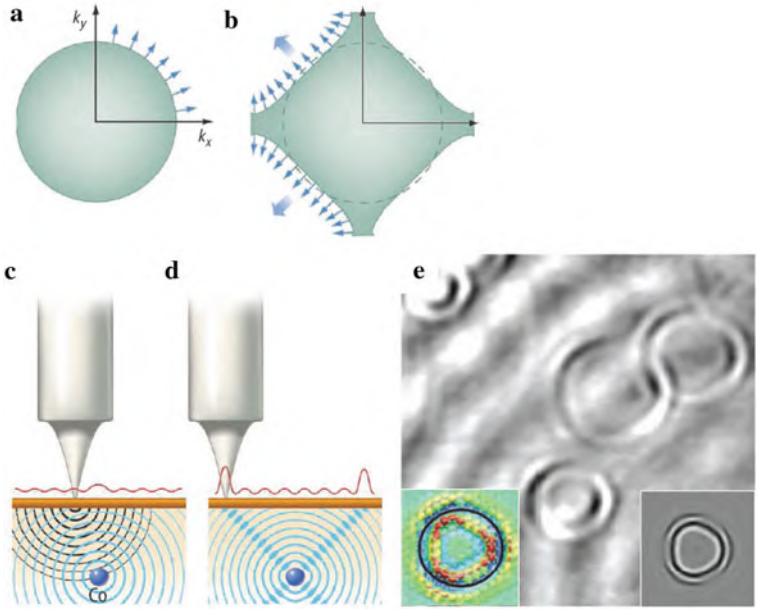

Fig. 2.7 (**a**) A nearly free-electron gas has a spherical Fermi surface. The *blue* arrows indicate the direction of electron propagation at the Fermi surface. (**b**) In the Fermi surface of Cu certain directions become preferred due to the non-spherical shape of the Fermi surface. The *thick* arrows indicate directions of electron focusing. (**c**) When a scatterer is present under the surface, the electron wave can be reflected. For a spherical Fermi surface this results in a weak interference pattern at the surface. (**d**) When the Fermi surface is not spherical, electron focusing is observed along certain directions which can give rise to a pronounced interference pattern at the surface [2.31]. (**e**) Scanning tunneling micrographs (STM) of four Co atoms below the Cu (111) surface (9 by 9 nm). The *right inset* shows (4 by 4 nm) the calculated local density of states (LDOS), whereas the *left inset* refers to density-functional theory (DFT) calculations. (Reprinted with permission from [2.28]. © 2009 AAAS)

electron and the empty states. The simplest model for electrons in a solid is the nearly-free electron gas with a spherical Fermi surface (Fig. 2.7a). A small deviation from a sphere, such as in Cu (Fig. 2.7b), allows to measure the shape of the bulk Fermi surface which is most frequently measured by quantum oscillations or photo-emission spectroscopy and calculated with density-functional theory (DFT) [2.31]. When an electron is injected from the tip of an STM into a sample, it propagates as a wave and eventually scatters or arrives back at the tip. This wave behavior of the electrons in the bulk is not visible in most STM images. The situation changes dramatically when a point defect is incorporated under the surface. A dramatic increase of the surface interference pattern is observed for Co atoms buried several layers underneath (Fig. 2.7e). This is ascribed to the shape of the Fermi surface: Along certain spatial directions, the amplitude of the scattered wave decays very slowly (see arrows in Fig. 2.7b). The electrons are scattered along beams of electron waves, a phenomenon referred to as electron focusing. When these beams

intersect the surface of the crystal, a strong and characteristically shaped interference pattern is observed containing information about the propagation of electrons through the bulk of the material, the shape of the Fermi surface, and the characteristics of the scattering potential below the surface. According to calculations [2.28], separate interference patterns (Fermi surfaces) should be observed for minority spin versus majority spin electrons in magnetic materials. Kondo resonances of electron scattering at a magnetic atom on a non-magnetic host were studied earlier [2.29, 2.30].

2.1.6 Radiofrequency STM

STM with an electronic band width as high as 10 MHz has been demonstrated [2.32]. This allows for high-sensitivity detection of high-frequency mechanical motion and is expected to be capable of quantum-limited position measurements (see Sect. 7.2).

2.2 Atomic Force Microscopy (AFM)

The scanning force microscope or atomic force microscope has been invented by Binnig et al. [2.33]. As shown in Fig. 2.8 a probetip is mounted on a cantilever type spring. The force interaction between the sample and the tip after approaching each other causes the cantilever to deflect according to Hooke's law

$$F = C \times \Delta z$$

where C denotes the spring constant and Δz the deflection. The AFM can be operated either in the contact regime or in the non-contact regime where, e.g., small van der Waals forces may be probed.

The most critical component is the cantilever-type spring with a sharp tip on one end. For a high sensitivity, a large deflection of a soft spring (with a low spring constant) for a given force is desirable. On the other hand, a high resonance frequency

$$\omega_0 = (C/m)^{1/2}$$

is necessary in order to minimize the influence of mechanical vibrations. Both conditions can be achieved only by keeping the mass, m, and therefore the geometrical dimensions small so that microfabrication techniques must be employed. Challenges in receiving atomic resolution and optimization of imaging parameters have been discussed [2.21].

The applicability of AFM techniques to bulk insulators is of particular importance where electron microscopical, spectroscopical, and STM studies are difficult because of charging effects.

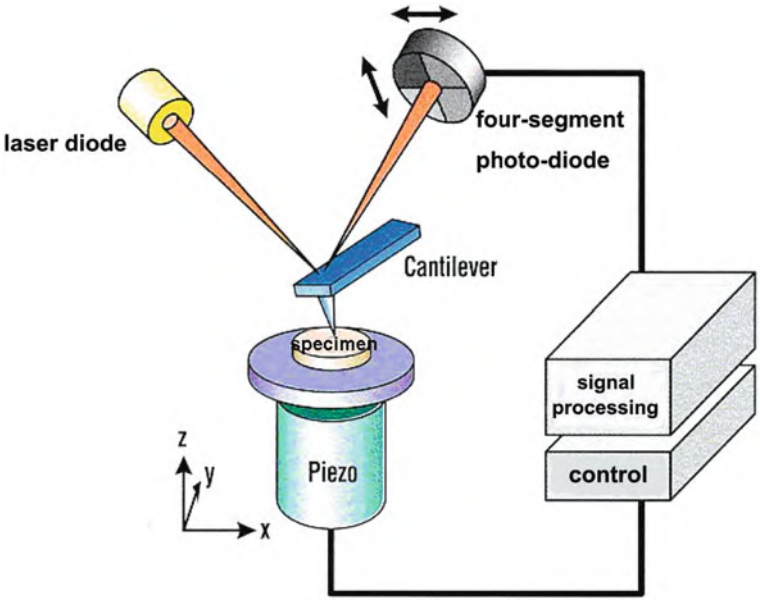

Fig. 2.8 Schematic set-up of an atomic force microscope (AFM) with a four-segment photodiode for detection of the laser beam deflection due to bending and twisting of the cantilever. (Reprinted with permission from [2.34]. © 1999 Karlsruher Institut für Technologie)

Mainly optical techniques (see Fig. 2.8) are employed in order to detect the cantilever deflection. In this set-up a laser beam is reflected from the cantilever and the cantilever displacement is measured by the detection of the reflected laser beam using a position-sensitive detector consisting of, e.g., four photoactive segments with eventually sub-Ångström sensitivity. By the four photoactive cells, vertical and lateral deflections (for, e.g., friction measurements) can be registered.

2.2.1 Topographic Imaging by AFM in Contact Mode

In this mode, where the tip and the sample are in contact, the interaction force causes the cantilever to deflect. In the constant force imaging (CFI) mode of AFM which is analogous to the constant current mode in STM, the cantilever deflection is kept constant by means of a feedback circuit. The output signal of the feedback loop U_z is recorded as a function of the (x, y) coordinates and can be translated into the "topography" $z\,(x, y)$. As equiforce surfaces are measured by AFM we have to consider the tip-surface interaction forces in the contact regime.

The invention of the AFM has considerably contributed to an increased interest in the force picture of quantum mechanical systems. The fundamental relationship

between energy and force pictures in quantum theory is expressed by the Hellmann–Feynman theorem [2.35–2.37] which states that if ψ is an exact eigenfunction of a Hamiltonian H with the eigenvalue E, then

$$\frac{\partial E}{\partial \lambda} \langle \psi | \psi \rangle = \left\langle \psi \left| \frac{\partial H}{\partial \lambda} \right| \psi \right\rangle$$

for any parameter λ occurring in the Hamiltonian H. This means that for a normalized wave function, the derivative of the energy with respect to a parameter λ is equal to the expectation value of the corresponding derivative of the Hamiltonian. If λ is taken as a coordinate of a nucleus, then one can derive the electrostatic Hellmann–Feynman theorem [2.37] resulting in the statement that the force acting on a nucleus in a system of nuclei and electrons can exclusively be interpreted in terms of classical electrostatics, once the electronic charge density has been obtained by an accurate self-consistent quantum-mechanical electronic structure calculation. The theorem is of central importance for the interpretation of AFM data similar to Bardeen's transfer Hamiltonian formalism for STM.

From these considerations one can deduce that in the contact regime, AFM measurements are expected to probe primarily the ion–ion repulsion forces which decrease rapidly with increasing tip-surface separation. This is in contrast to STM where the observation is dominated by the local surface electronic structure near the Fermi level which can substantially differ from the location of the ion cores. The strong distance dependence of the ion repulsion forces provides the key for the high spatial resolution achieved by contact force microscopy.

The atomic forces in real space can be derived by differentiating those terms in the Hamiltonian which explicitly depend on the positions of the ions [2.38].

The expression obtained exhibits two components. The first – denoted as F_{ion} – originates from the Coulomb repulsion between the ion cores, and the second, which is denoted by F_{el}, is due to the interaction of the valence electrons with the ion cores.

From this it is expected that in an AFM operated in the repulsive contact mode, $|F_{\text{ion}}| > |F_{\text{el}}|$ varies more rapidly with the position of the outermost tip atom than does F_{el}.

As the tip surface separation is increased, $|F_{\text{el}}|$ decays more slowly than $|F_{\text{ion}}|$ and $F_{\text{total}} = F_{\text{ion}} + F_{\text{el}}$ changes sign yielding a net attractive force. Yet, many AFM studies are performed in the strongly repulsive regime. With the high AFM spatial resolution, atomic-scale periodicities can be resolved by AFM in the case of, e.g., graphite, BN, Na, Cl, Au etc. Under the assumption of a monatomic tip it has been shown theoretically that repulsive forces of around 10^{-8}N can lead to a large elastic compression of, e.g., a graphite surface (see [2.20]). For a conclusive demonstration of the AFM atomic resolution capability of contact force microscopy, the observation of surface defects has particularly been important (see [2.20]). This means that the force interaction must, indeed, be highly spatially localized offering the possibility of probing single atomic sites with AFM, similar to the STM capabilities.

2.2.2 Frictional Force Microscopy

In friction of two contacting bodies the frictional force

$$F_{\mathrm{f}} = \mu \times F_1$$

is proportional to the loading force F_1 and independent of the apparent area of contact. The AFM geometry is well suited for nanoscale friction studies [2.39]. In addition to the cantilever bending normal to the surface, torsion mode deflections of the cantilever while scanning may occur in lateral motion with friction (see Fig. 2.9). The tip sliding process was found to be non-uniform with a stick-slip behavior. The slips actually exhibit the same spatial periodicity as, e.g., the graphite surface leading to the conclusion that the atomic surface structure determines the tip-surface interface (see Fig. 2.9).

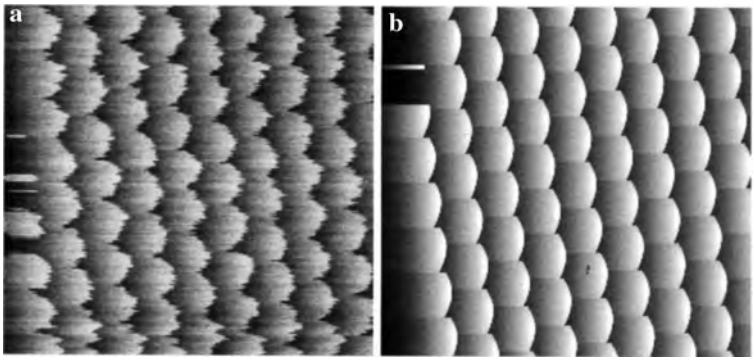

Fig. 2.9 (**a**) Comparison of the measured lateral forces F_1 on a graphite surface and (**b**) the correspondingly simulated forces. The image dimensions are 2 nm × 2 nm. (Reprinted with permission from [2.40]. © 1998 Wiley-VCH)

2.2.3 Non-contact Force Microscopy

The short-range interatomic forces are probed by measuring the quasistatic deflections of a cantilever beam with a well-known effective spring constant when the sample is scanned against the cantilever tip.

By increasing the tip-surface separation to 10–100 nm, only the long-range interaction forces as, e.g., van der Waals, electrostatic, or magnetic dipole forces remain. These forces can be probed by non-contact force microscopy. Instead of measuring quasistatic cantilever deflections, the cantilever is driven to vibrate near its resonance frequency by means of a piezoelectric element [2.33]. Changes in the resonance frequency as a result of tip-surface interaction are measured. This a. c.

technique is sensitive to force gradients rather than to the interaction forces themselves. The presence of the force gradient results in a modification of the effective spring constant.

If tip and sample are clean, electrically neutral and non-magnetic van der Waals forces are the sole sources of tip-sample interactions in the non-contact regime. In this case the spatial resolution achievable depends critically on the tip geometry and the tip-surface separation. For a good lateral resolution a, both the tip radius R and the tip surface separation s have to be small.

Van der Waals forces measured in vacuum are always attractive. An important field of electrostatic force microscopy (EFM) is direct imaging of domains and domain walls in ferroelectrics [2.41]. The charge signal changes its sign as the tip passes over the ferroelectric domain wall.

2.2.4 Chemical Identification of Individual Surface Atoms by AFM

By the force patterns emerging in AFM, the chemical nature of individual atoms on a surface that contains a mixture of elements can be identified [2.5, 2.42]. This is of interest because – in contrast to STM – AFM can be used for both insulating and conducting samples.

In the non-contact mode of the AFM, the resonance frequency of the AFM changes according to the specific interaction of the tip with the surface of the sample. By this the characteristic dependence of the force on the distance between the AFM tip and an individual atom can be measured [2.5]. The interaction between the tip and Si atoms in a Si–Sn–Pb surface alloy (see Fig. 2.10a, b) is strongest. The interaction forces observed between the tip and Si, Sn, or Pb atoms well match

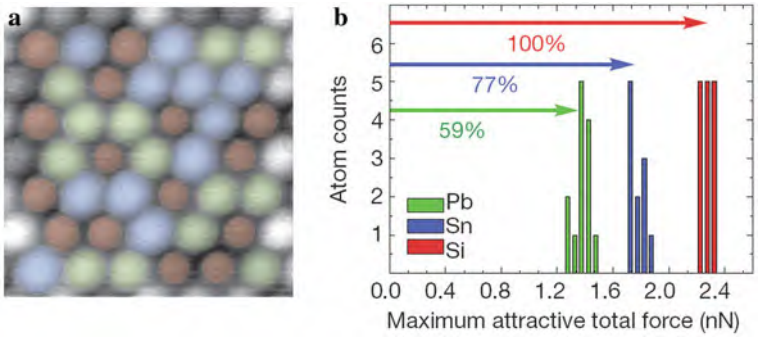

Fig. 2.10 (Fig. 698 P.C.): Single atom chemical identification of a Si–Sn–Pb surface alloy by AFM. (**a**) Local chemical composition of the surface. *Blue*, *green*, and *red* atoms correspond to Sn, Pb, and Si atoms, respectively. (**b**) Distribution of maximum attractive total forces measured over the atoms in (**a**). By using the relative interaction ratio determined for Sn/Si and Pb/Si, each of the three groups of forces can be attributed to interactions measured over Sn, Pb, and Si atoms. (Reprinted with permission from [2.5]. © 2007 Nature Publishing Group)

with atomistic modeling [2.5]. This technique provides the local composition and structure of a semiconductor surface on the atomic level.

By AFM techniques also the charge state of individual Au and Ag atoms on a NaCl film can be determined by quantifying the force response of a few piconewtons caused by a surplus charge [2.43].

2.2.5 AFM in Bionanotechnology

Atomic force microscopy is the only technique that provides sub-nanometer resolution under physiological conditions, needed for imaging biological species like proteins and living cells. Measurements of molecular recognition forces provide insight into the function and structure of biomolecular assemblies [2.44]. AFM is a companion technique to x-ray crystallography and electron microscopy (EM) for the determination of protein structures (see [2.44]).

For the investigation of soft biological membranes and supramolecular complexes, unfavorable probe-surface interactions in contact mode AFM, especially lateral forces, have been largely overcome by the development of dynamic force microscopy (DFM). The cantilever is oscillated close to its resonance frequency at an amplitude of a few nanometers as it scans the surface and touches the sample only at the end of its downward movement.

AFM images of plasmid DNA (pDNA) immobilized on mica (Fig. 2.11a) show the DNA molecules in a supercoiled state with two or more chains tightly overwound. DFM has been also used for studying the human rhinovirus (HRV), which causes the common cold, under physiological conditions (Fig. 2.11b). Topographical imaging of the virus capsid reveals a regular arrangement of 3 nm sized protrusions similar to that seen in cryoelectron microscopy studies (see [2.44]). Moreover, the binding of an antibody to surface antigens embedded in cell membranes has been studied by DFM. This is the primary event in the specific immune defense of vertebrates. Figure 2.11c, d shows a high-resolution image of a single antibody bound to its antigenic recognition sites (epitopes) on the 2D crystalline arrangement of bacteriorhodopsin (BR) molecules of mutant purple membranes from *Halobacterium salinarum*. Fab fragments, i.e., the fragment antigen binding regions (∼50 kDa) on membrane-bound antibodies, are allocated to antigenic sites at 1.5 nm lateral resolution on the purple membrane, allowing the identification and localization of individual epitopes [2.44].

2.3 Scanning Near-Field Optical Microscopy (SNOM)

By making use of scanning near-field optical microscopy, the spatial resolution can be substantially enhanced compared to classical optical microscopy and can reach nanometer resolution.

In classical optical microscopy the spatial resolution is limited by diffraction to about half the wavelength $\lambda/2$ (Abbé limit [2.48]). This limit originates from the

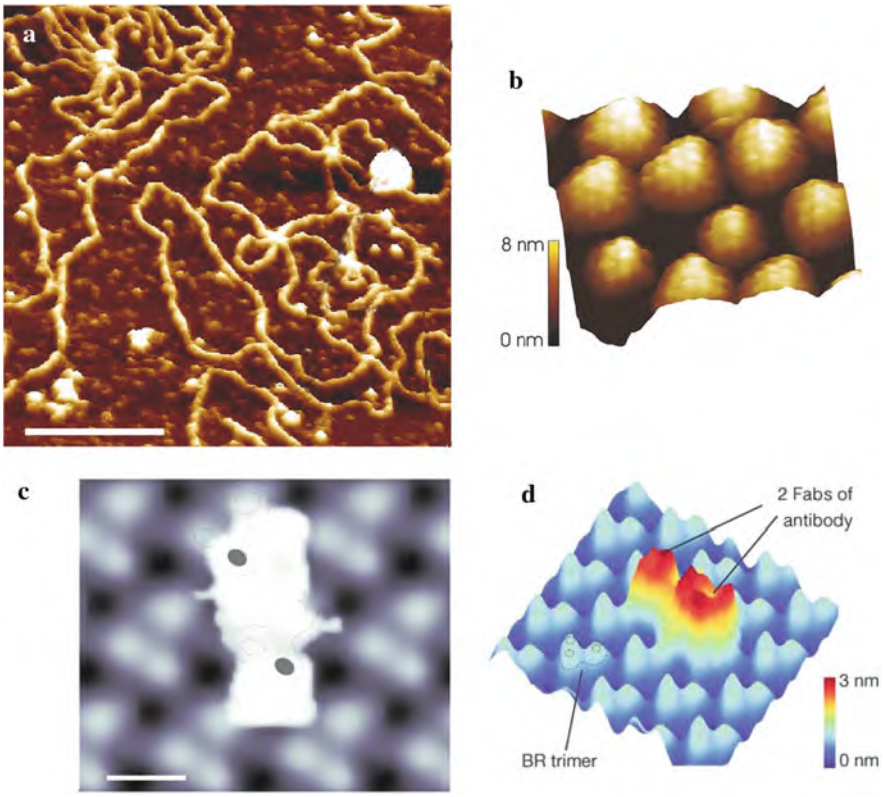

Fig. 2.11 High-resolution topographical imaging of biomolecular assemblies by atomic force microscopy (AFM). (**a**) 3 kbp (base pairs) plasmid DNA (pDNA) on mica; scale bar 150 nm [2.45]. (**b**) Dense packing of human rhinovirus (HRV) particles with regular patterns of small protrusions $\sim$ 0.5 nm high and $\sim$ 3 nm in diameter; width of the figure, ca. 70 nm [2.46]. (**c**) Topographical image of the purple membrane to which a single antibody is bound and (**d**) a 3D representation of two Fabs (fragment antigen binding regions of an antibody) bound to the bacteriorhodopsin (BR) molecules of mutant purple membranes from *Halobacterium salinarum* [2.44, 2.47]. (Reprinted with permission from [2.45] (**a**), [2.46] (**b**) and [2.47] (**c**) (**d**). © 2007 Elsevier (**a**), © 2005 Elsevier (**b**), © 2004 Nature Publishing Group (**c**) (**d**))

fact that electromagnetic waves interacting with an object are always diffracted into two components:

1. Propagating waves with low spatial frequencies ($< s/\lambda$), and
2. evanescent waves with high spatial frequencies ($> s/\lambda$)

where s is the tip-to-specimen spacing in near-field microscopy.

Whereas classical optics are concerned with the far-field regime where only the propagating fields survive, the evanescent waves are confined to sub-wavelength distances from the object corresponding to the near-field regime. Information about the high spatial frequency components of the diffracted waves is lost in the far-field

regime and therefore sub-wavelength features of the object to be imaged cannot be retrieved. On the other hand, by operating a microscope in the near-field regime the Abbé resolution limit can be surpassed [2.49]. The invention of the STM triggered increased effort in developing scanning near-field optical microscopy (SNOM).

As a characteristic of all scanning probe near-field microscopy methods the tip-to-specimen spacing s is small and typically far below the optical wavelength λ of the particular interaction to be studied. This means that the scanning probe near-field microscopes are operated in the near-field (NF) regime ($s \leq \lambda$) where the spatial resolution is determined by the tip-to-sample spacing and the effective radius of curvature of the probe tip, rather than the wavelength λ. In the far-field (FF) regime ($s > \lambda$), however, the optical resolution is diffraction limited.

2.3.1 Scanning Near-Field Optical Microscopy (SNOM)

In SNOM experiments a tiny aperture illuminated by a laser beam from the rear side is scanned across the sample surface (see Fig. 2.12). To achieve a high lateral resolution, which was of the order of 25 nm ($\lambda/20$) in the first experiments [2.50], the aperture had to be maintained at a distance of less than 10 nm from the object. This requirement arises because with increasing distance s from the aperture the evanescent waves are damped out rapidly with the field intensity $I \propto s^{-4}$. This fourth power dependence on distance in the NF regime is in contrast to the behavior in the FF regime where the field intensity decreases quadratically with distance.

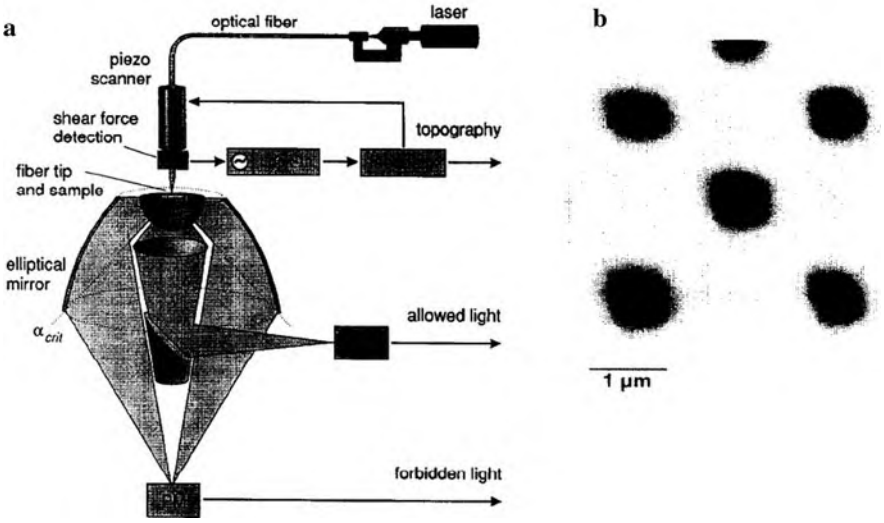

Fig. 2.12 (**a**) Set-up of a scanning near-field optical microscope (SNOM) combined with a conventional optical microscope. (**b**) SNOM signal of a Cr pattern on a glass substrate, imaged in transmission. (Reprinted with permission from [2.52]. © 1996 Elsevier)

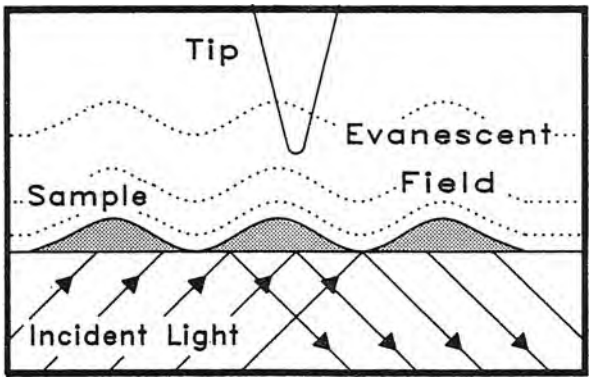

Fig. 2.13 Schematics of the photon scanning tunneling microscope (PSTM). The tip probes the sample-modulated evanescent field produced by an internally reflected light beam. (Reprinted with permission from [2.53]. © 1989 American Physical Society)

The optical probes (see Fig. 2.12) are formed by a sharpened glass or fiber tip coated with a thin metallic layer. The capability of fabrication of a nanometer-sized aperture is essential but is gained only at the expense of signal intensity. The tip-surface distance can be controlled by exploiting the force interaction [2.51]. SNOM can be performed in reflection or in transmission. In addition, SNOM can be combined with all techniques known in classical optical microscopy including the investigation of luminescence, polarization, or phase contrast (see [2.20]).

In close analogy to STM, a sharpened optical fiber tip can be used to probe the evanescent field above a dielectric in which total internal reflection (TIR) is made to occur. The specimen may form the TIR surface and spatially modulates the evanescent field (see Fig. 2.13). The tunneling of photons to the tip end of the optical fiber is detected by a photomultiplier tube connected to the other end of the fiber, while the object surface is scanned relatively to the tip by means of a piezostage. The lateral resolution achieved with this photon STM (PSTM) or evanescent field optical microscope (EFOM) is typically 50–100 nm.

2.3.2 Near-Field Scanning Interferometric Apertureless Microscopy (SIAM)

Unlike in regular near-field optical microscopy (SNOM), where the contrast results from a weak source (or aperture) dipole interacting with the polarizability of the sample, SIAM relies on sensing the dipole–dipole coupling of two externally driven dipoles (the tip and the sample dipoles) as their spacing is modulated. One can measure the scattered electric-field variation caused by a vibrating and scanning probe tip in close proximity to a sample surface (Fig. 2.14a) by encoding it as a modulation in the phase of one arm of an interferometer. In the transmission mode a laser beam is focused on the back surface of a transparent substrate holding the

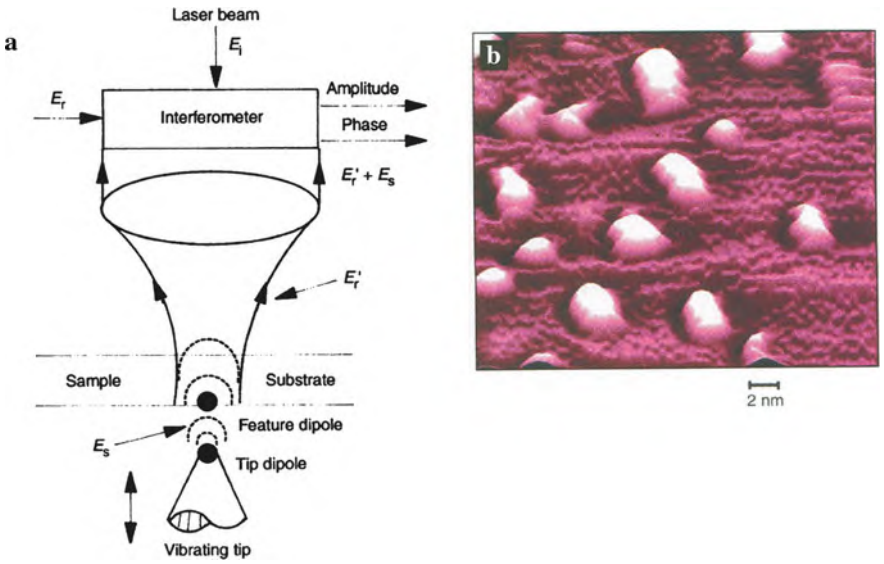

Fig. 2.14 (**a**) Principle of the near-field scanning interferometric apertureless microscope (SIAM) imaging method. (**b**) Optical SIAM image showing oil droplets as bright scattering regions on mica; smallest resolvable feature $\approx$ 1 nm. (Reprinted with permission from [2.54]. © 1995 AAAS)

sample (Fig. 2.14a). A tip vibrating with a frequency $f_z = 250$ kHz and an amplitude of 6–10 nm is brought close to the focused spot over the sample surface with an attractive mode atomic force microscope. The return beam $E_r' + E_s$ (reflection from the substrate plus tip-sample scattering) is detected with an interferometer by combining it with a reference beam E_r. The output signal of the interferometer measures either the amplitude of $(E_r' + E_s)$ or its phase difference with E_r, which represents the contrast mechanism [2.54]. Optical images and AFM can be recorded simultaneously. The optical image (Fig. 2.14b) shows oil droplets as enhanced scattering centers on mica. The smallest feature resolved optically is about 1 nm across and a phase change of 10^{-4} radian can be measured.

2.3.3 Mapping Vector Fields in Nanoscale Near-Field Imaging

The vectorial nature of electric fields can be mapped optically down to the nanoscale [2.55, 2.56] in addition to the detection of the intensity of light by conventional optical probes. Making use of an apertureless scanning near-field optical microscope, a polarizer is placed immediately before the CCD camera that is used to collect the light scattered by the nanoparticle tip in the near-field position (Fig. 2.15). For each tip position during the scan process the polarizer is rotated between 0° and 360° and a complete map of the vector state of the electric field at the tip position is

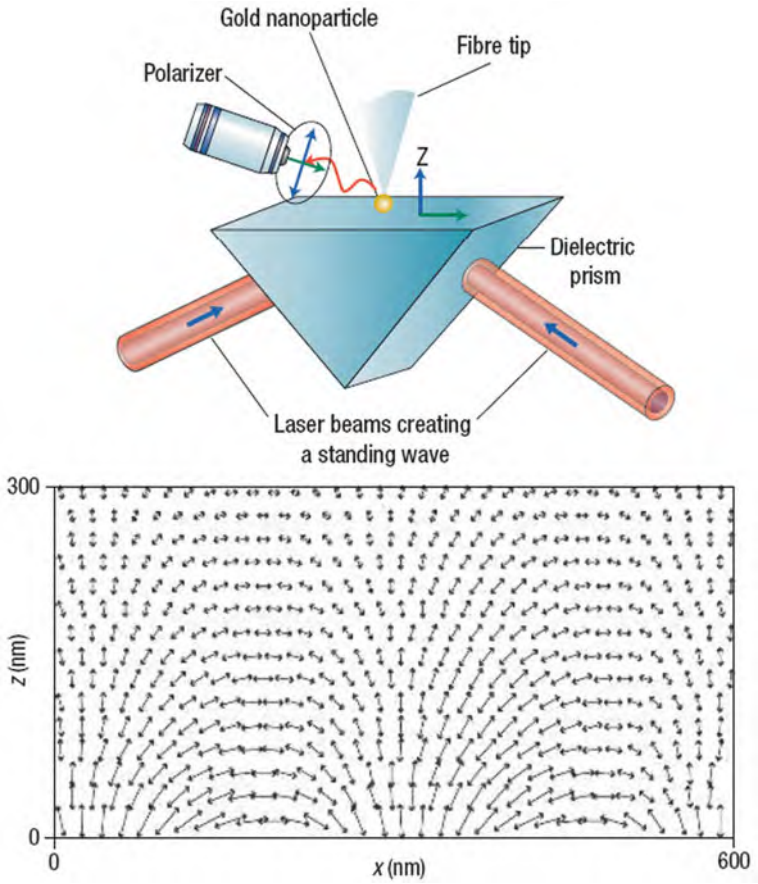

Fig. 2.15 The vector-field imaging device [2.55] combines an apertureless scanning near-field optical microscope with a polarizer, which allows for mapping both the size and the direction of electric-field vectors. (Reprinted with permission from [2.56]. © 2007 Nature Publishing Group)

derived. The knowledge of the electric vector field on the nanoscale could help in the design of miniaturized optical components and may be of importance in biosensing (see [2.56]).

2.3.4 Terahertz Near-Field Nanoscopy of Mobile Carriers in Semiconductor Nanodevices

Ultraresolving terahertz (THz) near-field microscopy based on THz scattering at atomic force microscope tips can specifically image charge carrier concentrations in semiconductor devices [2.6]. This is due to light-matter interactions at the low-energy THz frequencies exciting molecular vibrations and phonons, as well as plasmons and electrons of non-metallic conductors.

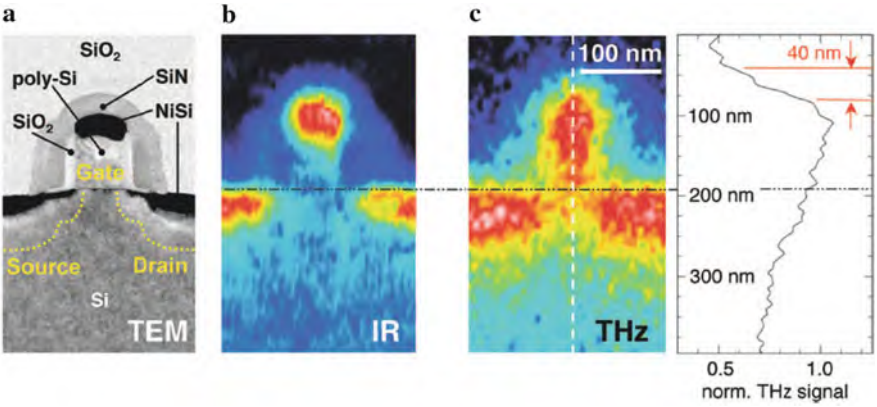

Fig. 2.16 Transmission electron micrograph (TEM) of a transistor. The highly doped regions below the source and drain NiSi contacts are marked by *dashed yellow lines*. (**b**) Infrared ($\lambda \approx 11\ \mu m$) image of a transistor. (**c**) High-resolution THz ($\lambda = 118\ \mu m$) image of the same transistor as in (**b**) showing all essential parts of the transistor: source, drain, and gate. The THz profile extracted along the *dashed white line* allows the estimation of a spatial resolution of about 40 nm. (Reprinted with permission from [2.6]. © 2008 American Chemical Society)

Nanoscale resolution is achieved by THz field confinement to a tip apex to within 30 nm, yielding a 40 nm ($\lambda/3000$) spatial resolution at 2.54 THz (wavelength $\lambda = 118\ \mu m$) for imaging of semiconductor transistors (see Fig. 2.16). Near-field THz microscopy provides a detection technique for mobile carriers in a concentration range centrally important for semiconductor science and technology ($n = 10^{16} - 10^{19}$ carriers/cm^3) where visible and infrared methods lack sensitivity. This is demonstrated in Fig. 2.16b, c where a transistor is illuminated with an infrared (IR) CO_2 laser at 28 THz ($\lambda = 11\mu m$) or a continuous-wave 2.54 THz CH_3OH gas laser, respectively. In contrast to the IR image (Fig. 2.16b), the THz image (Fig. 2.16c) also reveals the highly doped poly-Si gate and the highly doped Si regions (both $n \approx 10^{19}$cm^{-3}) just below the metallic NiSi source and drain contacts. In addition, THz near-field microscopy allows for probing the mobile carriers in the 65 nm wide region between source and drain which may open the possibility of future measurements of the carrier mobility in this most important part of nanoscale conductor devices.

2.4 Far-Field Optical Microscopy Beyond the Diffraction Limit

Light microscopy plays an enormous role in life sciences. It allows the detection of specific cellular constituents such as proteins, nucleic acids, and lipids under physiological conditions through fluorescence tagging but is conventionally restricted to the Abbé limit of spatial resolution of about 200 nm. Near-field optical techniques are qualified to enable high-resolution optical microscopy but only on surfaces and not in the interior of, e.g., living cells, where electron microscopy with atomic resolution power is inadequate because of intolerable radiation damage. Recently

developed far-field optical microscopy techniques such as stimulated emission depletion (STED) microscopy [2.7], stochastic optical reconstruction microscopy (STORM) [2.8], or photoactivated localization microscopy (PALM) [2.57] can substantially surpass the Abbé diffraction limit down to spatial resolutions of ~ 10 nm and potentially to molecular sizes [2.8, 2.9]. In addition, they can be used for 3D imaging [2.58, 2.59] and for video-rate imaging of fast nanoscale processes in living cells [2.9]. In these techniques, photoswitching of fluorophore molecules [2.60] plays an important role.

2.4.1 Stimulated Emission Depletion (STED) Optical Microscopy

This far-field fluorescence optical microscopy [2.61, 2.62] yields a focal plane resolution of 15–20 nm in biological samples which is a 20–40-fold increase in resolution beyond the diffraction limit. STED microscopy typically uses a scanning excitation illumination spot that is overlapped with a doughnut-shaped counterpart (see Fig. 2.17) for deexcitation of fluorophores by light, a phenomenon referred to as stimulated emission depletion. Oversaturation in the deexcitation suppresses emission in the doughnut and squeezes the fluorescence spot to sub-diffraction dimensions so that superresolved optical images emerge by scanning this spot through the object.

Making use of the 20 nm resolution provided by STED, optical studies of the nucleus of a fixed but otherwise intact mammalian cell can be performed. This appears to be suitable to bring further critical insight into how nuclear organization ensures regulated gene expression.

Figure 2.18 displays the protein-heavy subunit of neurofilaments in the human neuroblastoma cell line SH-SY5Y (retinoic acid–BDNF–differentiated), which establishes cross-links to organize and stabilize neurofilaments in axons (long process of a nerve fiber that conducts impulses to the nerve cell). Neurofilaments play an essential role in many neurodegenerative diseases, such as

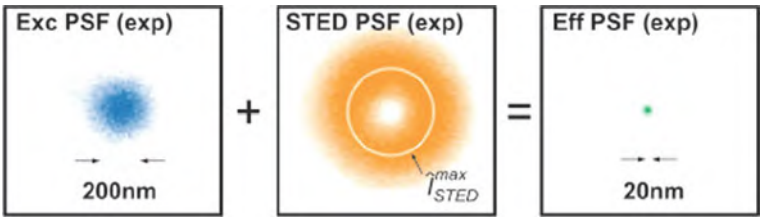

Fig. 2.17 Stimulated emission depletion (STED) microscopy. ExsPSF: measured focal spot for excitation (wave length 470 nm; *blue*; FWHM 190 nm); STED PSF:STED excitation, *doughnut shape*; (603 nm; *orange*); Eff PSF: the final spot yields a 22 nm effective size; $\hat{I}^{max}_{STED}$: crest intensity of the STED beam. (Reprinted with permission from [2.61]. © 2006 National Academy of Sciences U.S.A)

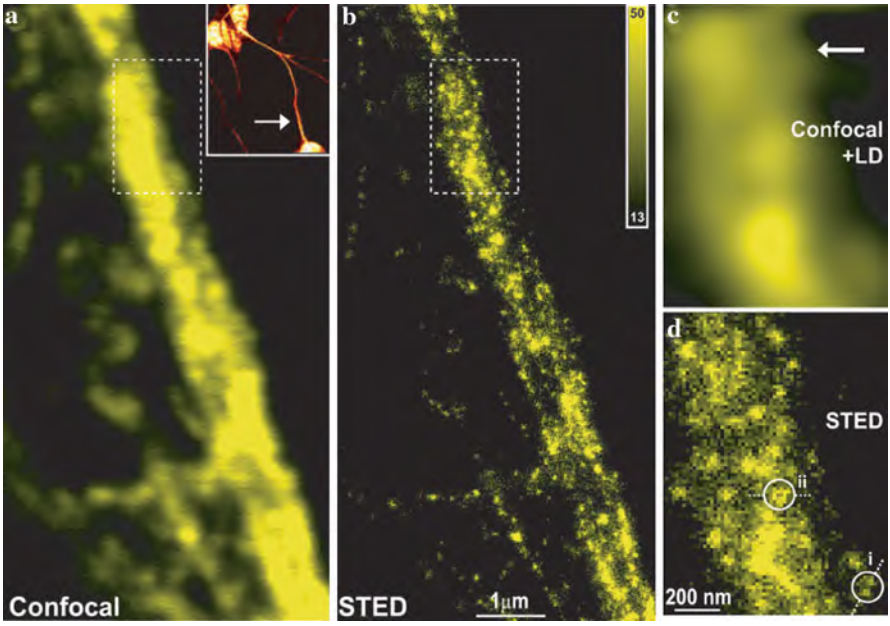

Fig. 2.18 Imaging nanofilaments in human neuroblastoma. (**a** inset) Low-magnification confocal image indicates the site of recording. (**a**–**d**) Contrary to the confocal recording (**a**), stimulated emission depletion (STED) recording (**b**) displays details <30 nm, as also highlighted by the comparison of image sub-regions shown in (**c**) and (**d**) bordered by *dashed lines* in (**a**) and (**b**) respectively. LD – linear deconvolution; (i) and (ii): measurements of line intensities for the determination of the imaging resolution. (Reprinted with permission from [2.61]. © 2006 National Academy of Sciences U.S.A)

Parkinson's disease. In contrast to the confocal image, the STED image identifies neurofilamental substructures of 20–30 nm.

In addition to the imaging of biomaterials, STED can image the position of color centers (atomic defects) in diamond with an accuracy of 0.15 nm and a resolution 28-fold smaller (8 nm; see Fig. 2.19) than can conventional fluorescence microscopy. This enables the addressing of the diamond color centers in much higher concentrations which may be of interest in quantum computing or cryptography. Fluorescent nanodiamonds could also be favorably used as biological markers because of their bleaching resistance [2.63].

2.4.2 Stochastic Optical Reconstruction Microscopy (2D-STORM)

In each cycle of this technique (see [2.8]), only a fraction of each of the fluorophores in the field of view is switched on, such that no images of the active fluorophores are overlapping. This allows the position of these separate fluorophores to be determined with high accuracy by fitting the point-spread function (PSF) of

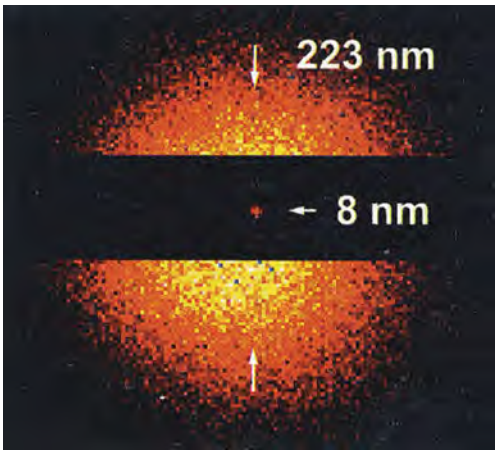

Fig. 2.19 High-resolution stimulated emission depletion (STED) optical microscopy for imaging of vacancy-nitrogen color centers in diamond with a resolution of 8 nm, 28-fold narrower than with conventional fluorescence microscopy which yields a focal spot of 223 nm in diameter. (Reprinted with permission from [2.63]. © 2009 Eva Rittweger and Stefan W. Hell, Max-Planck-Institut für Biophysikalische Chemie)

the emission by a Gaussian which gives the position of the PSF centroid with high precision. Repeating this process for multiple cycles, each causing a stochastically different subset of fluorophores to be turned on, allows the position of many fluorophores to be determined and thus an overall image to be reconstructed. Imaging resolutions of approximately 20 nm can be achieved by using a fluorescence microscope, low-power continuous-wave lasers, and a photo switchable cyanine dye [2.8].

2.4.3 Three-Dimensional Far-Field Optical Nanoimaging of Cells

Three-dimensional STED imaging deep inside a cell can be achieved by generating a spherical focal spot of ~ 45 nm ($\lambda/16$) in diameter by making use of two lasers. This gives rise to a spherical (isotropic) fluorescence spot (isoSTED) with essentially a diameter of

$$d \approx \lambda \Big/ (n\pi \sqrt{I_\mathrm{m}/I_\mathrm{s}}$$

where n is the refractive index of the sample, I_m the peak intensity of the doughnut beam (Fig. 2.17), and I_s the characteristic intensity for the quenching of the dye used [2.58]. By this isoSTED technique the distribution of mitochondrial proteins in mammalian cells has been studied [2.58]. Mitochondria are spherical or tubular organelles with inner and outer membranes. They contain genetic material and enzymes important for cell metabolism. In these organelles with diameters of 200–400 nm the protein distribution cannot be visualized by conventional light microscopy. The translocase of the mitochondrial outer membrane (TOM complex) serves as the mitochondrial entry gate for nuclear-encoded protein precursors. Acting as an import receptor, Tom20 is a subunit of TOM. For

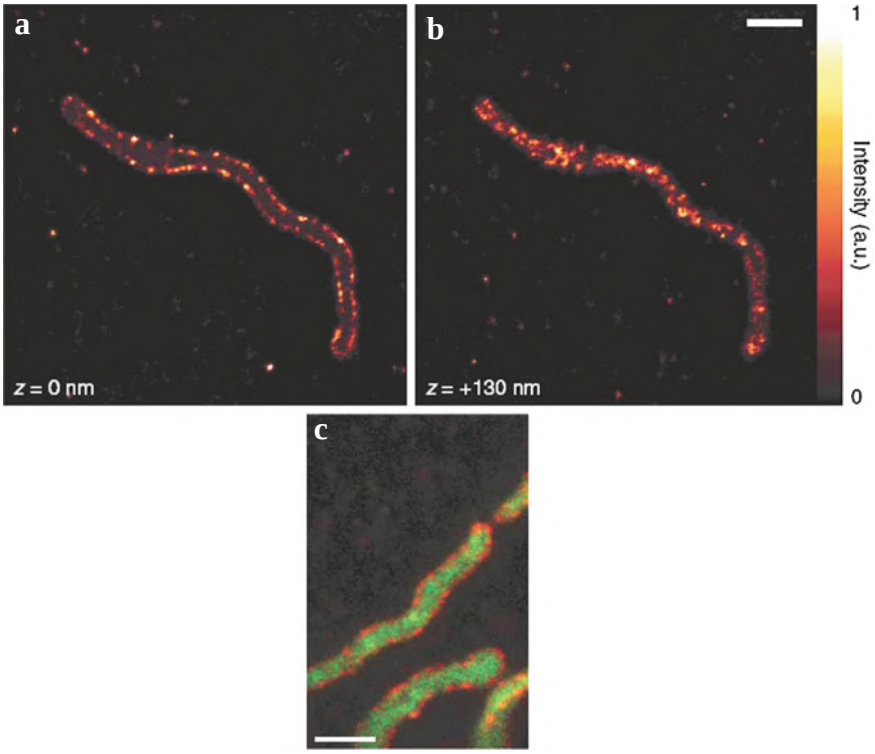

Fig. 2.20 (**a**–**b**) Stimulated emission depletion (isoSTED) fluorescence microscopy optical sections through the center (**a**) and the top (**b**) plane of a mitochondrion by focusing light into the interior of a mammalian cell with imaging the distribution of the Tom20 protein clusters. The *x*–*y* image through the center plane shows that the clusters are located at the rim of the organelle; scale bar, 1 μm. (**c**) Two-color isoSTED imaging of a mitochondrion of a mammalian cell with the outer membrane protein Tom20 labeled with NK51 (*red*) and the matrix protein mtHsp70 labeled with DY-485XL (*green*). Scale bar, 1 μm. (Reprinted with permission from [2.58]. © 2008 Nature Publishing Group)

visualization, Tom20 has been labeled with the orange-emitting fluorophore NK51 (see [2.58]). Two optical sections (*x*–*y* images) through the center and the top of mitochondrion inside a mammalian cell in Fig. 2.20a, b show that Tom20 forms distinct clusters at the boundary of the organelle. The isotropic 3D sub-diffraction resolution is essential to identify the peripheral localization of Tom20 [2.58]. As a demonstration of multiprotein imaging on the nanoscale, additionally the matrix protein mtHsp70, a component of the mitochondrial import motor conjugated with the fluorophore DY-485XL, has been visualized (see Fig. 2.20c).

Three-dimensional (3D) far-field optical imaging can also be achieved by stochastic optical reconstruction microscopy (STORM) with nanoscale resolution

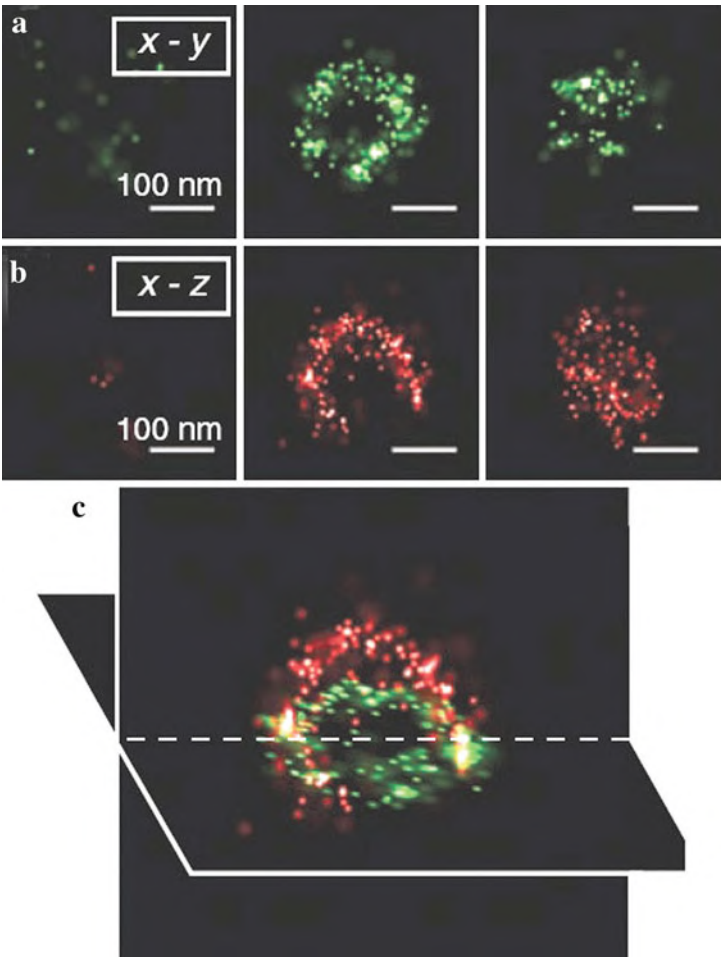

Fig. 2.21 Three-dimensional stochastic optical reconstruction microscopy (STORM) imaging of a clathrin-coated pit (CCP) in a monkey kidney epithelial (BS-C-1) cell. (**a**) Serial *x*–*y* cross-sections (each 50 nm thick in *z*) and (**b**) *x*–*z* cross-sections (each 50 nm thick in *y*) of a CCP and (**c**) an *x*–*y* and *x*–*z* cross-sections presented in a 3D perspective, showing the half-spherical cage-like structure of the pit. (Reprinted with permission from [2.59]. © 2008 AAAS)

making use of photoswitchable cyanine dyes [2.59]. In Fig. 2.21 *x*–*y* and *x*–*z* sections and a 3D rendering of clathrin-coated pits (CCPs) in monkey kidney epithelial (BS-C-1) cells are visualized by STORM. CCPs are spherical cage-like structures, about 200 nm in size, assembled on the cytoplasmic side of the cell membrane to facilitate endocytosis. The half-spherical cage-like morphology of the nanoscopic CCP structure can only be observed with 3D imaging and not with 2D images.

2.4.4 *Video-Rate Far-Field Nanooptical Observation of Synaptic Vesicle Movement*

In addition to nanoscale structural studies in cells, the investigation of fast physiological phenomena in vivo is of particular interest. Recently, the movement of synaptic vesicles in cultured hippocampal neurons (brain cells) has been recorded by video-rate (28 frames per second) STED microscopy with a focal spot size of 62 nm [2.9]. Vesicle movement has been difficult to study by conventional optical microscopy because of the small size of the ~40 nm diameter vesicles which are housed in presynaptic nerve terminals of ~1 μm in diameter, referred to as synaptic boutons. By video-rate STED, the vesicle movement with a speed peaking at 2 nm/ms (see Fig. 2.22) can be studied, showing that drugs can reduce vesicle mobility which indicates that active transport plays a role in vesicle traffic in axons. This study [2.9] demonstrates the emerging ability of optical microscopy to investigate intracellular nanoscale processes in real time.

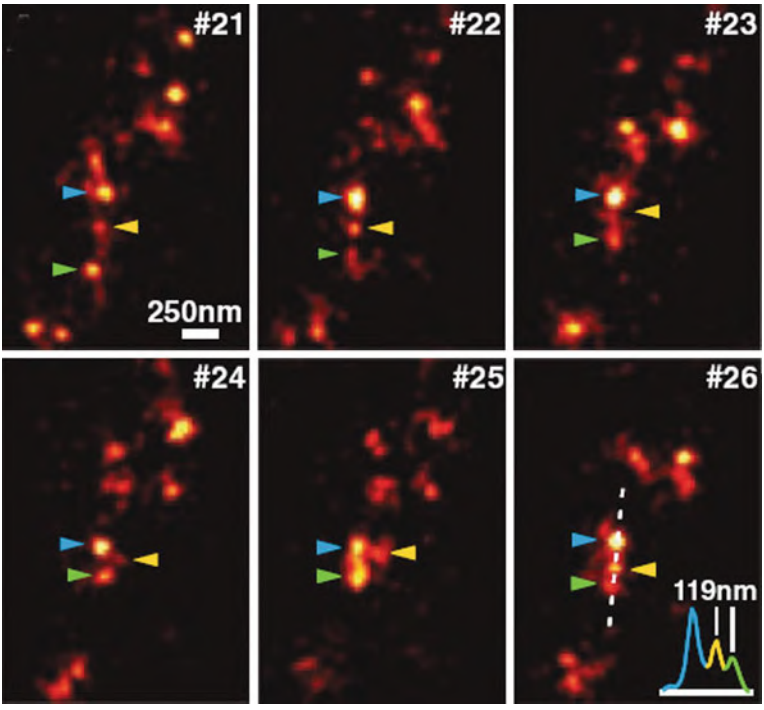

Fig. 2.22 Characteristics of synaptic vesicle movement. Successive frames of stimulated emission depletion (STED) microscopy. The *arrowheads* indicate three vesicles, which were tracked in all frames, localized in a sub-diffraction space. The inset in frame #26 shows an intensity profile along the *dotted white line*. (Reprinted with permission from [2.9]. © 2009 AAAS)

2.5 Magnetic Scanning Probe Techniques

The magnetic properties of solids, which arise due to the spin alignment of electrons, can be studied by scanning probe microscopy such as magnetic force microscopy (MFM; see [2.20, 2.64]) or, with atomic resolution, by spin-polarized scanning tunneling microscopy (SP-STM; see [2.10]). In addition to the brief survey given here, a more detailed discussion of magnetic nano-imaging will be given in Sect. 8.1.

2.5.1 Magnetic Force Microscopy (MFM)

The MFM non-contact imaging mode is sensitive to the magnetostatic dipole–dipole interaction between tip and sample. If a ferromagnetic tip approaches a magnetic sample surface within a distance of typically 10–50 nm, the tip interacts magnetically with the stray field emanating from the sample [2.65]. The long-range magnetic dipole interaction is usually probed by using the a. c. detection technique and gradients rather than the magnetic dipole forces are measured.

For a magnetic domain in the tip, that is small compared to the extent of the sample stray field B_s, the tip can be considered as a point dipole with the magnetic moment m yielding [2.66] a force

$$F(\text{dipole}) = \nabla\,(m \cdot B_s) = (m \cdot \nabla)\,B_s.$$

Therefore, in the point-dipole limit, the MFM images are closely related to the spatial distribution of the magnetic stray field gradient rather than the stray field.

Since magnetic forces F_{mag} may be either attractive or repulsive, problems with the feedback loop stability may emerge. Therefore, an attractive electrostatic force F_{el} via a bias voltage of 1–10 V between tip and specimen is applied. A separation of topography and magnetic structure has been demonstrated by imaging a discrete-track magnetic recording sample with the magnetic structure of bits (see Fig. 2.23).

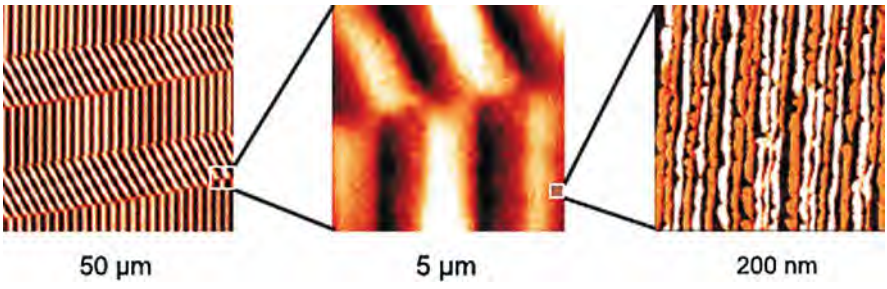

Fig. 2.23 Comparison of the different length scales involved in magnetic data storage. (**a**) and (**b**) show magnetic force microscopy (MFM) images of bit tracks of a magnetic tape whereas (**c**) shows a nanoscale magnetic medium where the imaging has been performed by spin-polarized tunneling microscopy (SP-STM) which is directly sensitive to the local magnetization rather than to the magnetic stray field sensed by MFM. (Reprinted with permission from [2.10]. © 2000 Wiley-VCH)

Care should be taken for not destroying the magnetic surface structure by the interaction of the magnetic tip (Ni or Ni-coated W) with the magnetic surface [2.64].

A requirement for high spatial resolution in MFM is to operate the probe tip close to the sample surfaces. Standard experimental resolution is typically of the order of 50–100 nm with a theoretical MFM resolution limit of about 5–10 nm (see [2.20]).

2.5.2 Spin-Polarized Scanning Tunneling Microscopy (SP-STM)

For distinguishing electrons with different spin alignments in magnetic solids by STM techniques, the probe tip can be coated with a thin film of magnetic material which exhibits a strong difference in the number of states with different spin orientations [2.67]. This leads to a difference in tunneling conductance for parallel or antiparallel alignment of the spins in the tip and the substrate. Due to the atomic resolution capabilities of the STM, spin structures down to the atomic level can be studied as demonstrated for ferromagnetic [2.68] or antiferromagnetic [2.69] specimens (see Fig. 2.24). In addition, novel magnetic devices for ultradense data storage

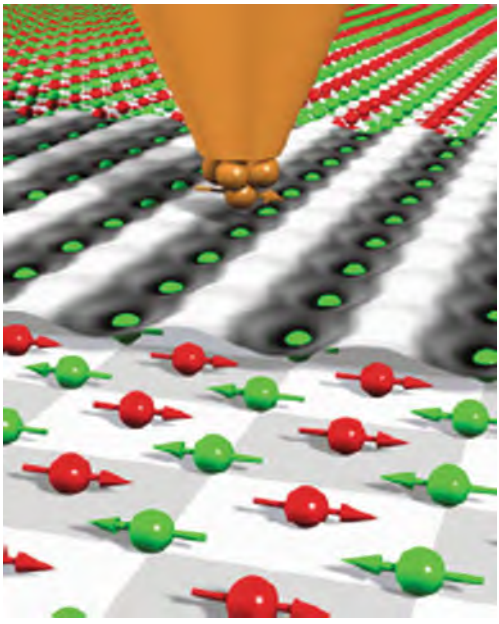

Fig. 2.24 Schematic of imaging a 2D antiferromagnet by means of spin-polarized scanning tunneling microscopy (SP-STM) making use of a magnetically coated probe tip. Depending on the relative spin orientation in the tip and in the substrate, the tunneling current differs and therefore enables the direct visualization of the antiferromagnetic structure on an atomic level. A single atomic layer of manganese on a tungsten substrate has been imaged by making use of an iron-coated probe tip at 16 K [2.69, 2.10]. The *green* and *red spheres* with the arrows symbolize the manganese atoms with opposite directions of the magnetic moments. The *black* and the *white* stripes in the center of the figure are experimental STM images (see [2.69]). (Reprinted with permission from [2.10]. © 2000 Wiley-VCH)

may be studied and controlled by the direct detection of the local magnetization in the near-field regime (Fig. 2.23c) instead of probing the long-range magnetic stray field (Fig. 2.23a, b).

2.6 Progress in Electron Microscopy

The transmission electron microscope, which was invented in the early thirties of the last century [2.11] (Nobel prize 1985 for Ernst Ruska) has since played a most important role in basic research, engineering, and medicine. Recent development in aberration correction, however, accelerated atomic resolution routines providing fundamental insight into nanotechnology. In addition, cryoelectron tomography is an important technique for the 3D observation in cell biology and electron tomography is also making progress in materials science.

2.6.1 Aberration-Corrected Electron Microscopy

One of the highest obstacles in improving the resolution of an electron microscope has always been the blurring of the image caused by lens aberrations, notably the spherical aberration. Rays passing through a spherically aberrated lens at a high angle to the optical axis are brought to a focus closer to the lens than the rays passing at a small angle to the optical axis (Fig. 2.25). These incorrectly focused high-angle rays produce a smearing in the image. The point resolution is given by $\sim C_s^{1/4}\lambda^{3/4}$ [2.70] where λ is the wave length and C_s the coefficient of spherical aberration. The point resolution limit can, therefore, be improved by reducing λ or by reducing C_s. In the past, by increasing the voltage of the electron beam to 1250 keV (electron wave length $\lambda = 0.74$ nm) a resolution of 0.10 nm could be obtained [2.71]. High-voltage electron microscopy, though, is inappropriate for many specimens because of radiation damage.

Aberration correction by reducing or eliminating C_s is a recent route to improving microscope performance. Additional multipole lenses, such as hexapoles [2.72] as aberration correctors, can yield a negative C_s to match the positive C_s of the microscope objective lens so that the point resolution can be improved.

Two basically different technical variants of transmission electron microscopes (TEMs) are used [2.12]. In conventional TEM, the specimen is illuminated by a near-parallel bundle of electrons, and the image is formed by a sequence of lenses equivalent to the lenses used in a light microscope. In scanning TEM (STEM), a fine probe is formed by focusing the incident electrons and is then scanned across the specimen. The transmitted electrons are registered by detectors and the resulting signal is displayed on a video screen. In conventional TEM, the aberrations of the objective lens determine the image quality, whereas in STEM, the aberrations of the probe-forming lens are of relevance for the quality.

The basis of the quantum mechanical interaction of the incident electron wave field with the atomic potentials, which is the basis of TEM imaging, is contained

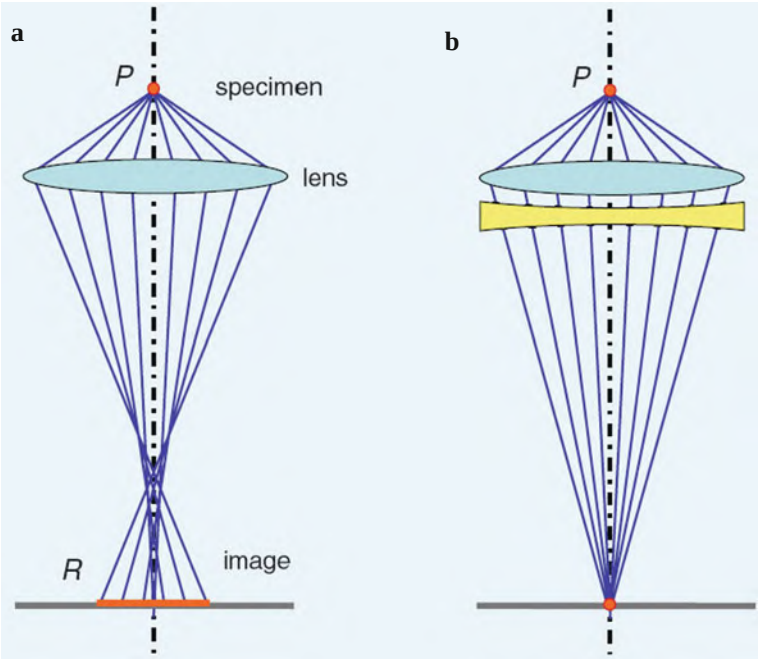

Fig. 2.25 (**a**) Schematic of spherical aberration of a converging lens. The scattering power increases with increasing angle (with respect to the optical axis) at which the electrons enter the lens. As a result, the electrons passing the lens at its periphery are focused at a distance in front of the image that is defined by low-angle beams. The image of a point *P* of the specimen is broadened into a "point-spread disk" of radius *R* (*red*). (**b**) Aberration correction. Spherical aberration is compensated by combining the converging lens with a suitable diverging lens. In electron optics, diverging lenses are realized by combinations of multipole lenses. (Reprinted with permission from [2.12]. © 2008 AAAS)

in the exit plane wave function (EPWF). This can be derived by focus-variation techniques (see [2.12]) where EPWF is calculated by fitting model functions to a series of images taken under different defocus values. Then the EPWF is calculated for a model structure of the sample which is iteratively improved to obtain the best fit between the calculated and experimental EPWFs. The result is generically not an image in the conventional sense but a computer model of the structure that gives the atomic species and coordinates.

Theoretically, the optimum imaging contrast is achieved by combining a small defocus with a small negative value of the spherical-aberration parameter C_s (see [2.12]). Under these negative spherical-aberration imaging (NCSI) conditions, atoms appear bright on a dark background. The strong contrast achieved by NCSI, which makes few-electron atoms such as oxygen, nitrogen, or even boron visible, is considered to be one of the major advances of spherical-aberration correction (see [2.12]). In a $\sum 3$ {111} twin boundary of $BaTiO_3$ (Fig. 2.26), all the atom species including oxygen (arrows) can be identified. By evaluating the local intensity signal,

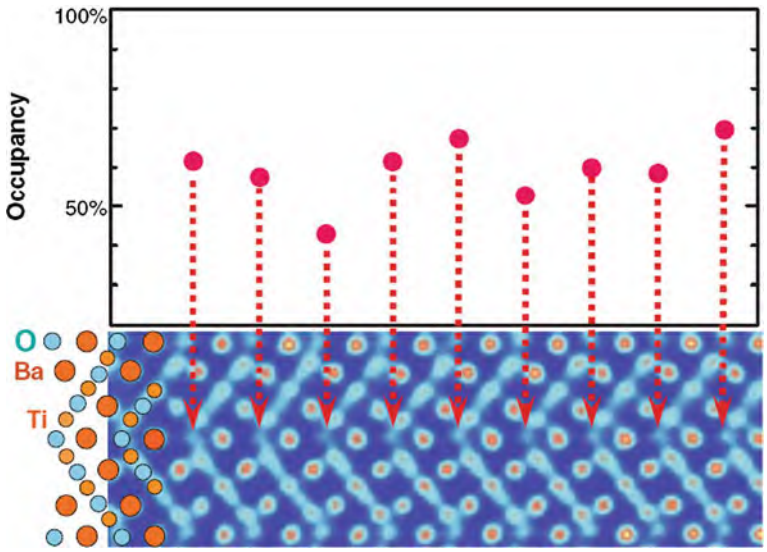

Fig. 2.26 $\sum 3$ {111} twin boundary in $BaTiO_3$. All atomic species, including oxygen, can be identified as confirmed by image simulation. Quantitative site-occupation measurements derived from the local intensity values indicate that in the interfacial oxygen columns only about 40–70% of the sites are occupied. This provides evidence for oxygen deficiency, which is presumed to have a strong influence on the electronic properties of interfaces. (Reprinted with permission from [2.12, 2.73]. © 2008 AAAS)

the oxygen occupancies (see upper part of Fig. 2.26) in the boundary can be determined to 40–70% of the bulk value, providing direct evidence of oxygen deficiency in the boundary.

The resolution of aberration-corrected 300 keV electron microscopes is about 0.08 nm. A resolution of 0.05 nm is achieved in the transmission electron aberration-corrected microscope (TEAM; [2.12] and Fig. 5.43). The TEAM instrument offers both TEM and STEM operation, a monochromator in the electron-beam forming system and a future additional corrector for chromatic aberration (see [2.12, 2.13]). The accuracy at which the separation of well-isolated atoms can be measured is with about 0.006 nm much better than the resolution (see [2.12]). This accuracy was demonstrated in a study of polarization domain walls in ferroelectric $Pb(Zr_{0.2}Ti_{0.8})O_3$ (PZT) (Fig. 2.27). The high-precision measurement of the shifts of the individual atoms enables the derivation of the local polarization vector and thereby the determination of the structure of the domain wall.

In STEM, the prevailing imaging mode is high-angle annular dark-field (HAADF; see [2.12]), where the contrast arises from incoherent scattering intensity which can be understood directly in terms of the atomic number. The HAADF mode is also referred to as *Z*-contrast imaging. In imaging a silicon crystal along a [112] direction by aberration-corrected STEM the atom-pair separation of 0.078 nm can be clearly resolved (Fig. 2.28a). The low-angle scattered electrons passing the

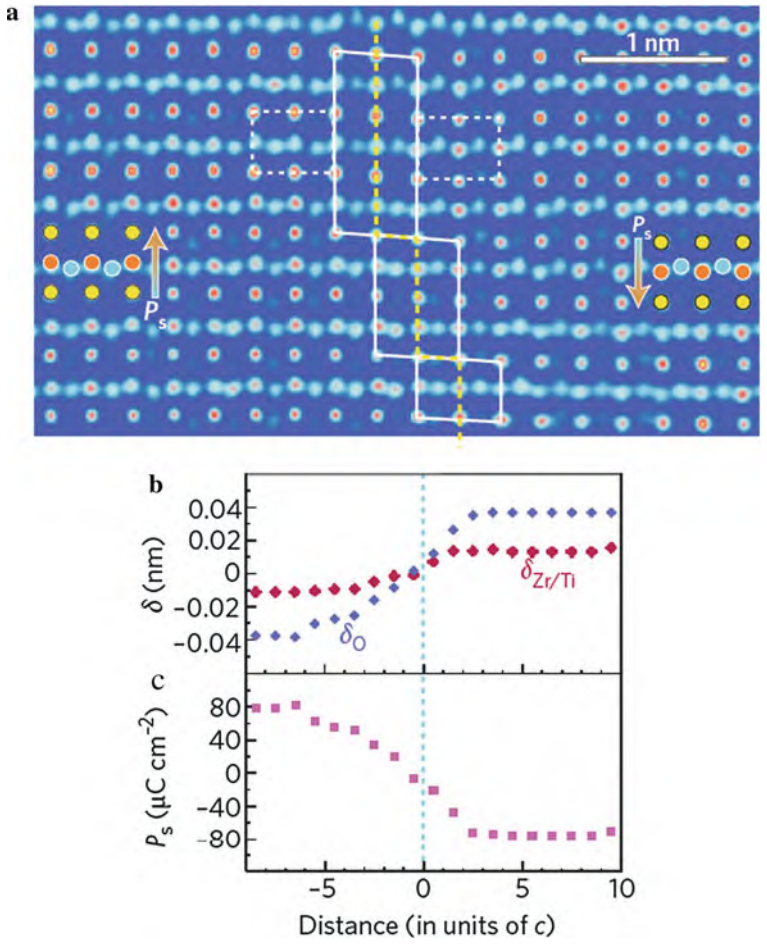

Fig. 2.27 (**a**) Transversal inversion polarization domain wall in ferroelectric $Pb(Zr_{0.2}Ti_{0.8})O_3$ (PZT). *Arrows* give the direction of the spontaneous polarization, which can be deduced from the local atomic displacements. The shifts of the oxygen atoms (*blue* circles) out of the Ti/Zr atom rows (red circles) can be seen. (**b**) Atomic resolution measurements of the shifts of oxygen (δ_O), and titanium/zirconium ($\delta_{Ti/Zr}$) atoms in a longitudinal inversion domain wale and the value of the local polarization *P* that can be calculated from theses data [2.12, 2.74, 2.75]. (Reprinted with permission from [2.74]. © 2009 Nature Publishing Group)

annular HAADF detector can be used for electron-energy-loss spectroscopy (EELS) providing an analysis of the electronic structure with atomic-scale resolution (see Fig. 2.29 and [2.79, 2.80]). In Fig. 2.28b the atomic resolution EELS spectrum of a $La_{0.7}Sr_{0.3}MnO_3/SrTiO_3$ multilayer is imaged. A spectral electron-energy resolution of 55 meV has been achieved at the sub-electron volt sub-Ångström microscope (SESAM) which can be exploited to study changes in the width of the local electron-energy band gap near interfaces in semiconductor nanodevices (see [2.12]).

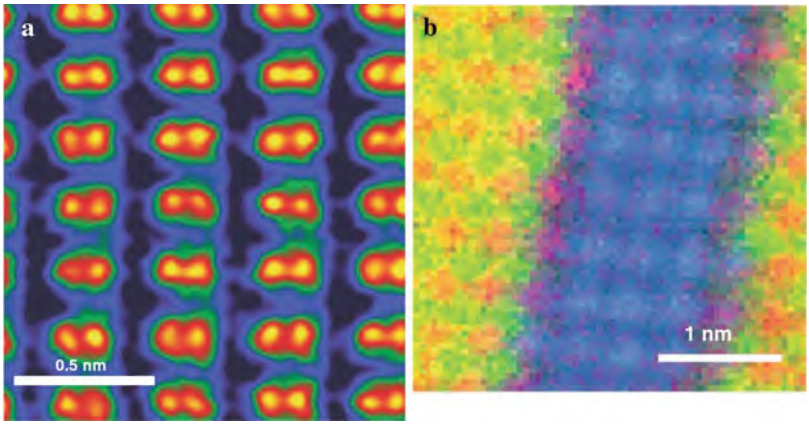

Fig. 2.28 (**a**) High-angle annular dark-field (HAADF) image in scanning transmission electron microscopy (STEM), of Si along a [112] direction. The atom-pair separation of 0.078 nm is clearly resolved in the 300 keV instrument [2.12, 2.76]. (**b**) Spectroscopic imaging of a $La_{0.7}Sr_{0.3}MnO_3/SrTiO_3$ multilayer showing the different chemical sub-layers in a 64 ×-64 pixel spectrum extracted from 650 eV wide electron-energy-loss spectroscopy (EELS) data recorded at each pixel. *Red* (Mn-L edge)-*green* (La–M edge)-*blue* (Ti-L edge) false-color image showing the Mn, La, and Ti sub-lattices as derived from the EELS data. The *purple color* at the interface indicates Mn–Ti intermixing at the Ti sub-lattice [2.12, 2.77]. (Reprinted with permission from [2.12]. © 2008 AAAS)

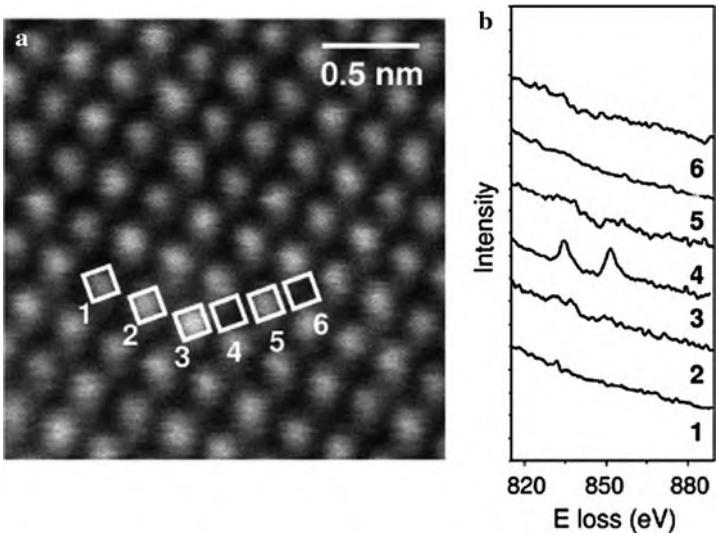

Fig. 2.29 Spectroscopic imaging of a single La atom inside $CaTiO_3$ by an aberration-corrected scanning transmission electron microscope with electron energy loss spectroscopy (EELS). (**a**) *Z*-contrast image with (**b**) EELS traces showing spectroscopic identification of a single La atom of atomic resolution with the same beam used for imaging [2.78]. The characteristic $M_{4,5}$ lines of La are seen strongly in spectrum 3. (Reprinted with permission from [2.78]. © 2004 American Physical Society)

2.6.2 TEM Nanotomography and Holography

For high-resolution ($\sim 1^3$ nm^3) 3D tomographic imaging in TEM, images are recorded every one or two degrees about a tilt axis. Typically, the ensemble of images is then "back-projected" to form a 3D reconstruction. The STEM HAADF signal is most appropriate for tomographic applications and is also sensitive to changes in composition (see [2.14, 2.81, 2.82]) because it is approximately proportional to $Z^{1.8}$, where Z is the atomic number. STEM tomography can be used to relate the distribution of ruthenium-platinum catalyst nanoparticles to the underlying surface curvature (see Fig. 2.30a), showing in this case the strong preference of the particles (red) for saddle-shaped anchor points. 3D compositional information can be extracted from energy-filtered transmission electron micrograph (EF-TEM) series. Electron tomography can also be used for studying dislocation networks and EF-TEM tomography is useful for the investigation of precipitates in alloys (see [2.14]). True atomic resolution tomography appears to be possible by using aberration-corrected TEM or STEM instruments (see [2.14]).

Electron holography [2.83], which is based on the formation of an interference pattern in the TEM, overcomes the TEM limitations of using only intensities in imaging. By contrast, holography allows the phase shift of the electron wave to be recovered (see [2.14]). As the phase shift is sensitive to local variations in magnetic and electrostatic potential, the technique can be used to obtain quantitative information about magnetic and electric fields in materials and devices with spatial resolution that can approach the nanometer scale. In the TEM off-axis electron holography mode (Fig. 2.30b), a field-emission electron gun is used to provide a highly coherent source of electrons. By electron holography, magnetic fields in fine-particle recording media, flux vortices in superconductors, the Aharonov–Bohm effect (see [2.14]), or spontaneous polarization [2.84] have been observed. In Fig. 2.30c the holographic imaging of the magnetic interaction of closely spaced cobalt nanoparticles is shown. The images indicate an approximately 50:50 mixture of clockwise and anticlockwise ground-state configurations to which the rings relax after exposure to a magnetic field (see [2.14]). Electron holography can also provide quantitative information about electrostatic potentials in doped semiconductors and in ferroelectrics (see [2.14]). In a silicon *p*-*n* junction (Fig. 2.30d) the *p*-type and *n*-type regions are delineated clearly as darker and lighter holographic contrast, respectively.

An exciting prospect is the combination of electron holography with electron tomography to characterize electrostatic and magnetic fields inside nanostructured materials with nanometer spatial resolution in three dimensions (see [2.14]).

2.6.3 Cryoelectron Microscopy and Tomography

Cryoelectron microscopy is a technique in nanobiology for imaging single organelles ($\sim$5 nm) in cells such as the protein-packaging Golgi apparatus or energy producing mitochondria [2.85, 2.86] for a better understanding of their

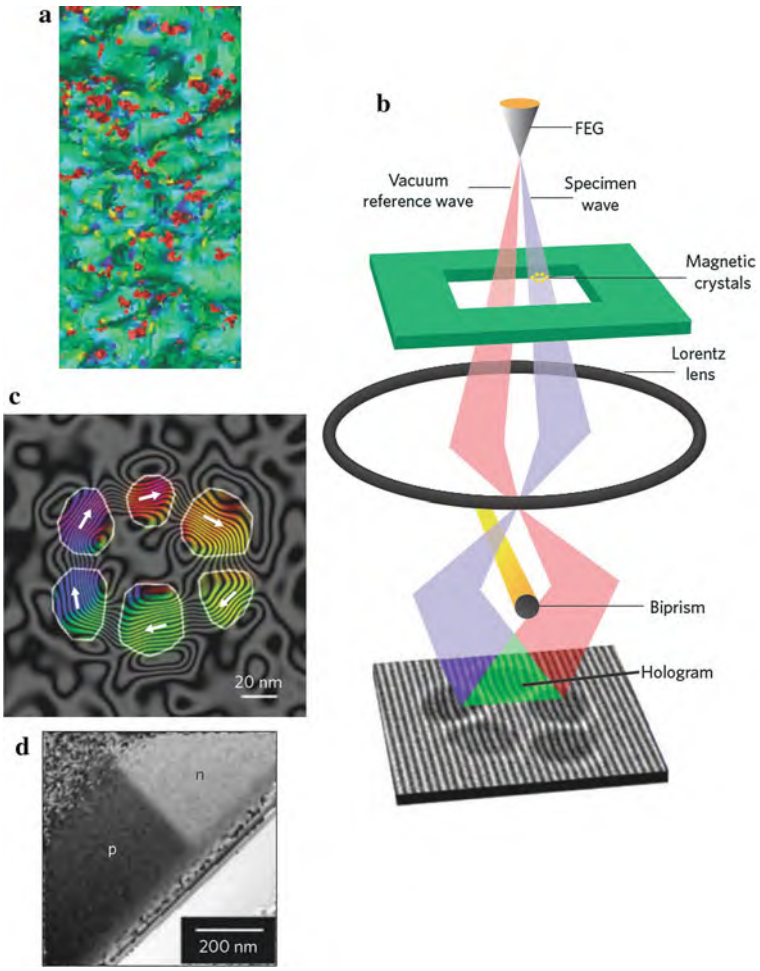

Fig. 2.30 (**a**) Electron tomography for reconstruction of a heterogeneous catalyst. Ruthenium–platinum nanoparticles on disordered mesoporous silica. The surface has been color-coded according to the curvature of the surface. The nanoparticles (*red*) appear to prefer to anchor themselves at the (*blue*) saddle points (width 20 nm) [2.14]. (**b**) Schematic of electron holography microscopy. A voltage is applied to an electron biprism located close to a conjugate image plane in a field-emission electron gun (FEG) TEM, to overlap a vacuum reference electron wave that has passed through a region of the specimen to form an off-axis electron hologram. Variations in the spacing and direction of the holographic interference fringes contain information about the projected magnetic flux density inside and outside the crystals. (**c**) Magnetic phase contours formed by the magnetic contributions to the electron phase shift measured on a cobalt nanoparticle ring in magnetic-field-free conditions. The magnetization of the nanoparticles is indicated by arrows [2.14]. (**d**) Representative electrostatic phase image reconstructed from an off-axis electron hologram of a silicon p–n junction sample. (Reprinted with permission from [2.14]. © 2009 Nature Publishing Group)

functionalities. For this purpose the cells are flash-frozen (10^5 K/s) to, e.g., 4.2 K. They then do not need to be fixed or have their membranes disrupted and additionally can withstand a ten times higher electron dose for imaging (6500 e^- nm^2 [2.87]) than at ambient temperatures. By the electron beam, 2D projection slices of the particle are imaged with subsequent processing to a 3D image by computer back projection routines. A few examples of cell components imaged by cryoelectron microscopy are shown in the following.

In Fig. 2.31a stereoview of the human SF3b splicing factor complex imaged by cryoelectron tomography is given at a resolution of less than 1 nm [2.88]. The splicing factor SF3b with a mass of ∼450 kDa consists of seven proteins and is essential for the accurate excision of introns (segments of a gene that do not function in coding for protein synthesis) from pre-messenger RNA. The SF3b factor is involved in the recognition of the pre-messenger RNA's branch site and is required for the pre-messenger RNA splicing [2.88]. 3D reconstruction of SF3b reveals the architecture of an envelope (wall thickness ∼2.5 nm) enclosing a large inner cavity containing a single density element (yellow) like a pearl in an oyster (see Fig. 2.31a) and the protrusions (see Fig. 2.31b) might be identified as possible RNA-recognition motif (RRM) domains.

Microtubule doublets (see Fig. 2.32) are structural components of axonemes which form the core of eukaryotic flagella and cilia, e.g., in sea urchin sperm. The axoneme is one of the largest macromolecular machines. The structure of the microtubule doublet derived from cryoelectron tomography provides insight into tubulin–protein interaction and into the functions doublets perform in axoneme machines, and may be used as basis for quantitative modeling of the mechanical properties [2.87].

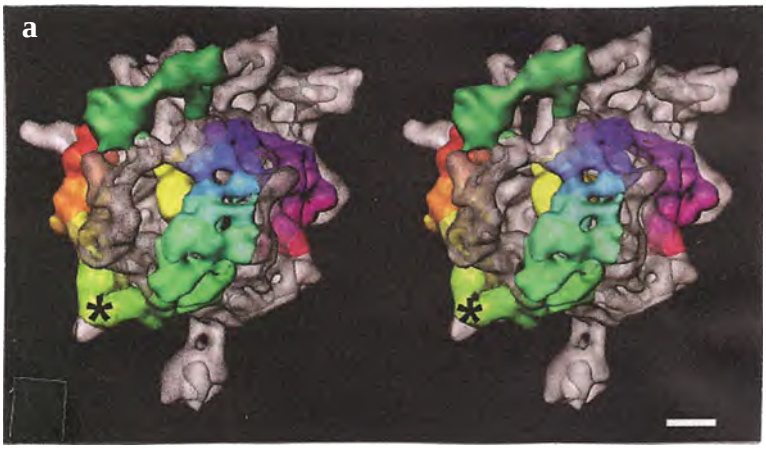

Fig. 2.31 (**a**) Stereoview of the SF3b complex by cryoelectron tomography. The SF3b155 proteins are shown in rainbow colors, the two RNA recognition motifs (RRM) of SF3b49 protein in *green* color, and the p14 RRM in the center of the complex in *yellow*. The potential hinge region in the SF3b155 protein is indicated by asterisks. Scale bar, 2 nm. (Reprinted with permission from [2.88]. © 2003 AAAS)

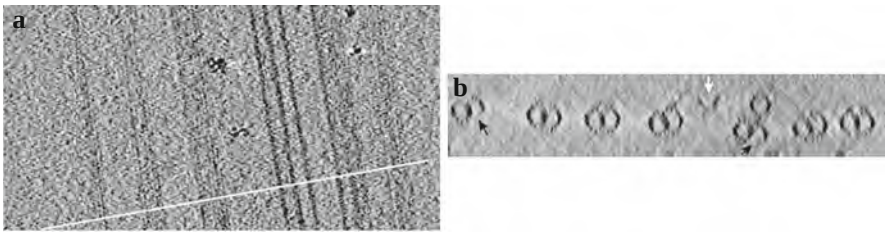

Fig. 2.32 Electron tomography of microtubule doublets. (**a**) Protofilaments are well resolved in the reconstruction, roughly parallel to the doublets. (**b**) A projection of a 26 nm thick cross-section along the *white line* in (**a**). The field includes five complete and two broken doublets (*black arrows* at missing proto filaments). A partially disassembled singlet microtubule is designated by a *white arrow*. (Reprinted with permission from [2.87]. © 2006 Nature Publishing Group)

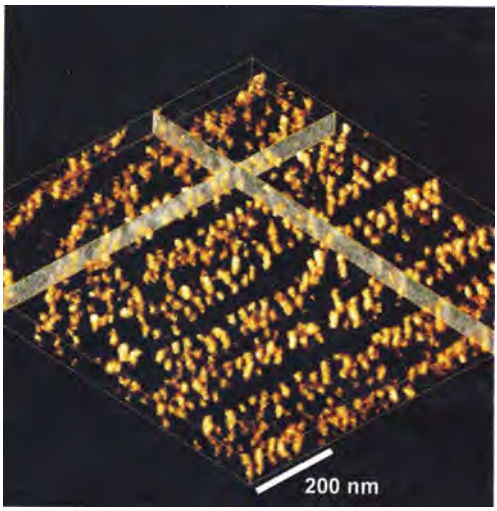

Fig. 2.33 A voxel (volume pixel) projection of ribosomes in the nematode *C. elegans* from EF-TEM tomography reconstructed from maps of the characteristic electron energy losses of phosphorus; the ribosomes show no contrast in a bright field (BF) TEM image [2.89, 2.90]. (Reprinted with permission from [2.90]. © 2004 Elsevier)

Tomography of energy-filtered transmission electron microscopy (EF-TEM) was employed to reconstruct the ribosomes of the *Caenorhabditis elegans* nematode worm by specifically detecting the *P* atoms in the ribosomes (Fig. 2.33) which are particles composed of RNA and protein found in the cytoplasma of living cells and which are active in the synthesis of proteins.

2.7 X-Ray Microscopy

X-ray microscopy in some sense fills the "resolution gap" between light microscopy and electron microscopy [2.91]. Fresnel zone plate lenses, which focus light by diffraction, or mirrors are used as optical elements for imaging (see [2.92, 2.93]). This type of microscopes successfully employs near-edge x-ray absorption

fine-structure (NEXAFS) for the analysis of organic and magnetic materials [2.15]. X-ray nanotomography is applied in materials science [2.94] and biology [2.95, 2.96]. Spatial resolution down to 5 nm has been demonstrated by lens-less coherent x-ray diffraction imaging [2.91, 2.97, 2.98] with prospects of atomic resolution imaging [2.97]. The intense, brief pulses of x-rays from upcoming free-electron lasers (see [2.16]) will greatly extend x-ray microscopy to the femto-second time domain and to interatomic length scales [2.17, 2.99] enabling the analysis of free single molecules.

2.7.1 Lens-Based X-Ray Microscopy

Here, commonly Fresnel zone plates (FZPs; Fig. 2.34a) are used to condense the beam unto the sample and then to use a micro FZP as a high-resolution objective to produce a magnified full-field image of the object. Zernike phase contrast (see Fig. 2.34a) is based on partially coherent illumination and uses a phase shifting plate inserted in the back focal plane of the imaging FZP to phase shift the illumination beam by $\pi/2$ (positive phase contrast) or $3\pi/2$ (negative phase contrast) with respect to the light scattered by the sample. The combination of the phase shifted and scattered light from the sample produces an image in the detector plane that has the appearance of an absorption contrast image, but varies with the phase shift of the sample structures (see [2.93]). The diffraction-limited spatial resolution achievable with FZPs having d_r as the outer most zone width is given by (see [2.93])

$$\delta \sim 1.22\, d_r/m$$

where m is the diffraction order. Resolutions to 15 nm have been achieved in a soft x-ray microscope making use of an overlaid objective zone plate with 80 nm thick gold plated opaque zones and a 15 nm outer zone width (Fig. 2.34b, c). Zone-plate-based microscopes are of two main types (see [2.15]): In the scanning transmission x-ray microscopes (STXMs) the sample is mechanically raster-scanned through the focal spot provided by a zone plate. In the transmission x-ray microscope (TXM), a zone plate magnifies the sample onto a 2D detector.

Compound lenses (Fig. 2.34d) can be made by chaining individual parabolic lenses made from Al or Be to form the optic element of a hard x-ray microscope [2.100].

Near-edge x-ray absorption fine-structure (NEXAFS) microscopy provides excellent compositional contrast in organic materials and is much less damaging than electron energy loss spectroscopy in electron transmission (see [2.15]). Similarly, the interaction of x-rays with magnetic materials provides element-specific contrast that allows the determination of magnetic properties in multielement antiferromagnetic and ferromagnetic materials by making use of x-ray magnetic circular dichroism (XMCD; see [2.15]), which also is used for studying dynamic magnetic phenomena (see [2.15]). In Fig. 2.35 the magnetic domains of a bilayer of 1.0 nm

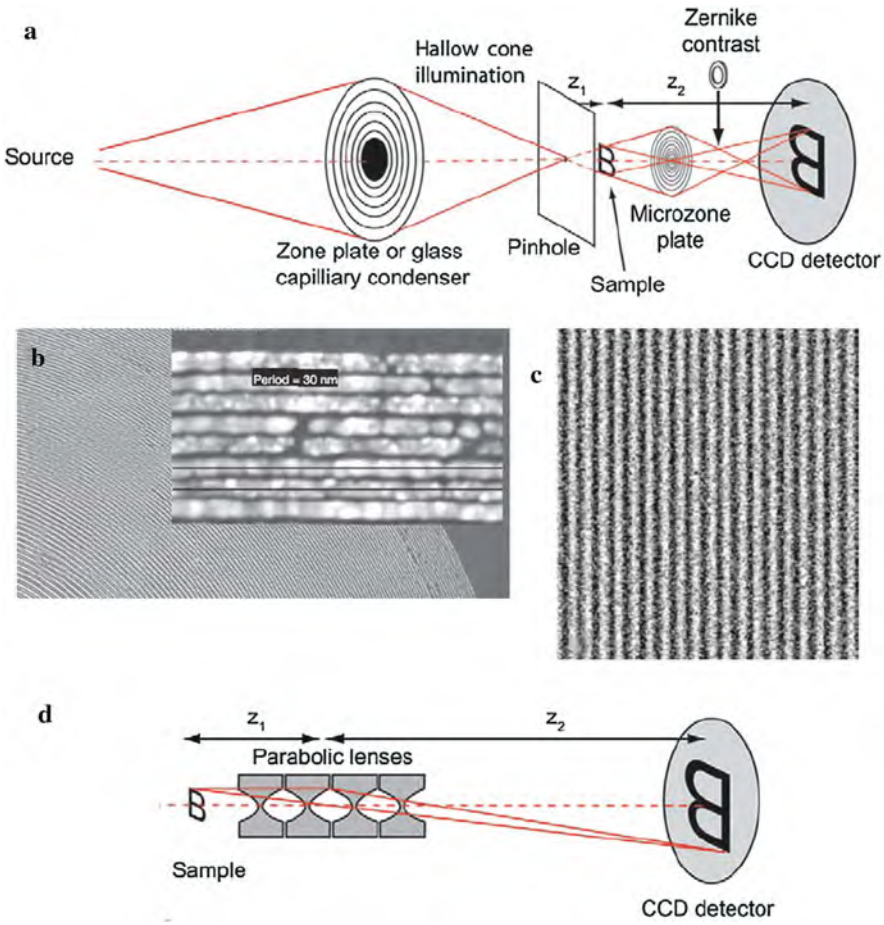

Fig. 2.34 Lens-based x-ray microscopy systems. (**a**) Fresnel zone plate (FZP) system (see [2.93]). (**b**) Scanning electron micrograph of a zone plate with 15 nm outermost zone showing a detailed view in the inset. The zonal period as indicated by the two *black lines* in the inset is 30 nm with a zone overlay placement accuracy of 1.7 nm. (**c**) Soft x-ray image 15.1 nm half-period Cr/Si multilayer image with the 15 nm zone plate shown in (**b**) at a photon energy of 815 eV and a pixel size of 1.6 nm [2.92]. (**d**) Compound refractive imaging system (see [2.93]). (Reprinted with permission from [2.93] (**a**), (**d**) and [2.92] (**b**), (**c**). © 2007 Elsevier (**a**), (**d**) and 2005 Nature Publishing Group (**b**), (**c**))

of platinum on 1.2 nm cobalt on an antiferromagnetic $LaFeO_3$ (100) substrate are shown as imaged by soft x-ray XMCD microscopy. The contributions of the various elements to the magnetic properties can be clearly distinguished because each element has its absorption edge at a different photon energy and the antiferromagnetic domains of the substrate could be clearly correlated with the cobalt-specific ferromagnetic domains above it. The imaging of magnetic nanofeatures is reviewed in Sect. 8.1.

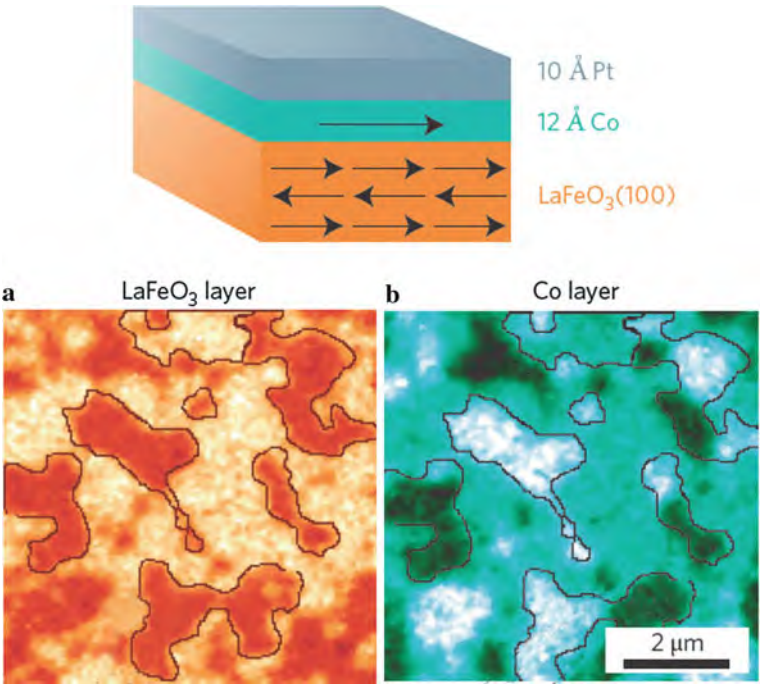

Fig. 2.35 Domain structure of a platinum–cobalt bilayer on an antiferromagnetic $LaFeO_3$ substrate observed by photoelectron emission microscopy (PEEM). X-ray magnetic circular dichroism (XMCD) can be used as a contrast mechanism in PEEM. The antiferromagnetic domains (**a**) and the cobalt domains (**b**) are visualized. Comparison of the images shows that the ferromagnetic cobalt domains align with the antiferromagnetic domains (*light* and *dark* regions inside outlined areas) [2.15, 2.101]. (Reprinted with permission from [2.15]. Figure courtesy of J. Stöhr)

2.7.2 X-Ray Nanotomography

For imaging tungsten plugs at 60 nm resolution (Fig. 2.36), 890 nm-thick Au FZPs have been used. These plugs interconnect the different layers of an integrated circuit. When a plug contains a defect in its center (a "keyhole" defect) formed during the electroplating process, it can cause the breakdown of the circuit.

X-ray microscopy can favorably image small biological objects containing elements of lower atomic numbers by using photon energies within the "water window" between the absorption edge energies of carbon (284 eV or 4.4 nm wavelength) and oxygen (543 eV or 2.3 nm) for probing whole hydrated biological cells. In this energy range water is transparent to a 10 µm thickness whereas the more carbon-rich organelles and other sub-cellular structures are more absorptive providing a natural contrast. 3D x-ray maps with 60 nm resolution of cryogenically fixed, fully hydrated and unstained yeast [2.95] and bacterium cells [2.96] are shown in Fig. 2.37.

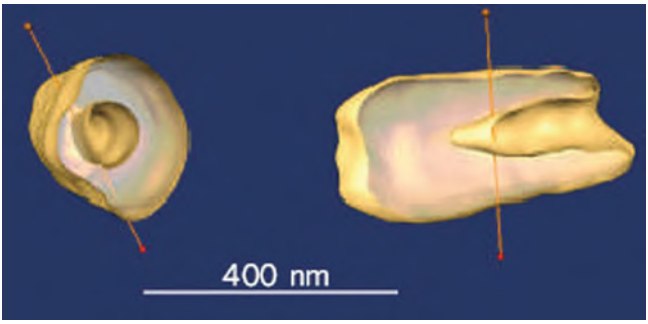

Fig. 2.36 Three-dimensional x-ray data set of tungsten plugs (with a "keyhole" of 50–80 nm diameter) used as electrical interconnects between layers of a computer chip. The 3D image is obtained from 141 2D images using a photon energy of 10.5 keV just above the tungsten absorption edge. (Reprinted with permission from [2.102]. Figure courtesy of G. C. Yin)

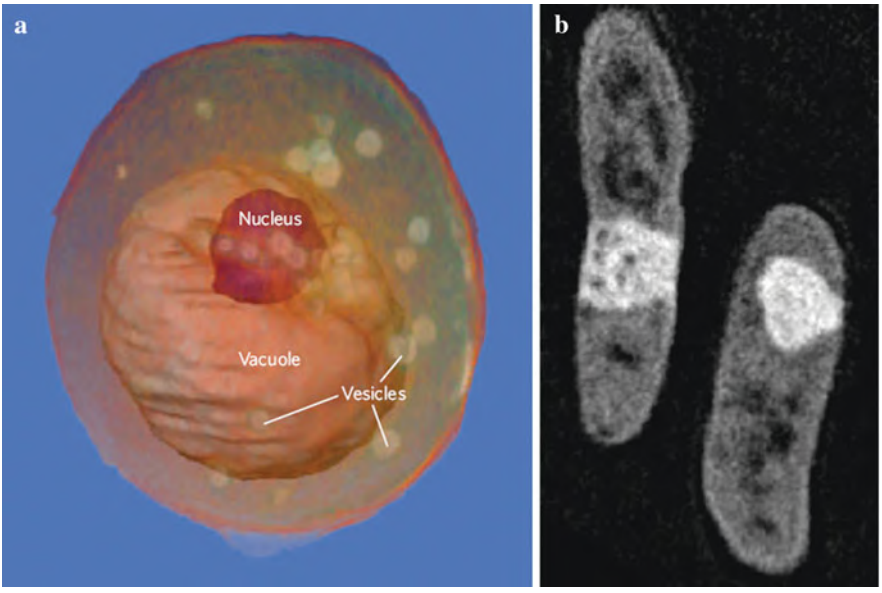

Fig. 2.37 Nanoscale 3D x-ray bio-tomography: (**a**) 3D image of a whole, hydrated yeast cell [2.102] about 5 μm wide imaged with a 517 eV photon energy where water is relatively transparent and carbon absorbs, providing a natural contrast mechanism. The cell nucleus, a large vacuole and several lipid-filled vesicles are visible. (**b**) Section through two Escherichia coli bacteria [2.102], each about 0.5 μm wide from a data set taken at ∼530 eV. The nature of the large white bands and of the dark sub-structure are unknown. (Reprinted with permission from [2.102]. Figure courtesy of C. Larabell)

2.7.3 Lens-Less Coherent X-Ray Diffraction Imaging

Coherent x-ray diffraction imaging (CXDI) is an x-ray microscopy technique with the potential of reaching spatial resolutions well beyond the limits of x-ray microscopes based on optics. In CXDI, the object is illuminated with coherent x-rays from modern synchrotron radiation sources or future free-electron laser sources [2.97]. From the far-field diffraction pattern of the coherent x-rays (Fig. 2.38a) the wave field behind the object is reconstructed by iteratively solving the phase problem (see [2.97]). A gold crystallite with a diameter smaller than 90 nm (Fig. 2.38b) was irradiated in the focus (100×100 nm^2) of coherent x-rays (energy $E = 15.25$ keV, wavelength $\lambda = 0.0813$ nm) at the European Synchrotron Radiation Facility (ESRF Grenoble, France) [2.97]. The size of the gold nanocrystallite was reconstructed from the diffraction pattern (Fig. 2.38c) by using the HIO algorithm (see [2.97]) with a spatial resolution of $\sim$5 nm, which might be pushed to below 1 nm by a 10^3 increase in x-ray flux density for radiation-hard scatterers.

Beside investigating small isolated objects, it is possible to study extended objects by combining scanning microscopy with CXDI (see [2.91, 2.97]). In this technique, also called ptychography, the sample is scanned with spatially confined illumination, e.g., a nanofocused hard x-ray beam, recording a diffraction pattern at each position. When the scanning steps have an overlap with that of the neighboring scan points (see Fig. 2.38d), then ambiguities in the image reconstruction can be avoided. A breakthrough in high-resolution scanning x-ray diffraction microscopy has been achieved by using the fast Pilatus x-ray detector [2.98].

2.7.4 Upcoming X-Ray Free-Electron Lasers (XFEL) and Single Biomolecule Imaging

The coherent flux of x-ray sources increased by an order of magnitude every 18 months for the past 20 years (see [2.99]). Starting in September 2009, the Linac Coherent Light Source (LCLS) at the Stanford linear AC-celerator Center (SLAC) USA will start to generate the brightest x-ray pulses, almost nine orders of magnitude beyond current synchrotron-based x-ray facilities [2.16]. Other projects are gearing up: the Japanese XFEL at Riken in Japan, and the 3 km-long European XFEL in Hamburg are under construction. The FLASH facility at DESY in Hamburg, an extreme ultraviolet FEL operating since 2005, is already demonstrating new capabilities with pulses of duration less than 30 fs and wavelengths in the range 6–40 nm. The LCLS, and the other XFELS, will produce laser-like x-ray pulses of about 100 fs duration and 10^{12} photons per pulse [2.16].

The key to achieving ultrafast and extremely intense x-ray pulses in an XFEL is the process of self-amplification of spontaneous emission, which occurs when an electron pulse travels through a periodic magnetic structure called an undulator. These new sources are expected to have a great impact on structural biology, chemistry, atomic physics, and materials science. The coherent x-ray pulses will enable

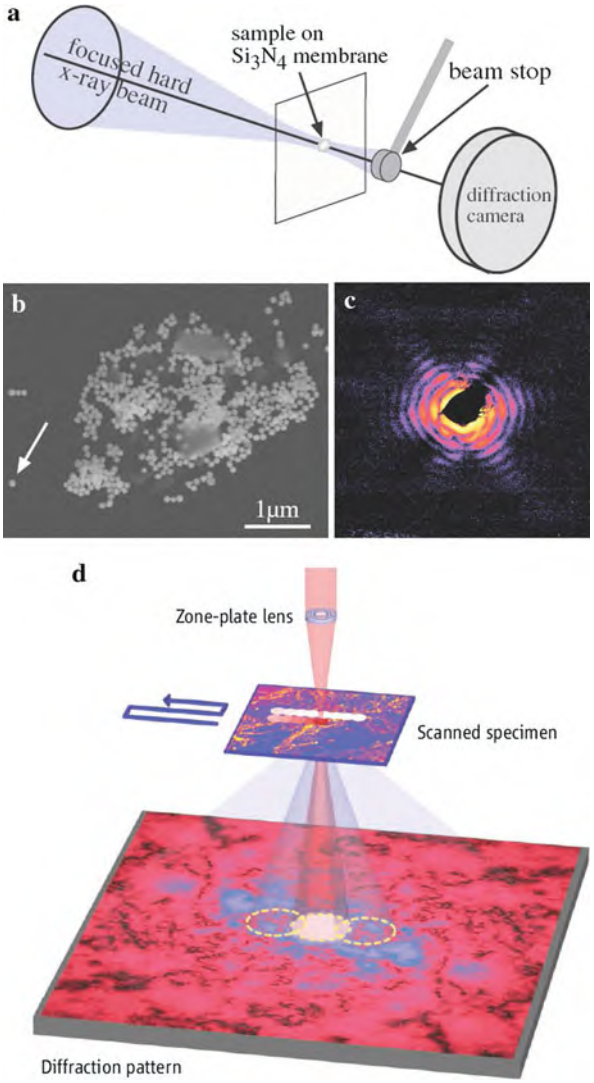

Fig. 2.38 Lens-less coherent x-ray diffraction imaging. (**a**) Schematic sketch of the coherent diffraction imaging setup with nanofocused illumination. (**b**) Scanning electron micrograph of gold nanoparticles deposited on a Si_3N_4 membrane. (**c**) Diffraction pattern (logarithmic scale) recorded of the single gold particle pointed to by the arrow in (**b**) and illuminated by a hard x-ray beam with lateral dimensions of about $100 \times 100\ nm^2$. The maximum momentum transfer, both in horizontal and in vertical direction is $q = 1.65\ nm^{-1}$ [2.97]. (**d**) Image creation in the scanning transmission x-ray diffraction microscope (ptychography) [2.91]. (Reprinted with permission from [2.97] (**a**–**c**) and [2.91] (**d**). © 2008 American Physical Society (**a**–**c**) and 2008 AAAS (**d**))

x-ray microscopy to be extended beyond the limits of x-ray objective lenses (see last section above). In essence, if the coherent scattering pattern of a single object can be recorded, then the image can be constructed numerically, with the computer performing the task usually undertaken by a high-quality lens [2.16].

Radiation damage will be an issue when unprecedented x-ray intensities of 10^{19} Wcm^{-2} will be achieved by focusing the 0.15 nm wavelength pulses to a 100 nm spot which will turn any material into a plasma but only after the pulse has traversed the sample ("diffraction before destruction"). Nevertheless, it is expected that spatial resolution of 1 nm can be achieved on whole unsectioned cells irradiated by soft x-ray pulses (see [2.16]). Image resolution may be even extended to the interatomic length scale to resolve the secondary structure of proteins (see Fig. 2.39), by combining many diffraction patterns from single particles, e.g., in a liquid droplet stream.

By powerful x-ray bursts from XFEL sources to determine the structure of single molecules, viruses, and nanoparticles, the limitations of current techniques can be circumvented, including the need to condense molecules into pure crystals. A new approach [2.17] demonstrates the recovery of the structure of a spinning or randomly oriented macromolecule with a weak scattering that gives rise to extremely low signal levels. In a simulation study [2.17] the orientation of a molecule is determined by analyzing the set of all possible intensity measurements in terms of the three degrees of rotational freedom. Phasing of the diffraction data and recovery of the molecular structure (see Fig. 2.39) then follow. From the study [2.17] it is concluded that the structure of even a relatively small 8 kDa molecule can be identified by the diffraction signal generated from a single XFEL pulse. This will contribute to realizing the full potential of the next generation of XFEL sources.

2.8 Three-Dimensional Atom Probes (3DAPs)

In 1951, E. W. Müller became the first person to observe single atoms, with the aid of the field-ion microscope (FIM) [2.19]. Later, the combination of position-sensitive detection with the time-of-flight mass spectrometry of single atoms in the atom probe enabled the reconstruction of the 3D atomic distribution of elements in a material [2.18, 2.103]. The instruments capable of microanalysis on this level are called generically 3D atom probes (3DAPs).

The principles of 3DAP are simple. Specimens for 3DAP are in the form of sharp needles of 50–100 nm end radius. The specimen is held at low temperatures (< 100 K) in ultrahigh vacuum at 0.5–1.0 m from a position-sensitive detector for the detection of single ions (Fig. 2.40). A combination of a high dc voltage and nanosecond-long high dc voltage pulses raises the electric field at the apex of the specimen to a level where individual atoms are ionized and removed on nearly radial

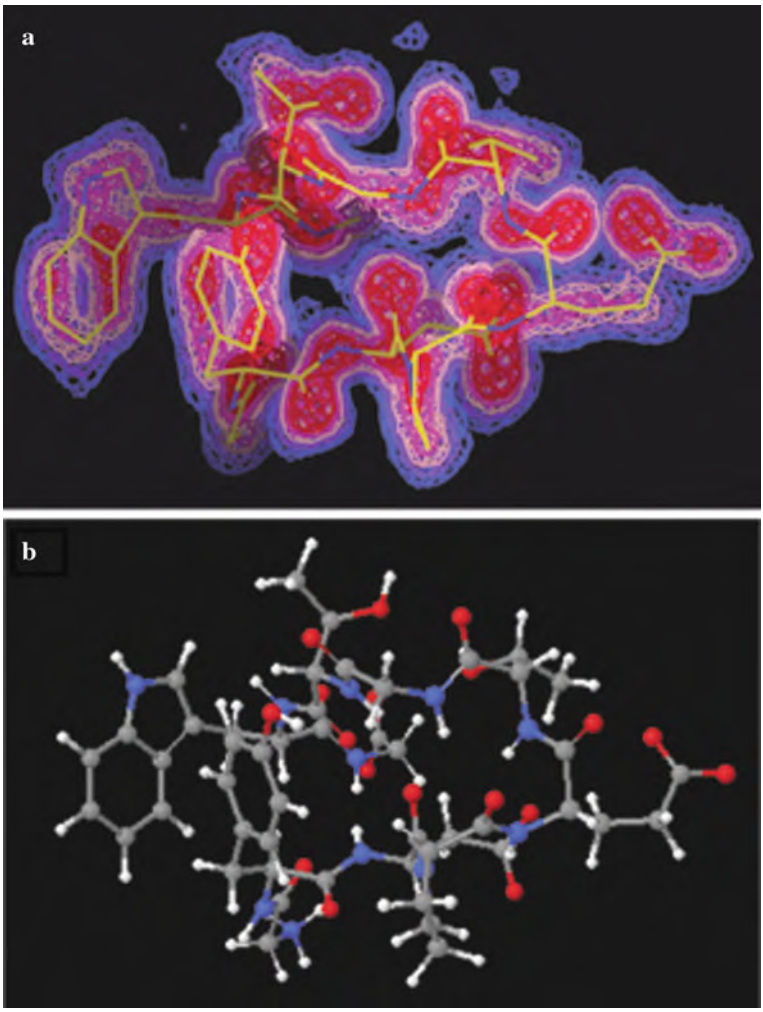

Fig. 2.39 Simulation of single molecule structure recovery by the diffraction signal from a single XFEL pulse. (**a**) Isosurfaces of electron density of the protein chignolin (a protein with 10 amino acid residues), recovered from 72,000 diffraction patterns of unknown orientation at a scattered mean photon count (MPC) of 4×10^{-2} per pixel. (**b**) The molecular model is represented by the stick figure, with C bonds shown in *yellow*, N in *blue,* and O in *red*. The 1, 2, and 3σ electron density contours are shown in *blue*, *pink,* and *red*, respectively, with σ denoting the r.m.s. deviation from the mean electron density. (Reprinted with permission from [2.17]. © 2009 Nature Publishing Group)

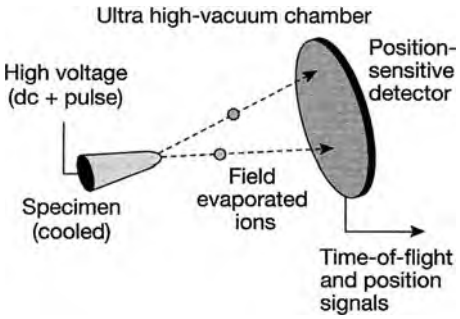

Fig. 2.40 Schematic illustration of the design of a 3D atom probe (3DAP). (Reprinted with permission from [2.105]. © 2001 Materials Research Society)

paths so that the instrument acts as a simple point-projection microscope with a very high magnification (several million times). The impact of an ion on the detector directly relates to its original surface position, and by time-of-flight mass spectrometry the nature of the ion is identified. Continued removal of ions produces a layer-by-layer sectioning of the specimen and generates a full 3D reconstruction of the element distribution in the material.

An example of detailed, ultrahigh-resolution provided by 3DAP is given in Fig. 2.41. Upon aging of an Al – 1.9wt% Cu – 0.3wt% Mg – 0.2wt% Ag alloy at 180°C for 10 h an Ω-phase plate forms in the alloy with a thickness of 10–13 $[111]_\alpha$ layers corresponding to 3 unit cells of Ω. In addition to the segregation of Ag and

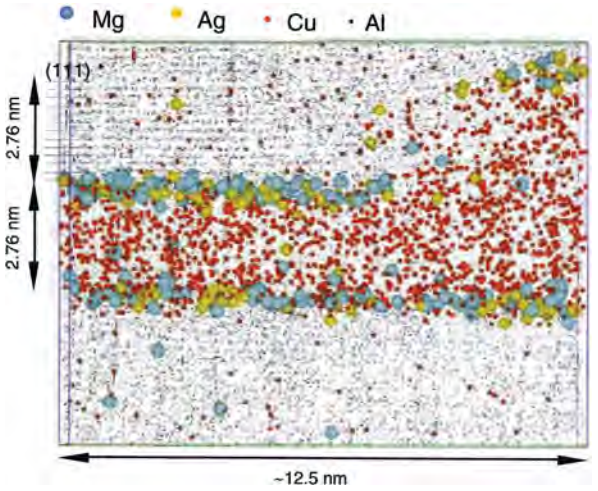

Fig. 2.41 3D atom probe (3DAP) elemental map with a step at the interface of an Ω-phase precipitate formed in an alloy aged at 180°C for 10 h. Segregation of Mg and Ag occurs to the precipitate interface as well as the enhancement of Cu in the vicinity of the step. (Reprinted with permission from [2.105]. © 2001 Materials Research Society)

Mg to the α/Ω interface, an interface step is apparent. The Cu concentration immediately ahead of the step is higher than in the matrix far from the precipitate. This indicates a process of redissolution as the precipitate shrinks during the coarsening process.

In the soft-magnetic nanocrystalline $Fe_{73.5}Si_{13.5}B_9Nb_3Cu_1$ alloy, 3DAP studies [2.104] demonstrated that Cu precipitates (Fig. 2.42) provide nucleation sites for Fe–Si primary crystallization, most important for the magnetic properties of the material (see Sect. 8.3).

For thin films and functional multilayers, as, e.g., giant magnetoresistance (GMR) devices (see Sect. 1.4), the structural and chemical control at the atomic scale is of importance. 3DAP studies of NiFe/CoFe/Cu/CoFe multilayers (Fig. 2.43) were performed by the development of appropriate tip preparation techniques. By these studies the effects of interface roughness and intermixing to properties such as GMR could be demonstrated (see [2.105]).

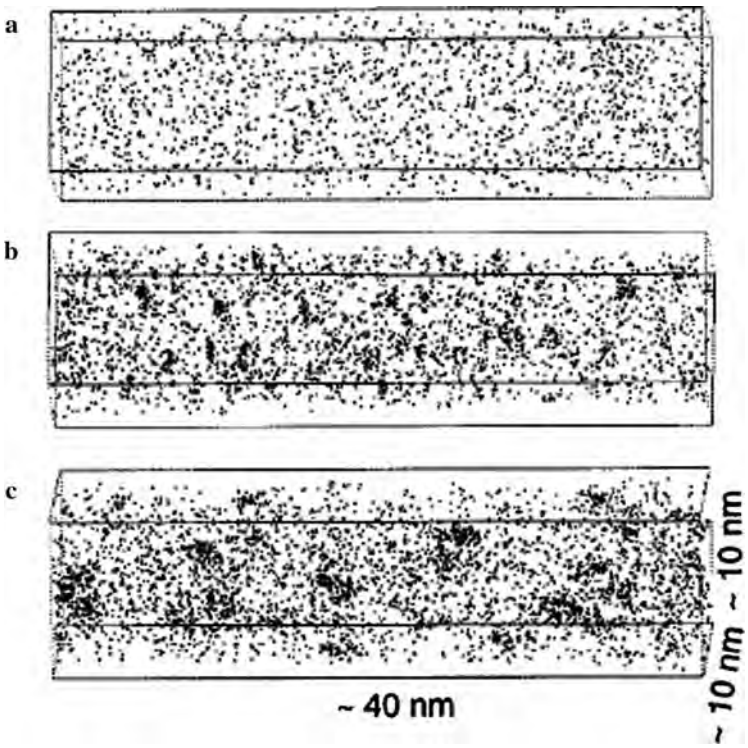

Fig. 2.42 3DAP elemental map of Cu of, the melt-spun amorphous $Fe_{73.5}Si_{13.5}B_9Nb_3Cu_1$ alloy which gives rise to a soft-magnetic behavior (see Sect. 8.3) due to nanocrystallization upon annealing at 515°C. (**a**) as quenched; (**b**) annealed at 400°C for 5 min.; (**c**) annealed at 400°C for 60 min. The data clearly show the nucleation of Cu precipitates as precursors of the Fe–Si nanocrystals. (Reprinted with permission from [2.104]. © 1999 Elsevier)

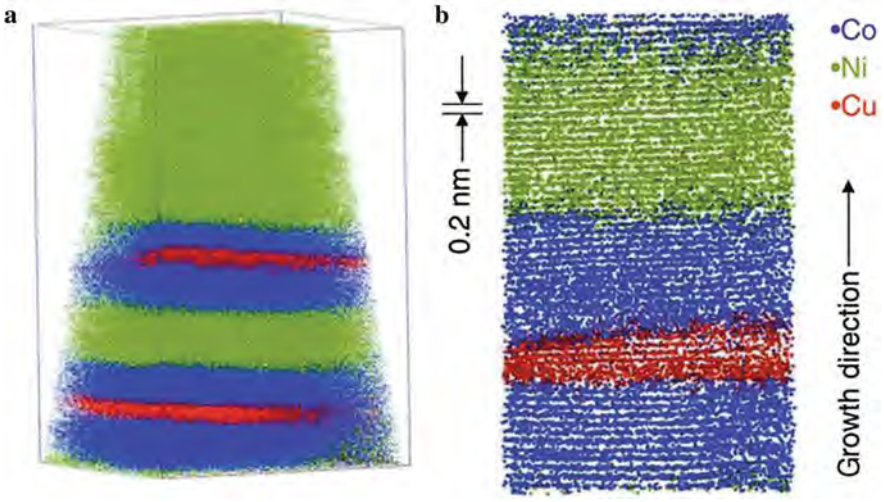

Fig. 2.43 (**a**) 3DAP analysis of a NiFe/CoFe/Cu/CoFe multilayer for giant magnetoresistance (GMR) devices (see Sect. 1.4). The Ni (*green*), Co (*blue*), and Cu (*red*) atom positions are shown. Height of the volume ∼35 nm. (**b**) Magnified view showing individual (111) planes along the growth direction. (Reprinted with permission from [2.105]. © 2001 Materials Research Society)

2.9 Summary

Microscopical imaging techniques are of outstanding importance for the characterization of nanosystems. The invention of scanning probe microscopy with partially atomic resolution has very much promoted the progress of nanoscience. A variety of scanning tunneling microscopes (STMs; where magnetic imaging is basically reviewed in Sect. 8.1), atomic force microscopes (AFMs), and scanning near-field optical microscopes (SNOMs) is available for imaging and manipulation. But also optical far-field stimulated emission depletion (STED) microscopy provides us with lateral resolution below 10 nm and qualifies for 3D imaging of biological nanosystems. Enormous progress has been achieved in topographic, tomographic, and analytical transmission electron microscopy by aberration correction techniques. With the generation of high-intensity and coherent x-ray beams, topographic, chemical, and magnetic imaging by x-rays with some 10 nm resolution have become feasible and strategies are being developed for imaging the atomic structure of single molecules. The 3D atomic probe (3DAP) is capable of 3D topographic and chemical atomic resolution.

References

2.1 G. Binnig, H. Rohrer, Helv. Phys. Act. **55**, 726 (1982)
2.2 G. Binnig et al., Phys. Rev. **56**, 930 (1986)
2.3 D.W. Pohl et al., Appl. Phys. Lett. **44**, 651 (1984)

2.4 T. Okuda et al., Phys. Rev. Lett. **102**, 105503 (2009)
2.5 Y. Sugimoto et al., Nature **446**, 64 (2007)
2.6 A.J. Huber et al., Nano Lett. **8**, 3766 (2008)
2.7 S.W. Hell, Science **316**, 1153 (2007)
2.8 M.J. Rust et al., Nat. Meth. **3**, 793 (2006)
2.9 V. Westphal et al., Science **320**, 246 (2008)
2.10 R. Wiesendanger, Ann. Phys. (Leipzig.) **9**, 895 (2000)
2.11 M. Knoll, E. Ruska, Z. Physik **78**, 318 (1932)
2.12 K.W. Urban, Science **321**, 506 (2008)
2.13 M. Haider et al., Ultramicrosc. **108**, 167 (2008)
2.14 P.A. Midgley, R.E. Dunin-Borkowski, Nature Mater. **8**, 271 (2009)
2.15 H. Ade, H. Stoll, Nat. Mater. **8**, 281 (2009)
2.16 H.N. Chapman, Nat. Mater. **8**, 299 (2009)
2.17 R. Fung et al., Nat. Phys. **5**, 64 (2009)
2.18 A. Cerezo et al., Mater. Today **10**, Dec. 2007, p. 36
2.19 E.W. Müller, Z. Physik **131**, 136 (1951)
2.20 R. Wiesendanger, *Scanning Probe Microscopy and Spectroscopy – Methods and Applications*, (Cambridge University Press, Cambridge, 1994)
2.21 F.J. Giessibl, Rev. Mod. Phys. **75**, 949 (2003); F.J. Giessibl, Mater. Today, May 2005, p. 32
2.22 J. Bardeen, Phys. Rev. Lett. **6**, 57 (1961)
2.23 J. Tersoff, D.R. Hamann, Phys. Rev. Lett. **50**, 1998 (1983)
2.24 D.M. Eigler et al., Phys. Rev. Lett. **66**, 1189 (1991)
2.25 J.W. M. Frenken et al., Mater. Today, May 2005, p. 20
2.26 F. Besenbacher et al., Mater. Today, May 2005, p. 26
2.27 P.K. Hansma, J. Tersoff, J. Appl. Phys. **61**, R1 (1987)
2.28 A. Weismann et al., Science **323**, 1190 (2009)
2.29 V. Madhavan et al., Science **280**, 567 (1998)
2.30 H.C. Manoharan et al., Nature **403**, 512 (2000)
2.31 A.J. Heinrich, Science **323**, 1178 (2009)
2.32 U. Kemiktarak et al., Nature **450**, 85 (2007)
2.33 G. Binnig, C.F. Quate, Ch. Gerber, Phys. Rev. Lett. **56**, 930 (1986)
2.34 T. Schimmel, Nachrichten FZ Karlsruhe **31**, 2–3, 217 (1999)
2.35 H. Hellmann, *Einführung in die Quantentheorie*, Franz Deuticke, Leipzig 1937
2.36 R.P. Feynman, Phys. Rev. **56**, 340 (1939)
2.37 B.M. Deb, Rev. Mod. Phys. **45**, 22 (1973)
2.38 F. Ciraci et al., Phys. Rev. **41**, 2763 (1990)
2.39 R. Bennewitz, Mater. Today, May 2005, p. 42
2.40 U.D. Schwarz et al., Phys. Bl. **54**, Nr. 12, 1127 (1998)
2.41 F. Saurenbach, B.D. Terris, Appl. Phys. Lett. **56**, 1703 (1990)
2.42 A. Shluger, T. Trevethan, Nature **446**, 34 (2007)
2.43 L. Gross et al., Science **324**, 1428 (2009)
2.44 G. Kada et al., Nanotoday **3**, Feb-Apr. 2008, p. 12
2.45 F. Kienberger et al., Biomaterial **28**, 2403 (2007)
2.46 F. Kienberger et al., Structure **13**, 1247 (2005)
2.47 F. Kienberger et al., EMBO Rep. **5**, 579 (2004)
2.48 E. Abbé, Archiv. Microskopische Anal. **9**, 413 (1873)
2.49 E.H. Synge, Phil. Mag. **6**, 356 (1928)
2.50 D.W. Pohl et al., Appl. Phys. Lett. **44**, 651 (1984)
2.51 E. Betzig et al., Appl. Phys. Lett. **60**, 2484 (1992)
2.52 H. Heinzelmann et al., Thin Solid Film. **273**, 149 (1996)
2.53 R.C. Reddick et al., Phys. Rev. **39**, 767 (1989)
2.54 F. Zenhausern et al., Science **269**, 1083 (1995)
2.55 K.G. Lee et al., Nat. Photon. **1**, 53 (2007)

2.56 F.J. García-Vidal, Nat. Photon. **1**, 13 (2007)
2.57 E. Betzig et al., Science **313**, 1642 (2006)
2.58 R. Schmidt et al., Nat. Meth. **5**, 539 (2008)
2.59 B. Huang et al., Science **319**, 810 (2008)
2.60 M. Heilemann et al., Laser Photon. Rev. **3**, 180 (2009)
2.61 G. Donnert et al., Proc. Nat. Acad. Sci. (USA. **103**, 11440 (2006)
2.62 V. Westphal, S.W. Hell, Phys. Rev. Lett. **94**, 143903 (2005)
2.63 E. Rittweger et al., Nat. Photon. **3**, 144 (2009)
2.64 U. Hartmann, J. Appl. Phys. **64**, 1561 (1988)
2.65 Y. Martin, H.K. Wickramasinghe, Appl. Phys. Lett. **50**, 1455 (1987)
2.66 H.J. Mamin et al., Appl. Phys. Lett. **55**, 318 (1989)
2.67 M. Bode et al., Phys. Rev. Lett. **81**, 4256 (1998)
2.68 R. Wiesendanger et al., Science **255**, 583 (1992)
2.69 S. Heinze et al., Science **288**, 1805 (2000)
2.70 O. Scherzer, J. Appl. Phys. **20**, 20 (1949)
2.71 F. Philipp et al., Ultramicroscopy **56**, 1 (1994)
2.72 M. Haider et al., Nature **392**, 768 (1998)
2.73 C.L. Jia, K. Urban, Science **303**, 2001 (2004)
2.74 K.W. Urban, Nat. Mater. **8**, 260 (2009)
2.75 C.L. Jia et al., Nat. Mater. **7**, 57 (2008)
2.76 P.D. Nellist et al., Science 305, 1741 (2004)
2.77 D.A. Muller et al., Science **319**, 1073 (2008)
2.78 M. Varela et al., Phys. Rev. Lett. **92**, 095502 (2004)
2.79 N. Shibata et al., Nat. Mater. **8**, 654 (2009)
2.80 K. Suenaga et al., Nat. Chem. **1**, 415 (2009)
2.81 G. Möbus, B.J. Inkson, Mater. Today **10**, December 2007, p. 18
2.82 K. van Benthem, S.J. Pennycook, Appl. Phys. A **96**, 161 (2009)
2.83 G. Möllenstedt, H. Düker, Naturwissenschaften **42**, 41 (1955)
2.84 M. Albrecht et al., Inst. Phys. Conf. Ser. **164**, 361 (1999)
2.85 M. van Heel et al., Quart. Rev. Biophy. **33**, 307 (2000)
2.86 O. Medalia et al., Science **298**, 1209 (2002)
2.87 H.X. Sui, K.H. Downing, Nature **442**, 475 (2006)
2.88 M.M. Golas et al., Science **300**, 980 (2003)
2.89 R.D. Leapman et al., Ultramicroscopy **100**, 115 (2004)
2.90 M. Weyland, P.A. Midgley, Mater. Today, December 2004, p. 32
2.91 H.N. Chapman, Science **321**, 352 (2008)
2.92 W.L. Chao et al., Nature **435**, 1210 (2005)
2.93 P.J. Withers, Mater. Today **10**, December 2007, p. 26
2.94 G.-C. Yin et al., Appl. Phys. Lett. **88**, 241115 (2006)
2.95 C.A. Larabell, M.A. Le Gros, Mol. Biol. Cell. **15**, 597 (2004)
2.96 M.A. Le Gros et al., Curr. Opin. Struct. Biol. **15**, 593 (2005)
2.97 C.G. Schroer et al., Phys. Rev. Lett. **101**, 090801 (2008)
2.98 P. Thibault et al., Science **321**, 379 (2008)
2.99 K.A. Nugent, Nat. Phys. **5**, 17 (2009)
2.100 B. Lengeler et al., Appl. Phys. Lett. **74**, 3924 (1999)
2.101 F. Nolting et al., Nature **405**, 767 (2000)
2.102 D. Attwood, Nature **442**, 642 (2006)
2.103 A. Cerezo et al., Rev. Sci. Intrum. **59**, 862 (1988)
2.104 K. Hono, Acta Mater. **47**, 3127 (1999)
2.105 A. Cerezo et al., MRS Bull. **26**, Feb. 2001, p. 102

Chapter 3
Synthesis

In this chapter a survey will be given on the variety of "bottom-up" and "top-down" synthesis techniques for nanostructures focusing first to structures of different dimensionality such as nanocrystals, nanowires, and nanolayers including shape control and more complex nanostructures. After the preparation of bulk nanocrystalline systems the synthesis of carbon nanostructures is discussed with a subsequent overview of nanoporous systems. Finally, the present development of lithography, which is of outstanding importance for the computer industry, will be presented.

3.1 Nanocrystals and Clusters

3.1.1 From Supersaturated Vapors

In nanosciences the term nanoparticle [3.1] is often used for the entire range from dimers to entities with 100 nm in diameter. The term cluster is used for small nanoparticles with less than 10^4 atoms. For cluster synthesis from supersaturated vapors classical nucleation theory is employed. Here, the reversible free energy

$$W(n) = -nk_{\mathrm{B}}T \ln S + 4\pi\sigma \left(\frac{3v}{4\pi}\right)^{2/3} n^{2/3}$$

for forming a cluster with n atoms or molecules contains a "bulk" and a "surface" free energy term where $S = p/p_{\mathrm{e}}$ is the ratio of the vapor pressure p and the equilibrium vapor pressure p_{e} at the temperature T and σ and v denote the surface energy and the volume of a molecule, respectively. From the condition $\partial W/\partial n = 0$ the critical values n^*, r^*, and $W(n^*)$ for cluster nucleation can be derived.

Clusters of atoms from supersaturated vapors may be formed by physical cooling, by supersonic expansion, by gas phase chemical reaction, or by thermal evaporation, sputtering or laser ablation. Mass spectra of clusters formed by evaporation of the cluster material and expansion of the carrier gas in an oven source [3.2] are shown in Fig. 3.1. The predominant cluster sizes of $n = 8, 20, 40$, etc., are called magic numbers which are governed, e.g., by filling the major electronic shells of the clusters at

H.-E. Schaefer, *Nanoscience*, DOI 10.1007/978-3-642-10559-3_3,

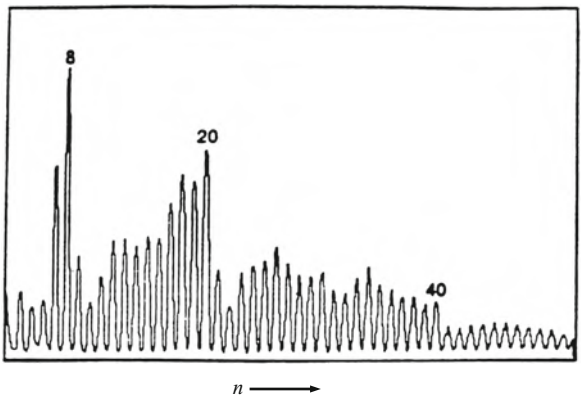

Fig. 3.1 Mass spectra showing the abundance of potassium clusters from a supersonic beam of an oven source as a function of cluster size *n*. (Reprinted with permission from [3.1]. © 1996 Institute of Physics)

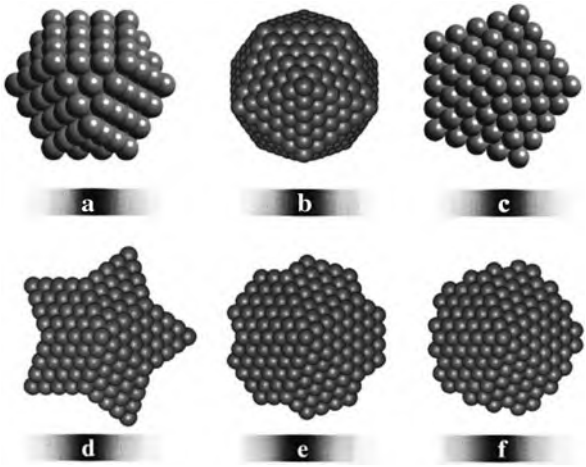

Fig. 3.2 Main shapes observed for small Au clusters. (**a**) fcc cuboctahedron, (**b**) icosahedron, (**c**) regular decahedron, (**d**) star decahedron, (**e**) marks decahedron, and (**f**) round decahedron. (Reprinted with permission from [3.4]. © 2001 American Institute of Physics)

particular sizes. At larger clusters the magic numbers originate from closing shells and subshells of icosahedral clusters [3.3]. Small metallic clusters can assume different shapes (Fig. 3.2) depending on the size and environmental conditions such as ligands or substrates [3.4]. Laser vaporization cluster beams were introduced by Smalley [3.5] yielding 100 torr pressures with laser powers generating temperatures of 10^4 K at the target.

Larger quantities of nanoparticles used for compaction to form nanocrystalline solids may be prepared by thermal evaporation, sputtering, or laser techniques (Fig. 3.3) [3.6].

The distribution of the cluster size r follows a log–normal relation

$$F(r) = \frac{C}{\sqrt{2\pi\sigma^2}} \frac{1}{r} \exp\left(\frac{-\left[\ln(r/r_{\mathrm{M}} - \sigma^2)\right]}{2\sigma^2}\right)^2$$

originating from the coalescence for the growth of particles, where σ is the width of the distribution and r_{M} is the most probable radius.

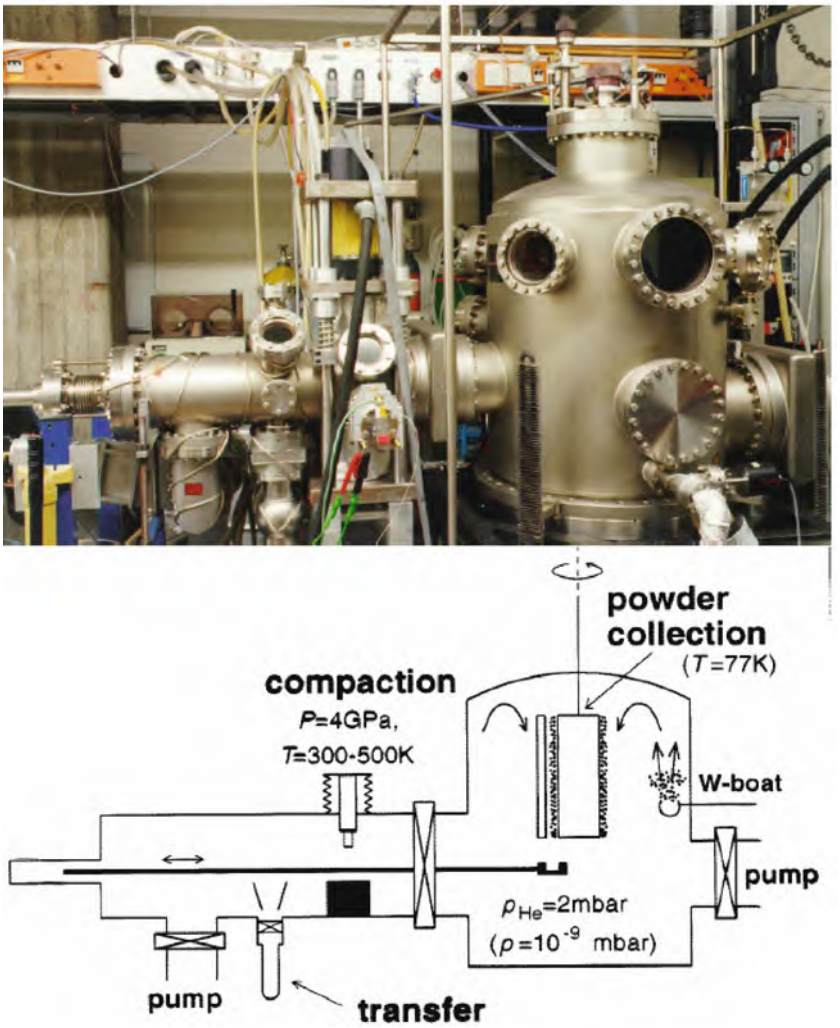

Fig. 3.3 Synthesis facility with a ultrahigh vacuum (UHV) chamber for production of nanocrystalline materials by materials evaporation in a dilute noble gas atmosphere, crystallite condensation, and compaction

3.1.2 Particle Synthesis by Chemical Routes

Chemical synthesis permits the manipulation at the molecular level and with high-compositional homogeneity. Scaling up for economical production of large quantities of materials may be relatively easy in many systems [3.7]. The nanosized particles may be precipitated from a supersaturated liquid solution or a co-precipitation of the batched ions to multinary materials. For many applications (paints, electronic inks, ferrofluids) the agglomeration of the nanoparticles should be suppressed either by particle charging and electrostatic repulsion or by steric

manipulation via surfactants reducing the surface tension. The surfactant molecules can adsorb unto the particle surface and their lyophilic (solution supporting) chains extend into the solvent and prevent the particles from agglomeration. Metals and intermetallics nanocrystallites can be synthesized from aqueous solutions. Noble metals are prepared from aqueous solutions of salts at adjusted pH. Amorphous particles can be produced by adding, e.g., boronhydride at reaction temperatures below the glass temperature. In addition, particles of conventionally immiscible alloys as n-Fe–Cu or n-Co–Cu were prepared by aqueous techniques.

In non-aqueous solutions crystalline metal particles can be prepared such as nanocrystalline iron (n-Fe) by pyrolysis of $Fe(CO)_5$ in polymers or n-Co, n-Ni, n-Cu in ethylene glycol. Alloys as n-PdCu were synthesized by reduction of the acetates or n-Fe/Co by co-reduction of the chlorides with $LiBEt_3H$ in THF, where BEt_3 is triethylboron and THF is tetrahydrofuran.

Nanocrystalline ceramic greenbodies can be sintered at substantially lower temperatures than micrometer-sized powders due to the high interface driving force (see Fig. 3.4). Ultrafine ceramic particles can be obtained by precipitation from solution such as 16 nm tetragonal ZrO_2 powders from precipitated amorphous hydrous

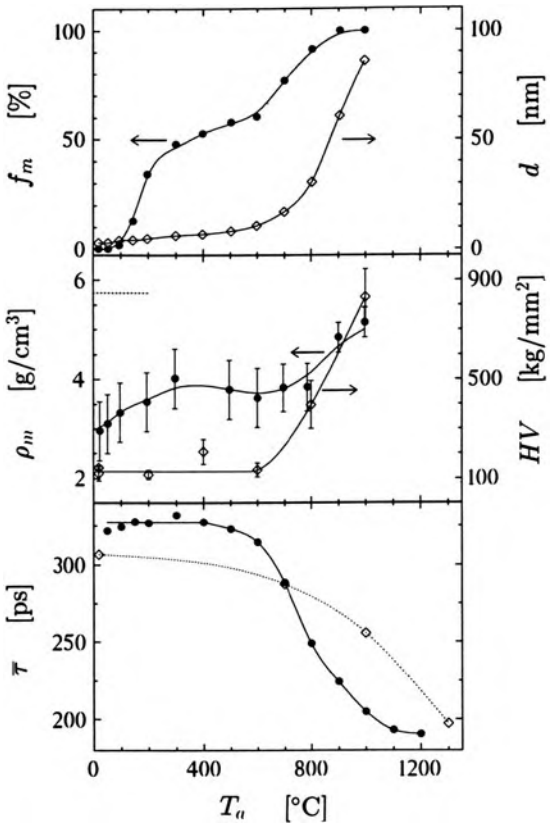

Fig. 3.4 Isochronal annealing ($t_a = 60$ min) of nanocrystalline zirconium dioxide (n-ZrO_2). (**Top**) Fraction f_m of monoclinic phase (•) and crystallite diameter d (◇) as determined from x-ray diffraction. (**Middle**) Mass density ρ_m (•) and Vickers hardness HV(◇). The bulk density of monoclinic ZrO_2 is indicated (· ·). (**Bottom**) Mean positron lifetimes $\bar{\tau}$ of cluster-condensed n-ZrO_2 (•) and of a specimen compacted from commercial ZrO_2 powder (◇) [3.8]. The decrease of $\bar{\tau}$ with increasing annealing temperature indicates the disappearance of nanovoids upon sintering which occurs in n-ZnO_2 at lower T_a than for commercial ZrO_2 powder. (Reprinted with permission from [3.8]. © 1993 Elsevier)

zirconia with subsequent hydrothermal treatment. MoC and WC nanopowders with 2 nm primary particles were synthesized by the ambient temperature reduction of the halides with $LiBEt_3H$.

The advantage of chemical homogeneity on the molecular scale is used for the production of WC/Co composites for cutting tool applications from the aqueous precipitation of tris(ethylenediamine) cobalt (II) tungstate, tungstic acids, and ammonium hydroxides. The extremely fine mixtures of the spray-dried W and Co salts are reduced with H and reacted with CO in a fluidbed reactor to yield WC/Co nanophase powder [3.9]. Furthermore, n-Si_3N_4/SiC nanoceramics can be prepared from a liquid organosilazane precursor $[CH_3SiHNH]_n$ ($n = 3,4$) by laser treatment [3.10] or pyrolysis [3.11].

One important chemical process for the formation of nanophase ceramics is the sol–gel process where powder size, morphology, and surface chemistry are controlled simultaneously [3.12]. In this case the precursors for ceramics synthesis are, e.g., alkoxides or colloidal sols. When using organometallic alkoxide precursors, e.g., $Al(OC_4H_9)_3$ for alumina synthesis, reactions such as hydrolysis and polymerization are employed to the irreversible sol–gel transition (see Fig. 3.5). Multicomponent nanophase oxides can be prepared by initially mixing several alkoxides.

For the controlled synthesis of nanoscale particles self-assembled membranes [3.13] are employed which include micelles, microemulsions (Fig. 3.6), liposomes (water droplets covered by several layers of phospholipids), and vesicles with diameters down to 3–6 nm. The membrane structure serves as reaction cage to control supersaturation (nucleation and growth of the particles) and acts as agglomeration barrier.

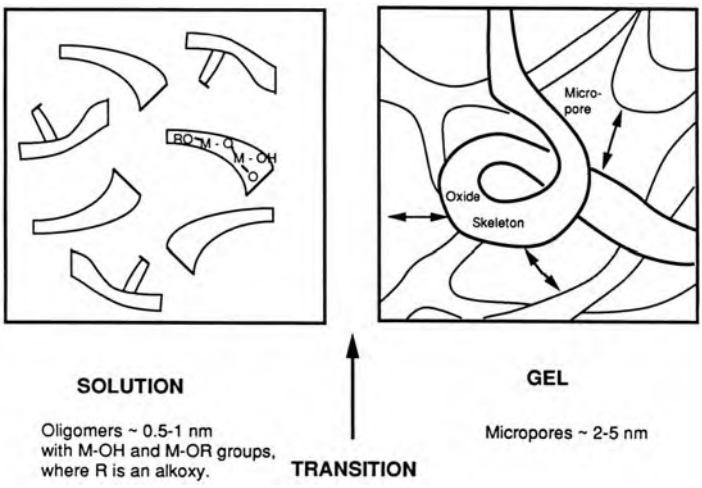

Fig. 3.5 Schematic of the oxide skeleton of a dried gel following the alkoxide solution route. (Reprinted with permission from [3.12]. © 1996 Institute of Physics)

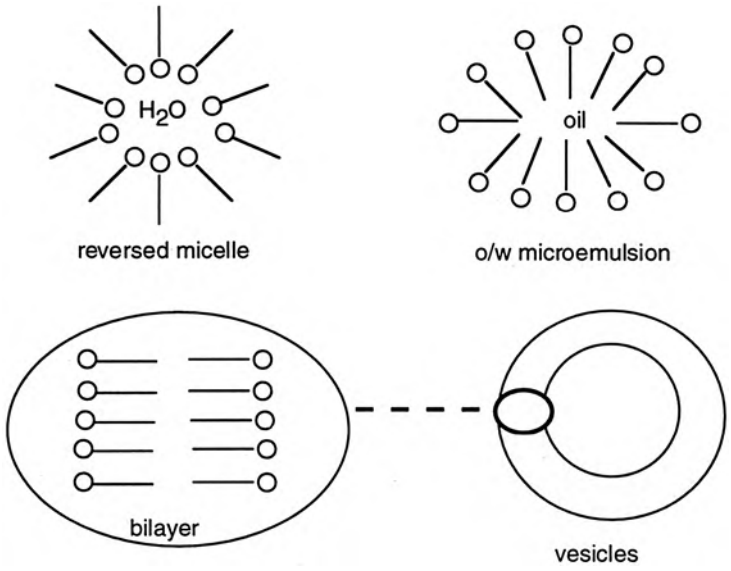

Fig. 3.6 Sketch showing different self-assembled membrane structures. (Reprinted with permission from [3.7]. © 1996 Institute of Physics)

3.1.3 Semiconductor Nanocrystals (Quantum Dots)

Semiconductor nanocrystals of CdSe were initially produced making use of reversed micelles [3.14]. The main goal in nanocrystals synthesis of II–VI, IV–VI, or III–V semiconductor clusters for quantum size effects, nonlinear optical properties, or photoconductivity [3.15] is to narrow the size distribution to below 10–20%. The semiconductor clusters can be prepared as dispersed colloids and stabilized within micelles, polymers, glasses, or zeolites.

For the characterization of semiconductor nanoclusters mainly x-ray diffraction and EXAFS techniques are used to identify the chemical surrounding and coordination. Quantum confinement effects in quantum dots can be nicely demonstrated by the optical behavior of semiconductor nanoparticles. The photoluminescence of CdTe quantum dots shifts from red (wave length 623 nm) to green (520 nm) (Fig. 3.7), which is called blue shift, when the dot size is decreased from 5.1 to 3.0 nm [3.16].

3.1.4 Doping of Nanocrystals

Doping enhances the properties of nanocrystals by controlling their electronic, optical, transport, and magnetic behavior (see [3.17]). The most common strategy for doping is to include a precursor containing the dopant in the solid-, gas-, or

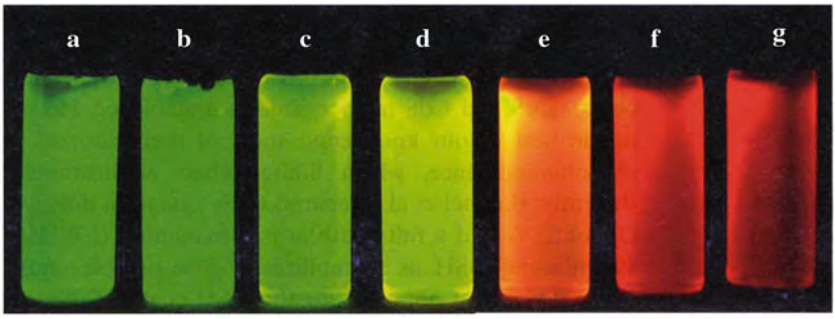

Fig. 3.7 Photoluminescence colors (wave length 623–520 nm) of crystalline CdTe quantum dots with sizes from 5.1 nm (*right*) to 3.0 nm (*left*) with absorption peaks between 570 and 495 nm in the UV excitation light. (Reprinted with permission from [3.16]. © 2006 Wiley-VCH)

liquid-phase synthesis. In contrast to the ultraviolet emission from undoped ZnSe nanocrystals, a range of colors is observed upon doping with Mn and Cu (Fig. 3.8). For Mn doping, electron paramagnetic resonance can distinguish dopants on the surface from those inside the nanocrystal (see [3.17]).

3.1.5 Magnetic Nanoparticles

A variety of monodisperse magnetic nanoparticles can be synthesized for application in high-power hard magnets (see Sect. 8.4), in high-density data storage (see Sect. 9.5), or for magnetic resonance imaging (see Sect. 12.2).

Metallic Fe and Co nanoparticles are of importance due to their high magnetization but chemically instable. Monodisperse Fe nanoparticles can be prepared by thermolysis of $Fe(CO)_5$ in 1-octadecene (ODE) with subsequent oxidation in air in order to prepare superparamagnetic core/shell nanoparticles of Fe/Fe_3O_4 (5 nm/5 nm; Fig. 3.9a). Nanocubes of 7-nm of Fe were made by thermolysis of $(Fe[N(SiMe_3)_2]_2)$ and hollow Fe nanoframes were formed via molten salt corrosion (see [3.18]). Co particles were obtained by either cobalt carbonyl decomposition or cobalt salt reduction (see [3.18]). Hollow Co particles were produced by fast outdiffusion of CoO species and surface reduction of the oxides by oleylamine (OAm) [3.18, 3.19].

Magnetic ferrite nanoparticles with cubic spinel structures such as superparamagnetic Fe_3O_4 nanoparticles can be reacted in an organic phase from metal acetylacetonates (acac) and 1, 2-alkanediols [3.18, 3.20] (Fig. 3.9b). Nanodisks of α-Fe_2O_3 (Fig. 3.9c) are prepared from a solution of $FeCl_3$ and NaH_2PO_4. The disk-shape is generated by the blocking of the growth process on the (001) plane, owing to high-density phosphate adsorption on this plane. The enhanced coercive field of these multidomain particles is ascribed to the pinning of surface domain walls by the adsorbed phosphate molecules [3.21].

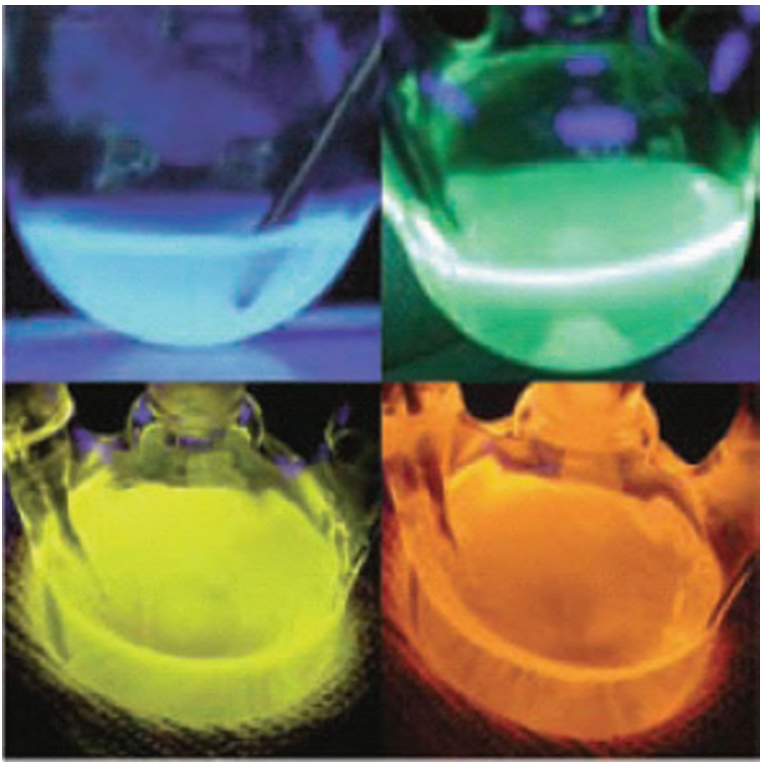

Fig. 3.8 Fluorescence of Cu- (*top* two images) and Mn- (*bottom* two images) doped ZnSe nanocrystals. The fluorescence color depends on the position of the dopant atom inside the ZnSe nanocrystals. (Reprinted with permission from [3.17]. © 2008 AAAS)

Nanosized FePt and FeCo alloys are of importance because FePt is considered for high-density data storage devices (see Sect. 9.5) and FeCo has the highest magnetic moment at ambient conditions (see [3.21]). Nanoparticles of fct-FePt can be obtained via thermal annealing of MgO-coated fcc-FePt particles followed by MgO removal. FeCo particles of 20-nm (Fig. 3.9d) were made by polyol co-reduction of Fe(III)- and Co(II)-acetylacetonates in oleic acid/oleylamine under a reductive atmosphere [3.18].

Nanomagnets of SmCo and NdFeB alloys are at the center of hard-magnet research (see Sect. 8.4) and can be prepared by solution-phase chemical synthesis (see [3.18]). Polyvinyl pyrrolidone (PVP)-assisted co-reduction of Sm and Co nitrates in tetraethylene glycol (TEG) were used to make SmCo [3.22] with 10 nm × 100 nm $SmCo_5$ nanocrystals and a slight Sm_2Co_{17} content (Fig. 3.9e), yielding a coercivity of 6.1 kOe and a magnetization of 40 emu/g at ambient temperature.

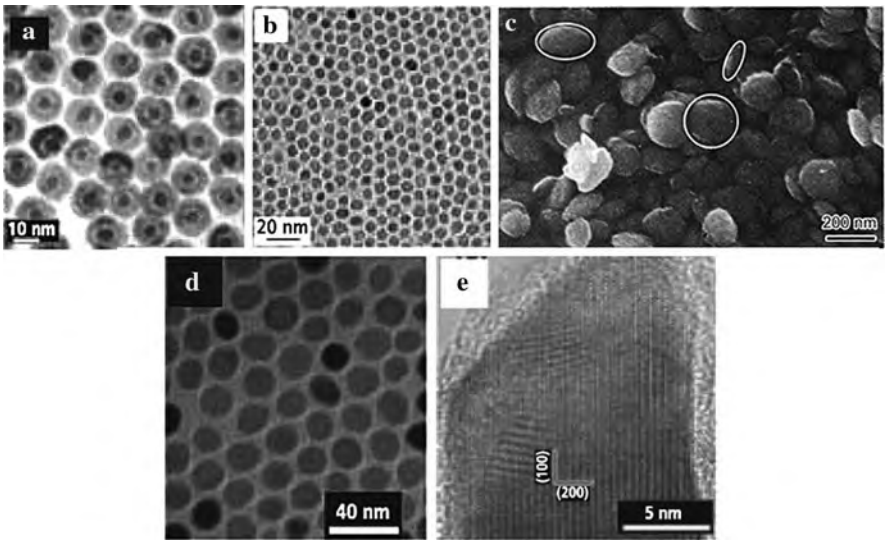

Fig. 3.9 (**a**) Transmission electron micrograph (TEM) of 5 nm/5 nm Fe/Fe_3O_4 core/shell particles. (**b**) TEM of 6 nm Fe_3O_4 particles (see [3.18]). (**c**) Scanning electron micrograph (SEM) of α-Fe_2O_3 nanodisks [3.21]. (**d**) TEM of 20 nm FeCo particles. (**e**) High-resolution TEM of $SmCO_5$ magnet particles prepared by the polyvinyl pyrrolidone (PVP) process (see [3.18]). (Reprinted with permission from [3.18] (**a**) (**b**) (**d**), [3.21] (**c**), and [3.22] (**e**). © 2008 Sigma-Aldrich (**a**) (**b**) (**d**), © 2009 Chinese Society of Metal (**c**), and © 2008 American Institute of Physics (**e**))

3.2 Superlattices of Nanocrystals in Two (2D) and Three (3D) Dimensions

By functionalization of nanocrystals or by choosing nanocrystals with two different compositions or sizes, long-range ordered 2D or 3D structures (superlattices) with novel properties can self-assemble (see Sect. 1.5) as discussed in the following.

3.2.1 Free-Standing Nanoparticle Superlattice Sheets

Free-standing monolayer superlattices of alkyl-conjugated [3.23] or DNA-ligated [3.24] gold nanoparticles were synthesized in a drying-mediated self-assembly process starting from solution droplets on microholes. These free-standing layers exhibit thicknesses from 9.6 to 66 nm and interparticle spacings from 1.2 to 20 nm.

Close-packed nanoparticle arrays [3.23] can be formed by letting dodecanethiol-ligated Au nanocrystals (6 nm in diameter) suspended in toluene spread across the top of a water droplet resting on a Si_3N_4 substrate with microholes (Fig. 3.10a). As

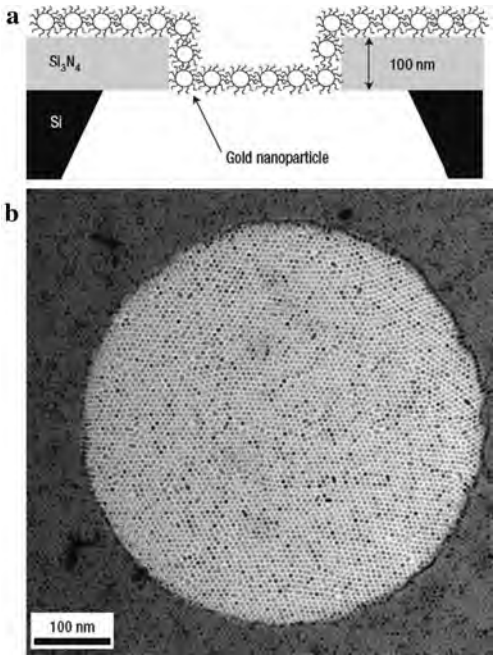

Fig. 3.10 Self-assembled ultrathin nanoparticle layers. (**a**) Schematic diagram of the nanoparticle layer configuration inside a microhole. The layer recedes into the hole. The projection of nanoparticles on the vertical wall of the hole shows up as a dark band at the edge in (**b**). (**b**) Transmission electron micrograph (TEM) of a Au nanoparticle monolayer freely suspended over a hole with a 0.5 μm diameter in the Si_3N_4 substrate. (Reprinted with permission from [3.23]. © 2007 Nature Publishing Group)

the water evaporates, the monolayer drapes itself over the substrate and the holes with an average interparticle spacing of ∼1.4 nm, high order (Fig. 3.10b), and a thickness of ∼9.4 nm. The high Young's modulus of $E = 6$ GPa is a consequence of the confinement of the ligands to the nanoparticle surface and to the spaces between the particles, which is consistent with molecular dynamics simulations (see [3.23]). In addition to the high Young's modulus, the ultrathin membranes possess a high bending flexibility (see Fig. 3.10) which should make it well suited for a wide range of applications.

Free-standing nanoparticle superlattice sheets controlled by DNA ligands can have both structural and functional properties rationally controlled by adjusting the DNA length up to 20 nm [3.24]. Monodisperse 13 nm diameter gold nanoparticles are capped with 5′-thiolated single-stranded DNA (ssDNA; Fig. 3.11a); when a droplet of colloidal solution dries on a holey substrate, 2D free-standing well-ordered films of the capped gold nanoparticles form with interparticle spacings depending on the DNA length (Fig. 3.11b, c) and with sheet thicknesses between ∼37 and ∼66 nm [3.24]. The optical properties of the sheets show color variations from blue to pink under white-light illumination (Fig. 3.11d, e) as interparticle spacing is varied which can be understood by discrete dipole approximation simulations (see [3.24] and Sect. 7.6), suggesting dominant dipole plasmon coupling resonance in the sheets. This behavior could enable the integration of free-standing monolayer sheets into future optoelectronic devices [3.24].

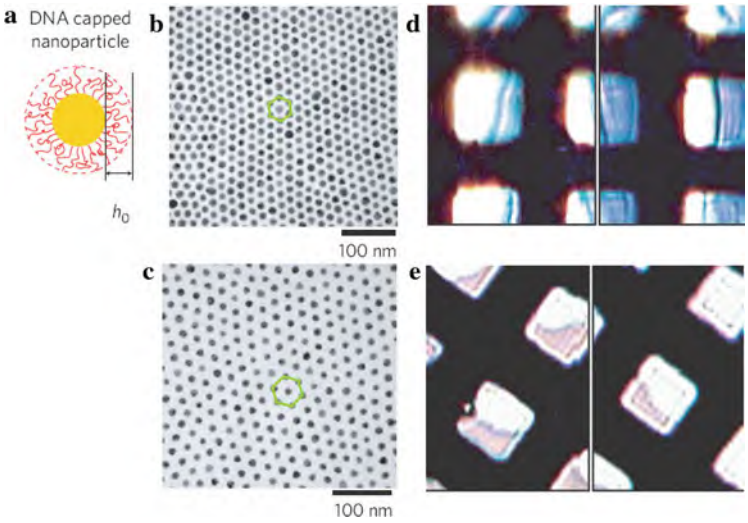

Fig. 3.11 Free-standing Au nanoparticle superlattice sheets controlled by DNA. (**a**) Schematic of a DNA-capped Au nanoparticle. (**b**–**c**) Regulation of the interparticle spacing by the DNA length DNA-T15 (**b**) and DNA-T90 (**c**). (**d**–**e**) DNA regulated plasmon coupling of superlattice sheets. Representative photographic images of sheets with the ligands DNA-T5 (**d**) and DNA-T30 (**e**), which were acquired in transmission mode under white-light illumination. (Reprinted with permission from [3.24]. © 2009 Nature Publishing Group)

3.2.2 3D Superlattices of Binary Nanoparticles

A wide-structural diversity can be achieved by the assembly of nanoparticles of two different materials into a binary nanoparticle superlattice (BNSL) [3.25], which can provide a general path to a large variety of materials (metamaterials) with precisely controlled chemical composition and tight placement of the components. In combinations of semiconducting (PbS, PbSe), metallic (Au, Ag, Pd), and magnetic (Fe_2O_3) nanoparticle building blocks, space-filling, particle charging, the relative concentrations of A and B particles, and the nanocrystal shape can be used to engineer the structure of the self-assembled BNSLs.

Nearly spherical nanoparticles can self-assemble into BNSLs with domains coherently packed over up to 10 μm in lateral dimensions with different structures (see Fig. 3.12a–c). By addition of oleic acid, PbSe nanoparticles are charged positively and dodecanethiol-capped metal particles negatively, whereas the addition of tri-*n*-octylphosphine oxide (TOPO) yields negatively charged PbSe nanocrystals and neutral metal particles [3.25]. Therefore, the structure of BNSLs of the same composition can be entirely changed by changing from oleic acid to TOPO (Fig. 3.12d–g). The nanocrystal shape can be used as an additional tool to control the BNSL structure as shown for a combination of LaF_3 triangular nanoplates and spherical Au nanocrystals in Fig. 3.12 h.

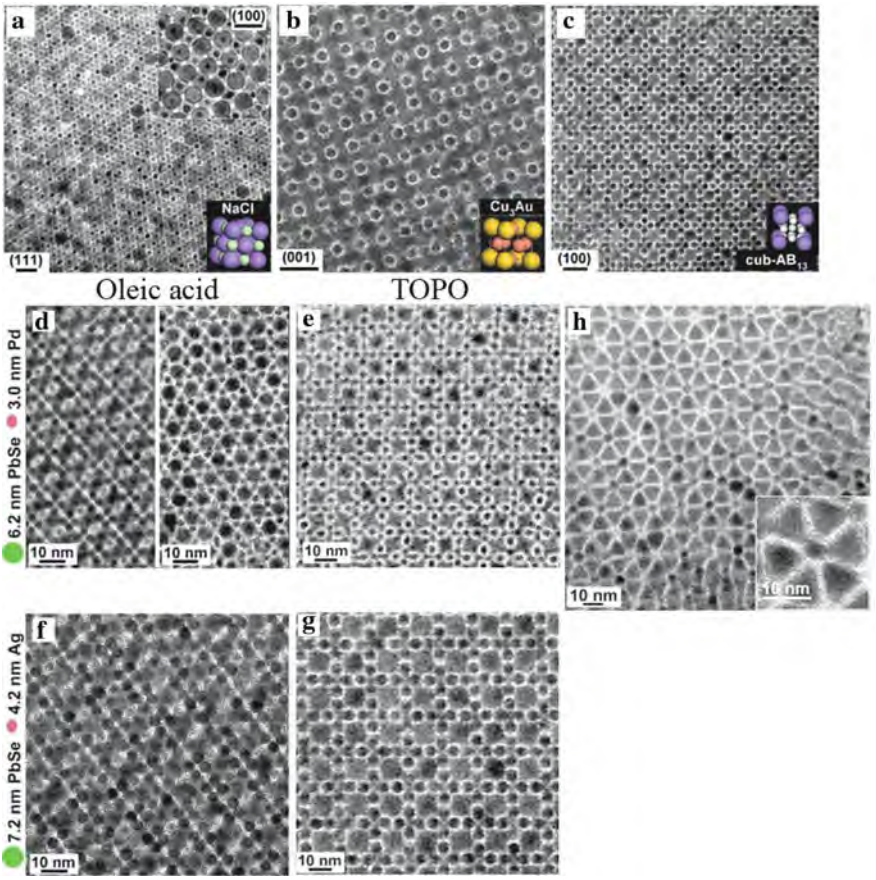

Fig. 3.12 (**a**–**c**) Transmission electron micrographs (TEM) of the characteristic projections of binary superlattices, self-assembled from different nanoparticles, and modeled unit cells of the corresponding 3D structures. (**a**) 13.4 nm diameter γ-Fe_2O_3 and 5.0 nm Au nanoparticles, NaCl structure, (111) scale bar 20 nm; (**b**) 7.2 nm PbSe and 4.2 nm Ag, Cu_3Au structure, scale bar 10 nm; (**c**) 6.2 nm PbSe and 3.0 nm Pd nanoparticles, cubic AB_{13} structure, scale bar 20 nm. The lattice projection is labeled in each panel above the scale bar. (**d**–**g**) TEM images of binary nanoparticle superlattices (BNSLs) self-assembled in the presence of oleic acid (*left column*) or tri-*n*-octylphosphine oxide, TOPO (*right column*). (**d**) 6.2 nm PbSe and 3.0 nm Pd nanoparticles self-assembled into orthorhombic AB- and AlB_2-type BNSLs and (**e**) into $NaZn_{13}$-type BNSL. (**f**–**g**) 7.2 nm PbSe and 4.2 nm Ag nanoparticles self-assembled into *orthorhombic* AB and *cuboctahedral* AB_{13} BNSLs, respectively. (**h**) TEM image and unit cell of BNSL self-assembled from *triangular* LaF_3 (9.0 nm side) nanoplates and *spherical* nanoparticles (5.0 nm) of Au. (Reprinted with permission from [3.25]. © 2006 Nature Publishing Group)

Nanocrystallites of Ag (diameter 5.1 nm) and Au (4.8 nm) functionalized with alkane thiols to final diameters of ~8.6 and ~8.36 nm, respectively, self-assemble to binary nanoparticle crystals (micrometers in diameter) with a non-close-packed diamond-like lattice and a lattice constant $a = 19$ nm [3.26]. Formation of this non-close-packed structure, which is stable versus NaCl and CsCl lattices, is a

consequence of electrostatic effects specific of the nanoscale, where the thickness of the screening layer is commensurate with the dimensions of the assembling objects [3.26].

3.3 Nanowires and Nanofibers

In the early 1980s it was theoretically predicted that quantum wires may have applications in high-performance transport devices due to their saw tooth like density of states (see Sect. 1.3). Novel techniques for nanowire formation were reviewed [3.27–30].

A popular technique for producing sub-10 nm features is "top-down" nanofabrication where a pattern is transferred on a material by selective irradiation (lithography by electrons, ions, photons) of a resist wire, subsequent development and etching. This approach, however, is hardly capable of producing structures with dimensions in a single-digit-nanometer range. Scanning tunneling microscopy (STM) and atomic force microscopy (AFM) fabrication techniques can achieve these dimensions but large area patterning produced in this fashion would be time consuming. Therefore, new techniques are required which, e.g., involve templates for the formation of natural-forming self-organizing 1D nanostructures which are to be discussed in the following.

Quantum wires can be grown at surface steps as templates. Atoms and molecules adsorbed on surfaces tend to stick to the step edges of a surface where they find extra bonding partners (see Fig. 3.13). The coverage determines the stripe width, the miscut angle of the substrate the stripe separation. In Fig. 3.14, 3 nm wires of Cu with a low surface energy not alloying with the high-surface energy Mo(110) substrate are shown.

In step-flow surface growth all the familiar equilibrium growth modes reappear such as row-by-row growth (equivalent to layer by layer), Stranski–Krastanov (layer and island growth) and island growth.

More universal techniques emerge for structuring the surfaces of the ubiquitous semiconductor material Si. On the reconstructed Si(111) (7×7) surface regular step arrays appear giving rise to natural grooves (see Fig. 3.15). On this surface epitaxial CaF_2 stripes can be deposited as masks (see Fig. 3.15). Selectively between these

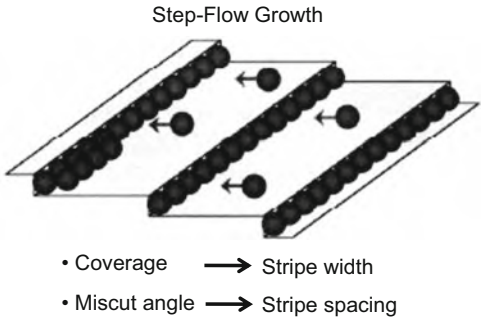

Fig. 3.13 Fabrication of nanowire arrays by self-assembly of atoms at stepped surfaces with stripe rows formed by step-growth flow. (Reprinted with permission from [3.27]. © 1999 Materials Research Society)

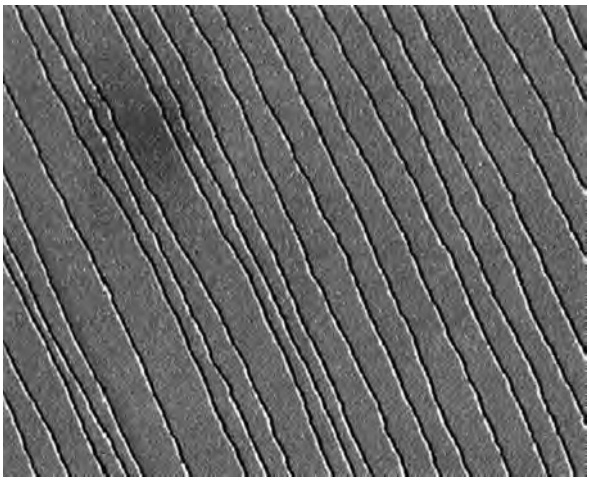

Fig. 3.14 STM image of Cu wires with a 3 nm width and a 50 nm separation grown by step flow on a Mo(110) surface. Copper appears bright as a result of resonant tunneling into a surface state. (Reprinted with permission from [3.27]. © 1999 Materials Research Society)

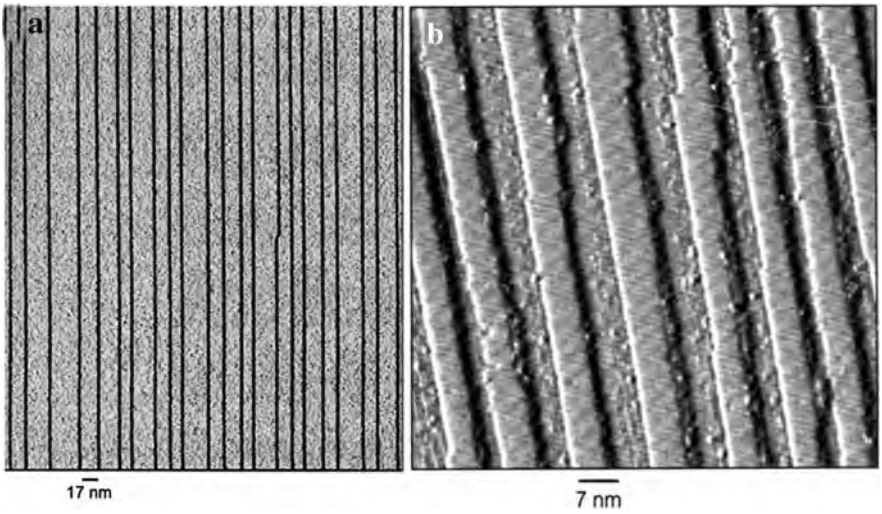

Fig. 3.15 Array of straight steps on Si(111) (7×7). In (**a**) only a single kink is detected in 20,000 edge atoms. Epitaxial CaF_2 mask deposited on a stepped Si(111) (7×7) surface. (Reprinted with permission from [3.27]. © 1999 Materials Research Society)

CaF_2 stripes, e.g., organic precursor molecules for metal–organic chemical vapor deposition (MOCVD) of metals can be deposited [3.27].

III–V semiconductor quantum wires such as gate-controlled GaAs nanowires can be formed by using Schottky in-plane or wrap gates (Fig. 3.16) for a selective depletion of a 2D molecular beam epitaxy (MBE) grown AlGaAs/GaAs quantum well electron gas [3.28]. The structures are formed by standard electron beam

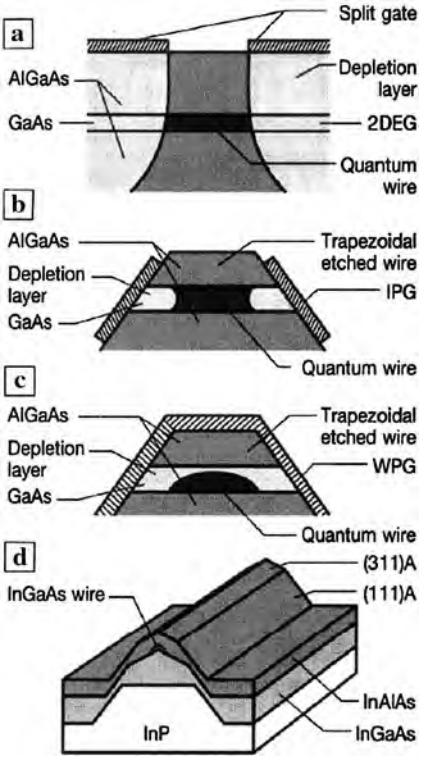

Fig. 3.16 Approaches for III–V nanowire formation. (**a**) Standard split-gate approach, (**b**) cross-section of a Schottky in-plane gate (IPG)-controlled GaAs wire, (**c**) cross-section of a Schottky wrap gate (WPG) controlled GaAs wire, and (**d**) a schematic view of an InGaAs nanowire embedded in InAlAs formed by selective molecular-beam epitaxy on an InP-patterned substrate. 2 DEG denotes a 2D electron gas. (Reprinted with permission from [3.28]. © 1999 Materials Research Society)

lithography, metal deposition, and etching. These gate-controlled semiconductor nanowires exhibit quantization of conductance.

The InGaAs/InAlAs heterostructure system on a InP substrate may be attractive for quantum devices operating at high temperatures due to its large conduction band discontinuity and a superb electron transport. InGaAs ridge nanowires were grown by selective MBE making use of self-organization during crystal growth on InP substrates [3.28] (see Fig. 3.16d).

3.3.1 Vapor–Liquid–Solid (VLS) Growth of Nanowires

Semiconductor nanowires can be grown from metal nanodroplets (e.g., Au) on a substrate. First a gold droplet reacts with Si from the gas phase to form droplets of liquid AuSi upon Si supersaturation, then Si precipitates beneath the droplets (see [3.31]). The droplets remain on the tips of the Si nanowires and allow them to continue growing fed by the Si supply from the gas phase. The diameter of the wire, which may be much less than achieved by lithography, depends on the size of the Au particle and the length depends on the growth time. By switching between source

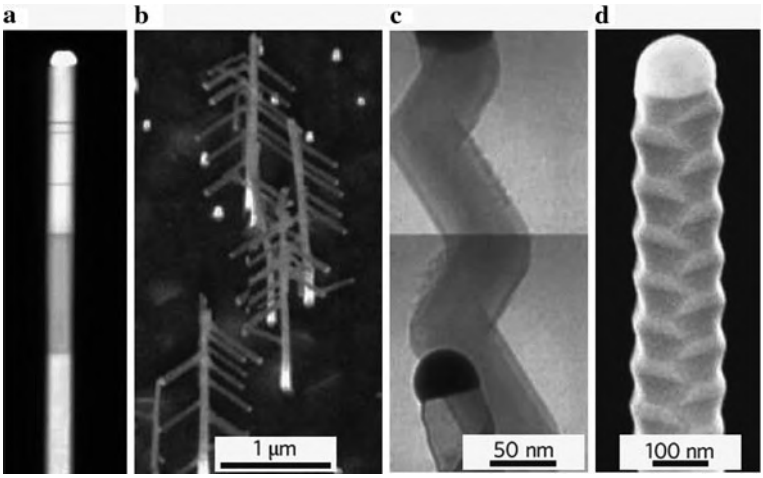

Fig. 3.17 Different types of semiconductor nanowires [3.31]. (**a**) Axially modulated InAs/InP nanowire (30 nm in diameter) grown by chemical beam epitaxy and imaged using high-angle annular dark-field scanning transmission electron microscopy [3.31]. The InP segments appear darker. (**b**) GaP nanowires with branches of GaP, grown by metallorganic chemical vapor deposition (MOCVD) and imaged by scanning electron microscopy (SEM) [3.33]. (**c**) Si nanowires grown by CVD and imaged by transmission electron microscopy. The growth direction is changed by the periodic addition of 10% oxygen to the disilane source gas [3.31]. (**d**) Periodically twinned InP nanowire imaged by SEM [3.34]. (Reprinted with permission from [3.31] (**a**) (**c**), [3.33] (**b**), and [3.34] (**d**). © 2009 Nature Publishing Group (**a**) (**c**), 2004 Nature Publishing Group (**b**), 2008 Nature Publishing Group (**d**))

gases, nanowires of modulated composition can be created (Fig. 3.17a). Varying the growth conditions allows cladding layers to be deposited around the wires to create core/shell geometries. Electronic confinement within these structures is exploited in sensors and nanoelectronic and nanophotonic devices [3.32] (see Sect. 4.2). The addition of fresh particles to previously grown wires allows the creation of branched structures (Fig. 3.17b). Growth direction and changes in diameter can be controlled through surface chemistry (Fig. 3.17c).

The dependence of the structure of InP nanowires – wurtzite or zincblende – of growth temperature, diameter, and doping level (see [3.31]) is of interest because the two types of crystals have different band structures. In pure zincblende InP nanowires a periodic sequence of twin planes appears (Fig. 3.17d) which is predicted to give rise to new electronic properties, including the formation of minibands and the opening of gaps. It has been shown that in nanowires unprecedented control of the crystal structure can be achieved [3.31, 3.34, 3.35].

The formation of nanowires in carbon nanotubes was studied soon after the discovery of the nanotubes (see [3.29]). For this process capillarity, wetting, and surface tension play an important role. For the synthesis of a carbon nanotube with encapsulated Ni (see Fig. 3.18) the following mechanism is suggested [3.30].

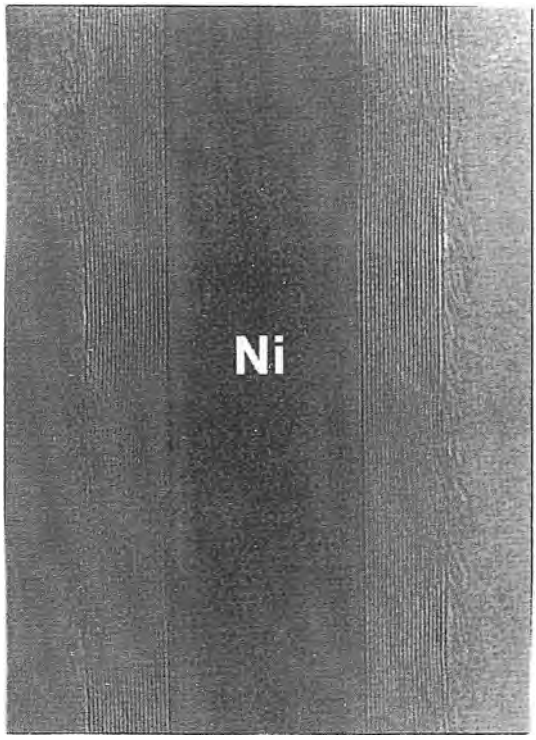

Fig. 3.18 Ni-filled carbon nanotube grown by pyrolysis of C_{60}–Ni substrates [3.29]; interlayer spacing of the carbon nanotubes about 0.34 nm. (Reprinted with permission from [3.29]. © 1999 Materials Research Society)

Initially the metal atoms react at high temperatures with the C particles. Then a carbide surface layer is formed and C extruded to form a concentric covering of C nanotubes. Further Ni_3C/Ni is drawn into the tube with a simultaneous growth of wall and core. Finally the carbon tube may be closed at decreasing temperatures (Fig. 3.19) reaching a length of up to 2.5 μm. In the C nanotubes long Fe nanowires can be protected from oxidation and may prove advantageous in the design of magnetic-storage devices.

The growth process of nanowires has been studied on an atomic scale by high-resolution electron microscopy and density functional theory in the case of catalyzed growth of carbon nanofibers [3.36]. The growth process occurs by surface diffusion of C atoms to the step edges of the Ni catalytic nanocrystals (Fig. 3.20) where the step edges act as dynamic growth sites for the carbon nanofiber. From concomitant density functional theory (DFT) calculations, diffusion energy barriers of 0.1 eV for Ni and 0.5 eV for C adatoms at the graphene–Ni(111) interface are deduced. DFT shows that Ni step edges can be induced by absorbed C atoms because the C binding energy to a Ni step is higher than the energy required for step formation. It, furthermore, yields an estimate of the total energy for incorporation of a C atom from the gas phase to the growing nanofiber of 1.6 eV which is in agreement with the measured activation energy of carbon fiber growth.

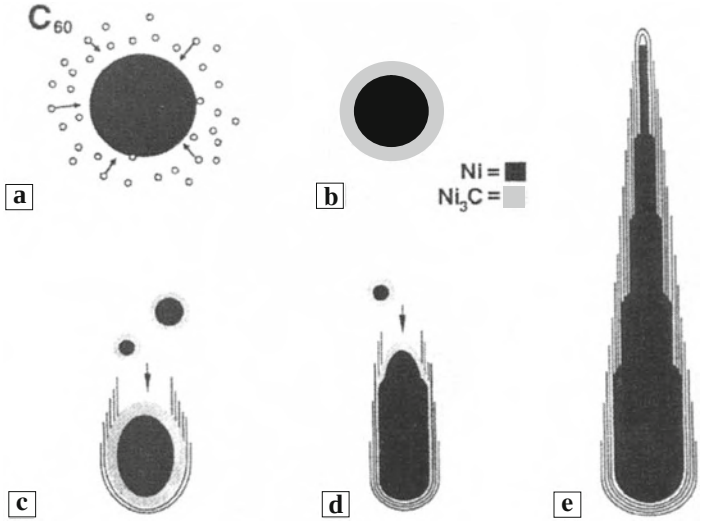

Fig. 3.19 Schematic of a growth process of a Ni-filled carbon nanotube. After the reaction of the metal with the C source, e.g., Ni-filled C_{60} molecules (**a**) or carbon-coated Ni clusters (**b**) may be formed. Then carbon extruded from the coated nanoclusters may form concentric tubes (**c**). Upon further uptake of Ni_3C/Ni the nanotube and the core grow simultaneously (**d**) and the carbon edges close (**e**) when the C supply ceases. (Reprinted with permission from [3.29]. © 1999 Materials Research Society)

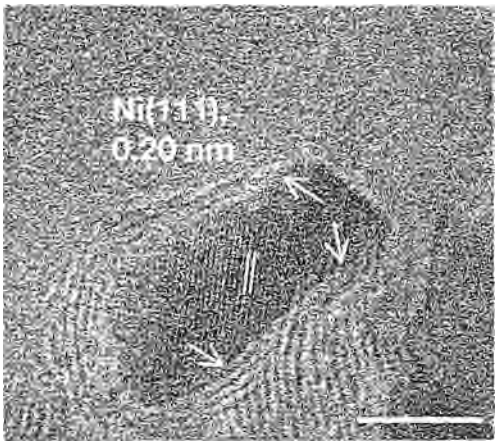

Fig. 3.20 In situ TEM image showing a Ni nanocrystal ((111) lattice fringes) during carbon nanofiber growth. *Arrows* indicate monoatomic step edges of the Ni surface. The Ni catalyst is exposed to a CH_4:H_2 = 1:1 mixture of a total pressure of 200 Pa and a temperature of ~800 K; scale bar 5 nm. (Reprinted with permission from [3.36]. © 2004 Nature Publishing Group)

3.3.2 Pine Tree Nanowires with Eshelby Twist

Hierarchical nanostructures of lead sulfide nanowires resembling pine trees (see Fig. 3.21) were synthesized by chemical vapor deposition [3.37]. Structural characterization reveals a screw-like dislocation in the nanowire trunks with

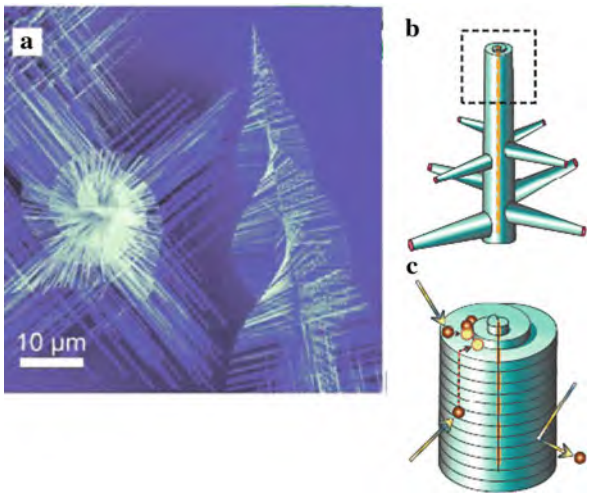

Fig. 3.21 (**a**) High-magnification scanning electron micrograph (SEM) of PbS pine tree nanowires highlighting the twisting (Eshelby twisting) of the central trunk and helical rotating branches. (**b**) Scheme of the magnified tip of a tree structure highlighting the combined faster dislocation-driven trunk nanowire growth and slower vapor–liquid–solid (VLS) driven branched nanowire growth. (**c**) A simplified scheme illustrating that the self-perpetuating steps of a screw dislocation spiral at the tip of a trunk can enable 1D crystal growth of nanowires. (Reprinted with permission from [3.37]. © 2008 AAAS)

helically rotating epitaxial branch nanowires. It is suggested that the screw component of an axial dislocation provides the self-perpetuating steps to enable 1D crystal growth, in contrast to mechanisms that require metal catalysts. Using elasticity theory, Eshelby [3.38] has shown that in a finite cylindrical rod containing an axial screw dislocation at the center, the stress field of the dislocation exerts a torque at the free ends of the rod, resulting in a twist of the rod along the axial direction. The rotating trunks and branches are the consequence of the Eshelby twist of screw dislocations with a Burgers vector along the <110> directions having an estimated magnitude of 0.6 nm for the screw component. A screw dislocation-driven nanowire growth process may be more general for other materials or may coexist with vapor–liquid–solid (VLS) growth.

3.3.3 Ultrathin Nanowires

Ultrathin nanowires are considered to be less than 10 nm in diameter with an especially large interest emerging in nanowires below ~2–3 nm [3.39] with particular emphasis to nanowires of Al, Pb, Bi, Si, Rh, Ag, Cu, and Au. The synthesis methodologies comprise templating ligand control and oriented attachment.

In the *templating* strategy the isotropicity of crystal growth is constrained by the templates which may be mesoporous materials, nanocrystals, structured surfaces, or

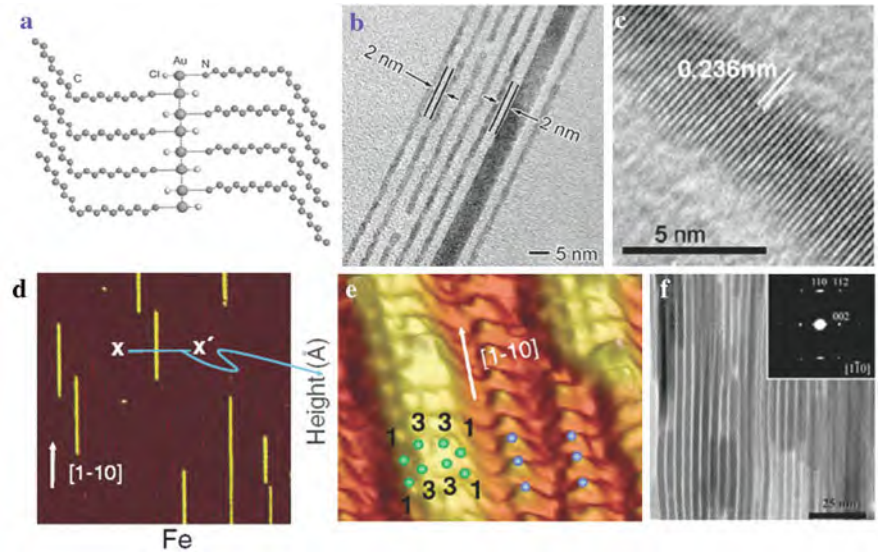

Fig. 3.22 *Templating strategies:* (**a**) Drawing of the [(oleylamine)AuCl]$_n$ inorganic polymer which templates the gold nanowire depicted in (**b**) [3.39]. (**b**) A group of parallel nanowires separated by a distance of ~2 nm [3.40]. (**c**) High-resolution transmission electron micrograph (HRTEM) of a 3 nm Au nanowire [3.41]. (**d**) Scanning tunneling micrograph (STM; 57 x 57 nm^2) of iron nanowires after deposition of 0.05 ML of Fe on a Cu_3N–Cu (110) molecular network [3.43]; (**e**) STM of a Fe atomic nanowire from (**d**) (3.9 × 4.8 nm^2) superimposed upon the Fe atom positions from an ab initio study; the *light green circles* designate the Fe atoms and the *blue circles* the N atoms in the top layer of Cu_3N [3.43]. *Ligand control strategy:* (**f**) TEM of Cu_2S nanowire bundles [3.44]. (Reprinted with permission from [3.39] (**a**), [3.40] (**b**), [3.41] (**c**), [3.43] (**d**) (**e**), [3.44] (**f**). © 2009 Wiley-VCH (**a**), © 2008 American Chemical Society (**b**) (**c**), © 2009 American Physical Society (**d**) (**e**), © 2005 American Chemical Society (**f**))

micelles. In mesoporous materials, e.g., 5 nm magnetite nanowires were produced. Nanocrystals are used in the vapor–liquid–solid (VLS, see above) technique to grow thin Si nanowires (see [3.39]. Thin Au nanowires (Fig. 3.22b) were grown by reducing gold chloride salts through oleylamine (Fig. 3.22a) and silver nanocrystals, forming an [(oleylamine) AuCl]$_n$ inorganic polymer, which templates the formation of ultrathin nanowires with uniform thickness [3.40]. Single-crystalline Au nanowires of 9 nm diameter (Fig. 3.22c) were found to have a good conductivity, a high failure current density, and a high resistance to electromigration and, therefore, are very promising for nanoelectronic circuitry [3.41]. Monatomic Co chains were synthesized on Pt (997) surfaces [3.42] (see Sect. 8.2). Nanowires of Fe with a width of 1.08 nm (see Fig. 3.22d, e) and of other transition metals [3.43] were deposited by molecular beam epitaxy (MBA) on a self-corrugated Cu_3N–Cu (110) molecular network.

For *ligand control* synthesis strategies the principle is simple: one ligand caps very strongly the crystallographic plane of the side of the nanostructure, thus strongly reducing its surface energy and therefore its growth rate, while the other

ligand caps selectively and loosely the tips. This selective ligand shielding, coupled with the high chemical potential of the tips (due to their curvature and different lattice terminations), allows for the formation of nanowires with high aspect ratios. Nanowires of Cu_2S as thin as 1.7 nm and lengths up to tens of micrometers (Fig. 3.22f) can be synthesized by thermal decomposition of copper diethyldithiocarbamate (CuS_2CNEt_2) in a mixed surfactant solvent of dodecanethiol and oleic acid at 160°C [3.44]. Nanowires of Sm_2O_3 (Fig. 3.23a, b, c) with a rectangular cross section are grown by decomposing hydrated samarium acetate in the presence of oleylamine and decanoic acid. This reaction is sensitive to the specific fatty acid, giving with oleic acid ultrathin platelets instead of wires [3.45].

Oriented attachment is maybe the most fascinating growth strategy for ultrathin nanowires, where single-crystalline nanowires are produced by oriented aggregation

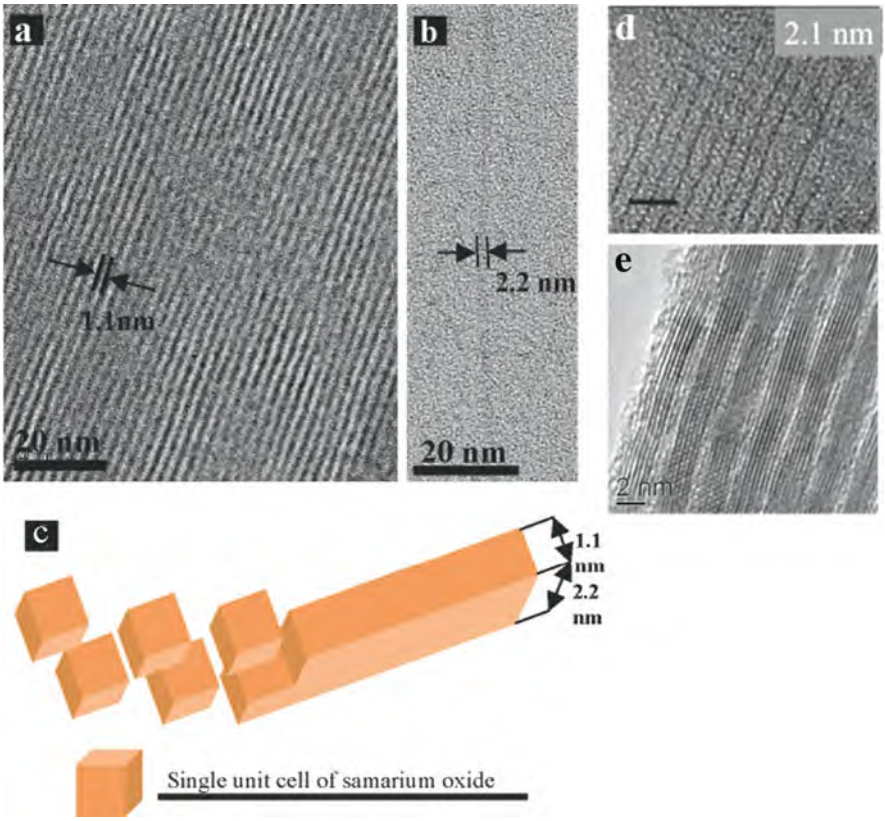

Fig. 3.23 (**a**), (**b**) TEM images of rectangular-shaped samarium oxide nanowires [3.45]. (**c**) Model for the structure of the rectangular-shaped samarium oxide nanowires [3.45]. *Oriented attachment strategy:* (**d**) CdSe nanowires with a diameter of 2.1 nm; scale bar, 10 nm [3.46]. (**e**) HRTEM of ultranarrow PbS wires self-assembled into 2D supercrystalline arrays [3.48]. (Reprinted with permission from [3.45] (**a**) (**b**) (**c**), [3.46] (**d**), [3.48] (**e**). © 2006 American Chemical Society (**a**) (**b**) (**c**) (**d**), © 2007 American Chemical Society (**e**))

of faceted nanocrystals. This methodology has some similarity with polymerization reactions, in which monomers are added to the tip of the growing polymer (see [3.39]). Ultrathin CdSe nanowires (Fig. 3.23d) were obtained by reacting cadmium acetate ($CdAc_2$) and selenourea in long-chain amines. Longer chain amines produced larger wires [3.46]. The formation of low aspect ratio nanocrystals followed by oriented attachment was theoretically found [3.47] to be the energetically most viable route to nanowires, confirming the experimental data [3.46]. PbS nanowires of 2 nm thick (Fig. 3.23e) can be fabricated by the simple decomposition of lead hexadecyl xanthate in trioctylamine. The PbS nanowires self-assemble (see Sect. 1.5) into 2D supercrystalline arrays [3.48].

3.3.4 Electrospinning of Nanofibers

Fibrous nanomaterials are attractive for a range of applications due to their high porosities and large surfaces areas. Electrospinning (see Fig. 3.24a) is a simple, versatile techniques for generating nanofibers from polymers, composites, ceramics [3.49–3.51], etc. The spinning process is a result of whipping rather than splaying of a liquid jet. The whipping instability originates from the electrostatic interactions between the external electric field and the surface charges on the jet. Stretching and acceleration of the unstable fluid filament, where the liquid phase has to have an appropriate viscosity in order to survive the whipping process, yield fibers with diameters as thin as tens of nanometers, much smaller than in conventional spinning techniques.

Electrospinning can be used not only for polymeric nanofibers but also to generate composite and inorganic nanofibers [3.51, 3.52] from, e.g., the oxides Al_2O_3,

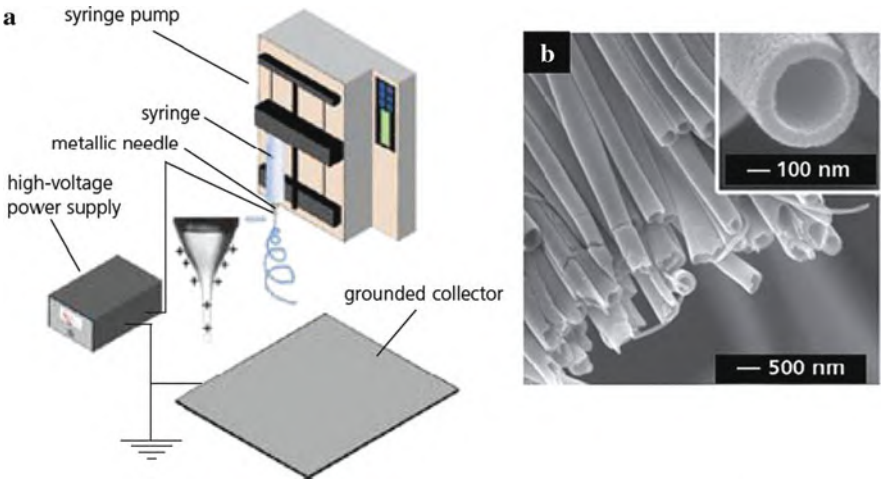

Fig. 3.24 (**a**) Schematic of a typical setup for electrospinning. (**b**) Scanning electron micrograph (SEM) of an aligned array of TiO_2 (anatase) nanotubes fabricated by electrospinning with a coaxial spinneret, followed by calcination in air. (Reprinted with permission from [3.51]. © 2008 Sigma-Aldrich)

TiO_2, ZnO, Nb_2O_5, $BaTiO_3$ by using metal alkoxides as precursors or non-oxide ceramics such as silicon carbide and boron carbide. In addition, nanotubes (see Fig. 3.24b) can be fabricated. Long copper nanofibers have been prepared from electrospinning of copper nitrate–polyvinylbutyral (PVB) solutions with subsequent thermal treatment [3.53].

Aligned arrays of biocompatible and biodegradable electrospun fibers are developed for biomedical applications. Aligned poly(propylene carbonate) (PPC) fiber material containing glial cell line-derived neurotrophic factor (GDNF) are designed for nerve conduits. Electrospun fibrous scaffolds can be combined with gene therapy and stem cell biology to provide a new route to blood vessel regeneration. For example, a vascular graft has been fabricated by seeding genetically modified autologous mesenchymal stem cells (MSCs) onto a scaffold of electro-spun poly(propylene carbonate) and the seeded cells could then be integrated into the microstructure of the graft to form a 3D cellular network [3.54]. Furthermore, bone marrow MSCs in poly(L-lactic) acid (PLLA) nanofibrous vascular grafts have been demonstrated to be antithrombogenic in vivo [3.55]. Figure 3.25a, b shows confocal micrographs of the human aortic smooth muscle cells (SMCs) and bone marrow MSCs seeded on aligned PLLA nanofibers. The cellular organization and alignment are similar to that of the native artery. In Fig. 3.25c, a vascular graft of PLLA nanofibers and MSCs is sutured to the common carotid artery (CCA) of a rat. These results demonstrate that nanofibrous scaffolds allow the remodeling of vascular grafts in both cellular and extracellular matrix (ECM) contents, similar to that of the native artery [3.51].

3.3.5 Bio-Quantum-Wires

Biosystems with the inherent capabilities of molecular recognition and self-assembly are an attractive template for organizing nanostructures. Viruses have been used for fabricating nanowires of cobalt oxide which exhibits excellent electrochemical properties as an electrode for advanced lithium batteries [3.56].

The M13 virus employed consists of ~2700 major coat proteins (p8) wrapped around its single-stranded DNA. The functionality of these proteins can be

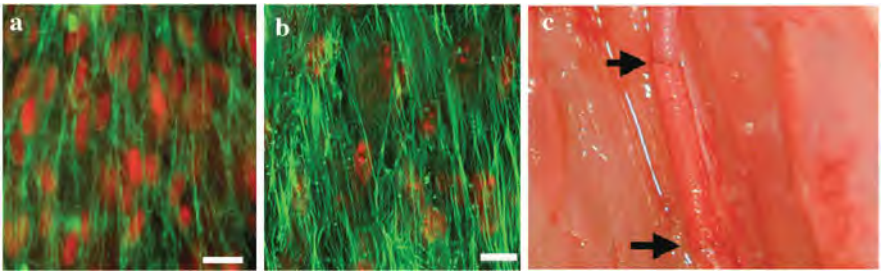

Fig. 3.25 (**a**) Human aortic smooth muscle cells and (**b**) bone marrow stem cells seeded on thin films of aligned poly(L-lactic) acid (PLLA) nanofibers. The actin filaments were stained with FITC-conjugated phalloidin (*green*) and the nuclei with propidium iodide (*red*). (**c**) An end-to-end view of the vascular graft sutured (*arrows*) to the common carotid artery in a rat [3.51, 55]. (Reprinted with permission from [3.55]. © 2007 National Academy of Sciences USA)

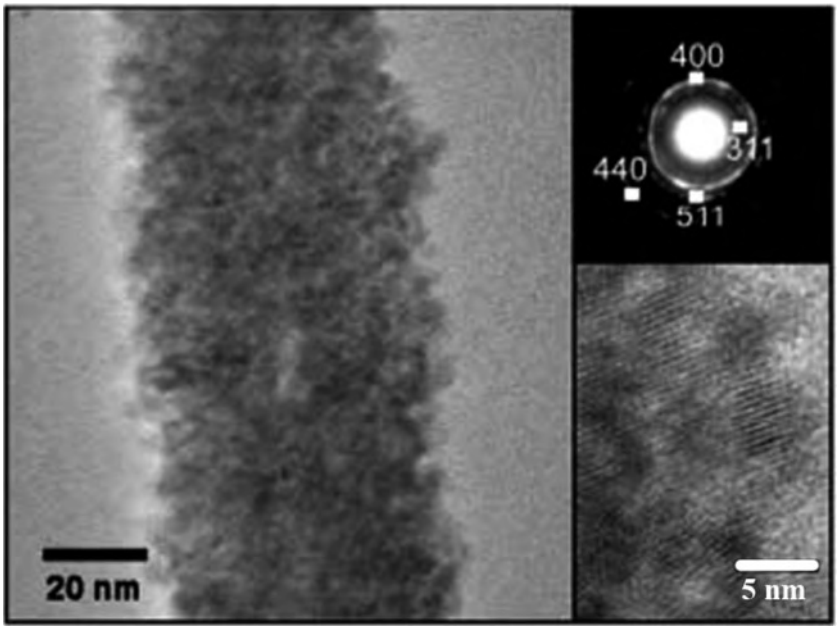

Fig. 3.26 High-resolution TEM image of a Co_3O_4 nanowire templated by a M13 virus. The electron diffraction pattern in the *inset* confirms the structure of the 3 nm Co_3O_4 crystallites with the lattice fringes shown in the *lower panel* of the *inset*. (Reprinted with permission from [3.56]. © 2006 AAAS)

specifically modified by additions in the M13 genome. Tetraglutamate was fused to the terminus of each coat p8 protein yielding a particular interaction capability with various metal ions. With this virus as a template, Co_3O_4 nanowires can be grown (Fig. 3.26) because of the strong binding of Co ions to the glutamate carboxyl groups. For these Co_3O_4 nanowires a reversible Li capacity of 600 mAh/g is found [3.56] which is about twice that of current carbon-based negative electrodes in Li^+ ion batteries. This capacity can even be increased by interdispersing a small fraction of 5 nm Au nanoparticles.

3.3.6 Formation of Arsenic Sulfide Nanotubes by the Bacterium Shewanella sp. Strain HN-41

The dissimilatory metal-reducing bacterium *Shewanella* sp. strain HN-41 forms long (up to $\approx$ 30 μm), variable diameter (20–100 nm), extracellular As–S nanotubes (Fig. 3.27) when grown anaerobically in the presence of thiosulfate and arsenate [3.57]. The As–S nanotubes comprise amorphous As_2S_3 at the early stage of the formation and are subject to mineralogical alterations over time, resulting in the formation of polycrystalline phases of different As–S compounds. In the structural evolution of the biogenic As–S nanotubes, the arsenate AsO_4^{3-} in the initial culture solution is likely "adsorbed" onto HN-41 cells or the extracellular

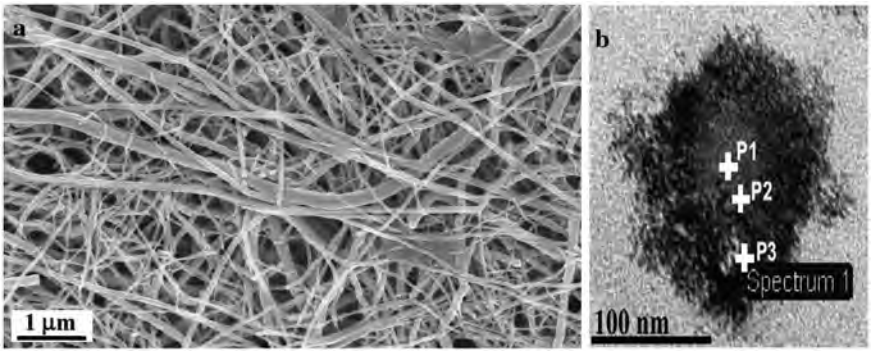

Fig. 3.27 (**a**) Scanning electron micrograph of biogenic As–S nanotubes from bacterium *Shewanella* sp. strain HN41. (**b**) Scanning electron transmission microscopy with energy dispersive x-ray analysis (STEM-EDX) of the cross section of an As–S nanotube with the As/S ratio increasing from the center (P1; As/S = 0.27) to the rim (P3; As/S = 5.84). (Reprinted with permission from [3.57]. © 2007 National Academy of Sciences USA)

polymeric substance (EPS). The electrons produced from the oxidation of lactate by strain HN-41 likely reduce $S_2O_3^{2-}$ to S^{2-} and the absorbed AsO_4^{3-} to AsO_3^{3-}, followed by the formation of polycrystalline As–S in association with the EPS as a possible template or nucleation site leading to an enhanced As density on the rims of the As–S EPS cross sections (see Fig. 3.27b). The As–S nanotubes can behave as metals or semiconductors in terms of their electrical and photoconductive properties and may be useful as building blocks for nanoscale optoelectronic devices (see [3.57]).

3.4 Nanolayers and Multilayered Systems

Artificially multilayered materials with nanometer sizes [3.58] in one dimension are prepared since the advent of advanced thin-film processing techniques. Since the early 1970s when Esaki and co-workers at IBM [3.59] suggested that semiconductor multilayers with layer thicknesses smaller than the electron mean free path could be the basis of novel devices.

A great variety of synthesis techniques are available for the various types of multilayers. Initially, Langmuir-Blodgett [3.60] and self-assembly [3.61] methods were used for preparing organic multilayered films composed of monomolecular layers. Multilayers of organic and inorganic macromolecules were synthesized [3.62] by sequential adsorption of polydiallyldimethylammonium chloride and exfoliated sheets of synthetic hectorite (a mica-type layered silicate) onto silicon substrates.

Electrodeposition is used for depositing metallic, ceramic, semiconductor, and polymer multilayers [3.63]. Multilayers may either be prepared by alternately plating between two deposition potentials in a single electrolyte or by periodic transfer of the substrate from one electrolyte to another. The low-cost techniques can be scaled up to large areas and high total thicknesses (tens of microns).

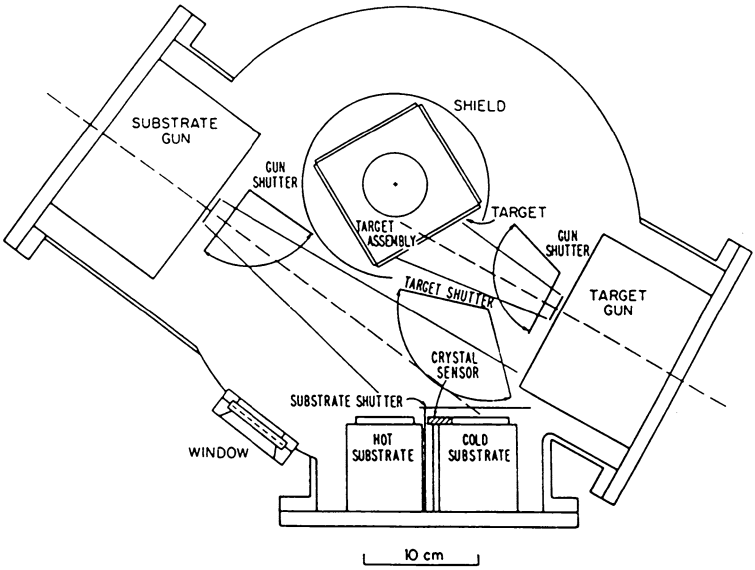

Fig. 3.28 Diagram of a multiple-target ion beam sputtering system used to produce multilayers [3.64]. The target-gun plasma sputters the atoms from the target onto the substrate which may be cleaned by the substrate gun. (Reprinted with permission from [3.64]. © 1985 American Institute of Physics)

Sputtering involves the collision of energetic ions (e.g., of a noble gas as Ar) with the surface of a target material, leading to the ejection of target atoms that are collected in their film form on a substrate (Fig. 3.28). Sputtering is used for ceramic or metal–ceramic multilayers or, because of its high quenching rate, for amorphous metal or amorphous semiconductor layers.

In evaporation systems the films are deposited by electron beam evaporization or a resistively heated source. Molecular beam epitaxy (MBE, Fig. 3.29) is employed to prepare single-crystal superlattices [3.65]. An MBE facility is a sophisticated and expensive evaporator where deposition occurs under ultrahigh vacuum (UHV) conditions (Fig. 3.30) with in situ characterization as reflection high-energy electron diffraction (RHEED) and Auger electron spectroscopy (AES). A computer-controlled shutter system is used to control the layering and an ion gun for cleaning the substrate prior to deposition of the film.

Pulsed laser deposition also referred to as laser ablation makes use of short laser pulses to rapidly vaporize material from the surface of a target. The material is then collected unto a substrate [3.67] with a material thickness per pulse of about 0.1 nm. This allows the deposition of a multicomponent film of the target composition for, e.g., high-temperature superconductor oxides.

Chemical vapor deposition (CVD) is commonly used for the preparation of semiconductor superlattices such as GaAl $-$ $Al_xGa_{1-x}As$ [3.65]. A volatile gaseous compound is adsorbed on a substrate and reacted by pyrolysis, reduction or oxidation to semiconductors and metals or oxides and nitrides.

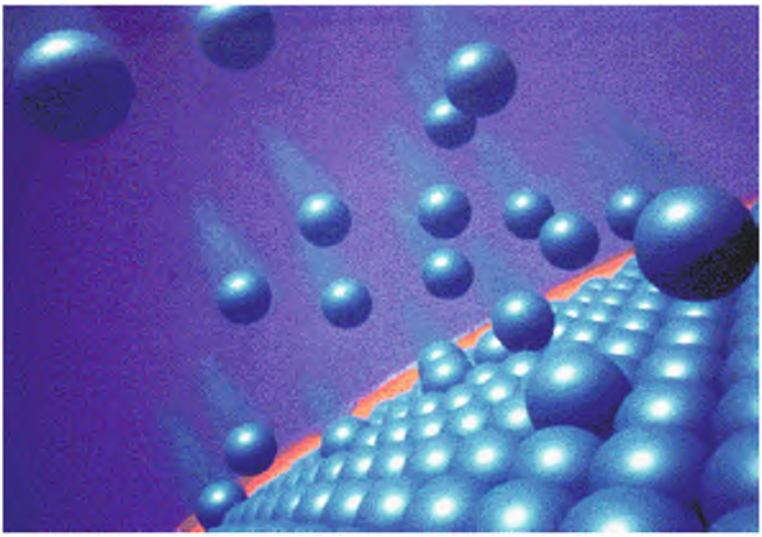

Fig. 3.29 Deposition of atoms on a substrate surface during molecular beam epitaxy (MBE) (*schematic drawing*). (Reprinted with permission from [3.66]. © 1998 Max-Planck-Society)

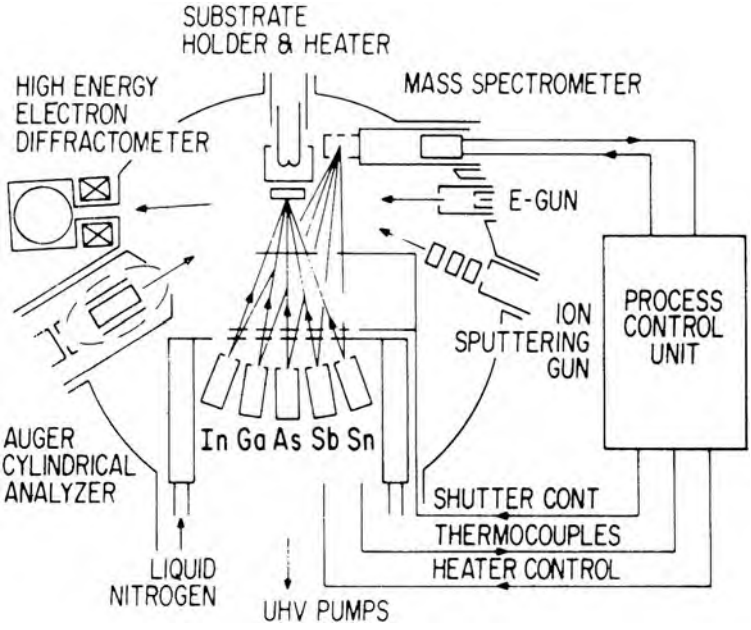

Fig. 3.30 MBE facility for the preparation of $In_{1-x}Ga_xAs-GaSb_{1-y}As_y$ superlattices [3.68]. The Knudsen cells are labeled by the evaporants In, Ga, As, Sb where the Sn cell is used for doping. (Reprinted with permission from [3.68]. © 1980 Elsevier)

Metal–organic chemical vapor deposition (MOCVD) is a basic technique for depositing compound semiconductor films and superlattices [3.65] by reactions such as

$$Ga(CH_3)_3(g) + AsH_3(g) \rightarrow GaAs(s) + 3CH_4(g)$$

$$xAl(CH_3)_3(g) + (1-x)Ga(CH_3)_3(g) + AsH_3(g) \rightarrow Al_xGa_{1-x}As(s) + 3CH_4(g).$$

By precisely controlling temperature, pressure, and gas composition, high-quality superlattices can be prepared on an atomic thickness level.

With respect to the microstructure multilayers are often referred to as compositionally modulated materials with a composition modulation wavelength of Λ (Fig. 3.31). Multilayers composed of single-crystal layers with perfect interfacial atomic registry are called superlattices. An ideal superlattice without structural variation at the interface is called coherent. A lattice parameter misfit of a semicoherent interface may be accommodated by misfit dislocations. A pseudomorphic change of the crystal structure may occur within multilayers with, e.g., bcc Ge formed in Mo–Ge multilayers as an example [3.69].

Multilayers are specifically characterized by x-ray diffraction. In addition to the patterns from the crystal lattice diffraction of the single layers, satellite peaks appear due to the superlattice. The higher the order of the detectable diffraction peaks the

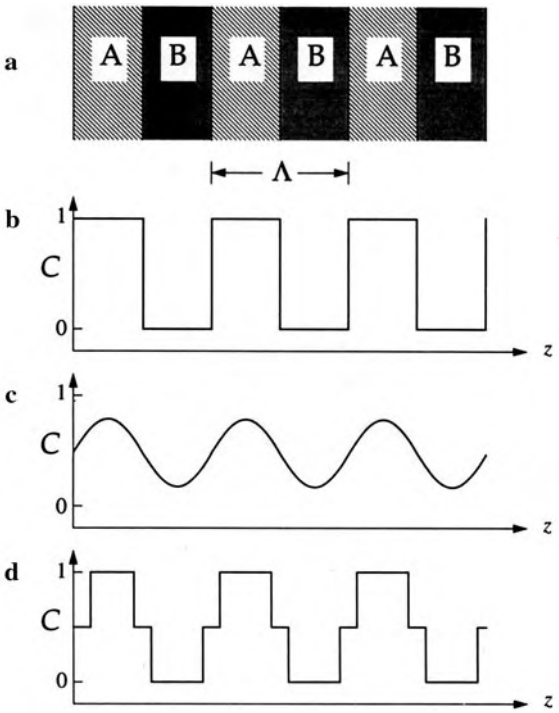

Fig. 3.31 Composition profiles for an artificially multilayered material of bilayer repeat length Λ. (**a**) Artificially layered material with alternating A and B layers; (**b**) ideal rectangular composition profile; (**c**) sinusoidal composition profile; (**d**) composition profile of a multilayer with a third interfacial phase of, e.g., an intermetallic. (Reprinted with permission from [3.58]. © 1996 Institute of Physics)

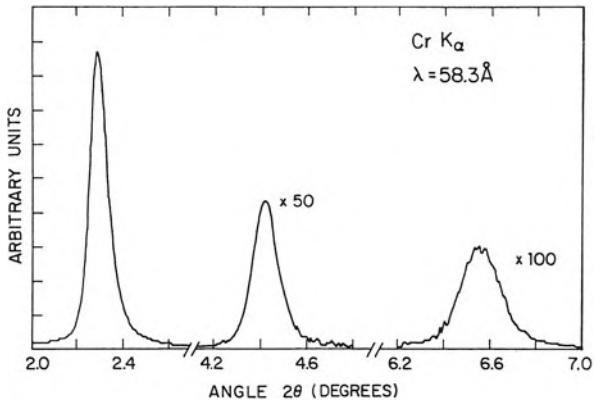

Fig. 3.32 X-ray diffraction of an amorphous Si–amorphous Ge multilayer with a 5.8 nm bilayer repeat length. (Reprinted with permission from [3.70]. © 1985 American Institute of Physics)

sharper are the interfaces. In amorphous multilayers the crystalline diffraction peaks are missing and only the satellites appear (Fig. 3.32).

From the diffraction patterns with satellite peaks, structural information on the bilayer repeat length Λ and on the real part n_r of the index of refraction can be derived. The roughness of the interfaces can be derived by fitting simulations of the x-ray interference function. Neutron and electron diffractions yield additional information.

From diffraction studies information only on the average layer quality can be derived. Investigations on a more atomistic scale can be performed by high-resolution electron microscopy HRTEM (see Fig. 3.33) or by the analysis of the extended x-ray absorption fine structure (EXAFS) . Thin-film characterization methods such as Rutherford back scattering (RBS) or Auger-electron spectroscopy (AES) can be used for the chemical analysis of artificially multilayered thin films.

3.4.1 Layered Oxide Heterostructures by Molecular Beam Epitaxy (MBE)

Molecular beam epitaxy has achieved unparalleled control in the integration of semiconductors at the nanometer level. Metal oxides and their interfaces can now be prepared with the same atomic precision due to advances in heteroepitaxy of complex oxides [3.71, 3.72]. At complex oxide interfaces electrons interact and order in unique ways, so that novel types of quantum Hall systems and unique superconductors can be obtained (see Sect. 4.3 and [3.72]).

MBE systems dedicated to the layer growth of oxides (see [3.71]) are equipped with molecular beams of metals (Sr, Ba, Pb, Bi, etc.,) and oxidation is achieved by purified ozone or molecular oxygen. The composition of the atomic oxide layers on substrates can be controlled to within less than 1% of the cation ratio and

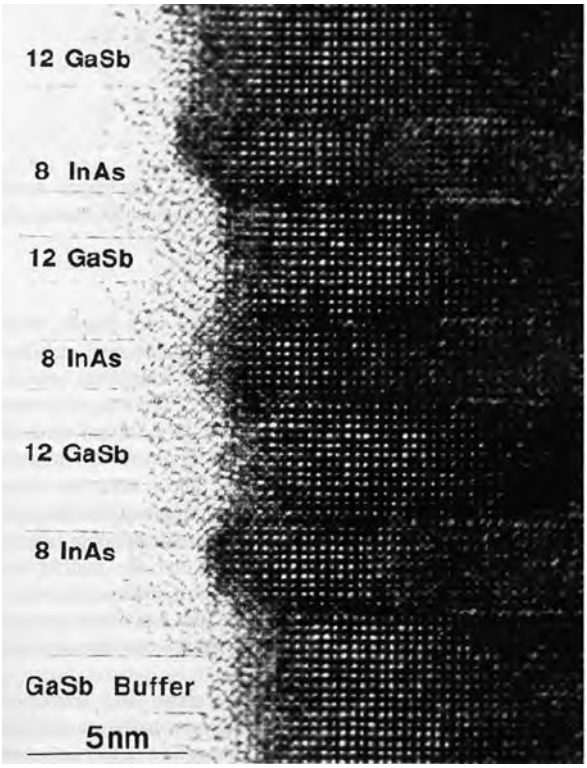

Fig. 3.33 HRTEM cross-sectional transmission electron micrograph of an InAs–GaSb superlattice with the numbers indicating the monolayers per layer. (Reprinted with permission from [3.58]. © 1996 Institute of Physics)

the absolute dose of cations. The films can be characterized by RHEED, by x-ray diffraction, and by HRTEM (see [3.71]).

In Fig. 3.34a, b HRTEM images of $PbTiO_3/SrTiO_3$ and $BaTiO_3/SrTiO_3$ superlattices with a high degree of uniformity in the structural order are shown. Superlattices digitally graded from pure $SrTiO_3$ to pure $BaTiO_3$ by linearly increasing the fraction of $BaTiO_3$ unit cell thick layers are shown in Fig. 3.34c.

3.4.2 Atomic Layer Deposition (ALD)

Atomic layer deposition can be used to process extremely thin insulating layers or Zr and Hf high-*k* (high dielectric constant) materials such as silicates and aluminates [3.73] onto large-area silicon substrates and is additionally useful for surface modification of complex nanostructures [3.74]. The technique is based on successive, surface-controlled reactions from the gas phase to produce thin films and overlayers in the nanometer range with high homogeneity and controllability. The principle of ALD is schematically shown in Fig. 3.35a where the thin film growth cycle for a binary compound (TiO_2) from gaseous precursors ($TiCl_4$ and H_2O) is presented. The reactant does not need to be controlled as the process is surface

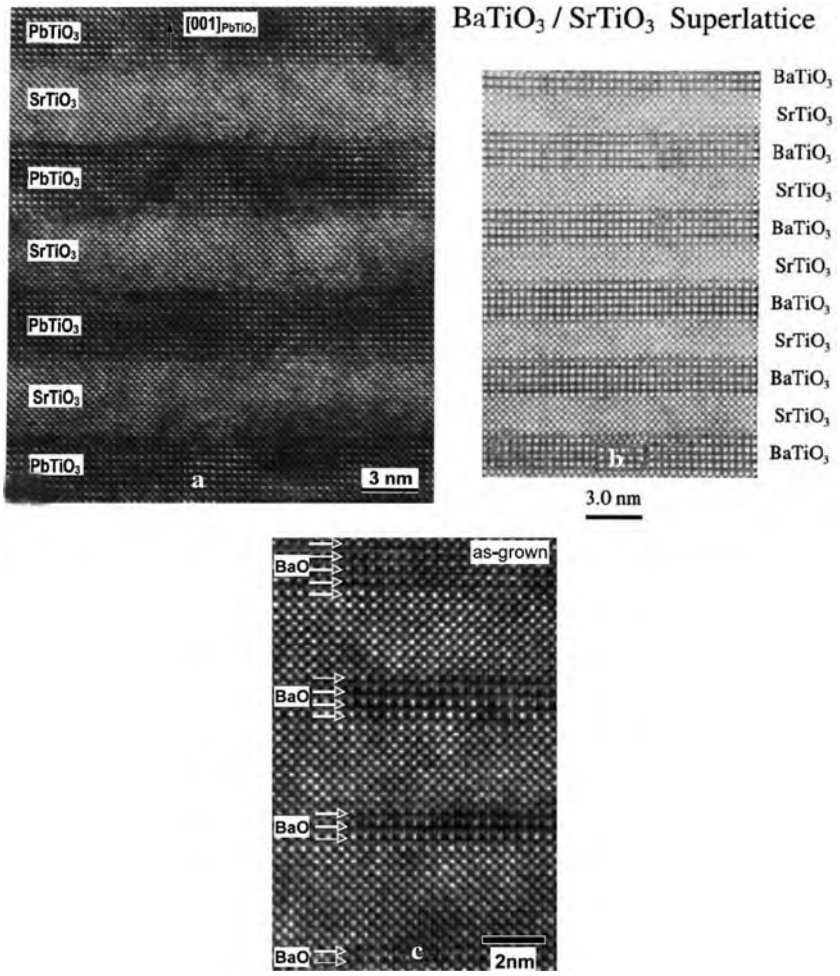

Fig. 3.34 High-resolution transmission electron micrographs (HRTEM) of (**a**) a $PbTiO_3/SrTiO_3$ superlattice and (**b**) a $BaTiO_3/SrTiO_3$ superlattice grown by molecular beam epitaxy (MBE). (**c**) HRTEM image of a digitally graded $BaTiO_3/SrTiO_3$ multilayer that goes from pure $SrTiO_3$ to pure $BaTiO_3$ in unit cell thick increments. (Reprinted with permission from [3.71]. © 2001 Elsevier)

controlled. Currently studied ALD deposition materials are, e.g., HfO_2 as a high-k insulator (see Sect. 9.7), to serve as gate dielectrics in MOSFETS, and also metal oxides and nitrides including ZnO, TiO_2, WN_x, or Al_2O_3.

The high potential of ALD for deposition of thin layers of material into high aspect ratio (AR) nanopores and trenches was demonstrated with the fabrication of uniform arrays of TiO_2 nanotubes, where the precursors $TiCl_4$ and H_2O were deposited into the nanopores of Al_2O_3 on a silicon substrate (Fig. 3.35b). The Al_2O_3 template was then chemically removed to reveal nanotubes with controllable tube

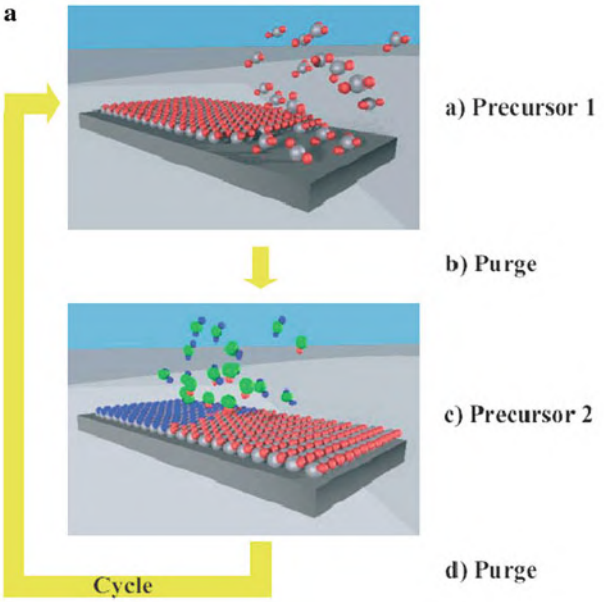
a
a) Precursor 1
b) Purge
c) Precursor 2
d) Purge
Cycle

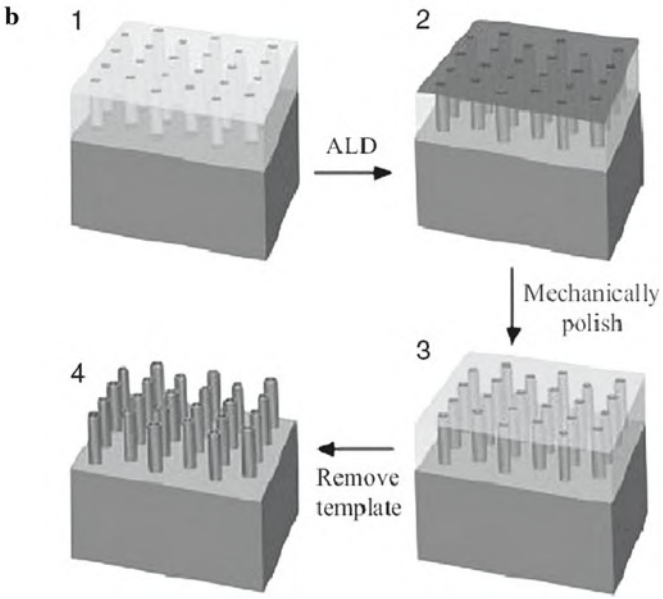
b
1
2
ALD
Mechanically
polish
3
4
Remove
template

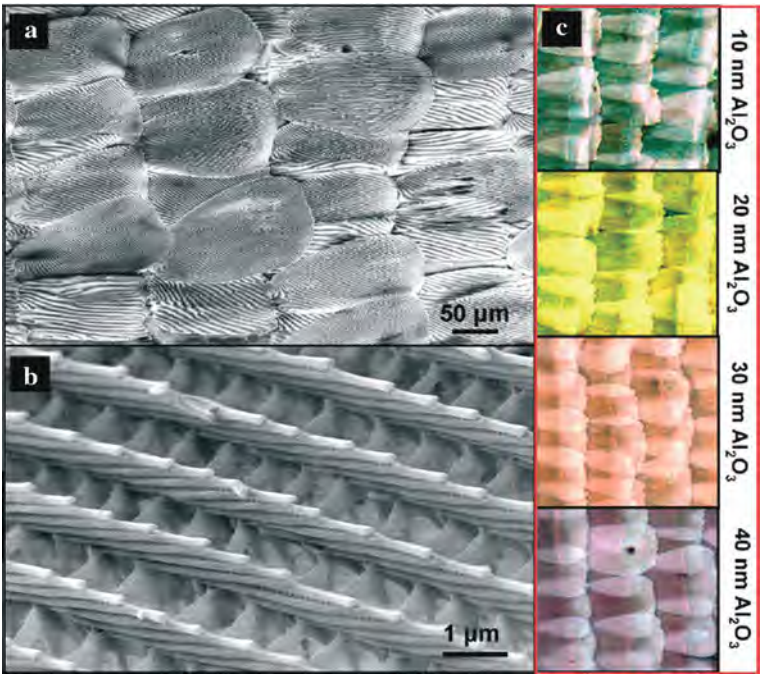

Fig. 3.36 Images of the alumina replicas of butterfly wing scales prepared by atomic layer deposition (ALD). (**a**), (**b**) Scanning electron micrographs (SEM) of the alumina replicas of the butterfly wing scales on a silicon substrate after the butterfly template was completely removed. (**c**) Micrographs of the replicas with various thicknesses of deposited Al_2O_3. (Reprinted with permission from [3.76]. © 2006 American Chemical Society)

diameter, spacing, and wall thickness (see [3.74]). By low-temperature ALD for organic nanostructures, butterfly wings were covered with Al_2O_3, showing a change in coloration with the thickness of the alumina layer (see Fig. 3.36) which may be of interest for the development of optical elements.

Fig. 3.35 (**a**) Schematic of an atomic layer deposition (ALD) process. In step (a) the substrate is exposed to the molecules of precursor 1 which adsorb ideally as a monolayer on the surface. In step (b) the excess precursor 1 in the gas phase is removed by inert gas purging. In step (c) the substrate is exposed to precursor 2 which reacts with the adsorbed precursor 1 to form a layer of the desired material. In step (d) the excess precursors 2 and the reaction by-products are removed by purging. The cycle is repeated (*yellow-arrow*) until the desired thickness of the deposit [3.74] is obtained. (**b**) Schematic of the process to create TiO_2 nanotube arrays on a substrate. (*1*) Formation of the nanoporous Al_2O_3 template by anodization of an aluminum film. (*2*) TiO_2 deposition on the template by ALD. (*3*) Top layer of TiO_2 on alumina removed by mechanical polishing. (*4*) Alumina template chemically etched away to reveal an array of titania nanotubes on the substrate [3.75]. (Reprinted with permission from [3.74] (**a**) and [3.75] (**b**). © 2007 Wiley-VCH (**a**) and © 2004 Wiley-VCH (**b**))

Metallic multilayers with thin individual layers date back to the medieval forging of Damascus [3.77] or Japanese [3.78] swords composed of layers of wrought iron and hardened steel that were repeatedly folded and rolled. Metallic multilayers of Ni–Er were produced with 5 nm individual layer thicknesses and a total thickness up to 200 μm [3.79].

Multilayered polymer composites such as polystyrene–polyethylene multilayers can be composed of thousands of layers with an individual layer thickness of a few tens of nanometers [3.80].

3.5 Shape Control of Nanoparticles

It has been shown that the shape of nanoparticles may be modified by the reaction conditions, particle irradiation, doping, etc. The various nanoparticle shapes obtained making use of various reaction conditions are schematically shown in Fig. 3.37.

The sensitivity of the nanoparticle shape to the reaction conditions implies that the reaction is under kinetic rather than thermodynamic control [3.81]. Silver nanocubes can be synthesized with edge lengths between 70 and 175 nm depending on the reaction time (Fig. 3.38).

By shape-controlling synthesis, nanosized Au octahedra [3.83], Au decahedra [3.84], triangular Pd plates [3.85], Pt multipods [3.86], and Ag nanowires with pentagonal cross section (see [3.87]) can be prepared.

The shape of silica particles can be modified by irradiation with Xe ions (Fig. 3.39). The particles shrink in beam direction and expand perpendicular to this direction [3.88]. This is ascribed to the melting of the silica material along the ion track giving rise to a perpendicular shear stress with local plastic expansion and expansion of the particle normal to the ion beam. In contrast to that an initially spherical Au particle coated by silica expands in ion beam direction (Fig. 3.40) due to the silica shell because this effect is not observed without this shell. The surface

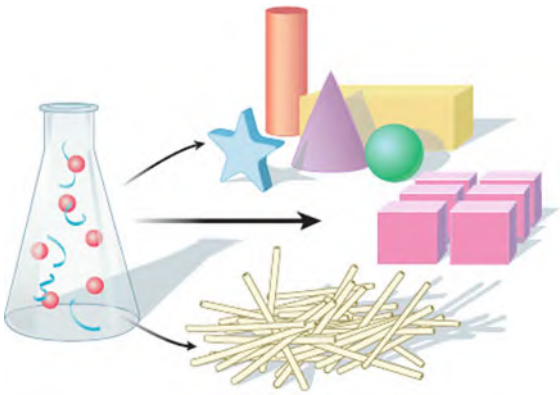

Fig. 3.37 A variety of nanoparticle shapes (*right*) can be synthesized from precursors (*left*) depending on the reaction conditions. (Reprinted with permission from [3.81]. © 2002 AAAS)

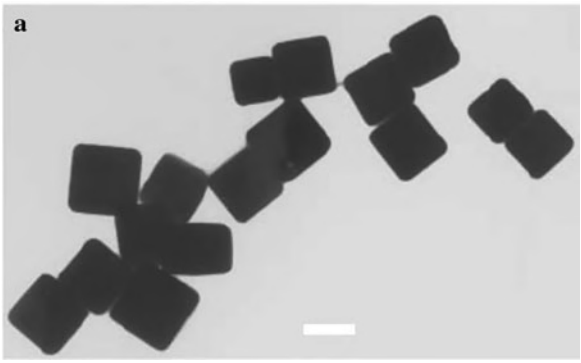

Fig. 3.38 Transmission electron microscopy (TEM) image of silver nanocubes with {100} faces synthesized by a reduction of $AgNO_3$ with ethylene glycol at 160°C. Scale bar, 100 nm. (Reprinted with permission from [3.82]. © 2002 AAAS)

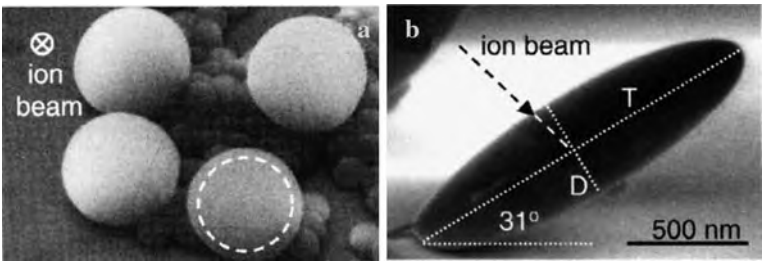

Fig. 3.39 SEM imaging of initially spherical silica particles on a Si substrate after irradiation with 4 MeV Xe ions to 3×10^{18} Xe ions/m^2 at 85 K. (**a**) View along the Xe beam. The lateral expansion of the *spheres* is indicated by a comparison with the *dashed sphere* before irradiation. (**b**) View perpendicular to the beam with the shrinkage of the particle in beam direction. (Reprinted with permission from [3.88]. © 2007 Elsevier)

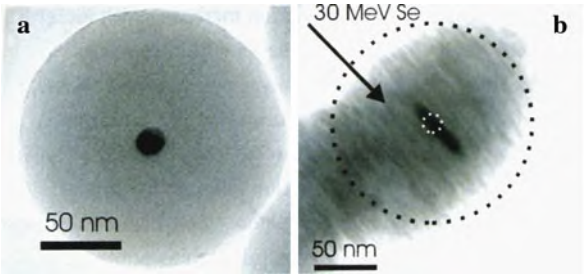

Fig. 3.40 TEM images of a 14 nm Au particle coated by a 54 nm silica shell. (**a**) Before ion irradiation. (**b**) After irradiation with 30 MeV Se ions to a fluence of 2×10^{18} ions/m^2 at 85 K, giving rise to an elongation of the coated Au nanoparticle in beam direction. (Reprinted with permission from [3.89]. © 2004 Elsevier)

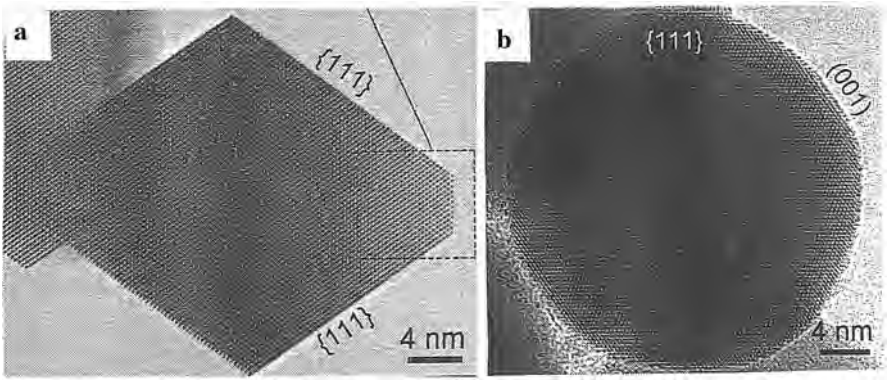

Fig. 3.41 (**a**) High-resolution TEM image of a CeO_2 nanocrystal with a faceted shape. (**b**) Spherical shape of CeO_2 particles doped with 6 at % of Ti. (Reprinted with permission from [3.93]. © 2006 AAAS)

plasmon absorption (see Sect. 7.6) of the elongated Au nanoparticle is red shifted compared to the spherical particle [3.89].

The preparation of hollow nanoparticles such as hollow CuO pyramids [3.90] or hollow CoSe nanoparticles [3.91, 3.92] may offer new possibilities in catalysis, drug delivery, or the field of lightweight structural materials.

A conversion of polyhedral nanoparticles into nanospheres by doping has been shown in the case of ceria [3.93]. The polyhedral shape of the pure CeO_2 particles (Fig. 3.41) can be transformed into a spherical shape by doping with Ti. This is ascribed to a minimization of the surface energy during high-temperature crystallization of the CeO_2 particles when a thin liquid titania shell encapsulates the nanoparticle. This transformation is important for the abrasive properties of ceria in the planarization of integrated circuits because by a spherical shape of the particles the polishing defects on nanoelectronics chips can be substantially reduced.

3.6 Nanostructures with Complex Shapes

From some materials such as ZnO with a wurtzite structure (Fig. 3.42a), nano structures with a more complex shape can be synthesized [3.94]. By sublimation of ZnO, nanobelts (Fig. 3.42b) with photoluminescence blue shifting with decreasing belt width (Fig. 3.42c), nanosprings (Fig. 3.42d), nanopropellers (Fig. 3.42e), or patterns of aligned quantum wires (Fig. 3.42f) can be synthesized.

Quantum wires may be prepared as branched systems to form, e.g., CdSe tetrapods or tetrapods with extended branching [3.95] as well as controlled heterostructures (Fig. 3.43) with tunable properties.

Even more complex structures can be formed in the case of *dendrimers* [3.96] which are covalent hierarchical assemblies of branched polymers with surface functionalization or container capabilities.

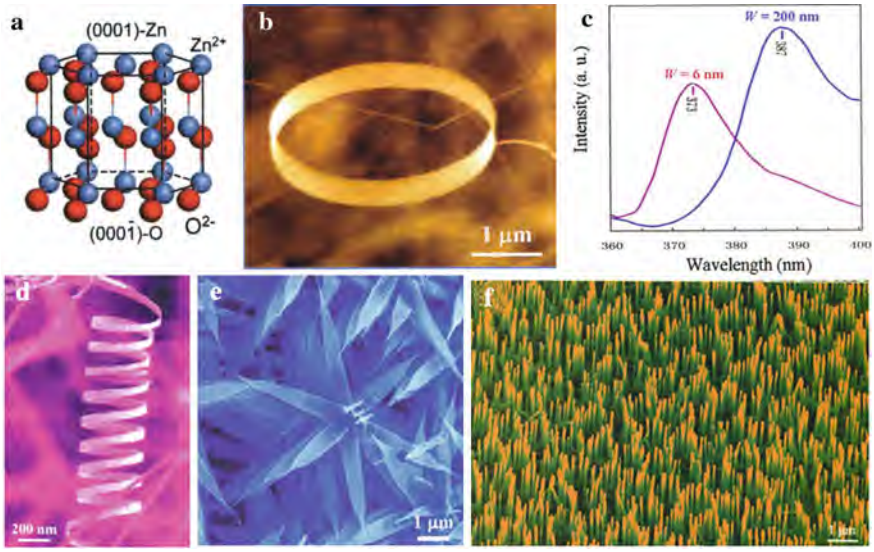

Fig. 3.42 Complex nanostructures of ZnO [3.94] with a (**a**) wurtzite structure. (**b**) Nanobelts showing a (**c**) photoluminescence blue shifting with decreasing belt width, *W*, (**d**) nanospring, (**e**) nanopropellers, and (**f**) patterns of aligned quantum wires on a single-crystalline alumina substrate; scale bar 1 μm. (Reprinted with permission from [3.94]. © 2004 Elsevier)

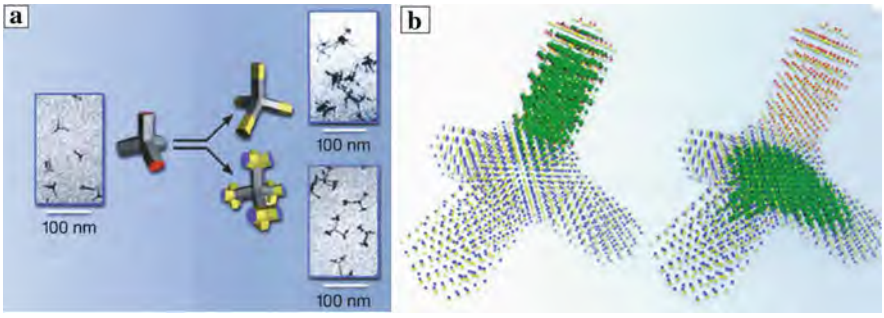

Fig. 3.43 (**a**) CdSe tetrapods (*left*) extended with CdTe segments (*upper right*) which branch in turn (*lower right*). (**b**) Calculations by local density approximation, the charge patching method, and the folded spectrum method yield electronic maps for the four legs. On the *left*, *green* marks the conduction band's lowest state which is separated in the structure from the valence band's highest state (*green* on the *right*). The branches have diameters of 2.2 nm and lengths of 4.2 nm. (Reprinted with permission from [3.95]. © 2004 Materials Research Society)

3.7 Nanostructures by Ball Milling or Strong Plastic Deformation

Nanosized crystallites (metals, alloys, ceramics) down to 2–100 nm can be fabricated by ball milling. This originates from the formation and self-organization of a large number of large-angle grain boundaries by strong plastic deformation during milling [3.97]. This procedure can be scaled up to industrially relevant amounts of nanocrystalline materials. In ball-mills the hard balls (steel, WC) are impacted to each other by shaking in order to deform, fracture, and weld the material between the balls (see Fig. 3.44).

From x-ray diffraction experiments the mean size $< d >$ and the root-mean-square (RMS) strains in the coherently scattering domains or crystallites can be determined from plotting the full width at half maximum (FWHM) $\Delta K = \Delta K(K)$ of a Bragg reflection $K = 2 \sin \Theta / \lambda$ in reciprocal space where Θ is the scattering angle and λ the x-ray wavelength [3.98, 3.99].

The grain size of ball-milled metals decreases with milling time to about $d = 12$ nm with strain levels of $< \varepsilon^2 >^{1/2} = 1, ..., 3\%$ [3.97].

The mechanisms of grain size reduction by ball milling or strong plastic deformation can be summarized as following:

i. Initially, the high-strain rate deformation is localized in shear bands with a high dislocation density and slightly rotated grains of $d = 20$ nm.
ii. With longer milling the shear bands extend, and the dislocations recombine to small-angle grain boundaries with grain sizes of about 20 nm and some orientational correlation. The transition from (i) to (ii)/(iii) occurs when dislocation multiplication is balanced by dislocation annihilation [3.97].
iii. After even longer milling times the entire sample disintegrates into sub-grains with a crystallite orientation correlation entirely random. According to the Hall–Petch relationship $\sigma = \sigma_0 + kd^{-1/2}$ with the typical experimental values [3.97] $k = 0,5 \text{MNm}^{-3/2}$ and $\sigma_0 = 50$MPa the yield stress at a 10 nm grain size is about 5 GPa or 15% of the theoretical shear stress which limits the further reduction of the grain size.

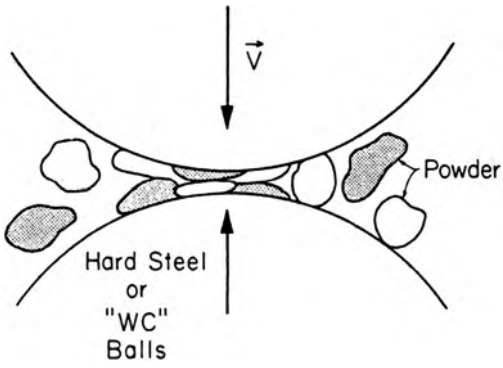

Fig. 3.44 Schematics of the mechanical attrition of a metal powder by ball milling. (Reprinted with permission from [3.97]. © 1996 Institute of Physics)

Nanocrystallization of materials after deformation by high strain rates also occurs after severe torsional deformation [3.101], as well as in tribology and wear [3.102].

In addition to the grain refinement process, alloying of conventionally immiscible components such as Fe and Cu can be achieved by ball milling due to mechanical alloying. The dissolution of 4 nm Fe particles in a Cu matrix may be thermodynamically favorable when the difference $\Delta G_{\mathrm{Fe}} = 2V_{\mathrm{m}}\sigma_{\mathrm{FeCu}}/r$ of the Gibbs free enthalpy between the Fe and the Cu structures is offset, where V_{m} denotes the molar volume and $\sigma_{\mathrm{FeCu}} = 1.37\,J/m^2$ the interface energy [3.100], and thus the solubility limits drastically change with grain size.

By reactive milling in gaseous or liquid atmospheres oxides, carbides, nitrides or, e.g., metal/carbide composites [3.103] with improved ductility may be synthesized.

3.8 Carbon Nanostructures

Three novel nanostructured modifications of carbon, namely fullerenes (0D [3.104]), carbon nanotubes (1D [3.105]), and graphene (2D [3.106, 3.107]), have been prepared during the last two decades in addition to diamond and graphite (Fig. 3.45). The preparation techniques for these novel nanostructures with an enormous impact in solid-state physics, chemistry, and materials science will be briefly outlined in the following.

3.8.1 Fullerenes

In 1985 the teams of H. Kroto and R. Smalley discovered highly stable clusters of 60 carbon atoms in mass spectra of laser-ablated graphite [3.104]. For this cluster a soccer ball-shaped molecule (C_{60}), a truncated icosahedron comprising 12 carbon pentagons and 20 carbon hexagons, was suggested (Fig. 3.45).

Because of its similarity to the geodesic domes of the architect Buckminster Fuller this cage-shaped carbon cluster was named buckminsterfullerene and a number of larger clusters was detected. In 1990 the synthesis of macroscopic quantities of fullerenes was announced [3.113] (see Fig. 3.46) yielding crystallized C_{60} fullerenes, higher fullerenes as C_{70}, C_{76}, C_{84}, C_{92}, C_{96} and giant fullerenes with hundreds of carbon atoms [3.114].

For producing fullerene (C_{60}) molecules graphite rods are vaporized by an arc discharge, by electron beam heating, or by sputtering in a production chamber with a dilute atmosphere of He or an other noble gas. The C atoms are thermalized in the gas atmosphere to form clusters which are very reactive as long as they are small because of unsatisfied bonds at the edges. These clusters grow and finally the totally closed, inert C_{60} molecules without dangling bonds survive together with higher fullerenes. The fullerenes are extracted from the carbon soot by dissolution via a non-polar solvent (e.g., toluene) or by sublimation. Separation of the various fullerenes and purification can be achieved by chromatographic techniques or by selective complexation with calixarenes [3.115].

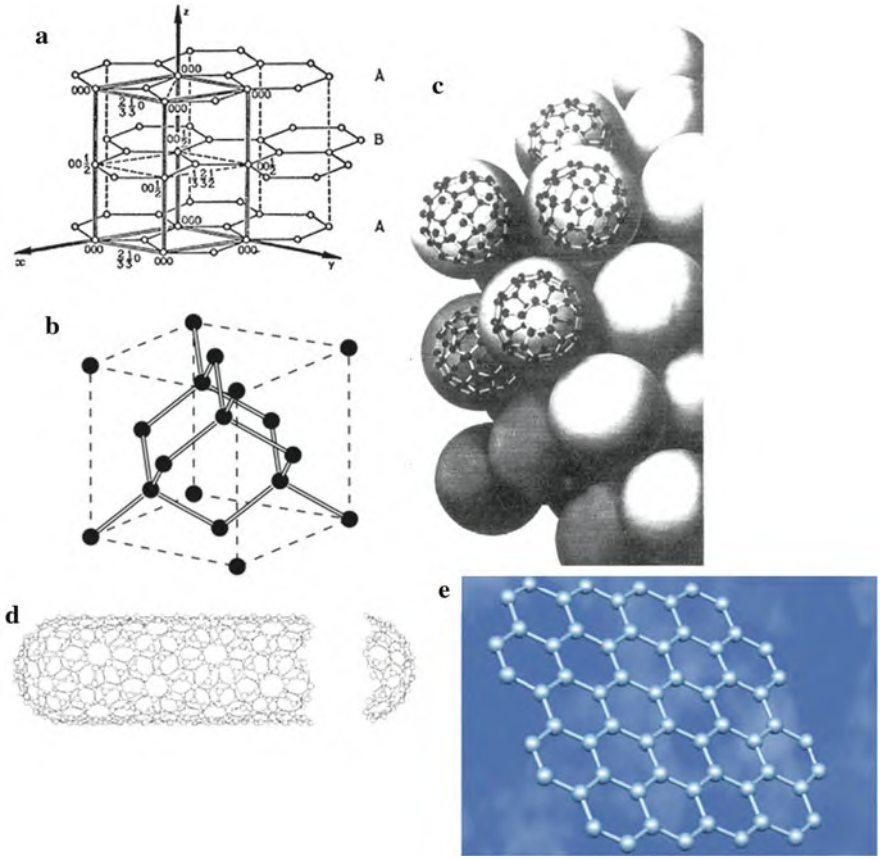

Fig. 3.45 Crystal structures of the five forms of carbon: (**a**) graphite [3.108], (**b**) diamond [3.109], (**c**) crystallized fullerene molecules (C_{60}) [3.110], (**d**) carbon nanotube [3.111], and (**e**) graphene [3.112]. (Reprinted with permission from [3.108] (**a**), [3.109] (**b**), [3.110] (**c**), [3.111] (**d**), and [3.112] (**e**). © 1964 Wiley Intersience (**a**), © 2002 Oldenburg (**b**), © 1996 Institute of Physics (**c**), © 1999 Springer Verlag (**d**), and © 2006 Nature Publishing Group (**e**))

The distance between two C atoms in the truncated icosahedral C_{60} molecule is 0.14–0.145 nm yielding a diameter of the molecule of about 0.7 nm. The C_{60} molecules are about 0.29 nm apart in the solid, called fullerite, compared to the 0.34 nm distance of the graphite planes.

It has been detected that C_{60} [3.116] and higher fullerenes [3.117] are also synthesized in nature as deduced from the analysis of the Allende meteorite. This indicates that fullerenes existed either in the early solar nebula or as a component of presolar dust.

Onion-shaped graphitic spheres were formed by high-intensity electron irradiation of carbon soot in a high-voltage electron microscope [3.118]. This structure without dangling bonds may be the most stable form of graphite. If these graphitic

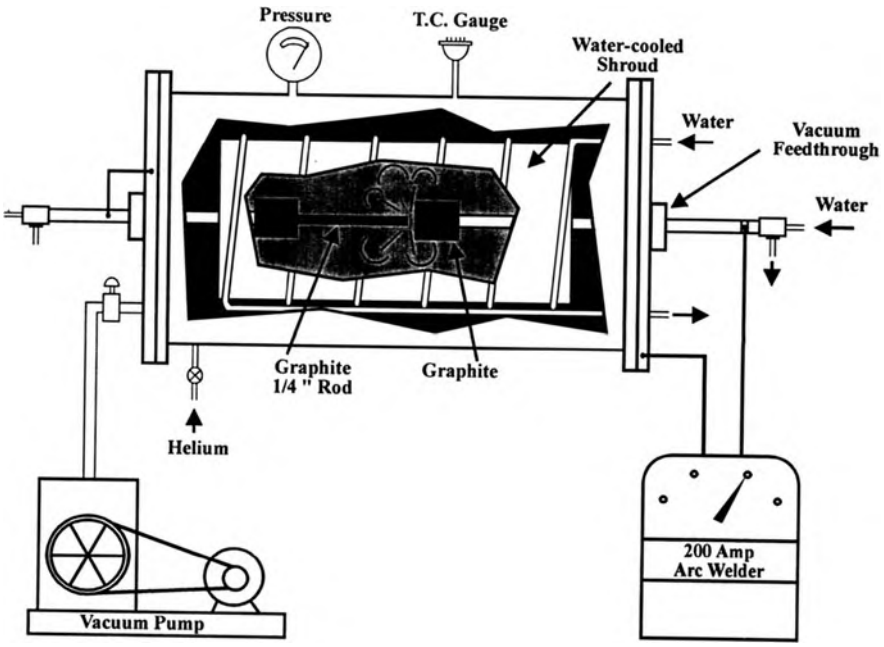

Fig. 3.46 Fullerene soot production chamber with a He atmosphere and graphite electrodes. (Reprinted with permission from [3.110]. © 1996 Institute of Physics)

spheres are further electron irradiated at 700°C, their cores transform into diamonds. From the outer layers to the more interior layers of these spheres the spacings of the graphitic layers decreases from 0.31 to 0.22 nm in contrast to the 0.34 nm layer separation in graphite indicating high compression [3.119] (see Fig. 3.47).

3.8.2 Single-Walled Carbon Nanotubes (SWNTs) – Synthesis and Characterization

Using an arc discharge method, carbon nanotubes were initially grown on the negative end of the electrode [3.105]. The tubes consist of cylindrical graphitic layers separated by 0.34 nm (see Fig. 3.48) and capped on the ends with fullerene-like domes [3.29].

For the synthesis of carbon nanotubes, carbon arc, laser ablation, and chemical vapor deposition (CVD) processes are available (see [3.120]). The CVD processes offer the best approach to the manufacturing of larger SWNT quantities, with perhaps the most scalable being the CoMoCAT process which uses a fluidized bed reactor (see Fig. 3.49a) similar to those in petroleum refining, albeit, on a much smaller scale. In this CoMoCAT method, SWNTs are grown by CO disproportionation (decomposition into C and CO_2) at 700–950°C in flow of pure CO at a

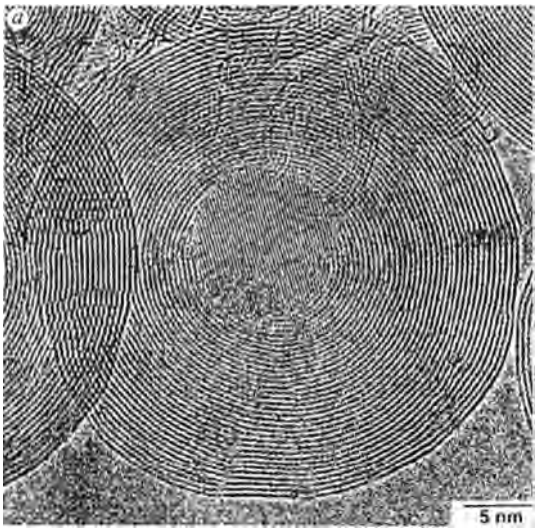

Fig. 3.47 Spherical graphitic particle (*onion*) with a diamond core 10 nm in size (1.8×10^{-17} carat) and the diamond lattice fringes separated by 0.206 nm, after electron irradiation at 700°C. (Reprinted with permission from [3.119]. © 1996 Nature Publishing Group)

pressure of 1–10 atm with a selectivity toward SWNTs with a diameter between 0.72 and 0.92 nm (> 90%) and a (6, 5) chirality of 52% [3.120]. The catalyst is effective when both metals, Co and Mo, are simultaneously present on a silica support.

For the characterization of SWNTs, the microscopy techniques (see Chap. 2) of scanning tunneling microscopy (STM), atomic force microscopy (AFM), and transmission electron microscopy (TEM) are available, as well as Raman spectroscopy, optical absorbance spectroscopy, and thermogravimetric analysis (TGA) . In Raman spectroscopy (Fig. 3.49b), the radial breathing mode (RBM) from 120 to 300 cm^{-1} is unique to SWNTs and can be used to determine the tube diameter d (in nm) from the wave number ν (in cm^{-1}) according to

$$\nu = 238/d^{0.93}.$$

The D band at 1300–1350 cm^{-1} is indicative of disordered carbon, multiwall tubes, and microcrystalline graphite, and the G band at 1500–1586 cm^{-1} is a result of the tangential stretching mode from graphitic-like materials and the G/D ratio has been used as a measure of the purity of the SWNTs [3.120]. The optical absorption measurements in the UV–Vis–NIR region show peaks which are characteristic of individual (n, m) species. For example the (6, 5) species absorb at 566 and 976 nm and fluoresce at 983 nm, whereas a (7, 6) SWNT absorbs at 645 and 1024 nm and fluoresces at 1030 nm. The main peak of the TGA trace represents the oxidation of SWNTs, while the second peak is indicative of the presence of other forms of carbon [3.120].

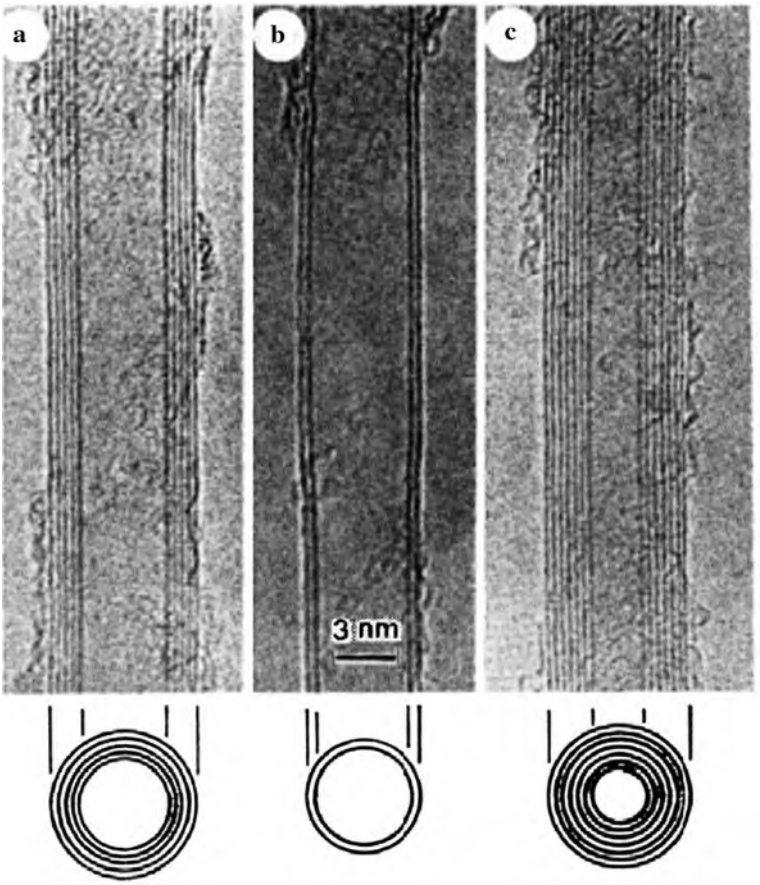

Fig. 3.48 Electron micrographs of nanotubes of graphitic carbon [3.105]. A cross section of each tubule is illustrated. (Reprinted with permission from [3.105]. © 1991 Nature Publishing Group)

The caps of carbon nanotubes can be opened by oxidation [3.121] and filled [3.122] with various materials in order to synthesize nanowires. Large areas of highly aligned, isolated carbon nanotubes were prepared by 700°C deposition of acetylene on sol–gel synthesized mesoporous silica with iron nanoparticles in the pores [3.123].

Crystalline ropes of metallic regularly ordered 2D arrays of SWNTs can be synthesized [3.124] by a laser-oven method with a uniform SWNT diameter of ∼1.38 nm. They self-organize to hexagonal 2D rope-like crystallites 5–20 nm in diameter and tens to hundreds of micrometers long with a 1.7 nm lattice constant as evidenced by transmission electron microscopy (TEM) and x-ray diffraction (XRD) (see Fig. 3.50). All SWNTs terminate together at the end of the rope.

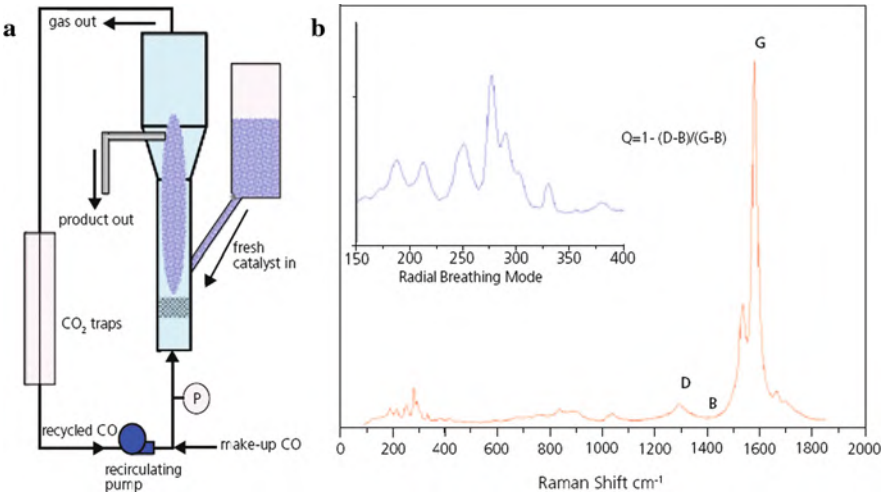

Fig. 3.49 (**a**) Illustration of a fluidized bed reactor which is able to scale up the generation of SWNTs using the CoMoCAT process. (**b**) Typical Raman spectrum of (6, 5) SWNTs, obtained with 633 nm laser excitation. (Reprinted with permission from [3.120]. © 2009 Sigma-Aldrich)

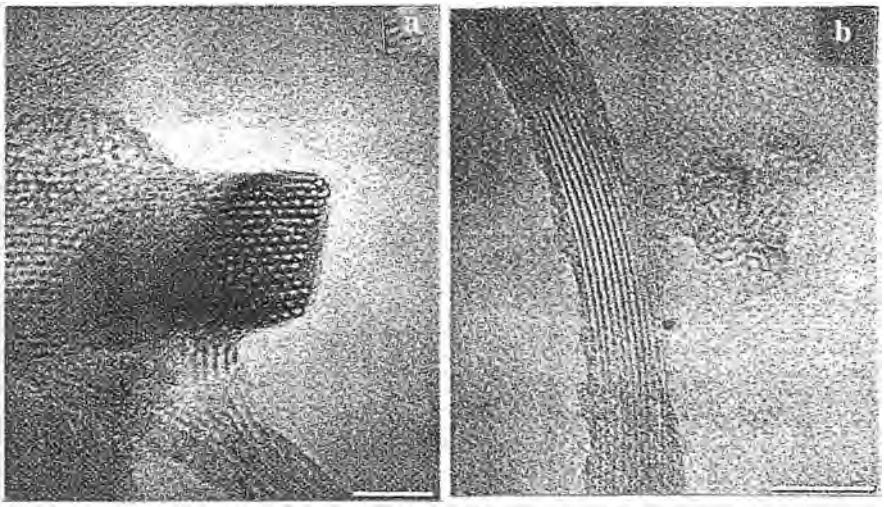

Fig. 3.50 Scanning electron micrographs (SEM) of single-wall carbon nanotube (SWNT) bundles (ropes). (**a**) SWNT rope consisting of ~100 SWNTs bending through the image plane of the microscope, showing uniform diameter and triangular packing of the tubes within the rope. (**b**) Imaging of the SWNT rope perpendicular to the tube axes. Scale bars 10 nm (**a**) and 20 nm (**b**). (Reprinted with permission from [3.124]. © 1996 AAAS)

3.8.3 Graphene

Graphene is a single layer of sp^2-bonded carbon which can be seen as an individual atomic plane pulled out of bulk graphite. This material was found in its free state only recently when individual graphene samples of a few microns in width were isolated by micromechanical cleavage of graphite. The current intense interest in graphene is driven by the high crystal quality and ballistic transport at sub-micron distances [3.125, 3.126] as well as the behavior of quasi-particles as massless Dirac fermions so that the electronic properties are governed by quantum electrodynamics rather than the standard physics of metals based on the (non-relativistic) Schrödinger equation [3.125, 3.126].

Preparation and stability: Graphene up to sizes of 100 μm (Fig. 3.51b) can be obtained by micromechanical cleavage of bulk graphite [3.127] although graphene

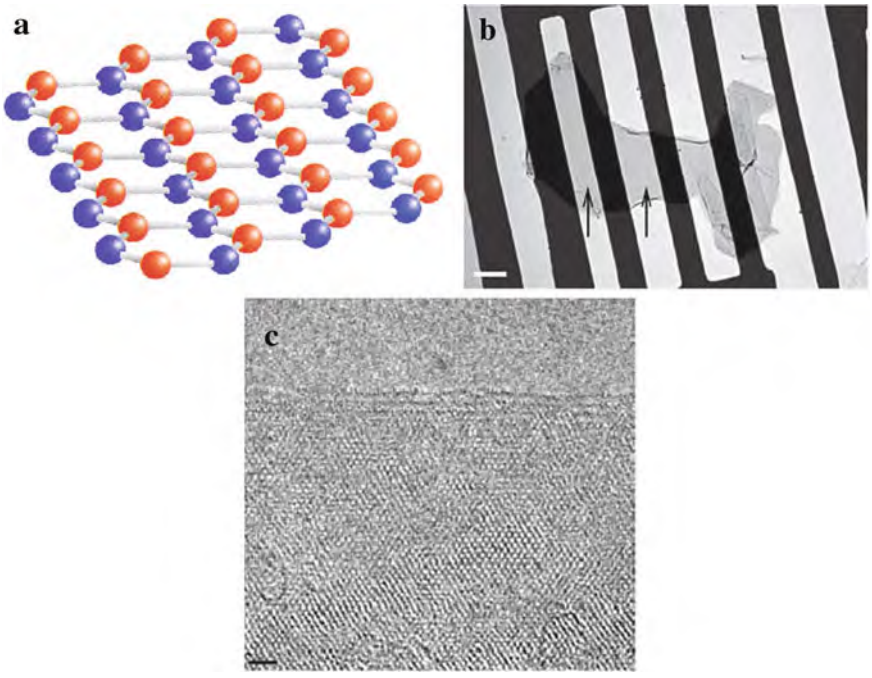

Fig. 3.51 (**a**) Crystallographic structure of graphene. Atoms of the two sub-lattices (*A* and *B*) are marked by different colors [3.128]. (**b**) TEM image of a suspended graphene membrane. Its central part (*arrows*) is monolayer graphene. Electron diffraction shows that it is a single crystal without domains. Scrolled top and bottom edges and a strongly folded region are visible on the *right*. Scale bar, 500 nm [3.135]. (**c**) TEM atomic resolution image of a few-layer graphene membrane near its edge, where the number of horizontal *dark lines* indicates the thickness of two to four layers. Because the electron contrast depends strongly on the incidence angle, small (few degrees) variations of the surface normal are visible. Scale bar, 1 nm [3.135]. (Reprinted with permission from [3.128] (**a**) and [3.135] (**b**) (**c**). © 2007 Materials Research Group (b) (c))

crystallites left on a substrate are extremely rare [3.129]. Graphene crystals with a few layers (1,2,3,4,5) can be discerned by Raman spectroscopy [3.130].

The fact that 2D atomic crystals do exist and are stable under ambient conditions is amazing by itself. Peierls [3.131] and Landau [3.132] predicted that strictly 2D crystals were thermodynamically unstable and could not exist because a divergent contribution of thermal fluctuations in low-dimensional crystals should lead to such large displacements of atoms that they become comparable to interatomic distances and dislocations should appear in 2D crystals [3.133] at any finite temperature. However, strong interatomic bonds can ensure that thermal fluctuations cannot lead to the generation of dislocations [3.133] and 2D crystals are intrinsically stabilized by gentle crumpling in the third dimension [3.134] which is reported from x-ray diffraction experiments [3.135].

For future large-scale application of graphene, two requirements are of importance as discussed in the following. Convenient synthesis of larger quantities and control of the pattering, morphology, and crystallinity of the edges of graphene nanoribbons, because these nanoribbons can exhibit either quasi-metallic or semiconducting behavior, depending on the atomic structure of their edges [3.136]. Nanoribbons less than 10 nm wide are expected to be semiconductors, independent of their edge patterns (see [3.137]).

Gram-scale production of graphene (see Fig. 3.52) has been achieved [3.138] by reacting ethanol and sodium to an intermediate solid that is then pyrolyzed, yielding a fused array of graphene sheets that are dispersed by mild sonication. By a solution-based method for large-scale production, uniform films of single and/or few-layer chemically converted graphene can be produced over the entire area of a silicon/SiO_2 wafer [3.139]. Epitaxial graphene layers have been grown on single-crystal 4-inch silicon carbide wafers [3.140] and a number of additional chemical methods are available for the production of graphene (see [3.141]).

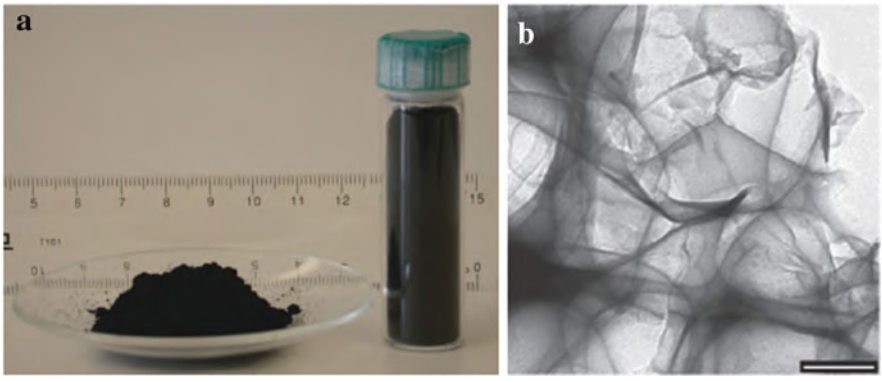

Fig. 3.52 (**a**) Example of the bulk quantity (∼2 g) of the graphene product. (**b**) Transmission electron micrograph of the agglomerated graphene sheets. Scale bar, 200 nm. (Reprinted with permission from [3.138]. © 2009 Nature Publishing Group)

3.9 Nanoporous Materials

Bulk materials with a nanoporous structure can be synthesized (see below) from oxides with widespread applications in catalysis, photocatalysis, and separation, from semiconductors due to band gap engineering, and from metals for improved fuel cell electrodes or optical and electronic applications. The field of nanoporous materials is sometimes subdivided into microporosity (pore diameter less than 2 nm) and mesoporosity (pore diameter 2–100 nm). Between these two length scales the transition between monolayer and multilayer adsorption occurs and the assumptions of classical adsorption theories can break down (see [3.142]). Recent developments in zeolite synthesis could bridge this gap with the generation of ever larger pore sizes. It may be not catalysis or separation where the nanoporous materials with larger pore sizes will find use. They may be more important in the field of sensors or photonics or low-dielectric constant materials.

3.9.1 Zeolites and Mesoporous Metal Oxides

Zeolites are crystalline oxide materials with a tetrahedral atomic framework structure that contains cavities in which "guest" molecules can move relatively freely. Such molecules can rapidly be adsorbed, react and desorb, making zeolites particularly useful for catalytic and separation application (see [3.142]). The framework is composed mainly of silica tetrahedra, but many other elements, such as Al, Ti, or Ge, can be incorporated. One of the most useful properties of zeolites is their ability to select molecules based on size (molecular sieving). But for some applications, such as cracking of hydrocarbons, and specifically hydrocracking, this is in fact a limitation, as the large molecules one may wish to react do not have access to the reaction sites located inside the crystals. A measure of pore size is how many oxygen atoms form the ring that define a pore channel. An 18-ring zeolite (ITQ-33) with a pore diameter of 1.3 nm (Fig. 3.53a, b) has been synthesized [3.143] making use of an organic hexamethonium template and additional fluoride and germanium ions, yielding a large void fraction of 0.37 cm^3/g. The additional medium-size pores (10-ring, 0.56 nm, see Fig. 3.53b) that run perpendicular to the 18-ring pores can bypass blocked pores. It should be pointed out that the structure of the ITQ-33 was "predicted" theoretically by algorithms that generate framework structures of zeolites [3.144].

One may ask the question whether materials with even larger pores are needed [3.142]. Some of the unique properties of zeolites arise from the large curvature of their pores. As the pores get larger, the interaction of adsorbates increasingly resembles the interaction with a flat surface. Yet, large pore materials will find use as sensors or in photonics, or where the low dielectric constant (low k) of such materials, arising from their porosity, can be exploited in the manufacture of improved microelectronic devices (see Sect. 9.8).

Zeolitic materials with extralarge pores and channels displaying only one enantiomorph have been synthesized with the ITQ-37 chiral zeolite [3.145] of the

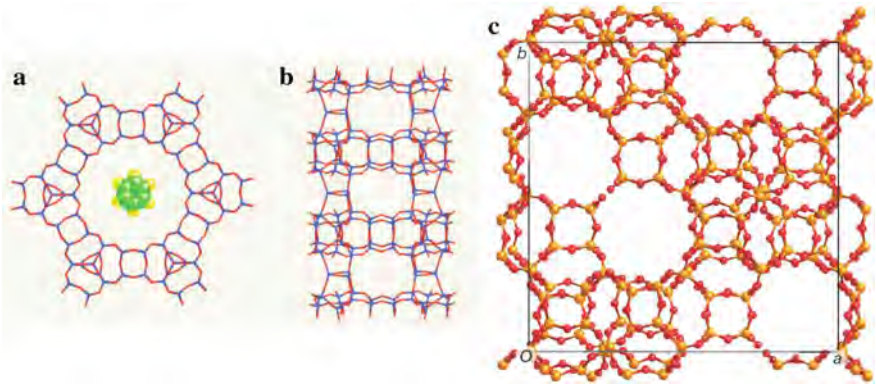

Fig. 3.53 (**a**) Structure of the Si–Ti–Ge zeolite ITQ-33 [3.143]. View of the framework down the 18-member ring (a pore defined by a ring containing 18 oxygen atoms). The *green* and *yellow* molecule is benzene, which is 0.55 nm in diameter and is included for size comparison. (**b**) The 10-ring pore windows that interconnect the 18-ring channels [3.142], [3.143]. (**c**) The framework structure model of the 30-ring ITQ-37 zeolite, viewed along the *c*-axis, derived from the electron density map which is deduced from selected area electron diffraction (SAED) and powder x-ray diffraction (PXRD). The Si and Ge atoms are in *yellow* and oxygen atoms are in *red* [3.145]. (Reprinted with permission from [3.142] (**a**) (**b**) and [3.145] (**c**). © 2006 Nature Publishing Group (**a**) (**b**) and © 2009 Nature Publishing Group (**c**))

formula $|(C_{22}N_2H_{40})_{10.5}(H_2O)|\,[Ge_{80}Si_{112}O_{400}H_{32}F_{20}]$ (Fig. 3.53c). The stable 30-ring ITQ-37 zeolite with an asymmetric pore opening of 0.43 nm × 1.93 nm, a low framework density of 10.3 Si and Ge atoms per cubic nanometer, a BET (Brunauer–Emmett–Teller) surface area of 900 $m^2\ g^{-1}$, and a micropore volume of 0.38 $cm^3\ g^{-1}$ approaches the mesoporous range [3.145].

Mesoporous transition metal oxides with ∼20-nm pore size, high crystallinity and high thermal stability can be synthesized [3.146] by making use of transition metal oxide sols and amphiphilic diblock copolymers. Mesoporous TiO_2 and Nb_2O_5 may be used in photovoltaic cells and fuel cells, respectively [3.146]. When mesoporous TiO_2 is applied in photocatalysis, a highly crystalline TiO_2 matrix is required, because amorphous regions are known to be trap sites for the recombination of photoexcited electrons and holes, limiting the device efficiency (see [3.146]). For the synthesis of the mesoporous crystalline metal oxide, first a mixture of the block copolymer poly(isoprene-*block*-ethylene oxide) (PI-*b*-PEO) with the metal oxide sol leads to a film of hexagonally arranged PI cylinders embedded in a matrix containing PEO and the metal oxide sol (Fig. 3.54a). For PEO burn-off, PI conversion to amorphous carbon and crystallization of the oxide walls, the film is heated under argon to 700°C (Fig. 3.54b). Finally, the residual carbon is removed by heating the film in air to 450°C, leaving a highly crystalline mesoporous transition metal oxide behind (Fig. 3.54c). Mesoporous TiO_2 (anatase) prepared by this procedure contains pores with a size of ∼24 nm and fully crystalline walls of a thickness of 5 nm, and exhibits a surface area of 89 $m^2\ g^{-1}$ [3.146].

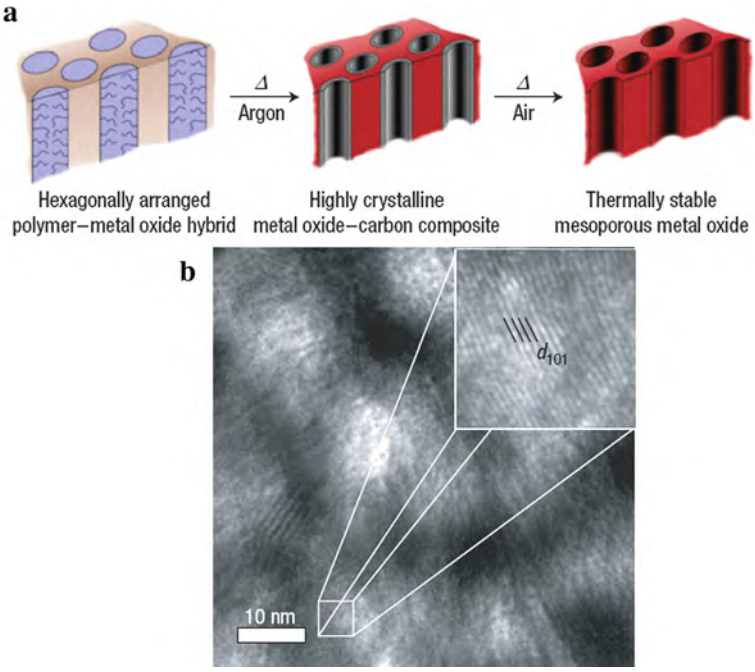

Fig. 3.54 (**a**) Schematic representation of the formation of mesoporous transition metal oxides. In situ formed carbon acts as a rigid support and enables the synthesis of highly crystalline mesoporous oxides with large uniform pores. (**b**) High-resolution transmission electron micrograph (HRTEM) of a TiO_2 mesoporous film. *Inset*: Image showing the d_{101} lattice spacing, $d_{101} = 0.348$ nm, of the TiO_2 anatase structure consistent with literature values. (Reprinted with permission from [3.146]. © 2008 Nature Publishing Group)

Nanoporous anodic aluminum oxide (AAO) with self-organized hexagonal arrays of uniform parallel nanopores have been used for sensing, storage, separation, and nanowire synthesis (see [3.147]). Self-ordered AAOs have been obtained by mild anodization (MA) within limited processing windows, whereas hard anodization (HA) with high current densities using sulfuric acid is a faster process but the pores are less ordered than those in the MA process. By a combination of the MA and HA processes in a periodic pulse sequence consisting of a low-potential pulse followed by a high-potential pulse, a tailoring of the pore structure as well as of the chemical composition of the AAO along the pore axis can be achieved (see Fig. 3.55).

Nanoporous membranes can be used as templates for nanoscopic metal particles. The optical properties of the nanometal–insulator composites are of particular interest [3.148]. The length and aspect ratios of the wires or nanotubes can be controlled by the amount of metal deposited and the pore diameter. For obtaining nanotubes the pore walls are chemically modified for preferential deposition of the metal ions. As a molecular anchor for metal ions a cyanosilane is used to react with the hydroxyl

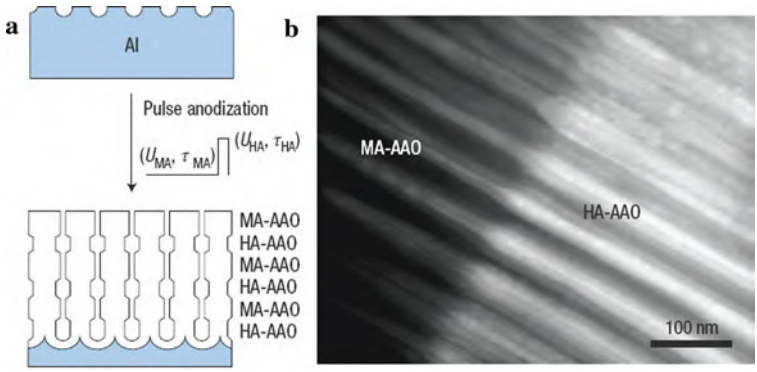

Fig. 3.55 (**a**) Scheme for the fabrication of nanoporous anodic aluminum oxide (AAO) with modulated pore diameters by pulse anodization. (**b**) Image taken at the interface of the mild anodization (MA) and the hard anodization (HA) AAO slabs. (Reprinted with permission from [3.147]. © 2008 Nature Publishing Group)

groups on the alumina pore wall yielding attractive centers for Au deposition and a general route to chemically tailor the pore walls in alumina. At longer deposition times the nanotubes close up to form nanowires. The optical properties of a metal nanowire ensemble in an insulating matrix depend strongly on the size and aspect ratio of the wires (see Fig. 3.56). The optical extinction generated by the metallic nanoparticles originates from the plasmon resonance band (see Sect. 7.6) of the nanoparticles where the wavelength of the highest extinction in the metal particle composite corresponds to the condition where the induced field in the metal is

Fig. 3.56 Optical micrographs of alumina membranes containing gold nanowires with diameters decreasing from the *top row* (150 nm) to the *bottom row* (20 nm) and aspect ratios increasing from left to right. The membranes are transparent so that the colors originate from the gold nanowires [3.148]. The real shift of the transmission light from *top* to *bottom* and from *left* to *right* is due to a blue shift of the surface plasmon absorption. (Reprinted with permission from [3.148]. © 1994 AAAS)

maximum. This gives rise to a blue shift of the extinction maximum at 550 nm or a red shift of the specimen colors with decreasing particle size and increasing aspect ratio.

Nanoporous materials by self-assembly (e.g., MCM-41) can be synthesized of structure-directing amphiphiles, usually surfactants or block copolymers, combined with solutions of sol–gel precursors (e.g., metal alkoxides) as schematically shown in Fig. 3.57. The surface functionality of the pores can be modified by adding organically modified precursors [3.149]. By the wide range of amphiphilic templates the pore-size constraints of zeolites can be overcome to allow more facile diffusion of bulky molecules for application in catalysis and absorption technologies. Nanoporous aluminosilicates are investigated for uses in fluid catalytic cracking and condensed media chemical conversion processes (see [3.149]). Large, optically active molecules, such as dyes and conjugated polymers (see [3.149]), can be incorporated into the pores to make hybrid materials with attractive optoelectronic properties.

A most complex silica mesoporous nanostructure IBN-9 with three unconnected interwoven channels 2–50 nm in diameter has been synthesized [3.151] by using a specially designed cationic surfactant template, *N, N*-dimethyl-L-phenylalanine, which has a large and tunable head group and a long hydrophobic hydrocarbon tail. The IBN-9 morphology contains both ultralong and ultrashort channels, which makes it possible to have distinct diffusion rates in different directions [3.151, 3.152].

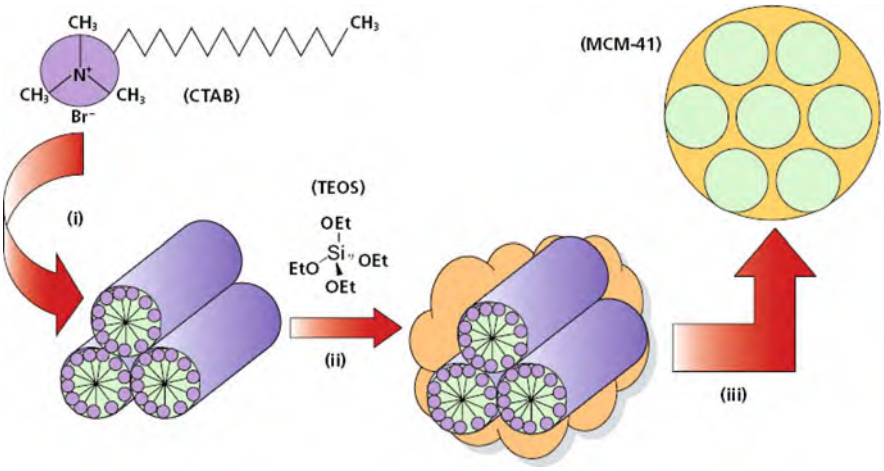

Fig. 3.57 Schematic of the classical mesoporous silica (MCM-41) synthesis route [3.150]. (i) Surfactant, e.g., cetyltrimethylammonium bromide (CTAB), is used to form liquid crystalline micelles in water. (ii) Ceramic sol–gel precursor, e.g., tetraethylorthosilicate (TEOS), is added to the micellar solution to make, upon hydrolysis and condensation, a silica network around the micelles. (iii) Removal of the organic template by thermal treatment (calcination) or solvent extraction yields a mesoporous ceramic material, in this case a hexagonally ordered MCM-41 mesoporous silica framework. (Reprinted with permission from [3.149]. © 2008 Sigma-Aldrich)

3.9.2 Nanostructured Germanium

Nanoporous semiconductors can be of interest because their electronic and optical properties may contrast with those of bulk, thin film, and nanocrystalline forms. Cubic mesostructured germanium (MSU-Ge-1 [3.153] with gyroidal channels (see Fig. 3.58) containing surfactant molecules were synthesized using Ge^{4-} anions from Mg_2Ge via a metathesis reaction with $GeCl_4$ in the presence of the cationic surfactant *N*-eicosane-*N*-methyl-*N*, *N*-dis(2-hydroxyethyl)ammonium bromide (EMBHEAB). The thin Ge walls in the MSU-GE-1 mesostructure – only 1 nm thick – give rise to a substantial blue shift of the optical absorption edge (1.42 eV in MSU-Ge-1) relative to bulk Ge (0.66 eV). This marked blue shift can be understood by considering the changes in the density of the electronic energy states due to the thin Ge walls [3.153].

3.9.3 Nanoporous Metals

Nano- or mesoporous metallic structures can be fabricated by dealloying [3.154], [3.155] or by pyrolysis of block copolymers self-assembled with ligand stabilized metal nanoparticles [3.156].

Nanoporous metals by dealloying. The model system for dealloying is the Ag–Au alloy which can be transformed to nanoporous gold by electrochemical dissolution

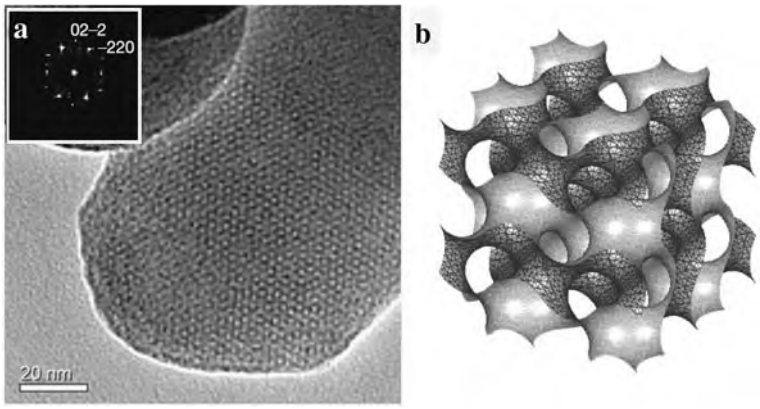

Fig. 3.58 (**a**) Transmission electron micrograph of the mesoporous germanium semiconductor MSU-Ge-1, taken along the [3.111] porosity direction. (**b**) The bi-continuous gyroid minimal surface of the nanoporous germanium. The elemental germanium framework follows the gyroid surface and the surfactant molecules occupy the pore channels. The two different shades of the surface belong to the two independent channel systems in the structure. (Reprinted with permission from [3.153]. © 2006 Nature Publishing Group)

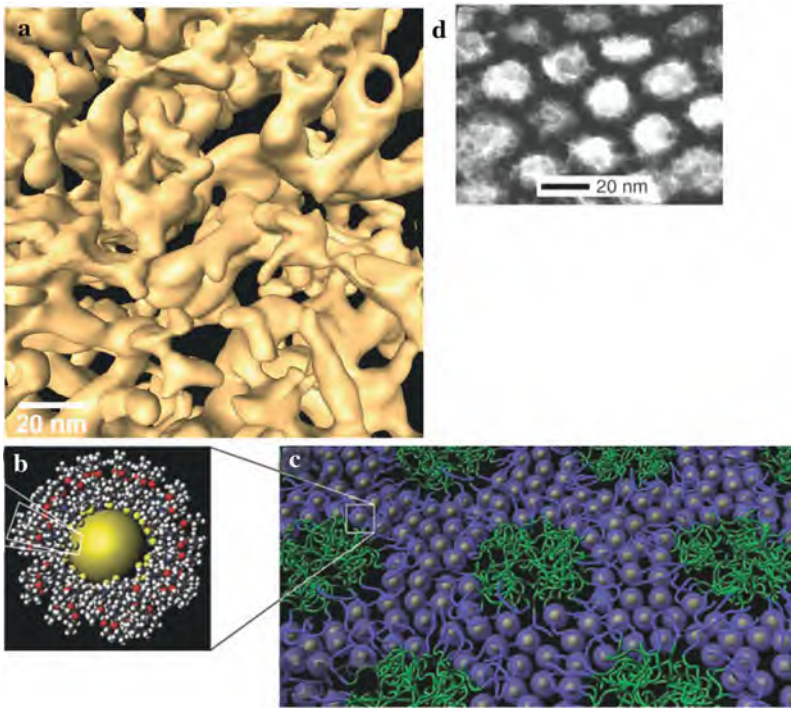

Fig. 3.59 (**a**) Electron tomographic surface rendering of the solid phase of nanoporous gold prepared by dealloying of $Ag_{80}Au_{20}$ [3.155]. (**b**) Model of a Au nanoparticle (NP) with a 1.8-nm diameter metal core and a 1.4-nm shell of *N*, *N*-di-2-propoxyethyl-*N*-3-mercaptopropyl-*N*-methylammonium chloride, the ligand used to produce moderately hydrophilic PtNPs with high solubility. Part of the metal surface is artificially exposed for illustrative purposes. (**c**) Illustration that attempts to convey the approximate mesostructure geometry with the block copolymer (*green*) and violet Au-NPs with ligands. (**d**) Mesoporous Pt after heating at 410°C and carbon removal with an Ar–O plasma [3.156]. (Reprinted with permission from [3.155] (**a**) and [3.156] (**b**–**d**). © 2007 Wiley-VCH (**a**) and © 2008 AAAS (**b**–**d**))

of Ag in 1 M perchloric acid (see [3.155]) and curvature-driven diffusion of Au. From electron tomographic imaging (see Sect. 2.6) of nanoporous Au (Fig. 3.59a) prepared from a $Ag_{80}Au_{20}$ alloy, a porosity of 76%, mean radii for pores (28 nm) and ligaments (16 nm), and a mean curvature of $<\kappa> = 55\ \mu m^{-1}$ [3.155] can be determined.

Mesoporous Pt by self-assembly, with a highly ordered pore structure (see Fig. 3.59d) can be fabricated by self-assembling ligand-stabilized Pt nanoparticles (NPs, Pt core size 1.8 nm, see Fig. 3.59b) and a block copolymer (Fig. 3.59c). This pore structure is pyrolyzed at 410°C under an inert gas atmosphere, leaving behind ordered porous Pt-C composites. Finally, the carbon is removed through use of an Ar–O plasma or acid etch to produce ordered porous Pt mesostructures (Fig. 3.59d).

3.9.4 Single Nanopores – Potentials for DNA Sequencing

A nanopore-based device can provide single-molecule detection and analytical capabilities that are achieved by electrophoretically driving molecules in solution through a nanoscale pore [3.157–3.159]. In the highly confined space of the nanopore, single-nucleic acid polymers can be analyzed at high throughput by a variety of means so that the native order of the nucleobases in a polynucleotide is reflected in the sequence of signals that is detected. Kilobase (kb) length polymers (single-stranded genomic DNA or RNA) or small molecules (e.g., nucleosides) can be identified without amplification or labeling, a unique analytical capability that makes inexpensive, rapid DNA sequencing a possibility to reach the goal set by the US National Institute of Health to sequence a diploid mammalian genome for ∼US$ 1000 in ∼24 h [3.157].

A protein nanopore from, Myobacterium smegmatis porin A (MspA) (Fig. 3.60), with a ∼1 nm long, ∼1 nm wide constriction flanked by regions of significantly larger diameter, has been selected as a candidate nanopore for nucleic acid analysis [3.158]. It has been shown that single-stranded DNA (ssDNA) can be electrophoretically driven through MspA mutants, giving rise to blockades of the ionic current through the pore, when a bias voltage is applied [3.158].

Solid-state nanopores (Fig. 3.61a) articulated with nanoprobes have been proposed to be capable of distinguishing among the four nucleobases of ssDNA (see [3.157, 3.159]. Single bases should be resolved because it is the transverse tunneling current from an emitter probe tip of ≤ 1-nm diameter – resembling a scanning

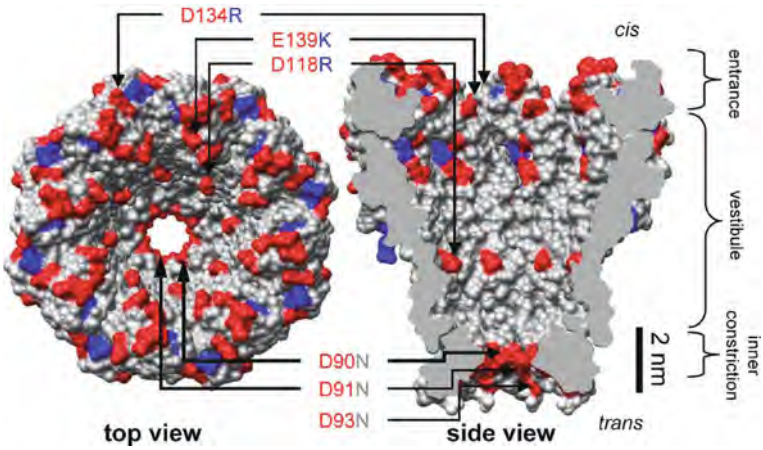

Fig. 3.60 Structure and charge distribution of the protein nanopore from *Mycobacterium smegmatis* porin A (MspA). Aspartate and glutamate residues are colored *red* and arginine and lysine residues are colored *blue*. At an experimental pH 8, the acidic (*red*) residues are expected to be predominantly negatively charged and the basic (*blue*) residues to be positively charged. Locations and identities of mutations are indicated by *arrows* and *labels*. (Reprinted with permission from [3.158]. © 2008 National Academy of Sciences USA)

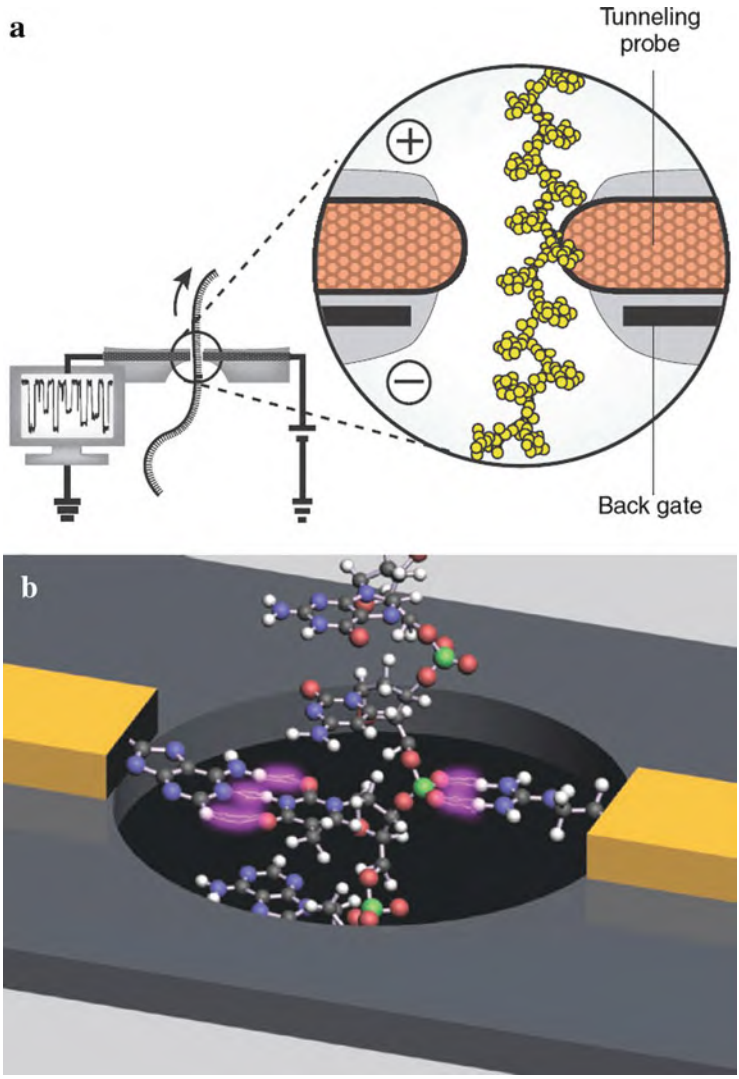

Fig. 3.61 Approach to nanopore sequencing. (**a**) Strand-sequencing in a solid-state nanopore using transverse electron currents. DNA is driven through a nanopore functionalized with embedded emitter and collector tunneling probes (*orange*) and backgate (*black*). The amplitude of the tunneling currents that traverse through the nucleotides is expected to differentiate each nucleobase as the DNA is electrophoretically driven through the pore (*arrow*). (**b**) Design of a nanopore reader with chemically functionalized probes. As a strand of DNA emerges from a nanopore, a "phosphate grabber" on one functionalized electrode and a "base reader" on the other electrode form hydrogen bonds (*light blue ovals*) to complete a transverse electrical circuit through each nucleotide as it is translocated through the nanopore. (Reprinted with permission from [3.157]. © 2008 Nature Publishing Group)

tunneling microscope (STM) – that generates the nucleobase-indentifying signal rather than the nucleotide occupancy through the entire length of nanopore channel. Simulations of the attainable base contrast have presented encouraging but differing insights into the challenges this approach must address. However, the ability of a STM to reveal the atomic-scale features of matter is well established (see Sect. 2.1). A nanopore reader bearing pair of two chemically functionalized probes has been proposed, one probe of each pair able to couple to the nucleotide's phosphate moiety while the other probe base pairs with the nucleobase (Fig. 3.61b). The nucleobase can be identified by the tunneling current–distance response as the DNA moves through the nanopore and past the reader, rather than the tunneling current in a static configuration (see [3.157]).

However, in spite of the progress achieved up to now, important challenges remain until the application of nanopore DNA sequencing [3.157].

Individual DNA base molecules for DNA sequencing can also be directly imaged and identified with a combination of scanning tunneling microscopy (STM) and scanning tunneling spectroscopy (STS) [3.160].

3.10 Lithography

Very large-scale integration (VLSI) of computer components is the fundamental issue of powerful and cheap computers. During the last decades, feature sizes shrank by a factor of two roughly for every 18 months (Moore's law; Fig. 3.62). The challenge now is to stay on this exponential curve for the next decades.

Since matter is not continuous anymore at the nanoscale it will be impossible to build a 10 nm device that works anything like the current CMOS transistor (complementary metal oxide semiconductor). It will be a nanodevice with new physics, new operation principles, and new manufacturing processes. These challenges will appear in the near future when, as predicted, the 45-nm device node will be in production by 2010 and the 32-nm device to follow by 2013. This will not only have impact on the development of IC computer hardware but also on sensor technology, energy conversion, catalysis, nanoelectromechanical systems (NEMS), nanobiology, etc.

The pivotal issue in this development is lithography but the boundaries to function and materials begin to blur. "Top-down" and "bottom-up" approaches will compete and even may merge.

The ability of nanolithography to tailor the structure and chemical composition of a surface at the sub-100 nm length scale is important for studying topics ranging from electronics to materials assembly and for investigating biological recognition at the single biomolecule level [3.161].

In the following, a concise overview of the lithographic techniques such as UV optical lithography, nanoimprinting, block copolymer self-assembly, use of supercritical fluids, nonlinear two-photon lithography, or electron beam lithography, available for coping with these challenges, will be given.

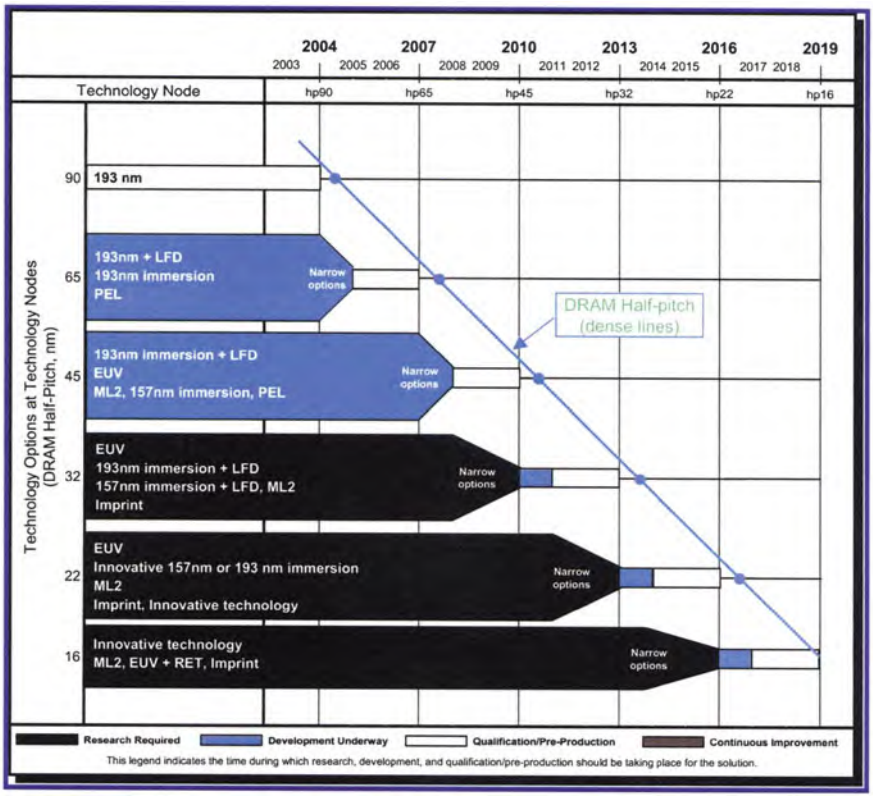

Fig. 3.62 Moore's law for the evolution of the half-pitch (half the distance between the centers of adjacent features in periodic structures) of DRAMs (dynamic random access memory) in nanometer over the years (https://www.itrs.net/common/2005update/2005_07_Lithography.pdf)

3.10.1 UV Optical Lithography

Nanoelectronics nearly exclusively relies on projection lithography (Fig. 3.63) where a predetermined pattern on a photomask is imaged with great fidelity on a photoresist-coated wafer [3.162]. The electronic elements such as transistors and leads are then prepared by lift-off processes, etching, evaporation, diffusion, oxidation, etc.

From 2003 to 2005 the "half-pitch" (half the distance between the centers of adjacent features in periodic structures) has been 90 and 65 nm with 193 nm light sources in 2006 [3.163]. It is expected to be 32 nm in 2013 making use of extreme ultraviolet light sources (EUV) combined with mirror systems (see below).

Optical lithography is the most common patterning technology because of high throughput and economical mass production. However, miniaturization is limited by the wavelike nature of light leading to diffraction and therefore a reduced contrast

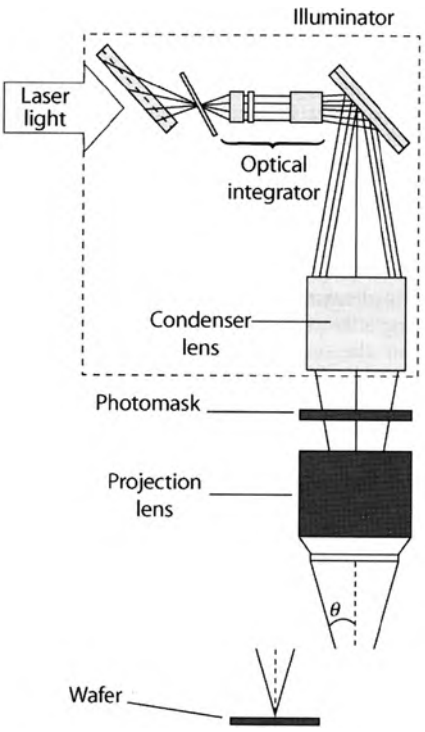

Fig. 3.63 Schematics of an optical lithography system with the main sub-systems the light source (laser), the illuminator, the photomask, the projection lense, and the photoresist-coated wafer. (Reprinted with permission from [3.162]. © 2005 Materials Research Society)

between bright and dark pattern areas. The minimum half-pitch HP is related to the wave length λ of the illuminating light and the numerical aperture $\mathrm{NA} = n \sin\theta$ of the imaging system with n the refractive index of the medium above the photoresist-coated wafer and θ the half-angle of the converging beam in the image plane (Fig. 3.63) by

$$HP = k_1 \lambda / \mathrm{NA} = k_1 \lambda / (n \sin\theta) .$$

Here, k_1 is determined by the illumination conditions, the structure of the photomask, the imaging optics, and the photoresist.

The k_1 factor is at present ~0.4 and can only be lowered to the theoretical limit of 0.25. According to the equation in p. 99 the half-pitch can be reduced by a reduction of λ which, however, requires appropriate light sources, transparent lenses, and suitable photoresists.

The 193 nm argon fluoride eximer lasers as lithography light sources yield a half-pitch of 90 nm and an option is the 157 nm molecular fluorine laser. Single-crystal CaF_2 is used as lense material. In liquid immersion lithography HP can be reduced by introducing a high n fluid (water $n = 1.44$) between the last optical element and the photoresist on the wafer (Fig. 3.63) yielding a reduction of the exposure wave

length from, e.g., 193 to 134 nm in water. This technology can be used for 65 and 45 nm half-pitch manufacturing.

In parallel to immersion lithography, extreme ultraviolet lithography (EUV lithography) is currently developed for the sub-32 nm node with joint research platforms of the IC manufacturers. For implementing this technique novel technologies of light sources and of projection systems are going to be developed (see Sect. 9.2).

3.10.2 Electron Beam Lithography

Lateral dimensions of about 10 nm or less are necessary to define, e.g., single-electron transistors working at ambient temperature. These structures can be fabricated by electron-beam lithography [3.164] making use of low-energy electrons and a high-resolution resist such as calixarene (see Fig. 3.64). This high-resolution lithographic technique is, however, limited by the slow serial writing process whereas for commercial application parallel lithographic processes are mandatory.

3.10.3 Proton-Beam Writing

Proton-beam writing uses a focused beam of MeV protons to pattern resist material at nanodimensions [3.165]. In contrast to electrons, the more massive protons maintain a straight path, enabling p-beam writing to fabricate 3D, high aspect ratio structures with vertical, smooth sidewalls (Fig. 3.64b), and lateral resolutions down to 22 nm [3.165].

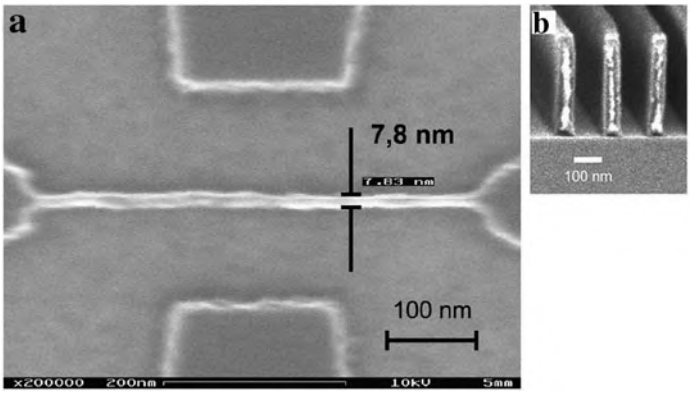

Fig. 3.64 (**a**) Scanning electron micrograph (SEM) of an 8-nm wide nanowire patterned in a 40-nm thick hexaacetate *p*-methylcalixarene (MC6A0Ac) resists using a 10 keV electron beam [3.164]. (**b**) SEM of parallel lines within in a 350-nm thick poly (methyl metacrylate) (PMMA) layer. The structure is written with a focused 2 MeV proton beam, and the structure has a wall width of 50 nm [3.165]. (Reprinted with permission from [3.164] (**a**) and [3.165] (**b**). © 2001 Elsevier (**a**) and © 2007 Elsevier (**b**))

3.10.4 Nanoimprint Lithography (NIL)

This technique is a potentially low-cost, high-resolution patterning technique which may be appropriate for the sub-45-nm integrated circuit regime [3.166]. In this technique, patterns can be repeatedly transferred from a mold to some polymeric material with a 5-nm horizontal patterning resolution. This may be of interest for semiconductor devices, microfluidic devices, optical components, photonic devices, and biological applications [3.167].

The processing flow for ultraviolet-assisted nanoimprint lithography (UV-NIL) is shown in Fig. 3.65. The research at present is focused to the chemistry of the photo-setting materials. An example of a UV-NIL pattern is given in Fig. 3.66. Nanoimprint lithography, furthermore, has been studied in order to fabricate plasmonic arrays [3.168].

3.10.5 Dip-Pen Nanolithography (DPN)

Dip-pen nanolithography (DPN)is a scanning probe microscopy-based nanofabrication technique that combines direct-write soft-matter compatibility with the high resolution and registry of atomic force microscopy (AFM), which makes it a versatile tool for depositing soft and hard materials on a variety of surfaces [3.161]. DPN uses an "ink"-coated AFM tip to pattern a surface (Fig. 3.67a) with a sub-50-nm resolution and without premodification of the surface. DPN patterning has been used for a wide variety of inks, including small organic molecules, polymer, DNA, proteins, nanoparticles, and metal ions (see [3.161, 3.169]).

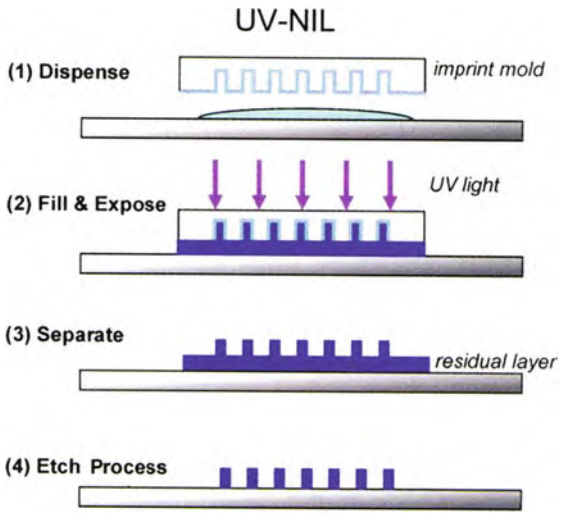

Fig. 3.65 Schematics of the processing flow of ultraviolet-assisted nanoimprint lithography (UV-NIL). (Reprinted with permission from [3.166]. © 2005 Materials Research Society)

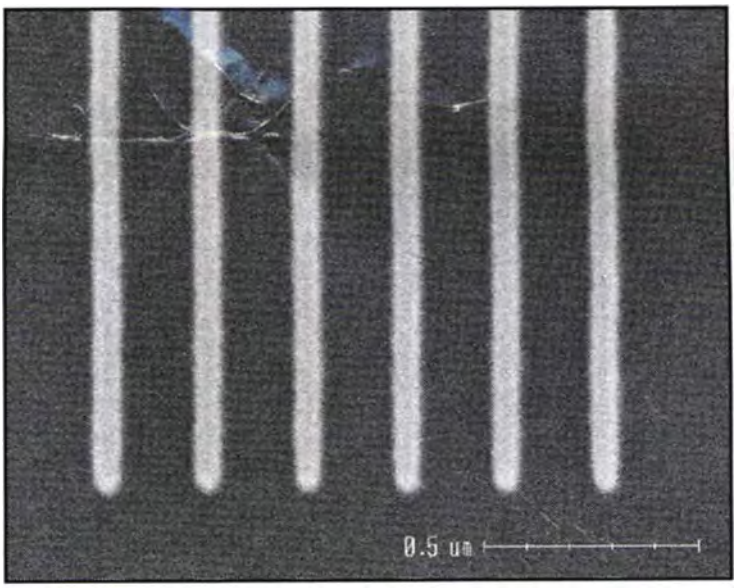

Fig. 3.66 Scanning electron microscopy of a UV-NIL pattern with 30 nm lines on a semi-isolated pitch. (Reprinted with permission from [3.166]. © 2005 Materials Research Society)

Nanoarrays of biomolecules are of interest because they can screen a larger number of targets more rapidly than conventional microarrays, they can lead to lowering the limits of molecular detection, and they can be used to address questions of biomolecular recognition, since biorecognition is inherently a nano- rather than a microscopic phenomenon [3.161].

Nanoarrays of the anti-p24 antibody can be used to screen for the human immunodeficiency HIV-1 virus (HIV-1) p24 antigen in serum samples [3.170]. The nanoarrays are fabricated using DPN-patterned 16-mercaptohexadecanoic acid (MHA) dot features as templates for antibody immobilization. On capturing the p24 antigen, the anti-p24 features (Fig. 3.67b) increased in height by ∼2.3 nm (measured by AFM, see Fig. 3.67c). This height increase can be further amplified by sandwiching the captured p24 protein with anti-p24-functionalized gold nanoparticles (Fig. 3.67a). This demonstrates that nanoarray-based assays can exceed the detection limit of conventional enzyme-linked immunosorbent assays (ELISA) by orders of magnitude [3.161].

3.10.6 Block Copolymer Lithography

This may be an additional alternative for fabricating feature sizes less than 45 nm. Here, tailored self-assembly processes (“bottom-up” approaches) may be combined with conventional microfabrication processes (“top-down”) [3.171]. In block

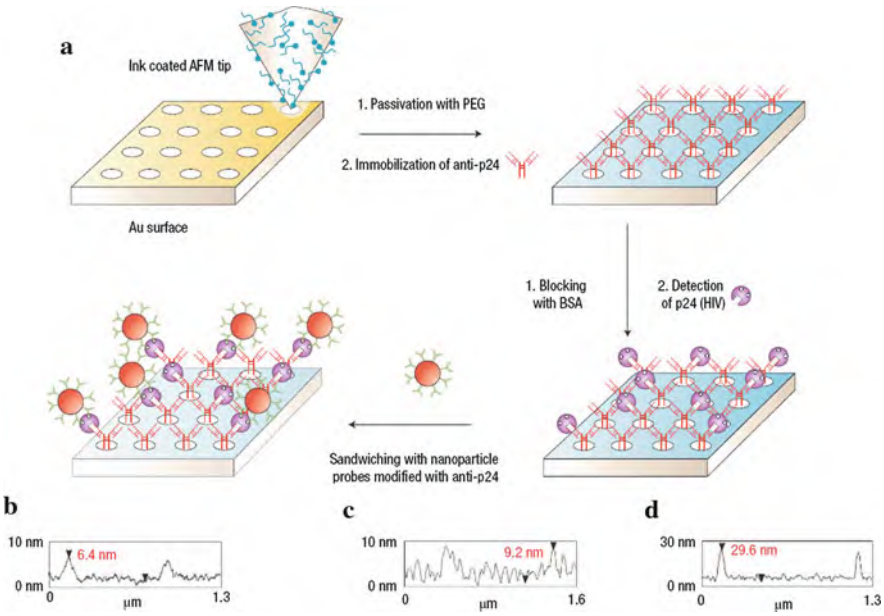

Fig. 3.67 Detection of HIV-1 p24 antigen using a dip-pen nanolithography (DPN) generated nanoarray of anti-p24 antibodies. (**a**) DPN-generated nanoarrays of mercaptohexadecanoic acid (MHA) dots with a diameter of ~83 nm are used to immobilize anti-p24 antibodies on a Au substrate. The bare regions were passivated with 11-mercaptoundecyl-tri(ethylene glycol) (PEG) and non-specific protein adsorption was minimized by blocking with bovine serum albumin (BSA). The presence of HIV-1 p24 in patient plasma is probed by measuring the height profile of the anti-p24 antibody array. The height increase signal as a result of specific antigen–antibody binding is further amplified by a sandwich assay with Au nanoparticles. (**b**–**d**) Atomic force microscopy (AFM) traces that demonstrate the detection of HIV-1 p24 antigen. (**b**) Topography trace of adsorbed anti-p24 IgG on MHA. (**c**) After p24 binding to anti-p24 IgG, a height increase for the IgG features is observed. (**d**) p24 detection after amplification with anti-p24 IgG-coated Au nanoparticles (diameter 20 nm) [3.161, 3.170]. (Reprinted with permission from [3.161]. © 2007 Nature Publishing Group)

copolymers two chemically dissimilar polymer chains are covalently linked together at one end. They are in general immiscible and phase-separate microscopically. However, in the case of block copolymers phase separation is limited to the dimensions of the copolymer chain (5–20 nm) due to the connectivity of the two chains. Therefore, upon heating, amorphous block copolymers containing blocks such as polystyrene (PS), poly(methyl methacrylate) (PMMA), poly(ethylene-*alt*-propylene) (PEP), or poly(vinylpyridine) (PVP) will self-assemble into arrays of nanosized domains (Fig. 3.68). with morphologies changing with composition.

In the case of cylindrical domains in, e.g., PS-PMMA diblock copolymers these domains may be oriented in parallel or perpendicularly to the substrate depending on the chemical interaction with the substrate (Fig. 3.69).

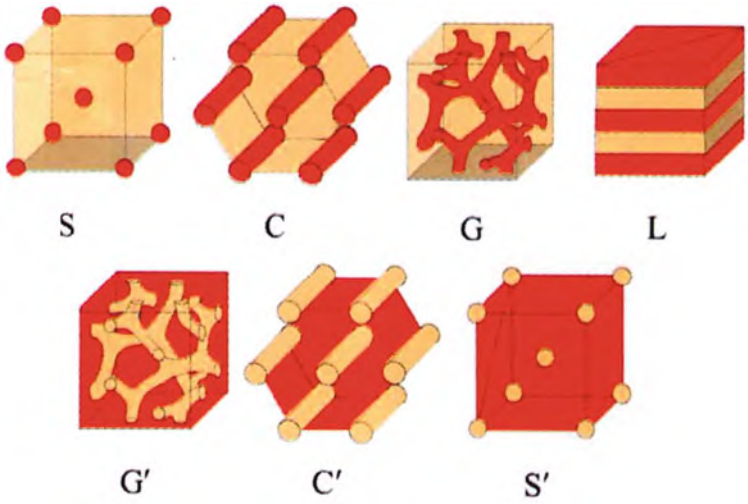

Fig. 3.68 Schematics of nanodomain morphologies of diblock copolymers with morphologies changing with the volume fraction of the components from spherical (S, S′) to cylindrical (C, C′) to gyroid (G,G′) to lamellar (L). The molecular weight of the block copolymer determines the size of the domains of typically 10 nm. (Reprinted with permission from [3.171]. © 2005 Materials Research Society)

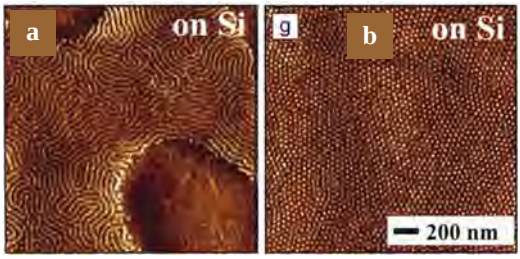

Fig. 3.69 Atomic force micrographs of a PS-PMMA diblock copolymer on a Si substrate with (**a**) domain orientation parallel to the substrate and (**b**) with perpendicular domain orientation on a chemically modified substrate. (Reprinted with permission from [3.171]. © 2005 Materials Research Society)

It may be noted that cylindrical polymer nanodomains oriented perpendicular to a film plane, can be selectively removed in order to fabricate highly selective biological nanofiltration membranes, e.g., for the separation of human rhinovirus type 14 with a 30 nm diameter. This virus is a major pathogen of the common cold in humans [3.171].

Square patterns of block copolymers complying with nanoscale industry standards can be generated by combining supramolecular assembly of hydrogen-bonding units with controlled phase separation of diblock copolymers [3.172].

3.10.7 Protein Nanolithography

Nanopatterned protein arrays offer significant advantages for sensing biomedical protein–protein interactions, due to short diffusion times, parallel detection of multiple targets, and the requirement of only tiny amounts of samples (see [3.173]). Protein nanolithography can be used for the nanostructured assembly of even fragile proteins under native conditions. Immobilized proteins are detached by a vibrational atomic force microscopy (AFM) mode and replaced by other proteins, which are selectively self-assembled (see Fig. 3.70a). This nanolithography permits rapid writing, reading, and erasing of arrays of functional proteins at dimensions down to 50 nm [3.173] (see Fig. 3.70b).

Nanolithography of protein arrays under native conditions (aqueous buffer, physiological pH, and ionic strength) is a prerequisite for biochip applications (see Sect. 12.3). The interaction of a receptor protein and its ligand was studied specifically for the nanoarrayed extracellular domain of the human type I interferon receptor (ifnar2-His_{10}) to monitor the binding of interferon-α2 (IFNα2, a glycoprotein) labeled with quantum dots (see Fig. 3.70b). This medically relevant antivirus

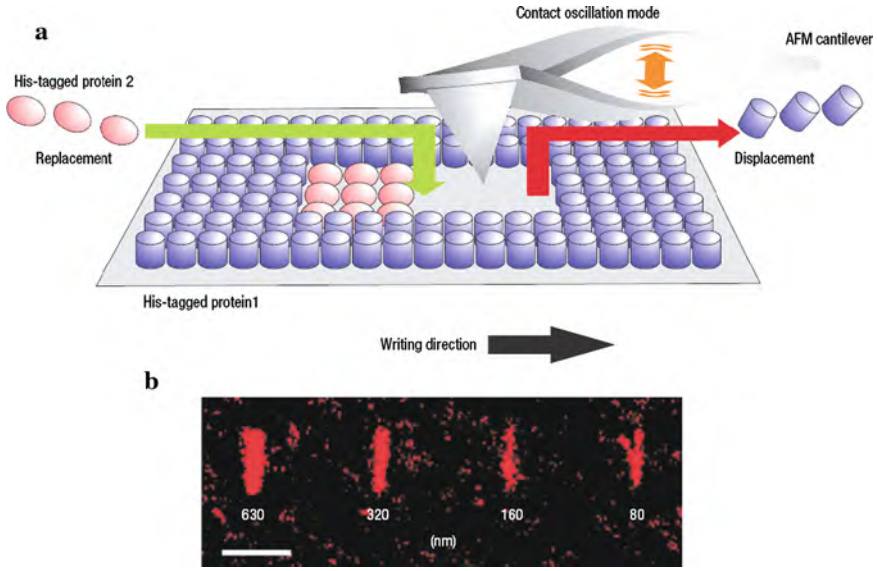

Fig. 3.70 (**a**) Fabrication of rewriteable protein nanoarrays on self-assembled nanolayers (SAMs) by native protein nanolithography. His is a oligohistidine peptide, where histidine is the amino acid $C_6H_9N_3O_2$. Uniformly His-tagged proteins are removed ("displacement") with the tip of an atomic force microscope (AFM, see Sect. 2.2) in contact oscillation mode and substituted with other His-tagged proteins ("replacement"). (**b**) Protein–protein interaction in micro- and nanostructured arrays: specific binding of IFN α2 (*red*) conjugated with the Quantum Dot 655 to immobilized ifnar2-His_{10} nanostructure arrays is probed by confocal laser scanning fluorescence microscopy. Strong fluorescence emission at 655 nm was detected only in the arrays. Scale bar, 5 μm. (Reprinted with permission from [3.173]. © 2007 Nature Publishing Group)

defense system is well suited for demonstrating the functional organization of fragile and dynamic protein assemblies. The ligand IFNα2 binds exclusively to the nanoarrayed receptor ifnar2, but not to the surrounding protein matrix (Fig. 3.70b). This shows the possibility of probing specifically protein–protein interaction in nanoscale dimensions [3.173].

3.10.8 Fabrication of Nanostructures in Supercritical Fluids

Supercritical fluids such as CO_2 offer a combination of properties well suited for the fabrication of nanostructures: Liquid-like densities, favorable transport properties, and the absence of surface tension enable solution-based processing in media that behave like gases. Therefore, "top-down" methods such as metal deposition, etching, surface modification as well as "bottom-up" approaches as deposition reactions in template structures may be conducted in order to overcome existing limitations to device scaling beyond 45 nm [3.174].

Any substance heated beyond its critical temperature T_c cannot be liquefied at any pressure. A convenient system is CO_2 with the critical parameters $T_c = 30.98°C$ and $p_c = 7.38$ MPa. The combination of properties of supercritical fluids is often very favorable for manufacturing nanostructures: The mass density can be as high as in liquids, the viscosity low as in gases, reasonable diffusivities and, most important, zero surface tensions. Therefore, the material can penetrate easily into the smallest features without limitations of wetting or flow in confined geometries or concerns about residual solvent contaminations as the solvents dissipate completely upon depressurization. Thus, deposition reactions, e.g., on polymer templates dilated in CO_2 can provide device-quality nanostructured silica, titania (Fig. 3.71), carbon, or ultralow-dielectric constant thin films for microelectronics.

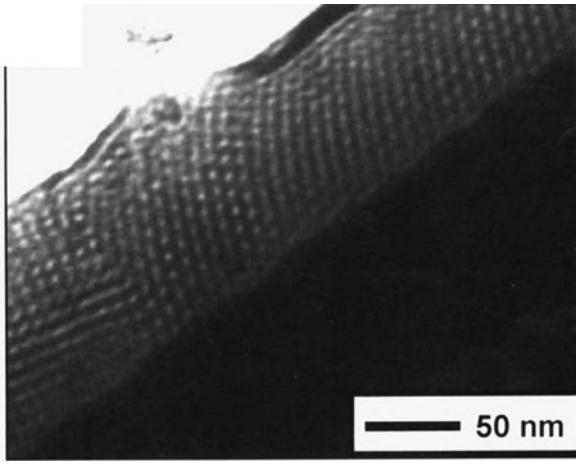

Fig. 3.71 Transmission electron micrograph (TEM) of a mesoporous TiO_2 film prepared by supercritical CO_2-assisted infusion and condensation of titanium diisopropoxide bisacetylacetonate within a block copolymer template blend. (Reprinted with permission from [3.174]. © 2005 Materials Research Society)

3.10.9 Two-Photon Lithography for Microfabrication

Two-photon lithography is based on two-photon absorption processes in certain chromophores that can simultaneously absorb two photons to produce a photochemical reaction characteristic for radiation of twice the energy [3.175]. The advantage of this process is that outside the focal point, the incident light is below the absorbance threshold and passes without reaction through the material. Therefore, by tightly focusing a femtosecond laser beam into a resin, photo-induced reactions such as polymerization occur only close to the focal point allowing the direct writing of 3D patterns by sample scanning.

By two-photon absorption, structures of the order of 250 nm can be fabricated since the width of the absorption depends quadratically on the excitation intensity and is therefore confined to the excitation wavelength.

The desired 3D structure is fabricated via two-photon absorption and subsequent photopolymerization followed by the removal of the unreacted resin. Current research efforts are focused to the synthesis of high-efficiency two-photon initiator and sensitizer molecules with high two-photon absorption cross sections. Polymerization is presumably initiated by a two-photon induced electron transfer from a photoexcited chromophore (e.g., organic stilbene-based π-conjugated compounds) to an acrylate or subsequent radical products. The most widely applied commercial two-photon resin, SCR 500 (Japan Synthetic Rubber Co.) is a free radical resin consisting of urethane acrylate monomers and oligomers as well as photo initiators (Fig. 3.72).

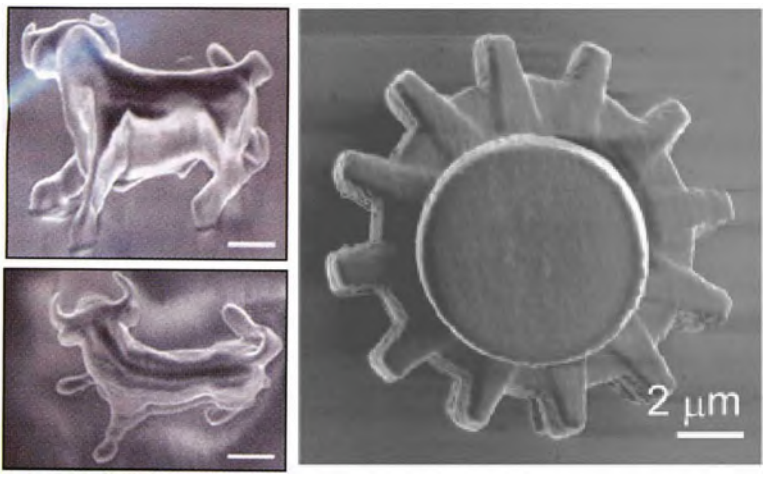

Fig. 3.72 "Micro-bull" sculptures manufactured by two-photon polymerization of SCR 500 resin [3.176] and a microgearwheel [3.177]. (Reprinted with permission from [3.176] and [3.177]. © 2001 Nature Publishing Group and © 2002 American Institute of Physics)

3.11 Summary

For the synthesis of 0D nanocrystals, of arrays of nanocrystals, of 1D nanowires, of 2D nanolayers or multilayers, and of bulk nanomaterials of metals, semiconductors, or insulators, numerous techniques are available. The synthesis of carbon nanostructures plays a particular role. The shape of nanocrystals can be precisely controlled and complex nanostructures can be fabricated. Nanoporous structures can be synthesized from oxides (e.g., zeolites) for application in catalysis or separation, from semiconductors for band gap engineering or from metals for improved fuel cell electrodes or optical applications. Single nanopores offer potentials for DNA sequencing. Lithographic techniques for preparing nanostructures extend from optical to extreme ultraviolet (EUV) wavelengths, to particle beam nanowriting, nanoimprint lithography, and dip-pen nanolithography.

References

3.1 M.S. El-Shall, A.S. Edelstein, in *Nanomaterials: Synthesis, Properties, Applications*, eds. A.S. Edelstein, R.C. Cammarata (IOP Publishing, Bristol, 1996), p. 13
3.2 M. Cohen et al., J. Phys. Chem. **91**, 3141 (1987)
3.3 A.C. Mackay, Acta Crysta. **15**, 916 (1962)
3.4 M.J. Yacaman et al., J. Vac. Sci. Technol. **319**, 1091 (2001)
3.5 T. Dietz et al., J. Chem. Phys. **73**, 4816 (1980)
3.6 C.G. Granquist, R.A. Buhrmann, J. Appl. Phys. **47**, 2200 (1976)
3.7 G.M. Chow, K.E. Gonsalves, in [3.1], p. 55
3.8 R. Würschum et al., Nanostructured Materials **3**, 225 (1993)
3.9 L.E. McCandlish et al., Mat. Res. Soc. Symp. Proc. **132**, 67 (1989)
3.10 K. Gonsalves et al., Adv. Mater. **3**, 202 (1991)
3.11 T.D. Xiao et al., J. Mat. Sci. **255**, 1098 (1992)
3.12 L.C. Klein, in [3.1], p. 147
3.13 A.H. Heuer et al., Science **255**, 1098 (1992)
3.14 A.R. Kortan et al., J. Am. Chem. Soc. **112**, 1327 (1990)
3.15 N. Herron, Y. Wang, in [2.1], p. 73
3.16 H.F. Qian et al., Small **2**, 747 (2006)
3.17 D.J. Norris et al., Science **319**, 1776 (2008)
3.18 S. Peng, S. Sun, Mater. Matt. (Sigma-Aldrich) **4**(1), 14 (2009)
3.19 K.M. Nam et al., Angew. Chem. Int. Edn. **47**, 9504 (2008)
3.20 S.H. Sun et al., J. Am. Chem. Soc. **126**, 273 (2004)
3.21 B.L. Lv et al., J. Mater. Sci. Technol. **25**, 155 (2009)
3.22 C.N. Chinnasamy et al., Appl. Phys. Lett. **93**, 032505 (2008)
3.23 K.E. Mueggenburg et al., Nat. Mater. **6**, 656 (2007)
3.24 W.L. Cheng et al., Nat. Mater. **8**, 519 (2009)
3.25 E.V. Shevchenko et al., Nature **439**, 55 (2006)
3.26 A.M. Kalsin et al., Science **312**, 420 (2006)
3.27 F.J. Himpsel et al., MRS Bull. **24**, 8; 20 (1999)
3.28 H. Hasegawa et al., MRS Bull. **24**, 8; 25 (1999)
3.29 M. Terrones et al., Adv. Mater. **11**, 655 (1999); M. Terrones et al., MRS Bull. **24**, 8; 4 (1999)
3.30 H.J. Fan et al., Small **2**, 700 (2006)

3.31 F.M. Ross, Nat. Nanotech. **4**, 17 (2009)
3.32 W. Lu, C.M. Lieber, J. Phys. D: Appl. Phys. **39**, R387 (2006)
3.33 K.A. Dick et al., Nat. Mater. **3**, 380 (2004)
3.34 P. Caroff et al., Nat. Nanotech. **4**, 50 (2008)
3.35 R.E. Algra et al., Nature **456**, 369 (2008)
3.36 S. Helveg et al., Nature **427**, 426 (2004)
3.37 M.J. Bierman et al., Science **320**, 1060 (2008)
3.38 J.D. Eshelby, J. Appl. Phys. **24**, 176 (1953)
3.39 L. Cademartiri, G.A. Ozui, Adv. Mater. **21**, 1013 (2009)
3.40 X.M. Lu et al., J. Am. Chem. Soc. **130**, 8900 (2008)
3.41 C. Wang et al., J. Am. Chem. Soc. **130**, 8902 (2008)
3.42 P. Gambardella et al., Nature **416**, 301 (2002)
3.43 X.-D. Ma et al., Phys. Rev. Lett. **102**, 205503 (2009)
3.44 Z.P. Liu et al., J. Phys. Chem. B **109**, 10699 (2005)
3.45 T.Y. Yu et al., J. Am. Chem. Soc. **128**, 1786 (2006)
3.46 N. Pradhan et al., NanoLett. **6**, 720 (2006)
3.47 A.S. Barnard et al., Nanotechnol. **17**, 5707 (2006)
3.48 I. Patla et al., NanoLett. **7**, 1459 (2007)
3.49 D. Li, Y. Xia, Adv. Mater. **16**, 1151 (2004)
3.50 Y. Dzenis, Science **304**, 1917 (2004)
3.51 J.W. Xie, Y. Xia, Material Matters (Sigma-Aldrich) **3** (1), 19 (2008)
3.52 D. Li et al., J. Am. Ceram. Soc. **89**, 1861 (2006)
3.53 M. Bognitzki et al., Adv. Mater. **18**, 2384 (2006)
3.54 J.J. Stankus et al., Biomaterials **28**, 2738 (2007)
3.55 C.K. Hashi et al., Proc. Natl. Acad. Sci. USA **104**, 11915 (2007)
3.56 K.T. Nam et al., Science **312**, 885 (2006)
3.57 J.-H. Lee et al., Proc. Natl. Acad. Sci. USA **104**, 20410 (2007)
3.58 R.C. Cammarata in [3.1], p. 113
3.59 L. Esaki, R. Tsu, IBM, 7. Res. Dev. **14**, 61 (1970)
3.60 G.G. Roberts, Adv. Phys. **34**, 475 (1985)
3.61 N. Tillman et al., Langmuir **5**, 101 (1989)
3.62 E.R. Kleinfeld, G.S. Ferguson, Science **265**, 370 (1994)
3.63 C. Ross, Annu. Rev. Mater. Sci., **24**, 159 (1994)
3.64 F. Spaepen et al., Rev. Sci. Inst. **56**, 1340 (1985)
3.65 K.N. Tu et al., in *Electronic Thin Film Science for Electrical Engineers and Materials Scientists*, MacMillan, New York (1996) Ch. 6
3.66 Max-Planck-Gesellschaft, Berichte und Mitteilungen, München, 3/98
3.67 G.K. Hubler, MRS Bull. **17**, 26 (1992)
3.68 L.L. Chang, L. Esaki, Surf. Sci. **98**, 70 (1980)
3.69 L. Wilson, A. Bienenstock, Mat. Res. Soc. Symp. Proc. **103**, 69 (1988)
3.70 S.M. Prokes, F. Spaepen, Appl. Phys. Lett. **47**, 234 (1985)
3.71 D.G. Schlom et al., Mater. Sci. Eng. **B87**, 282 (2001)
3.72 J. Mannhart et al., MRS Bull. **33**, 1027 (2008)
3.73 W.K. Kim et al., J. Chem. Eng. Jpn. **38**, 578 (2005)
3.74 M. Knez et al., Adv. Mater. **19**, 3425 (2007)
3.75 M.S. Sander et al., Adv. Mater. **16**, 2052 (2004)
3.76 J.Y. Huang et al., NanoLett. **6**, 2325 (2006)
3.77 G. Slayter, Sci. Am. **206**, 124 (1962)
3.78 M. Chigashige, *Alchemy and other chemical achievements of the ancient orient*, Engl. Transl. N. Sasaki (Rokakuho Uchide, Tokyo, 1936), p. 84
3.79 M. Atzmon et al., J. Appl. Phys. **58**, 3865 (1985)
3.80 E. Baer et al., Science **235**, 1015 (1987)
3.81 C.J. Murphy, Science **298**, 2139 (2002)

3.82 Y.G. Sun, Y.Xia, Science **298**, 2176 (2002)
3.83 C. Li et al., Angew. Chem. Int. Edn. **46**, 3264 (2007)
3.84 D. Seo et al., J. Phys. Chem. B **112**, 2469 (2008)
3.85 Y. Xiong et al., J. Am. Chem. Soc. **127**, 17118 (2005)
3.86 J. Chen et al., Angew. Chem. Int. Edn. **44**, 2589 (2005)
3.87 M.J. Jiang et al., Mater. Matt. (Sigma-Aldrich) **4** (1), 8 (2009)
3.88 T. van Dillen et al., Materials Today **7**, July – August 2004, p. 40
3.89 S. Roorda et al., Adv. Mater. **16**, 235, (2004)
3.90 G.W. Zhou et al., Phys. Rev. Lett. **94**, 246101 (2005)
3.91 Y.D. Yin et al., Science **304**, 711 (2004)
3.92 K.N. Tu, U. Gösele, Appl. Phys. Lett. **86**, 093111 (2005)
3.93 X.D. Feng et al., Science **312**, 1504 (2006)
3.94 Z.L. Wang, Materials Today, June 2004, p. 26
3.95 MRS Bull. Sept. 2004, p. 608
3.96 D.A. Tomalia, Materials Today, March 2005, p. 34
3.97 H.J. Fecht in [3.1], p. 89
3.98 A. Guinier, *x-ray diffraction*, Freeman, San Francisco (1963), p. 124
3.99 G.M.J. Wagner, M.S. Boldrick, J. Mater. Sci. Eng. A **133**, 26 (1991)
3.100 A.R. Yavari, P.J. Desré, in *Ordering and Disordering in Alloys*, ed. A.R. Yavari (Elsevier, Amsterdam, 1992), p. 414
3.101 R.Z. Valiev, in *Nanophase Materials*, eds. G.C. Hajipanayis, R.W. Siegel (Kluwer, Dordrecht, 1994), p. 275
3.102 D.A. Rigney, Annu. Rev. Mater. Sci. **18**, 141 (1988)
3.103 R.B. Schwarz et al., Nanostr. Mat. 1, **37** (1992)
3.104 H.W. Kroto et al., Nature **318**, 162 (1985)
3.105 S. Iijima, Nature **354**, 56 (1991)
3.106 K.S. Novoselov et al., Science **306**, 666 (2004); Proc. Nat. Acad. Sci. USA. **102**, 10451 (2005)
3.107 S. Stankovich et al., Nature **442**, 282 (2006)
3.108 R.W.G. Wyckoff, *Crystal Structures*, vol. 1 (Interscience, New York, 1964)
3.109 C. Kittel, Einführung in die Festkörperphysik (Oldenbourg, München, 2002)
3.110 D.R. Huffman, in [3.1], p. 477
3.111 M.S. Dresselhaus et al., Europhys. J. **D9**, 69 (1999)
3.112 R.V. Norden, Nature **442**, 228 (2006)
3.113 W. Kraetschmer et al., Nature **347**, 354 (1990)
3.114 C. Smart et al., Chem. Phys. Lett. **188**, 171 (1992)
3.115 J.L. Atwood et al., Nature **368**, 229 (1994)
3.116 L. Becker et al., Nature **372**, 507 (1994)
3.117 L. Becker et al., Nature **400**, 227 (1999)
3.118 D. Ugarte, Nature **359**, 707 (1992)
3.119 F. Banhart, P.M. Ajayan, Nature **382**, 453 (1996)
3.120 R. Jansen, P. Wallis, Mater. Matt. (Sigma-Aldrich) **4**(1), 23 (2009)
3.121 P.M. Ajayan et al., Nature **362**, 522 (1993)
3.122 P.M. Ajayan, S. Iijima, Nature **361**, 333 (1993)
3.123 W.Z. Li et al., Science **274**, 1701 (1996)
3.124 A. Thess et al., Science **273**, 483 (1996)
3.125 K.S. Novoselov et al., Nature **438**, 197 (2005)
3.126 Y.B. Zhang et al., Nature **438**, 201 (2005)
3.127 K.S. Novoselov et al., Science **306**, 666 (2004); Proc. Natl. Acad. Sci. USA **102**, 10451 (2005)
3.128 M.I. Katsnelson, Materials Today **10**, Jan–Feb 2007, p. 20
3.129 Y. Zhang et al., Nature **438**, 201 (2005)
3.130 A.C. Ferrari et al., Phys. Rev. Lett. **97**, 187401 (2006)

3.131 R.E. Peierls, Ann. I. H. Poincaré **5**, 177 (1935)
3.132 L.D. Landau, Phys. Z. Sowjetunion **11**, 26 (1937)
3.133 N.D. Mermin, Phys. Rev. **176**, 250 (1968)
3.134 D.R. Nelson et al., eds., *Statistical Mechanics of Membranes and Surfaces* (World Scientific, Singapore, 2004)
3.135 J.C. Meyer et al., Nature **446**, 60 (2007)
3.136 X. Jia et al., Science **323**, 1701 (2009)
3.137 M. Terrones, Nature **458**, 845 (2009)
3.138 M. Choucair et al., Nat. Nanotech. **4**, 30 (2009)
3.139 V.C. Tung et al., Nat. Nanotech. **4**, 25 (2009)
3.140 C. Berger et al., Science **312**, 1191 (2006)
3.141 S.J. Park, R.S. Ruoff, Nat. Nanotech. **4**, 217 (2009)
3.142 R.F. Lobo, Nature **443**, 757 (2006)
3.143 A. Corma et al., Nature **443**, 842 (2006)
3.144 M.M. Treacy et al., Micropor. Mesopor. Mater. **74**, 121 (2004)
3.145 J.L. Sun et al., Nature **458**, 1154 (2009)
3.146 J.W. Lee et al., Nat. Mater. **7**, 222 (2008)
3.147 W. Lee et al., Nat. Nanotech. **3**, 234 (2008)
3.148 C.R. Martin, Science **266**, 1961 (1994)
3.149 Material Matters (Sigma-Aldrich) **3** (1), 17 (2008)
3.150 J.S. Beck et al., J. Am. Chem. Soc. **114**, 10834 (1992)
3.151 Y. Han et al., Nat. Chem. **1**, 123 (2009)
3.152 C. Sealy, Nanotoda. **4** (3), 214 (2009)
3.153 G.S. Armatas, M.G. Kanatzidis, Nature **441**, 1122 (2006)
3.154 G. Tammann, Z. Anorg. Allg. Chem. 107, 1 (1919)
3.155 H. Rösner et al., Adv. Eng. Mater. **9**, 535 (2007)
3.156 S.C. Warren et al., Science **320**, 1748 (2008)
3.157 D. Branton et al., Nat. Biotech. **26**, 1146 (2008)
3.158 T.Z. Butler et al., Proc. Natl. Acad. Sci. USA **105**, 20647 (2008)
3.159 M. Zwolak, M. DiVentra, Rev. Mod. Phys. **80**, 141 (2008)
3.160 H. Tanaka, T. Kawai, Nat. Nanotech. **4**, 518 (2009)
3.161 K. Salaita et al., Nat. Nanotech. **2**, 145 (2007)
3.162 M. Rothschild et al., MRS Bull. **30**, 942 (2005)
3.163 Physik J. **5**, Nr. 4, 18 (2006)
3.164 A.T. Tilke et al., Prog. Quantum Electron. **25**, 97 (2001)
3.165 F. Watt et al., Materials Today **10**, June 2007, p. 20
3.166 M.D. Stewart, C.G. Wilson, MRS Bull. **30**, 947 (2005)
3.167 C.A. Mills et al., Nanotechnology **16**, 369 (2005)
3.168 B.D. Lucas et al., Adv. Mater. **20**, 1129 (2008)
3.169 D.S. Ginger et al., Angew. Chem. Int. Edn. **43**, 30 (2004)
3.170 K.B. Lee et al., NanoLett. **4**, 1869 (2004)
3.171 C.J. Hawker, Th. P. Russel, MRS Bull. **30**, 952 (2005)
3.172 C.B. Tang et al., Science **322**, 429 (2008)
3.173 A. Tinazli et al., Nat. Nanotech. **2**, 220 (2007)
3.174 A. O'Neil, J.J. Watkins, MRS Bull. **30**, 967 (2005)
3.175 D. Yang et al., MRS Bull. **30**, 976 (2005)
3.176 S. Kawata et al., Nature **412**, 697 (2001)
3.177 T. Tanaka et al., Appl. Phys. Lett. **80**, 312 (2002)

Chapter 4
Nanocrystals – Nanowires – Nanolayers

The dimensionality of nanosystems plays an important role in nanoscience and nanotechnology. In nanostructures with 0D macroscopic extension (0D – nanocrystals), 1D macroscopic extension (1D – nanowires), or 2D macroscopic extensions (2D – nanolayers), novel properties emerge compared to macroscopic bulk systems due to quantum confinement, charge quantization, magnetic exchange length, etc. In the case of semiconductor systems, the nanostructures of different dimensionality are often called quantum dots, quantum wires, and quantum wells.

Dimensionality effects of nanostructures have been introduced with some exemplary features in Chap. 1 and have been shown to be of relevance in synthesis (Chap. 3). In the present section some generic characteristics of nanocrystals, nanowires, and nanolayers will be discussed. Dimensionality effects will be resumed later in nanoscale carbon systems (Chap. 5) and in the discussion of nanomagnetism (Chap. 8).

4.1 Nanocrystals

Nanodots exhibit in all three spatial directions and dimensions smaller than the de Broglie wave length of the charge carriers. Semiconductor nanodots are often embedded in another dielectric semiconductor matrix [4.1, 4.2]. Single quantum dots may provide innovative components for quantum information processing, quantum cryptography, or hybrid DRAM/Flash data storage. In large numbers (billions) they may form optoelectronic components, lasers or amplifiers, and new systems for communication technology, consumer electronics, or high-precision metrology.

4.1.1 Synthesis of Nanocrystals

Some more specific features of the synthesis of nanocrystals will be discussed in the following in addition to the more general discussion in Chap. 3.

Metal seeds have been used as catalysts for growing semiconductor or oxide nanowires either in the gas phase, using the vapor–liquid–solid mechanism, or

H.-E. Schaefer, *Nanoscience*, DOI 10.1007/978-3-642-10559-3_4,

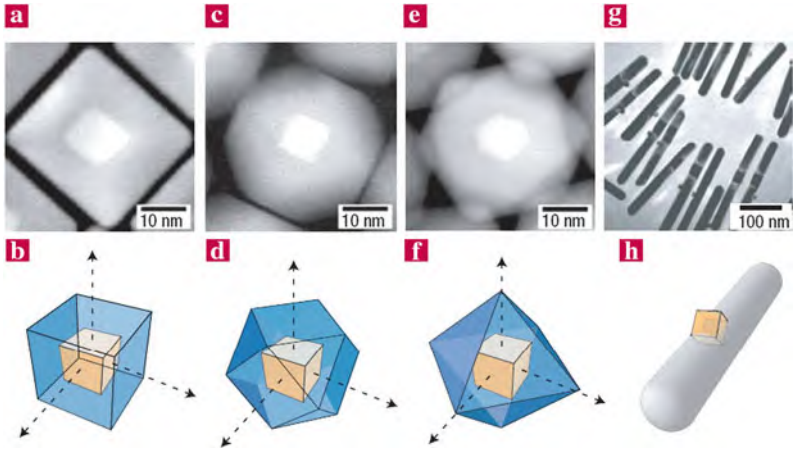

Fig. 4.1 Shape-controlled bimetallic Pt–Pd core–shell nanoparticles grown by the seeded-growth approach [4.4] using Pt cubes as seeds; high-angle annular dark-field scanning transmission electron micrographs (HAADF-STEM), and models of the core–shell nanoparticles. (**a, b**) Cubic Pt seed within the Pd shell. (**c–f**) Control over the directed growth of Pd on Pt nanocubes is achieved by the addition of increasing amounts of NO_2, which alters the growth rates along the <100> and <111> directions to give Pt/Pd core–shell cuboctahedra (**c**, **d**) or octahedra (**e**, **f**). (**g, h**) For Pt/Au, where the lattice mismatch is large, anisotropic growth of Au rods is observed, with the Pt seed on the perimeter [4.3, 4.4]. (Reprinted with permission from [4.3]. © 2007 Nature Publishing Group)

in solution via the solution–liquid–solid mechanism (see [4.3]). When using Pt nanocubes as seeds for growing Pt–Pd bimetallic core–shell nanocubes (see Fig. 4.1a, b), it could be demonstrated that the growth rates along specific crystal directions can be varied by controlling the concentration of the NO_2 atmosphere [4.4]. With increasing concentrations of NO_2, cuboctahedra or octahedra (Fig. 4.1c–f) can be grown. In addition, lattice mismatch is critically important in this type of epitaxial growth. When Au was reacted with the cubic Pt seeds, where the lattice mismatch is 4% compared with less than 1% for Pt–Pd, anisotropic growth of rods was obtained, with a Pt seed partially embedded on the perimeter (Fig. 4.1g, h). The ability to tune the faceting of the Pd shell is of relevance for the application of bimetallic particles in catalysis. Varying the preparation conditions, various facet orientations between all Pd {100} facets (nanocubes) to all Pd {111} facets (octahedra) can be obtained, exhibiting different catalytic properties (see [4.4]).

Infrared quantum dots promise application in fiberoptic and free-space communication photonic components; in in vivo biological tagging in infrared spectral bands in which living tissue is optically penetrable to a depth of 5–10 cm; in solar photovoltaics for energy conversion; and in infrared sensing and imaging based on non-visible signatures (see [4.5]). The size-dependent properties of quantum-confined states of PbS nanodots (Fig. 4.2a, b) can be tuned for exciton absorption peaks between 800 and 1,800 nm (Fig. 4.2c, d). Room-temperature amplified spontaneous emission has been reported at infrared wavelengths for PbSe and PbS

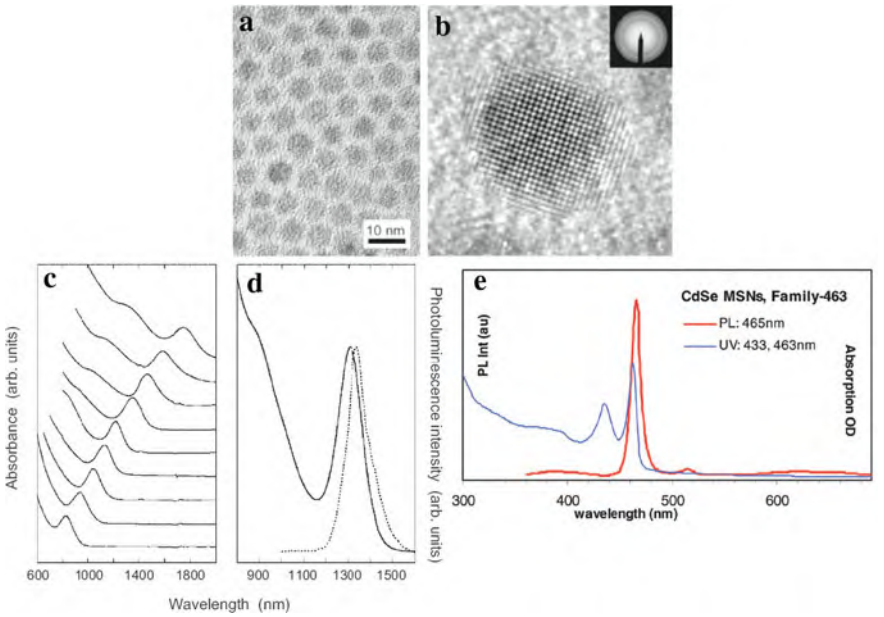

Fig. 4.2 Properties of PbS quantum dots synthesized by an organometallic route [4.6]. (**a**), (**b**) High-resolution transmission electron micrographs (HRTEM) of quantum dots with peak luminescence at 1440 nm. (**c**) Absorption spectra of PbS dots with exciton peaks size effect tuned from 800–1800 nm. (**d**) Absorption and photoluminescence features of 6.5 nm diameter dots [4.6]. (**e**) Single-sized CdSe quantum dot ensembles dispersed in toluene demonstrate a narrow absorption line (*blue line*, *right y*-axis) and emission line [4.7]. (Reprinted with permission from [4.6] (**a**–**d**) and [4.7] (**e**). © 2003 Wiley-VCH (**a**–**d**) and © 2008 American Chemical Society (**e**))

nanocrystals (see [4.5]). Very sharp light absorption near the absorption band edge and very narrow (pure color) photoluminescence in the visible range with bandwidths as narrow as 10 nm have been observed for single-sized ensembles of CdSe quantum dots (see Fig. 4.2e).

Dimer clusters of Au nanocrystals and clusters of differently sized Au nanocrystals (Fig. 4.3) can be prepared with high definition and high yield by assembling DNA-encoded nanoparticles [4.8].

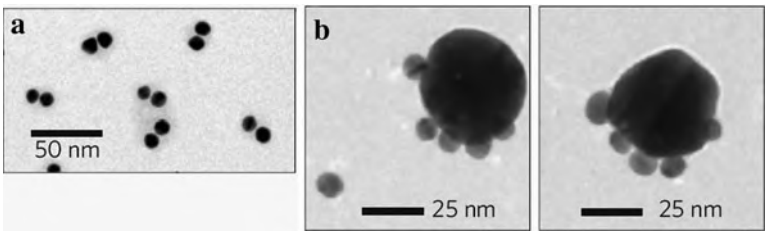

Fig. 4.3 Au dimers (**a**) and Au clusters composed of Au particles of different sizes (**b**) assembled by DNA linkers. (Reprinted with permission from [4.8]. © 2009 Nature Publishing Group)

4.1.2 Metal Nanocrystallites – Structure and Properties

The ground-state crystallographic structure of nanocrystals in dependence of size [4.9], the surface atomic structure [4.10], the crystallinity of nanocrystals [4.11], and the structural changes of nanocrystals on substrates [4.12] play an important role for the modification of properties and for application. Therefore, structural control of nanocrystals during synthesis [4.13] is of interest.

The ground-state structures of Fe nanocrystals are icosahedral isomers for a few dozens of atoms (see [4.9]) and for Fe-55 a shell-wise transformed morphology where the innermost shell turns into an almost perfect cuboctahedron, while the outermost shell largely retains its icosahedral shape [4.9]. According to density functional theory [4.9], isomers with the body-centered cubic (bcc) structure of bulk α-Fe are found to be the lowest in energy when the clusters contain more than 100 atoms.

Surface atomic structures of 3–5 nm Au nanocrystals have been probed by electron diffraction [4.10] making use of a 40-nm-diameter electron beam (see Fig. 4.4). Surface reconstruction and bond length contraction are expected to be very important in nanocrystals, where it will affect many phenomena such as interfacial stability and heterogeneous catalysis. The diffraction data of Au nanocrystals together with molecular dynamics studies suggest that the surface atoms do contract, but the amount of contraction depends on the crystallographic orientations of the crystal facet: large out-of-plane bond length contractions for the edge atoms (∼ 20 pm); a significant contraction (∼ 13 pm) for {100} surface atoms; and a much smaller contraction (∼ 5 pm) for atoms in the middle of the densely packed {111}

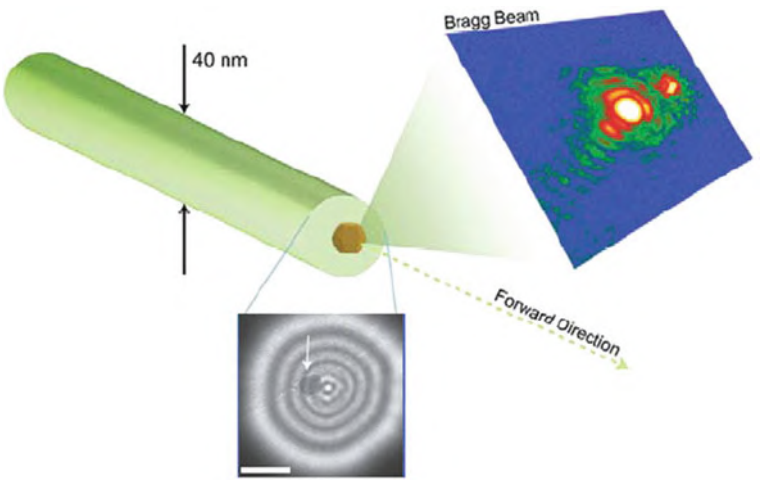

Fig. 4.4 The atomic structure of nanocrystal surfaces can be extracted from diffraction patterns obtained using a coherent electron beam focused to 40 nm. The Au nanocrystal (4 nm) is visible in the *inset* (*white arrow*). The scale bar in the *inset* is 10 nm [4.10, 4.14]. (Reprinted with permission from [4.14]. © 2008 Elsevier)

facets. This indicates a coordination/facet dependence that markedly differentiates the structural dynamics of nanocrystals from bulk crystalline surfaces [4.10].

Raman scattering has been introduced as a new way to measure crystallinity by monitoring changes in the way the crystal vibrates [4.11]. In single-crystalline Au nanocrystals, two separate Raman modes are found [4.11] which can be ascribed to two characteristic quadrupolar Raman modes of the elastically anisotropic spherical Au nanocrystals. Polycrystalline nanocrystals produce only one broad Raman peak because they are a blend of different structures. Thus, Raman scattering can offer a simple alternative to, e.g., electron microscopy for characterizing crystallinity [4.11].

Interface structures of Au nanoparticles on metal oxide supports may substantially determine the catalytic activity (see Sect. 10.4). By high-angle annular dark-field scanning transmission electron microscopy (HAADF-STEM) with aberration correction (see Sect. 2.6) it was found (Fig. 4.5) that when the gold

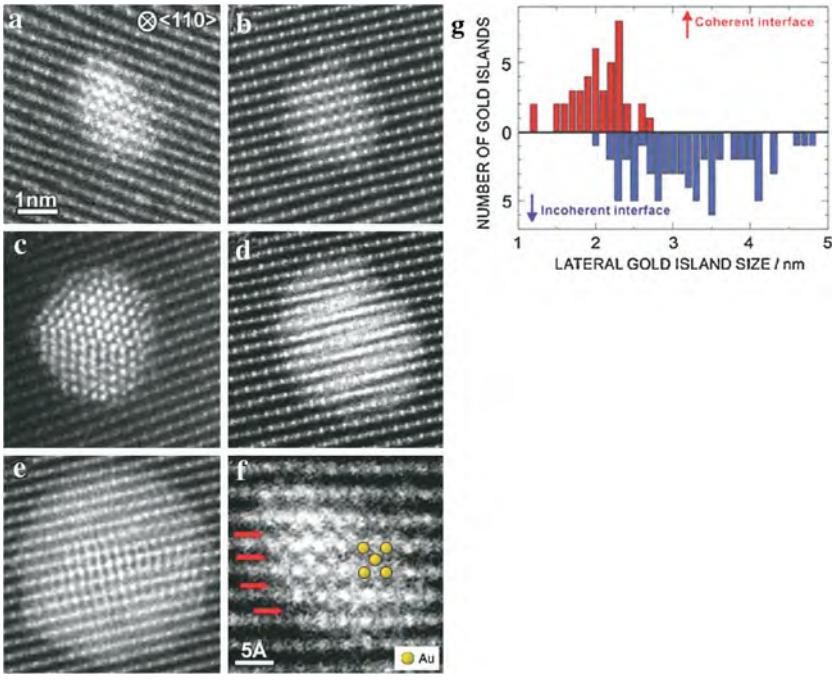

Fig. 4.5 (**a**–**e**) High-angle annular dark-field scanning transmission electron micrographs (HAADF-STEMs) of Au nanoparticles arranged in the order of the size of the projected particles. The lattice coherency between the Au nanoparticles and the TiO_2 substrate clearly changes according to the Au particle size: (**a**) and (**b**) are coherent but (**c**–**e**) are incoherent. (f) Magnified image of the epitaxial Au structure shown in (**a**). Not only Au sites on top of the TiO substrate columns but also Au sites on top of the O columns in the troughs of Ti-containing columns (along the arrows) are resolved. (**g**) Histogram of the formation of coherent or incoherent interfaces as a function of Au nanoparticle lateral size estimated from the HAADF-STEM images. (Reprinted with permission from [4.12]. © 2009 American Physical Society)

nanoparticle size on a Ti_2O (110) substrate is smaller than a few nanometers, gold atoms preferentially form an epitaxial and coherent interface. When the Au nanocrystallite is larger, the gold–Ti_2O interface loses lattice coherency in order to accommodate the large lattice mismatch between the dissimilar crystals [4.12].

Crystallinity engineering of Ag nanocrystallites, i.e., selective synthesis of single-crystalline (SC) nanocrystallites or multiply twinned (MT) nanocrystallites, has been achieved [4.13] by chemically modifying the silver phosphine precursor complexes (see Fig. 4.6a). By using NO_3-functionalized precursors (**1**), MT silver nanocrystallites are fabricated (Fig. 4.6d), whereas Cl functionalizing (**2**) results in SC Ag nanocrystallites (Fig. 4.6b). This is ascribed to the preferential etching of the initial metal twinning nuclei by the chloride ions in an oxidative environment, which inhibits the growth of MT clusters [4.13]. The SC and MT nanocrystals exhibit drastically different properties. Upon a chemical reaction with Se, a hollow structure (Fig. 4.6c) is found in the SC nanoparticle (SC-NP) by a mechanism analogous to the excess-vacancy based Kirkendall effect. In contrast, the MT nanoparticle (MT-NP) is transformed into a Ag_2Se single crystal without hole (Fig. 4.6e), owing to the modification of the atomic diffusion processes by the twin boundaries. For the electron–phonon (e–ph) interaction coupling constants G, values of 15×10^{15} $JK^{-1}m^{-3}s$ and 3.7×10^{15} $JK^{-1}m^{-3}s$ are determined for MT- and SC-NPs, respectively [4.13]. This suggests that e–ph scattering is significantly enhanced due to the existence of twinning defects which eventually could lead to sizeable modulation of electronic and heat conductivity and/or superconductivity of metals at the nanoscale. Elastic moduli are derived to be higher in SC-NPs (111 GPa) than in MT-NPs (81 GPa) [4.13] and, from x-ray diffraction studies [4.15], higher in Ag-NPs and Au-NPs than in the bulk materials. The sensitivity of surface plasmons (see Sect. 7.6) in Ag NPs for the refractive index of a solvent or the chain lengths of alkanethiols [4.13] is higher for SC-NPs than for MT-NPs. This is of importance for the optimization of plasmonic metal-NP-based sensing devices [4.13].

4.1.3 Semiconductor Quantum Dots

In semiconductors excitons, i.e., bound electron–hole pairs can be formed by the association of electron and hole charge carriers or directly by photoexcitation creating an electron in the conduction band and leaving a hole in the valence band. The luminescence resulting from exciton recombination is the basic process of light-emitting diode technology. Conversely, excitons that are formed by photo-excitation can dissociate into free unbound carriers and thus play a central role in detectors or photovoltaic and solar cell devices. Therefore, the properties of excitons confined in quantum dots can change the way that diodes, lasers, or solar cells operate (see [4.2]).

Semiconductor quantum dots are characterized by discrete energy levels where calculations show (see Fig. 4.7) that the centers of gravity of the electron charge and the hole charge are not directly located on top of each other.

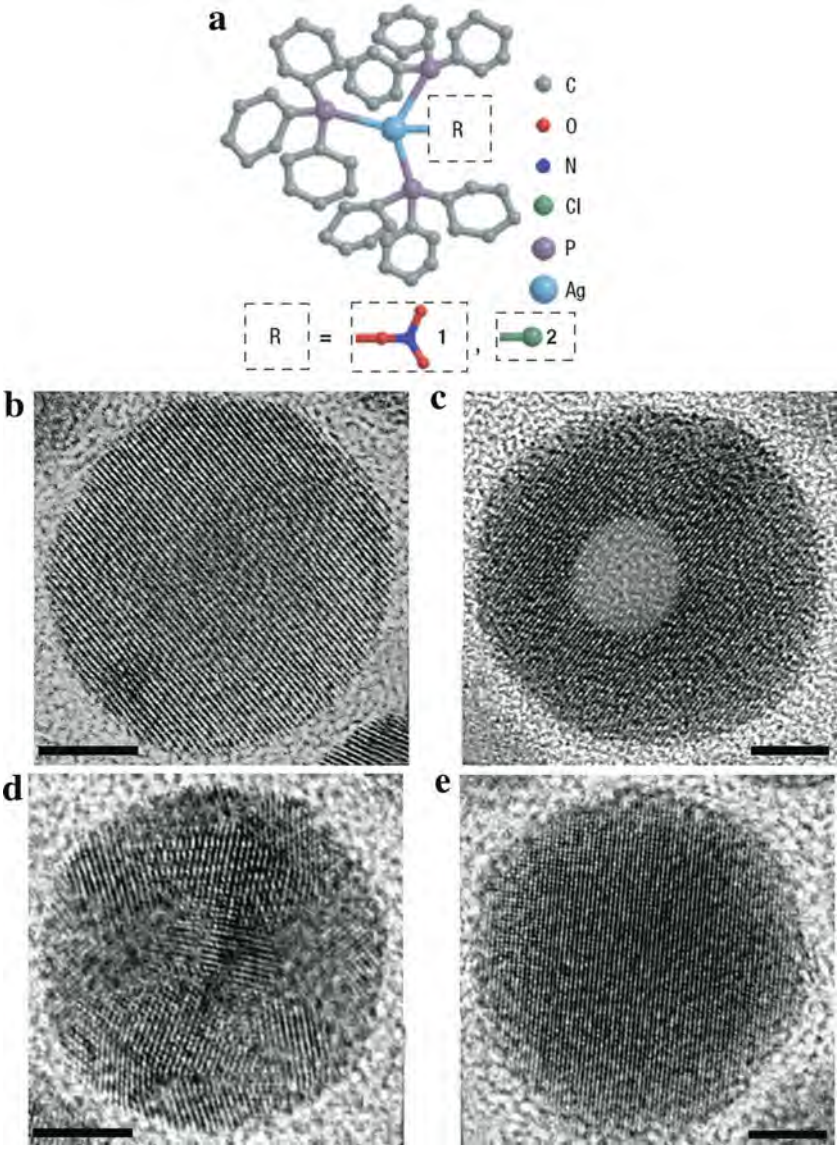

Fig. 4.6 Controlled synthesis of silver nanoparticles (NPs) with selective crystallinity and chemical transformation to Ag_2Se. (**a**) Molecular structure of the phosphine complex precursor $(PPh_3)_3Ag$-R with functional groups R = $-NO_3$ (*1*) or R = –Cl (*2*). (**b**) High-resolution transmission electron micrograph (HRTEM) of a single-crystalline (SC) nanoparticle (NP) of silver. (**c**) HRTEM of SC-Ag_2Se NP with a hollow core. (**d**) HRTEM of a multiply twinned nanoparticle (MT-NP) of silver and (**e**) after reaction with Se to a SC-Ag_2Se NP. Scale bars of the HRTEMs: 5 nm. (Reprinted with permission from [4.13]. © 2007 Nature Publishing Group)

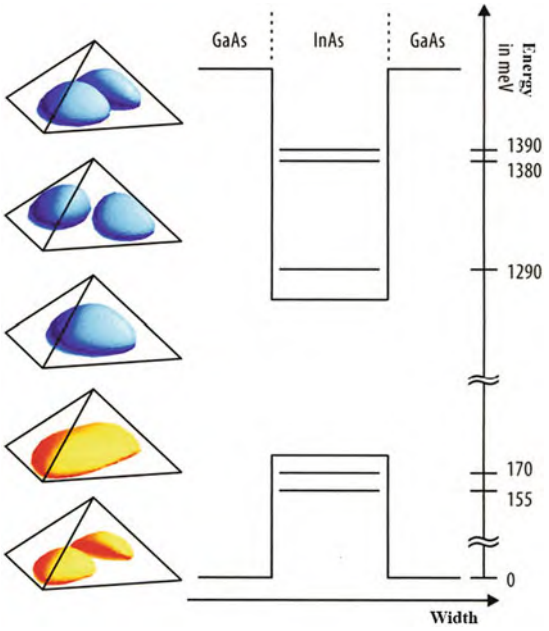

Fig. 4.7 Wave functions and energy levels calculated for the three lowest electron states and the two lowest hole states in a pyramidal InAs quantum dot (baseline 13.3 nm) in a GaAs matrix [4.16]. (Reprinted with permission from [4.1]. © 2006 Wiley-VCH)

Due to the discrete energy levels, the luminescence spectra of semiconductor quantum dots are composed of only a few, extremely narrow lines (see Fig. 4.8) originating from different types of exciton complexes. By modifying size, shape, and composition of the quantum dots, the emission wavelength can be tuned over a wide range (Fig. 4.9).

The size tuning of the quantum dot properties is attributed to the confinement of the exciton in a nanocrystal substantially smaller than the bulk exciton. For example, the exciton Bohr radius of PbS is ~20 nm and its bulk band gap is 0.41 eV. Absorption spectra for PbS quantum dots of radii ranging from 1.3 to 3.5 nm, however, reveal quantum dot exciton energies from 1.5 to 0.7 eV (Fig. 4.10a).

The size-tunable optical excitation energies derive from the semiconductor band gap as well as the exciton binding energy and the quantum mechanical exchange interaction, which are both intimately tied to the size of the exciton [4.2]. The exciton binding energy which is about 10 meV in bulk semiconductors increases to 200-50 meV in quantum dots of radii R=1–2 nm and scales approximately as $1/R$, according to the size dependence of the electron–hole Coulomb interaction. The electron–hole exchange interaction mixes the single-exciton configurations in a quantum dot, experimentally evident as a splitting between the bright and dark exciton states at the band edge (Fig. 4.10b). This exchange interaction is of the order of milli-electron volts in bulk semiconductors but increases 1,000 fold in quantum dots (see [4.2]) and is predicted to scale as R^{-3} as partially confirmed experimentally by the bright-dark splitting of CdSe, CdTe, and GaAs quantum dots (Fig. 4.10b).

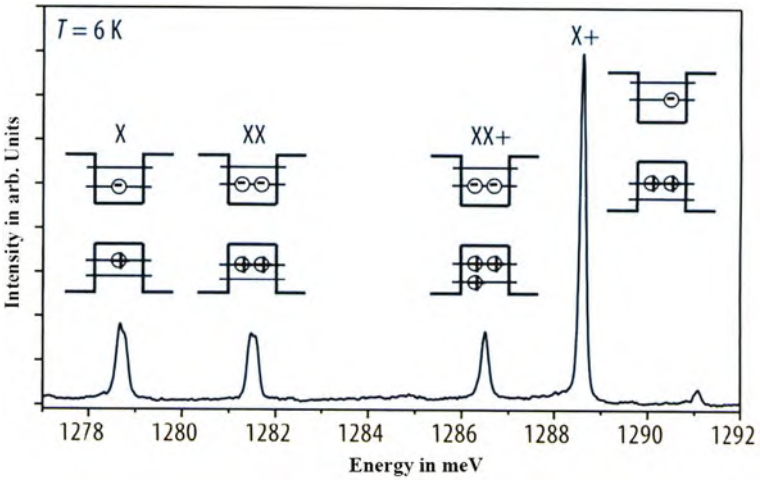

Fig. 4.8 Luminescence spectrum of a single InAs quantum dot in a GaAs matrix. The emission lines are ascribed to various excitonic complexes as exciton (X), biexciton (XX), positively charged biexciton (XX+), or positively charged exciton (X+). In all cases an electron recombines with a hole where the Coulomb interaction with the additional charge carriers gives rise to an energy shift. (Reprinted with permission from [4.1]. © 2006 Wiley-VCH)

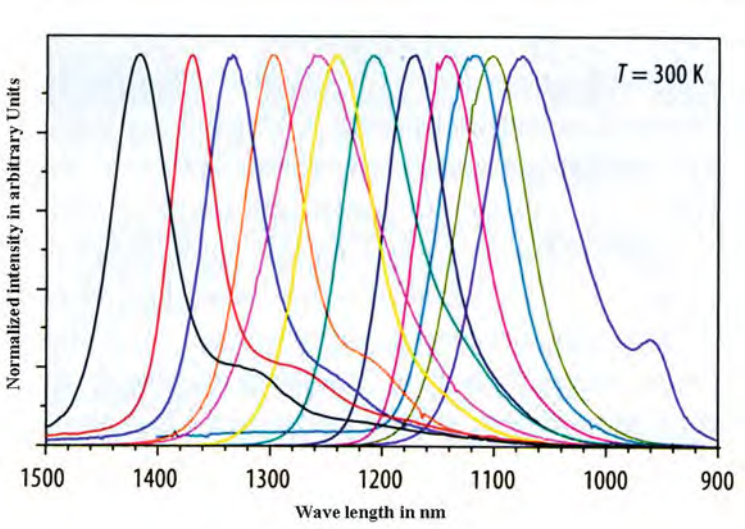

Fig. 4.9 By variation of size, shape, and composition of quantum dots the wavelength of the emission can be selectively modified over a wide range as shown for In(Ga)As quantum dot ensembles embedded in a GaAs matrix. (Reprinted with permission from [4.1]. © 2006 Wiley-VCH)

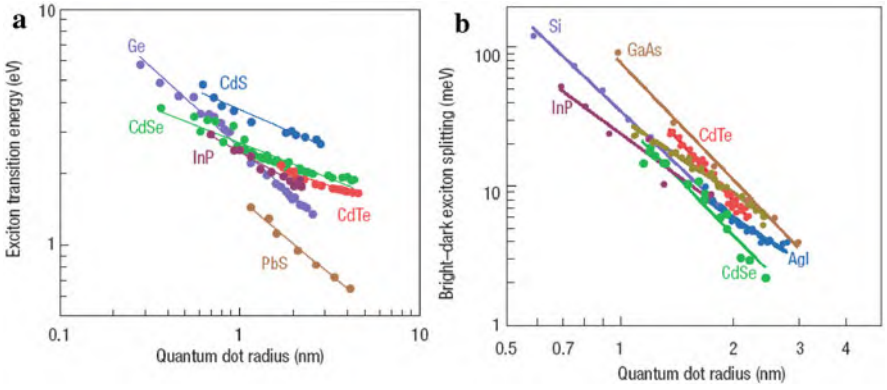

Fig. 4.10 (**a**) Size tuning of excitation energies for various quantum dot materials: Ge calculated by ab initio theory; CdSe, CdS, and CdTe measured at 250 K; PbS measured at 293 K, and InP measured at 10 K. (**b**) Data of bright-dark exciton splitting representing the exciton exchange interaction in quantum dots of Si (calculations), InP (measured at 10 K), GaAs (calculations), CdTe (measured at 10 K), AgI (2 K), and CdSe (10 K) (for references see [4.2]). (Reprinted with permission from [4.2]. © 2006 Nature Publishing Group)

For single-photon and entangled photon sources and photon detectors based on quantum dots, the reader is referred to Sect. 7.4. Quantum dot lasers are discussed in Sect. 7.5.

4.1.4 Colorful Nanoparticles

Nanoparticles or nanoparticle ensembles may give rise to colors, covering the entire visible spectrum (Fig. 4.11). These effects may be used for biomedical detection, sensors, color displays, etc.

Fig. 4.11 Color variation of solutions of nanoparticles in dependence of size, shape, oxidation state, or external magnetic field. (**a**) Fluorescence of CdSe–ZnS core–shell nanoparticles, after excitation at $\lambda = 470$ nm, in dependence of particle size, showing the characteristic blue shift with decreasing particle size [4.17]. (**b**) Size, shape, and composition of metallic nanocrystals can be controlled and manipulated to produce nanoparticles with distinct light-scattering profiles [4.18]. (**c**) Carbon nanoparticles produced in the flame of a candle show luminescence in the visible range of light depending on the particle size [4.19, 4.20]. (**d**) Photos of colloidal photonic crystals of superparamagnetic nanoparticles in solution formed in an external magnetic field which increases from the *right* to the *left* [4.21]. (**e**) Schematic illustration of a polyacrylate-capped Fe_3O_4 colloidal nanocrystal cluster [4.21]. (**f**) Hysteresis loop of 180 nm Fe_3O_4 colloidal nanocrystal clusters (CNCs) measured at room temperature, showing superparamagnetic behavior [4.21]. (**g**) TEM image of polyacrylate-capped Fe_3O_4 colloidal nanocrystal cluster; scale bar: 100 nm [4.21]. (Reprinted with permission from [4.17] (**a**), [4.18] (**b**), [4.19] (**c**), and [4.21] (**d**–**g**). © 2005 Nature Publishing Group (**a**), © 2005 American Chemical Society (**b**), © 2007 Nature Publishing Group (**c**), and © 2007 Wiley-VCH (**d**–**g**))

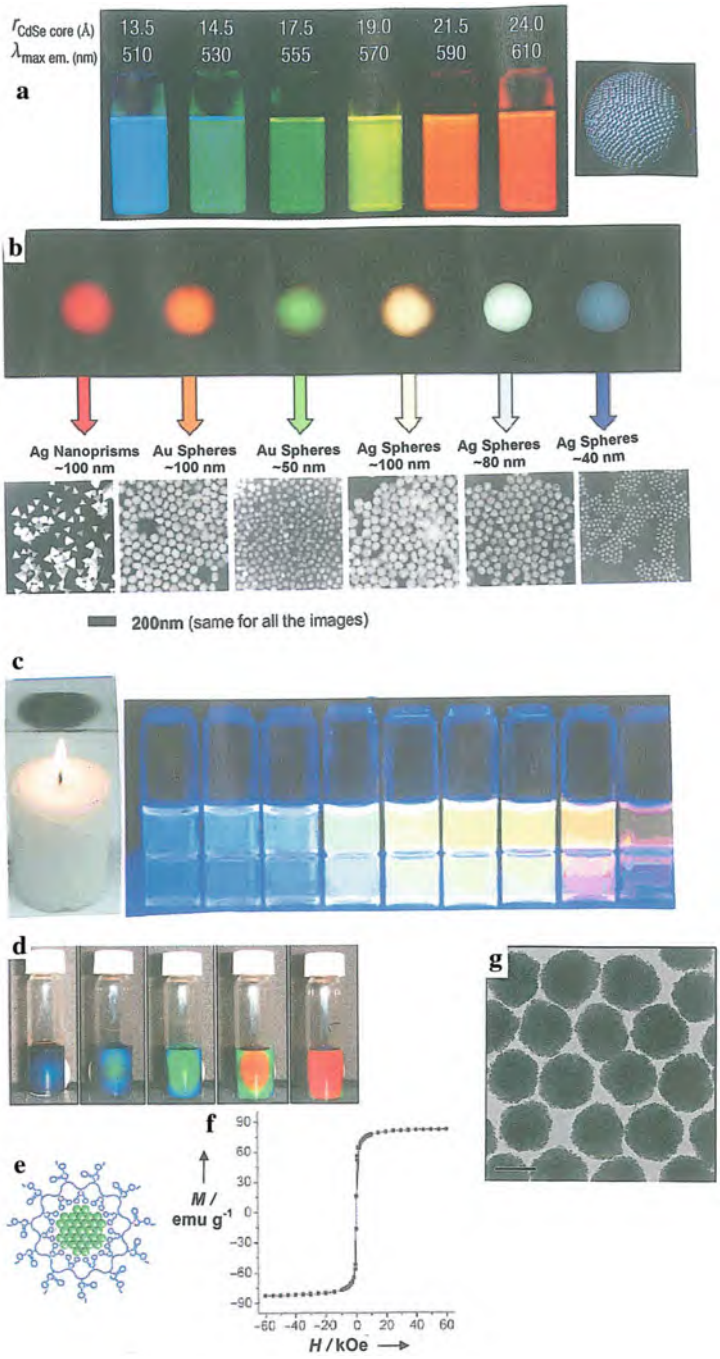
$r_{CdSe\ core}$ (Å)
$\lambda_{max\ em.}$ (nm)
13.5 510
14.5 530
17.5 555
19.0 570
21.5 590
24.0 610
a
b
Ag Nanoprisms ~100 nm
Au Spheres ~100 nm
Au Spheres ~50 nm
Ag Spheres ~100 nm
Ag Spheres ~80 nm
Ag Spheres ~40 nm
200nm (same for all the images)
c
d
e
f
M / emu g-1
H / kOe
g

In *semiconductor nanoparticles* (quantum dots), where the optical response is due to the excitation of single electron–hole pairs, the wavelength of light emission (fluorescence, Fig. 4.11a) can be controlled by the size of the particle when this compares with the electron wavelength, so that the electron motion is "confined" by potential barriers in all three dimensions. This was followed closely by the realization that quantum dots, with the typical size of a protein, could be used for biological labeling [4.22, 4.23] as very stable light emitters with a larger linear absorption cross section for excitations compared with phycoerythrin and orders of magnitude larger cross section for two-photon excitation compared with conventional organic chromophores, where the optical response is due to the excitation of single electron–hole pairs [4.24].

In *metallic nanoparticles* [4.25, 4.26], incident light can couple to the plasmon excitation of the metal (see Sect. 7.6) which involves the light-induced motion of all the valence electrons [4.27]. Thus, the cross section for elastic light scattering from a 50-nm gold nanocrystal can be a million-fold larger than the cross section of even a quantum dot chromophore. It has been shown that plasmon resonance is strongly dependent on shape and size of the nanoparticles (Fig. 4.11b). Using specific organic molecules or DNA, it appears possible to design discrete aggregates of nanoparticles, in which the spectra will depend sensitively on the particle arrangement, providing a rich system for detection. The electromagnetic field in the near-field region around a metallic nanoparticle is greatly enhanced, providing new mechanisms for detection (see Sect. 7.6). When gold nanoparticles are located close to each other, their plasmon resonances can couple, shifting the plasmon resonance to higher energy. This change in optical response can be used to sensitively detect nucleic acids [4.28]. The large field enhancement in the vicinity of gold nanocrystals is well known to lead to the surface-enhanced Raman scattering (SERS). This makes it possible to detect a wide range of biological macromolecules through binding events involving gold nanocrystals that have been coated with specific molecules that offer a distinct Raman signature (see [4.24]).

Carbon nanoparticles from candlelight. From the soot of a candle flame, solutions containing 1-nm carbon nanoparticles can be deduced [4.19, 4.20] which in ultraviolet light luminesce with yellow or blue light (Fig. 4.11c) depending on whether the group used nitric acid (yellow) or aqueous hydrogen peroxide and acetic acid (blue) as an oxidizing agent. The acid oxidation step, therefore, is the key to enriching the soot with luminescent, hydrophilic, and individually dispersed carbon nanoparticles with carbonyl groups on their surfaces.

*Photonic crystals of superparamagnetic nanopart*icles. Photonic crystals are media with artificially designed regions of varying index of refraction in order to control the density of photon states [4.29]. Photonic crystals can be fabricated by self-assembly from monodisperse nanoparticles. It is desirable from the envisioned applications that a photonic crystal possesses a tunable stop band yielding a variable color scale in the visible range that can be conveniently controlled by external stimuli. Solutions of polyacrylate-capped superparamagnetic magnetite (Fe_3O_4) colloidal nanocrystal clusters (CNCs; Fig. 4.11 g) can form photonic crystals in an external magnetic field [4.21]. Each cluster with a size of 120 nm is composed of many magnetite crystallites of approximately 10 nm,

thus retaining superparamagnetic properties at room temperature. The Fe_3O_4 CNCs readily self-assemble in an aqueous solution in the field of an external FeNdB magnet (see Sect. 1.5). The light intensity peak resulting from the diffraction of (111) planes blue shifts from 730 to below 450 nm (Fig. 4.11d) as the magnetic field increases from 8.8 to 35.2 mT by moving the magnet to the sample (3.7–2.0 cm) with a decrease of the interplanar spacing from 274 to 169 nm. Larger clusters ($\sim$ 170 nm) diffract red light, whereas smaller clusters diffract blue light. The change in diffraction wavelength reversibly responds to a 2 Hz periodic magnetic field. The 3D order of the photonic crystal in the magnetic field is the balanced result of the interparticle electrostatic repulsive force due to the polyacrylate capping of the superparamagnetic clusters and the attractive magnetic forces exerted in the external magnetic field. These forces are estimated to be 10^{-12} N [4.21].

4.1.5 Double Quantum Dots for Operating Single-Electron Spins as Qubits for Quantum Computing

The use of quantum mechanical superposition states and entanglement in a computer can theoretically solve important mathematical and physical problems much faster than classical computers (see [4.30]). Electron spin states (see Sect. 1.4) were identified early as an attractive realization of a quantum bit (qubit) [4.31] in a quantum computer, because they are relatively robust against decoherence (uncontrolled interaction with the environment). Advances in the field of semiconductor quantum dots have made this system a valuable host for the electron spin. The quantum state of the electron spin can be coherently controlled [4.30] by applying short bursts of an oscillating magnetic field giving rise to oscillations of the spin state (so-called Rabi oscillations), which can be detected by measuring the dot current (Fig. 4.12c).

The spin state of a single electron confined in a double quantum dot can be controlled via electron spin resonance (ESR). In a double dot GaAs/AlGaAs system (see Fig. 4.12a), spin flips can be detected through the transition of an electron from one dot to the other (see [4.30]) rather than between a dot and a reservoir, as would be the case for a single dot. This has the advantage that there is no need for the electron spin Zeeman splitting to exceed the temperature of the reservoir and that the experiment can thus be performed at a smaller static magnetic field and consequently with lower excitation frequencies (see [4.30]). Furthermore, in a double dot, single-spin operations can in future experiments be combined with two qubit operations to realize universal quantum gates (see [4.30]).

To detect the ESR-induced spin rotations, electrical transport measurements through the two dots (Fig. 4.12a) in the spin blockade regime are used [4.30] where current flow depends on the relative spin state of the electrons in the two dots. The device is operated so that current is blocked owing to spin blockade (Fig. 4.12b), but this blockade is lifted if the ESR condition $hf_{ac} = g\mu_B B_{ext}$ is satisfied. Here, f_{ac} is the frequency of the oscillating magnetic field B_{ac}, μ_B the Bohr magneton, and g the electron spin g-factor. The spin blockade regime is accessed by tuning the gate voltages such that one electron always resides in the right dot and a second electron

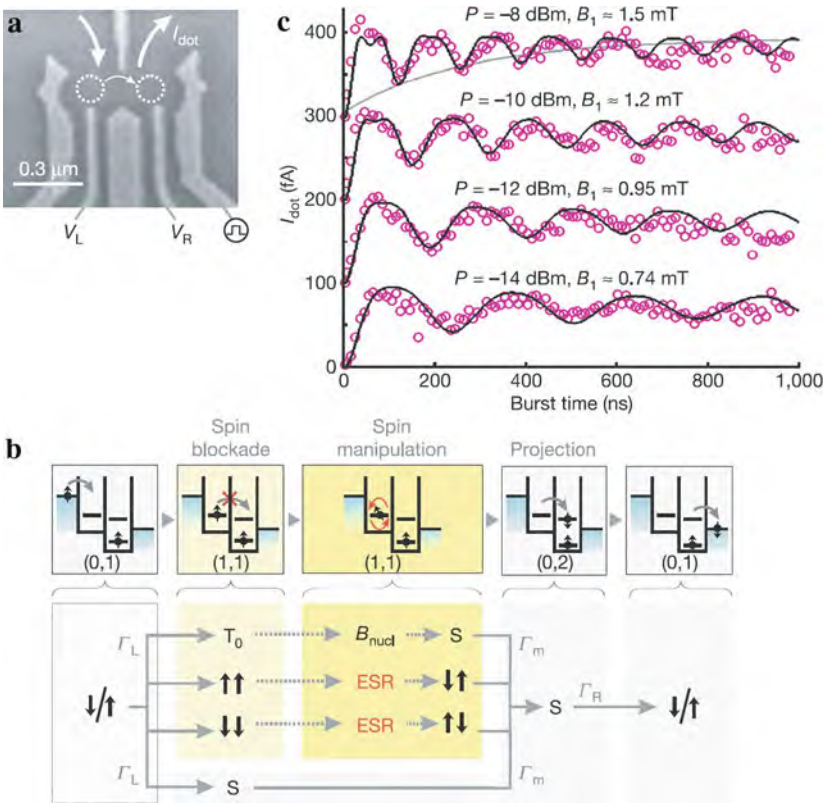

Fig. 4.12 (**a**–**b**) Device and electron spin resonance (ESR) detection scheme for operating single-electron spins as qubits for quantum computing. (**a**) Scanning electron micrograph (SEM) of the device with Ti/Au gates deposited on top of a GaAs/AlGaAs heterostructure containing a 2D electron gas. *White arrows* indicate current flow through the two coupled dots (*dotted circles*). (**b**) Diagrams illustrating the transport cycle in the spin blockade regime, which is described via the occupation numbers (m, n) of the left and right dots as (0, 1) → (1, 1) → (0, 2) → (0, 1). When an electron enters the left dot (with rate Γ_L) starting from (0, 1), the two-electron system that is formed can be either a singlet S(1, 1) or a triplet T(1, 1). From S(1, 1), further current flow is possible via a transition to S(0, 2) (with rate Γ_m). When the system is in T(1, 1), current is blocked. (**c**) Coherent spin rotations. The dot current – reflecting the spin state at the end of the radiofrequency (RT) burst – oscillates as a function of RF burst length. The period of the oscillation increases and is more strongly damped for increasing RF power P. (Reprinted with permission from [4.30]. © 2006 Nature Publishing Group)

can tunnel from the left reservoir to the left dot (Fig. 4.12a, b). If this electron forms a double-dot singlet state (↑↓) with the electron in the right dot, it is possible for the left electron to move to the right dot and then to the right lead, since the right dot singlet state is energetically accessible. If the electrons, however, form a double-dot triplet state (↑↑ or ↓↓), the left electron cannot move to the right dot because the right dot's triplet state is much higher in energy. The electron also cannot move back to the lead and therefore further current flow is blocked as soon as any of the (double-dot) triplet states is formed [4.30].

The oscillating magnetic fields for driving the spin transitions are generated by applying a radiofrequency (RF) signal. As shown in Fig. 4.12c the dot current oscillates periodically with the RF burst length. This oscillation indicates that driven, coherent electron spin rotations, or Rabi oscillations, have been performed [4.30]. This single spin rotation offers new opportunities, such as measuring the violation of Bell's inequalities or the implementation of simple quantum algorithms [4.30].

Fast quantum control of a single quantum dot spin has been achieved by using ultrafast optical pulses, promising nearly 10^5 gate operations within the qubit's coherence time of about 3 μs [4.32].

4.1.6 Quantum Dot Data Storage Devices

Future quantum dot storage devices may combine the properties of dynamic random access memories (DRAM) with rapid data access and the properties of non-volatile Flash memories. Recent studies of quantum dots (see [4.1]) have demonstrated charge storage times of more than 5 ms which may be extended into the 5 s range [4.1]. Addressing of single quantum dots seems to be possible [4.1].

4.2 Nanowires and Metamaterials

Nanowires can be prepared from metals, semiconductors, organic molecules, etc. and offer prospects in mechanical, electronic, optical, or medical applications. Here, we discuss metallic nanowires and their recent introduction into metamaterials for the generation of negative refractive index materials in the optical range, semiconductor quantum wires for transistors, biosensors, light sources, detectors, and molecular nanowires. Finally, the conduction of single rows of atoms is considered.

4.2.1 Metallic Nanowires

Nanowires can be grown from Cu, Ag, and Au (see [4.33]). Copper nanowires (Fig. 4.13a) grown by chemical vapor deposition (CVD) with a fivefold twinned structure are suitable for integration into devices. The confinement for the 1D growth arises from a passivation of the {100} side planes of the wires by phosphate ligands derived from the precursor compound, so that the growth only occurs on the capping {111} planes. These Cu nanowires may be useful as a promising electron emitter [4.33]. Bismuth nanowires (Fig. 4.13b) can be grown by the anodic alumina membrane (AAM) template technique [4.34] (see Sect. 3.9). Bismuth is a semimetal with a small effective electron mass, long carrier mean free path, and a small energy overlap between the conduction and the valence band, which can lead to a semimetal–semiconductor transition in Bi nanowires with decreasing wire diameter (see [4.34]). The fabrication of Bi nanowires has attracted attention due to potential application in thermoelectric devices (see [4.34]). Alloy nanowires

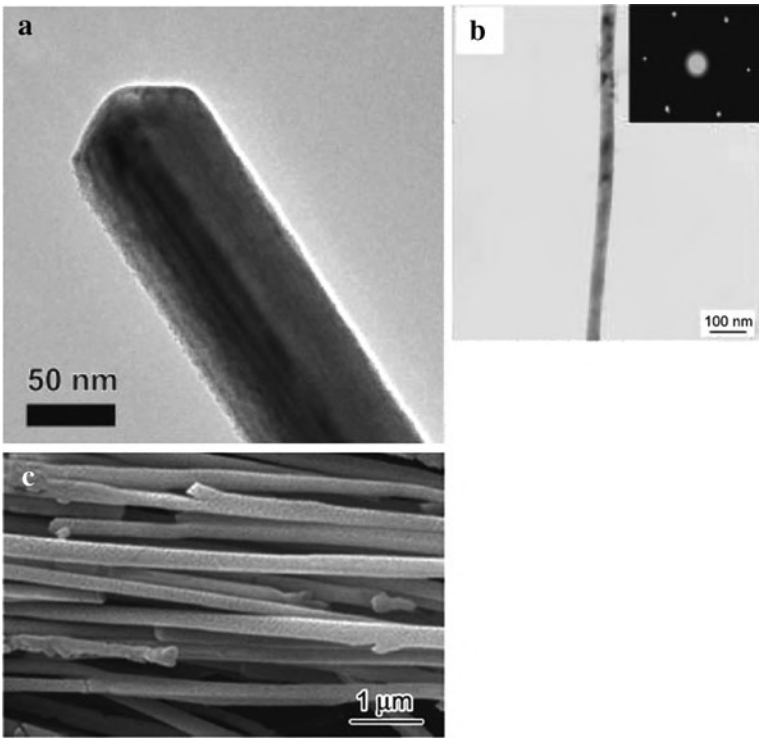

Fig. 4.13 (**a**) Transmission electron micrograph (TEM) of a Cu nanowire [4.33]. (**b**) TEM of a Bi nanowire [4.34]. (**c**) Scanning electron micrograph of Pd–Ag nanowires [4.35]. (Reprinted with permission from [4.33] (**a**), [4.34] (**b**), and [4.35] (**c**). © 2008 Wiley-VCH (**a**), © 2007 Chinese Society of Metal (**b**), and © 2008 Chinese Society of Metal (**c**))

of Pd–Ag (Fig. 4.13c) can be fabricated by the AAM template technique and are expected to be employed for hydrogen sensors [4.35].

Mechanical properties. The mechanical properties of gold nanowires are found to change substantially with the diameter of the wire. Whereas wires with a diameter of 70 nm exhibit a yield stress of 600 MPa, this increases to 1400 MPa for a 30 nm diameter and increases further, down to 5 nm. Transmission electron microscopy shows that deformation is caused by dislocation motion and possibly twinning [4.36]. Nanoporous gold – obtained from leaching Au–Ag alloys – with a relative density of 0.2–0.45 and a ligament size of 5–500 nm shows a high strength of 1–15 GPa [4.36].

4.2.2 Negative-Index Materials (Metamaterials) with Nanostructures

Metallic nanowires [4.37–4.39] and nanolayers of metals and insulators [4.40] or of semiconductors [4.41] are the building blocks for the recently developed

2D or 3D negative-index materials (NIMs) or "metamaterials." The NIMs have negative electrical permittivity (ε), negative magnetic permeability (μ), and negative index of refraction (n) at a common frequency band (for introductory reviews see [4.42–4.44]. Although it has been well known how to obtain a $\varepsilon < 0$ material easily, e.g., by using wire arrays (see [4.45]), the realization of a $\mu < 0$ response (especially at high frequencies) has been a challenge, due to the absence of naturally occurring magnetic materials with negative μ. Materials with $\mu < 0$ can be realized [4.46] by arrays of metallic rings with gaps, called split-ring resonators (SRR), which exhibit a $\mu < 0$ regime in the vicinity of a magnetic resonance frequency. Artificial materials with negative ε and μ have been predicted (see [4.47]) to have the remarkable property of a negative refractive index: a light ray entering such a NIM bends the "wrong" way from the surface normal (see Fig. 4.14). Making use of NIM materials, the realization of invisibility cloaks (see [4.49]) and of "perfect" lenses is envisaged.

The existence of NIMs has been initially demonstrated in the gigahertz frequency range (see [4.45]) and shifted to the optical region [4.37, 4.39] by the use of pairs of finite length nanowires (cut wires) and the fishnet topology (see Fig. 4.15a) in 2D arrays. The resonance at 720 nm in Fig. 4.15b is a magnetic resonance, yielding a negative refractive index (see [4.39]). 3D NIM materials [4.38, 4.40] which are required for practical applications have been developed from 3D fishnet materials

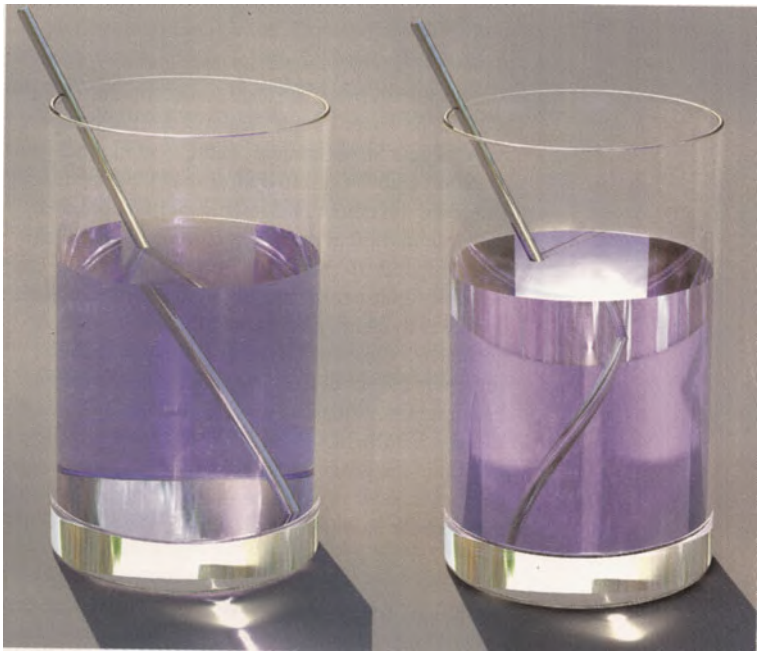

Fig. 4.14 The simulation of a metal rod in a glass filled with water (*left*, index of refraction of water, $n = 1.3$) would be drastically changed for a fictitious liquid with a negative index of refraction, $n = -1.3$ (*right*). (Reprinted with permission from [4.48]. © 2006 Wiley-VCH)

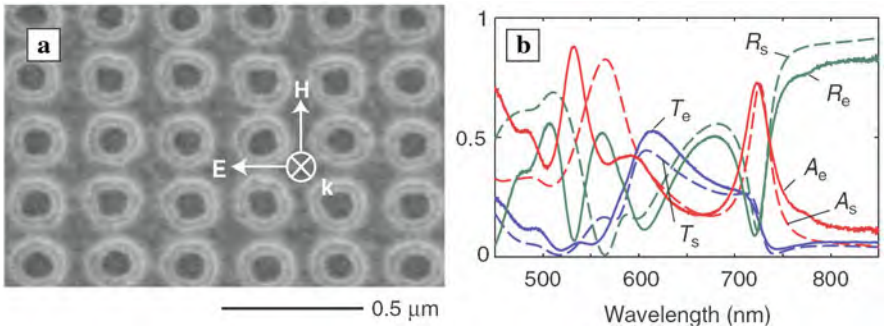

Fig. 4.15 (**a**) Scanning electron micrograph (SEM) and (**b**) experimental and simulated spectra of a double-negative negative-index fishnet material (DN-NIM) silver sample. *H*, *E*, and *k* define the directions of the magnetic field, the electric field, and the wave propagation, respectively. *T* is transmittance, *R* is reflectance, and *A* is absorbance, with *solid lines* and subscript *e* representing experimental data and *dashed lines* and subscript s representing simulated data. (Reprinted with permission from [4.39]. © 2008 Materials Research Society)

and gold nanowire 3D-SRR arrays (see Fig. 4.16), where plasmon-like oscillations couple between adjacent SRRs. With the 3D fishnet material negative refraction of a laser beam, i.e., "wrong" deflection (Fig. 4.16b), can be demonstrated. 3D metamaterials with a tunable plasma frequency in the visible regime were prepared from InGaAs/GaAs/Ag multilayers with a single-layer thickness of 17 nm [4.50].

4.2.3 Semiconductor Nanowires

Semiconductor nanowires are emerging as a powerful class of materials that, through controlled growth and organization, are opening up novel opportunities for nanoscale electronic and photonic devices [4.51].

A host of techniques are available for growing semiconductor nanowires (see Sect. 3.3). Homogeneous quantum wires (Fig. 4.17a) can be grown with diameters down to 3 nm with specific dopants to control their electronic properties. Recently controlled growth of axial (Fig. 4.17b) and radial heterostructures (Fig. 4.17c) has been achieved where the composition or doping is modulated on an atomic level along or perpendicular to the axes of quantum wires, respectively. This wide range of controlled structures enables the development of powerful and unique nanoscale electronic and optoelectronic devices for future applications.

Mechanical properties. The mechanical properties of semiconductor nanowires are of interest given the potential applications in electronic and electromechanical devices. Zinc oxide is a semiconductor with a direct wide band gap of 3.37 eV, piezoelectric properties (see [4.52]), good biocompatibility, and therefore a number of application prospects (see [4.52]). Whereas the Young's modulus of ZnO turns out to be independent of diameter, the ultimate strength increases for small diameter wires and exhibits values up to 40 times that of the bulk [4.52].

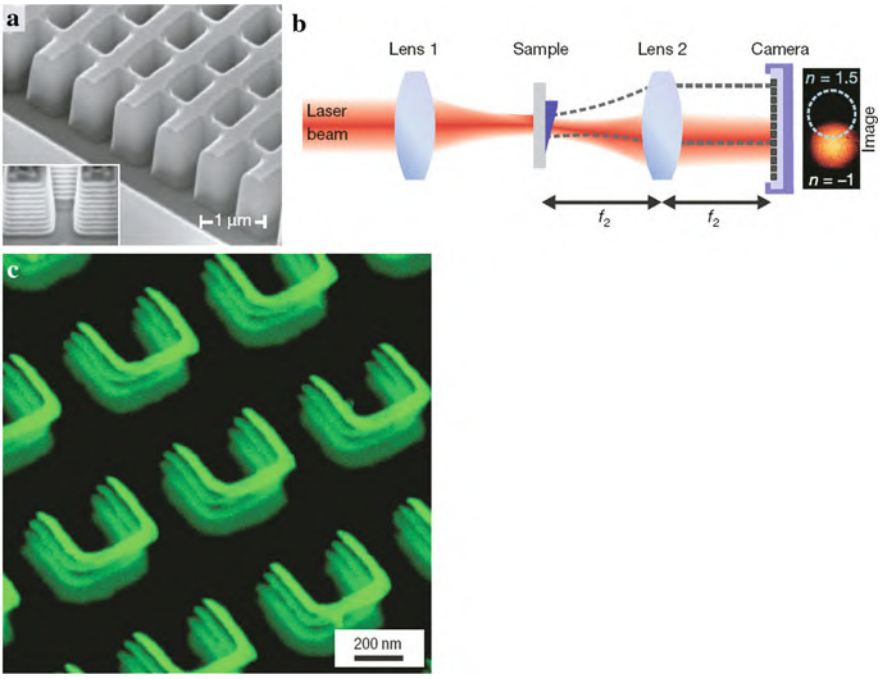

Fig. 4.16 (**a**) Scanning electron micrograph (SEM) of a 21-layer fishnet structure with the side etched, showing the cross section. The structure consists of alternating layers of 30 nm Ag and 50 nm MgF_2. The *inset* shows a cross section of the pattern. (**b**) Experimental setup for a laser beam refraction measurement. The focal length of lens 1 is 50 mm and that of lens 2 is $f_2 = 40$ mm. Lens 2 is placed in a 2f configuration, resulting in the image at the camera position. A prism of the metamaterial refracts the laser beam with a negative index of refraction $n = -1$ for wavelengths between 1,500 and 1,800 nm. The *dashed circle* indicates the expected image of the beam for a positive index of refraction $n = 1.5$ [4.40]. (**c**) Field-emission scanning electron micrographs (*oblique view*) of a 3D four-layer gold split-ring resonator (SRR) array that mimics magnetism at high frequencies [4.38]. (Reprinted with permission from the [4.40] (**a**) (**b**), and [4.38] (**c**). © 2008 Nature Publishing Group)

Field-effect transistors: It has been shown [4.51] that quantum wire materials including Si, Ge, and GaN can be prepared with complementary n-type and p-type doping. For example, studies of quantum wires fabricated from boron (phosphorus)-doped silicon have been used in field-effect transistors (FETs) that are switched on with a negative (positive) gate voltage characteristic of p-(n-) channel FETs (Fig. 4.18). In these quantum wires long mean free paths of carriers have been observed and the high quality of these wires has been demonstrated [4.51].

From these quantum wires, logic gates such as inverters or oscillators can be built. By the crossed quantum wire architecture [4.51] the key device properties can be designed making use of a bottom-up assembly of two nanowire components and not of top-down lithography. This concept was first demonstrated using a Si

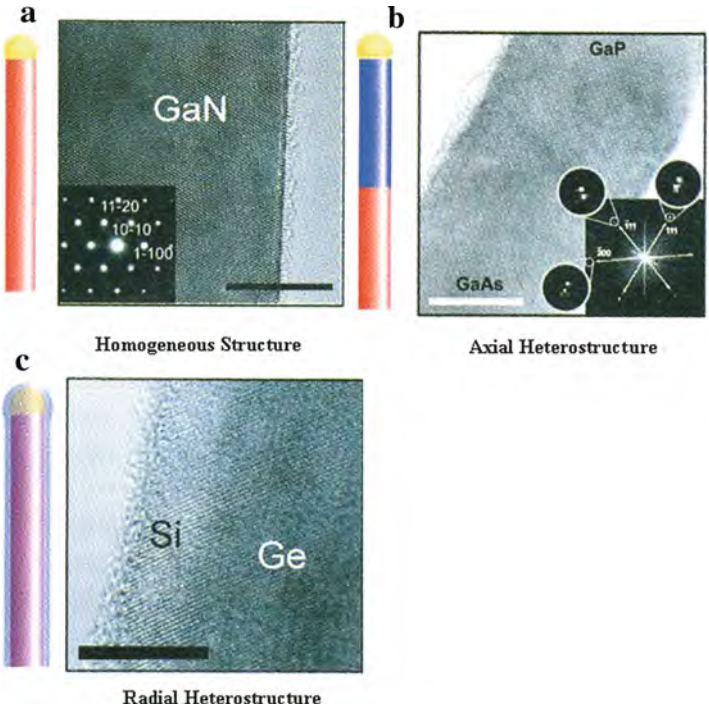

Fig. 4.17 Semiconductor nanowires and heterostructures, schematics, and transmission electron micrographs (TEM). (**a**) Uniform single-crystal GaN quantum wire, (**b**) axial GaP/GaAs heterostructure, and (**c**) radial (core/shell, core/multishell) heterostructure. All scale bars 10 nm. (Reprinted with permission from [4.51]. © 2006 Elsevier)

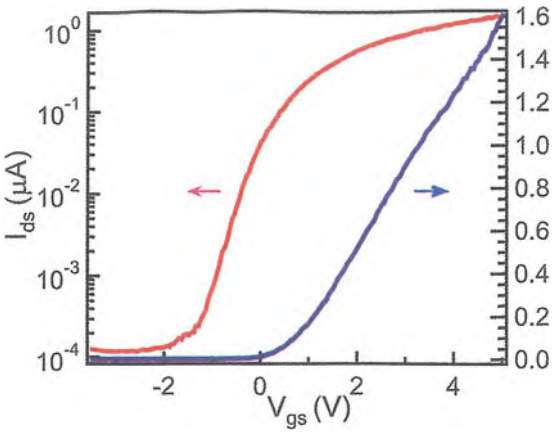

Fig. 4.18 Electrical transport characteristics of a lightly doped (Si/P=4000) 20 nm n-type Si quantum wire field-effect transistor (FET) device with the drain-source current I_{ds} versus the gate voltage V_{gs} on linear and logarithmic scales. (Reprinted with permission from [4.53]. © 2004 Wiley-VCH)

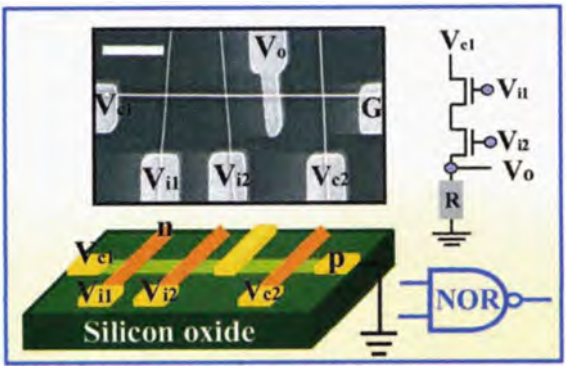

Fig. 4.19 Crossed quantum wire electronic device. Left: Schematic of a logic NOR gate constructed from a Si wire crossed by three GaN wires. *Insets* show a scanning electron micrograph of the device (scale bar: 1 μm) and a symbolic electronic circuit. (Reprinted with permission from [4.51]. © 2006 Elsevier)

quantum wire with a thin SiO_2 dielectric shell as the channel and GaN quantum wires as gate electrodes to fabricate both NOR logic gate structures (Fig. 4.19) and basic computation devices [4.54].

Biosensors: Quantum wire FETs have emerged as powerful sensors for label-free detection of biological and chemical species [4.51]. Binding of molecules to the surface of the FET is mimicking the application of a gate voltage which leads to the depletion or accumulation of carriers and subsequent specific changes in the quantum wire conductance.

For example, for the specific detection of a particular type of viruses (see Fig. 4.20a), the small sizes and the high performance of the quantum wire FETs with attached specific antibody receptors yield a high sensitivity, as shown in the FET conductance, upon virus binding and unbinding (Fig. 4.20a). The conductance of a second quantum wire with antibodies not specific to the present virus does not change.

For the diagnosis of prostate cancer, the multiplexed real-time detection of three cancer marker proteins, f-PSA (prostate specific antigen), CEA (carcinoembryonic antigen), and mucin-1 was demonstrated [4.56] making use of Si quantum wire devices functionalized with monoclonal antibodies (mAbs) for f-PSA (quantum wire 1), CEA (quantum wire 2), and mucin-1 (quantum wire 3) (see Fig. 4.20b). These cancer marker proteins can be identified by the subsequent concentration-dependent conductance changes on the differently functionalized wires upon sequential delivery of the different protein solutions (see Fig. 4.20c). These results show multiplexed real-time, label-free marker protein detection with sensitivity to the femtomolar level and complete selectivity which may offer a significant improvement of future health care.

Light-emitting diodes (LEDs), lasers, and photodetectors: Crossed nanowires can also be used to fabricate nanoscale p-n diodes for, e.g., band-edge emission LEDs at the nanoscale cross-points (Fig. 4.21a). The capability to assemble a

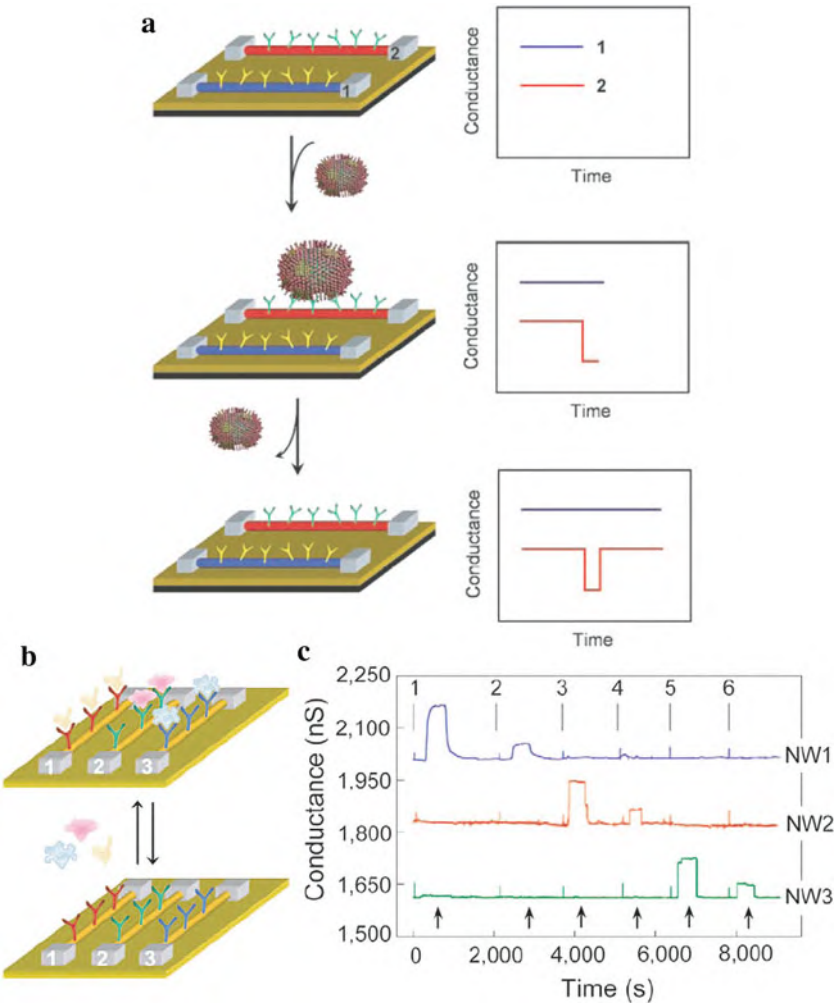

Fig. 4.20 (**a**) Schematics of quantum wire-based detection of single viruses making use of two nanowire devices, 1 and 2, where the nanowires are modified with different antibody receptors. Specific binding of a single virus to the receptors on quantum wire 2 produces a conductance change characteristic of the surface charge of the virus only in quantum wire 2. When the virus unbinds from the surface the conductance returns to the initial value [4.55]. (**b**) Schematics illustrating multiplexed protein detection by three Si quantum wire devices in an array. Devices 1, 2, and 3 are made of similar wires which are selectively functionalized with distinct monoclonal receptors specific to three different cancer markers. (**c**) Time-dependent conductance for simultaneous detection of prostate antigen (PSA), carcinoembryonic antigen (CEA), and mucin-1 on a p-Si wire array in which the wires 1, 2, and 3 are functionalized with monoclonal receptors for PSA, CEA, and mucin-1, respectively. Protein solutions were delivered sequentially on the wire array: (1) 0.9 ng/ml PSA, (2) 1.4 pg/ml PSA, (3) 0.2 ng/ml CEA, (4) 2 pg/ml CEA, (5) 0.5 ng/ml mucin-1, and (6) 5 pg/ml mucin-1. Buffer solutions were injected following each protein solution at points indicated by black arrows [4.51]. (Reprinted with permission from [4.55] (**a**) (**b**) and [4.51] (**c**). © 2004 National Academy of Sciences, USA (**a**) (**b**) and © 2006 Elsevier (**c**))

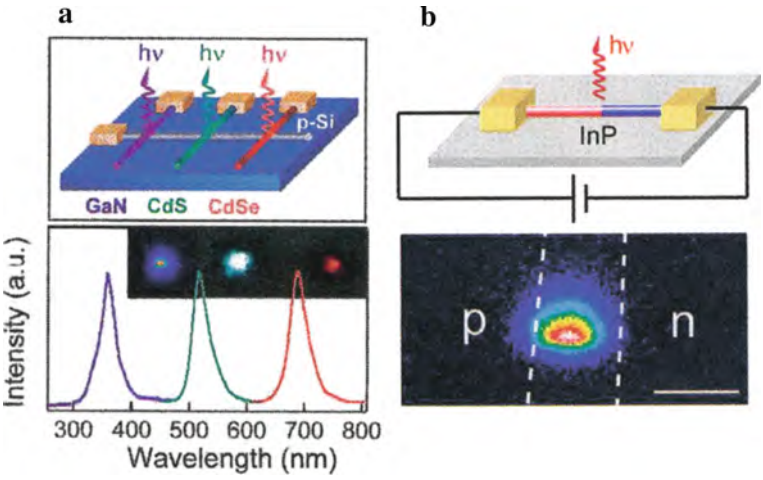

Fig. 4.21 (**a**) Schematic of the electroluminescence of a tricolor nano light-emitting diode (LED) array of a p-type Si quantum wire crossed with n-type GaN, CdS, and CdSe wires. (**b**) Schematic of a modulation-doped InP quantum wire LED and image of the emission from the device. The *dashed white lines* indicate the edges of the electrodes. Scale bar: 3 μm. (Reprinted with permission from[4.51]. © 2006 Elsevier)

wide range of different n-type direct band gap quantum wires of GaN (ultraviolet), CdS (green), and CdSe (near infrared) with p-type Si quantum wires has enabled the simple creation of multicolor light-emitting diodes (LEDs) on a single substrate in a manner not possible formerly. Light emission can also be obtained at p–n interfaces of modulation doped InP quantum wire axial heterostructures (Fig. 4.21b).

A nanoscale electronic injection laser has been constructed from n-type CdS quantum wires assembled unto p-type Si electrodes [4.57]. This device shows a superlinear increase in the electroluminescence intensity at the end of the quantum wire together with peak narrowing (Fig. 4.22a) when the injection current increases above the threshold.

Photodetectors for use in integrated photonics can also be fabricated from crossed quantum wire p–n junctions. Avalanche multiplication of the photocurrent has been detected in nanoscale p–n diodes of crossed Si/CdS quantum wires (Fig. 4.22d) [4.58]. These nanoscale avalanche photodiodes exhibit ultrahigh sensitivity with detection limits of less than 100 photons and sub-wavelength spatial resolution of 250 nm.

Manipulation of quantum wires by means of optical traps. For the manipulation of quantum wires for further integration, an optical trap can be employed [4.59]. This makes use of the effect that a light beam can exert a force on a particle and therefore can grip a quantum wire and transport it into a desired location (Fig. 4.23a). By this technique, e.g., a GaN quantum wire could be transported close to a human cervical cancer cell and attached there (Fig. 4.23b).

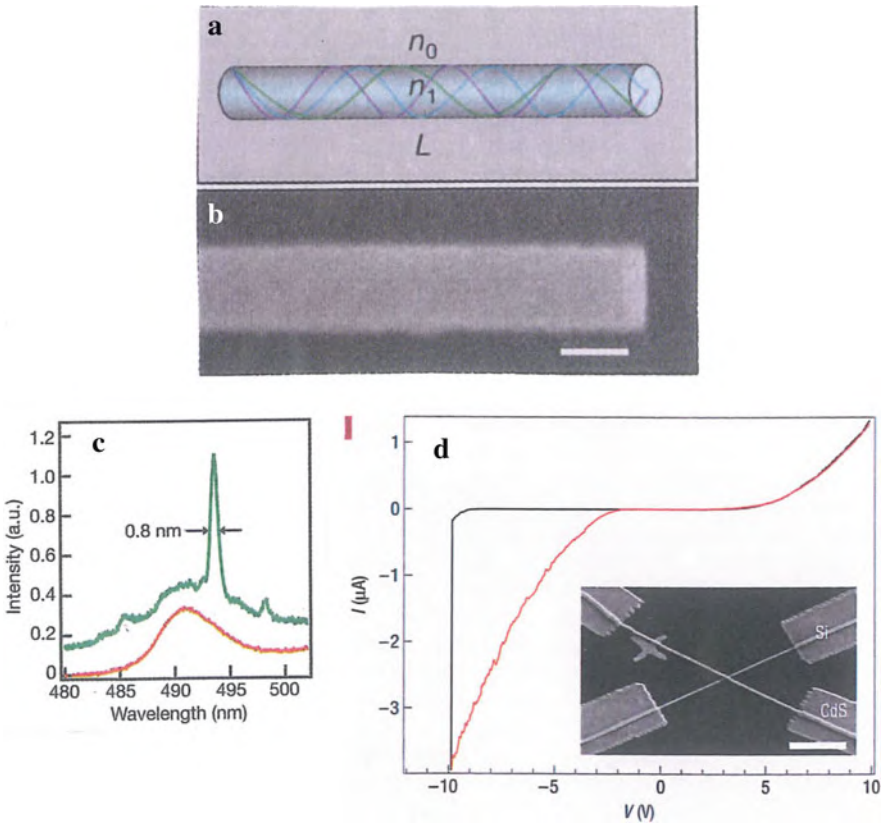

Fig. 4.22 (**a**) Schematics of a Fabry–Perot optical cavity of a quantum wire as an optical waveguide and with cleaved ends defining the Fabry–Perot cavity. (**b**) SEM image of a cleaved CdS quantum wire end. Scale bar: 100 nm [4.57]. (**c**) Electroluminescence spectra from the end of an n-CdS quantum wire laser deposited on a p-Si substrate with injection currents below (200 μA, *lower curve*) and above (280 μA, *upper curve*) the lasing threshold. The spectra are offset by 0.1 intensity for clarity. (**d**) I–V characteristics of an n-CdS/p-Si crossed quantum wire avalanche photodiode in dark (step function line) and under illumination (*curved line*); the *inset* represents the optical micrograph of an array of an n-CdS quantum wire crossing a p-Si quantum wire; the larger rectangular features are the metal contacts. Scale bar, 10 μm [4.58]. (Reprinted with permission from [4.57] (**a**) (**b**) and [4.58] (**c**) (**d**). © 2003 Nature Publishing Group (**a**) (**b**) and © 2006 Nature Publishing Group (**c**) (**d**))

4.2.4 Molecular Nanowires

For the bottom-up approach of designing electronic components for future information technology or signal conductance in artificial nerves, the exploitation of the features of organic molecules and molecular wires are of interest. Poly(z-vinylpyridine) nanowires were loaded with Au, Ag, or CdS nanoparticles [4.60]. Highly conductive and relatively long (~40 nm) molecular wires can be synthesized by the coordination of terpyridine-based ligands to metal ions such as Fe or

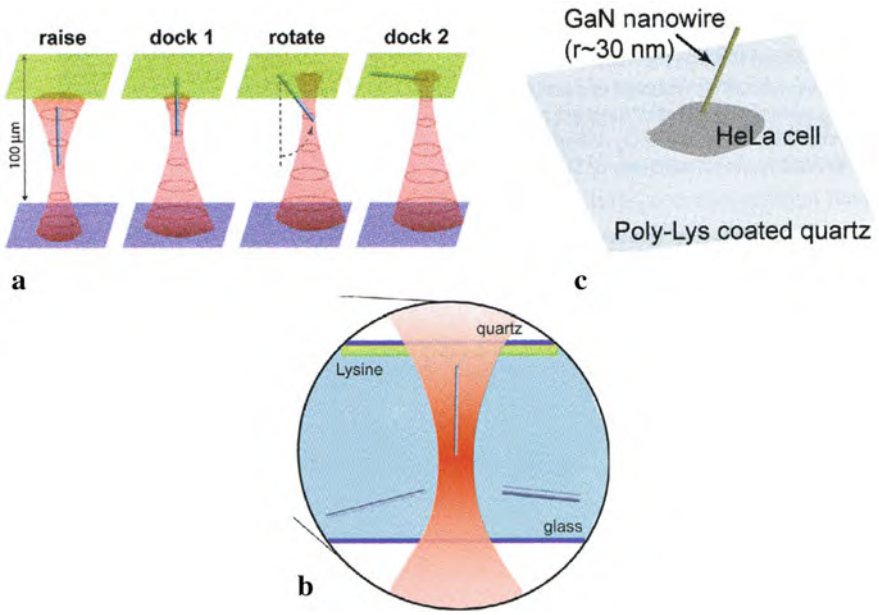

Fig. 4.23 (**a**) Schematic of a four-step nanowire positioning procedure in an optical trap aqueous chamber with a light beam. (**b**) Schematic of the experimental chamber cross section. The top surface is a 170 µm quartz coverslip (*blue*) coated with lysine (*green*) and the bottom surface a glass coverslip. The quantum wires sink to the bottom and can be picked up there by the light beam. (**c**) Schematic of a GaN quantum wire attached to a human cervical cancer cell by optical trapping. (Reprinted with permission from [4.59]. © 2006 Elsevier)

Co [4.61]. By π-stacking of 6,13-bis(methylthio)pentacene, molecular nanowires were self-assembled, achieving four-level switching in a multiwire transistor and demonstrating their suitability for the production of multilogic devices [4.62].

In spite of all the present progress in quantum wire synthesis, characterization, and their attractive physical features, researchers are aware of further challenges to be overcome before nanowires are implemented in high-end products [4.63].

4.2.5 Conduction Through Individual Rows of Atoms and Single-Atom Contacts

The quantized conductance through individual rows of freely suspended Au atoms [4.64], the manipulation of these single-atom metallic wires [4.65], and the detection of the signature of the chemical valence in the electrical conduction through single-atom contacts [4.66] will be discussed in the following.

By a combination of conductance measurements and high-resolution electron microscopy [4.64], it was shown that the conductance of a single strand of gold atom (Fig. 4.24) is about equal to the conductance quantum $2e^2/h$ $\left(\sim 13\,\mathrm{k}\Omega^{-1}\right)$

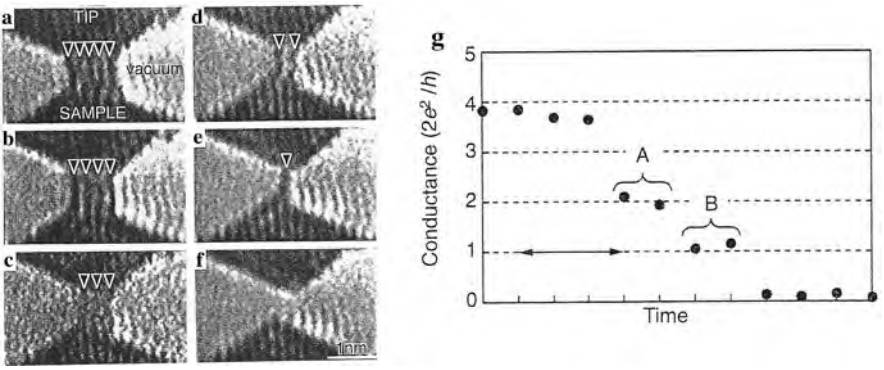

Fig. 4.24 Electron micrographs of an Au contact while withdrawing the Au tip (*top*) from the Au substrate (*bottom*). The gold contact is thinned from (**a)** to (**e**) during withdrawing and ruptured at (**f**). *Dark lines* indicated with arrow heads are single rows of gold atoms. (**g)** Conductance change of a Au contact in units of $G_0 = 2e^2/h \sim (13\ \mathrm{k\Omega})^{-1}$ while withdrawing the tip from the substrate. (Reprinted with permission from [4.64]. © 1998 Nature Publishing Group)

and that the conductance of a double strand is twice as large. By straining the atomic gold bridge (Fig. 4.24) the strands presenting a row of atoms each disappear one by one until the contact breaks. Simultaneously the conductance changes in units of $2e^2/h$ (see Fig. 4.24 g). The Au bridges can sustain high electrical current densities up to $8 \times 10^{14}\mathrm{A/m^2}$ [4.65] indicating that the electron transport is ballistic without dissipation.

In chains of two atoms of the noble gas Xe the conductance is two orders of magnitude lower than $2e^2/h$ due to the non-metallic bonding [4.67].

If the length of an atomic wire shrinks to one atom, we arrive at a single-atom contact or an atomic constriction. Experimental [4.66] and theoretical studies [4.68] show that the electrical conductance in single-atom contacts evidences the signature of the chemical valence of the metals investigated. The extended quantum states of the leads that carry the current from one bank of the constriction to the other necessarily proceed through the valence orbitals of the constriction atom. It has been conjectured that the current-carrying modes (or "channels") of a one-atom contact is determined by the number of available orbitals and so should strongly differ for metallic elements in different series of the periodic table.

The electrical conductance of a quantum coherent structure with N channels is given by the Landauer formula $G = G_0 \sum_{n=1}^{N} T_n$ [4.69] with the conductance quantum $G_0 = 2e^2/h$ and the transmission probability T_n which can be derived from the nonlinearities in the current–voltage characteristics of superconducting constrictions. These nonlinearities are sensitive to the individual transmission values $\{T_n\}$ of the channel ensemble.

It turns out that the maximum number of channels N_{max} for an atomic contact is characteristic for a given metal. For Pb three or four channels contribute to the atomic conductance where in Al three and in Nb five channels are detected. These results support the hypothesis that N_{max} for one-atom contacts is given by the number of the valence orbitals N_{orb} of the central atom [4.66, 4.68].

4.3 Nanolayers and Multilayers

In this section 2D nanostructures with a confinement of the charge carriers in one dimension will be discussed. These structures which are also termed quantum wells exhibit novel electronic properties in particular in high magnetic fields, such as the integral quantum Hall effect (IQHE) and the fractional quantum Hall effect (FQHE). In addition, 2D electron gases in oxide interfaces and nanomultilayers for x-ray mirror fabrication will be outlined.

4.3.1 2D Quantum Wells

When an electron is confined in a thin metal or semiconductor film where the film thickness scales with the de Broglie wavelength $\lambda = h/p$ of the charge carriers (p – carrier momentum; h – Planck's constant), new physical phenomena occur [4.70, 4.71]. For an electron the film represents a potential well (quantum well) with the width a (film thickness) and the depth Φ (work function) which may be considered as infinitely deep because $\Phi = 4 - 5\,eV >> kT$. In this thin quantum well the electron assumes discrete quantized energy levels

$$E_N = \frac{\pi^2 \hbar^2 N^2}{2ma^2}$$

with $N = 1,\ 2,$ ... and m the effective mass of the carrier (Fig. 4.25a).

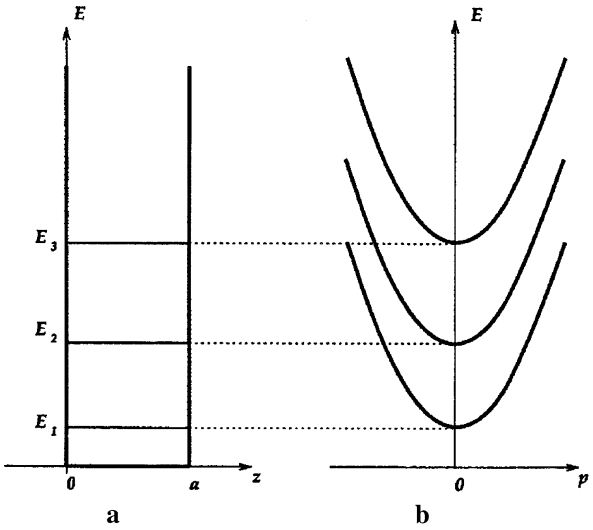

Fig. 4.25 (**a**) Energy spectrum of a quantum well with quantized levels for the carrier motion in z-direction perpendicular to the plane of the quantum well and (**b**) taking into account additionally the in-plane carrier motion with the momentum $p = \left(p_x^2 + p_y^2\right)^{1/2}$. (Reprinted with permission from [4.70]. © 1997 World Scientific)

For the total energy of an electron in a quantum well, the in-plane motion of the carriers has to be taken into account additionally, yielding the energy spectrum

$$E = E_N + \frac{p_x^2 + p_y^2}{2m}$$

with the discrete component E_N for the motion perpendicular to the film (z-direction) and a continuous component with the in-plane carrier momenta p_x and p_y (see Fig. 4.25b). This energy spectrum gives rise to the step-like density of states in a 2D quantum well (see Sect. 1.3).

4.3.2 2D Quantum Wells in High Magnetic Fields

In the case of a magnetic field H oriented perpendicularly to the plane of the 2D quantum well, the total energy spectrum of the carriers including the motion in the direction of the field H is given by

$$E = E_N + E_\perp = E_N + \hbar\omega_c\,(M + 1/2)\,,\ M = 0,\ 1,\ 2,\ ...$$

The equidistant energy levels $\hbar\omega_c\,(M + 1/2)$ are called Landau levels with the cyclotron frequency $\omega_c = eH/mc$ [4.70]. The most remarkable feature of this spectrum is its purely discrete character.

It is convenient to discuss the effects of 2D quantum wells in high magnetic fields employing the dimensionless filling factor

$$\nu = 2\pi n_s \hbar c/eH$$

which is the number of Landau levels completely filled by electrons at $T = 0$, where the critical fields $H_N = 2\pi hcn_s/eN$ correspond to integer filling factors. Since $2\pi h/e = \Phi_0$ represents the magnetic flux quantum, the filling factor $\nu = n_s/\,(B/\Phi_0)$ can alternatively be interpreted as the number of electrons per flux quantum and much of the physics of 2D electrons in a magnetic field can be cast in terms of this filling factor.

4.3.3 The Integral Quantum Hall Effect (IQHE)

Most of the experiments performed on 2D electron systems in high magnetic fields H are electrical resistance measurements [4.71]. These measurements (see inset of Fig. 4.26) yield the magneto-resistance R_{xx}, which reduces to the regular resistance in zero H field, and the Hall resistance R_{xy}, which increases linearly with the field in an ordinary conductor. In 1980 K. v. Klitzing [4.72] discovered novel plateaus in the Hall resistance R_{xy} of a semiconductor quantum well structure (see Fig. 4.26) and was awarded the Nobel prize in 1985. The effect is called the Integer Quantum

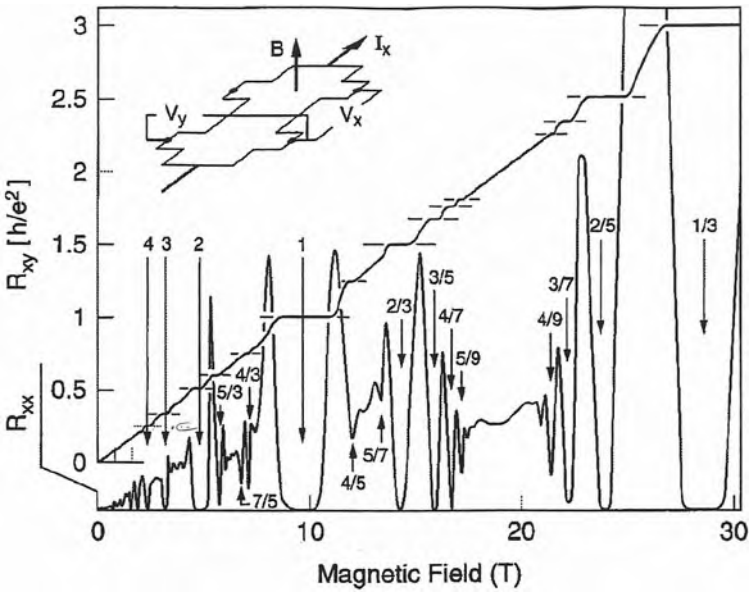

Fig. 4.26 Composite view showing the Hall resistance $R_{xy} = V_y/I_x$ and the magnetoresistance $R_{xx} = V_x/I_x$ of a 2D electron system of the density $n = 2.33 \times 10^{11}$ cm^{-2} at $T = 85$ mK in dependence of the magnetic field H. The numbers designate the filling factor ν, which indicates the degree to which the sequence of Landau levels is filled with electrons. In contrast to a linear rise with H, R_{xy} exhibits plateaus, quantized to $h/\left(\nu e^2\right)$ with simultaneous minima in R_{xx}. The features of the integer quantum Hall effect (IQHE) result from the quantization conditions for individual 2D electrons in a H field, whereas the fractional quantum Hall effect (FQHE) is of many-particle origin. The *inset* shows the measuring geometry. (Reprinted with permission from [4.71]. © 1999 American Physical Society)

Hall Effect (IQHE) because it occurs at integer filling factors ν and displays the quantization of the Hall resistance $R_{xy} = R_H = V_y/I_x = h/\left(\nu e^2\right)$ (see Fig. 4.26) as a consequence of the quantization of *non-interacting electrons* in a 2D quantum well in a magnetic field H. It, therefore, is a result of the discretization of the energy spectrum due to the 2D confinement of the charge carriers *plus* Landau and spin quantization in the magnetic field.

A microscopic picture of the IQHE is at present [4.73] characterized by a striped structure along the edges of the quantum well where the stripes of constant electron density n_s are incompressible ($\partial\mu_{ch}/\partial n_s \rightarrow \infty$; μ_{ch} – chemical potential) and the stripes of varying n_s are compressible. By this striped structure, which has been demonstrated experimentally [4.74], the formation of the plateaus of the IQHE can be described microscopically [4.73].

The quantum Hall resistance has applications in metrology [4.73] since the value $R_H = 25812.807\Omega$ has been taken as a resistance standard. In comparative measurements of several national institutions, deviations of less than 2×10^{-9} from this value have been reported.

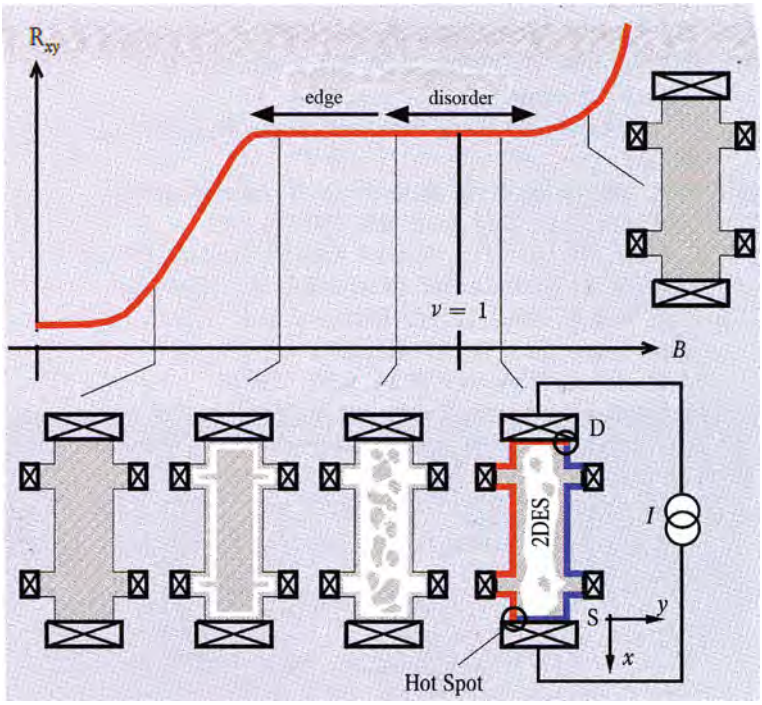

Fig. 4.27 Schematics of the evolution of compressible (*gray*) and incompressible (*white*) stripes or domains in a real inhomogeneous quantum well structure over an integer quantum Hall effect (IQHE) plateau in dependence of the magnetic field. (Reprinted with permission from [4.73]. © 2005 Wiley-VCH)

4.3.4 The Fractional Quantum Hall Effect (FQHE)

In contrast to the IQHE the Fractional Quantum Hall Effect (FQHE), which was discovered by Tsui and Störmer [4.75] and theoretically interpreted by Laughlin [4.76] (Nobel prize 1998), occurs at fractional filling factors and its quantum numbers are not integers but rational fractions p/q.

The FQHE results from the highly correlated motion of many 2D electrons in a magnetic field. The driving force is the reduction of the Coulomb interaction between the like-charged electrons by a magnetic field. The many-particle states of this system are of inherently quantum mechanical nature [4.76]. Fractional quantum numbers and fractionally charged quasi-particles are the most spectacular of its implications.

At present, the attachment of magnetic vortices to electrons (Fig. 4.28) represents the unifying principle for the description of the multiple many-particle states of the FQHE [4.77] where Laughlin's wave function [4.76] describing the $\nu = 1/3$ states is the prime example for this principle at work. Since electrons are charge accumulations and magnetic flux quanta (vortices) charge deficits they attract each

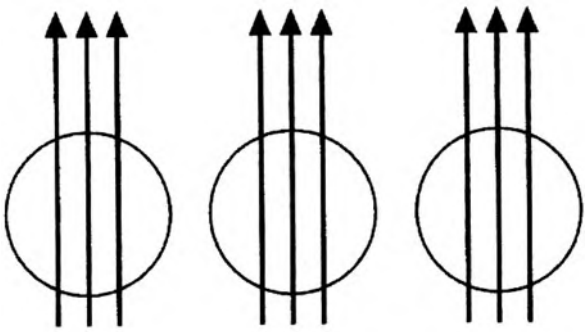

Fig. 4.28 Sketch of composite particles in the fractional quantum Hall effect FQHE for the filling factor $\nu = 1/3$. The arrows represent the magnetic flux quanta attached to the electrons (*circles*). (Reprinted with permission from [4.78]. © 1999 Karlruher Institut für Technologie)

other. Coulomb energy can be gained by placing vortices onto electrons (composite particle model; see [4.71] and Fig. 4.28). At $\nu = 1/3$ there exist three times as many vortices as there are electrons. The attachment of exactly three vortices to each electron is the origin of the prominent $\nu = 1/3$ FQHE state described by the Laughlin wave function

$$\psi_{1/3} = \prod_{i<j}^{n} \left(z_i - z_j\right)^3 \exp\left(-\frac{1}{4}\sum_{k}^{n} |z_k|^2\right)$$

where the $z_{i,j,k}$ represent the coordinates of n electrons in a complex 2D plane. The exponent 3 is a manifestation of the attachment of 3 vortices to the position of each electron and changes to q if the electrons are dressed by q vortices. Here, only odd q values are allowed in order to guarantee the antisymmetry of this electron wave function.

A bound state of an electron and an even number of flux quanta is itself a fermion and hence called a *composite fermion* (see [4.79]). Numerous properties of these composite fermions and the quantum fluids they form have been established. Their Fermi sea, their Shubnikov–de Haas oscillations, their cyclotron orbits, and their quantized Landau levels have been demonstrated experimentally. The particles' charge, spin, statistics, mass, magnetic moment, and thermopower have been measured (see [4.79]).

4.3.5 2D Electron Gases (2DEG) at Oxide Interfaces

Advances in the heteroepitaxy of complex oxides [4.80] provide the possibility of fabricating interfaces in oxides with atomic precision, including oxides with strongly correlated electrons. 2D electron gases (2DEG) can be formed at these interfaces [4.81]. The electrons interact and order at the interfaces in unique ways (see [4.81–4.83]) so that, for example, novel types of quantum Hall systems [4.84], unique superconductors [4.85], ferromagnetic ground states [4.86],

and field-effect transistor behavior [4.87] can be observed. It turns out that everything depends on the precise crystalline structure of the interface (see [4.81]): only when the right atomic layers meet, the internal electric fields on each side push electrons toward the junction so that they can form the electron gas with a thickness < 4 nm [4.88]. The quality of oxide films on silicon has been improving steadily [4.89] so that the integration of oxide heterostructures into silicon wafers could be possible.

Quantum Hall effect. In a (MgZn)O/ZnO heterostructure the 2DEG accumulates at the interface through a discontinuity in the electric polarization (see Fig. 4.29a).

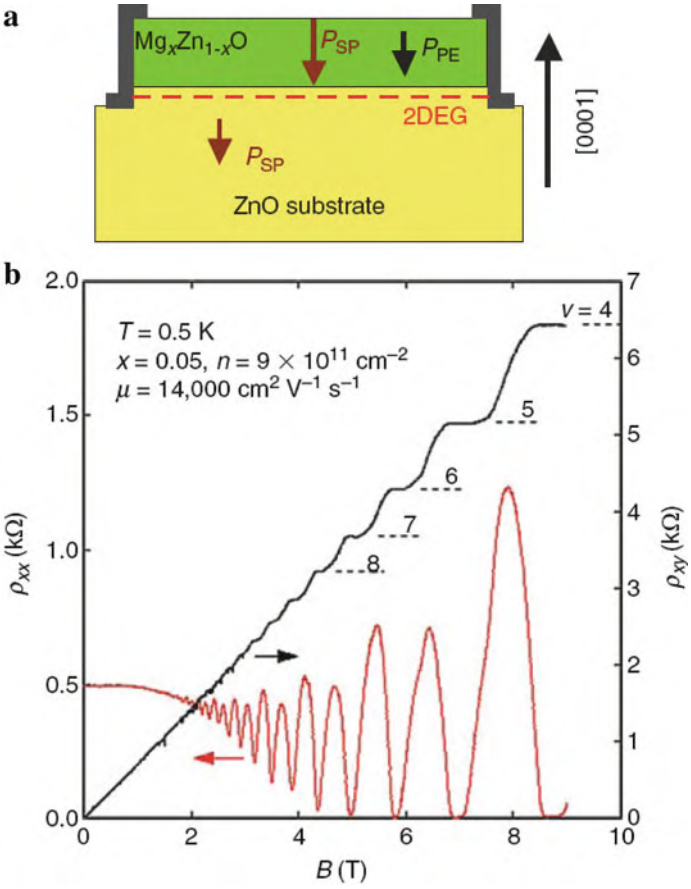

Fig. 4.29 (**a**) Schematic of (MgZn)O/ZnO heterostructures in which a discontinuity in polarization (P) induces a 2D electron gas (2DEG). P_{SP} is the spontaneous polarization and P_{PE} is the piezoelectric polarization. (**b**) Magnetotransport properties of the 2DEG show Shubnikov–de Haas oscillations (ρ_{xx}) and the quantum Hall effect (ρ_{xy}). The integers ν indicate Landau filling factors. (Reprinted with permission from [4.82]. © 2008 Materials Research Society)

ZnO is a piezoelectric material with a finite spontaneous polarization, P_{SP}. When a (MgZn)O layer is grown on the ZnO substrate pseudomorphously, piezoelectric polarization, P_{PE}, appears as a result of epitaxial strain in addition to P_{SP}. At the interface, the sums of P_{SP} and P_{PE} for the two layers do not necessarily match and a sheet charge is formed in the layer of the narrower band gap material (ZnO) at the interface to relax the electrostatically unfavorable situation. By forming a degenerate 2DEG in the nominally undoped and clean interface channel, a clear oscillation is observed in the magnetoresistance and plateaus in the Hall resistance (quantum Hall effect; Fig. 4.29b). These effects result from the quantum interference of free electrons in a strong magnetic field (Lorentz force) and have been observed only in a clean channel with a Hall mobility $\mu_H > 10{,}000\ cm^2/(V\ s)$ [4.82, 4.84].

Superconductivity. In $LaAlO_3/SrTiO_3$ samples, a superconducting condensate has been found to be in the ground state [4.85] with critical temperatures of ~200 mK (Fig. 4.30). Critical field measurements with the magnetic field aligned parallel and perpendicular to the interface plane reveal a large anisotropy with the in-plane coherence length estimated to ~ 50–100 nm and the thickness of the superconducting sheet to only ~ 4 nm. From these data, the interface is expected to behave as a 2D superconductor such as described by the Berezinskii–Kosterlitz–Thouless theory [4.90, 4.91]. In field-effect transistor configurations, perpendicular electric fields allow the sheet carrier density of $LaAlO_3/SrTiO_3$ interfaces to be substantially modulated in both the normal and the superconducting states (see [4.81]). At low temperatures an insulator-to-superconductor phase transition can be induced with electric fields [4.92]. This might suggest to write complex patterns into such a 2DEG, potentially allowing the definition of entire electronic circuits (see [4.83]).

4.3.6 Multilayer EUV and X-Ray Mirrors with High Reflectivity

In extreme ultraviolet (EUV) lithography for future chip production (see Sect. 9.2) or in research at high-power soft x-ray sources, such as free electron lasers (FLASH, XFEL), high-reflectivity mirrors are required as optical components for beam formation [4.94]. As well known from visible optics, λ/4 multilayer structures enhance the reflectivity by constructive interference of the light waves reflected at the layer interfaces (Fig. 4.31). The multilayer stack consists of alternating layers of absorber and spacer materials with different refractive indices. The absorber material is selected according to a high reflectivity at the boundary with the spacer while still having an extinction coefficient as low as possible, whereas the spacer material should have the lowest extinction coefficient at the desired wavelength.

The multilayers can be fabricated by DC sputtering [4.95]. For the fabrication of multilayers with a period of 1.0–5.0 nm for radiation wavelengths of 2–10 nm, the layer density, smoothness, and the ability to produce continuous thin layers with abrupt and smooth interfaces are pivotal.

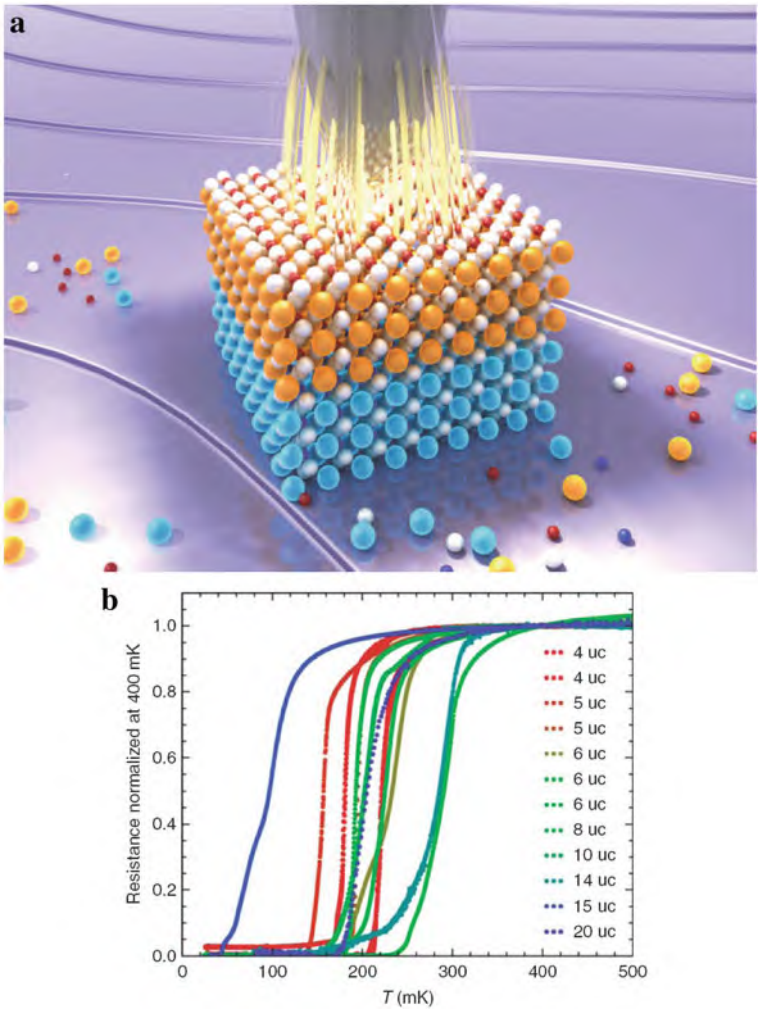

Fig. 4.30 (**a**) The artist's impression shows the interface between lanthanum aluminate ($LaAlO_3$; *top*) and strontium titanate ($SrTiO_3$; *bottom*). The atoms are shown in different colors: La (*orange*), Al (*red*), Sr (*pale blue*), Ti (*dark blue*), O (*white*) [4.93]. (**b**) Resistance measurements of several $LaAlO_3/SrTiO_3$ oxide heterostructures with a variety of $LaAlO_3$ thicknesses measured in unit cells (uc). The resistances are normalized to the values measured at 400 mK. The figure shows samples with superconducting transitions at $\sim$ 200 mK [4.81]. (Reprinted with permission from [4.93] (**a**) and [4.81] (**b**). © 2009 Nature Publishing Group (**a**) and © 2008 Materials Research Society (**b**))

Mirrors with the spectral range from 40 to 120 nm are of particular interest for astrophysical applications making use of Al layers with protecting MgF_2 or LiF layers (see Table 4.1). For the wavelength range 35–50 nm Sc/Si multilayers appear to be favorable. For wavelengths from 12.5 nm (above the Si

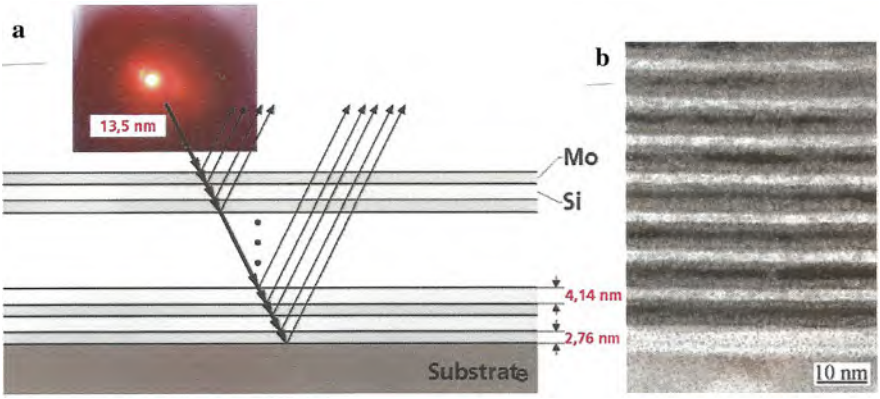

Fig. 4.31 (**a**) Schematic representation of high-reflectivity multilayer extreme ultraviolet (EUV) and soft x-ray mirrors due to constructive interference of the radiation reflected at the multilayer interfaces with the 13.5 nm EUV radiation as an example. (**b**) Transmission electron micrograph of a Mo/Si multilayer for EUV mirrors. (Reprinted with permission from [4.94]. © 2008 Photonik; S. Yulin)

Table 4.1 UV, EUV, and x-ray mirrors and multilayer mirrors [4.94]

Multilayer system	λ range (nm)	λ (nm)	Number of layer periods (*N*)	Reflectivity (%)	FWHM (nm)
Al	70–150	110	–	60	–
Sc/Si	40–50	46	20	52	4.6
Mo/Si	12.4–40	26	25	25.8	2.6
Mo/Si	13.5 (EUV)	13.5	60	69.5	0.5
Mo/B_4C	6.4–11.0	6.7	200	26.0	0.04
Cr/Sc	3.1–4.4	4.4	300	7.1	0.021
		3.1	400	17.1	0.008
Cr/V	2.4–2.7	2.5	400	5.2	0.005

L-absorption edge) to 40 nm, Mo/Si multilayer mirrors are used. For the 13.5 nm EUV radiation, maximum reflectivity (see Table 4.1) has been achieved by minimizing interdiffusion making use of barrier layers [4.94]. From the wavelength regime from 6 to 12 nm, which is of interest for studies with soft x-rays at free electron lasers, Mo/B_4C multilayer mirrors are used, whereas for the so-called water window between the K absorption edges of oxygen ($\lambda = 2.3$ nm, 543 eV) and carbon (4.4 nm, 284 eV), which is of particular interest for x-ray microscopy, multilayers of Cr/Sc, Cr/Ti, and Cr/V are employed (Table 4.1, Fig. 4.32).

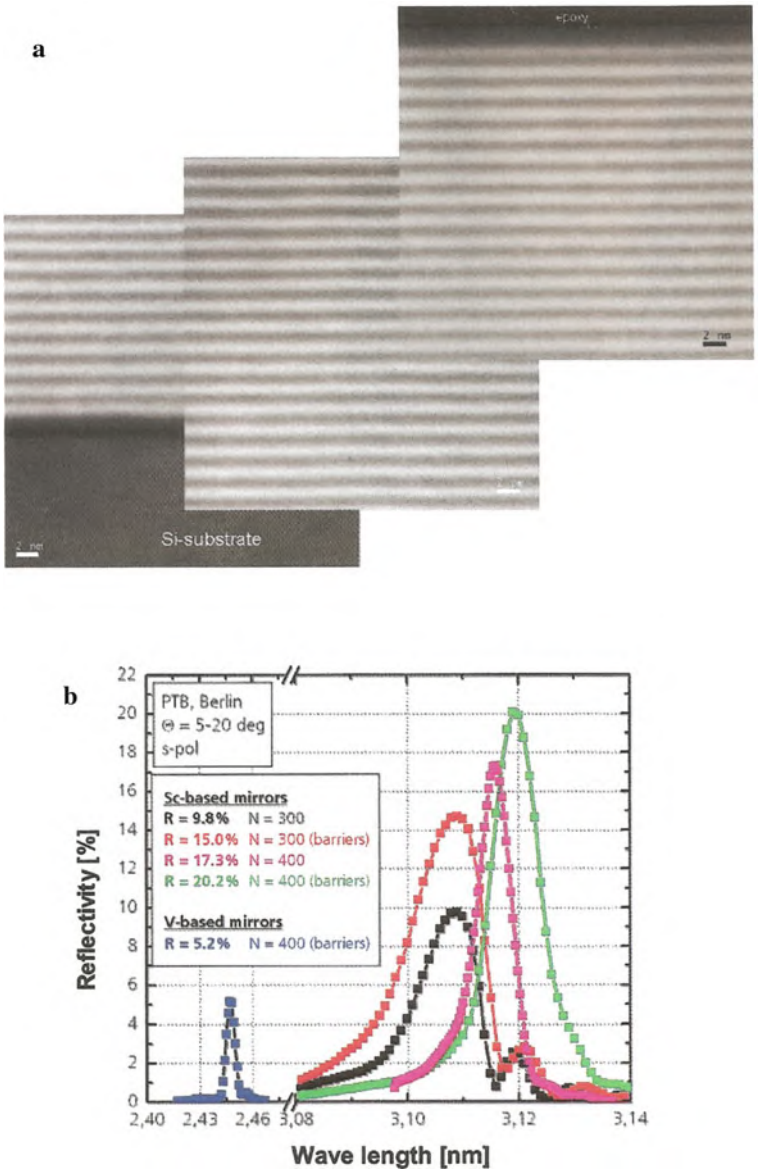

Fig. 4.32 (**a**) Transmission electron micrograph of the layer structure of a diffusion-barrier-optimized Cr/Sc multilayer ($N = 300$) mirror for soft x-ray reflection; near the substrate (*bottom*), in the stack center and near the surface (*top*); scale bar: 2 nm. (**b**) Enhancement of the reflectivity of Cr/Sc and Cr/V multilayers by optimization of the diffusion barriers. (Reprinted with permission from [4.94]. © 2008 Photonik; S. Yulin)

4.4 Summary

Nanocrystals or nanocrystal ensembles may give rise to colors due to quantum confinement, plasmonic excitation, or photonic-crystal effects for use in biomedical detection or sensors. Metallic nanowires exhibit enhanced mechanical properties and can be used for the construction of negative-index materials (metamaterials), whereas semiconductor nanowires offer potentials for transistors, logic gates, multicolor light-emitting diodes (LEDs), and photodetectors. In the conductance through individual rows of atoms or single-atom contacts, the valency of the particular metal is manifested. Semiconductor nanolayers (quantum wells, 2D electron gases – 2DEG) in a magnetic field show the integral quantum Hall effect of non-interacting electrons with application in metrology or – at higher fields – the fractional quantum Hall effect of electrons interacting via magnetic vortices. 2DEGs can also be generated at oxide interfaces demonstrating quantum Hall effect, superconductivity, and ferromagnetic features. Nanostructural multilayers are used as high-reflectivity mirrors for extreme ultraviolet (EUV) and x-ray radiation.

References

4.1 D. Bimberg, Phys. J. **5**(8/9), 43 (2006)
4.2 G.D. Scholes, G. Rumbles, Nature Materials **5**, 683 (2006)
4.3 U. Banin, Nat. Mater. **6**, 625 (2007)
4.4 S.E. Habas et al., Nat. Mater. **6**, 692 (2007)
4.5 E.H. Sargent, Adv. Mater. **17**, 515 (2005)
4.6 M.A. Hines, G.D. Scholes, Adv. Mater. **15**, 1844 (2003)
4.7 J.Y. Ouyang et al., J. Phys. Chem. C **112**, 13805 (2008)
4.8 M.M. Maye et al., Nat. Mater. **8**, 388 (2009)
4.9 G. Rollmann et al., Phys. Rev. Lett. **99**, 083402 (2007)
4.10 W.J. Huang et al., Nat. Mater. **7**, 308 (2008)
4.11 H. Portales et al., Proc. Natl. Acad. Sci. USA **105**, 14784 (2008)
4.12 N. Shibata et al., Phys. Rev. Lett. **102**, 136105 (2009)
4.13 Y. Tang, M. Ouyang, Nat. Mater. **6**, 754 (2007)
4.14 J. Wood, Materials today **11**, May 2008, p. 8
4.15 Q.F. Gu et al., Phys. Rev. Lett. **100**, 045502 (2008)
4.16 D. Stier et al., Phys. Rev. B**59**, 5688 (1999)
4.17 I.L. Medintz et al., Nat. Materials **4**, 435 (2005)
4.18 N.R. Rosi, C.A. Mirkin, Chem. Rev. **105**, 1547 (2005)
4.19 M. Bottini, T. Mustelin, Nat. Nanotech. **2**, 599 (2007)
4.20 H. Liu et al., Angew. Chem. Int. Edn. **46**, 6473 (2007)
4.21 J.P. Ge et al., Angew. Chem. Int. Edn. **46**, 7428 (2007)
4.22 M. Bruchez et al., Science **281**, 2013 (1998)
4.23 W.C.W. Chan, S.M. Nie, Science **281**, 216 (1998)
4.24 P. Alivisatos, Nat. Biotechnol. **22**, 47 (2004)
4.25 Y.G. Sun, Y.N. Xia, Science **298**, 2176 (2002)
4.26 R.C. Jin et al., Nature **425**, 487 (2003)
4.27 U. Kreibig, M. Vollmer, *Optical Properties of Metal Clusters* (Springer, Berlin, 1995)
4.28 R. Elghanian et al. Science **277**, 1078 (1997)
4.29 E. Yablonovitch, Sci. Am. **285**, 47 (2001)
4.30 F.H.L. Koppens et al., Nature **442**, 766 (2006)

4.31 D.P. DiVincenzo, Science **270**, 255 (1995)
4.32 D. Press et al., Nature **456**, 218 (2008)
4.33 C.W. Kim et al., Adv. Mater. **20**, 1859 (2008)
4.34 L. Li et al., J. Mater. Sci. Technol. **23**, 166 (2007)
4.35 E.H. Yue et al., J. Mater. Sci. Technol. **24**, 850 (2008)
4.36 B. Derby, 7th Brazilian – MRS Meeting (São Paulo, 2008)
4.37 G. Dolling et al., Optics Lett. **32**, 53 (2007)
4.38 N. Liu et al., Nat. Mater. **7**, 31 (2008)
4.39 U.K. Chettiar et al., MRS Bull. **33**, 921 (2008)
4.40 J. Valentine et al., Nature **455**, 376 (2008)
4.41 A.J. Hoffmann, Nat. Mater. **6**, 946 (2007)
4.42 W.J. Park, J.S. Kim, MRS Bull. **33**, 907 (2008)
4.43 Ch. Caloz, Materials Today. **12**, March 2009, p. 12
4.44 G.V. Eleftheriades, Materials Today **12**, March 2009, p. 30
4.45 C.M. Soukoulis et al., J. Phys.: Condens. Matt. **20**, 304217 (2008)
4.46 J.B. Pendry et al., IEEE Trans. Microw. Theory Tech. **47**, 2075 (1999)
4.47 G. Shvets, Nat. Mater. **7**, 7 (2008)
4.48 S. Linden, M. Wegener, Physik Journal **5** (12), 29 (2006)
4.49 U. Engelhardt, T. Tyc, Science **323**, 110 (2009)
4.50 S. Schwaiger et al., Phys. Rev. Lett. **102**, 163903 (2009)
4.51 Y. Li et al., Materials today **9**, Nr. 10, 18 (2006)
4.52 B.M. Wen et al., Phys. Rev. Lett. **101**, 175502 (2008)
4.53 G.F. Zheng et al., Adv. Mater. **16**, 1890 (2004)
4.54 Y. Huang et al., Science **294**, 1313 (2001)
4.55 F. Patolsky et al., Proc. Natl. Acad. Sci. (USA. **101**, 14017 (2004)
4.56 G. Zheng et al., Nat. Biotechnol. **23**, 1294 (2005)
4.57 X.F. Duan et al., Nature **421**, 241 (2003)
4.58 O. Hayden et al., Nat. Mater. **5**, 352 (2006)
4.59 P.J. Pauzauskie, P.D. Yang, Materials Today **9**, Nr. 10, 36 (2006)
4.60 A. Walther et al., NanoLett. **9**, 2026 (2009)
4.61 N. Tuccitto et al., Nat. Mater. **8**, 41 (2009)
4.62 Y. Wakayama et al., Nano Lett. **8**, 3273 (2008)
4.63 C. Thelander et al., Materials Today **9**, Nr. 10, 28 (2006)
4.64 H. Ohnishi et al., Nature **395**, 780 (1998)
4.65 A.I. Yanson et al., Nature **395**, 783 (1998)
4.66 E. Scheer et al., Nature **394**, 154 (1998)
4.67 A. Yazdani et al., Science **272**, 1927 (1996)
4.68 J.C. Cuevas et al., Phys. Rev. Lett. **80**, 1066 (1998)
4.69 R. Landauer, Phil. Mag. **21**, 863 (1970)
4.70 A. Shik, Quantum Wells – *Physics and Electronics of Two-Dimensional Systems*, (World Scientific, Singapore, 1997)
4.71 H.L. Stormer et al., Rev. Mod. Phys. **71**(2), S298 (1999)
4.72 K. v. Klitzing et al., Phys. Rev. Lett. **45**, 494 (1980)
4.73 K. v. Klitzing et al., Phys. J. **4**(6), 37 (2005)
4.74 Y.Y. Wei et al., Phys. Rev. Lett. **81**, 1674 (1998)
4.75 D.C. Tsui et al., Phys. Rev. Lett. **48**, 1559 (1982)
4.76 R.B. Laughlin, Phys. Rev. Lett. **50**, 1395 (1983)
4.77 S. Das Sarma, A. Pinczuk, Eds., *Perspectives of Quantum Hall Effects*, Wiley, New York (1997)
4.78 A.D. Mirlin, P. Wölfle, Nachrichten Forschungszentrum Karlsruh. **31**, 94 (1999)
4.79 J.K. Jain, Physics Today, April 2000, p. 39
4.80 A. Ohtomo, H.Y. Hwang, Nature **427**, 423 (2004)
4.81 J. Mannhart et al., MRS Bull. **33**, 1027 (2008)

4.82 T. Kamiya, M. Kawasaki, MRS Bull. **33**, 1061 (2008)
4.83 J. Heber, Nature **459**, 28 (2009)
4.84 A. Tsukazaki et al., Science **315**, 1388 (2007)
4.85 N. Reyren et al., Science **317**, 1196 (2007)
4.86 A. Brinkmann et al., Nature Mater. **6**, 493 (2007)
4.87 C. Cen et al., Science **323**, 1026 (2009)
4.88 M. Sing et al., Phys. Rev. Lett. **102**, 176805 (2009)
4.89 M.P. Warusawithana et al., Science **324**, 367 (2009)
4.90 V.L. Berezinski, Zh. Eksp. Teor. Fiz. **61**, 1144 (1971)
4.91 J.M. Kosterlitz, D.J. Thouless, J. Phys. C **5**, L124 (1972)
4.92 A.D. Caviglia et al., Nature **456**, 624 (2008)
4.93 D.H.A. Blank, G. Rijnders, Nat. Nanotech. **4**, 279 (2009)
4.94 S. Yulin et al., Photonik 2/2008, p. 48
4.95 S. Yulin et al., Sixth Int. Conf. on the Physics of x-ray Multilayer Structures (Chamonix, France, 2002)

Chapter 5
Carbon Nanostructures – Tubes, Graphene, Fullerenes, Wave-Particle Duality

The discoveries of the carbon nanostructures, such as the 0D fullerenes [5.1] and their mass production [5.2], the 1D carbon nanotubes [5.3], and 2D graphene [5.4] substantially contributed to the fast development of nanoscience. More than 1,000 PhDs have been awarded for research on carbon nanotubes alone [5.5]. However, the carbon nanostructures have emerged as likely candidates for a wide range of applications, driving research into novel techniques for synthesizing these nanostructures. In this chapter we will first discuss carbon nanotubes, then graphene layers which have been studied only recently, and finally fullerenes such as C_{60} and similar molecular structures with a brief summary of the limits of wave-particle duality studied with fullerene nanoparticles.

5.1 Nanotubes

Here, we first will resume a few synthesis techniques, then discuss some other 1D carbon nanostructures in order to proceed to nanotubes of other layered materials. After that an overview of the properties will be given, followed by field emission phenomena, field effect transistors, and some applications.

5.1.1 Synthesis of Carbon Nanotubes

Arc discharge in an inert gas is the technique where carbon nanotubes were found in the cathode deposit for the first time [5.3] (see also Sect. 3.8). When a graphite rod containing a metal catalyst (Fe, Co, etc.) is used as the anode with pure graphite as cathode, single-walled carbon nanotubes (SWNTs) are generated (see [5.6]). For the efficient production of multiwalled carbon nanotubes (MWNTs) a mixture of hydrogen and He or Ar is preferable. The smallest carbon nanotubes with a diameter of 0.3 nm observed up to now (see Fig. 5.1) are ascribed to an armchair (2,2) structure (see below) whereas the longest SWNTs are about 2 mm long [5.7]. Mass production of SWNTs by arc discharge has been achieved using Ni–Y catalyst in He [5.9].

H.-E. Schaefer, *Nanoscience*, DOI 10.1007/978-3-642-10559-3_5,

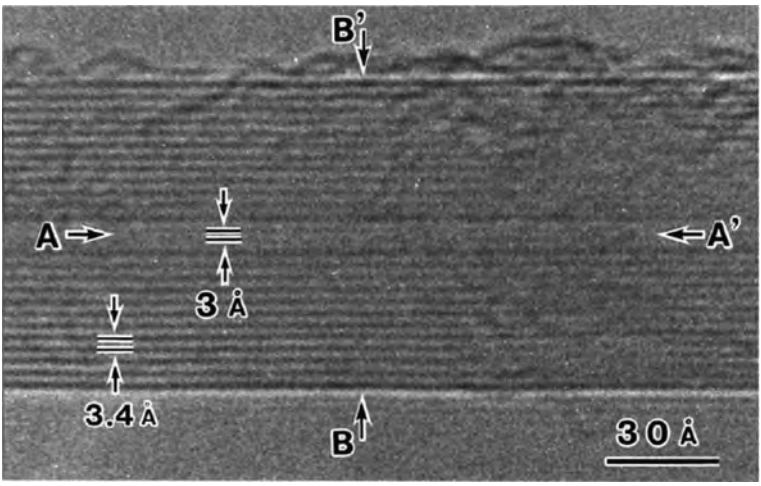

Fig. 5.1 High-resolution transmission electron micrograph of a 0.3 nm CNT inside a MWNT. The diameter of the 0.3 nm CNT and the 0.34 nm interlayer spacing of the MWNT are indicated. Each end is marked by the *horizontal arrows*, A and A′, and is capped by half a C_{12} cage containing two tetragons. (Reprinted with permission from [5.8]. © 2004 American Physical Society)

By means of the *laser-furnace method* (see [5.6]) high-quality SWNTs can be produced where the diameter can be controlled by the furnace temperature and the type of catalyst.

Chemical vapor deposition (CVD; see [5.6]) is a simple and economic technique for synthesizing carbon nanotubes at low temperatures and ambient pressure. By means of CVD and plasma-enhanced CVD (PECVD), in particular, arrays of CNTs for electronics can be fabricated [5.10] (Fig. 5.2). Carbon species catalytically decomposed from hydrocarbons are assumed to dissolve in the metal nanoparticles present and, after supersaturation, precipitate in the form of a fullerene dome extending into a carbon cylinder (Fig. 5.2). Formation of SWNTs (900–1,200°C) or MWNTs (600–900°C) is governed by temperature and the size of the metal catalyst nanoparticles (Fe, Co, Ni). High-purity vertically aligned carbon nanotubes can be produced in an atmospheric-pressure glow discharge [5.11].

The atomic processes of carbon nanofiber growth could be partially observed by in situ electron microscopy [5.12] (see also Sect. 2.6). Carbon nanofibers are shown to develop from methane decomposition through a reaction-induced reshaping of the catalyst nickel nanocrystals. Specifically, the nucleation and growth of graphene layers (Fig. 5.3) are found to be assisted by a dynamic formation and restructuring of monatomic step edges at the nickel surface. Density-functional theory indicates that the observations are consistent with a growth mechanism involving surface diffusion of carbon and nickel atoms.

Use of PECVD has allowed the growth of MWNTs at substrate temperatures as low as 120°C [5.13] and SWNTs were synthesized by CVD at temperatures as low as 350°C [5.14] where these low synthesis temperatures are particularly valuable

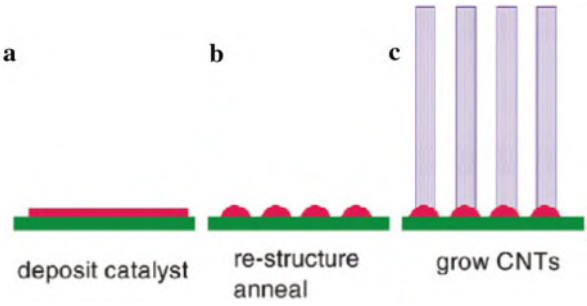

Fig. 5.2 Schematic of the three stages of CVD growth of CNTs. (**a**) Deposit of the catalyst; (**b**) restructuring the initial catalyst layer into nanoparticles under specified conditions; and (**c**) growing the nanotubes. (Reprinted with permission from [5.10]. © 2007 Elsevier)

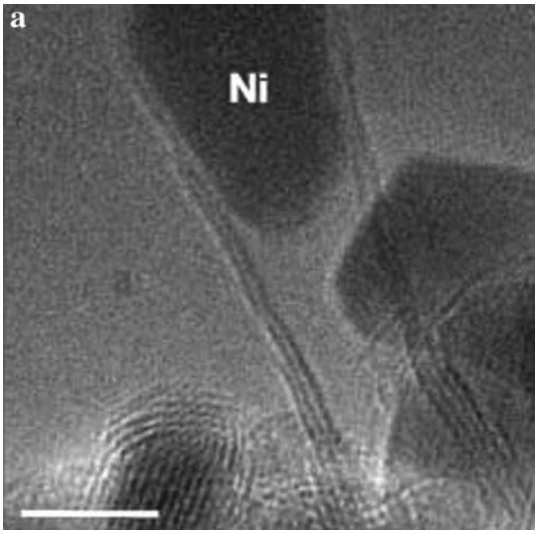

Fig. 5.3 Transmission electron micrograph (TEM) of a Ni catalyst and a carbon nanofiber growing from methane decomposition. TEM image showing a multiwalled tubular carbon nanofiber structure. Scale bar, 5 nm. (Reprinted with permission from [5.12]. © 2004 Nature Publishing Group)

for electronic applications. SWNT growth at these low temperatures can only occur because carbon rapidly diffuses over the surfaces of the metal catalyst particles and because of a restructuring of these surfaces at low temperatures [5.10].

MWNTs can be produced in few-kilogram quantities per hour [5.15] whereas 10 g of SWNTs are produced per day [5.16]. By B-doping (acceptors) or N-doping (donors) (see [5.17] the electronic and mechanical properties of carbon nanotubes can be substantially modified.

As most practical technologies require predictable and uniform performance of carbon nanotubes, strategies are sought for preparing samples of single-walled carbon nanotubes with well-defined diameters, lengths, chiralities, and electronic properties. Postsynthetic approaches for sorting single-walled carbon nanotubes have been developed [5.18] employing, e.g., chromatography (Fig. 5.4a). High-density arrays of aligned single-walled nanotubes (Fig. 5.4b) are grown that are almost entirely semiconducting [5.20].

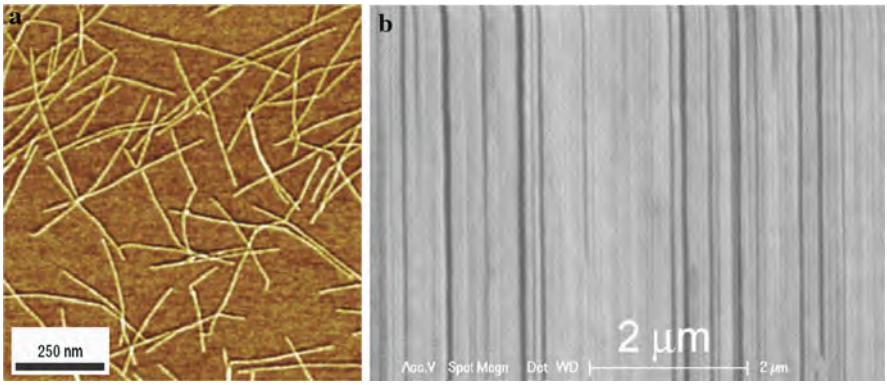

Fig. 5.4 (**a**) Chromatographic sorting of SWNTs. Sequential sorting of size exclusion chromatography and ion exchange chromatography results in SWNTs of uniform diameter and length as observed in this atomic force microscopy image [5.19]. (**b**) Scanning electron micrograph of aligned semiconducting SWNT arrays on quartz [5.21]. (Reprinted with permission from [5.19] (**a**) and [5.21] (**b**). © 2007 American Chemical Society (**a**) and © 2009 Elsevier (**b**))

5.1.2 Structure of Carbon Nanotubes

The structure of carbon nanotubes (CNTs) is formed by a seamless bending of a graphene sheet where each C atom is covalently bonded to its three neighbors and the fourth electron is smeared (sp^2 hybridization) over the entire structure. Three different structures "armchair," "zigzag," and "chiral" (see Fig. 5.5) can be discerned. The CNTs are characterized by the vector (n, m) which is given in terms of

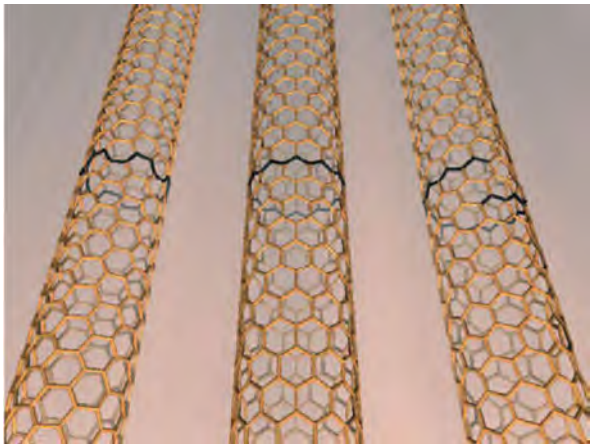

Fig. 5.5 The carbon nanotubes (CNTs) can be thought to be formed by seamless bending of graphene layers with triply coordinated C atoms. Three different types of CNTs can be differentiated as "armchair" (*left*), zigzag (*center*), and chiral (*right*). (Reprinted with permission from [5.22]. © 2004 Wiley-VCH)

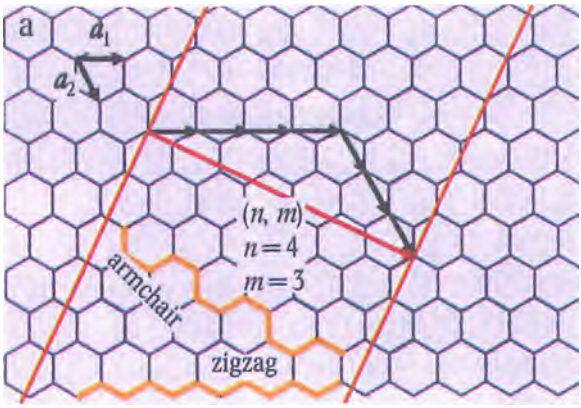

Fig. 5.6 The vector (n, m) perpendicular to the CNT axis, defined by the base vectors $\mathbf{a}_1$ and $\mathbf{a}_2$. (Reprinted with permission from [5.22]. © 2004 Wiley-VCH)

the base vectors $\mathbf{a}_1$ and $\mathbf{a}_2$ (see Fig. 5.6) where the magnitude of the vector is the circumference of the tube. The *(n, m)* indices can be determined experimentally by photoluminescence studies in conjunction with resonant Raman experiments. The $n = m$ tubes are of the armchair structure, whereas the $n = 0$ or $m = 0$ tubes are of the zigzag structure.

The phonon structure of SWNTs can be studied optically by using resonance Raman spectroscopy [5.23]. In Fig. 5.7 the Raman spectra from two isolated

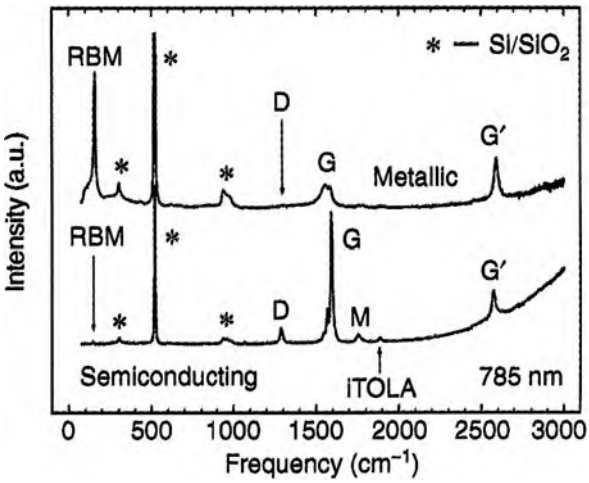

Fig. 5.7 Raman spectra from a metallic and from a semiconducting isolated SWNT on a Si/SiO_2 substrate obtained with a 785 nm laser excitation. The strong first-order features – the radial breathing mode (RBM) and the tangential G band-mode vibrations – are assigned in the spectra. The *D*, *M*, iTOLA, and G' features are modes activated by defects (*D*) or combination of two modes. The features with an *asterisk* originate from the Si/SiO_2 substrate. (Reprinted with permission from [5.23]. © 2004 Materials Research Society)

SWNTs show features of the radial breathing mode (RBM) where all C atoms vibrate radially and the graphite-like G band mode characteristic for tangential vibrations. The RBM frequency ω can be used for measuring the tube diameter d_t making use of the relationship $\omega = \alpha/d_t$. The G mode is different for metallic and semiconducting SWNTs due to the presence of plasmons in metallic SWNTs which couple to phonons (see [5.23]).

5.1.3 Electronic Properties of Carbon Nanotubes

It is often stated that one-third of single-walled carbon nanotubes are metallic (see [5.24]), which means there should not be an energy gap between their valence and conduction bands. However, in samples of ultraclean carbon nanotubes that should, according to theory, be metallic, an appreciable band gap has been observed [5.25]. This shows that all pure undoped carbon nanotubes are actually insulators. The gap is assigned [5.25] to an insulating state first proposed by Mott [5.26]. The Mott metal–insulator transition is a quantum-phase transition (see [5.24]). It occurs when the Coulomb interactions of the electrons overwhelm the total kinetic energy of the electron gas and then the system becomes a Mott insulator. Taking into account the effect of electron–electron interactions, the metallic state in armchair nanotubes was predicted [5.27] to be unstable for small diameters and that the ground state would instead be a Mott insulator – a prediction that has been confirmed experimentally [5.25]. This shows that carbon nanotubes offer another way of exploring electron correlation phenomena and quantum-phase transitions in quasi-1D systems (see [5.24]). The interesting electrical properties of CNTs are due in large part to the peculiar electronic structure of graphene (see, e.g., [5.28]). In going from graphene to a CNT, additional quantization arises from electron confinement around the CNT circumference. As a result, each graphene band splits into a number of sub-bands. These allowed energy states are cuts of the graphene band structure.

In contrast to metals with a ∼40 nm free path of charge carriers, CNTs exhibit values of several micrometers. This is due to the 1D confinement of electrons, which allows motion only along the tube. This constraint, along with energy and momentum conservation, severely reduces the phase space for scattering. Without scattering at defects and with low electron–phonon interaction, extremely high current densities up to 10^{10} A/cm^2 can be achieved. Metallic SWNTs have a Fermi velocity $v_F = 8 \times 10^5$m/s that is comparable to typical metals [5.29] and a room temperature resistivity of $\rho \approx 10^{-6}\,\Omega\,\mathrm{cm}$ even outperforming the room temperature resistivity of Cu [5.29]. For the thermal conductivity values of $\sim 6000\,\mathrm{W/(Km)}$ and for the piezoelectric strain ($\Delta l/l$) a value of 0.11% at 1 V has been reported [5.22].

Semiconducting SWNTs with the diameter d_t (in nanometers) have a band gap of $E_g = 2\gamma_0 a_{C-C}/d_t = 0.9\,\mathrm{eV}/d_t$ increasing with decreasing d_t where γ_0 is the nearest neighbor overlap integral and a_{C-C} the nearest neighbor spacing of carbon

atoms. Electron and hole effective masses m^* decrease with increasing d_t [5.28]. Hole mobilities as high as $20,000\ \mathrm{cm}^2/\mathrm{V\,s}$ have been reported [5.30].

The semiconducting properties of carbon nanotubes have also attracted much interest because due to their small dimensions these structures could lead to conceptually new miniaturized strategies in electronics and computer industries. The use of individual molecules as functional electronic devices was first proposed in the 1970s [5.31].

Quasi-1D excitons (electron–hole pairs) are known to be the primary photoexcitations in carbon nanotubes (see [5.32]). The electron–hole distance or correlation length, ξ_e, is of relevance for the understanding of optical, optoelectronic, and photonic properties of CNTs. From femtosecond laser spectroscopy [5.32] on CNTs the exciton size is estimated to be 2.0 ± 0.7 nm in good agreement with theoretical studies.

Advances in nanotechnology resulted in achieving electrical contacts to nanotubes and in manufacturing a field-effect transistor (FET) at ambient temperatures [5.33], a three-terminal switching device that consists of one semiconducting single-wall carbon nanotube connected to two metal electrodes. By applying a gate electrode, the nanotube can be switched from a conducting to an insulating state. In Fig. 5.8a FET device of a single- or multiwalled carbon nanotube with Au contacts and a gate electrode is shown. As demonstrated in Fig. 5.9 the source-drain current decreases strongly (by five orders of magnitude) with increasing positive gate voltage. This is evidence for a FET behavior and transport through positive carriers (holes). The doping with acceptors may be a result of the nanotube processing. In order to maximize device performance, the tube gate capacitance C_g should be maximized. This can be achieved by a thin layer of a high-κ dielectric material such as ZrO_2 [5.35]. The excellent electrical characteristics of the nanotube FET may be described by the transductance with a maximum value of $dI/dV_G = 12\,\mu\mathrm{A/V}$ at $V_G = 0.4\,\mathrm{V}$. Normalizing this to a device width $2d \approx 4\,\mathrm{nm}$ [5.29] gives a transductance per unit width of $3\ \mathrm{mS}/\mu\mathrm{m}$ which is significantly better than in current-generation MOSFETs [5.29].

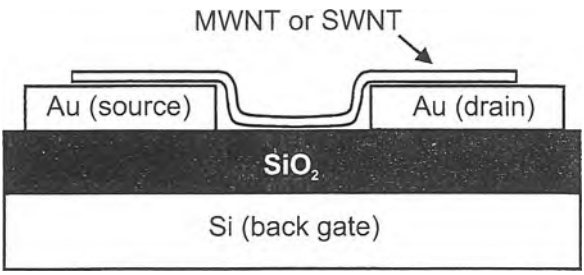

Fig. 5.8 Schematic cross section of a FET device. A single nanotube (NT) of either SWNT- or MWNT-type bridges the gap between two gold electrodes. The Si substrate is used as backgate. (Reprinted with permission from [5.34]. © 1998 American Institute of Physics)

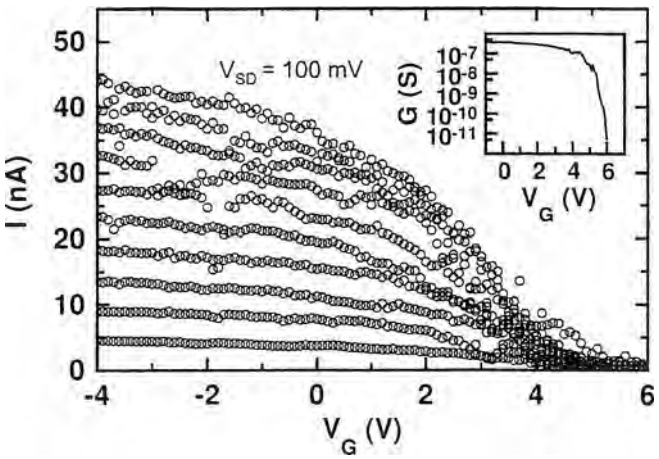

Fig. 5.9 Output and transfer characteristics of a field-effect transistor of a single-walled carbon nanotube (SWNT–FET). $I - V_G$ curves for $V_{SD} = 10 - 100$ mV in steps of 10 mV. The *inset* shows that the gate modulates the conductance by five orders of magnitude ($V_{SD} = 10$ mV). (Reprinted with permission from [5.34]. © 1998 American Institute of Physics)

The electronic wave functions that correspond to quantized energy levels in short metallic carbon nanotubes were observed by scanning tunneling microscopy (STM) [5.36]. Limiting the length of a carbon nanotube leads to a "particle-in-a-box" quantization of the energy levels. The electron wave functions corresponding to these discrete states can in principle be imaged by STM. A 30-nm long single-walled metallic carbon nanotube with an "armchair" structure determined by STM (see Fig. 5.10) and 1.4 nm diameter was prepared on a Au (111) substrate at 4.2 K. Steps in the *I–V* curves (see Fig. 5.11) correspond to the quantized electronic energy levels. The plateau width is determined by the total energy-level spacing plus single electron charging energy to add an electron to the tube.

The height of the dI/dV peaks (see Fig. 5.11b) varies with the position x along the tube axis with a period ~0.4 nm which clearly differs from the lattice constant

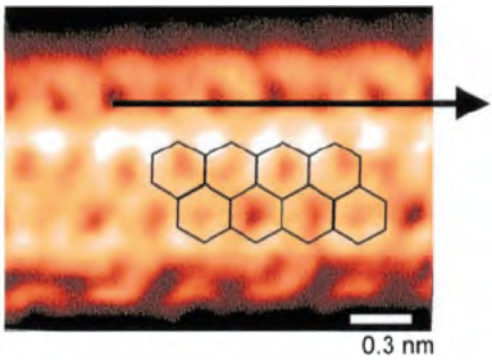

Fig. 5.10 Atomically resolved STM image of an armchair nanotube with the arrow in the direction of the tube axis and a tube diameter of 1.3 nm. Feedback parameters are $V = 0.1$ V, $I = 20$ pA with images taken in constant current mode. (Reprinted with permission from [5.36]. © 1999 AAAS)

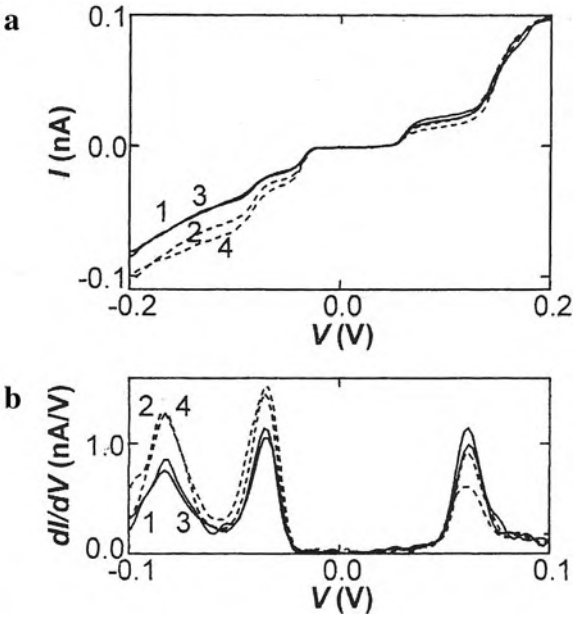

Fig. 5.11 Scanning tunneling microscopy (STM) spectroscopy measurements on a 30-nm long armchair tube. (**a**) *I–V* characteristics of the tube shown in Fig. 5.10, taken at positions about 0.18 nm apart on a straight line along the tube axis. Current steps correspond to discrete energy states. *Dashed curves*, maximum values; *solid curves*, minimum values. (**b**) Differential conductance *dI/dV* versus *V* calculated from *I* to *V* curves. Peaks appear at the voltage positions of current steps in the *I–V* curves. The data points 1–4 indicate the positions along the tube at which the four *I–V* curves plotted in (**a**) and the *dI/dV* curves in (**b**) were obtained. (Reprinted with permission from [5.36].© 1999 AAAS)

of 0.25 nm. The quantity dI/dV is a measure of the squared amplitude of the quantized electron wave function $|\psi(E,x)|^2$. The separation of 0.4 nm between the peaks corresponds to half the wavelength λ because dI/dV measures the square of the wave function. The wavelengths obtained from a fitting procedure vary from 0.66 to 0.76 nm.

The discrete levels are probed at energies near the Fermi energy E_F and therefore the wavelength of the electron waves is close to the Fermi wavelength λ_F. The experimentally observed wavelengths [5.36] correspond well to the theoretical values confirming the predicted band structure with two linear bands crossing near E_F [5.36]. This result provides quantitative evidence for the interpretation of the oscillations of dI/dV in terms of wave functions of discrete electron states. A short carbon nanotube therefore resembles the textbook model for a particle in a 1D box.

Orbital magnetic moments μ_{orb}, along the CNT axis, that are much larger than the Bohr magneton μ_B (the magnetic moment of an electron due to its spin) are predicted for electron states near the energy gap in carbon nanotubes [5.37]. This large moment is due to the motion of electrons around the circumference of the

nanotube and is thought to play a role in the magnetic susceptibility of CNTs and in the magneto-resistance observed in MWNTs (see [5.38]). It has been shown experimentally that the orbital magnetic moment μ_{orb} for an electron traversing the waistline of a nanotube is exactly what is predicted. It scales with the tube diameter and is 10–20 times larger than that for an electron in an atom – consistent with the difference in their diameters [5.38].

In addition to the transistor behavior of nanodevices, spin-electronics may play a role for the development of future devices. From the injection of spin-polarized electrons from ferromagnetic Co contacts into multiwalled carbon nanotubes, direct evidence for coherent transport of electron spins has been derived with an estimate of the spin-flip scattering length in carbon nanotubes to be at least 130 nm [5.39, 5.40]. This is derived from a hysteretic magneto-resistance effect which is attributed to spin-polarized injection between the ferromagnetic contacts and the MWNT [5.39].

In CNTs the *Aharonov–Bohm effect* has been observed [5.41, 5.42]. When electrons pass through a cylindrical conductor in an axial magnetic field, their wave-like nature yields a periodic oscillation in the electrical resistance in dependence of the enclosed magnetic flux. This phenomenon reflects the dependence of the phase of the electron wave on the magnetic field, the so-called Aharonov–Bohm effect [5.43]. This causes a phase difference and, therefore, an interference between partial waves encircling the conductor in opposite directions. Magneto-resistance measurements on individual multiwalled carbon nanotubes exhibit pronounced oscillations of the resistance in dependence of the magnetic field [5.41] in good agreement with theoretical predictions for the Aharonov–Bohm effect in a hollow conductor with the diameter of the outermost shell of the nanotubes.

Superconductivity in 1D systems as CNTs may be obstructed by Tomonaga–Luttinger liquid (TLL; see Sect. 1.3) states due to repulsive electron–electron (e–e) interaction, by charge–density waves (Peierls transition), and by a small density of states (see [5.44]). However, since the interplay between TLL states and superconductivity in CNTs is highly sensitive to strong electron–phonon (e–p) coupling, to the phonon modes, and to the structure of CNT ropes, the appearance of superconductivity may be permitted in specific cases [5.44]. Proximity-induced superconductivity was observed in Nb/MWNT/Al junctions [5.45] which showed that Cooper pairs can be efficiently transported through the interface of the CNT/metal junctions. Recently it was demonstrated that multiwalled carbon nanotubes (MWNTs) exhibit type II superconductivity with a transition temperature $T_c = 12$ K (see Fig. 5.12), a superconducting gap of $\Delta \approx 1.15$ meV, and a magnetic penetration length estimated to be >10 nm. The measurements suggest that the competition of the TLL states and superconductivity is strongly associated with the number N of electrically active shells of the MWNTs and that intershell effects play a key role in the emergence of superconductivity in the MWNTs [5.44].

Nuclear magnetism and electronic order in ^{13}C nanotubes. The physics of conduction electrons interacting with localized magnetic moments is central for a number of fields in condensed matter such as nuclear magnetism, heavy fermions, or ferromagnetic semiconductors (see [5.46]). Electron–electron interactions are most

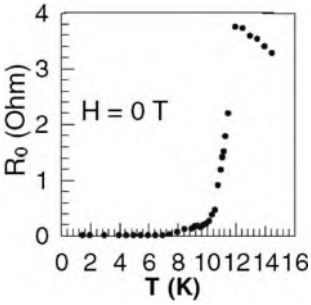

Fig. 5.12 Zero-bias resistance R_0 of MWNTs as a function of temperature at zero magnetic field. (Reprinted with permission from [5.44]. © 2006 American Physical Society)

important in 1D systems such as metallic single-wall carbon nanotubes (SWNTs) where they lead to Luttinger liquid physics (see [5.46]). Calculations performed for SWNTs made of ^{13}C demonstrate that even a weak hyperfine interaction can lead to a helical ferromagnetic order of the ^{13}C nuclear spins coexisting with an electron density order that combines charge and spin degrees of freedom [5.46]. The ordered phases stabilize each other up into the millikelvin range.

5.1.4 Heteronanocontacts Between Carbon Nanotubes and Metals

Heterojunctions between different materials are of increasing interest in nanotechnology. Junctions between carbon nanotubes (CNTs) and metals or semiconducting nanowires are desirable to exploit the excellent electronic and mechanical properties of CNTs. In electronic devices making use of CNTs, metallic electrodes need to be established to link the nanotubes with each other and the periphery. Many studies indicate that the properties of such a device are dominated by the electronic behavior at the nanotube–metal contact (see [5.47]). In some studies the interconnections between metal electrodes and multiwall carbon nanotubes (MWNTs) occurred only with the outermost wall of the MWNTs. By controlling the nanotube–metal heterojunction formation in an electron microscope with lattice resolution imaging, it is demonstrated [5.47] that the metal can be strongly bonded to all layers of a MWNT. Two MWNT segments can be joined by a short transition metal nanowire and the atomistic details of the interfaces are elucidated by density-functional theory (DFT) calculations [5.47].

5.1.5 Optoelectronic Properties of Carbon Nanotubes

Semiconducting CNTs are, unlike Si, direct-gap materials; this, along with the 1D confinement, makes them promising candidates for optoelectronic applications. The electron–electron and electron–hole interactions, which should be particularly strong in a 1D system [5.48], give rise to a strong binding of the photoexcited electron and hole states and the formation of Wannier-like excitons [5.49].

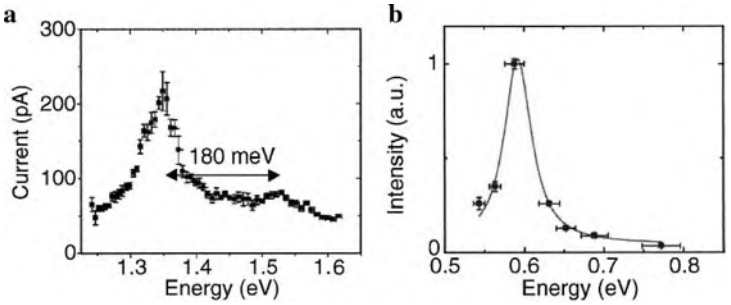

Fig. 5.13 (**a**) Photoconductivity spectrum of a single CNT. The main peak arises from the excitation of the second exciton state of the CNT, while the side band involves the additional excitation of one quantum of the C–C stretching optical phonon mode. (**b**) Electroluminescence spectrum of a long single CNT. (Reprinted with permission from [5.28]. © 2004 Materials Research Society)

For optoelectronic applications, electrically driven CNT light-emitting devices and light detectors are desirable. Photocurrents (Fig. 5.13a) from individual CNTs in a CNT–FET were reported [5.50]. Thus, CNT–FETs can act as efficient light detectors with the additional capability of polarization detection.

CNT–FETs can also be used to produce a gate-controlled light source [5.51] with the light emission generated by the radiative recombination of electrons and holes (Fig. 5.13b). Spatially resolved studies of the light emission provides insight into the electrical transport processes in a CNT and can identify local sources of e–h pair creation [5.28].

Photoluminescence quantum yields of SWNTs can be quenched by sidewall chemisorption of oxygen. A coverage of SWNTs by an aliphatic (docecyl) analog of flavin mononucleotide, FC12, is sufficiently tight to exclude oxygen from the SWNT surface, which leads to quantum yields as high as 20% [5.52].

5.1.6 Thermal Properties of Carbon Nanotubes

Individual nanoscale systems can be studied up to extreme temperatures in the transmission electron microscope (TEM) [5.53]. Multiwall carbon nanotubes (MWNTs) turn out to be stable up to 3,200 K, a record for carbon-based materials and better than diamond or graphite. The nanotubes are exceptional electrical and thermal conductors even at extreme temperatures. Even just prior to failure, MWNTs retain 10% of their peak thermal conductivity and carry a current of 1.7×10^8 A/cm^2 [5.53].

5.1.7 Mechanical Properties of Carbon Nanotubes

Carbon nanotubes exhibit outstanding mechanical properties with a Young's modulus of 3.7×10^{12} Pa [5.54] by about a factor of 5 higher than for carbon fibers and

only slightly below theoretical predictions of 5 TPa [5.55]. A composite of SWNTs and polyvinyl alcohol with a tensile strength of 1.8 GPa is tougher than any natural or synthetic fiber described so far [5.56]. This toughness results from a high strength and a high strain to failure. The toughness may be due to chain extension in the amorphous polyvinyl alcohol and the slipping of nanotubes within bundles. Although the 80 GPa Young's modulus is more than an order of magnitude less than that of SWNTs but, normalized for density, it is more than twice the value of a steel wire (see [5.56]).

Due to these high modulus values, CNTs are envisaged for ultrahigh strength lightweight composite materials (see Sect. 6.9). Due to their high elasticity and strength, carbon nanotubes can be reversibly bent strongly to buckle and form kinks [5.57]. By bending or twisting (Fig. 5.14) the CNTs, a strong increase of the electrical resistance is expected.

The tensile rupture of CNTs has been studied [5.59] and the plastic deformation has been investigated theoretically by tight binding and ab initio molecular dynamics studies [5.60]. They demonstrate that a "transverse" tension applied perpendicularly to a C–C bond, as in a tensile strain to an armchair tube, gives rise to a ductile deformation. In contrast to that a "longitudinal" tension in parallel to the C–C bond as in tensile strain to a zigzag tube leads to a brittle rupture. The transverse tension finds a natural release in the rotation of the C–C bond perpendicular to it (the so-called Stone–Wales transformation [5.61] which produces two pentagons and two heptagons coupled in pairs (5-7-7-5) (Fig. 5.15). The appearance of the (5-7-7-5) defect can be interpreted as the nucleation of a dislocation loop in the planar hexagonal network of the graphene sheet. Once nucleated, the (5-7-7-5) can further relax by separating the two dislocation cores which glide through successive Stone–Wales bond rotations. This corresponds to a flow of dislocations on spiral glide planes (Fig. 5.15) and gives rise to a ductile behavior with the final creation of higher order rings whose extensions lead to a brittle fracture of the tube. Tubes with $n, m \leq 14$ are calculated to be completely ductile while larger tubes are moderately or completely brittle.

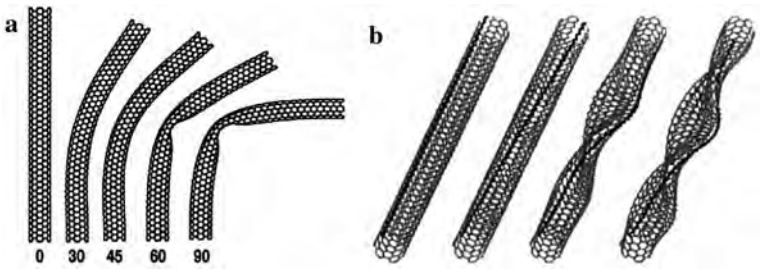

Fig. 5.14 (**a**) Computed structures of isolated bent carbon nanotubes with the indices referring to the bending angles (in degrees). (**b**) Relaxed nanotube structures upon twisting. (Reprinted with permission from [5.58]. © 1999 American Physical Society)

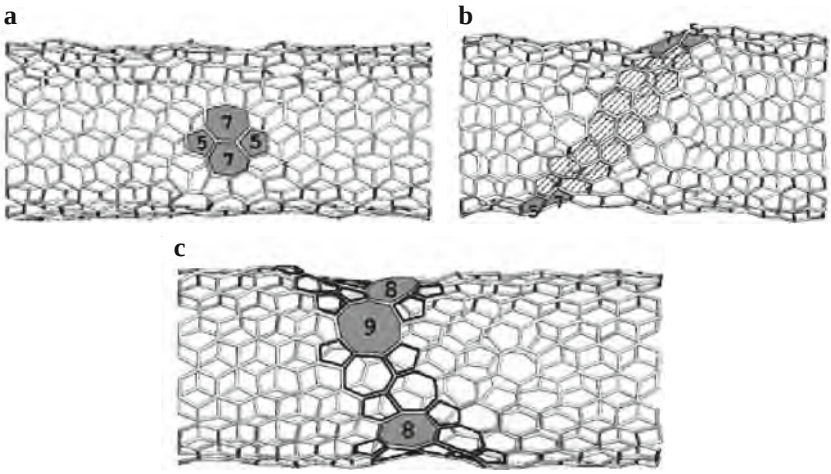

Fig. 5.15 Snap-shots of a molecular dynamics simulation of a (10,10) carbon nanotube under axial tension. (**a**) Formation of a Stone–Wales defect at $T = 2{,}000$ K and 10% strain; (**b**) plastic behavior at $T = 3{,}000$ K and 3% strain. The *shaded area* indicates the migration path of the (5–7) edge dislocation; (**c**) nucleation of large open rings and initiation of the brittle failure at $T = 1{,}300$ K and 15% strain. (Reprinted with permission from [5.60]. © 1996 American Physical Society)

Although in many calculations carbon nanotubes display some plastic-like behavior, recent experiments suggest [5.62] that nanotubes behave like brittle materials.

Enhanced ductile behavior of tensile-elongated individual carbon nanotubes is found at high temperatures [5.63]. Single-walled carbon nanotubes (SWNTs) become superplastic and can accommodate extremely large plastic strains to 280% (see [5.63]). Double-walled (DWNTs; see Fig. 5.16) and triple-walled carbon nanotubes (TWNTs) exhibit above 2000°C tensile elongations of 190% and diameter reduction of 90%. This superelongation is attributed to a high-temperature creep deformation mechanism mediated by atom or vacancy diffusion, dislocation climb, and kink motion at high temperatures [5.63].

Enormous pressures can be produced by carbon nanotubes on enclosed crystals when the tubes are irradiated by high-energy electrons at elevated temperatures in an electron microscope (Fig. 5.17). This high pressure originates from radiation-induced vacancies which anneal out and lead to a reconstruction of the lattice [5.65, 5.66] reducing the surface area and generating local tension in the graphene sheet. The pressures exceeding 40 GPa inside the CNT initiate the extrusion and final cutting of an enclosed Fe_3C crystal (see Fig. 5.17). The pressures thus generated in the nanotubes are only an order of magnitude below the pressure in the center of the Earth (∼360 GPa) or the highest pressures achieved in a diamond anvil cell (∼400 GPa).

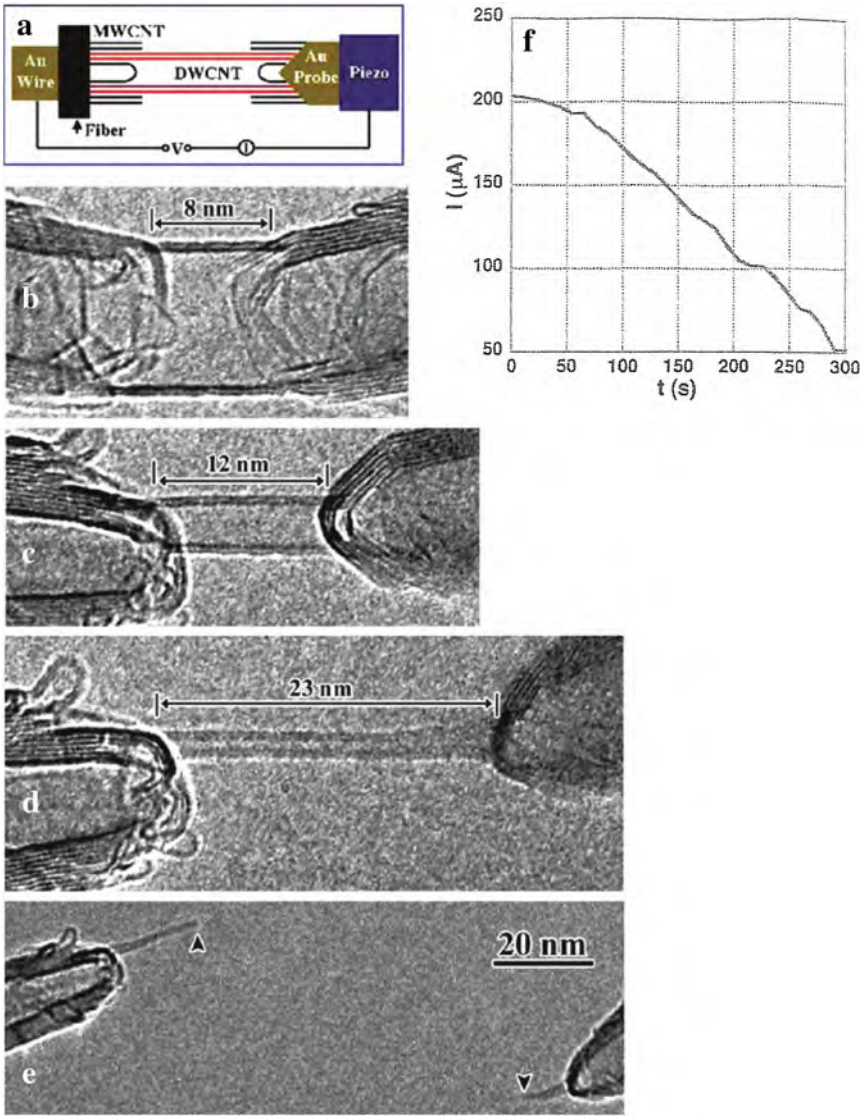

Fig. 5.16 Tensile elongation (190%) of a double-walled carbon nanotube (DWNT). (**a**) Experimental setup. A dog-bone-shaped sample was produced by electric break down of a multiwalled carbon nanotube (MWCT). (**b–e**) Sequential high-resolution transmission electron micrographs (HRTEM) showing the tensile elongation of a DWNT. In (**e**) the nanotube is broken near the middle (*arrowheads*). (**f**) Current (*I*) versus time (*t*) plot for the same DWNT as in (**b–d**). (Reprinted with permission from [5.63]. © 2007 American Physical Society)

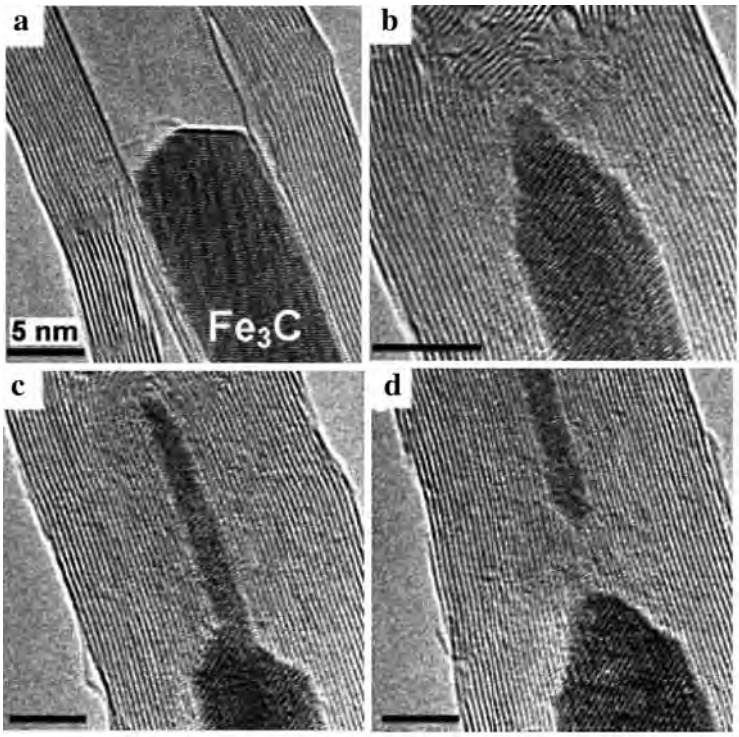

Fig. 5.17 Shrinkage of a MWNT partly filled with a Fe_3C nanowire under irradiation with an electron beam (60 nm in diameter and 200–400 A/cm^2 in intensity) for 50 min at 600°C. (**a**) Tube before irradiation. (**b**, **c**) Irradiation leads to a collapse of the tube and deformation of the Fe_3C crystal. (**d**) The collapsing tube cuts off the thinned Fe_3C crystal. Scale bars, 5 nm. (Reprinted with permission from [5.64]. © 2006 AAAS)

5.1.8 Carbon Nanotubes as Nanoprobes and Nanotweezers in Physics, Chemistry, and Biology

Carbon nanotubes can be employed as ultrafine nanoprobes in atomic force microscopes (AFM) [5.67] or scanning tunneling microscopes (STM) for high-resolution imaging of sharp recesses in surface topography [5.68], as chemically or biologically sensitive probes [5.69] or as nanotweezers for grabbing and manipulating nanoparticles [5.70]. This is due to the slenderness, the flexibility, the robustness, and the electrical conductivity of carbon nanotubes.

For application in an AFM [5.68], multiwalled nanotubes (MWNTs) were bonded to a conventional Si cantilever. This allows the nanotube to bend away from its connection whenever the tip is inadvertently "crashed" into a hard surface and then to snap back to its original straight position when the tip is withdrawn. The buckling, therefore, serves as an insurance policy during AFM imaging.

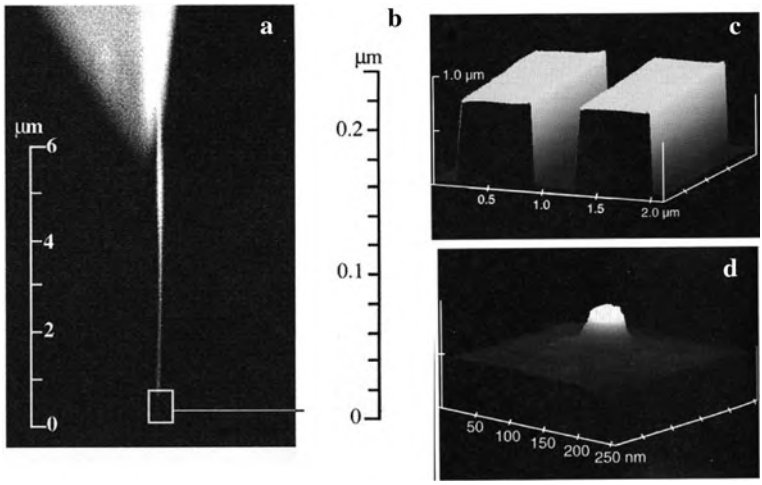

Fig. 5.18 Single nanotube (MWNT; ca. 10 nm in diameter, 1 µm long) attached to the pyramidal tip of a silicon cantilever for atomic force microscopy (AFM). The multiwalled carbon nanotube was attached to the Si tip with an acrylic adhesive. (**a**) Scanning electron microscope (SEM) image of the MWNT attached to the Si pyramid. (**b**) TEM image of the MWNT tip; scale bar, 20 nm.(c) Tapping-mode AFM image of a deep trench etched through a TiN-coated Al film on a Si wafer. Image taken with a nanotube attached to the Si pyramid of (**a**). (**d**) Tapping-mode AFM image of a 40 nm diameter, 30 nm high carbon cluster formed on the bottom of the trench by applying a –5 V pulse to the nanotube. (Reprinted with permission from [5.68]. © 1996 Nature Publishing Group)

As shown in Fig. 5.18c, d the long, narrow MWNT tips can reach into deep trenches previously inaccessible to high-resolution scanning probes permitting even a carbon dot at the bottom to be imaged.

One of the principle limits of the AFM technique in air has been the surface coverage with a layer of water giving rise to relative high-capillary adhesive forces of 10–100 µN when the conventional tip makes contact. Owing to the small diameter of the nanotube the capillary adhesion forces are reduced to 0.05–5 nN permitting tapping-mode imaging with cantilevers having force constants as small as 0.01 N/m at a peak-to-peak amplitude of 10 nm. Employing the nanotube probe, imaging under water is feasible as the frequency dependence of the cantilever oscillation is only slightly affected when only the end of the nanotube is immersed, e.g., in a trench. According to their electrical conductivity, MWNTs can also be used for scanning tunneling microscopy, e.g., in order to image charge–density waves [5.71].

Used either bare or with chemical derivatization, thin SWNTs were suggested as good candidates for an ultimate chemical nanoprobe. Nanotubes with acidic or basic functionalities or additional biomolecular probes offer in combination with AFM techniques the capability of chemical and biological discrimination on a nanometer scale [5.69]. Thus, nanotubes with carboxyl (COOH) groups at the open-tip ends were used as AFM tips to titrate acid and base groups on a substrate, to image patterned samples based on molecular interaction, and to measure the binding force

between single protein–ligand pairs [5.69] yielding potential applications in chemistry and biology. In these experiments carboxyl (COOH) functional groups are attached to the nanotube tip with a coupling of amines (RNH_2 with $R = CH_2C_6H_5$ or $R = CH_2CH_2NH_2$) to this carboxyl group. This enables further attachment of amide-linked groups (see Fig. 5.19a) yielding a broad applicability to aqueous and non-aqueous chemistry.

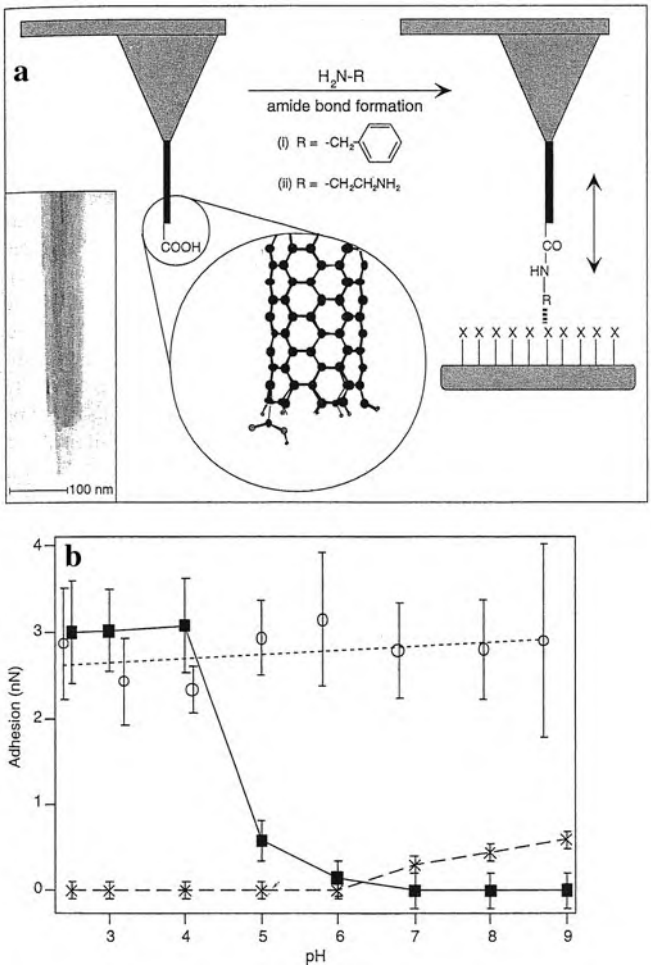

Fig. 5.19 Preparation and characterization of functionalized carbon nanotube tips. (**a**) Modification of a nanotube tip by coupling an amine (RNH_2) to a pendant carboxyl group and the application of this probe to sense specific interactions with functional groups (X) of a substrate. *Inset*: TEM image of the open end of a shortened nanotube tip. (b) Adhesion force as a function of pH between the nanotube tips and an OH-terminated self-assembled monolayer (11-thioundecanol on Au-coated mica): *filled squares*, COOH tips (unmodified) showing a characteristic drop with pH variation; *open circles*, phenyl-modified tip; and *crosses* amine-modified tip. (Reprinted with permission from [5.69]. © 1996 Nature Publishing Group)

The presence of COOH groups at the very nanotube tip ends [5.69] can be tested by measuring the adhesion force to a substrate with varying pH with a drop at pH = 4.5 (see Fig. 5.19b) which is known (see [5.69]) to be characteristic of the deprotonation of carboxyl acid. A lateral resolution of 3.3 nm for separating adjacent chemically distinct regions can be achieved [5.72].

Covalently modified nanotube tips also offer the possibility of probing biological systems at the nanometer scale shown in the ligand–receptor interaction of biotin–streptavidin, where the biotin ligand (see triangle in Fig. 5.20a) was covalently linked to the nanotube tip by the formation of an amide bond. Force versus displacement measurements (see Fig. 5.20b) made on mica surfaces containing the immobilized protein streptavidin show well-defined binding force effects of $F_b \approx$ 200 pN per biotin–streptavidin pair (see Fig. 5.20c). The observed binding force is specific for the biotin–streptavidin interaction because no adhesion is measured in control experiments when the receptor sites are blocked or when the nanotube tip is unmodified. These results may lead to a high-resolution mapping of the binding domains of, e.g., proteins and membranes.

In the above discussion the problem remains that a single tip cannot grab an object. This problem has been solved by the preparation of nanotweezers [5.70] making use of electrically conducting and mechanically robust carbon nanotubes attached to independent electrodes fabricated on pulled glass micropipettes (see Fig. 5.21). Voltages applied to the electrodes close and open the free ends of the nanotubes and this electromechanical response can be understood quantitatively making use of the known nanotube properties [5.70]. Free-standing electrically independent electrodes were deposited onto tapered glass micropipettes, which can be routinely drawn with end diameters of 100 nm. The carbon nanotubes (4 μm long, 50 nm thick) are fixed to the Au electrodes by an adhesive [5.68]. By applying a voltage to the electrodes the ends of the nanotubes bend to each other elastically performing the tweezer action. By this tweezer action nanoscale objects can be grabbed as shown in Fig. 5.21c for a SiC nanocluster or a GaAs nanowire. In addition, with the electrically conducting nanotubes the *I–V* behavior of the grabbed object can be tested as demonstrated by Fig. 5.21c.

5.1.9 Other Tubular 1D Carbon Nanostructures

A variety of tubular carbon nanostructures of different shape such as peapods, CNT rings, coiled CNTs, tubular graphite cones, or CNTs with amorphous beads were developed for potential applications in nanoelectronics and nanomechanics. Carbon peapods are CNTs containing fullerene C_{60} molecules [5.73] (see Fig. 5.22a). Rings of CNTs with an average diameter of 540 nm (see Fig. 5.22b) were synthesized by closing the oxygen-containing tube ends by means of a 1,3 dicyclohexyl carbodiimide (DCC) reaction. Coils of CNTs (see Fig. 5.22c) were grown in a CVD process

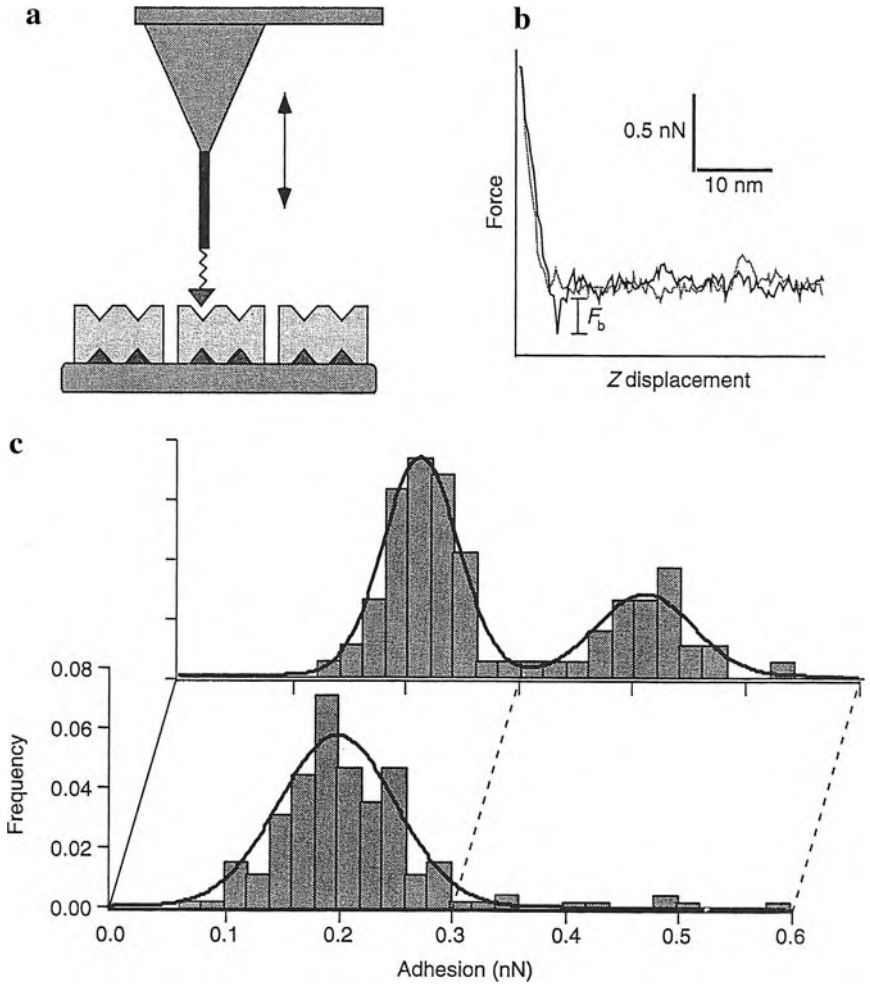

Fig. 5.20 Ligand-derivatized nanotube tips as biological probes. (**a**) Sketch of a nanotube tip covalently modified with a biotin ligand (*dark-gray triangle*) interacting with a streptavidin protein receptor (*light gray blocks*); the receptors are linked to the surface by biotin groups. Force versus displacement curve recorded with a biotin-modified nanotube tip on a streptavidin surface in pH 7.0 with the binding force F_b. (**c**) Adhesion *histograms* representing 200–400 force–displacement curves obtained from two separate biotinylated nanotube tips on streptavidin-derivatized surfaces. One tip showed a single peak centered at 200 pN that corresponds to the unbinding of a single biotin–streptavidin ligand–receptor complex. The other tip exhibited a bimodal distribution peak at 200 and 400 pN that corresponds to an unbinding of two biotin–streptavidin complexes, respectively. (Reprinted with permission from [5.69]. © 1996 Nature Publishing Group)

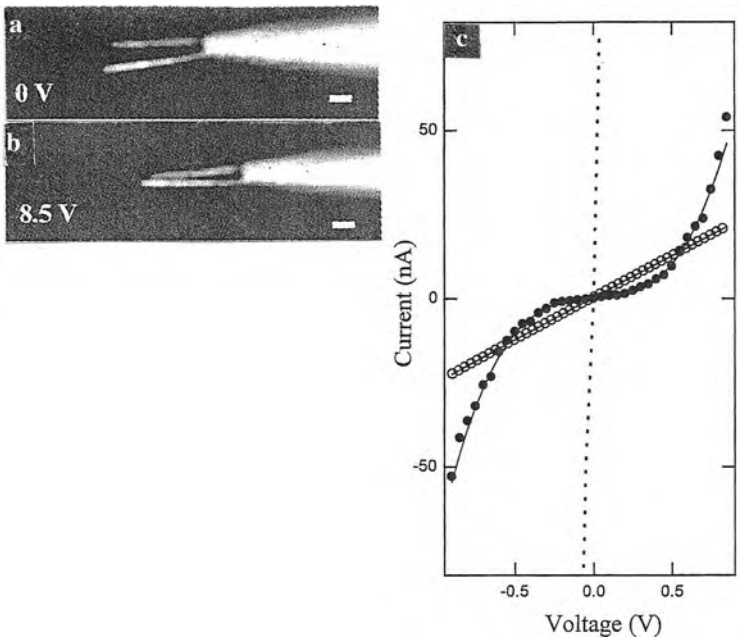

Fig. 5.21 Electromechanical response of the nanotube nanotweezers (**a**, **b**). Dark-field optical micrographs of the nanotube arms at the potentials indicated. Scale bars, 1 μm. The mechanical deflection of the nanotweezers in response to the bias voltage applied to electrodes is shown. Although the nanotweezer arms (50 nm thick) are substantially smaller than the optical wavelengths they sufficiently scatter light to be readily observed in the dark-field images. (**c**). Electrical characterization of nanostructures by means of nanotweezers. *I–V* data: ··· closed nanotube tweezers (ohmic behavior), ○○○ SiC nanoclusters (ohmic behavior), and ●●● GaAs nanowire (tunneling transport through a surface oxide layer). (Reprinted with permission from [5.70]. © 1999 AAAS)

feeding a methane/nitrogen gas mixture and thereby periodically introducing heptagonal and pentagonal rings into the hexagonal network of the graphitic layers along the tube axis.

Tubular graphite cones (see Fig. 5.23a, b) are synthesized by microwave plasma-assisted chemical vapor deposition (MPCVD) with a N_2/CH_4 reaction gas. Nanosized beads of amorphous carbon nanotubes (Fig. 5.23c, d) are fabricated in a carbon arc in a He atmosphere. Herringbone carbon nanofibers (Fig. 5.23e) are produced by catalytic plasma-enhanced chemical vapor deposition (C-PECVD).

Junctions of carbon nanotubes, a prerequisite for employing CNTs in electronic devices and nanomechanical systems, may be generated during synthesis by pyrolysis of an organo-metallic nickelocene precursor (see Fig. 5.24a), by chemical functionalization (Fig. 5.24b), or by radiation-induced defects in an electron microscope (Fig. 5.24c–f) which promote the joining of tubes via cross-linking of dangling bonds.

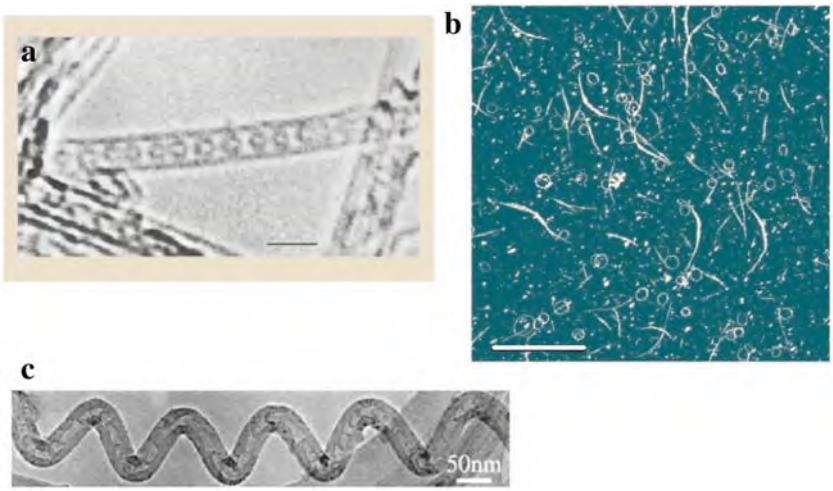

Fig. 5.22 (**a**) High-resolution transmission electron microscopy (HRTEM) of a carbon peapod, i.e., a SWNT filled with C_{60} molecules [5.73]; scale bar, 2.0 nm; (**b**) AFM images of CNT rings in the reaction mixture on mica; scale bar, 5 μm [5.74]. (**c**) TEM image of typical CVD synthesized coiled CNTs with a nanobell structure [5.75]. (Reprinted with permission from [5.73] (**a**), [5.74] (**b**), and [5.75] (**c**). © 1998 Nature Publishing Group (**a**), © 2001 AAAS (**b**), and © 2003 American Institute of Physics (**c**))

5.1.10 Filling and Functionalizing Carbon Nanotubes

Inside carbon nanotubes (CNTs) molecular species can be capsulated in the nanometer-scale 1D cavity to form novel 1D crystals. Furthermore, this encapsulation can allow for a direct observation of chemical reactions in confined space [5.82] or of molecules in motion [5.83].

CNTs filled with metals (Fig. 5.25a) could provide potential application in catalysis, separation, or magnetic technologies. An ionic KI crystal in a SWNT (Fig. 5.25b) displays substantial lattice distortions as compared with its bulk structure because a differential expansion is observed with the I columns being more compressed than the K columns. In metallofullerene Gd@C_{82} crystals in SWNTs, the Gd atoms can be imaged due to their high atomic number (Fig. 5.25c) and also located by electron energy-loss spectroscopy (EELS) [5.87]. By inserting Gd@C_{82} endohedral fullerenes, a semiconductor CNT can be divided into multiple quantum dots with lengths of about 10 nm with spatial modulation of the nanotube electronic band gap narrowing down to 0.1 eV at the sites of the Gd@C_{82} metallofullerenes [5.88]. 1D linear polyyne $C_{10}H_2$ molecules (*sp* bonding) inside a nanotube (sp^2) (Fig. 5.26a) constitute a unique combination of *sp*- and sp^2-hybridized carbon network systems. Other organic molecules such as tetrathiafulvalene (TTF), tetramethyl tetraselenafulvalene (TMSF), or tetracyano-*p*-quinodimethane (TCNQ) have been filled into CNTs [5.90].

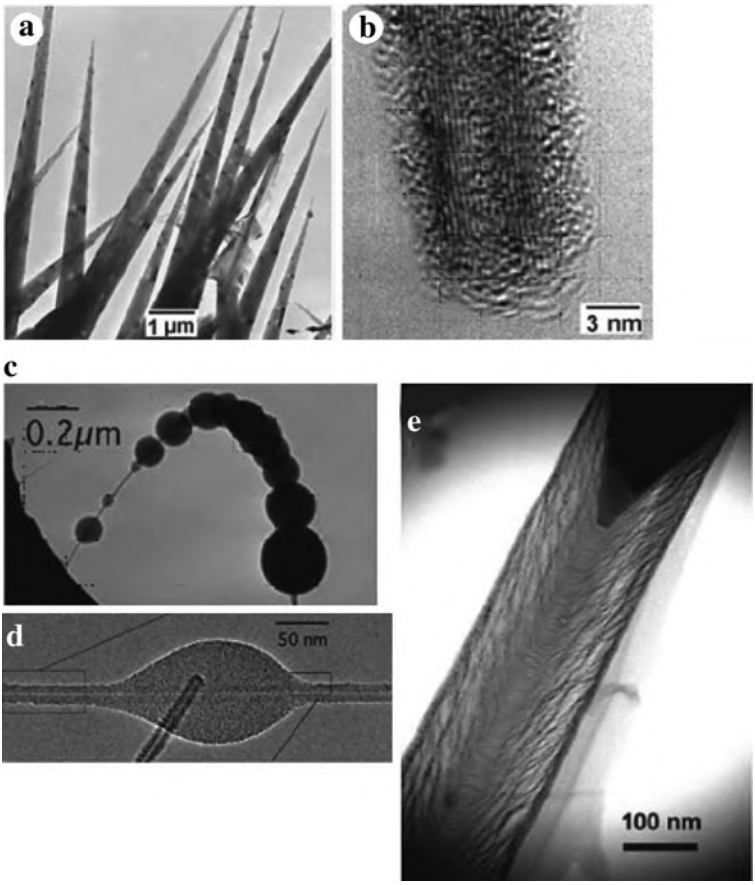

Fig. 5.23 (**a**) TEM image of tubular graphite cones (TGCs) and (**b**) the TGC tip [5.76]. (**c**) TEM of a CNT with amorphous carbon beads and (**d**) TEM image of an amorphous carbon bead with the CNT clearly visible [5.77]. (**e**) Scanning transmission electron micrograph (STEM) of a carbon nanofiber produced by C-PECVD with a Ni catalyst [5.78]. (Reprinted with permission from [5.76] (**a**) (**b**), [5.77] (**c**) (**d**), and [5.78] (**e**). © 2003 AAAS (**a**) (**b**), © 2005 AAAS (**c**) (**d**), and © 2005 American Institute of Physics (**e**))

Fig. 5.24 (**a**) TEM image of a typical y-junction after pyrolysis of an organometallic precursor [5.79]; (**b**) Schematic representation of a SWNT intermolecular end-to-end junction via two amide linkages [5.80]; (**c**), (**d**) TEM image and molecular model of a thin (0.9 nm diameter) and a thicker (2.0 nm diameter) SWNT crossing each other; (**e**), (**f**) 60 s of electron irradiation (1.25 MeV; electron current 10 A/cm^2) promotes a molecular connection between the two tubes. In the molecular model (**f**) heptagonal rings are indicated in *red* [5.81]. (Reprinted with permission from [5.79] (**a**), [5.80] (**b**), and [5.81] (**c**–**f**). © 2000 American Institute of Physics (**a**), © 2002 American Institute of Physics (**b**), and © 2002 American Physical Society (**c**–**f**))

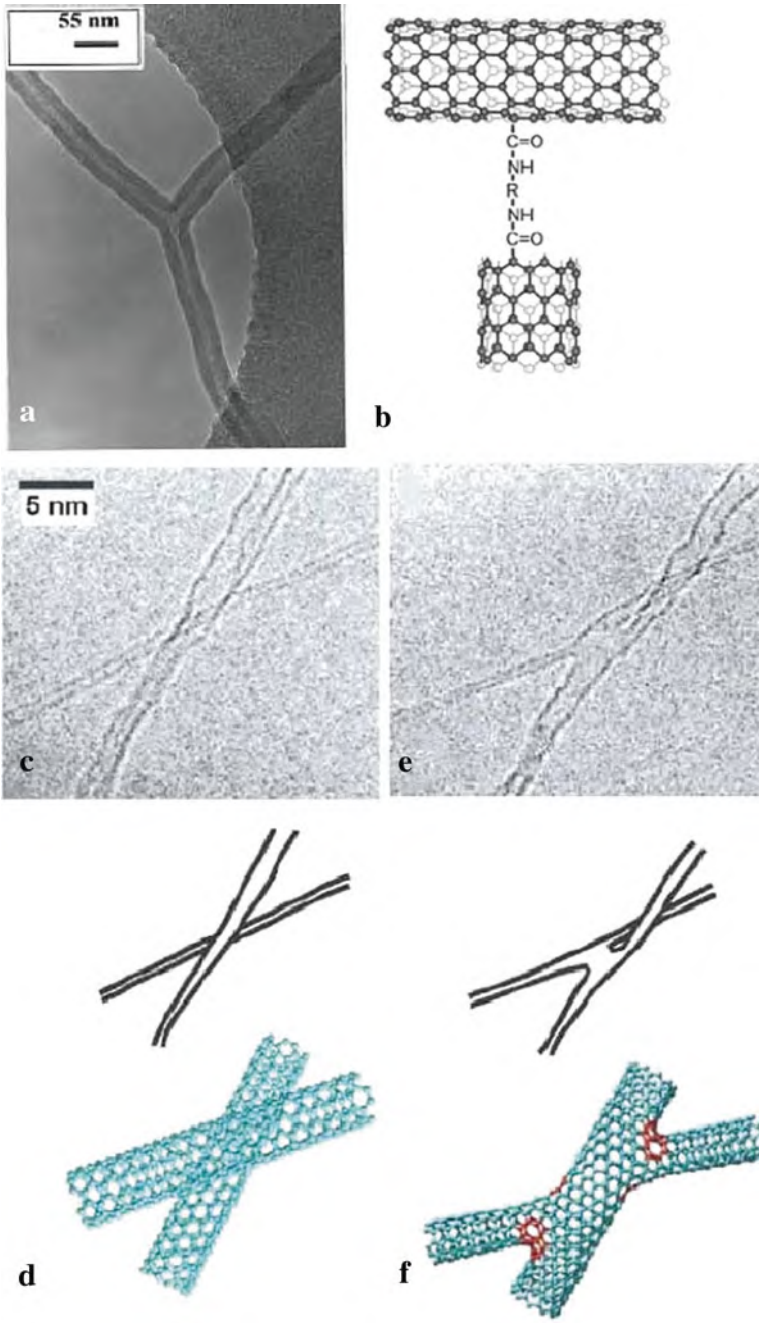
55 nm
a
C=O
NH
R
NH
C=O
b
5 nm
c
e
d
f

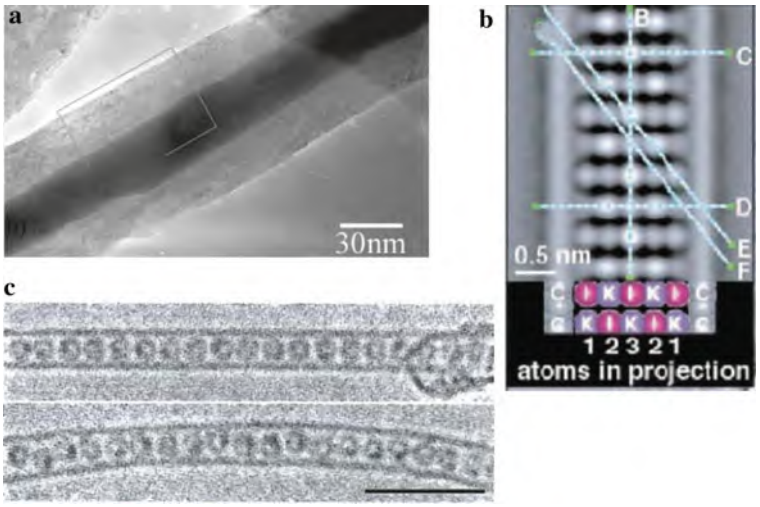

Fig. 5.25 (**a**) HRTEM of a Cu-filled CNT with a diameter of the CNT of 70 nm and of the Cu quantum wire of about 27 nm [5.84]. (**b**) Super-resolved HRTEM image (tilt or focal series of HRTEM images for removing key aberrations) of a 3×3 KI crystal formed in a ∼1.6 nm diameter SWNT [5.85]. The columns of the heavy iodine and the weaker columns of potassium atoms are visible. (**c**) HRTEM images of the isolated SWNTs containing $Gd@C_{82}$ fullerenes. The encapsulated Gd atoms (*dark spots* in the fullerene cages) are oriented randomly with respect to the tube axis (scale bar, 5 nm) [5.86]. (Reprinted with permission from [5.84] (**a**), [5.85] (**b**), and [5.86] (**c**). © 2003 American Institute of Physics (**a**), © 2000 AAAS (**b**), and © 2000 American Physical Society (**c**))

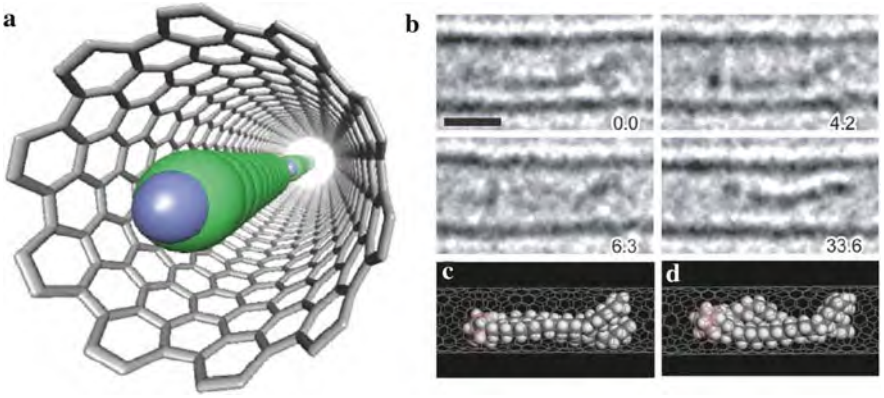

Fig. 5.26 (**a**) A schematic drawing of a "polyyne peapod"; $C_{10}H_2$ polyyne molecules aligned inside the (10,10) nanotube [5.89]. (**b**) Translation of a molecule bearing double alkyl chains through a 1.2 nm diameter CNT. Transmission electron micrographs of two intertwined hydrocarbon chains of $C_{22}H_{45}$ at consecutive times in seconds. (**c**–**d**) Model of the intertwined chain at 4.2 and 6.3 s, respectively [5.83]. (Reprinted with permission from [5.89] (**a**) and [5.83] (**b**–**d**). © 2006 Elsevier (**a**) and © 2007 AAAS (**b**–**d**))

The first successful imaging of the process of motion of a molecule (Fig. 5.26b) has been achieved by encapsulation of a small hydrocarbon chain into a 1.2 nm diameter CNT.

On the surface of carbon nanotubes, the outside functionalization is of interest for materials science, nanoelectronics, biological application. Making use of the extremely strong SWNTs together with polymers, the mechanical properties such as stiffness of these composites could, in theory, be enhanced by a factor of ten or more. At present the materials are, however, far from approaching these values because of the inability to disperse CNTs effectively into conventional polymers. A step into the direction of solving this problem is the functionalization of SWNTs with pH-sensitive poly (acrylic acid) molecules (see Fig. 5.27a) providing a pH-controlled solubility and dispersion in water. By an oligonucleotide functionalization of the ends of CNTs, these CNTs can be self-assembled for a localized deposition as interconnects for, e.g., integrated circuits. The functionalized sites can be imaged by attaching Au clusters (see Fig. 5.27b).

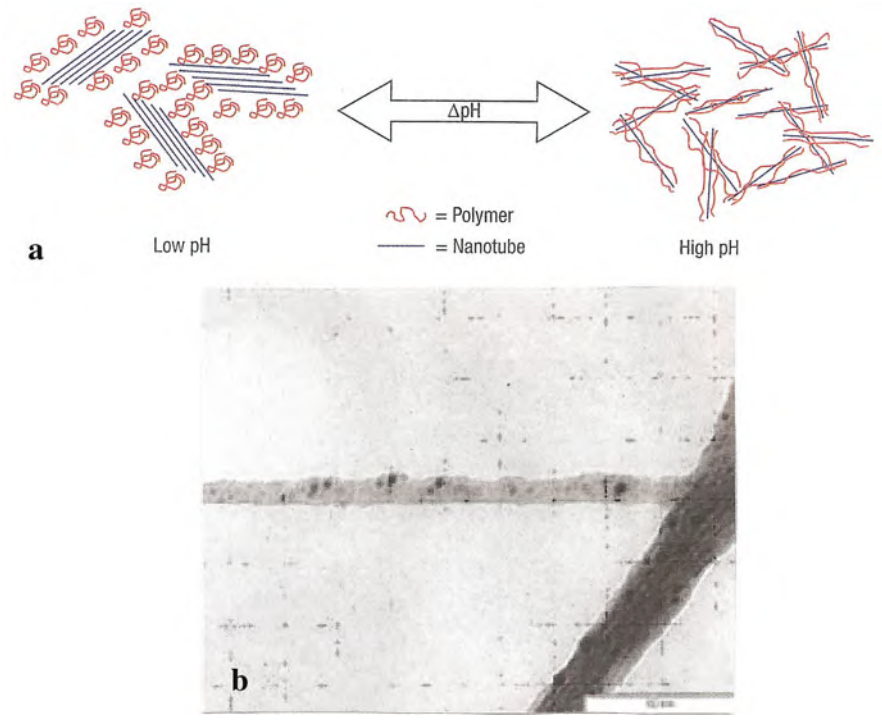

Fig. 5.27 (**a**) Change in nanotube microstructure when the pH of poly(acrylic acid) is changed. At low pH the polymer is highly coiled, allowing the CNTs to bundle together. At high pH, the polymer is negatively charged and becomes more extended as the side groups repel each other. This leads to a more disperse network of nanotubes [5.91, 5.92]. (**b**) TEM of gold clusters attached to CNTs by oligonucleotides [5.93]; scale bar, 90 nm. (Reprinted with permission from [5.91] (**a**) and [5.93] (**b**). © 2006 Nature Publishing Group (**a**) and © 2006 M. Mertig (**b**))

5.1.11 Nanotubes from Materials Other than Pure Carbon

With the advent of carbon nanotubes, nanosized tubular structures from a plethora of materials have been developed. In addition, biological tubules such as nanotubes of proteins [5.94] or phospholipids [5.95] perform numerous biochemical operations in nature.

Metallic nanotubes can be fabricated in a great variety (see Fig. 5.28 and Table 5.1). A selection of elemental (Si) and compound semiconductors is given in Fig. 5.29 and Table 5.1. The boron nitride nanotubes [5.119] are isoelectronic to carbon nanotubes but with electronic properties quite different due to the wide BN band gap and the influence of excitons. Nanotubes of MoS_2, WS_2 (see Fig. 5.30), or $NbSe_2$ (see Table 5.1) are semiconducting or superconducting, respectively. Metal oxide nanotubes (see Table 5.1 and Fig. 5.31) were fabricated from TiO_2 which is a material for solar energy conversion and catalysis, from Al_2O_3 and $ZnAl_2O_4$, from SrBiTaO which is a piezoelectric material, from the manganite LaPrCaMnO which is a colossal magneto-resistance (CMR) ceramic, or from Fe_3O_4 with a curling-type magnetization.

Polymer nanotubes synthesized by, e.g., electrospinning [5.112] (Fig. 5.32a) or by stretching of polymersomes (polymers vesicles composed of amphiphilic diblock copolymers) [5.113] (see Fig. 5.32b) may be used for the transport of biological molecules with potentially significant applications in biotechnology such as biosensorics, catalysis, or drug delivery.

Biological nanotubes called tunneling nanotubes (TNTs) (see Fig. 5.32c) interconnect cells, e.g., rat pheochromocytoma (tumor) PC12 cells or human embryonic kidney cells. These nanotubes have a diameter of about 100 nm with a length of several cell diameters and can transfer organelles unidirectionally from one cell to another.

Nanotubes can also be produced by living organisms as demonstrated for the bacterium *Shewanella* sp. HN-41 which produces arsenic sulfide (AsS) nanotubes

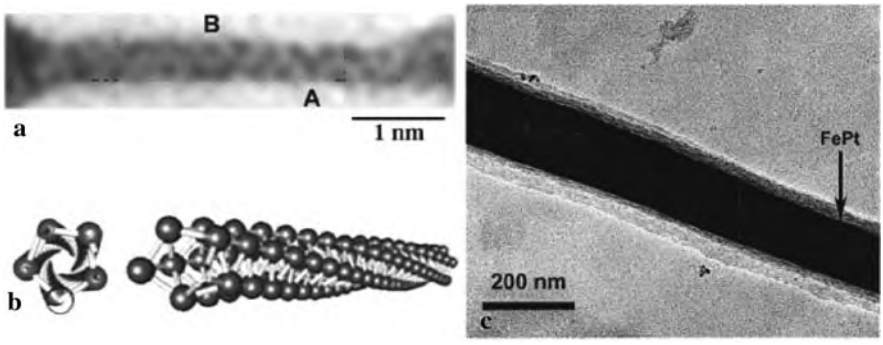

Fig. 5.28 (**a**) TEM image of a gold (5,3) nanotube. (**b**) Structure model of the gold nanotube in (**a**) [5.96]. (**c**) TEM of a FePt nanotube [5.97]. (Reprinted with permission from [5.96] (**a**) (**b**) and [5.97] (**c**). © 2003 American Physical Society (**a**) (**b**) and © 2004 American Institute of Physics (**c**))

Table 5.1 Selection of nanotubes from materials other than pure carbon

Material	Dimensions diameter (nm)	References
Au	0.4	[5.96]
Pt, Pd, Au	50–100	[5.98]
Fe, Co		[5.99]
FePt	200	[5.97]
Co/polymer	180	[5.100]
Si	15	[5.101]
GaN	100	[5.102]
BN	20	[5.103]
CN	30	[5.115]
BCN	250	[5.104]
SiC	30	[5.105]
AsS, AS_4S	20–100	[5.114]
MoS_2	4	[5.106]
WS_2	40	[5.107]
$NbSe_2$		[5.118]
ZnO	10^5	[5.116]
TiO_2	20	[5.117]
Al_2O_3	15	[5.108]
$ZnAl_2O_4$	30	[5.109]
SrBiTaO	1,000	[5.110]
LaPrCaMnO	700	[5.111]
Fe_3O_4	200 magnetic	[5.97]
Polymers	400	[5.112]
Biological nanotubes (TNTs)		[5.95]

(20–100 nm in diameter by $\approx$ 30 μm in length; see Fig. 5.33). The nanotubes are initially amorphous As_2S_3 but evolve with incubation time toward polycrystalline phases of realgar (AsS) and duranosite (AS_4S) which behave as metals or semiconductors [5.114].

5.1.12 Application of Carbon Nanotubes

A great many of applications of carbon nanotubes (CNTs) has been suggested due to their particular mechanical and electronic properties as well as their high aspect ratios. Since the supply situation is now improving with several companies producing on a larger scale [5.120] a critical assessment from a more business view is worthwhile.

Composites containing CNTs exhibit a number of excellent properties. The conduction percolation threshold can be reduced to very low values (0.004%) due to the high CNT aspect ratio. This has been used for electrostatically applying paint to car components [5.121] or as antistatic shielding on airplane wings or fuselages. These composites can be used as transparent conductors, which is a huge market, in particular that they are truly flexible and compatible with polymer substrates.

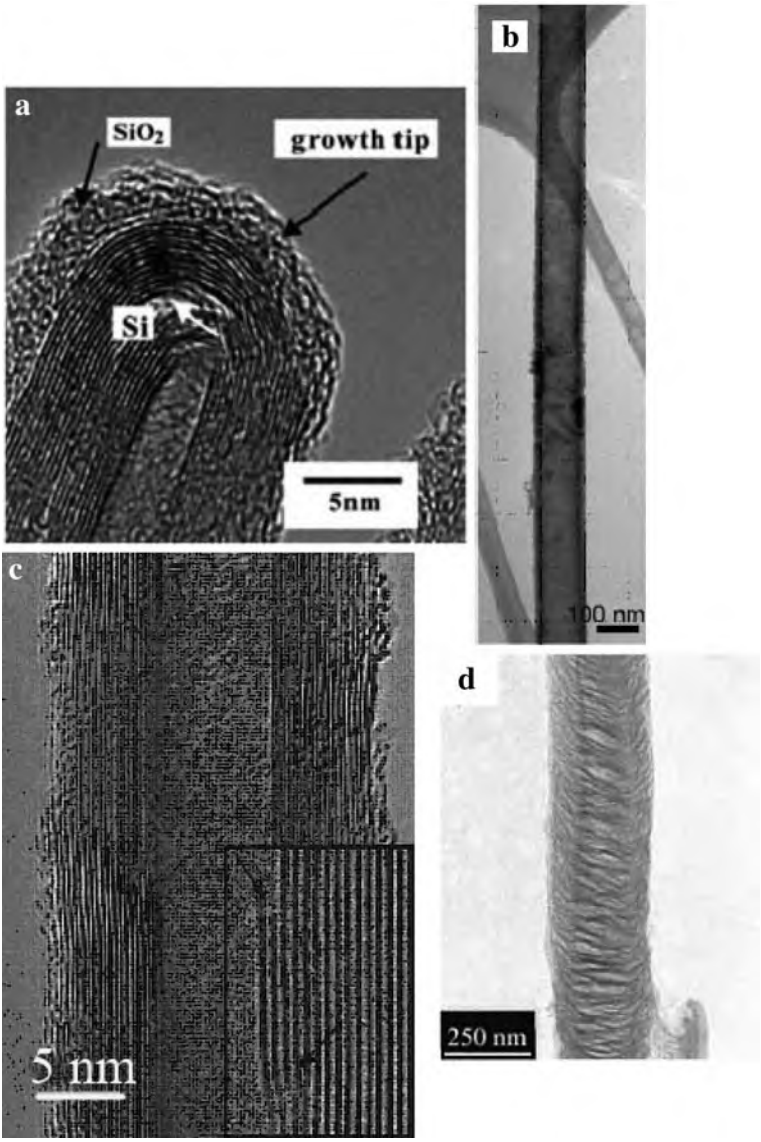

Fig. 5.29 (**a**) HRTEM image of the closed tip of a Si nanotube. A defect is pointed out by the *white arrow* [5.101]. (**b**) TEM image of a GaN nanotube [5.102]. (**c**) HRTEM image of a BN nanotube with (*inset*) an edge dislocation among the walls and truncated layers at the innermost surface. Defects are common in BN nanotubes because of the strong interlayer interaction [5.103]. (d) B–C–N nanotube with high B and N atomic concentrations [5.104]. (Reprinted with permission from [5.101] (**a**), [5.102] (**b**), [5.103] (**c**), and [5.104] (**d**). © 2005 American Physical Society (**a**), © 2003 Nature Publishing Group (**b**), © 2005 American Institute of Physics (**c**), and © 2002 American Institute of Physics (**d**))

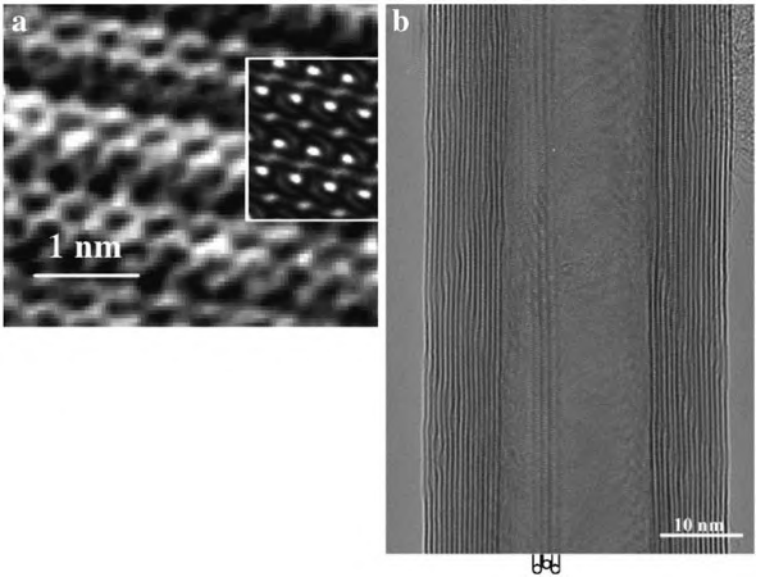

Fig. 5.30 (**a**) HRTEM image of a MoS_2 bundle with image simulation revealing ordered stacking of nanotubes; *bright spots* correspond to the positions of Mo atoms [5.106]. (**b**) HRTEM image of a 15-walled WS_2 nanotube containing SWNTs [5.107]. (Reprinted with permission from [5.106] (**a**) and [5.107] (**b**). © 2001 AAAS (**a**) and © 2001 American Institute of Physics (**b**))

The mechanical performance of the CNT composites has been rather disappointing because of insufficient dispersion and weak bonding across the CNT/host interface which may be improved by functionalization along the tubes. It, e.g., has been possible to fabricate protein–CNT composites (Fig. 5.34). CNT fibers can be drawn and spun with final impregnation with epoxy to make a composite. These fibers (Fig. 5.35) presently have a failure strength up to 1 GPa.

Field emission and AFM tips: CNTs can carry a huge current density of 10^{13} A/m^2 and have a better performance than other forms of carbon. The field emission electron current from a solid is controlled by the Fowler–Nordheim equation with an exponential dependence on the local field. This suggests an application for electron guns in the next generation electron microscopes (Fig. 5.36). In a low-voltage scanning electron microscope (SEM), the largest market, the lateral resolution is limited by chromatic aberration and an electron source with a small energy spread is needed. A single-MWNT field emission source is found to have a factor of 30 higher brightness than existing electron sources and a small energy width of 0.25 eV.

An interesting application of CNTs is in field effect displays (FEDs) because of the huge market of US$ 50 billion per annum. A market gap might exist for FEDs in large displays (see Fig. 5.37); but in competition with organic light emitting diodes (OLEDs), liquid crystal displays (AMLDCs), and plasma display panels (PDPs) they will have a difficult future.

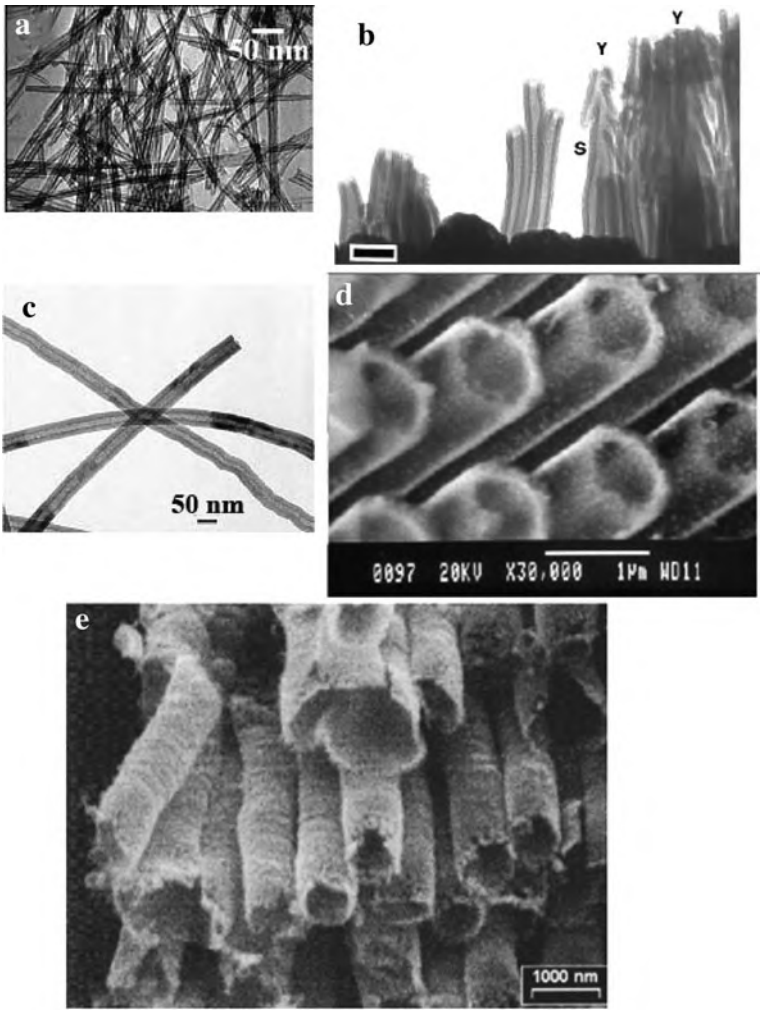

Fig. 5.31 (**a**) Transmission electron micrograph (TEM) of TiO_2 nanotubes [5.117]. (**b**) TEM side view of branchy alumina nanotubes [5.108] (scale bar, 100 nm). (**c**) TEM image of $ZnAl_2O_4$ spinel nanotubes [5.109]. (**d**) Scanning electron micrographs of $SrBi_2Ta_2O_9$ nanotubes [5.110]. (**e**) Nanotubes of LaPrCaMnO manganites with a colossal magneto-resistance (CMR) behavior [5.111]. (Reprinted with permission from [5.117] (**a**), [5.108] (**b**), [5.109] (**c**), [5.110] (**d**), and [5.111] (**e**). © 2006 American Chemical Society (**a**), © 2002 American Institute of Physics (**b**), © 2006 Nature Publishing Group (**c**), © 2003 Institute of Physics (**d**), and © 2003 American Institute of Physics (**e**))

For atomic force microscopy (AFM) imaging, an SWNT can be directly grown on Si [5.125] to protrude from the AFM Si tip apex in order to yield a significantly improved resolution.

Electronics: The interconnects between transistors in integrated circuits have to carry ever larger current densities so that the current density capabilities of

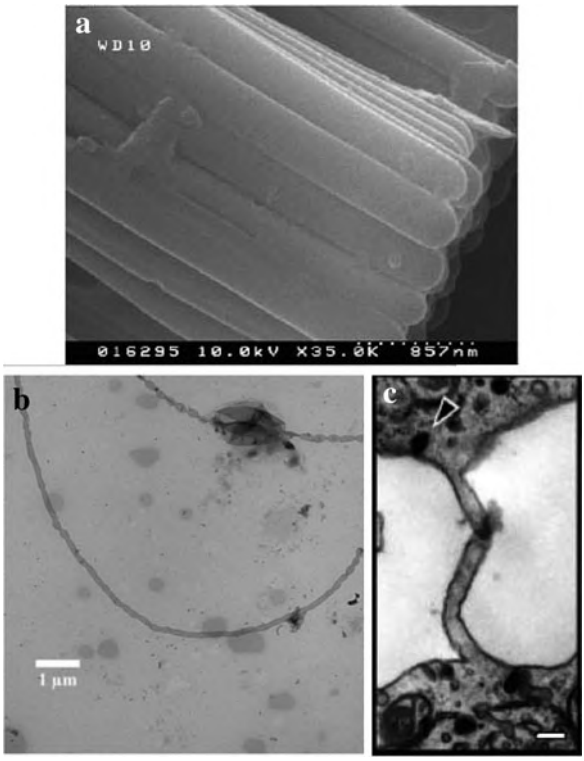

Fig. 5.32 (**a**) Polystyrene nanotubes produced by template wetting [5.112]. (**b**) TEM image of a polymer nanotube stretched from a polymersome. A polymersome is visible in the *upper* part of the image [5.113]. (**c**) TEM of a biological tunneling nanotube (TNT) between PC 12 cells. The TNT contains actin but no microtubules [5.95]; scale bar, 200 nm. (Reprinted with permission from [5.112] (**a**), [5.113] (**b**), and [5.95] (**c**). © 2006 Springer Verlag (**a**), © 2006 National Academy of Sciences USA. (**b**), and © 2004 AAAS (**c**))

CNTs 1,000 times that of Cu could be employed. Infineon [5.126] has replaced the vertical connects known as vias by CNTs (Fig. 5.38). However, the greatest demand is not for vias but for horizontal interconnects. They can be fabricated by applying a horizontal electric field between the starting and the finishing electrode which favors the CNT between the electrodes [5.127], however, with low yield. Nevertheless, researchers from Intel are confident [5.128] that CNTs can replace Cu in microelectronics.

Field effect transistors (FET) can be built from CNTs. In the first example the substrate is used as the bottom gate electrode. The second generation FET requires a separate "top gate" over each individual nanotube and by the use of ZrO_2 gate oxide best turn-on performance of any nanotube device has been achieved [5.129] but this approach occupies a huge wafer area because of its connections. One possibility which takes up much less space is the vertical CNT–FET concept of Infineon (see Fig. 5.39). However, it is expected that Si CMOS technology will continue in its present form until at least 2016 [5.120]. For these applications it is necessary to grow a specific type of tube at a defined position in a defined direction with nearly 100% yield. CNTs can be sorted by both diameter and electronic-type making use of surfactants and centrifugation [5.130].

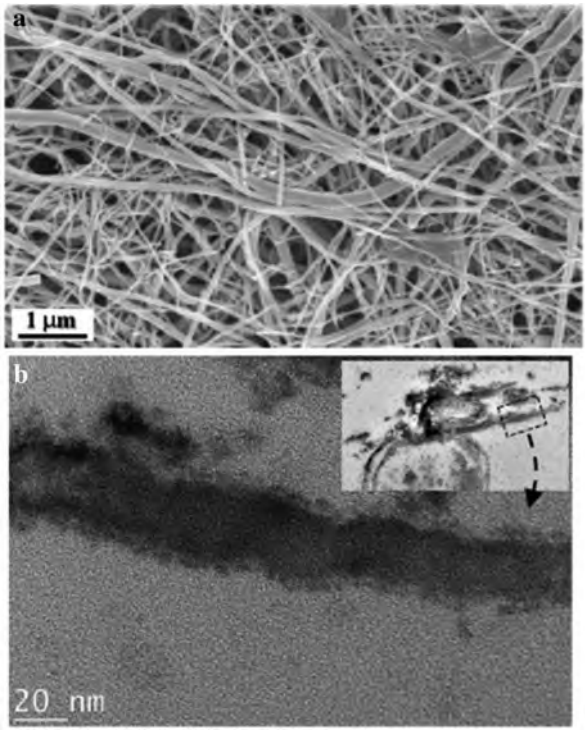

Fig. 5.33 Electron micrographs of biogenic AsS nanotubes. (**a**) Scanning electron micrograph. (**b**) Laterally sectioned transmission electron micrographs. (Reprinted with permission from [5.114]. © 2007 National Academy of Sciences USA)

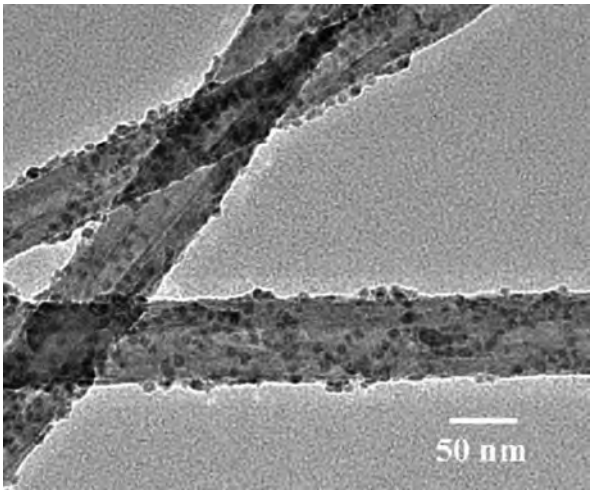

Fig. 5.34 Transmission electron micrograph of a ferritin-MWNT (N-doped) composite [5.122]. Ferritin is a protein found, e.g., in the liver that functions as the primary form of iron storage in the body. (Reprinted with permission from [5.122]. © 2004 Royal Society of Chemistry)

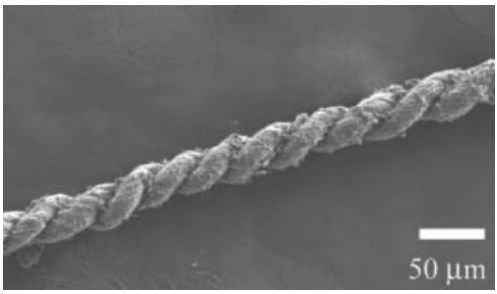

Fig. 5.35 Scanning electron micrograph of a spun CNT fiber. (Reprinted with permission from [5.123]. © 2004 AAAS)

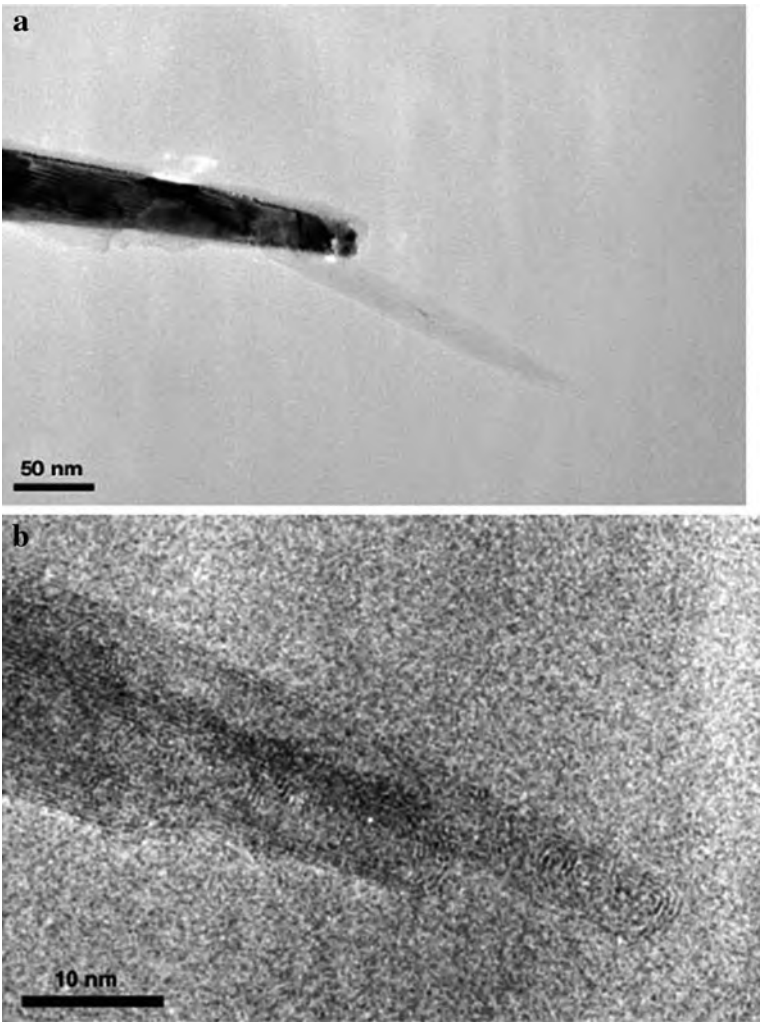

Fig. 5.36 TEM image of a carbon MWNT mounted on a tungsten tip. (**a**) MWNT attached to the W tip. (**b**) High-resolution TEM of the apex of the MWNT with a radius of 2.7 nm. (Reprinted with permission from [5.124]. © 2002 Nature Publishing Group)

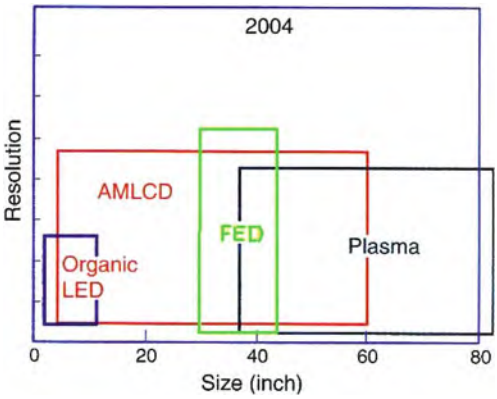

Fig. 5.37 In 2004, liquid crystal displays (AMLCD) span small- and large-area applications, plasma has taken over at larger areas while organic light-emitting diodes (OLEDs) are entering the small-area display market. This leaves FEDs as a large-area display market around 34″. (Reprinted with permission from [5.120]. © 2004 Elsevier)

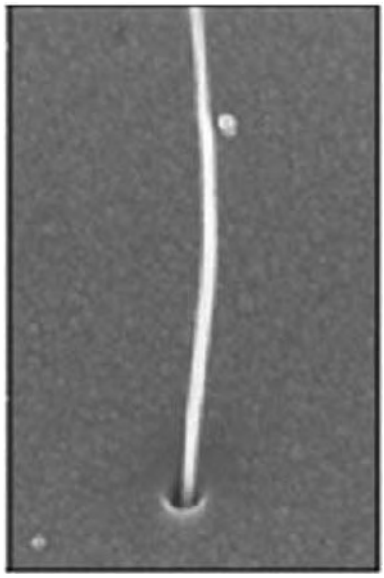

Fig. 5.38 Growth of one carbon MWNT (diameter 15 nm) for vias. (Reprinted with permission from [5.126]. © 2007 Elsevier)

Nanotubes with their charge carrier mobilities as high as 20,000 $cm^2/V\,s$ [5.30] have a number of near-term competitors for replacing complementary metal oxide semiconductor (CMOS) transistor technology [5.10]. CMOS is reaching the stage where many high-mobility channel materials are being considered for use instead of Si [5.10]. Strained Si is in use to increase mobility. Ge has higher mobility than Si and alloying Ge with Si can increase mobilities. Replacing Si by InSb increases electron mobilities by a factor of 100 and decreases power consumption. Power dissipation is a major problem in general CMOS and has arrived at a power density up to the limit of $\sim$200 W/cm^2 (see Fig. 5.40). It does not matter if Si is replaced by nanotubes because it will not get round the power limit – it is purely a function

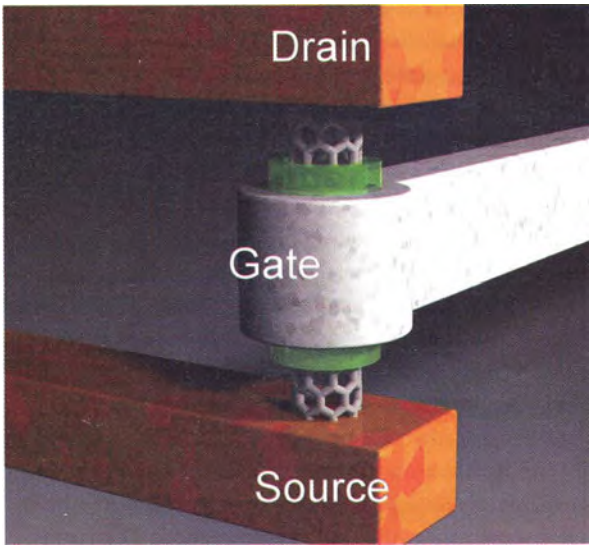

Fig. 5.39 Infineons vertical CNT–FET concept. The nanowire is grown on the source contact (*bottom*), a top drain contact is put on, a gate insulator (*green*) is grown around the CNT with a final wrap-around gate electrode [5.120, 5.126]. (Reprinted with permission from [5.120]. © 2004 Elsevier)

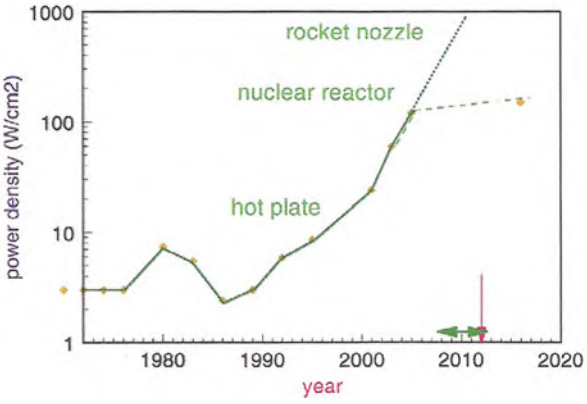

Fig. 5.40 Power density against year for Intel microprocessor chips. (Reprinted with permission from [5.10]. © 2007 Elsevier)

of a switch operating on charge [5.10]. For introducing more novel materials into integrated circuit (IC) technology, 20 years are suggested to develop the necessary processes economically [5.131]. The estimate for nanotubes may be a lot later than 2012 [5.10].

High-precision mass and charge measurements. The masses of single atoms adsorbed on CNTs [5.132–5.134] or the addition of single electrons to CNTs [5.135,

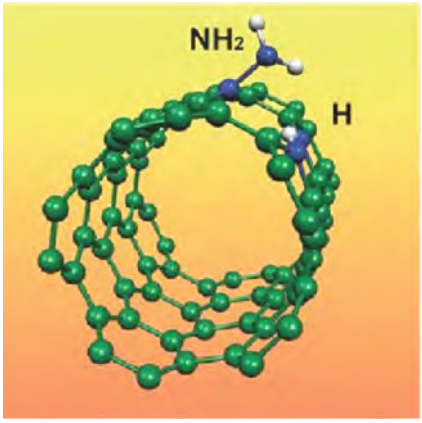

Fig. 5.41 Molecular model for a (5,5) CNT doped with pyridinic sites on its surface with NH_3 molecules absorbed in the vicinity of such a site [5.17, 5.139]. (Reprinted with permission from [5.17]. © 2004 Elsevier)

5.136] can be detected by measuring the resonant frequency of a suspended carbon nanotube.

A large nonlinear absorption of light is observed in CNTs [5.137] because of their 1D band structure with singularities in the electronic density of states. Due to the rapid decay of excited electrons in picoseconds this could be employed for fast saturable absorbers, limiters, and optical switches [5.120].

Li^+ batteries: N-doped CNTs and nanofibers have shown efficient Li storage (480 mA h/g) much higher than commercial carbon materials used for Li^+ batteries (330 mA h/g) [5.138] (see Sect. 10.11).

Sensors: N-doped MWNTs display a fast response within milliseconds when exposed to toxic gases and organic solvents [5.139]. The sensitivity to $\sim 1\%$ NH_3 originates from chemisorption due to the strong interaction between the pyridinic sites of the tube with the NH_3 molecule (Fig. 5.41) giving rise to an increase in the electrical resistance of the tube due to a decrease in the electronic density of states at the Fermi level. It is envisaged [5.17] that N-doped or B-doped MWNTs could be used to detect low concentrations of ethanol, important in the fabrication of alcohol meters.

5.2 Graphene

Graphene is a flat monolayer of carbon atoms densely packed into a 2D honeycomb lattice (see Sect. 3.8) and it is the building block for graphitic materials of all other dimensionalities. Although graphene has been studied theoretically since 60 years [5.140], it only has been prepared recently [5.4, 5.141]. This material exhibits physical properties at the interface between traditional condensed matter physics and the theory of relativistic electrons in vacuum–quantum electrodynamics (QED) [5.4, 5.142] (see the recent reviews [5.143–5.145]).

Graphene has attracted a great deal of attention due to its high-charge carrier mobility at room temperature, its control of the band gap by patterning to nanoribbons, and its potential for many-body-correlated effects (see [5.146]). Chemically synthesized graphene appears to be available in sufficient quantities [5.147] to seriously consider its use in a wide range of applications (see [5.148]), including composite reinforcement, electronic devices, batteries, sensors, catalysis. (see [5.147]).

5.2.1 Imaging of Graphene, Defects, and Atomic Dynamics

Graphene sheets on insulating substrates were imaged by scanning tunneling microscopy (STM; Fig. 5.42a) showing the hexagonal symmetry. Free-standing single-layer graphene sheets were imaged (Fig. 5.42b) in a high-angle annular dark-field mode (HAADF) using a 100-keV scanning transmission electron microscope (STEM) with aberration correction. In these experiments, moreover, vacany defects in a graphene sheet could be detected (Fig. 5.43a, b). In Fig. 5.43c–f, furthermore, the appearance (d) and disappearance (f) of a Stone–Wales (SW) defect (see Sect. 5.1) are shown comprising two heptagons and two pentagons. This type of defects is proposed to play a key role in the formation and transformation of sp^2-bonded

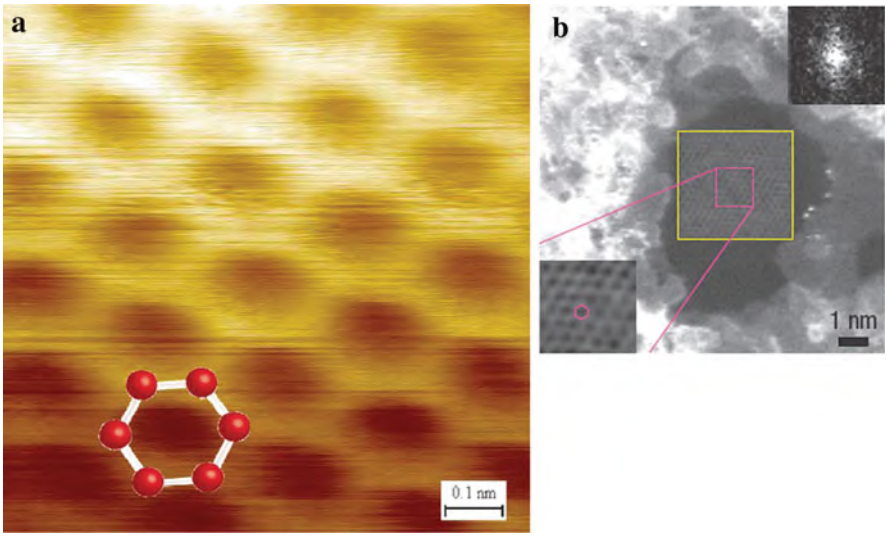

Fig. 5.42 (**a**) Scanning tunneling micrograph (STM) of a single layer of graphene. A model of the underlying atomic structure is shown as a guide to the eye [5.149]. (**b**) Scanning transmission electron micrograph (STEM) in high-angle dark-field (HAADF) mode of monolayer graphene. By applying a band-pass filter, the atomic structure is apparent in the *bottom left inset* [5.150]. (Reprinted with permission from [5.149] (**a**) and [5.150] (**b**). © 2007 National Academy of Sciences USA. (**a**) and © 2008 Nature Publishing Group (**b**))

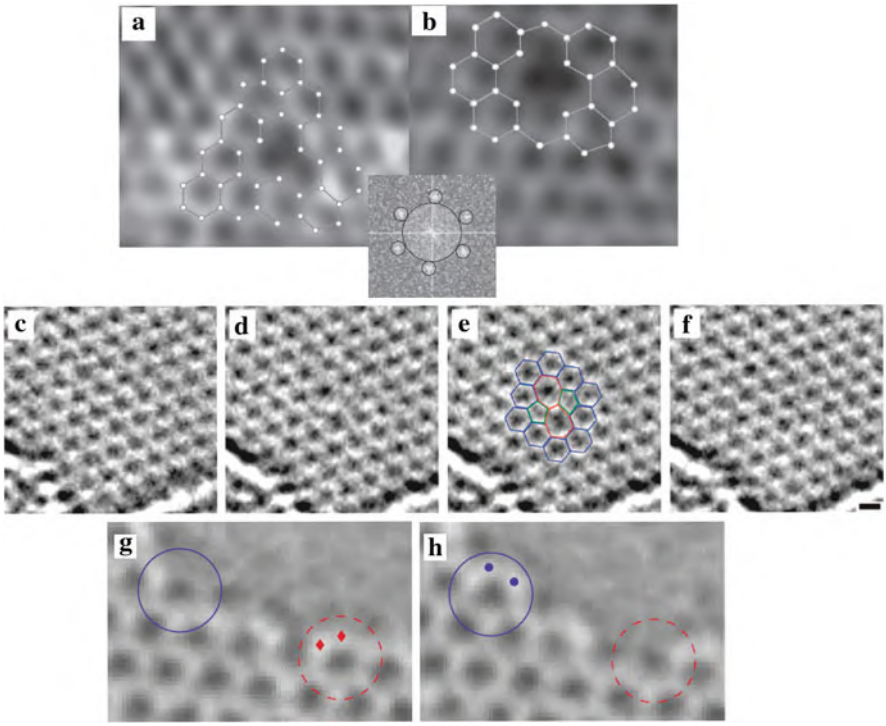

Fig. 5.43 Defects and atomic dynamics in graphene. (**a, b**) High-resolution transmission electron micrograph (HRTEM) of vacancy defects in graphene which may occur due to electron bombardment. The images were obtained with a filter applied to the fast Fourier transform of the raw images as indicated by the *inset* and show a monovacancy (**a**) and a divacancy (**b**) [5.150]. (**c–f**) HRTEM of a Stone–Wales defect (SW) comprising two heptagons and two pentagons: (**c**) unperturbed lattice before appearance of the defect, (**d**) SW defect, (**e**) same image as (**d**) with atomic configuration superimposed, (**f**) relaxation to the unperturbed lattice (after ca. 4 s) [5.151]. (**g–h**) Aberration-corrected transmission electron micrographs of the edge of a hole in single-layer graphene where (**h**) follows 4 s after (**g**). Two carbon atoms (*red* diamonds in the *dashed circle* of (**g**)) are removed while two carbon atoms nearby (*blue* dots in (**h**)) bind to their neighbors to close a hexagon (*solid circle*) [5.152]. (Reprinted with permission from [5.150] (**a**) (**b**), [5.151] (**c–f**), and [5.152] (**g**) (**h**). © 2008 Nature Publishing Group (**a**) (**b**), © 2008 American Chemical Society (**c–f**), and © 2009 AAAS (**g**) (**h**))

carbon nanostructures [5.151]. These defects are involved in the coalescence of fullerenes and nanotubes and their mobility may be relevant for the plastic response of carbon nanotubes under strain (see Sect. 5.1). Moreover, the dynamics of carbon atoms at the edge of a hole in a suspended graphene sheet can be observed (see Fig. 5.43g, h) by high-resolution transmission electron microscopy as a result of either knockon damage from the electrons in the electron beam (80 keV) or migration of vacant sites nearby (see [5.152]).

2D nanosheets of other materials can be created starting from nanowires. When tungsten oxide nanorods with a diameter of ∼5 nm and a length of 30 nm are treated

in the presence of CS_2 in a hot hexadecylamine solution, sulfidation of the nanorods occurs, and the strain between the heterogenous phases cause the rods to unroll. The result is square WS_2 sheets, ~ 40 nm along each side. These sheets stack up in groups of about six [5.153].

5.2.2 Electronic Structure of Graphene, Massless Relativistic Dirac Fermions, and Chirality

The electronic structure of graphene follows from a nearest-neighbor tight-binding approximation calculation [5.140, 5.145]. The two atoms per graphene unit cell and therefore the two graphene sub-lattices give rise to two "conical" points per Brillouin zone where band crossing occurs, K and K' (Fig. 5.45), and where the electron energy $E = \hbar \mathbf{k} v_F$ is linearly dependent on the wave vector $\mathbf{k}$ with the Fermi velocity $v_F = c/300$ (c – velocity of light).

What makes graphene so interesting is that the energy spectrum closely resembles the energy spectrum derived from the Dirac equation for massless relativistic fermions, such as electrons [5.154]. For Dirac particles with the mass m, the energy $E = c\hbar\mathbf{k}$ is *linearly dependent* on the wave vector $\mathbf{k}$ when $E >> E_0 = mc^2$ and for *massless* Dirac fermions the gap between the electron and the positron energy is zero. Yet, no such particles have been observed before. According to the above analogies for relativistic Dirac fermions in graphene, the graphene electrons may be used for studying the properties of these massless Dirac particles where the role of the speed of light is played by the Fermi velocity. Because of the linear energy spectrum, one can expect that quasi particles in graphene behave differently from those in conventional metals and semiconductors with a parabolic (free electron-like) dispersion relation.

Above zero energy the current-carrying states in graphene are, as usual, electron like and negatively charged. At negative energies, if the valence band is not full, unoccupied electronic states behave as positively charged holes. However, in contrast to electrons and holes in solid-state physics described by different Schrödinger equations and different effective masses, electrons and holes in graphene should be interconnected in analogy to the charge-conjugation (electron–positron) symmetry in quantum electrodynamics (QED) [5.154]. In the case of graphene, the latter symmetry is a consequence of the two-component wave functions arising from the two sub-lattices. The two-component description for graphene is very similar to the spinor wave functions in QED, but the "spin" index for graphene indicates the sub-lattice rather than the real spin of the electrons and is usually referred to as pseudospin σ. This allows one to introduce *chirality* [5.144, 5.154] – formally a projection of pseudospin on the direction of motion – which is positive for electrons and negative for holes.

Due to the exceptional electronic quality of the isolated graphene crystallites, the electron and hole concentrations n can be as high as $10^{13}/\text{cm}^2$. Their mobilities μ can exceed 15,000 $\text{cm}^2/\text{V s}$ even under ambient conditions [5.4] and may be improved to 100,000 $\text{cm}^2/\text{V s}$ [5.143]. This demonstrates ballistic charge carrier

transport up to 300 nm at 300 K. A further indication of the system's high electronic quality is the quantum Hall effect (QHE) discussed below, that can be observed in graphene even at room temperature [5.155].

Studies of charge dynamics in graphene integrated in gated devices indicate the relevance of many-body interactions to the electromagnetic response of graphene [5.156]. For zigzag graphene nanoribbons magnetic ordering has been found at the edges (see [5.157]) and by first principle simulations [5.157] for spin-valve devices, magneto-resistance values have been predicted that are thousand times higher than previously reported experimental values (see Sect. 1.4). The thermoelectric power of graphene is gate dependent [5.158].

Confinement gaps up to 0.5 eV for semiconducting behavior can be opened in graphene by nanoribbon patterning (see Fig. 5.44a) employing scanning tunneling microscope (STM) lithography [5.159]. This method for fabricating semiconducting graphene components may prove useful in the realization of complete integrated circuits, operating as room temperature ballistic electronic devices (see [5.159]). The atomic structure of the edges is of importance for the electronic behavior of the graphene ribbons. The edges can be efficiently reconstructed by Joule heating and electron irradiation of the nanoribbons [5.160], yielding sharp edges with zigzag- or armchair-edge configurations activated by point defect annealing [5.160]. Unzipping of multiwalled carbon nanotubes may pave the way for bulk fabrication

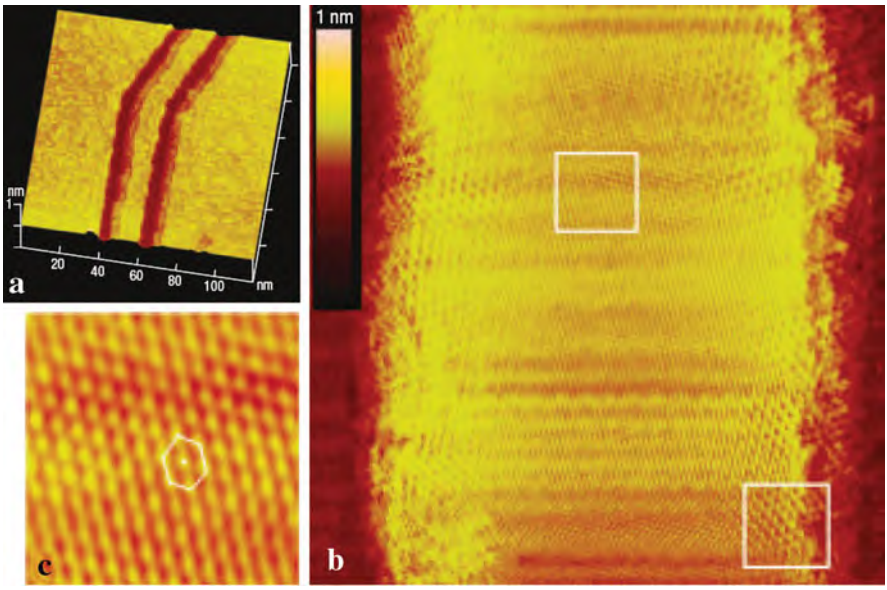

Fig. 5.44 Graphene nanoribbons patterned by STM lithography. (**a**) An 8 nm wide 30° graphene nanoribbon (GNR) bent junction connecting an armchair and a zigzag ribbon. (**b**) Atomic-resolution STM image of a 15 nm wide GNR displaying an atomically flat and defect-free structure. (**c**) Magnified image of the defect-free lattice taken at the center of the ribbon (**b**). (Reprinted with permission from [5.159]. © 2008 Nature Publishing Group)

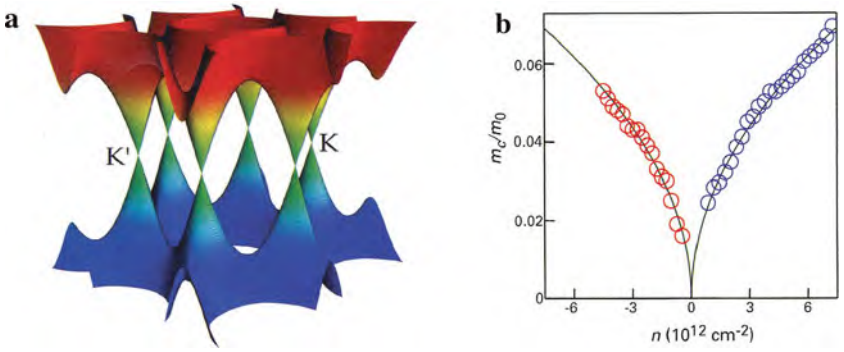

Fig. 5.45 (**a**) Band structure of graphene. The conduction band touches the valence band at the K and K' points [5.144]. (**b**) Electron and hole cyclotron masses as a function of carrier concentration in graphene. The square-root dependence suggests a linear dispersion relation. (Reprinted with permission from [5.164]. © 2007 Elsevier)

of nanoribbons [5.161]. In this process, the tubes are partially embedded in a polymer film and subsequently etched with an argon plasma, yielding semiconducting ribbons 10–20 nanometers wide.

Graphene transistors have been fabricated that operate at frequencies as high as 26 GHz with a gate length of 150 nm [5.162].

5.2.3 Quantum Hall Effect

Magneto-oscillation effects as the de Haas–van Alphen or the Shubnikov–de Haas effects are the most reliable tools to investigate electron-energy spectra in metals and semiconductors [5.163]. In a 2D system with a magnetic field B perpendicular to the system's plane, the energy spectrum is discrete (Landau quantization). In the case of massless Dirac fermions the energy spectrum yields the form

$$E_{\nu\sigma} = \pm\sqrt{2\,|e|\,B\hbar v_{\mathrm{F}}^2\,(\nu + 1/2 \pm 1/2)}$$

where ν is the quantum number and the term $\pm 1/2$ is connected with the chirality (see [5.144]). By varying B at a given electron concentration n one can tune the Fermi energy E_{F} to coincide with one of the Landau levels. This drastically changes the properties of the solid and various properties will oscillate with $1/B$. From the amplitude of the oscillations the effective cyclotron mass of the charge carriers can be derived. For massless Dirac fermions this quantity should be proportional to $\sqrt{n}$, which is exactly the behavior found experimentally [5.142, 5.164] (see Fig. 5.45b). A peculiarity of the Landau levels of massless Dirac fermions is the existence of zero

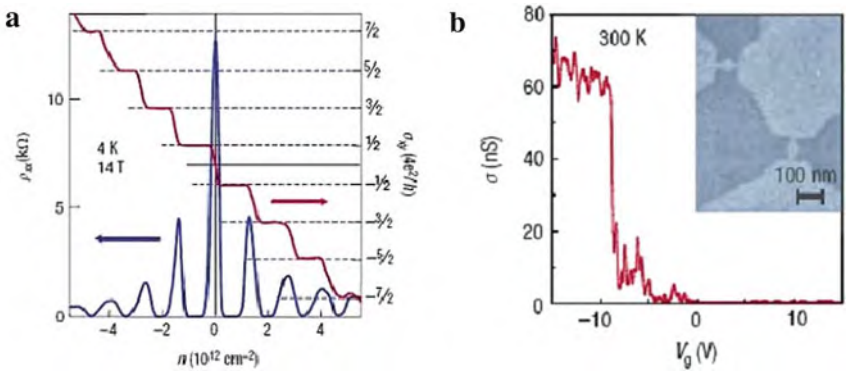

Fig. 5.46 (**a**) Anomalous quantum Hall effect (QHE). The hallmark of massless Dirac fermions is QHE plateau in the Hall conductivity σ_{xy} at half integers of $4e^2/h$ [5.143, 5.164]. (b) 10-nm-scale graphene structures show a high-quality transistor action even at room temperature so that this conductance can be pinched-off completely over a large range of gate voltages. The *inset* shows a scanning electron micrograph of two graphene dots of ∼40 nm in diameter with narrower (∼10 nm) constrictions. (Reprinted with permission from [5.143]. © 2007 Nature Publishing Group)

energy states (with $\nu = 0$ and a minus sign in the equation above) which leads to an anomalous quantum Hall effect (QHE) with *half-integer* quantization of the Hall conductivity (see Fig. 5.46a) instead of an *integer* one (see Sect. 4.3). The anomalous QHE is the most direct evidence for Dirac fermions in graphene (see [5.144]). One view of the anomalous QHE in graphene is based on the concept of a Berry's phase (see [5.144]). Since the electron wave function is a two-component spinor, it has to change sign when the electron moves along a closed contour. Thus, the wave function gains an additional phase $\Phi = \pi$. In quasi-classical terms, stationary states are nothing but electron standing waves and they can exist if the electron orbit is, at least, half the wavelength. As a result of the additional phase shift by the Berry phase, this condition is already satisfied for the zeroth length of the orbit, that is for zero energy.

5.2.4 Anomalous QHE in Bilayer Graphene

The discovery of graphene opens an opportunity to investigate *chiral* particles in a *parabolic* (nonrelativistic) energy spectrum which is available for *bilayer* graphene. For two carbon layers a gapless state with *parabolic* bands touching at the K and K' points are predicted instead of conical bands [5.165] so that bilayer graphene can be treated as a gapless semiconductor. The energy states in a B field are given by $E_\nu \propto \sqrt{\nu\,(\nu-1)}$ and, thus, the number of zero energy states ($\nu = 0$ and $\nu = 1$) is

twice that of monolayer graphene. Therefore, the QHE in bilayer graphene differs from both single-layer graphene and conventional semiconductors [5.166].

5.2.5 Absence of Localization

In graphene, the transmission probability for normally incident electrons is always equal to unity, irrespective of the height and width of the barrier, which again fits into the QED picture of Dirac fermions (see [5.144]). In conventional 2D systems, disorder results in electronic states separated by barriers with exponentially small transparency [5.167] which is known to lead to Anderson localization. However, in graphene, potential barriers are rather transparent. Therefore, different electron and hole "puddles" induced by disorder are not isolated but percolate effectively, thereby suppressing localization. This is important for understanding the minimum conductivity $= e^2/h$ observed experimentally in graphene [5.164, 5.166].

5.2.6 From Graphene to Graphane

The electronic properties of graphene can be controlled by chemical modification. By hydrogenation, graphene is transformed into an insulator (graphane) [5.168]. By attaching hydrogen atoms to graphene, the carbon bond is shortened and transformed in such a way that conduction electrons are removed and an energy gap is opened. Whereas graphene shows a resistivity independent of temperature, after exposure to an hydrogen plasma, the resistivity increases and shows a temperature dependence typical for insulators. The modification can be perfectly reversed by annealing the hydrogenated sample [5.168].

5.2.7 Graphene Devices

A number of features of graphene may be employed for devices. Ten nanometer scale graphene structures show high-quality transistor action (Fig. 5.46b). Best candidates for graphene-based FETs will be devices based on quantum dots and devices using p–n junctions in bilayer graphene [5.144]. Negligible spin–orbit coupling makes the spin polarization in graphene to survive over sub-micrometer distances yielding applications in spintronics. Superconductivity can be induced through the proximity effect and the supercurrent can be controlled by an external gate voltage giving prospects for usage in superconductive FETs (see [5.144]). The sensitivity of the graphene electrical resistivity to the absorption of gases may be employed for sensor operation (see [5.144]).

5.3 Fullerenes, Large Carbon Molecules, and Hollow Cages of Other Materials

The C_{60} molecule, discovered in 1985 [5.1], was the first carbon nanostructure. Later on, a variety of different sizes of fullerenes, compounds, doped fullerenes, endohedral fullerenes, and intercalated fullerene crystals were synthesized. In addition, hollow nanospheres of other materials could be prepared. Finally C_{60} molecules and larger compounds have been used in order to study quantum objects and the limits of wave-particle duality.

5.3.1 Fullerenes

The initial C_{60} molecule of carbon atoms (soccer ball) is a truncated icosahedron with 20 hexagons and 12 pentagons (Fig. 5.47). The carbon atoms are connected by sp^2 bonds in the sphere surface and weaker π bonds of the orbitals perpendicular to the surface. For the hexagon–hexagon carbon–carbon bonds a length of 0.1388 nm and for the pentagon–hexagon-type bond a length of 0.1432 nm is determined yielding a C_{60} diameter of 0.71 nm. These molecules can crystallize in an fcc lattice where the molecules with a 1-nm nearest-neighbor distance freely rotate at ambient temperature. This crystal is a semiconductor with a direct band gap of 1.5–2.0 eV. By intercalation of, e.g., C_{60} [5.169] or C_{70} crystals [5.170] with alkali atoms a metallic behavior is obtained and in intercalated C_{60} crystals superconductivity is observed with transition temperatures of 33 K for Rb_2Cs C_{60} [5.169]. By adding five hexagons (10 carbon atoms) to the C_{60} structure, the C_{70} fullerene molecule (rugby ball; Fig. 5.47) is formed and many larger fullerenes such as C_{76} [5.171], C_{82}, C_{84} [5.172], C_{96} [5.173], up to C_{300} [5.174] and also the smallest fullerene, C_{20} [5.175], have been synthesized. It may be mentioned here that fullerenes also

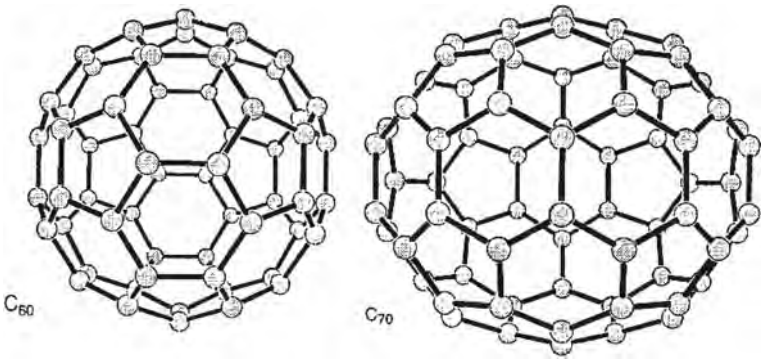

Fig. 5.47 Structure of the fullerenes C_{60} (*soccer ball*) and C_{70} (*rugby ball*). (Reprinted with permission from [5.190]. © 1993 H. Eickenbusch)

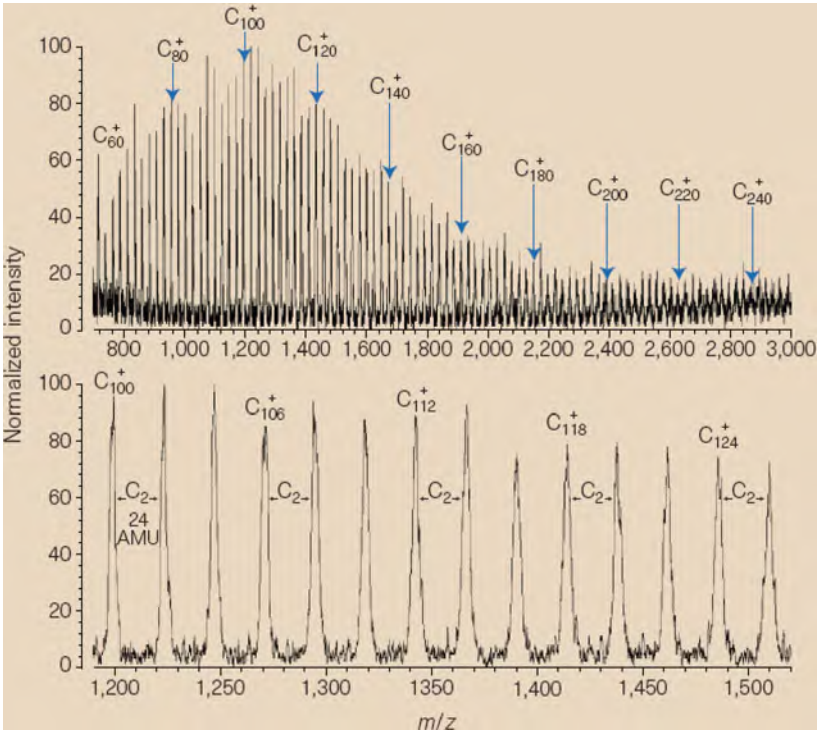

Fig. 5.48 Mass spectra from an extract of the Allende meteorite containing C_{60} and larger carbon clusters. (Reprinted with permission from [5.177]. © 1999 Nature Publishing Group)

occur naturally in minerals [5.176] or in the Allende meteorite (see Fig. 5.48 and Sect. 3.8). Fullerenes have also been detected in the soot of candle lights (see [5.178]). Thus, we now realize that humans have been synthesizing fullerenes for thousands of years.

5.3.2 Fullerene Compounds

Endohedral metallofullerenes were synthesized where single or a few metal atoms as La [5.179], Y [5.180], U [5.181], Fe [5.182], Co [5.183], and Gd [5.184] were encapsulated in fullerene molecules and purified. A Sc dimer was encaged in C_{66} ($Sc_2@C_{66}$; Fig. 5.49 a) and $Sc_2@C_{84}$ in a carbon nanotube (Fig. 5.49b) forming a peapod.

Attachment of foreign atoms to the fullerene shell and *integration* of foreign atoms into the shell have also been studied. When charge-donating K atoms are attached to the C_{60} host, spectroscopic measurements show that each attached K atom donates ~0.6 electrons to the C_{60} molecule, thereby enabling its electronic

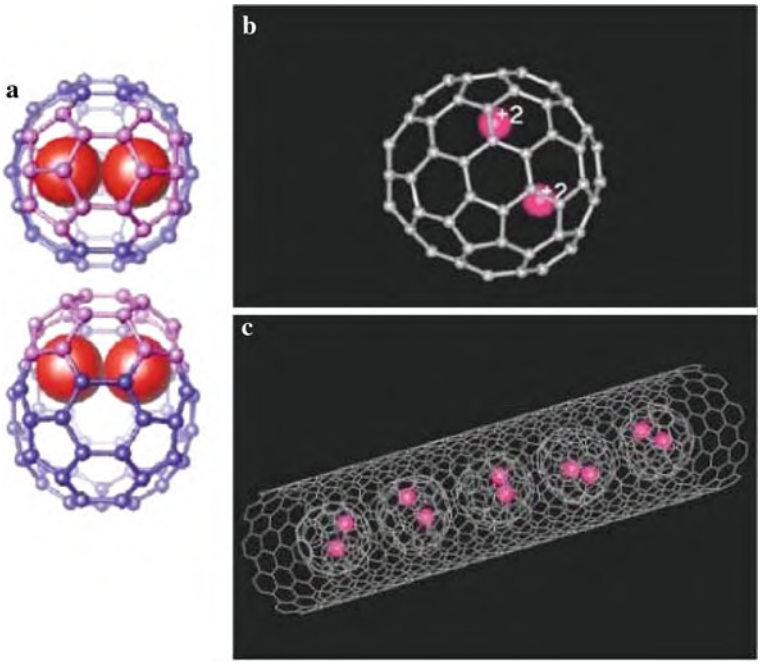

Fig. 5.49 (**a**) Top view and side view of a Sc–Sc dimer in C_{66} derived from x-ray powder diffraction and ^{13}C nuclear magnetic resonance. The C_{66} molecule is stabilized by a charge transfer from Sc–Sc (Sc–Sc distance 0.287 nm) resulting in a formal electronic state $(Sc_2)^{2+}@C_{66}^{2-}$ of the endohedral metallofullerene [5.185]. (**b**) The atomic positions in $Sc_2@C_{84}$. Two divalent Sc atoms are located at a 0.20 nm distance to the molecular center with the Sc–Sc distance 0.35 nm [5.186]. (**c**) Schematic presentation of the peapod with $Sc_2@C_{84}$ molecules aligned in a SWNT [5.186]. (Reprinted with permission from [5.185] (**a**) and [5.186] (**b**) (**c**). © 2000 Nature Publishing Group (**a**) and © 2003 American Physical Society (**b**) (**c**))

structure to be precisely and reversibly tuned (Fig. 5.50a). After incorporation of a nitrogen atom into a C_{60} sphere by replacing a carbon atom, this $C_{59}N$ molecule (Fig. 5.50e) exhibits a rectifying effect. Further replacement of carbon atoms by nitrogen yields the $C_{48}N_{12}$ azafullerene (see Fig. 5.50f) with a high hardness of 7 GPa and a Young's modulus of 37 GPa.

A cornucopia of organofullerenes can be created by, e.g., bonding organic molecules to fullerenes or by polymerization of fullerenes (Fig. 5.51).

5.3.3 Superheating and Supercooling of Metals Encapsulated in Fullerene-Like Shells

As discussed earlier (see Sect. 3.8), high pressures can be built up in the interior of fullerenes under electron irradiation. Nanometer-sized tin and lead crystals

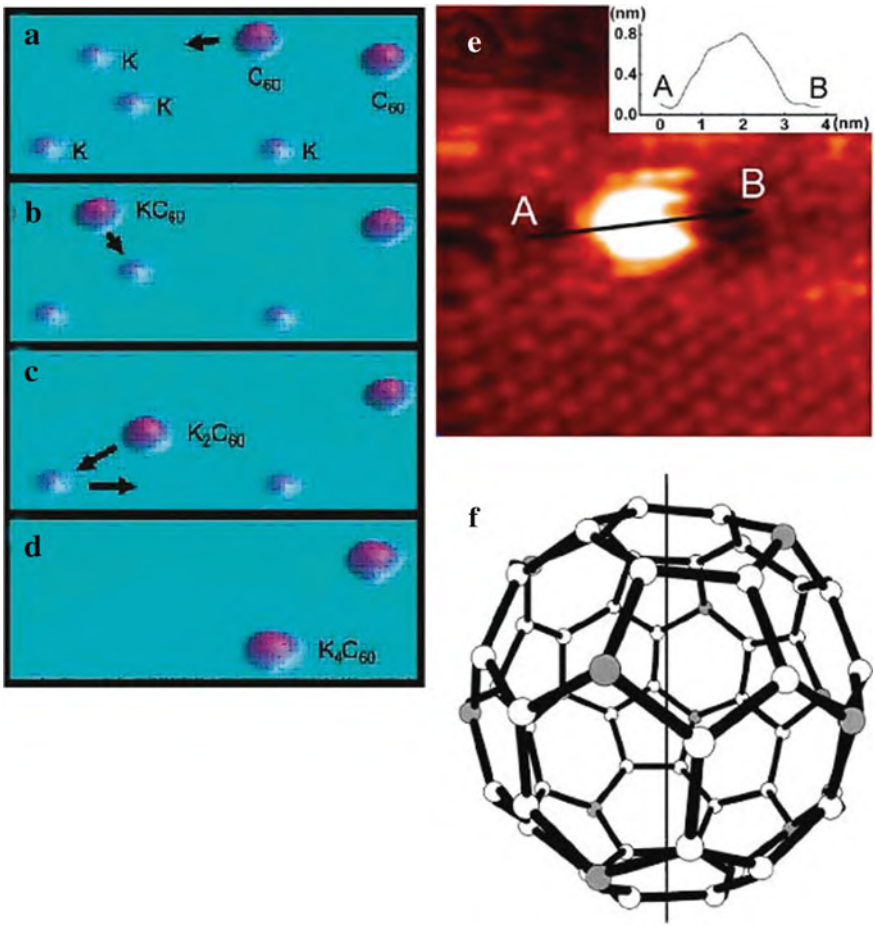

Fig. 5.50 (**a**–**d**) STM images showing the formation of K_4C_{60} (22.7 nm by 11.5 nm) [5.187]. (**e**) STM image of $C_{59}N$ molecule on an alkanethiol self-assembled monolayer (SAM). The height profile along A–B is shown in the *inset*. The asymmetry induced by the N atom is visible [5.188]. (**f**) Structure of $C_{48}N_{12}$ azafullerene; N is shown in *gray*. The *solid line* shows the (C_6) symmetry axis [5.189]. (Reprinted with permission from [5.188] (**a**–**e**) and [5.189] (**f**). © 2005 American Physical Society (**a**–**e**) and © 2001 American Physical Society (**f**))

exhibit drastically altered melting and solidification behavior when encapsulated in fullerene like graphitic shells. The melting transition of encapsulated Sn is shown in an in situ electron microscopy study to occur at temperatures higher than 770 K (Fig. 5.52), significantly higher than the melting point of bulk β-Sn ($T_m = 505$ K). The liquid Sn droplets were found to solidify below 370 K, well below T_m. The driving force for superheating is a pressure buildup of up to 3 GPa that prevails inside graphitic shells under electron irradiation [5.192].

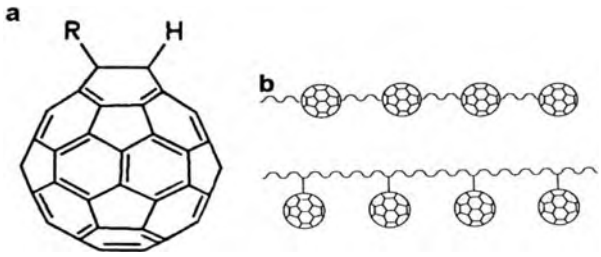

Fig. 5.51 (**a**) Organofullerene $C_{60}HR$ (R=methyl, ethyl, etc.) [5.190]. (**b**) Polymers with C_{60} units [5.191]. (Reprinted with permission from [5.190] (**a**) and [5.191] (**b**). © 1993 H. Eickenbusch (**a**) and © 1993 Nature Publishing Group (**b**))

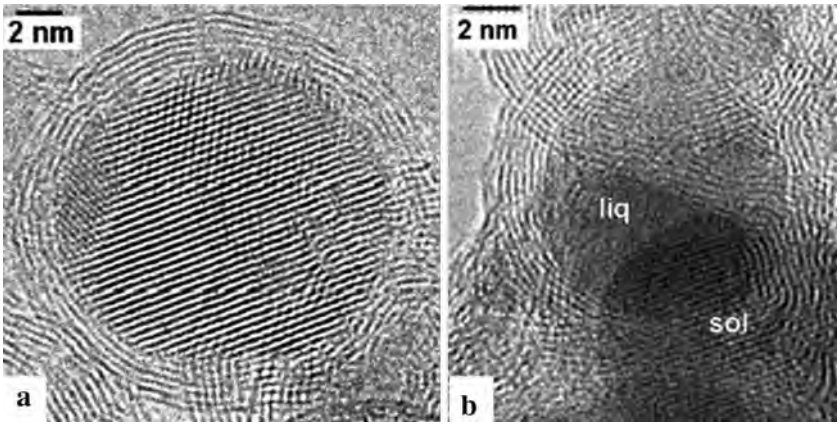

Fig. 5.52 Sn nanocrystals encapsulated by graphitic onion-like shells. (**a**) Sn nanocrystal superheated at 770 K. The spacing of the lattice fringes is 0.29 nm corresponding to the (200) lattice planes of β-Sn. (**b**) Supercooled liquid Sn droplet ("liq") at 370 K which was previously subject to melting at high temperatures. Several adjacent particles overlap in the projection. (Reprinted with permission from [5.192]. © 2003 American Physical Society)

5.3.4 Large Carbon Molecules

The basic unit of an armchair nanotube, referred to as "carbon nanohoop," (Fig. 5.53a) has been synthesized by solution-phase chemistry [5.193]. These molecules (also called cycloparaphenylenes) consist of a circle of benzene rings, where each ring is connected by a carbon–carbon single bond. This chemistry may be used to prepare nanotubes with specific structures and hence specific properties. Nanoscale carbon molecular spoked wheels (Fig. 5.53b, c) can be synthesized with various sizes and properties [5.194].

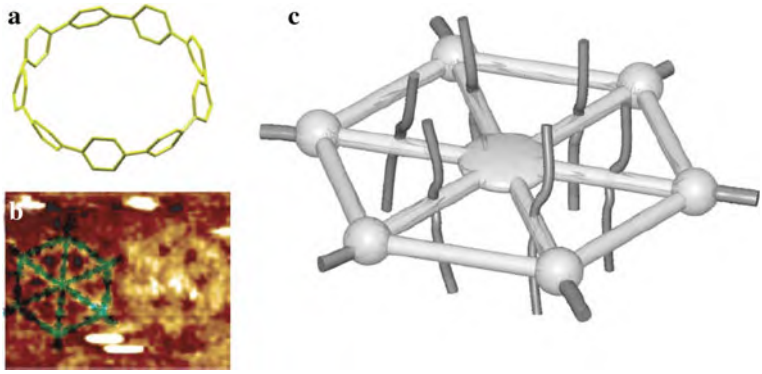

Fig. 5.53 (**a**) Energy-minimized geometry of a carbon nanohoop with nine benzene rings as calculated by density-functional theory [5.193]. (**b**) Scanning tunneling microscopy of a carbon molecular spoked wheel. (**c**) Detailed structure of this wheel [5.194]. (Reprinted with permission from [5.193] (**a**) and [5.194] (**b**) (**c**). © 2008 American Chemical Society (**a**) and © 2007 Wiley-VCH (**b**) (**c**))

5.3.5 Hollow Cages of Other Materials

Forming football-shaped molecules is no longer the sole preserve of carbon atoms. Clusters of 20 gold atoms or less can form clusters from pyramids to gold cages (Fig. 5.54a) with diameters >0.55 nm. Larger hollow spheres have been prepared from semiconductors such as GaN (Fig. 5.54b), ZnS [5.195], CdS [5.196] or from uranium [5.197] and the existence of a stable boron buckyball B_{80} has been predicted [5.198].

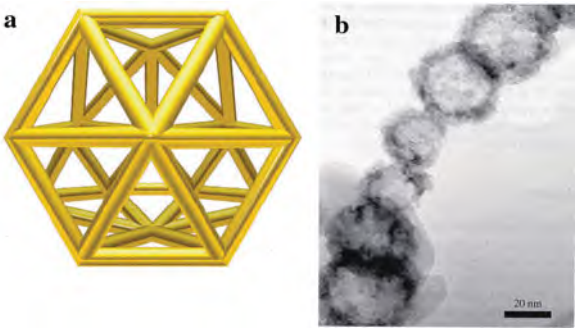

Fig. 5.54 (**a**) Nanocage of gold atoms [5.199, 5.200]. (**b**) TEM image of aligned hollow GaN spheres [5.201]. (Reprinted with permission from [5.200] (**a**) and [5.201] (**b**). © 2006 Nature Publishing Group (**a**) and © 2005 Wiley-VCH (**b**))

5.4 Fullerenes and the Wave-Particle Duality

Since the early days of quantum theory it has been a fundamental question whether the concepts of quantum physics do apply to every day "classical" objects as well as to those in the atomic and sub-atomic regime. Can we meaningfully attribute wave properties to an every day object such as a football or does quantum theory break down at some level? More than 80 years ago Louis de Broglie suggested that "atomic" particles such as electrons had wave as well as particle properties with the wavelength $\lambda = h/mv$ where h is Planck's constant, m the mass of the particle, and v its velocity. This suggestion received early confirmation from the Davisson and Germer electron diffraction experiments [5.202].

An archetypal example demonstration of wave-particle duality is the two-slit experiment with particles (Fig. 5.55a). A particle wave crosses a screen with two slits. The wave splits into two parts, which are re-united on a screen, yielding an interference pattern. It is the creation of an interference pattern that is an unambiguous signature of a wave. Interference – the addition or cancellation of overlapping waves – is in this case a purely quantum effect and cannot be understood if the molecules are viewed as discrete particles. It is possible only if the molecules are in a superposition of states (see Sect. 7.2) – in several places at once (see [5.203]. On the other hand, when the object reaches the screen it is always detected as a particle – hence the term "wave-particle duality." The central question, if and how quantum theory applies to macroscopic objects, has been extended to C_{60} molecules [5.204, 5.205]. A C_{60} beam emerging from an oven at a temperature of 900 K is collimated, velocity selected, and passed through a grating whose slits are 50 nm wide and 100 nm apart. The emerging beam is detected and found to form an interference pattern (Fig. 5.55b) that is completely explicable on the basis that the beam has wave properties.

C_{60} is of course not a macroscopic object but it is an order of magnitude more massive than anything else studied before. For studying even heavier particles, Talbot–Lau interferometry [5.206–5.208] is employed which investigates near-field effects where the curvature of the molecular wave fronts has to be taken into account. By using this technique, the wave nature of the biomolecule tetraphenylporphyrin, serving as a color center, e.g., in chlorophyll and in hemoglobin, and of the fluorofullerene $C_{60}F_{48}$ more than twice as heavy as C_{60} (see Fig. 5.56), or of perfluoroalkyl-functionalized azobenzenes ($C_{30}H_{12}F_{30}N_2O_4$ [5.209]) could be demonstrated. By a further development of this type of interferometry, tests of the wave nature of particles thousand times heavier than C_{60} such as viruses, giant proteins, or nanocrystals are envisioned [5.210].

For answering the question where the boundary between quantum behavior and classical behavior of particles is located, not only the size but also the particles interaction with its environment is of importance. When a hot particle cools in the interferometer it loses its diffraction fringe-forming coherence by radiating to the environment. The photons emitted from a hot C_{60} molecule carry information that can localize its path. This information entangles the environment in a state that picks out one path. This leads to decoherence and the particle becomes classical [5.213].

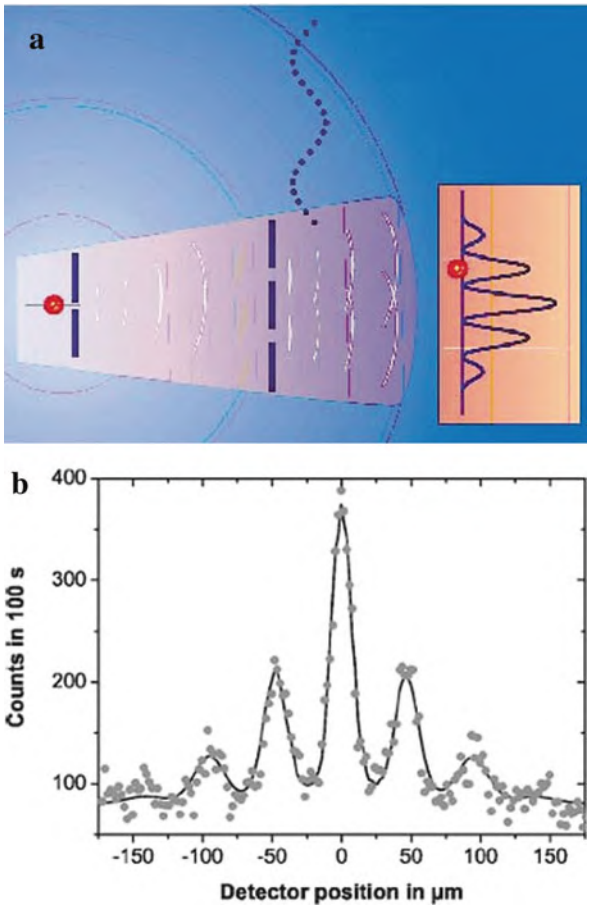

Fig. 5.55 (**a**) Two-slit diffractometer setup for demonstrating the wave-particle duality. A beam of particles passes through a double slit in the form of a wave and produces an interference pattern. The experiments on C_{60} (**b**) demonstrate this effect. The molecule may absorb or emit radiation when passing through the apparatus (*dotted wave*). Provided the wavelength of this radiation is much larger than the distance of the slits, the interference pattern is unaffected, i.e., decoherence is negligible [5.211]. (**b**) Far-field diffraction of C_{60} using velocity selection with a mean velocity $\bar{v} = 117$ m/s and a width $\Delta v/v \sim 17\%$. The *circles* are the experimental data and the *line* represents a Kirchhoff–Fresnel diffraction model. The van der Waals interaction between the molecule and the grating is taken into account by a reduced slit width [5.205]. (Reprinted with permission from [5.211] (**a**) and [5.205] (**b**). © 1999 Nature Publishing Group (**a**) and © 2003 American Association of Physics Teachers (b))

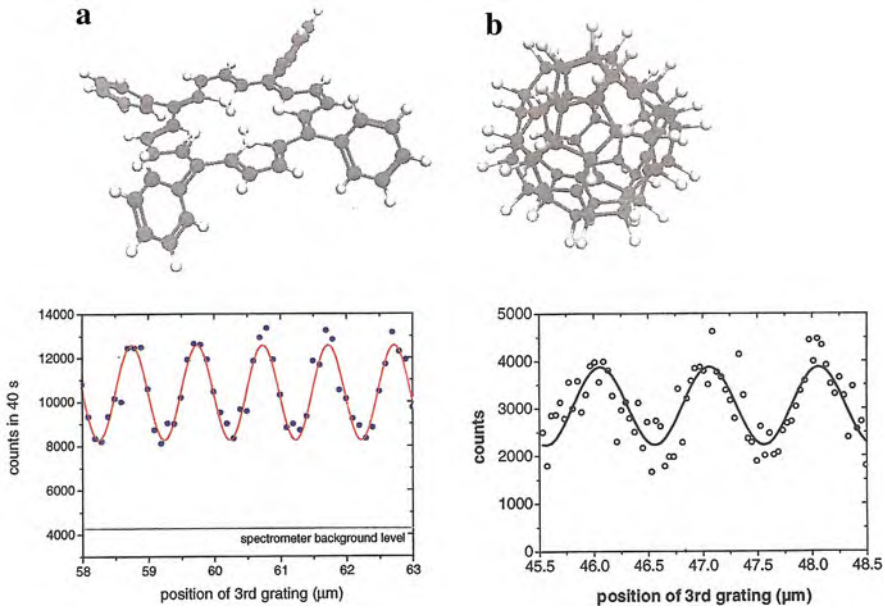

Fig. 5.56 *Upper panels*: 3D structures of tetraphenylporphyrin (TPP) $C_{44}H_{30}N_4$ ($m = 614$ amu; *left*) and the fluorofullerene $C_{60}F_{48}$ ($m = 1{,}632$ amu; *right*). *Lower panels*: (**a**) De Broglie near-field interference fringes of TPP using a Talbot–Lau interferometer. (**b**) Quantum interference fringes of $C_{60}F_{48}$ in a Talbot–Lau interferometer. (Reprinted with permission from [5.212]. © 2003 American Physical Society)

It was found that the decay of quantum coherence (see Sect. 7.2) and interference happened at precisely the rate predicted by theory (see [5.203].

5.5 Summary

Three types of carbon nanostructures have been synthesized: carbon nanotubes, monatomic layers of carbon atoms (graphene), and fullerenes. Carbon nanotubes are because of their high mechanical strength and their high thermal and electronic conductivities of particular interest for application. In addition, they can be used as tips for scanning probe microscopy in deep trenches or with chemical sensitivity. Starting from carbon nanotubes, more complex nanostructures (pea pods, etc.) can be fabricated. A great many of nanotubes of other materials have been synthesized. In graphene, the electrons exhibit the behavior of massless Dirac fermions and quantum Hall effect. Graphene nanostripes are semiconducting with high-quality transistor action even at room temperature. Fullerene molecules with the most prominent C_{60} structure and many other cage-like carbon molecules can be doped and form a variety of carbon compounds. Fullerene-like structures

have also been formed from other materials. Fullerenes have been used for probing the quantum mechanical wave-particle duality up to particles masses of ca. 1,600 amu.

References

5.1 H.W. Kroto et al., Nature **318**, 162 (1985)
5.2 W. Krätschmer et al., Nature **347**, 354 (1990)
5.3 S. Iijima, Nature **354**, 56 (1991)
5.4 K.S. Novoselov et al., Science **306**, 666 (2004); Proc. Natl. Acad. Sci. USA **102**, 10451 (2005)
5.5 S. Iijima, Nat. Nanotechnol. **2**, 590 (2007)
5.6 Ando et al., Materials today, October 2004, p. 22
5.7 S.M. Huang, et al., J. Am. Chem. Soc. **125**, 5636 (2003)
5.8 X. Zhao et al., Phys. Rev. Lett. **92**, 125502 (2004)
5.9 C. Journet et al., Nature **388**, 756 (1997)
5.10 J. Robertson, Materials today **10**, Jan – Feb 2007, p. 36
5.11 T. Nozaki, K. Okazaki, Plasma Process. Polym. **5**, 300 (2008)
5.12 S. Helveg et al., Nature **427**, 426 (2004)
5.13 S. Hofmann et al., Appl. Phys. Lett. **83**, 135 (2003)
5.14 M. Cantoro et al., Nano Lett. **6**, 1107 (2006)
5.15 Y. Wang et al., Chem. Phys. Lett. **364**, 568 (2002)
5.16 M.J. Bronikowski et al., J. Vac. Sci. Technol. A **19**, 1800 (2001)
5.17 M. Terrones et al., Materials today, October 2004, p. 30
5.18 M.C. Hersam, Nat. Nanotechnol. **3**, 387 (2008)
5.19 M. Zheng, E.D. Semke, J. Am. Chem. Soc. **129**, 6084 (2007)
5.20 L. Ding et al., Nano Lett. **9**, 800 (2009)
5.21 C. Sealy, Nanotoday, April 2009, p. 109
5.22 W. Hönlein, F. Kreupl, Physik Journal **3**, Nr. 10, 39 (2004)
5.23 A. Jorio et al., MRS Bull. April 2004, p. 276
5.24 Ch. Schönenberger, Nat. Nanotechnol. **4**, 147 (2009)
5.25 V.V. Deshpande et al., Science **323**, 106 (2009)
5.26 N.F. Mott, Proc. Phys. Soc. **A62**, 416 (1949)
5.27 L. Balents, M.P.A. Fisher, Phys. Rev. B **55**, 11973 (1997)
5.28 P. Avouris, MRS Bull. **29**, June 2004, p. 403
5.29 P.L. McEuen, J.-Y. Park, MRS Bull. April 2004, p. 272
5.30 T. Dürkop et al., in *Structural and Electronic Properties of Molecular Nanostructures*, eds. by H. Kuzmany et al. AiP Conference Proceedings, vol. 633 (American Institute of Physics, New York, 2002), p. 242
5.31 A. Aviram, M.A. Ratner, Chem. Phys. Lett. **29**, 277 (1974)
5.32 L. Lüer et al., Nat. Phys. **5**, 54 (2009)
5.33 S.J. Tans et al., Nature **386**, 474 (1997)
5.34 R. Martel et al., Appl. Phys. Lett. **73**, 2447 (1998)
5.35 A. Javey et al., Nat. Mater. **1**, 241 (2002)
5.36 L.C. Venema et al, Science **283**, 52 (1999)
5.37 J.P. Lu, Phys. Rev. Lett. **74**, 1123 (1995)
5.38 E.D. Minot et al., Nature **428**, 536 (2004)
5.39 K. Tsukagoshi et al., Nature **401**, 572 (1999)
5.40 B.W. Alphenaar et al., J. Appl. Phys. **89**, 6863 (2001)
5.41 A. Bachtold et al., Nature **397**, 673 (1999)
5.42 S. Zaric et al., Science **304**, 1129 (2004)

5.43 Y. Aharonov, D. Bohm, Phys. Rev. **115**, 485 (1959)
5.44 I. Takesue et al., Phys. Rev. Lett. **96**, 057001 (2006)
5.45 J. Haruyama et al., Appl. Phys. Lett. **84**, 4714 (2004)
5.46 B. Braunecker et al., Phys. Rev. Lett. **102**, 116403 (2009)
5.47 J.A. Rodríguez-Manzo et al., Proc. Natl. Acad. Sci. USA **106**, 4591 (2009)
5.48 J. Lefebre et al., Phys. Rev. Lett. **90**, 217401 (2003)
5.49 C.D. Spataru et al., Phys. Rev. Lett. **92**, 077402 (2004)
5.50 M. Freitag et al., Nano Lett. **3**, 1067 (2003)
5.51 A. Misewich et al., Science **300**, 783 (2003)
5.52 S.-Y. Ju et al., Science **323**, 1319 (2009)
5.53 G.E. Begstrup et al., Phys. Rev. Lett. **99**, 155901 (2007)
5.54 G. Overney et al., Z. Phys. **D27**, 93 (1993)
5.55 M.M. J. Treacy et al., Nature **381**, 678 (1996)
5.56 A.B. Dalton et al., Nature **423**, 703 (2003)
5.57 T. Hertel et al., J. Phys. Chem. **B102**, 910 (1998)
5.58 A. Rochefort et al., Phys. Rev. B **60**, 13824 (1999)
5.59 M. Zhang et al., Science **309**, 1215 (2005)
5.60 M.B. Nardelli et al., Phys. Rev. Lett. **81**, 4656 (1996)
5.61 A.J. Stone, D.J. Wales, Chem. Phys. Lett. **128**, 501 (1986)
5.62 B. Peng et al., Nat. Nanotechnol. **3**, 626 (2008)
5.63 J.Y. Huang et al., Phys. Rev. Lett. **98**, 185501 (2007)
5.64 L. Sun et al., Science **312**, 1199 (2006)
5.65 A.V. Krasheninnikov et al., Chem. Phys. Lett. **418**, 132 (2006)
5.66 A.V. Krasheninnikov, J. Banhart, Nat. Mater. **6**, 723 (2007)
5.67 N.R. Wilson, J.V. Macpherson, Nat. Nanotech. **4**, 483 (2009)
5.68 H.J. Dai et al., Nature **384**, 147 (1996)
5.69 S.S. Wong et al., Nature **394**, 52 (1998)
5.70 P. Kim, C. Lieber, Science **286**, 2148 (1999)
5.71 H.J. Dai, C.M. Lieber, Ann. Rev. Phys. Chem. **44**, 237 (1993)
5.72 S.S. Wong et al., J. Am. Chem. Soc. **120 B**, 557 (1998)
5.73 B.W. Smith et al., Nature **396**, 323 (1998)
5.74 M. Sano et al., Science **293**, 1299 (2001)
5.75 D.Y. Zhong et al., Appl. Phys. Lett. **83**, 4423 (2003)
5.76 G.Y. Zhang et al., Science **300**, 472 (2003)
5.77 W.A. de Heer et al., Science **307**, 907 (2005)
5.78 A.V. Melechko et al., J. Appl. Phys. **97**, 041301 (2005)
5.79 B.C. Satishkumar et al., Appl. Phys. Lett. **77**, 2530 (2000)
5.80 P.W. Chin et al., Appl. Phys. Lett. **80**, 3811 (2002)
5.81 M. Terrones et al., Phys. Rev. Lett. **89**, 075505 (2002)
5.82 T. Okazaki et al., J. Am. Chem. Soc. **123**, 9673 (2001)
5.83 M. Koshino et al., Science **316**, 853 (2007)
5.84 G.Y. Zhang, E.G. Wang, Appl. Phys. Lett. **82**, 1926 (2003)
5.85 R.R. Meyer et al., Science **289**, 1324 (2000)
5.86 K. Hirahara et al., Phys. Rev. Lett. **85**, 5384 (2000)
5.87 K. Suenaga et al., Science **290**, 2280 (2000)
5.88 J.H. Lee et al., Nature **415**, 1005 (2005)
5.89 D. Nishide et al., Chem. Phys. Lett. **428**, 356 (2006)
5.90 T. Takenobu et al., Nat. Mater. **2**, 683 (2003)
5.91 M.S. Strano, Nat. Mater. **5**, 433 (2006)
5.92 J.C. Grunlan et al., Nano Lett. **6**, 911 (2006)
5.93 M. Mertig, Info Phystech, VDi Technologiezentrum Nr. 65/2006
5.94 L. Letellier et al., Res. Microbiol. **154**, 283 (2004)
5.95 A. Rustom et al., Science **303**, 1007 (2004)

5.96 Y. Oshima et al., Phys. Rev. Lett. **91**, 205503 (2003)
5.97 Y.C. Sui et al., Appl. Phys. Lett. **84**, 1525 (2004)
5.98 Y. Sun et al., Adv. Mater. **15**, 641 (2003)
5.99 G. Tourillon et al., Electrochem. Sol. Stat. Lett. **3**, 20 (2000)
5.100 K. Nielsch et al., Adv. Eng. Mater. **7**, 217 (2005)
5.101 Y.H. Tang et al., Phys. Rev. Lett. **95**, 116102 (2005)
5.102 J. Goldberger et al., Nature **422**, 599 (2003)
5.103 A. Celik-Aktas et al., Appl. Phys. Lett. **86**, 133110 (2005)
5.104 C.Y. Zhi et al., J. Appl. Phys. **91**, 5325 (2002)
5.105 Cuong Pham-Huu et al., J. Catalysis **200**, 400 (2001)
5.106 M. Remskar et al., Science **292**, 479 (2001)
5.107 R.L. D. Whitby et al., Appl. Phys. Lett. **79**, 4574 (2001)
5.108 J.P. Zou et al., Appl. Phys. Lett. **80**, 1079 (2002)
5.109 H.J. Fan et al., Nat. Mater. **5**, 627 (2006)
5.110 J.L. Shen et al., J. Phys.: Condens. Matter **15**, L527 (2003)
5.111 P. Levy et al., Appl. Phys. Lett. **83**, 5247 (2003)
5.112 A. Greiner et al., Appl. Microbiol. Technol. **71**, 387 (2006)
5.113 J.E. Reiner et al., Proc. Natl. Acad. Sci. USA **103**, 1173 (2006)
5.114 J.H. Lee et al., Proc. Natl. Acad. Sci. USA **104**, 20410 (2007)
5.115 G.Y. Zhang et al., J. Appl. Phys. **91**, 9324 (2002)
5.116 J.P. Cheng et al., Appl. Phys. Lett. **85**, 5140 (2004)
5.117 Y.B. Mao, S.S. Wong, J. Am. Chem. Soc. **128**, 8217 (2006)
5.118 M. Nath et al., Chem. Phys. Lett. **368**, 690 (2003)
5.119 M. Terrones et al., Materials Today **10**, May 2007, p. 30
5.120 J. Robertson, Materials Today, October 2004, p. 46
5.121 R.H. Baughman et al., Science **292**, 787 (2002)
5.122 K. Jiang et al., J. Mater. Chem. **14**, 37 (2004)
5.123 Y.L. Lie et al., Science **304**, 276 (2004)
5.124 N. de Jonge et al., Nature **420**, 393 (2002)
5.125 J.H. Hafner et al., Am. Chem. Soc. **121**, 9750 (1999)
5.126 A.P. Graham et al., Diamond Relat. Mater. **13**, 1296 (2004)
5.127 Y. Zhang et al., Appl. Phys. Lett. **79**, 3155 (2001)
5.128 J.J. Plombon et al., Appl. Phys. Lett. **90**, 063106 (2007)
5.129 A. Javey et al., Nano Lett. **4**, 447 (2004)
5.130 M.S. Arnold et al., Nat. Nanotech. **1**, 60 (2006)
5.131 S.E. Thompson, S. Parthasarthy, Materials Today **9** (6), 20 (2006)
5.132 K. Jensen et al., Nat. Nanotech. **3**, 533 (2008)
5.133 B. Lassagne et al., Nano Lett. **8**, 3735 (2008)
5.134 H.-Y. Chiu et al., Nano Lett. **8**, 4342 (2008)
5.135 B. Lassagne et al., Science 1174290 (2009). doi: 10.1126/science
5.136 G.A. Steele, Science 1176076 (2009). doi: 10.1126 science
5.137 Y.C. Chen et al., Appl. Phys. Lett. **81**, 975 (2002)
5.138 D.Y. Zhang et al., Appl. Phys. Lett. **79**, 3500 (2001)
5.139 F. Villalpando-Paez et al., Phys. Chem. Lett. **386**, 137 (2004)
5.140 P.R. Wallace, Phys. Rev. **71**, 622 (1947)
5.141 J.C. Meyer et al., Nature **446**, 60 (2007)
5.142 Y. Zhang et al., Nature **438**, 201 (2005)
5.143 A.K. Geim, K.S. Novoselov, Nat. Mater. **6**, 183 (2007)
5.144 M.I. Katsnelson, Materials Today **10**, Jan-Feb 2007, p. 20
5.145 A.H. Castro Neto et al., Rev. Mod. Phys. **81**, 109 (2009)
5.146 K.L. Wang et al., Proc. IEE. **96**, 212 (2008)
5.147 M. Choucair et al., Nat. Nanotechnol. **4**, 30 (2009)
5.148 G. Brumfiel, Nature **458**, 390 (2009)

5.149 E. Stolyarova et al., Proc. Natl. Acad. Sci. USA **104**, 9209 (2007)
5.150 M.H. Gass et al., Nat. Nanotechnol. **3**, 676 (2008)
5.151 J.C. Meyer et al., Nano Lett. **8**, 3582 (2008)
5.152 C.Ö. Girit et al., Science **323**, 1705 (2009)
5.153 J.-W. Seo et al., Angew. Chem. Int. Ed. **46**, 8828 (2007)
5.154 F.D. M. Haldane, Phys. Rev. Lett. **61**, 2015 (1988)
5.155 K.S. Novoselov et al., Science **315**, 1379 (2007)
5.156 Z.Q. Li et al., Nat. Phys. **4**, 532 (2008)
5.157 W.Y. Kim, K.S. Kim, Nat. Nanotechnol. **3**, 408 (2008)
5.158 Y.M. Zuev et al., Phys. Rev. Lett. **102**, 096807 (2009)
5.159 L. Tabasztó et al., Nat. Nanotechnol. **3**, 397 (2008)
5.160 X.T. Jia et al., Science **323**, 1701 (2009)
5.161 L. Jiao et al., Nature **458**, 872 (2009)
5.162 Y.-M. Lin et al., Nano Lett. **9**, 422 (2009)
5.163 N.W. Ashcroft, N.D. Mermin, *Solid State Physics* (Holt, Rinehart and Winston, NY, 1976)
5.164 K.S. Novoselov et al., Nature **438**, 197 (2005)
5.165 E. McCann, V.I. Fal'ko, Phys. Rev. Lett. **96**, 086805 (2006)
5.166 K.S. Novoselov et al., Nat. Phys. **2**, 177 (2006)
5.167 J.M. Ziman, *Models of Disorder* (Cambridge University Press, Cambridge, 1979)
5.168 D.C. Elias et al., Science **323**, 610 (2009); Nat. Mater. **8**, 163 (2009)
5.169 R.C. Haddon, Physics Today, Nov. 1992
5.170 T. Hara et al., Phys. Rev. B **68**, 045401 (2003)
5.171 F. Dieterich et al., Science **252**, 548 (1991)
5.172 K. Kikuchi et al., Nature **357**, 142 (1992)
5.173 K. Kikuchi et al., Chem. Phys. Lett. **188**, 177 (1992)
5.174 H. Shinohara et al., J. Phys. Chem. **95**, 8449 (1991)
5.175 H. Prinzbach et al., Nature **407**, 60 (2000)
5.176 P.R. Buseck et al., Science **257**, 215 (1992)
5.177 L. Becker et al., Nature **400**, 217 (1999)
5.178 M. Bottini, T. Mustelin, Nat. Nanotechn. **2**, 599 (2007)
5.179 K. Kikuchi et al., Chem. Phys. Lett. **216**, 67 (1993)
5.180 H. Shinohara et al., J. Phys. Chem. **96**, 3571 (1992)
5.181 T. Guo et al., Science **257**, 1661 (1992)
5.182 T. Pradeep et al., J. Am. Chem. Soc. **114**, 2272 (1992)
5.183 D.S. Bethune et al., Nature **363**, 605 (1993)
5.184 E. Gillan et al., J. Phys. Chem. **96**, 6869 (1992)
5.185 C.R. Wang et al., Nature **408**, 426 (2000)
5.186 K. Suenaga et al., Phys. Rev. Lett. **90**, 055506 (2003)
5.187 R. Yamachika et al., Science **304**, 281 (2004)
5.188 J. Zhao et al., Phys. Rev. Lett. **95**, 045502 (2005)
5.189 L. Hultman et al., Phys. Rev. Lett. **87**, 225503 (2001)
5.190 H. Eickenbusch, VDI Technologiezentrum, Technologieanalyse Fullerene (1993)
5.191 R. Taylor, D.R.M. Walton, Nature **363**, 685 (1993)
5.192 F. Banhart et al., Phys. Rev. Lett. **90**, 185502 (2003)
5.193 R. Jasti et al., J. Am. Chem. Soc. **130**, 17646 (2008)
5.194 D. Mössinger et al., Angew. Chem. Int. Edn. **46**, 6802 (2007)
5.195 K.P. Velikov, A. van Blaaderen, Langmuir **17**, 4779 (2001)
5.196 J.J. Zhu et al., Adv. Mater. **15**, 156 (2003)
5.197 G.E. Sigmon et al., Angew. Chem. Int. Edn. **48**, 2737 (2009)
5.198 N.G. Szwacki et al., Phys. Rev. Lett. **98**, 166804 (2007)
5.199 S. Bulusu et al., Proc. Natl. Acad. Sci. USA **103**, 8326 (2006)
5.200 Nature **441**, 386 (2006)
5.201 L.-W. Yin et al., Small. **1**, 1094 (2005)

5.202 C.J. Davisson, L.H. Germer, Nature **119**, 558 (1927)
5.203 P. Ball, Nature **453**, 22 (2008)
5.204 M. Arndt et al., Nature **401**, 680 (1999)
5.205 O. Nairz et al., Am. J. Phys. **71**, 319 (2003)
5.206 H.F. Talbot, Phil. Mag. **9**, 401 (1836)
5.207 E. Lau, Ann. Phys. (Leipzig) **6**, 417 (1948)
5.208 B. Brezger et al., J. Opt. B: Quantum Semiclass. Opt. **5**, S82 (2003)
5.209 S. Gerlich et al., Nat. Phys. **3**, 711 (2007)
5.210 M. Arndt et al., Phys. Unserer Zeit **37**, Nr. 1, 24 (2006)
5.211 A.I.M. Rae, Nature **401**, 651 (1999)
5.212 L. Hackermüller et al., Phys. Rev. Lett. **91**, 090408 (2003)
5.213 L. Hackermüller et al., Nature **427**, 711 (2004)

Chapter 6
Nanocrystalline Materials

The design of nanocrystalline solids with novel properties different from the chemically identical coarse-grained counterparts was an early and most fruitful contribution to nanoscience [6.1, 6.2]. Nanocrystalline materials are polycrystals with a crystallite size usually in the 10-nm range and atomically disordered crystallite interfaces with a substantial volume fraction. The macroscopic properties are, therefore, dominated by the small crystallite size, giving rise to confinement effects, and the interfacial structure. Crystallites and interfaces may be of the same or of different chemical composition, composites of different materials may be fabricated, dimensionality may play a role, and a plethora of synthesis routes is available (see Chap. 3). The wide field is covered by early reviews [6.3–6.6], monographs [6.7, 6.8], and an encyclopedia (see [6.9]). In this chapter, recent developments in the field of nanocrystalline solids will be reviewed, including aspects such as atomic simulation, structure of interfaces, plasticity, strength, superplasticity, fatigue, composites, ceramics, diffusion, and surface-induced manipulation of the properties of nanomaterials.

6.1 Molecular Dynamics Simulation of the Structure of Grain Boundaries and of the Plastic Deformation of Nanocrystalline Materials

Among the various atomic-level simulation approaches, molecular dynamics (MD) has proven particularly useful for studying nanocrystalline solids [6.10–6.13]. In deformation studies by MD, rather large plastic strains can be considered, enabling the deformation under very high grain boundary and dislocation densities. However, in addition to being limited to relatively small model systems consisting of typically millions of atoms, the fundamental limitations inherent to the MD approach are well known, pertaining mainly to the reliability of the interatomic potentials used and the relatively short time period (of typically 10 ns) over which the dynamics of the system can be probed. This leads to extremely high strain rates exceeding 10^7 s^{-1}, much higher than in experiments, requiring rather high stresses. While the empirical interatomic forces used in most MD simulations are computationally highly

H.-E. Schaefer, *Nanoscience*, DOI 10.1007/978-3-642-10559-3_6,

efficient, they are unable to fully capture the many body nature of electronic bonding. Interestingly, however, a comparison between many body and pair potentials used in simulations of grain boundaries (see [6.11]) revealed only few qualitative differences, suggesting that many body effects may not dominate, e.g., the grain boundary (GB) behavior. The dynamic properties of defects (e.g., dislocations, grain boundaries, and precipitates) which dictate the mechanical properties of materials should be computed directly using quantum mechanics-based total-energy methods. However, the number of atoms necessary to do so exceeds available computational resources and will for years to come (see [6.14]). The challenge, therefore, is to identify the real physical processes (see [6.11]), so that the information extracted from simulations focuses on a careful classification of the atomic processes occurring, e.g., during plastic deformation (see [6.12]), taking into account the interplay between GB structure and deformation mechanisms, as discussed in the following sections.

6.2 Grain Boundary Structure

Coarse-grained polycrystals contain GBs with very much differing structures and with a wide spectrum of energies and properties (see [6.11, 6.15]). *Special high-angle GBs* contain no dislocations and their properties are perfect-crystal like (Fig. 6.1a) with low energies, low atomic diffusivities, and low mobilities but with high sliding resistance and cohesion. Grain boundaries of this type, i.e., twin boundaries, play a role in the process of deformation twinning (see [6.11]). In *low-angle or dislocation boundaries* the atomic structure consists of periodic arrays of dislocations and their properties are characterized by isolated lattice dislocations and their interactions. In the *general high-angle GB*, dislocation cores are completely overlapping yielding a GB structural atomic disorder similar to an amorphous material, which is characterized by the local radial distribution function, $g(r)$ (Fig. 6.1b).

According to MD simulations [6.11], the structure of GBs in nanocrystalline Pd (Fig. 6.1c) is fully disordered and virtually identical to that of high-angle (110) twist boundaries (Fig. 6.1b), i.e., to the universal structure of the high-energy GBs in coarse-grained Pd. These simulations for nanocrystalline Si and Pd [6.11] show that the randomly oriented grains are connected by a glassy intergranular "phase". These observations are consistent with simulations of the phonon density of states and of the related free energy [6.16] which indicate that below a critical grain size (1.5–3 nm) nanocrystalline microstructures are thermodynamically unstable with respect to the amorphous phase.

Temperature-dependent structural and dynamical transitions in thermal equilibrium are additionally predicted by MD simulations in highly disordered high-energy GBs in Si and Pd bicrystals (see [6.11]) at a critical temperature T_c below the melting temperature T_m (Fig. 6.1d). At $T>T_c$ the splitting of the second $g(r)$ peak observed at low temperatures (Fig. 6.1c) has disappeared. This transition has a profound influence on the high-temperature GB properties, such as GB migration,

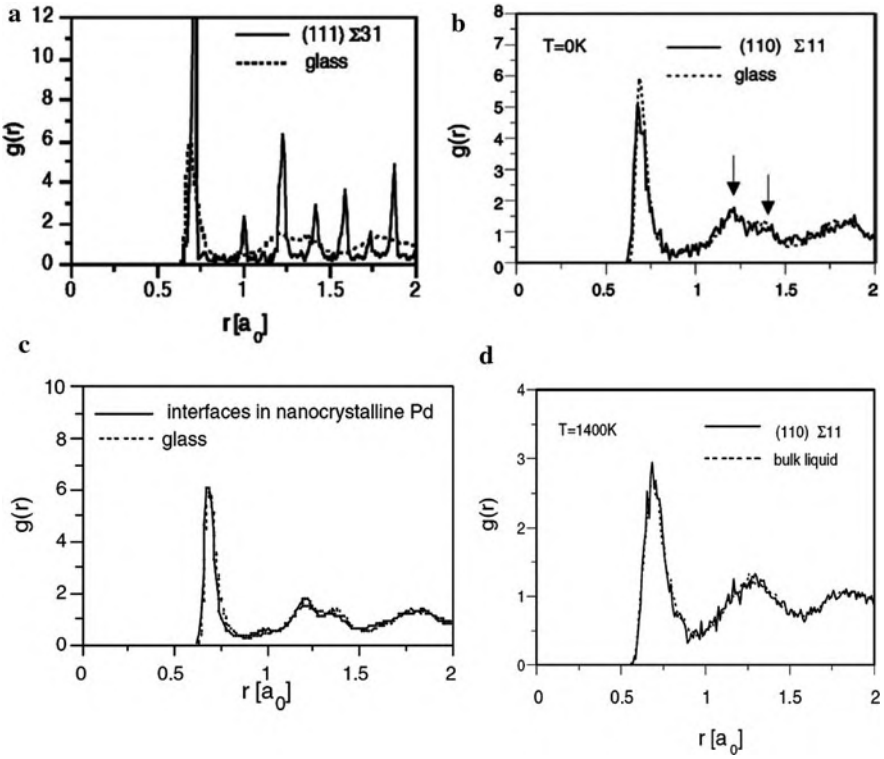

Fig. 6.1 Local radial distribution functions, $g(r)$, determined from MD simulations for high-angle twist GBs on densest lattice planes of fcc Pd, described by an embedded atom model (EAM) potential. The radial distribution function, $g(r)$, is normalized such that for large r, $g(r) = 1$. For comparison, the *dotted lines* show $g(r)$ for bulk Pd glass or bulk liquid Pd. (**a**) Bicrystal (111) $\Sigma 31$ twist boundary (Σ is the inverse density of coincidence-site lattice sites) with an energy of 300 mJ/m^2; (**b**) (110) $\Sigma 11$ twist boundary at T=0 K with an energy of 1025 mJ/m^2. The *arrows* indicate the split second peak present in both the GB and the bulk glass. (**c**) Local radial distribution function for the GB atoms in a Pd nanocrystalline solid with a grain size of 8 nm, compared to the $g(r)$ of bulk Pd glass. (**d**) High-temperature radial distribution function for the atoms in the two central planes of the (110) $\Sigma 11$ twist GB in Pd at T=1400 K compared to that of the bulk melt supercooled to the same temperature. (Reprinted with permission from [6.11]. © 2005 Elsevier)

sliding, and diffusion and hence on the mechanical behavior of nanocrystalline solids. The temperature-dependent changes of the GB mobility and GB diffusivity (Fig. 6.2) are ascribed to a transition from a low-temperature solid-like atom hopping to a high-temperature liquid-like reshuffling of the GB atoms (see [6.11]). This is consistent with an early suggestion by Mott [6.17] that the mechanism for GB migration involves local disordering, or "melting," of small groups of atoms at the boundary, thereby enabling atoms belonging to one grain to reshuffle collectively while aligning themselves to the opposite grain. According to this idea, the activation energy for GB migration at high temperatures can be substantially smaller than the activation energy for atomic diffusivity in GBs (see [6.11]).

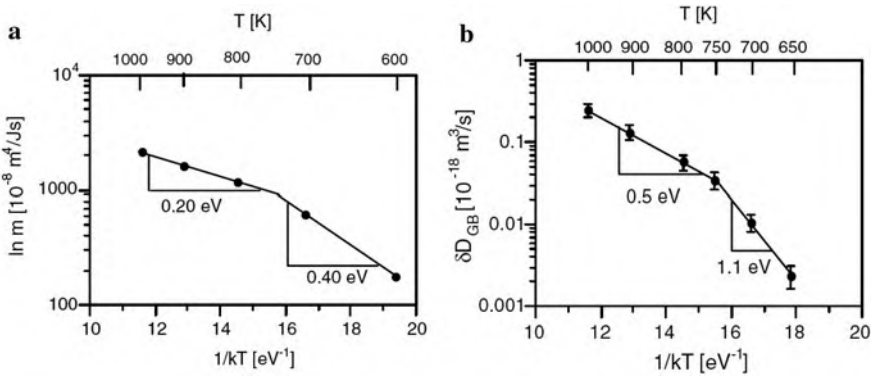

Fig. 6.2 Arrhenius plots derived from MD simulations, making use of a Lennard-Jones potential, for (**a**) the GB mobility, m, and (**b**) the GB diffusivity, δD_{GB}, for the (001) $\Sigma 29$ twist GB in Cu. (Reprinted with permission from [6.11]. © 2005 Elsevier)

Experimental evidence of the structure of grain boundaries may be derived from x-ray diffraction (XRD), high-resolution transmission electron microscopy (HRTEM), extended x-ray absorption fine-structure (EXAFS), positron annihilation (PA), or atomic diffusion (AD). From XRD of n-Pd [6.18], the atomic coordination numbers in the GBs were determined to depend on the time–temperature history of the sample, indicating that the structure of well-relaxed GBs is similar to the structure of microstructurally unconfined bicrystalline GBs. For the direct test whether the atomic structure of GBs changes reversibly with temperature, temperature-dependent XRD on fine-grained nanostructured specimens are required. Initial XRD studies on nanocrystalline $Fe_{73}Si_{16}B_7Nb_3Cu_1$ (grain size 12 nm) at ambient temperature and at T=773 K showed a reversible change of the GB radial distribution function at nearest-neighbor sites (Fig. 6.3a).

For the *lateral* resolution of atom columns in general high-angle GBs by HRTEM, 0.1-nm resolution of the microscope is required (see Fig. 6.4). One should, however, have in mind that sample preparation and high-energy electron irradiation in HRTEM may affect the GB structure. For characterization of grain boundaries *along* the columns, the application of electron microscopes with aberration correction may be promising [6.22]. From EXAFS studies a reduction of the atomic coordination in the GBs has been reported which appears to depend on the time–temperature history of the specimen [6.18, 6.23, 6.24].

By positron–electron annihilation techniques, atomic free volumes in GBs can be studied specifically [6.25]. In defect-free crystals, positrons exhibit diffusion lengths of ~100 nm prior to annihilation with electrons. In nanocrystalline solids they are, however, efficiently trapped by atomic size free volumes, which can be characterized by the annihilation signals. In nanocrystalline Pd, agglomerates of a few vacancies were detected by positron lifetime studies [6.20] with positron trapping rates varying reversibly with temperature (Fig. 6.3b). This variation may be ascribed to a temperature-dependent structural change of the agglomerates in the GBs. In GB

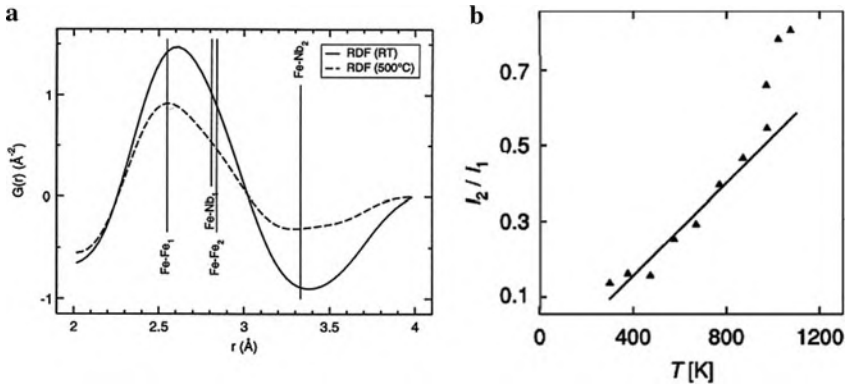

Fig. 6.3 (**a**) Nearest neighbor part of the radial distribution function $G(r)$ of atoms in the GBs of nanocrystalline $Fe_{73}Si_{16}B_7Nb_3Cu_1$ measured reversibly by x-ray diffraction at ambient temperature (RT) and at 737 K [6.19] with the bulk nearest-neighbor distance of iron atoms (Fe–Fe_1) or iron and niobium atoms (Fe–Nb_1) or the next-nearest neighbor distances (Fe–Fe_2, Fe–Nb_2) indicated. (**b**) Reversible temperature variation of the positron trapping at vacancy-size free volumes with the concentration C_1 and at vacancy agglomerates (C_2) in the grain boundaries of nanocrystalline $Pd_{84}Zr_{16}$ with a grain size of d<250 nm. The change of the intensity ratio $I_2/I_1 = \sigma_2 C_2/\sigma_1 C_1$ of the two positron lifetimes $\tau_1 = 175$ ps and $\tau_2 = 370$ ps, characteristic for the two types of interfacial free volumes, indicates a reversible change of the interfacial free volumes with temperature. σ_1 and σ_2 are the specific positron trapping rates of vacancy-size free volumes and of vacancy agglomerates, respectively [6.20]. (Reprinted with permission from [6.19] (**a**) and [6.20] (**b**). © 2005 Landesstiftung Baden-Württemberg (**a**) and © American Physical Society (**b**))

diffusion experiments, a change of the temperature dependence of the atomic diffusivity at high temperatures [6.26] is consistent with the MD simulation study of the diffusion behavior shown in Fig. 6.2b. A reversible transition from an amorphous to a liquid structure of interfaces in n-Si has been deduced from molecular dynamics simulations [6.27].

6.3 Plasticity and Hall–Petch Behavior of Nanocrystalline Materials

Low-temperature plastic deformation of coarse-grained metals involves the nucleation of dislocations from a Frank–Read source and their glide through the crystal on well-defined slip systems. In a polycrystalline material, the size L of the sources is restricted to the grain size. Since the stress $\sigma = Gb/L$ needed for their operation (G – shear modulus, b – Burgers vector) rapidly increases with decreasing L, this deformation mechanism can operate only down to a grain size of typically 1 μm. For the plastic deformation of nanocrystalline metals with smaller grain sizes (Fig. 6.5), mobile dislocations must be nucleated from other sources, such as grain boundaries or grain junctions. Recent MD simulations (see [6.11, 6.12]) suggest the existence

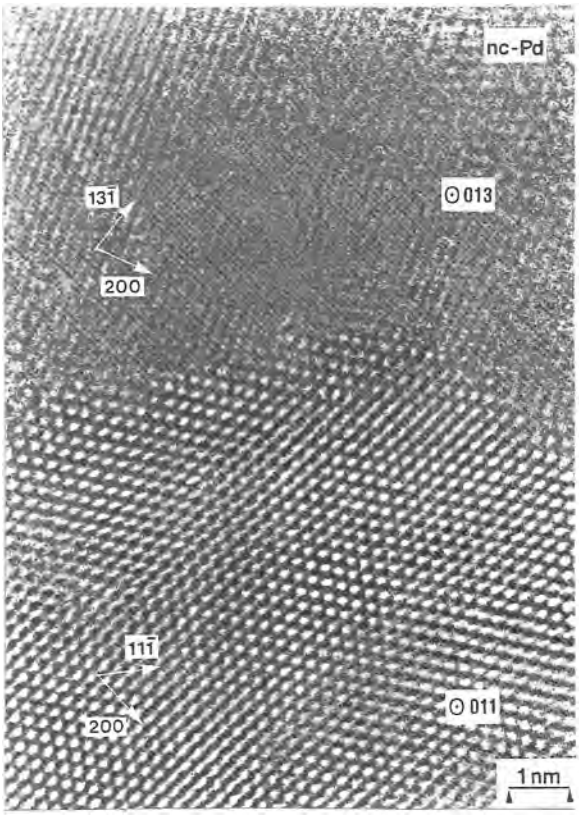

Fig. 6.4 Atomic resolution transmission electron micrograph of nanocrystalline Pd with <013> and <011> zone axes and an orientation correlationship $\Sigma>39$ of the two crystallites, giving rise to a general, high-energy grain boundary in the center of the micrograph. (Reprinted with permission from [6.21]. © 2000 Elsevier)

of a length-scale competition between the grain size d and the dislocation splitting distance r which renders, with decreasing d, the dislocation process less and less effective until, at a critical grain size d_c, grain boundary-based deformation processes dominate. The simulations also show a propensity for deformation twinning, giving rise to strain hardening.

According to the simulations, in the case of the largest nanosized grains the GBs act as sources for complete extended dislocations that subsequently glide across the grains to be finally re-incorporated into the GBs. Although Frank–Read sources cannot be operated, the material still seems to deform by the conventional dislocation–slip mechanism, including dislocation–dislocation reactions and cross slip.

When the grain size decreases well below 100 nm the deformation behavior seems to change fundamentally because of the appearance of deformation twinning in the simulations in Al with a high stacking fault energy (Fig. 6.6a). Twin deformation occurs through emission of groups of partial dislocations from grain boundaries into grain interiors (see [6.29, 6.30]). Deformation twinning in nanomaterials has been observed [6.31], [6.32] by high-resolution electron microscopy (Fig. 6.6b). Although it is unknown whether the increase in yield stress follows the $\sigma \sim d^{-1/2}$ Hall–Petch relation, two hardening mechanisms are envisaged,

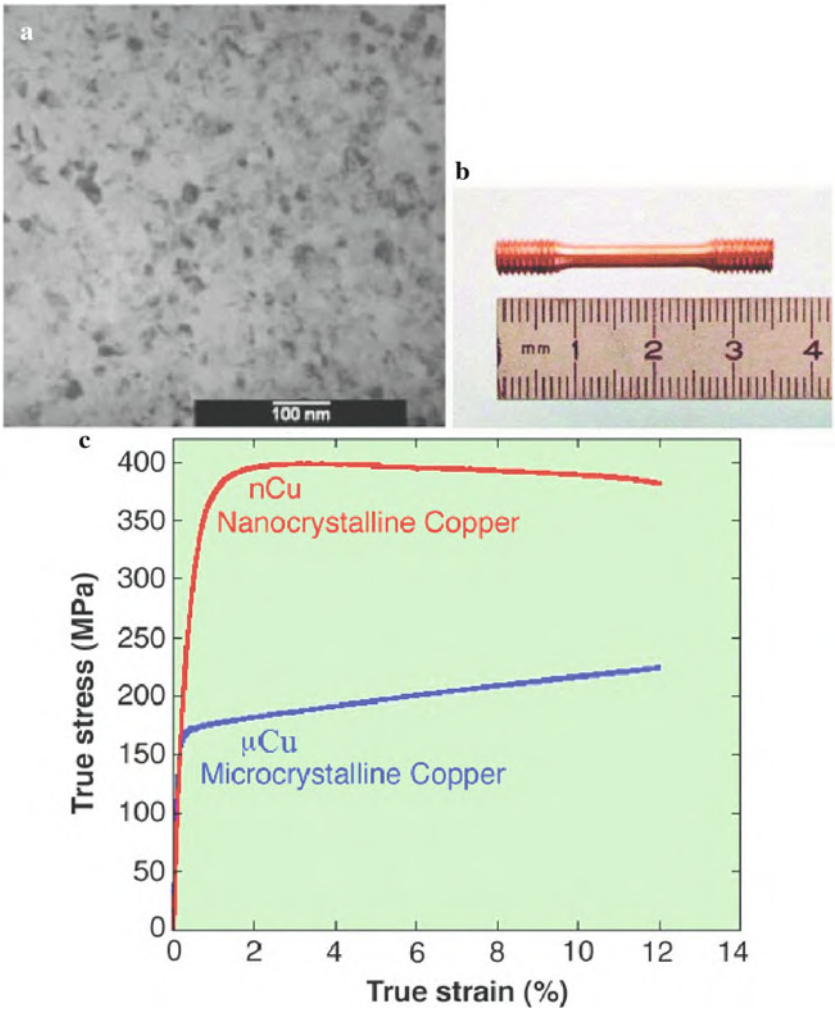

Fig. 6.5 (**a**) Transmission electron micrograph of a nanocrystalline Cu sample (grain size, 20 nm) synthesized by inert gas condensation [6.12]. (**b**) Tensile test specimen cut from nanocrystalline Cu, prepared by powder metallurgy [6.28]. (**c**) Comparison of the stress–strain curves of nanocrystalline and microcrystalline Cu, showing a higher yield strength in n-Cu; the tests were performed at a strain rate of $\dot{\varepsilon} = 5 \times 10^{-6}\mathrm{s}^{-1}$ [6.28]. (Reprinted with permission from [6.12] (**a**) and [6.26] (**b**) (**c**). © 2006 Elsevier (**a**) and © 2003 AAAS (**b**) (**c**))

including dislocation pile-ups against GBs and pile-ups against complex networks of deformation twins (see [6.11]).

As the grain size is even smaller and similar to the size of extended dislocations, slip of complete dislocations seems to be gradually replaced by the slip of partial dislocations in the MD simulations, which is also indicated in experiments [6.32].

The transition from complete- to partial-dislocation slip in simulations with decreasing grain size is accompanied by a rapid increase in the stress required to

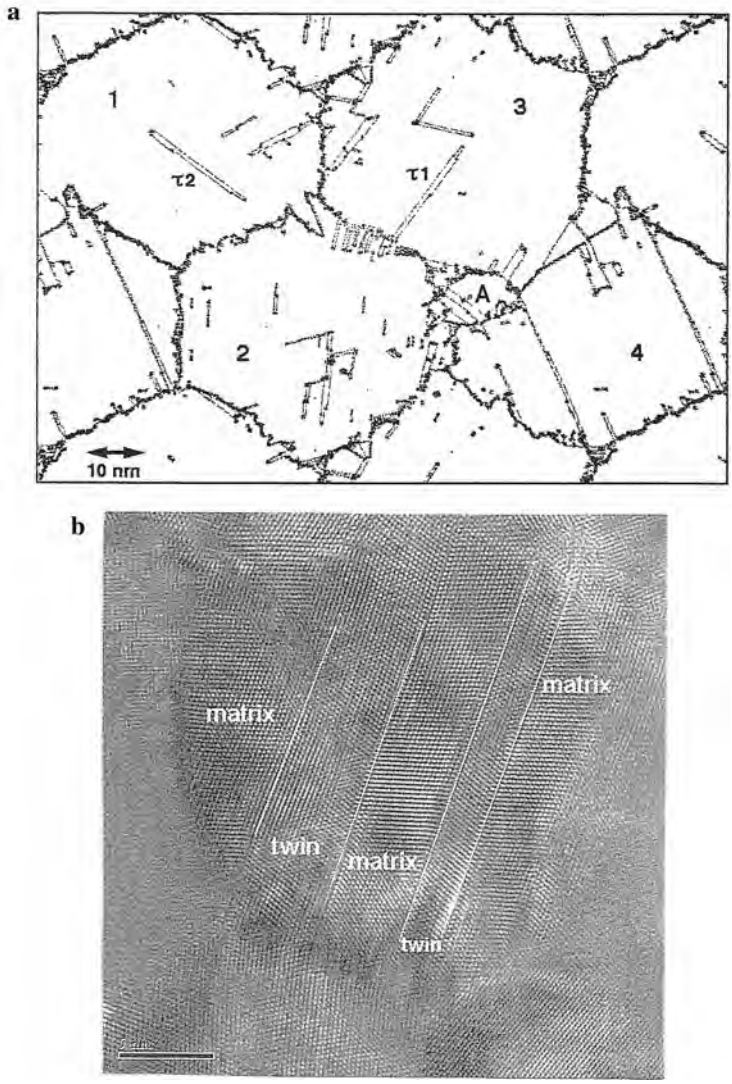

Fig. 6.6 (**a**) MD simulation of plastic deformation (strain $\varepsilon = 0.119$) of nanocrystalline Al. Formations $\tau = 1$ and $\tau = 2$ in grains 3 and 1 mark two types of deformation twins. The formation of a new grain, labeled A, is also seen (see Video 3 in [6.11]). (**b**) High-resolution transmission electron micrograph of nanocrystalline Pd deformed to $\varepsilon = 0.32$ by rolling at a strain rate $\dot{\varepsilon} = 0.3\ s^{-1}$ [6.31]. (Reprinted with permission from [6.11] (**a**) and [6.31] (**b**). © 2005 Elsevier (**a**) and © 2005 Wiley-VCH (**b**))

nucleate dislocations from the GBs. The dislocation activity therefore decreases rapidly until a GB-based deformation process takes over. The simulations reveal that this crossover in the dominating deformation mechanisms from Hall–Petch hardening to softening gives rise to a minimum in the strain rate and a maximum in the yield stress at the "strongest grain size" d_c where a maximum in hardness (Fig. 6.7a) is observed experimentally. Hardness measurements covering the crossover from normal to inverse Hall–Petch behavior have been critically discussed [6.33]. According to the simulations [6.10, 6.11], Coble creep (i.e., GB diffusion-induced grain elongation accommodated by Lifshitz sliding) characterized by a strain rate dependence $\dot{\varepsilon} \sim \sigma D_{GB}/Td^3$ (see [6.11]) seems to dominate the deformation mechanism at small grain size $d < d_c$, giving rise to a softening at small grain

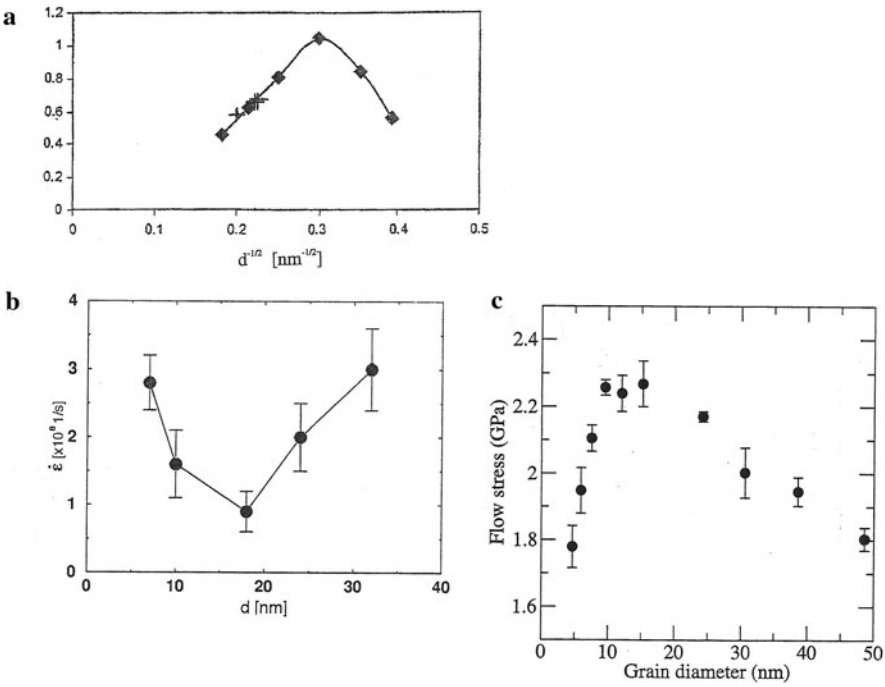

Fig. 6.7 Experimental data and MD simulation results of the Hall–Petch relation and the crossover to inverse Hall–Petch behavior in dependence of grain size d in the plastic deformation of nanocrystalline materials. (**a**) Hall–Petch plot (yield strength versus $d^{-1/2}$) for Cu. The yield strengths are obtained from tension, compression, and hardness tests on nanocrystalline Cu [6.12]; (**b**) MD simulation of the grain-size dependence of the strain rate $\dot{\varepsilon}$ of nanocrystalline Al. The minimum in $\dot{\varepsilon}$ at $d_c = 18$ nm suggests the existence of a "strongest size" at which the grains are too small to sustain the dislocation–slip process, but are still too large for GB sliding processes to dominate the deformation [6.11]; (**c**) flow stress versus d in nanocrystalline Cu [6.10]. (Reprinted with permission from [6.12] (**a**), [6.11] (**b**), and [6.10] (**c**).)

sizes. Here, σ is the stress and D_{GB} the GB diffusivity. This gives rise to the $\dot{\varepsilon}$ minimum or a maximum of the simulation data for the flow stress in Fig. 6.7b and c, respectively. In simulations of Coble creep (see [6.11]) it has been found that the activation energy for creep is similar to the diffusion activation energy in high-energy bicrystal GBs. In addition, the excess free volume in GBs is expected to play an important role in GB creep [6.12]. Simulations suggest (see [6.11]) that lowering the stacking fault energy (SFE) results in a decrease of d_c which is confirmed by the simulations for Al (high SFE, $d_c = 18$ nm) and Cu (lower SFE, $d_c = 14$ nm) shown in Fig. 6.7b and c, respectively.

6.4 Plasticity Studies by Nanoindentation

The development of indentation and impression tests has a long tradition for measuring the mechanical properties of a material by making a contact of well-known geometry [6.34]. Owing to the development of new sensors and actuators, indentations can now be performed on sub-micron scales, a technique termed nanoindentation. Recently, a nanoindenter has been coupled in situ to a transmission electron microscope (TEM) for monitoring the stress–strain curve of the material together with the microstructure of the material throughout the test [6.34]. The indenter is made from B-doped diamond for electrical conductivity to suppress electrical charging from the TEM electron beam so that no electrostatic force is exerted between the indenter probe and the specimen.

In Fig. 6.8 the stress–strain curve and TEM images of nanoindentation studies on Al are shown with an initially dislocation-free Al crystallite in Fig. 6.8b. Figure 6.8c and e shows the grain's microstructure immediately after each of the first two dislocation bursts which, surprisingly, coincide with the barely discernible load transients 1 and 2 in Fig. 6.8a, i.e., they occur before a sustained rise in load. This shows that plasticity in a dislocation free volume of polycrystalline aluminum can begin at very small forces, remarkably, even before the first sustained rise in repulsive force (indicated by a star in Fig. 6.8a). However, the shear stress associated with these very small forces do approach the theoretical shear strength of aluminum ($\sim$2.2 GPa). The data in Fig. 6.8 supply evidence that a sub-micrometer grain of aluminum, plastically deformed to a dislocation density of $\sim 10^{14} m^{-2}$, is also capable of supporting shear stress close to the theoretical shear strength [6.35] which is contrary to earlier assumptions that a dislocation free volume is necessary to achieve shear stresses near the theoretical shear strength (see [6.35]). This behavior may be attributable to grain boundaries acting as a barrier to dislocation motion [6.35]. The data are, furthermore, at odds with the prevalent notion that the first obvious displacement excursion in a nanoindentation test is indicative of plastic deformation (see [6.35]).

Atomic simulation of nanoindentation in nanocrystalline gold with a grain size of 12 nm shows dislocation nucleation within the grains at the onset of plastic deformation with the grain boundaries as an efficient sink for partial and full dislocations. Intergranular sliding and a decrease in Young's modulus are observed as the grain

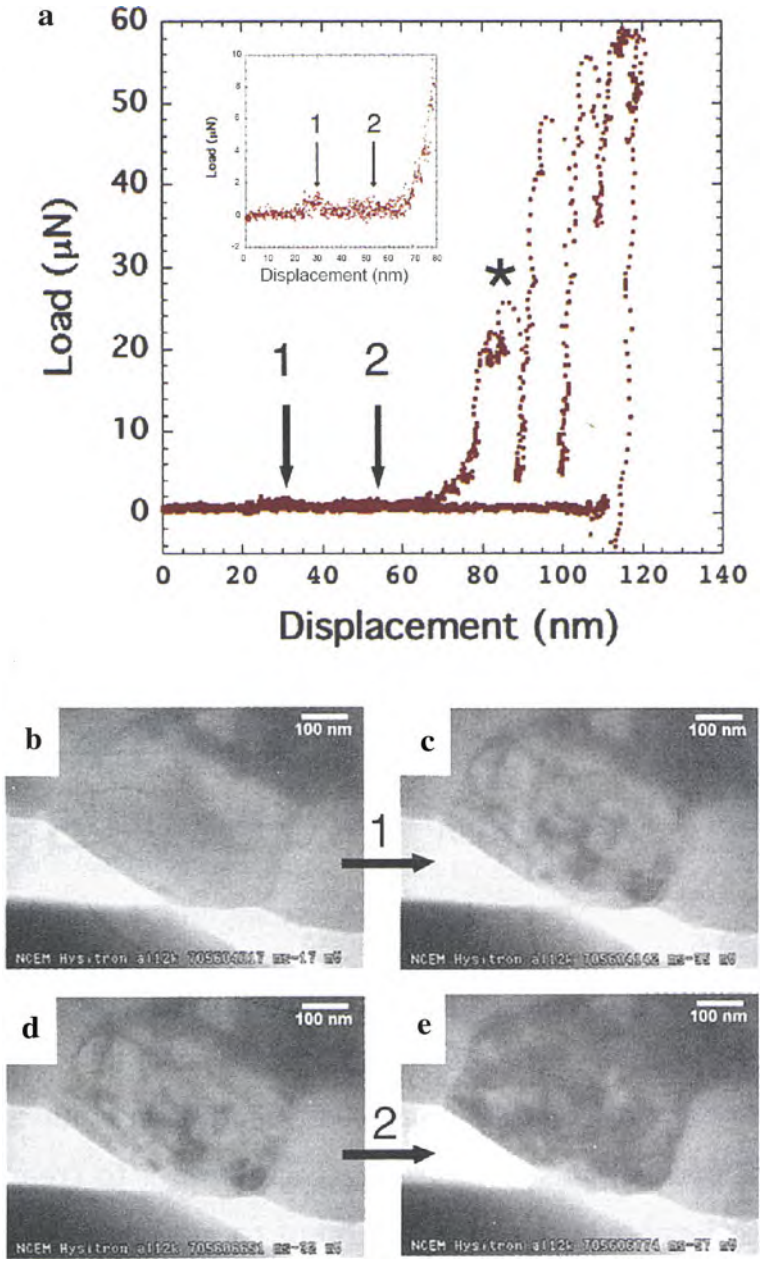

Fig. 6.8 (**a**) Load–displacement curves, measured in an integrated nanoindenter–TEM facility. The *curve* exhibits several load-drop events as the indenter (*lower part* in (**b**)) moves into the Al grain (*upper part* in (**b**)). Inset: Initial portion of the loading segment: *Arrows* point to tiny load peaks, corresponding to the first two dislocation bursts within the grain. The *star* indicates the first major load-drop event. (**b**), (**c**) and (**d**), (**e**) Sequential TEM images from the first and second dislocation bursts [6.34, 6.35]. (Reprinted with permission from [6.34]. © 2007 Elsevier)

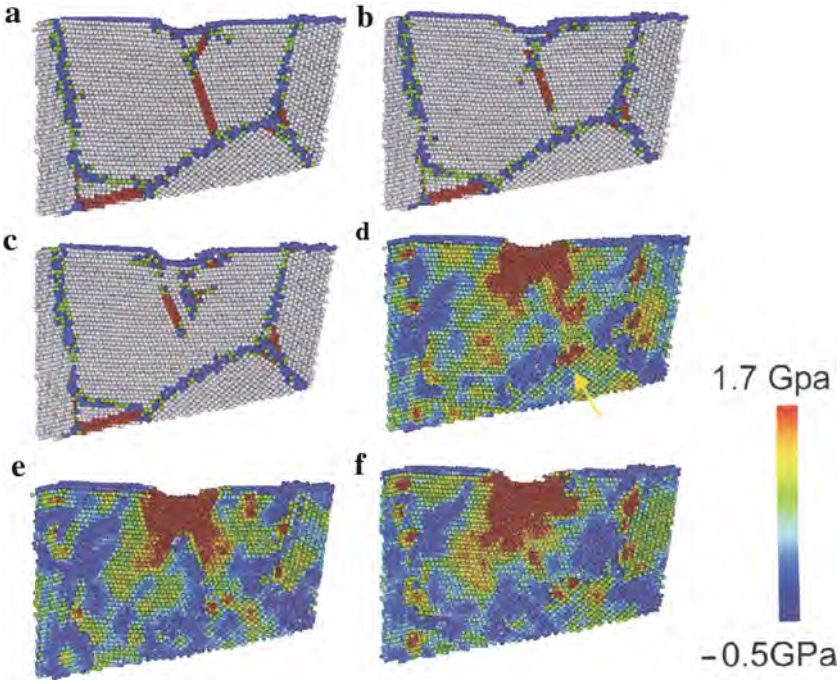

Fig. 6.9 Molecular dynamics indentation simulation of nanocrystalline Au showing the interactions between dislocations and grain boundaries (GB). (**a**–**c**) Atomic configuration during loading and (**d**–**f**) corresponding stress distribution. Upon indentation, dislocations are emitted from under the indenter and propagate through a grain until absorption by GBs. A dislocation is represented by two *red lines* (parallel planes) that mark a stacking fault left behind a propagating partial dislocation. The *yellow arrow* in (**d**) marks the region where the leading partial dislocation arrives. (Reprinted with permission from [6.37]. © 2004 Elsevier)

size is refined to 5 nm [6.36]. When the indenter size is smaller than the grain size, the grain boundaries not only act as sinks but also reflect or emit dislocations (Fig. 6.9).

Molecular dynamics simulation of nanoindentation has been furthermore performed on nanocrystalline SiC ceramics [6.38, 6.39] with an 8-nm grain size and 19 million atoms in total. As the indenter depth h increases, a crossover is observed from a cooperative deformation mechanism involving multiple grains to a decoupled response of individual grains, e.g., grain rotation, sliding, and intragranular dislocation activity. The crossover is also reflected in a switch from deformation dominated by crystallization of the grain boundary material to deformation dominated by disordering (see Fig. 6.10). In the early stages of plastic deformation, the soft (amorphous) GB phase "screens" the crystalline grains from deformation, thus making nanocrystalline SiC more ductile than its coarse-grained counterpart. Fracture toughness (a measure of how much energy it takes to propagate a crack) measured experimentally in nanocomposites (see [6.39]) exceeds that of a polycrystalline

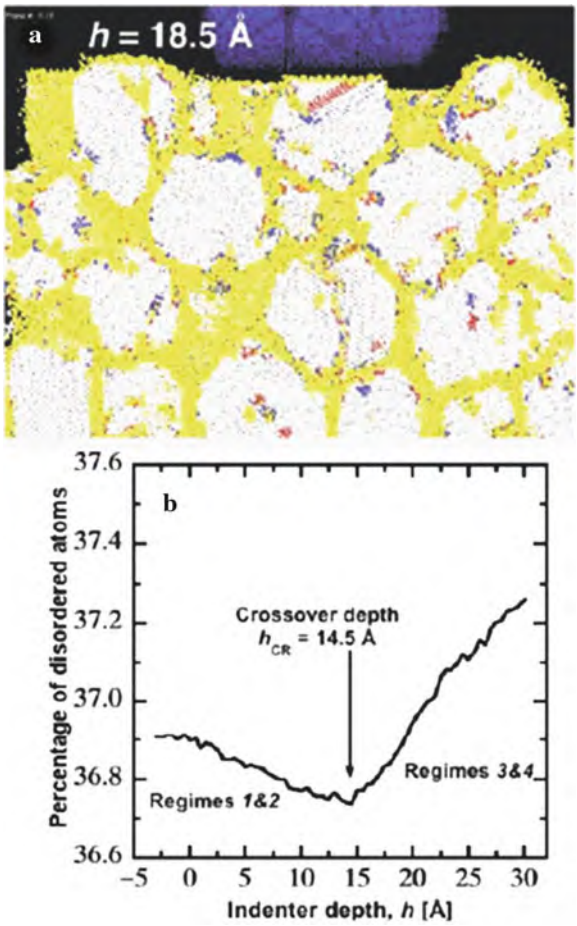

Fig. 6.10 (**a**) Atomic configuration of nanocrystalline SiC with *white* grains and *yellow* GBs. At lower indentation depths h, the deformation of the material is dominated by recrystallization (*blue* atoms). At depths $h > h_{cr}$, deformation is dominated by disordering (*red* atoms). (**b**) Percentage of disordered atoms in the material as a function of h reflects the crossover in the deformation mechanism. (Reprinted with permission from [6.38]. © 2005 AAAS)

matrix by about 50%. Increased fracture toughness does not necessarily lead to a lower value of hardness. Nanoindentation experiments of nanocrystalline SiC with grain sizes of 5–20 nm show the opposite trend [6.40] and report nanocrystalline SiC to be superhard with hardness values of 30–50 GPa, higher than that of coarse-grained SiC, and a similar value (39 GPa) has been derived from the molecular dynamics simulations [6.39].

6.5 Ultrastrength Nanomaterials

Ultrastrength nanomaterials (Table 6.1) have been reviewed before [6.41]. The strength of metals is dictated by dislocation nucleation and motion at low temperatures (see [6.13]). In the absence of mobile dislocations in nanocrystallites, plastic

Table 6.1 Experimentally measured ultrahigh strengths. CNT, carbon nanotubes; NW, nanowires; NP, nanopillars; NS, nanospheres; ML, monolayer; SW, single wall; MW, multiwall; *E*, Young's modulus. For references see [6.41]

Material	Number of layers or diameter (nm)	Measured strength (GPa)	Ideal strength $\sim E/10$ (GPa)
CNT	SW	30	100
CNT	MW	30	100
Ag-NW	16.5	7.3	8
Au-NW	40	5.6	8
Au-NP	300	0.8	8
Si-NS	20–50	20–50	17
Graphene	ML	130	100

deformation will not proceed until new dislocations are nucleated, which can lead to a high strength, approaching the ideal strength, which is the stress required to deform a perfect crystal to its elastic limit while maintaining perfect periodicity.

Ultrastrength can be achieved by dislocation exhaustion [6.41] or starvation [6.42], a concept explaining the high compressive strength of Au nanopillars (see [6.41]) of about 800 MPa which is about 50 times higher than that of bulk Au and which is not so far from the prediction of the ideal shear strength from ab initio calculations (see Table 6.1). Unlike in bulk samples, dislocations in nanostructures can travel only very small distances before being annihilated at free surfaces, thereby reducing the overall dislocation multiplication rate. Gliding dislocations leave the crystal more rapidly than they multiply, decreasing the overall mobile dislocation density which requires very high stresses to nucleate new mobile dislocations (see [6.41]).

Insight into source-controlled dislocation plasticity in a sub-micrometer Al crystal (300 nm × 400 nm × 400 nm) has been gained by in situ transmission electron microscopy in tensile tests [6.43]. Single-ended sources emit dislocations that escape the crystal before being able to multiply (Fig. 6.11). As dislocation nucleation and loss rates are counterbalanced, the dislocation density remains constant throughout the deformation at strain rates of about 10^{-4} s^{-1}. However, an increase in strain rate to 10^{-3} s^{-1} causes a surge in dislocation density as the nucleation rate outweighs the loss rate. This demonstrates that the deformation of nanometer crystals is strain rate sensitive [6.43].

One possible application of the extremely high strength of nanoparticles is to exploit their role as reinforcement to improve the mechanical properties of bulk materials. In this case strengthening is induced through the introduction of nanoscale precipitates, hindering the propagation of dislocations in the crystalline matrix [6.14]. The precise mechanism of the strengthening depends on the size of the nanoparticles [6.44] and their structure can be altered through their interaction with the dislocations. Small nanoparticles of 3–5 nm in diameter can be structurally stable at high temperatures and lead to a six orders-of-magnitude increase in creep resistance (see [6.13]). The limit of precipitate strengthening is determined by both

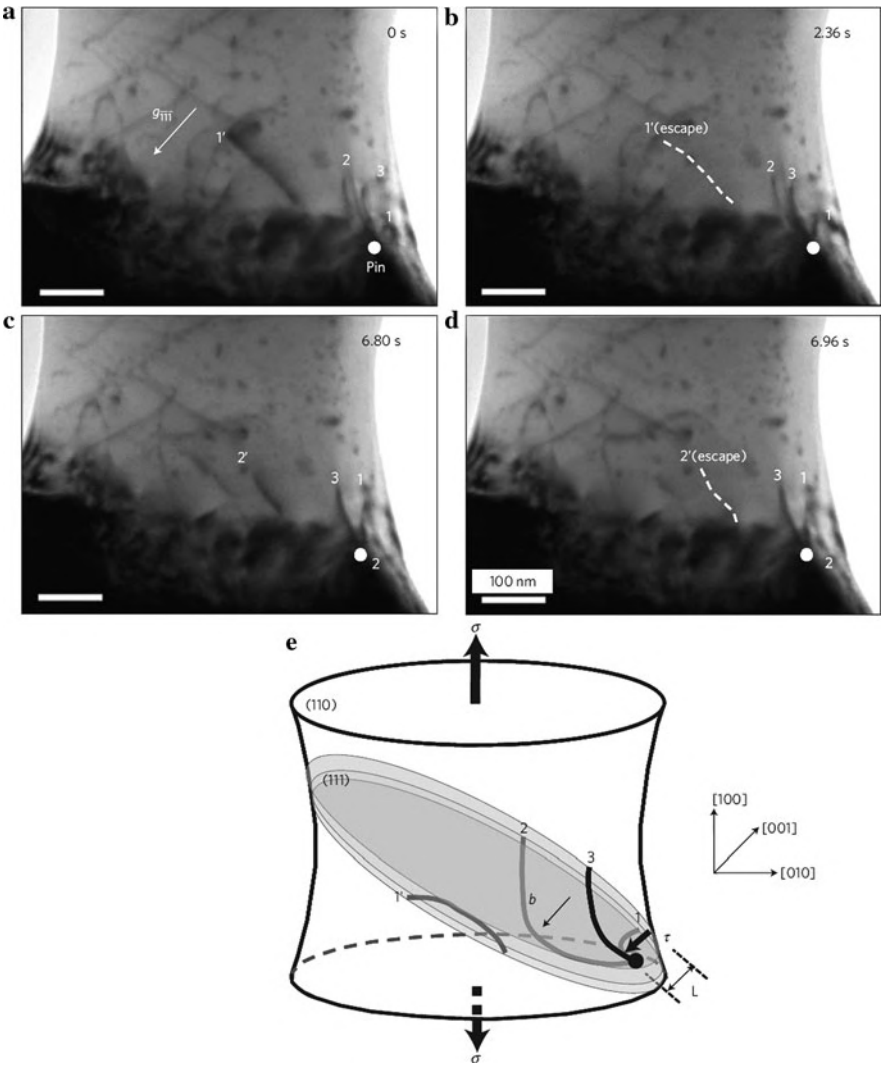

Fig. 6.11 Dislocation emission in the tensile test of an Al nanocrystal by the operation of a single-ended source. (**a**–**d**) Sequence of transmission electron micrographs (TEM) showing single-ended dislocation sources lying on a set of parallel slip planes 1, 2, and 3 at $\varepsilon \approx 140\%$. (**e**) Schematic of the dislocation configuration corresponding to (**a**). The previously generated dislocations from sources 1 and 2 are labeled as 1' and 2', respectively. The source size is 70 ± 20 nm. Upon generation, the dislocations glide and reach the surface in proximity with aligning their lines in parallel to the surface in edge character and intersecting the surface perpendicularly owing to image forces. (Reprinted with permission from [6.43]. © 2009 Nature Publishing Group)

the strength of the nanoscale precipitates and the elastic properties of the matrix and may approach the ideal strength [6.14].

6.6 Enhancement of Both Strength and Ductility

When designing materials, there is often a trade-off between strength and ductility – properties that are critically important to the performance of materials. This is also true for bulk nanostructured materials, which usually have a high strength, but disappointingly low ductility (see [6.45, 6.46]). Techniques have been developed to make a nanostructured material both strong and ductile [6.46, 6.47], and by simulation methods [6.45] it has been revealed why some nanodesigned materials behave with that desirable compromise between strength and ductility by visualizing the simulation of materials deformation on a timescale of minutes.

Nanocrystalline metals are several times stronger than conventional microcrystalline metals (Fig. 6.5) but often more brittle (less ductile). However, in many

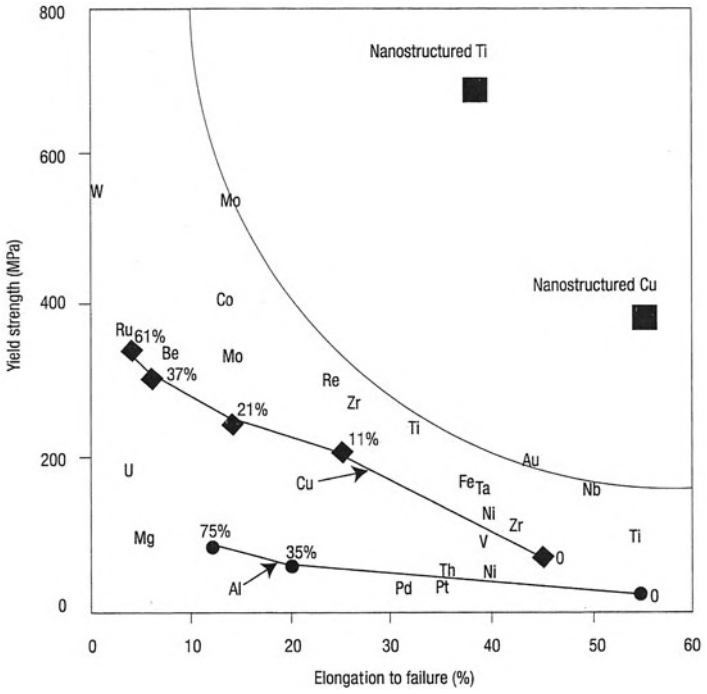

Fig. 6.12 Strength and ductility of severely plastically deformed nanostructured Cu and Ti compared with coarse-grained metals. Conventional cold rolling of Al and Cu (*full lines* with percentage of rolling indicated) increases the yield strength but decreases the ductility. In contrast, the high strength and ductility of nanostructured Cu and Ti differ very much from the behavior of coarse-grained metals. (Reprinted with permission from [6.48]. © 2004 Nature Publishing Group)

applications one needs optimum combinations of strength and ductility [6.45] which has been demonstrated in severely plastically deformed nanocrystalline Cu and Ti (Fig. 6.12) and in nanotwinned copper [6.47], by a bimodal distribution of grain sizes and by low-temperature/high-strain rate deformation (see [6.49]). Copper with tunable combinations of strength and ductility could be produced by controlling the thickness and nanospacing of twin boundaries inside small grains [6.47] (Fig. 6.13a, b). Internal interfaces such as grain boundaries and twin boundaries play a critical role in the strength and ductility of metals. When there are smaller grains in the metal structure, and hence more grain boundaries, there is more interaction between the boundaries and dislocations (string-like defects in the material) that move inside and between grains during mechanical deformation. The larger portion of these boundaries contributes to the brittleness of the metal. Adding nanoscale twin boundaries has a similar strengthening effect, but the twin boundaries do not promote the same level of brittleness as grain boundaries do (see [6.45]). Simulations reveal [6.45] that the ductility of nanotwinned copper can be

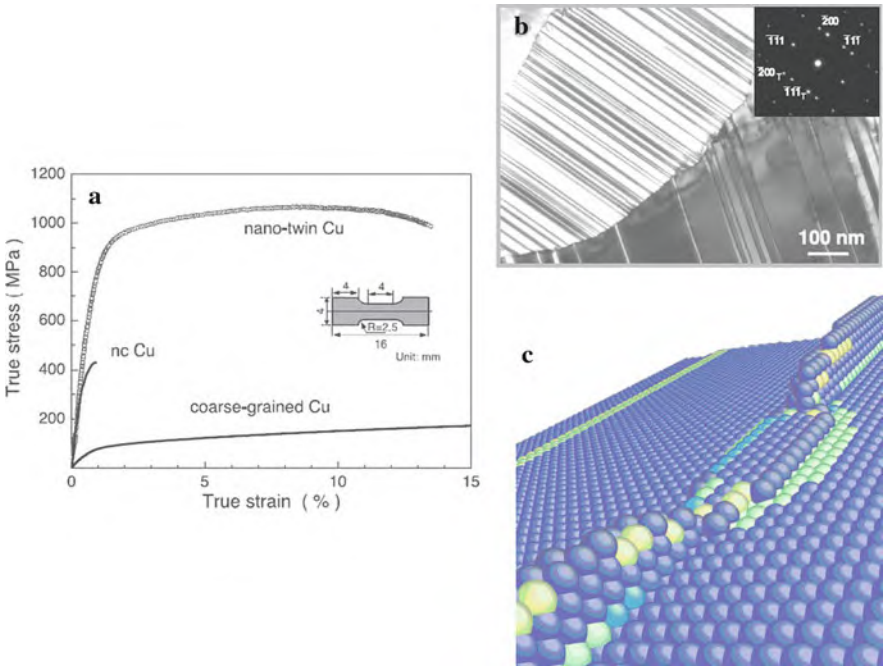

Fig. 6.13 High mechanical strength and ductility of nanotwinned Cu. (**a**) Stress–strain curves of electrodeposited nanotwinned Cu, of nanocrystalline Cu, and of coarse-grained Cu [6.47]. (**b**) Electron diffraction patterns (*inset*) indicate that the twins in each grain (transmission electron micrograph – TEM) are parallel to each other in {111} planes [6.47]. (**c**) Atomic simulation shows the absorption of a line defect by a twin boundary in nanotwinned Cu [6.45, 6.50]. (Reprinted with permission from [6.47] (**a**) (**b**) and [6.45] (**c**). © 2004 AAAS (**a**) (**b**) and © 2007 National Academy of Sciences USA (**c**))

attributed to changes in the atomic structure of the twin boundaries as the material is deformed (Fig. 6.13c). From molecular dynamics (MD) simulations for copper it is concluded [6.51] that, since the dislocation nucleation is suppressed in the vicinity of the coherent twin boundaries (TBs) and each TB plane hinders dislocations from propagating, the coherent TBs can be regarded as an intrinsic strengthening phase relative to a perfect crystal. Furthermore, a comparison of experimental evidence and calculations (see [6.52]) demonstrates that dislocation/interface interactions, rather than dislocation/dislocation interactions, are the rate-controlling mechanisms in the TB-dominated materials. It was found in nanotwinned copper [6.53] that the strength increases with decreasing twin thickness, reaching a maximum at 15 nm, followed by a softening at smaller values.

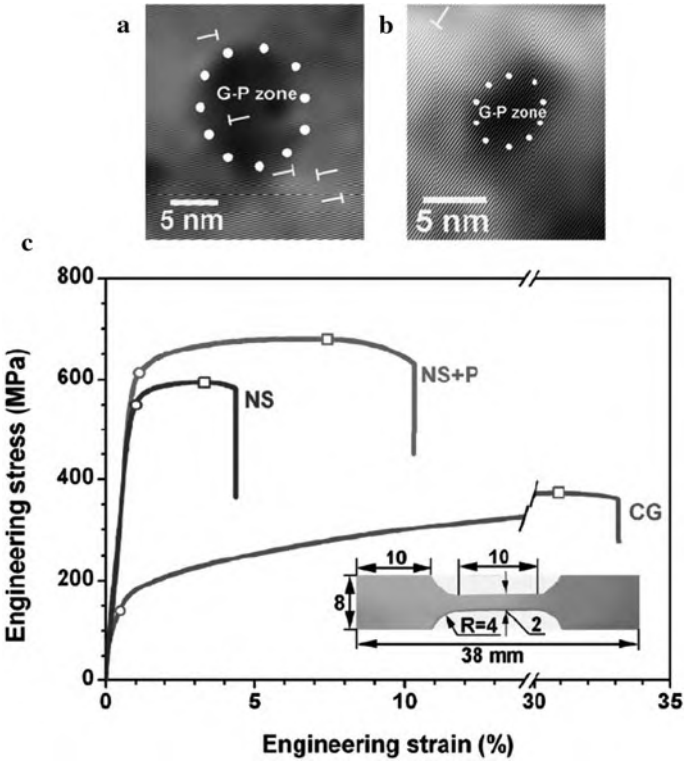

Fig. 6.14 (**a**) High-resolution transmission electron micrograph (HRTEM) of a {111} matrix plane of a nanostructured 7075 Al alloy with a Guinier–Preston zone precipitate (NS+P specimen) before and (**b**) after tensile testing. The *white dots* mark the particle/matrix interface and the *white T symbols* designate edge dislocations. (**c**) Tensile engineering stress–strain curves of the coarse grained (CG), nanostructured (NS), and the nanostructured Al alloy specimen with nanoprecipitations (NS+P). The *inset* shows the tensile specimen with a thickness of 1 mm. (Reprinted with permission from [6.46]. © 2006 Wiley-VCH)

Another technique for a simultaneous increase of strength and ductility has been demonstrated by engineering very small second-phase particles into a nanostructured alloy matrix [6.46]. In a cryogenically rolled 7075 Al alloy with a 100-nm grain size (NS sample), second-phase nanoparticles (such as Guinier–Preston zones; Fig. 6.14a, b) with sizes between 4 and 10 nm were precipitated (NS+P specimen) yielding an increased strength (engineering stress) and ductility (engineering strain) compared to coarse-grained (CG) or nanocrystalline (NS) specimens (Fig. 6.14c). The high dislocation density and the fine grain size of the NS specimen are responsible for its enhanced strength over the CG sample, while the high density of second-phase particles in the NS+P specimen is responsible for the increased strength compared with the NS specimen. The enhanced elongation (ductility) of the NS+P specimen (Fig. 6.14c) is ascribed to the increased work hardening rate, θ (slope of the stress–strain curve), through dislocation accumulation at the precipitates with an increase of the dislocation density from 3.5×10^{14} m^{-2} before tensile testing to 5.4×10^{14} m^{-2} after testing (Fig. 6.14a, b). The second-phase precipitates significantly reduce dynamic recovery and increase the dislocation storage capability, leading to an enhancement of the hardening rate, θ, and of the ductility.

6.7 Superplasticity

Superplasticity is the deformation process that produces essentially neck-free elongations of many hundreds of percents without failure in materials deformed in tension (see [6.29, 6.54, 6.55]). A reduction in grain size decreases the temperature and increases the strain rate of superplastic flow. Examples for superplasticity tensile tests on nanocrystalline materials are shown in Fig. 6.15. Exceptionally high superplastic elongations of 3050% have been achieved at 473 K with a strain rate of 10^{-4} s^{-1} in a commercial Mg – 5.5 wt% Zn – 0.5 wt% Zr alloy with a grain size of 800 nm after processing by equal-channel angular pressing [6.56]. Superplastic behavior is of industrial interest, as it allows for net-shape fabrication of components with complex shape from materials that are hard to machine, such as composites or intermetallics.

Superplasticity of nanocrystalline materials is characterized by very high values of the flow stress, the strengthening in the first stage of deformation and a softening in a second deformation stage (Fig. 6.16a). Dangerous stress concentrations leading to cracking and failure must be avoided. It is thought (see [6.29]) that superplastic deformation occurs in nanocrystalline materials, if grain boundary sliding serves as the dominant deformation mechanism whose operation and effective accommodation are provided by lattice dislocation slip, fast atomic diffusion, diffusion-controlled deformation by grain rotation, and triple-junction migration.

According to a detailed discussion [6.29], grain boundary sliding is supported by the slip of lattice dislocations which are generated under a critical stress $\sigma_c \sim Gb/ML$ (G – shear modulus, b – Burgers vector, $M \approx 0.5$ a geometrical factor,

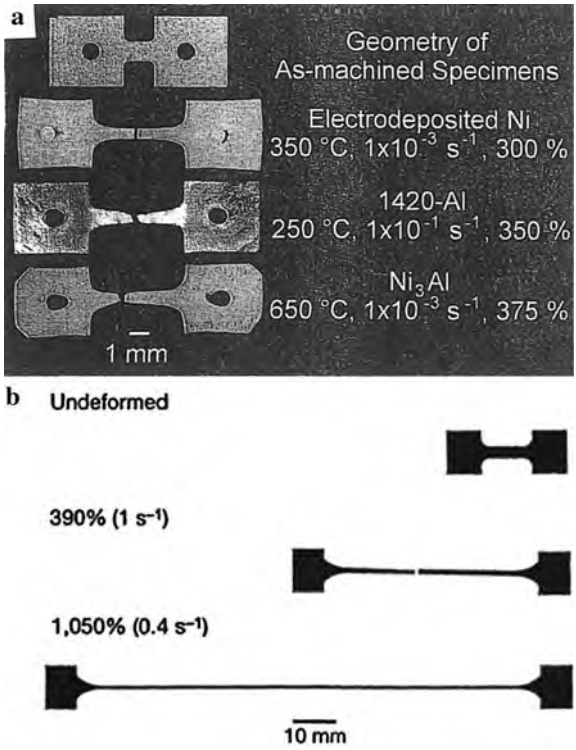

Fig. 6.15 (**a**) Tensile specimens of Ni (grain size 20 nm), Al alloy (100 nm), and Ni_3Al (50 nm), shown in the initial geometry and after deformation [6.57]. (**b**) Superplasticity of a ceramic specimen composed of ZrO_2 (180 nm) with α-Al_2O_3 (250 nm) and $MgO{\cdot}1.3Al_2O_3$ spinel (180 nm) [6.61]. (Reprinted with permission from [6.57] (**a**) and [6.61] (**b**). © 1999 Nature Publishing Group (**a**) and © 2001 Nature Publishing Group (**b**))

$L \approx 0.3d$ the length of a Frank–Read dislocation segment in a grain of the size d [6.58]). An estimate for nanocrystalline materials yields $\sigma_c \sim G/60 - G/30$ which is close to experimental values (see [6.29, 6.57]). This shows that the measured flow stress is high enough to activate Frank–Read sources for the generation of lattice dislocations in intermediate grains of nanocrystalline materials. The lattice dislocations then move to grain boundaries to be absorbed there and to be transformed into mobile grain boundary dislocations that carry grain boundary sliding. The storage of GB dislocations (Fig. 6.16b–i) causes the experimentally observed strengthening of nanocrystalline materials in the first stage of superplastic deformation, in contrast to coarse-grained materials where strengthening originates from the storage of lattice dislocations in the grains.

The storage of grain boundary dislocations at triple junctions may lead to stress sources, inducing nanocracks and failure. Nanocrack nucleation under superplastic deformation of nanomaterials can be suppressed by accommodation effects of lattice dislocation slip, diffusion-assisted grain rotation, local diffusion processes, and, in particular, by the emission of lattice dislocations from triple junctions. Grain rotation which occurs through diffusion-assisted climb of GB dislocations serves as the key recovery process for the GB dislocation density and thereby can suppress nanocrack nucleation.

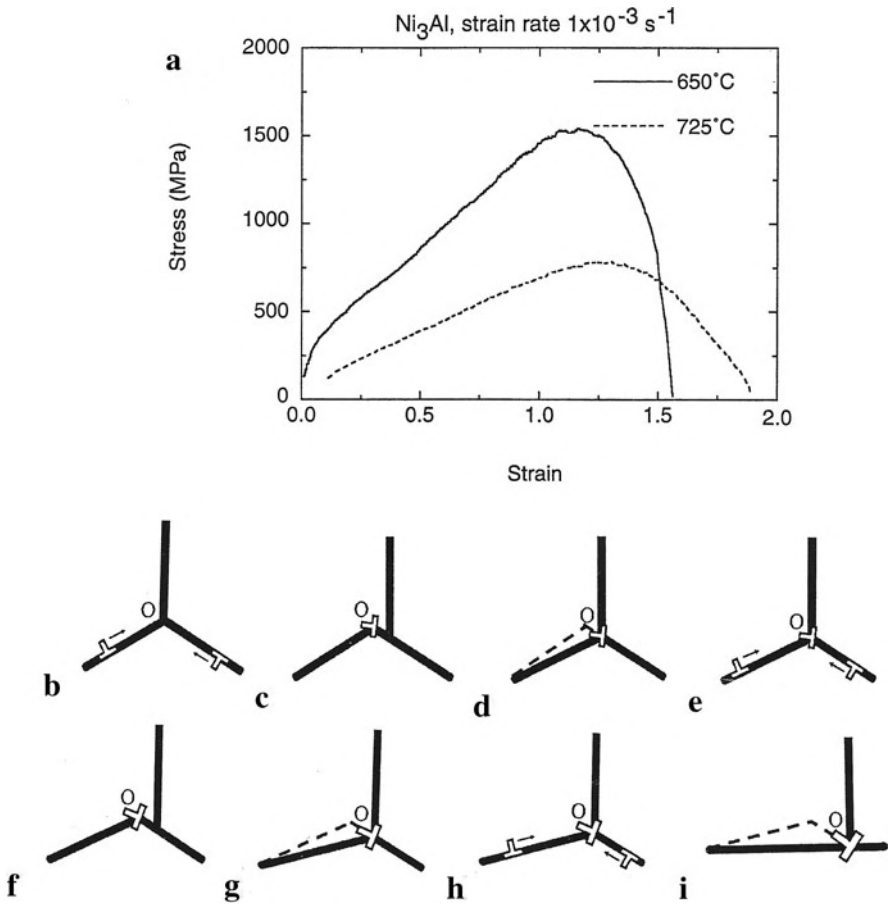

Fig. 6.16 (**a**) Superplastic stress–strain curves of nanocrystalline Ni_3Al (grain size 50 nm) prepared by severe plastic deformation [6.57]; (**b–i**) Grain boundary sliding and transformation of defect structures near a triple junction of grain boundaries; (**i**) the transfer of grain boundary dislocations across the triple junction O results in the increase of the magnitude of the Burgers vector of a sessile dislocation and the formation of a planar array of GBs for easy GB sliding giving rise to softening in the second superplastic deformation stage [6.29]. (Reprinted with permission from [6.57] (**a**) and [6.29] (**b–i**). © 1999 Nature Publishing Group (**a**) and © 2005 Advanced Study Center (**b–i**))

The softening of nanomaterials under superplastic deformation is related to triple junction migration that accommodates GB sliding (Fig. 6.16b–i) [6.29, 6.59]. This results in the experimentally observed [6.60] formation of plane arrays of GBs (Fig. 6.16i). In this geometry, triple junctions stop being obstacles for GB sliding along coplanar grain boundaries. The subsequent cooperative grain boundary sliding gives rise to the softening in the second stage of superplastic deformation.

Notwithstanding the recent progress in the field, the achievement of superplasticity or good ductility of superstrong nanocrystalline materials at commercially desired high strain rates and at room temperature are major unresolved topics in this research area.

6.8 Fatigue

Fatigue of metallic materials is an important issue in the field of mechanical behavior. Because enhanced fatigue properties are associated with high tensile strength and good ductility, nanocrystalline materials are particularly susceptible to fatigue failure when strength and/or ductility are poor (see [6.62, 6.63]). Although most nanocrystalline metals (e.g., manufactured by severe plastic deformation [6.63]) exhibit a shorter fatigue life compared to their coarse-grained counterparts because some ductility is lost during manufacturing, an enhancement of the fatigue life has been observed for nanocrystalline Ti and for CuCrZr alloys after severe plastic deformation (SPD; see [6.63]).

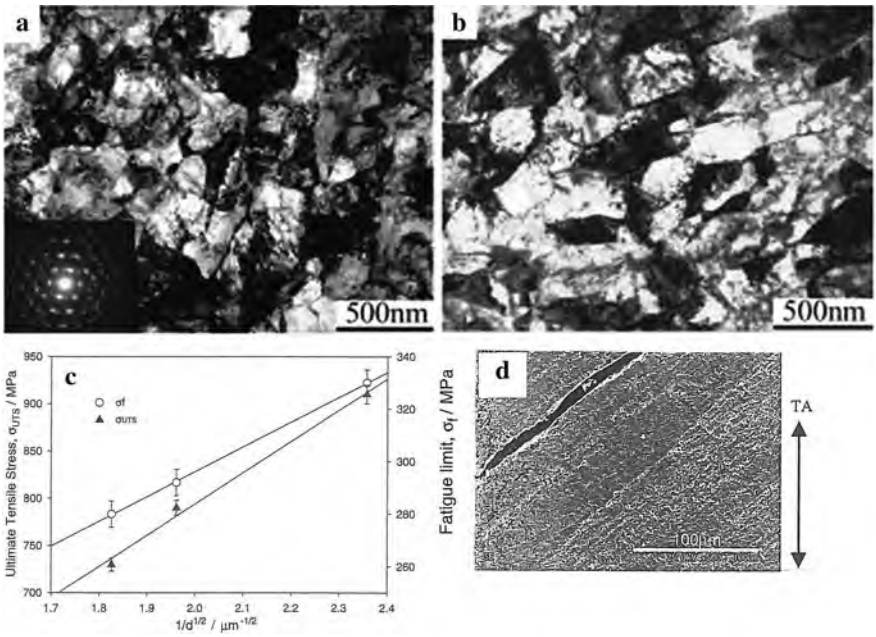

Fig. 6.17 (**a**) Invar, manufactured by severe plastic deformation (SPD), before and (**b**) after fatigue at a cumulated fatigue strain of $\Delta\varepsilon_{pe}/2 = 10^{-3}$; (**c**) Hall–Petch behavior of the ultimate tensile strength σ_{UTS} and the fatigue limit σ_f of a SPD manufactured nanocrystalline Invar alloy. (**d**) Shear bands on the surface of SPD nanocrystalline Cu deformed cyclically to $\Delta\varepsilon_{pe}/2 = 10^{-3}$. (Reprinted with permission from [6.63]. © 2003 Wiley-VCH)

As an example, the structure of SPD nanocrystalline Fe–36Ni (Invar) with equiaxed sub-micron-sized grains before fatigue and after fatigue with a cumulated plastic strain $\Delta\varepsilon_{pe}/2 = 10^{-3}$ and significantly elongated grains are shown in Fig. 6.17a, b. For the ultimate tensile strength σ_{UTS} and the fatigue limit σ_f a Hall–Petch behavior is found (Fig. 6.17c). Detailed studies on ultrafine-grained pure metals have been performed for Cu [6.64, 6.65] and Ni [6.66]. In cyclic deformation of SPD nanocrystalline materials, strain localization in shear bands oriented at 45° to the tensile loading axis are observed (Fig. 6.17d). In the shear bands, where the strain localization occurs primarily along the grain boundaries, cracks are initiated and propagated (see [6.63]).

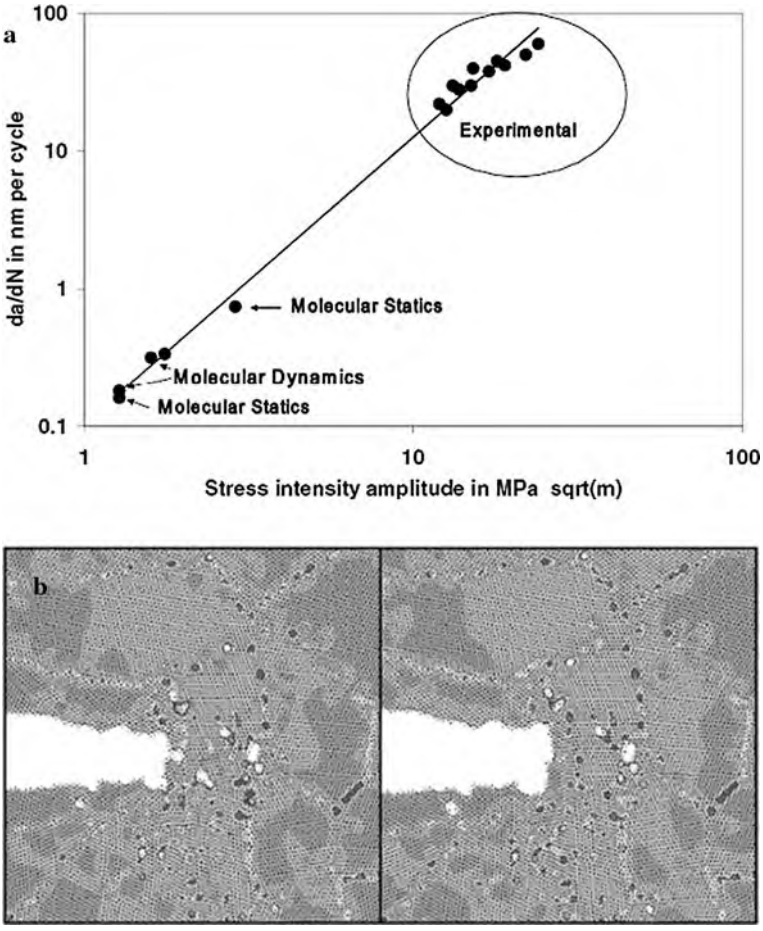

Fig. 6.18 (**a**) Rate of crack advance for both molecular statics and dynamics simulations [6.62] together with experimental data [6.67]; (**b**) Crack tip configurations for 26 (*left*) and 31 (*right*) cycles showing nanovoids essentially within the grain where the crack tip is located. (Reprinted with permission from [6.62]. © 2005 American Physical Society)

Although the details of the microsopic mechanism of fatigue damage of nanocrystalline materials have still to be uncovered [6.63], atomic simulation studies may shed some light on these processes [6.62]. In these studies, a combination of molecular statics and molecular dynamics making use of an embedded-atom method (EAM) potential for Ni has been utilized. The calculated rates of crack advance are compared to experimental values (Fig. 6.18a). Regarding the mechanism of crack advance, the calculations suggest nanovoids to be created in the grain where the crack tip is located (Fig. 6.18b), with most of the dislocations being unable to continue to glide across the grain boundary. However, the experimental data of fatigue failure of nanograined Pt films are ascribed to dislocation–slip mediated processes [6.68], known to operate in fcc metals during fatigue, and not to plastic blunting and void coalescence mechanisms observed in MD simulations.

6.9 Nanocomposites

A critical challenge in nanocomposite fabrication is the ability to realize materials that allow the transfer of the exceptional mechanical properties (e.g., tensile strength, σ_{UTS}; Young's modulus, E) of the nanoscale materials to the macroscale properties of the bulk material [6.69]. In addition, novel optical features will arise from the interfaces of, e.g., metal oxides/polymer interfaces. This will be discussed in the following, comprising recent examples of nanocomposites from metals, ceramics, and polymers.

6.9.1 Metallic Nanocomposites

Materials with both high strength and high ductility can be manufactured from Zr based Zr-Nb-Cu-Ni-Al alloys [6.70] by simple casting of appropriate alloy compositions. These composites consist of a ductile dendritic bcc-Zr phase and a strong nanostructured matrix (Fig. 6.19a, c). The dendritic phase exhibits work hardening and enhances the ductility of the composites reaching plastic strains of 17.5% whereas the nanostructured matrix enhances the strength to high values of about 1900 MPa (Fig. 6.19d). Catastrophic failure can be avoided for composites with larger amounts of dendrites (alloys C3–C5; see Fig. 6.19d). On the other hand, the yield strength decreases with increasing bcc dendrite volume fraction. The glassy sample (alloy G in Fig. 6.19d), the nanocrystalline sample (NC), and the quasi-crystalline alloy (QC) show practically no ductility. Due to the heterogeneous structure, the deformation mechanisms of the nanocomposite are quite complicated. The shear bands, spreading in the matrix and interacting with the dendrites, exhibit inter-band spacings of about 150 nm [6.70], yielding essentially homogeneous strain distribution during deformation. After nucleation, cracks propagate through the shear bands, whereas the dendrites act as crack blunting objects, thus enhancing the toughness of the nanocomposite.

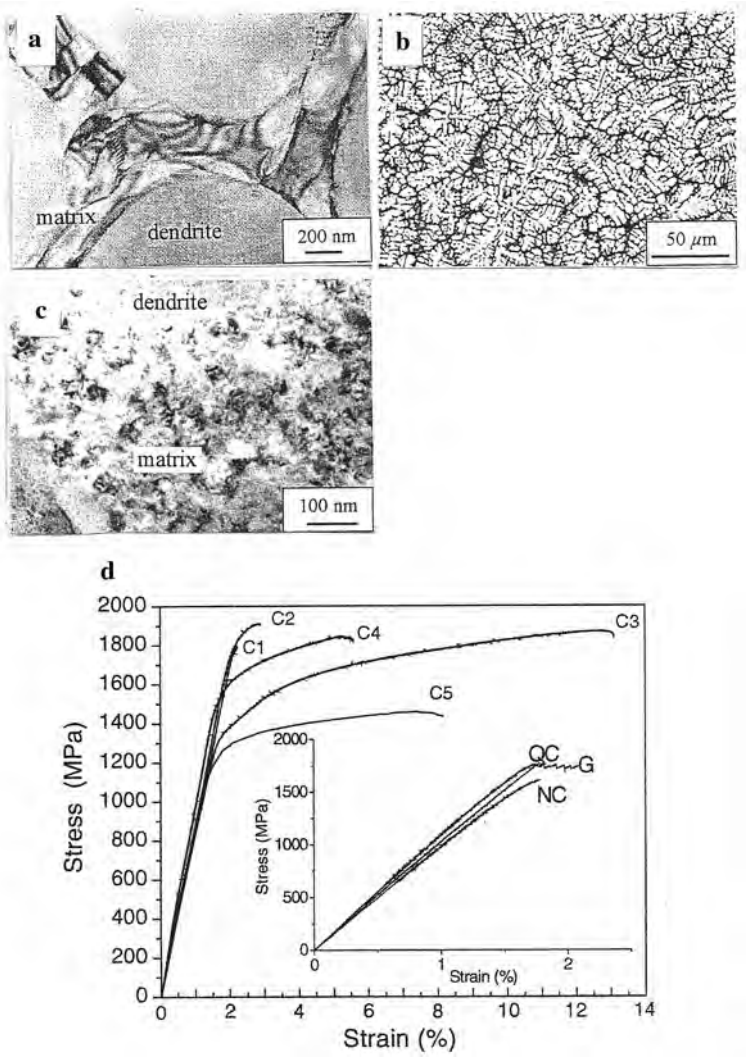

Fig. 6.19 (**a**) TEM image of $Zr_{66}Nb_{13}Cu_8Ni_{6.8}Al_{6.2}$ dendrites in a nanostructured matrix. (**b**) SEM image of a $Zr_{74.5}Nb_8Cu_7Ni_1Al_{9.5}$ nanocomposite (alloy C4) with 88 vol% dendrites in a (**c**) $CuZr_2$-type nanocrystalline matrix (TEM). (**d**) Stress–strain curves of Zr-Nb-Cu-Ni-Al nanocomposites with various compositions and dendrite volume fractions (alloys C1–C5) or of Zr-Ti-Nb-Cu-Ni-Al alloys (G – bulk metallic glass, QC – 90 vol% quasi-crystalline + glassy composite, NC – 10 vol% nanocrystalline + glassy composite. (Reprinted with permission from [6.70]. © 2005 Wiley-VCH)

The combination of high ductility, strength, and elasticity of these nanocomposites is promising for engineering applications for springs, microgears, medical devices, sporting equipment, etc.

6.9.2 *Ceramic/Metal Nanocomposites with Diamond-Like Hardening*

The design of materials with a hardness similar to diamond is an ongoing challenge because diamond cannot be used in machining steels due to its reactivity with materials such as Fe, Ti, or Si. The synthesis of alternative superhard materials including carbides, nitrides, and borides, however, requires extreme conditions [6.71]. Therefore, the superhard behavior of alumina (grain size 300 nm) and Ni (< 60 nm) nanocomposites (Fig. 6.20) were studied [6.72] after spark-plasma sintering, making use of the strategies of Hall–Petch strengthening of nanocrystalline solids (see Sect. 6.3) and of percolation theory. When the concentration of Ni increases, the hardness of the composite increases (Fig. 6.20e). It is initially enhanced due to an increase of the number of Ni particles. However, when the metal concentration is further increased, it reaches a critical value with maximum hardness until single Ni particles start to coalesce, leading to increased particle sizes and a decrease in hardness. In fact, the hardness of the present alumina-n-Ni (2.5 vol%) nanocomposite corresponds to an alumina–diamond (6 vol%) composite with a substantially higher diamond contents, if the rule of mixing is applied. In addition, the alumina-n-Ni (2.5 vol%) nanocomposite was found to exhibit an excellent wear

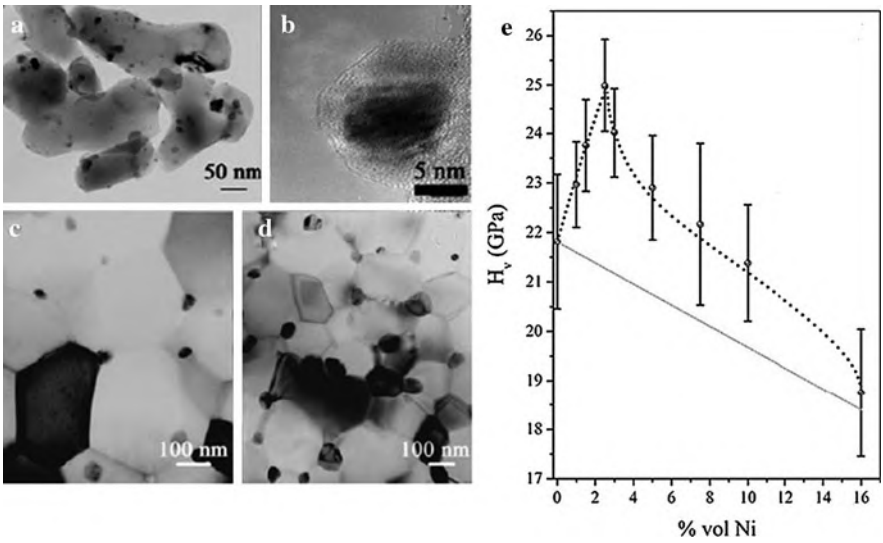

Fig. 6.20 Transmission electron micrographs of (**a**) alumina/n-Ni powder containing 1 vol% Ni, (**b**) high-resolution electron micrograph of the alumina-n-Ni interface of the powder containing 1 vol% n-Ni particles, (**c**) spark-plasma sintered alumina-n-Ni composite (1.5 vol% Ni), (**d**) sintered alumina-n-Ni composite (5 vol% Ni), and (**e**) hardness as a function of Ni contents. Measured and theoretically predicted (*dashed line*) hardness values plotted as a function of the Ni contents. The *solid line* represents the rule of mixing. (Reprinted with permission from [6.72]. © 2007 Wiley-VCH)

behavior with a wear rate by a factor of 30 smaller than that of pure alumina and about 15 times lower than that of B_4C.

6.9.3 Oxide/Dye/Polymer Nanocomposites – Optical Properties

Nanocomposites of oxides and polymers (e.g., PMMA) can fluoresce emitting photons of a particular wave length (fluorescence) when excited by irradiation with shorter wave lengths. The fluorescence is excited by photon absorption in the ceramic core (~5 nm) of the composite and the energy is transferred to the (C=O)–O bond in the ceramic/PMMA interface (Fig. 6.21a) for fluorescence between 400 and 475 nm. In ZrO_2/m-PMMA nanocomposites with a particle diameter changing from 4.5 to 2.0 nm the emission spectra (Fig. 6.21c) blue shift from 434 to 418 nm and the emission intensity increases upon decreasing the particle

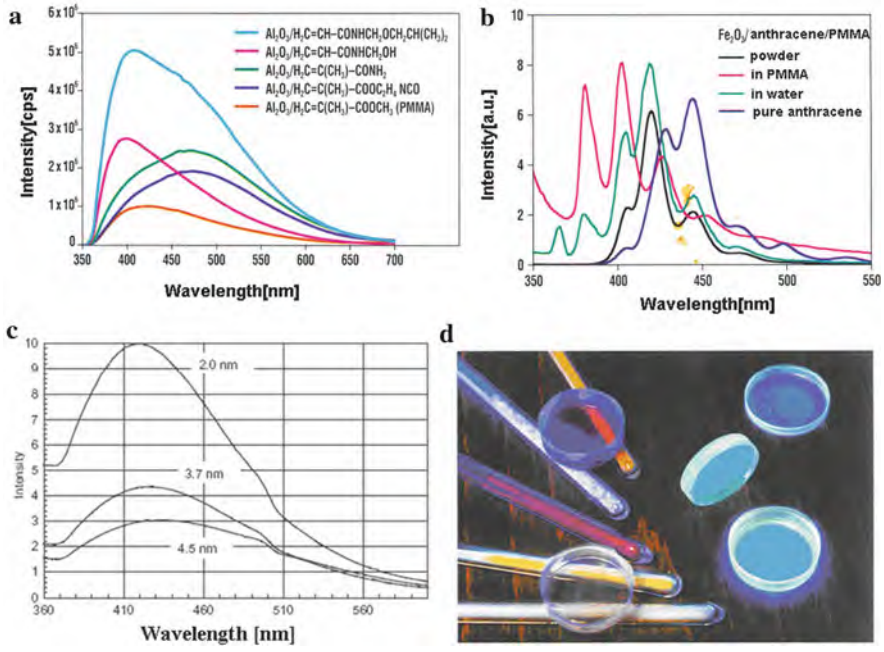

Fig. 6.21 (**a**) Fluorescence spectra of Al_2O_3/polymer nanocomposites. Polymers including amide or isocyanate groups enhance the fluorescence intensity. (**b**) Fluorescence spectra of γ-Fe_2O_3/anthracene/PMMA nanocomposites with emission wave lengths depending on the surrounding chemistry [6.73]. (**c**) Influence of the particle diameter (4.5–2.0 nm) of ZrO_2/m-PMMA nanocomposites on the emission spectra. The emission wave length blue shift (from 434 to 418 nm) and the emission intensity increases with decreasing particle size [6.74]. (**d**) Metal oxide/dye/polymer nanocomposite powders in glass tubes and dispersed in a PMMA matrix [6.73]. (Reprinted with permission from [6.73] (**a**) (**b**) (**d**) and [6.74] (**c**). © 2005 Karlsruher Institut für Technologie (**a**) (**b**) (**d**) and © 2004 Springer Verlag (**c**))

size. The range of fluorescence wave lengths can be widely expanded by making use of an intermediate monolayer of organic dyes, such as the model dye anthracene. In Fig. 6.21b the fluorescence spectra of paramagnetic Fe_2O_3/anthracene/ PMMA nanocomposites are shown which could be of interest in biological analysis and medical diagnosis. By introducing such a nanocomposite into a PMMA matrix, transparently colored materials can be manufactured (Fig. 6.21d).

6.9.4 Polymer Nanocomposites

This term has evolved to refer to a multicomponent system in which the major constituent is a polymer and the minor constituent has at least one dimension below 100 nm [6.75–78]. Hybrid organic–inorganic nanocomposites of polymer and clay nanoplatelets (see also Sect. 11.6) have received special attention because of the very low cost of the inorganic component and the relatively simple preparation [6.69] with growing commercial importance [6.79]. Polymer nanocomposites are preferred over metals for moderate temperature applications (C 300°C) based on their weight savings, fatigue resistance, and corrosion suppression [6.80]. The advantages of polymer nanocomposites result primarily from the filler size reduction with the concomitant increase in the volume fraction of the relatively thick organic–inorganic interface structure [6.78] which extends into the polymer matrix on the order of $R_g \approx 6$ nm [6.78], the radius of gyration [6.81], or approximately the expanse of the polymer molecule. The interfacial volume fraction additionally depends on the aspect ratio of the nanoparticles [6.78]. The patent and literature activity in this field has been rapidly increasing during the last decade [6.78]. Some recent studies will be briefly discussed in the following.

Polymer nanocomposites have been produced [6.69] with properties that approach the theoretical maxima using spatial and orientational control of clay platelets in a polymer matrix at the nanoscale and retaining this order at the macroscale. Montmorillonite (MTM) clay (aluminosilicate, ∼1-nm thick by 100–1000 nm sheet diameter, Fig. 6.22a) with a theoretical in-plane elastic modulus of ∼270 GPa [6.82] should yield polymer composites with theoretical stiffness values of ∼100 GPa, but values achieved to date were at least one order of magnitude lower because of clay aggregation and phase separation. Layer-by-layer (LBL) assembly was utilized [6.69] to sequentially coat a surface (Fig. 6.22a) with nanometer-thick layers of poly(vinyl alcohol) PVA and MTM, yielding, e.g., 300-bilayer films with a thickness of 1.5 μm (Fig. 6.22c, d) and an average thickness of ∼5 nm per bilayer. The PVA/MTM pair has two unique properties. First, the hydrogen bonding is highly efficient because the distance between the O atoms of clay with 0.275 nm and of the H atoms of PVA with 0.265 nm makes hydrogen bonding epitaxial. Second, a substantial part of the efficient bonding and load transfer between the PVA and the inorganic MTM is attributed to the cyclic cross-linking to easily accessible Al atoms on the surface and along the edges of MTM platelets. One Al atom, two O atoms, and three C atoms from PVA participating in this bond form a

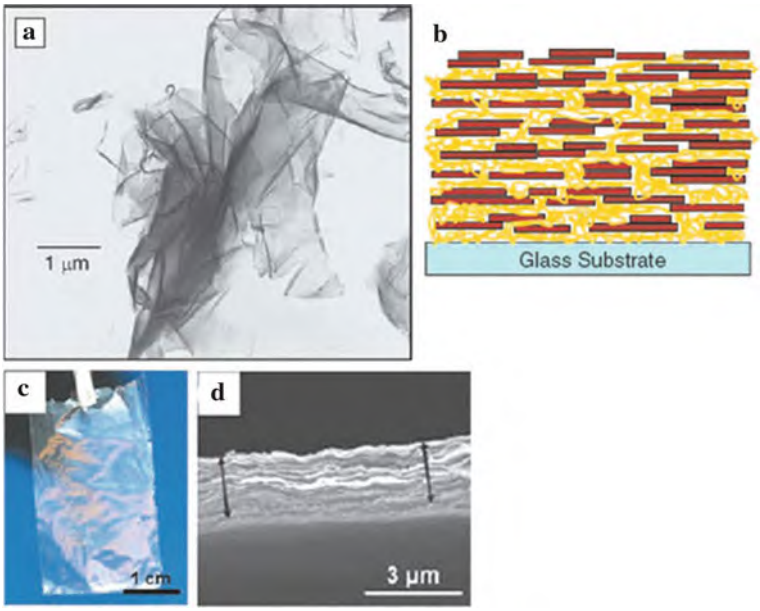

Fig. 6.22 (**a**) Transmission electron micrograph of refined montmorillonite [6.79]. (**b**) Schematic representation of the nanoarchitecture of a PVA/MTM (poly(vinylalcohol)/montmorillonite) nanocomposite with eight bilayers and a ∼5 nm bilayer thickness. (**c**) Free standing, 300-bilayer PVA/ MTM composite film showing high flexibility and transparency. (**d**) Scanning electron micrograph of the cross section of the multilayer film with the *arrows* indicating the span of the cross section [6.69]. (Reprinted with permission from [6.79] (**a**) and [6.69] (**b**–**d**). © 2007 Materials Research Society (**a**) and © 2007 AAAS (**b**–**d**))

six-membered ring structure, which is known to be particularly stable (Fig. 6.23a, b). Experimental data from Fourier transform infrared (FTIR) spectroscopy, nuclear magnetic resonance (NMR), and x-ray photoelectron spectroscopy (XPS) evidence the formation of Al-PVA covalent linkages. In addition, the PVA/ MTM films were treated with glutaraldehyde (GA) to further the bonding and load transfer between the –OH groups and the clay surface, as again demonstrated by NMR and FTIR studies. GA is a highly efficient cross-linking agent for PVA that forms covalent acetal bridges between –OH groups of the polymer chains as well as the hydroxyl groups present on the MTM sheets. The cross-linked free-standing PVA/ 50 vol% MTM films show a high strength (Fig. 6.23c), flexibility, and an 80–90% transparency [6.69]. This can be explained by the nanoscale dimensions of the inorganic phase and the nearly perfect orientation and dispersion of the MTM platelets. The ultimate tensile strength is increased by nearly a factor 3 over that of PVA/MTM without cross-linking and 10 times that of pure PVA, to values as high as 480 MPA. The modulus of cross-linked PVA/MTM exceeds that of PVA/MTM without cross-linking by a factor of 10 and that of pure PVA by a factor of 100, with the high values of 125 GPa, similar to that of Kevlar (80–200 GPa). In addition, the cross-linked

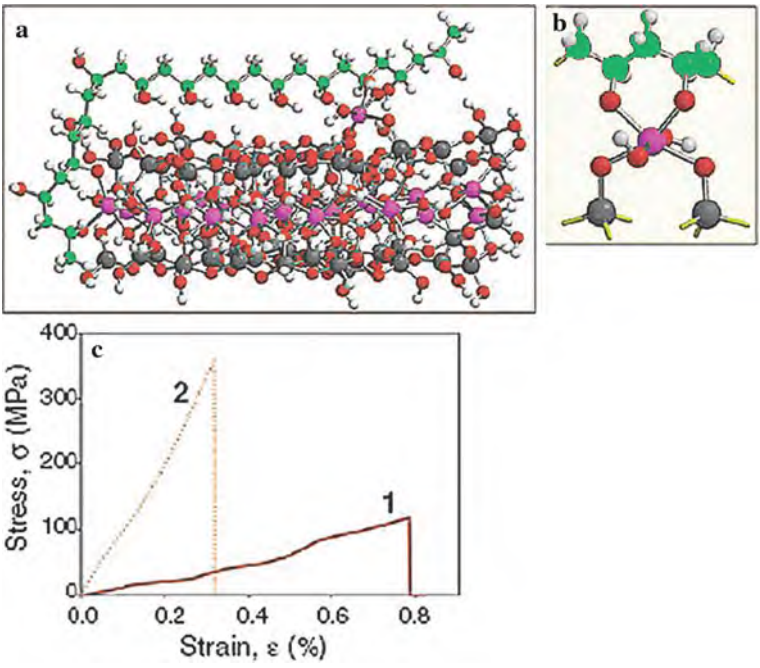

Fig. 6.23 (**a**) Characterization of the molecular interaction between poly(vinyl alcohol) (PVA) and montmorillonite (MTM) clay. Energy optimized geometry of bonding between PVA and MTM obtained by calculations with a semi-empirical algorithm. (**b**) Enlarged portion of the six-membered cycle formed between PVA and MTM. Al, *purple*; O, *red*; H, *light gray*; Si, *dark gray*; C, *green*. (**c**) Stress–strain curves for 300-bilayer PVA/ MTM composites (*1*) without and (*2*) with glutaraldehyde (GA) cross-linking. (Reprinted with permission from [6.69]. © 2007 AAAS)

PVA/MTM composites show exceptional stability to humidity due to the covalent character of the bonding. It is believed [6.69] that the understanding of these results lies in the effective stiffening of the PVA matrix (due to a constrained motion of the polymer chains) because of its close proximity to and many interactions with the MTM platelets. The strengthening and modulus enhancement in the PVA/MTM nanocomposites with GA is considered to be a result of the likelihood that a polymer chain interacts strongly with two or more clay platelets, thereby improving the particle-to-matrix-to-particle load-transfer process over that in PVA/MTM.

The secret of nacre (see Fig. 6.24a and Sect. 11.6), which combines both high strength and toughness with lightweight, is the embedding of ceramic platelets in a polymer matrix (see [6.83]). This has been used as a stimulation for a composite film of 200-nm-thick alumina platelets and a chitosan polymer (Fig. 6.24b) that is both strong (tensile strength ∼300 GPa) and ductile (fracture at a strain of ∼20%; see Fig. 6.24c) [6.84]. This artificial material is stronger and absorbs about one order of magnitude more energy during fracture than nacre [6.84].

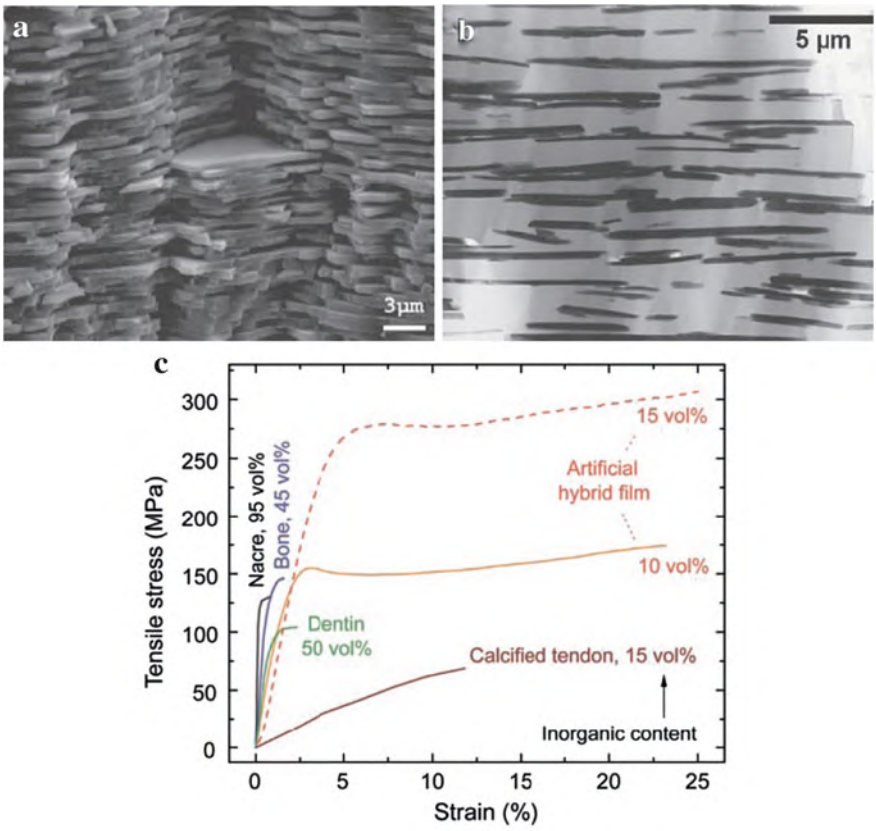

Fig. 6.24 (**a**) Scanning electron micrograph of the cross section of natural nacre. (**b**) Transmission electron micrograph of the cross section of the layered Al_2O_3/chitosan composite [6.83]. (**c**) Stress–strain curves for nacre (red abalone, *Haliotis rufescens*), bone, dentin, and calcified tendon; for references see [6.84]. (Reprinted with permission from [6.83] (**a**), (**b**) and [6.84] (**c**). © 2008 Elsevier (**a**), (**b**) and © 2008 AAAS (**c**))

In nanocomposites of carbon nanotubes and polymers [6.85] one could take advantage of the very high Young's modulus and the extraordinary strength of the nanotubes if one can cope with the matrix-to-nanotube stress transfer, i.e., enhance the strength of the interface [6.86]. Here, key questions emerge concerning wetting, mechanisms of nanotube–polymer adhesion, or measuring techniques for interfacial strength at the nanoscale. From molecular dynamics simulations, interfacial shear strengths between single-walled carbon nanotubes (SWNTs) and polymers in the 100–160 MPA range have been deduced (see [6.86]). Experimental studies have been performed by pulling a single multiwalled carbon nanotube (MWNT) from a polymer surface. The MWNT is attached to an AFM tip (Fig. 6.25) and pushed into

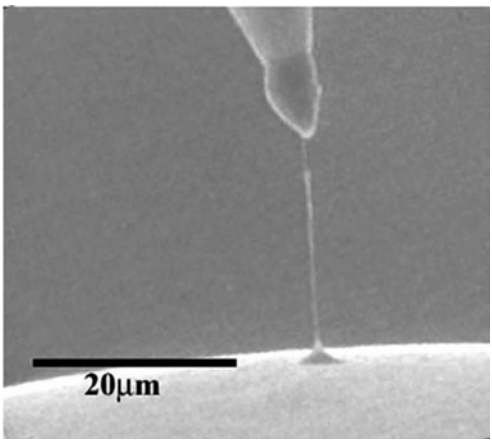

Fig. 6.25 Pullout of a carbon nanotube (MWNT) from a polymer surface. AFM pullout testing of a single MWNT from a solid polymer droplet. (Reprinted with permission from [6.86]. © 2004 Elsevier)

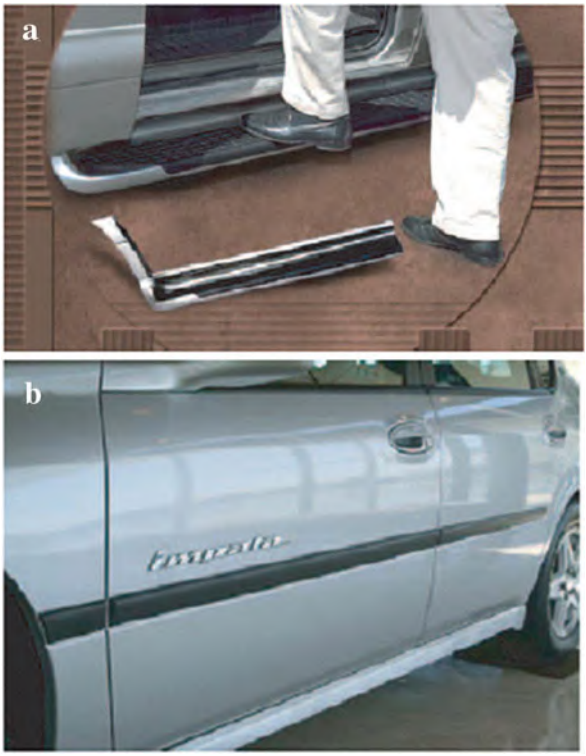

Fig. 6.26 Thermoplastic olefin nanocomposites: applications for automotive parts: (**a**) M-Van step assist: first commercial launch and (**b**) Impala: second nanocomposite application. (Reprinted with permission from [6.91]. © 2006 SAGE Pub)

a melt of polyethylene–butene. After cooling, the MWNT can be pulled out and an interfacial strength of 50 MPa is measured, which is by a factor of 10 higher than the adhesion level of this polymer and carbon fibers and far in excess of the polymer matrix tensile strength, but substantially lower than the above simulation values. The high interfacial strength has been ascribed to the formation of a crystalline layer of material around the nanotube surface (see [6.86]).

Graphene sheet (0.05 wt%, see Sect. 5.2) nanocomposites with poly(methyl methacrylate) can rival values of modulus, ultimate strength and thermal stability of single-walled carbon nanotube–poly(methyl methacrylate) composites [6.87]. Cellulose nanofibrils in polymer matrices produce reinforced composites. The stiffness (145 GPa) and tensile strength (7.5 GPa) of these glucose based, most abundant polymer nanofibrils with diameters of 5–20 nm and hundreds of nanometers in length approach those of carbon nanotubes and should be much cheaper [6.88].

Major applications for polymer nanocomposites are forecast for large commercial opportunities such as automobile parts, aerospace wings and fuselages, flame retardants and packing, with global consumption of polymer nanocomposites of tens of thousands of tons [6.78] (∼US $250 million) with an envisaged increase to 50,000 tons annually in 2011 (∼US $500–800 million) [6.78]. The most common use of polymer–clay nanocomposites is for mechanical reinforcement of *thermoplastics*, e.g., by Ube/Toyota, to replace a metal component near the engine block for weight savings [6.89]. A clay/polyolefin nanocomposite was developed by Basell Polyolefins, General Motors (GM) R&D and Southern Clay products for a GM M-Van step assist (2001), and for side trim moldings of the Impala line (2004) (Fig. 6.26). Here, the interest is based on factors such as mass savings, large processing windows, improved scratch/mar resistance, improved recyclability [6.79]. Mass saving is also an outstanding issue in *aerospace* applications where the costs for launching into the lower Earth orbit are approximately US $15,000 and for a geosynchronous orbit $36,000 per kg [6.80]. The *toughness* of thermoplastic olefin materials can be dramatically increased by adding nanoclay particles, as they interfere with the process of droplet coalescence, a key parameter in controlling toughness [6.79]. The use of polymer–clay nanocomposites for *flame retardant* application [6.90] has led to two commercial products: a Wire and Cable jacket material (organoclay + aluminum hydroxide) produced by Kabelwerk Eupen AG, and a series of polypropylene + organoclay + flame retardant systems (Maxxam^{TM} FR) produced by PolyOne® [6.89]. A number of applications appeared for clay nanocomposites as *gas-barrier* materials. Exxon Mobile has announced improvements of about 35% in air impermeability of a tire inner liner by using less than 10 wt% organoclay in brominated isobutylene-*p*-methylstyrene copolymers (see [6.79]). The gas leakage of a nanocomposite-overwrapped cryogenic hydrogen tank can be reduced by a factor of five and the structural weight by 50%, when layered silicates within the resin are used (Fig. 6.27). Clay nanocomposites can decrease the diffusivity of oxygen and water so that they are successfully used in food/liquid packaging to keep foods fresher longer [6.75], [6.89].

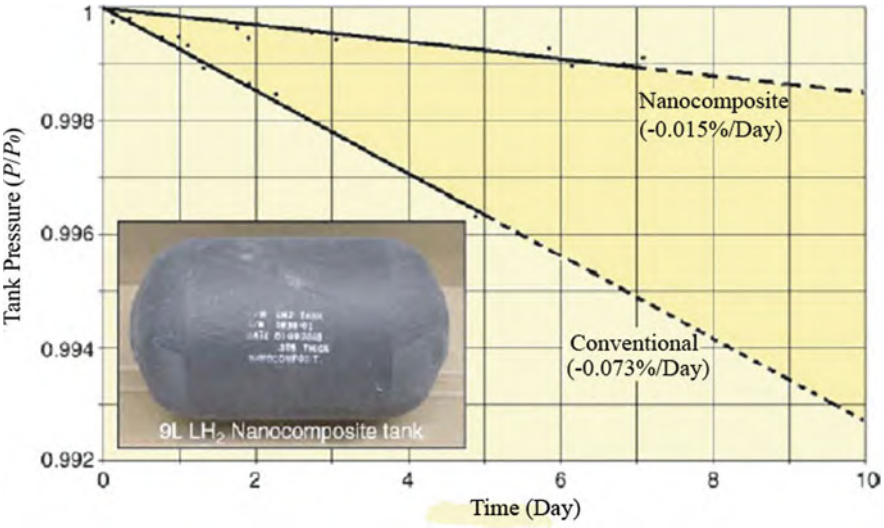

Fig. 6.27 Comparison of leak rates for a nanocomposite-overwrapped liquid-hydrogen tank using layered silicates within the resin. Nanoclays show reduced permeability for tank applications (helium is used for leak detection). P_0 is the initial helium pressure in the tank. The *inset* shows a photograph of a liquid-hydrogen tank. (Reprinted with permission from [6.80]. © 2007 Materials Research Society)

6.10 Nanocrystalline Ceramics

The properties of ceramics for application as structural materials, solid-state electrolytes [6.92], sensors [6.93], catalysts [6.94], for nanoelectronics, photovoltaics, membrane technologies [6.93], or medical techniques can often be substantially enhanced by nanostructuring. Nanosized ceramics can be synthesized [6.95] by gas-phase condensation and oxidation [6.92, 6.96], chemical vapor synthesis [6.93], sol–gel techniques [6.97], etc. Sintering of these ceramics can be achieved at significantly reduced temperatures (Fig. 6.28a) because of the small atomic diffusion distances required for densification which also facilitate superplasticity at moderate temperatures (Fig. 6.15b). Grain growth during sintering may be suppressed by doping, as demonstrated in nanocrystalline (n-)$ZrO_2{\cdot}Y_2O_3$ by Al_2O_3 doping [6.93, 6.98]. The main features of nanoceramics are characterized on the one hand by the small crystallite size which may give rise to a blue shift of fluorescence emission (see Sect. 4.1) or to optical transparency (Fig. 6.28c) because of suppression of the light scattering probability when the crystallite size is substantially smaller than the wave length of light [6.93]. On the other hand, the high volume fraction of interfaces in n-ceramics causes an enhanced atomic diffusivity of, e.g., oxygen [6.92] because of excess interfacial free volume [6.22] or to a reduction of the ion conductivity due to charge barriers at the interfaces [6.100]. It should be mentioned here that

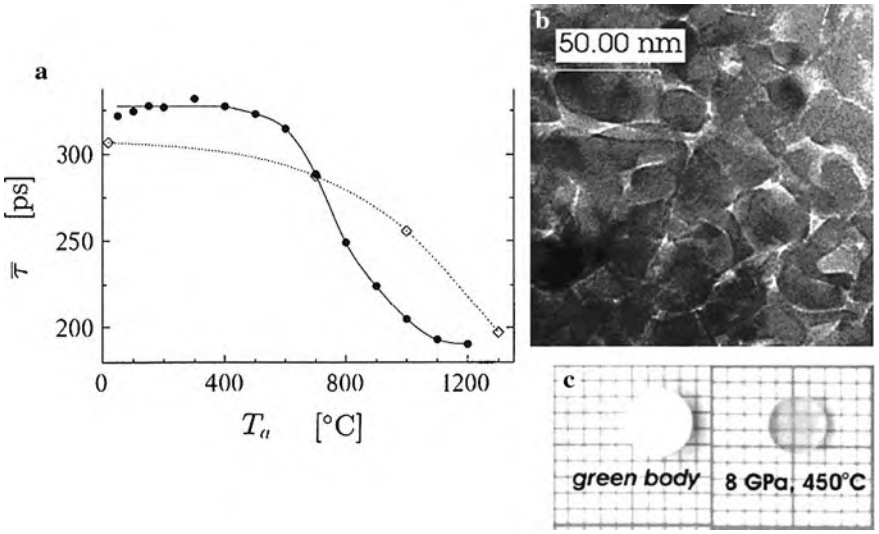

Fig. 6.28 (**a**) Mean positron lifetime as a function of the isochronal annealing temperature, monitoring the sintering process of compacted ZrO_2 powders, which occurs in gas-phase condensed nanocrystalline ZrO_2 powders (crystallite size 4 nm, ●●●) at substantially lower temperatures than in commercial ZrO_2 powders (7 nm, ◇ ◇ ◇). The higher positron lifetimes at low annealing temperatures are due to the presence of nanovoids which disappear upon sintering [6.96]. (**b**) Transmission electron microscopy of nanocrystalline Nd^{3+}-doped $Y_3Al_5O_{12}$ (YAG) with residual porosity (*white areas*) after high pressure sintering at 8 GPa, 450° C for 1 min. (**c**) Optical transparency of the Nd–YAG pellets before (*green* body) and after sintering (8 GPa, 450° C) [6.99]. (Reprinted with permission from [6.96] (**a**) and [6.99] (**b**) (**c**). © 1992 Materials Research Society (**a**) and © 2007 Elsevier (**b**), (**c**))

for solid-state electrolyte applications fully dense, crack-free nanoceramics [6.101] are a prerequisite whereas for filter membranes or sensors controlled porosity is desirable [6.93]. Schematic designs of nanoceramics for solid-state electrolytes for high-temperature fuel cells, for an oxygen sensor, and for a filtration membrane are presented in Fig. 6.29.

6.10.1 Low Thermal Expansion Nanocrystallite-Glass Ceramics

In lithium–aluminum–silicate glasses, nanocrystallites (see Fig. 6.30a) with a diameter of ∼50 nm and a volume fraction of 70% can be grown by long-term thermal treatment (Fig. 6.30b). The positive thermal expansion of the glassy matrix is nearly compensated by the negative thermal expansion of the nanocrystallites, resulting in an integral linear thermal expansion coefficient of $5 - 1.4 \times 10^{-8} K^{-1}$, by a factor of ∼1000 smaller than that of Al [6.102].

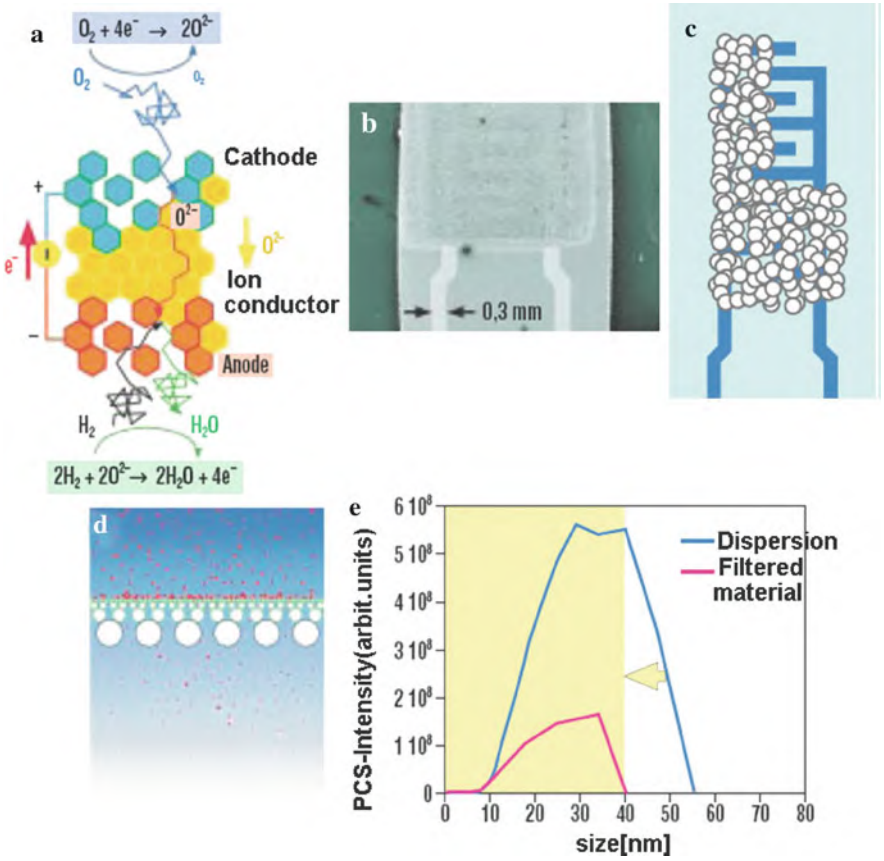

Fig. 6.29 Schematic designs of nanoceramic device applications. (**a**) Structure of a fuel cell with n-$ZrO_2 \cdot Y_2O_3$ solid electrolyte (ion conductor), cathode, anode, and operation principle. (**b**) Scanning electron micrograph of a nanocrystalline TiO_2 oxygen sensor with platinum electrodes. (**c**) Schematic of the n-TiO_2 oxygen sensor ("ceramic nose"). (**d**) Schematic of a nanocrystalline filtration membrane ("artificial kidney") on a macro-porous substrate. (**e**) Separation behavior of the filtration membrane measured by means of a suspension of latex spheres [6.93] before and after filtering. (Reprinted with permission from [6.93]. © 2005 Karlsruher Institut für Technologie)

Due to its extremely low thermal expansion, this nanoceramic is used for observatory mirror carriers for, e.g., the Very Large Telescope (VLT) at Cerro Paranal, Chile, with a mirror diameter of 8.2 m, for high-precision gyroscopes, as carrier for multilayer mirrors in extreme ultraviolet (EUV) lithography and large TV screens. Glass ceramic mirror carriers are also an option for the future European Extremely Large Telescope (E-ELT), which is scheduled to use in 2017 a 42-m-diameter mirror with more than 900 hexagonal segments [6.102].

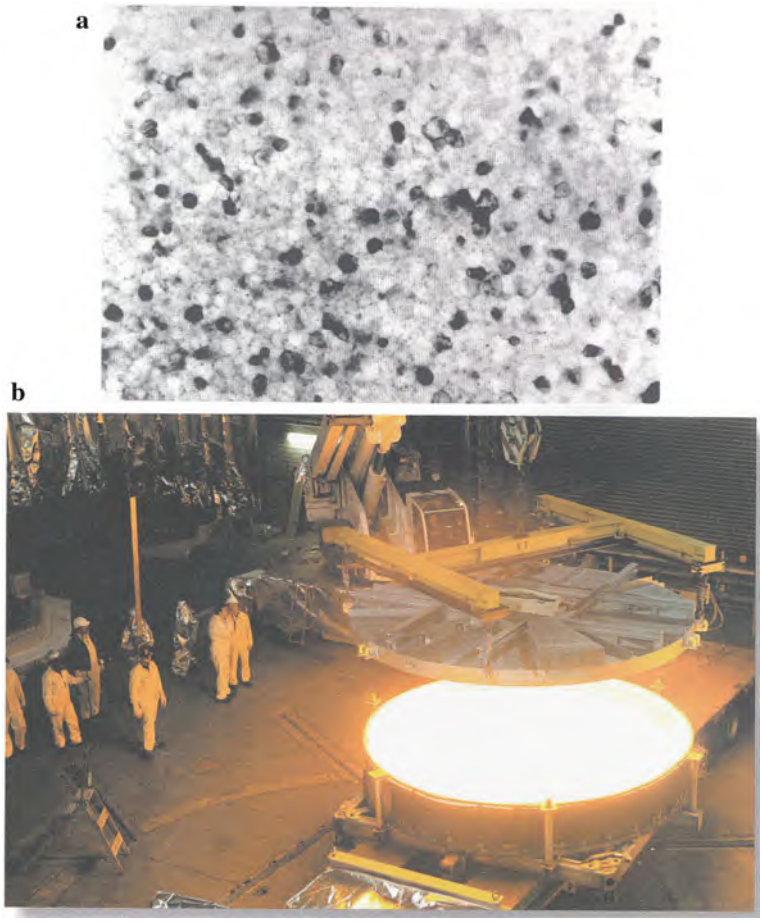

Fig. 6.30 (**a**) Nanostructured glass ceramics with the nanocrystallites (*black*) and the remnant glass phase (*white*). (**b**) Casting of a 4-m-diameter telescope mirror carrier of glass ceramics at more than 1500°C. In a cooling procedure over 11 months the nanocrystallites grow to their final size of ∼50 nm. (Reprinted with permission from [6.102]. © 2008 Photonik Th. Döring)

6.11 Atomic Diffusion in Nanocrystalline Materials

Atomic diffusion processes in nanocrystalline materials differ fundamentally from the processes in their coarse-grained or single-crystalline counterparts (see [6.103]). An illustrative example can be given for copper. Whereas the atomic diffusion length $L_\mathrm{v} = \sqrt{D_\mathrm{v} t}$ in a copper crystal at ambient temperature is completely negligible, a copper atom in a grain boundary of nanocrystalline copper will travel across $L_\mathrm{GB} = \sqrt{D_\mathrm{GB} t} = 10\,\mathrm{nm}$, i.e., the length of the size of a crystallite, within 2 h (see [6.104]), where D_v is the diffusivity in a bulk crystal and D_GB in a grain

boundary. Therefore, diffusion may control a number of application-oriented properties of nanocrystalline materials, such as enhanced ductility, diffusion-induced magnetic anisotropy, enhanced ionic mass transport, or improved catalytic activity (see [6.103]). In this section a short survey of recent diffusion studies in nanocrystalline alloys and ceramics will be given and the reader is referred to earlier reviews [6.103–6.109].

For experimental diffusion studies, the radio tracer technique with sputter or mechanical sectioning, electron-beam microanalysis, Auger electron spectroscopy (AES) or secondary ion-mass spectrometry (SIMS) with depth profiling, Rutherford backscattering, or nuclear magnetic resonance were employed. In the simplest case of nanocrystal diffusion, the two processes of rapid diffusion (D_{GB}) in the interfaces or grain boundaries and the slower diffusion from the interfaces into the crystallites (D_V) have to be considered for the analysis of the experimental diffusion profiles. According to Harrison's scheme, the three types – A, B, and C – of diffusion profiles can be differentiated [6.110]. From the type A ($L_V > d$, diffusion length > crystallite size) or type C ($L_V < \delta$, interface thickness) diffusion profiles, an average of D_V and D_{GB} or D_{GB} can be derived, respectively. From the tail in the type B profiles ($d > L_v > \delta$) the product $s\delta D_{GB} D_V^{-0.5}$ (segregation factor s) may be deduced. Transitions between the regimes A, B, and C can be treated numerically and GB migration due to grain growth or the appearance of several types of interfaces can be taken into account (see [6.103]). It has been shown in nanocrystalline iron that the interfacial diffusivity decreases after specimen preparation in dependence of time at slightly elevated temperatures due to structural relaxation of the grain boundaries [6.111] and in fully relaxed grain boundaries the values of diffusivities appear to be rather similar to the values of grain boundary diffusivities in bicrystals (see [6.103]). Atomic simulations show (see [6.103]) that in low-energy coincidence grain boundaries atomic diffusivity is mediated at moderate temperatures by point defects with reduced activation energies of formation and migration [6.112, 6.113], whereas high-energy grain boundaries may undergo a transition from a solid to a liquid state, accompanied by a decrease in the activation energy of diffusion [6.114].

An exemplary compilation of grain boundary self-diffusivities in metals and alloys is given in Fig. 6.31 for the case of iron and iron-based alloys. The ^{59}Fe diffusivity in relaxed nanocrystalline iron [6.111] is many orders of magnitude higher than the volume diffusivity and similar to the diffusivity in grain boundaries of coarse-grained iron (g-Fe). In nanocrystalline Fe–Ni, two ^{59}Fe diffusivity processes are reported (Fig. 6.31a) where the higher values are ascribed to interfaces between agglomerates of nanocrystallites and the lower values to interfaces between the nanocrystallites within agglomerates. Diffusion processes may play a role in the desirable build-up of magnetic anisotropy in modern soft-magnetic or hard-magnetic nanocrystalline alloys, by annealing, e.g., in an external magnetic field at elevated temperatures. The ^{59}Fe diffusivity measured in nanocrystalline $Fe_{73.5}Si_{13.5}B_9Nb_3Cu_1$ [6.115] (Fig. 6.31a) with superior soft-magnetic properties (see Chap. 8.3) is lower than in grain boundaries of pure iron, presumably due to intergranular amorphous phases. However, magnetic anisotropy formation in this material has been found (see [6.103]) to be due to the much slower Si diffusion

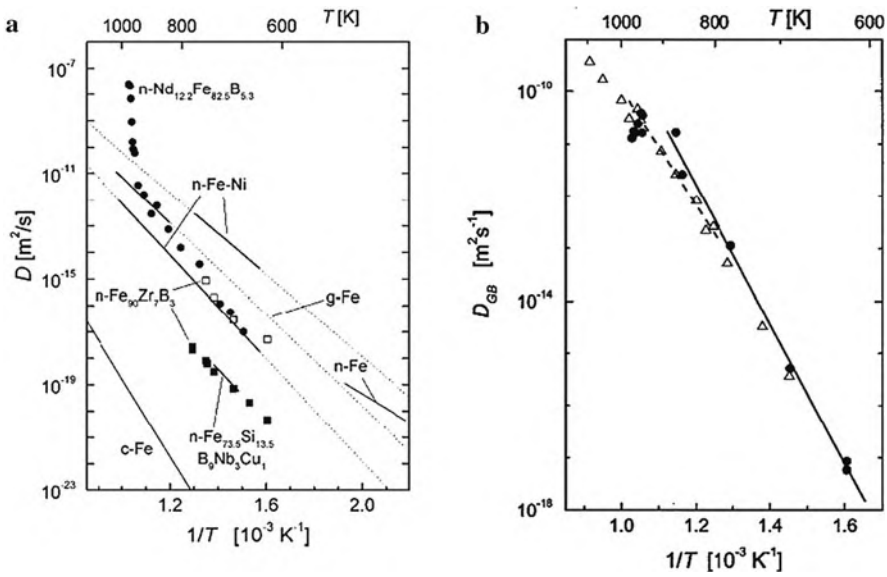

Fig. 6.31 (**a**) Arrhenius plots of ^{59}Fe-tracer diffusivities in the interfaces of nanocrystalline Fe (n-Fe) and the Fe-rich nanocrystalline alloys $Fe_{73.5}Si_{13.5}B_9Nb_3Cu_1$, $Fe_{90}Zr_7B_3$, and $Nd_{12.2}Fe_{81.8}B_6$ (interface thickness $\delta = 1$ nm). For $Fe_{90}Zr_7B_3$ the diffusivities in two types of interfaces (■ and □) are shown. The data of n-Fe refer to relaxed grain boundaries. Diffusion data for crystalline α-Fe (c-Fe), for Fe grain boundaries (g-Fe), and for nanocrystalline γ-Fe–Ni are shown for comparison. See for references text and [6.103]. (**b**) Comparison of grain boundary diffusivities of ^{147}Nd (●) and of ^{59}Fe (Δ) in nanocrystalline $Nd_2Fe_{14}B$, obtained from a type B analysis assuming a volume diffusivity of ^{147}Nd equal to that of Fe in α-Fe (see [6.103]) and $\delta = 0.5$ nm [6.116]. (Reprinted with permission from [6.103] (**a**) and [6.116] (**b**). © 2003 Wiley-VCH (**a**) and © 2005 American Institute of Physics (**b**))

within the crystallites which finally enables the ordering of the Fe–Si pairs. In the hard-magnetic nanocrystalline $Nd_2Fe_{14}B$-based system the ^{59}Fe diffusivity is similar to the grain-boundary diffusivity in pure iron (Fig. 6.31a) with a similar diffusion behavior of ^{59}Fe and ^{147}Nd [6.116] (Fig. 6.31b). The steep high temperature increase of the ^{59}Fe diffusivity in n-$Nd_2Fe_{14}B$ indicates interfacial melting (Fig. 6.31a).

Self-diffusivities in nanocrystalline metal oxides have been studied comprehensively in nanocrystalline ZrO_2 and in the oxygen ion conductor $ZrO_2{\cdot}Y_2O_3$ (Fig. 6.32). The ^{18}O diffusivity in the grain boundaries of fully dense nanocrystalline ZrO_2·6.9 mol% Y_2O_3 is found to exceed the high oxygen diffusivity in $ZrO_2{\cdot}Y_2O_3$ single crystals by about three orders of magnitude which may be of particular interest for application in gas sensors and electrolytes in solid oxide fuel cells (SOFCs). Open questions concerning the relationship between oxygen diffusion and ion conductivity [6.92] may be elucidated by a careful characterization of the specimen material. A similar enhancement of the oxygen diffusivity in interfaces over that in the crystalline volume, but on a much lower diffusivity level, has been observed in nanocrystalline monoclinic ZrO_2 [6.118] (see Fig. 6.32). The cation diffusivity

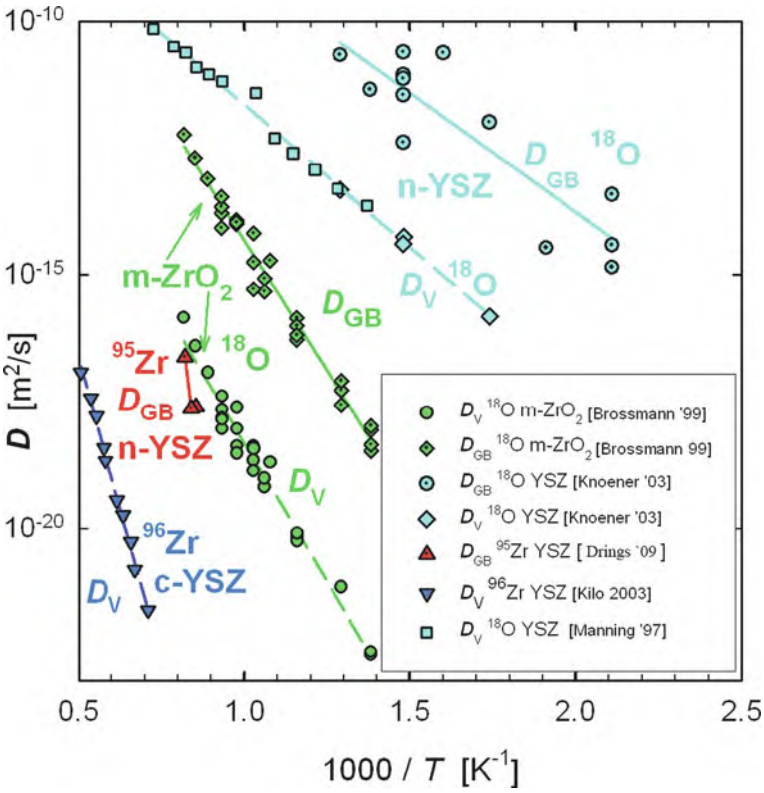

Fig. 6.32 Temperature dependence of the ^{18}O and ^{95}Zr or ^{96}Zr self-diffusivities in single crystals and in grain boundaries of nanocrystalline $ZrO_2{\cdot}Y_2O_3$ and in undoped nanocrystalline monoclinic m-ZrO_2. The volume diffusivities are designated by D_V whereas D_{GB} is the grain boundary diffusivity [6.117]. For references see text

in nanocrystalline ceramics may be of relevance for crystallite growth and degradation of solid oxide fuel cell electrolytes. Studies in fully dense nanocrystalline $ZrO_2{\cdot}9.5$ mol% Y_2O_3 with a grain size of 50 nm showed a ^{95}Zr diffusivity by about seven orders of magnitude higher than in single crystals [6.119] (Fig. 6.32). It may be pointed out here, as demonstrated by the data in Fig. 6.32, that the atomic diffusivities in metal oxides can cover a wide range of ~20 orders of magnitude upon doping and nanostructuring.

6.12 Surface-Controlled Actuation and Manipulation of the Properties of Nanostructures

Actuator materials and mechanisms that convert electrical, chemical, thermal, or photonic energy to mechanical energy have been sought for a long time (see [6.120]). Moreover, the manipulation of magnetic properties of materials by bias

voltages could be of relevance for convenient design of magnetic data storage devices. Here, some recent progress in charge-induced strain in nanocrystalline metals and carbon nanotube composites, modification of magnetic properties by electric fields, and chemistry-driven actuation will be discussed.

6.12.1 Charge-Induced Reversible Strain in Nanocrystalline Metals

Length changes in the order of 0.1% or more in response to an applied voltage have been reported for many materials, including ceramics, polymers, and carbon nanostructures, which in these cases arise from atomic rearrangements or charge transfer throughout the entire solid. In metals, voltage-induced length changes have been observed making use of nanometer-sized porous metal nanostructures [6.121]. In this case, the length change is due to a controlling of the surface charge density σ in, e.g., a nanoporous Pt sample (grain size 6 nm; see Fig. 6.33a, b) through an applied

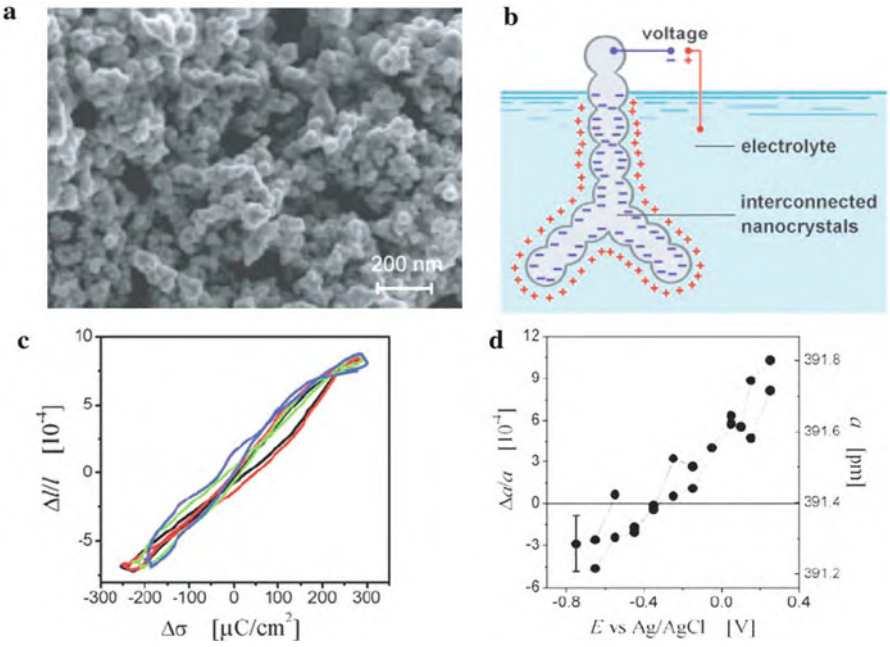

Fig. 6.33 (**a**) Scanning electron micrograph of the fracture surface of a nanoporous Pt sample. (**b**) Schematic representation of an array of charged nanoparticles immersed in an electrolyte. (**c**) Relative length change $\Delta I/I$, as measured by dilatometry, versus the surface charge density $\Delta\sigma$. (**d**) Lattice parameter a determined by x-ray diffraction (*right ordinate*) and lattice strain $\Delta a/a_0$ (*left ordinate*) versus E. The *horizontal line* indicates the lattice parameter of the dry powder. The *error bar* refers to the reproducibility of $\Delta a/a_0$; the uncertainty in the absolute value of a is estimated to be $\pm$ 0.3 pm. (Reprinted with permission from [6.121]. © 2003 AAAS)

potential E relative to an electrolyte impregnating the pores. The nanocrystalline Pt sample shows a reversible macroscopic length change $\Delta I/I = 0.0015$ in a potential E which induces a variation $\Delta\sigma \approx 500\mu C/cm^2$ of the surface charge density (Fig. 6.33c). This coincides with the voltage-induced variation of the lattice parameter $\Delta a/a_0 \approx 0.0014$ as measured by x-ray diffraction (Fig. 6.33d). A microscopic discussion of the charge-induced strain in nanocrystalline Pt starts from the effects of the electronic band structure on the interatomic spacing in late transition metals, where the antibonding interaction due to the upper d-band states is balanced by the bonding effect of the sp-hybridized states. Injecting electrons into the band structure changes the population of both bands, and the lattice contraction found experimentally upon injecting electrons at the surface would be compatible with the notion of a dominant effect on the bonding sp orbitals [6.121]. Even larger strain amplitudes than at present can be envisioned in porous metals with higher surface-to-volume ratios.

6.12.2 Artificial Muscles Made of Carbon Nanotubes

An aerogel – a lightweight (1.5 mg/cm^3), sponge-like material consisting of bundles of multiwalled carbon nanotubes (12 nm in diameter) – is light as air, yet stronger than steel and bendier than rubber. These characteristics are combined in a material that twitches like a bionic man's biceps when a voltage is applied [6.120]. Applying a voltage across the width of a ribbon of the material electrically charges the nanotubes that thread through the material (see [6.122]). This makes them repel one another and the ribbon can expand sideways by up to three times its original width with an actuation rate of $3.7\times10^4\%s^{-1}$, much faster than the 50% s^{-1} maximum rate of natural muscle (see [6.120]).The maximum achieved work per actuation cycle is ~30 J/kg, compared with the maximum capability of ~40 J/kg for natural muscle. Applying a voltage along the length of the ribbon has a very different effect. It triggers the nanotube structure to contract, making the material more dense and very stiff. The material can withstand extreme temperatures between 80 and 1900 K and, therefore, could be easily used in harsh environment.

6.12.3 Electric Field-Controlled Magnetism in Nanostructured Metals

The *magnetic anisotropy* of a bcc Fe (001)/MgO 001 junction (see Fig. 6.34a) can be modified by an electric field. Magnetic hysteresis loops, in a 0.48-nm-thick Fe layer under the application of a bias voltage, obtained from Kerr ellipticity, η_K, measurements are shown in Fig. 6.34b. From these data, a change of the magnetic anisotropy by 39% is derived when the electric field is switched from 200 to –200 V. The effect is largest for an Fe film thickness of 0.48 nm and is tentatively attributed to a suppression of the number of electrons in the $d_{3z^2-r^2}(m_z = 0)$ electron states of Fe atoms adjacent to the MgO barrier (Fig. 6.34c) under a negative voltage due to

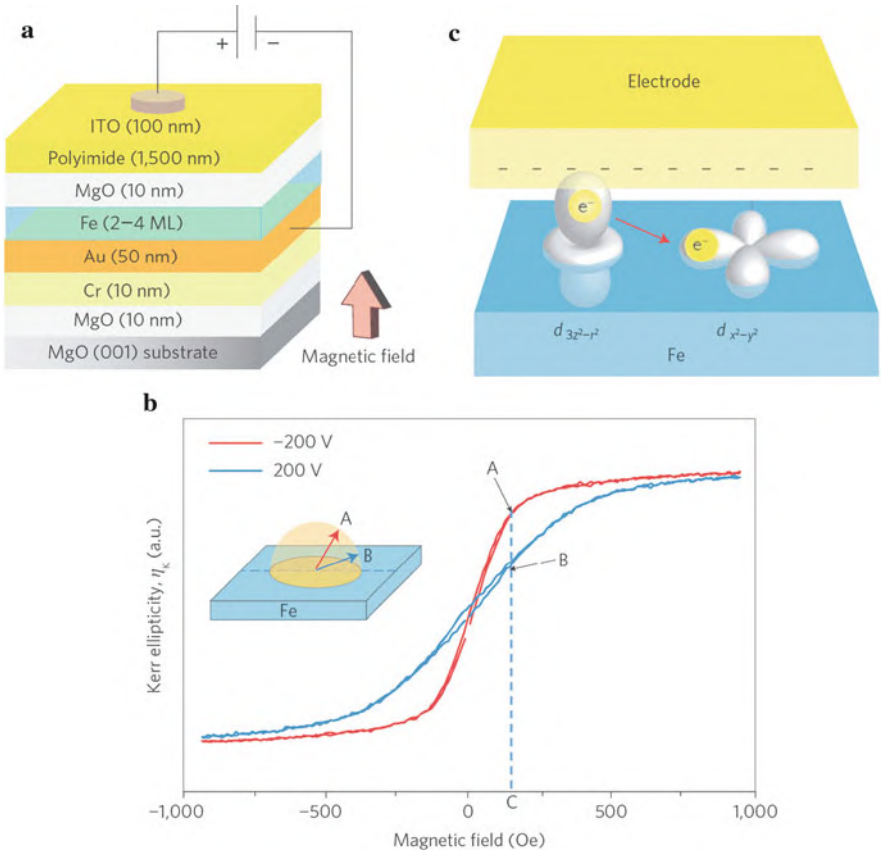

Fig. 6.34 (**a**) Schematic of the sample used for a voltage-induced magnetic anisotropy change. The magnetic field was applied perpendicular to film plane for magneto-optical Kerr effect (MOKE) ellipticity measurements, η_K. (**b**) Measurements of η_K for different applied voltages on a Fe/MgO junction (Fe thickness 0.48 nm) as a function of the applied magnetic field. The change in the hysteresis curve upon the change of the bias voltage indicates a large change in the perpendicular magnetic anisotropy of the Fe film. (**c**) Schematic of the effect of the electric field on electron filling of the 3*d* orbitals in the ultrathin Fe layer. (Reprinted with permission from [6.123]. © 2009 Nature Publishing Group)

an increase in energy of these electron states. Therefore, the electron occupancy in the d_{xy} and $d_{x^2-y^2}$ states could be changed relative to one another, leading to a modulation of the magnetic anisotropy [6.123]. This approach may provide a technique for high-speed voltage-controlled magnetization switching.

The *orientation of the magnetization* in ferromagnetic Co, which is exchange-bias coupled to multiferroic (see Sect. 8.9) antiferromagnetic $BiFeO_3$, can be controlled and switched through the application of an electric field to the $BiFeO_3$ structure [6.124], [6.125].

The *magnetization* at the surface of a ferromagnetic electrode in an electrochemical cell has been demonstrated to be electric field tunable [6.126].

6.12.4 Surface Chemistry-Driven Actuation in Nanoporous Gold

The powering of actuation by chemical energy which is used in biological systems has been demonstrated for man-made actuator technologies in high-surface area nanoporous gold [6.127]. Reversible strain amplitudes of the order of a few tenths of a percent were achieved by alternating exposure of nanoporous Au to ozone and carbon monoxide. The effect can be explained by adsorbate-induced changes of the surface stress and can be used to convert chemical energy directly into mechanical response [6.127].

6.13 Summary

Nanocrystalline bulk materials are polycrystals with nanometer-sized crystallite dimensions. Due to the high volume fraction of interfaces with a disordered atomic structure they are expected to show novel mechanical, thermal, electrical, and diffusive properties. Molecular dynamics studies have contributed to the understanding of the interface structure and the plastic behavior of bulk nanomaterials showing a yield strength increasing with decreasing crystallite size (Hall–Petch behavior) and turning to an inverse Hall–Petch behavior at small ($\sim$15 nm) crystallite sizes. Both ductility and strength can be enhanced in metals with nanotwin structures and superplasticity is observed. Nanocomposites of inorganic and organic materials and nanoceramics play an interesting industrial role. Due to the rapid atomic diffusion in interfaces, the diffusion processes in nanocrystalline solids are strongly enhanced. The properties of nanocrystalline materials can be surface controlled by charges and electrical fields.

References

6.1 H. Gleiter, in *Deformation of Polycrystals: Mechanisms and Microstructures*, eds. by N. Hansen et al. (Risø Nat. Lab., Roskilde, 1981) p. 15
6.2 R. Birringer et al., Phys. Lett. **A102**, 365 (1984)
6.3 R.W. Siegel, H. Hahn, in *Current Trends in Physics of Materials*, ed. by M. Yusouff (World Scientific Publ., Singapore, 1987) p. 403
6.4 H.-E. Schaefer et al., in *Physical Research*, Vol. **8**, ed. K. Henning (Akademie Verlag, Berlin, 1988), p. 580
6.5 H. Gleiter, Prog. Mat. Sci. **33**, 223 (1989)
6.6 H. Gleiter, Acta Mater. **48**, 1 (2000)
6.7 A.S. Edelstein, R. Cammarata (eds.), *Nanomaterials* (IOP, Bristol, 1996)
6.8 C.C. Koch (ed.), *Nanostructured Materials* (Noyes Publications, Norwich NY, 2002)
6.9 H.S. Nalwa (ed.), *Nanoclusters and Nanocrystals* (American Scientific Publ., California, 2003)

6.10 J. Schiøtz, W. Jacobsen, Science **301**, 1357 (2003)
6.11 D. Wolf et al., Acta Mater. **53**, 1 (2005)
6.12 H.V. Swygenhoven, J.R. Weertman, Mater. Today **9**, May 2006, p. 24
6.13 H.C. Huang, H. Van Swygenhoven, MRS Bull. **34**, 160 (2009)
6.14 D.C. Chrzan et al., MRS Bull. **34**, 173 (2009)
6.15 A.P. Sutton, R.W. Balluffi, *Grain boundaries in Crystalline Materials* (Oxford Sci., Oxford, 1996)
6.16 D. Wolf et al., Phys. Rev. Lett. **77**, 2965 (1996)
6.17 N.F. Mott, Proc. Phys. Soc. **60**, 391 (1948)
6.18 J. Löffler, J. Weissmüller, Phys. Rev. **B52**, 7076 (1995)
6.19 H.-E. Schaefer et al., *Bericht zum Kompetenznetz Funktionelle Nanostrukturen* (Landesstiftung Baden-Württemberg, Germany, 2005), p. 407
6.20 R. Würschum et al., Phys. Rev. **B62**, 12021 (2000)
6.21 H.-E. Schaefer et al., Mat. Sci. Eng. **A286**, 24 (2000)
6.22 K.W. Urban, Science **321**, 506 (2008)
6.23 T. Haubold et al., Phys. Lett. **A135**, 461 (1989)
6.24 S. Ranganathan et al., Scripta Mater. **44**, 1169 (2001)
6.25 H.-E. Schaefer, R. Würschum, Phys. Lett. **A119**, 370 (1987)
6.26 E. Budke et al., Acta Mater. **47**, 385 (1999)
6.27 P. Keblinski et al., Phil. Mag. Lett. **76**, 134 (1997)
6.28 Y. Champion et al., Science **300**, 310 (2003)
6.29 I.A. Ovid'ko, Rev. Adv. Mater. Sc. **10**, 89 (2005)
6.30 M. Yu. Gutkin, I.A. Ovid'ko, *Plastic Deformation in Nanocrystalline Materials* (Springer, Berlin 2004)
6.31 J. Weissmüller, J. Markmann, Adv. Eng. Mater. **7**, 202 (2005)
6.32 X.Z. Liao et al., Appl. Phys. Lett. **83**, 632 (2003)
6.33 C.C. Koch, J. Narayan, MRS Symp. Proc., vol. 634, p. B.5.1.1 (2000)
6.34 O.L. Warren et al., Mater. Today **10**, April 2007, p. 59
6.35 A.M. Minor et al., Nature Mater. **5**, 697 (2006)
6.36 D. Feichtinger et al., Phys. Rev. **B67**, 024113 (2003)
6.37 A. Hasnaoui et al., Acta Mater. **52**, 2251 (2004)
6.38 I. Szlufarska et al., Science **309**, 911 (2005)
6.39 I. Szlufarska, Mater. Today **9**, 42 (2006)
6.40 F. Liao et al., Appl. Phys. Lett. **86**, 171913 (2005)
6.41 T. Zhu et al., MRS Bull. **34**, 167 (2009)
6.42 J.R. Greer, W.D. Nix, Phys. Rev. B**73**, 245410 (2006)
6.43 S.H. Oh et al., Nat. Mater. **8**, 95 (2009)
6.44 D.N. Seidman et al., Acta Mater. **50**, 4021 (2002)
6.45 T. Zhu et al., Proc. Natl. Acad. Sci. US. **104**, 3031 (2007)
6.46 Y.-H. Zhao et al., Adv. Mater. **18**, 2280 (2006)
6.47 L. Lu et al., Science **304**, 422 (2004)
6.48 R.Z. Valiev, Nat. Mater. **3**, 511 (2004)
6.49 C. Suryanarayana, Adv. Eng. Mater. **7**, 983 (2005)
6.50 A. Trafton, MIT TechTalk, March 7, 2007, p. 5
6.51 Y.F. Luo et al., J. Mater. Sci. Technol. **25**, 211 (2009)
6.52 P.M. Derlet et al., MRS Bull. **34**, 184 (2009)
6.53 L. Lu et al., Science **323**, 607 (2009)
6.54 A.K. Mukherjee, Mater. Sci. Eng. **A322**, 1 (2002)
6.55 K.C. Chan et al., Mat. Sci. Technol. **23**, 677 (2007)
6.56 R.B. Figueiredo, T.G. Laugdon, Adv. Eng. Mater. **10**(1–2), 37 (2008)
6.57 S.X. McFadden et al., Nature **398**, 684 (1999)
6.58 J.P. Hirth, J. Lothe, *Theory of Dislocations* (McGraw-Hill, New York, 1968)
6.59 K.A. Padmanabhan, H. Gleiter, Mater. Sci. Eng. **A381**, 28 (2004)

6.60 J. Markmann et al., Scr. Mater. **49**, 637 (2003)
6.61 B.N. Kim et al., Nature **413**, 288 (2001)
6.62 D. Farkas et al., Phys. Rev. Lett. **94**, 165502 (2005)
6.63 A. Vinogradov, S. Hashimoto, Adv. Eng. Mater. **5**, 351 (2003)
6.64 H.W. Höppel et al., Phil. Mag. **A82**, 1781 (2002)
6.65 X.–W. Li et al., Adv. Eng. Mater. **10** (8), 720 (2008)
6.66 E. Thiele et al., Z. Metallkunde **93**, 730 (2002)
6.67 T. Hanlon et al., Scr. Mater. **49**, 675 (2003)
6.68 R.A. Meirom et al., Phys. Rev. Lett. **101**, 085503 (2008)
6.69 P. Podsiadlo et al., Science **318**, 80 (2007)
6.70 J. Eckert et al., Adv. Eng. Mater. **7**, 587 (2005)
6.71 V.L. Solozhenko, E. Gregoryanz, Mater. Today **8** (11), 44 (2005)
6.72 J.S. Moya et al., Adv. Eng. Mater. **9**, 898 (2007)
6.73 D.V. Szabó et al., Nachr. Forschungsz. Karlsruhe **37**(1-2) 64 (2005); D. Vollath, D.V. Szabó, J. Nanopart. Res. **6**, 18 (2004)
6.74 D. Vollath et al., J. Nanopart. Res. **6**, 181 (2004)
6.75 S.S. Ray, M. Okamoto, Progr. Polym. Sci. **28**, 1539 (2003)
6.76 S.C. Tjong, Mat. Sci. Eng. **R53**, 73 (2006)
6.77 S.S. Ray, M. Bousmina, *Polymer Nanocomposites and their Applications* (American Scientific, Stevenson Ranch, CA, 2006)
6.78 K.I. Winey, R.A. Vaia, MRS Bulletin **32**, April 2007, p. 314
6.79 D.L. Hunter et al., MRS Bulletin **32**, April 2007, p. 323
6.80 J. Baur, E. Silverman, MRS Bulletin **32**, April 2007, p. 323
6.81 R.A. Vaia, H.D. Wagner, Mater. Today, November 2004, p. 32
6.82 O.L. Manevitch, C.G. Rutledge, J. Phys. Chem. **B108**, 1428 (2004)
6.83 C. Sealy, Mater. Today **11**, April 2008, p. 15
6.84 L.J. Bonderer et al., Science **319**, 1069 (2008)
6.85 M. Moniruzzaman, K.I. Winey, Macromolecule. **39**, 5194 (2006)
6.86 H.D. Wagner, R.A. Vaia, Mater. Today, November 2004, p. 38
6.87 T. Ramanathan et al., Nature Nanotechnol. **3**, 327 (2008)
6.88 J.F. Beecher, Nat. Nanotechnol. **2**, 466 (2007)
6.89 A.B. Morgan, Mater. Matters, Sigma-aldric. **2**(1), 20 (2007)
6.90 A.B. Morgan, C.A. Wilkie (eds.), *Flame Retardant Nanocomposites* (Wiley, New York, 2007)
6.91 F. Hussain et al., J. Compos. Mater. **40**, 1511 (2006)
6.92 G. Knöner et al., Proc. Natl. Acad. Sci USA **100**, 3870 (2003)
6.93 H. Hahn et al., Nachrichten-Forsch. Zentr. Karlsruh. **37**(1-2), 12 (2005)
6.94 A. Weidenkaff, Adv. Eng. Mater. **6**, 709 (2004)
6.95 M. Winterer, *Nanocrystalline Ceramics – Synthesis and Structure* (Springer, Heidelberg, 2002)
6.96 R. Würschum et al., Mat. Res. Soc. Symp. Prog. **238**, 733 (1992)
6.97 L.C. Klein, in *Nanomaterials*, eds. by A.S. Edelstein, R.C. Cammerata (IOP, Bristol, 1996), p. 147
6.98 A. Madubuonu et al., Phys. Stat. Sol. (a. **203**, R64 (2006)
6.99 R. Fedyk et al., Opt. Mater. **29**, 1252 (2007)
6.100 J. Maier, Sol. State Ionics **131**, 13 (2000)
6.101 H. Drings et al., Phys. Stat. Sol. (RRL. **1**, R7 (2007)
6.102 Th. Döring, Photonik 2/2008, p. 52
6.103 R. Würschum et al., Adv. Eng. Mater. **5**, 365 (2003)
6.104 H. Mehrer, *Diffusion in Solids* (Springer, Berlin 2007)
6.105 H. Gleiter, Phys. Stat. Sol. (b. **172**, 41 (1992)
6.106 R. Würschum, H.-E. Schaefer, in *Nanomaterials*, eds. by A.S. Edelstein, R.C. Cammarata (IOP, Bristol, 1996), p. 277

6.107 R. Würschum et al., *Nanostructured Materials*, ed. by C.C. Koch (Noyes Publications, Norwich NY, 2002), p. 267
6.108 P. Heitjans, S. Indris, J. Phys.: Condens. Matter. **15**, R1257 (2003)
6.109 A.V. Chadwick, in *Diffusion Fundamentals*, eds. by J. Kärger et al. (Leipziger Universitätsverlag, Leipzig, 2005), p. 204
6.110 I. Kaur et al., *Fundamentals in Grain and Interphase Boundary Diffusion* (John Wiley, Chichester, 1995)
6.111 H. Tanimoto et al., Nanostruct. Mater. **12**, 681 (1999)
6.112 Q. Ma et al., Acta Metall. Mater. **41**, 143 (1993)
6.113 M.R. Sørensen et al., Phys. Rev. **62**, 3658 (2000)
6.114 P. Keblinski et al., Phil. Mag. **A79**, 2735 (1999)
6.115 R. Würschum et al., Phys. Rev. Lett. **79**, 4918 (1997)
6.116 W. Sprengel et al., J. Appl. Phys. **98**, 074314 (2005)
6.117 H. Drings et al., Phys. Status Solidi **A206**, 54 (2009)
6.118 U. Brossmann et al., J. Appl. Phys. **85**, 7646 (1999)
6.119 M. Kilo et al., J. Appl. Phys. **94**, 7547 (2003)
6.120 A.E. Aliev et al., Science **323**, 1575 (2009)
6.121 J. Weissmüller et al., Science **300**, 312 (2003)
6.122 K. Sanderson, Nature doi:10.1038/news.2009.178
6.123 T.M. Maruyama et al., Nat. Nanotechn. **4**, 158 (2009)
6.124 N.A. Spaldin, R. Ramesh, MRS Bull. **33**, 1047 (2008)
6.125 Y.-H. Chu et al., Nat. Mater. **7**, 478 (2008)
6.126 M. Weisheit et al., Science **315**, 349 (2007)
6.127 J. Biener et al., Nat. Mater. **8**, 47 (2009)

Chapter 7
Nanomechanics – Nanophotonics – Nanofluidics

A number of novel phenomena emerge for mechanical, optical, or fluidic properties on nanometer scales. Nanoelectromechanical systems (NEMS) are developed for high-sensitivity detection and for investigating the boundary between classical mechanics and quantum mechanics. By the adhesion properties of nanostructured gecko toe pads, the fabrication of highly sticky adhesive materials is stimulated.

In the rapidly expanding field of nanophotonics, single-photon sources and detectors may be of importance for cryptography and quantum computing. Quantum dot lasers and amplifiers are expected to play a role in communication technology. The field of plasmonics, where photons are coupled to the oscillations of conduction electrons in metal nanostructures, is of relevance from the coloring of stained glass in antiquity to future biomedical technology.

Fluidics on the nanoscale are governing many biological processes and have to be taken into account for the scaling down of biomedical assays. Here, recent studies of wetting and spreading, of enhanced transport rates in nanotubes, on nanodroplets, and on nanobubbles will be outlined.

In addition, first steps of unifying the above fields, such as the combination of nanomechanics and nanophotonics [7.1] or the fusion of nanophotonics and nanofluidics [7.2–7.4] appear to be particularly promising (see Sect. 7.6).

7.1 Nanoelectromechanical Systems (NEMS)

Microelectromechanical systems (MEMS) have become mainstream devices such as optical switches, inkjets, and accelerometers. As an advancement, nanoelectromechanical systems (NEMS) [7.5, 7.6] with nanoscale dimensions not only show great progress in sub-single-charge electrometry [7.7], single-electron spin paramagnetic resonance [7.8], nuclear spin relaxation (see [7.9]), zeptogram-scale mass sensing [7.10] in vacuum and attogram-scale sensing in liquids [7.11], zeptonewton-scale force sensing [7.12], sub-femtometer displacement sensing [7.13], and high-sensitivity energy sensing [7.14] (see also Sects. 1.7 and 7.2) but also provide a way to observe the imprint of quantum phenomena directly [7.15]. Displacements of microscale cantilevers are typically measured optically

H.-E. Schaefer, *Nanoscience*, DOI 10.1007/978-3-642-10559-3_7,

by bouncing a laser off the sensor. Diffraction effects make it far more difficult to apply this method at the nanoscale, so electric currents are used to drive and detect the motion of tiny mechanical NEMS structures such as beams and cantilevers by employing, e.g., effects of piezoelectricity discovered by the Curie brothers [7.16] in 1880 [7.6]. Recent developments in the fields of nanoelectromechanical high-frequency resonators, rotational activators, and switches will be discussed in the following.

7.1.1 High-Frequency Resonators

Self-sensing nanocantilevers with fundamental mechanical resonances up to some hundred MHz [7.17, 7.18] can make use of integrated electronic displacement transducers based on piezoresistive thin metal films, (e.g., a 30 nm thick gold layer on a nanosized SiC cantilever; see Fig. 7.1a), which undergo a resistance change in response to the motion-induced strain. By circumventing optics, piezoresistive transduction yields access to dimensions far below the diffraction limit of ~ 200 nm. Sufficiently small cantilevers with a resonance frequency of 127 MHz (Fig. 7.1a) can be operated at atmospheric pressure and room temperature (mean free path of air molecules ~ 65 nm) because enhanced damping due to viscous flow can be suppressed [7.17]. Under these conditions, mass resolutions of ~ 100 zg (10^{-19} g) are achieved.

Substantially higher resonance frequencies up to 1.85 GHz have been observed for 3.5 nm thick carbon nanotubes (CNTs) suspended over a trench (Fig. 7.1b) where the vibrating motion is detected by changes in the source-drain current through the carbon nanotube [7.19]. The resonance frequency of a CNT can be tuned by employing a gate voltage (Fig. 7.1c) in a similar fashion like tightening a guitar string [7.20].

Rotational actuator. Repeated rotary oscillations and free rotations of a 440 nm diameter thin metal plate fixed on a multiwalled carbon nanotube (MWNT; diameters 10–40 nm) have been demonstrated (Fig. 7.2), promising torsional oscillator mechanical resonance frequencies of the order of tens to hundreds of megahertz. For large-displacement rotary operation, the outer MWNT shells between the rotor plate and the anchors (see Fig. 7.2a) were removed by a strong torque past the elastic limit of the outer shells initiated by a ~ 80 V dc stator voltage (see Fig. 7.2a). Subsequently, due to the low intershell friction of the atomically smooth MWNT surface, complete rotor-plate revolutions can be performed controlled by quasi-static dc stator voltages (Fig. 7.2b). In principle very high-frequency operation should be possible [7.21].

7.1.2 Nanoelectromechanical Switches

Several switching devices based on microelectromechanical (MEMS) and nanoelectromechanical (NEMS) systems have been proposed recently in order to suppress

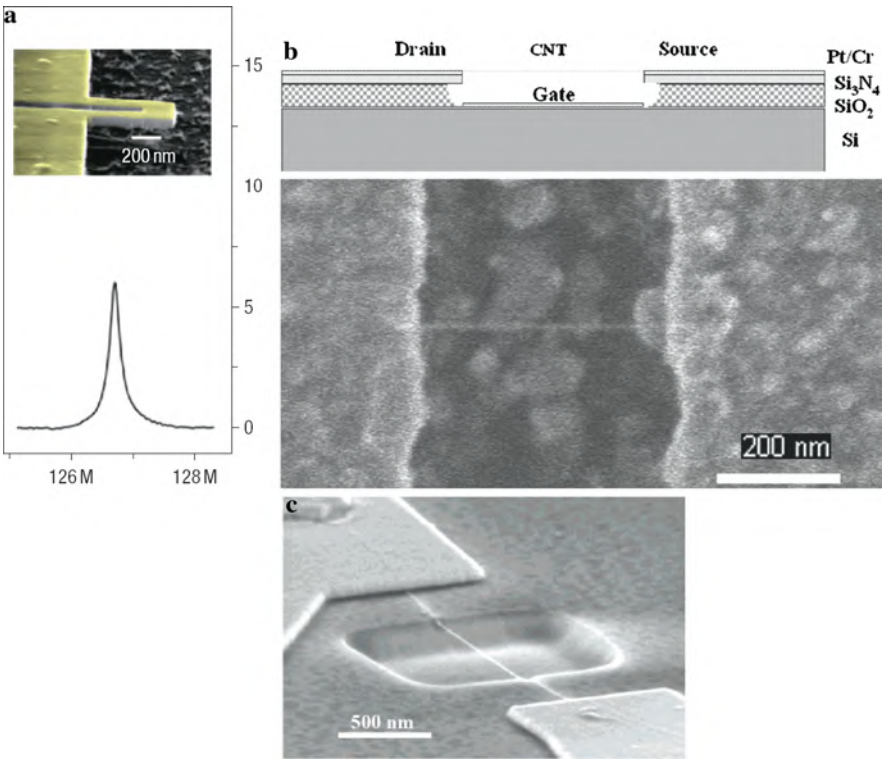

Fig. 7.1 High-frequency nanoelectromechanical system (NEMS) resonators. (**a**) Piezoresistively detected resonant response from a SiC nanocantilever ($600 \times 400 \times 70$ nm^3) covered with a 30 nm thick gold film as piezoresistive transducer [7.17]; (**b**) Schematic cross-section and scanning electron micrograph (SEM) of a suspended CVD-grown carbon nanotube (CNT) resonator crossing a trench [7.19]. (**c**) SEM image of a suspended CNT with a p-Si gate on the bottom of the trench [7.20]. (Reprinted with permission from [7.17] (**a**), [7.19] (**b**), and [7.20] (**c**). © 2007 Nature Publishing Group (**a**), © 2006 American Physical Society (**b**), and © 2006 American Chemical Society (**c**))

power dissipation, parasitic leakage currents, and short-channel effects, emerging in the scaling of complementary metal-oxide semiconductor (CMOS) devices (see [7.22]). Cantilever-type switches with a 35 nm thick TiN beam could be fabricated by and integrated into conventional CMOS technology [7.22]. The beam material TiN (see Fig. 7.3a, b) was selected owing to its low electrical resistivity of 20 $\mu\Omega$ cm, a high Young's modulus of 600 GPa, and its chemical inertness. The switch has a pull-in voltage of $\sim$ 13.45 V for switch closing, an essentially zero off current, an excellent on/off current ratio of 10^5 (Fig. 7.3c), and can be stably operated over several hundreds of switching cycles under dc and ac biases at ambient conditions.

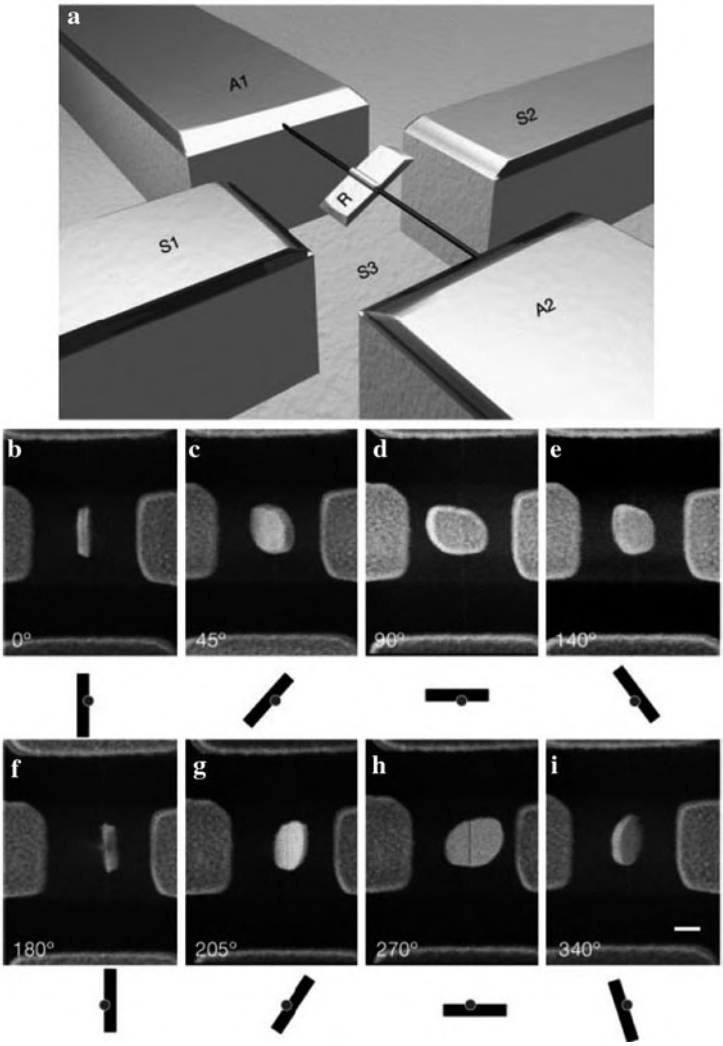

Fig. 7.2 Integrated rotational NEMS actuator. (**a**) Conceptual drawing of the nanoactuator. A metal plate rotor (R) of gold (90 nm thick) covered with chromium (10 nm) and a diameter of $\sim$ 440 nm is attached to a multiwalled carbon nanotube (MWNT) which acts as a support shaft and yields rotational freedom. Electrical contact to the rotor plate is made via the MWNT and its anchor pads (*A1, A2*). Three stator electrodes, two on the SiO_2 surface (*S1, S2*) and one buried beneath the surface (*S3*), provide additional voltage control elements. The SiO_2 surface has been etched down to provide full rotational freedom for the rotor plate. The entire actuator assembly is integrated on a Si chip. (**b–i**) Series of scanning electron micrographs (SEM) showing the actuator rotor plate at different angular displacements. The MWNT, barely visible, runs vertically through the middle of each frame. The schematic diagrams located beneath each SEM image illustrate a cross-sectional view of the position of the nanotube/rotor-plate assembly. Scale bar, 300 nm. (Reprinted with permission from [7.21]. © 2003 Nature Publishing Group)

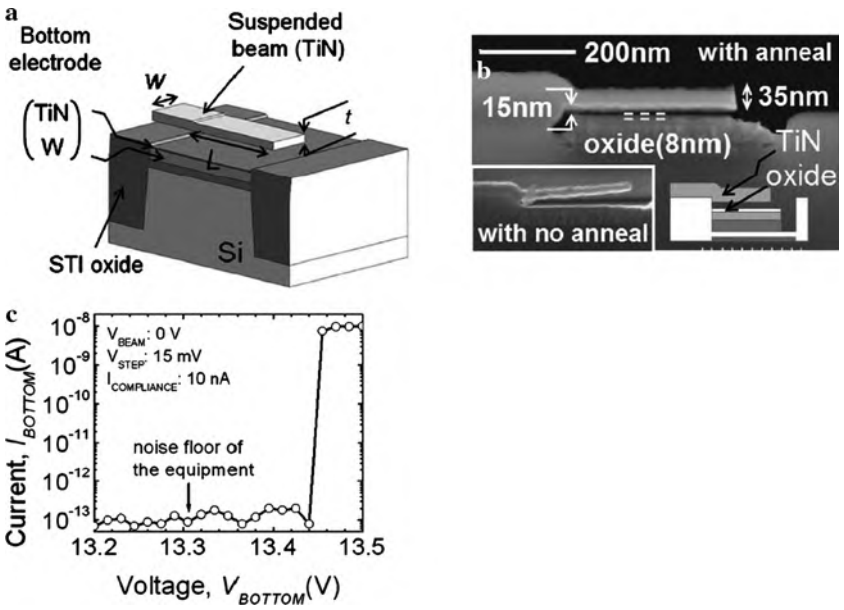

Fig. 7.3 (**a**) Schematic diagram of the cantilever-type NEMS switch composed of the suspended TiN beam and the bottom electrode STI (shallow trench isolation). (**b**) Scanning electron micrograph (SEM) of a cantilever-type NEMS switch by employing a thin oxide layer. (**c**) *I–V* curve of the pull-in regime of the cantilever-type NEMS switch ($w/L/t = 200/300/35$ nm), showing ideal on/off current characteristics. (Reprinted with permission from [7.22]. © 2008 American Institute of Physics)

7.2 Putting Mechanics into Quantum Mechanics – Cooling by Laser Irradiation

Nanoelectromechanical structures are starting to approach the ultimate quantum mechanical limits for detecting and exciting motion at the nanoscale [7.15]. These structures at the quantum limit may further illuminate the boundary between the microscopic realm, governed by quantum mechanics, and our macroscopic world, governed by classical mechanics [7.15]. For generating very low temperatures and for measuring the motion of a mechanical resonator, laser light may be used as a coolant (see [7.23, 7.24]), a technique by which atoms were brought to the quantum ground state earlier. If this could be achieved for nanoscale or even microscale objects of the order of 10^{14} atoms [7.25], this could elucidate whether the laws of quantum mechanics also apply to these size scales.

In the quantum world, many properties such as energy, location, or speed can take a range of values simultaneously, so that all one can say is that this value has that probability. When that is the case, physicists say that a quantum object is in a superposition of states [7.26]. The great conundrum of modern physics is the quantum-classical transition which is crucial for the emerging field of quantum

information technology. What happens to the superposition as one goes to objects of more and more atoms (see [7.26])? The most favored answer to this question involves a phenomenon known as decoherence [7.27]. Crudely speaking, decoherence is a sort of leaking away of quantum behavior when a particle interacts with its surroundings. Decoherence predicts, that the quantum-classical transition is not really a matter of size, but of time. So larger objects, which generally have more ways of interacting, decohere almost instantaneously. Even in a perfect vacuum, particles will decohere through interactions with photons in the omnipresent cosmic microwave background. The decoherence description shows that there is no abrupt boundary, no critical size, at which quantum behavior switches to classical.

An alternative theory of quantum-classical transition suggests, that the "collapse" of superposition, rather than being a gradual affair resulting from environment-induced decoherence, is a rather abrupt event that is mediated by gravity [7.28, 7.29]. It is thought [7.29, 7.26] that the cost in gravitational potential energy in keeping objects in a superposition becomes too great as objects get bigger, so that the objects "go classical" on a definite timescale, which is estimated [7.29] to be about a second for dust particles [7.26].

Assuming that quantum mechanics applies for mesoscale structures, the energy of each resonator mode is given by $E = h\omega(N + 1/2)$ where $N = 0, 1, 2 \ldots$ is the occupation factor of the mechanical mode of the frequency ω. The quantum ground state $N = 0$ has a zero-point energy of $h\omega/2$ and is described by a Gaussian wave function of the width $(x^2)^{1/2} = \Delta x_{\mathrm{SQL}} = \sqrt{h/(2m\omega)}$. This quantity, known as the standard quantum limit, is the root-mean-square amplitude of quantum fluctuations of the resonator position [7.30]. The larger the zero-point fluctuations, the easier they are to detect. For example, a radio-frequency (10–30 MHz) nanomechanical resonator with a typical mass of $\sim 10^{-12}$ g has $\Delta x_{\mathrm{SQL}} = 10^{-14}$m, only a little larger than the size of an atomic nucleus.

This Δx_{SQL} value is readily detectable by today's advanced methods (see Sect. 7.1 and [7.15]). A much larger $\Delta x_{\mathrm{SQL}} \approx 10^{-10}$m of a 1 μm long carbon nanotube makes this device very attractive for displaying and exploring quantum phenomena with mechanical systems. A crucial consideration for reaching the quantum limit of a mechanical mode is the thermal occupation factor N_{th} given by the average energy

$$\langle E \rangle = \hbar\omega\, N_{\mathrm{th}} = \hbar\omega \left(\frac{1}{2} + \frac{1}{e^{\hbar\omega/k_{\mathrm{B}}T}}\right)$$

of a mechanical mode coupled to a thermal bath where N_{th} follows the Bose–Einstein distribution. Figure 7.4 a displays the deviation from classical behavior that occurs at low temperatures. When $k_{\mathrm{B}}T \ll \hbar\omega$, N_{th} is less than 1 and the mode becomes "frozen out," which occurs for a 1 GHz resonator for $T < 50$ mK – a regime well within standard dilution refrigeration [7.15]. For displacement sensing of nanoelectromechanical systems (NEMS) optical detection is complicated dramatically by diffraction effects and transduction is performed from the mechanical to an electrical signal by making use of amplifiers such as quantum dots or

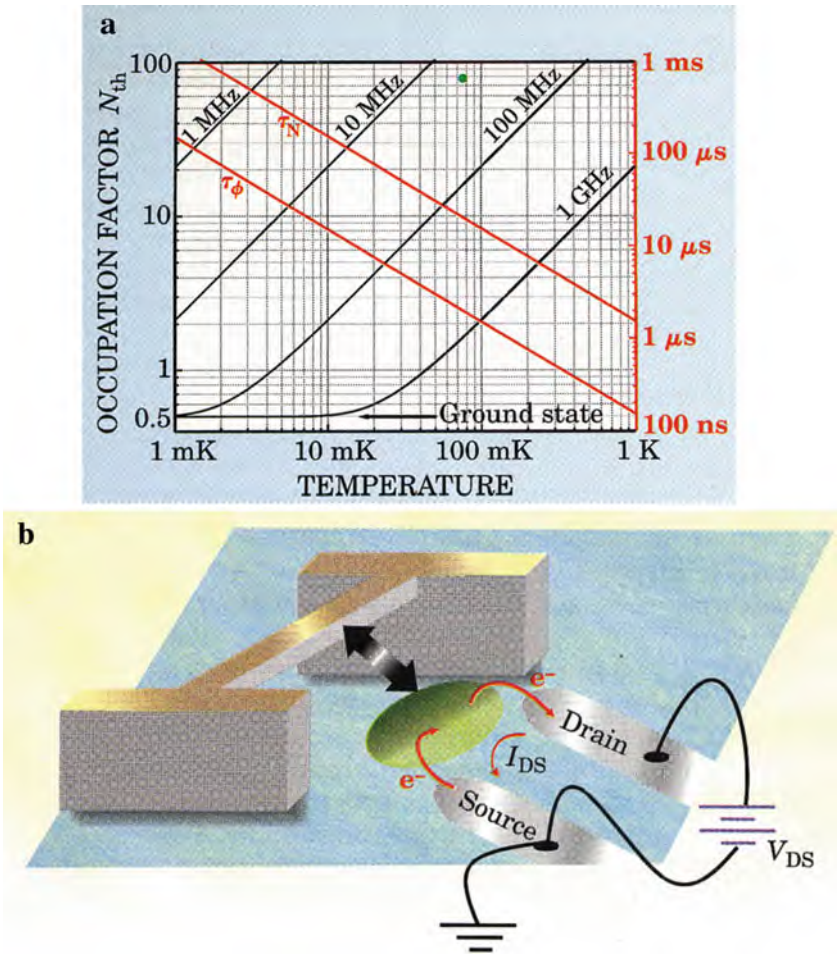

Fig. 7.4 (**a**) Quantum limits. The occupation factor N_{th} (*black curves*) for various mechanical resonator frequencies is a function of resonant frequency and temperature T. Shown in *red* is the lifetime τ_N of a given number state for a 10 MHz resonator with a quality factor $Q = 200{,}000$ [7.31]. Also in *red* is the expected decoherence time τ_ϕ for a superposition of two coherent states in that resonator displaced by 100 fm. (**b**) Detection techniques for nanomechanical displacements in a nanoelectromechanical system (NEMS). Coupling of the NEMS to a mesoscopic detector such as a quantum dot or a single-electron transistor. The current I_{DS} through the detector is modulated by the NEMS motion. (Reprinted with permission from [7.15]. © 2005 American Institute of Physics)

single-electron transistors (SET; see Fig. 7.4b). The resonator's motion induces a change in the charge on the gate electrode of the SET and the SET's conductance can be directly monitored, so that nanomechanical measurements only a factor of about 6 from the quantum limit could be performed [7.31] with an occupation factor $N_{\text{th}} = 58$ of the mechanical mode. This demonstrates that the quantum

ground state ($N_{th} < 1$) is within reach [7.15]. The generation and detection of the uniquely quantum states of a small mechanical device, such as energy eigenstates (so-called Fock states), superposition states, or entangled states, which are predicted for temperatures up to even $\sim$ 20 K [7.32] are particularly interesting because the mechanical structures may be considered "bare systems" [7.15]: There is no macroscopic quantum condensate to protect the device from excitation or decoherence [7.15]. However, cooling of NEMS to low temperatures is less straightforward than initially thought [7.15] and active cooling through controllable external interactions such as laser cooling of a nanomechanical resonator mode to its motional ground state has been proposed [7.33]. In fact, stimulated by theoretical work [7.34, 7.35], laser cooling was demonstrated to reduce the temperature of micromirrors by more than two orders of magnitude [7.36–38]. In addition, by sideband laser irradiation of a silica microresonator (Fig. 7.5), cooling has been observed [7.24]. This cooling is due to light absorption in a sideband with lower energy and subsequent emission of higher-energy light.

By optical sideband cooling, mechanical resonators can be refrigerated to fewer than 60 phonons and will soon be operating in the mechanical quantum regime. There may be surprises waiting in the quantum behavior of these very large (observable to the naked eye) systems [7.39].

Quantum-limited displacement sensitivities can also be achieved by making use of a superconducting interference device (SQUID) which can detect flexing displacement of a bar down to about 10^{-13} m. This may correspond to a sensitivity that is 36 times larger than the bar's quantum zero-point displacement uncertainty [7.40, 7.41].

For approaching the regime where quantum aspects are important, a coupling of nanomechnical resonators is suggested [7.43] with quantum-controlled atomic ensembles into an entangled Einstein–Podolsky–Rosen state.

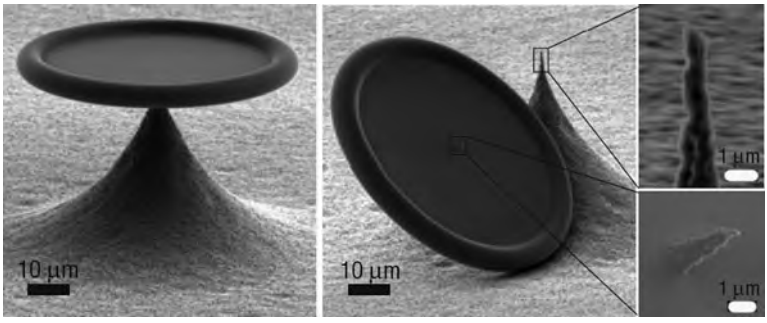

Fig. 7.5 Resolved-sideband regime of a mesoscopic optomechanical oscillator. Scanning electron microscope image of the silica microtoroidal optical cavity supporting both optical resonances and radial breathing modes with a high quality factor $Q = 30{,}000$, held by a nanosized "needle" pillar. An image of an intentionally broken cavity structure is also shown with a 500 nm diameter pillar which reduces the coupling to the pillar and enables high Q factors. (Reprinted with permission from [7.24]. © 2008 Nature Publishing Group)

7.3 Nanoadhesion: From Geckos to Materials

Nanosized attachment structures enable some larger animals, such as geckos, or small insects (see Fig. 7.6) to easily climb vertical walls and even walk on the ceiling. This is made possible by a hierarchical structure of fibrils that become smaller toward the contact region of the feet with the surface and that attach the feet strongly but reversibly to a variety of surfaces – smooth or rough, hydrophilic or hydrophobic, clean or containing contaminants. The surface is contacted by thousands of 200 nm long and 15 nm thick stiff keratin structures (elastic modulus $E \approx 1$ GPa [7.45]) called spatulae – thin fibers tipped with tapered plates – which form individual attachment points [7.46]. Such a structure may rely solely on van der Waals forces [7.47] to stick to the surface because of the multiple attachment points and the nanosized structure of the contacting elements. A water layer present on the majority of real surfaces may enhance adhesion by capillarity (see [7.46]). This demonstrates the close links between mechanics, chemistry, and physics when considering adhesion. Geckos can move on a vertical stone wall during heavy rain although van der Waals interaction between two surfaces is already negligibly small at a separation of a few nanometers. Thus, the first step in building up adhesive contact is to squeeze out most of the water between the gecko's toe pad and the stone wall. This is a complex problem in elastohydrodynamics (see [7.45]).

During pull-off, the bond between the toe pad and the substrate is not broken uniformly over the contact area but rather via crack propagation (or peeling) from the periphery to the center in analogy with peeling adhesive tape (Fig. 7.7). The normal component of the pull-off force of a tape is given by $F_\perp = F \sin\theta = \Delta\gamma B \sin\theta(1 - \cos\theta)$, where θ is the peel angle, $\Delta\gamma$ the adhesion energy per unit area, and B the width of the film. The gecko adheres by applying muscle force that keeps the angle θ between its legs and the substrate very small. This maximizes the pull-off force which is important on rough and contaminated surfaces. The toe

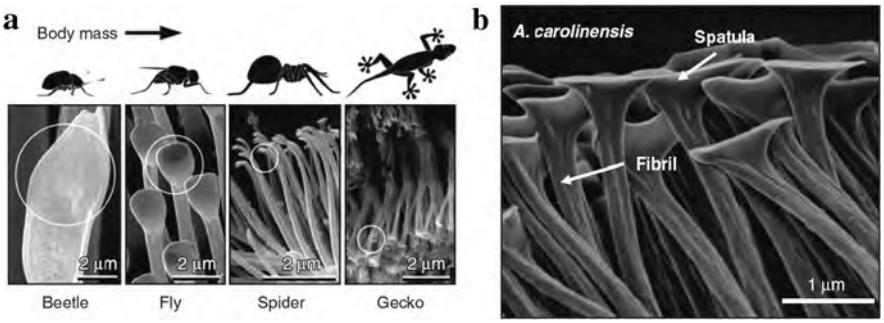

Fig. 7.6 (**a**) Examples of natural fibrillar attachment structures of the foot pads of the beetle, fly, spider, and gecko. They consist of a hierarchical arrangement of nanoscale fibrillar structures called setae. The tips of the fibrils are terminated by flat plate-like structures called spatulae (*circled*) [7.42]. (**b**) Example of a spatulated fibrillar array of the green anole lizard (*Anolis carolinensis*) [7.44]. (Reprinted with permission from [7.42] (**a**) and [7.44] (b). © 2007 Materials Research Society)

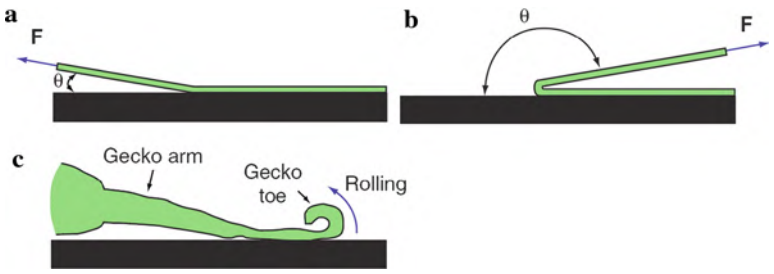

Fig. 7.7 Peeling adhesive tape from a substrate. (**a**) The peel angle θ is small, the pull-off force is large, while the opposite is true when the peel angle is large (**b**). (**c**) The gecko removes the contact to the substrate by rolling its toes upward from the substrate. (Reprinted with permission from [7.48]. © 2006 National Academy of Sciences USA)

pad-substrate bond can be quickly broken for fast motion by rolling or peeling the toe, from the tip, off the substrate (Fig. 7.7c). It has been suggested that the gecko keeps its toe pads clean for good adherence by scratching away solid particles trapped on the toe pad surface [7.45].

7.3.1 Materials with Bioinspired Adhesion

The details of the mechanism for attachment and detachment of animal feet with nanoscopic structures remain complex and difficult to reproduce artificially but several laboratories have designed biologically inspired artificial surfaces for enhanced and removable adhesion. A gecko tape has been developed by transferring arrays of carbon nanotubes (8 nm in diameter) on a polymer tape simulating the structure found on the foot of a gecko lizard. The gecko tape can support a sheer stress (36 N/cm^2) nearly four times higher than the gecko foot, can be used repeatedly, and sticks to a variety of surfaces, including Teflon [7.49]. A biologically inspired adhesive, consisting of an array of nanofabricated polymer pillars coated with a synthetic polymer that mimics the wet adhesive proteins found in mussel holdfasts, maintains its adhesive performance for over a thousand contact cycles in both dry and wet environments [7.50]. Tapes with sub-micrometer poly (glycerol sebacate acrylate) (PGSA) pillars and a coating of oxidized dextran with aldehyde functionalities were developed for bonding to wet tissues in medical application. When implanted into rats, the coated tapes show enhanced adherence and cause minimal inflammation [7.51]. Furthermore, bioinspired micropatterned surfaces with switchable adhesion have been designed [7.52].

7.3.2 Climbing Robots and Spiderman Suit

Biologically inspired adhesives may also be employed for the design of vertically climbing robots [7.53] or a Spiderman suit [7.54]. Whereas conventional robots are vacuuming horizontal household floors, exploring the surface of Mars and performing other tasks that humans find tedious or hazardous, robots with gecko

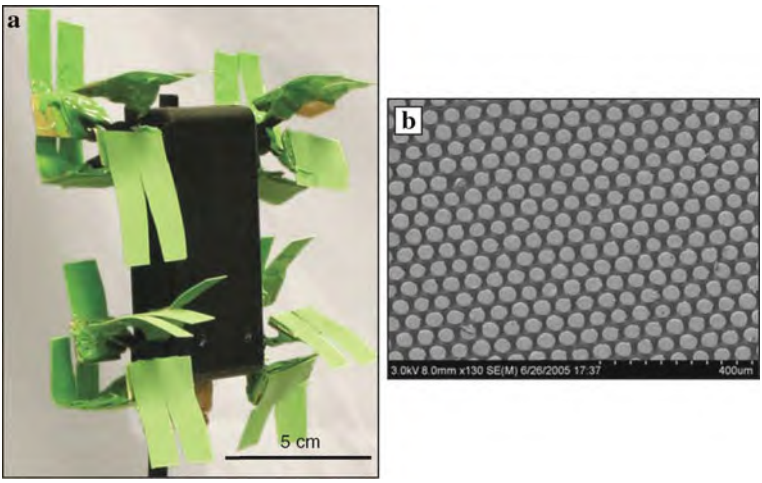

Fig. 7.8 (**a**) Mini-Whegs7^{TM} (87 g) on vertical glass with poly (vinyl siloxane) (PVS) microstructured polymer feet. (**b**) PVS surface with a hexagonally patterned microstructure. (Reprinted with permission from [7.53]. © 2007 Materials Research Society)

capabilities might be walking on ceilings, changing high light bulbs, or cleaning building exteriors. A Mini Whegs ^{TM} is a robot with four multispoke wheel-leg appendages (Fig. 7.8a). A foot made of flexible material is bounded to the end of each spoke and acts as a hinge between the foot and the spoke. The feet contact the substrate, bend as the wheel-leg turns, peel off the substrate gradually, and spring back to their initial orientation for the next contact. Walks of 58 cm were performed on a vertical glass wall with 2.3 cm/s [7.53] where the structured feet retained their traction and adhesive properties for several hours and could be renewed by washing.

Spiderman suits are thought to become feasible in the near future [7.54]. According to a recent analysis [7.54], a man (palm surfaces of $\sim$200 cm^2) with gecko-material gloves ($\sigma_{\text{gecko}} \approx 0.58$ MPa) could support a mass of $\sim$1160 kg, or with spider-material gloves ($\sigma_{\text{spider}} \approx 0.24$ MPa) a mass of 480 kg. As a good material for a Spiderman suit, branched long carbon nanotubes [7.55] are suggested [7.54], with a number of hierarchical levels sufficient to activate self-cleaning. A highly sticky material with vertically oriented carbon nanotubes yielding a shear adhesion force of 1 MPa and a normal adhesion force of 0.1 MPa has been developed recently [7.56].

7.4 Single-Photon and Entangled-Photon Sources and Photon Detectors, Based on Quantum Dots

7.4.1 Single-Photon Sources

Conventional sources of light, such as light-emitting diodes and lasers, generate radiation that can be described with classical Maxwell's equations (see [7.57, 7.58]).

On the other hand, applications in the field of quantum information science require optical sources with strong quantum correlations between single photons [7.59]. This is particularly true for quantum cryptography, which makes use of the principles of quantum mechanics to provide unconditional security for communication. An essential element of secure key distribution in quantum cryptography is an optical source emitting a train of signals that contains each one single photon (see [7.57, 7.60]). In addition, the availability of a single-photon source enables the implementation of quantum computation using only linear optical elements and photodetectors (see [7.57]).

An emission behavior where the emission of two or more photons simultaneously is precluded is called photon antibunching. It represents the ultimate limit in the quantum control of the photon generation process and has been observed in a variety of single quantum emitters, including an atom, a stored ion, a molecule, a semiconductor quantum dot, or a single nitrogen-vacancy center in diamond (see references in [7.57]). In a single-photon emitter based on semiconductor quantum dots (QDs), the quantum dots with a small band gap, e.g., InAs and an emission wavelength of ~ 950 nm are embedded in a semiinsulating GaAs substrate (see Fig. 7.9a). Upon pulsed (~ 250 fs) illumination with a Ti: sapphire laser (750 nm), which supplies the trigger signal for the single-photon sequence, charge carriers are formed in the GaAs layers and trapped at the QDs where they form confined excitons with discrete energy states. The exciton recombination radiation with an energy of 1.322 eV is predominantly emitted from the edge of the disk (Fig. 7.9a) due to a coupling to the whispering gallery modes located there.

In order to assess whether the exciton recombination radiation from the quantum dots is single-photon emission, one has to consider photon statistics. A classical light source, such as a laser, can be described by a *coherent* or *Glauber state*. The distribution of photon numbers $P(n)$ with a mean photon number N and the measurement of n photons in this state is given by a Poisson distribution which leads to the broad distribution shown in Fig. 7.9b. This prohibits the application of the Glauber state in quantum cryptography. A non-classical state of light is the so-called *Fock state*.

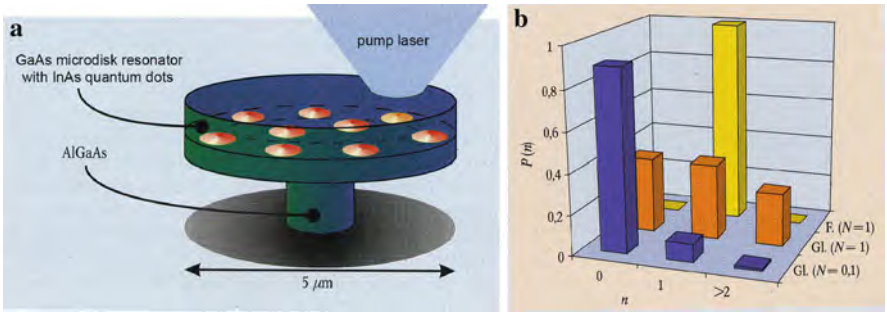

Fig. 7.9 (**a**) Schematic representation of a single-photon source based on semiconductor quantum dots. The InAs quantum dots with a diameter of ~ 40 nm and a height of ~ 3 nm are embedded between two semiinsulating 100 nm thick GaAs layers. (**b**) Distribution $P(n)$ of photon numbers for the Fock state ($F.$) with a mean photon number $N = 1$ and for Glauber states (Gl.) with $N = 1$ and $N = 0.1$. (Reprinted with permission from [7.58]. © 2001 Wiley-VCH)

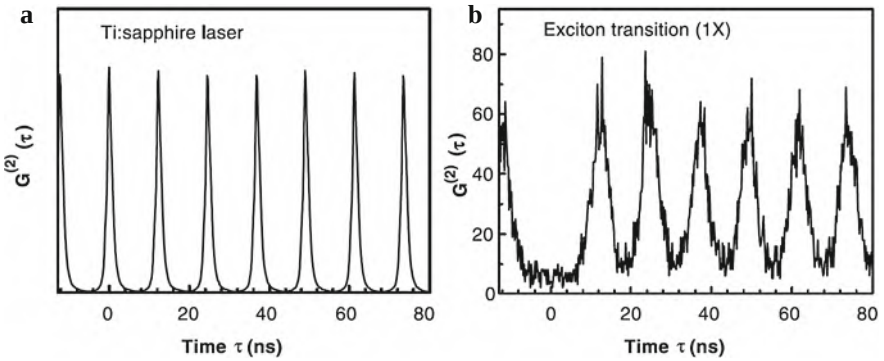

Fig. 7.10 Measured unnormalized correlation function $G^{(2)}(\tau)$ of (**a**) a mode-locked Ti: sapphire laser (FWHM = 250 fs) and (**b**) a single QD excitonic ground state (1X) emission under pulsed excitation conditions (82 MHz). (Reprinted with permission from [7.57]. © 2000 AAAS)

In a mode excited in this state, precisely N photons are available with the variance $\Delta N = 0$, as sketched in Fig. 7.9b. This is the characteristic signature of a single-photon source. For measuring the emission statistics a single QD can be excited [7.57]. The unnormalized correlation function $G^{(2)}(\tau) = \langle I(t)I(t+\tau)\rangle$, with I the time-dependent intensity for the pulsed Ti:sapphire laser, is given in Fig. 7.10 for the exciton transition radiation of a QD at $T = 4$ K. Whereas the $G^{(2)}(\tau)$ of the pulsed Ti:sapphire laser shows integer multiples of the repetition period $\tau_{\text{rep}} = 12.27$ ns, the $G^{(2)}(\tau)$ of the QD exciton emission also shows peaks at the same τ_{rep}, but in contrast to the laser, the peak at $\tau = 0$ is not present; that is, the probability of finding a second photon at $\tau = 0$ vanishes. The absence of a peak at $\tau = 0$ provides strong evidence for an ideal single-photon source operation.

Quantum dot structures can also be used for single-photon sources which are electrically operating [7.61], which are operating at elevated temperatures up to 200 K [7.62], or which emit photons with polarization control at high emission rates [7.63]. In addition, single-photon sources based on single carbon nanotubes have been demonstrated [7.64].

7.4.2 Entangled-Photon Sources

Entanglement, the intriguing correlation of quantum systems [7.65, 7.66], is an essential resource of quantum information and communication (see, e.g., [7.67]). It has been demonstrated that the biexciton–exciton radiative cascade in single InAs quantum dots on a GaAs substrate is a source for entangled-photon pairs satisfying the Peres criterion for entanglement (see [7.67]).

Entangled photons are a basic tool in quantum optics, e.g., to demonstrate the violation of Bell's inequalities, teleportation, or quantum cryptography [7.59]. Making use of quantum dots, a compact source of entangled photons on demand has become available [7.68]. In a single InAs quantum dot a single entangled-photon pair can be generated at a well-defined time [7.68]. Here, initially a biexcition (XX) is generated

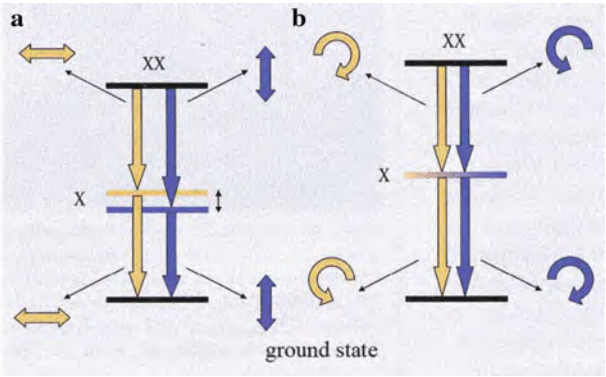

Fig. 7.11 In the generation of entangled photons in a cascade decay in a symmetric quantum dot (**b**) the two degenerate decay channels cannot be distinguished (entanglement). In the case of an asymmetry a splitting of the exciton state (X) emerges and the two channels can be distinguished (**a**). The *arrows* indicate the polarization of the photons. (Reprinted with permission from [7.69]. © 2006 Wiley-VCH)

by optical excitation. These two electron–hole pairs can subsequently recombine in a cascade decay, first to the exciton state (X) and then to the "empty" ground state. In an ideal symmetric quantum dot either first a right circular polarized photon and then a left circular polarized photon are emitted or the other way round (Fig. 7.11a). These two decay paths are principally indistinguishable so that the resulting state is a polarization entangled state

$$|\psi\rangle = \left(|\sigma^+\rangle|\sigma^-\rangle + |\sigma^-\rangle|\sigma^+\rangle\right)\Big/\sqrt{2}$$

which is generated within a narrow time window of about 1 ns.

Asymmetries in the quantum dot lead via the electron–hole exchange interaction to a splitting of the ideally degenerated exciton state (Fig. 7.11a) giving rise to the emission of non-entangled linearly polarized photon pairs. This splitting can be controlled or removed by an external magnetic field so that the entanglement of the photons can be switched on and off.

The entanglement of two photons can be demonstrated by studying the tomographic reconstruction of the two-photon density matrix (Fig. 7.12). The appearance of off-diagonal elements in the density matrix (Fig. 7.12b) in accordance with theoretical predictions (Fig. 7.12d) is a clear signature of entanglement which cannot be observed in asymmetric quantum dots (Fig. 7.12a, c).

7.4.3 Single-Photon Detection

Practical systems for optical quantum information technology require in addition to single-photon sources also efficient, low noise single-photon detectors. It has been

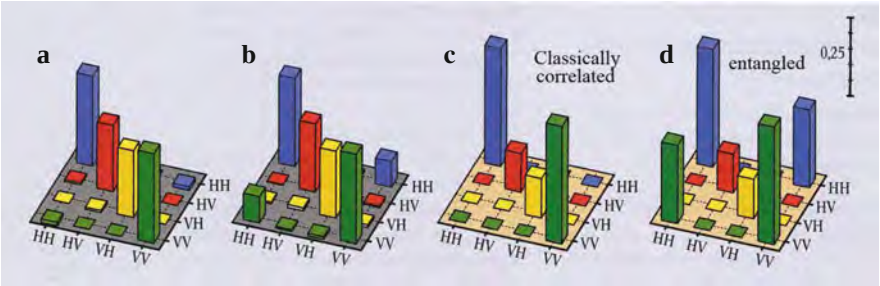

Fig. 7.12 The experimentally reconstructed density matrix of the two-photon state differs substantially for quantum dots with splitting (**a**) and without splitting (**b**, entanglement) of the exciton state (X). This is in accordance with the theoretically predicted density matrices for a classically correlated (**c**) and an entangled (**d**) photon state. (Reprinted with permission from [7.69]. © 2006 Wiley-VCH)

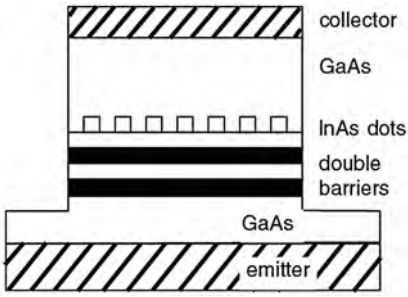

Fig. 7.13 Schematic for a quantum dot resonant tunneling diode for efficient single-photon detection. (Reprinted with permission from [7.70]. © 2005 American Physical Society)

demonstrated that the resonant tunnel current through a double-barrier structure (Fig. 7.13) is sensitive to the capture of single photo-excited holes by an adjacent layer of quantum dots. This is due to the fact that the current flowing between the emitter and collector contacts in response to an applied voltage is limited by tunneling through the double-barrier structure. The resonant tunneling process is now sensitively modified by the electrostatic potential of the nanosized quantum dots when these quantum dots trap and confine single electrons or holes upon single-photon absorption [7.70]. This phenomenon can be used for low noise detection of single photons with an efficiency of up to 12.5% and a time resolution of 150 ns, promising a maximum detection rate of 10–100 MHz [7.70]. Single-photon detection at 800 nm has been reported for a quantum dot transistor [7.71].

7.5 Quantum Dot Lasers

Diode lasers are based on current injection into a semiconductor active medium, resulting in charge carrier population inversion (i.e., the higher energy level becomes more populated than the lower energy level) and sufficient modal gain

(an exponential increase of the intensity of the amplified emission per unit length once it propagates through the active medium) to achieve lasing. Thin or ultrathin layers of a narrow-gap semiconductor embedded in a wide-gap barrier are traditionally used as the active media in such lasers. Later on, self-organization effects on semiconductor surfaces leading to the formation of coherent semiconductor nanoislands (see [7.72]) made the use of quantum dots (QDs) as active media in semiconductor lasers possible.

Here, a semiconductor quantum dot is a nanometer-scale coherent insertion of a narrow-gap semiconductor into a wider-gap semiconductor [7.72]. A QD combines the properties of a single atom with those of a semiconductor, such as a discrete energy spectrum of the charge carriers, which is a quantum mechanical effect due to the confinement of the charge carriers to a distance similar to its de Broglie wavelength (see Fig. 7.14a). Stable levels are formed for energies that correspond to an integer number of electron wave function half-waves.

It was proposed in 1976 [7.73] to apply size-quantization effects to improving laser performance. If the number of translational degrees of freedom of charge carriers is reduced to below two, a singularity occurs in the density of states [7.73] (see Sect. 1.3), which increases light absorption or light amplification. Among the anticipated advantages of QD lasers are decreased transparency current, which is the current at which the gain overcomes losses in the active medium; increased material gain, which is an exponential increase in the intensity of amplified emission; large characteristic temperature T_0, which is higher the higher the temperature stability of the threshold current, etc. The fabrication of QDs for GaAs-based QD lasers employs the self-organized growth of uniform nanometer-scale islands (Fig. 7.14b).

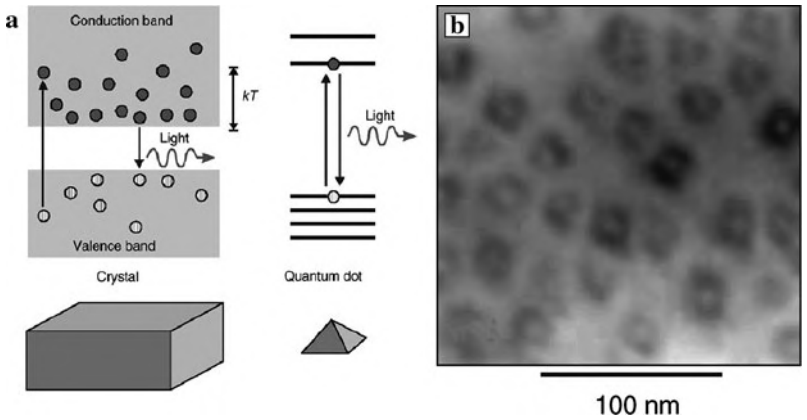

Fig. 7.14 (**a**) Schematic illustration of the energy diagrams of charge carriers in a bulk semiconductor crystal and a quantum dot (QD). The width of energy bands is close to kT, where k is Boltzmann's constant and T the temperature. (**b**) Plan view transmission electron micrograph of QDs formed by a two-monolayer InAs deposition followed by overgrowth with a 5 nm thick $In_{0.15}Ga_{0.85}As$ layer prior to GaAs deposition. (Reprinted with permission from [7.72]. © 2002 Materials Research Society)

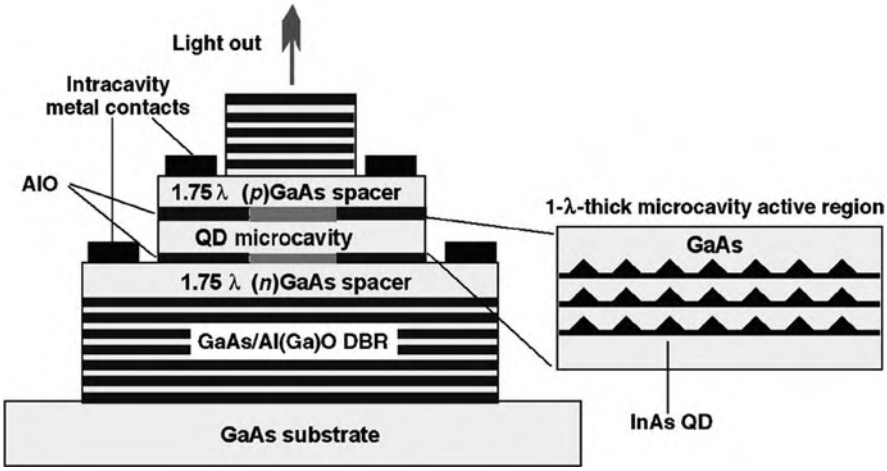

Fig. 7.15 Schematic representation of a quantum dot vertical-cavity surface-emitting laser (QD VCSEL) with a distributed Bragg reflector (DBR). (Reprinted with permission from [7.72]. © 2002 Materials Research Society)

Interaction of the islands via the substrate allows for lateral island ordering [7.72]. Due to the interest in the application of QDs in vertical-cavity surface-emitting lasers (QD VCSELs; see Fig. 7.15), the first surface-emitting QD lasers were demonstrated [7.74, 7.75] and QD VCSELs with threshold current densities down to 170 A/cm^2 [7.76] and 1.3 μm emission [7.77] were shown.

Using InGaAsN nanodots in a GaAs matrix (see [7.72]) the wavelength range of QD lasers can be extended to 1.55–1.6 μm. From CdSe QD lasers visible light [7.78] and from core–shell CdS/ZnS QD lasers blue light [7.79] is emitted. A high-speed QD laser transferring 10 gigabits/s across a temperature range of 20–70°C was predicted to reach the market in July 2008 [7.80]. For future metropolitan area networks the demand for inexpensive ultrafast amplifiers is probably even larger than that for lasers and quantum dot semiconductor optical amplifiers (SOAs) are expected to play a decisive role there [7.81–7.83].

It may be mentioned here that nanoscale lasers can also be fabricated making use of quantum wires (see, e.g., [7.84, 7.85]) or photonic crystals (see, e.g., [7.86]).

7.6 Plasmonics

The science of plasmonics [7.87–7.89] describes how metals can essentially transmit and manipulate light waves at length scales much smaller than their wavelengths and therefore enable the diffraction limit imposed on conventional optics to be overcome. The interaction of light with free electrons in gold or silver nanoparticles or surfaces gives rise to collective oscillations known as *surface plasmons*

(*SPs*) [7.90]. SPs are essentially composite particles composed of both light and charge, thereby providing a potential means to unify photonics and electronics. Plasmonics can generate signals in the soft x-ray range of wavelengths (between 10 and 100 nm) by exciting materials with visible light. The wavelength can, at the same frequency (resonance), be reduced by more than a factor of 10 relative to its free-space value, where the fundamental relation between the two – frequency times wavelength equals the speed of light – is preserved because the electromagnetic waves slow as they travel along the metal surface [7.87]. For millennia, alchemists and glassmakers have unwittingly taken advantage of plasmonic effects when they created stained glass windows or goblets that incorporate small metallic particles in the glass [7.87].

When light interacts with a metal, the free electrons of the metal can oscillate as in a plasma relative to the lattice of the positive ions at the resonant plasma frequency

$$\omega_\mathrm{p} = (Ne^2/\varepsilon_0 m_\mathrm{e})^{1/2}$$

where N is the number density of the electrons, ε_0 is the vacuum dielectric constant, and e and m_e are the charge and the effective mass of an electron, respectively. Quantized plasma oscillations are called *plasmons*. Since an electromagnetic light wave impinging on a metal surface only has a penetration depth <50 nm for Ag and Au, just the electrons on the surface are the most significant [7.90]. Their collective oscillations are properly termed surface plasmon polaritons (SPPs), but are often referred to as propagating surface plasmons (SPs; see Fig. 7.16a). Another type of resonant SP (localized SPs or LSPs) corresponds to collective excitations of free electrons confined to the finite volume of a metal nanocrystal (see Fig. 7.16b). By resonance, one means a condition in which the frequencies and wave vectors are approximately the same, leading to constructive interference,

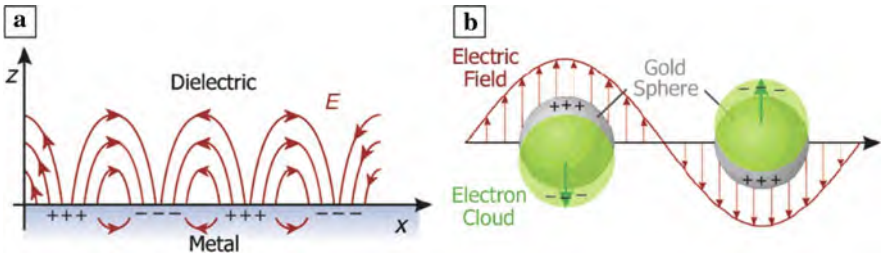

Fig. 7.16 Schematic of the collective oscillations of free electrons for (**a**) a metal–dielectric interface and (**b**) a spherical gold nanocrystal. Excited by the electric field of the incident light, the free electrons can be collectively displaced from the lattice of positive ions. While the plasmon shown in (**a**) can propagate across the surface as a charge density wave, the plasmon depicted in (**b**) is localized to each particle. (Reprinted with permission from [7.90]. © 2005 Materials Research Society)

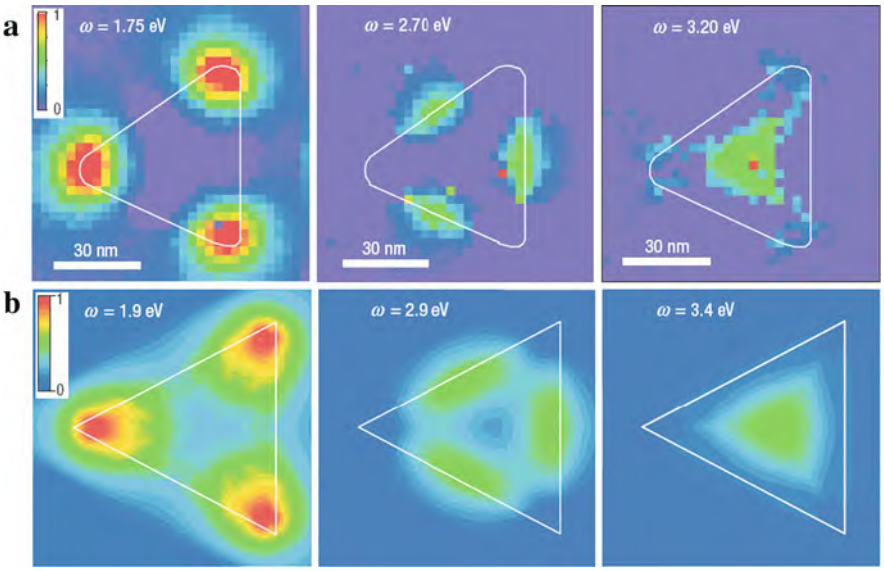

Fig. 7.17 Experimental and simulated electron-energy-loss spectroscopy (EELS) maps of plasmons in a silver nanotriangle. (**a**) Distribution of the modes centered at 1.75, 2.70, and 3.20 eV, respectively. The outer contour of the nanotriangle, deduced from its high-angle annular dark-field (HAADF) scanning transmission electron micrograph, is shown as a *white line*. (**b**) Simulated amplitude maps of the three main plasmon modes resolved in the simulated EELS of the Ag nanoprism, calculated by the boundary element method (see [7.91]). The color linear scale is common to the three maps. The simulated amplitude distributions of the three different modes qualitatively match the experimental maps in (**a**). (Reprinted with permission from [7.91]. © 2007 Nature Publishing Group)

a stronger signal, and peaks in the extinction spectra (extinction = scattering + absorption). Surface plasmon excitation in the infrared/visible/ultraviolet domain in, e.g., a silver nanotriangle can be directly mapped by measuring resonance peaks in the energy-loss spectra of a sub-nanometer electron beam probe scanned on a nanoparticle (Fig. 7.17a). The three modes peak respectively at the corners, the edges, and the center of the particle, and simulations of the amplitude maps (Fig. 7.17b) nicely match the experimental results in Fig. 7.17a. Single surface plasmons exhibit both wave and particle properties [7.92], similar to those of single photons.

Large local-field enhancement near the particle surface is a consequence of the excitation of plasmon resonances due to illumination. Local-field calculations have been performed for a range of particle sizes and shapes (see [7.94]) using a variety of computational tools such as finite-difference time domain (FDTD) [7.96], discrete dipole approximation (DDA) [7.93], or multiple multipole (MMP) techniques [7.97]. As shown in Fig. 7.18, the magnitude of the field enhancement in resonance depends strongly on the particle size and shape and the proximity to sharp points and narrow gaps. The vectorial nature of the electric fields can be captured and mapped

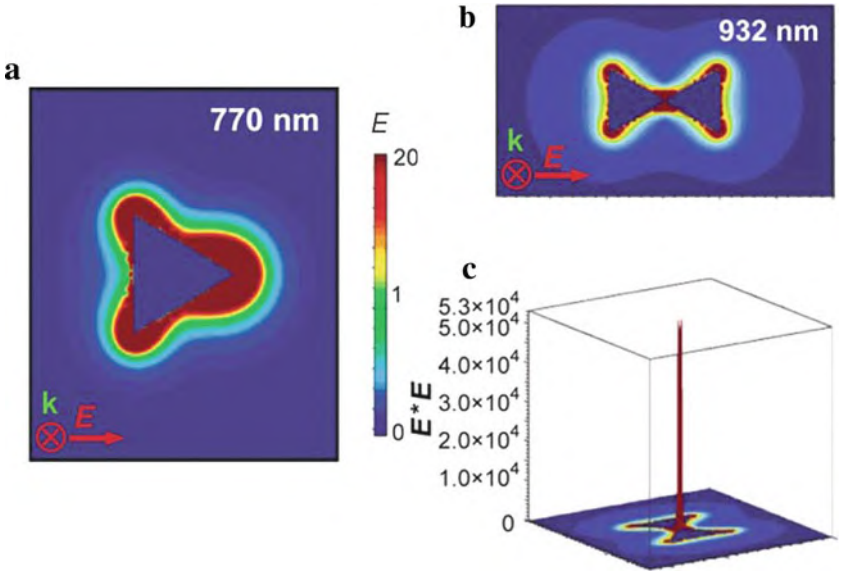

Fig. 7.18 (**a**) Local electric-field enhancement around a silver nanoprism (100 nm sides) calculated for polarized incident light (770 nm wavelength) at the resonance frequency using discrete dipole approximation (DDA) calculations. At the resonance frequency, the nanoparticle concentrates the incident E field strength ∼ 20-fold [7.93, 7.94]. (**b**) Electric-field intensity (E^* E) enhancement between two triangular prisms (∼ 60 nm side length, 12 nm thickness) showing (**c**) a hot spot of more than 50,000 times the incident electric-field intensity [7.94, 7.95]. (Reprinted with permission from [7.93] (**a**) and [7.94] (**b**) (**c**). © 2003 American Chemical Society (**a**) and © 2008 Materials Research Society (**b**) (**c**))

down to the nanoscale [7.98]. These highly confined electric fields have been used in a variety of near-field enhanced spectroscopies, including surface-enhanced Raman spectroscopy (SERS; see [7.99]) or surface-enhanced fluorescence [7.100] (see below).

7.6.1 Plasmon-Controlled Synthesis of Metallic Nanoparticles

Metallic nanoparticles can be fabricated by electron-beam lithography, ion-beam lithography, or chemical synthesis, etc. (see [7.90]). Surfactants are employed for growing nanowires [7.101]. It is interesting that the growth of, e.g., anisotropic triangular silver nanoprisms can be controlled by plasmon excitation in order to produce particles with desired edge lengths from solution [7.102]. By using selectively excitation wavelengths between 450 and 750 nm, nanoprisms with well-defined sizes between 38 and 120 nm could be grown (see Fig. 7.19). It is assumed that

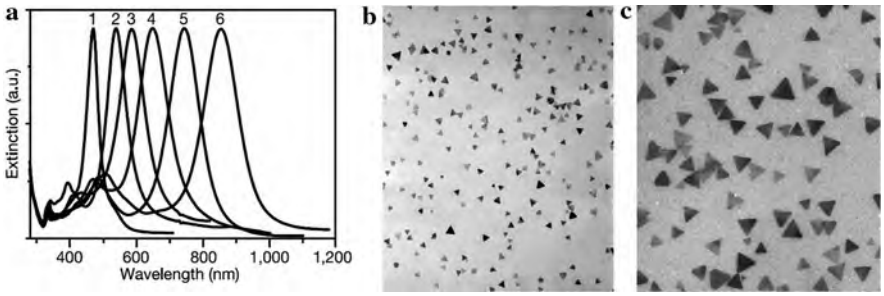

Fig. 7.19 Light-induced unimodal growth of silver nanoprisms. (**a**) Excitation wavelengths between 450 and 750 nm for controlled solution synthesis of unimodal silver nanoprisms with sizes of, e.g., 38 nm (**b**) or 120 nm (**c**). (Reprinted with permission from [7.102]. © 2003 Nature Publishing Group)

dipole plasmon excitation in the nanoprisms could facilitate the addition of silver atoms at the corners and edges leading to a growth of the nanoprisms up to a certain size limit [7.102].

7.6.2 Extinction Behavior of Nanoparticles and Arrays

The extinction behavior of metallic nanoparticles due to plasmon excitation can be controlled by the particle size, shape, aspect ratio, by the type of material, or by the medium surrounding the particle, as discussed in the following. The localized surface plasmon resonance extinction spectra can easily be tuned all the way from the near-UV through the visible spectrum (see [7.103, 7.104]) by changing the size or shape (triangle or hemisphere) of the nanoparticles (see Fig. 7.20a). This is demonstrated by the change of colors in solutions containing Ag nanoparticles of different sizes and shapes (Fig. 7.20b). The red shift from Ag spheres (diameter of 50 nm) to Ag pyramids with the same volume (Fig. 7.20c) is due to the availability of longer plasmon wavelengths in non-spherical particles. The red shift of the plasmon resonance of Ag nanoparticles in solution increases linearly with the refractive index of the solvent (Fig. 7.21). This can be used for molecular detection with high spatial resolution [7.105].

The interaction of localized surface plasmons (LSPs) plays a role in the case of large-area uniformly oriented nanoparticle arrays which can be prepared, e.g., by nanoimprint lithography (NIL, see [7.106], Sect. 3.10) or soft interference lithography (SIL; see [7.107]). The tunability of the extinction is demonstrated by the blue shift with increasing height of the nanoparticles (Fig. 7.22), which may be attributed to the appearance of additional resonances characteristic of Ag [7.106]. Arrays of different metallic (Ag, Cu, Au) or dielectric (Si) nanoparticles with the same

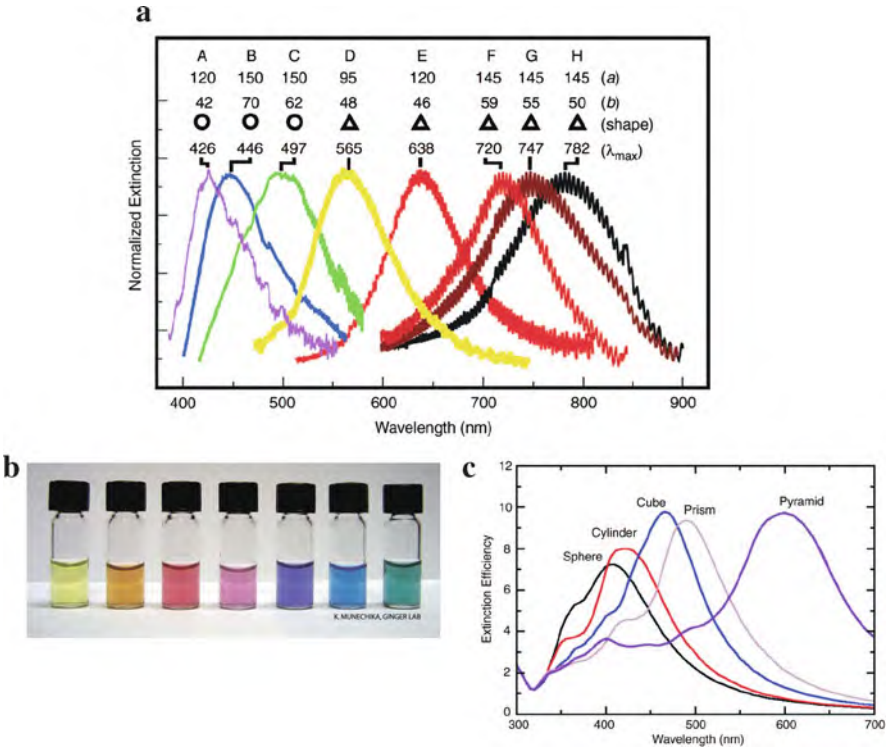

Fig. 7.20 Extinction due to plasmon resonance on silver nanoparticles. (**a**) Size- and shape-tunable localized plasmon resonance extinction spectra of Ag nanoparticles fabricated by nanosphere lithography (NSL). The extinction is changed by varying the in-plane width *a* and the out-of-plane height *b* of the nanoparticles [7.104]. (**b**) The solutions of Ag nanoparticles show a variety of colors due to the different sizes and shapes of the Ag nanoparticles within each solution [7.94]. (**c**) Extinction spectra of Ag nanoparticles in vacuum having the shapes indicated. Each particle type has the same volume, taken to be that of a *sphere* with a radius of 50 nm [7.104]. (Reprinted with permission from [7.104] (**a**) (**c**) and [7.94] (**b**). © 2005 Materials Research Society (**a**) (**c**) and © 2008 Materials Research Society (**b**))

geometrical parameters (see Fig. 7.23) show dark-field (DF) scattering peaks from ultraviolet to visible wavelengths which is in good agreement with the calculated scattering properties [7.107]. In anisotropic arrays of nanoparticles, the extinction spectra additionally depend on the polarization of the incident light [7.106].

Plasma resonances of hollow gold nanospheres (Fig. 7.24a) in the near-infrared spectrum are of particular interest for targeted medical diagnosis and therapy (see Sects. 12.6, 12.7, [7.108]). A wide range of absorption wavelengths can be covered by varying the Au sphere size or shell thickness (Fig. 7.24b) and the absorbance can be blue shifted by coating with a Ag layer (Fig. 7.24c). The scattering and absorption of metallic nanostructures due to localized surface plasmon resonances can be simulated by employing the discrete dipole approximation (DDA; [7.93]).

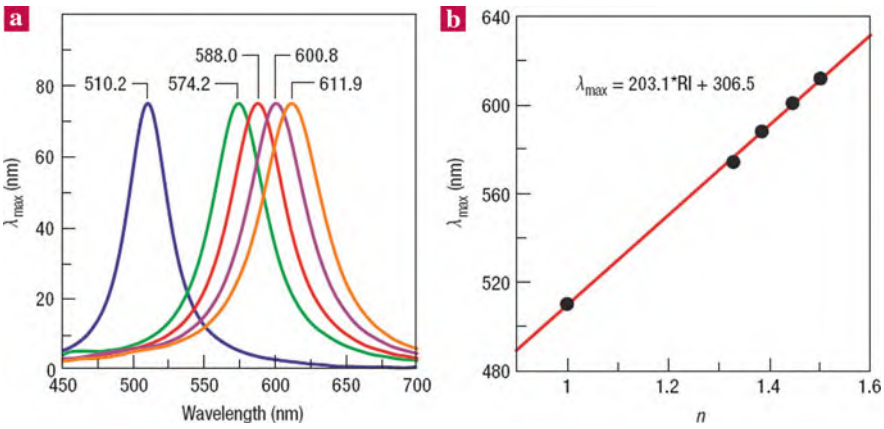

Fig. 7.21 Localized surface plasmon resonance (LSP) of single silver nanoparticles in various solvent environments. (**a**) Resonant Raleigh scattering spectrum from a single Ag nanoparticle in (*left* to *right*): nitrogen, methanol, propan-1-ol, chloroform, and benzene. (**b**) Linear relationship between the solvent refractive index n and the LSP λ_{max}. (Reprinted with permission from [7.105]. © 2008 Nature Publishing Group)

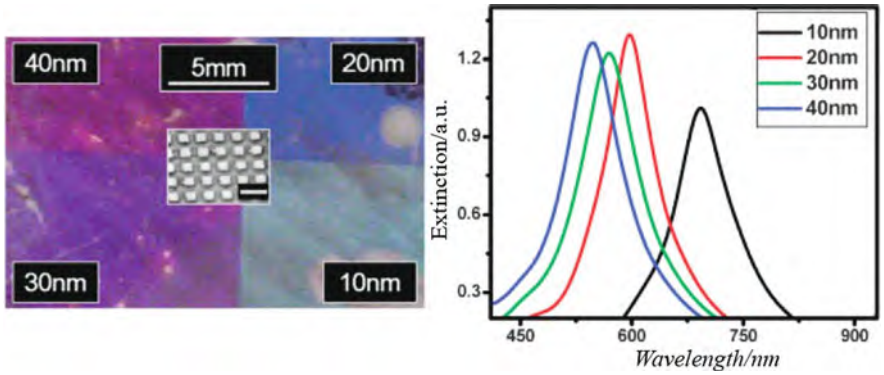

Fig. 7.22 (*Left*) Photograph of a Ag nanoparticle array with four areas of structures that only differ in nanoparticle height as indicated by the labels. A scanning electron micrograph of the array is shown in the center inset (scale bar = 350 nm). (*Right*) Measured extinction spectra corresponding to the four different areas shown in the photograph. (Reprinted with permission from [7.106]. © 2008 Wiley-VCH)

7.6.3 Plasmonic Nanocavities

For highly integrated optical systems, light propagation in nanooptical systems is a prerequisite. However, because of diffraction, the propagation of light fields is limited to structures with sizes larger than the wavelength (Abbé limit of some hundred nanometers). This limitation is lifted in the case of near-field optics where plasmons can propagate along metallic nanowires with a diameter much smaller than

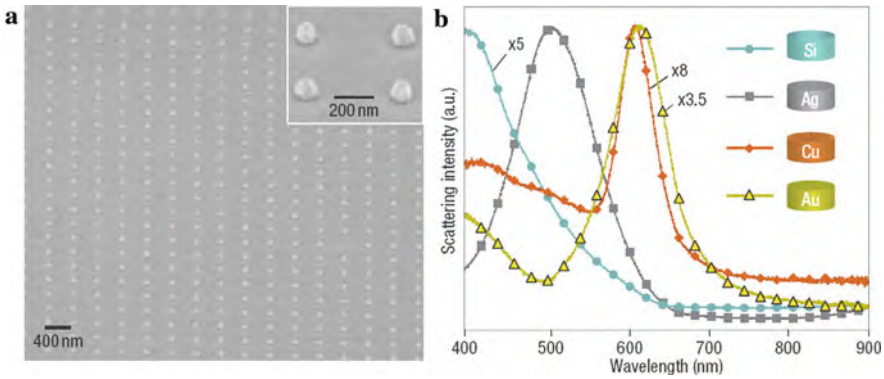

Fig. 7.23 Localized surface plasmon extinction of nanoparticle arrays of different single component materials. (**a**) Scanning electron micrograph of an array of Au nanoparticles with a pitch of 400 nm, a nanoparticle diameter of 100 nm and a nanoparticle height of 50 nm. (**b**) Dark-field (DF) scattering spectra for metal (Ag, Cu, Au) and dielectric (Si) nanoparticle arrays with the same nanoparticle parameters as in (**a**). The peaks are scaled to the height of the Ag peak as indicated on the graph. (Reprinted with permission from [7.107]. © 2007 Nature Publishing Group)

the free-space wavelength of light. This is demonstrated by plasmon propagation from an illuminated Au stripe into a Au nanowire (see Fig. 7.25) with a 1/e propagation length of 2.5 μm in agreement with theoretical predictions [7.110]. In this experiment, the lateral width of the plasmon field is 115 nm (Fig. 7.25b) – only 14% of the 800 nm wavelength of the incident light. The surface plasmons excited in a silver nanowire by the emission of a CdSe quantum dot (Fig. 7.26) can propagate over a length of 30 μm at 809 nm [7.111] with an optical decay time of 16 ps in the nanowire.

7.6.4 Surface-Enhanced Raman Spectroscopy (SERS) and Fluorescence

The sensitivity of a number of spectroscopy techniques for the characterization of molecules can be substantially enhanced in the high electric fields generated by plasmon excitation. Raman spectroscopy is a highly specific technique used to detect and identify molecules on the basis of their unique vibrational energy levels. When molecules absorb onto a plasmonic nanoparticle (see Fig. 7.27a) enhancement of Raman scattering by as much as 10^{14}–10^{15} is observed (see [7.105]). Two principal enhancement mechanisms are generally thought to explain the large SERS signals [7.105]. First, an electromagnetic enhancement factor arises because the LSP modes increase the density of states at Stokes-shifted Raman wavelengths. Second, chemical enhancement factors arise from changes in the molecular electronic states.

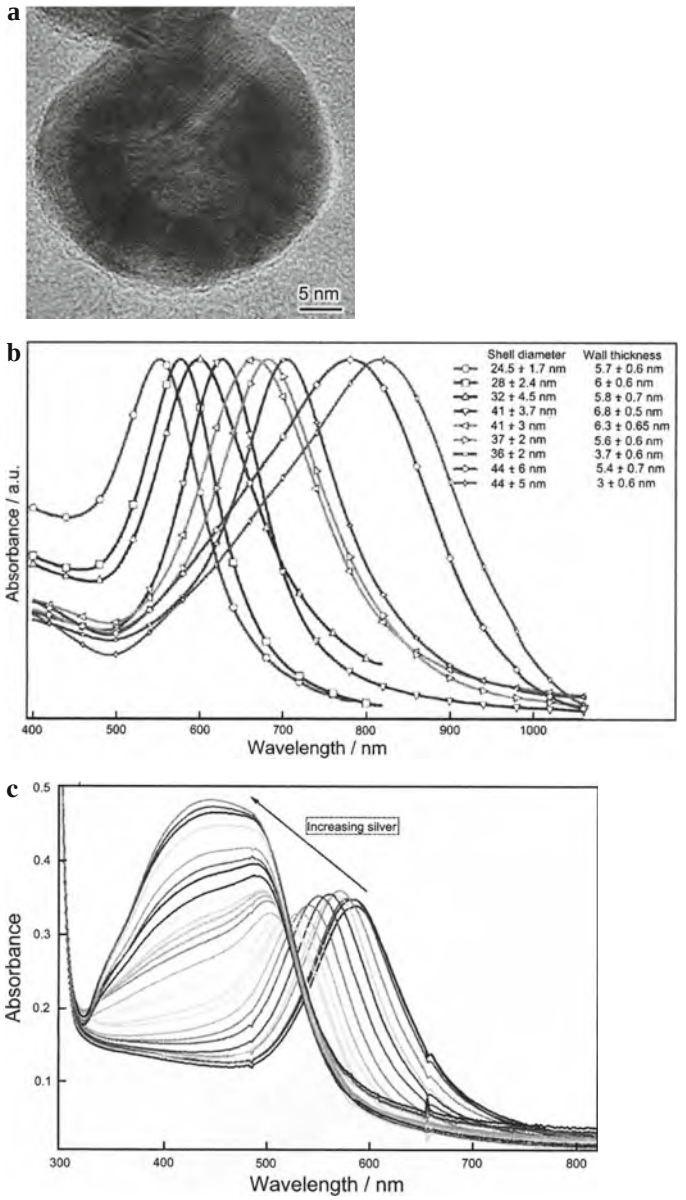

Fig. 7.24 Plasmon absorbance spectra of Au spheres. (**a**) Hollow Au nanosphere with a Ag shell. (**b**) The surface plasmon resonance occurs throughout the visible to the near-IR wavelength range depending on diameter and thickness of the gold shell. (**c**) The absorbance of a hollow gold nanosphere is blue shifted by coating with a Ag layer. (Reprinted with permission from [7.108]. © 2008 Chinese Society of Metals)

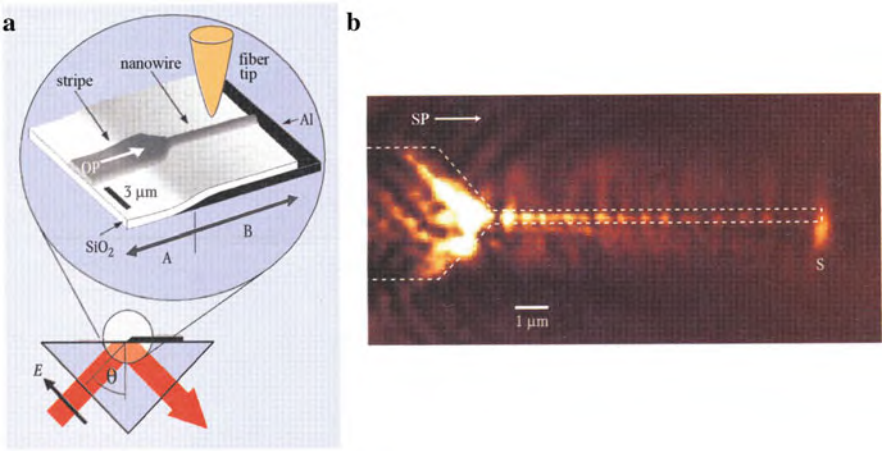

Fig. 7.25 Light propagation via surface plasmons in a gold nanowire. (**a**) Schematic representation of the experimental set-up. An Al film shields the wire from the excitation light. (**b**) Scanning near-field optical micrograph (SNOM) of light propagation from an illuminated Au stripe (left) along a 200 nm wide, 50 nm high, and 8000 nm long Au wire. The wavelength of the excitation light is 800 nm. *S* indicates plasmon scattering at the end of the wire. (Reprinted with permission from [7.109]. © 2002 Wiley-VCH)

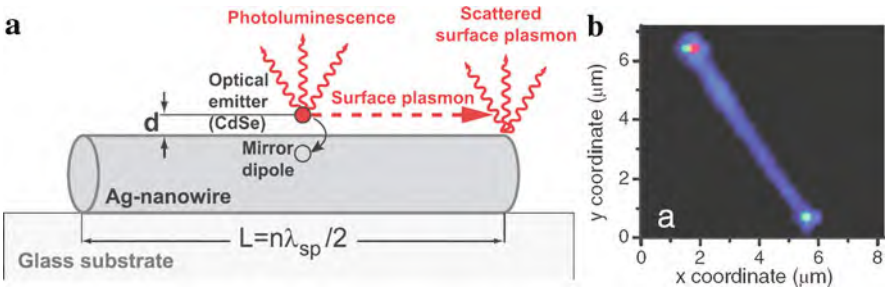

Fig. 7.26 (**a**) Plasmonic nanocavity consisting of a Ag nanowire with a CdSe nanocrystal on top of a SiO_2 shell of thickness *d*. (**b**) Microphotoluminescence image of the 635 nm emission from a CdSe quantum dot for a 7.5 µm long Ag nanowire with a 22 nm thick SiO_2 shell. (Reprinted with permission from [7.111]. © 2007 American Physical Society)

Raman spectroscopy with nanometer lateral resolution can be achieved by making use of laser illumination of fine metallic tips close to the sample (tip-enhanced Raman spectroscopy – TERS [7.112]; see Sect. 1.7).

In addition, fluorophores (components that fluoresce) can be positioned near metal nanostructures (see Fig. 7.27b) with the goal of producing more intense and stable fluorescence for a variety of applications (see [7.94]). It has been demonstrated that fluorescence spectra of molecules can be shaped by plasmonic

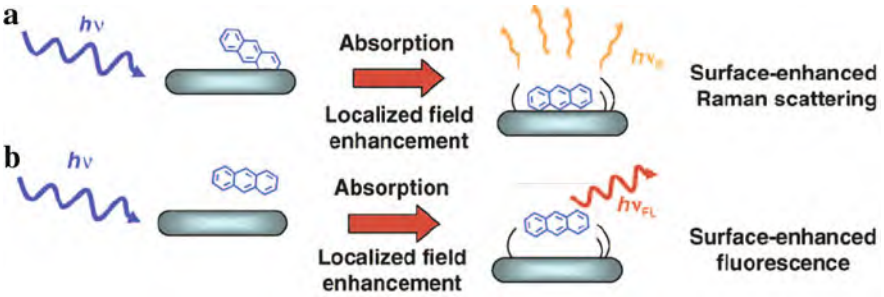

Fig. 7.27 Schematic showing surface-enhanced Raman scattering $h\nu_R$ and surface-enhanced fluorescence $h\nu_{FL}$. Photons are indicated by $h\nu$. (Reprinted with permission from [7.101]. © 2005 Elsevier)

nanoresonators [7.113]. The fluorescence enhancement can be understood as arising from an enhanced excitation rate due to enhanced light intensity near a nanoparticle antenna and from an enhanced emission due to an increased radiative decay rate [7.94].

7.6.5 Receiver–Transmitter Nanoantenna Pairs

"Receiver" gold nanodisks couple to input light at their characteristic resonant frequency [7.114]. When the nanodisk receivers are excited, their local optical field couples to the adjacent "transmitter" single-walled carbon nanotubes that function as a polarization-dependent, near-field detector. The local fields of the nanodisks excite the Raman vibrational modes of the carbon nanotubes, providing a characteristic signature to the far-field optical signal of the carbon nanotube antennas, which is finally detected as the output signal (see [7.103]).

7.6.6 Electro-optical Nanotraps for Neutral Atoms

It has been suggested [7.115] to study the effect of the fields, exerted by plasmon resonances excited in Ag nanoparticles, on the motion of atoms (Fig. 7.28). A plasmon-resonant laser field that is blue detuned from an atomic resonance causes a dramatic repulsion of atoms from the nanostructure surface and when combined with attractive electrostatic forces creates a trap minimum at nanometer distances from that surface. The atom nanotrap is expected to cast new light on the interplay between quantum fluctuations in the radiation field, the atom, and the nanostructure, with a proper description ultimately involving entangled eigenstates of the strongly coupled atom-nanostructure system (see [7.115]).

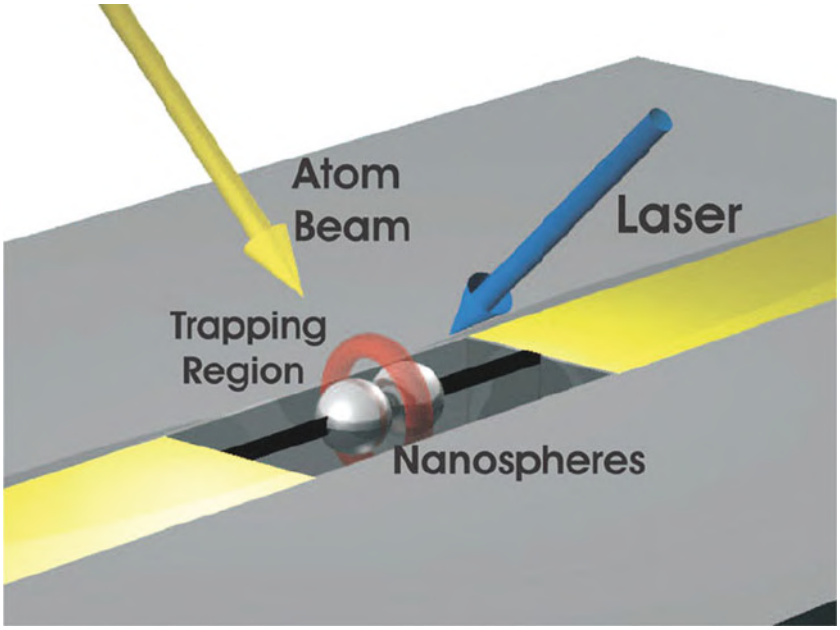

Fig. 7.28 The nanotrap. A suspended carbon nanotube (10 μm long, 4 nm diameter), attached at each end to an electrode supports two Ag nanospheres (diameter 90 nm, separation 2 nm) across a gap in a silicon nitride membrane. A laser field excites plasma oscillations in the spheres, and large electric fields near the structures are generated. In addition, a dc voltage is applied to the electrodes to create a toroidal trapping region (*red*). The radius of the toroid can be controlled with nanometer precision and the trap may be loaded directly from an incident atom beam. (Reprinted with permission from [7.115]. © 2009 American Physical Society)

7.6.7 Unifying Nanophotonics and Nanomechanics

Light can exert a mechanical force on an object in two ways – through radiation pressure or through a force that arises from gradients in a light beam. The approach with forces exerted by the radiation pressure cannot be extended down to the nanoscale. The gradient force has been measured [7.1] by suspending a silicon waveguide (Fig. 7.29) above a substrate and passing a laser beam through it. The beam in the waveguide couples to the substrate, leading to an asymmetry in the electromagnetic field that results in a gradient force acting on the waveguide. The approach could have applications in all-optical switching and optomechanical signal processing.

7.6.8 Integration of Optical Manipulation and Nanofluidics

A slot waveguide comprises a nanoscale slot sandwiched between two materials of high refractive index (Fig. 7.30a). At the horizontal boundaries of the slot region, there exists a large electric-field discontinuity. This results in a high-intensity

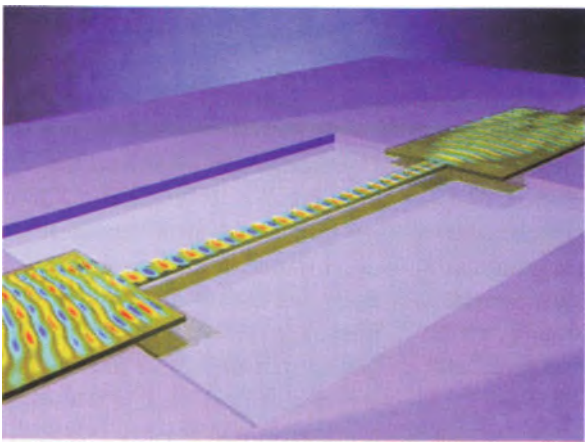

Fig. 7.29 The Si beam (10 μm long, 500 nm wide, 110 nm thick, 300 nm above the SiO_2 substrate) unifies nanophotonics and nanomechanics by simultaneously operating as a waveguide and a nanomechanical component. A strong gradient force of the optical mode overlaps with the substrate and forces the waveguide toward the substrate. By modulation of the laser beam at the mechanical resonance frequency, vibrations can be generated in the waveguide [7.1, 7.116]. (Reprinted with permission from [7.116]. © 2009 Wiley-VCH)

eigenmode in the slot making the majority of the optical energy accessible within the low-index fluid region in the slot (Fig. 7.30b). This sub-wavelength-scale slot waveguide can be used for optical capture, trapping, and transport of dielectric nanoparticles or λ-DNA molecules. Optical propulsion of 100 nm dielectric particles, which can be considered as models for biological species such as viruses, was demonstrated at an average speed of 1.5 μms^{-1} [7.4]. λ-DNA molecules 48 kb long were captured from solution and stably trapped (Fig. 7.30c). As the trapping stability is likely to be strongly dependent on molecular conformation, analysis of the release kinetics in such systems may result in a new method of single-molecule analysis. Sub-wavelength slot waveguides can be integrated into lab-on-a-chip platforms using existing manufacturing techniques [7.4].

7.6.9 Single-Photon Transistor

In analogy with the electronic transistor, a photon transistor is a device where a small optical "gate" field is used to control the propagation of another optical signal field via a nonlinear optical interaction. Such a device could be most valuable for designing fast plasmonic circuits [7.87]. The creation of such a single-photon transistor has been discussed [7.117] making use of nanoscale surface plasmons.

7.6.10 Application Prospects of Plasmonics

Research in the emerging field of plasmonics could lead to an entirely new class of devices [7.87]. The use of plasmonic components may improve the resolution of

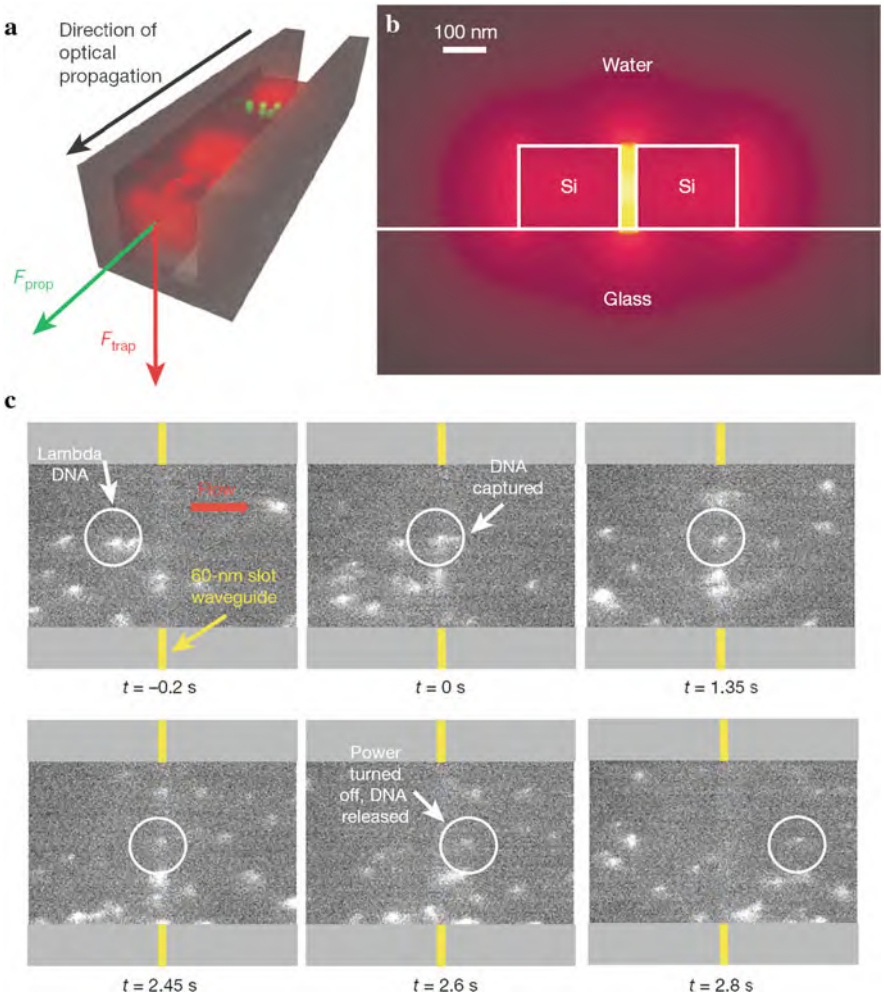

Fig. 7.30 (**a**) Nanoscale optofluidic transport. Schematic illustrating the transport of two different sizes of nanoparticles in a slot waveguide. The force F_{prop} is the radiation pressure force responsible for optofluidic transport, and F_{trap} is the trapping force that holds nanoparticles within the slot region. (**b**) Mode profile for a silicon-on-insulator 40 nm slot waveguide immersed in water, calculated by finite-element techniques. The main trapping region is the high-intensity slot mode. (**c**) Capture and trapping of λ-DNA. The images show individual 48 kb λ-DNA flowing over an optically excited 60 nm wide slot waveguide. At the time $t = 0$, the encircled DNA is trapped. The DNA is released at the 2.6 s mark and flows downstream. The images were taken using a sensiCam CCD camera. (Reprinted with permission from [7.4]. © 2009 Nature Publishing Group)

microscopes, the efficiency of light-emitting diodes (LED), and the sensitivity of chemical and biological detectors [7.87]. Gold nanospheres, silica–gold nanoshells, and nanorods were investigated as biological and cell imaging agents, where the gold nanorods were shown to offer the best near-infrared absorption and scattering properties [7.118]. The uptake of hollow gold nanospheres conjugated

to cancer-specific antibodies directed at the epidermal growth factor receptor was demonstrated for targeted delivery to and destruction of tumor cells by photothermal treatment [7.119]. Due to the near-infrared absorption properties of the gold nanospheres (see Fig. 7.24a), laser wavelength in this region, to which human and animal tissue materials are transparent, was used to illuminate the particles in vitro. The cancer cells then can be selectively destroyed by photothermal ablation (see Sect. 12.6). This technique has also been demonstrated in vivo [7.108] and permission from the U.S. Food and Drug Administration is sought to conduct clinical trials of nanoshell therapy in patients with head and neck cancer [7.87].

Perhaps the most fascinating potential application of plasmonics would be the invention of an invisibility cloak. In 1897 H. G. Wells published *The Invisible Man*, a tale of a young scientist who discovered how to make his own body's refractive index equal to that of air, rendering him invisible (see [7.87]). Exciting a plasmonic structure with radiation that is close to the structure's resonance frequency can make its refractive index equal to air's, meaning that it would neither bend nor reflect light. In addition, the absorption losses would be offset by an increase in intensity when the structure was laminated with a material that produces optical gain. A true invisibility cloak would be more difficult, but some physicists say it is possible [7.120], making use of a shell of metamaterials that, in theory, could reroute the electromagnetic waves traveling through it, diverting them around a spherical region within it (see Fig. 7.31).

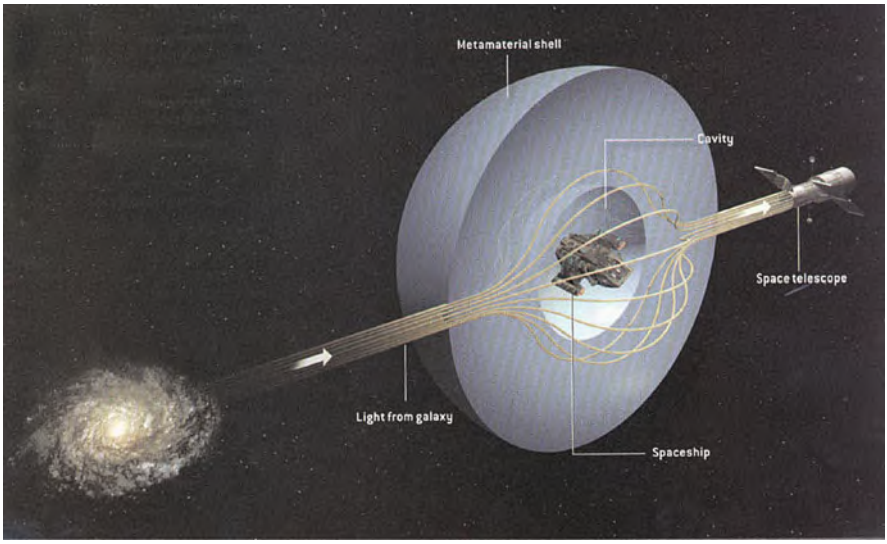

Fig. 7.31 How a cloaking device might work. It has been theorized that plasmonic materials could render objects invisible [7.120]. The cloaking device could be a thick shell constructed of metamaterials, which exhibits unusual optical properties for electromagnetic radiation around a central cavity, in which a spaceship could be hidden [7.87]. (© 2010 Space Channel)

7.7 2D-Confinement of Fluids, Wetting, and Spreading

Surface interactions can significantly alter fluid properties on the nanoscale. Confining fluids in nanometer-scale channels can affect how the molecules pack together, how they withstand compression, and their ability to rapidly mix or flow [7.121]. By molecular dynamics simulations [7.122] of the behavior of hard-sphere fluids in confined spaces (Fig. 7.32), changes of the fluid mobility and entropy were compared to the bulk quantities. Both properties are affected by confinement, but the relationship between them essentially remains the same down to very small scales [7.123]. Layered ordering imposed on liquid aluminum by a solid alumina interface has been experimentally confirmed by electron microscopy [7.124].

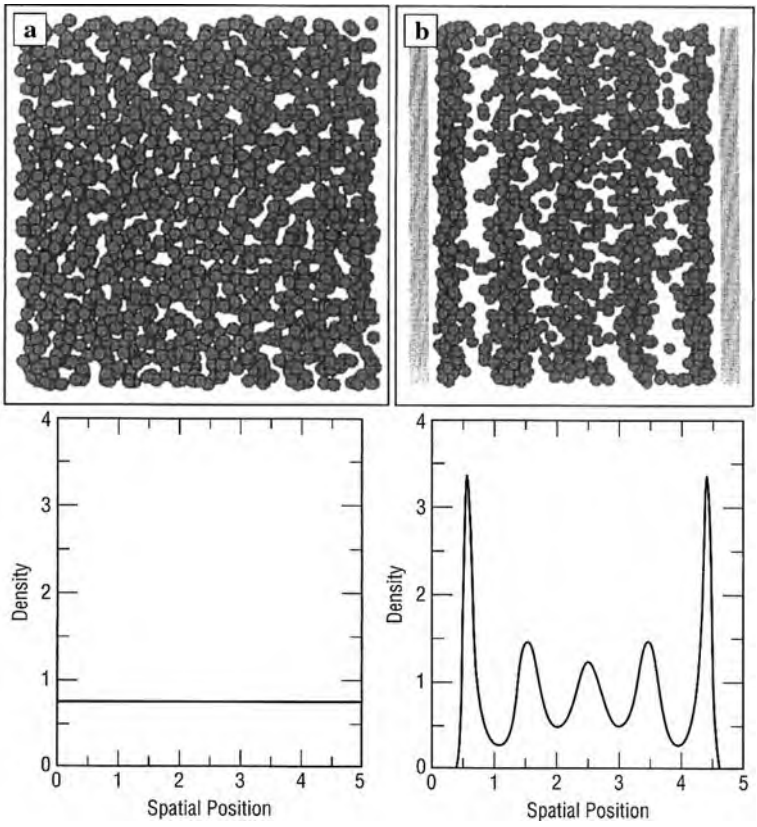

Fig. 7.32 Molecular dynamics (MD) simulations graphics showing a comparison between the packing arrangements and spatial density profiles of a hard-sphere fluid in (**a**) bulk and (**b**) confined environments [7.122, 7.123]. (Reprinted with permission from [7.123]. © 2008 Materials Research Society)

7.7.1 Phase Transitions Induced by Nanoconfinement of Liquid Water

The structure and properties of water in nanometerscale confinement are important in numerous fields including biological self-assembly, fuel-cell technology, nanotribology, etc. (see [7.125]). Molecular dynamics (MD) simulations of water confined by two parallel hydrophobic walls with a wall–wall separation of 0.8 nm show at $T = 300$ K and low water density ($\rho = 0.8$ g/cm^2) two peaks in the density $\rho\,(z)$ (Fig. 7.33a), whereas at high density ($\rho = 1.15$ g/cm^2) a transition to three peaks occurs. In the latter case, the molecules next to the walls arrange in a crystal-like structure – templated by the wall – and do not diffuse (Fig. 7.33b). The central slab is liquid-like (Fig. 7.33c) without long-range order of the molecules, which readily diffuse. When the water density is decreased to $\rho = 1.05$ g/cm^3 a few vacancy defects are observed in the crystal-like structure (Fig. 7.33d), which disappears in an order-to-disorder or "melting" transformation at $\rho = 0.8$ g/cm^3, where the bilayer is stable.

The dynamics of nanoconfined water, as studied by atomic force microscopy (AFM), are found to be orders of magnitude slower than those of bulk water [7.126] and comparable to the dynamics measured in supercooled water at 170–210 K.

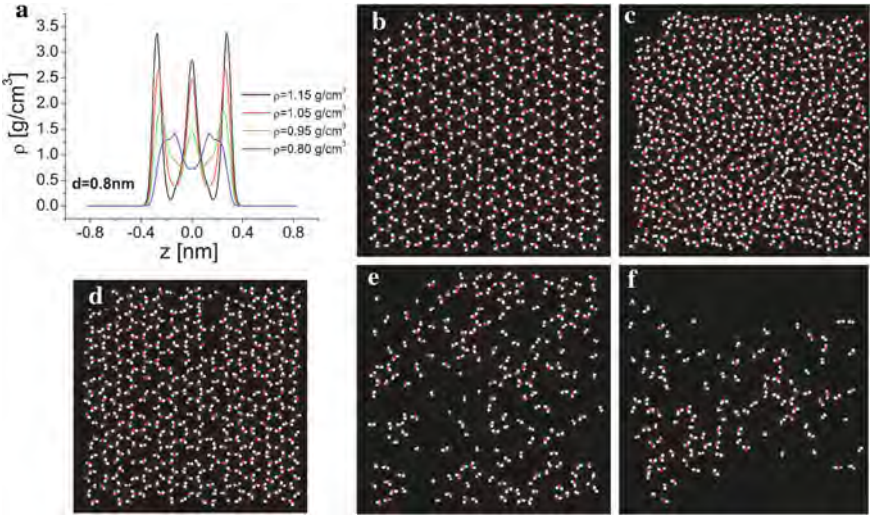

Fig. 7.33 (**a**) Molecular dynamics simulation of the density profiles $\rho\,(z)$ of water between two walls in a distance $d = 0.8$ nm for densities above ($\rho = 1.15, 1.05$ g/cm^3) and below ($\rho = 0.8$ g/cm^3) the phase transition from a trilayer to a bilayer. (**b**) and (**c**) Snapshots of the system at $\rho = 1.15$ g/cm^3, $d = 0.8$ nm, and $t = 500$ ps with a layer close to a wall (b) which is ordered and a central slab (**c**) which is disordered. (**d**–**f**) Same as (**b**) for the densities 1.05, 0.8, and 0.5 g/cm^2, respectively. As the density decreases, first vacancy-like defects are introduced into the ordered structure next to the wall. Then, an order–disorder structural change occurs. (Reprinted with permission from [7.125]. © 2009 American Physical Society)

7.7.2 Fluid Flow and Wetting

Steady-state flow of incompressible fluids in a channel width 2 h, driven for example, by gravity ρg or a pressure gradient dP/dy, can be described by the Navier–Stokes equations. The solution for the velocity in the direction of flow, y, as a function of the distance from the wall, z, has a parabolic profile (Fig. 7.34) given by

$$U_y(z) = (\rho g/2\eta)\,[\delta + h]^2 - z^2$$

where η is the viscosity and δ, the slip length, is the distance into the wall at which the velocity extrapolates to zero. Conventionally, the slip length is assumed to be zero for wetting fluids but it may be non-zero for non-wetting fluids, which for very small channels can significantly enhance the fluid flow. Integrating the velocity profile over the cross-sectional area of, e.g., a pipe gives for no-slip boundary conditions the Hagen–Poiseuille law for the flux through the pipe, yielding a flow rate proportional to the pressure difference between the tube ends and to the fourth power of the tube's internal radius, and inversely proportional to the tube length and to the viscosity of the fluid.

By taking into account the force exerted by the wall on the fluid, the evolution of the boundary conditions with the wetting properties can be reproduced [7.128, 7.129]. In particular, a transition from a no-slip boundary condition in a wetting situation (contact angle $\theta \sim 0°$) to a partial-slip boundary condition with a slip length of some tens of nanometers in a non-wetting situation ($\theta \sim 120°$) is obtained [7.128].

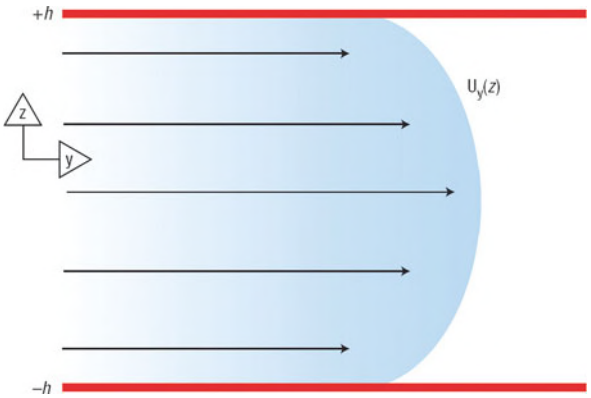

Fig. 7.34 Parabolic velocity profile $U_Y(z)$ for Poiseuille flow in a capillary of width 2 h. (Reprinted with permission from [7.127]. © 2007 Nature Publishing Group)

7.7.3 Superhydrophobic Surfaces

Non-wettability or superhydrophobicity is a well-known effect in many natural materials, such as the "lotus effect" of lotus leaves (see Sect. 11.9). Artificial

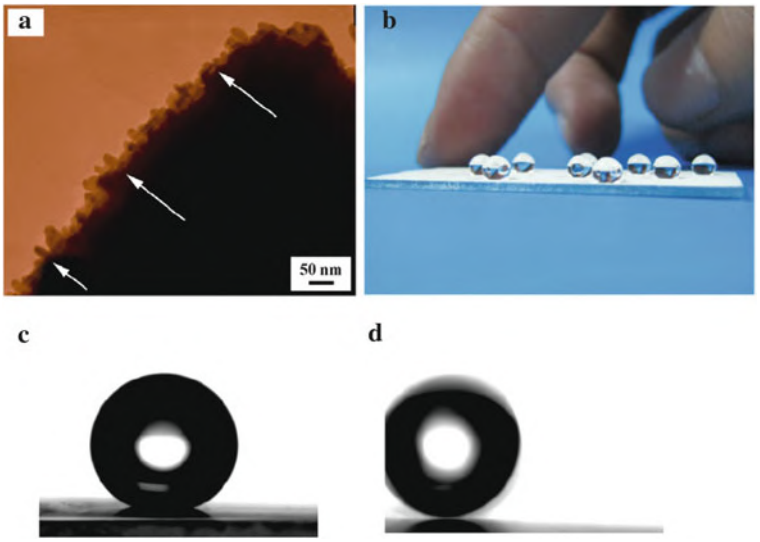

Fig. 7.35 (**a**) Scanning electron micrograph (SEM) of a superhydrophobic Sb_2O_3 film. (**b**–**d**) Optical images of water drops of different sizes (17–22 μl) on the as-synthesized Sb_2O_3 film (**b**), the water droplet profile (4 μl) on the Sb_2O_3 film (**c**) and a sliding water drop (4 μl) on the surface tilted by less than 5° (**d**). (Reprinted with permission from [7.130]. © 2008 Institute of Physics)

superhydrophobicity has been demonstrated by antimony oxide (Sb_2O_3) micro-nanoscale hierarchical surface structures [7.130]. For the preparation of the nanocrystalline Sb_2O_3 surface coating a solution of hexadecylamine (HDA, $CH_3(CH_2)_{15}NH_2$) is added to the $Sb(OCH(CH_3)_2)_3$ precursor yielding cilium-like nanostructures 10–30 nm in diameter and 5–30 nm in length with interspaces of 5–15 nm (see Fig. 7.35a). Water drops on the surface (Fig. 7.35) show superhydrophobic behavior with a contact angle of about $159° \pm 2°$ (Fig. 7.35c). Moreover, the water drop is hardly able to stick to the surface, as indicated by a small sliding angle (less than 5°), allowing water drops to roll off quite easily (Fig. 7.35d). By x-ray photoelectron spectroscopy (XPS) a substantial surface contribution of carbon is detected. From this it is concluded that the presence of alkyl chains contributes to the hydrophobicity of the microscale–nanoscale Sb_2O_3 structures [7.130].

7.7.4 Liquid Spreading Under Nanoscale Confinement

The macroscopic spreading of a liquid droplet on a solid surface proceeds via the formation of a very thin "precursor film" ahead of the droplet's contact line (see [7.131]) where the length of the precursor is predicted by de Gennes [7.132] to be

$$L_\mathrm{p} = a\sqrt{S/\gamma}\,Ca^{-1}$$

where $S = \gamma_{Sv} - \gamma_{SL} - \gamma$ is the spreading parameter, with γ the liquid surface tension and γ_{SV} and γ_{SL} the solid–vapor and solid-liquid interfacial energies, respectively. The capillary number $Ca = \eta V/\gamma$ depends on the viscosity η and the spreading velocity V of the liquid, a is a molecular length scale. The film thickness h is expected to decrease as the inverse of the distance from the apparent droplet contact line until the film is "truncated" at a thickness $h_0 = a\sqrt{3\gamma/2S}$ significantly larger than a molecular size. The truncation region corresponds to the *microscopic* contact line. The investigation of these spreading processes is important for emerging technologies aiming at the formation and manipulation of smaller and smaller amounts of liquid.

The spreading of the non-volatile liquid squalone ($C_{30}H_{62}$) along wettable nanostripes embedded in a non-wettable (CH_3 terminated) surface of an octadecyltrichlorosilane (OTS) monolayer on a Si wafer is studied by atomic force microscopy (AFM) [7.131] (see Fig. 7.36). The maximum liquid thickness turns out to depend on the stripe width (Fig. 7.36b). The film is thinner (by about 0.4 nm)

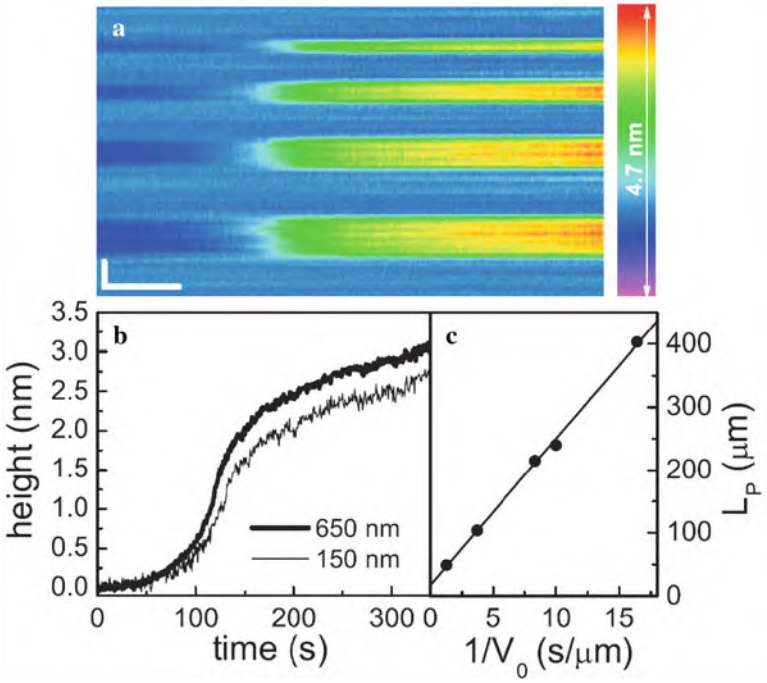

Fig. 7.36 (**a**) Temporal evolution of a transverse cross-sectional AFM profile of liquid nanostripes (lateral scale bar 50 s, vertical scale bar 400 nm). (**b**) Height of the liquid versus time on the narrow (150 nm wide) and wide (650 nm) stripe, as extracted from (**a**). (**c**) The length L_p of the precursor film versus the inverse of the spreading velocity V_0. From the linear fit, the spreading parameter $S = 3 \times 10^{-4}$N/m can be estimated. (Reprinted with permission from [7.131]. © 2009 American Physical Society)

on the narrow line (150 nm) compared to the wider line (650 nm). This is the effect of the nanoscale lateral confinement on the fluid morphology. The pinning of the contact line along the boundaries of the wettable stripe imposes a curvature to the liquid's free surface. Consequently for sufficiently narrow stripes, the film height is expected to decrease with the stripe width [7.133]. From the measurements carried out at various velocities V_0, it is found that L_p scales as $1/V_0$ (Fig. 7.36c), as predicted by de Gennes' model above.

Water molecules form a locally ordered superstructure on TiO_2 anatase (101), a most efficient photocatalyst for the dissociation of water [7.134].

7.8 Fast Transport of Liquids and Gases Through Carbon Nanotubes

Molecularly smooth hydrophobic graphitic walls and nanoscale inner diameters of carbon nanotubes (CNTs) give rise to ultraefficient transport of water and gas, by orders of magnitude faster than through other pores of similar size. The water transport mechanism has a similarity to the transport mechanisms of biological membrane ion channels. The combination of transport efficiency and selectivity makes CNT membranes a promising technology for future water desalination, water purification, nanofiltration, and gas separation applications [7.135].

7.8.1 Limits of Continuum Hydrodynamics at the Nanoscale

Advances in nanoscience, which have pushed the dimensions of synthetic objects closer to the molecular scale, pose a fundamental question: does the continuum-based description of fluid flow, governed by the Navier–Stokes equations, still work in a situation where the reduction in size causes the variables to vary appreciably over the molecular length. The size of a water droplet that still can be treated as a continuum object with less than 1% statistical fluctuation of a property can be estimated to contain 10^4 water molecules with a droplet diameter of $\sim$ 27 molecules, or $\sim$ 6.5 nm. According to molecular dynamics (MD) simulations (see [7.135]), Navier–Stokes theory predictions are approached by channel widths of ten molecular diameters. Flow through CNTs with lateral dimensions of less than 2 nm evidently falls in the field of non-continuum fluidics, or *nanofluidics*.

7.8.2 Water Transport in CNTs

It is surprising that hydrophilic liquids, especially water, enter and fill very narrow and hydrophobic CNTs. MD simulations (see [7.135]) confirm this behavior and demonstrate that water molecules confined in such a small space, form a single-file

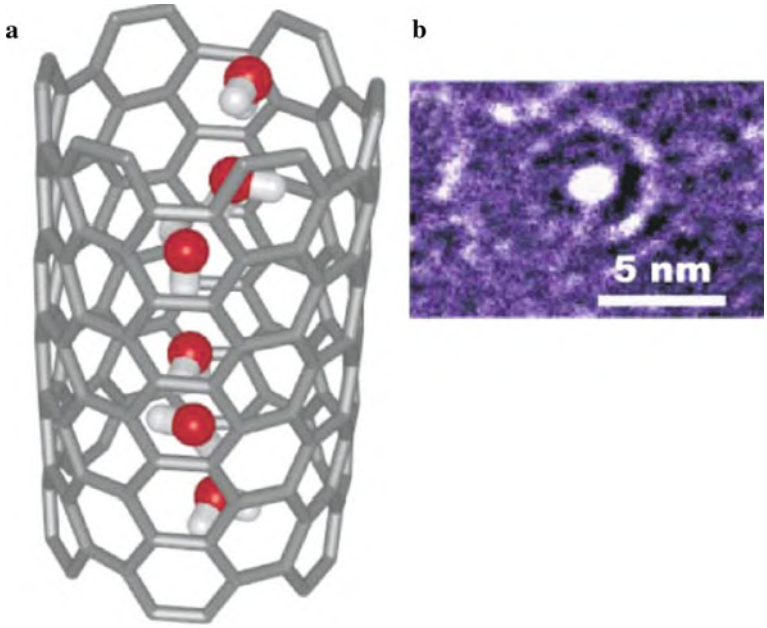

Fig. 7.37 (**a**) Structure of the hydrogen-bonded water chain inside a carbon nanotube (CNT) [7.136]. (**b**) High-resolution transmission electron micrograph (HRTEM) of the cross-section of a double-walled carbon nanotube (DWNT) in a Si_3N_x membrane [7.137]. (Reprinted with permission from [7.136] (**a**) and [7.137] (**b**). © 2001 Nature Publishing Group (**a**) and © 2006 AAAS (**b**))

configuration (Fig. 7.37a) that is unseen in bulk water. Such 1D hydrogen-bonded structures are highly reminiscent of the water wires observed in the biological aquaporin water-transporting channels (see Sect. 11.5) with also a hydrophobic lining inside (see [7.135]). In CNTs, the friction at the channel walls is so low that the water transport is no longer governed by Hagen–Poiseuille flow, but nanotube entrance and exit. The calculated water transport rates approach 5.8 water molecules per nanosecond per nanotube, similar to the transport rates in aquaporins (see [7.135]), yet – due to the different dimensions of the two systems – one cannot imply that the same mechanism is responsible for CNTs and aquaporins.

The experimentally determined water transport rates in sub-2 nm double wall carbon nanotube (DWNT, Fig. 7.37b) membranes reveal a flow enhancement that is at least 2–3 orders of magnitude faster than no-slip, hydrodynamic flow calculated using the Hagen–Poiseuille equation whereas the calculated slip length for sub-2 nm CNTs is as large as hundreds of nanometers, which is almost three orders of magnitude larger than the pore size [7.135]. The measured water flux compares well with that predicted by MD simulations (see [7.135]).

MD simulations further show that water infiltration into and defiltration out of CNTs is influenced by gas molecules [7.138].

7.8.3 Gas Transport in CNTs

MD simulations (see [7.135]) show that gas flux in CNTs reaches a value almost three orders of magnitude higher than in zeolites with equivalently sized pores. Transport of hydrogen in CNTs is calculated to be as fast as 10 cm^2/s due to the predominantly specular nature of the molecule-wall collisions inside the CNTs. The measured gas flows are up to 100 times higher than the predictions of the conventional Knudsen model for gas transport (see [7.135]).

7.9 Nanodroplets

Nanodroplets are of interest in a variety of fields. As discussed in the following, the behavior of water in nanoconfinement can be studied in water nanopools enclosed in reverse micelles [7.139]. Nanoscale emulsions are extensively used by the foods, cosmetic, and coating industries, where double emulsions provide the ability to carry both polar and non-polar cargos [7.140]. By employing zeptoliter (10^{-21} l) alloy droplets, the crystallization mechanisms of nanometer-sized fluid drops can be investigated [7.141] and in suprafluid He nanodroplets, spectroscopy and low-temperature chemical reactions of molecules can be performed [7.142] (see below).

7.9.1 Dynamics of Nanoscopic Water in Micelles

A wide variety of biological processes occurs in very crowded aqueous surroundings with the solvating water often playing an important role. Thus it has been shown that the dynamics of water in the first hydration layer of a protein are slowed down relative to bulk water. Fluctuations in this hydration shell may dictate internal protein motions [7.143]. The dynamics of water in the nanopores of Nafion fuel-cell membranes differ substantially from those of bulk water and vary with the hydration level (pore size) of the membrane (see [7.139]). This makes the understanding of the properties of water in confined environments and near interfaces desirable.

The dynamics of water confined in two different types of reverse micelles (see Fig. 7.38) in dependence of the diameter of the water pool can be studied by spectroscopy of the OD stretch of HOD in H_2O [7.139]. Reverse micelles of the surfactant AOT (ionic head group) in isooctane and of the surfactant Igepal CO520 (non-ionic head group) in cyclohexane/hexane are prepared with the same diameter of 4 nm of the water nanopools. The infrared absorption spectra of the hydroxyl stretch are in both micelles blue shifted relative to bulk water. The orientational dynamics of the water molecules are found to be very similar for the confined water in the two types of reverse micelles and slowed down compared to bulk water. The results demonstrate that confinement by an interface to form a nanoscopic water pool is the primary factor governing the dynamics of nanoscopic water rather than the presence of the charged groups at the interface.

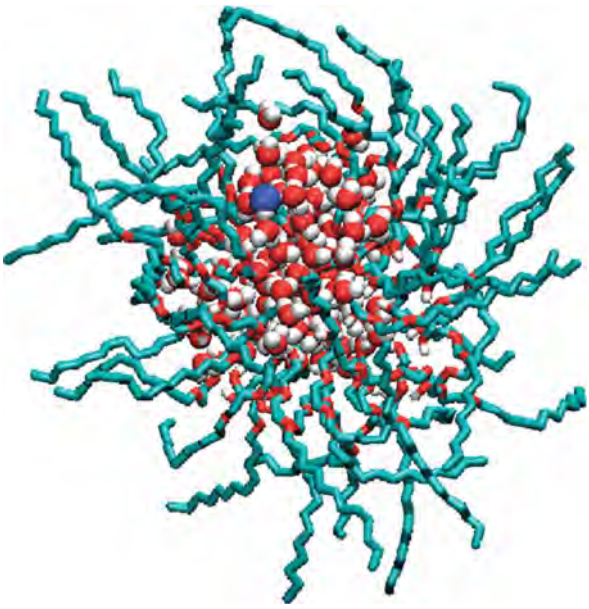

Fig. 7.38 A protonated non-ionic aqueous inverse micelle with the neutral surfactant diethylene glycol monodecyl ether $[CH_3(CH_2)_{11}(OC_2H_4)_2OH]$ ($C_{12}E_2$). Oxygens (*red*), hydrogens (*white*), surfactants (*cyan*), and hydronium (*blue*, larger size). (Reprinted with permission from [7.144]. © 2009 Royal Society of Chemistry)

7.9.2 Nanoscale Double Emulsions

Water-in-oil-in-water (WOW) double emulsions can be prepared by using block copolypeptide surfactants with the structure poly(L-lysine · HBr)$_x$-*b*-poly(*racemic*-leucine)$_y$, K$_x$(*rac*-L)$_y$ (Fig. 7.39a). For the preparation of a nanoscale double emulsion, ultrasonic homogenization is used to generate a K$_{40}$(*rac*-L)$_{20}$ emulsion with subsequent passages through a microfluidic homogenizer and ultra-centrifugation, yielding droplets ranging from 10 to 100 nm in diameter (Fig. 7.39b). The compartmentalization of hydrophilic quantum dots (red) into the inner aqueous phase, hydrophobic pyrene (blue) into the oil phase and the labeled polypeptide (green) stabilizing the outer interface is shown in Fig. 7.39c.

7.9.3 Zeptoliter Liquid Alloy Droplets and Surface-Induced Crystallization

The controlled delivery of fluids is a key process in many areas of science and technology. The volume of a droplet from an inkjet printer is about 2 picoliters (2×10^{-12} l) [7.145]. Recently a pipette has been developed [7.141], which, observed by electron microscopy, delivers a $Au_{72}Ge_{28}$ alloy melt with zeptoliter (10^{-21} l = 1 zl) resolution. The liquid–solid transition provides evidence for a crystallization pathway of nanosized fluid drops that avoids nucleation in the interior, but instead proceeds via liquid-state surface faceting as a precursor to surface-induced crystallization.

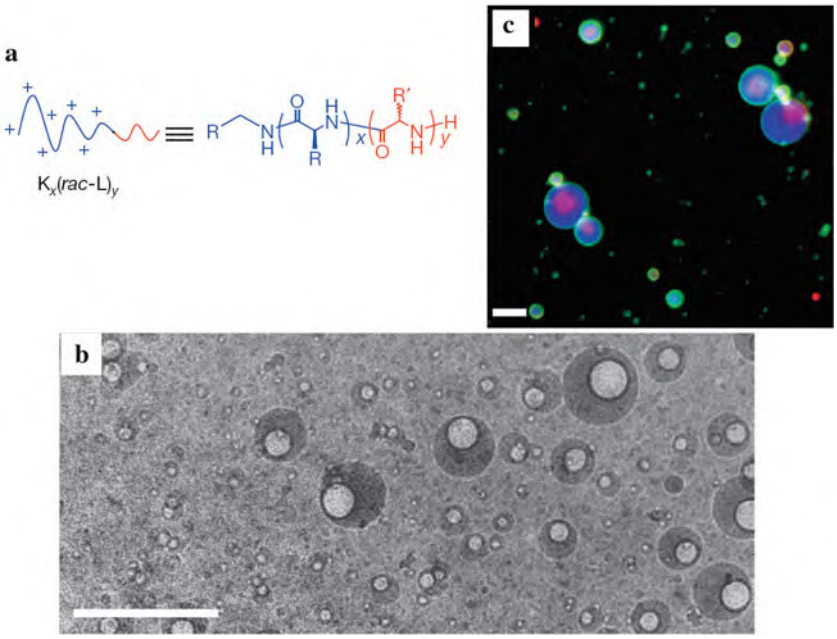

Fig. 7.39 (**a**) Structure of the $K_x(rac\text{-}L)_Y$ block copolypeptide surfactant. (**b**) Cryogenic transmission electron micrograph of size-fractionated double emulsion droplets isolated from a $K_{40}(rac\text{-}L)_{20}$-stabilized double emulsion by centrifugation and ultra-centrifugation. Scale bar, 200 nm. (**c**) Fluorescence micrographs of double emulsions containing polar and non-polar cargos. Double emulsion stabilized by FITC-labeled $K_{40}(rac\text{-}L)_{10}$, loaded with both pyrene and quantum dots. The oil phase fluoresces blue because of the entrapped pyrene and the internal aqueous phase fluoresces *red* because of encapsulation of InGaP quantum dots. The polypeptides are labeled with fluorescein isothiocyanate (FITC) and therefore fluoresce *green*; scale bar, 5 μm. (Reprinted with permission from [7.140]. © 2008 Nature Publishing Group)

The zeptoliter pipette with the Au–Ge alloy (Fig. 7.40a) encapsulated in a multilayer shell of crystalline carbon (Fig. 7.40b) is heated in a transmission electron microscope above the eutectic temperature $T_E = 361°C$. The expulsion of alloy melt (Fig. 7.40d) with an initial volume of 3 zl is triggered by opening a pipette "nozzle" in the C-shell by briefly focusing a tight ($\sim$ 1 nm) electron beam onto the shell (Fig. 7.40c). The high pressure (>1 GPa) generated by the C-shell [7.146] plays the key role of driving the fluid flow and expulsion.

The "pendant droplet" geometry (Fig. 7.40d) permits the observation that a few centigrades above the crystallization point, the droplets develop surface facets (Fig. 7.40e, f) which continuously form and decay without showing distinct reflections characteristic for crystalline order. From this it is concluded [7.141] that the nanoscale liquid $Au_{72}Ge_{28}$ droplets close to crystallization develop some degree of ordering, at least locally, in the areas showing transient faceting.

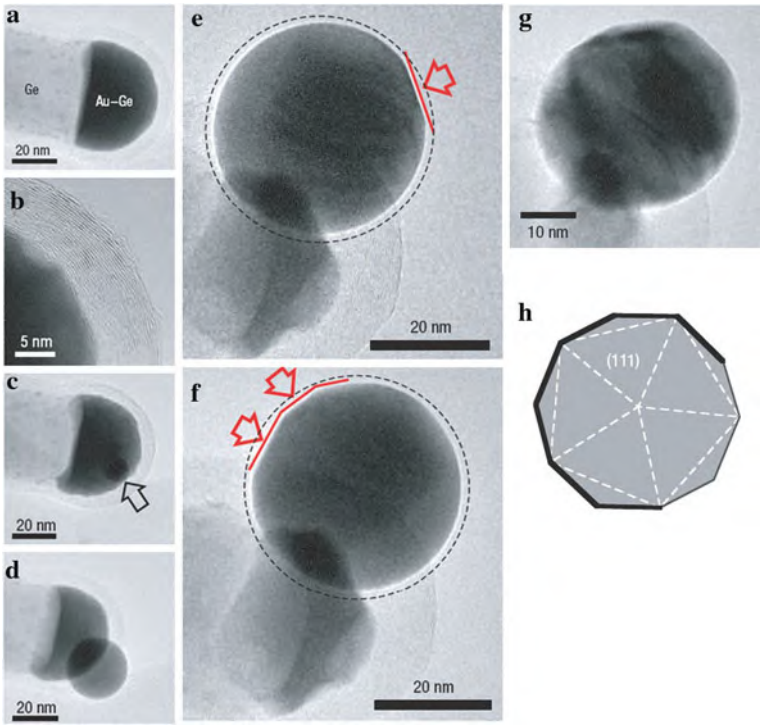

Fig. 7.40 Dispensing and surface-induced crystallization of zeptoliter liquid $Au_{72}Ge_{28}$ droplets. (**a**) Fluid Au–Ge melt reservoir encapsulated into a multilayer carbon shell (**b**). (**c**) Opening of the carbon coating by a nanometer electron beam and expulsion of a Au–Ge melt droplet (**d**) during operation of the zeptoliter pipette at 425°C. (**e–f**) Transient faceting of a 30 nm $Au_{72}Ge_{28}$ liquid droplet near the liquid–solid phase transition. The same droplet is imaged at various times. The *arrows* mark extended planar surface facets. (**g**) Frozen in crystalline shape of a "free" $Au_{72}Ge_{28}$ cluster. Transmission electron micrograph (TEM) of a crystalline cluster that underwent extensive transient surface faceting in the liquid state. (**h**) Projections of the icosahedral motif bounded by (111) facets, oriented to match the facets in the upper left section of the cluster shown in (**g**). (Reprinted with permission from [7.141]. © 2007 Nature Publishing Group)

Lowering of the temperature induces freezing of the pendant droplets with transient surface faceting into a cluster shape containing faceted segments that match the projection of an icosahedral cluster (Fig. 7.40g, h). Given the preference of larger Au nanoclusters for the stable fcc structure and truncated octahedron morphology, the formation of facets with icosahedral symmetry suggests (see [7.141]) crystallization originating at close-packed (111)-like surface planes, that is, a surface-induced crystallization templated by the transient surface facets of "free" liquid droplets.

7.9.4 Superfluid Helium Nanodroplets

Helium nanodroplets (Fig. 7.41a) with typical diameters of 4.4 nm containing about 10^3 ^{4}He atoms are used as containers for spectroscopy with little broadening due

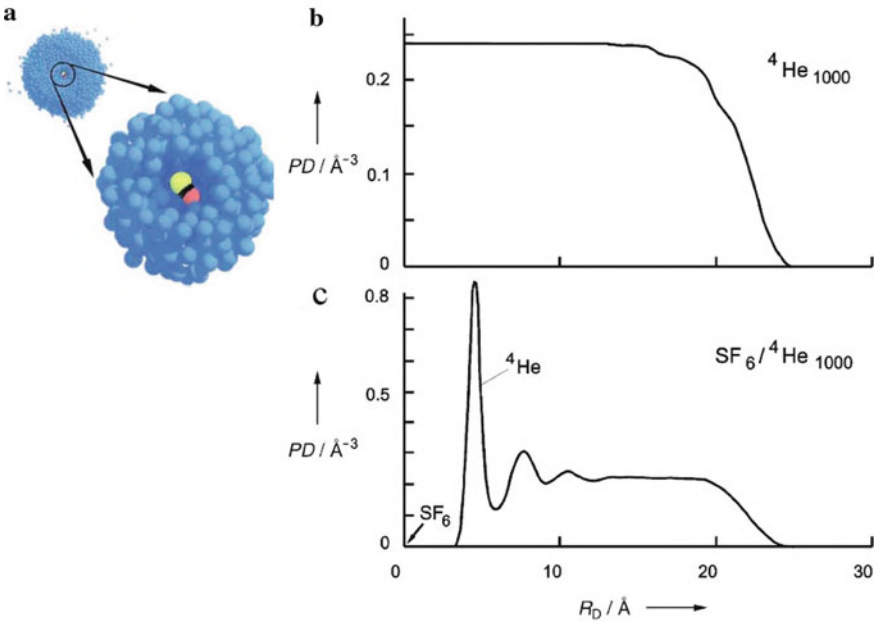

Fig. 7.41 (**a**) Computer simulation showing an OSC molecule inside a ^{4}He droplet made up of 500 atoms; ^{4}He *blue*, O *red*, S *yellow*, C *black*. (**b**–**c**) Results of density-functional calculations of the dependence of particle density (*PD*) on droplet radius (R_D) of a pure ^{4}He droplet of $N = 1000$ atoms (**b**) [7.142] and a ^{4}He droplet of $N = 1000$ atoms doped with a single SF_6 molecule (**c**) [7.147]. (Reprinted with permission from [7.142] (**a**) (**b**) and [7.147] (**c**). © 2004 Wiley-VCH (**a**) (**b**) and © 1998 American Institute of Physics (**c**))

to the superfluid characteristics and for the synthesis of new molecular complexes [7.142]. By doping, e.g., with an SF_6 molecule, a strong restructuring of the He droplet density appears (Fig. 7.41c) compared to the homogeneous density of a pure ^{4}He droplet (Fig. 7.41b). The temperature of ^{4}He droplets from free jet gas expansion is about 0.4 K whereas the temperature of ^{3}He droplets is ≈ 0.15 K. For SF_6 in ^{4}He droplets sharp rotational lines of the vibrational transition can be observed where, however, the moments of inertia are about three times higher than in the gas phase which is attributed to a stronger coupling of the molecular rotation to the ^{4}He bath [7.142].

Nanodroplets of ultracold helium can serve as nanoscopic cryoreactors for probing reactions of, e.g., alkali–metal clusters with water clusters [7.148].

For para-H_2 (pH_2) it was predicted [7.149] that, since at low temperatures para-H_2 molecules are spinless bosons, these molecules might undergo a transition to a superfluid state, which may be located between 2 and 3 K (see [7.142]. It was additionally predicted [7.150] that small pH_2 clusters with less than 18 molecules should remain fluid at $T = 0$ and exhibit superfluidity below about 2 K. From rotational spectroscopy of pH_2 clusters with $n = 14$–17 molecules in helium droplets a large decrease in the moment of inertia was observed, much below the expected classical

value. This is considered to be a manifestation of superfluidity of pH_2 clusters (see [7.142]) which is also studied theoretically [7.151].

7.10 Nanobubbles

Gas–liquid two-phase system with bubbles down to sub-micrometer scales play a role as contrast agents for ultrasound imaging, aerated food and personal care products, and foamed construction materials (see [7.152]). In addition, highly stable nanobubbles are present, e.g., on hydrophobized surfaces submerged in water (see [7.153]). Furthermore, as finally discussed her, a single electron immersed into liquid helium forms a nanobubble which can be employed for tracking the motion of the electron [7.154].

7.10.1 Stable Surface Nanobubbles

Surface nanobubbles (diameter $\sim$ 100 nm) on hydrophobic surfaces submerged in water (see Fig. 7.42) appear to be much more stable than anticipated taking into account the high Laplace pressure inside the bubbles causing a fast diffusive outflux of gas. This stability has been modeled by a dynamic equilibrium mechanism [7.155]. It is, moreover, demonstrated [7.153] that these nanobubbles do not act as nucleation sites for shock wave-induced cavitation on surfaces.

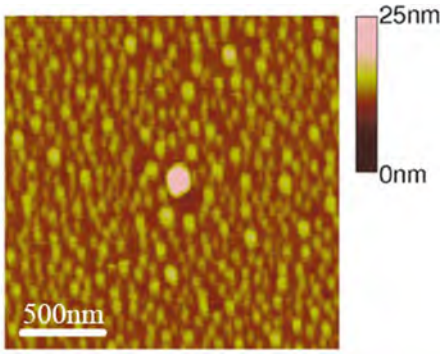

Fig. 7.42 Atomic force micrograph (AFM) of nanobubbles on a Si (100) wafer hydrophobized by a layer of 1H, 1H, 2H, 2H-perfluorodecyldimethylchlorosilane (PFDCS) and immersed in water. (Reprinted with permission from [7.153]. © 2007 American Physical Society)

7.10.2 Polygonal Nanopatterning of Stable Microbubbles

A nanometer-scale hexagonal patterning of microbubbles (Fig. 7.43) can arrest the shrinkage of bubbles and identify a route to fabricate highly stable dispersions of microbubbles [7.152].

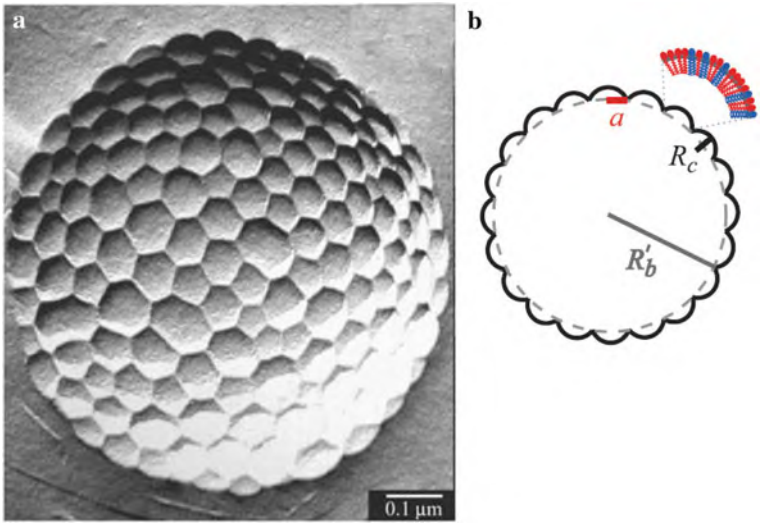

Fig. 7.43 Nanotextured surfaces of microbubbles. (**a**) Transmission electron micrograph (TEM) of a micrometer-sized bubble covered with hexagons ∼ 50–100 nm in diameter. The platinum shadowing of the surface replica reveals that the domains are buckled outward. (**b**) Schematic of the air–liquid interfacial structure. The domains are modeled with spherical caps whose geometry (a, R_c) results from the packing of sucrose mono- and distearate (*red* and *blue*), respectively. (Reprinted with permission from [7.152]. © 2008 AAAS)

A very stable gas dispersion can be obtained by trapping air into sucrose stearate surfactant shells within a viscous glucose syrup bulk phase with gas cells ranging from hundreds of nanometers to tens of micrometers [7.152]. Hexagonal nanometer-scale domains that buckle outward from the bubble fully cover the air–liquid interface (Fig. 7.43a). This structuring originates from the self-assembly of the sucrose stearate surfactant molecules with the hydrophilic head groups (in the aqueous phase) occupying substantially more surface area than the microbubbles (Fig. 7.43b). According to thermodynamic modeling [7.152], the bending elasticity of the nanoscale domains resists the compression of the interface and, thereby, stops or substantially reduces bubble shrinkage. This gives rise to the observed longevity of the dispersion.

7.10.3 Bubbles for Tracking the Trajectory of an Individual Electron Immersed in Liquid Helium

An electron injected into liquid helium forms a tiny bubble (diameter ∼ 4 nm) around itself (see [7.154]) due to the repulsive interaction between the electron and the electrons of the helium atoms, which arises from the Pauli exclusion principle. A

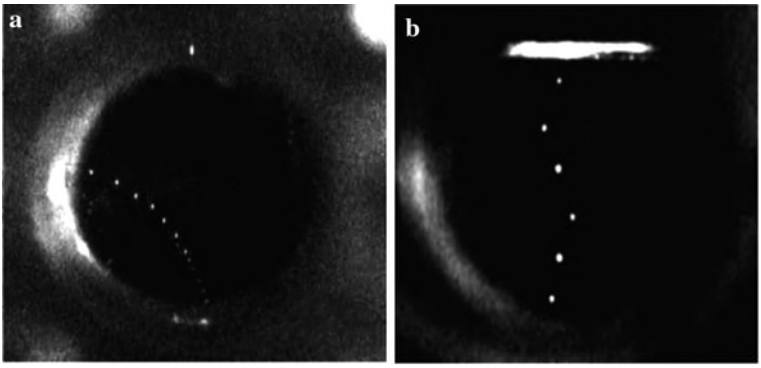

Fig. 7.44 Image of a bubble with an electron moving under the combined influence of an upward convective flow of liquid He at 2.4 K and an electric field of –150 V applied to the electrode shown as a bright spot at the top of the window. (**b**) Image of an electron bubble following a snake-like track which may relate to the electron being trapped on and sliding along a vortex line in superfluidic He at 1.5 K. (Reprinted with permission from [7.154]. © 2009 American Physical Society)

negative pressure in an acoustic pulse causes the electron bubble to expand to about 10 μm making it visible due to strong light scattering.

Figure 7.44a shows an electron bubble moving upward in liquid He at 2.4 K following the convective fluid flow until it is deflected to the left by a repelling –150 V voltage applied to an electrode. In Fig. 7.44b an electron bubble is shown moving in superfluid liquid He at 1.5 K. The zigzag motion evident in this picture can be attributed to the trapping of the electron on the core of a quantized vortex line yielding a constraint to follow the meandering of the vortex core across the cell. The electron bubble can be trapped on the vortex because of the Bernoulli force exerted on the bubble that arises from the increasing velocity of the superfluid flow near the vortex core.

7.11 Summary

Mechanical, optical, and fluid properties of nanostructures are of growing interest. Nanoelectromechanical systems (NEMSs) are used for sub-single charge electrometry, single-electron spin paramagnetic resonance, zeptogram mass sensing, zeptonewton sensing and they can also provide a way to observe the imprint of quantum phenomena directly. The transition from mechanics to quantum mechanics is going to be studied by means of high-frequency laser-cooled NEMS structures. Nanomaterials mimicking gecko toes are developed for bioinspired adhesion. Single-photon and entangled-photon sources and photon detectors based on quantum dots may be most useful for quantum communication and computation. Plasmon excitation on metallic nanostructure is of interest for sensors, medical therapy, and potential invisibility cloaks. Nanophotonics can be unified with

nanomechanics and nanofluidics. Fluid properties may be significantly altered on the nanoscale by surface interactions. The boundary conditions for a fluid on a wall depend on the wetting properties – no-slip for a wetting situation and slip lengths of some tens of nanometers in a non-wetting situation or on superhydrophobic surfaces. The hydrophobic walls in carbon nanotubes give rise to transport of water and gas by orders of magnitudes faster than in other pores of the same size, similar to the transport mechanism in biological membrane ion channels. Nanodroplets in emulsions are used extensively by the foods, cosmetics, and coating industries and double emulsions provide the ability to carry both polar and non-polar cargos. In 4 nm water nanodroplets, the dynamics of water molecules are slowed down compared to bulk water. Nanobubbles in gas–liquid systems play a role as contrast agents for ultrasound imaging, aerated food, and personal care products.

References

7.1 M. Li et al., Nature **456**, 480 (2008)
7.2 D. Psaltis et al., Nature **442**, 381 (2006)
7.3 C. Monat et al., Nat. Photon. **1**, 106 (2007)
7.4 A.H.J. Yang et al., Nature **457**, 71 (2009)
7.5 H.G. Craighead, Science **290**, 1532 (2000)
7.6 S.C. Masmanides et al., Science 317, 780 (2007)
7.7 A.N. Cleland, M.L. Roukes, Nature **392**, 160 (1998)
7.8 D. Rugar et al., Nature **430**, 329 (2004)
7.9 C.L. Degen et al., Phys. Rev. Lett. **100**, 137601 (2008); C.L. Degen et al., Proc. Natl. Acad. Sci. **106**, 1313 (2009)
7.10 Y.T. Yang et al., Nano Lett. **6**, 583 (2006)
7.11 T.P. Burg et al., Nature **446**, 1066 (2007)
7.12 H.J. Mamin, D. Rugar, Appl. Phys. Lett. **79**, 3358 (2001)
7.13 A. Naik et al., Nature **443**, 193 (2006)
7.14 W.C. Fon et al., Nano Lett. **5**, 1968 (2005)
7.15 K.C. Schwab, M.L. Roukes, Phys. Today. **58** (7), 36 (2005)
7.16 P. Curie, J. Curie, Bull. Soc. Minéral. Fr. **3**, 90 (1880)
7.17 M. Li et al., Nat. Nanotechnol. **2**, 114 (2007)
7.18 X.L. Feng et al., Nat. Nanotechnol. **3**, 342 (2008)
7.19 H.B. Peng et al., Phys. Rev. Lett. **97**, 087203 (2006)
7.20 B. Witkamp et al., Nano Lett. **6**, 2904 (2006)
7.21 A.M. Fennimore et al., Nature **424**, 408 (2003)
7.22 W.W. Jang et al., Appl. Phys. Lett. **92**, 103110 (2008)
7.23 J. Eisert, Phys. J. **6** (3), 22 (2007)
7.24 A. Schliesser et al., Nat. Phys. **4**, 415 (2008)
7.25 W. Marshall et al., Phys. Rev. Lett. **91**, 130401 (2003)
7.26 P. Ball, Nature **453**, 22 (2008)
7.27 M. Schlosshauer, *Decoherence and the Quantum-to-Classical Transition* (Springer, Heidelberg, 2007)
7.28 F. Károlyházy, Nuovo Ciment. **52**, 390 (1966)
7.29 R. Penrose in *Mathematical Physics 2000*, eds. by A. Fokas et al. (Imperial College, London, 2000), p. 226
7.30 V.B. Braginsky, F. Ya. Khalili, *Quantum Measurements* (Cambridge University Press, New York, 1992)

7.31 M.D. LaHaye et al., Science **304**, 74 (2004)
7.32 D. Vitali et al., Phys. Rev. Let. **98**, 030405 (2007)
7.33 I. Wilson-Rae et al., Phys. Rev. Lett. **92**, 075507 (2004)
7.34 S. Mancini et al., Phys. Rev. Lett. **88**, 120401 (2002)
7.35 M. Pinard et al., Europhys. Lett. **72**, 747 (2005)
7.36 S. Gigan et al., Nature **444**, 67 (2006)
7.37 D. Kleckner, D. Bouwmeester, Nature **444**, 75 (2006)
7.38 A. Schliesser et al., Phys. Rev. Lett. **97**, 243905 (2006)
7.39 A.N. Cleland, Nat. Physics **5**, 458 (2009)
7.40 S. Etaki et al., Nat. Phys. **4**, 785 (2008)
7.41 M.P. Blencowe, Nat. Phys. **4**, 753 (2008)
7.42 E.P. Chan et al., MRS Bull. **32**, June 2007, p. 496
7.43 K. Hammerer et al., Phys. Rev. Lett. **102**, 020501 (2009)
7.44 A. Jagota et al., MRS Bull. **32**, June 2007, p. 492
7.45 B.N. J. Person, MRS Bull. **32**, June 2007, p. 486
7.46 C. Creton, S. Grob, MRS Bull. **32**, June 2007, p. 466
7.47 K. Autumn, Am. Sci. March-April 2006, p. 124
7.48 Y. Tian et al., Proc. Natl. Acad. Sci. USA **103**, 19320 (2006)
7.49 L.H. Ge et al., Proc. Natl. Acad. Sci. USA **104**, 10792 (2007)
7.50 H.S. Lee et al., Nature **448**, 338 (2007)
7.51 A. Mahdavi et al., Proc. Natl. Acad. Sci. USA **105**, 2307 (2008)
7.52 S. Reddy et al., Adv. Mater. **19**, 3833 (2007)
7.53 K.A. Daltorio et al., MRS Bull. **32**, June 2007, p. 504
7.54 N.M. Pugno, J. Phys.: Condens. Matter **19**, 395001 (2007)
7.55 B. Yurdumakan et al., Chem. Commun. **30**, 3799 (2005)
7.56 L.T. Qu et al., Science **322**, 238 (2008)
7.57 P. Michler et al., Science **290**, 2282 (2000)
7.58 P. Michler, C. Becher, Physikal. Blätter **57** (9), 55 (2001)
7.59 D. Bouwmeester, A. Ekert, A. Zeilinger, *The Physics of Quantum Information* (Springer, Berlin 2000)
7.60 B. Lounis, M. Orrit, Rep. Prog. Phys. **68**, 1129 (2005)
7.61 Z.L. Yuan et al., Science **295**, 102 (2002)
7.62 S. Kako et al., Nat. Mater. **5**, 887 (2006)
7.63 S. Strauf et al., Nat. Photo. **1**, 704 (2007)
7.64 A. Högele et al., Phys. Rev. Lett. **100**, 217401 (2008)
7.65 A. Einstein et al., Phys. Rev. **47**, 777 (1935)
7.66 J.S. Bell, Rev. Mod. Phys. **40**, 229 (1968)
7.67 N. Akopian et al., Phys. Rev. Lett. **96**, 130501 (2006)
7.68 R.M. Stevenson et al., Nature **439**, 179 (2006)
7.69 O. Benson, Phys. J. **5**, Nr. 4, 22 (2006)
7.70 J.C. Blakesley et al., Phys. Rev. Lett. **94**, 067401 (2005)
7.71 E.J. Gansen et al., Nat. Photon. **1**, 585 (2007)
7.72 D. Bimberg et al., MRS Bull. July 2002, p. 531
7.73 R. Dingle, C.H. Henry, U.S. Patent No. 3, 982, 207 (1976)
7.74 H. Saito et al., Appl. Phys. Lett. **69**, 3140 (1996)
7.75 R. Schur et al., Jpn. J. Appl. Phys., Part 2: Lett. **35**, L357 (1997)
7.76 J.A. Lott et al., Electron. Lett. **33**, 1150 (1997)
7.77 N.N. Ledentsov et al., *Memories of the Institute of Scientific and Industrial Research*, vol. 57 (March 2001), special issue "Advanced Nanoelectronics: Devices, Materials and Computing", 3rd Sanken International Symposium (ISIR, Osaka, 2000), p. 80
7.78 V.I. Klimov, M.G. Bawendi, MRS Bull. Dec. 998 (2001)
7.79 Y.T. Chan et al., Appl. Phys. Lett. **86**, 073102 (2005)
7.80 Nat. Nanotechnol. **3**, 5 (2008)

7.81 D. Bimberg. J. Phys. D: Appl. Phys. **38**, 2055 (2005)
7.82 V.I. Klimov et al., Nature **447**, 441 (2007)
7.83 T. Akiyama et al., Proc. IEEE **95**, 1757 (2007)
7.84 C.M. Lieber, Z.L. Wang, MRS Bull. **32**, February 2007, p. 99
7.85 Y. Nakayama et al., Nature **447**, 1098 (2007)
7.86 K. Nozaki et al., Opt. Express **15** (12), 7506 (2007)
7.87 H.A. Atwater, Sci. Am., April 2007, p. 38
7.88 S. Kawata et al., Nat. Photo. **3**, 388 (2009)
7.89 S.A. Maier, Plasmonics: Fundamentals and Applications (Springer, Heidelberg, 2007)
7.90 Y.N. Xia, N.J. Halas, MRS Bull. **30**, May 2005, p. 338
7.91 J. Nelayah et al., Nat. Phys. **3**, 348 (2007)
7.92 R. Kolesov et al., Nat. Phys. **5**, 470 (2009)
7.93 K.L. Kelly et al., J. Phys. Chem. **B107**, 668 (2003)
7.94 Y. Chen et al., MRS Bull. **33**, May 2008, p. 536
7.95 E. Hao et al., J. Chem. Phys. **120**, 357 (2004)
7.96 A. Taflove, G. Hagness, *Computational Electrodynamics: The Finite-Difference Time-Domain Method, Second Edition* (Artech House, Boston, 2000)
7.97 L. Novotny, B. Hecht, *Principles of Nanooptics* (Cambridge University Press, Cambridge, 2006)
7.98 K.G. Lee et al., Nat. Photon. **1**, 53 (2007)
7.99 K.A. Willets, R.P. Van Duyne, Annu. Rev. Phys. Chem. **58**, 267 (2007)
7.100 S.L. Pan et al., J. Phys. Chem. B **110**, 17383 (2006)
7.101 C.J. Murphy et al., MRS Bull. **30**, May 2005, p. 349
7.102 H.C. Jin et al., Nature **425**, 487 (2003)
7.103 N.J. Halas, Proc. Natl. Acad. Sci. USA **106**, 3643 (2009)
7.104 A.J. Haes et al., MRS Bull. **30**, May 2005, p. 368
7.105 J.N. Anker et al., Nat. Mater. **7**, 442 (2008)
7.106 B.D. Lucas et al., Adv. Mater. **20**, 1129 (2008)
7.107 J. Henzie et al., Nat. Nanotechnol. **2**, 549 (2007)
7.108 T.Y. Olson, J.Z. Zhang, J. Mater. Sci. Technol. **24**, 433 (2008)
7.109 J.R. Krenn, F.R. Aussenegg, Phys. J. **1** (3), 39 (2002)
7.110 J. Takahara et al., Opt. Lett. **22**, 475 (1996)
7.111 Y. Fedutik et al., Phys. Rev. Lett. **99**, 136802 (2007)
7.112 T. Ichimura et al., Phys. Rev. Lett. **102**, 186101 (2009)
7.113 M. Ringler et al., Phys. Rev. Lett. **100**, 203002 (2008)
7.114 E. Cubukcu et al., Proc. Natl. Acad. Sci. USA **106**, 2495 (2009)
7.115 B. Murphy, L. Vestergaard Hau, Phys. Rev. Lett. **102**, 033003 (2009)
7.116 T.J. Kippenberg, Phys. J. **8** (2), 16 (2009)
7.117 D.E. Chang et al., Nat. Phys. **3**, 807 (2007)
7.118 P.K. Jain et al., J. Phys. Chem. **B110**, 7238 (2006)
7.119 M.P. Melancon et al., Cancer Mol. Ther. **7**, 1730 (2008)
7.120 J.B. Pendry et al., Science **312**, 1780 (2006)
7.121 J. Edel, A.J. de Mello (eds.) *Nanofluidics, Nanoscience and Nanotechnology* (RSC Publishing, 2008)
7.122 J. Mittal et al., Phys. Rev. Lett. **96**, 177804 (2006)
7.123 MRS Bull. **31**, August 2006, 588
7.124 S.H. Oh et al., Science **310**, 661 (2005)
7.125 N. Giovambattista et al., Phys. Rev. Lett. **102**, 050603 (2009)
7.126 T.-D. Li, E. Riedo, Phys. Rev. Lett. **100**, 106102 (2008)
7.127 M. Whitby, N. Quirke, Nat. Nanotech. **2**, 87 (2007)
7.128 T. Biben, L. Joly, Phys. Rev. Lett. **100**, 186103 (2008)
7.129 M. Rauscher, S. Dietrich, Annu. Rev. Mater. Res. **38**, 1 (2008)
7.130 K.S. Liu et al., Nanotech. **19**, 165604 (2008)

7.131 A. Checco, Phys. Rev. Lett. **102**, 106103 (2009)
7.132 P.G. de Gennes et al., Rev. Mod. Phys. **57**, 827 (1985)
7.133 C. Bauer, S. Dietrich, Phys. Rev. E 60, 6919 (1999)
7.134 J.B. He et al., Nat. Mater. **8**, 585 (2009)
7.135 A. Noy et al., Nanotoday. **2**, December 2007, p. 22
7.136 G. Hummer et al., Nature **414**, 188 (2001)
7.137 J.K. Holt et al., Science **312**, 1034 (2006)
7.138 Y. Qiao et al., J. Am. Chem. Soc. **129**, 2355 (2007)
7.139 D.E. Moilanen et al., J. Am. Chem. Soc. **129**, 14311 (2007)
7.140 J.A. Hanson et al., Nature **455**, 85 (2008)
7.141 P.W. Sutter, E.A. Sutter, Nat. Mater. **6**, 363 (2007)
7.142 J.P. Toennies, A.F. Vilesov, Angew. Chem. Int. Ed. **43**, 2622 (2004)
7.143 H. Frauenfelder et al., Nat. Phys. **5**, 251 (2009)
7.144 J. Rodrigues et al., Phys. Chem. Chem. Phys. **11**, 1484 (2009)
7.145 S. Colin, Spektrum der Wissenschaft, Jan 2004, p. 46
7.146 F. Banhart, Rep. Prog. Phys. **62**, 1181 (1999)
7.147 F. Garcias et al., J. Chem. Phys. **108**, 9102 (1998)
7.148 S. Müller et al., Phys. Rev. Lett. **102**, 183401 (2009)
7.149 V.L. Ginzburg, A.A. Sobyanin JETP Lett. **15**, 343 (1972)
7.150 P. Sindzingre et al., Phys. Rev. Lett. **67**, 1871 (1991)
7.151 S.A. Khairalla et al., Phys. Rev. Lett. **98**, 183401 (2007)
7.152 E. Dressaire et al., Science **320**, 1198 (2008)
7.153 B.M. Borkent et al., Phys. Rev. Lett. **98**, 204502 (2007)
7.154 W. Guo et al., Phys. Rev. B **79**, 054515 (2009)
7.155 M.P. Brenner, D. Lohse, Phys. Rev. Lett. **101**, 214505 (2008)

Chapter 8
Nanomagnetism

"Magnetism goes nano" is the slogan that describes the present activities in research on ferromagnetic systems [8.1]. These activities include basic research as well as profit-oriented industrial development laboratories. In basic research, imaging and dimensionality play an important role, as the size can be reduced to the dimensions where the collective phenomenon "ferromagnetism" will be affected. The study of the transition from atomic to molecular magnetism and ferromagnetism is going to become feasible, envisioning new and highly fascinating insight into collective phenomena. For this aim, the fabrication and the analysis of nanostructures together with a nanoscale understanding of the properties is of pivotal interest.

The progress in the understanding of magnetism at the nanoscale and the development of magnetic nanoelements [8.2–8.8] has been stimulated by advances in film growth and device fabrication techniques, by the development of new measurement methods, and by the increase in computing power that has allowed the modeling of materials and properties at the nanoscale [8.4, 8.9].

In this section recent advances in magnetic imaging, dimensionality effects in nanomagnetism, magnetically soft, hard, and antiferromagnetic nanomaterials, ferromagnetic nanorings, current-induced domain wall motion, single molecule magnets, multiferroic nanostructures, and nanomagnets in bacteria will be discussed. It should be pointed out that nanomagnetism also plays a role in other fields as described in Chap. 1 or in Chaps. 3, 9, and 12.

8.1 Magnetic Imaging

Developments toward high-resolution magnetic imaging are fueled by demands of current magnetic data storage and sensor technologies, as well as by the interest in the fundamentals of magnetic phenomena. A wide range of techniques have been developed for the imaging of magnetic domain patterns, such as the Bitter decoration technique (see [8.10]) or magneto-optical microscopy in reflection (Kerr effect [8.11], MOKE; lateral resolution $\sim 0.15\ \mu m$), and transmission (Faraday effect). Here, we will discuss recent developments in magnetically sensitive scanning probe techniques [8.12, 8.13], of magnetically sensitive electron microscopy, and of

H.-E. Schaefer, *Nanoscience*, DOI 10.1007/978-3-642-10559-3_8,

high-resolution x-ray magnetic circular dichroism (XMCD). These techniques have recently developed the capabilities of nanometer or even atomic scale resolution.

8.1.1 Magnetic Force Microscopy (MFM) and Magnetic Exchange Force Microscopy (MEx FM)

Both techniques, MFM and MEx FM, utilize an atomic force microscope (AFM; see Sect. 2.2) [8.13]. MFM [8.14] senses the dipolar magnetostatic force between a ferromagnetic tip and a ferromagnetic sample. Since the magnetostatic force is long range, typical tip–sample separations are larger than 10 nm. To exceed the nanometer resolution capability of MFM it was proposed earlier [8.15] to use the short-range magnetic exchange force for magnetic imaging (MEx FM). This force acts between two closely spaced atomic magnetic moments (spins) and, therefore, can only be detected at small tip–sample distances in the range of 0.5 nm. Theoretical studies (see [8.16]) have predicted the feasibility of MEx FM with atomic resolution and an experimental breakthrough has been reported [8.17].

For a MFM or a MEx FM setup an atomic force microscope is used containing a tip coated with a ferromagnetic material to attain magnetic sensitivity (Fig. 8.1b). The device is operated with a frequency modulation (FM) mode ($f_0 = 50$–200 kHz) in a non-contact (NC) regime, where because of the tip–sample interaction the resonance frequency is characteristically shifted by $\Delta f = f - f_0$. Data acquisition is performed in the constant height plane-subtraction mode so that the $\Delta f(x, y)$ maps recorded in this mode reflect the magnitude and sign of the tip–sample interaction (see [8.13]).

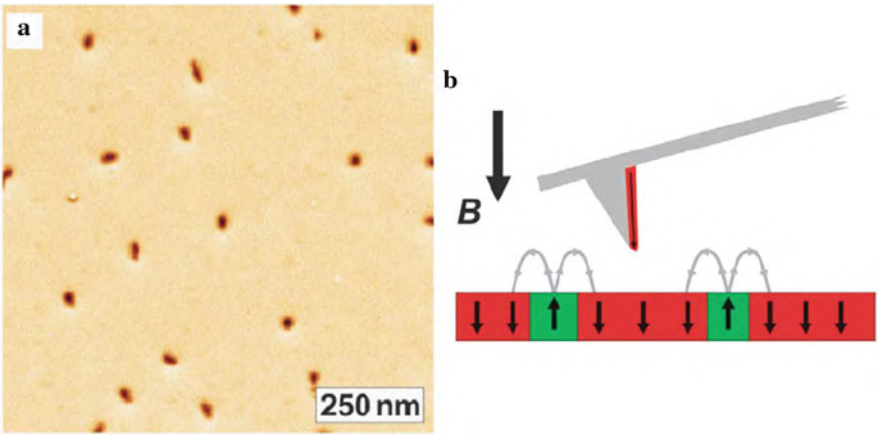

Fig. 8.1 MFM tip with pure out-of-plane sensitivity. (**a**) The image of a $La_{0.7}Sr_{0.3}MnO_3$ layer on a $LaAlO_3$ substrate was recorded at 5.1 K in the constant height plane subtraction mode at $B = 0.295$ T. (**b**) The magnetic configuration of tip and sample ($La_{0.7}Ca_{0.3}MnO_3/LaAlO_3$) relative to B is shown. (Reprinted with permission from [8.13]. © 2008 Elsevier)

For *MFM imaging*, the magnetostatic and the electrostatic interactions can be separated (see [8.13]). Thus the force gradient perpendicular to the surface $\partial F_z = \partial z$, i.e., the second derivative of the tip–sample interaction energy E_{TS}, is detected and is related to the measured frequency shift by $\partial F_z/\partial z = 2c_z \cdot \Delta f/f_0$, where c_z is the force constant. When the tip is approximated by a dipole $\boldsymbol{m}_{\mathrm{T}} = (m_x, m_y, m_z)$ the force gradient of the tip in the stray field H of the sample is given by

$$\frac{\partial}{\partial z}F_z = \mu_0 \left(m_x \frac{\partial^2 H_x}{\partial z^2} + m_y \frac{\partial^2 H_y}{\partial z^2} + m_z \frac{\partial^2 H_z}{\partial z^2} \right)$$

demonstrating that the image interpretation is easiest when the dipole points in the z-direction ($m_x = m_y = 0$) and thereby $\partial F_z \big/ \partial z$ depends only on $J^2 H_z \big/ \partial z^2$. The physical meaning of the MFM image can be understood by looking at the interaction energy

$$E_{\mathrm{TS}} = -\int \rho_{\mathrm{S}} \phi_{\mathrm{T}} dV - \int \sigma_{\mathrm{S}} \phi_{\mathrm{T}} dS,$$

where $\rho_{\mathrm{S}} = -\mathrm{div}\, J_{\mathrm{S}}$ and $\sigma_{\mathrm{S}} = \mathbf{n}\, J_{\mathrm{S}}$ are the volume and surface magnetic pole densities, respectively, with $\boldsymbol{J}_{\mathrm{S}}$ the sample magnetic polarization, $\mathbf{n}$ the surface normal unit vector, and ϕ_{T} the scalar potential of the tip stray field $\boldsymbol{H}_{\mathrm{T}}$. The force gradient is obtained when ϕ_{T} is replaced by $\partial^2 \phi_{\mathrm{T}} = \partial z^2$. The above relationship for E_{TS} shows that MFM images reflect the distribution of north and south poles (magnetic charges) smoothed by the spatial extend of ϕ_{T}, which is related to the stray field of the tip via $H_{\mathrm{T}} = -\boldsymbol{D}\phi_{\mathrm{T}}$ (see [8.13]).

Suitable MFM tips should exhibit emanating stray fields as localized as possible. This can be achieved by coating only one side of the tip (Fig. 8.1b) so that complex domain structures at the tip apex can be avoided facilitating image interpretation because only m_Z is non-zero. By this MFM approach isolated circular out-of-plane polarized magnetic domains in a $La_{0.7}Sr_{0.3}MnO_3$ (LSMO) layer on a $LaAlO_3$ (LAO) substrate are imaged in Fig. 8.1a with a lateral resolution down to 10 nm [8.13].

MEX FM imaging can supply atomic resolution spin configurations with an atomically sharp tip and a tip–sample distance of below 0.5 nm, using the FM technique in the NC regime. To detect a magnetic contrast on the magnetic scale unambiguously, the problem of separating the magnetic exchange interaction from the usual chemical interaction arises because both types of interactions are electron mediated with similar decay lengths of ~ 0.1 nm. This complication is completely absent in antiferromagnetic samples (see, e.g., NiO in Fig. 8.2a) where chemically identical atoms carry spins that point into opposite directions. Moreover, antiferromagnets do not possess a magnetic stray field and their spin configuration is much less affected by an external magnetic field than that of ferromagnets. In the topographical AFM image of a NiO (001) surface in Fig. 8.2b the positions of increased valence charge density (protrusions) or of decreased charge density (depressions)

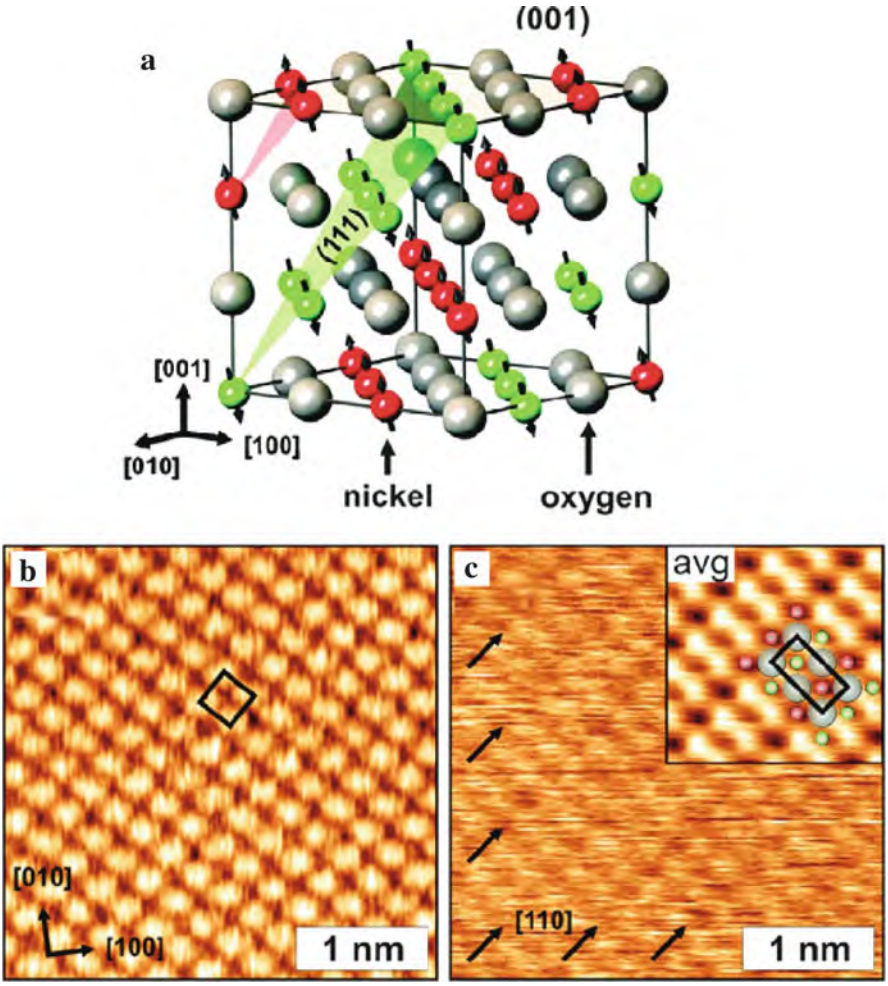

Fig. 8.2 (**a**) Chemical and magnetic structure of NiO. (**b**) Atomic resolution with chemical contrast on NiO (001). The AFM image is recorded with a non-magnetic tip at 8.1 K and a frequency shift $\Delta f = -11$ Hz. Protrusions and depressions correspond to O and Ni atoms, respectively. The square indicates the (1×1) surface unit cell. (**c**) Magnetic exchange force microscopy (MEx FM) image using an Fe-coated tip at 7.9 K and $\Delta f = -24.3$ Hz in an external flux density of $B = 5$ T. As in (**b**), chemical resolution is obtained. In addition, a contrast modulation on neighboring rows of depression (Ni atoms) demonstrates the simultaneous detection of the magnetic exchange interaction between tip and sample spins. The *inset* in (**c**) is obtained after unit cell averaging of the raw data. (Reprinted with permission from [8.13]. © 2008 Elsevier)

indicate the lattice sites of O or Ni ions, respectively. The magnetic properties of the NiO lattice are determined by the strongly localized Ni d-electrons. They couple antiferromagnetically via superexchange across bridging O atoms. The (001) surface shows a row-wise antiferromagnetic structure exhibiting a (2×1) magnetic surface unit cell with canted magnetic moments pointing into <112> directions. This configuration is reflected by the atomic scale contrast visualized in Fig. 8.2c using a tip coated with Fe showing the atomic O protrusions and Ni depressions with neighboring rows of Ni atoms exhibiting different contrasts (see (2×1) surface unit cell in the inset of Fig. 8.2c). Since these contrasts arise from chemically and structurally identical nickel atoms, they must be of magnetic origin. Thus, it can be inferred that this atomic scale contrast stems from the short-range magnetic exchange force between the tip and sample spins.

One way to describe the magnetic exchange interaction between spins is the Heisenberg model with the Hamiltonian $H_{ij} = -\sum_{ij} J_{ij} S_i S_j$, where J_{ij} is the exchange integral which determines strength and type (ferro- or antiferromagnetic) of the coupling between the spins $\boldsymbol{S}_i$ and $\boldsymbol{S}_j$. Its physical origin is the Coulomb interaction between electrons and the Pauli exclusion principle of indistinguishable particles. If, for simplicity, only the spin $\boldsymbol{S}_\mathrm{T}$ of the foremost tip atom and the spin $\boldsymbol{S}_\mathrm{S}$ of the sample atom directly underneath are considered, the equation for H_{ij} infers that the magnitude of the MEx FM signal is maximum for parallel or antiparallel alignment of these spins. From this it can be concluded that the spin of the foremost tip atom should be oriented perpendicular to the sample surface (see Fig. 8.3). This can be accomplished by a high external field of 5 T, exceeding the saturation magnetization of the ferromagnetic tip material but leaving the antiferromagnetic structure of the NiO unaltered. A favorable alignment of the spins at the tip apex seems to be the crucial issue for successfully imaging antiferromagnetic ordering on an atomic scale by MEx FM [8.13, 8.17]. Future

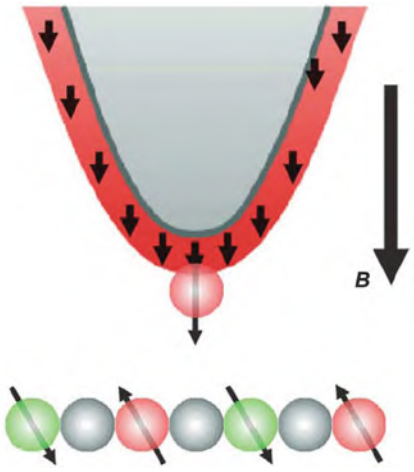

Fig. 8.3 Most likely configuration of the spin of the foremost tip atom for $B > J_\mathrm{sat}$. The magnetic polarization is aligned to B. This configuration is suitable for studying surface spin structures that are mainly independent of the external B field, like in antiferromagnetic NiO. (Reprinted with permission from [8.13]. © 2008 Elsevier)

perspectives of MEx FM are wide (see [8.13]). With this technique atomic scale magnetic structures of insulators can be studied in contrast to spin-polarized scanning tunneling microscopy (SP-STM) [8.18] with similar resolution but restricted to conductors. The exchange bias effect [8.19] may be studied which might be related to uncompensated spins at the interface. The magnetic structure of individual magnetic molecules deposited on insulators could be studied without any coupling because of the large band gap. In addition, dissipative processes due to, e.g., spin excitation (magnons) could be accessible or, if the interaction is not direct but RKKY-like (Ruderman–Kittel–Kasuya–Yosida), the then expected oscillatory behavior might be observable.

8.1.2 Spin-Polarized Scanning Tunneling Microscopy (SP-STM) and Manipulation

Spin-polarized tunneling microscopy combines the atomic resolution capabilities of conventional spin-averaged STM with spin sensitivity (see [8.20, 8.21]). This is achieved by making use of the tunneling magnetoresistance effect which is based on the conservation of a spin of an electron during tunneling across a vacuum barrier. Since magnetic materials exhibit an intrinsic imbalance between the spin-majority and spin-minority electronic densities of states (DOS) this leads to a junction transmittance which depends on the relative magnetization directions of STM tip and substrate.

According to a simple theoretical description [8.22] the tunneling current in a SP-STM experiment

$$I(r_\mathrm{T}, U, \theta) = I_0(r_\mathrm{T}, U) + I_\mathrm{SP}(r_\mathrm{T}, U, \theta)$$

can be decomposed into the spin-averaged component I_0 and the spin-dependent contribution I_SP, where r_T is the tip position, U the bias voltage, and θ the angle between the magnetization vectors of tip and sample, m_T and m_S. A possibility to separate topographic, electronic, and magnetic information is the measurement of the local differential conductance dI/dU, where the spin-averaged measurement of the differential conductivity, $dI/dU_0(r_\mathrm{T}, U) \propto n_\mathrm{S}$, gives access to the sample's non-spin-polarized LDOS [8.23, 8.24]. If a magnetic tip is applied, spin-polarized components additionally contribute [8.22] yielding

$$\frac{dI}{dU}(r_\mathrm{T}, U) = \frac{dI}{dU}(r_\mathrm{T}, U)_0 + \frac{dI}{dU}(r_\mathrm{T}, U)_\mathrm{SP} \propto n_\mathrm{T} n_\mathrm{S}(r_\mathrm{T}, E_\mathrm{F}+eU) + \boldsymbol{m}_\mathrm{T}\boldsymbol{m}_\mathrm{S}(r_\mathrm{T}, E_\mathrm{F}+eU)$$

This local differential conductance mode dI/dU is sensitive to the spin polarization within a narrow energy interval ΔE around $E_\mathrm{F} + eU$ and, therefore, can be nicely applied to spin polarized surface states (see [8.21]) where the dI/dU signal is maximum for parallel or antiparallel spin orientations of tip and sample.

A separation of spin-averaged electronic from magnetic effects can be accomplished by first recording a dI/dU image with a bias voltage for which the spin asymmetry defined by

$$A = \frac{dI/dU_{\uparrow\downarrow} - dI/dU_{\uparrow\uparrow}}{dI/dU_{\uparrow\downarrow} + dI/dU_{\uparrow\uparrow}}$$

becomes zero (electronic contrast image) and simultaneously recording a second dI/dU image with a bias voltage for which the spin asymmetry is maximum (magnetic contrast image) [8.25]. Three examples of imaging by SP-STM – magnetic vortices, dynamic processes, and atomic resolution – will be discussed in the following [8.21].

Magnetic vortices can develop in small magnetic disks. In this case the magnetic polarization follows the disk curvature and rotates out of plane toward the center, where it finally orients perpendicular to the surface (Fig. 8.4a). Maps of the spin-resolved dI/dU signal measured on Fe islands (Fig. 8.4b, c) with Cr-coated tips are sensitive to the in-plane and out-of-plane components of the magnetization $\boldsymbol{M}_S$, depending on the thickness of the Cr coating. While the in-plane-sensitive signal (Fig. 8.4b, d) shows the rotating magnetization by a contrast inversion, the out-of-plane image (Fig. 8.4c, e) shows a homogeneous dI/dU signal for the entire island except for a small bright spot approximately located in the center of the island. This spot is caused by the perpendicular orientation of the magnetization in the vortex core with a width of about 9 nm. It was predicted theoretically [8.10] that the shape of the vortex core is determined by the minimum total energy, which is dominated by the exchange and the magnetostatic energy. Compared to the latter, the magnetocrystalline anisotropy energy, which is relevant for the width of bulk Bloch walls, and the surface anisotropy are negligible. The calculated vortex width $\omega = 2\sqrt{A/K_d} \approx 6.4$ nm is in reasonable agreement with the experimental data, where A is the exchange stiffness and $K_d = \mu_0 M_{\text{sat}}^2/2$ is given by the saturation magnetization.

Dynamic processes in superparamagnetic particles have been studied in Fe islands on Mo(110) (see [8.21]) in the so-called line mode (see Fig. 8.5a, b) in order to enhance the conventionally restricted time resolution of STM. By repeatedly scanning along the same line for about 40 min, thereby crossing islands A–D at a rate of 1 Hz, one obtains spin-resolved dI/dU maps in dependence of time (Fig. 8.5c). At lower temperatures ($T = 13$ K; lower panel), only in the smallest island B switching processes due to thermally activated magnetization reversal are observed, i.e., about 50 times within the 40 min time interval. As the temperature is raised to 19 K (upper panel in Fig. 8.5c), however, larger islands become magnetically unstable, too.

Atomic resolution can be achieved by SP-STM of, e.g., a 1.1 atomic layer of Fe on W(001) (see Fig. 8.6). Early density-functional calculations [8.26] predicted an antiferromagnetic ground state of the Fe atoms that has been confirmed experimentally (see Fig. 8.6) by a dI/dU map with a periodicity of about 0.5 nm which is in good agreement with the expected 0.45 nm.

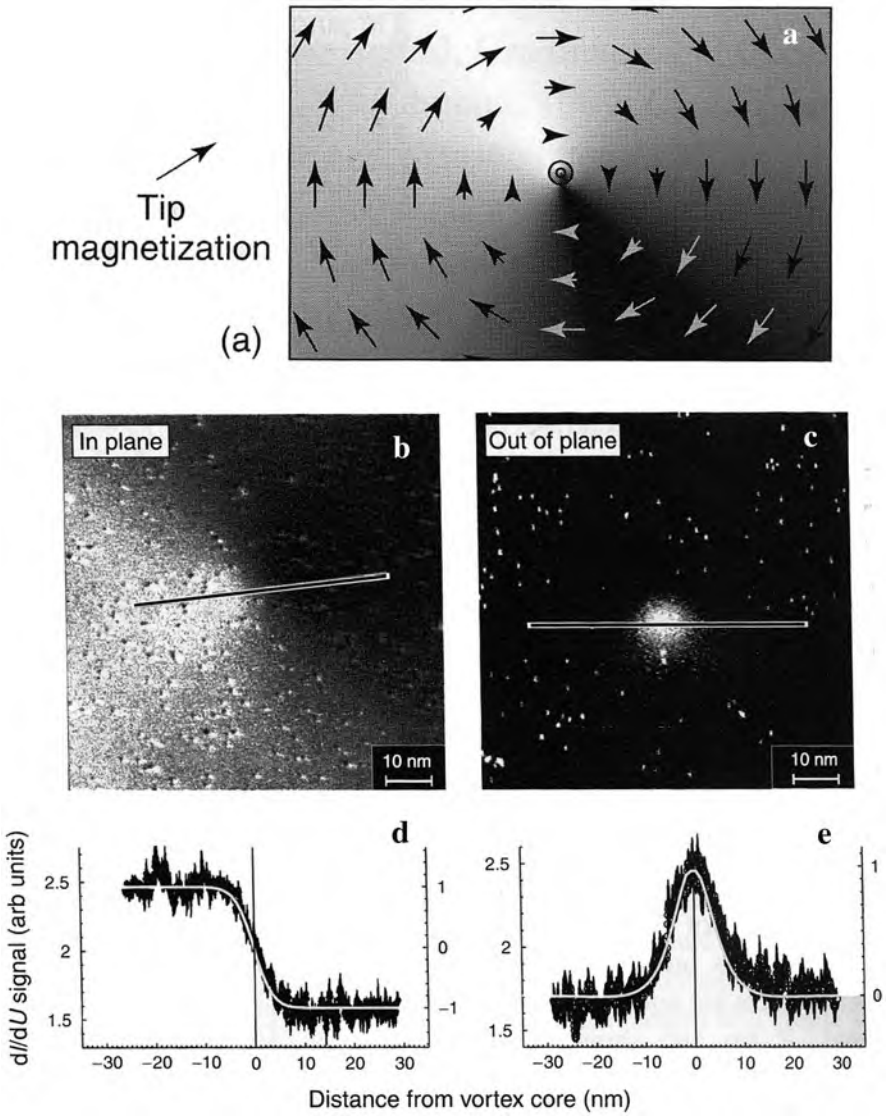

Fig. 8.4 (**a**) Schematic arrow representation of the magnetic structure in the vicinity of a vortex core (*right*) and the tip magnetization (*left*). (**b**, **c**) High-resolution spin-resolved dI/dU maps of a magnetic vortex in an Fe island (size about 250×500 nm^2; thickness about 7 nm) on a W (110) surface taken with an in-plane sensitive (**b**, **d**) and an out-of-plane sensitive Cr-coated tip (**c**, **e**). Experimental line sections (**d**, **e**) taken along the *black line* in (**b**, **c**) are compared to micromagnetic simulations (*white lines*). (Reprinted with permission from [8.21]. © 2007 Wiley Interscience)

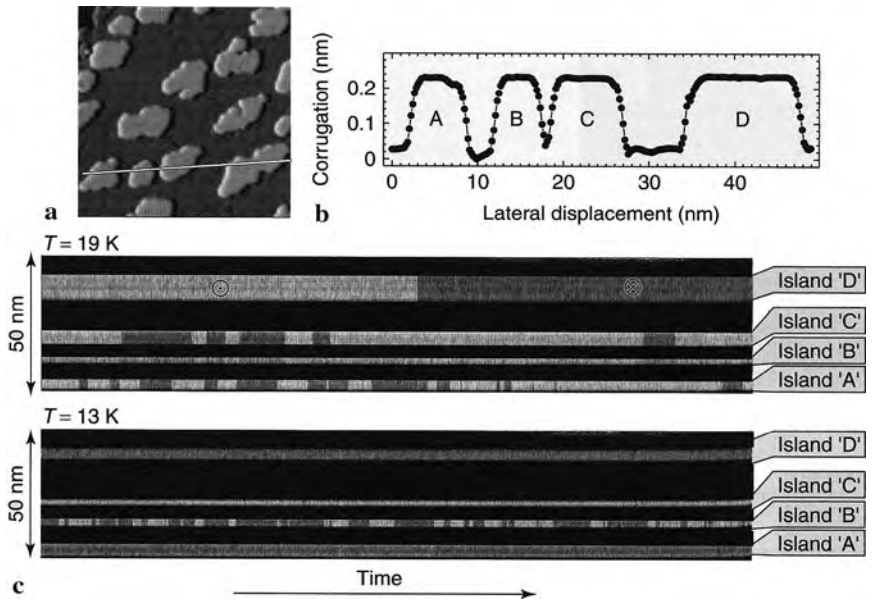

Fig. 8.5 (**a**) Topography of Fe monolayer islands on Mo (110). The scan range amounts to 40×40 nm^2. (**b**) Line section showing the profiles of four individual islands labeled A–D. (**c**) Spin-resolved dI/dU maps of the islands A–D shown in (**b**) as measured in the line mode at $T = 13$ K (*bottom*) and $T = 19$ K (*top panel*). (Reprinted with permission from [8.21]. © 2007 John Wiley)

Chiral magnetic order may be caused by the Dzyaloshinskii–Moriya interaction (DMI) [8.27] (see [8.28]), which arises from spin-orbit scattering of electrons in an inversion-asymmetric crystal field such as at surfaces. Such a chiral magnetic surface order has been observed for a Mn monolayer on a W (110) substrate by SP-STM using a Cr-coated tip, sensitive to the in-plane magnetization. The SP-STM data reveal periodic stripes (Fig. 8.7a) running along the [001] direction, with an inter-stripe distance of 0.47 nm matching the surface lattice constant along the [110] direction. The magnetic amplitude is additionally modulated with a period of about 6 nm. With the help of SP-STM studies in an external magnetic field and of applying density functional theory it could be shown that the magnetic surface order of the Mn monolayer on W (110) is a left-handed cycloidal spin spiral (c-ss; Fig. 8.7b, c) where the handedness arises from the spin-orbit interaction on the surface. It should be kept in mind that an STM image of the cycloidal modulation of an atomic scale antiferromagnetic structure repeats twice across a period (Fig. 8.7b, c), so that the period of the spin spiral structure is about 12 nm.

Chirality in nanoscale magnets may play a role in spintronic devices, where the spin rather than charge is used for data transmission and manipulation. For instance, a spin-polarized current flowing through chiral magnetic structures will exert a spin torque on the magnetic structure, causing a variety of excitations or manipulations of

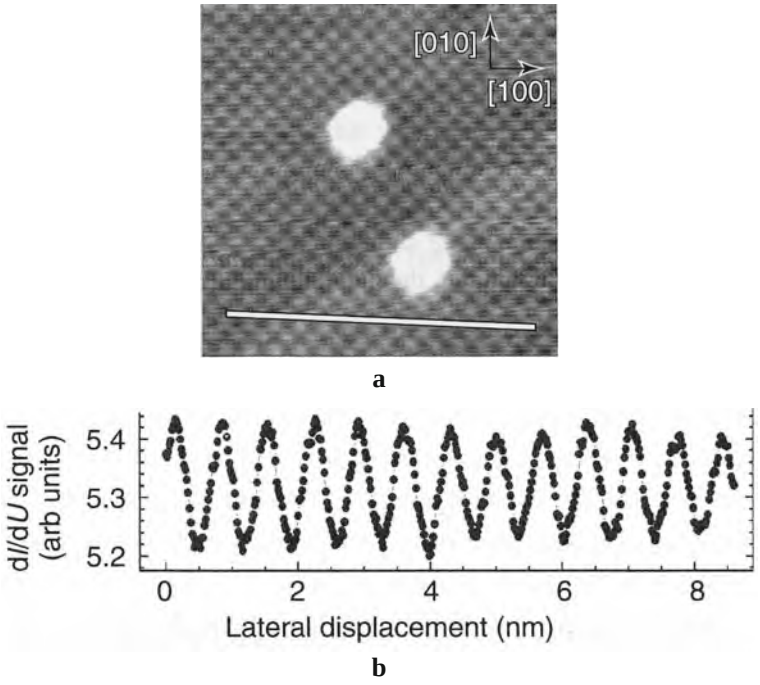

Fig. 8.6 (**a**) Spin-resolved dI/dU map of 1.1 atomic layers of Fe on W (001) with atomic magnetic resolution. Note that the two adsorbates appear to exhibit a lower dI/dU signal strength. (**b**) Line section taken along the line in (**a**). (Reprinted with permission from [8.21]. © 2007 Wiley Interscience)

the magnetization and giving rise to microwave emission, magnetization switching, or magnetic motors [8.28].

Magnon excitation, i.e., collective excitations of the spin system in a ferromagnet, can be studied by SP-STM techniques as demonstrated, e.g., for bulk iron and Co-nanolayers on Cu (111) [8.30]. This approach with its high lateral resolution may allow the investigation of laterally confined magnons in nanostructures and the study of the impact of magnon generation on the magnetic configuration.

Toward magnetization switching by means of SP-STM. The increase of hard disk and memory capacities is a result of continuously decreasing bit size. For example, the area of one bit in today's magnetic hard disks is of the order of $(60\ \text{nm})^2$. Two different effects are used for reading and writing information: the giant magnetoresistive effect for reading (see Sect. 1.4), whereas in writing a magnetic field is used. However, due to the non-local character of magnetic fields, the stored information of nearby bits may be accidentally destroyed. One solution of this problem may be the substitution of a magnetic switching field for writing by a spin polarized current locally exerting a magnetic torque (see Sect. 8.7) that leads to the reversal of magnetization at sufficient current density, as has been proposed theoretically [8.31]

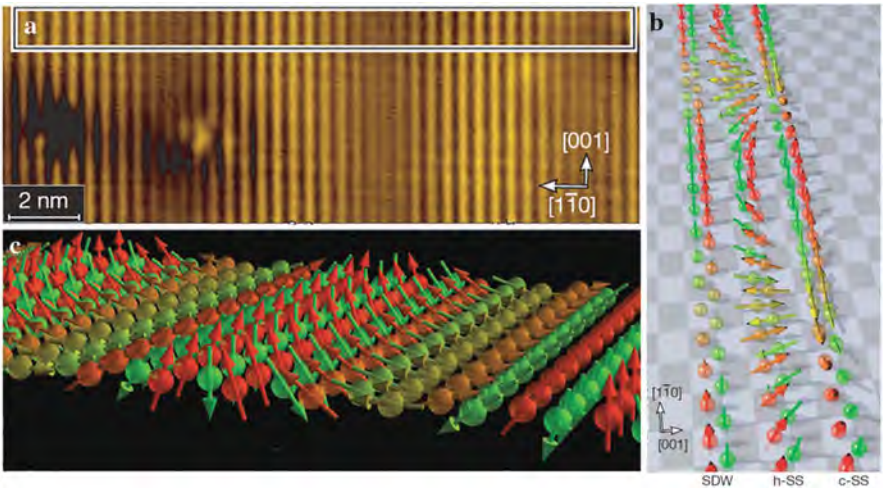

Fig. 8.7 Spin-polarized scanning tunneling microscopy (SP-STM) of a Mn monolayer on W (110) and potential spin structures. (**a**) SP-STM image taken with a Cr-coated tip. The stripes along the [001] direction are caused by spin-polarized tunneling between the magnetic tip and the sample, showing a 0.448 nm periodicity and a long-wavelength modulation. (**b**) Artist's view of considered spin structures: spin-density wave (SDW), a helical spin spiral (h-ss), and a left-handed cycloidal spin spiral (c-ss) [8.28]. (**c**) Schematic view of a left-handed cycloidal spin spiral surface [8.29]. (Reprinted with permission from [8.28] (**a**) (**b**) and [8.29] (**c**). © 2007 Nature Publishing Group)

and demonstrated experimentally in nanopillar devices [8.32]. This technique may reduce circuit complexity and may further miniaturize data storage devices, because the same electrical line to address a bit could be used to read information at low currents (by measuring the magnetoresistance) and to write information at high currents (by the spin torque effect).

In order to study magnetization reversal initiated by SP-STM, monolayer superparamagnetic islands of Fe were deposited on a W (110) substrate and imaged by an antiferromagnetic Cr-coated W tip [8.33] which is sensitive to the in-plane sample magnetization (Fig. 8.8a). Then the dI/dU SP-STM signal is observed as a function of time, with the tip positioned stationary above the central region of a small Fe nanoisland with a typical surface area of 7 nm^2 (i.e., consisting of about 100 atoms).

At a low tunneling current, the dI/dU signal statistically switches between the two levels "0" and "1" (top panel of Fig. 8.8b) with the two states occurring with the same probability (see histogram in Fig. 8.8c) as expected because the two states are energetically degenerate. As I is increased, however, an imbalance between "0" and "1" evolves, until one state clearly dominates for $I = 2000$ nA (Fig. 8.8c). The study [8.33] indicates that the current-induced magnetization switching by SP-STM with high spatial resolution is dominated by the spin torque induced by the spin-polarized current, whereas the effects of the Oersted field and of the heating by the tunneling current are small.

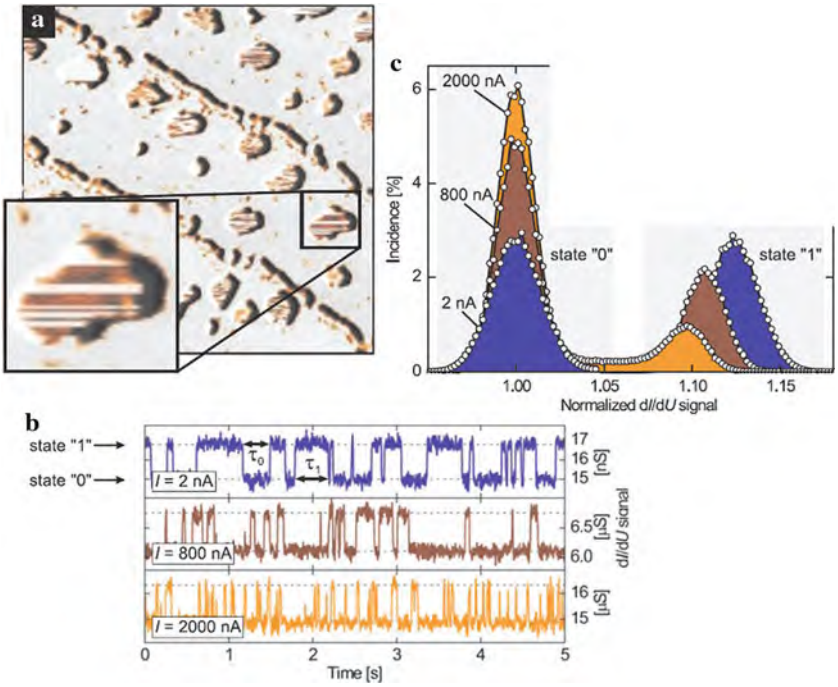

Fig. 8.8 (**a**) In-plane magnetic dI/dU map of Fe monolayer islands on W (110) measured by SP-STM at 56 K. A dark or bright signal on the islands represents a magnetization direction parallel or antiparallel to the tip magnetization, respectively. Stripes appear on small islands (see *inset*) because they switch their magnetization state frequently. (**b**) Trace section of the time-dependent magnetic dI/dU signal of one particular nanoisland (area: 5.7×0.4 nm^2) recorded at different tunneling currents $I(T = 48.4$ K). (**c**) Histogram of the overall magnetic dI/dU signal normalized with respect to the state "0" level at different tunneling currents. Whereas states "0" and "1" are equally populated at low currents, a substantial asymmetry toward state "0" can be recognized at high currents. (Reprinted with permission from [8.33]. © 2007 AAAS)

8.1.3 Electron Microscopy

Whereas Lorentz microscopy [8.34] (see [8.35]) has been used early for magnetic imaging, electron holography [8.35, 8.36], scanning electron microscopy with polarization analysis [8.1], or circular dichroism electron microscopy [8.37] have been developed recently. Electron microscopy can visualize the magnetic induction B due to the Lorentz force $F_L = q \cdot v \times B$, where $q = -e$ is the electron charge and v the electron velocity. As shown by Aharonov and Bohm [8.38], the vector potential $\boldsymbol{A}(r)$ generated by a magnetic induction distribution $B(r)$ gives rise to a phase shift of a bypassing electromagnetic wave.

Lorentz microscopy can be performed – utilizing a scanning transmission microscope (STEM) – in the differential phase contrast (DPC) mode (see [8.35]; Fig. 8.9) which can detect the spatial derivative of the phase shift along the electron

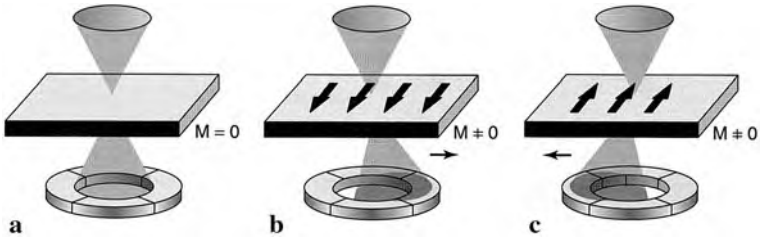

Fig. 8.9 Schematic representation of the electron beam tilt and the corresponding shift of the electron beam in the detector's plane due to the magnetization of the specimen. (**a**) For a non-magnetic specimen where the beam is not deflected. (**b**, **c**) Owing to a non-zero magnetization of the specimen the beam is tilted, causing different segments of the detector to record intensity. Therefore, the four-segment position-sensitive device can measure the direction and magnitude of the local magnetization in the specimen. (Reprinted with permission from [8.35]. © 2007 Wiley Interscience)

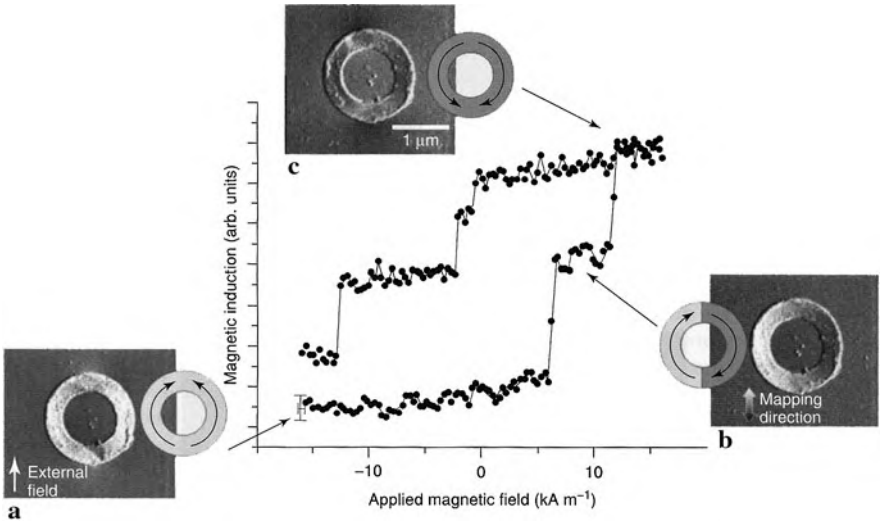

Fig. 8.10 Hysteresis loop of a magnetic permalloy ring measured by differential phase contrast (DPC) Lorentz microscopy. It is obvious from the DPC images, (**a**), (**b**), and (**c**) together with the attached schematic drawings, that the ring switches with changing magnetic field (10 kA m^{-1} = 0.01257 T) from an upward oriented "onion state" (**a**) into a "vortex state" (**b**) and then into a "reversed onion state" (**c**). Each change of the magnetic configuration is accompanied by specific features in the hysteresis loop. (Reprinted with permission from [8.35]. © 2007 Wiley Interscience)

trajectories by measuring the shift of the electron beam on a detector. Lorentz microscopy can provide an image of the magnetization structure of the specimen at every point of the magnetization loop as shown in Fig. 8.10. The jumps in the hysteresis loop of a 20 nm thick permalloy ring indicate a switching process, when the initial onion state changes into a flux-closure state at an external field of

6.1 kA m^{-1} and into the reversed onion state at 11.6 kA m^{-1}. Lateral resolutions of the magnetization imaging of 5 nm have been demonstrated (see [8.35]).

Holography [8.39] (see also Sect. 2.6) can measure the phase shifting action of a magnetic specimen on the phase of a bypassing initially plane electron wave. To record the phase of a wave, an interference experiment has to be carried out. If the electron wave after transmission through the specimen interferes with a coherent reference wave yielding an interference pattern the phase shift and therefore the specimen magnetization distribution can be recorded by mathematical procedures. In practice, the specimen is placed in one half of the illuminating electron beam, while the unaffected second half of the beam can act as a reference wave (Fig. 8.11). A positively charged wire with a diameter in the sub-micrometer range is used as a biprism (see [8.35]) to tilt the two partial beams toward each other, producing an interference pattern in the recording plane.

In a strongly simplified mathematical model (see [8.35]), the object wave $\Phi_{\mathrm{Obj}}(r)$, that is the primary wave modulated by the specimen's transmission function, can be written as $\phi_{\mathrm{Obj}}(r) = U(r)\exp(ik_0 r + \varphi(r))$, while the reference wave would be written as $\phi_{\mathrm{ref}} = \exp(ik_0 r)$. If both waves are tilted toward the optic axis by $\pm k'$, the intensity in the plane of observation can be formulated as $I(r) = U^2(r) + 1 + 2U(r)\cos(2\,k' r - \varphi(r))$. In this equation the phase information $\varphi(r)$ of the magnetic specimen is contained in the interference cosine term. It can, however, be extracted in Fourier space by Fourier transformation of the recorded image, i.e., of $I(r)$.

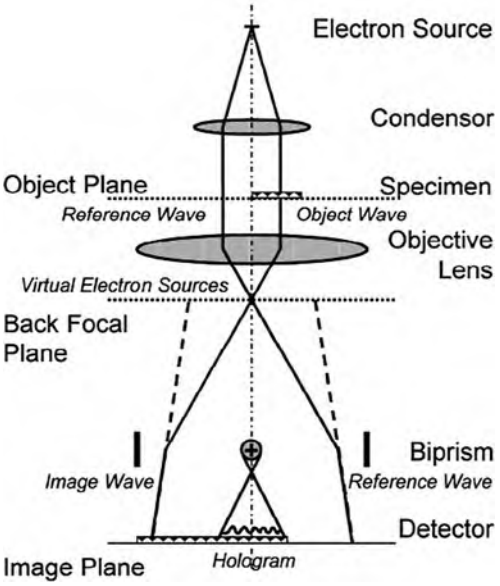

Fig. 8.11 A schematic diagram of off-axis electron holography. An image wave that travels through the specimen overlaps with a reference wave that does not travel through the specimen. The resulting interference fringes carry information about the magnetic and electric potentials of the specimen. (Reprinted with permission from [8.40]. © 2002 Cambridge University Press)

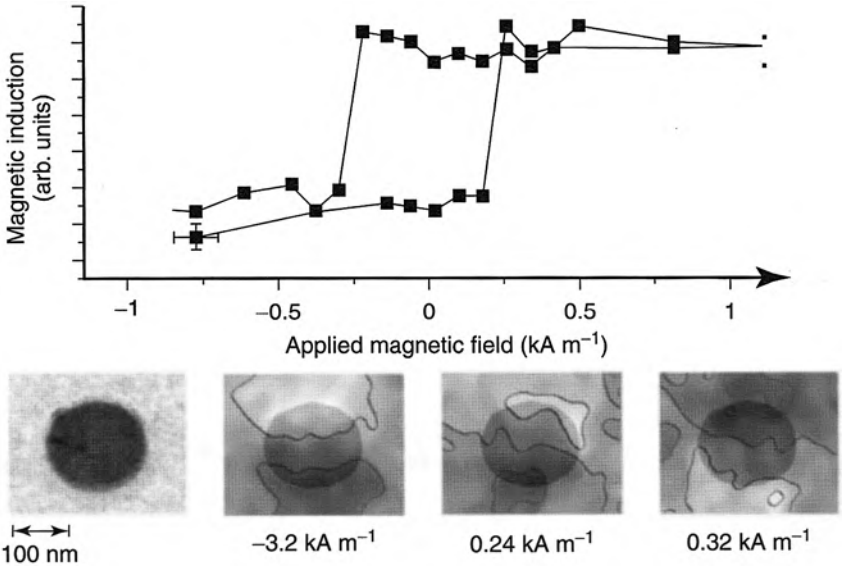

Fig. 8.12 Hysteresis loop of a $Ni_{80}Fe_{20}$ particle with a diameter of approximately 160 nm. The hysteresis loops taken from holograms at various external fields show single domain behavior of the specimen, that is, a switching between two magnetic states without any intermediate state. The micrographs below the hysteresis loop show (*left* to *right*) a shadow image of the specimen used to determine the holographic phase reconstructions of the magnetization distribution within the specimen for the applied fields indicated. Between 0.24 and 0.32 kA m^{-1} a switching occurs as can be seen from the inverted *gray* scale contrast. (Reprinted with permission from [8.35]. © 2007 Wiley Interscience)

A study of the magnetization behavior of a 6 nm thick permalloy disk by electron holography is shown in Fig. 8.12 as recorded with electron holography. The disk with a diameter of about 160 nm shows a single domain switching behavior between 0.24 and 0.32 kA m^{-1} (1 kA m^{-1} = 0.01257 T) without any intermediate states as would be expected for nucleation of domain walls. The gray scale indicates the slope of the electron wave which was generated by the specimen's vector potential acting on the initially plane electron wave. The magnetization of the specimen is directed perpendicular to the slope of the gray scale. Lines of constant phase shift are displayed which indicate the magnetic field lines inside and outside of the specimen.

For deducing the magnetization of the specimen from the electron micrographs, the transport-of-intensity equation has to be utilized together with image simulation of magnetization distributions (see [8.35]).

Scanning electron microscopy with polarization analysis (spin-SEM) can bridge the scales from micrometers to nanometers for magnetic surface imaging [8.1]. When a solid is irradiated by electrons with energies of a few kiloelectronvolts, a maximum of emitted secondary electrons (SE) appears at energies of a few electronvolts, i.e., near the Fermi level E_F. In itinerant ferromagnets such as Fe, Cu, or Ni, these electrons show a strong unbalance of the spins aligned antiparallel (spin-up) or

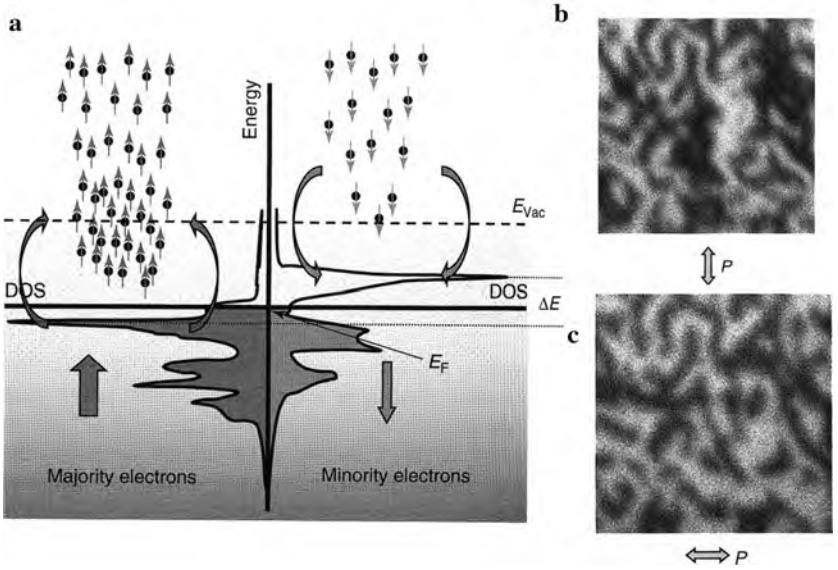

Fig. 8.13 (**a**) Spin resolved densities of states for a hypothetical itinerant ferromagnet. The electrons with minority spin have a high density of states above the Fermi level while majority spin electrons occupy states below E_F. The shaded energy ranges indicate the band states below the vacuum level E_{Vac}. Electrons above E_{Vac} can leave the solid and contribute to the secondary electrons. A rough sketch of the process is given that causes the polarization of the electrons emitted from the itinerant ferromagnet. (**b**, **c**) Domain image obtained from the spin-STEM of a $(Co/Pt)_8$ multilayer on a Si wafer. The polarization components *P* within the film plane are shown. Image size $2.35 \times 2.35\ \mu m^2$. (Reprinted with permission from [8.1]. © 2007 Wiley Interscience)

parallel (spin-down) with respect to the magnetization of the specimen. Hence, upon electron irradiation, mostly electrons of majority spin character are ejected, because close to the Fermi energy the occupied states are mostly majority states (Fig. 8.13). This can be utilized for imaging magnetic surface domain structures by means of a scanning electron microscope (SEM) equipped with an electron polarization detector, which, e.g., is based on low-energy electron diffraction on a W (001) surface (see [8.1]). The magnetic domain structure of a $(Co/Pt)_8$ multilayer on a Si wafer imaged by spin-SEM is shown in Fig. 8.13b, c.

Magnetic circular dichroism studies by transmission electron microscopy were performed on Fe films [8.37]. A material is said to exhibit dichroism if its photon absorption spectrum depends on the polarization of the incident radiation. In the case of x-ray magnetic circular dichroism (XMCD; see below) the absorption cross section of a ferromagnet changes when the helicity of a circularly polarized photon is reversed relative to the magnetization direction. In analogy to that, a dichroic behavior of magnetic materials has been detected by electron energy loss spectroscopy under particular scattering conditions [8.37]. This may lead to an element-specific magnetic imaging technique with high lateral resolution and additional depth information.

8.1.4 X-Ray Magnetic Circular Dichroism (XMCD)

This technique has developed to a high impact method based on synchrotron radiation: it has made practical the concept of "local magnetometry" and magnetic moment analysis based on the sum rules. Orbital, spin, and quadrupolar magnetic moments can be retrieved with elemental specificity notably from $L_{2,3}$ x-ray absorption edges of transition metals and from $M_{4,5}$ edges of rare earth metals and actinides (see [8.37]). Microscopy applications of XMCD have been developed both by focusing soft x-rays by means of diffractive optics (Fresnel zone plates) or by passing the photoemitted electrons through electron optical lenses to form high-resolution images. In some cases, 50 nm resolution has been demonstrated, with expectations of reaching 10 nm in the next few years (see [8.37]). The x-rays with a well-defined polarization for the XMCD experiments [8.42] are emitted by highly relativistic electrons in the gigavolt range. For x-rays in the 0.1–100 keV energy range the photoeffect related absorption in matter gives rise to element-specific binding energy of an inner atomic electron level, such as the $L_{2,3}$ edge of the 3d transition metals.

The magnetism of a material is introduced by the fact that, in the vicinity of an absorption edge in a magnetic material, the density of electron states (DOS) is spin-split in a simple band structure model (Fig. 8.13). Therefore, the excitation probability of polarized electrons depends on the spin-polarized DOS of the final state atom, and the strength of the absorption depends on the polarization of the empty states available in the absorption process following Pauli's exclusion principle. This results in a difference in the absorption coefficients when the helicity of the photon beam is flipped with respect to the sample magnetization (Fig. 8.14). Since the spin moment yields a different sign for the absorption at both edges (see Fig. 8.14) and since the orbital moment yields the same sign, both the spin moment and the orbital moment can be deduced from a comparison of the dichroic profiles at the L_2 and L_3 edges separated by a spin–orbit coupling of 13 eV in Fe (see Fig. 8.14). The separation of the spin and orbital moment contributions to the absorption difference can be achieved by employing a theory resulting in the "sum rules" (see [8.41, 8.42]).

Time-resolved imaging of magnetic nanostructures by means of XMCD can be performed by utilizing x-ray microscopy and sub-100-ps synchrotron x-ray pulses (see [8.42]). This forms the basis for the implementation of stroboscopic pump and probe experiments with sub-nanosecond time resolution [8.43] as shown for the dynamics of an out-of-plane magnetic vortex core (Fig. 8.15) in a permalloy ($Ni_{80}Fe_{20}$) film with a Landau magnetic domain structure. The extension of the vortex core ($\sim$ 20 nm) is imaged at the Ni L_3 XMCD absorption edge. From the gyrotropic motion in the alternating magnetic field, the speed of a vortex core pointing up can be deduced to 140 ms^{-1}. The dynamics of magnetic vortices excited by current pulses, which may be of interest for the development of new magnetic storage media, has been studied by resistance measurements [8.44] and x-ray microscopy [8.45]. The high static out-of-plane magnetic fields of about 0.5 T required for switching the core polarization can be lowered to *mT* values by applying sub-nanosecond in-plane magnetic field pulses [8.46].

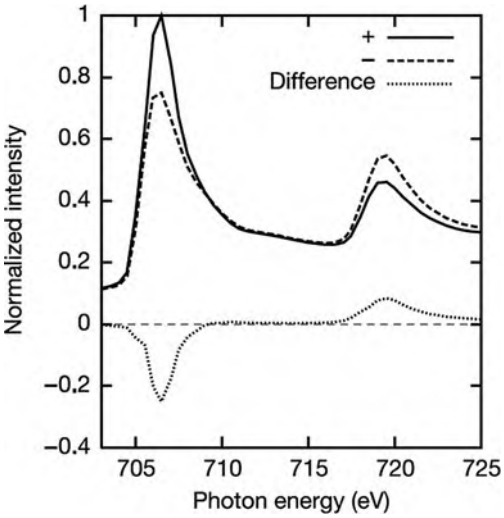

Fig. 8.14 X-ray magnetic circular dichroism in the $L_{2,3}$ absorption edge of epitaxial Fe on GaAs (001) remanently magnetized along the in-plane [100] direction. The *full* and *dashed curves* are obtained by reversing the handedness (+/−) of the circularly polarized x-rays. The magnitude of the dichroism is represented by the difference spectrum (*dotted line*). (Reprinted with permission from [8.37]. © 2006 Nature Publishing Group)

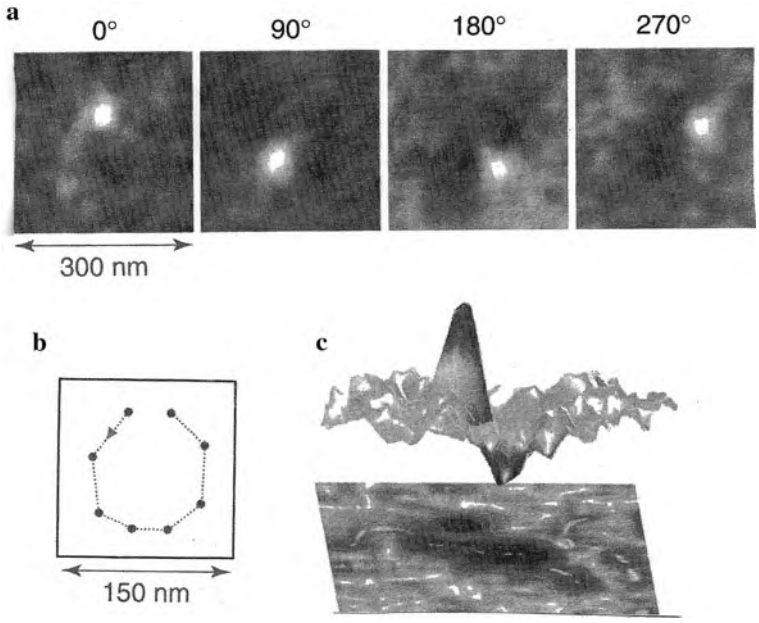

Fig. 8.15 Dynamic response of a vortex structure in a permalloy film (500×500 nm^2, 40 nm thick, Landau structure) due to an in-plane alternating magnetic field ($f = 437.5$ MHz, $H_0 = 710$ Am^{-1}) with a vortex core pointing up. (**a**) The out-of-plane magnetic contrast of the Landau structure at different phases of the external field. The position of the different phases is depicted in (**b**), and (**c**) is a 3D representation of the vortex structure (300×300 nm) at phase 270°. (Reprinted with permission from [8.42]. © 2007 Wiley Interscience)

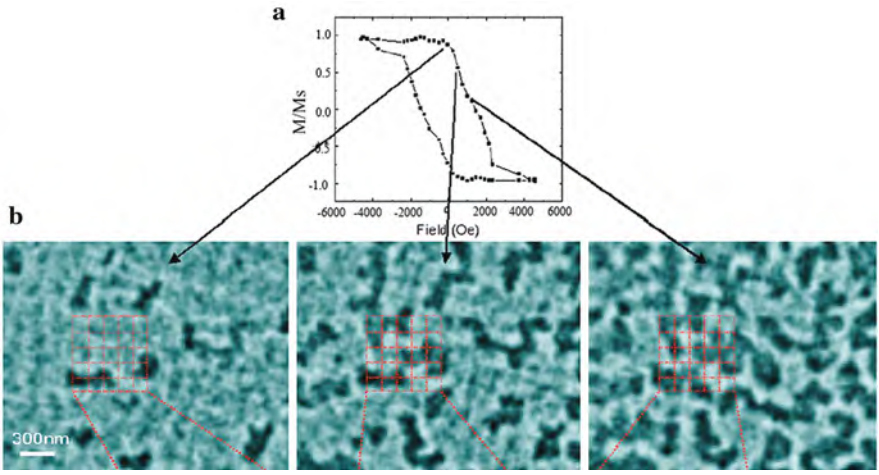

Fig. 8.16 (**a**) Hysteresis loop of a nanogranular $(Co_{83}Cr_{17})_{87}Pt_{13}$ alloy thin film derived from XMCD images taken at the CoL_3 absorption edge. (**b**) Field-dependent XMCD magnetic domain patterns at various magnetic fields indicated in the hysteresis loop; image size, $100 \times 100\ nm^2$ [8.47, 8.48]. (Reprinted with permission from [8.48]. © 2006 American Institute of Physics)

Local magnetic hysteresis loops have been studied by XMCD with a lateral resolution of <15 nm on CoCrPt films (see [8.47]) which have received attention as possible high-density magnetic recording media because of their strong perpendicular magnetic anisotropy and low media noise resulting from the decoupling of the exchange interaction between magnetically isolated grains via compositional segregation at grain boundaries (see [8.47]). The magnetic domain structure in Fig. 8.16 deduced by XMCD for various external magnetic fields exhibits dark and bright areas where the Co magnetization is pointing into and out of the film plane, respectively. The variation of this pattern in the external field is a direct and element-specific measure of the Co magnetization and by means of the integration of the gray scale intensity the macroscopic hysteresis of the film can be derived. The high-spatial XMCD resolution allows for zooming into the details of magnetization reversal of each grain demonstrating the stochastical character of the nucleation processes which is of technological relevance.

8.2 Size and Dimensionality Effects in Nanomagnetism – Single Atoms, Clusters (0D), Wires (1D), Films (2D)

Although there is a wealth of experimental and theoretical data available for magnetic phenomena in free atoms and bulk materials, systems on the nanometer length scale of the characteristic magnetic exchange interaction have been investigated only recently. This has been made possible by the development of fabrication techniques of 0D cluster, 1D wire, and 2D film nanostructures of 3*d* transition metals with

atomic control (see [8.49]). The link for understanding the magnetic properties of these nanosized structures is provided by the electronic structure of the *d*-states, (see [8.50]), which sensitively respond to the electronic nature of the neighboring atoms. An additional key role is played by the supporting substrate where, e.g., a platinum substrate is found to contribute to the nanostructure's magnetic anisotropy energy via strong electronic hybridization and hence stabilizes ferromagnetic long-range order in very small structures. This may be technically utilized to increase the bit density in magnetic memories (see [8.49]).

For the preparation of nanostructures on substrates, the deposition rate, the atomic diffusivity with a hierarchy of diffusion barriers, self-ordering strategies [8.51], and surface templates are dominating factors (see [8.49]).

8.2.1 Single Atoms

The magnetic properties of single atoms on surfaces have been studied by measuring the magnetization curves of individual magnetic Co atoms adsorbed on a non-magnetic metallic Pt substrate making use of a scanning tunneling microscope with a spin-polarized tip [8.52]. For isolated Co adatoms, that are more than 8 nm distant from a Co monolayer (ML) stripe with a magnetization perpendicular to the substrate (inset in Fig. 8.17e), an S-shaped magnetization curve is found at 0.3 K. This is characteristic for a paramagnetic behavior which implies the dominance of a temperature-independent switching process, for example, quantum tunneling of the magnetization (see [8.52). Focusing on adatoms close to the ML stripe (see inset in Fig. 8.17e) with a distance of ~ 1.5 nm, a square-like hysteresis is found (Fig. 8.17a) corresponding to a ferromagnetic behavior with an antiferromagnetic coupling to the stripe. With an increasing distance d of the adatoms from the ML the coupling, i.e., the exchange energy, J, oscillates to ferromagnetic–antiferromagnetic–ferromagnetic and the ferromagnetic behavior (see hysteresis in Fig. 8.17b, c) of the adatoms decays with distance (Fig. 8.17e). These characteristics are reminiscent of Ruderman–Kittel–Kasuya–Yosida (RKKY) – like exchange [8.54–8.56] with an oscillation period of the exchange energy of 1.5 nm and a wavelength $\lambda_F = 2\pi/k_F \approx 3$ nm of the range function $J(d) = J_0 \cos(2k_F d)/(2k_F d)^D$ (D – dimensionality; see [8.52]) which is by a factor 2–6 larger than typical Fermi wavelengths of the Pt (111) surface.

The magnetism of single atoms has been studied experimentally in various configurations in the case of Co (see [8.49] and Table 8.1). For an isolated Co impurity on a Pt (111) substrate a large magnetocrystalline anisotropy energy with an energy constant $K = 9.3$ meV is observed, much higher than in all other configurations (see Table 8.1). This originates from a strong orbital magnetic moment m_L (Table 8.1) which is mainly due to the reduced atomic coordination and the strongly interacting substrate, as confirmed theoretically (see [8.49]). Ab initio calculations predict [8.60] that the spin direction of single adatoms (Fe, Co) on Cu (001) can be controlled by varying the position of a spin-polarized Cr STM tip.

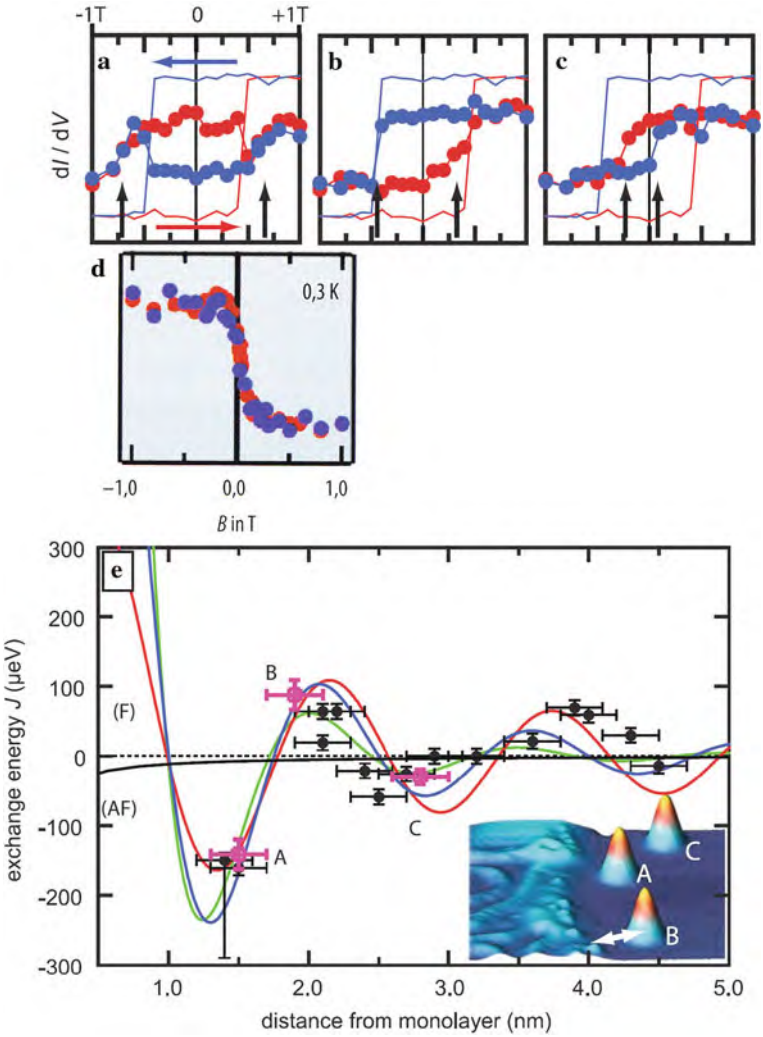

Fig. 8.17 Magnetic exchange between Co adatoms on a Pt substrate and a Co monolayer (ML) stripe. (**a**–**c**) Magnetization curves measured at 0.3 K on the ML (straight lines) and on the three adatoms (dots) **a**, **b**, and **c** visible in the *inset* topograph of (**e**). The *blue* color indicates the field downsweep from $B = +1$ T to -1 T and *red* the upsweep from -1 T to +1 T. The *vertical arrows* indicate the exchange bias field, B_{ex}, which is converted into the exchange energy (using the magnetic moment $m = 3.7\ \mu_B$) for the corresponding magenta points in (**e**). (**d**) S-shaped magnetization curve without hysteresis of a Co adatom with a distance much larger than 1.5 nm from the Co ML stripe [8.52, 8.53]. (**e**) Dots show the measured exchange energy as a function of distance d from ML as indicated by the *arrow* in the *inset*. The *black line* is the dipolar interaction calculated from the stray field of a 10-nm wide stripe with saturation magnetization 1.3×10^6 A/m. The *red*, *blue*, and *green lines* are fits to 1D, 2D, and 3D range functions for indirect exchange. (Reprinted with permission from [8.52]. © 2008 AAAS)

Table 8.1 Magnetic properties per Co atom in the gas phase, of a single Co atom on a Pt (111) substrate, in a monatomic Co chain on Pt (997), in a monatomic Co layer on Pt (997), and in a bulk Co crystal. The values of the calculated spin magnetic moment m_S, of the orbital magnetic moment m_L, and of the magnetocrystalline anisotropy energy constant K per atom are given. The K values of Co are compared to the values for $Fe_{50}Co_{50}$ and $Fe_{50}Pt_{50}$ monolayers on Pt and to the value of the high-anisotropy $L1_0$ FePt bulk alloy

	m_S (μ_B)	m_L (μ_B)	K (meV)	
– Co atom in the gas phase	3	3		(see [8.49])
– single Co atom on Pt (111)	2.1	1.1	9.3	[8.49]
– Co atom in a monatomic Co chain on Pt (997)	2.08	0.68	2.00	[8.57]
– Co atom in a monatomic Co layer on Pt (997)	2.03	0.31	0.14	(see [8.57])
– $Fe_{50}Co_{50}$ on Pt (111)			0.5 per atom	[8.58]
– $Fe_{50}Pt_{50}$ on Pt (997)			0.35 per Fe atom	[8.59]
– Co atom in bulk Co	1.52	0.15	0.05	(see [8.57])
– $L1_0$ FePt bulk alloy			0.8 per Fe atom	[8.59]

8.2.2 Finite-Size Atomic Clusters

For magnetic nanoparticles, the research is stimulated by the effort to overcome the superparamagnetic limit in magnetic storage devices (see [8.61]).

Small clusters show magnetic orbital and spin moments that can be assessed by x-ray magnetic circular dichroism (XMCD). While investigations on relatively simple structures in pure 3d metal particles yield insight into the basic mechanisms of the dimensionality and size dependence of magnetic properties, alloy nanoparticles seem to be more promising in terms of technical application. Alloys consisting of, e.g., Fe–Co have very high magnetic moments and are soft magnetic, whereas binary clusters of 3d metals (e.g., Co) in combination with heavy elements (Sm, Ag, or Pt) are candidates for materials with high magnetic anisotropies and increased superparamagnetic blocking temperatures [8.61].

Theoretical approaches (see [8.61]) relate the magnetic properties such as the spin and orbital magnetic moments per atom, magnetic order, and magnetic anisotropy energy (MAE) to the magnitudes that characterize the cluster electronic structure, such as Coulomb and spin–orbit interaction, local electronic density of states, spin-density distribution, etc. The calculated spin moments m_s per atom in pure Fe clusters or Co-coated Fe clusters, and the calculated orbital moments m_L per atom in Ni_N clusters in dependence of the cluster size are given in Fig. 8.18. The atomic spin moment in pure Fe clusters is highest in small clusters. It is enhanced

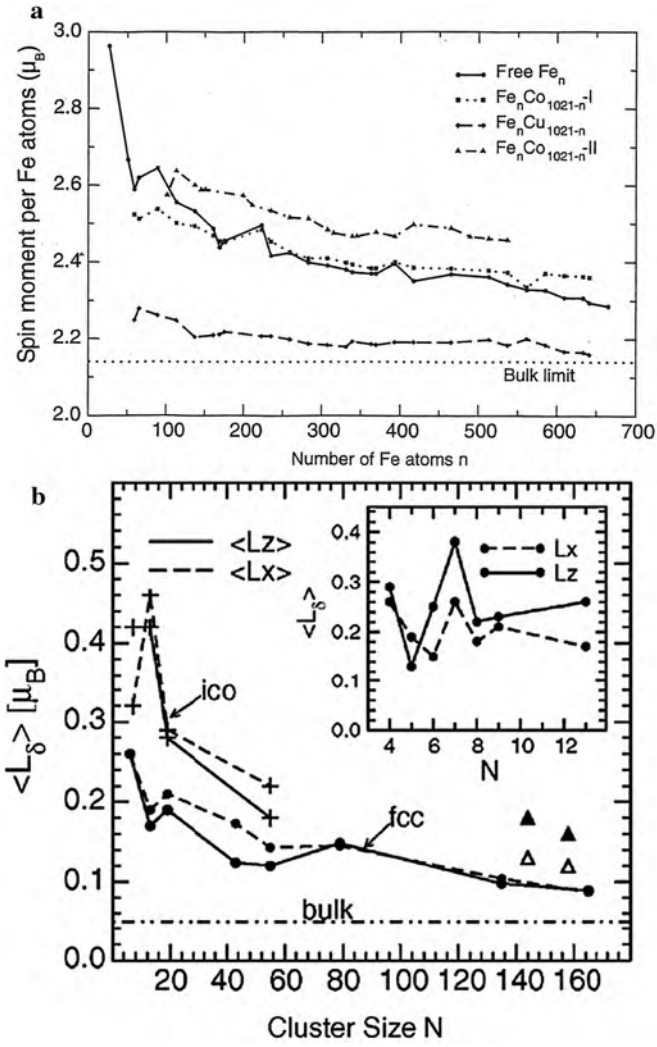

Fig. 8.18 (**a**) Average local spin moment of Fe atoms in clusters of size n for free Fe clusters, Cu-coated Fe clusters (Fe$_n$Cu$_{1021-n}$), Co-coated Fe clusters (Fe$_n$Co$_{1021-n}$-I), Co-coated Fe clusters with intermixing at the interface (Fe$_n$Co$_{1021-n}$-II) [8.61]. (**b**) Average orbital magnetic moment <L_d> per atom of Ni$_N$ clusters with fcc-like (*dots*) and icosahedron-like structures (*crosses*) [8.61, 8.62]. Filled (*open*) triangles refer to coin-like bilayer clusters with perpendicular (in-plane) magnetization. Results for small clusters are given in the *inset*. (Reprinted with permission from [8.61]. © 2005 Elsevier)

by intermixing with Co atoms. As shown in Fig. 8.18b, the reduction of the atomic coordination number with decreasing N causes a decrease of the local spin polarization which induces larger orbital moments m_L per atom in Ni$_N$ by means of spin–orbit coupling. The calculated MAE values in small Fe clusters [8.61] are

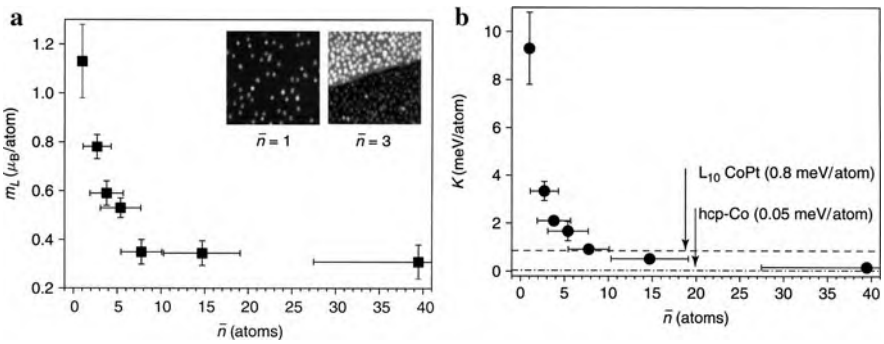

Fig. 8.19 (**a**) Orbital magnetic moment m_L of Co nanoparticles on Pt (111) measured as a function of their average size along the easy magnetic direction. (**b**) Magnetic anisotropy energy K as a function of average particle size. The *dashed* and *dash–dot lines* indicate the magnetic anisotropy energy K per Co atom of the CoPt $L1_0$ alloy and hcp-Co, respectively. The *inset* in (**a**) shows 18×18 nm^2 STM images of single Co impurities ($\bar{n} = 1$) and particles ($\bar{n} = 3\pm1$atoms). (Reprinted with permission from [8.49]. © 2007 Wiley Interscience)

much larger than in bulk solids, in agreement with experiments [8.63]. The MAE depends much more sensitively than the spin moments on the geometrical structure of the clusters and the anisotropy energy surface is complex with alternating off-plane and in-plane MAEs.

It could also be shown experimentally for small Co clusters that the orbital magnetic moment m_L is much more sensitive to progressive quenching with increasing particle size (Fig. 8.19a) than the spin magnetic moment, which slightly decreases from 2.1 μ_B for impurity atoms to 2.03 μ_B for monatomic Co layers on Pt (997). The MAE energy (Fig. 8.19b), due to its spin–orbit origin [8.64], is strongly correlated to the decrease of m_L and the anisotropy energy constant K for clusters of three atoms decreases to a value of 30% of that of single impurity atoms. The trend of K shows that a huge gain in MAE with respect to bulk Co or Co 2D films can be achieved by reducing the size of magnetic particles to a few tens of atoms or less on suitable substrates [8.49].

8.2.3 Ferromagnetic Nanowires

Monatomic 1D chains of magnetic atoms on metallic substrates (such as Co atoms on Pt surfaces [8.57] have been shown to exhibit ferromagnetic order [8.57], although ferromagnetic order has been predicted by spin lattice models not to occur [8.65] (see [8.61]) for infinite 1D linear chains at finite temperatures. The ferromagnetic long-range ordered state appears owing to the presence of magnetic anisotropy energy barriers [8.61]. The magnetic behavior of these monoatomic chains differs very much from that of magnetic 2D monolayers on substrates and oscillates when going from monatomic chains to double chains, triple chains, etc. [8.66] which can

be understood by ab initio calculations [8.67] as discussed below. In addition to that, the magnetic domain structure of monolayer nanowires with a lateral width of about 100 nm [8.68] and the magnetic properties of nanowires in carbon nanotubes [8.69] will be described.

8.2.3.1 Atomic Chains

Co monatomic chains of variable width can be prepared by epitaxial deposition of Co atoms on the step edges of a vicinal Pt (997) substrate with a 2.0 nm step separation [8.66] (Fig. 8.20a). By increasing the Co coverage from 0.13 ML (monolayers) to 1.3 ML, monatomic Co chains, double chains, triple chains, etc., and finally a 2D monolayer can be generated (Fig. 8.20b). The magnetic properties of the Co chains can be specifically probed by x-ray magnetic circular dichroism (XMCD) [8.70] taking spectra at the Co L edges (770–820 eV) [8.66], where the amplitude of the dichroic signal is a measure of the magnetization of the Co wire array and contains information on the local character of the atomic moments.

The spin magnetic moment (m_S) per atom in a Co/Pt (997) monatomic chain is – according to local spin density calculations (see Table 8.1) – increased to 2.08 μ_B compared to the bulk value (1.57 μ_B) or the value for a monolayer (2.03 μ_B). This is due to the narrowing of the Co 3d band in Co/Pt (997) and the corresponding increase in the density of states at the Fermi level. The increase of the orbital

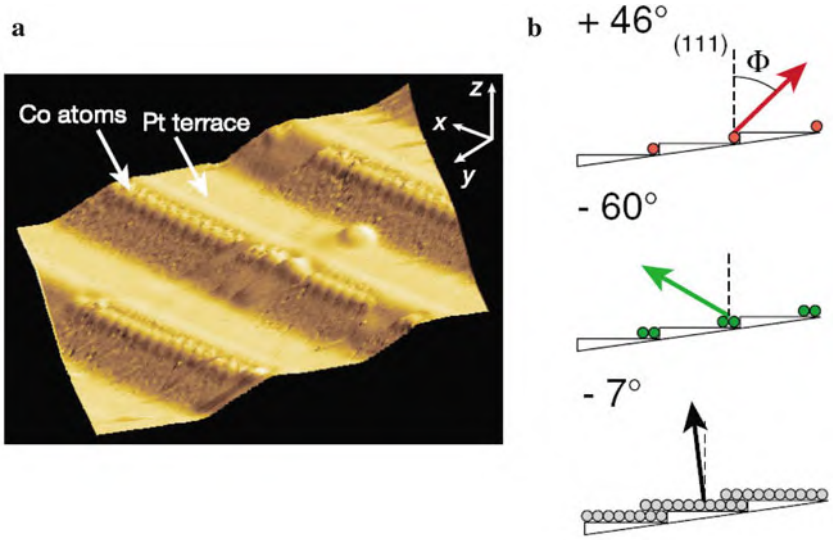

Fig. 8.20 (**a**) STM topograph of the Pt (997) surface with Co monatomic chains decorating the step edges (the vertical dimension is enhanced for better contrast) [8.61]. (**b**) Easy magnetic directions in a plane perpendicular to the chains for (from *top*) monatomic chains ($n = 1$), double chains ($n = 2$), and for a 2D monolayer of Co [8.66]. (Reprinted with permission from [8.61] (**a**) and [8.66] (**b**). © 2002 Nature Publishing Group (**a**) and © 2004 American Physical Society (**b**))

atomic moment per atom (m_L) is expected to be much larger due to the sensitivity to changes in the atomic coordination because of its dependence of the crystal field. From the XMCD studies of monatomic Co/Pt (997) wires a value of $m_L = 0.68\ \mu_B$ per atom is derived [8.61] which is much higher than the Co bulk value (0.14 μ_B) and steeply drops for Co biatomic wires (0.37 μ_B), a value similar to that for a Co monolayer (0.31 μ_B; see Table 8.1).

Short-range magnetic order and therefore significant interatomic magnetic exchange coupling is derived from measurements of the magnetization curves of the Co/Pt (997) monatomic wires at 45 K, although at this temperature long-range ferromagnetic order is absent [8.61]. This behavior is that of a 1D superparamagnetic system composed of spin blocks each containing ca. 15 exchange-coupled Co atoms. In addition, the magnetic anisotropy energy (MAE) of 2.0 meV per Co atom in the Co/Pt (997) monatomic chain can be deduced from the dependence of the superparamagnetic magnetization curve from the direction of the external magnetic field. This MAE value is large compared to bulk h.c.p. Co (50 μeV) or to that of a Co monolayer on Pt (997) (0.14 meV) (see [8.61] and Table 8.1). The high MAE value is directly related [8.71] to the anisotropy of m_L, measured in the easy and hard directions, which is unusually high (0.12 μ_B) for the Co/Pt (997) monatomic chains [8.61].

A transition of the system to a long-range ferromagnetically ordered state is observed below the so-called blocking temperature $T_B = 15$ K [8.61] by the appearance of a hysteretic magnetization curve at 10 K. Below T_B, the magnetization of each spin block is pinned by magnetic anisotropy energy barriers and aligned in the easy axis direction [8.61]. The easy magnetization axis of the Co/Pt (997) monatomic chains is oriented in a plane perpendicular to the chains and 46° off the Pt [111] direction (Fig. 8.20b, upper panel).

The easy magnetization direction and the magnetic anisotropy energy (MAE) of the Co/Pt (997) chains are found to oscillate when the monatomic chain ($n = 1$) is extended to a double chain ($n = 2$), a triple chain ($n = 3$), etc. (see Table 8.2). The easy direction reverses from $\theta = 46°$ (step-up direction) in the monatomic chain to $-60°$ (step-down) for the double wire (see Fig. 8.20b). Simultaneously, a sharp drop of the MAE is found (together with the decrease of m_L; see above) with a

Table 8.2 Oscillations of the easy magnetization axes in the plane perpendicular to the Co chains (see angle θ in Fig. 8.20b) and of the magnetic anisotropy energy (MAE) in dependence of the width n of the Co/Pt (997) chains; experimental [8.66] and theoretical [8.67] data

	$n = 1$	$n = 2$	$n = 3$	$n = 4$	Monolayer
Orientation θ of the easy axis					
– experiment	+46	−60	−45	−61	−7
– theory	+51	−19	−15	−40	
MAE (meV/atom)					
– experiment	2.0	0.33	0.45		0.14
– theory	2.5	0.15	0.99	0.82	

subsequent re-increase. All this behavior in dependence of n is well reproduced by ab initio theory [8.67]. The oscillation of the MAE from a decrease of the initially high value (at $n = 1$) to the low value of the double chain ($n = 2$) originates – according to ab initio theory [8.67] – from the contributions of the two strands which nearly cancel each other. When the number of strands exceeds $n = 2$, the two outer strands still compensate each other, but the contribution of the remaining strands now gives rise to a larger MAE.

8.2.3.2 Magnetic Domain Walls in Nanowires

The structure of ferromagnetic domains on the nanoscale are of importance, e.g., for data storage media. Nanostructure domain walls have been studied experimentally and theoretically in iron nanowires on tungsten substrates [8.68, 8.72, 8.73].

The magnetic domain structure of Fe nanowires (20 nm wide, two atomic layers thick) on a (110) tungsten substrate as studied with high resolution by spin-sensitive scanning tunneling microscopy (see [8.72]) shows domain walls (thickness ~ 7 nm) preferentially along $[1\bar{1}0]$ as dark stripes (see Fig. 8.21a). This anisotropic behavior

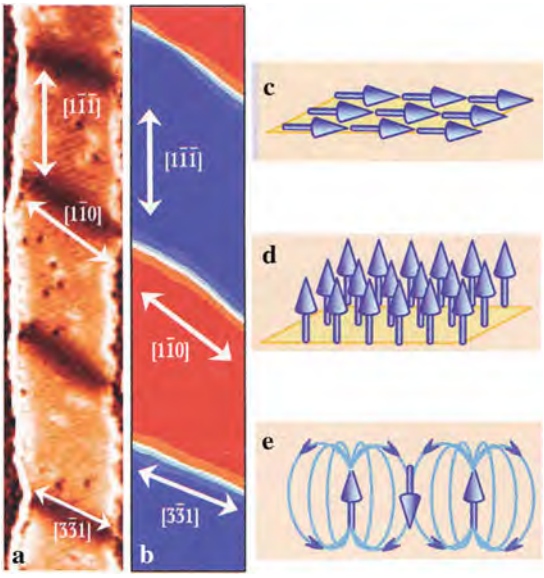

Fig. 8.21 (**a**) Experimental study and (**b**) simulation (see text) of 20 nm wide Fe nanowires with a thickness of two monolayers on a W (110) substrate with the domain walls (**a** – *dark*, **b** – *white*) along $[1\bar{1}0]$ directions. (**c**, **d**) Models of ferromagnetic coupling in a thin film with two different magnetic crystal anisotropy energies: (**c**) In-plane configuration, (**d**) perpendicular configuration. (**e**) Dipole interaction showing the coupling of the central magnetic moment with the adjacent moments via the dipole fields. (Reprinted with permission from [8.73]. © 2005 Wiley-VCH)

of the domain walls has been modeled by Monte Carlo simulations taking into account the bcc lattice structure of iron and making use of the Hamiltonian

$$H = -\sum_{<ij>} \boldsymbol{J}_{[xyz]} \boldsymbol{S}_i \cdot \boldsymbol{S}_j + K_1 \sum_i \sin^2\theta + D \sum_{ij} \left(\frac{\boldsymbol{S}_i \cdot \boldsymbol{S}_j}{r_{ij}^3} - 3\frac{(\boldsymbol{S}_i \cdot r_{ij})(\boldsymbol{S}_j \cdot r_{ij})}{r_{ij}^5} \right).$$

Here, the $\boldsymbol{S}_i$, $\boldsymbol{S}_j$ are the 3D magnetic moments, $\boldsymbol{J}_{[xyz]}$ the magnetic exchange interaction, D the dipole energy coupling constant, K_1 the constant of the magnetocrystalline anisotropy which is oriented perpendicular to the surface, and $\boldsymbol{r}_{ij}$ the distance between the lattice sites i and j. The magnetic exchange interaction, based on Pauli's principle, gives rise to the parallel orientation of neighboring magnetic moments in a ferromagnet. The magnetocrystalline anisotropy determines the crystallographic direction of the magnetization in zero external field where the configurations in Fig. 8.21c, d represent different anisotropy energies. The dipole interaction accounts for the coupling of a magnetic moment with the fields of all other moments (Fig. 8.21e). The difference between the dipole energy of the in-plane magnetization (Fig. 8.21c; low-energy configuration) and of the high-energy perpendicular magnetization (Fig. 8.21d) is called shape anisotropy.

The calculations show that the magnetic exchange energy for a bcc film with a (110) surface is minimized when the domain walls are oriented along the $[1\bar{1}0]$ directions (Fig. 8.21b), as observed experimentally (Fig. 8.21a).

8.2.3.3 Magnetization Behavior of Fe Nanowires in Carbon Nanotubes

Arrays of Fe nanowires inside carbon nanotubes – where they are prevented from oxidation – (see Fig. 8.22a) exhibit high magnetic coercivities and therefore could be used as high-density magnetic storage media with, e.g., an individual wire corresponding to an information bit. The hysteresis loop in an external field parallel to the wires exhibits step-like sudden changes (Fig. 8.22c), whereas a smoother hysteresis loop is found in a perpendicular field (Fig. 8.22d). The sudden changes are attributed to particular spin configurations due to the presence of strong dipolar interactions among the closely packed nanowires [8.74].

The spin configurations in dependence of the external field were calculated (see Fig. 8.23) making use of a Heisenberg Hamiltonian including ferromagnetic exchange coupling, dipole–dipole interaction, and the external magnetic field [8.69]. In fact, the calculations initially show a canted spin configuration (Fig. 8.23a) that starts to change abruptly in a parallel external field (Fig. 8.23d) – similar to the experimental hysteresis curve – promoting the creation of helical vortices (Fig. 8.23b). For magnetization in a perpendicular field a flowerlike configuration is calculated initially (Fig. 8.23e) that transforms into a frustrated helical vortex state when the field is increased (Fig. 8.23f). The hysteresis loop calculated for the case of a perpendicular field is relatively smooth (Fig. 8.23h), similar to the experimental behavior.

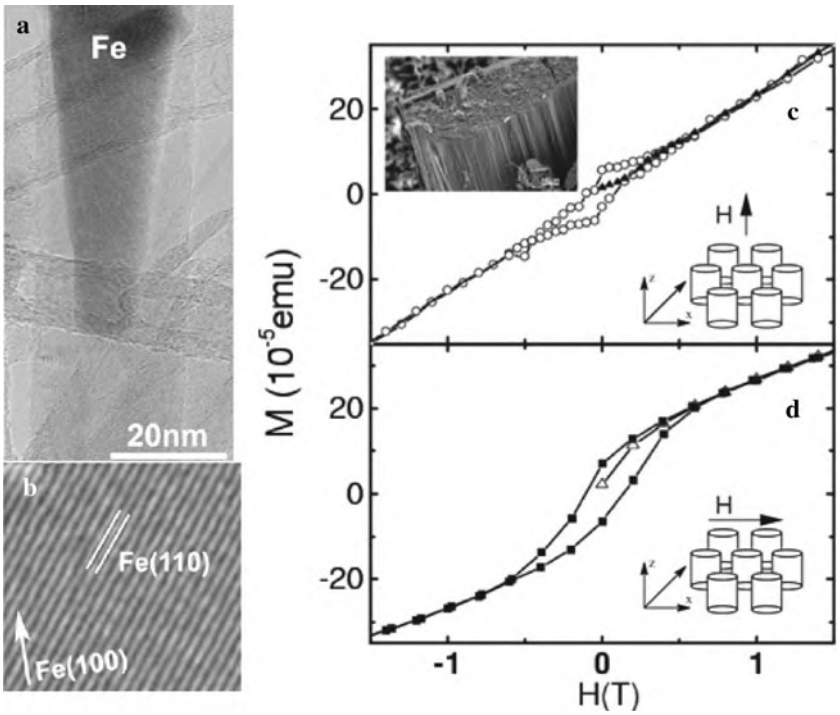

Fig. 8.22 (**a**) High-resolution transmission electron micrograph (HRTEM) of a carbon nanotube filled with a relatively short Fe nanowire (< 60 nm); (**b**) HRTEM of the monocrystalline Fe nanowire with the Fe (100) plane parallel to the nanotube axis. (**c**, **d**) Hysteresis loops measured at 1.8 K for a carpet (see *inset*) of Fe nanowires encapsulated inside carbon nanotubes with the magnetic field applied (**c**) parallel and (**d**) perpendicular to the nanowires. When the applied magnetic field is parallel to the wires, the hysteresis loop exhibits steps (**c**) which are absent in the case of a perpendicular field (**d**). (Reprinted with permission from [8.69]. © 2005 American Physical Society)

In order to obtain high magnetic storage densities in the Tbin/in^2 range, close-packed pellet-like 2D nanowire arrays with wire aspect ratios between 0.5 and 1.5 are suggested [8.69].

8.2.4 Magnetic Films (2D)

Whereas in monatomic Co wires on Pt the preferred magnetization direction is perpendicular to the wire axis but closer to the substrate surface, the magnetization axis in complete Co films reorients gradually toward the out-of-plane direction (Table 8.2). Complete Fe and Co monolayers have an easy axis close to the sample normal (see [8.49]). In the thickness range between 0.5 and 5 atomic Fe layers on Pt (997), the easy magnetization axis reorients from the perpendicular direction into

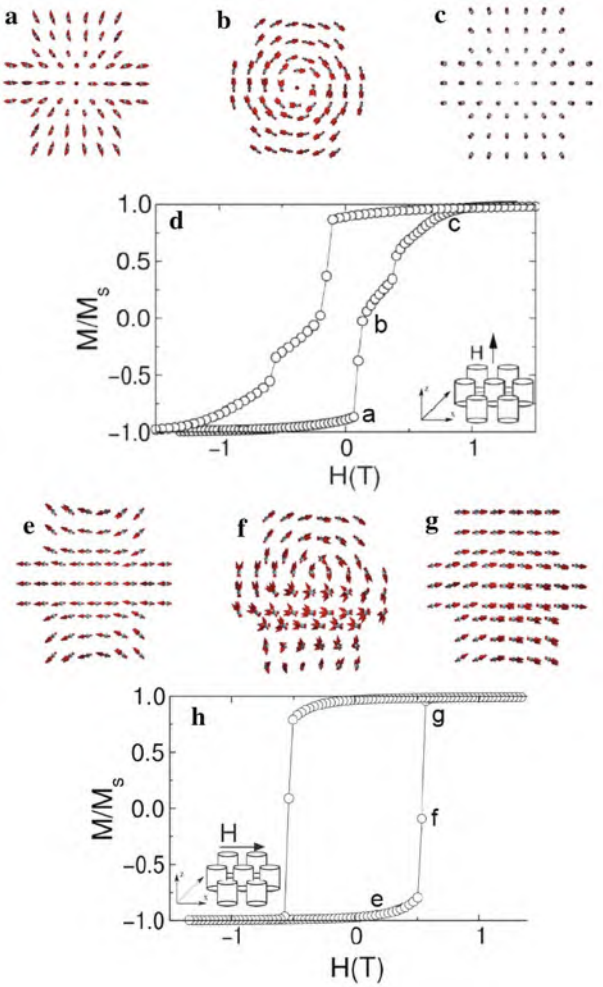

Fig. 8.23 Hysteresis loop simulations for a hexagonal array of nanowires in carbon nanotubes with an interwire distance of 0.72 nm. (**a**–**c**) Spin configurations in a wire depending on the external field parallel to the wires (see hysteresis curve in (**d**)); (**e**–**g**) spin configurations of a wire depending on the external field perpendicular to the wires (see hysteresis curve in (**h**)). (Reprinted with permission from [8.69]. © 2005 American Physical Society)

the film plane at 2.6–3 monolayers (see Fig. 8.24a), accompanied by a structural transition from fcc (111) to bcc (110) of the Fe film. Above a three-monolayer coverage the easy axis is oriented in-plane with a hard axis along the substrate steps.

A key role for the surface magnetic structures is played by the supporting substrate. Pt is found to contribute to the nanostructure's MAE via strong electronic hybridization with the consequence of induced magnetization in Pt.

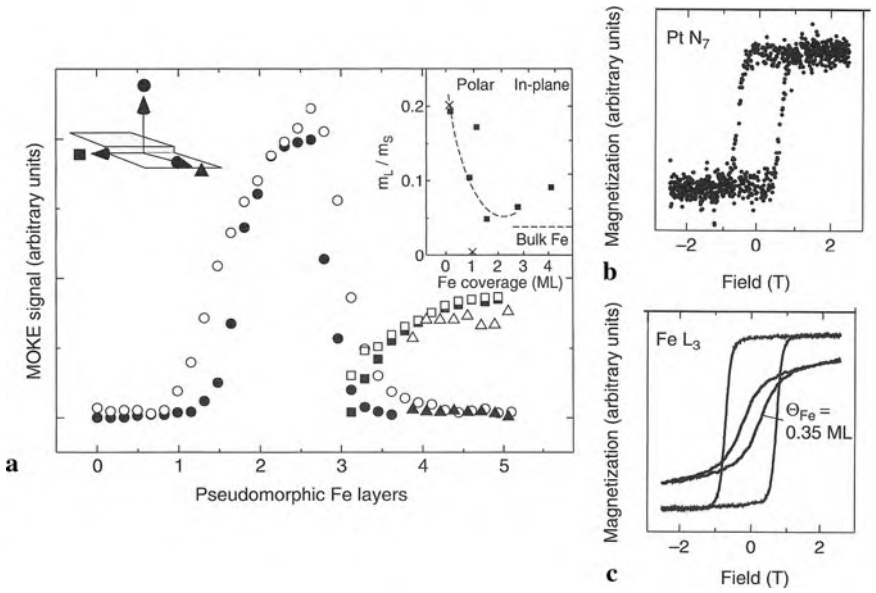

Fig. 8.24 (**a**) Evolution of the easy magnetization axis for 2D Fe films on Pt substrates with Fe coverage. *Open* and *solid symbols* correspond to the saturation and the remanent magnetization as obtained from magneto-optical Kerr effect (MOKE) hysteresis loops at 300 K. A magnetization reorientation from perpendicular to in-plane direction is observed at the critical thickness of $t_{crit} = 2.8$ atomic layers. Above t_{crit} the films show pronounced in-plane anisotropy with the easy axis along the step edges. *Inset*: For films thinner than one atomic layer the ratio m_L/m_S (from XMCD measurements) increases in favor of larger m_L values, in qualitative agreement with calculations (*x*, from [8.75]). (**b**), (**c**) XMCD dichroic signals to obtain element-specific hysteresis loops of the Fe and the Pt sublattices in a $Fe_{50}Pt_{50}$ surface alloy layer. The hysteresis loop of the Fe sublattice is compared to the FeL_3 loop of a diluted $Fe_{35}Pt_{65}$ monolayer. (Reprinted with permission from [8.49]. © 2007 Wiley Interscience)

Films of the intermetallic compound FePt with an $L1_0$ structure and a high magnetocrystalline anisotropy energy (MAE) of >1 meV per atom are considered for upcoming high-density storage media [8.75]. The exchange interaction between Fe atoms across adjacent fcc (100) layers, and hence the 3D nature of the alloy, is considered to be important for a large MAE. A key role is played by the induced magnetism in Pt which gives additional MAE contributions due to its large spin–orbit interaction (see [8.49]). The tetragonal $L1_0$ lattice distortion and chemical disorder give access not only to the magnetic anisotropy energy but also to the Curie temperature T_C, the exchange interaction J, or the saturation magnetization M_S. The coordination of Fe with Pt atoms in monolayer thin films increases the MAE so that values close to bulk FePt could be measured (see [8.49] and Table 8.1). The element specificity of XMCD is ideal for probing the magnetism of the Fe and Pt sublattices separately with a large dichroic signal at both the Fe $L_{3,2}$ and the Pt $N_{7,6}$ absorption edges, making visible congruent magnetization loops for Fe and Pt (Fig. 8.24b, c). The presence of a dichroic signal for Pt is the result of an induced magnetic moment

due to the hybridization between Fe 3d and Pt 5d electron states. The existence of a magnetic moment in Pt evidences ferromagnetic coupling between the Fe chains. In a simple picture the Fe atoms act as the source of magnetization, whereas the Pt sublattice, owing to its large spin–orbit interaction, provides the main contribution to the large MAE [8.49]. Reducing the Fe concentration by only 30% results in S-shaped hysteresis loops with a remanence reduced by 78% and the coercivity reduced by 68% (Fig. 8.24c).

8.2.5 *Curie Temperature* T_C *in Dependence of Size, Dimensionality, and Charging*

In ferromagnetic structures the ferromagnetic ordering temperature T_C (Curie temperature) is determined by the strong, short-range spin exchange interaction, and the disordering by the lattice thermal vibrations (see [8.76]). In nanostructures on inert substrates (moderate interaction), there exist different degrees of spin–spin interactions between inner and surface atoms because of the reduction in the number of spin interactions at the surface which leads to an increase of lattice vibrations and a decrease of T_C with decreasing particles size D (see Fig. 8.25a, b). For increasing dimensionalities d of nanoparticles ($d = 0$ for nanocrystals, $d = 1$ for nanorods, and $d = 2$ for films), the surface-to-volume ratios decreases and the decrease of T_C (D) is shifted to lower D values (see Fig. 8.25b).

When in modeling the effects induced by the surface and the interface on T_C (D) are assumed to be additive, then the relationship

$$T_C(D)/T_C(\infty) = \left\{\exp\left[-(\alpha_s - 1)/(D/D_0 - 1)\right] + \exp\left[-(\alpha_i - 1)/(D/D_0 - 1)\right]\right\}/2$$

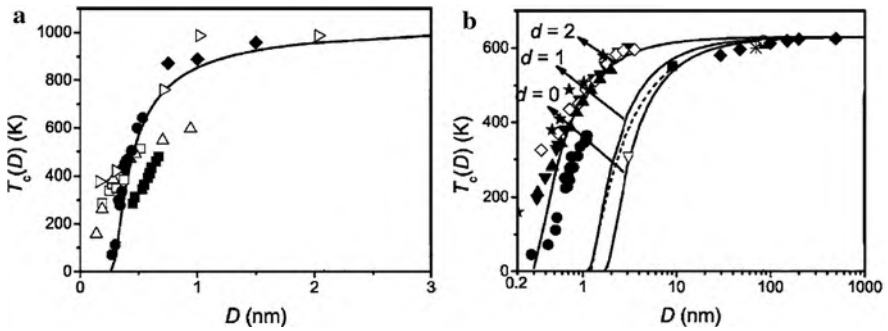

Fig. 8.25 (**a**) Comparison of the calculated dependence of the Curie temperature $T_C(D)$ on the thickness D of Fe films on a substrate (*solid line*; see relationship in the text) with experimental data; for references see [8.76]. (**b**) Calculations (*solid lines*) of $T_C(D)$ for Ni nanoparticles (dimensionality $d = 0$), nanorods ($d = 1$), and thin films ($d = 2$). The decrease of T_C with decreasing particle size D shifts to lower D values when going from nanocrystals ($d = 0$) to films ($d = 2$) due to the decrease of the surface-to-volume ratio. (Reprinted with permission from [8.76]. © 2006 American Physical Society)

is obtained [8.76]. Here, $T_C(\infty)$ is the bulk Curie temperature and α_s or α_i are characterized by the root mean square (rms) thermal average amplitudes of atomic vibrations at the surface or at the interface, respectively, and are coupled by $\alpha_i = \alpha_s J_s/J_i$, where J_s and J_i are the corresponding magnetic exchange coupling constants [8.76]. The quantity $D_0 = 2(3-d)h$ contains the dimensionality d and the atomic diameter h. The above model function can nicely describe the variation of T_C with D (Fig. 8.25a) and with d (Fig. 8.25b).

The Curie temperature T_C may increase with decreasing D when the interaction at a film/substrate interface is strong [8.76].

8.2.5.1 Control of T_C by Surface Charges

The Curie temperature T_C of the transition metals Ni, Co, and Fe depends on the surface charge σ according to theoretical studies based on the Ginzburg–Landau functional and ab initio data [8.77]. By a typical electric saturation polarization of lead zirconate titanate (PZT) ($\sigma \approx 30\ \mu C/cm^2$) on $D = 2$-nm thick films of Ni[001], Co[0001], or Fe [001], T_C shifts ΔT_C of (13.6, 7.9, 6.9) K or (19.1, 7.0, 4.7) K are predicted for the in- or out-of-plane magnetic orderings, respectively [8.77]. A similar $\Delta T_C = 20$ K has been found experimentally [8.78] for a PZT contact on a 4-nm wide layer of the ferromagnetic oxide LaSrMnO with a density of free carriers almost at the metallic level (10^{21} cm^{-3}). Additionally, the magnetic properties of nanostructured metals, such as the magnetic anisotropy or the magnetization, can be controlled by electric fields (see Sect. 6.12).

8.3 Soft-Magnetic Materials

When in a nanocrystalline ferromagnet the crystallite size D is smaller than the ferromagnetic correlation length $L_0 = \varphi\sqrt{A/K_1}$ (typically 5–40 nm), where A is the ferromagnetic exchange stiffness, K_1 the local magnetocrystalline anisotropy constant and, $\varphi \approx 1$, an extremely soft-magnetic behavior with low values of the coercivity $H_c = 0.4$ Am^{-1} and high values of the initial permeability $\mu_i = 1.1 \cdot 10^5$ may be observed (see [8.79]). In these nanocrystalline soft magnets, the coercivity shows a D^6 dependence of the crystallite size D whereas for conventional polycrystalline ferromagnets a *1/D* law applies (Fig. 8.26a). The key to understanding the soft-magnetic properties in nanocrystalline materials is the nanostructure with a distribution of magnetic anisotropy axes with random orientations on a scale smaller than the ferromagnetic correlation length L_0 (Fig. 8.26b). The smoothing of these anisotropies by the ferromagnetic exchange interaction across the amorphous interfaces, however, impedes the magnetization to follow the easy axes of the individual grains. The effective anisotropy constant for the magnetization process will, therefore, be an average over several grains and, hence, is strongly reduced in magnitude (random anisotropy model, see [8.79]), yielding the average anisotropy constant $< K_1 >= K_1 \cdot (D/L_0)^6$. This is essentially different from coarse-grained materials where the magnetization follows the randomly oriented easy axes of the

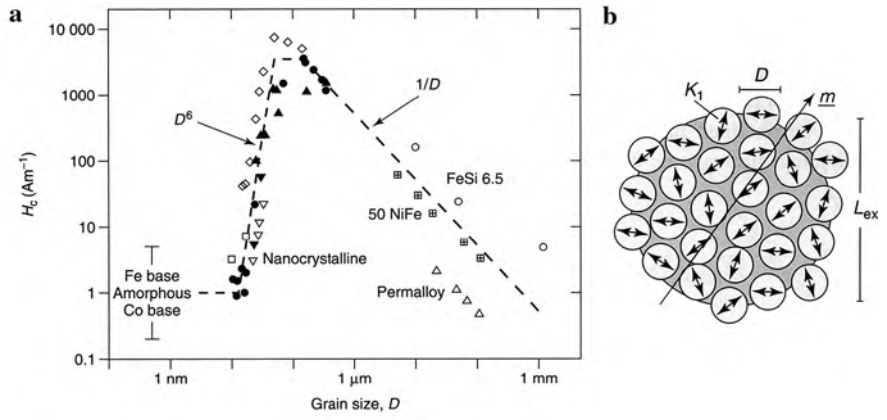

Fig. 8.26 (**a**) Coercivity, H_c, versus grain size, D, for various soft-magnetic metallic alloys: Fe–Nb–Si–B (▲), Fe–Cu–Nb–Si–B (●), Fe–Cu–V–Si–B (▼, ▽), Fe–Zr–B (□), Fe–Co–Zr (◊), NiFe alloys (⊞, △), and Fe Si 6.5 wt% (○). For reference see [8.79]. (**b**) Schematic representation of the random anisotropy model for grains embedded in an ideally soft ferromagnetic matrix. The double *arrows* indicate the randomly fluctuating anisotropy axes, the hatched area represents the ferromagnetic correlation volume determined by the exchange length L_{ex} within which the orientation of the magnetization is constant. (Reprinted with permission from [8.79]. © 2007 Wiley Interscience)

various grains and, accordingly, the magnetization process is controlled by full local magnetocrystalline anisotropy.

For pure random anisotropies averaged out by exchange interaction and no other types of anisotropy, the coercivity is given within the framework of the random anisotropy model [8.79] by $H_c = p_c < K > /J_S$ and the permeability by $\mu_i = p_\mu J_s^2/(\mu_0 < K >)$ where J_s is the average saturation magnetization and p_c and p_μ are prefactors of the order of unity. Accordingly, coercivity and permeability are expected to vary with grain size as $H_c \propto D^6$ and $\mu_i \propto D^{-6}$ which coincides with the experimental observation at small grain sizes (Fig. 8.26a).

Soft-magnetic nanocrystalline materials with FeSi crystallites of a diameter of ∼12 nm in an amorphous Fe–Si–B matrix (Fig. 8.27a) can be preferentially prepared by annealing the amorphous alloy $Fe_{73.5}Si_{13.5}B_9Nb_3Cu_1$ at temperatures between 500 and 600°C [8.80]. Iron yields the highest saturation magnetization, copper provides by the formation of Cu-rich clusters [8.82] (see Sect. 2.8) a high density of nucleation sites, Si and B are the glass formers, and Nb stabilizes the amorphous matrix.

For application, the hysteresis loop of these nanocrystalline soft-magnetic materials can be widely modified by magnetic field annealing or tensile stress axial anisotropy with the induced anisotropy energy constant, K_u (see [8.79]). The anisotropy formation is related to atomic ordering along the direction of the local magnetization in order to minimize the spin–orbit coupling energy [8.83]. Highest permeabilities can be achieved with rectangular hysteresis loops. Since the domain

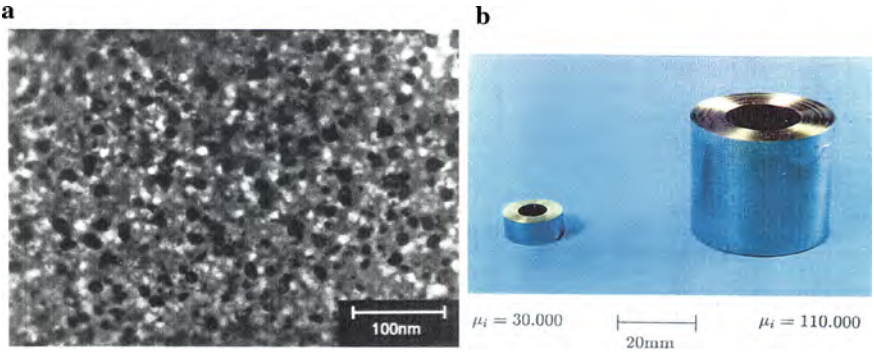

Fig. 8.27 (**a**) Transmission electron micrograph of nanocrystalline $Fe_{73.5}Si_{13.5}B_9Nb_3Cu_1$ after crystallization at 540°C [8.81]. (**b**) Toroidal strip wound magnetic cores of nanocrystalline Fe–Si–B–Nb–Cu (VITROPERM; courtesy of G. Herzer, Vacuumschmelze, D-63412 Hanau, Germany).

wall energy is proportional to $\sqrt{K_u}$, low induced anisotropies facilitate domain refinement which results in good dynamic properties such as reduced anomalous eddy current losses (see [8.79]). In addition, high electrical resistivities ($\sim$ 115 $\mu\Omega$ cm) minimize the eddy current losses in nanocrystalline ribbons. Consequently the frequency dependence of the permeability and the core losses of nanocrystalline Fe–Si–B–Nb–Cu are comparable to those of amorphous Co-based alloys and surpass by far that of conventional ferrites up to frequencies of several 100 kHz. Magnetoelastic anisotropies $K_\sigma = -\frac{3}{2}\lambda_s\sigma$, where λ_s is the saturation magnetostriction and σ the mechanical stress, are low or negligible in the Fe–Si–B–Nb–Cu nanocrystalline alloys because of the mutual compensation of the magnetostrictions of the nanocrystalline and the amorphous phases to near-zero magnetostriction. This gives rise to an insensitivity to stresses which is a basic requirement for excellent soft-magnetic properties.

Due to their high technical performance and the inexpensive raw materials Fe and Si, the above nanocrystalline soft-magnetic materials exhibit an increasing level of application in magnetic cores for ground fault interrupters, common mode chokes, and high-frequency transformers. The worldwide production rate meanwhile approaches $\sim$ 1,000 tons/year (see [8.79]).

8.4 Nanostructured Hard Magnets

With decreasing particle size, the coercivity initially increases (Fig. 8.26). For very small crystallites the intergranular exchange interaction can be strong enough to "pull" the magnetization of the adjacent crystallites together [8.84–8.86]. This "remanence enhancement" phenomenon is often used in nanocrystalline permanent (hard) magnets and – due to their excellent hard-magnetic properties – the exchange

coupled rare-earth nanocrystalline magnets are sometimes referred to as the "next-generation permanent magnets" [8.85]. If the magnet consists of two nanophases with different magnetic properties as, e.g., α-Fe providing a high magnetization and $Nd_2Fe_{14}B$ with the high magnetocrystalline anisotropy causing a high coercitivity H_c, the "exchange coupling" of nanoparticles with a diameter less than 10 nm [8.87] allows us to benefit from the combination of both properties in advanced hard magnets, a phenomenon which was discovered in melt-spun Nd–Fe–B alloys [8.88] and subsequently modeled [8.89, 8.90]. In the following the synthesis and the properties of nanocrystalline hard magnets will be discussed with respect to recent development in high coercivity H_c, high remanence J_r, and the maximum energy product $(BH)_{max}$ (Fig. 8.28). The energy product is the maximum magnetostatic energy that would be stored in the free space between the pole pieces made of the permanent magnetic material in question, with a theoretical upper bound of 1146 kJ/m^3 [8.91].

Nanocrystalline permanent magnets can be prepared by rapid solidification and annealing (see [8.85, 8.92]), by mechanical alloying [8.93], or by severe plastic deformation [8.94]. For the processing of nanocrystalline hard magnets such as *n*-$Nd_2Fe_{14}B$, the atomic diffusion processes are of interest where the diffusivities of ^{59}Fe [8.95] and of ^{147}Nd [8.96] have been reported.

Single-phase ribbons of nanocrystalline $Nd_2Fe_{14}B$ and of $Pr_2Fe_{14}B$ and also two-phase α-Fe/$Nd_2Fe_{14}B$ or α-Fe/$Pr_2Fe_{14}B$ materials with good hard-magnetic properties were reported (see Table 8.3). Gallium substitution for Fe in the α-Fe/$R_2Fe_{14}B$ type (R – rare earth metal) nanocomposite magnet $Pr_9Fe_{74}Co_{12}GaB_5$ (Table 8.3) leads to an improvement of the magnetic properties compared to the Ga-free specimens due to microstructure refinement. After die-upsetting

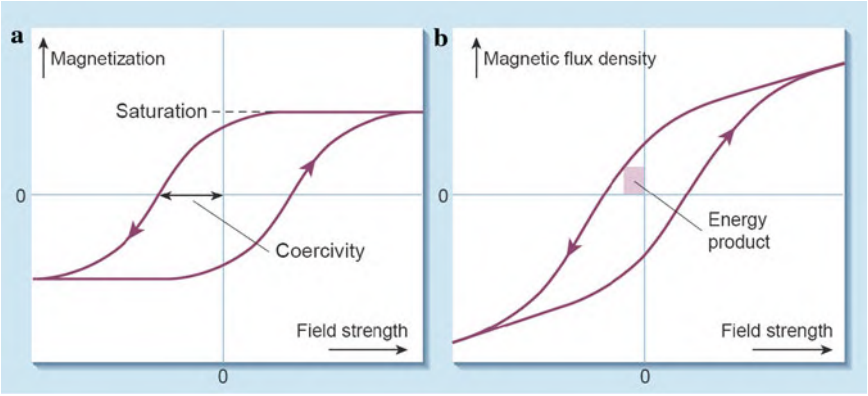

Fig. 8.28 Typical hysteresis loops for a permanent magnet showing the magnetization (**a**) and the magnetic induction or flux density (**b**) in dependence of the field strength with the coercivity and the energy product indicated. (Reprinted with permission from [8.91]. © 2002 Nature Publishing Group)

Table 8.3 Particle diameter D, coercivity H_c, remanence J_r, and energy product $(BH)_{max}$ of some nanostructured magnetically hard compounds

	D (nm)	H_C (MAm^{-1})	J_r (T)	$(BH)_{max}$ (kJm^{-3})	References
$Nd_2Fe_{14}B$		0.96		150	[8.97]
$Pr_2Fe_{14}B$		0.95	1.42	181	[8.98]
α-Fe/$Nd_2Fe_{14}B$	10	0.485	10	160	[8.99]
α-Fe/$Pr_2Fe_{14}B$				181	[8.98]
$Pr_9Fe_{74}Co_{12}GaB_5$			1.22	178	[8.100]
α-Fe/(Nd, Pr, Dy)$_2Fe_{14}B$	150			336	[8.101]
$Nd_{13.5}(Fe_{0.975}Co_{0.025})_{80}Ga_{0.5}B_6$	100	1.05		433	[8.102]
Sm_2Co_{17}				240	[8.85]
α-Fe/Sm_2(Fe, Si)$_{17}C_x$	12			199	[8.104]

(strong plastic deformation at about 1,000°C), α-Fe/(Nd, Pr, Dy)$_2Fe_{14}B$ and $Nd_{13.5}(Fe_{0.975}Co_{0.025})_{80}Ga_{0.5}B_6$ exhibit very high $(BH)_{max}$ values (Table 8.3).

The Sm_2Co_{17}, or briefly 2:17, magnets are attractive due to their temperature stability and good corrosion resistance, but rather expensive. They consist of 70-nm cells of rhombohedral Sm_2Co_{17} (2:17R) surrounded by $SmCo_5$ (1:5) layers (Fig. 8.29a, b). Although the 2:17 magnets exhibit a high energy product of 240 kJ/m^3 at ambient temperature (see [8.85] they hardly can compete with the less expensive Nb–Fe–B magnets. The predominant magnetization reversal model suggests for the 2:17 Sm–Co magnets domain wall pinning at the waved cell boundaries (Fig. 8.29c) owing to a large gradient of domain wall energy (see [8.85]).

Modifications of the R_2Fe_{17} compounds by interstitial atoms are well known to dramatically change the magnetic properties [8.103]. Owing to a lattice expansion caused by the solution of interstitial nitrogen or carbon, the Curie temperature and the saturation magnetization increase significantly, yielding, e.g., in nanocrystalline α-Fe/Sm_2(Fe, Si)$_{17}$ C_x high $(BH)_{max}$ values (see Table 8.3).

8.5 Antiferromagnetic and Complex Magnetic Nanostructures

While the ferromagnetic state of surfaces is accessible by various surface-sensitive techniques, it is more challenging to image the antiferromagnetic (AFM) behavior of surfaces [8.110], such as the surface of the bulk AFM NiO (see Fig. 8.2) or AFM Mn monolayers on W (001) (see Sects. 2.5 and 8.1). Here, recent investigations of domain walls in AFM monolayers [8.105] as well as the properties of AFM monatomic chains [8.106, 8.107] and of nanocrystalline AFMs [8.108] will be discussed with a subsequent outline of the complex magnetic structure of Fe monolayers on Ir (111) [8.110] with antiferromagnetic coupling.

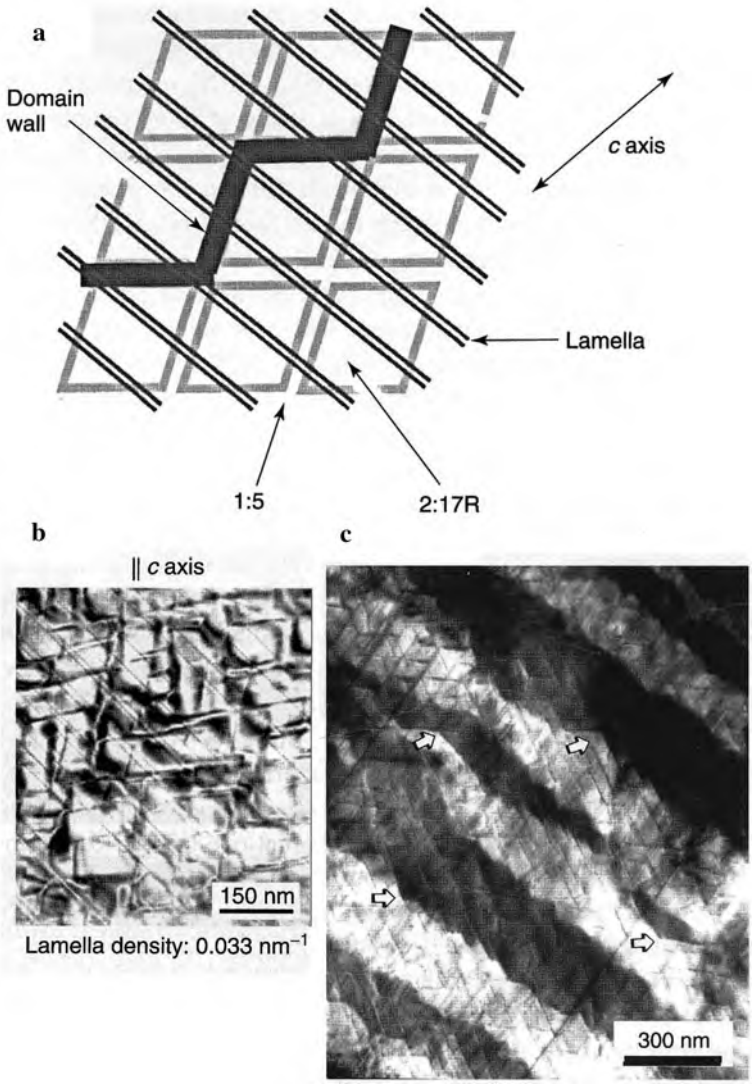

Fig. 8.29 (**a**) Schematic representation of the microstructure in 2:17 Sm–Co magnets. (**b**) Typical cellular and lamellar microstructure in 2:17 Sm–Co magnets parallel to the *c*-axis. (**c**) Typical magnetic domain structure in the 2:17 Sm–Co magnets; Foucault mode of Lorentz microscopy for imaging. (Reprinted with permission from [8.85]. © 2007 Wiley Interscience)

8.5.1 Spin Structure of Antiferromagnetic Domain Walls

Antiferromagnetic surfaces play an important role in information technology as they are used to pin the magnetization direction of bistable thin ferromagnetic films by the exchange bias (EB) effect in spin valves (see Sect. 1.4) and in magnetic storage devices (see [8.105]). Only a few uncompensated spins are thought to contribute to the effect. Uncompensated moments of phase domain walls in antiferromagnetic surfaces – in addition to moments that arise from known sources as grain size, step edges, and non-magnetic defect sites (see [8.105]) – may contribute to EB.

Domain walls were studied by spin-polarized scanning tunneling microscopy (SP-STM) in the perpendicular antiferromagnet of a Fe monolayer on W (001) where the magnetic moments of nearest-neighbor atoms are pointing alternately up and down (see Fig. 8.30b, inset). Segments of a phase domain wall (p-DW) are shown in Fig. 8.30c. In the p-DW (Fig. 8.30a) the phase of the magnetic lattice shifts at the position of the wall by one atomic site. Within the p-DW, which is only a few lattice sites wide (Fig. 8.30c), the magnetic signal appears to be rather blurred because here the magnetic moments of the tip and the sample are orthogonal. According to Monte Carlo (MC) simulations, the [110]-oriented p-DWs carry a finite perpendicular magnetic moment of about 0.6 μ_B per nm DW length. As sketched in Fig. 8.30 the wall is 6–8 atomic rows wide and Bloch-like; the in-plane component of rows 4 and 5 is already very small. In Fig. 8.30e and f calculated and experimental SP-STM images of such a wall are shown.

8.5.2 Antiferromagnetic Monatomic Chains

In monatomic chains of manganese atoms on an insulating CuN layer on Cu (100), the ground-state spin of the chain can be determined by measuring the conductivity dI/dU in inelastic tunneling spectroscopy by means of a scanning tunneling microscope (Fig. 8.31a). The alternation of the ground-state spin between zero for even-length chains (2, 4, 6, 8, 10 Mn atoms) and non-zero values for odd-length chains (1, 3, 5, 7, 9 Mn atoms) indicates antiferromagnetic coupling between the atomic spins (Fig. 8.31b). Theoretical studies [8.107] by means of the Korringa–Kohn–Rostoker (KKR) Green function method based on density functional theory (DFT) and local spin density approximation (LSDA) show that even-numbered antiferromagnetic Mn chains on Ni (001) exhibit a non-collinear structure whereas odd-atom chains have a collinear ferromagnetic structure.

8.5.3 Antiferromagnetic Nanoparticles

Nanoparticles of antiferromagnetic materials may have applications in new types of hard-magnetic materials consisting of composites of antiferromagnetic and ferromagnetic nanoparticles (see [8.108]). In the following, the properties and the

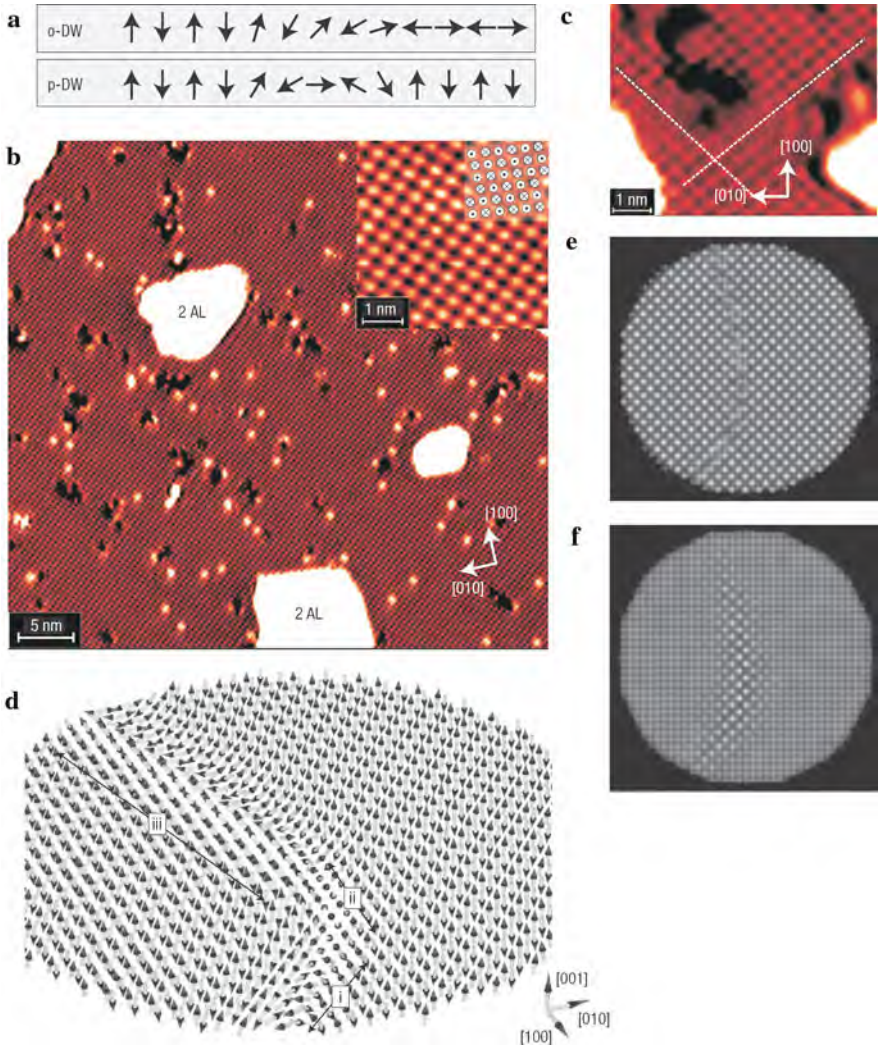

Fig. 8.30 Schematic representation of domain walls (DWs) at antiferromagnetic surfaces, experimental observations, and theoretical spin structure. (**a**) Scheme of an orientational domain wall (o-DW) and a phase domain wall (p-DW). (**b**) Spin-polarized scanning tunneling micrograph (SP-STM) of a 1.1 Fe monolayer on W (001). The antiferromagnetic structure (higher resolution in the *inset*) exhibits long-range periodicity without any DWs. (**c**) p-DWs (*dashed lines*) at higher defect densities (double-layer islands). (**d**) Theoretical spin structure of a <110>-oriented p-DW. (**e**) Simulated and (**f**) experimental SP-STM image of a p-DW in the out-of-plane antiferromagnetic Fe monolayer on W (001). (Reprinted with permission from [8.105]. © 2006 Nature Publishing Group)

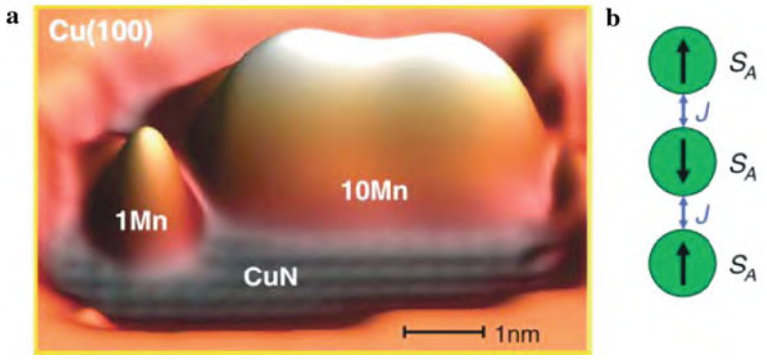

Fig. 8.31 Mn chains on CuN. (**a**) Scanning tunneling micrograph (STM) perspective rendering of a chain of 10 Mn atoms. The observed double-peak structure suggests the existence of 1D delocalized electronic states as seen in metallic chains constructed on metal surfaces (see [8.106]). (**b**) Schematic of the antiferromagnetic coupling of three atomic spins described by the Heisenberg model [8.106]. (Reprinted with permission from [8.106]. © 2007 Institute of Physics)

interaction of antiferromagnetic nanoparticles will be discussed which can be studied by magnetization measurements, by Mössbauer spectroscopy, or by neutron scattering.

In contrast to bulk antiferromagnets with a zero magnetic moment, nanocrystalline antiferromagnets have a non-zero magnetic moment because of imperfections or finite size effects. Nanoparticles of antiferromagnetic NiO exhibit spin canting and a reduction of the antiferromagnetic ordering temperature (Néel temperature – T_N). From neutron diffraction data it has been deduced that 15 nm hematite (α-Fe_2O_3) nanoparticles are single domain particles. In bulk α-Fe_2O_3, the sublattice magnetization changes at the Morin temperature $T_M \approx 263$ K from a direction in the (001) plane to the hexagonal [001] direction because of a change of sign of the magnetocrystalline anisotropy constant, K. In nanocrystalline α-Fe_2O_3, however, T_M decreases with decreasing particle size and disappears for sizes below 20 nm because of a size-dependent K (see [8.108]). The magnetization of NiO nanoparticles appears to be proportional to $N^{1/3}$, where N is the total number of spins in a particle, which has been theoretically suggested for a random occupation of surface sites (see [8.108]). From temperature-dependent measurements, values of the magnetic anisotropy constant K can be derived for ferritin, an iron storage protein with an antiferromagnetic 8-nm iron oxyhydroxite core ($K = 25$ kJ/m^3) [8.109], and for α-Fe_2O_3 nanoparticles ($K \approx 4$ kJ/m^3) (see [8.108]).

Uncoated antiferromagnetic α-Fe_2O_3 nanoparticles show a strong interaction as shown in their Mössbauer spectra (Fig. 8.32) as compared to the spectra of coated, weakly interacting particles. In the weakly interacting particles, the low-temperature Mössbauer sextet disappears at 240 K which is characteristic for fast superparamagnetic relaxation above this temperature. In contrast to that, the sextet is maintained

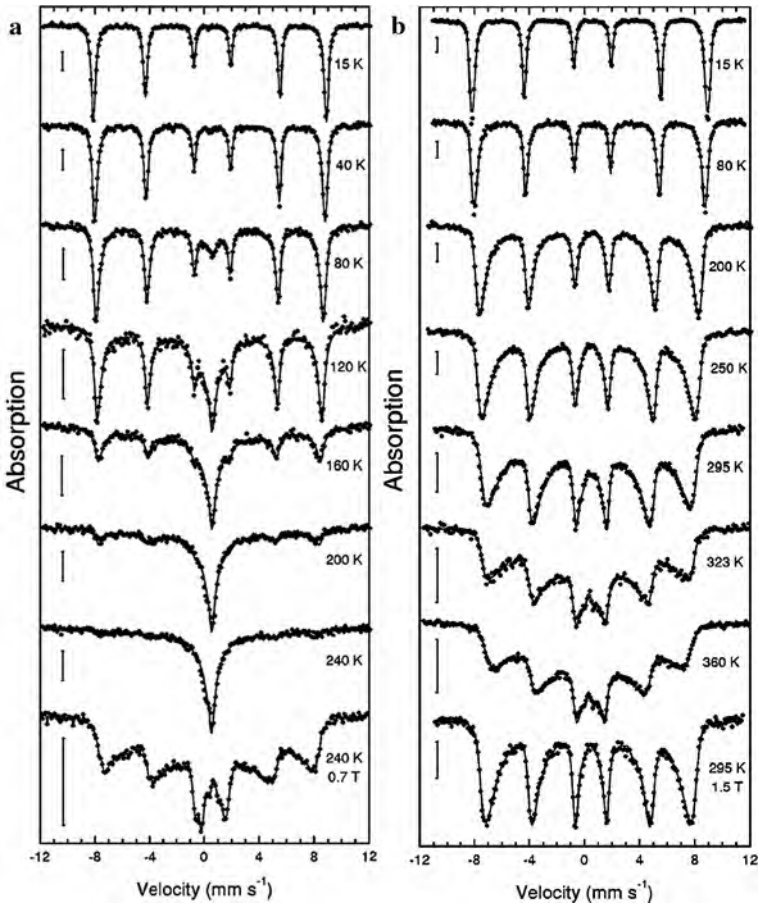

Fig. 8.32 Mössbauer spectra of (**a**) 20 nm α-Fe_2O_3 nanoparticles coated with oleic acid (weakly interacting) and (**b**) uncoated (strongly interacting) nanoparticles, measured at the temperatures indicated. The lowest spectrum in each panel is measured in an external magnetic field. (Reprinted with permission from [8.111]. © 2000 American Physical Society)

in the uncoated, strongly interacting particles to temperatures above 360 K. The strong interaction is ascribed to a magnetic exchange interaction of the nanoparticles because the magnetic dipole interaction is negligible due to the very small magnetic moments of the antiferromagnetic particles. Exchange interaction implies that the particles are in such a close proximity that the electronic wave functions of atoms at the interfaces overlap (see [8.108]). Neutron diffraction experiments suggest [8.112] that about three α-Fe_2O_3 nanoparticles may be aligned in chains with common crystallographic orientation and a magnetic correlation in the [001] direction, which has been confirmed by high-resolution electron microscopy [8.112].

8.5.4 Complex Magnetic Structure of an Iron Monolayer on Ir (111)

Using spin polarized scanning tunneling microscopy, a nanometer-sized 2D magnetic unit cell of Fe atoms on Ir (111) is observed which is also favored by first-principles calculations. A collinear magnetic structure is proposed for the magnetic unit cell (Fig. 8.33) consisting of 15 atoms with 7 magnetic moments pointing in one and 8 moments in the opposite direction. This structure is induced by the strong Fe–Ir hybridization. The Fe atoms in the mosaic structure have a magnetic moment of $\bar{m}_{Fe} = 2.96\ \mu_B$ and the Ir atoms a value of $\sim 0.1\ \mu_B$.

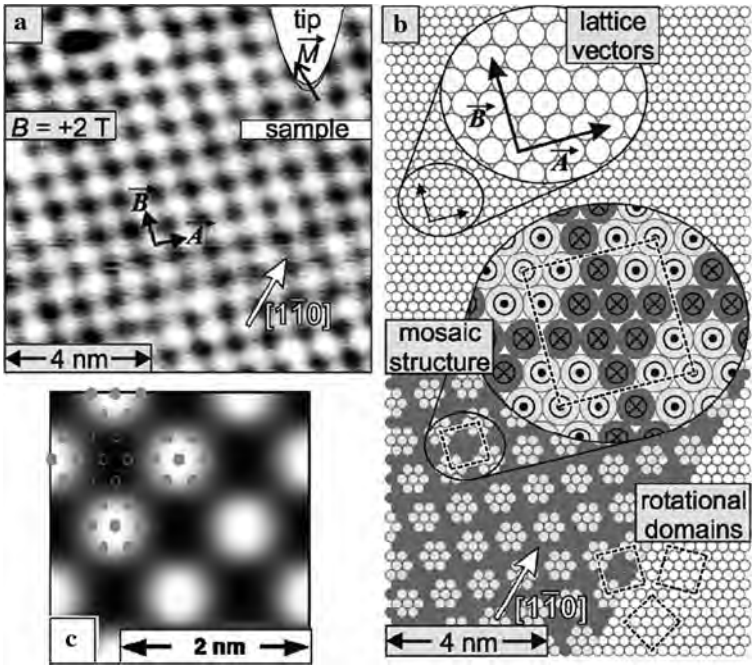

Fig. 8.33 Magnetism of the face-centered cubic (fcc) Fe monolayer on fcc Ir (111). (**a**) Spin-polarized scanning tunneling micrograph (SP-STM) of the Fe monolayer in a magnetic field of $B = 2$ T. (**b**) Structural model based on the experimental data. (**c**) Calculated SP-STM image for the 7:8 domain of the Fe magnetic mosaic structure. (Reprinted with permission from [8.110]. © 2006 American Physical Society)

8.6 Ferromagnetic Nanorings

Ferromagnetic rings with a diameter of 1–3 μm and of nanometer widths and thicknesses exhibit new spin states (Fig. 8.10), switching behavior, and spin dynamics which can be controlled via geometry, materials composition, and applied field.

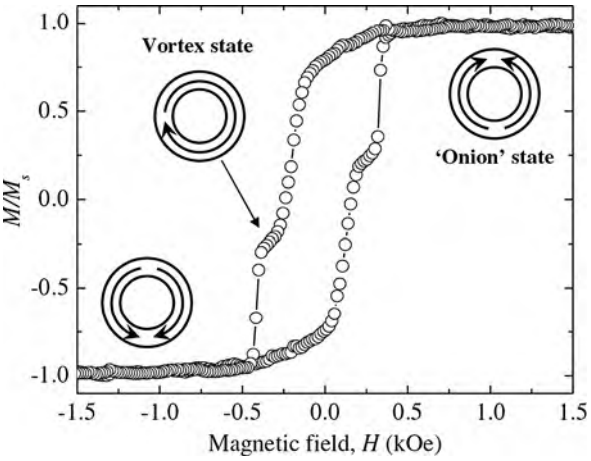

Fig. 8.34 Hysteresis loop of an array of polycrystalline Co rings with an outer diameter of 1.65 μm, a width of 350 nm, and a thickness of 16 nm. The *insets* show schematic diagrams of the onion and vortex states of a ring which are attained during the magnetization reversal process. (Reprinted with permission from [8.9]. © 2007 Institute of Physics)

These characteristics make the rings an attractive geometry for devices, including MRAMs (magnetic random access memories) and magnetic sensors [8.9]. These nanorings are prepared by a combination of electron beam lithography (EBL), metal molecular beam epitaxy, and lift-off techniques (see [8.9]).

A hysteresis loop of an array of micrometer-sized magnetic nanorings (Fig. 8.34) is characterized by the "onion" magnetization state from positive saturation down to zero field. As the magnetic field is reversed, a jump of the magnetization to a state close to zero remanence is characteristic for the transition from the "onion" to the "vortex" state. When the reverse field is further increased, the transition to the reverse onion state occurs. The equilibrium magnetic configuration of nanorings is determined by the exchange energy and the magnetostatic energy, where in 3*d* transition metal ferromagnets the magnetocrystalline anisotropy plays a minor role (see [8.9]).

In field-induced magnetic switching of ring elements, the switching time and switching field amplitude depend on the particular reversal mechanisms favored by the magnetic system. In the case of double switching, from onion to vortex and vortex to reverse onion, domain wall propagation, and domain nucleation plus wall propagation are prevalent. In the transition from the onion to the vortex state one of the 180° walls is displaced and propagates along one half of the ring (annihilating the other domain wall or forming metastable 360° domain walls, depending on the relative winding [8.113]), where the onion-to-vortex switching field strongly depends on the ring width (see [8.9]). The magnetic switching properties of ring elements have been studied by using resistance measurements, yielding jumps in resistance when a domain wall is located within or outside the measuring section (see Fig. 8.35a, c).

Magnetization dynamics in confined geometries have also been studied by means of Brillouin light scattering for investigating the spin wave modes (see, e.g., [8.115]), showing in the case of 1 μm permalloy rings 2D quantization of spin waves in radial and azimuthal direction which partially disappears in larger rings.

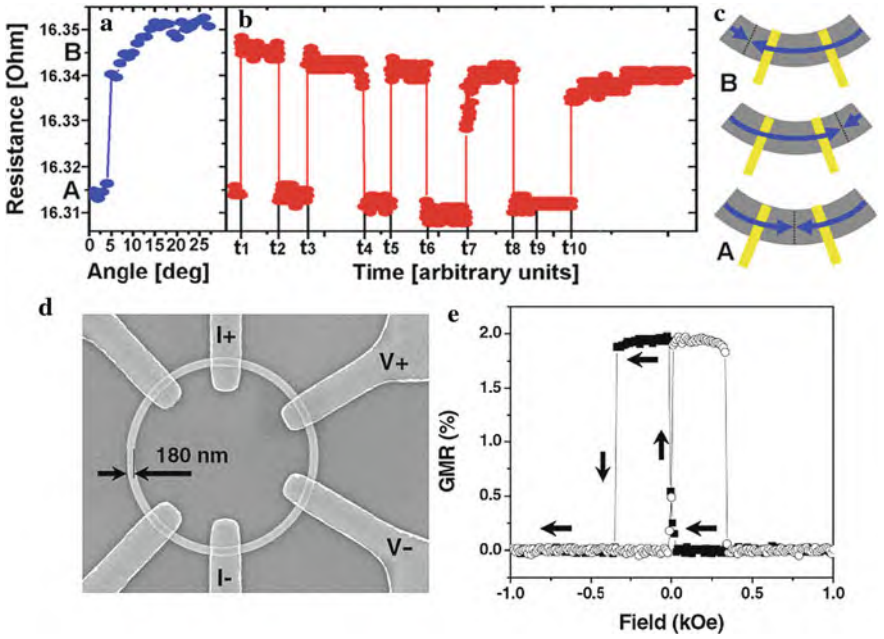

Fig. 8.35 (**a**) Resistance response of a permalloy nanoring due to domain wall movement by an applied magnetic field; level A corresponds to the presence of the domain wall in between the voltage contacts (see (**c**)), while for level B the domain wall is outside the voltage contacts (for these measurements, the ring is severed to exclude contributions from other portions of the ring). (**b**) Resistance across the voltage contacts after successive positive and negative current pulses (width: 20 μs, amplitude: 5×10^{12} Am^{-2}), demonstrating current-induced domain wall motion. (**c**) Schematic diagrams of the voltage contacts and of the domain wall position [8.114]. (**d**) Scanning electron microscopy (SEM) of a pseudo-spin valve ring with a diameter of 5 μm and the structure Au (4 nm)/Co (7 nm)/Cu (5 nm)/NiFe (4 nm)/SiO_x/Si (001). (**e**) Magnetoresistive characteristics for the ring in (**d**). The magnetic field is applied in the direction of the current contacts [8.9]. (Reprinted with permission from [8.114] (**a**–**c**) and [8.9] (**d**) (**e**). © 2005 American Physical Society (**a**–**c**) and © 2007 Institute of Physics (**d**) (**e**))

Current-induced magnetic switching can be performed by switching the magnetization or by displacing domain walls by means of a spin polarized current. This is of much interest for the switching of magnetic memory elements with the advantage of much simplified wiring as compared to conventional magnetic field switching. The ring geometry has been used for the study of current-induced domain wall propagation. A domain wall initially outside two voltage contacts (Fig. 8.35c) can be positioned by a current pulse into the region between the two voltage contacts which is monitored by a lowering of the resistance (Fig. 8.35b). A reverse current pulse can move the wall back.

Pseudo-spin-valve multilayer ring structures of the type Au (4 nm)/Co (7 nm)/Cu (5 nm)/NiFe (4 nm)/SiO_x/Si (001) (Fig. 8.35d) exhibiting giant magnetoresistance (GMR; see Sect. 1.4) have been fabricated and their magnetization reversal investigated using magnetoresistance measurements and micromagnetic modeling

[8.116]. The GMR data for the ring show a flat baseline interrupted by jumps (Fig. 8.35e) as domain walls are created and move through the ring; this leads to an increase in resistance as the parallel arrangement of the magnetization of the NiFe and the Co at high fields (both in the same onion state) changes to an antiparallel spin arrangement following the reversal of the NiFe layer to the reverse onion state.

8.7 Current-Induced Domain Wall Motion in Magnetic Nanostructures

Domain walls in nanoscale ferromagnetic structures exhibit complex spin arrangements that strongly deviate from the wall types in bulk and thin film systems [8.117]. Recently, a new aspect of magnetic domain walls has been attracting attention, i.e., the domain walls are considered as possible objects for high-speed logic, where each wall represents a single bit [8.118]. The pioneering prediction [8.119–8.121] and confirmation [8.122, 8.123] that domain walls cannot only be moved by magnetic fields but also by spin-polarized electrical current offer an attractive alternative in designing novel devices such as sensors and magnetic non-volatile memories [8.124, 8.125].

The transition of the magnetization direction in one ferromagnetic domain to the opposite direction in the adjacent domain occurs in the domain wall between the two domains. The width of the wall in a bulk system is governed by the magnetocrystalline anisotropy energy and the quantum mechanical magnetic exchange energy. Lateral confinement in nanostructured films (see Fig. 8.36a) leads to pronounced geometrical effects, i.e., to modifications of the domain wall structure because of the demagnetization energy at the edges. This in turn offers the possibility to finely tune the wall properties, such as the wall width from a few nanometers to several hundred nanometers which determines, e.g., the electrical resistance and the dynamic properties of the domain wall (see [8.117, 8.126, 8.127]). Wall positions can be detected by anisotropic or giant magnetoresistance, by induced Hall voltage, by magnetic force microscopy, by magneto-optical Kerr effect, or by spin-polarized scanning electron microscopy (see [8.117]).

An electrical current flowing in a magnetic element can be used, instead of a magnetic field, to move a domain wall. This was first observed in continuous films [8.128, 8.129]. The predominant mechanism for this process is believed to be the exchange interaction between the 3*d* electrons in the ferromagnet and the spin-polarized conduction electrons which results in a torque and a transfer of spin momentum from the drifting electrons to the domain wall. In theoretical treatments the underlying Landau–Lifshitz–Gilbert equation has been extended by additional torque terms (see [8.117]).

For the movement of a domain wall, relatively high current densities of $10^{11} - 10^{12}$ A/m^2 are required (Fig. 8.36b, c). Domain wall velocities up to 80 m/s have been observed [8.130], a value similar to that expected theoretically (100 m/s; see [8.117]). Domain walls pinned at notches of a ferromagnetic wire can be excited

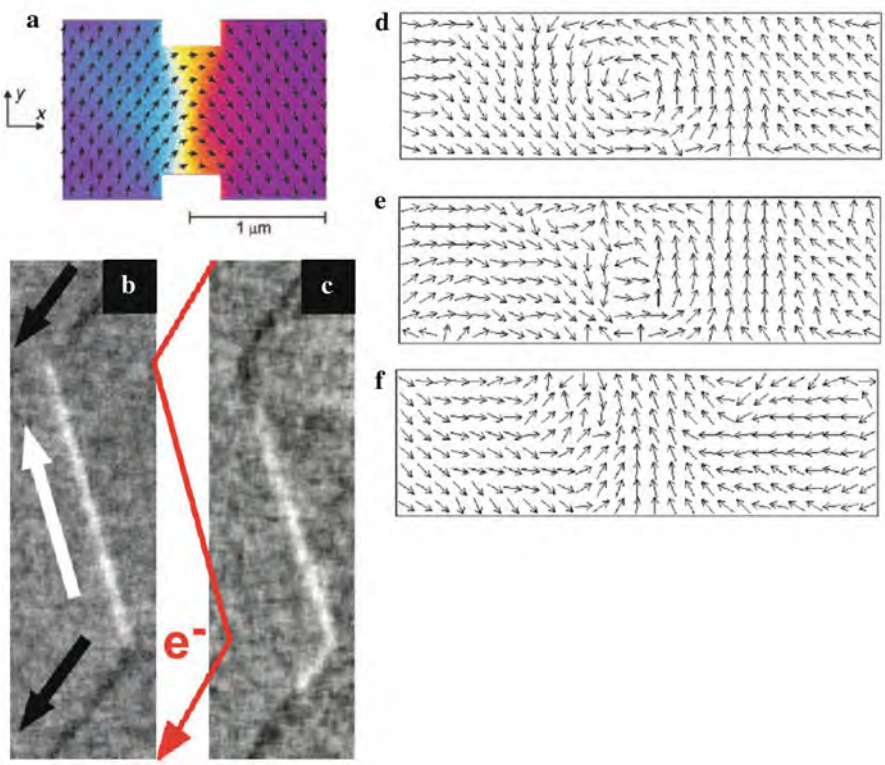

Fig. 8.36 Magnetic domain walls in nanowires, their motion, and their deformation. (**a**) Magnetic domain wall in a constriction in a 7.5-nm thick $Fe_{20}Ni_{80}$ film as measured by spin-polarized scanning electron microscopy (spin SEM). The color code shows the in-plane magnetization component along the $+y$ (*left*) and the $-y$ (*right*) directions. The *arrows* give the in-plane magnetization directions. The magnetization configuration is asymmetric, showing a wall that is wider toward the top than the bottom constriction (colored *yellow* for vanishing magnetization component in *y*-direction). (**b**–**c**) $Fe_{20}Ni_{80}$ nanowires with a width of 500 nm, a thickness of 10 nm, and a length of the central straight segment of 20 μm. The spin-SEM studies yield the black and white magnetization contrasts according to the magnetization directions given by the *black* and *white arrows*. The walls move from the initial positions at the bends shown in (**b**) to a position in the straight wire shown in (**c**), after injection of a 10 μs long current pulse with the current direction indicated by the *red arrow*. Current density, 2.2×10^{12} A/m^2. (**d**–**f**) Arrow images constructed from high-resolution experimental images of the spin structure of a domain wall in a $Fe_{20}Ni_{80}$ wire of a width of 500 nm and a thickness of 20 nm after subsequent current injections. The wall transforms from (**d**) the initial vortex state to (**e**) a vortex core with a large transverse component and (**f**) to a transverse wall. This wall no longer moves with a current density of 2.2×10^{12} A/m^2. The *arrow* images are constructed from the spin-SEM studies. Image size: 1600 nm × 500 nm. (Reprinted with permission from [8.117]. © 2006 Materials Research Society)

to oscillations by a high-frequency current. From this experiment quasi-particle domain wall masses between 5.6×10^{-25} kg and 6.2×10^{-24} kg were derived, depending on the type of wall [8.131]. The pinning potential can be completely characterized [8.132].

In analogy to the current-induced domain wall motion, the motion of a domain wall by a magnetic field can generate a current [8.133].

8.8 Single Molecule Magnets

The observation of a magnetic memory effect [8.134] in single molecule magnets (SMMs) has opened the perspective of exploiting the information storage capability of individual SMMs. In fact, the combination of a large spin of the molecule with an easy-axis magnetic anisotropy results in an energy barrier for the reversal of the magnetization, although the barrier can be cross-cut by a tunneling mechanism for some particular values of the magnetic field [8.135–8.137]. Anchoring SMMs on conducting surfaces is required to make them individually addressable. Evidence that SMMs retain molecular magnetic hysteresis has been presented [8.138].

SMMs comprising four high-spin iron(III) ions, Fe_4 (Fig. 8.37a, b), and having a diameter of ~ 2.5 nm [8.138] are stable and robust. The outer three individual $s = 5/2$ spins interact antiferromagnetically with the center spin to give a ground state $S = 5$ spin state with an anisotropy barrier of about 15 K to be overcome for magnetization reversal. At low temperatures of 0.5 K a magnetic hysteresis (Fig. 8.37c) of purely molecular origin is observed. This may open the possibility to control magnetization reversal by conduction electrons in a metal–molecule–metal nanojunction which would mimic at the molecular scale the current-induced motion of domain walls for memory nanostructures (see Sect. 9.4).

8.9 Multiferroic Nanostructures

Three forms of ferroic order are widely known: ferromagnetism, a spontaneous magnetization; ferroelectricity, a spontaneous polarization; and ferroelasticity, a spontaneous strain. It is currently debated whether to include an ordered arrangement of magnetic vortices as a fourth form of ferroic order, termed ferrotoroidicity [8.139].

Multiferroic materials that display simultaneously ferromagnetic and ferroelectric ordering have recently gained interest [8.140–8.142] because they couple magnetic and electric behavior. In these materials the electrical polarization P can be reoriented by means of magnetic fields H and the magnetization M by electrical fields E as predicted more than 100 years ago [8.143]. Since E fields can be generated in integrated circuits more easily than H fields, it would be of interest to switch (write) magnetic multiferroic bits by E fields, whereas for reading, the magnetization could be more convenient [8.144]. The coupling of ferroelectric

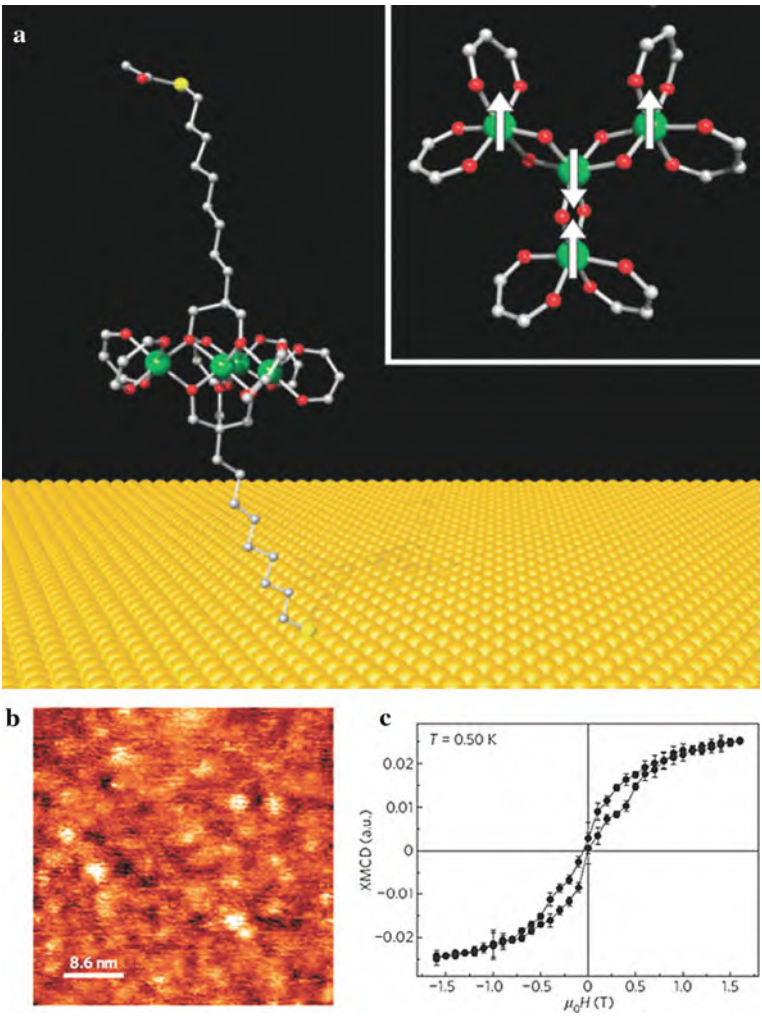

Fig. 8.37 (**a**) Schematic diagram of the anchoring on a gold surface of the Fe_4 derivative molecule through its thiolate-terminated aliphatic chains (Fe atoms in large *green* spheres, oxygen in *red*, carbon in *gray*, and sulfur in *light yellow*). *Inset*: A view of the magnetic core structure of the Fe_4 molecule, with the ground-state spin arrangement (*white arrows*). (**b**) Room-temperature scanning tunneling micrograph (STM) of a monolayer of Fe_4 molecules. (**c**) Magnetic hysteresis of the Fe_4 monolayer monitored through the x-ray magnetic circular dichroism (XMCD) intensity. (Reprinted with permission from [8.138]. © 2009 Nature Publishing Group)

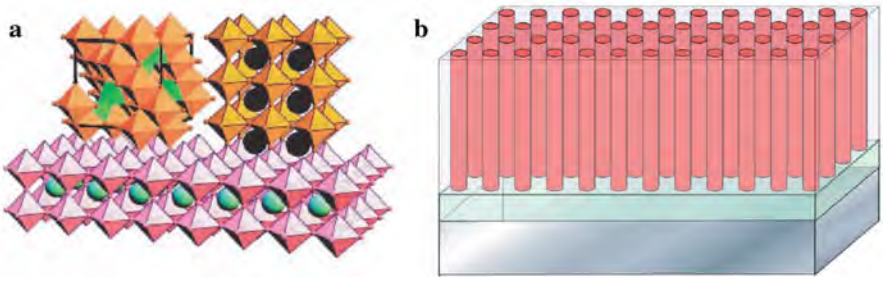

Fig. 8.38 (**a**) Epitaxial alignment of a spinel (*top left*) and a perovskite (*top right*) on a perovskite substrate (*bottom*). (**b**) Schematic illustration of a self-assembled nanostructured columnar thin film formed on a substrate. (Reprinted with permission from [8.145]. © 2004 AAAS)

and magnetic order parameters in a two-phase nanostructured $BaTiO_3$–$CoFe_2O_4$ multiferroic ferroelectromagnet has been demonstrated [8.145]. The intrinsic similarities in crystal chemistry (i.e., oxygen coordination) between the perovskite ($BaTiO_3$) and the spinel ($CoFe_2O_4$) families lead to lattice dimensions that are compatible. This presents the possibility of heteroepitaxy in three dimensions, e.g., of nanopillars of the ferromagnetic spinel in a ferroelectric perovskite matrix (Fig. 8.38).

The connection between the polarization P and the magnetization M as well as $P(H)$ and $M(E)$ dependences can be derived from the minimization of the free energy

$$F = (1-\alpha)\left[\phi_{\mathrm{P}}(P) - EP\right] + \alpha\left[\phi_{\mathrm{M}}(M) - HM\right] + e\left[\varepsilon_0^P(P), \varepsilon_0^M(M)\right]$$

where α is the fraction of the ferromagnetic phase, $\phi_{\mathrm{P}}(\phi_{\mathrm{M}})$ the specific free energy of uniform ferroelectrics (ferromagnets), e the energy of elastic interaction, $\varepsilon_0^P(P) = QP^2$ the spontaneous ferroelectric strain with Q the electrostriction coefficient, and $\varepsilon_0^M(M)$ the spontaneous magnetostriction (see [8.145]). It is clear from the above equation that a strong magnetoelectric coupling requires a strong interphase elastic interaction.

The two-phase oxide films with self-assembled $CoFe_2O_4$ nanopillars (30 nm in diameter; volume fraction 35%; Fig. 8.39a, b) in a $BaTiO_3$ matrix are prepared by pulsed laser deposition. The nanopillars exhibit a compressive out-of-plane strain of 0.8% due to a vertical heteroepitaxial mismatch between $CoFe_2O_4$ and $BaTiO_3$ [8.145]. In quasi-static ferroelectric measurements a ferroelectric hysteresis is observed with a dielectric constant of 350 (normalized to the $BaTiO_3$ fraction) at 100 kHz. In magnetometry measurements a saturation magnetization (normalized to the $CoFe_2O_4$ fraction) of ~350 electromagnetic units (emu)/cm^3 are found.

Temperature-dependent magnetization measurements (Fig. 8.38c; upper curve) show coupling between the electric and magnetic order parameters in a $CoFe_2O_4$–$BaTiO_3$ films as manifested by a drop in the magnetization of ~16 emu/cm^3

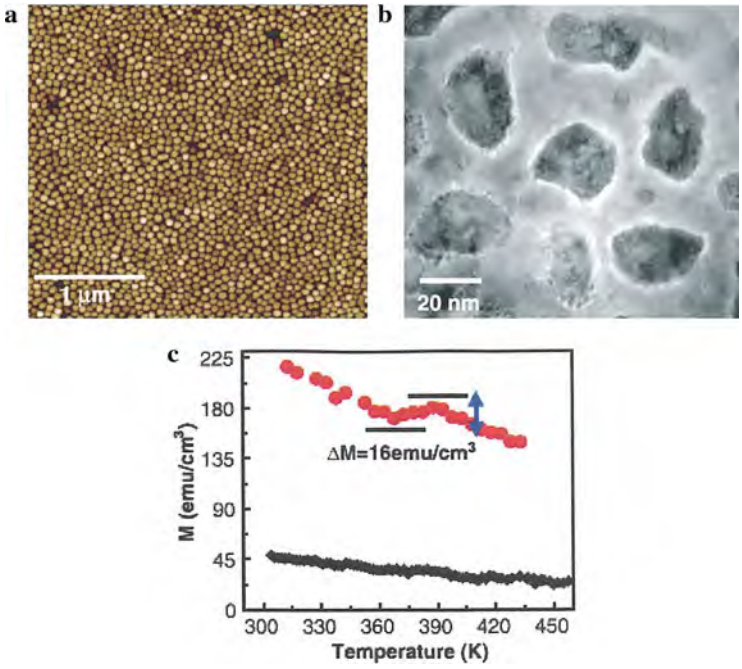

Fig. 8.39 (**a**) AFM topography image of a film showing a quasi-hexagonal arrangement of $CoFe_2O_4$ nanopillars in a $BaTiO_3$ matrix. (**b**) TEM planar view image of the $CoFe_2O_4$ nanopillars in the $BaTiO_3$ matrix. The heteroepitaxy of the two structures can be shown by electron diffraction. (**c**) Temperature dependence of the magnetization of the $CoFe_2O_4$–$BaTiO_3$ film at $H = 100$ Oe, showing a drop in magnetization at the ferroelectric Curie temperature $T_C \sim 390$ K for the vertically self-assembled nanostructure (*upper curve*); a multilayered nanostructure (*lower curve*) shows negligible change in magnetization. (Reprinted with permission from [8.145]. © 2004 AAAS)

around the ferroelectric Curie temperature $T_C \sim 390$ K upon cooling. At temperatures $>T_C$, the $CoFe_2O_4$ is compressed due to the lattice mismatch with $BaTiO_3$. At temperatures $<T_C$, the tetragonal distortion in $BaTiO_3$ decreases this compression in $CoFe_2O_4$. Because $CoFe_2O_4$ has a negative magnetostriction, it results in a reduction of the magnetization as experimentally observed [8.145].

A number of applications are envisaged for multiferroic materials. Composite multiferroics with strong magnetostriction and large piezoelectric coefficients enable the creation of tiny magnetic sensors with the sensitivity exceeding that of even superconducting quantum interference devices (SQUIDs) [8.146].

Domain walls in multiferroics, intrinsically nanoscopic because of their small thickness, could be used as active device components [8.147]. In the insulating room-temperature multiferroic $BiFeO_3$, domain walls separating regions with polarization orientations differing by 180° or 109° show the signature of electric conductance [8.148] which is correlated to a local structural distortion in the

otherwise insulating material. This distortion reduces the electronic band gap in the region of the domain wall. A possible application could be as a highly sensitive local strain sensor.

In a Néel magnetic domain wall of a multiferroic an electric polarization could form [8.141]. This domain wall can be moved by an inhomogeneous electric field exerted, e.g., by a voltage pulse on a Cu tip [8.149]. This interaction could be a means of controlling the domain structure, and consequently a magnetic memory, by applying a voltage rather than electric currents (see Sect. 8.7 and 9.4) or magnetic fields (see [8.141]).

8.10 Magnetically Tunable Photonic Crystals of Superparamagnetic Colloids

Colloidal crystals, i.e., periodic structures typically self-assembled from monodisperse colloidal building blocks, are a low-cost photonic band gap material. In analogy to the electronic band gaps of semiconductor crystals, photonic crystals exhibit photonic band gaps giving rise to the disappearance of the transparency for radiation with particular wavelengths. For application it is desirable that the tunability of the photonic band gap (stop band) can be conveniently controlled by external stimuli.

As building blocks for a photonic crystals, polyacrylate-capped superparamagnetic magnetite (Fe_3O_4) colloidal nanocrystal clusters (CNCs) with a diameter of 120 nm have been synthesized [8.150] (see Fig. 8.40). The CNCs consist of 10-nm superparamagnetic primary particles (Fig. 8.40a). The polyacrylate binds to the particle surface through a strong coordination of the carboxylate groups with iron cations, whereas the non-coordinated carboxylate groups of the polymer chains extend into the aqueous solution and render the particle surface highly charged (Fig. 8.40b). The Fe_3O_4 CNCs readily self-assemble in deionized water into colloidal photonic crystals upon application of a magnetic field. Figure 8.40d, e shows the photos and reflection spectra of an aqueous solution of 120-nm CNCs (ca. 8.6 mg mL^{-1}) in response to a varying magnetic field achieved by controlling the distance between a NdFeB magnet and the sample. The peaks resulting from the diffraction of the (111) planes blue shift from 730 to below 450 nm as the magnetic field increases from 8.8 to 35.2 mT moving the magnet toward the sample (3.7–2.0 cm). The blue shift corresponds to a decrease of the interplanar spacing from 274 to 169 nm. The 3D order of the colloidal photonic crystal formed within $\sim$ 200 ms [8.150] in the magnetic field is the balanced result of the interparticle electrostatic repulsive force and the magnetic forces [8.151]. The above studies demonstrate that medium-sized superparamagnetic clusters can reversibly form stable colloidal photonic crystals in a magnetic field with tunable stop bands and therefore tunable colors covering the whole visible spectrum [8.150].

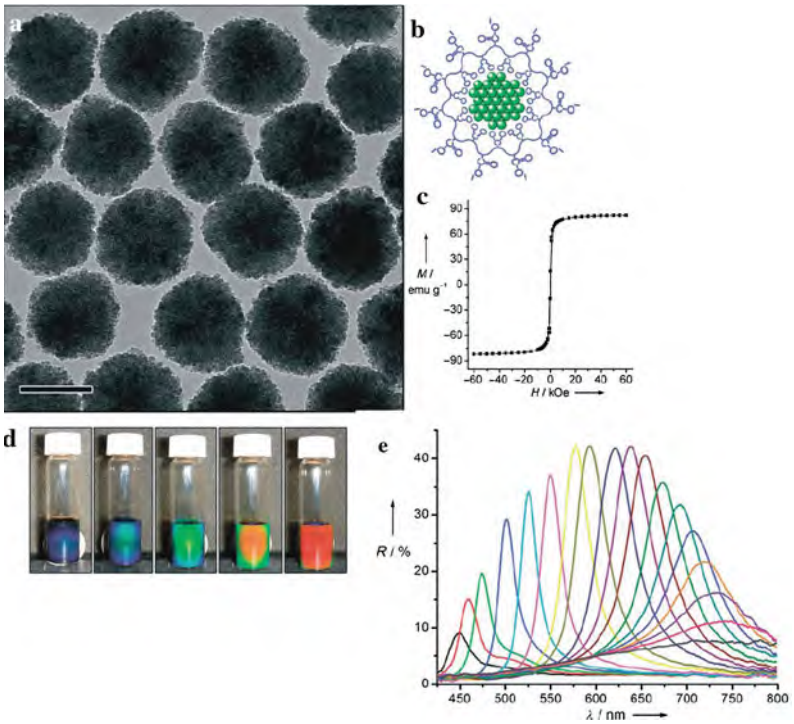

Fig. 8.40 (**a**) Transmission electron micrograph and (**b**) schematic illustration of polyacrylate-capped Fe_3O_4 colloidal nanocrystal clusters (CNCs) with a nanocrystal size of $\sim$ 10 nm; scale bar: 100 nm. (**c**) Magnetization curve of CNCs measured at room temperature exhibiting superparamagnetic behavior. (**d**) Photographs of solutions of colloidal photonic crystals formed in response to an external magnetic field; the magnet–sample distance decreases gradually from *right* to *left*. (**e**) Variation of the reflectance spectra at normal incidence on the colloidal photonic crystals with the magnet–sample distance. Diffraction peaks blue shift (from *right* to *left*) as the magnet–sample distance decreases from 3.7 to 2.0 cm in steps of 0.1 cm. (Reprinted with permission from [8.150]. © 2007 Wiley-VCH)

8.11 Nanomagnets in Bacteria

Magnetotactic bacteria, such as the bacterium *Magnetospirillum magnetotacticum*, biomineralize iron into magnetite (Fe_3O_4) nanoparticles ("magnetosomes"), which enable the bacteria to respond to magnetic fields in their environments. These magnetosomes have considerable potential for use in nanotechnological, biotechnical, and medical application because of their narrow size distribution and inherent biocompatibility (see [8.152]). Furthermore, magnetotactic bacteria are the simplest single-cell organisms in which biomineralization occurs and, as such, offer a model system to study biomineralization mechanisms. Models of the biomineralization of

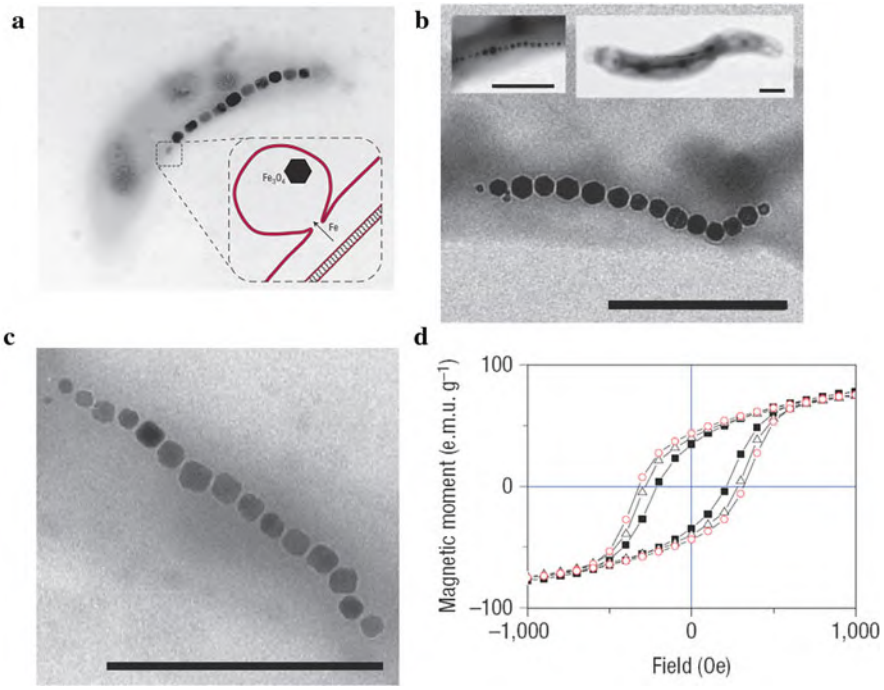

Fig. 8.41 (**a**) Electron micrograph of a chain of magnetosomes in a magnetic bacterium where a small magnetite crystal at the left end of the chain is still growing [8.153]. The *inset* shows a model of magnetite formation: As the inner membrane (*red*) forms a membrane vesicle, iron can be transported inside to eventually precipitate as magnetite [8.154, 8.155]. (**b**) Electron micrograph of Co-doped magnetosomes of the bacterium *M. gryphiswaldense*. *Insets*: undoped magnetosome chain (*left*) and undoped magnetosomes in a whole cell (*right*); scale bars are 500 nm. (**c**) *M. magnetotacticum* MS1; scale bar is 500 nm. (**d**) Magnetic hysteresis loops of MS1 measured at 300 K. *Closed squares*, *open triangles*, and *open circles* indicate the magnetosomes corresponding to [Fe], [FeCo], and [Co] growth conditions [8.152]. (Reprinted with permission from Refs. [8.155] (**a**) and [8.152] (**b**–**d**). © 2008 Nature Publishing Group)

magnetosomes with a typical size of about 50 nm (Fig. 8.41a) propose that in a first step iron, e.g., incorporated in the cage protein ferritin, is accumulated in the space between the outer and inner cell membrane (see inset in Fig. 8.41a). In a second step, the inner membrane expands inward to form an empty magnetosome vesicle (see [8.155]), into which the stored iron can be released to eventually precipitate as magnetite.

8.11.1 In Vivo Doping of Magnetosomes

Pure magnetite has the highest saturation magnetization of the iron oxides but is magnetically soft and therefore less suitable for applications that require the nanoparticles to remain magnetized in zero-field. It is, however, well known that magnetite particles can be magnetically stabilized when small amounts of iron are

substituted by cobalt, a technique which has been employed for iron oxide nanoparticles used in videotapes and floppy disks (see [8.155]). Recently it could be shown that for magnetosomes in bacteria fed in vivo with cobalt-containing quinate (CoQ), the coercive field, which is a measure of the magnetic stability of the particles, could be increased by up to 50% (see Fig. 8.41d). This is due to the biological introduction of a Co content up to 1.4%, as determined by induced coupled plasma optical emission spectroscopy (ICP-OES) and x-ray magnetic circular dichroism [8.152] (see Sect. 8.1). This demonstrates the possibility of tuning the properties of biosynthesized nanoparticles in vivo, but retaining the advantageous biological growth control.

8.11.2 Magnetosomes for Highly Sensitive Biomarker Detection

A biomarker is a biochemical compound (see Sect. 12.2), such as a protein, which can be used to specifically and sensitively monitor a health status. Furthermore, in various fields such as agriculture, drug development, or doping control, biomarkers are of interest (see [8.156]).

Magnetosomes have been developed for sensitive detection of the hepatitis B surface antigen (HBs Ag) in human serum by employing a magneto immuno polymerase chain reaction (M-IPCR) [8.156, 8.157]. Magnetite ferromagnetic magnetosomes derived from the bacterium *Magnetospirillum gryphiswaldense* are modified with oligonucleotides and antibodies (see Fig. 8.42) for the detection

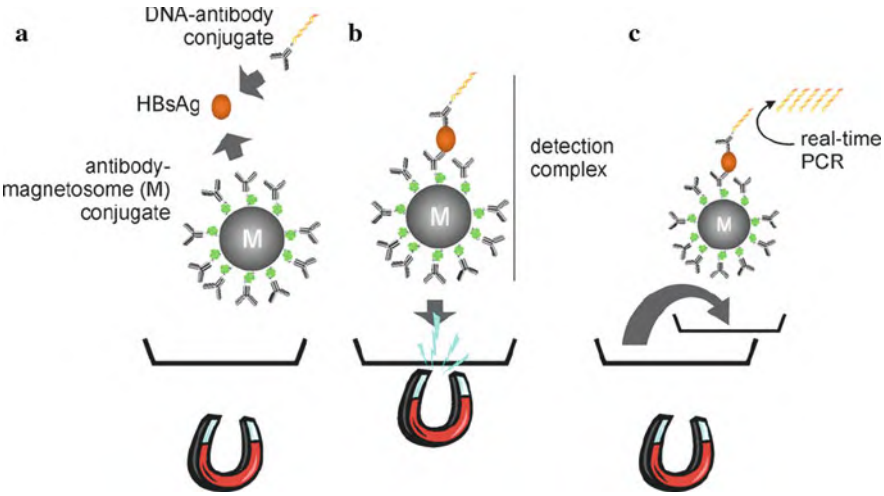

Fig. 8.42 Schematic drawing of the magneto immuno polymerase chain reaction (M-IPCR) assay. (**a**) Hepatitis B surface antigen (HBsAg)-specific magnetosome–antibody conjugate and DNA–antibody conjugate are incubated with the serum sample containing HBsAg resulting in a signal-generating detection complex. (**b**) The detection complex is concentrated using an external magnetic field. (**c**) The detection complex solution is transferred to a microplate containing the polymerase chain reaction (PCR) amplification mastermix for highly sensitive detection of the HBsAg antigen. (Reprinted with permission from [8.156]. © 2007 Elsevier)

of the HBsAg antigen biomarker where additionally a DNA–antibody conjugate is attached to the HBsAg for PCR amplification (Fig. 8.42). A 125-fold increase in sensitivity is observed for this M-IPCR assay as compared to enzyme-linked immunosorbent analysis (M-ELISA [8.156]) and a 25-fold increased sensitivity compared to the limit of HBsAg detection using commercial magnetic beads. Most likely, the enhanced performance of the magnetosomes, compared to conventional magnetic microbeads, results from their smaller size, monodispersity, and higher magnetization [8.156].

8.12 Summary

The progress in the understanding of magnetism on the nanoscale has been stimulated by advances in film growth, by new imaging methods, and by the increase in computer power for modeling. Imaging of magnetic nanostructures can be performed by various scanning probe microscopy techniques, even down to the magnetic behavior of single atoms on surfaces, by electron microscopy and holography, and by x-ray magnetic circular dichroism (XMCD) microscopy. Substantial size and dimensionality effects are found in nanomagnetism going from single atoms and clusters to nanowires and nanolayers. Soft- and hard-magnetic materials can be improved by nanostructuring. Antiferromagnetic structures are modified and complex magnetic structures appear at the nanoscale and the motion of magnetic domain walls can be induced by electrical currents. Single-molecule magnets may be exploited for information storage. Multiferroic behavior may be induced in nanostructures. Magnetic nanostructures can be biomineralized and doped in bacteria.

References

8.1 H.P. Oepen, R. Frömter, in [8.21], p. 1488
8.2 C.M. Schneider, J. Kirschner in *Handbook of Surface Science*, vol. 2, ed. by K. Horn, M Scheffler (Elsevier, Amsterdam, 2000), p. 511
8.3 J. Shen, J. Kirschner, Surf. Sci. **500**, 300 (2002)
8.4 D.L. Mills, J.A.C. Bland, *Nanomagnetism* (Elsevier, Amsterdam, 2006)
8.5 U. Hartmann, *Nanotechnologie und Nanostrukturtechnik* (Oldenburg, München, 2008)
8.6 S.D. Bader, Rev. Mod. Phys. **78**, 1(2006)
8.7 A.P. Guimarães, *Principles of nanomagnetism* (Springer, Heidelberg), 2009
8.8 D. Fiorani (ed.), *Surface Effects in Magnetic Nanoparticles* (Springer, New York, 2005)
8.9 C.A.F. Vaz et al., J. Phys.: Condens. Matt. **19**, 255207 (2007)
8.10 A. Hubert, R. Schäfer, *Magnetic Domains* (Springer, Heidelberg, 1998)
8.11 J. Kerr, Phil. Mag. **3** (5), 321 (1877)
8.12 H. Hopster, H.P. Oepen (Eds.) *Magnetic Microscopy of nanostructures* (Springer, Berlin, 2005)
8.13 A. Schwarz, R. Wiesendanger, Nano Today **3**, Feb-Apr. 2008, p. 28
8.14 U. Hartmann, Annu. Rev. Mater. Res. **29**, 53 (1999)
8.15 R. Wiesendanger et al., J. Vac. Sci. Technol. **B9**, 519 (1991)
8.16 H. Momida, T. Oguchi, Surf. Sci. **590**, 42 (2005)

8.17 U. Kaiser et al., Nature **446**, 522 (2007)
8.18 S. Heinze et al., Science **288**, 1805 (2000)
8.19 J. Nogués, I.K. Schuller, J. Magn. Magn. Mater. **192**, 203 (1999)
8.20 M. Bode, Rep. Prog. Phys. **66**, 523 (2003)
8.21 A. Schwarz et al., in *Handbook of Magnetism and Advanced Magnetic Materials*, eds. by H. Kronmüller, S. Parkin (Wiley, Chichester, 2007) p. 1687
8.22 D. Wortmann et al., Phys. Rev. Lett. **86**, 4132 (2001)
8.23 J. Tersoff, D.R. Hamann, Phys. Rev. Lett. **50**, 1998 (1983)
8.24 A. Selloni et al., Phys. Rev. **B31**, 2602 (1985)
8.25 O. Pietzsch et al., Phys. Rev. Lett. **92**, 057202 (2004)
8.26 R. Wu, A.J. Freeman, Phys. Rev. B **45**, 7532 (1992)
8.27 E. Dzyaloshinski, Sov. Phys. JET. **19**, 960 (1964)
8.28 M. Bode et al., Nature **447**, 190 (2007)
8.29 Ch. Pfleiderer, U.K. Rößler, Nature **447**, 157 (2007)
8.30 T. Balashov et al., Phys. Rev. Lett. 97, 187201 (2006)
8.31 J.C. Slonczewski, J. Magn. Magn. Mater. **159**, L1 (1996)
8.32 F.J. Albert et al., Phys. Rev. Lett. **89**, 226802 (2002)
8.33 S. Krause et al., Science **317**, 1537 (2007)
8.34 H. Boersch, H. Raith, Naturwissenschaften **46**, 574 (1959)
8.35 J. Zweck, T. Uhlig, In [8.21], p. 1393
8.36 M.R. McCartney, D.J. Smith, in [8.21], p. 1428
8.37 P. Schattschneider et al., Nature **441**, 486 (2006)
8.38 Y. Aharonov, D. Bohm, Phys. Rev. **115**, 485 (1959)
8.39 D. Gabor, Nature **161**, 777 (1948)
8.40 M. Lehmann, H. Lichte, Microsc. Microanal. **8**, 447 (2002)
8.41 J. Stöhr, J. Magn. Magn. **200**, 470 (1999)
8.42 G. Schütz et al., in [8.21] Vol. 3, p. 1311
8.43 H. Stoll et al., Appl. Phys. Lett. **84**, 3328 (2004)
8.44 R. Moriya et al., Nat. Phys. **4**, 368 (2008)
8.45 M. Bolte et al., Phys. Rev. Lett. **100**, 176601 (2008)
8.46 M. Weigand et al., Phys. Rev. Lett. **102**, 077201 (2009)
8.47 P. Fischer et al., Mater. Today **9**, Jan-Feb 2006, p. 34
8.48 D.-H. Kim et al., J. Appl. Phys. **99**, 08H303 (2006)
8.49 A. Enders et al., in [8.21], vol. 1, p. 577
8.50 S. Blügel, G. Bihlmayer, in [8.21], vol. 1, p. 598
8.51 J.V. Barth et al., Phys. Rev. **B42**, 9307 (1990)
8.52 F. Meier et al., Science **320**, 82 (2008)
8.53 M. Morgenstern, Phys. J. **7** (7), 16 (2008)
8.54 M.A. Ruderman, C. Kittel, Phys. Rev. **96**, 99 (1954)
8.55 T. Kasuya, Prog. Theor. Phys. **16**, 45 (1956)
8.56 K. Yosida, Phys. Rev. **106**, 893 (1957)
8.57 P. Gambardella et al., Nature **416**, 301 (2002)
8.58 G. Moulas et al., Phys. Rev. **B78**, 214424 (2008)
8.59 J. Honolka et al., Phys. Rev. Lett. **102**, 067207 (2009)
8.60 K. Tao et al., Phys. Rev. Lett. **103**, 057202 (2009)
8.61 J. Bansmann et al., Surf. Sci. Rep. **56**, 189 (2005)
8.62 G.M. Pastor, in *Lecture Notes of the Les Houches Summer School of Theoretical Physics* (Springer, Berlin, 2001)
8.63 F. Bodker et al., Phys. Rev. Lett. **72**, 282 (1994)
8.64 P. Bruno, Phys. Rev. **B39**, 865 (1989)
8.65 N.D. Mermin, H. Wagner, Phys. Rev. Lett. **17**, 1133 (1966)
8.66 P. Gambardella et al., Phys. Rev. Lett. **93**, 077203 (2004)
8.67 S. Baud et al., Surf. Sci. **600**, 4301 (2006)

8.68 E.Y. Vedmedenko et al., Phys. Rev. Lett. **92**, 077207 (2004)
8.69 F. López-Urías et al., Phys. Rev. Lett. **94**, 216102 (2005)
8.70 J. Stöhr, R. Nakajima, IBM J. Res. Devel. **48**, 73 (1998)
8.71 D. Weller et al., Phys. Rev. Lett. **75**, 3752 (1995)
8.72 M. Getzlaff et al., Phys. Unserer Zeit **31**, 110 (2000)
8.73 E.Y. Vedmendenko, Phys. J. **4** (8/9), 81 (2005)
8.74 M. Knobel et al., J. Magn. Magn. Mater. **249**, 60 (2002)
8.75 C. Ederer et al., Phys. Rev. **B68**, 052402 (2003)
8.76 X.Y. Lang et al., Phys. Rev. **B73**, 224444 (2006)
8.77 I.V. Ovchinnikov, K.L. Wang, Phys. Rev. **B80**, 012405 (2009)
8.78 H.J.A. Molegraaf et al., Adv. Mater. **21**, 1 (2009)
8.79 G. Herzer in [8.21], p. 1882
8.80 Y. Yoshizawa et al., J. Appl. Phys. **64**, 6044 (1988)
8.81 R. Würschum, Habilitationsschrift, Universität Stuttgart (1997)
8.82 K. Hono et al., Acta Metall. **40**, 2137 (1992)
8.83 L. Neel, J. Phys. Radium **15**, 225 (1954)
8.84 E. Callen et al., Phys. Rev. **B16**, 263 (1977)
8.85 M. Marinescu et al., in [8.21], p. 2005
8.86 K.H.J. Buschow in *Magnetism and Processing of Permanent Magnetic Materials*, ed. by K.H.J. Buschow (Elsevier Science, 1997), Vol. 10, p. 463
8.87 E.F. Kneller, R. Hawing, IEEE Trans. Mag. **27**, 3588 (1991)
8.88 R. Coehoorn et al., J. Magn. Magn. Mater. **80**, 101–104 (1989)
8.89 J. Fukunaga, H. Inoue, Jap. J. Appl. Phys., Part 1, **31**, 1347 (1992)
8.90 H. Kronmüller, D. Goll, Scripta Mater. **47**, 551 (2002)
8.91 D.J. Sellmyer, Nature **420**, 374 (2002)
8.92 W. Zhang, A. Inoue, Appl. Phys. Lett. **80**, 1610 (2002)
8.93 L. Schultz in *Science and Technology of Nanostructured Materials*, NATO ASI Series, vol. 259, eds. by G.C. Hadjipanayis, G.A. Prinz (Springer, Berlin, 1990), p. 538
8.94 A.G. Popov et al., J. Magn. Magn. Mater. **158**, 33 (1996)
8.95 S. Herth et al., Phys. Rev. Lett. **92**, 095901 (2004)
8.96 W. Sprengel et al., J. Appl. Phys. **98**, 074314 (2005)
8.97 G.B. Clemente et al., J. Appl. Phys. **64**, 5299 (1988)
8.98 D. Goll et al., J. Magn. Magn. Mater. **185**, 49 (1998)
8.99 H.A. Davies et al., J. Magn. Magn. Mater. **115**, 211 (1992)
8.100 M. Zhang et al., J. Alloys Compounds **372**, 267 (2004)
8.101 D. Lee et al., IEEE Trans. Magn. **40**, 2904 (2004)
8.102 T. Saito et al., J. Appl. Phys. **83**, 6390 (1998)
8.103 J.M.D. Coey, H Sun, J. Magn. Magn. Mater. **87**, L 251 (1990)
8.104 X.Y. Zhang et al., Adv. Mater. **12**, 1441 (2000)
8.105 M. Bode et al., Nat. Mater. **5**, 477 (2006)
8.106 C.F. Hirjibehedin et al., Science **312**, 1021 (2006)
8.107 S. Lounis et al., Phys. Rev. Lett. **101**, 107204 (2008)
8.108 S. Mørup et al., J. Phys.: Condens. Matter **19**, 213202 (2007)
8.109 D. Resnick et al., J. Appl., Phys. **95**, 7127 (2004)
8.110 K. von Bergmann et al., Phys. Rev. Lett. **96**, 167203 (2006)
8.111 M.F. Hansen et al., Phys. Rev. **B62**, 1124 (2000)
8.112 C. Frandsen et al., Phys. Rev. **B72**, 214406 (2005)
8.113 F.J. Castaño et al., Phys. Rev. **B67**, 184425 (2003)
8.114 M. Kläui et al., Phys. Rev. Lett. **94**, 106601 (2005)
8.115 H. Schultheiss et al., Phys. Rev. Lett. **100**, 047204 (2008)
8.116 J.J. Hayward et al., Phys. Rev. **B74**, 134405 (2006)
8.117 R. Allenspach, P.-O. Jubert, MRS Bull. **31**, May 2006, p. 395
8.118 D.A. Allwood et al., Science **309**, 1688 (2005)

8.119 L. Berger, J. Phys. Chem. Sol. **35**, 947 (1974)
8.120 L. Berger, Phys. Rev. **B54**, 9353 (1996)
8.121 J. Slonczewski, J. Magn. Magn. Mater **159**, L1 (1996)
8.122 M. Yamanouchi et al., Nature **428**, 539 (2004)
8.123 M. Hyashi et al., Phys. Rev. Lett. **98**, 037204 (2007)
8.124 S.S.P. Parkin, U.S. Patent 6834005 (December 21, 2004)
8.125 M. Hayashi et al., Science **320**, 209 (2008)
8.126 P. Bruno, Phys. Rev. Lett. **83**, 2425 (1999)
8.127 O. Pietzsch et al., Phys. Rev. Lett. **84**, 5212 (2000)
8.128 P.P. Freitas, L. Berger, J. Appl. Phys. **57**, 1266 (1985)
8.129 C.-Y. Hung, L. Berger, J. Appl. Phys. **63**, 4276 (1988)
8.130 A.V. Khvalkovskiy et al., Phys. Rev. Lett. **102**, 067206 (2009)
8.131 D. Bedau et al., Phys. Rev. Lett. **99**, 146601 (2007)
8.132 D. Bedau et al., Phys. Rev. Lett. **101**, 256602 (2008)
8.133 S.A. Yang et al., Phys. Rev. Lett. **102**, 067201 (2009)
8.134 R. Sessoli et al., Nature **365**, 141 (1993)
8.135 D. Gatteschi et al., *Molecular Magnets* (Oxford University Press, Oxford, 2006)
8.136 B. Barbara, Phys. J. **7**(8/9), 81 (2008)
8.137 C. Schlegel, Phys. Rev. Lett. **101**, 147203 (2008)
8.138 M. Mannini et al., Nat. Mater. **8**, 194 (2009)
8.139 B.B. Aken et al., Nature **449**, 702 (2007)
8.140 C.-W. Nan et al., J. Appl. Phys. **103**, 031101 (2008)
8.141 D. Khomskii, Physics **2**, 20 (2009)
8.142 A. Loidl et al., J. Phys.: Condens. Matter **20**, 430301 (2008)
8.143 P. Curie, J. Physique 3e Série III, 393 (1894)
8.144 J. Mannhart, D.G. Schlom, Phys. J. **4**, Nr. 6, 45 (2005)
8.145 H. Zheng et al., Science **303**, 661 (2004)
8.146 J. Zhai et al., Appl. Phys. Lett. **88**, 062510 (2006)
8.147 H. Béa, P. Paruch, Nat. Mater. **8**, 168 (2009)
8.148 J. Seidel et al., Nat. Mater. **8**, 229 (2009)
8.149 A.S. Logginov et al., Appl. Phys. Lett. **93**, 182510 (2008)
8.150 J.P. Ge et al., Angew. Chem. Int. Ed. **46**, 7428 (2007)
8.151 X. Xu et al., Chem. Mater. **14**, 1249 (2002)
8.152 S. Staniland et al., Nat. Nanotechnol. **3**, 158 (2008)
8.153 V.P. Shcherbakov et al., Eur. Biophys. J. **26**, 319 (1997)
8.154 D. Faivre et al., Angew. Chem. Int. Edn. **46**, 8495 (2007)
8.155 M. Winklhofer, Nat. Nanotechnol. **3**, 135 (2008)
8.156 R. Wacker et al., Biochem. Biophys. Res. Commun. **357**, 391 (2007)
8.157 C.M. Niemeyer et al., Trends Biotechnol. **23**, 208 (2005)

Chapter 9
Nanotechnology for Computers, Memories, and Hard Disks

The field of computer and data storage development is of particular importance in nanoscience. The design and fabrication of computer components, such as transistors, or of data bits in storage media are governed by the principles of physics, chemistry, and materials science on the nanoscale. On the other hand, the nanotechnical semiconductor industry with its current revenues of ∼200 billion US $ annually [9.1] is presumably the largest economic factor where nanotechnology plays a central role.

The continuous development of computers is driven by scientific projects such as the 1,000 Genomes Project or the Large Hadron Collider (LHC) at the CERN European particle-physics lab, by search engines such as Google (see [9.2]), by military supercomputers with petaflop (10^{15}) operations per second [9.3], but also by consumers' demands for increasing computation power, for digital video, digital cameras in cell phones, interactive multimedia, game products, etc., with ever increasing data storage densities and data transfer rates in addition to random access and removability (the ability to separate the media from the drive) [9.4]. In a computer, the memories that directly provide data bits to the microprocessor are semiconductor devices known as the static random access memory (SRAM) and the dynamic random access memory (DRAM). They are fast but need power to maintain the stored bits. When a personal computer (PC) is turned off, the information stored in these memory devices vanishes. The only archival memory in a computer today is a hard disc drive (HDD). Its access time, however, is six orders of magnitude slower than that of SRAM, as seen in the all too familiar wait when a computer is turned on [9.5].

Established by Intel co-founder Gordon Moore in 1965 [9.6], the empirical rule of Moore's law states that the density of transistors on a silicon-based integrated circuit (IC), and so the attainable computing power, doubles about every 18 months, with similar rules for data storage. This had the consequence that the IC components, such as transistors or capacitors, or data bits on HDD shrank to nanometer dimensions so that novel designs and materials concept had to and have to be developed in the future. The rapid development of computers has also initiated novel mathematical techniques. Whereas the computation of a particular equation took more than 2 days in 1980, this only took 10 ms in 2007 (20 million times faster),

H.-E. Schaefer, *Nanoscience*, DOI 10.1007/978-3-642-10559-3_9,

although the computer velocity increased in this period only by a factor of 4,000. This demonstrates that a similar acceleration in computation has been contributed by novel calculation methods [9.7].

Moore's law has held for more than 40 years but there is a sobering consensus in the industry that the miniaturization process or scaling can continue for only another decade or so [9.8]. Therefore, in this section, the present state and future prospects of integrated circuits including strategies beyond complementary metal-oxide-semiconductor (CMOS) technology, of modern lithography technologies, of solid state memory, and of hard disk drives will be discussed. In addition materials (high k, low k) for ultrahigh-density circuit integration will be outlined.

9.1 Transistors and Integrated Circuits

After the invention of the transistor in 1947, the monolithic integrated circuit (IC) was devised in 1958–1959 and in 1971 Intel unveiled the 4004 microprocessor (2,300 transistors) [9.9]. Back in 1993, the Pentium processors with $\sim$ 10 million transistors were released and the current transistor count (see Fig. 9.1) is $\sim$ 4 billion. In 2009 the chip industries had an annual turnover of US$ 212 billion [9.10]. A modern factory costs about US$ 4.5 billion and for a successful operation of this factory an annual output of US$ 7 billion is required [9.10].

The 45 nm technology is available in Penryn processors since November 2007 (P. Otellini, Intel). Prototypes of the 32 nm technology have been manufactured in September 2007 and fabrication started in 2009.

The basic transistor structure in the gate conductors is going to be re-engineered in the current decade. Figure 9.2 shows a transistor structure with a silicon base, a top gate, and a few-monolayer standard SiO_2 (1.2 nm) gate insulator. As the leakage current increases substantially when the insulator is made thinner and thinner, the SiO_2 insulator has to be replaced by a higher-k material (Fig. 9.2, right). Since it is much thicker than the SiO_2 insulator, it has one-hundredth of the leakage current (see Sect. 9.7).

For further scaling, a redesign of the transistor structure, with a very thin conduction channel ($\sim$ 2.0 nm) is suggested (Fig. 9.3, left). The performance of a transistor, which is usually compromised in disordered Si by a high-leakage current due to defect states in the band gap, E_g, is enhanced in nanometer-thin films due to quantum confinement. This gives rise to band edge shifts in both the conduction and the valence bands, and thereby an effective increase of E_g (see [9.11]), which results in an enhanced ratio $I_{ON}/I_{OFF} > 10^{11}$ of the ON and OFF currents, the holy grail of IC designers. Another example is the source-gated transistor (SGT) concept (Fig. 9.3, right), which leads to much less susceptibility to short-channel effects and a higher output independence due to the source barrier being screened from the drain field by the gate (see [9.11]).

The exponential advances in the technologies of complementary metal oxide semiconductor (CMOS) transistors and integrated circuitry predicted by Moore's

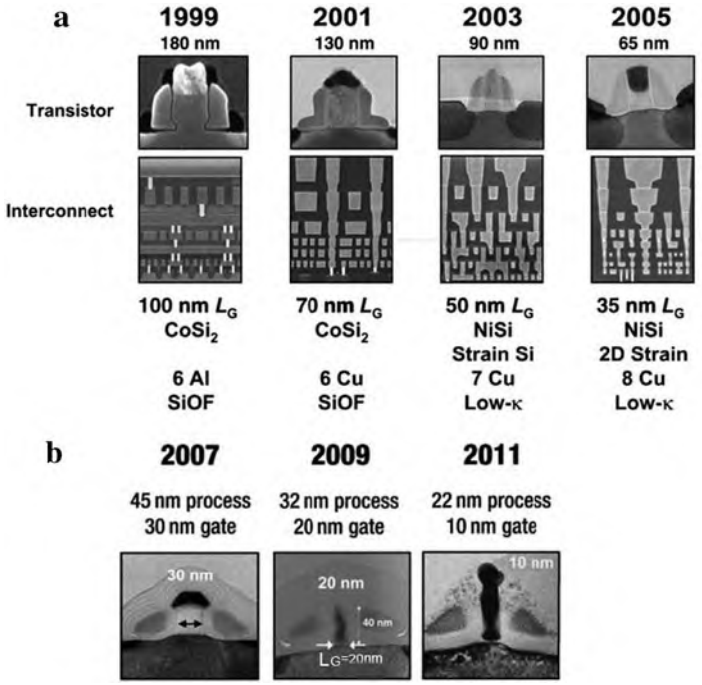

Fig. 9.1 The rate of innovation in transistor density. (**a**) The generations 1999, 2001, 2003, and 2005 with cross sections of the transistors (*upper panels*) and cross sections of the metal interconnects at different magnifications (*lower panels*). L_G is the gate length, "6 Al" means six layers of aluminum, "8 Cu" means eight layers of Cu, etc., $CoSi_2$ or NiSi is the materials of source, drain, and gate electrodes. (**b**) Transistor generations of 2007, 2009, 2011 extending Moore's law. (Reprinted with permission from [9.1]. © 2006 Materials Research Society)

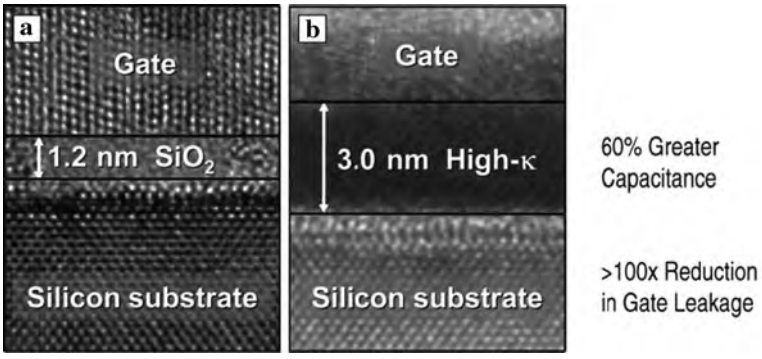

Fig. 9.2 High-resolution cross-sectional images of a transistor structure for SRAMs with a silicon base, a gate on the top, and the dielectric in between. The dielectric layer in (**a**) is a standard SiO_2 gate, 1.2 nm thick. The gate in (**b**) shows a high-*k* dielectric. Although it is much thicker than the gate in (**a**), it has 60% more capacitance and, more importantly, one-hundredth the leakage current because of the thicker gate dielectric. (Reprinted with permission from [9.1]. © 2006 Materials Research Society)

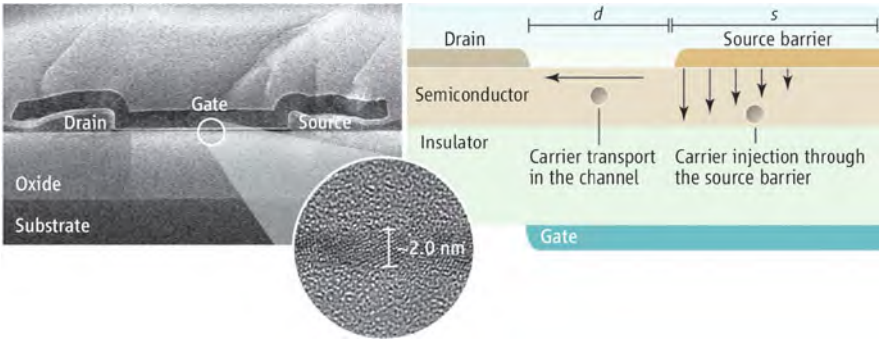

Fig. 9.3 Structure for high-performance transistors in disordered semiconductors. (*Left*) Cross-sectional scanning electron micrograph and transmission electron micrograph of the fabricated nanocrystalline silicon thin film transistors (the minimum channel thickness is 2.0 nm). (*Right*) Schematic of a source-gated transistor (SGT). The arrows in the channel indicate the carrier conduction in the device. (Reprinted with permission from [9.11]. © 2008 AAAS)

law must eventually come to a halt imposed by a hierarchy of physical limits. The five levels of this hierarchy are defined as fundamental, material, device, circuit, and system (see [9.12]). An early analysis of these limitations [9.12] revealed that silicon technology has the potential to achieve a year 2011 terascale integration of more than 1 trillion transistors (with a channel length in the 10 nm range) per chip.

After the termination of the downscaling, conventional transistors could be replaced by a number of devices. One of these could be a silicon-based single-electron transistor (SET; see Fig. 9.4). In a SET, a thin silicon-on-insulator (SOI) may be patterned to form a Si electron island connected to source and drain by two constrictions. The electron island can only be charged at discrete gate voltages and therefore acts as a switch for electrons based on the quantization of electric charge

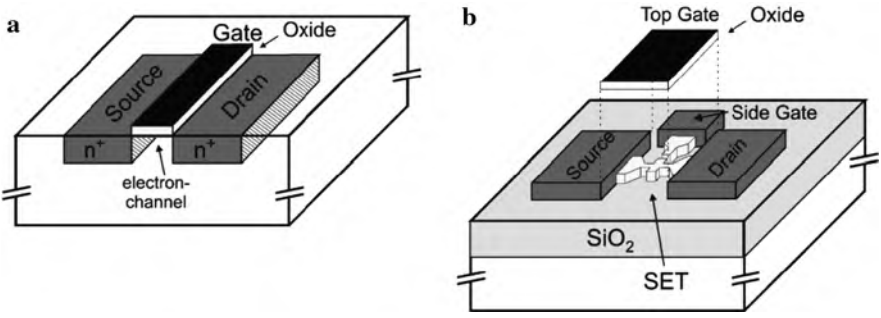

Fig. 9.4 Comparison of (**a**) a MOSFET and (**b**) a silicon-based single-electron transistor. Whereas in the conventional MOSFET a conductive electron channel is formed between two highly doped source and drain regions by applying a gate voltage to a top electrode, the SET uses the charge quantization in a laterally structured electron island which has to be fabricated out of a silicon-insulator film. (Reprinted with permission from [9.13]. © 2001 Elsevier)

(see Sect. 1.3) rather than on the charging of a capacitor like in a metal oxide–semiconductor field-effect transistor (MOSFET). The outstanding property of SETs is to switch the device by adding only one electron to the gate whereas common MOSFETs need about 10^3–10^4 electrons. In addition, the switching times are short because of the low RC time constants of the small constrictions. First SETs working at ambient temperature have been demonstrated earlier [9.14, 9.15]. Carbon nanotube electronics is another approach with a remarkable pace of advances. The first nanotube-based transistor appeared in 1998 [9.16]. Logic circuits [9.17] as, e.g., an inverter (NOT gate) (see Fig. 9.5) or a ring oscillator [9.18], build from nanotube transistors appeared in 2001. In 2006 a five-stage, ten-transistor ring oscillator built as an IC on a single nanotube [9.20] was demonstrated. As a further step for building reliable devices it was shown that carbon nanotubes can be sorted out by both diameter and electronic type (metallic or semiconducting) [9.21].

Graphene nanoribbons with sub-10 nm width were theoretically predicted to be semiconducting (see [9.22]), as demonstrated experimentally [9.22]. Graphene nanoribbon field-effect transistors (GNRFETs; see Fig. 9.6) were demonstrated with I_{ON}/I_{OFF} ratios up to 10^6, an on-state current density as high as $\sim$ 2,000 μA/μm, a carrier mobility of $\sim$ 200 cm^2/Vs, and a scattering mean free path of $\sim$ 10 nm [9.22]. Scattering by edges, acoustic phonons, and defects may play a role [9.22]. The sub-10 nm GNRFETs are comparable to small diameter ($d \leq 1.2$ nm) carbon nanotube FETs with Pd contacts in on-state current density and I_{ON}/I_{OFF} ratio, but have the advantage of producing all-semiconducting devices [9.22].

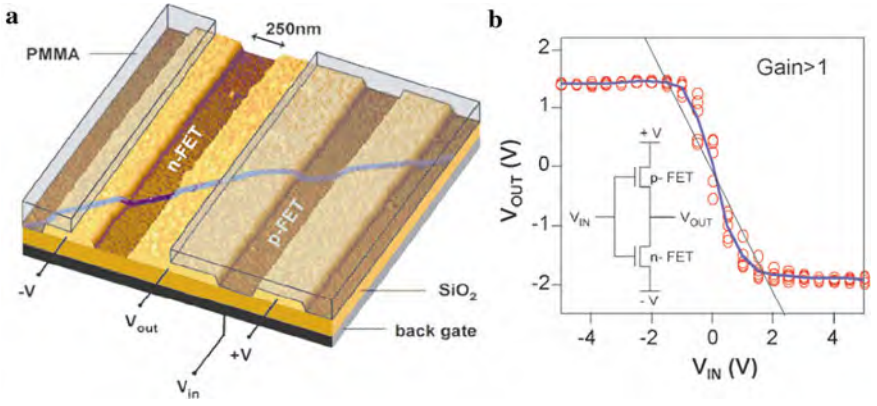

Fig. 9.5 Atomic force microscope (AFM) image showing the design of an intramolecular logic gate. A single-nanotube bundle is positioned over the gold electrodes to produce two p-type CNTFETs (carbon nanotube field-effect transistor) in series. The device is covered by poly(methyl methacrylate) (PMMA) and a window is opened by e-beam lithography to expose part of the nanotube. Potassium is then evaporated through this window to produce a n-CNTFET, while the other CNTFET remains p-type. (**b**) Characteristics of the resulting intramolecular voltage inverter. Open *red circles* are measuring data and the *blue line* is the average of these data. The thin straight line corresponds to an input/output gain of one. (Reprinted with permission from [9.19]. © 2004 Materials Research Society)

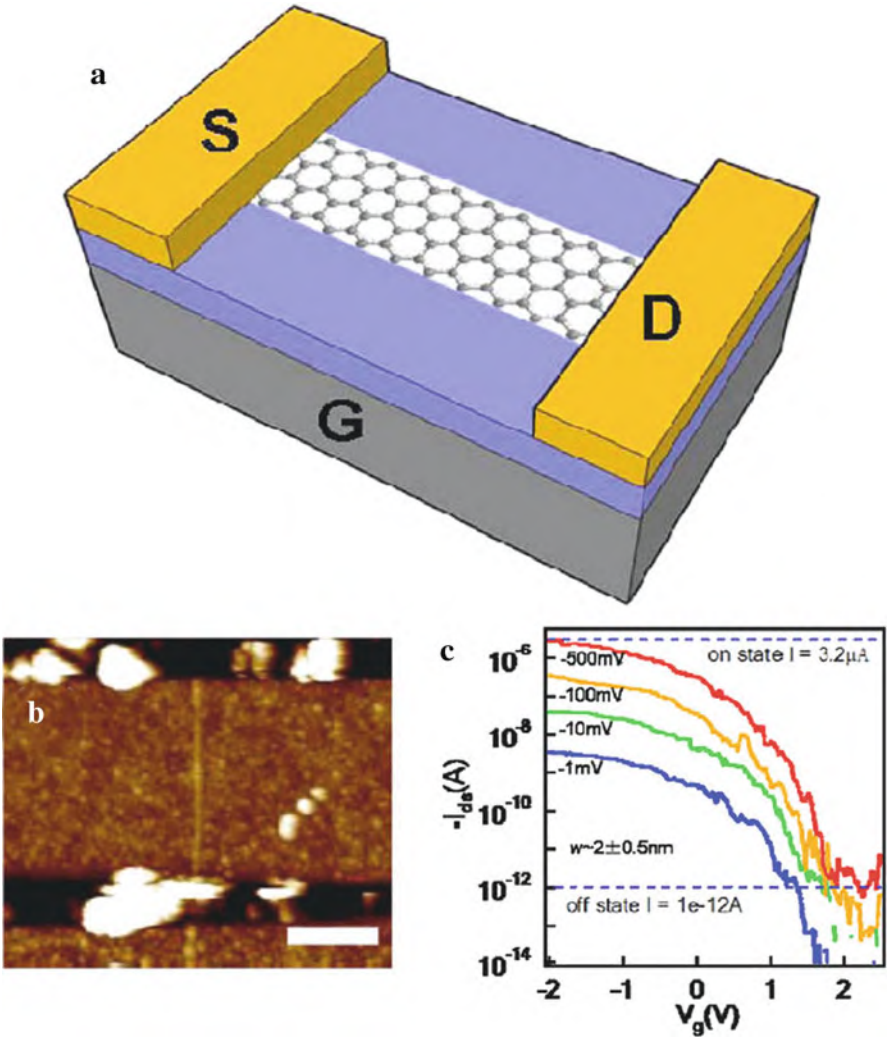

Fig. 9.6 The graphene nanoribbon field-effect transistor (GNRFET). (**a**) Schematics of GNRFET on 10 nm SiO_2 with Pd source-drain electrodes. $P^{++}Si$ is used as backgate. (**b**) Atomic force microscope (AFM) image of a GNRFET with a width of $\omega \sim 2 \pm 0.5$ nm and a length of $L \sim 236$ nm. Scale bar is 100 nm. (**c**) Transistor performance of the GNRFET in (**b**) with current versus gate voltage $I_{ds} - V_{gs}$ under various V_{ds} and an I_{ON}/I_{OFF} ratio of $> 10^6$ achieved at room temperature. (Reprinted with permission from [9.22]. © 2008 American Physical Society)

High-speed integrated circuits may find many new applications when they could be printed with inks containing high-performance semiconducting materials. In inks with a dispersion of single-walled carbon nanotubes the conductivity of the metallic nanotubes can be suppressed by attaching fluorinated olefins which depletes the density of states at the Fermi level [9.23]. Transistors manufactured using this ink

show a high mobility of 100 cm^2 $(Vs)^{-1}$ *and* an on/off ratio as high as 10^5. Thin-film transistors can be printed with a spatial resolution of 1 μm or less by inkjet printing. Since individual nanotubes have mobilities of 10,000 cm^2 $(Vs)^{-1}$ and more, it is possible that a mobility superior to that of single-crystal silicon (1,000 cm^2 $(Vs)^{-1}$) can be achieved.

9.2 Extreme Ultraviolet (EUV) Lithography – The Future Technology of Chip Fabrication

Extreme ultraviolet lithography (EUVL; see [9.24]) appears to be the most promising fabrication technology for future computer chips [9.25]. With the first-generation ASML demotools for 13.5 nm EUVL scanners deployed in 2006 (see Fig. 9.7b), the first 45 nm logic test chips with functional transistors were fabricated [9.27] with properties consistent with those printed by a standard 193 nm immersion process. With the ASML EUV "preproduction tool" available in 2009, this development will be continued for a test fabrication of 22 nm structural sizes, so that in 2011 EUV lithography will be the most likely technical option for the production of computer chips (see Fig. 9.7a).

For the reduction of the structural sizes in computer chips, the minimum half-pitch (HP; see Sect. 3.10) or the

$$\text{resolution} = k_1 \cdot \lambda/\text{NA}$$

of the optical production tools is of particular importance. According to this relationship the resolution can be improved by reducing the wavelength λ of the light for imaging, by increasing the numerical aperture NA of the optical system, and by reducing the process parameter k_1 which characterizes the printing of a pattern on the mask. Small k_1 values can only be achieved by complex and costly production processes. For $k_1 < 0.25$, dense structures cannot be printed in a single-illumination process but multiple illumination is required (double patterning, spacing [9.28]). A decreased λ and an increase of NA can enhance the resolution, independent of k_1.

In the production of computer chips with 193 nm wave length ArF lasers, where the maximum NA = 1.35 is already approached, the production of structures 32 nm wide (32 nm logic node) in the near future requires the lowering of k_1 to below 0.25 which makes the mask cost escalate. That means that only the lowering of λ to EUV can provide long-term solutions with good prospects, also beyond the 22 nm node.

For EUV lithography novel techniques had to be developed. For powerful radiation sources with several hundreds of watts in the 13.5 nm wavelength regime (Fig. 9.8a) plasmas of Sn or Xe, generated by laser focusing or discharge, are employed. For the manipulation of the 13.5 nm wavelength radiation no lenses but only multilayer interference mirrors (see Sect. 4.3.6) can be used, where Mo–Si multilayers with a layer thickness of λ/4 = 3–4 nm exhibit a high reflectivity (Fig. 9.8a) when fabricated with 150 pm shape and positioning precision [9.25]. This precision

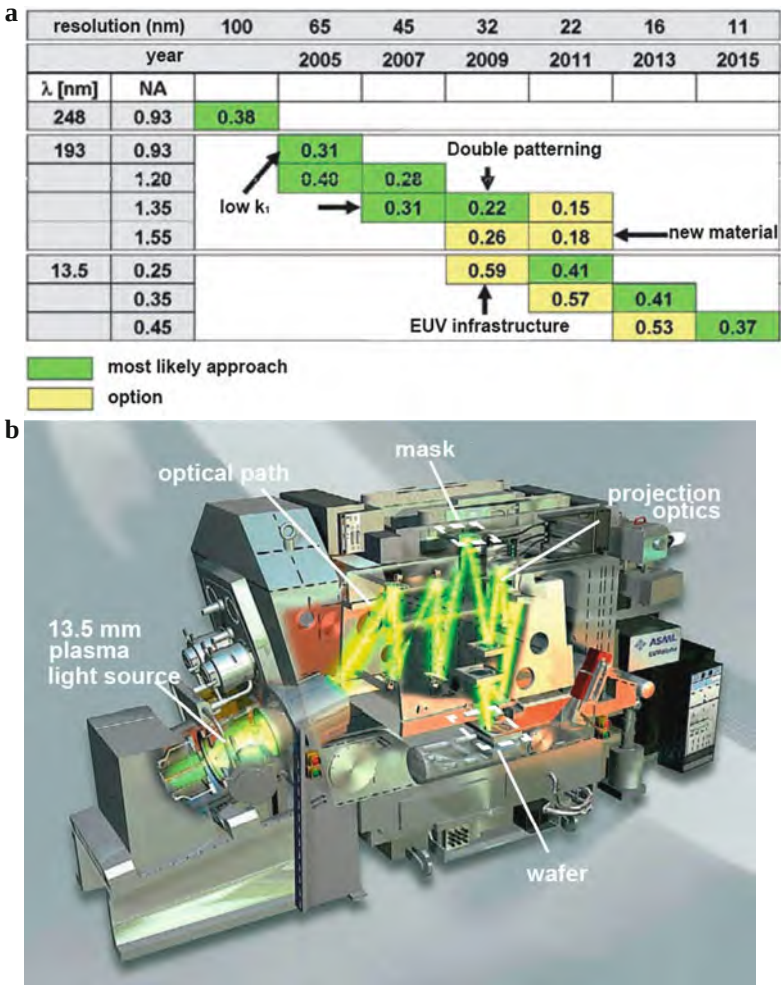

Fig. 9.7 (**a**) The ASML/Carl Zeiss SMT roadmap indicates which technological option – conventional 193 nm lithography or 13.5 nm EUV lithography – will most likely be employed at which time in order to meet the requirements of a particular resolution. The comments indicate the outstanding challenges. (**b**) ASML EUV wafer scanner with the optical system by Carl Zeiss STM [9.26]. The 13.5 nm EUV irradiation generated by a plasma source illuminates the mask and the projection optics image the mask unto the wafer [9.25]. (Reprinted with permission from [9.26] and [9.25]. © 2008 Photonik; T. Heil and M. Lowisch, Zeiss, ASML)

is equivalent to a 2 mm high hill on a 1,000 km distance. The mask with a similar multilayer structure as the mirrors is operated in reflection. The mask patterns are written on the surface of this multilayer where they suppress reflection. Corrections have to be applied to the chip mask to compensate for flare, i.e., variations in the power spectral density of the optical path differences, and of the mask shadowing

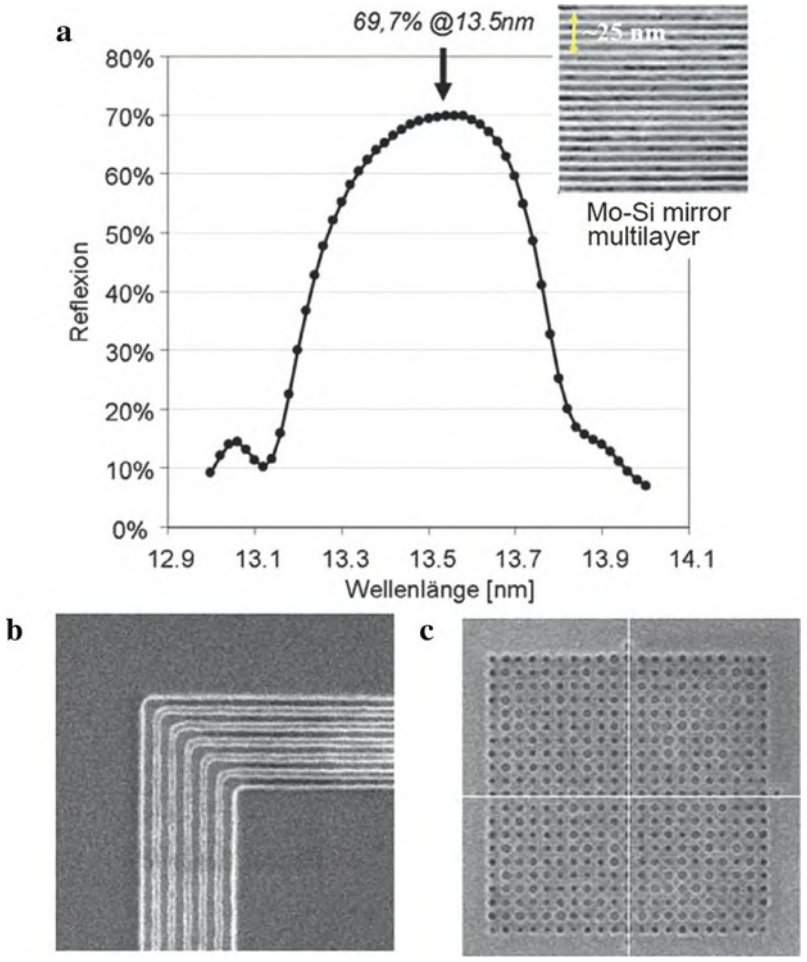

Fig. 9.8 (**a**) Reflection spectrum of a Mo–Si mirror multilayer. The inset shows a transmission electron micrograph of the Mo–Si multilayer. (**b**, **c**) Scanning electron micrograph of 35 nm wide conduction lines (**b**) and 32 nm diameter contact points (**c**) generated by EUV lithography. (Reprinted with permission from [9.25]. © 2008 Photonik; T. Heil and M. Lowisch, Zeiss.)

effects due to a non-normal illumination of the mask plane [9.27]. The projection optics have to image the mask structures without defects over the width of 26 mm of the chip onto the wafer, which is covered with a high-sensitivity resist [9.29], in a time-saving single scan. Since the width of the single nanostructures on the chip differs from the total chip size by 6 orders of magnitude, the information contents of 10^{12} pixels – corresponding to a HDTV image of the size of 1 km^2 – can be transferred to the wafer in a single illumination. This may demonstrate the enormous productivity of the EUV technology. In Fig. 9.8b, c structures generated by means of EUV lithography are shown.

9.3 Flash Memory

Flash memory relies for data storage on controlling electrons stored in a transistor's gate circuit [9.30–9.32]. Floating gate flash memory is a fast growing memory segment [9.30], driven by the rapid growth of portable devices such as digital cameras and cell phones. The technology allows for data stored in multiple memory cells to be erased in a single action (a "flash") by means of an applied voltage. Flash memory cells have been scaled down to 32 nm half-pitch with a cell size of 0.0112 μm^2 and a word line spacing of 20 nm where, however, crosstalk becomes an issue [9.33]. Flash data storage devices with 3 gigabytes per cm^2 [9.34] have been achieved. For further decreasing size, the scaling constraints will require new materials, [9.32] and novel concepts such as charge storage in nanocrystals [9.35] in a non-conducting floating node, which replaces the normally conducting floating gate, or organic flash memory devices based on alterations of a polymer's conformation [9.36]. A conventional floating gate non-volatile flash memory cell (Fig. 9.9) contains a metal oxide semiconductor (MOS) transistor with two gates, a floating gate and a control gate. The memory cell consists of an *n*-channel transistor with the addition of an electrically isolated polysilicon. Any charge present on the floating gate is retained due to the inherent $Si–SiO_2$ energy barrier height, leading to the non-volatile nature of the memory cell. Characteristic of the structure is a thin tunneling oxide (~10 nm), an oxide-nitride-oxide (ONO) interpoly dielectric (IPD) that resides between the two polysilicon gates, and a short electrical channel length. The threshold voltage of the device can be changed by modifying the charge on the floating gate, which can retain this charge for many years. Data can be stored in the memory by adding or removing charge.

Programming of a flash cell can be performed with channel electrons of high kinetic energy – so called hot electrons – which can surmount the 3.2 eV $Si–SiO_2$ energy barrier. When these electrons experience a collision with the Si lattice, they

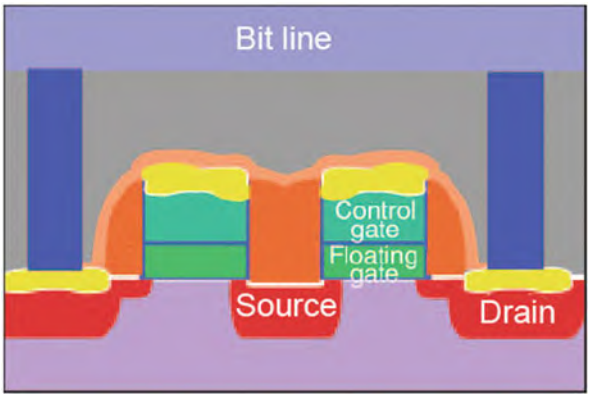

Fig. 9.9 Flash memory cell: cross section along the channel. (Reprinted with permission from [9.30]. © 2004 Materials Research Society)

are directed toward the Si–SiO_2 interface with the aid of the gate field. The electron is subsequently captured on the floating gate and retained as stored charge. The electrical *erasure* of flash memory is achieved by electron tunneling in a high field (8–10 MV/cm) between the floating gate and the channel. When the erase operation has been completed, electrons have been removed from the floating gate, reducing the cell threshold. While programming is selective to each individual cell, erasing is not, with many cells (typically, 64 kbytes) being erased simultaneously [9.30].

Scaling limitations of the flash memory will emerge below the 70 nm lithography node due to the inability of a shorter channel length to withstand the required programming voltage. By choosing dielectric alternatives to SiO_2, the barrier can be tailored to allow hot electron injection to occur at lower voltages. Scaling also affects the adequate coupling of the control gate to the floating gate by the IPD, while minimizing any leakage through the dielectric. An alternative may be to replace the IPD with higher-dielectric constant (high k) materials compared to SiO_2. One thrust to overcome the limitations of the scaling of flash memory is electron storage in nanocrystals in a non-conducting floating node, instead of the conventional conducting floating gate. In Fig. 9.10 3 nm HfO_2 nanodots with densities of 6×10^{12} cm^{-2} in a SiO_2 film on a Si substrate are shown. Memory cells with HfO_2 nanodots can be erased in 0.1–1 ms and exhibit retention times of 10^8 s (>3 years). They are considered suitable as charge storage nodes in future 45 and 32 nm generations [9.35].

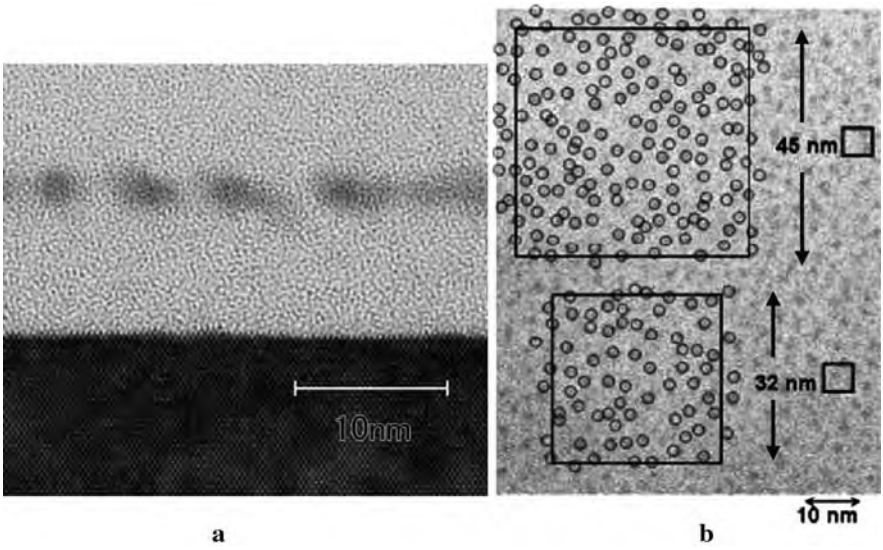

Fig. 9.10 (**a**) Cross-sectional and (**b**) plane-view transmission electron micrographs of ultrahigh-density HfO_2 nanodots in SiO_2 on a Si substrate. The thickness of the initially deposited HfO_2 film was 0.5 nm. In (**b**), nanodots are marked with open circles for clarity. The dimensions of the gate areas of the future 45 nm and the 32 nm technology nodes are also shown. (Reprinted with permission from [9.35]. © 2006 Japan Society of Applied Physics)

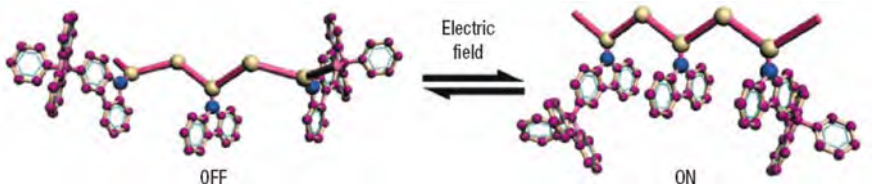

Fig. 9.11 Schematic diagram for the switching transition of the poly(*N*-vinylcarbazole)-phenylfluorene (PVK-PF) molecule from the low conductivity to the high-conductivity states. (Reprinted with permission from [9.36]. © 2008 Nature Publishing Group)

Another choice for scalable flash memories could be organic semiconductor polymers which transport charge via their π orbitals, the orientation of which depends on the conformation of the polymer and affects the charge mobility. The first organic non-volatile flash memory devices were designed [9.36] by taking poly(*N*-vinylcarbazole) (PVK), which transports charge via intrachain stacked π orbitals that result from face-to-face conformation of the carbazole (Cz) group (Fig. 9.11). By adding to PVK the bulky phenylfluorene (PF) as a side group, the steric effects were used to tune the conformation of the polymer. When applying a voltage of 2.2 V to a PVK-PF sandwich device, a sharp increase of the current was observed – the ON state ("write" process) with Cz stacked face to face. The application of a reverse voltage induces conformational changes of the PF groups to the initial state, blocking the face-to-face orientation of Cz – the OFF state (Fig. 9.11). An ON/OFF current ratio of $>10^4$ has been obtained and no degradation was observed of the OFF and ON states after 10^8 read cycles at –1 V [9.36]. Experts see flash and random-access memory (RAM) technologies reaching scale limitations in a similar time-frame after 2010 [9.31]. A new non-volatile technology – phase-change random access memory (RAM) or PRAM – is viewed as the most promising among alternatives to flash. In PRAM (see below), data are stored by altering the chip material's atomic structure, obtaining improved data density and other benefits over standard flash [9.31].

9.4 Emerging Solid State Memory Technologies

Currently, there are three commercially available families of memory: dynamic random access memory (DRAM), static random access memory (SRAM), and flash memory. Consumer products typically use combinations of these three memory families, each having their unique advantages: DRAM is cheap, SRAM is fast, and flash is non-volatile (see [9.37]). In the semiconductor industry, increasing miniaturization is beginning to place strains on existing technologies for data storage and computer memory, which could soon reach fundamental physical limitations. In addition, there is a need to develop new memory technologies that can provide low-power operation and low standby battery drain. These trends have accelerated

Table 9.1 Performance characteristics of conventional and emerging memory technologies. SRAM – static random access memory; DRAM – dynamic random access memory; Flash – flash memory; PRAM – phase change memory; MRAM – magnetoresistive memory; FeRAM – ferroelectric memory; NRAM – nanotube random access memory. The NRAM data should be considered as a target established by Nantero, Inc. [9.37]

	Conventional technologies			Emerging technologies			Prototypes
Parameter	SRAM	DRAM	Flash	PRAM	MRAM	FeRAM	NRAM
Read speed	Fastest	Medium	Fast	Fast	Fast	Fast	Fast
Write speed	Fastest	Medium	Slow	Fast	Fast	Med.	Fast
Cell density	Low	High	Medium	High	High	Med.	High
Process technology, nm	130	80	56	90	130	130	22
Nonvolatility	No	No	Yes	Yes	Yes	Yes	Yes
Future scalability	Good	Limited	Limited	Exell.	Good	Limited	Scalable

the development efforts in universal memory products that integrate the best features of existing memory types into a single package. The new universal memory chip should be cheap and compact with the density of DRAM, draw and dissipate little power, switch in nanoseconds and should be compatible with CMOS architectures [9.38]. There are several possible candidates for a universal memory that are being actively explored by the industry. The new technologies that have already found a niche in the memory market include phase-change memory (PRAM), magnetoresistive RAM (MRAM), and ferroelectric RAM (FeRAM). A number of other technologies including resistance RAM (ReRAM), carbon nanotube RAM (NRAM), and race track memory (RM), which will be briefly discussed below, are being developed to compete in non-volatility with flash memory and in speed and density with conventional SRAM and DRAM [9.37].

Although existing memory technologies continue to advance, providing faster, smaller, and cheaper memory, they are not expected to scale down beyond a very few additional process technology nodes. The most widely used commercial nonvolatile memory – flash – has a low write speed leading to a slow random access. New emerging memory technologies such as FeRAM, MRAM, and PRAM are currently in use in a number of applications where the limitations of flash are an issue. A comparison of the performance characteristics of conventional and novel advanced memory technologies including carbon-nanotube-based (NRAM) prototypes is given in Table 9.1.

9.4.1 Phase-Change Memory Technology

Phase-change non-volatile semiconductor memory technology is based on an electrically initiated, reversible rapid amorphous-to-crystalline phase-change process in multicomponent chalcogenide alloy materials similar to those used in rewritable optical disks (see Sect. 9.6) [9.39, 9.40]. Long cycle life, low programming energy,

and excellent scaling characteristics are advantages that make phase-change semiconductor memory (PCM) a promising candidate [9.41, 9.42] to replace flash memory in future applications [9.39], [9.43]. Under R&D scrutiny for years, Intel Corp. and STMicroelectronics announced in February 2008 the shipment of a 128 Mb device codenamed "Alverstone" using PCM technology, fabricated on a 90 nm process. This may bring PCM technology one step closer to adoption (see [9.43]).

A schematic cross section of a phase-change memory cell together with the corresponding current–voltage curves is shown in Fig. 9.12. The cell is a nonlinear resistor and the readout is performed at low bias (READ in Fig. 9.12b), where the low-field resistance changes by orders of magnitude depending whether the Ge–Sb–Te chalcogenide semiconductor material in the active region of the device is crystalline or amorphous. The propensity to amorphize is due to the chalcogenide (Group VI) components such as Te, which are good glass formers because of their two-fold-coordinating chemical bonds that can produce linear, tangled polymer-like clusters in the melt. This increases the viscosity of the liquid, inhibiting the atomic motion necessary for crystallization (see [9.39]). To reach the switching regions (SET for crystallization and RESET for amorphization due to subsequent quenching, see Fig. 9.12b), the bias is raised above the switching voltage so that enough current can flow through the cell, heating up the active region (Fig. 9.12a) and resulting in either the amorphous–crystalline phase change to the SET state (programming) within <20 ns (see [9.39]) or the crystalline–amorphous phase change to the RESET state at higher temperatures within a few nanoseconds (see [9.39]) with subsequent quenching-in of the amorphous state.

The crucial problem for electronic phase-change data storage is understanding electronic transport which is different in the crystalline and amorphous phases (see [9.40]). While the resistivity in the crystalline phase exhibits an ohmic behavior the

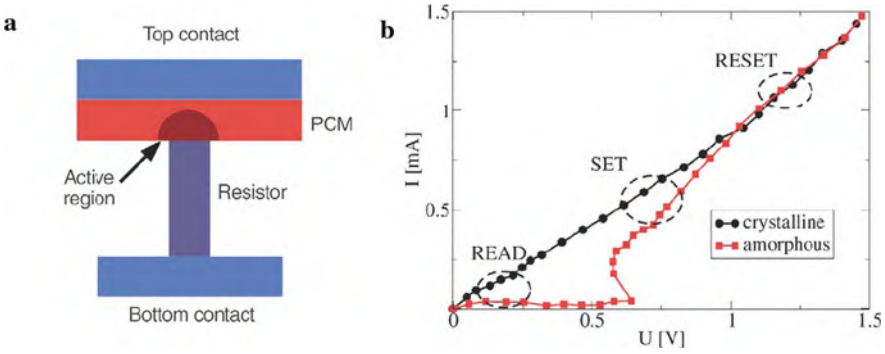

Fig. 9.12 (**a**) Schematic of a phase change memory cell. Depending on the state of the active region (crystalline or amorphous), the resistance of the cell changes by several orders of magnitude. (**b**) Current–voltage curve for a phase-change memory cell. SET and RESET denote the switching regions, while READ denotes the region of readout [9.40, 9.44]. (Reprinted with permission from [9.40]. © 2008 Materials Research Society)

amorphous phase shows threshold switching, allowing the phase transition to occur at modest voltages. The current which is low at small electric fields, increases dramatically when a critical electrical field is exceeded. This leads to a high current in the amorphous phase, generating significant heating which gives rise to the desired phase transition. In modeling of the threshold behavior, at zero electrical field V_A an electron trapped in the amorphous structure needs to overcome the energy barrier E_C–E_T in order to hop onto the neighboring trap, where E_C and E_T are the energies of the conduction band edge and of the trap state, respectively. The application of a sub-threshold voltage changes the shape and the height of the barrier, and therefore the activation energy for electron transport, leading to the generation of carriers and a current

$$I = 2qAN_T \frac{\Delta z}{\tau_0} \exp\left[(E_F - E_C)/kT\right] \sinh\left(\frac{qV_A \Delta z}{\mathrm{k}T2u_a}\right)$$

exponentially rising as a function of voltage. Here A is the area of the contact, N_T the integral of the trap distribution, Δz the intertrap distance, τ_0 the escape time for a trapped electron, E_F the Fermi energy, q the elementary charge, and u_a the thickness of the amorphous chalcogenide. This relation correctly reproduces the current–voltage characteristics of the sub-threshold regime. At large electric fields, the equilibrium distribution of electrons in sub-threshold traps is suggested [9.45] to change into a non-equilibrium distribution at which electrons acquire an effective temperature. As a result of this electron heating, charge carriers from deep traps are allowed to access shallow trap states at higher energies closer to the conduction band edge via thermal emission or tunneling. Because of the exponentially rising emission and the finite relaxation time of the trapped carriers, the occupation of the shallow traps increases with increasing voltage, moving the electron distribution from the equilibrium Fermi distribution to a non-equilibrium distribution. This causes the conductivity to increase exponentially, which leads to a steep enhancement of the current in the system.

Crystallization kinetics is the time-limiting step in the application of phase-change materials. Since an atomistic understanding of these kinetics is missing, experimental studies have focused to the determination of activation barriers for the overall crystallization process, making use of Johnson–Mehl–Avrami concepts (see [9.40]). More recently, the contributions of nucleation and crystal growth to crystallization have been separated, being facilitated by the substantial density change between the amorphous and crystalline phases of 5–10% [9.46]. From atomic force microscopy studies the temperature dependences of nucleation and crystal growth with the corresponding activation energies were determined in dependence of composition. The ratio T_G/T_M of a phase-change material, where T_G is the glass transition temperature and T_M the melting temperature, obviously can provide a first approach to predict the crystallization mechanism: within the interval $0.5 \leq T_G/T_M \leq 0.55$, the materials with lower T_G/T_M values show nucleation-dominated crystallization while materials with values at the upper limit are characterized by growth-dominated crystallization (see [9.40]).

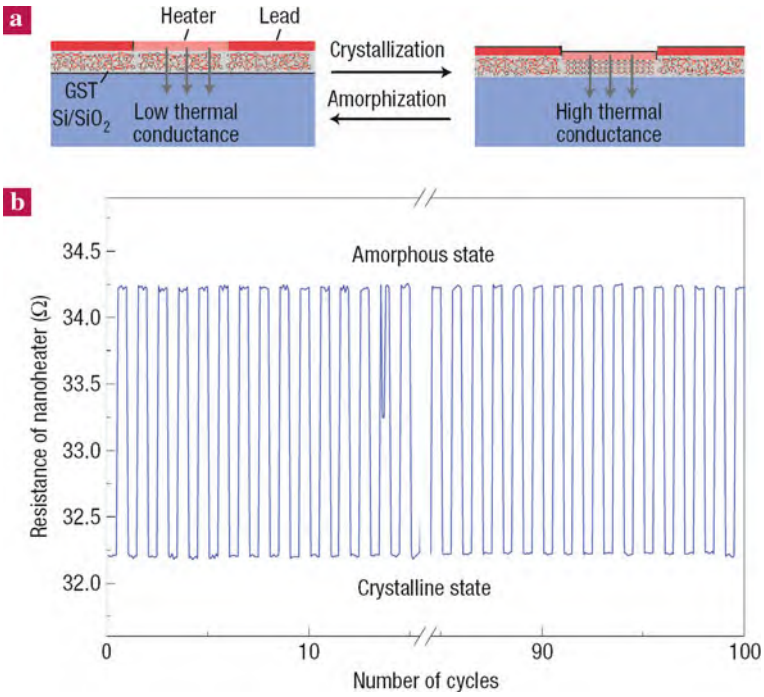

Fig. 9.13 An all-thermal phase-change memory concept. (**a**) Illustration of the concept. By applying the appropriate current (heat) pulse the $Ge_2Sb_2T_5$ film is written (amorphized) and erased (crystallized) by a nanoheater. The phase of the film is read at lower currents by sensing the thermal resistance of the heater, which depends on the phase of the $Ge_2Sb_2Te_5$ film underneath the heater. (**b**) A portion of 100 cycles of successful amorphizing and crystallizing using the all-thermal memory cell. (Reprinted with permission from [9.47]. © 2006 Nature Publishing Group)

An all-thermal phase-change memory concept has been presented (Fig. 9.13) by using a nanoheater, which can be fabricated with a size less than 50 nm, for reversible phase-change recording and reading. Because the amorphous phase has a lower thermal conductivity, the resulting temperature of the substrate and thus the resistance of the platinum heater is higher than in the crystalline phase for a given bias current. The amorphization and crystallization kinetics can, in principle, be as fast as 8 GHz for dimensions smaller than 50 nm (see [9.47]). Another promising approach for optimizing the performance of phase-change electronic memories is the use of nanostructures. Phase change nanostructures were prepared by filling prepatterned holes with a GeSbTe alloy [9.48] or by self-assembling sublithographic GeSbTe nanowires to construct a phase-change device with a threshold voltage of 1.8 V [9.38].

The endurance of phase-change memory cells has been reported as being between 10^9 and 10^{13} write/erase cycles – considerably in excess of nominal 10^6 cycle endurance of flash memory. Data retention and life times of 10 years at

110°C have been anticipated (see [9.39]). One of the strongest advantages of phase-change memory cells is that no physical limit to scaling has been identified for the next lithography generations. Nevertheless, a number of challenges remain before the potential of phase-change memories can realized in high-density commercial products [9.39]. The identification of extremely fast phase-change materials would help to produce a memory that combines the attractive features of the two existing memory technologies, namely the non-volatility of flash memory and the speed of dynamic random access memory (DRAM). This would provide a truly universal memory [9.40]. The threshold switching of phase change materials has been modeled numerically [9.49].

9.4.2 Magnetoresistive Random-Access Memories (MRAM)

The magnetic random-access memory (MRAM) making use of magnetic tunnel junctions (see Sect. 1.4) can provide a non-volatile memory with the density of DRAM (dynamic random-access memory), the speed of SRAM (static random-access memory), unlimited write cycles, and significantly lower write-power requirements than flash memory (commonly used in USB sticks, digital cameras and cell phones) [9.50]. MRAM could be the "dream memory" since it has the potential to replace all the existing memory devices in a computer. This "universal" memory then could become an enabling technology for integrating a computer on a single chip [9.5]. In a magnetic tunnel junction (MTJ), which is the building block of the MRAM, two ferromagnetic layers are separated by a thin (1.2 nm) insulating layer, giving a much larger change in resistance (∼60%; see Fig. 9.14c) from the parallel to the antiparallel magnetization states than a GMR device. The sense and write lines of a magnetic tunnel junction are shown in Fig. 9.14a together with the detailed structure of the MTJ in Fig. 9.14b. A recent development, already in use by Freescale Comp., a former spin-out of Motorola and IBM, is the "toggle" switching of the magnetization in the free layer (see Fig. 9.15) by which switching errors can be suppressed. The synthetic antiferromagnet (SAF) with toggle switching provides another benefit for scaling, because the magnetic anisotropy of the composite structure can be more easily controlled than that of a single layer in order to maintain the anisotropy energy of the shrinking bit by a factor of 30–50 larger than kT.

Magnetic tunnel junctions with much higher magnetoresistive ratios (∼ 350%) were theoretically predicted for Fe/MgO/Fe sandwiches oriented in the (100) direction [9.53] and demonstrated experimentally [9.54, 9.55] (see Fig. 9.16) with tunneling magnetoresistance ratios of more than 400% (see [9.57]). This shows that not exclusively the nature of the ferromagnetic electrodes but the chemical bonds formed at the ferromagnet/insulator interface influence the magnitude of the tunneling current as described in terms of a tunneling current matrix element. The tunneling current is proportional to the density of states multiplied by the corresponding tunneling matrix element, which will be strongly influenced by the conduction band wave functions in the ferromagnet. Since the electronic wave

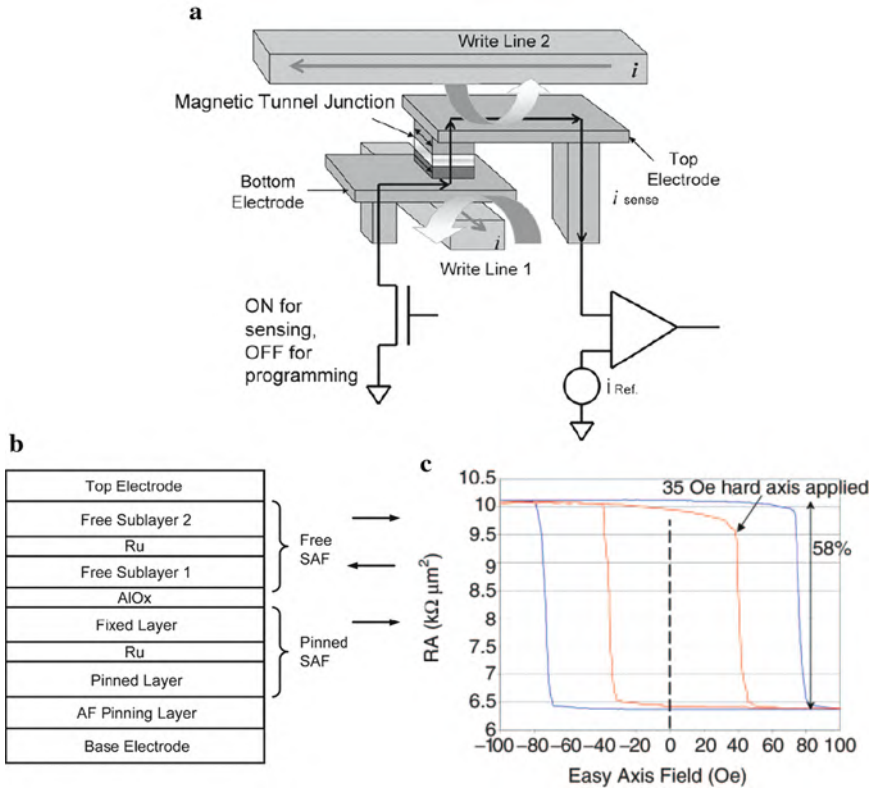

Fig. 9.14 (**a**) MRAM (magnetoresistive random-access memory) bit cell structure, showing the sense path and programming lines. (**b**) Bit cell material stack of a magnetic tunnel junction (MTJ) showing the synthetic antiferromagnetic (SAF) free layer [9.51]. (**c**) Resistance (expressed as resistance-area product RA of the MTJ material) versus field for a 0.6 μm × 1.2 μm bit with (*red curve*) and without (*blue curve*) hard axis field applied. The parallel magnetization is low resistance and the antiparallel state is high resistance with a ratio in this case of 58% [9.52]. (Reprinted with permission from [9.51] (**a**) (**b**) and [9.52] (**c**). © 2005 IEEE (**a**) (**b**) and © 2004 Materials Research Society (**c**))

functions decay into the tunnel barrier depending on the symmetry of the wave function, states with a more delocalized character will decay less quickly into the barrier and, therefore, have a correspondingly larger matrix element. This means that the majority and minority spin-polarized conduction band states in the ferromagnet, with significantly different symmetries, will decay at different rates across the tunnel barrier, leading to an increased (or decreased) spin polarization of the tunneling current. Thus the tunneling barrier can act as a spin filter, giving rise to a resistivity strongly dependent on the mutual orientations of magnetizations in the magnetic tunneling junction.

Further scaling of MRAM is expected from nanoscale current-induced magnetization reversal by spin torque (see Sect. 8.7) in trilayer GMR structures [9.50].

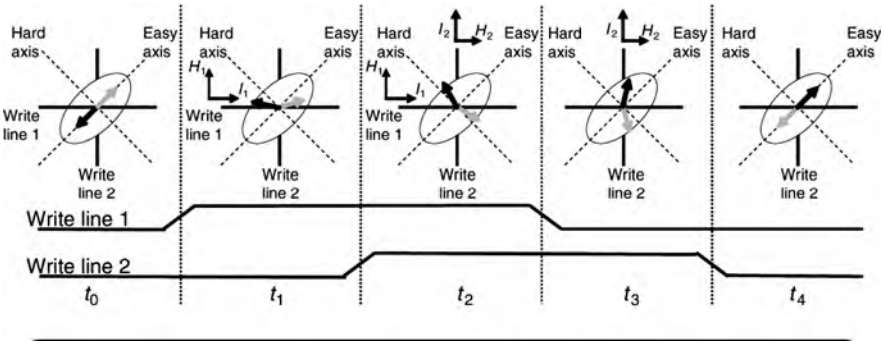

Fig. 9.15 The pulse sequence for toggling a magnetic tunnel junction MRAM bit. The pulses of the two write lines rotate the synthetic antiferromagnet (SAF) by 180° to switch between the antiparallel (high resistance) and parallel (low resistance) orientation of the magnetization. Only the bottom layer of the SAF, close to the insulating layer, determines the resistance of the bit. I_1 and I_2 are the programming currents in the lines 1 and 2, respectively, whereas H_1 and H_2 are the corresponding magnetic fields. Timing intervals between pulses are indicated by t_1, t_2, t_3, t_4. (Reprinted with permission from [9.52]. © 2004 Materials Research Society)

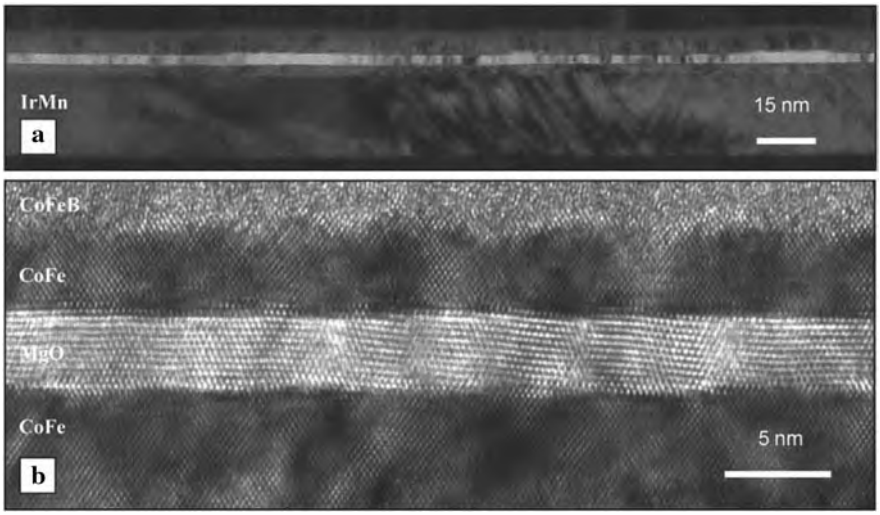

Fig. 9.16 Transmission electron micrographs of a magnetic tunnel junction showing a highly oriented (100) MgO tunnel barrier. (**a**) Growth of ultrasmooth underlayers formed from TaN, Ta, the antiferromagnetic exchange-bias layer of $Ir_{76}Mn_{24}$, the ferromagnetic reference layer, the MgO layer with the subsequent counter ferromagnetic electrode of amorphous $[Co_{70}Fe_{30}]_{80}B_{20}$. (**b**) High-resolution image along the [9.110] zone axis showing atomically resolved lattice planes with (100) planes perpendicular to the growth direction. (Reprinted with permission from [9.56]. © 2006 Materials Research Society)

This development is key for scaling MRAM to at least the 32 nm lithography node. The requirement for this novel spin momentum transfer (SMT) effect is that the dimensions of the bit must be well under 100 nm. This innovation will significantly shrink the size of the bit and allow the bit to be switched at much lower energy than the "toggle" bit [9.50]. The key features of future MRAMs incorporating SMT switching are compiled in Table 9.2. Future SMT MRAMs may outperform volatile DRAMs and SRAMs or flash memories which exhibit long program times, limited write ability, and high-power consumption.

For current-induced spin torque in an MTJ, the tunneling current arriving at the storage layer is spin-polarized because the population of the tunneling electrons with one sign of spin is higher than with the other sign (see [9.57]). The net spin moment of the tunneling current is proportional to both the degree of polarization and the current density, and can generate a torque, on the local magnetization. Depending on the direction of the tunneling current, the spin torque switches the storage layer magnetization to a state either parallel or antiparallel to the magnetization of the reference layer. When a spin-polarized current flows from the fixed layer to the free layer with antiparallel magnetization then they are aligned in parallel. When a spin-polarized current flows from the free layer to the fixed layer with parallel magnetization, then the magnetization of the free layer is reversed to an antiparallel direction, which is ascribed to the action of the electrons reflected from the field layer [9.57].

Calculations of MRAM elements with perpendicular magnetization (see Fig. 9.17a) based on spin torque switching with dynamic micromagnetic modeling

Table 9.2 Projected performance of MRAM, SMT MRAM, and conventional semiconducting memories [9.50]

	Standard			SMT			SMT
	MRAM (90 nm)[a]	DRAM (90 nm)[b]	SRAM (90 nm)[b]	MRAM (90 nm)[a]	Flash (90 nm)[b]	Flash (32 nm)[b]	MRAM (32 nm)[a]
Cell size (μm^2)	0.25	0.25	1–1.3	0.12	0.1	0.02	0.01
Mbit/cm^2	256	256	64	512	512	2500	5000
Read time (ns)	10	10	1.1	10	10–50	10–50	1
Program time (ns)	5–20	10	1.1	10	$0.1–10^8$	$0.1–10^8$	1
Program energy/bit (pJ)	120	5	5	0.4	$3–12\times10^4$	1×10^4	0.02
Endurance	Needs refresh $>10^{15}$	$>10^{15}$	$>10^{15}$	$>10^{15}$	$>10^{15}$ read $>10^6$ write	$>10^{15}$ read $>10^6$ write	$>10^{15}$
Nonvolatility	Yes	No	No	Yes	Yes	Yes	Yes

MRAM = magnetic random-access memory. SMT = spin momentum transfer; DRAM = dynamic random-access memory; SRAM = static random access memory

[a]MRAM values according to [9.50]

[b]These values are from the International Technology Roadmap for semiconductors [9.50]

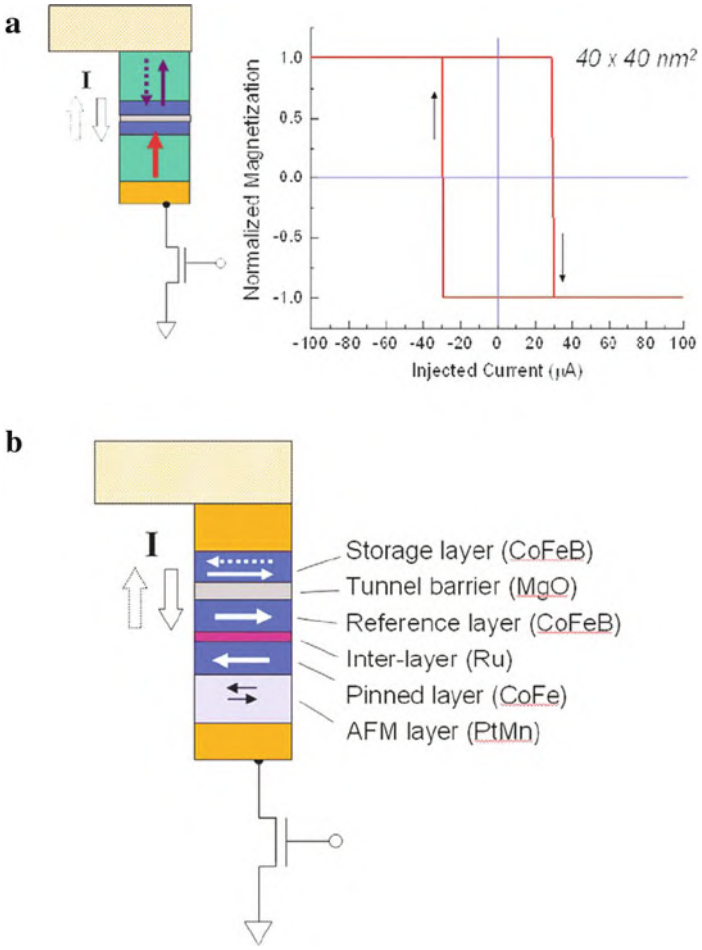

Fig. 9.17 (**a**) Calculated magnetic switching of the free-storage layer of a perpendicular magnetic tunneling junction (MTJ) memory element by direct current injection using spin torque. The magnetization in the MTJ element is perpendicular and the junction area is 40 nm × 40 nm. The perpendicular magnetization can be accomplished by using materials with magnetocrystalline anisotropy that forces the magnetization to be oriented along certain crystallographic axes. The magnetization of the two nanosized layers (*green* and *blue*) within a bilayer is strongly coupled by the ferromagnetic exchange energy, so that the magnetization of the thinner layer is completely perpendicular to the film. The anisotropy strengths of the two bilayers are chosen to be different, yielding different switching field thresholds which enable well-defined parallel and antiparallel states to be reached. The two spin-polarization layers adjacent to the tunnel barrier are assumed to be $Co_{90}Fe_{10}$. A switching current threshold of 30 μA is obtained. (**b**) Schematic of Sony's spin-RAM memory element with direct current injection using spin torque to switch the free-storage layer. (Reprinted with permission from [9.57]. © 2006 Elsevier)

have suggested that such a design may enable MRAM chips to reach many gigabits of storage capacity with low operating power [9.57].

Freescale Semiconductor Comp. has shipped 4 Mbit toggle MRAM devices in 2006 where writing is performed via magnetization reversal of the free-storage layer in an MTJ induced by the magnetic fields generated by the current pulses in the writing lines. The 4 Mbit chip has a relatively small bit count, but applications where battery backup (which cost money and space) can be eliminated will benefit by replacing SRAM or flash with MRAM. This represents the commercial emergence of a truly new memory technology [9.58].

The first on-chip demonstration of a spin-torque-operated non-volatile memory device, a 4 kbit MRAM device named spin-RAM, has been performed by Sony Company in 2005. In this demonstration, the memory elements (see Fig. 9.17b) are CoFeB/MgO/CoFeB MTJs with a tunneling magnetoresistance (TMR) ratio of >160% and a low RA (resistance-area) product of 20 $\Omega\ \mu m^2$ [9.57].

9.4.3 Ferroelectric Random-Access Memories (FeRAM)

Ferroelectric random-access memory (FeRAM) is a type of non-volatile RAM that uses a ferroelectric film as a capacitor for storing data. FeRAM has low access times, high-speed read/write operations, comparable to volatile dynamic RAM (DRAM), it offers the advantages of easy embedding into large-scale integration (LSI) circuits, and it exhibits low power consumption [9.59].

A conventional memory cell for storing one data bit is composed of a cell-selection transistor and a capacitor in the case of a 1T1C (one transistor, one capacitor)-type FeRAM. For higher reliability, the number of transistors (T) and capacitors (C) has been enhanced. In commercially available FeRAMs, PZT [$Pb(Zr_{0.3}Ti_{0.7})O_3$] or SBT ($SrBi_2Ta_2O_9$) is used as ferroelectric material. In order to realize a high-speed system, LSI circuits with embedded non-volatile RAM, a 6T4C type FeRAM (see Fig. 9.18) with a non-destructive readout, unlimited endurance to read/write cycling, an access time of < 10 ns, and a compatibility with standard CMOS LSI components have been developed (see [9.59]). The memory cells in 6T4C-type FeRAMs are larger than those in SRAMs but can be scaled down more easily than in conventional FeRAMs.

Another type of ferroelectric memory, called FET-type FeRAM, is developed from an MFSFET (metal-ferroelectric-semiconductor FET) transistor, in which the gate insulator is composed of a ferroelectric material. In this FET, the polarization direction of the film can be read out non-destructively using the drain current. Based on $Ba_4Ti_3O_{12}$ films, FeRAMs have been developed to be embedded into a complementary metal oxide semiconductor (CMOS) device. This FeRAM with a size of 180 nm exhibits extended read cycle endurance with more than 10^{11} cycles [9.60].

Fe-RAM embedded LSI circuits have been used in smart cards, radiofrequency identification (RFID) tags, and as a replacement for battery-backed-up static RAMs

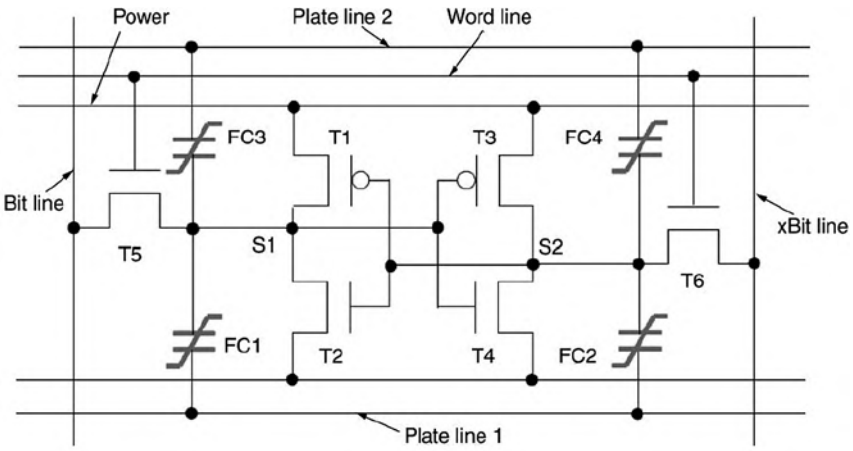

Fig. 9.18 Memory cell circuit of a 6T4C (six transistors, four capacitors) –type FeRAM; FC = ferroelectric capacitor. (Reprinted with permission from [9.59]. © 2004 Materials Research Society)

(BBSRAM), as well as in many other systems on a chip (SoC) (see [9.59]). Recent studies showed that material volumes down to $(20\ \text{nm})^3$ can be ferroelectric and, by making use of scanning probe techniques, storage densities up to 1.5 Tbit/in^2 could be demonstrated [9.61]. Ferroelectric polymers [9.62, 9.63] can be easily transformed into high-density arrays of nanostructures by a nanoembossing protocol, with integration densities larger than 33 Gbits/inch^2 [9.63]. Each nanocell shows a narrow square-shaped hysteresis curve, with low energy losses and a coercive field of $\sim 10\ \text{MVm}^{-1}$, well below previously reported bulk values.

9.4.4 Resistance Random Access Memories (ReRAMs)

Resistance random access memories (ReRAMs) are capacitor-like structures composed of insulating or semiconducting metal oxides, manganites, or titanates that exhibit reversible resistive switching on applying voltage pulses. Recent studies indicate that a thermal or electrochemical redox reaction in the vicinity of the interface between the oxide and the metal electrode is a plausible mechanism for resistive switching (see [9.64, 9.65]).

In the resistive switching phenomenon, a large change of resistance (>1,000%) occurs on applying pulsed voltages (Fig. 9.19). The resistance of the cell can be set to a desired value by making use of an appropriate voltage pulse, with a switching velocity faster than a few nanoseconds [9.66]. Prototype ReRAM devices composed of $Pr_{0.7}Ca_{0.3}MnO_3$ (PCMO) and NiO have been demonstrated recently by Sharp Corporation [9.67] and Samsung [9.68], respectively. However, an integrated circuit

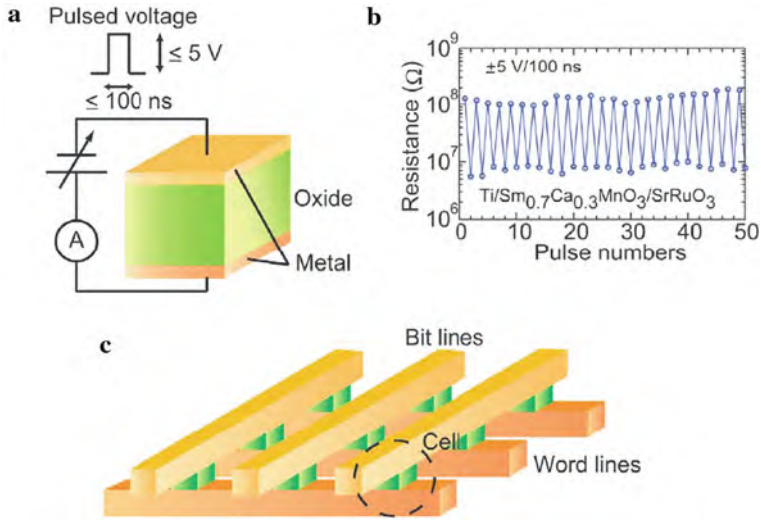

Fig. 9.19 (**a**) Diagram of a ReRAM memory cell with a capacitor-like structure in which an insulating or semiconducting oxide is sandwiched between two metal electrodes. (**b**) Resistive switching in a $Ti/Sm_{0.7}Ca_{0.3}MnO_3/SrRuO_3$ (MIM) cell at room temperature. By applying a pulsed voltage of ±5 V, the resistance of the cell changes reversibly between high- and low-resistance states. (**c**) Diagram of a cross-point memory structure. Word and bit lines are used for selecting a memory cell and writing/reading data respectively. (Reprinted with permission from [9.64]. © 2008 Elsevier)

ReRAM memory, consisting of a sufficient number of cells to be practical, has not yet been demonstrated [9.64].

Based on the *I*–*V* characteristics, two different switching behaviors – unipolar and bipolar – can be observed in different materials [9.64]. The unipolar switching process in, e.g., NiO is ascribed to the formation of filamentary conduction paths (Fig. 9.20) occurring presumably in the grain boundaries [9.69]. In contrast, in bipolar-type switching as, e.g., in a $Ti/La_2\ CuO_4/La_{1.65}Sr_{0.35}CuO_4$ cell [9.64], electronical migration of oxygen ions (by a vacancy mechanism) in the vicinity of the interfaces is regarded as the driving force [9.70–9.72].

9.4.5 Carbon-Nanotube (CNT)-Based Data Storage Devices (NRAM)

Carbon-nanotube (CNT)-based data storage devices (NRAM) show fast write and read speeds, high cell densities, and allow for non-volatile operation [9.37]. Designs of CNT-based electromechanical data storage devices may exploit CNTs as both molecular device elements and molecular wires for the read–write scheme.

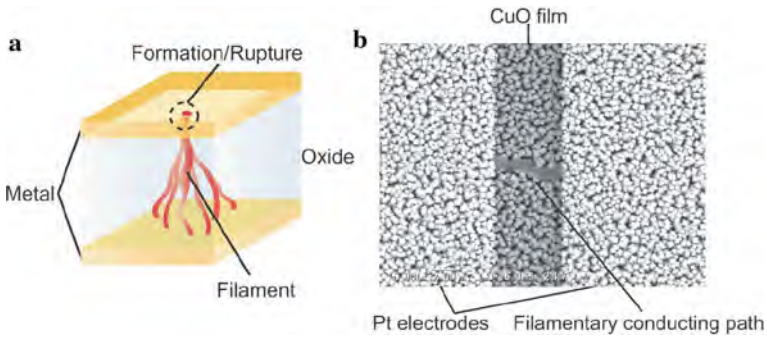

Fig. 9.20 (**a**) Proposed model for unipolar switching of a Pt/NiO/Pt (ReRAM) cell with filamentary conduction paths. (**b**) Scanning electron micrograph of a filamentary conduction path in a CuO film between Pt electrodes with a distance of 5 μm. (Reprinted with permission from [9.64]. © 2008 Elsevier)

The achievement of the controlled and reversible telescopic extension of multiwalled CNTs [9.73] led to a suggestion of an electromechanical switch, operated through the electrostatically initiated sliding of the inner core of a multiwalled CNT out of its sleeve (Fig. 9.21). The device requires a < 10 V of pull-in voltage on the drain electrode and <100 V of pull-out voltage on the gate electrode to produce reversible "0 → 1" conductance cycles with extremely fast switching (see Table 9.3).

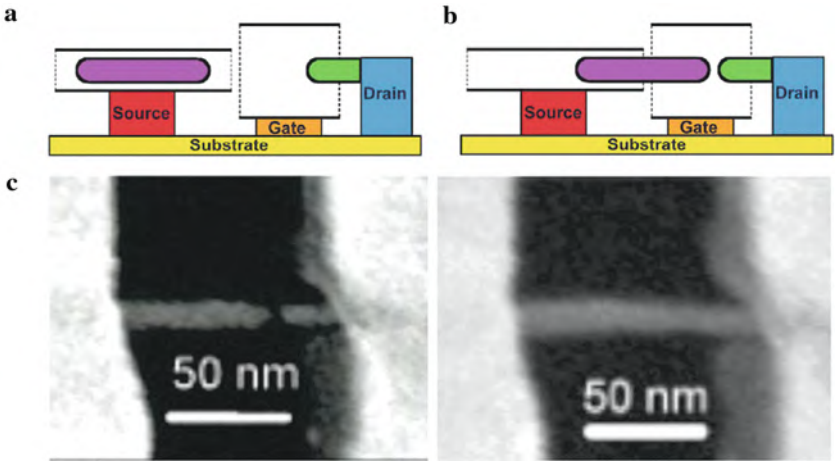

Fig. 9.21 A three-terminal memory cell based on telescoping carbon nanotubes. An all-carbon memory cell with a CNT attached to the gate electrode: (**a**) in non-conducting state "0" and (**b**) in the conducting state "1". (**c**) Scanning electron micrographs of a memory cell with a flat gate electrode [9.37, 9.74]. (Reprinted with permission from [9.37]. © 2008 Elsevier)

Table 9.3 Operational parameters of electromechanical data storage devices based on telescoping carbon nanotubes; for example see [9.37]

Type of study	Linear size, nm	Pull-in voltage, V	Operation frequency, GHz
Experiment	300	4–10	>1
Theory	5–60	6	<100

Memory devices based on CNTs (NRAM) may allow, at least in theory, storage densities higher than those of DRAM (see Table 9.3). Nantero Inc. has recently demonstrated a prototype of a 22 nm NRAM switch and suggested an NRAM scale down below the 5 nm technology node [9.37]. All these advances, however, will become commercial reality only if radical changes in processing are found that gain precise control over the number and spatial location of CNTs over large areas [9.37].

9.4.6 Magnetic Domain Wall Racetrack Memories (RM)

The roadmap for memories means that the size of the memory cell will need to go below 30 nm until 2013. This is made possible by developments that allow multiple bits of information to be stored in magnetic domain walls. This leads to the development of the racetrack memory [9.75]. The controlled movement of domain walls (DWs) in magnetic nanowires by short pulses of spin polarized current (see Sect. 8.7) gives promise of a non-volatile memory device, the magnetic racetrack memory (RM) [9.76–9.79], with the high performance and reliability of conventional solid-state memory but at low cost of conventional magnetic disc drive storage. The racetrack memory is, furthermore, an example of the move toward 3D microelectronic devices.

A domain wall in the section A and B of a nanowire (Fig. 9.22a) can be created by a current pulse from a pulse generator (PG-1 or PG-2) into line A. A current of a density of $\sim 2\times10^8$ A/cm^2 that flows into the nanowire drives the DW along the nanowire between A and B. The position of the DW can be controlled by varying the injection pulse length without using any magnetic field. Sequential injection and removal of two domain walls is detected by specific changes in the nanowire resistance (Fig. 9.22b, c). A DW shift register memory, namely a three-bit unidirectional serial-in, serial-out memory, in which the data are coded as the magnetization direction of individual domains, is shown in Fig. 9.23a. A left-pointing domain represents a 0 and a right-pointing domain a 1. The data was written into the left-most domain, was shifted by two domains, and then read from the state of the right-most domain. For example, when the data sequence 010 111 is written into the register, the resistance and the corresponding magnetization configuration

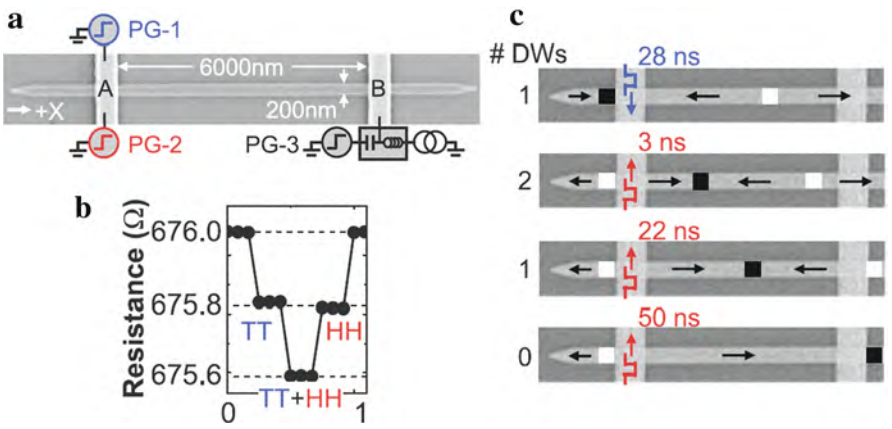

Fig. 9.22 (**a**) Scanning electron micrograph of a permalloy nanowire and the electrical contact lines A and B. PG, pulse generator. (**b**) Variation of the nanowire dc resistance and (**c**) illustration of the corresponding motion of tail-to-tail (TT; *white squares*) and head-to-head (HH; *black squares*) domain walls. *Black arrows* represent the magnetization direction within each domain, *blue* and *red arrows* represent the electron flow directions. (Reprinted with permission from [9.77]. © 2008 AAAS)

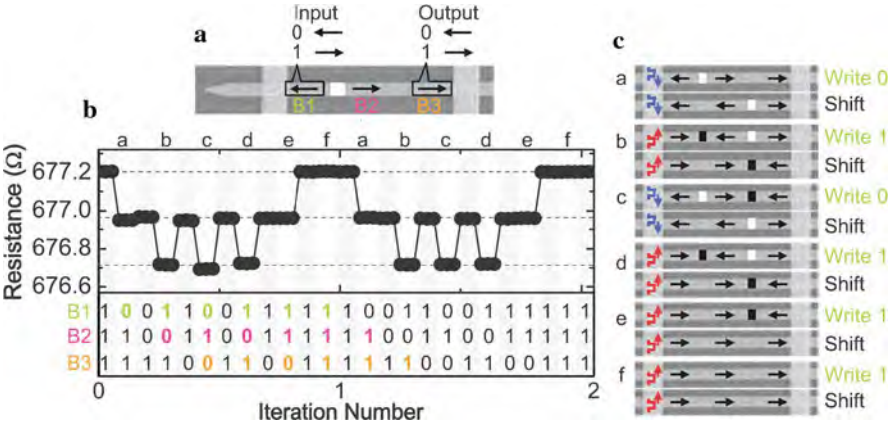

Fig. 9.23 Three-bit magnetic domain wall (DW) shift register. (**a**) The data is encoded by the magnetization direction of three domains in the nanowire. (**b**) Variation of the nanowire resistance when a pulse sequence is used to write and shift along the register the sequence 010 111 two times in succession. The *light* and *dark* regions indicate writing and shifting operations, respectively. The table shows the corresponding evolution of the states of the three bits during these operations. The *highlighted* digits show how the input bit sequence is transferred to the output after two write/shift operations. (**c**) Schematic illustration of the shift-register operation. *White squares* and *black squares* represent tail-to-tail and head-to-head DWs, respectively. *Black arrows* indicate the magnetization direction of each domain. *Blue* and *red arrows* show the electron flow directions. (Reprinted with permission from [9.77]. © 2008 AAAS)

evolved as shown in Fig. 9.23b, c. In Fig. 9.23b, the light regions correspond to write operation and the shaded regions to a shift operation. The input sequence is accurately transferred to the output after two write/shift operations, with a cycle time to write and shift one bit of ∼30 ns. The rapid motion of a series of DWs using nanosecond current pulses not only demonstrates the viability of a shift register memory but also indicates the possibility of current-controlled DW-based logic devices [9.77].

The concept of racetrack memories is to crate U-shaped wire loops, ∼100 nm in diameter, containing regions magnetized in opposite directions over a total length of tens of microns (Fig. 9.24). This series of domain walls, which represents a series of bits, could be passed up and down the nanowire (Fig. 9.24f) past reading or writing devices. The process involves the motion of only magnetic moments – no atoms move, and, therefore, exhibits no wear or fatigue. Each column may have its own reading/writing device with a read/write velocity of 100 m/s at a bit size of ∼1 μm. This makes the system much faster than disk drives with only one reading/writing device, yielding an average access time for RM of 10–50 ns, as compared to 5 ms for a hard disc drive (HDD) and perhaps ∼10 ns for advanced MRAM [9.79]. The RM data storage may be cheaper even than flash [9.78] because one could store in the same area of Si, that stores one bit in flash, 10 bits in the RM technology. If RM could replace disk drives and flash, it opens up the possibility of simplifying computers by reducing the number of memory storage technologies on which they rely. A challenge for the development of racetrack memories is the high-current densities of $\sim 2 \times 10^8$ A/cm^2 required at present for domain wall motion. The critical current can, however, be substantially reduced by resonantly amplifying the DW's oscillatory motion at pinning centers making use of properly engineered current pulse sequences (see [9.79]).

9.4.7 Single-Molecule Magnets

Single-molecule magnets (SMMs; see Sect. 8.8) could be a promising alternative for high-density data storage, but they need to be connected to a conducting surface. SMMs based around four atoms of iron with oxygen, carbon, and sulfur atoms can be attached to a gold substrate by self-assembly, showing the signature hysteresis loop at 0.5 K and a magnetization maintained for about 220 s [9.80].

9.4.8 10 Terabit/Inch^2 Block Copolymer (BCP) Storage Media

Ordered arrays of cylindrical nanodomains of block copolymers (two chemically dissimilar polymers joined together) 3 nm in diameter (Fig. 9.25) with areal densities in excess of 10 terabits per square inch can be produced [9.81]. These BCP films are promising candidates for the generation of ultrahigh density storage media that have the potential of being addressable [9.81].

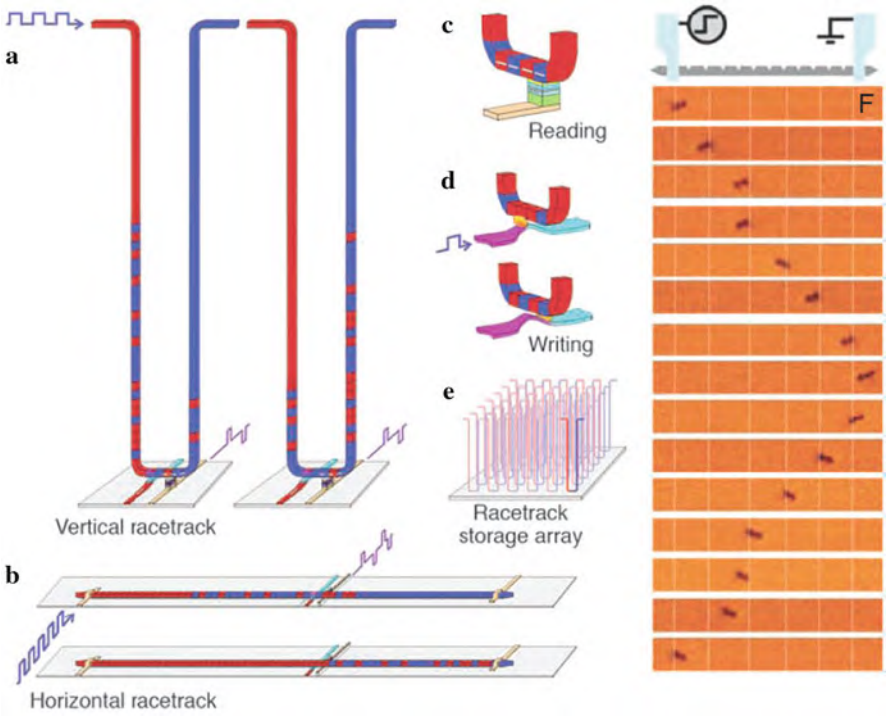

Fig. 9.24 The racetrack memory is a ferromagnetic nanowire, with data encoded as a pattern of magnetic domains. Pulses of highly spin-polarized current move the pattern of domain walls (DWs) coherently along the length of the wire past read and write elements. (**a**) A vertical-configuration racetrack offers the highest storage density in a U-shaped nanowire normal to the plane of the substrate. The two cartoons show the magnetic patterns before and after the DWs have moved down one branch of the U, past the read and write elements, and then up the other branch. (**b**) A horizontal configuration uses a nanowire parallel to the plane of the substrate. (**c**) Reading data from the stored pattern is done by measuring the tunnel magnetoresistance of a magnetic tunnel junction element connected to the racetrack. (**d**) Writing data is accomplished, for example, by the fringe fields of a DW moved in a second ferromagnetic nanowire oriented at right angles to the storage nanowire. (**e**) Arrays of racetracks are built on a chip to enable high-density storage. (**f**) Magnetic force microscopy (MFM) for imaging the motion of a single tail-to-tail vortex DW. The cartoon at top shows a schematic of the experiment. A nanowire with a series of notches for pinning the domain walls was connected to electrical contacts to allow for injection of current pulses. Experimental results are shown for a 40 nm thick, 100 nm wide permalloy nanowire with 11 triangular notches located 1 μm apart; a part of the nanowire with six notches, indicated by vertical *white lines*, is shown. Single current pulses, 8 V (26 mA) and 14 ns long, were applied between each image sequentially from top to bottom, applying pulses with negative polarity for the first eight images and pulses with positive polarity for the last seven images. (Reprinted with permission from [9.79]. © 2008 AAAS)

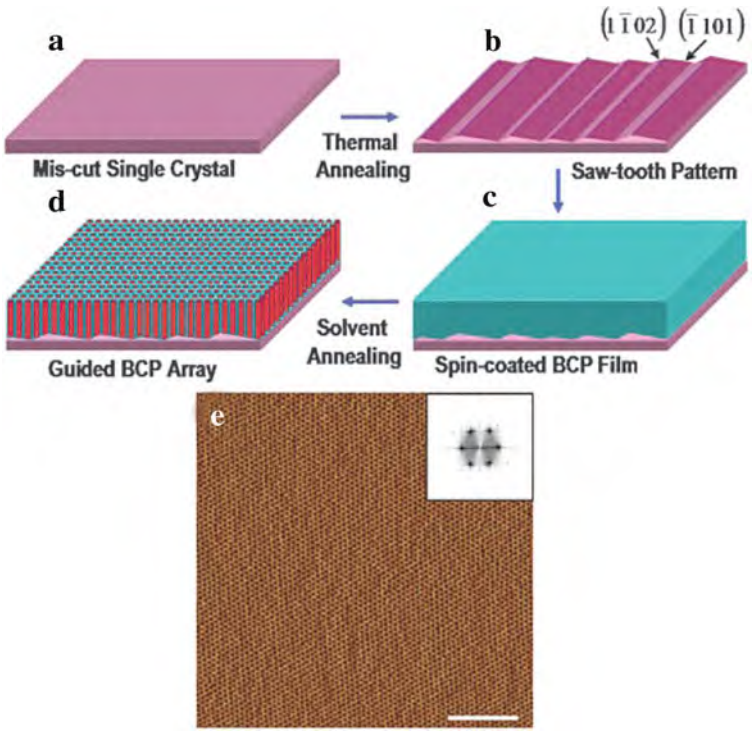

Fig. 9.25 (**a**–**d**) Schematic illustration of the strategy used for generating block co-polymer (BCP) cylindrical nanodomains on highly oriented facets on a single-crystal sapphire surface (**a**) after annealing at 1500°C to form sawtooth patterns (**b**). (**c**) Smooth polystyrene-*block*-poly(ethylene oxide) (PS-*b*-PEOs) thin films were spin-coated unto these surfaces that, upon annealing in *o*-xylene vapors (**d**), produced highly ordered cylindrical nanodomains oriented normal to the film surface. (**e**) Atomic force microscopy (AFM) of highly ordered PS-*b*-PEO nanodomains in PCB thin films. Scale bar, 100 nm. (Reprinted with permission from [9.81]. © 2009 AAAS)

9.5 Magnetic Hard Disks and Write/Read Heads

More than half a century of progress in magnetic data storage has fundamentally changed information technology (see [9.82–9.84]). Starting with the IBM350 disk drive in 1956 with over fifty 24 in disks and a total of 4.4 Mbytes storage capacity (0.002 Mbits/in.^{2}), devices with several hundreds of Gbits/in.^{2} are available at present (see Fig. 9.26) due to rapid down scaling enabled by technical breakthroughs and novel components. Apart from the fast scaling of the bit sizes in the magnetic media, the thickness t of the media of initially 30 μm and initial fly height of the writing/reading heads of ∼20 μm have been decrease up to now into the nanoregime of ∼15 and ∼10 nm, respectively [9.83]. The development from longitudinal to perpendicular recording and future approaches, as well as the structure of write heads

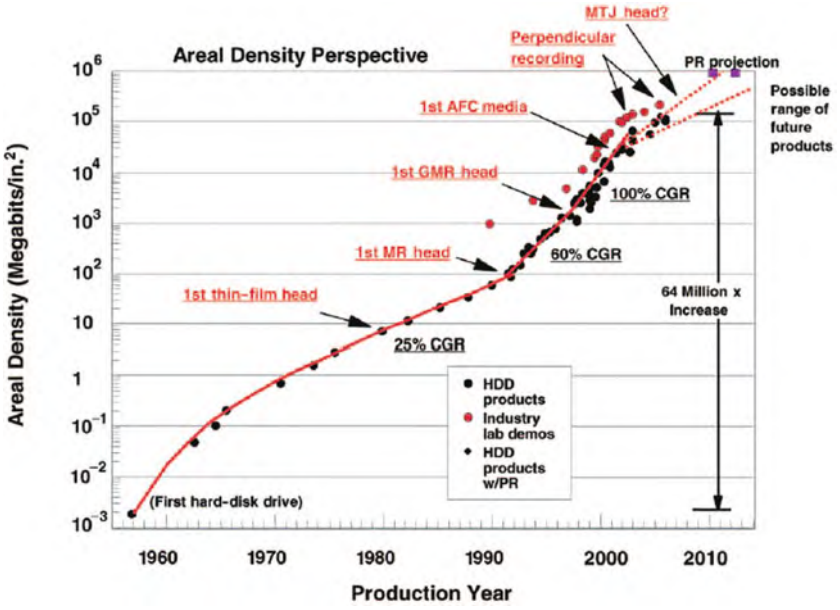

Fig. 9.26 Storage density of magnetic hard disk drives as a function of calendar year. The compounded growth rate (CGR) for some periods are indicated, as well as the technical breakthroughs. MR stands for the introduction of the magnetoresistance head, GMR for the giant magnetoresistance, AFC for antiferromagnetically coupled media, and PR for the introduction of perpendicular recording into the manufacturing of hard disk drives (HDDs). (Reprinted with permission from [9.82]. © 2006 Materials Research Society)

and particularly of giant magnetoresistance read back heads, will be outlined here. The areal density of magnetic recording on flexible tape is at present [9.85] two to three orders of magnitude lower than on hard disc drives. The mechanical and magnetic properties of materials that play a key role in the future of tape have been discussed recently [9.85].

In the magnetic recording process, the bits (containing each about 100 grains) are written as magnetization patterns, with the magnetization pointing either "left" or "right" within the plane of the magnetic medium for longitudinal recording and "up" or "down" for perpendicular recording. Typically, hcp Co alloys with uniaxial anisotropy are used for the recording media, i.e., with the easy magnetic axis along the *c*-axis. The energy that keeps the magnetization on the easy axis is $K_U V$, where K_U is the magnetocrystalline anisotropy energy density and V the volume of the grain. The scaling down of media is limited by thermal instability of the magnetization direction (bit) when $K_U V$ becomes comparable to the thermal energy $k_B T$, i.e., the transition probability or relaxation rate is given by $r = f_0 \exp(-K_U V / k_B T)$ with $f_0 = 10^{10} \ldots 10^{11}$ Hz. The minimum energy needed to maintain stability for > 10 years is $K_U V > 55\, k_B T$. Reduction in V for higher storage density can be countered by increasing K_U. Doping of Co with Pt is highly effective in increasing K_U, as the large atomic radius (0.1387 nm) engenders an expansion of the Co *c*-axis relative

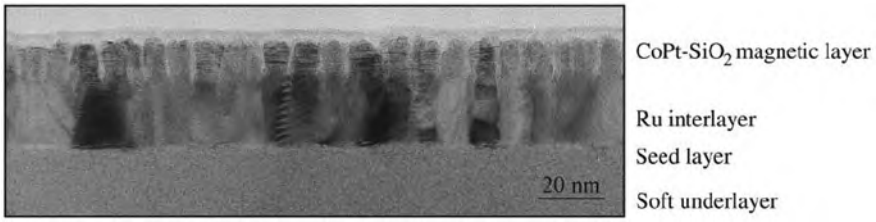

Fig. 9.27 Cross-sectional transmission electron micrograph of a typical perpendicular recording medium design. (Reprinted with permission from [9.84]. © 2006 Materials Research Society)

to the *a*-axis. However, K_U increases are limited by available write fields needed to overcome the media's coercive field, $\sim K_U/M_S$, where M_S is the saturation magnetization. The combination of signal-to-noise ratio (SNR) requirements, write-field limitations, and thermal activation of small particles is commonly referred to as the superparamagnetic limit. Since it is the grain volume V and not the grain area that enters in the magnetic energy $K_U V$, it is attractive to increase the film thickness – that is to make media with "tall and slim" grains. Film thicknesses up to 15–20 nm are indeed common for perpendicular recording media. The grain size in perpendicularly oriented (0001) Co alloys is dominated by the template grain size of the Ru alloy sublayer with a high surface energy, leading to a finely dispersed nucleation density, and a similar hcp structure and lattice parameter to enable parallel alignment with the top Co alloy (Fig. 9.27). The seed layer establishes the crystallographic texture for the Ru interlayer grown above. For the seed layer, low-surface-energy fcc materials are employed that wet the amorphous soft underlayer (SUL). The fcc (111) planes make suitable templates for hcp (0001) growth when the lattice parameters match. The porosity between the magnetic particles and the SiO_2 insulating layer are introduced in order to suppress quantum mechanical magnetic exchange coupling between the grains which causes a magnetic clustering of the grains and therefore a transition jitter [9.84].

9.5.1 Extensions to Hard Disk Magnetic Recording

A very promising extension to perpendicular recording is *composite media* [9.86] of a two-layer structure with materials of different properties. Material 1 has such a high anisotropy field $H_A = 2K_U/(\mu_0 M_S)$ that it cannot be written with available head fields, and Material 2 serves as a switching assist. Making use of a properly tuned exchange coupling between the two layers, the result is most effective when the contrast between the materials is well pronounced: $M_{S2}/M_{S1} \gg 1$ and $H_{A2}/H_{A1} \ll 1$. Another approach makes use of the effect that for all magnetic materials the anisotropy decreases when increasing the temperature. The basic idea of *heat-assisted magnetic recording* is to heat the media during the writing process

to temporarily lower the switching field [9.87]. The full anisotropy remains available during storage. Demonstrations of *perpendicular recording* [9.88, 9.89] have reached $\sim$ 400 Gb/in^2, with the potential for values of 1 Tbit/in^2. The superparamagnetic limit is also addressed by *bit-patterned media*: rather than recording one bit on a large number (50–100) of grains as nowadays, one single grain or magnetic island represents one bit. The entire volume of the bit contributes to the magnetic energy, and stable media can be achieved with much lower anisotropies [9.90] and with prospects of storage densities up to 5 Tb/in^2 [9.91] but, simultaneously, a completely new set of challenges for manufacturing [9.92] emerges. Still higher data storage densities are promised by *current-induced switching* of the magnetization as tentatively studied by spin-polarized scanning tunneling microscopy of 7 nm^2 Fe islands ($\sim$ 100 atoms) on a substrate [9.93] (see Sect. 8.1.2).

9.5.2 Magnetic Write Head and Read Back Head

For perpendicular magnetic recording, the writing is accomplished by a miniature electromagnet: a time-varying current in a conductor wrapped around the main pole (Fig. 9.28) generates the write flux that is sent through the magnetic storage layer, then through a magnetically soft underlayer (SUL) beneath the storage layer, and finally reenters the head structure through the return pole. The storage media can be thought of as traveling through the deep gap field of the head rather than the fringefield, thus, higher-coercivity media can be written.

The reading back of the data on the magnetic media occurs by measuring the stray fields (as described below) originating from transitions between opposite magnetization and not the magnetization itself. As the read density increased, the signal from the recorded transitions decreased and more sensitive detectors such as the giant magnetoresistance (GMR) head or spin-valve (since 1997), which enabled a thousand-fold increase in the storage capacity of hard disc drives in the last decade [9.79], were required with a GMR effect of 15% today. A view of this device, looking up from the media, is shown in Fig. 9.29. The GMR sensor is sandwiched between micrometer-thick magnetic shield layers (with a shield-to-shield spacing of 50 nm) which provide down-track spatial magnetic resolution by absorbing the magnetic flux from nearby media transitions. The sensor itself is lithographically patterned to half the track width, W, which is about 100 nm. As the track width scales to smaller dimensions, this is pushing magnetic recording past semiconductor processing in terms of the smallest feature size.

The basis of the GMR effect (see Sect. 1.4) is contained in only three layers: a cobalt alloy magnetic reference layer, a non-magnetic Cu spacer layer, and second magnetic free layer of a Co alloy. A current flowing in the magnetic layers is spin-polarized and the probability of electron scattering as they move between the magnetic layers depends on the relative orientation of the magnetization of these layers. This is a minimum, R_0, when the magnetizations of the free layer and reference layer are parallel. Spin-dependent scattering increases the resistance by maximum ΔR as the layer magnetizations deviate from parallel (see Sect. 1.4).

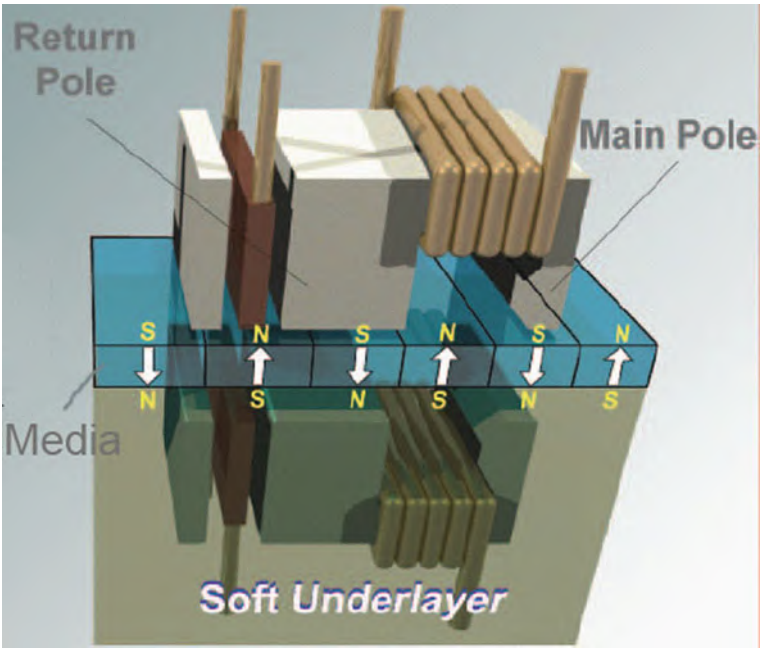

Fig. 9.28 Schematic illustration of perpendicular recording. The writing is performed by the main pole (on the *right*). The magnetic write flux penetrates the media and is conducted via the magnetically soft underlayer (SUL) back into the return pole. The field configuration in the presence of the SUL can be viewed as if the head structure were imaged in the SUL. (Reprinted with permission from [9.84]. © 2006 Materials Research Society)

In a GMR read head the magnetic moment of the reference layer points perpendicular to the medium surface. With zero field from the medium, the free layer moment points perpendicular to this direction ($\theta = 90°$). When the head passes over a magnetic transition in the medium, the free layer makes only a $\sim 10°$ deviation from 90°. The output signal is, then, fairly well linear with the field and the head uses only a 3% fraction of the $\Delta R = 15\%$ GMR effect.

The detailed structuring of the tiny and most sensitive GMR detector (Fig. 9.29), which impressively demonstrates the electronic, magnetic, and chemical interplay and adjustment of the various materials on the nanoscale, is discussed in the following. A typical underlayer structure is Ta (3 nm)/ NiFeCr (3 nm)/Ni Fe (0.8 nm). The Ta provides good adhesion and promotes a (111) texture, which is beneficial for the magnetic properties of the free layer. The deposition of NiFe gives rise to crystallization of NiFeCr to grain sizes as much as 22 nm, which decreases grain boundary scattering and increases the output of current-generation spin valves by 30% [9.83]. The next layer is the antiferromagnetic IrMn (for the properties of antiferromagnetic materials see [9.83]), which "pins" the ferromagnetic layer's magnetic moment through a mechanism called exchange anisotropy. This prevents the moment of the

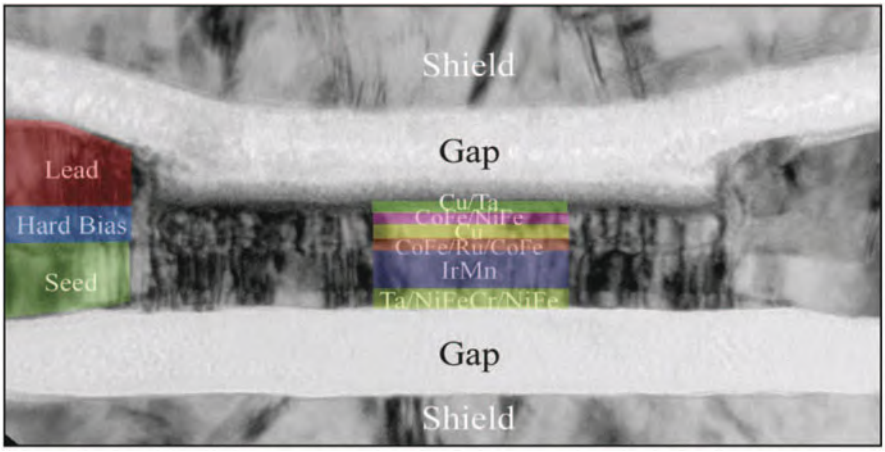

Fig. 9.29 Transmission electron micrograph of a giant magnetoresistance spin valve read head viewed as looking up at the head from the media. The 120 nm wide sensor is a multilayer stack. In addition to providing the sense current, the leads contain a magnetically hard bias layer that applies a small magnetic field to the sensor. The magnetic shields ensure that the sensor detects only the field from a single-magnetic transition at a time. (Reprinted with permission from [9.83]. © 2006 Materials Research Society)

ferromagnetic layer from rotating in moderate magnetic fields, making it useful as a reference layer. The magnetic CoFe/Ru/CoFe reference layer and the magnetic CoFe/NiFe free layer are coupled antiferromagnetically through the Cu spacer layer via the long-range Ruderman–Kittel–Kasuya–Yosida (RKKY) interaction. The Cu spacer layer not only separates the magnetic layers, but, since its band structure closely matches that of CoFe, it also allows electrons to pass with little spin-independent scattering, a key feature for GMR transport. In the free layer made of CoFe and NiFe, the $\sim$ 1 nm thick CoFe layer in contact with Cu gives high GMR and responds in contact with NiFe, due to a magnetic softening, more readily to low fields than CoFe alone. In addition CoFe and Cu are immiscible, yielding sharp interfaces, which improves GMR. The spin valve is capped with a Cu/Ta bilayer to protect the device from oxidation during processing.

The spin valve, from the seed layers to the cap, is fabricated in one deposition without breaking vacuum and is patterned afterward. Due to the small sensor dimensions, lithography techniques are used and electron-beam lithography will likely be required in the future. Conductive leads are deposited on the patterned spin valve to provide the sense current. The CoPtCr "hard bias" portion of the leads (see Fig. 9.29) provide a small magnetic bias field to stabilize the free layer, reducing noise. To the complete read head, a top alumina cap and magnetic shield layers are added (see Fig. 9.29). The write head is then fabricated on top of this read head (see [9.83]). A single wafer contains approximately 20,000 heads. The heads are finally mechanically lapped to expose the read sensor in the nanostructured device.

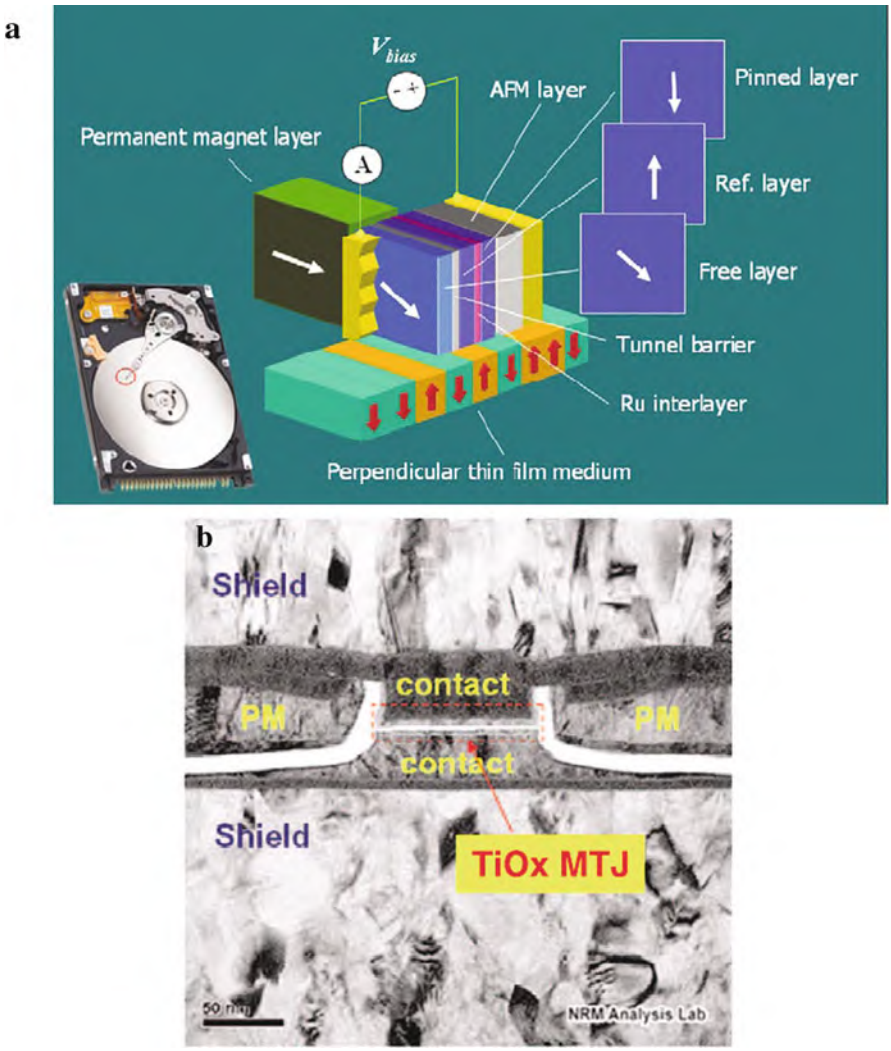

Fig. 9.30 (**a**) Magnetic tunneling junction (MTJ) reads head for a hard disk drive (HDD). One magnetic electrode is a free layer, and its magnetization rotates freely in response to the medium signal field. The magnetic moment of the other electrode is "fixed" through the interlayer magnetic coupling and functions as a reference to the free layer magnetization orientation. (**b**) Transmission electron micrograph of a commercial MTJ read head with a TiO_x barrier layer, viewed from the magnetic data storage medium, produced by Seagate Technology. (Reprinted with permission from [9.57]. © 2006 Elsevier)

In hard disk drive (HDD) read heads, also magnetic tunnel junctions (MTJs) have been commercialized by Seagate Technology since 2004 (see [9.57]) and many disc drive products have read heads with TiO_x-based MTJs (see Fig. 9.30). The TiO_x insulator provides a low resistance-area (RA) product. This is of importance when higher and higher data storage densities are packed on a disk and the size of the MTJ element needs to be reduced accordingly. In this case, the resistance must be prevented from increasing because this would lead to a longer time constant and – at high resistance – a sufficient current density would stress or damage the tunnel junction [9.57]. In the not-so-distant future [9.57], HDD read heads are very likely to use MgO-based MTJs when the high tunneling magnetoresistance ratio can be combined with an RA value for exceeding the present data rates of already 1 Gbit/s [9.57].

When the magnetic bits get smaller and smaller, this requires the significant reduction of the magnetic spacing which is the vertical distance between the read head and the magnetic storage layer (Fig. 9.31). Reducing the fly height of the read head requires ever thinner carbon films for disk and head protection with a present thickness of 4 nm. For 1 Tbit/in.^{2} devices the magnetic spacing will be 6.5 nm which implies ~1 nm disk and head overcoat. The ideal material for this would be tetrahedral amorphous carbon (ta-C) which is a diamond-like carbon (DLC) with a maximum C–C sp^3 bond content. This ta-C material has an ultralow roughness (rms roughness ~ 12 nm) that is independent of the film thickness [9.89].

Between 1997 and 2007 about 5 billion GMR read heads were shipped. Since 2005 these read heads were replaced by TMR (tunneling magnetoresistance in MTJ) and since recently by PMR (perpendicular magnetoresistance) [9.94].

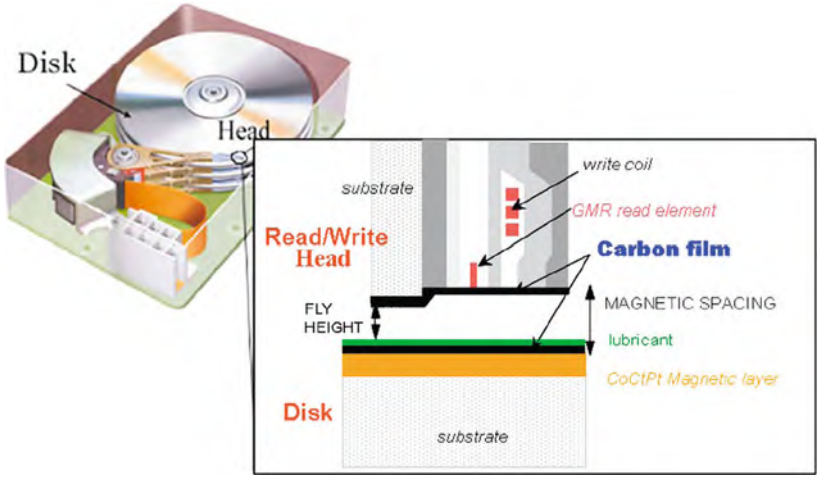

Fig. 9.31 Hard disk architecture. (Reprinted with permission from [9.89]. © 2007 Elsevier)

9.6 Optical Hard Disks

Optical data storage has become ubiquitous as a method for distributing content, archiving data, and managing information [9.95]. The progression of optical storage from high-fidelity stereo compact disks (CDs), storing approximately 74 min of audio, has required the evolution to digital versatile disks (DVDs), to high-definition DVDs and Bluray disks (BDs) (see Fig. 9.32). The disks contain surface structures called pits and lands. A semiconductor laser is used to reflect off of this structure to reconstruct the recorded data (Fig. 9.33). Concurrently with the development of CDs and DVDs, magneto-optical disks were developed which are based on the modulation of light by the magnetic state of the material, with current capacities of many gigabytes and expectations of terabytes of storage capacity (see [9.95]). Multilayer optical recording and holographic data storage may extend the optical storage roadmap to even higher performance. In the following an overview of these optical storage technologies will be given.

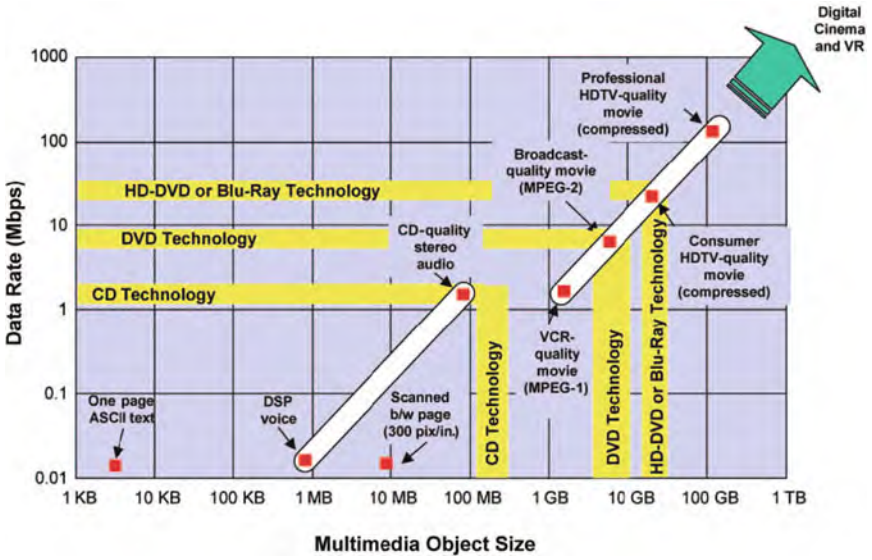

Fig. 9.32 The increase in storage capacity and complexity of multimedia objects has driven improvements in optical storage technologies. CD = compact disk, DSP = digital signal processor, DVD = digital versatile disk, HD-DVD = high-definition DVD, KB = kilobytes, MD = megabytes, GB = gigabytes, TB = terabytes, pix = pixel, Mbps = megabits per second, MPEG-1 = moving pictures expert group standard 1, MPEG-2 = moving pictures expert group standard 2, VR = virtual reality. (Reprinted with permission from [9.95]. © 2006 Materials Research Society)

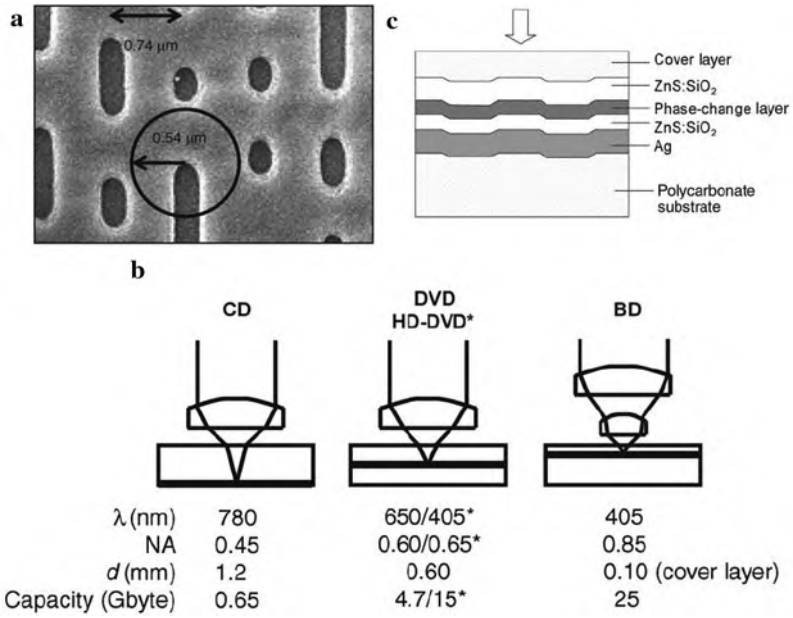

Fig. 9.33 (**a**) Electron micrograph of embossed pits in a DVD-ROM disk (viewed from the *top*). The track pitch is 740 nm, the shortest pit has a length of 400 nm, and the spot radius is 540 nm. (**b**) Roadmap of optical data storage and its key parameters. CD = compact disk, DVD = digital versatile disk, HD-DVD = high-definition digital versatile disk, BD = Blu-ray disk, λ = wave length of the laser light, NA = numerical aperture of the objective lens, and d = thickness of substrate or cover layer [9.96]. (**c**) Schematic illustration of a phase-change stack for blue recording [9.99]. (Reprinted with permission from [9.96] (**a**) (**b**) and [9.99] (**c**). © 2006 Materials Research Society)

9.6.1 Principles and Materials Considerations

A basic component for current optical disk systems is an objective lens with a specific numerical aperture (NA; see Fig. 9.33b) to focus a laser beam with the wavelength λ through a transparent cover layer onto the highly reflective information layer where the diffraction-limited spot radius is given by $s/2 = \lambda/(2\mathrm{NA})$ (see [9.96]). The reflectivity is modulated locally by the optical character (phase or amplitude objects) of the pits/marks. The information is digitally encoded in the lengths of the pits/marks (Fig. 9.33).

In prerecorded read-only memory, the embossed pits act as phase objects. The pit width is smaller than the laser beam to allow for destructive interference between light reflected from the pit and from the neighboring land area. For a high modulation depth of the readout signal, a pit height $H \approx \lambda/4n_0$, with n_0 the index of

refraction of the substrate, is optimum. The accuracy of the pit height replication in the fast molding fabrication process has to be kept within tight limits of a few nanometers.

In recordable or rewritable disks, an additional functional layer is located between the metallic refractive layer (usually Ag) and the transparent cover layer. Also, a spiral pregroove is embossed into the substrate for tracking and addressing purposes in the unrecorded state where the nanometer accuracy is again very important [9.96]. In the case of recordable disks the functional layer is an organic dye layer which decomposes thermally under laser writing and changes locally its complex index of refraction $n + ik$.

In the case of rewriteable disks (CD-RW, DVD-RW, DVD-RAM, BD), which can accommodate writing, reading, erasing, and rewriting of data, the functional layer comprises a thin phase-change layer ($\sim$ 10–15 nm) of, e.g., a chalcogenide alloy such as Ag–In–Sb–Te (see Fig. 9.33c), embedded in dielectric layers. The phase-change layer changes its index of refraction $n + ik$ between the amorphous and the crystalline states [9.40] due to differences in the electronic and chemical structure of the two phases [9.97]. The information is stored by means of amorphous marks which are written by local laser heating and rapid quenching. The change in the amplitude of the reflected light coming from the amorphous mark or the crystalline land is used for reading. Rewriting is effectuated by appropriate heating the amorphous marks for recrystallization and subsequent writing. The data rate, which is one of the key parameters in recording, is limited by the crystallization of the phase-change materials. A high crystallization rate may originate from a high vacancy concentration in the metastable crystalline structure [9.98]. By doping of phase-change Sb_2Te compounds, data rates of 60 Mbit/s for overwriting have been achieved. Another important parameter is the archival life stability. From temperature-dependent crystallization studies of phase-change materials, a lifetime of phase-change recorded data of 1,000 years at a storage temperature of 90°C can be estimated [9.99]. Erasable thermal phase-change recording at storage densities up to 2.2 Tb in^{-2} has been demonstrated (see Fig. 9.34).

It is anticipated that the vast majority of disks in blue recording are write-once disks. In such disks, a cost-effective dye layer could replace the more complex phase-change stack. Dyes sensitive to blue-violet lasers have been tested on prototype BD-R and HD-DVD-R disks (see [9.99, 9.100]). Another option for write-once disks is to replace the phase-change layer (Fig. 9.33c) by a 5 nm Si/6 nm Cu bilayer which by laser illumination transforms irreversibly into a Cu_3Si layer with optical characteristics quite different from those of the components [9.99].

In a CD the numerical aperture NA is typically 0.5 and λ is 780 nm. In a DVD, NA is 0.6 and $\lambda = 650$ nm. A third generation of optical devices with a blue laser of $\lambda = 400$ nm allows a storage density of 20–30 GB per disk [9.95]. In an emerging fourth generation of optical devices with near-field data storage, a dramatic reduction in spot size can be achieved by using a lens with NA >1, known as the solid immersion lens (SIL; Fig. 9.35). It is possible to have a SIL with a refractive index between 1.5 and 3 yielding $\sim$ 100 Gbytes per disk to be reached [9.101]. However, a carefully controlled gap between lens and disk is needed with a transparent coating on the disk in order to protect slider and disk during start-stop and crashes. The

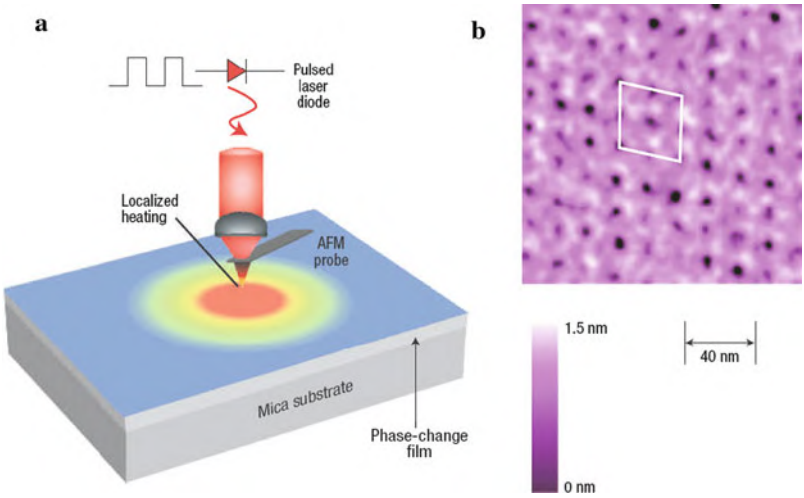

Fig. 9.34 Thermal recording of ultrahigh density phase-change bit patterns. (**a**) Experimental set-up. (**b**) AFM images of an array of crystalline phase-change bits in an amorphous $Ge_2Sb_2Te_5$ matrix with a storage density of 3.3^2 Tb in^{-2}. (Reprinted with permission from [9.47]. © 2006 Nature Publishing Group)

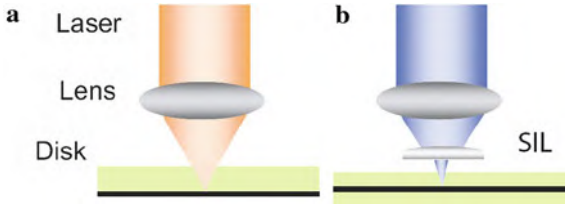

Fig. 9.35 (**a**) Optical data storage technology using far-field optics. (**b**) Near-field data storage technology using a solid immersion lens (SIL). CDs and DVDs use a metallic reflective layer (*black*) sandwiched between a substrate (*green*) and a lacquer surface (not shown). (Reprinted with permission from [9.89]. © 2007 Elsevier)

requirements for this coating can be satisfied by a layer of tetrahedral amorphous carbon with hydrogen (ta-C:H) (see [9.89]).

Approaches to further enhance the information storage density of optical recording exploit simultaneously wavelength, polarization, and spatial dimensions for multiplexing making use of the longitudinal surface plasmon resonance (see Sect. 7.6) of Au nanorods [9.102]. This concept leads to a storage capacity of 1.6 Tbytes for a DVD-sized disk and disk capacities of 7.2 Tbytes with recording speeds up to 1 Gbits/s are envisaged [9.102].

The substrate material has to meet different well-balanced requirements comprising optical, rheological, mechanical, and processing properties. The most appropriate performance profile is reached with BPA-PC and $\sim$ 800,000 tons of polycarbonates were used for ODS production in 2004 [9.96].

9.6.2 Magneto-Optical Recording

Magneto-optical recording (MO) has been first commercialized in 1988 (see [9.103]). Materials and technologies for MO disks may play an important role in recording for ultrahigh densities beyond 1 Tbit/in^2 [9.103].

In this technique the recorded marks are read out by the magneto-optical effect, where the axis of polarization of the light reflected from the magnetic layer is rotated at an angle called the Kerr rotation, with a typical value of 1° for the recorded area and an opposite rotation for the erased area. This difference is detected for the signal readout. Recording on an MO disk is called thermomagnetic recording because the magnetization is reversed at an area heated by laser irradiation where the coercivity at the elevated temperature is decreased below the external magnetic field (see Fig. 9.36b). The recorded mark has a magnetization upward, opposite to the erased state. A typical amorphous $Tb_{20}Fe_{74}Co_6$ recording layer (see Fig. 9.36a) has a high perpendicular anisotropy constant K_U of several 10^6erg/cm^3, which originates from the large magnetostriction coefficient and the large single-ion anisotropy of Tb, and a Tb spin directed opposite to the spins of the transition metals Fe and Co, giving rise to a ferrimagnetic behavior (Fig. 9.36a). Due to this behavior, the total magnetization approaches zero at the elevated temperature T_{comp} where it can be reversed by a moderate external field for recording (Fig. 9.36b). The recorded information is estimated to be stable for more than 100 years at ambient temperatures and a recording repeatability factor of more than 10^6 is achieved [9.103].

The storage capacity of MO disks has been favorably enhanced by the domain wall displacement detection (DWDD) technique. Here, the resolving power is not limited by the optical mark size but determined by the magnetic domain wall width which is estimated to 8 nm for Tb–Fe–Co (see Fig. 9.37a). DWDD technology has been used in high-density MiniDisks (HiMDs), which where commercialized in 2004 with storage capacities of 1 Gbyte per 64 mm diameter disk [9.103].

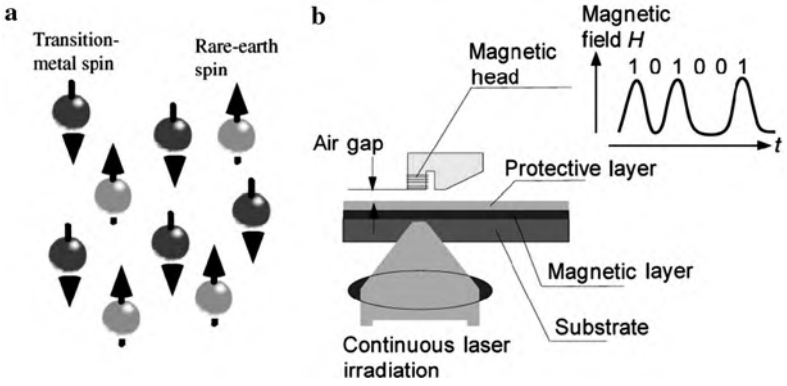

Fig. 9.36 (**a**) Antiparallel alignment of the magnetic moments of a ferrimagnetic rare-earth/transition-metal amorphous alloy. (**b**) Recording on a magneto-optical storage device by magnetic field modulation. H is the magnetic field and t is time. (Reprinted with permission from [9.103]. © 2006 Materials Research Society)

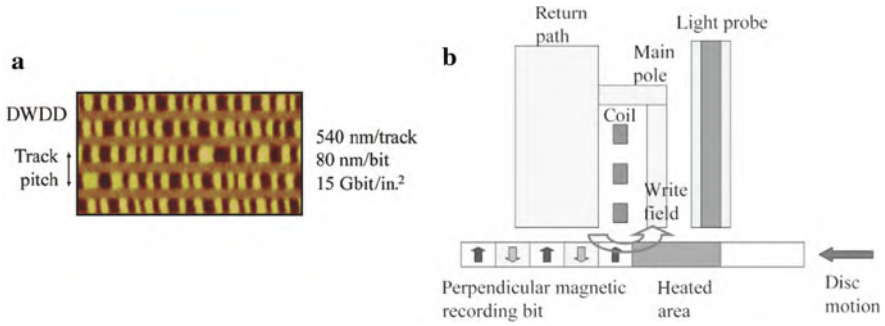

Fig. 9.37 (**a**) Magnetic force micrograph of recorded magnetic domains for domain wall displacement detection (DWDD) in magneto-optical data storage. Dark and light areas refer to two opposite magnetization directions. The track pitch for the DWDD media is 540 nm. (**b**) Schematic configuration for hybrid recording. (Reprinted with permission from [9.103]. © 2006 Materials Research Society)

Various MO technologies, including perpendicular recording media, are anticipated to achieve an areal density of 1 Tbit/in^2 [9.103]. For these high data storage densities, the coercivities H_C of the magnetic marks have to exceed 800 kA/m (10 kOe) in order to ensure the thermal stability at small sizes. In this case, heat-assisted recording, for reduction of H_C during recording (Fig. 9.37b) has been proposed, similar to the suggestion for high-density magnetic recording (see Sect. 9.5).

9.6.3 Multilayer Recording

The capacity of optical disks can be also increased by using multiple layers of bitwise data. Layers are spaced along the depth dimension of the disks (Fig. 9.38).

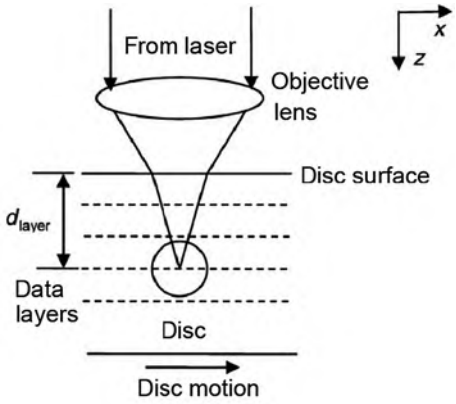

Fig. 9.38 Geometry of a bitwise volumetric optical data storage device. A data layer (*dashed lines*) is accessed by focusing a laser beam to different depths, d_{layer}. Readout is performed in reflection. (Reprinted with permission from [9.104]. © 2006 Materials Research Society)

Individual layers are recorded and information is retrieved in a manner that is very similar to conventional optical disk systems using a single layer. Bitwise volumetric multilayer recording is different from volumetric holographic recording (see below), in that holographic recording stores data as collections of gratings throughout the depth of the material.

In multilayer recording, two-photon (2P) absorption is used for the writing process (see [9.104]). The advantage of a 2P absorption process is its ability to selectively excite molecules inside the focus volume, e.g., of a short-pulse high-irradiance laser, without affecting molecules elsewhere in the storage material [9.104]. Data readout is often a simple one-photon process, because depth-discriminating techniques, such as scanning confocal microscopy, can be used.

For recording media, several categories of materials can be used including refraction near-field structure (super-RENS) materials, and thin-film refractive layers. To date, the most mature bitwise volumetric technology uses two-photon fluorescent media (see [9.104]).

9.6.4 Holographic Data Storage

Holographic storage is considered a promising successor to currently available storage technologies because of recent demonstration of significant gains in data transfer rates, densities and archival storage robustness, however, with challenges in the development of suitable recording materials [9.4].

Optical holography, on which holographic storage is based, can record the complete characteristics of a light wave. This recording of information is accomplished by overlapping two coherent light waves to produce an interference pattern (Fig. 9.39). The intensity profile of the pattern, determined by both the phases and the amplitudes of the interfering light waves, is imaged into a recording medium to produce a hologram. Either light wave can be regenerated by illuminating the hologram with the other light wave. Applying the reference beam to the recording medium (Fig. 9.39b) diffracts the light from the hologram to reconstruct the original 3d object [9.105]. The classic treatment of the behavior of light diffracted from volume holograms is known as coupled wave theory [9.106]. As shown in Fig. 9.39, laser light in a holographic storage system is split into the two arms, a reference path and a signal path, of the recording system. Digital data is recorded in a pagewise fashion – the bits of information are grouped into arrays and the arrays are encoded onto the pixels of a spatial light modulator. Light transversing the signal path is, therefore, patterned by the digital data array, or page. The light from the signal path overlaps with the light from the reference path within the recording medium to record an optical interference pattern that contains the information of the data page. Data is read out by diffracting light from the reference path off the optical interference pattern within the media to reproduce the recorded data array, which is imaged unto a detector to reconstruct the digital data (see [9.4]). Instead of recording and reading out data in a serial, bitwise manner, holographic storage

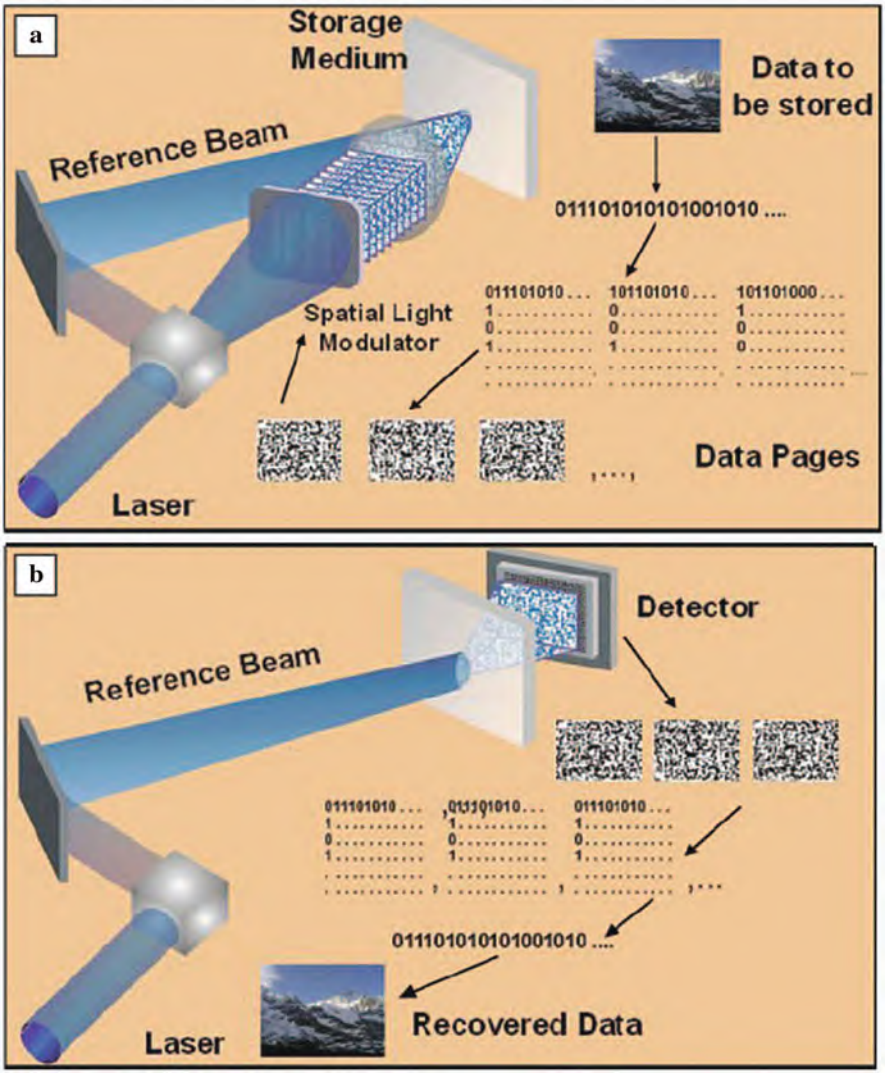

Fig. 9.39 Schematic illustrations of (**a**) the recording process in holographic storage and (**b**) the readout process in holographic storage. (Reprinted with permission from [9.4]. © 2006 Materials Research Society)

transfers data in a parallel, pagewise process, enabling significant improvements in recording and readout rates. In addition, holographic storage allows multiple pages of data to be recorded in the same volume of the recording media (multiplexing) enabling ultrahigh storage densities.

The requirements of the recording media are high optical quality, adequate dynamic range, high photosensitivity, long shelf and archival lives, and

manufacturability in a cost-effective manner [9.4]. Photopolymers with a two-chemistry approach can fulfill these requirements. These materials are, e.g., composed of two independently polymerizable systems – one system forms a 3D cross-linked polymer matrix, whereas the second photopolymerizable monomer is the imaging component, as it reacts during holographic recording. Using blue-wave length-sensitized, two-chemistry media with a 1.5 nm thick recording layer, 200 Gbits/in^2 was demonstrated [9.107]. From these materials, storage densities up to terabits/in^2 are expected [9.4].

9.7 High-*k* Dielectrics for Replacing SiO_2 Insulation in Memory and Logic Devices

In silicon-based information electronics, an important materials feature of silicon is, that it can be reacted with oxygen or nitrogen in a controlled manner to form superb insulators with excellent mechanical, electrical, and dielectric properties. These dielectrics are used as core components in two important device types in silicon semiconductor industry: as the capacitor dielectrics used for information storage in dynamic random access memories (DRAMs) and as the transistor gate dielectric in complementary metal oxide semiconductor (CMOS) field-effect transistor (FET) logic devices. In both cases, the thickness of the SiO_2 or Si–O–N dielectric is – with decreasing device size – becoming sufficiently thin (Table 9.4, Fig. 9.40a) that leakage currents arising from quantum mechanical electron tunneling through the dielectrics are posing a problem and are viewed as a major technical barrier [9.108–9.110]. When the thickness of the SiO_2 dielectric decreases below 1 nm, currents of a density of 1,000 A/cm^2 tunnel through the dielectric and increase by an order of magnitude when the dielectric thickness is reduced by a further 0.1 nm [9.110]. This gives rise to unacceptable energy consumption, cooling problems, and deleterious coupling between source-drain channel and gate. Continued device shrinkage will therefore require the replacement of the insulator with high-dielectric constant (high k) oxides [9.111], to increase its thickness, thus preventing tunneling currents while retaining the electronic properties of an ultrathin SiO_2 film ($k = 3.9$). Ultimately such insulators will require an atomically defined interface with silicon without an interfacial SiO_2 layer for optimal performance [9.109]. For application

Table 9.4 Roadmap predictions for dielectric gate oxide thickness (equivalent thickness of a SiO_2 dielectric) as a function of time (see [9.108])

Year	2005	2008	2011	2014
Technology node (nm)	100	70	50	35
Gate length (nm)	65	45	32	22
Equivalent oxide thickness (nm)	1.0–1.5	0.8–1.2	0.6–0.8	0.3–0.6

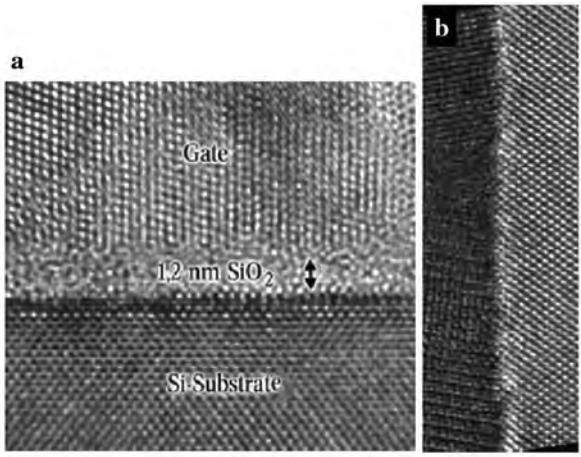

Fig. 9.40 (**a**) Transmission electron micrograph (TEM) of a cross section of a CMOS transistor in a Pentium-4 Processor (Intel Corp., see [9.110]). (**b**) High-resolution transmission electron micrograph (HRTEM) of the interface between a Si substrate (*right*) and a HfO_2 film (*left*), prepared at a deposition temperature of 350°C [9.116]. (Reprinted with permission from Refs. [9.110] (**a**) and [9.116] (**b**). © 2005 Wiley-VCH (**a**) and © 2009 Chinese Society of Metal (**b**))

as high-*k* insulators, amorphous Hf–Si–O–N compounds ($k \approx 11$–22) [9.112] and the application of oxides such as $LaAlO_3$ ($k \approx 25$) [9.113], Gd_2O_3 [9.114] or $LaLuO_3$ (see [9.111]) may enable industry companies to keep pace with Moore's law. High-quality oxide layers (see Fig. 9.40b) can be prepared by laser ablation techniques for highly precise compositional control and together with reflection high-energy electron diffraction (RHEED) techniques for structural control (see [9.110]). Processes for the preparation of ultrathin layers of high-*k* dielectrics have been reported [9.115].

High-*k* dielectric materials are used by Intel for transistors at the 45 nm technology node and by IBM for its 32 nm node CMOS technology [9.111].

9.8 Low-*k* Materials as Interlayer Dielectrics (ILD)

Modern ultralarge-scale integration (ULSI) electronic circuits contain 10^9 transistors in an area smaller than 1 cm^2. These basic elements must be interconnected and an advanced ULSI device may consist of 10 levels of metal lines. For this reason, the effective speed of the device is becoming ever more dominated by the signal propagation velocity through the interconnects of the components. The increase of the resistance (R) and the capacitance (C) of the interconnect materials give rise to a rapid increase in the delay time

$$RC = 2\rho k\varepsilon_0(4L^2/P^2 + L^2/T^2),$$

where ρ is the metal resistivity, ε_0 the vacuum permittivity, k is the relative dielectric constant of the interlayer dielectric (ILD), P is the metal line pitch (sum of line width and line spacing), T is the metal thickness, and L is the metal line length. Therefore, the device speed, increased through smaller feature sizes, will become overshadowed by this interconnect delay [9.117, 9.118]. The International Technology Roadmap for semiconductors (ITRS) predicts the necessary (maximum) k value of the ILD, and the estimated RC delay, for the various line width (DRAM half-pitch) "technology nodes", according to the expected year of production (see Fig. 9.41).

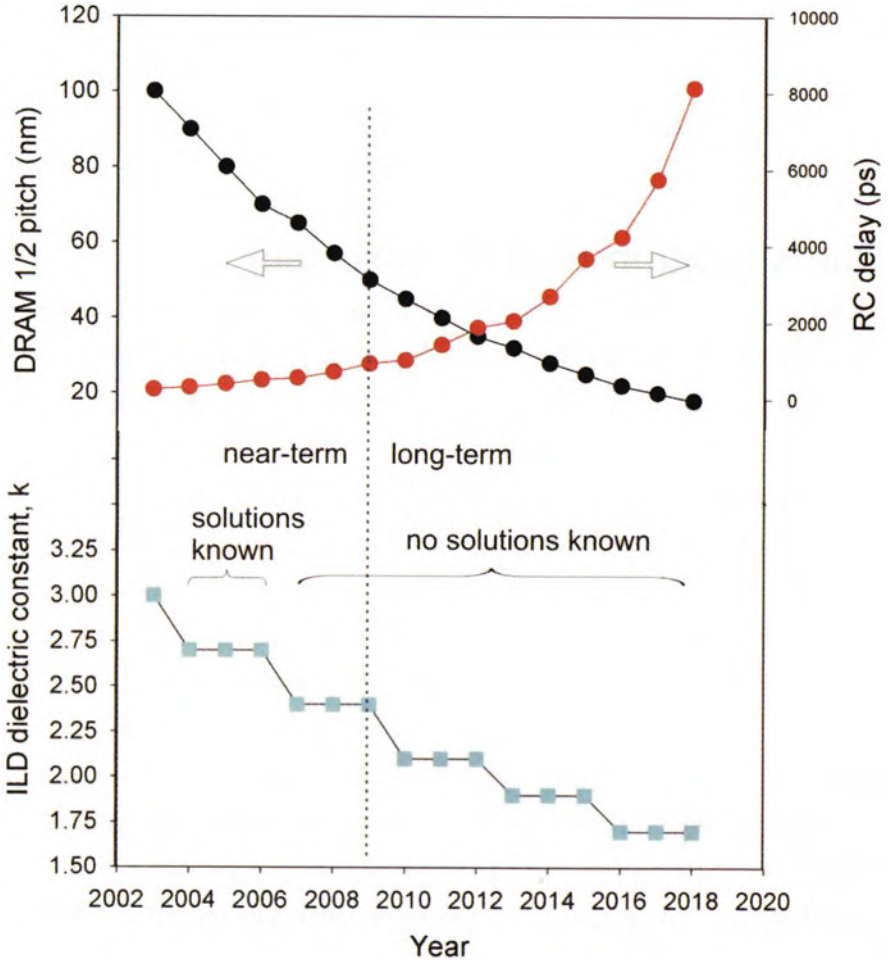

Fig. 9.41 The ITRS (2004 Update) industrial roadmap for the semiconductor industry, showing the planned decrease in device spacing (DRAM half-pitch), the expected increase in the RC delay, and the required k values of the interlayer dielectric (ILD), indicating the extent to which manufacturable solutions are known. (Reprinted with permission from [9.118]. © 2006 Elsevier)

Future low-*k* materials for ILDs [9.119] are porous materials such as periodic mesoporous organosilicas (PMOs; see [9.118, 9.120]) which are produced by template-based synthesis making use of bridged-organic silsesquioxane (SSQ) precursors to incorporate organic groups directly into the pore or channel walls (Fig. 9.42a). These PMOs have, however, polar silanol groups with OH bonds on the channel walls to be hydrophilic. The ingress of water with its high dielectric constant ($k \sim 80$) must be suppressed because this would cause the effective *k* to increase dramatically. This can be induced by thermal "hydrophobization" (Fig. 9.42b), where a proton from the hydrophilic hydroxyl group of a silanol (Si–OH) is transferred to a bridging group to break one Si–CH_2–Si bridge, thus creating a hydrophobic surface with terminal organic groups. This treatment causes *k* to decrease below 2.0 for the methenesilica, ethenesilica, and three-ring PMOs (see [9.118]). The film porosity – and thereby *k* – can be controlled by the template (surfactant)/precursor ratio *R* (see Fig. 9.42c) achieving values of $k \sim 1.75$ as required for ultralow-*k* ILDs. The mechanical properties of low-*k* dielectric materials are of importance for circuit reliability.

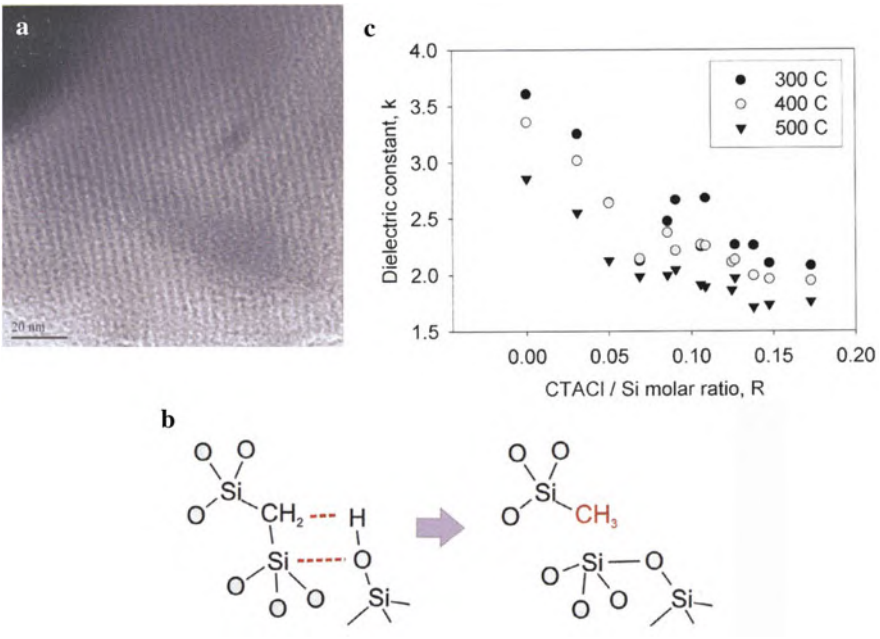

Fig. 9.42 (**a**) Transmission electron micrograph of periodic mesoporous organosilica (PMO) showing a 2D hexagonal structure of a ~ 4 nm channel spacing. (**b**) Illustration of the thermally activated chemical reaction that transforms an initial bridging organic group (*left*) to a terminal organic group (right), as a result of proton transfer from a silanol group in close proximity. (**c**) Decrease of the dielectric constant *k* for three-ring PMO films of increasing porosity as determined by the surfactant (CTACl)/precursor (Si-organo-of-silica) molar ratio *R*. The temperatures of the thermal treatments are given in centigrades. (Reprinted with permission from [9.118]. © 2008 American Institute of Physics)

9.9 Summary

The field of computer and data storage development with the fabrication of transistors or of data bits in storage media, respectively, is of particular importance for the application of nanoscience in computer industry with current revenues of US$ $\sim$ 200 billion annually. According to Moore's law the computing power – and in a similar fashion the data storage density – doubles about every 18 months due to a shrinkage of transistor sizes on an integrated circuit or of data bits to the nanometer scale. Due to physical limitations in the downscaling of transistors and data bits, novel strategies for the fabrication of these components have to be developed. Carbon nanotubes and graphene nanoribbons may provide us with future transistor technologies. Flash memories and magnetoresistive memories exhibit considerable downscaling potentials. With the implementation of nanoscale magnetic domain wall racetrack memories, the possibility of simplifying computers is opened by reducing the number of memory storage technologies. The storage capacity of magnetic hard disks could be dramatically increased by the use of GMR and TMR read heads based on nanoscale multilayers. For ultrahigh-density integration of computer components the development of high-dielectric constant (high k) and low-dielectric constant (low k) materials is indispensable.

References

9.1 C.R. Barrett, MRS Bull. **31**, Nov 2006, p. 906
9.2 C. Doctorov, Nature **455**, 17 (2008)
9.3 Nature **453**, 837 (2008)
9.4 L. Dhar, MRS Bull. **31**, Apr 2006, p. 314
9.5 J.-G. Zhu, C. Park, Mater. Today **9**, Nov 2006, p. 36
9.6 G.E. Moore, ISSCC Dig. Tech. Pap. 20 (2003)
9.7 C. Drösser, Die Zeit, Jan 24, (2008)
9.8 J.M. Tour, T. He, Nature **453**, 42 (2008)
9.9 A.G. Rinzler, Nat. Nanotechnol. **1**, 17 (2006)
9.10 P.S. Otellini, Die Zeit, Sept. 17, 2009, p. 28
9.11 X.J. Guo, S.R.P. Silva, Science **320**, 618 (2008)
9.12 J.D. Meindl et al., Science **293**, 2044 (2001)
9.13 A.T. Tilke et al., Prog. Quantum Electron. **25**, 97 (2001)
9.14 H. Ishikuro, H. Hiramoto, Appl. Phys. Lett. **71**, 3691 (1997)
9.15 L. Zhuang et al., Appl. Phys. Lett. **72**, 1205 (1998)
9.16 S.J. Tans et al., Nature **393**, 49 (1998)
9.17 A. Bachtold et al., Science **294**, 1317 (2001)
9.18 V. Derycke et al., Nano Lett. **1**, 453 (2001)
9.19 P. Avouris, MRS Bull. June 2004, p. 403
9.20 Z.-H. Chen et al., Science **311**, 1735 (2006)
9.21 M.S. Arnold et al., Nat. Nanotech. **1**, 60 (2006)
9.22 X.R. Wang et al., Phys. Rev. Lett. **100**, 206803 (2008)
9.23 M. Kanungo et al., Science **323**, 234 (2009)
9.24 B.Q. Wu, A. Kumar, J. Vac. Sci. Technol. **B25**, 1743 (2007)
9.25 T. Heil, M. Lowisch, Photonik 2, (2008), p. 44

9.26 www.asml.com (2009)
9.27 B.M. La Fontaine et al., Proc. SPIE **6921**, 6921 OP-1 (2008)
9.28 J. Finders et al., Microlithogr. World **17**, No. 1 (2008)
9.29 S. Grantham et al., *SEMA-TECH EUV Source Workshop* (Bolton Landing, New York) May 12, 2008
9.30 A. Fazio, MRS Bull. Nov. 2004, p. 814
9.31 F.J. Bartos, Control Eng. **55**, April 2008, p. 26
9.32 K.H. Kuesters et al., Adv. Eng. Mater. **11**, 241 (2009)
9.33 M.F. Beng et al., Solid-State Electron. **52**, 571 (2008)
9.34 C. Trinh et al., In ISSCC Proc. **246** (2009)
9.35 H. Wakai et al., Jap. J. Appl. Phys. **45**, 2459 (2006)
9.36 L.-H. Xie et al., J. Am. Chem. Soc. **130**, 2120 (2008); Research Highlights, Nat. Mater. **7**, 267 (2008)
9.37 E. Bichoutskaia et al., Mater. Today **11**, June 2008, p. 38
9.38 S.-H. Lee et al., Nat. Nanotechnol. **2**, 626 (2007)
9.39 S. Hudgens, B. Johnson, MRS Bull. Nov. 2004, p. 829
9.40 W. Wełnic, M. Wuttig, Mater. Today **11**, June 2008, p. 20
9.41 A.L. Lacaita, Solid-State Electron. **50**, 24 (2006)
9.42 D. Lencer et al., Nat. Mater. **7**, 972 (2008)
9.43 F.J. Bartos, Control Eng. **55**, April 2008, p. 26
9.44 A. Pirovano et al., IEEE Trans. Electron. Device **51**, 714 (2004)
9.45 D. Ielmini, Y. Zhang, J. Appl. Phys. **102**, 054517 (2007)
9.46 W.K. Njoroge et al., J. Vac. Sci. Technol. **20**, 230 (2002)
9.47 H.F. Hamann et al., Nat. Mater. **5**, 383 (2006)
9.48 D.J. Milliron et al., Nat. Mater. **6**, 352 (2007)
9.49 A. Radaelli et al., J. Appl. Phys. **103**, 111101 (2008)
9.50 S.A. Wolf et al., MRS Bull. **31**, May 2006, p. 400
9.51 B.N. Engel et al., IEEE Trans. Magn. **41**, 132 (2005)
9.52 G. Grynkewich et al., MRS Bull. Nov. 2004, p. 818
9.53 W.H. Butler et al., Phys. Rev. **B 63**, 054416 (2001)
9.54 S.S. P. Parkin et al., Nat. Mater. **3**, 862 (2004)
9.55 S.J. Yuasa et al., Nat. Mater. **3**, 868 (2004)
9.56 S.S. P. Parkin, MRS Bull. **31**, May 2006, p. 389
9.57 J.-G. Zhu, C. Park, Mater. Today **9**, November 2006, p. 36
9.58 C. Sealy, Mater. Today **9**, Sept 2006, p. 10
9.59 Y. Arimoto, H. Ishiwara, MRS Bull. Nov. 2004, p. 823
9.60 Y. Kato et al., Jap. J. Appl. Phys. **46**, 2157 (2007)
9.61 Y. Cho et al., Nanotechnology **14**, 637 (2003)
9.62 K. Asadi et al., Nat. Mater. **7**, 547 (2008)
9.63 Z.J. Hu et al., Nat. Mater. **8**, 62 (2009)
9.64 A. Sawa, Mater. Today **11**, June 2008, p. 28
9.65 T. Mikolajik et al., Adv. Eng. Mater. **11**, 235 (2009)
9.66 C. Yoshida et al., Appl. Phys. Lett. **91**, 223510 (2007)
9.67 W.W. Zhuang et al., Tech. Dig. IEDM 193 (2002)
9.68 I.G. Baek et al., Tech. Dig. IEDM 587 (2004)
9.69 G.-S. Park et al., Appl. Phys. Lett. **91**, 222103 (2007)
9.70 Z. Szot et al., Nat. Mater. **5**, 312 (2006)
9.71 D.-J. Seong et al., Electrochem. Solid-State Lett. **10**, H168 (2007)
9.72 Y.B. Nian et al., Phys. Rev. Lett. **98**, 146403 (2007)
9.73 J. Cumings, A. Zettl, Science **289**, 602 (2000)
9.74 V.V. Deshpande et al., Nano Lett. **6**, 1092 (2006)
9.75 S. Parkin, International Union of Materials Research Societies – International Conference on Electronicsic Materials (IUMRS ICEM), Sidney Australia (2008)

9.76 S.S.P. Parkin, U.S. Patent 6834005 (Dec. 21, 2004); S.S. P. Parkin, U.S. Patent 6898132 (May 24, 2005)
9.77 M. Hayashi et al., Science **320**, 209 (2008)
9.78 C. Sealy, Mater. Today **11**, June 2008, p. 16
9.79 S.S. P. Parkin et al., Science **320**, 190 (2008)
9.80 M. Mannini et al., Nat. Mater. **8**, 194 (2009)
9.81 S.J. Park et al., Science **323**, 1030 (2009)
9.82 H. Coufal et al., MRS Bull. **31**, May 2006, p. 374
9.83 I.R. McFadyen et al., MRS Bull. **31**, May 2006, p. 379
9.84 H.J. Richter et al., MRS Bull. **31**, May 2006, p. 384
9.85 R.H. Dee, MRS Bull. **31**, May 2006, p. 404
9.86 D. Suess et al., IEEE Trans. Magn. **41**, 3166 (2005)
9.87 J.J. M. Ruigrok et al., J. Appl. Phys. **87**, 5398 (2000)
9.88 www.seagate.com (2009)
9.89 C. Casiraghi et al., Mater. Today **10**, Jan–Feb 2007, p. 44
9.90 R.L. White et al., IEEE Trans. Magn. Pt. 2, **33**(1), 990 (1997)
9.91 H.J. Richter et al., IEEE Trans. Magn. **42** (10), 2255 (2006)
9.92 B.D. Terries, T. Thomson, J. Phys. D: Appl. Phys. **38**, R199 (2005)
9.93 S. Krause et al., Science **317**, 1537 (2007)
9.94 P.A. Grünberg, private communication (2008)
9.95 H. Coufal, L. Dhax, MRS Bull. **31**, Apr 2006, p. 294
9.96 F.-K. Bruder et al., MRS Bull. **31**, Apr 2006, p. 299
9.97 A. Klein et al., Phys. Rev. Lett. **100**, 016402 (2008)
9.98 M. Wuttig et al., Nat. Mater. **6**, 122 (2007)
9.99 A.E. T. Kuiper et al., MRS Bull. **31**, April 2006, p. 308
9.100 H. Nishiwaki et al., Jpn. J. Appl. Phys. **45**, 1452 (2006)
9.101 J. Hellmig, Phys. World **17**, 21 (2004)
9.102 P. Zijlstra et al., Nature **459**, 410 (2009)
9.103 M. Kaneko, MRS Bull. **31**, Apr 2006, p. 314
9.104 T.D. Milster, Y. Zhang, MRS Bulll. **31**, April 2006, p. 318
9.105 P.C. Hariharan, *Optical Holography* (Cambridge University Press, Cambridge, UK, 1996)
9.106 H. Kogelnik, Bell Syst. Tech. J. **48**, 2909 (1969)
9.107 E. Fotheringham et al., Proc. Int. Symp. Optical Memory and Optical Data Storage, ThE2 (2005)
9.108 A.I. Kingon et al., Nature **406**, 1032 (2000)
9.109 C.J. Först et al., Nature **427**, 53 (2003)
9.110 J. Mannhart, D.G. Schlom, Phys. J. **4** (6), 45 (2005)
9.111 D.G. Schlom et al., MRS Bull. **33**, Nov 2008, 1017
9.112 D.G. Schlom, J.H. Haeni, MRS Bull. **27**, 198 (2002)
9.113 B.-E. Park, H. Ishiwara, Appl. Phys. Lett **82**, 1197 (2003)
9.114 H.J. Osten et al., Phys. Stat. Sol. (a. **205**, 695 (2008)
9.115 J.C. Tinoco et al., Thin Solid Film. **496**, 546 (2006)
9.116 X.H. Zhu et al., J. Mater. Sci. Technol. **25**, 289 (2009)
9.117 M.R. Baklanov, K. Maex. Phil. Trans. R. Soc. **A364**, 201 (2006)
9.118 B.D. Hatton et al., Mater. Today **9**, March 2006, p. 22
9.119 B.R. Kim et al., Microelectr. Eng. **85**, 74 (2008)
9.120 C.A. Yuan et al., Appl. Phys. Lett. **92**, 061909 (2008)

Chapter 10
Nanochemistry – From Supramolecular Chemistry to Chemistry on the Nanoscale, Catalysis, Renewable Energy, Batteries, and Environmental Protection

Chemistry plays an important role in the synthesis of nanostructures (see Chap. 3 and [10.1]). In the present section, the main features of supramolecular chemistry and of inorganic hollow clusters will be outlined with a subsequent discussion of chemical reactions on the nanoscale and catalysis. Furthermore, nanochemistry and nanoscience appear to be of importance for future renewable energy production, battery development, and environmental protection.

10.1 Supramolecular Chemistry

Supramolecular chemistry [10.2–10.6] or – as sometimes called – supramolecular science is located at the meeting point provided by the design and investigation of organized, informed, and functional supramolecular architectures. As a bottom-up approach, supramolecular chemistry is concerned with the next step in increasing complexity beyond the molecule toward the supramolecule and organized polymolecular systems on a *nanometric* size scale, held together by non-covalent interactions. This type of molecular interactions forms the basis of the highly specific recognition, reaction, transport, and regulation processes that occur in biology. Due to weak intermolecular bonds, supramolecules are in general thermodynamically less stable, kinetically more labile, and dynamically more flexible so that a type of "soft chemistry" emerges. Binding of a substrate σ to a receptor ρ yields the supramolecule $\sigma\rho$ and involves recognition, transformation, and translocation. The association and organization of functional supramolecules may lead to molecular and supramolecular devices.

According to a consideration of Lehn [10.3] there was in the beginning the Big Bang and physics reigned. Then chemistry came along at milder temperatures; particles formed atoms; these united to give more and more complex molecules, which in turn associated into aggregates and membranes, defining primitive cells out of which life emerged. In this sense chemistry is settled between the laws of physics and the rules of life.

H.-E. Schaefer, *Nanoscience*, DOI 10.1007/978-3-642-10559-3_10,

However, not only nanoscaled organic entities are available but also nanometer-sized inorganic molecules, approaching the size range of bacteria, can be synthesized [10.7] which will be briefly discussed at the end of this section.

10.1.1 Architecture in Supramolecular Chemistry

Receptors are often mesomolecules, i.e., molecules with sizes intermediate between small organic molecules and large molecules of macromolecular chemistry.

Cyclic and non-cyclic elements can be combined (Fig. 10.1). Some trivial names, which characterize their functions and activities, have been given to these supramolecules: crown ether, cryptands, cavitands, carcerands. Spherical recognition cryptates of metal cations represent the simplest recognition process of spherical substrates, e.g., metal cations. In Fig. 10.1c, a natural macrocyclic molecule with antibiotic properties, such as valinomycin, is shown with a K^+ ion included in the macrocyclic cavity. By employing a receptor molecule with an appropriate size of hollow volume, a particular type of ion can be selected from a mixture of these ions by the formation of a cryptate compound [10.3]. This selectivity is of importance for electrical stimulation in nerve cells which is based on changes of the gradient in concentration of Na^+ and K^+ ions as well as of Ca^{2+} ions [10.8] in channels across membranes (see Sect. 11.5). Therefore, there should be molecules available in these membranes which are capable of differentiating these simple ions by the difference in diameter of about 0.06 nm.

Whereas macrocycles define a 2D hole, bicycles define a 3D hole which can be highly stabilized by alkali or alkali earth cations or protons giving rise to spherical

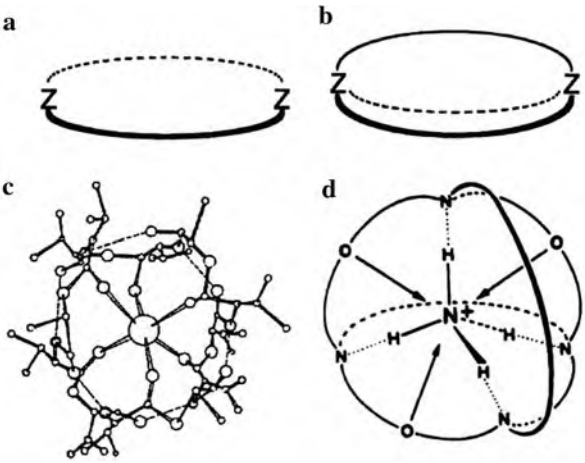

Fig. 10.1 (**a**) Macrocylic and (**b**) cylindrical macrobicyclic molecular structure. (**c**) Recognition of a K^+ ion included in a macrocyclic cavity. (**d**) Tetrahedral recognition of a NH_4^+ cation by a tricyclic cryptand. (Reprinted with permission from [10.2]. © 1995 Wiley-VCH)

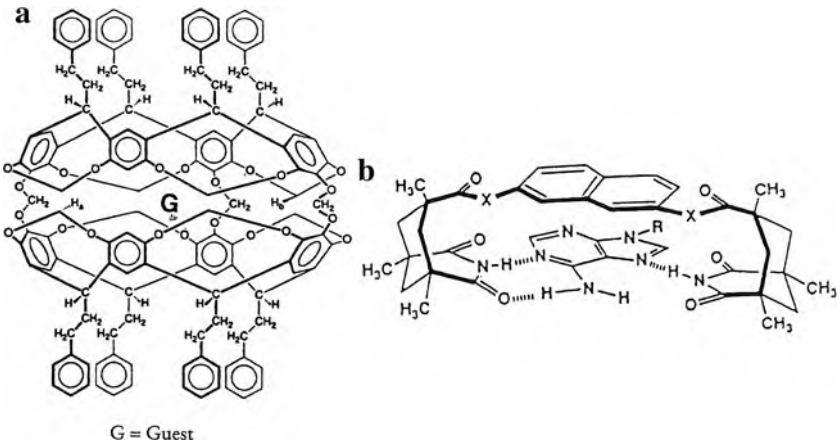

Fig. 10.2 (**a**) Nanosized supramolecular guest–host container molecule (carcerand). (**b**) Recognition of neutral molecules by hydrogen bonding in a cleft. (Reprinted with permission from [10.2]. © 1995 Wiley-VCH)

recognition. Such a 3D molecule shows a strong "cryptate effect" (buried atom) characterized by high stability and selectivity, slow exchange, efficient shielding of the bound ion from environment supplying, e.g., transition metal recognition. Tetrahedral recognition of the NH_4^+ cation is achieved by a tricyclic cryptand (Fig. 10.1d).

The supramolecular structures can get larger and larger as in the case of the guest–host container molecules (carcerand in Fig. 10.2a with a diameter of about 2.8 nm). They make the protection of highly reactive species possible. For example, highly reactive white phosphorus (P_4 tetrahedra) can be encapsulated in supramolecular complexes where the phosphorus becomes inert [10.9]. Recognition of neutral molecules may occur by hydrogen bonding in, e.g., a cleft (Fig. 10.2b).

10.1.1.1 *Cyclodextrin* Encaging

Cyclodextrins are cyclic shell molecules (Fig. 10.3) with a diameter of ~0.8 nm. They can be produced by enzymatic decomposition of starch. The molecule has a hydrophilic outer surface and a hydrophobic interior and exhibits typical host–guest complexing properties. Here, the driving force for incorporation of a hydrophobic guest molecule is a reduction of the total energy when the guest replaces water molecules. Pharmaceutical applications are due to a reduction of the irritation of the stomach lining when the drug is cyclodextrin encapsulated. The sensitivity of cosmetics, e.g., the anti-aging drug retinol, which can reduce the depth of wrinkles can be reduced by a cyclodextrin coating (see Fig. 10.3b). In food technology cyclodextrin may be used for removing unpleasant tastes by enclosing the aldehyde molecules released from the packaging material.

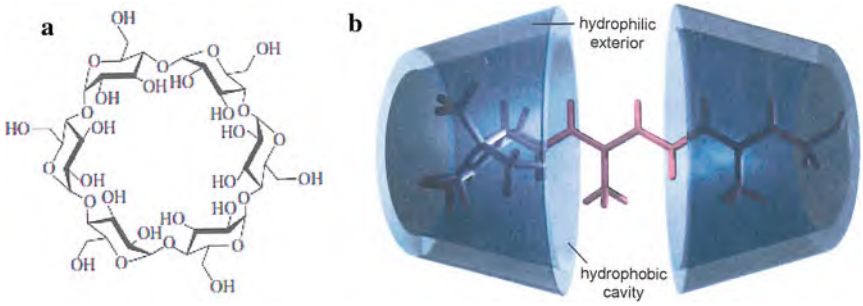

Fig. 10.3 (**a**) γ-Cyclodextrin ring. (**b**) Two cyclodextrin rings can enclose a retinol molecule for protection of this vitamin from oxygen and light. (Reprinted with permission from [10.10]. © 2005 Wiley-VCH)

10.1.1.2 Supramolecular Nanostructures at Metal Surfaces

The mastery of the non-covalent bond is the leitmotif in supramolecular chemistry. This issue can be directly addressed by the deposition of molecular building blocks on a substrate and the study of the mutual molecular interaction and the interaction with, e.g., a well-characterized metallic surface on a molecular level. The supramolecular patterning of carboxylic acids such as 4-[*trans*-2-(pyrid-4-yl-vinyl)]-benzoic acid (PVBA) and trimesic acid (1,3,5-benzenetricarboxylic acid) (TMA) on metal surfaces are shown in Fig. 10.4. The head-to-tail hydrogen bonding of the rod-like species PVBA with supramolecular chiral H-bonded twin chains yields 1D nanogratings on Ag(111). The threefold symmetry of TMA accounts for the formation of H-bonded honeycomb networks on Cu(100) at low temperatures.

10.1.2 Supramolecular Materials

Organic supramolecular materials are of interest because of their interaction and recognition capabilities. Examples are organic nanotubes formed by self-assembly of cyclic peptide units [10.12]. Networks of self-assembled actin filaments play a basic role in the physicochemical behavior of cells and vesicles [10.13]. Technologies resorting to self-organization processes should be able to bypass nanofabrication procedures by making use of the spontaneous formation of the desired suprastructures and devices from instructed and functional building blocks. In the future, supramolecular devices may be organized by recognition-directed self-assembly (see Sect. 1.5) into well-defined architectures with novel properties. Components and molecular devices such as molecular wires, channels, resistors, rectifiers, diodes, and photosensitive elements might be assembled into nanocircuits.

Artificial transmembrane ion channels. Tubes and channels are ubiquitous in living systems. Constructed from various proteins these conduits are responsible for numerous biological functions such as ion flow, signal transduction, and molecular transport. Artificial transmembrane ion channels were constructed from

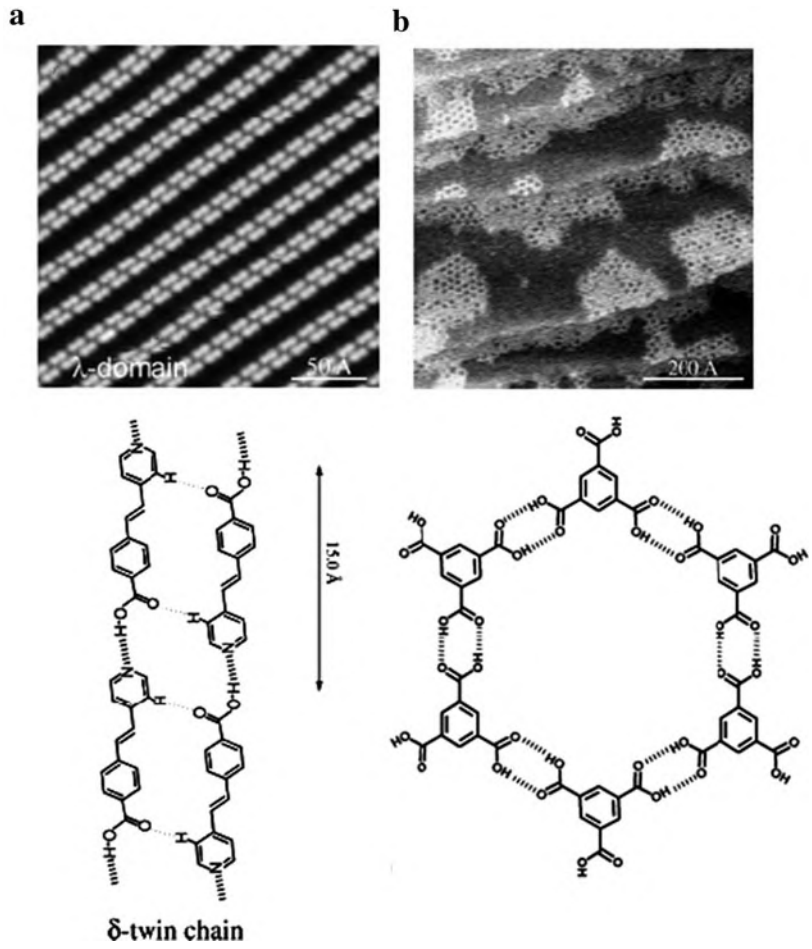

Fig. 10.4 (**a**) STM image of the formation of a regular 1D supramolecular PVBA nanograting by H-bond-mediated self-assembly and connection by the molecular end groups on the Ag(111) surface extended over micrometer domains. *Lower panel*: Schematic of the supramolecular chiral PVBA twin chains with OH. . .N and weak lateral CH. . .OC hydrogen bonds indicated. (**b**) STM image of TMA on Cu(100) taken at 205 K. In the islands decorating the step edges, a honeycomb motif is resolved which is associated with the extensively H-bonded 2D TMA networks. *Lower panel*: Schematic model for the honeycomb TMA structure with threefold dimerization of self-complementary carboxyl moieties. (Reprinted with permission from [10.11]. © 2003 Springer Verlag)

cyclic peptide structures containing alternating D- and L-aminoacids, where D and L refer to the amino acid chirality. These cyclic subunits adopt a flat ring conformation, allowing them to stack on top of one another to form a hydrogen-bonded, hollow tubular structure (Fig. 10.5). The rings are composed of the eight-residue cyclic peptide cyclo[-(TRP-D-Leu)$_3$-Gln-D-Leu-] with a pore diameter of 0.75 nm.

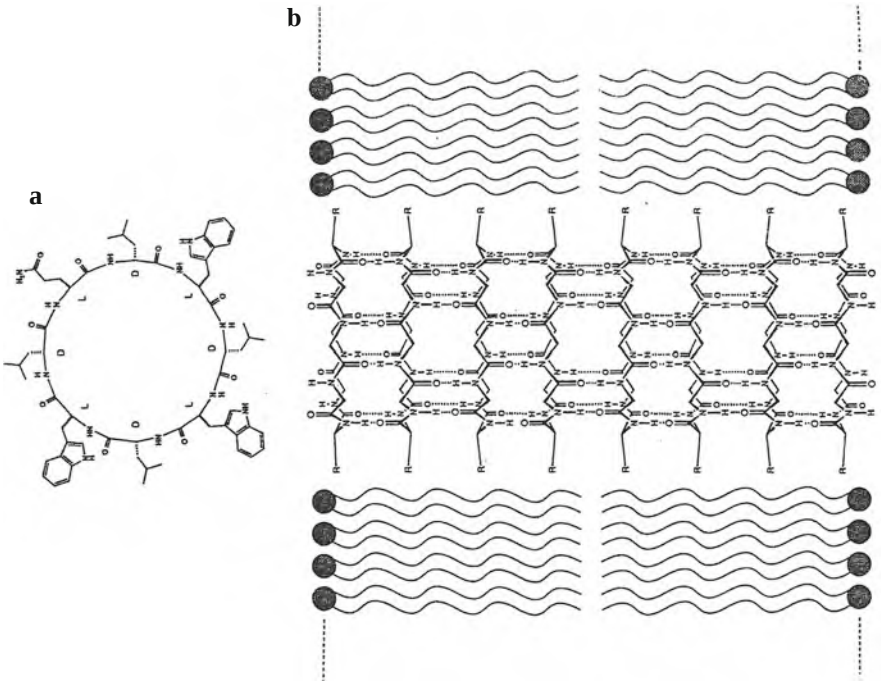

Fig. 10.5 (**a**) The chemical structure of the peptide subunit in a flat ring-shaped conformation. (**b**) Peptide subunits shown in a self-assembled tubular configuration (*horizontal*) embedded in a lipid bilayer membrane (*vertical*). The representation emphasizes the antiparallel ring stacking, the presence of inter-subunit hydrogen-bonding and side chain–lipid interactions. (Reprinted with permission from [10.14]. © 1994 Nature Publishing Group)

The incorporation of the tubules into lipid bilayers was demonstrated by specific Fourier transform infrared (FTIR) spectroscopy. In addition, the synthetic tubules showed ion transport activity with rates exceeding 107 ions/s, similar to biological channels such as gramicidin A [10.14, 10.15]. Supramolecular nanotubes have been shown to exhibit selective antibacterial activity in mice by increasing the permeability of bacterial membranes [10.16].

Supramolecular polymers. Polymers can respond to changes in temperature, solvent, or the presence of signal chemicals by reversible assembly/disassembly (see [10.17]). Scaffolds, such as those that constitute the cellular skeleton, are formed only where and when they are required, and they are dissembled in small building blocks when their task has been fulfilled. As opposed to a purely macromolecular approach, such a modular, supramolecular strategy allows a fast and efficient response to changing needs in the cellular cycle.

Whereas in macromolecular polymers [10.18] a large number of repeating units are *covalently* linked into long chains, in supramolecular polymers monomers are held together by *noncovalent* interactions [10.1, 10.2] such as directional and versatile hydrogen (H) bonds. Very stable complexes can be obtained when quadruple H-bonding units are employed as in 2-ureido-4[1H]-pyrimidinones (UPy; Fig. 10.6) dimerized in toluene.

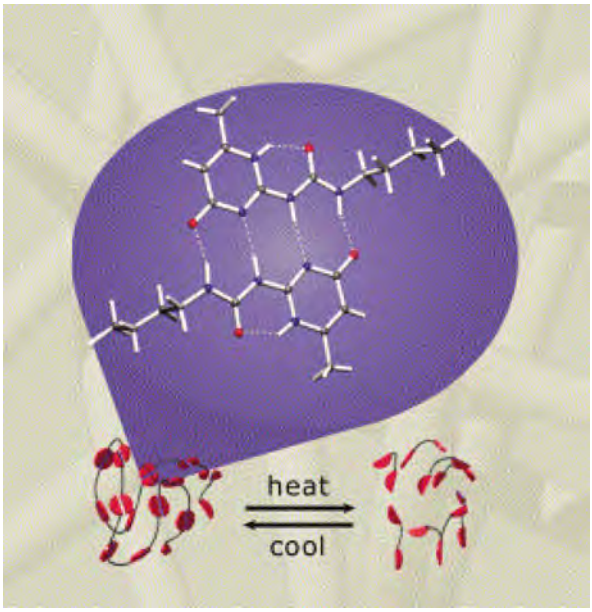

Fig. 10.6 Schematic representation of a linear supramolecular polymer. The enlargement shows a representation of the x-ray structure of the H-bonded dimer of the UPy group that holds the supramolecular polymer together. (Reprinted with permission from [10.17]. © 2004 Elsevier)

Supramolecular polymers such as UPy compounds exhibit a strongly temperature-dependent melt viscosity with an extremely high activation energy [10.17]. This originates from the mechanisms of stress relaxation that are available to supramolecular polymers [10.19]. Stress relaxation in supramolecular polymers occurs by reptation, such as in conventional polymers, but additionally, supramolecular chains can release strain by breaking and then recombine with other, strain-free chain ends which speeds up at higher temperatures. The strongly temperature-dependent melt viscosity gave rise to numerous application prospects for supramolecular polymers. Xerox has filed patents [10.20] for inks in inkjet printing. The ink has to be of low viscosity in order to be ejected in small droplets, but has to be highly viscous once the droplet hits the paper – otherwise the ink will smear out. Patents are also filed for printing plates [10.21] that make use of a supramolecular polymer as thermally sensitive coating.

Organometallic wheels – molecular magnets (see Sect. 8.8): Metal rings have excited mankind since mythological times [10.22]. Large cyclic metal organic structures with exclusively paramagnetic 3d transition metals have been synthesized with, e.g., 18 iron atoms [10.23], 24 nickel atoms [10.24], 12 cobalt atoms [10.25], or 10 chromium atoms [10.26]. These wheel molecules (Fig. 10.7) are by a factor of 2–3 smaller than the 3.6 nm giant wheels constructed from purely inorganic molybdate fragments [10.27]. They have been considered as candidates for observing quantum coherence phenomena and as qubits in quantum computing [10.28, 10.29].

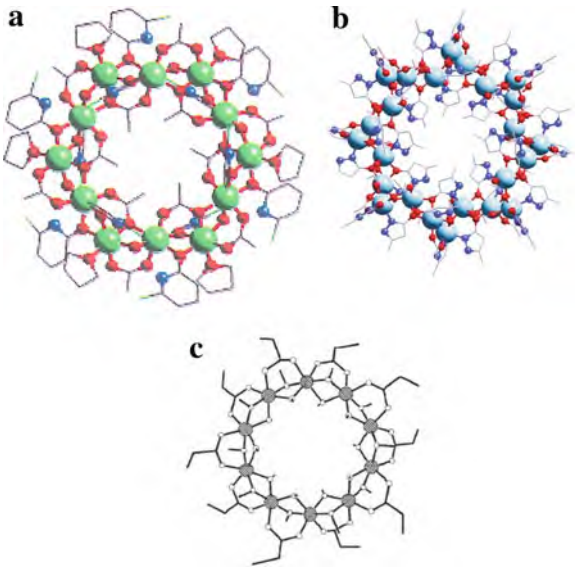

Fig. 10.7 (**a**) Dodecanuclear cobalt wheel $[Co_{12}(chp)_{12}(O_2CMe)_{12}(H_2O)_6(THF)_6]$ where chp is c-chloro-2-pyridonate and THF is tetrahydrofuran. The distances Co–Co of the green Co atoms are 0.3122 and 0.3176 nm [10.25]. (**b**) Ni_{24} wheel $[Ni_{24}(OH)_8(mpo)_{16}(O_2CMe)_{24}(Hmpo)_{16}]$ where Hmpo is 3-methyl-3-pyrazolin-5-one and mpo the deprotonated anion of Hmpo [10.24]. (**c**) Cr_{10} ring $[Cr_{10}(OMe)_{20}(O_2CEt)_{10}]$ with the Cr atoms cross-hatched [10.26]. (Reprinted with permission from [10.25] (**a**), [10.24] (**b**), and [10.26] (**c**). © 2002 Royal Society of Chemistry (**a**), © 2001 Wiley-VCH (**b**), and © 2006 Wiley-VCH (**c**))

The Co ring shows ferromagnetic interaction between the Co atoms [10.25] whereas the magnetic behavior of the 24 Ni ring appears to be dominated by antiferromagnetic exchange [10.24]. In the 10 Cr ring the magnetic exchange is found to be weakly antiferromagnetic or weakly ferromagnetic, depending on the precise composition [10.26].

10.1.3 Molecular Recognition, Reactivity, Catalysis, and Transport

Molecular recognition requires complementary properties of receptors and substrate as well as flexibility and rigidity. Recognition which enables selection is based on the information stored in the interacting molecules. Information storage is of pivotal importance for biological processes as demonstrated in the storage, the transfer, and the reading of genetic information in DNA. This is based on a somehow simple principle, namely the interaction between the two different pyrimidine–purine base pairs thymine ($C_5H_6N_2O_2$)–adenine ($C_5H_5N_5$) on the one hand and cytosine ($C_4H_5N_3O$)–guanine ($C_5H_5N_5O$) on the other hand in the DNA double helix (Fig. 10.8). All life is eventually controlled by the activation of sequences of the different connections, i.e., the formation of either two or three hydrogen bonds. The

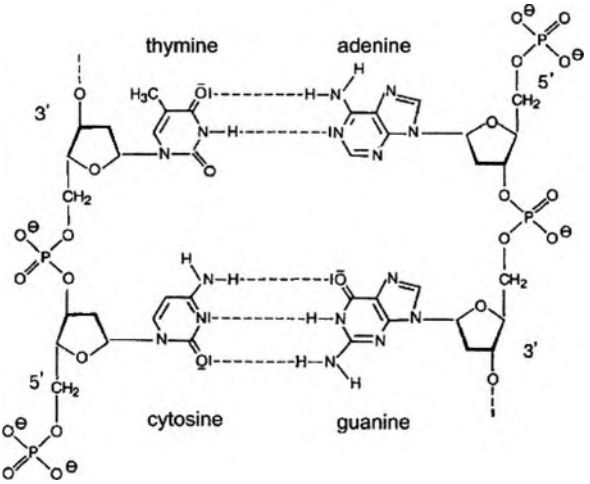

Fig. 10.8 Pairing of bases in the double helix of a deoxyribonucleic acid (DNA) molecule. (Reprinted with permission from [10.3]. © 1997 Leopoldina)

most complex processes of life are controlled by the wealth of information which is stored on the long DNA thread.

Catalytic reactions between a substrate and molecular receptors with appropriate bond sites and reactive groups may occur by forming first with a certain selectivity and velocity a complex. The reaction products then may be released so that the catalyst is again available for the next reaction cycle (see Fig. 10.9). Two steps are characteristic for this process: the selective binding of the substrate to the catalyst receptor and the transformation of the bound substrate to the reaction products. A prerequisite for the functioning of both processes is the availability of the appropriate information stored in the supramolecular system.

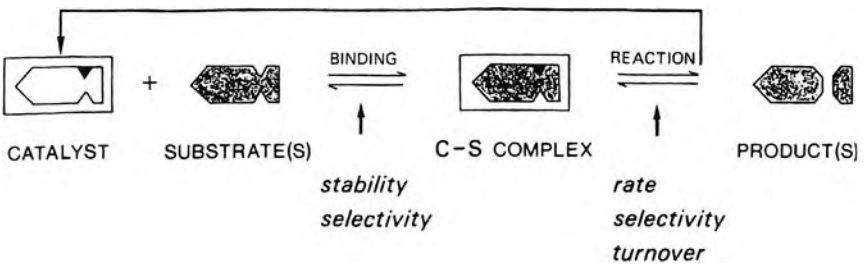

Fig. 10.9 Sketch of supramolecular catalysis: Catalyst receptor and substrate form a catalyst–substrate complex which, when the reaction is performed, decays in two reaction products and the catalyst, which then is available again for a further reaction cycle. (Reprinted with permission from [10.3]. © 1997 Leopoldina)

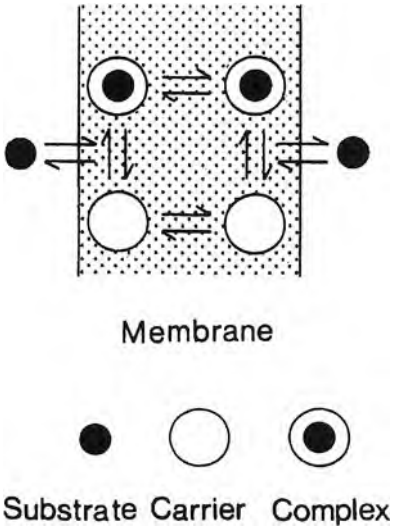

Fig. 10.10 Schematic representation of carrier-mediated transport of a substrate through a membrane in a four-step cycle: Association of the substrate–carrier complex in the membrane, diffusion of the substrate into the membrane, dissociation, and out-diffusion of the substrate. (Reprinted with permission from [10.3]. © 1997 Leopoldina)

By the design and the synthesis of receptors for selectively binding organic and inorganic substrates, a variety of compounds soluble in membranes were prepared which can effectuate, as carriers, reactive transport through a membrane. In Fig. 10.10 such a four-step transport cycle of association, diffusion, dissociation, and back diffusion is shown. Based on the above-mentioned cryptates with alkali cations (see Fig. 10.1c), simple carrier molecules were synthesized for these ions.

10.1.4 Molecular Photonics and Electronics

Light conversion. A photochemical molecular functional unit may consist of two components: a light collector and an emitter (see Fig. 10.11a) with an effective energy transfer (ET) between the two components. The functional unit works in three steps: light absorption (A) by a receptor (collector), intramolecular energy transfer (ET) to a substrate (emitter), and emission (E) of light of different wavelengths. For this process, e.g., a Eu(III)-cryptate with a macrobicyclic cryptand (structure sketched in Fig. 10.11b) is particularly suitable. This cryptand contains three 2,2′ bipyridine groups, which act as light collectors. The UV radiation absorbed by these groups is transferred to the Eu cation in the hollow space of the molecule which eventually emits visible red light. The Eu^{+} complex in aqueous

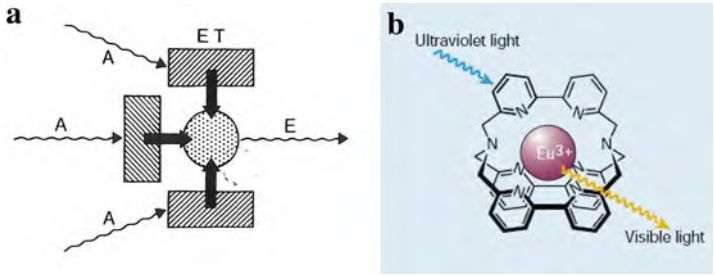

Fig. 10.11 (**a**) Photochemical molecular functional unit for light conversion consisting of two components: the light collectors (*hatched areas*) and a light emitter (*dotted area*) with the three processes absorption (A), energy transfer (ET), and emission (E). (**b**) Photochemical molecular functional unit of a europium(III)-cryptate ion with a cryptand of three 2,2′ bipyridine groups which act as light collectors. Ultraviolet light absorbed by the cryptand excites the metal ion, Eu(III), which then emits radiation at longer (visible) wavelengths [10.3, 10.27]. (Reprinted with permission from [10.3] (**a**) and [10.27] (b). © 1997 Leopoldina (**a**) and © 2000 Nature Publishing Group (**b**))

solution shows a long-lived luminescence which is missing in free Eu ions. This complex is of interest as an optical marker for biological species such as antibodies, oligonucleotides, and membrane components.

Molecular wires may be employed in order to make membranes permeable to electrons. In Fig. 10.12a molecular wire with a length equal to the thickness of the membrane double layer forms a supramolecular functional unit with the membrane. With the molecular wires in the membrane, the chemical reduction of the electron acceptor K-hexacyanoferrate (III) on the one side of the membrane to K-hexacyanoferrate (II) by a reducing agent, e.g., an electron donor as Na-dithionite on the other side of the membrane was accelerated by a factor of 4 demonstrating an electron transfer from the reducing phase on the one side to the oxidizing phase on the other side [10.3].

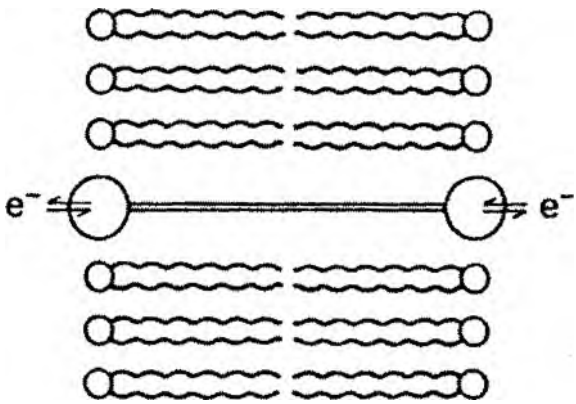

Fig. 10.12 Schematic representation of a molecular wire embedded in a phospholipid double layer membrane. (Reprinted with permission from [10.3]. © 1997 Leopoldina)

10.1.4.1 Polyrotaxanes as Semiconducting Molecular Wires in Electronics and Optoelectronics

In polyrotaxane supramolecular architectures (see Fig. 10.13a), backbones of conjugated polymers are threaded into insulating rings such as α- or β-cyclodextrins (CDs). The properties of conjugated polymers are dominated by the formation of a partially delocalized π-electron system giving rise to small energy gaps in the visible, which is crucial for optoelectronics, an intrachain mobility up to 0.5 cm^2/Vs, strong nonlinear effects, and ultrafast thermalization of optically excited states (see [10.30]). The "supramolecules" resulting from threading are insulated molecular wires that display the basic semiconducting and optical properties of uninsulated chains and can be used as molecular materials, e.g., in LEDs (Fig. 10.13c). The threading leads not only to a reduction of the aggregation of the polyrotaxane molecules but also to an increased electroluminescence efficiency, a blue shift of the emission, and an increased environmental stability (see [10.30]).

π–π stacks: self-assembly of anisotropic nanoarchitectures. The interaction between extended π-electron systems can be exploited as the driving force to form noncovalent architectures. Columnar architectures based on large polycyclic aromatic hydrocarbons are good candidates for the active components of organic

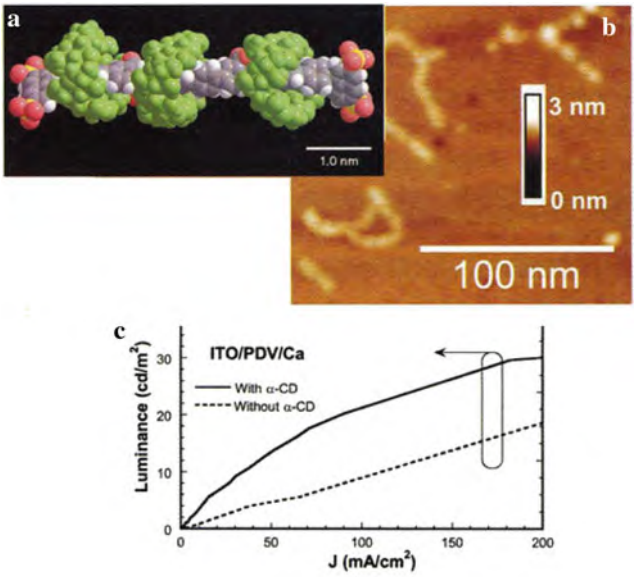

Fig. 10.13 (**a**) The van der Waals surface of the energy-minimized structure of a short (n=2) molecular wire of poly-para-phenylene insulated by β-cyclodextrine (β-CD-PPP). The molecular wire is threaded through the CD spacers to prevent close packing. (**b**) Tapping mode atomic force micrograph of β-CD-PPP spin coated on mica with a chain length of 30–50 nm and a chain width of ~1.6 nm. (**c**) Electroluminescence of wires insulated with cyclodextrine rings (α-CD-PVD; *solid line*) versus non-insulated (*dashed line*) molecular wires of poly(diphenylene vinylene). The insulated wires display a higher efficiency and luminescence up to high current densities. (Reprinted with permission from [10.30]. © 2004 Elsevier)

transistors [10.31]. Such columnar assemblies can also be reinforced with H-bonds [10.32] that can confer a helical motif to the supramolecular architecture [10.33]. Helical motifs of the columnar structure can also be induced by the presence of chiral groups in the aliphatic side chains (see [10.30]). An example is shown in Fig. 10.14 where the presence of crown ethers in between the aromatic core and the aliphatic tails allows manipulation of the helicity of the columnar structures. In the absence of ions, the molecules self-assemble into right-handed helices that in turn form coiled-coil aggregates with a left-handed helical motif. The addition of K^+ ions leads to the loss of the helicity in the fibers (Fig. 10.14f, g). Such tunable, chiral, and optically active materials provide potentials for optoelectronics, nonlinear optics, and ion sensing [10.34].

10.1.4.2 Signaling Supramolecular Receptor–Substrate Interaction with Luminescent Quantum Dots

Semiconductor quantum dots, which are inorganic nanoparticles with attractive photophysical properties, are becoming valuable analytical tools for biomedical applications and can complement, if not replace conventional organic fluorophores [10.35]. With their broad absorption bands, these quantum dots offer a wide range of excitation wavelengths and with their narrow emission luminescence bands they can be positioned within the visible optical region.

It has been demonstrated that quantum dots equipped with appropriate ligand receptors can specifically detect and signal, e.g., a particular protein by a supramolecular receptor–substrate interaction giving rise to a luminescence change [10.36]. For this purpose, CdSe–ZnS core–shell quantum dots were coated with hydrophilic mercaptoacetate groups in order to make them soluble in water giving rise to a 563 nm luminescence emission (Fig. 10.15c). The addition of the bipyridinium branch of an integrated bipyridinium–biotin molecule (Fig. 10.15a) to the hydrophilic quantum dots decreases ("quenches") the luminescence due to a capturing of the electrons photo-induced in the quantum dot. The specific supramolecular association of the biotin branch with a streptavidin protein molecule (Fig. 10.15b) prevents the electron capturing and, therefore, reactivates the luminescence of the quantum dot to re-increase the luminescence intensity in Fig. 10.15c. This supramolecular reaction shows that a particular protein can be specifically monitored by using luminescent quantum dots as probes.

10.1.5 Molecular Recognition and Self-Organization

Some of the above-mentioned functional units contain molecular receptors for recognition, catalysis, and transport processes. For self-organization additional information is required. As an example from biology the self-organization of the tobacco mosaic virus is considered (Fig. 10.16). This rod-shaped particle is ~300 nm long and 18 nm in diameter and is composed of over 2000 coat–protein subunits arranged into a right-handed helix. Running along the core of the virus is a single strand of ribonucleic acid (RNA). Under appropriate pH, the coat

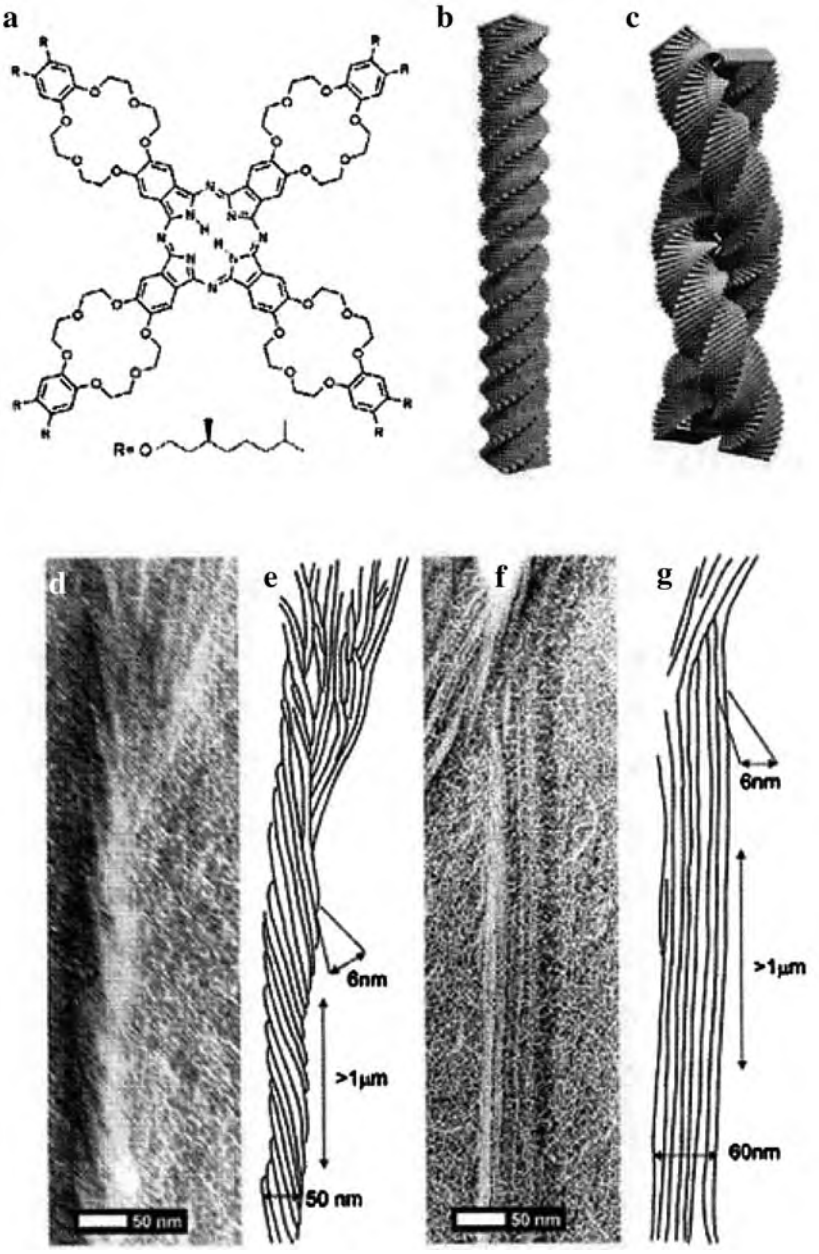

Fig. 10.14 (**a**) Chemical formula of the crown ether phthalocyanines. (**b**) Right-handed helix assembles into (**c**) a left-handed superhelix. Transmission electron micrographs (Pt shadowing) of gels from the compounds: (**d**) Left-handed coiled-coil aggregates and (e) its schematic representation. (**f**) Nonhelical rods formed in the presence of KCl and (**g**) their schematic representation [10.30, 10.34]. (Reprinted with permission from [10.30]. © 2004 Elsevier)

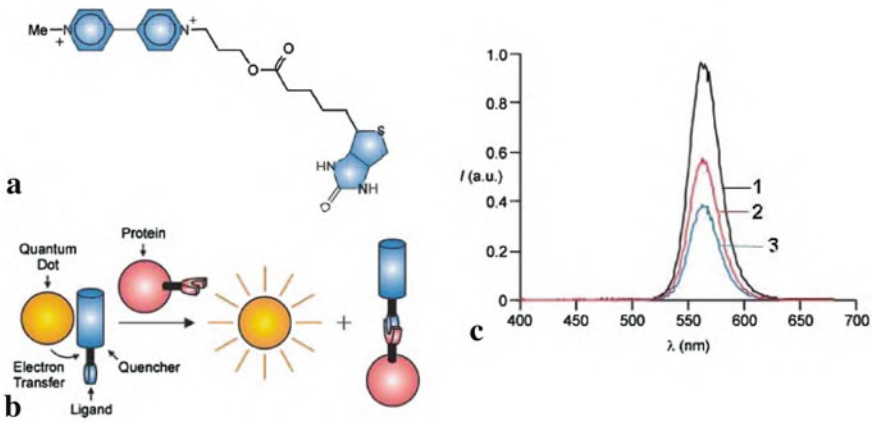

Fig. 10.15 (**a**) Molecular skeleton integrating a bipyridinium quencher and a biotin ligand. (**b**) The supramolecular association of protein and ligand prevents the electron transfer process and reactivates the luminescence of the quantum dot. (**c**) Influence of the bipyridinium–biotin (**a**) and streptavidin molecules on the emission behavior of hydrophilic CdSe–ZnS core–shell quantum dots recorded before (1) and after addition of bipyridinium–biotin (3) and streptavidin (2). (Reprinted with permission from [10.36]. © 2006 National Academy of Sciences USA)

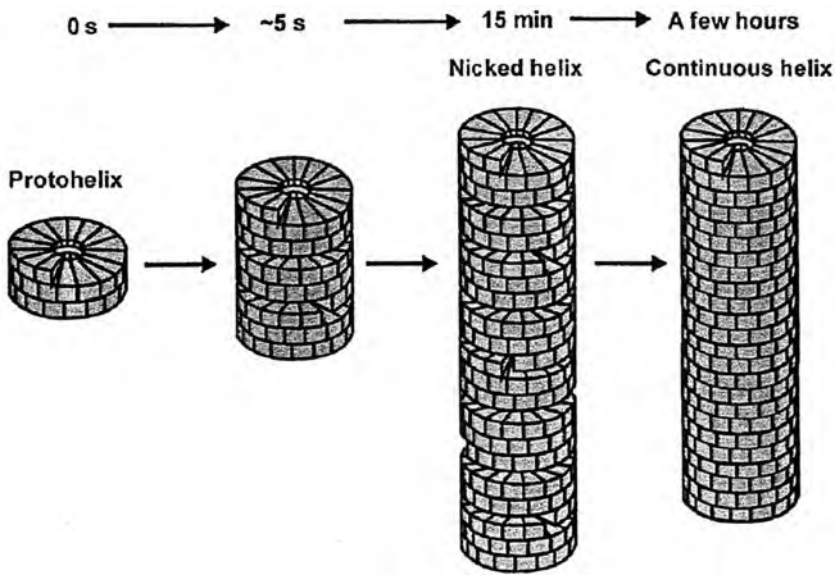

Fig. 10.16 Self-organization of tobacco mosaic virus coat proteins in the absence of RNA. (Reprinted with permission from [10.15]. © 2000 Materials Research Society)

proteins aggregate to form small "lock-washer" helices known as protohelices which specifically interact with the nucleotides of the central RNA strand to drive the self-organization of the final virus. This occurs by the initial formation of a "nicked," incomplete helix, which, over a few hours' time, anneals to form continuous helical protein rods (see Fig. 10.16).

One of the well-known examples of biological self-organization is the formation of the double helix structure of two complementary deoxyribonucleic acid strands. Can similar structures be synthesized in supramolecular chemistry based on binding phenomena non-existent in biology? Such supramolecular structures can be formed by bringing chain-like oligobipyridine ligands consisting of a few 2,2′ bipyridine units together with octahedrally coordinating Ni(II) ions forming together with the bipyridine units a triple helix (Fig. 10.17), where three strands are wrapped around the chain of the three Ni(II) ions.

Finally, an approach is presented which could lead to a refined and enormously simplified microelectronic functional unit if one could succeed in addressing these molecular electronic systems which still poses a problem [10.3]. The structure in Fig. 10.18 is considered as a so-called inorganic lattice of nine metal atoms and six

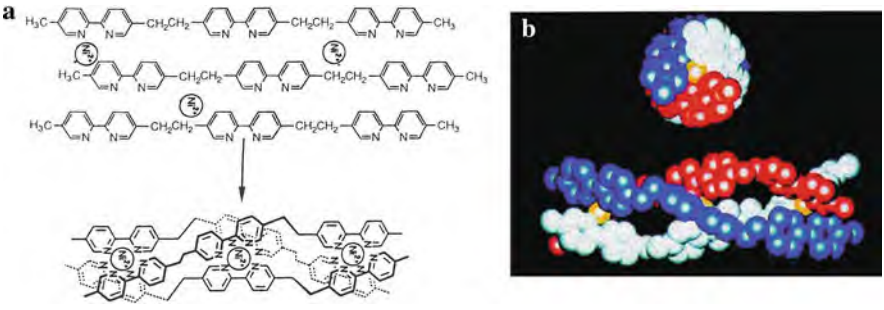

Fig. 10.17 (**a**) Self-organization of a triple helix of three ligand molecules with each three 2,2′ bipyridine units and three octahedrally coordinated Ni(II) ions. (**b**) 3D structure of the triple helix derived from x-ray diffraction. (Reprinted with permission from [10.3]. © 1997 Leopoldina)

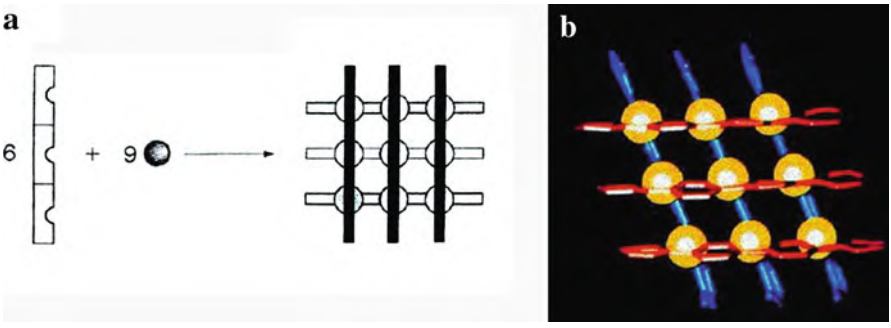

Fig. 10.18 (**a**) Schematics of the self-organization of a so-called inorganic lattice of six linear molecules, with each containing two pyridine and two pyridazine units yielding three binding sites, and nine Ag(I) ions. (**b**) 3D structure of such a lattice derived from x-ray analysis. (Reprinted with permission from [10.3]. © 1997 Leopoldina)

perpendicularly arranged linear molecules. Experimentally, such a lattice array of six linear molecules, each consisting of two pyridine and one bipyridine units and nine Ag^+ ions, can be formed spontaneously. These structures on an atomic scale are similar to quantum dot structures, however, with a much higher data storage capacity and without complex "machining" processes.

10.1.6 DNA Self-Assembled Nanostructures

DNA is an extremely favorable "constructional material" for nanoscale structures. It permits the informational character of macromolecules of biological systems to be utilized. In fact, the construction of sticky structures using branched DNA molecules as building blocks has been demonstrated to open the way to a large variety of DNA arrangements [10.37–10.40]. The double-helical DNA can form 2D square lattices (see Fig. 10.19) where the DNA chain forms the edges of these arrangements whereas the branching points of stable DNA branched junctions correspond to the vortices (see Fig. 10.19). A similar technique was applied to synthesize 2D and 3D periodic nanometer-sized DNA structures [10.40] with predefined topologies, e.g., cubes and truncated octahedra.

10.1.7 Supramolecular DNA Polyhedra

Basic DNA building units can be designed in such a way that many copies of identical units assemble into larger 3D structures [10.41] as nanosized tetrahedra, dodecahedra, or truncated icosahedra (see Fig. 10.20).

Some general aspects of the future prospects of supramolecular chemistry have been formulated by Lehn [10.3]. Under a chemical viewpoint, biology is restricted to

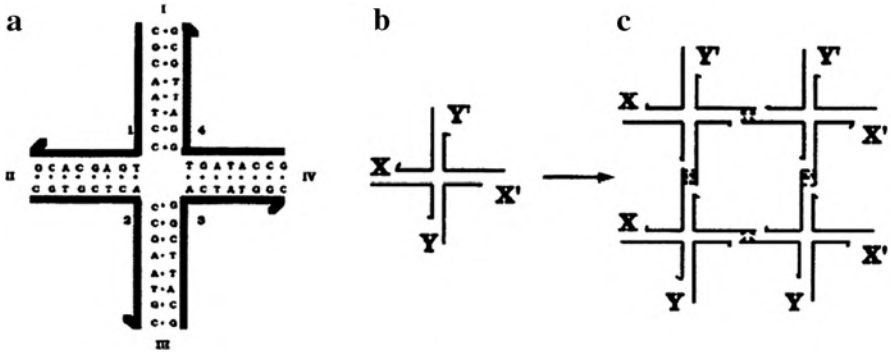

Fig. 10.19 (**a**) Stable branched DNA molecule. (**b**) Sticky ends of the DNA molecules. (**c**) Assembly of four sticky-ended DNA molecules into a square-shaped pattern [10.37, 10.38]. (Reprinted with permission from [10.3]. © 1997 Wilay-VCH)

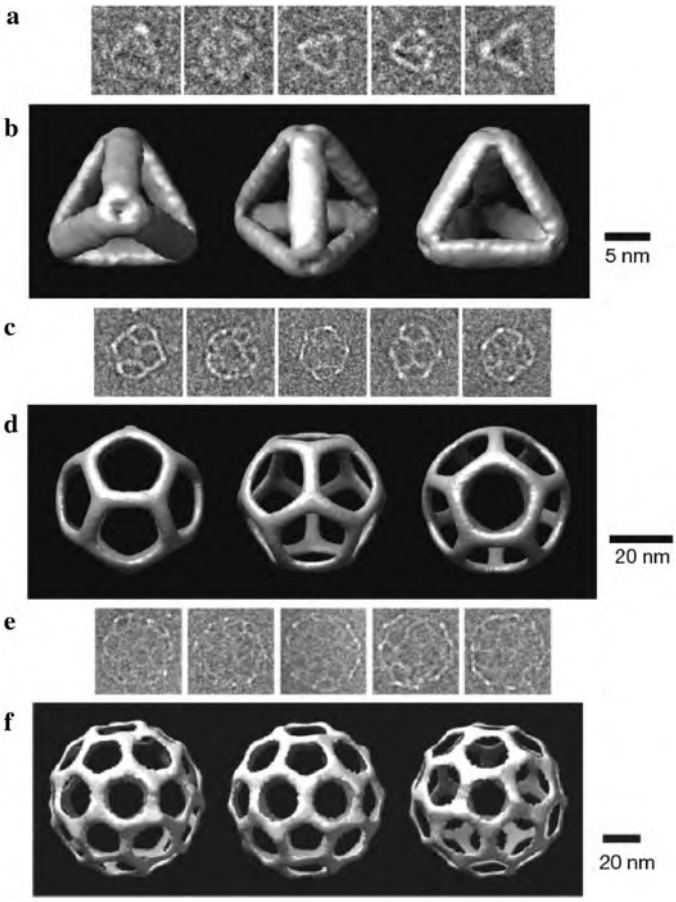

Fig. 10.20 Supramolecular DNA polyhedra. (**a**), (**c**), (**e**) Raw cryoelectron microscopy (cryo-EM) images in various projections of a tetrahedron, a dodecahedron, and a truncated icosahedron (buckyball), respectively. (**b**), (**d**), (**f**) Three views of a tetrahedron, a dodecahedron, or a buckyball structure reconstructed from cryo-EM images. (Reprinted with permission from [10.41]. © 2008 Nature Publishing Group)

a relatively narrow framework. Whereas the number of various molecules as carriers of biological functions is huge, the number of materials classes is not so wide. In contrast, chemistry offers a powerful wealth and variety of materials classes where the complexity of biomolecules is by far not reached but which implies enormous potentials of varieties, in particular taking into account supramolecular chemistry (see Fig. 10.21).

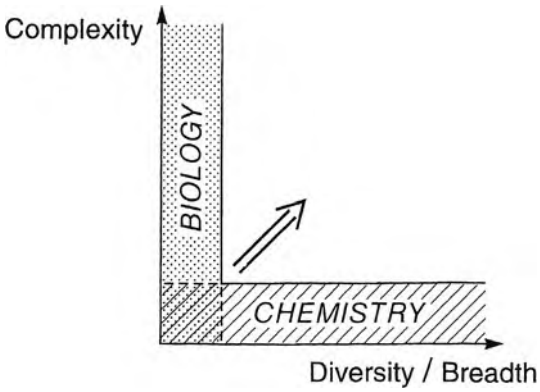

Fig. 10.21 Diagrammatic comparison of the potentials of biology and chemistry with the parameters complexity and diversity/breadth. (Reprinted with permission from [10.2]. © 1995 Wiley-VCH)

10.2 Large Inorganic Hollow Clusters

Not only in supramolecular organic chemistry large molecular entities with sizes of several or many nanometers can be constructed but also in inorganic chemistry large hollow clusters can be fabricated by bottom-up approaches. Here, the clusters, with extended cavities, formed by assembling molybdate fragments [10.28, 10.42] and the nitride clathrates formed by using phosphorus–nitrogen tetrahedra [10.43] will be discussed briefly.

10.2.1 Nano-hedgehogs Shaped from Molybdenum Oxide Building Blocks

For the construction of nanosized molecular units the appropriate building blocks must display a certain type of flexibility as a pre-requisite for linking, a condition well fulfilled by molybdenum oxide-based fragments [10.42]. Large, hollow hedgehogs of $Na_{48}[H_xMo_{368}O_{1032}(H_2O)_{240}(SO_4)_{48}]\cdot$ca. $1000H_2O$ with a cavity of $2.5\times2.5\times4.0$ nm^3 were synthesized (Fig. 10.22). These clusters have approximately the size of hemoglobin (6 nm in diameter). Reducing conditions can further favor the growth of the cluster which may enable a new type of nanochemistry, supramolecular reactions inside the cavity, and the understanding of the mechanisms of heterogeneous catalysis.

10.2.2 Vesicle-Like Structures with a Diameter of 90 nm

They can be formed in aqueous solution from a spherical composition of approximately 1,165 wheel-shaped $\{Mo_{154}\}$ clusters each with a diameter of 3.6 nm

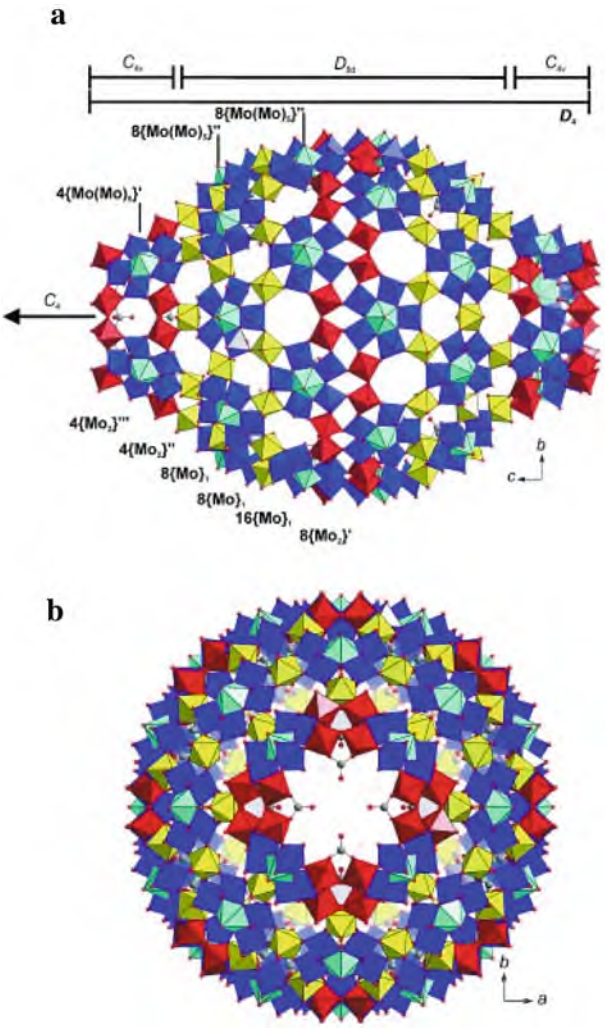

Fig. 10.22 Structure of the Mo_{368} hedghog perpendicular to the C_4 axis (**a**) and along the C_4 axis (**b**). Building units $\{Mo_1\}\equiv[MoO(H_2O)]$ (*yellow*), $\{Mo_2\}\equiv\{Mo_2O_3(H_2O)_2\}$ (*red*), and $\{Mo(Mo_5)\}$ (*blue*) with blue-turquoise pentagonal bipyramids. The cavity has a size of $2.5\times2.5\times4.0\,nm^3$. (Reprinted with permission from [10.42]. © 2002 Wiley-VCH)

(see Fig. 10.23). These clusters are stabilized by van der Waals attraction, electrostatic repulsion, and hydrogen bonding involving water molecules. The ensemble of the spherically arranged nanowheels yields a soft and flexible "surface membrane" of the vesicles as analyzed by light scattering and transmission electron microscopy. These vesicles partially collapse during the drying process. The vesicle built by the 1,165 nanowheels (Fig. 10.23c) is modeled by an icosadeltahedron which is a

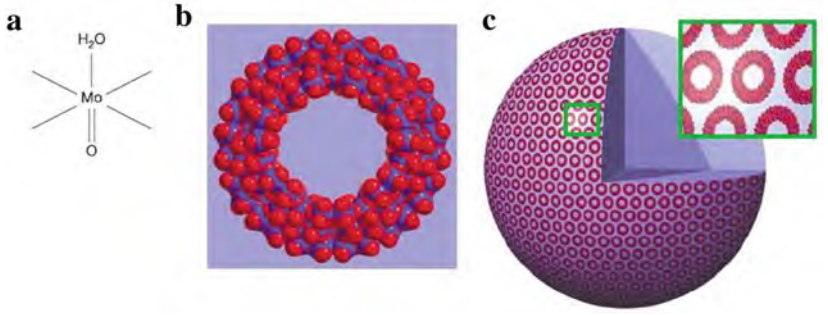

Fig. 10.23 Spherical 90 nm vesicles composed of 1,165{Mo_{154}} nanowheels. (**a**) Smallest fragment with a Mo atom and its coordinated sphere including one of the 70 H_2O ligands causing the hydrophilic nature. (**b**) Space-filling representation of the 3.6 nm size {Mo_{154}}-type nanowheel (*blue* and *light blue*, Mo atoms; *red*, O atoms). (**c**) Schematic representation of the vesicle structure formed of nanowheels in aqueous solution with the *inset* showing enlarged nanowheels. (Reprinted with permission from [10.28]. © 2003 Nature Publishing Group)

polytope with icosahedral symmetry where all faces are equilateral triangles and either five or six triangles are found adjacent to each vortex [10.28].

10.2.3 Nitride–Phosphate Clathrate

Clathrates are formed when a host compound encloses guest molecules without using strong ionic interactions or covalent bonds. A nitride–phosphate clathrate framework has been synthesized [10.43] (Fig. 10.24) which can trap neutral

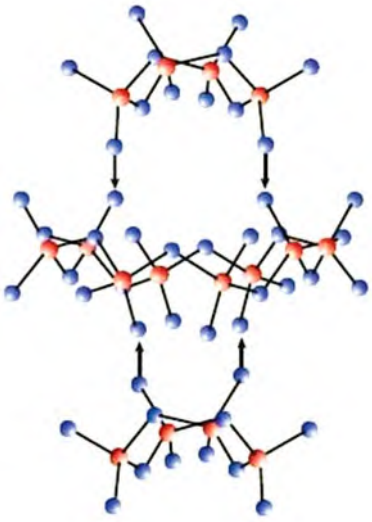

Fig. 10.24 Exploded view of a cavity via a nitride–phosphate clathrate framework, formed from a ring of eight tetrahedra capped with two rings of four tetrahedra. The *arrows* point between nitrogen atoms that are shared by the central and the capping rings. (Reprinted with permission from [10.43]. © 2006 Wiley-VCH)

ammonia molecules in small cages. The framework is constructed from tetrahedra which consist of a phosphorus atom (red) at the center of four nitrogen atoms (blue). To form a cage, eight of these tetrahedra form a ring which is capped above and below by two smaller rings, each formed from four tetrahedra (Fig. 10.24). This compound with a remarkable thermal stability up to 550°C could be useful in membrane reactors where the trapped molecules would participate in chemical reactions at solid–gas interfaces. The nitride may even exhibit electrical protonic conduction.

10.3 Chemistry on the Nanoscale

The availability of carbon nanotubes and nanodroplets as "nano test tubes" and "nanoreactors" allows for the investigation of novel chemical reactions in low-dimensional environments and confined geometries. Chemical reactions can be performed in attoliter (10^{-18} l) volumes on a zeptomole (10^{-21} mol) scale [10.44]. In addition, by employing nano-manipulation techniques [10.45], the interaction of single molecules can be studied, as outlined in the following.

10.3.1 Nano Test Tubes

Single-walled carbon nanotubes (SWNTs) were used as templates for forming covalent polymeric chains from $C_{60}O$ [10.46]; the resulting polymer topology is different from the 3D bulk polymer in that it is linear and unbranched. Above 250°C in the bulk solid state, $C_{60}O$ polymerizes via epoxide ring opening, with a rigid furan-type bridge linking the cages. The bulk fullerene oxide polymer forms a face-centered cubic lattice with an interfullerene spacing of 0.997 nm, close to that of C_{60}. For the reaction in the nanotubes, the $C_{60}O$ molecules were filled into the SWNTs and heated to 260°C.

The confinement of 1-heptene molecules inside of SWNTs was shown to result in lowering of their reactivity to atomic hydrogen compared to 1-heptene absorption on external SWNT sites [10.47]. The reaction of atomic hydrogen with 1-heptene to heptane

$$C_5H_{11}CH = CH_2 + \dot{H} \Rightarrow C_5H_{11}\dot{C}H - CH_3$$

$$2C_5H_{11}\dot{C}H - CH_3 \Rightarrow C_5H_{11}CH_2 - CH_3 + C_5H_{11}CH = CH_2$$

is nearly nonactivated and occurs readily even below 100 K. At SWNT temperatures of 270 K, when only the interior of the nanotube is populated with 1-heptene, a lower rate of reaction with atomic hydrogen is observed, compared to experiments in which both interior and surface sites are occupied. This suggests that the graphene framework shields the 1-heptene molecules from the incident hydrogen atoms and that nanotubes can be used to control the chemical reactivity of a molecule [10.47].

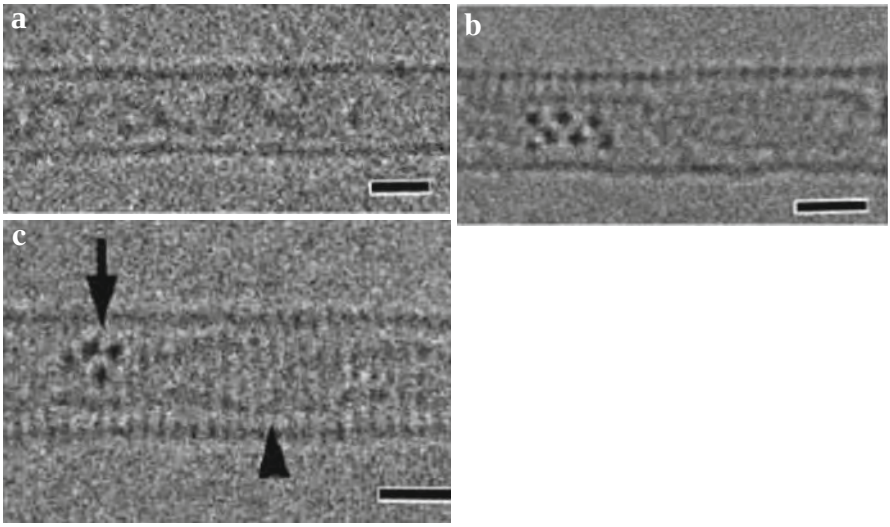

Fig. 10.25 (**a**) High-resolution transmission electron micrograph (HRTEM) of tris (cyclopentadienyl)cerium ($CeCp_3$) in a single-walled carbon nanotube SWNT ($CeCp_3$@SWNT). (**b**), (**c**) HRTEM of the sample transformed at 1000°C in vacuo into double-walled carbon nanotubes (DWNT) containing cerium (Ce@DWNT). The *undulating lines* in between the outer tube wall indicate an inner tube, while the *dark dots* are from cerium ions. Scale bar is 1 nm. (Reprinted with permission from [10.48]. © 2009 American Physical Society)

For the application of nano test tube chemistry, the 1D quantized electronic levels of SWNTs can be manipulated by doping [10.48], e.g., with tris(cyclopentadienyl)cerium ($CeCp_3$; see Fig. 10.25a).

10.3.2 Dynamics in Water Nanodroplets

There are many examples in the fields of biology, geochemistry, tribology, and nanofluidics, where water molecules are not present as a bulk liquid, but in confined geometries [10.49]. Near a surface, ordering of water molecules into layers occurs [10.50] as shown by x-ray diffraction. This ordering was found to extend up to several molecular diameters into the liquid. In the case of small water droplets, the confinement is 3D, and the overall structure and dynamics of the water are affected.

A solution of nanometer-sized droplets (see Sect. 7.9) forms when preparing an emulsion of water in an apolar solvent by addition of a surfactant. The anionic lipid surfactant sodium bis(2-ethylhexyl)sulfosuccinate (AOT) is known to form monodisperse micelles with radii ranging from 0.2 to 4.5 nm [10.49], depending of the water-to-AOT ratio, conventionally denoted by the parameter $w_0 = [H_2O]/[AOT]$. The dynamics of water molecules in nanodroplets was studied by using ultrafast mid-infrared pump-probe spectroscopy on the OH-stretch vibration of isotopically diluted water (HDO in D_2O) contained in reverse micelles. In

these experiments, the contributions of core and interfacial water molecules can be observed separately, demonstrating that the molecular mobilities are surprisingly different.

When the size of the water droplets is increased, the amplitude of the slow component in the vibrational relaxation, which can be assigned to the water molecules at the droplet interface, strongly decreases. From a quantitative analysis, a surface coordination of about six hydrogen bonds per surfactant molecule is derived. This number of hydrogen bonds is consistent with the fact that there are six lone electron pairs located at the oxygens of the sulfonate anion of the AOT surfactant molecule, which can accept one hydrogen bond each. Whereas the core water molecules reorient on a timescale close to that of bulk water (2–4 ps), the interfacial water is highly immobile with reorientation times >15 ps [10.49].

The strongly different orientational mobilities of core and interfacial water molecules have to be explained from their different intermolecular interactions and very different geometric arrangements. Molecular reorientation involves the subsequent breaking and formation of hydrogen bonds. For core water molecules (as for bulk water), the activation energy for reorientation is substantially lowered, because these molecules can break a hydrogen bond while simultaneously forming a new bond with another water molecule. For interfacial water molecules this process is inhibited because these molecules are hydrogen bonded to an immobile surfactant molecule. The slow orientational dynamics for the interfacial water molecules is supported by molecular dynamics simulations on micellar systems [10.51]. Water molecules with full bulk-like character only start to appear in the core of a cluster of at least 2,000 water molecules ($\omega_0 = 12$) [10.49].

10.3.3 Targeted Delivery and Reaction of Single Molecules

Scanning probe microscopy-based techniques can be used to manipulate and deliver single molecules in a precisely controlled manner to a specific target. Reactive polymer molecules, attached at one end to an atomic force microscope (AFM) tip (Fig. 10.26a), are brought into contact with a modified silicon substrate to which they become linked by a chemical reaction. When the AFM tip is pulled away from the surface, the mechanical force causes the weakest bond – the one between the tip and the polymer – to break. This process transfers the polymer molecule to a precisely defined site on the substrate where it can be modified by further chemical reactions [10.52].

An Au-coated AFM tip is modified by poly-*N*-succinimidyl acrylate (PNSA) and a silicon substrate with amino propyltrimethoxysilane. In an *N*,*N*-dimethylformamide solution containing 4-dimethylaminopyridine (DMAP), the functionalized AFM tip is brought into contact with the substrate to covalently link the polymer chains to the substrate (Fig. 10.26a). Upon retraction of the tip, the Au (tip)-c (polymer) bond is the weakest link and the most likely candidate for breaking. Upon cleavage, the polymer chain remains covalently attached to the substrate and can be easily modified by a wide range of nucleophilic compounds [10.52].

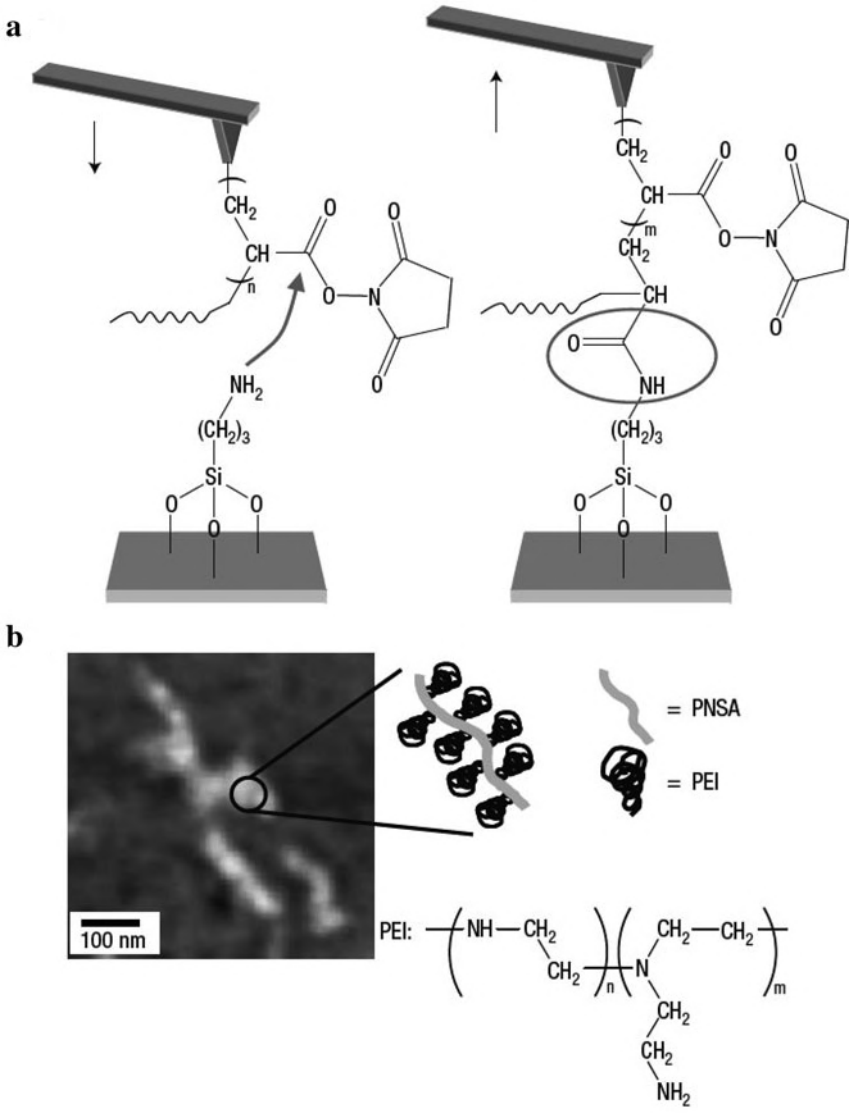

Fig. 10.26 (**a**) Molecule by molecule delivery process. *Left*: During the tip–sample contact a chemical reaction occurs between the activated esters of a poly-*N*-succinimidyl acrylate (PNSA) chain grafted to the tip and the amino groups of the substrate to form an amide bond, which covalently links the chain to the substrate. *Right*: When the tip is pulled away from the surface, the mechanical force causes the weakest bond – the bond between the tip and the polymer – to break. (**b**) Atomic force microscopy (AFM) topography images obtained in air after delivery. Image obtained in the area where four (PNSA) chains were deposited, one at a time. The chains are decorated by branched polyethyleneimine (PEI).The decorated molecules appear in an extended shape with a maximum vertical height of 4 nm. (Reprinted with permission from [10.52]. © 2006 Nature Publishing Group)

For visualization, the single organic PNSA chain on the substrate is reacted with branched polyethyleneimine (PEI). The resulting structure is a PNSA backbone with PEI side chains, which can be imaged by AFM (see Fig. 10.26b).

10.4 Catalysis

Catalysts are materials that accelerate the pace of chemical reactions, without changing their thermodynamics, and without being consumed during the reaction (see [10.53]). They come in many forms as nanocrystals, metal complexes, small organic molecules, enzymes. An industrial heterogeneous catalyst (see [10.54]) is typically a material of nanoparticles (see [10.55]) dispersed on a porous (often metal oxide) support [10.56]. Because of their inherent complexity and dispersed nature, most catalysts have been developed by trial and error methods in the past, but new challenges demand new concepts for designing and synthesizing catalysts. The altered geometric and electronic structure of nanoclusters may be employed – together with the potentials of density functional theory (DFT) ab initio calculations (see, e.g., [10.57–10.59]) – to develop novel and unique catalytic properties.

In heterogeneous catalysis, the reacting molecules are absorbed on the catalytically active solid surface. Chemical bonds are broken and formed on the surface and eventually the products are released back into the liquid or gas phase. For the elucidation of elementary processes in catalysis in his pioneering work [10.60, 10.61], Gerhard Ertl has been awarded the Nobel Prize in chemistry in 2007.

Most industrial reactions for chemical conversion are catalyzed [10.62]. Specifically, catalysis enables the cost-effective and environmentally sound production of fuels (e.g., transportation fuels) with about ten different catalysts during its transformation from curde oil [10.58]. Furthermore, catalysts are used in the catalytic converter in the exhaust of every car, for the production of chemicals (ammonia, methanol, flavors, fragrances), foods (hydrogenated fats), and pharmaceuticals (pain relievers). The value of the goods manufactured annually in the United States in processes that involve catalysts is estimated to be several trillion dollars [10.62].

In the following, studies of atomic-scale catalytic activities will be outlined on some metallic and nonmetallic nanocrystals, which can be specifically investigated by scanning tunneling microscopy [10.56, 10.63], high-resolution transmission electron microscopy (HRTEM; see Fig. 10.27), x-ray diffraction [10.64], extended x-ray absorption fine structure (EXAFS [10.65]), x-ray photoelectron spectroscopy (XPS [10.66]), etc.

10.4.1 Au Nanocrystals

Although extended gold surfaces are generally considered chemically inert, nanosized (<5 nm) gold particles can be effective catalysts for a number of oxidation

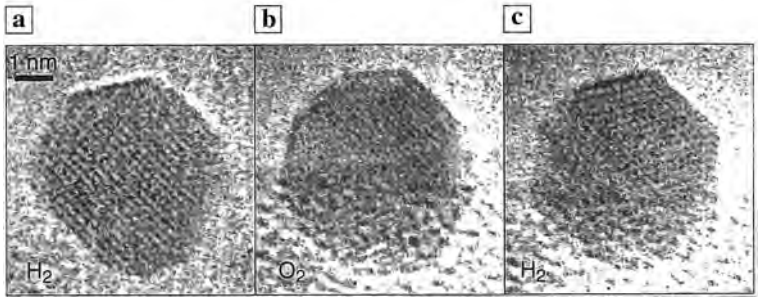

Fig. 10.27 Lattice-resolved environmental transmission electron microscopy of a Au cluster during exposure to a cycle of (**a**) H_2, 2 mbar; (**b**) O_2, 2 mbar; and (**c**) again H_2, 2 mbar at ambient temperature. The images show a reversible change from a faceted shape in hydrogen, to a more spherical shape during oxygen exposure to the final state again in hydrogen in which the faceted shape is recovered. (Reprinted with permission from [10.67]. © 2006 Elsevier)

reactions [10.68, 10.70], allowing significantly lowered reaction temperatures for the development of energy-efficient processes (see [10.58]). The reasons for the catalytic activity of small Au particles are seen, in addition to other effects, particularly in the role of low-coordinated Au atoms in Au nanocrystals.

The nobility of a metal is well illustrated by its ability to chemisorb oxygen dissociatively as characterized by the oxygen chemisorption energy. As shown in Fig. 10.28a, Au is the only metal with an endothermic chemisorption energy, illustrating its inert behavior in an oxygen atmosphere. This is due to the electron *d*-bond states in Au which are so low in energy that the interaction with oxygen 2*p* states is net repulsive. Nevertheless, the oxidation of CO is one of the reactions where Au nanoparticles with sizes <5 nm are a very good catalyst (Fig. 10.28b) on different support materials. This can be understood by the results of DFT calculations to simulate the absorption of molecules on ten-atom free Au clusters [10.58] (which also can be prepared experimentally [10.69]): CO oxidation by these clusters is possible at room temperature and, most importantly, the binding energy decreases to exothermic values with the coordination number (CN) of the Au atoms (Fig. 10.28c) to which the reactants bind. Au atoms on a close-packed surface have nine neighbors, at steps on a surface seven, and at the corners of small particles it can be as low as three to four. The increase in the fraction of corner atoms with decreasing Au particle size (Fig. 10.28d) coincides with the observed increase in CO oxidation activity (Fig. 10.28b). This indicates the enhanced reactivity of low-coordinated Au atoms which are abundant on the smallest nanometer-sized Au nanoparticles [10.58]. It, furthermore, has been shown – based on a set of DFT calculations of the full pathway of CO oxidation – that although platinum and palladium are the most active catalysts for extended surfaces at high temperatures (600 K), gold is the most active for very small particles at low temperatures (273 K) [10.70].

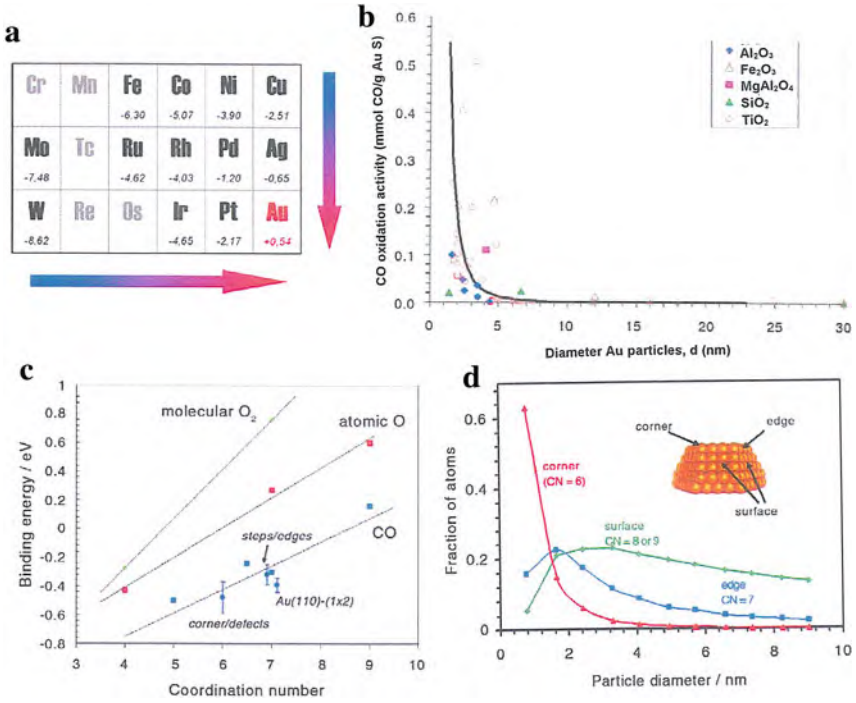

Fig. 10.28 Enhanced catalytic activity of low-coordinated atoms of Au nanoclusters. (**a**) The dissociative chemisorption energies for oxygen on transition metal surfaces with respect to a molecule in vacuum calculated by density functional theory (DFT) . All results are for adsorption at either a body-centered cubic (210) surface (for Fe, Mo, W) or a face-centered cubic (211) surface (other metals). (**b**) Reported catalytic activities for CO oxidation at 273 K as a function of gold nanoparticle size *d* for different support materials. The *solid curve* shows the calculated fraction of atoms located at the corners of nanoparticles as a function of *d* for uniform particles shaped as the top half of a regular cuboctahedron. (**c**) The correlation between the binding energies for O_2, O, and CO on Au and the coordination number of the Au atoms in different surfaces and clusters. The binding energies are calculated using density functional theory (DFT), for the experimental values see [10.58]. (**d**) Calculated fractions of Au atoms at corners (*red*), edges (*blue*), and crystal faces (*green*) in uniform nanoparticles with the shape of the top half of a truncated octahedron (see *insert*) as a function of Au particle diameter. (Reprinted with permission from [10.58]. © 2007 Elsevier)

At present, the most serious problem associated with Au nanocatalysts is probably their short long-term stability which appears to be enhanced by atomic defects in the support surface as shown by STM studies of Au clusters on rutile TiO_2 (110) surfaces [10.56]. Under reducing conditions (r-TiO_2), vacancies of the bridging oxygen (O_{br}) atoms can be introduced (see Fig. 10.29), by water doping (h-TiO_2) H adatoms can cap some of the O_{br} atoms, and by oxidation (o-TiO_2) O adatoms (O_{ot}) are introduced. O_{br} vacancies and O_{ot} atoms can stabilize small Au clusters on the terraces and heating experiments demonstrate that Au clusters bind most strongly to the o-TiO_2 surface which is corroborated by DFT calculations [10.56].

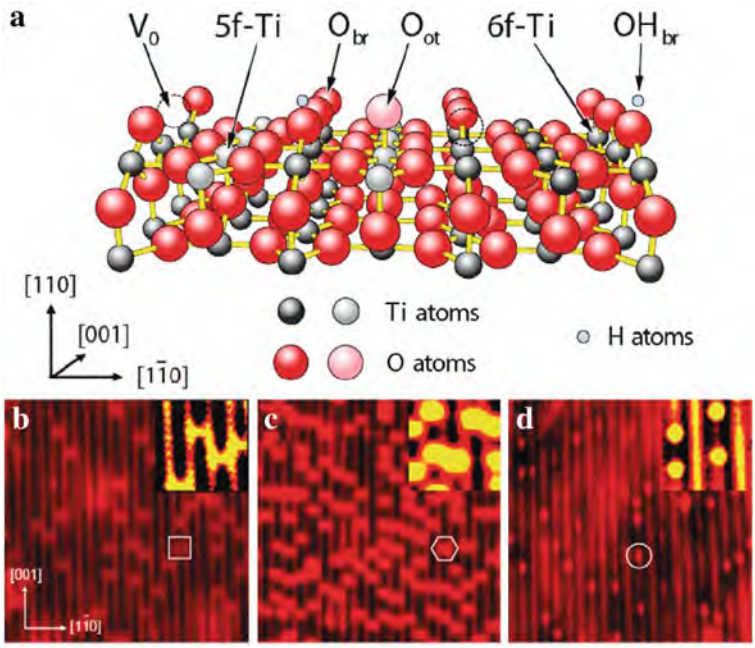

Fig. 10.29 Structure of a TiO_2 (110) surface with various types of atomic defects. (**a**) Ball model of the surface. Large *red* balls represent O atoms, medium-sized *black* balls sixfold coordinated Ti (6f-Ti), and medium-sized *gray* balls fivefold coordinated surface Ti atoms (5f-Ti). *Small light* balls indicate H atoms. The bridge-bonded O species (O_{br}), single oxygen vacancies (V_0), and on-top bonded O species (O_{ot}) are also indicated. Scanning tunneling microscopy (STM) images of reduced *r*- (**b**), water-doped *h*- (**c**) and oxidized *o*- (d) TiO_2 (110) surfaces before Au exposure. Size is 13×13 nm^2. In the STM images, the symbols indicate O_{br} vacancies (*square*), H adatoms on O_{br} sites (*hexagon*), and O_{ot} atoms in the Ti troughs (*circle*). *Insets* (3×3 nm^2) show the point defects of interest enlarged [10.56, 10.71]. (Reprinted with permission from [10.56]. © 2007 Elsevier)

10.4.2 Pt Nanocatalysts

Considerable research has been stimulated to use nanometer and sub-nanometer ($Pt_{8–12}$) Pt clusters as a catalyst [10.72–10.75] with high performance and utilization efficiency in the production of hydrogen and particularly in the direct methanol fuel cell (see [10.76]). It has been shown that high-index planes generally exhibit much higher catalytic activity than the stable planes, such as {111} and {100}, because the high-index planes have a high density of atomic steps, ledges, and kinks, which usually serve as active sites for breaking chemical bonds (see [10.77]). Pt nanocrystals with a tetrahexahedral (THH) shape [10.77] are enclosed by 24 high-index facets as {730}, {210}, and/or {520} surfaces (see Fig. 10.30a, c) that have a large density of atomic steps. These high-energy surfaces are stable to 800°C and exhibit much enhanced (up to 400%) catalytic activity for equivalent Pt surface

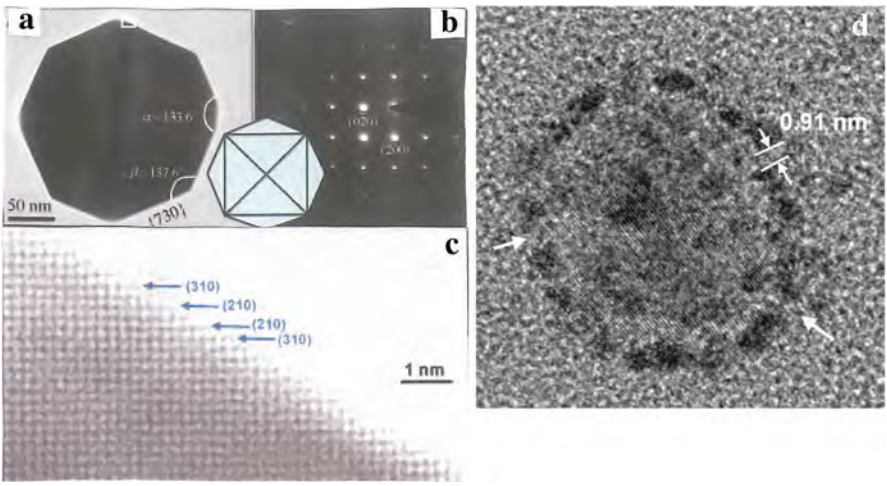

Fig. 10.30 (**a**) Transmission electron micrograph (TEM) of a tetrahexahedral (THH) Pt nanocrystal with {730} surfaces. The *inset* is a projected model of the THH. (**b**) Corresponding selected area electron diffraction (SAED) pattern, showing the single-crystal structure of the THH Pt nanocrystal. (**c**) High-resolution transmission electron micrograph (HRTEM) of a THH Pt nanocrystal showing the surface atomic steps made of (210) and (310) subfacets [10.77]. (**d**) Hollow Pt shell with nanochannels [10.76]. (Reprinted with permission from [10.77] (**a–c**) and [10.76] (**d**). © 2007 AAAS (**a–c**) and © 2008 American Chemical Society)

areas for electro-oxidation of small organic fuels as formic acid and ethanol [10.77]. The catalytic activity is also enhanced in the case of hollow Pt nanospheres with nanochannels (Fig. 10.30d). High thermal stability of Pt nanoparticles as catalysts for ethylene hydrogenation and CO oxidation can be achieved by coating with a mesoporous silica shell [10.78]. Enhanced catalytic activity for hydrogenation reactions in the aqueous phase was demonstrated for very small Pt nanocrystals with a diameter of 2–3 nm [10.79]. The (111) facets of tetrahedral Pt nanoparticles favor selectively the formation of *cis*-2-butene, despite the fact that, in the gas phase, it is energetically less stable than *trans*-2-butene, but more stable when adsorbed on the Pt (111) surface. DFT calculations indicate that the Pt (111) surface reconstruction is central to the adsorption of the isomers [10.80].

10.4.3 Pd Nanocatalysts

A TEM image of Pd nanocrystals on an Al_2O_3 support is shown in Fig. 10.31. The catalyst composition and oxidation state can be determined by x-ray photoelectron spectroscopy (XPS) . The properties of a catalyst may significantly change during a catalytic reaction due to surface restructuring by the adsorption of reactants or products, due to the formation of Pd hydrides during hydrogenation reactions, due

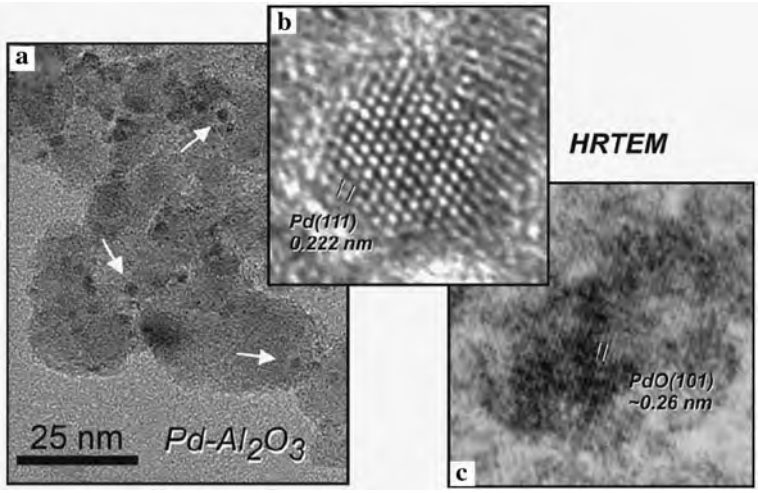

Fig. 10.31 (**a**) Transmission electron micrograph of a technological Pd–Al_2O_3 catalyst (5 wt% Pd). (**b**) Atomic structure of a cuboctahedral Pd nanoparticle by high-resolution imaging. (**c**) PdO nanoparticle of an initial Pd–Al_2O_3 catalyst used for methane combustion at ambient pressure at about 825 K. (Reprinted with permission from [10.81]. © 2007 Elsevier)

to carbon laydown, due to oxide formation (Fig. 10.31c), or due to changes of the surface composition in the case of bimetallic catalyst nanoparticles [10.81].

By alloying Pd nanoparticles with Ag, a higher fraction of CO can bind to single Pd atoms. Isolated Pd atoms in bimetallic Pd–Ag nanoparticles are also crucial for the selective hydrogenation of acetylene C_2H_2 to ethylene C_2H_4 [10.81]. When the surface of Pd–Au nanoparticles exhibits a maximum number of pairs of isolated Pd atoms, the rate of vinyl acetate synthesis shows a maximum, suggesting that the Pd monomer pair is the active site [10.81].

10.4.4 MoS_2 Nanocatalysts as Model Catalysts for Hydrodesulfurization (HDS)

Driven primarily by strict environmental regulations, a substantial decrease in the sulfur level in transportation fuels has been achieved. However, there is an urgent need for even cleaner fuels and better HDS catalysts (see [10.56]). The HDS catalyst, which separates S embedded in organic compounds in crude oil, consists of 2–3 nm diameter MoS_2 nanoparticles promoted for activity enhancement with Co or Ni and supported on a porous alumina carrier. STM studies have made it possible to investigate the cluster morphology, the atomic scale structure of the catalytically important MoS_2 cluster edges, their active sites, and the location of promoter atoms [10.56], as discussed below.

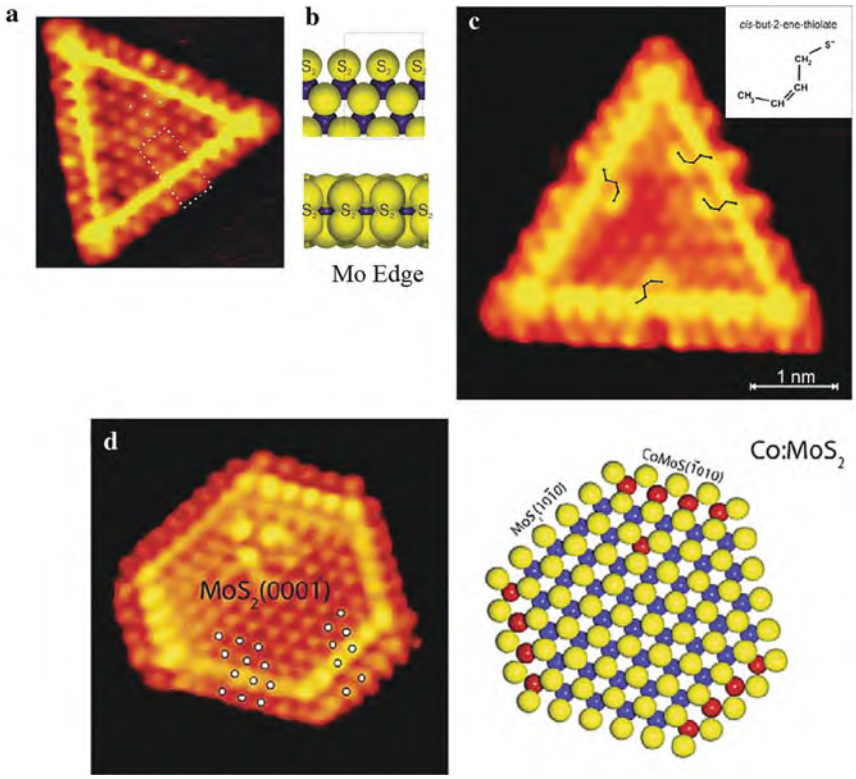

Fig. 10.32 (**a**) Atom-resolved STM image of a single-layer MoS_2 nanocluster (4.1×4.1 nm^2). (**b**) Ball model (*top view* above and *side view* below) of the edge structure determined as the Mo edge covered with S_2 dimers. Mo atoms are shown in *blue* and S atoms are *yellow*. (**c**) STM images of a MoS_2 nanocluster after exposure to hydrogen and the test molecule thiophene (C_4H_4S); 5×5 nm^2. (**d**) STM image and ball model of a single-layered Co–Mo–S nanoparticle; image size: 5.1×5.2 nm^2. Color code for the ball model: S – *yellow*, Mo – *blue*, Co – *red*. (Reprinted with permission from [10.56]. © 2007 Elsevier)

As an HDS model catalyst, MoS_2 nanoclusters are synthesized on a Au substrate [10.56]. In the STM image of Fig. 10.32a, a characteristic bright brim of high-electron state density is observed to extend all the way around the cluster edge. The electronic edge state is metallic in character, whereas bulk MoS_2 is a semiconductor with a bandgap of 1.2 eV. Experiments with hydrogenation of thiophene (C_4H_4S) to C_4H_7S on the MoS_2 nanocatalysts (see Fig. 10.32c) suggest together with DFT studies that the activation occurs on the metallic brim states on S vacancies.

Co and Ni are known to act as promoters for the MoS_2-based HDS catalysis. The Co-promoted nanoclusters adopt truncated shapes (Fig. 10.32d, e) relative to the triangular morphology of the unpromoted particles (Fig. 10.32a). The truncated shape implies that new types of edge terminations are present with the metallic

brim as a new type of active site for hydrogenation that in combination with sulfur vacancies can facilitate the full desulfurization of S-containing molecules [10.56].

10.4.5 In Situ Phase Analysis of a Catalyst

To gain insight into the mechanisms of heterogeneous catalysts, which would guide the design of novel catalysts, it is necessary to have a detailed characterization of the physicochemical composition of heterogeneous catalysts in their working state at the nanometer scale [10.82]. For this goal, a nanoreactor together with scanning transmission x-ray microscopy (STXM) is used at atmospheric pressure and up to 350°C to monitor in situ phase changes in an iron-based Fischer–Tropsch catalyst.

In the Fischer–Tropsch synthesis (FTS), synthesis gas ($CO + H_2$) is converted into hydrocarbon chains through a surface polymerization reaction for the production of chemicals and fuels from sources other than crude oil, most notably natural gas, coal, and biomass. The catalyst consists of an iron oxide phase dispersed on SiO_2. During FTS, iron oxide and metallic iron usually coexist with the iron phases largely converted into iron carbides. For in situ characterization of the catalyst, the x-ray absorption (see Sects. 2.7 and 8.1) at the carbon K edge (284.2 eV), at the oxygen K edge (543.1 eV), and at the iron L_2 and L_3 edges (706.8 eV and 719.9 eV, respectively) are used with a spatial resolution of ~15 nm [10.82]. Before the in situ experiments the iron phase of the catalyst is mainly present as α-Fe_2O_3 (Fig. 10.33a). After a 2 h exposure to H_2 at 350°C, a conversion to a mixture of iron

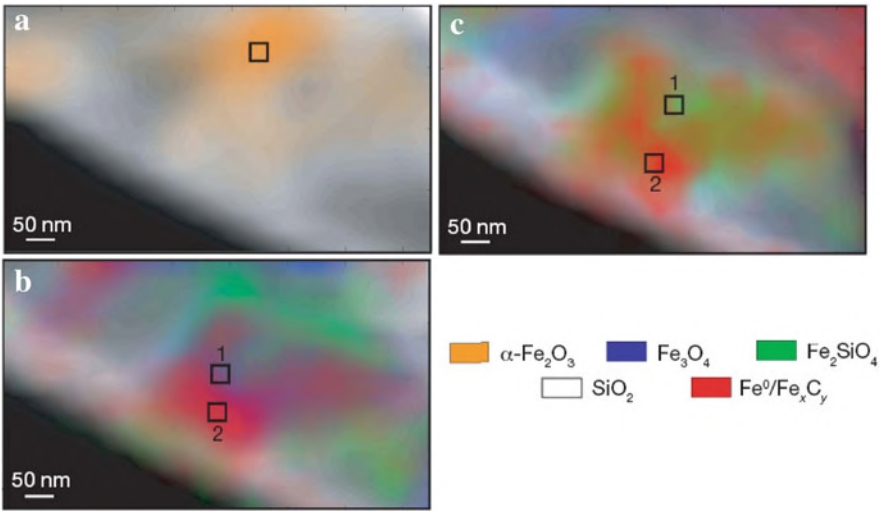

Fig. 10.33 Chemical contour maps (400 nm × 750 nm) derived by scanning transmission x-ray absorption microscopy (STXM). (**a**) Before treatment at 25°C 10^5 Pa He, (**b**) after 2 h in H_2 (~ 10^5 Pa), and (**c**) after 4 h in synthesis gas (~10^5 Pa) at 250°C. The *squares* indicate the sites where STXM spectra at the iron L_2 and L_3 edges and at the oxygen K edge are given in. (Reprinted with permission from [10.82]. © 2008 Nature Publishing Group)

oxides and metallic iron is visible (Fig. 10.33b) and during the subsequent FTS reaction in synthesis gas, the iron oxide is partially converted to Fe/Fe_xC_y and Fe_2SiO_4 (Fig. 10.33c). This demonstrates that STXM can image a complex catalyst under catalytically relevant reaction conditions.

10.5 Renewable Energy

The growing world population, rising standards of living in the developing world, and the limited supply of fossil fuels, which accounts for 85% of the world's energy needs, have an impact on global energy security, economics, and climate. Solutions to these global challenges require a global effort. In addition to energy conservation and increased efficiency in the use of energy, access to clean, affordable, reliable, and sustainable energy production – especially renewable energy – will be essential to enhancing global peace, alleviating poverty and growing our economics [10.83].

There is no doubt that many current developments in nanoscience have the potential to make a big impact on energy problems. Two recent reports (see [10.84]), published by the Basic Energy Science Advisory Committee (BESAC) of the US Department of Energy, at present with the physics Nobel laureate Steven Chu as Energy Secretary, paint an enticing picture of a sustainable and prosperous future facilitated by new technologies. European activities accelerate the development of new technologies as discussed at the conference on Nanotechnology for Sustainable Energy, organized by the European Science Foundation (ESF) [10.85].

New approaches involving nanotechnology as discussed in the following sections may make large-scale use of solar energy possible and will contribute to the further development of hydrogen storage and fuel cells. New batteries will permit the efficient storage of cleanly generated energy.

10.6 Solar Energy – Photovoltaics

Unlike other resources, solar energy is almost limitless. Several parts of Earth receive good solar radiation of about 600–800 watts/m^2. An hour of solar radiation on Earth provides 14 terawatt-years of energy, almost the same as the world's total annual energy consumption [10.86] and the resource presented by terrestrial insolation by far exceeds that of all other renewable energy sources combined [10.87]. Presently, solar collection contributes only a tiny amount (about 0.03%) to the world's energy needs, but the annual growth of the solar cell market is impressive, at about 40% per year, led in particular by Germany and Japan [10.86].

According to the radiation spectrum of the sun (Fig. 10.34), there are two routes for solar energy conversion: solar photovoltaics, including emerging nanotechnological developments discussed below and solar thermal energy generation making, e.g., use of thermoelectric materials, as discussed in the next section. Although the

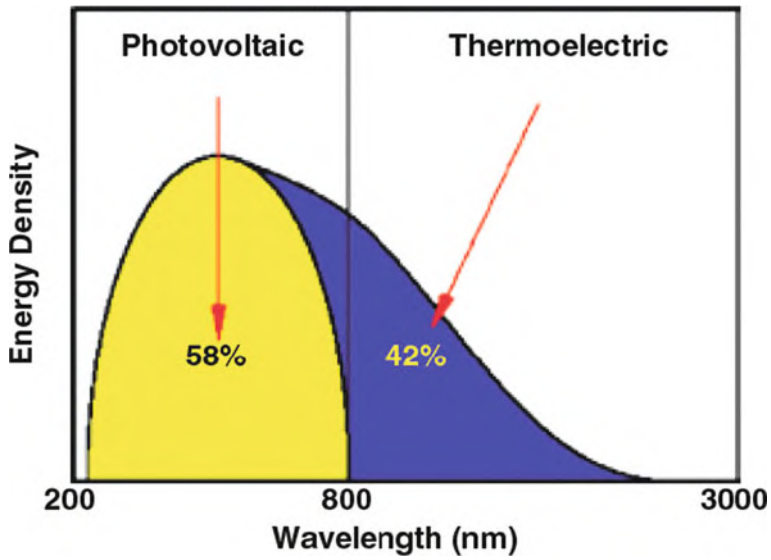

Fig. 10.34 The sun radiates energy as a 6,000 K blackbody radiator with part of the energy to be used for photovoltaic (~200–800 nm) and part (~800–3,000 nm) for thermoelectric conversion. (Reprinted with permission from [10.88]. © 2008 Materials Research Society)

performance of solar power is impressive, its costs continue to be daunting: an average of $0.25 per kilowatt-hour versus $0.05–0.08 for various biomass-based fuels (see [10.86]).

10.6.1 Nitrogen-Doped Nanocrystalline TiO_2 Films Sensitized by CdSe Quantum Dots

Two types of solar cells based on nanostructured semiconductor materials have been reported: the dye-sensitized solar cell (DSSC) [10.89] and the CdSe quantum dot solar cell [10.90]. In the DSSC, light-absorbing dye molecules inject under illumination electrons into TiO_2 nanocrystals. The electrons are transported through the porous TiO_2 layer and collected by a conductive fluorine-doped SnO_2 layer on the glass surface. In the organic–inorganic CdSe quantum dot system [10.90], light-induced charge separation and transport occur in the interface between a polymer and the CdSe quantum dots where both the quantum dots and the polymer provide continuous pathways to the electrodes.

Titanium dioxide has a wide band gap of 3.2 eV and absorbs only 5% of the solar spectrum. By nitrogen doping of TiO_2, electronic states in the band gap can be produced, thereby extending photoresponse to the visible region and improving photoactivity. The TiO_2/N nanoparticles can be efficiently sensitized by the attachment of CdSe quantum dots (Fig. 10.35) via a linking molecule, thioglycolic acid (TGA) [10.91].

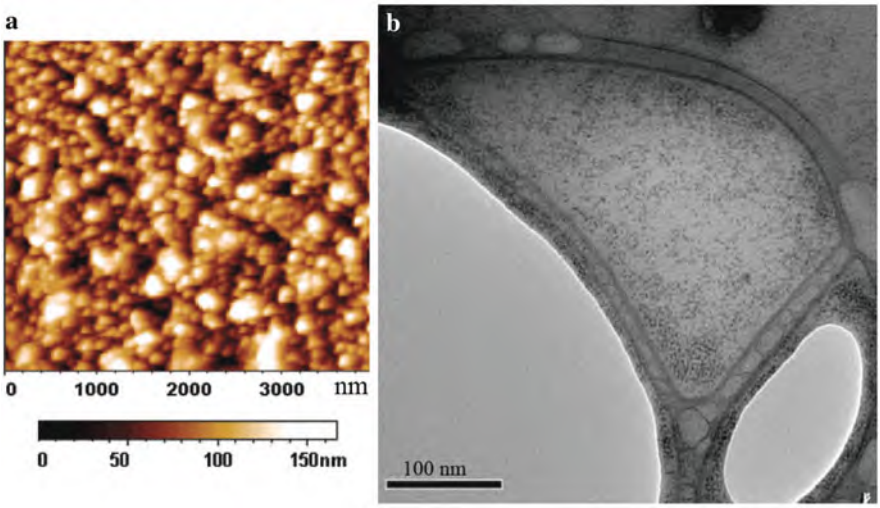

Fig. 10.35 (**a**) Atomic force microscopy (AFM) image of a thin film (175 nm) of nitrogen-doped TiO_2 nanoparticles. (**b**) Representative transmission electron microscope image of CdSe quantum dots showing an average particle size around 3.5 nm. (Reprinted with permission from [10.91]. © 2008 American Chemical Society)

10.6.2 Polymer-Based Solar Cells

Light weight and flexibility of polymers are qualities claimed to offer a reduction in the price of photovoltaic panels by reducing the installation costs. On photon absorption, in polymeric semiconductors bound excitons (electron–hole pairs) are generated. The bound excitons must migrate to an interface where there is a sufficient chemical potential energy drop to drive dissociation across the interface of the *donor* (material with low electron affinity) and *acceptor* (material with high electron affinity) [10.92]. Most successful organic/inorganic hybrid cells use a transparent metal oxide, such as TiO_2, as the n-type semiconductor because of the high electron mobility. TiO_2 templates can be made having continuous pores (Fig. 10.36) with a size matching the exciton diffusion length of a polymer (see [10.94]), allowing the possibility of complete exciton harvesting. The thickness of the nanostructure should be 300–500 nm so that the infiltrated polymer can absorb most of the incident light.

10.6.3 Silicon Nanostructures

Quantum confinement has been used to explore the increase of the Si band gap by embedding Si quantum dots in SiO_2 (Fig. 10.37). Transport of photogenerated carriers is determined by dot density because the closer the dots, the easier it is for carriers to tunnel between them. Stacks of either one or two of these quantum dot

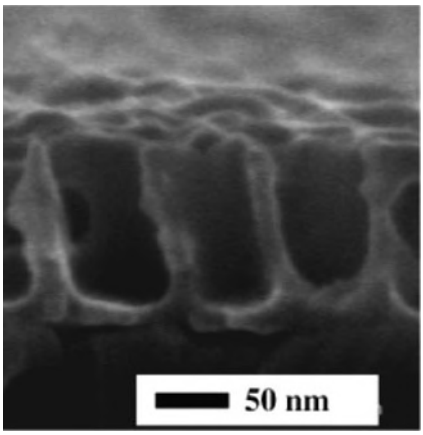

Fig. 10.36 Cross-sectional image of embossed TiO_2 after calcination. (Reprinted with permission from [10.93]. © 2005 American Chemical Society)

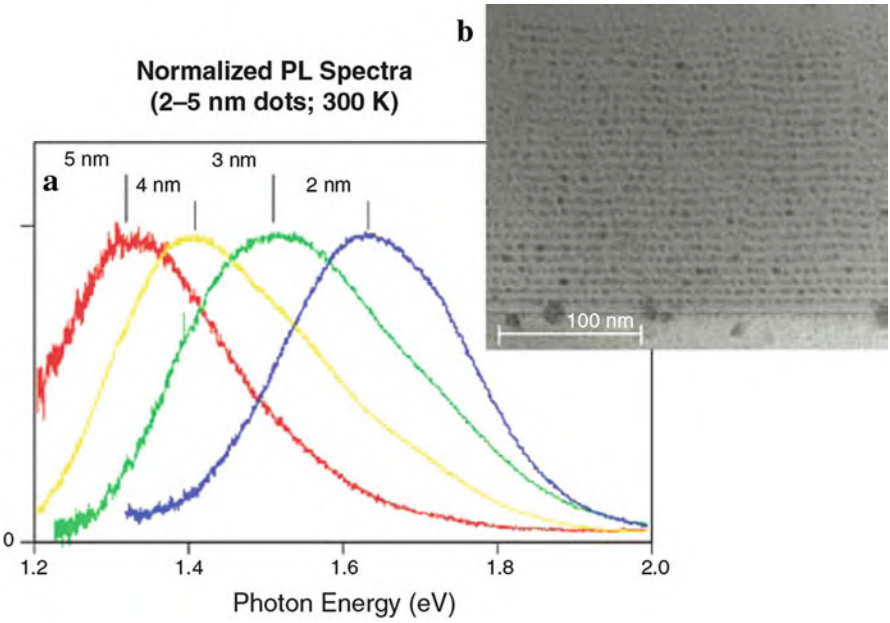

Fig. 10.37 Silicon quantum dots in an oxide material (micrograph) and resulting photoluminescence (PL) spectra as a function of quantum dot diameter. (**a**) Different particle sizes and associated PL wavelengths and (**b**) high-resolution transmission electron micrographs of the 5 nm Si particles. (Reprinted with permission from [10.95]. © 2008 American Chemical Society)

cells on top of a thin-film Si bottom cell have been proposed (see [10.95]), with the effective band gap of each cell determined by dot size. Coaxial nanowire solar cells of p-type/intrinsic/n-type (p–i–n) structures with a maximum power output of 200 pW per nanowire device and an apparent energy conversion efficiency of 3.4% might serve as integrated power sources of nanoelectronic systems [10.96].

10.7 Solar Energy – Thermal Conversion

In the thermoelectric effect [10.97], a voltage (ΔV) is generated when the junctions of two dissimilar materials are held at different temperatures (ΔT), yielding the thermopower $\alpha = -\Delta V / \Delta T$. When the circuit is closed, this couple allows for direct conversion of heat to electrical energy. The conversion efficiency, η_{TE} (see [10.88, 10.98]), is related to a quantity called the figure of merit, $ZT = \alpha^2 \sigma T / (\kappa_e + \kappa_{ph})$. Here, σ is the electrical conductivity and κ the thermal conductivity of electrons (κ_e) or phonons (κ_{ph}). The infrared (IR) region of the solar spectrum (Fig. 10.34) can supply the heat, whereas the IR radiation only generates waste heat in photovoltaic cells.

Current thermoelectric materials have $ZT = 1$, and new, e.g., nanostructured materials (see below) are sought with $ZT = 2 - 3$, according to theoretical and experimental evidence [10.99], to provide enhanced thermoelectric conversion efficiencies by reducing thermal conductivity while maintaining favorable electronic properties.

According to calculations for Bi nanorods [10.100], the ZT value substantially increases for rod diameters below 10 nm (see Fig. 10.38a). Compared to a bulk solid, the energy levels of the charge carriers in the rod are shifted by $\Delta E \approx 1 / (m_e^* d^2)$, where m_e^* is the effective mass of the charge carriers and d the diameter of the rod. The small value $m_e^* = 0.0001\ m_e$ of electrons in Bi gives rise to a considerable energy shift at relatively large diameters. In addition, the discrete energy states in the rods give rise to an enhanced density to states at the Fermi edge, enhanced conductivity, and increased ZT values. Bi_2S_3 nanorods can be prepared experimentally (Fig. 10.38b).

An enhanced thermoelectric performance has been observed in nanostructured $Bi_xSb_{2-x}Te_3$ bulk alloys due to a significant lowering of the thermal conductivity compared to the state-of-the-art BiSbTe coarse-grained alloy (see Fig. 10.39).

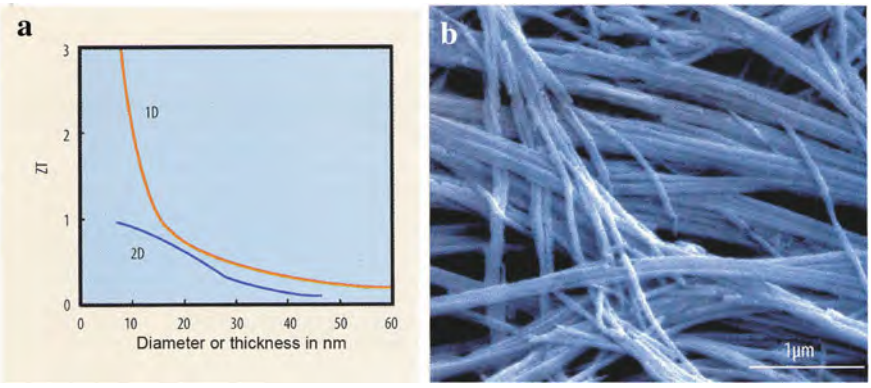

Fig. 10.38 (**a**) The calculated figure-of-merit ZT values of Bi nanorods (1D) and films (2D) substantially increase for small diameters or film thicknesses [10.100]. (**b**) Bi_2S_3 nanowires with a diameter of 50 nm [10.101]. (Reprinted with permission from [10.101]. © 2007 Wiley-VCH)

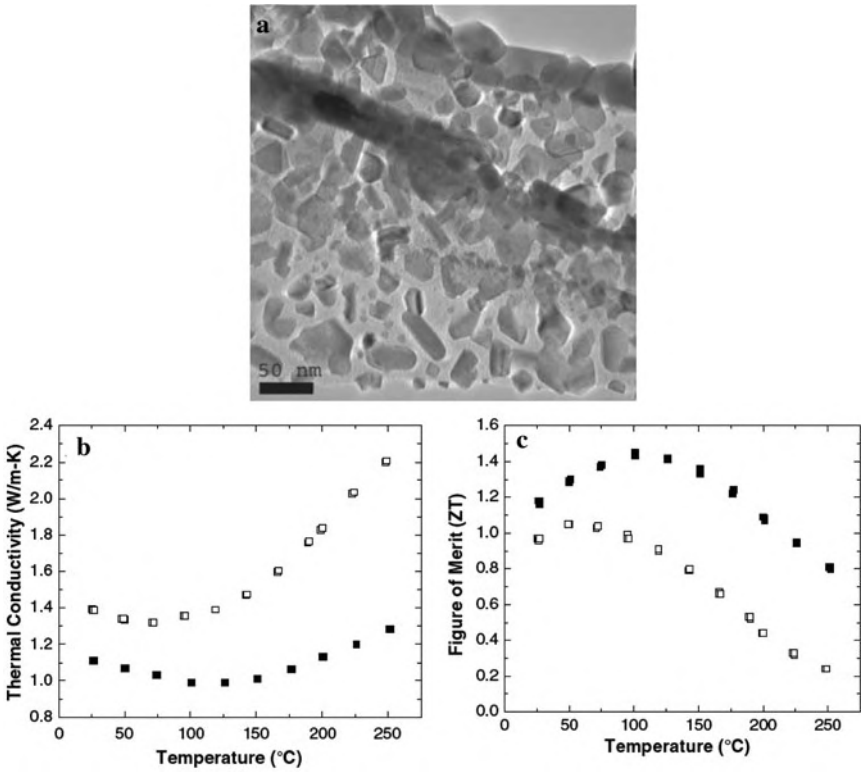

Fig. 10.39 (**a**) Transmission electron micrograph of a nanostructured $Bi_xSb_{2-x}Te_3$ bulk alloy. (**b**) Temperature dependence of the thermal conductivity and (**c**) of the *ZT* values of a hot-pressed nanocrystalline bulk BiSbTe sample (*black squares*) as compared with that of a state-of-the-art coarse-grained p-type BiSbTe alloy (*white squares*). (Reprinted with permission from [10.102]. © 2008 AAAS)

For achieving high *ZT* values, the surface decoration of ultra-thin Si nanowires is suggested [10.103].

10.8 Antireflection (AR) Coating

This coating can improve solar collection efficiency and, therefore, the overall solar-to-electricity efficiency. The AR coating needs to be effective over the entire solar spectrum and has to be effective for all angles θ of daily light incidence. Calculations predict an extremely low reflectance using the concept of a multilayer-graded index profile (see [10.104]) with, e.g., a quintic profile of the refractive index given by $n(Z) = n_{\min} + (n_{\max} - n_{\min})\left(10z^3 - 15z^4 + 6z^5\right)$, where z is the vertical optical distance measured from the air/AR-coating interface. An ultralow total reflectance of 1–6% has been obtained over a broad spectrum $\lambda = 400$–1600 nm, and a wide range of angles of incidence, $\theta = 0°$–$60°$ by the graded-index nanostructured AR coating shown in Fig. 10.40.

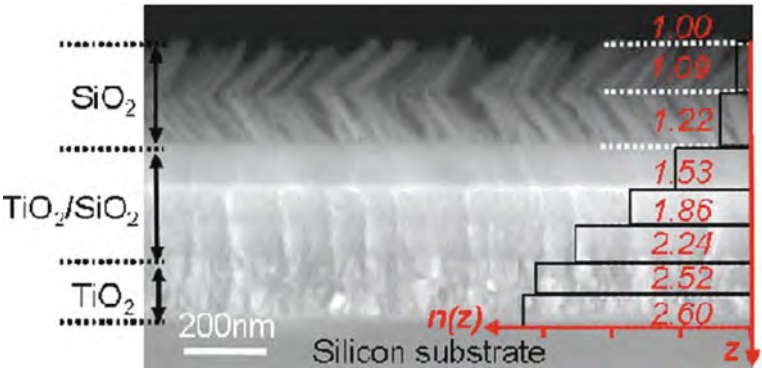

Fig. 10.40 Scanning electron micrograph of seven-layered, graded-index antireflection coating. (Reprinted with permission from [10.104]. © 2008 Optical Society of America)

10.9 Conversion of Mechanical Energy into Electricity

In addition to scavenging solar or thermal energy from the environment, mechanical energy may be converted into electricity owing to a coupled piezoelectric–semiconductor process (see [10.105]). By the vibration of piezoelectric zinc oxide nanowires grown radially around Kevlar 129 textile fibers (see Fig. 10.41), mechanical energy is transformed into electrical power.

Two fibers, one with ZnO nanowires and one with gold-coated ZnO nanowires (Fig. 10.41a, c) are firmly entangled (Fig. 10.41b) so that some of the gold-coated nanowires penetrate slightly into the spaces between the uncoated nanowires. When there is a relative sliding between the two fibers, the bending of the uncoated ZnO nanowires (Fig. 10.41e) produces a piezoelectric potential across their width and the Au-coated nanowires act as electrode for collecting and transporting the charges.

At a pulling and releasing frequency of 1.3 Hz of the fiber nanogenerator, a ~5 pA positive current is detected which can be increased to ~4 nA by reducing the inner resistance of the nanogenerator. Using ZnO nanowires grown on fibers, flexible, foldable, wearable, and robust power sources can be fabricated in any shape with an expected output density of 20–80 mW per square meter of fabric. The nanogenerator operates at low frequency, in the range of footsteps or heartbeats, which expands the application range of nanogenerators [10.105].

10.10 Hydrogen Storage and Fuel Cells

For the establishment of a clean and sustainable energy system, hydrogen-based technologies are considered to offer potential solutions [10.106]. Whereas, in the long term, the challenge is large-scale hydrogen production from renewable energy sources, the pressing issue is how to store hydrogen efficiently onboard of

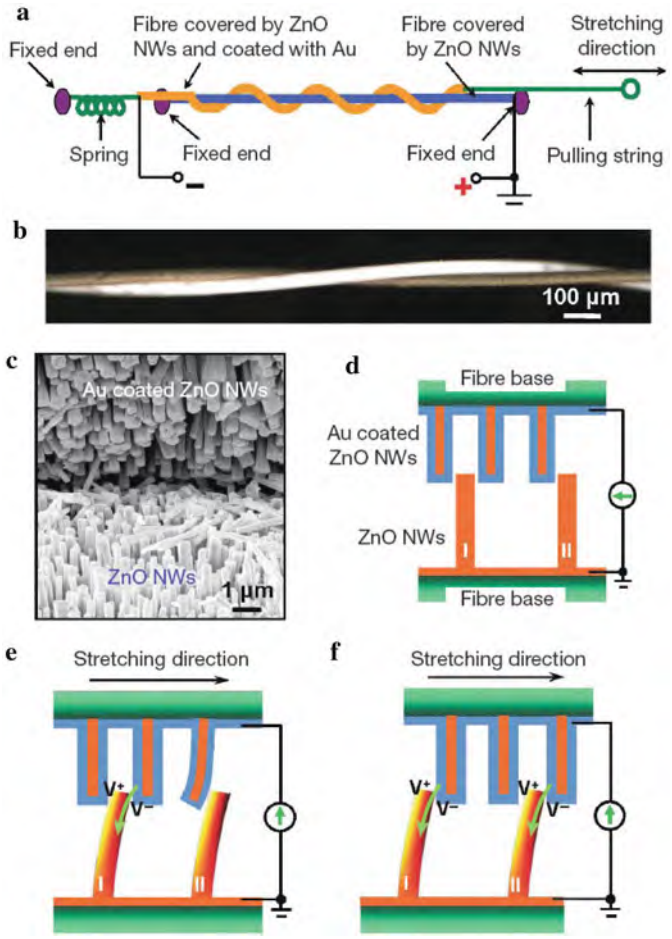

Fig. 10.41 Design and electricity-generating mechanism of the fiber-based nanogenerator driven by a low-frequency, external pulling force. (**a**) Schematic experimental setup of the fiber-based nanogenerator. (**b**) An optical image of a pair of entangled fibers, one of which is coated with Au (*darker contrast*). (**c**) Scanning electron image at the "teeth-to teeth" interface of two fibers covered by nanowires (NWs), with the top one coated with Au which serve as the conductive "tips" that deflect/bend the bottom ZnO nanowires. (**d**) Schematic of the teeth-to-teeth contact between the two fibers covered by nanowires. (**e**) The piezoelectric potential created across nanowire I and II under the pulling of the top fiber by an external force. The side with the positive piezoelectric potential does not allow the flow of current owing to the existence of a reverse-bias Schottky barrier. Once the nanowire is pushed to bend far enough to reach the other Au-coated nanowire, electrons in the external circuit will be driven to flow through the uncoated nanowire due to the forward-biased Schottky barrier at the interface. (**f**) When the top fiber is further pulled, the Au-coated nanowires may scrub across the uncoated nanowires. Once the two types of nanowires are in final contact, at the last moment, the interface is forward biased Schottky, resulting in further output of electric current, as indicated by *arrows*. The output current is the sum of all the contributions from all the nanowires, while the output voltage is determined by one nanowire. (Reprinted with permission from [10.105]. © 2008 Nature Publishing Group)

hydrogen fuel-cell vehicles. Experimental results show that grain refining of storage materials, especially to the nanoscale, significantly improves the kinetics of hybriding and dehybriding of metals and alloys. The desorption energy of MgH_2, which is 74 kJ/mol H_2 for the bulk, decreases to 65.3 kJ/mol H_2 for nanowires with a 30– 50 nm diameter which is consistent with theoretical predictions (see [10.106]). TiF_3-catalyzed MgH_2 nanoparticles desorb 4.5 wt% hydrogen in 6 min at 573 K, and hydrogen uptake can take place even at room temperature. The activation energy for MgH_2 decomposition was found to decrease significantly owing to the addition of the nanosized catalyst. In $Mg/MmM_5/Mg$ multilayer films (see Fig. 10.42), where MmM_5 is a $LaNi_5$-based rare-earth alloy, the hydrogen sorption temperature of the Mg layer is dramatically decreased, presumably due to the elastic interaction between the nanostructured Mg and MmM_5 layers (see [10.106]).

Polymer electrolyte membrane (PEM) fuel cells and hydrogen are promising candidates as power sources for cars with low-level emission of greenhouse gases as they function in the appropriate operating temperature range (80–120°C). To date, the best performing PEMs in H_2 fuel cells have been composed of Nafion, a perfluoro-sulphonated copolymer developed by DuPont in the 1960s (see [10.107]).

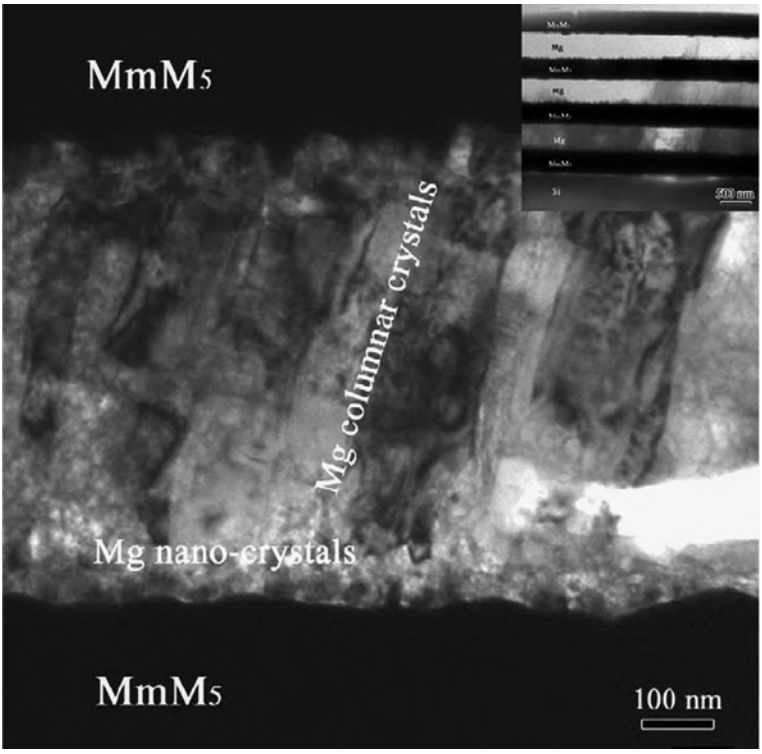

Fig. 10.42 Transmission electron micrograph of cross section of $MmM_5/Mg/MmM_5$ multilayer film. MmM_5 is a $LaNi_5$-based rare-earth alloy; the *inset* is a scanning electron micrograph. (Reprinted with permission from [10.106]. © 2008 Elsevier)

For explaining the electrochemical reactions during fuel–cell operation, a model of a tubular structure of Nafion, based on x-ray scattering data, has been suggested [10.108]. This structure comprises an array of oriented ionic nanochannels embedded within a locally aligned polymer matrix. The confined ions can thus diffuse easily in the tubular nanostructure. The specific development of a fabrication process that can create a macroscopic orientation of the proton channels could make Nafion the ideal PEM material [10.107].

10.11 Lithium Ion Batteries and Supercapacitors

Crucial environmental issues, which require the production and storage of renewable energy, together with the rapid advance and eagerness from the automotive industry toward the commercialization of hybrid electric vehicles and plug-in electric vehicles, have combined to make the development of improved rechargeable lithium batteries a worldwide imperative (see [10.109]). Whereas the Li-ion battery has conquered the portable market with an annual volume of $5 billion [10.110], its implementation into electric transportation is constantly postponed due to performance, cost, and more importantly, safety issues [10.109]. To address these issues, positive electrode materials are needed that are naturally abundant and react with Li at voltages within the thermodynamic stability range of non-aqueous Li-based electrolytes [10.109]. Some recent approaches for nanostructured Li battery electrodes will be discussed in the following.

10.11.1 Carbon Nanotube Cathodes

A combination of carbon nanotubes and nanoporous cellulose is suggested [10.111] for the fabrication of paper-thin and flexible batteries (Fig. 10.43). Vertical carbon nanotubes are grown on a silicon substrate cathode and impregnated with cellulose to form a nanocomposite paper, which is a few tens of micrometers thick, can be rolled up, twisted and bent to any curvature, and then returned to its original shape. This battery can light up a tiny light-emitting diode over several tens of charge/discharge cycles [10.111].

10.11.2 Tin-Based Anodes

Sony Comp. showed that amorphous nanostructured tin anodes (NP-FP71 camcorder battery) can be readily recharged (Fig. 10.44) and have a 30% higher volumetric energy density than carbon anodes [10.114]. Mesoporous carbon–tin nanocomposites have been synthesized as anode material for Li-ion batteries (Fig. 10.44b). The mesoporous structure of the carbon can effectively buffer the volume changes during the Li–Sn alloying and de-alloying cycles. The specific

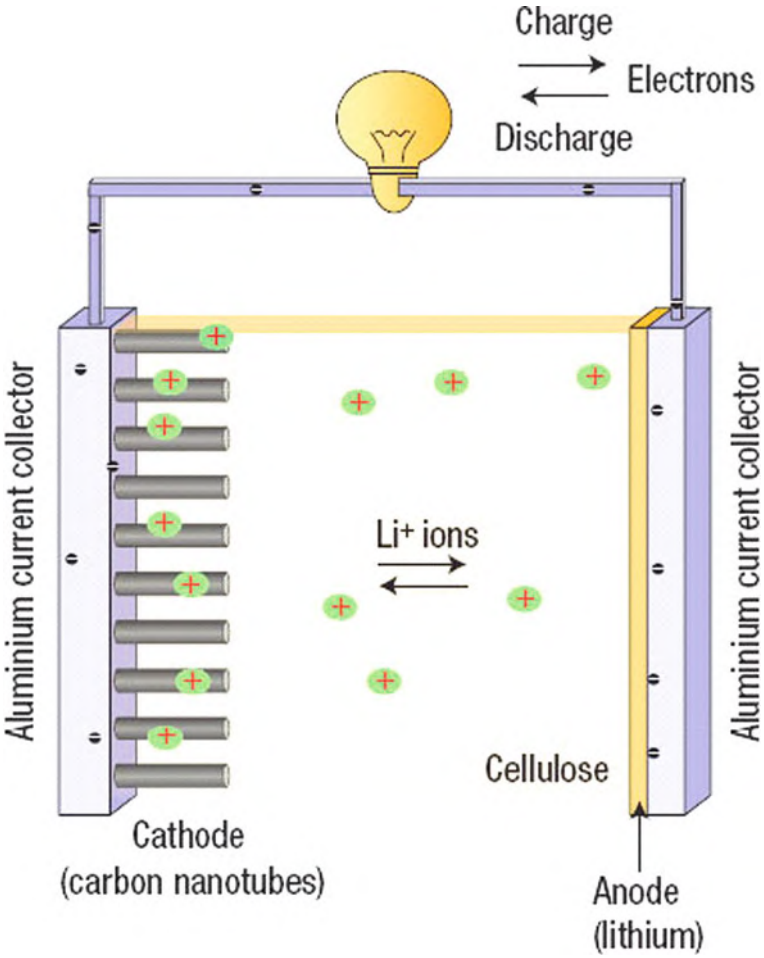

Fig. 10.43 A lithium-ion battery with a carbon nanotube cathode grown on a silicon substrate and cellulose infiltrated with the electrolyte. Electricity is produced when lithium on the anode is oxidized to form lithium ions, which are inserted into the nanotube cathode. Charging occurs when the lithium ions move in the opposite direction and are deposited as lithium metal on the anode. (Reprinted with permission from [10.112]. © 2007 Nature Publishing Group)

capacity of Sn in the composite electrode is calculated to be 0.96 Ahg^{-1}, which is 96.9% of the theoretical capacity (0.99 Ahg^{-1}) [10.115].

10.11.3 $LiFePO_4$ Cathodes

Electrodes made of $LiFePO_4$ nanoparticles (40 nm) [10.116, 10.109] formed by a low-temperature precipitation process (Fig. 10.45) exhibit sloping voltage charge/discharge curves, characteristic of a single-phase behavior. The presence

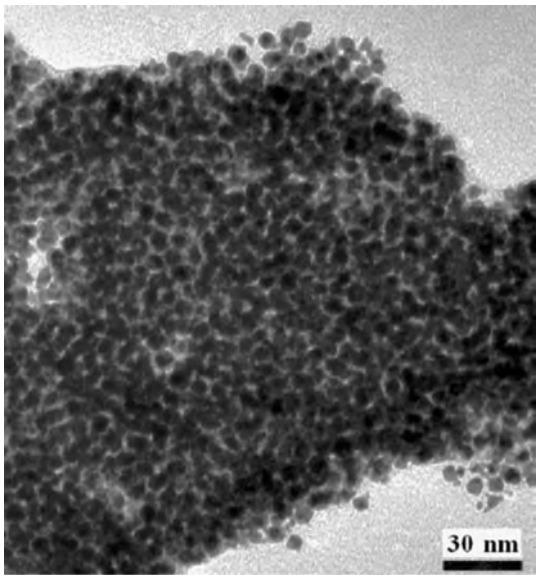

Fig. 10.44 Transmission electron micrograph (TEM) of a nanostructured tin–cobalt anode showing nanoparticles of ∼6 nm diameter embedded in a carbon matrix. (Reprinted with permission from [10.113]. © 2000 Elsevier)

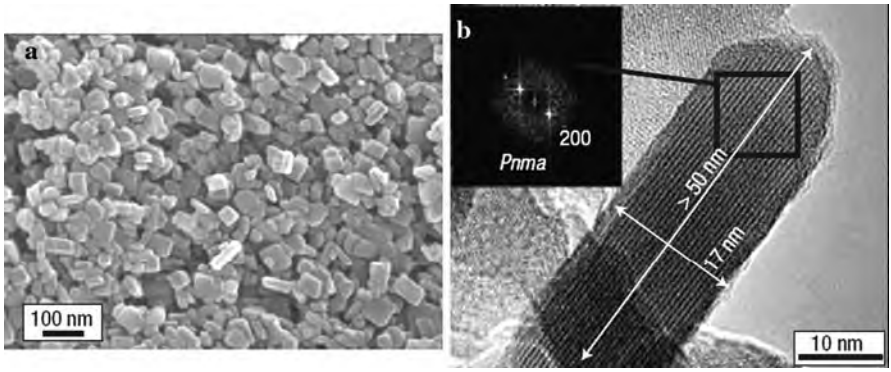

Fig. 10.45 Characterization of a 40 nm nanosized $LiFePO_4$ sample. (**a**) Scanning electron micrograph of the $LiFePO_4$ nanocrystallites. (**b**) High-resolution transmission electron micrograph of a crystallite combined with the Fourier transform of one box showing the orientation of the crystallite. (Reprinted with permission from referecne [10.109]. © 2008 Nature Publishing Group)

of defects and cation vacancies, as deduced by chemical/physical analytical techniques, is crucial for the properties [10.109]. Ultrahigh discharge rates with a rate capability equivalent to full battery discharge in 10–20 s can be achieved [10.117] by preparing a glassy lithium phosphate coating on the surface of nanoscale $LiFePO_4$ (see Fig. 10.46). These discharge rates are comparable to those of supercapacitors (see below), which, however, trade high power for low energy density.

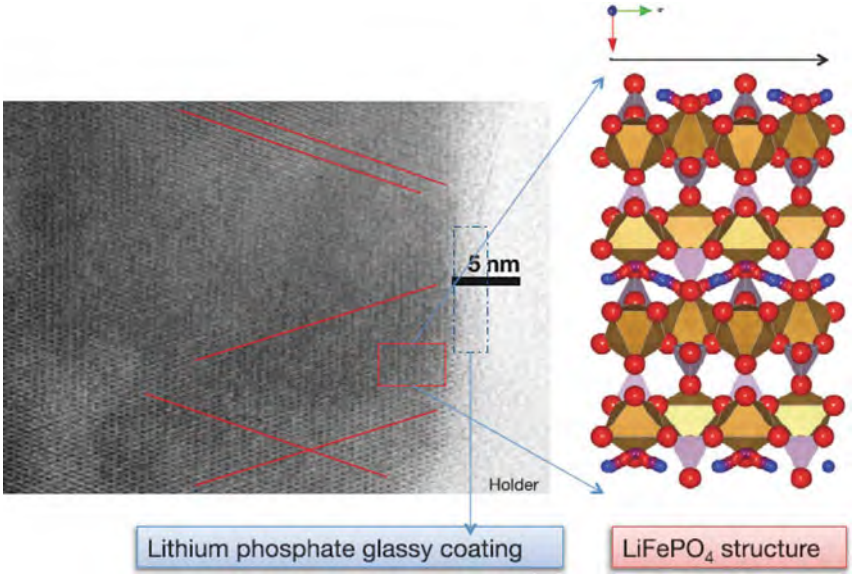

Fig. 10.46 Transmission electron microscopy (TEM) of a $LiFePO_4$ nanocrystallite coated with glassy lithium phosphate [10.117, 10.118]. (Reprinted with permission from [10.118]. © 2009 Elsevier)

10.11.4 Supercapacitors

It is thought that the energy and power for electronic devices cannot only be supplied by batteries but also by supercapacitors. In such a supercapacitor, carbon nanotube networks can comprise both the electrodes and the charge collectors [10.119] and are spray coated onto a plastic substrate from solution. A gel electrolyte is used, as it enables all components of the supercapacitor to be realized using printable materials. The energy and power densities of this device were measured at 6 Wh/kg and 23 kW/kg, respectively, which are comparable to values of commercially available devices, despite the use of printable materials.

10.12 Environmental Nanotechnology

In 1989, the Exxon Valdez ran aground in Alaska, releasing 11 million US gallons of crude oil and killing approximately 250,000 seabirds, seaotters, and eagles. This incident emphasized the need for materials that can effectively separate oil and water for cleaning up oil spills. Certain properties of nanomaterials – such as high surface-to-volume ratios and our ability to make surfaces that are either hydrophilic or hydrophobic – may provide solutions to this problem [10.120, 10.121].

Potassium manganese oxide nanowires each about 20 nm in diameter assemble into bundles that can be hundreds of micrometers long (Fig. 10.47a), resulting in

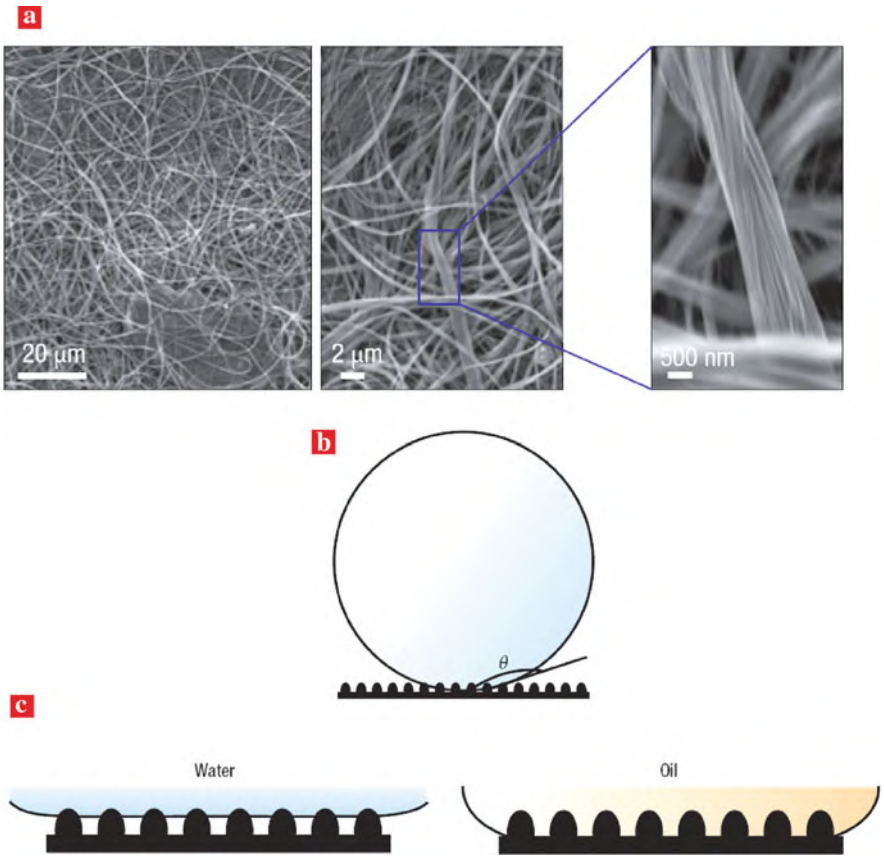

Fig. 10.47 The properties of nanomaterials make them ideal candidates for use in oil/water separation [10.120]. (**a**) The mesh of potassium manganese oxide nanowires provides a porous structure with high surface-to-volume ratio and is shown with increasing magnification from *left* to *right* [10.120]. (**b**) The contact angle, θ, quantifies the wetting behavior of a material. (**c**) The membrane surface displays heterogeneous wetting when in contact with water (*left*) but homogeneous wetting for oil (*right*) [10.121]. (Reprinted with permission from [10.121]. © 2008 Nature Publishing Group)

a membrane with a thickness of about 50 µm and an average pore size of about 10 nm, that causes a liquid to be sucked into the membrane by capillary action. Materials with contact angles θ (Fig. 10.47b) smaller than 90° are more hydrophilic, whereas those with contact angles above 90° are more hydrophobic (see Sect. 7.7). Superhydrophobic surfaces (see [10.121]) cause water droplets to freely roll off – like the self-cleaning properties of the lotus leaf (see Sect. 11.9). This is exactly what happens for water with the potassium manganese oxide nanowire membranes modified with a hydrophobic coating [10.120] (Fig. 10.47c, left). However, if a liquid that is less polar than water, such as oil, comes into contact with the surface, it will be drawn into the interstitial space, where it rapidly replaces the air (Fig. 10.47c,

right). This surface that repels water while allowing oil to selectively spread gives rise to an extraordinary selectivity and capacity for the separation of oil from water – the reported uptake capacities are as high as 20 times the initial weight of the nanomaterial. The membrane material exhibits a number of advantages, including its high-temperature stability and the ease with which it can be recycled and reused, confirming the potential of nanomaterials for protecting the environment [10.121].

10.13 Summary

Chemistry plays an important role in the bottom-up synthesis of nanostructures. By means of supramolecular chemistry or the formation of inorganic hollow clusters, nanometer-sized species can be fabricated conveniently. Chemical processes can be investigated on the nanoscale by using scanning probe microscopy-based techniques for manipulation and delivery of single molecules in a precisely controlled manner. In heterogeneous catalysis, where the reacting molecules are absorbed on catalytically active solid surfaces, experimental studies down to the atomic level are most successful in combination with ab initio calculations. Evidently, nanoscience may have an impact on future energy problems, in particular in the field of renewable energy such as solar energy (photovoltaics and thermal conversion), conversion of mechanical energy into electricity, fuel cells or energy storage by lithium ion batteries, supercapacitors, or hydrogen storage devices. For environmental protection strategies, nanostructures may be an optimum choice.

References

10.1 G.A. Ozin et al. (eds.) *Nanochemistry*, 2nd ed. (RSC Publ., Cambridge, 2008)
10.2 J.-M. Lehn, *Supramolecular Chemistry* (VCH, Weinheim, 1995)
10.3 J.-M. Lehn, Nova Acta Leopoldina **76**, 313 (1997)
10.4 J.W. Steed, J.L. Atwood, *Supramolecular Chemistry: An Introduction* (Wiley, New York, 2000)
10.5 K. Ariga, T. Kunitake, *Supramolecular Chemistry-Fundamentals and Applications* (Springer, Berlin, 2006)
10.6 J.F. Stoddart, Nat. Chem. **1**, 14 (2009)
10.7 A. Müller et al., Nature **426**, 59 (2003)
10.8 G. Matthews, Nature **406**, 835 (2000)
10.9 F. Mal et al., Science **324**, 1697 (2009)
10.10 C. Borchard-Tuch, Chem. Unserer Zeit **39**, 137 (2005)
10.11 J.V. Barth et al., Appl. Phys. **A**. **76**, 645 (2003)
10.12 M.R. Ghadiri et al., Nature **366**, 324 (1993)
10.13 E. Sackmann, Macromol. Chem. Phys. **195**, 7 (1994)
10.14 M.R. Ghadiri et al., Nature **369**, 301 (1994)
10.15 P. Kazmaier, N. Chopra, MRS Bull. April 2000, p. 30
10.16 S. Fernandez-Lopez et al., Nature **412**, 452 (2001)
10.17 A.W. Bosman et al., Mater. Today, April 2004, p. 34
10.18 H. Staudinger, *Die Hochmolekularen Organischen Verbindungen* (Springer, Berlin, 1932)
10.19 T.F. A. de Greef, E.W. Meijer, Nature **453**, 171 (2008)

10.20 H.B. Goodbrand et al., Patent number US2003/0105185A1, 2003; T.W. Smith et al., Patent number US2003/0079644A1, 2003
10.21 S.P. Pappas et al., Patent number WO 02053626A1 (2002)
10.22 R.W. Wagner, *Das Rheingold*, Schott, Mainz (1873)
10.23 S.P. Watton et al., Angew. Chem. Int. Edn. **36**, 2774 (1997)
10.24 A.L. Dearden et al., Angew. Chem. Int. Ed. **40**, 152 (2001)
10.25 E.K. Brechin et al., Chem. Commun. 1860 (2002)
10.26 D.M. Low et al., Chem. Eur. J. **12**, 1385 (2006)
10.27 G.S. Desirajou, Nature **412**, 397 (2000)
10.28 T.B. Liu et al., Nature **426**, 59 (2003)
10.29 F. Meier et al., Phys. Rev. **B 64**, 224411 (2001); Phys. Rev. **B 68**, 134417 (2003)
10.30 F. Cacialli et al., Mater. Today, April 2004, p. 24
10.31 A.M. van de Craats et al., Adv. Mater. **15**, 495 (2003)
10.32 R.I. Gearba et al., Adv. Mater. **15**, 614 (2003)
10.33 J.J. van Gorp et al., J. Am. Chem. Soc. **124**, 14759 (2002)
10.34 H. Engelkamp et al., Science **284**, 785 (1999)
10.35 B. Alberts et al., *The Molecular Biology of the Cell* (Garland Science, New York, (2002)
10.36 I. Yildiz et al., Proc. Natl. Acad. Sci. USA **103**, 11457 (2006)
10.37 N.C. Seeman, J. Theor. Biol. **99**, 237 (1982)
10.38 J. Chen, N.C. Seeman, Nature **350**, 631 (1991)
10.39 E. Winfree et al., Nature **394**, 539 (1998)
10.40 Y. Zhang, N.C. Seeman, J. Am. Chem. Soc. **114**, 2656 (1992); ibid. **116**, 1661 (1994)
10.41 Y. He et al., Nature **452**, 198 (2008)
10.42 A. Müller et al., Angew. Chem. **114**, 1210 (2002)
10.43 F. Karau, W. Schnick, Angew. Chem. Int. Edn. **45**, 4505 (2006)
10.44 P. Anzenbacher, M.A. Palacios, Nat. Chem. **11**, 80 (2009)
10.45 J.A. A.W. Elemans, Mater. Today **12**, (7–8), 34 (2009)
10.46 D.A. Britz et al., Chem. Commun. 37 (2005)
10.47 P. Kondratyuk, J.T. Yates, J. Am. Chem. Soc. **129**, 8736 (2007)
10.48 H. Shiozawa et al., Phys. Rev. Lett. **102**, 046804 (2009)
10.49 A.M. Dokter et al., Proc. Natl. Acad. Sci. USA **103**, 15355 (2006)
10.50 M.F. Reedijk et al., Phys. Rev. Lett. **90**, 066103 (2003)
10.51 S. Balasubramanian et al., Phys. Rev. Lett. **89**, 115505 (2002)
10.52 A.-S. Duwez et al., Nat. Nanotech. **1**, 122 (2006)
10.53 M. Mavrikakis, Nat. Mater. **5**, 847 (2006)
10.54 G. Ertl et al., Eds. *Handbook of Heterogeneous Catalysis* (Wiley-VCH, Weinheim, ed. 2, 2008)
10.55 U. Heiz, U. Landman (eds.) *Nanocatalysis (Nanoscience and Technology)* (Springer, Berlin, 2007)
10.56 F. Besenbacher et al., Nano Today **2**, August 2007, p. 30
10.57 J. Greeley et al., Nat. Mater. **5**, 909 (2006)
10.58 B. Hvolbaek et al., Nano Today, August 2007, p. 14
10.59 B. Yoon et al., Chem. Phys. Chem. **8**, 157 (2007)
10.60 G. Ertl, J. Vac. Sci. Technol. **A1**, 1247 (1983)
10.61 G. Ertl, H.-J. Freund, Phys. Today, January 1999, p. 32
10.62 B.C. Gates et al., MRS Bull. **33**, 429 (2008)
10.63 J. Frenken, B. Hendriksen, MRS Bull. **32**, 1015 (2007)
10.64 S. Ferrer et al., MRS Bul. **32**, 1010 (2007)
10.65 J. Evans et al., MRS Bul. **32**, 1038 (2007)
10.66 H. Bluhm et al., MRS Bull. **32**, 1022 (2007)
10.67 S. Giorgio et al., Ultramicroscop. **106**, 503 (2006)
10.68 M. Haruta et al., Chem. Lett. **16**, 405 (1987)
10.69 A.A. Herzing et al., Science **321**, 1331 (2008)

10.70 H. Falsig et al., Angew. Chem. Int. Ed. **47**, 4835 (2008)
10.71 D. Matthey et al., Science **315**, 1692 (2007)
10.72 S. Vaida et al., Nat. Mater. **8**, 213 (2009)
10.73 J.Y. Chen et al., Nano Today **4**, 81 (2009)
10.74 Z.M. Peng, H. Yang, Nano Today **4**, 143 (2009)
10.75 K. Yamamoto et al., Nat. Chem. **1**, 397 (2009)
10.76 H.M. Chen et al., J. Phys. Chem. C **112**, 7522 (2008)
10.77 N. Tian et al., Science **316**, 732 (2007)
10.78 S.H. Joo et al., Nat. Mater. **8**, 126 (2009)
10.79 M. Schrinner et al., Science **323**, 617 (2009)
10.80 I. Lee et al., Nat. Mater. **8**, 132 (2009)
10.81 G. Rupprechter, C. Weilach, Nano Today **2**, August 2007, p. 20
10.82 E. de Smit et al., Nature **456**, 222 (2008)
10.83 P. Jena et al., MRS Bull. **33**, Sept. 2008, p. 824
10.84 R. Jones, Nat. Nanotech. **4**, 75 (2009)
10.85 MRS Bull. **33**, Dec. 2008, p. 1141
10.86 V.S. Arunachalam, E.L. Fleischer, MRS Bull. **33**, April 2008, p. 264
10.87 N.S. Lewis, D.G. Nocera, Proc. Natl. Acad. Sci. USA **103**, 15729 (2006)
10.88 T.M. Tritt et al., MRS Bull. **33**, April 2008, p. 366
10.89 B. O'Regan, M. Grätzel, Nature **353**, 737 (1991)
10.90 D.J. Milliron et al., MRS Bull. **30**, January 2005, p. 41
10.91 T. López-Luke et al., J. Phys. Chem. C **112**, 1282 (2008)
10.92 A.C. Mayer et al., Mater. Today **10**, Nov. 2007, p. 28
10.93 C. Goh et al., Nano Lett. **5**, 1545 (2005)
10.94 M.D. McGehee, MRS Bull. **34**, 95 (2009)
10.95 D. Ginley et al., MRS Bull. **33**, April 2008, p. 355
10.96 B.Z. Tian et al., Nature **449**, 885 (2007)
10.97 T.J. Seebeck, Abh. K. Akad. Wiss. **265** (Berlin, 1823)
10.98 A.M. Rao et al., MRS Bull. **31**, Mar, 218 (2006)
10.99 M.S. Dresselhaus et al., Adv. Mater. **19**, 1043 (2007)
10.100 L. Yu-Ming et al., Appl. Phys. Lett. **81**, 2403 (2002)
10.101 J. Sommerlatte et al., Phys. J. **6**(5), 35 (2007)
10.102 B. Poudel et al., Science **320**, 634 (2008)
10.103 T. Markussen et al., Phys. Rev. Lett. **103**, 055502 (2009)
10.104 M.-L. Kuo et al., Optics Lett. **33**, 2527 (2008)
10.105 Y. Qin et al., Nature **451**, 809 (2008)
10.106 P. Chen, M. Zhu, Mater. Today **11**, December 2008, p. 36
10.107 O. Diat, G. Gebel, Nat. Mater. **7**, 13 (2008)
10.108 K. Schmidt-Rohr, Q. Chen, Nat. Mater. **7**, 75 (2008)
10.109 P. Gibot et al., Nat. Mater. **7**, 741 (2008)
10.110 M.M. Doeff et al., MRS Bull. **32**, October 2007, p. 755
10.111 V.L. Pushparaj et al., Proc. Natl. Acad. Sci. USA **104**, 13574 (2007)
10.112 B. Scrosati, Nat. Nanotech. **2**, 598 (2007)
10.113 R. Kötz, M. Carlen, Electrochim. Act. **45**, 2483 (2000)
10.114 M.S. Wittingham, MRS Bul. **33**, April 2008, p. 411
10.115 Z.W. Zhao et al., J. Mater. Sci. Techn. **24**, 657 (2008)
10.116 S.-Y. Chung et al., Nat. Mater. **1**, 123 (2002)
10.117 B. Kang, G. Ceder, Nature **458**, 190 (2009)
10.118 J. Agbenyega, Mater. Today **12**, May 2009, p. 10
10.119 M. Kaempgen et al., Nano Lett. **9**, 1872 (2009)
10.120 J. Yuan et al., Nat. Nanotech. **3**, 322 (2008)
10.121 J. Lahann, Nat. Nanotech. **3**, 320 (2008)

Chapter 11
Biology on the Nanoscale

Nanoscience plays an important role in the study of biological phenomena because the size of inorganic nanoparticles as probes and the spatial resolution of nanotools match the sizes of macromolecular components employed in living systems. Proteins, nucleic acid fragments, and their supramolecular complexes involved in the DNA replication and transcription, and the ribosome, have typical dimensions in the range of 2–200 nm.

An other interesting aspect is that the sizes of the physical world, that can be explored and controlled nowadays by nanotechnology will become very close to the sizes where the physicochemical bases and limits of living processes lie [11.1]. The orderliness necessary for the set of processes which characterize the living state can only be maintained against fluctuations in a system of a certain degree of complexity and, therefore, of a minimum size. However, what is the limiting value of this complexity? It has been shown [11.2] that, for spatio-temporal self-organization, the sizes as well as the dimensionality of the system are essential parameters. One model of the first living system to arise on Earth [11.3] yields a minimum value of about 6×10^6 atoms making up such a living system. This corresponds to a size of about 40–50 nm which is within the range of the size of a virus (30–500 nm) or of small biological structures (see Fig. 11.1).

In addition, nanoparticles of inorganic materials are essential building blocks in biomineralization, a fundamental biological process in which nature chemically generates morphology by means of genetic instructions.

The present section will start with a brief overview of the structure of the cell and a subsequent subsection on nanoparticles for bioanalysis. Then recent developments of biological nanomechanics will be reported. After a review of the structure of molecular motors and of membrane channels, some features of biomimetics and of the structure of bone and teeth will be outlined. Finally nanostructures in biophotonics, the lotus effect, in food and in cosmetics will be described.

H.-E. Schaefer, *Nanoscience*, DOI 10.1007/978-3-642-10559-3_11,

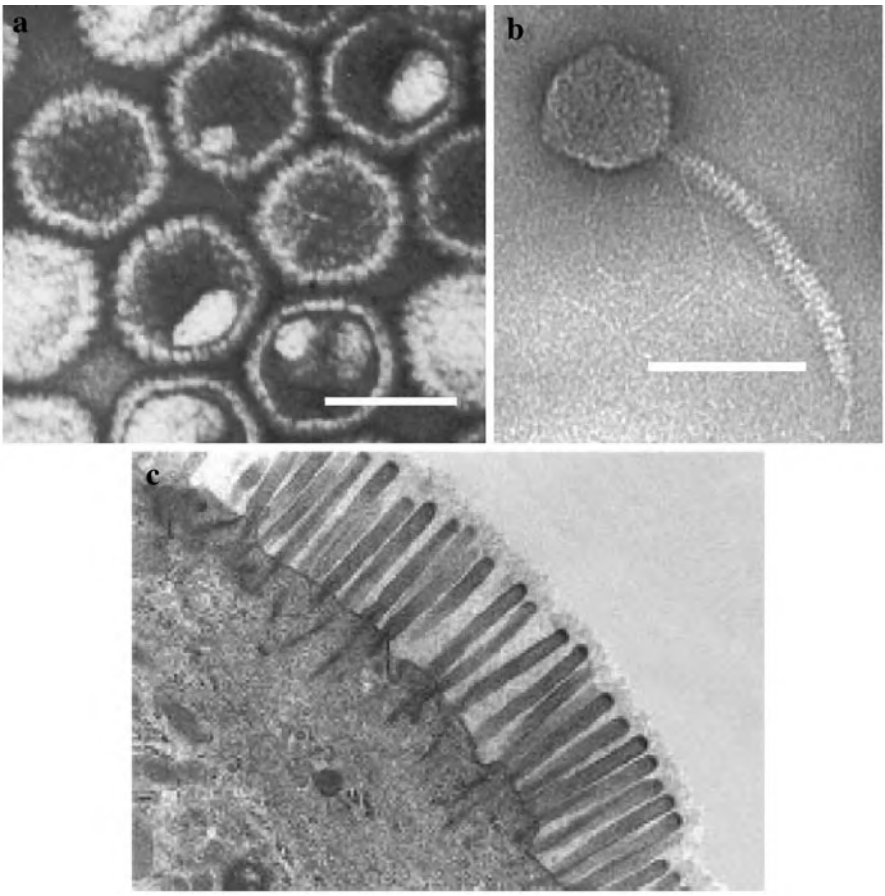

Fig. 11.1 Nanosized biological objects. (**a**) Human herpes virus 3; scale bar 100 nm. (**b**) Enterobacteria phage; scale bar, 50 nm. (**c**) Intestinal villi (fine, hair-like epidermal outgrows), diameter ∼100 nm [11.4]. (Reprinted with permission from [11.4] (**a**) (**b**) and Dennis Kunkel Microscopy (**c**). © 2009 Nature Publishing Group (**a**) (**b**) and © 2009 Dennis Kunkel Microscopy (**c**))

11.1 The Cell – Nanosized Components, Mechanics, and Diseases

Understanding of cells – that is understanding of life – is one of the great unanswered questions of science. The cell is the quantum of biology and the smallest and most fundamental unit. The cell contains a system of molecules and nanoscale machines, i.e., functional molecular aggregates of great complexity. Understanding the molecular nanostructures will help us to move closer to understanding human life and health, and thus toward "nanomedicine" [11.5].

11.1.1 Cell Structure

Most of the biological cells are 1–100 μm in size and they comprise many nanosized constituents (Fig. 11.2). Structural studies with nanoscale resolution can be performed by cryoelectron microscopy [11.7] (see Sect. 2.6), by electron microscopy [11.13] of whole cells in liquid [11.8], or by far-field stimulated emission depletion (STED) optical microscopy [11.9, 11.14] (see Sect. 2.4). The interior of the cell (Fig. 11.2) includes the cytoplasm and the nucleus which contains the chromosomes with the DNA strands carrying the genes and functions in the transmission of hereditary information. The cytoplasm contains the cytosol which is the "fluid" in the cell, the endoplasmic reticulum, microtubules, actin filaments, intermediate filaments, mitochondria, and the Golgi apparatus. The actin filaments (ca. 8 nm in diameter; see Fig. 11.3a) and the microtubules, in the shape of hollow tubes with a diameter of ca. 25 nm, form the cytoskeleton. The ribosomes found in the cytoplasm with a diameter of ca. 25 nm (see Fig. 11.3a, b) are minute round particles composed of RNA and protein which are active in the synthesis of proteins. The ribonucleoprotein of the ribosome represents the last step of the gene expression

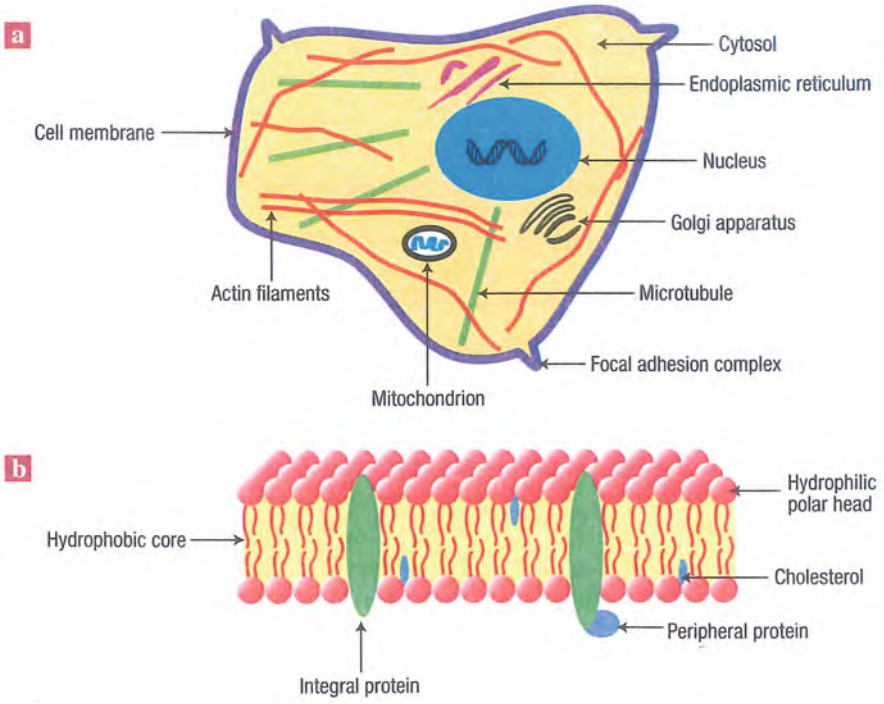

Fig. 11.2 (**a**) Schematic diagram of a typical eukaryotic cell which contains many nanoscale elements (see text). (**b**) The phospholipid bilayer membrane which covers the cell. (Reprinted with permission from [11.6]. © 2003 Nature Publishing Group)

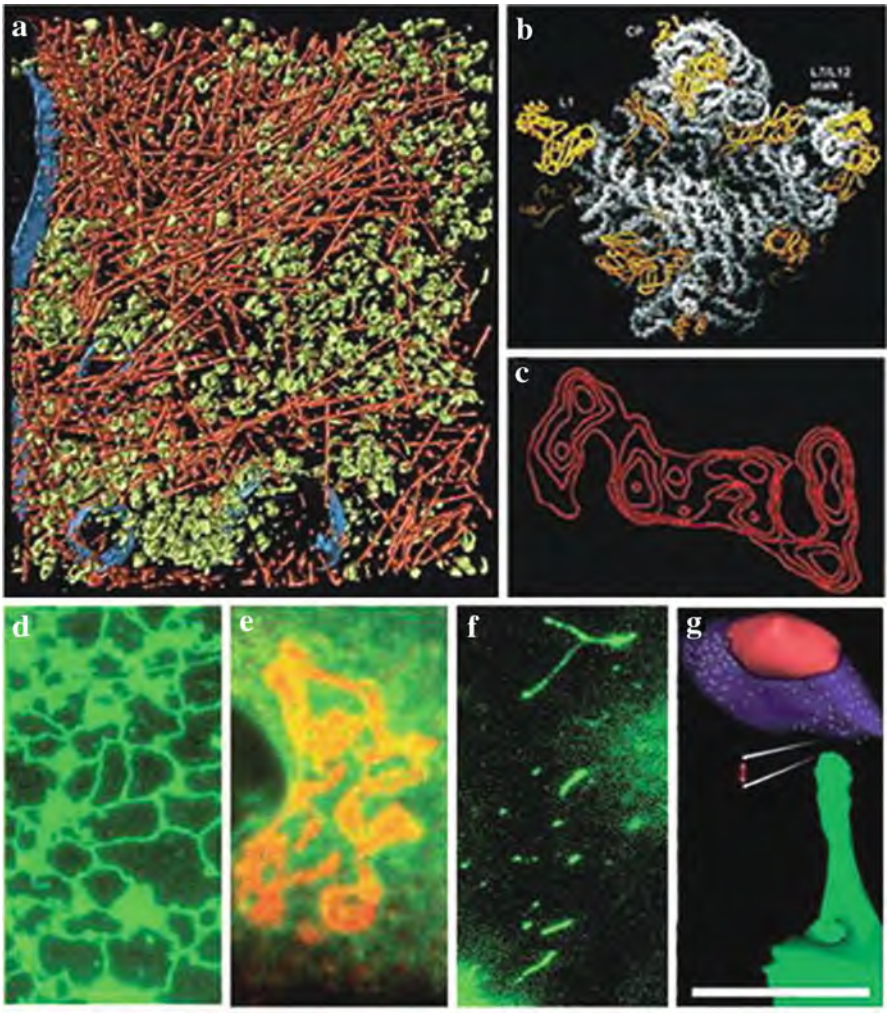

Fig. 11.3 (**a**) Cryoelectron tomography of the slime mold cell *Dictyostelium discoideum* (image 815 nm by 870 nm by 97 nm) with subjectively added colors to mark actins filaments (*reddish*), ribosomes (*green*), and membranes (*blue*) [11.7]. (**b**) The *Haloarcula marismortui* large ribosomal subunit [11.10]; RNA is shown in *gray*, the protein backbones are given in *gold*. The particle is ca. 25 nm across. The macromolecular structures, such as the ribosome, that populate the cell are functional nanostructures – "nanomachines" – with a much higher sophistication than that of artificial nanostructures. (**c**) Density profile of a 2D projection of a 26 S proteasome in the cell (**a**) derived from cryoelectrontomography. This molecular machine with a mass of 2.5 MDa has a characteristic elongation of 45 nm [11.7]. (**d–f**) The shapes of different biological membranes can be visualized by labeling them with fluorescently tagged proteins [11.12]: (**d**) endoplasmic reticulum (*green*; 30–100 nm), (**e**) Golgi apparatus (*red/yellow*; 30–100 nm), and (**f**) vesicular membrane carriers (*green*; spheres with a diameter of 40–100 nm) for transport tasks from Golgi complex to the plasma membrane. (**g**) Electron tomography of a neuronal filopodia (*green*) whose tip is in close contact with an axonal bouton (*blue*) in the adult mouse hippocampus [11.12]. (Reprinted with permission from [11.7] (**a**) (**c**), [11.10] (**b**), and [11.12] (**d–g**). © 2002 AAAS (**a**) (**c**), © 2000 AAAS (**b**), and © 2007 Nature Publishing Group (**d–g**))

pathway where the genomic information encoded in messenger RNAs is translated into protein. The large ribosomal subunit (Fig. 11.3b) includes the activity that catalyzes peptide bond formation – peptidyl transferase – and the binding site for the G-protein factors that assist in the initiation, elongation, and termination phases of protein synthesis [11.10].

A striking example of a large protein complex residing in the cytosol is the proteasome [11.11] (Fig. 11.3c) with proteolytic activities, responsible for degrading proteins that have been marked for destruction by the attachment of a small ubiquitin protein molecule. A mitochondrion (see Fig. 11.2a) is a membrane – bound organelle, about the size of a bacterium (500 nm in diameter and 1000 nm in length) that carries out oxidative phosphorylation and produces most of the ATP in eukaryotic cells. The endoplasmic reticulum is a membrane network (Figs. 11.2a, 11.3d and 11.4) within the cytoplasm where lipids, membrane-bound proteins, and secretory proteins are synthesized. Individual structural elements of the endoplasmic reticulum of a cell can be imaged optically by the STED technique (see Sect. 2.4) with a lateral resolution of <50 nm inside the living cell [11.9, 11.14] (Fig. 11.4). From the endoplasmic reticulum proteins and lipids are transferred to the Golgi apparatus (Figs. 11.2a and 11.3e), a network of stacked membranous vesicles, where they are modified and sorted. Vesicular membrane carriers (Fig. 11.3f) can perform transport tasks from the Golgi apparatus to the plasma membrane. Other cellular nanostructures are the protrusions of nerve cells (Fig. 11.3g) to make junctions with adjacent cells.

The cell is enclosed by a phospholipid bilayer membrane (Fig. 11.2b), with hydrophilic heads and hydrophobic tails whose mechanical rigidity is altered by the presence of integral protein molecules and cholesterol. Transmembrane protein receptors, such as integrins, provide links between the extracelluar matrix (ECM) and the cell interior.

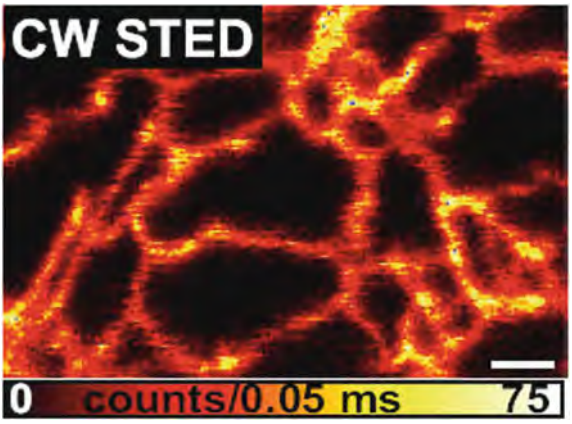

Fig. 11.4 Optical image of the endoplasmic reticulum, of a living mammalian cell making use of the stimulated emission depletion (STED) technique. Tubules as small as 60 nm can be seen (scale bar, 500 nm). (Reprinted with permission from [11.9]. © 2008 National Academy of Sciences USA)

11.1.2 Mechanics, Motion, and Deformation of Cells

Cells undergo mechanical deformation when subjected to external forces [11.4]. For the cell motion during cell migration contractile forces must be generated within the cell [11.15]. In addition, cells can signal stress, such as endothelial cells living in the interior walls of blood vessels, as they alter the expression of "stress-sensitive" genes in response to shear flow in the blood (see [11.6]). The deformability of a cell is determined largely by the cytoskeleton yielding an effective elastic modulus of 10^2–10^5 Pa, orders of magnitude smaller than that of metals or ceramics ($\sim 10^{11}$ Pa).

Experimental techniques for studying the mechanical behavior of cells are shown in Fig. 11.5. In addition to atomic force microscopy (AFM; see Sect. 2.2), magnetic twisting cytometry (MTC) is employed, where magnetic beads attached to a cell in a magnetic field can deform a cell locally. In the micropipette aspiration experiment, a cell is deformed by applying a suction through a micropipette on the cell surface. In the case of optical tweezers of a laser trap (Fig. 11.5) a force is created between a dielectric bead of high refractive index attached to a cell and a laser beam, pulling the bead toward the focal point of the trap.

Most living cells generate or sense forces. Skeletal, heart, and smooth muscle cells generate contractile forces on excitation, performing many essential functions of the body. Endothelial cells can recognize the magnitude, type, and duration of applied shear flow and respond accordingly (see [11.6]) in a healthy endothelium or in vascular diseases. Fibroplast cells "crawl" like an inchworm by pulling the cell body forward using contractile forces. These forces are generated by motor proteins, such as kinesin, myosin, or dynein, powered by the hydrolysis of adenosine triphosphate (ATP). It is not well understood how cells sense mechanical forces and deformation and how they convert such signals to biological response (see [11.6]).

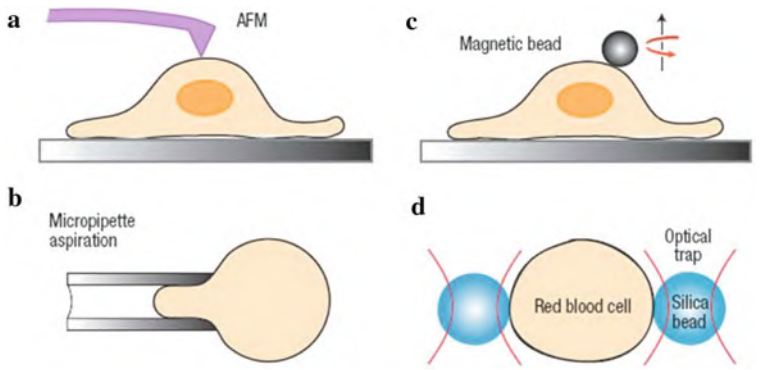

Fig. 11.5 Schematic representation of techniques for probing the mechanical properties of living cells. (**a**) Atomic force microscopy (AFM) and (**b**) magnetic twisting cytometry can probe cell components at a force resolution of 10^{-10} and 10^{-12} N, respectively, and a displacement resolution of less than 1 nm. (**c**) Micropipette aspiration (MA) and (**d**) optical trapping or optical tweezer stretching are techniques which can deform an entire cell at a force resolution of 10^{-10} and 10^{-11} N, respectively. (Reprinted with permission from [11.6]. © 2003 Nature Publishing Group)

Studies by modeling of the mechanical properties of a cell should exceed continuum-based models and include the cytoskeleton, the viscous cytoplasmic fluid, as well as the granularity and the heterogeneity of the cell.

The ability of cell membranes to adopt a great variety of shapes is one of the most striking and intriguing properties of cells. Computer simulations indicate that the forces necessary for this shaping arise from the concerted efforts of many proteins, integrated within the membrane, mediated by the 4.7–5.2 nm thick lipid bilayer that forms the membrane matrix and resists strong bending [11.12, 11.16]. In the cell there is a great variety of membrane shapes: plasma membranes are practically flat; the cylindrical membrane structures of the tubules 30–100 nm in diameter are strongly curved; the membrane structures that mediate endocytosis (the uptake into the cell from outside) and exocytosis (the export of material from the cell), and those that contribute to intracellular trafficking, form spheres of 40–100 nm diameter. In addition, saddle-like shapes are found at membrane necks and junctions as well as in the stacking-up of the membrane disks of the Golgi apparatus (see Fig. 11.3). Furthermore, these membranes undergo relentless shape transformations involving strong deformations and, in many cases, drastic rearrangements of membrane structures, leading to their fusion and fission.

The large-scale curving of a membrane requires the concerted effort of many membrane proteins forming domains. The physics of these long-range forces is a crucial open question. The reason for these forces is the interaction of individual membrane proteins which reduces the elastic energy and restricts the entropically favored thermal undulations of the membrane. Computer simulations showed [11.16] that the net interaction of the protein is attractive and that the attraction between proteins with sufficient intrinsic curvature is strong enough to cause them to cluster in domains giving rise to a driving force for membrane shaping in real biological conditions.

11.1.3 Cell Adhesion

When white blood cells fight viruses or bacteria or in the formation of metastases of cancerous cells, cell adhesion and cell mechanics play an important role [11.17–11.21]. In living cells, adhesion structures additionally have the ability to grow and strengthen under force. The adhesion is mediated by a selective bonding of ligands on one cell and receptors on an adjacent cell. The adhesion process is due to the formation of domains (ca. 1 μm in size) of ligand-receptor pairs.

A nanoscale modeling of cellular adhesion has been studied experimentally by the interaction of test vesicles containing arginine–glycine–asparagine (RGD) peptides as ligands with membranes containing integrin receptors as target cells [11.18, 11.19] (see Fig. 11.6a). Adhesion occurs by micrometer domains of agglomerated ligand-receptor pairs (see [11.18]). These domains are separated by non-adhering areas. This can be observed by reflection interference contrast (RIC) microscopy, yielding a vertical resolution of 5 nm and a lateral resolution of 50 nm [11.19]. When both ligands and receptors are mobile within their membranes, strengthening

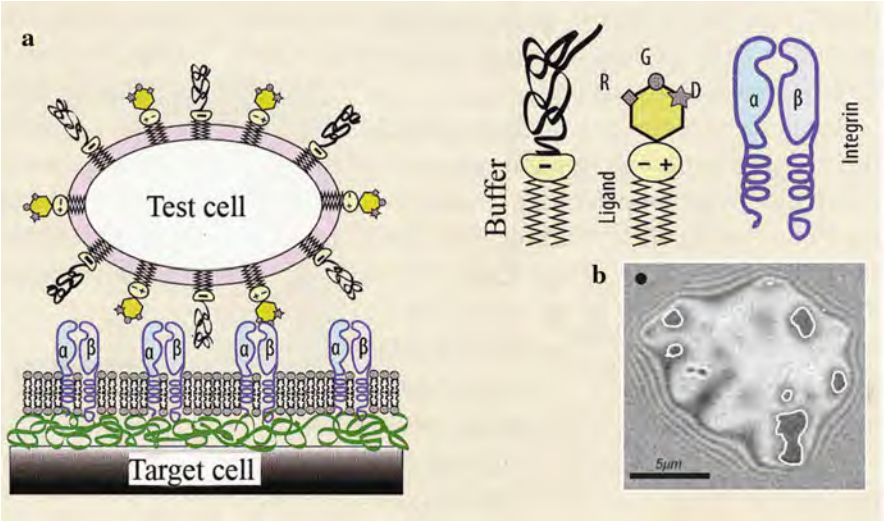

Fig. 11.6 (**a**) In a model of cell adhesion, vesicles containing arginine–glycine–asparagine (RGD) ligands are used as test cells whereas a membrane with integrin receptors on a substrate is employed as target cell [11.18]. (**b**) Adhesion domains (enclosed in white) as seen by optical reflection interference contrast (RIC) microscopy in a vesicle interacting with a membrane [11.19]. (Reprinted with permission from [11.18] (**a**) and [11.19] (**b**). © 2006 Wiley-VCH (**a**) and © 2008 National Academy of Sciences USA (**b**))

is aided by lateral movement of intact bonds as a transient response to force-induced membrane deformation [11.19].

A theoretical treatment has been given by calculating the total free energy of the vesicle-membrane system, including the elastic deformation energy, the binding energy of the ligand–receptor pair ensemble, and the positional entropy of mobile RGD ligands and integrin receptors [11.19]. The calculations show a strengthening of the adhesion domains under force as demonstrated in analogous experiments. In the model study, the application of force leads simultaneously to a decrease in the contact zone area and an increase in the adhesion energy density [11.19]. The identification of this phenomenon in living cells would be desirable.

11.1.4 Disease-Induced Alterations of the Mechanical Properties of Single Living Cells

This can be investigated by measuring the elastic properties at pN-level forces [11.22, 11.23] which could provide insight into the progression of diseases. The two examples of elastic measurements on human pancreatic cancer cells (Panc-1) and on human red blood cells (RBCs) infected with the malaria parasite *Plasmodium falciparum* will be briefly discussed.

Epithelial pancreatic cancer cells subjected to repeated tensile loading showed a three-fold decrease of the elastic modulus upon treatment with sphingosylphosphorylcholine (SPC), a bioactive lipid that promotes antiapoptotic (against controlled cellular death) effects in human blood components such as blood plasma and high-density lipoprotein (HDL) particles. The modulus decrease can be ascribed to a SPC-induced reorganization of the keratin network to perinuclear regions of the cell (see Fig. 11.7a). The modulus decrease and the increased deformability of cancer cells may increase the probability of cell migration to another site in the body, a critical step in cancer metastasis.

The malaria disease state occurs when the malaria-inducing parasite leaves the liver and invades red blood cells where it produces proteins that modify the RBC membrane and cytoskeleton. Healthy RBCs repeatedly deform from their biconcave shape to pass through small blood vessels or capillaries. In contrast, RBCs parasitized by *P. falciparum* show an up to 10-fold increase in elastic stiffness (Fig. 11.7b), they adhere to vascular endothelium, and therefore, sequester in microvasculature contributing to organ failure [11.22]. The stiffening may arise from the perturbation of the attachments between the membrane and the cytoskeleton. These attachments are facilitated by chemical interactions involving ankyrin and the RBC anion transporter as well as protein 4.1 and glycophorin A (see [11.22]). Alterations to this delicate molecular architecture due to abnormalities that mediate cross-linking of cytoskeletal proteins can result

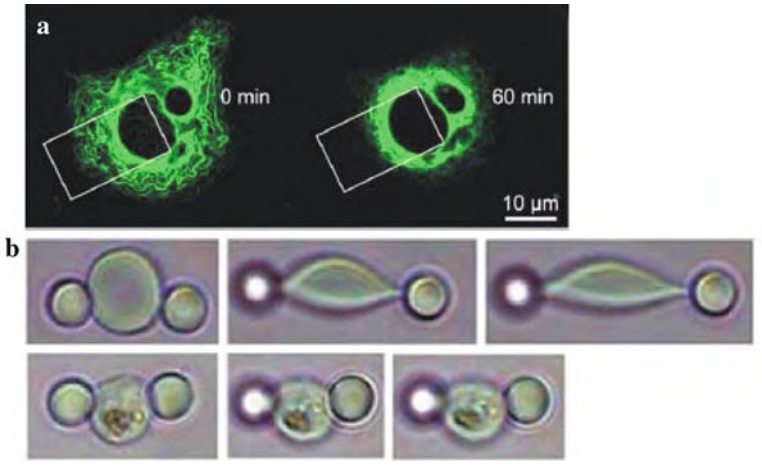

Fig. 11.7 (**a**) Treatment of human pancreatic cancer cells (Panc-1) with sphingosylphosphorylcholine (SPC) over a period of 60 min. causes significant reorganization of the keratin filaments to perinuclear regions which may be the reason for a three-fold decrease of the cellular elastic modulus. (**b**) Optical tweezers stretch a healthy red blood cell (*top row*) and a cell in a late stage of infection with the malaria parasite (*bottom row*). The parasite is visible in the centers of the bottom row images. Left column: tensile stretching of the cell by optical tweezers at a constant force of 68 ± 12 pN; right column: stretching at a constant force of 151 ± 20 pN. (Reprinted with permission from [11.22]. © 2005 Elsevier)

in severe stiffening of the RBCs. By the *P. falciparum* parasite, several parasite proteins are introduced into the RBC membrane and cytoskeleton, altering the mechanical response and the adhesive properties. Among these proteins, *P. falciparum* ring-infected erythrocyte surface antigen (RESA) or Pf 155 gets deposited into the cytoplasmic surface of the erythrocyte membrane from the dense granules in the apical region of the merozoite (parasitic protozoans which contribute to the proliferation of *P. falciparum*) during parasite invasion. It has been speculated that RESA interaction with the spectrin network underneath the RBC membrane contributes to the increased elastic modulus of parasite harboring RBCs (see [11.22]).

The structural and mechanical modifications of red blood cells (RBCs) due to parasitization by malaria-inducing *P. falciparum* can be extracted from optically measured maps of the refractive index and of nanoscale cell membrane fluctuations [11.24]. These findings may provide information on pathological states that cause or accompany human diseases. Furthermore, disease mutations in human intermediate filament (IF) proteins in the cell nucleus and in the cytoplasma indicate [11.25] that the nanomechanical properties of cell-type-specific IFs are central to the pathogenesis of diseases as diverse as muscular dystrophy and premature aging.

Theoretical and computational approaches, taking into account the data of advanced experimental techniques, may provide new insight into the connection between cell mechanics and function [11.26]. For these approaches the consideration of a wide range of length scales is of importance. For treating the overall mechanical response of individual cells, continuum-based computational models are favorable, whereas for nanostructural modeling molecular dynamics (MD) techniques are appropriate.

11.1.5 Control of Cell Functions by the Size of Nanoparticles Alone

To date, about 10 years after the regulatory approval of liposomaly encapsulated doxorubicin to treat various forms of cancer, no such "higher functionality" nanoparticle has reached the clinic yet. The reason is because it remains difficult to identify and validate biological targets that are specific enough for cancer cells [11.27]. New results [11.28] point to the importance of size as both a bioactive agent and an agent of toxicity. It was found that the uptake of Au or Ag nanoparticles (2–100 nm) decorated with Herceptin – a drug that binds Erb B2 receptors on breast cancer cells – was size dependent [11.28]. Most importantly, specific cell-growth pathways were inhibited and programmed cell death (apoptosis) was enhanced, particularly for particles in the 40–50 nm range.

11.2 Nanoparticles for Bioanalysis

Nanoparticles are used for efficient and selective tagging of a wide range of biologically and biomedically important targets, such as individual biomolecules, bacteria, and cancer cells. Metallic, semiconductor, oxide, or magnetic nanoparticles are used [11.29–11.35]. The further development of these nanoparticles with much higher photosensitivity and much higher stability against photobleaching than conventional organic dyes will provide a variety of advanced tools for molecular biology, genomics, proteomics, drug delivery, as well as diagnosis and therapy of infectious diseases and cancer.

11.2.1 Various Materials of Nanoparticles

One of the most widely used nanoparticle (NP) materials is Au-NPs as colorimetric probe due to the size and shape-dependent surface plasmon excitation (see Sect. 7.6) which changes upon aggregation with other molecules. Ultrasensitive analysis of oligonucleotides, proteins, and other biomolecules has been achieved using Au-NP biomarkers which are already commercial products [11.35]. One example is the lateral flow strip for fast pathogen detection and point-of-care diagnosis [11.36, 11.37].

Semiconductor nanoparticles of CdSe, CdTe, CdS, ZnSe, etc. [11.31, 11.35] with diameters of 2–10 nm and wide absorption bands provide bright (10–20-fold higher than an organic fluorophore) and narrow-fluorescence emission bands (see Fig. 11.8). The resistance of the semiconductor nanoparticles against photobleaching compared to the fast bleaching of organic dyes is demonstrated in Fig. 11.9a.

Silica nanoparticles with dye doping and high analytical sensitivity can be fabricated by a precursor technique that, e.g., integrates fluorescein isothiocyanate (FiTC) into the 3-amino propyltriethoxysilane precursor for a final incorporation of the dye into the silica matrix [11.38]. Besides single-dye doping, multiple-dye incorporation into silica NPs can be performed (see [11.35]).

Magnetic nanoparticles of, e.g., iron oxide (Fe_3O_4, γ-Fe_2O_3) are of biological and clinical interest (see [11.39]) since they are fully biocompatible because the human body already contains around 3–4 g Fe in the form of ferritin, hemoglobin, etc. These nanoparticles are superparamagnetic, i.e., they magnetize strongly in an applied magnetic field but retain no permanent magnetization once the field is removed. This magnetic behavior may improve drug delivery by literally dragging therapeutic agents attached to these nanoparticles to specific areas in the body under the influence of an external magnetic field (see Fig. 11.10). In addition, iron oxide nanoparticles have already been approved for clinical use as magnetic resonance imaging (MRI) contrast agents. These agents work by altering the relaxation rates

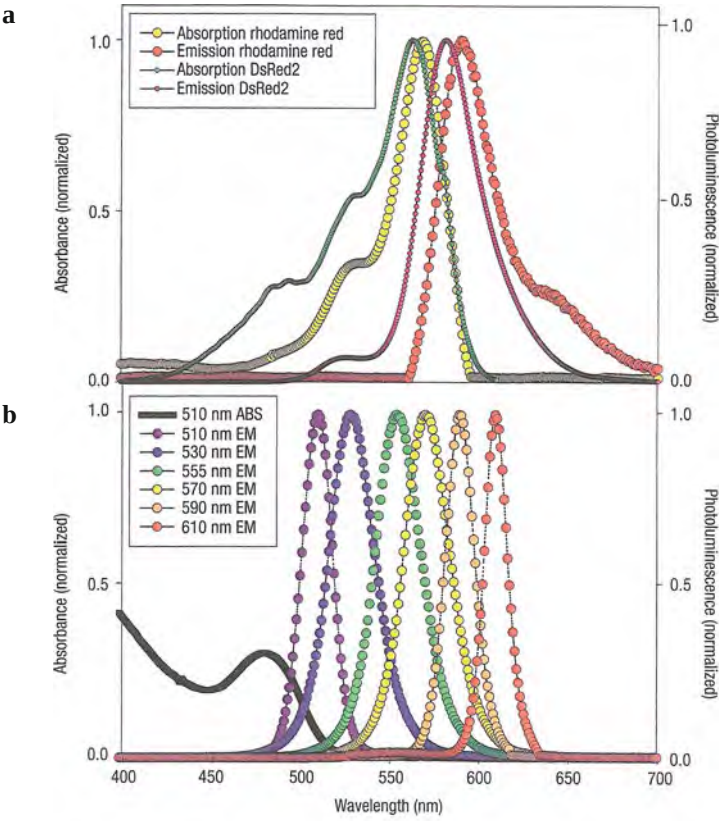
a
Absorption rhodamine red
Emission rhodamine red
Absorption DsRed2
Emission DsRed2
Absorbance (normalized)
Photoluminescence (normalized)
1.0
0.5
0.0
b
510 nm ABS
510 nm EM
530 nm EM
555 nm EM
570 nm EM
590 nm EM
610 nm EM
400
450
500
550
600
650
700
Wavelength (nm)

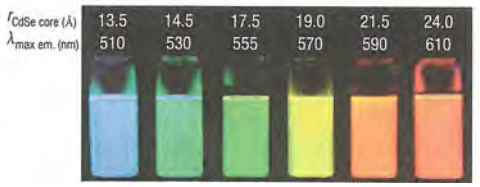
c
$r_{CdSe\ core}$ (Å)
$\lambda_{max\ em.}$ (nm)
13.5
510
14.5
530
17.5
555
19.0
570
21.5
590
24.0
610

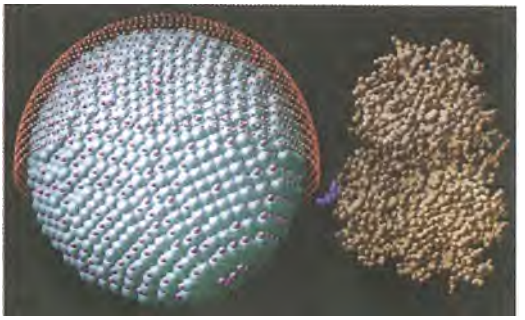
d

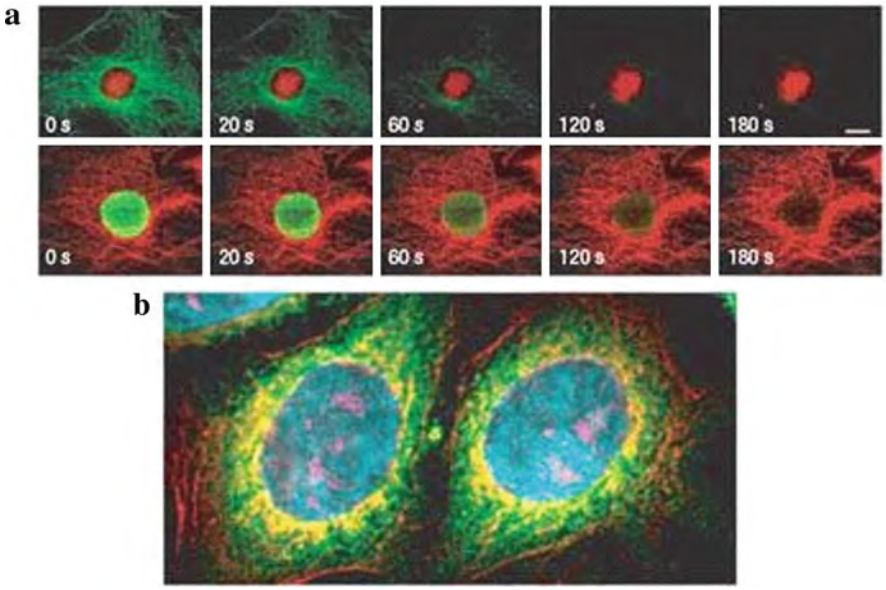

Fig. 11.9 Resistance of CdSe/ZnS nanoparticles to photobleaching and their ability of multicolor labeling. (**a**) *Top row*: antigens in a 3T3 cell nucleus were labeled with CdSe/ZnS streptavidin nanoparticles (630 nm emission, *red*) and microtubules were labeled with the organic dye Alexa Fluor 488 (488 nm emission, *green*); *bottom row*: microtubules labeled with the CdSe/ZnS nanoparticles (*red*) and nuclear antigens stained with Alexa 488 (*green*). The nanoparticles resist to photobleaching under continuous illumination [11.41]. (**b**) Pseudocolored image with nanoparticle staining in fixed human epithelial cells: Cyan (655 nm) corresponds to the nucleus, *magenta* (605 nm) labels Ki-67 protein, *orange* (525 nm) labels mitochondria, *green* (565 nm) labels microtubules, and *red* (705 nm) labeling actin filaments [11.31]. (Reprinted with permission from [11.41] (**a**) and [11.31] (**b**). © 2003 Nature Publishing Group (**a**) and © 2005 Nature Publishing Group (**b**))

of water protons (see Sect. 12.2) that are trying to realign with a static magnetic field following the application of radiofrequency (RF) pulses. The iron oxide nanoparticles affect the transverse relaxation times (T2) leading to negative contrast or dark spots on the T2-weighted MR images.

Fig. 11.8 Comparison of the absorption (ABS) and emission (EM) of the common organic dye rhodamine red and the genetically dye-encoded DsRed2 protein with that of six different sized ZnS-coated CdSe nanoparticles (**a**,**b**) [11.40]. (**c**) Photo of the size-tunable fluorescence and spectral range of the six CdSe/ZnS nanoparticles dispersions of (**b**). (**d**) Comparison of the size of the CdSe/ZnS nanoparticle ($r \sim 3.0$ nm; emitting at 555 nm) surface-functionalized with dihydrolipoic acid (red shell, ~1.0 nm) with that of a midsize maltose binding protein (MBP, mass ~44 kDa, $3 \times 4 \times 6.5$ nm^3) [11.31]. (Reprinted with permission from [11.40] (**a**) (**b**) and [11.31] (**c**) (**d**). © 2000 National Academy of Sciences USA (**a**) (**b**) and © 2005 Nature Publishing Group (**c**) (**d**))

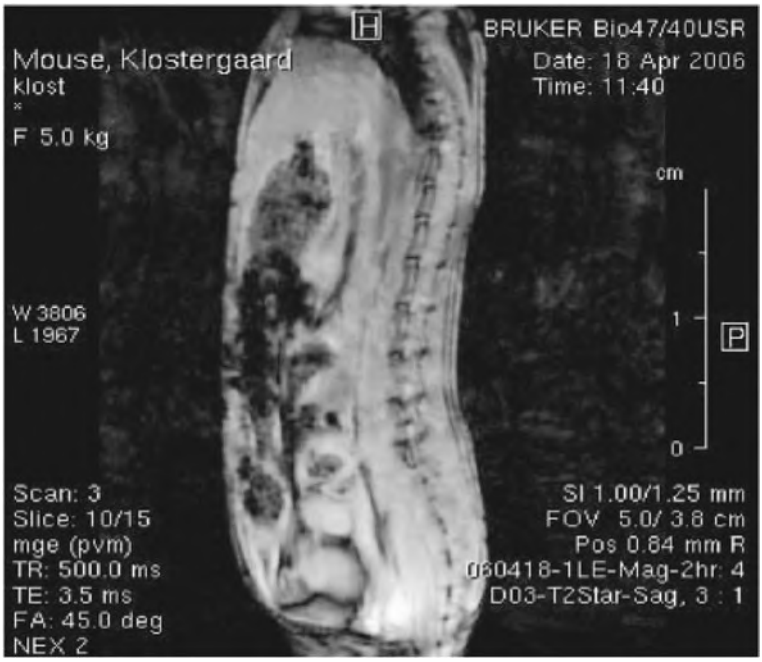

Fig. 11.10 T2-weighted MRI of a nude mouse with a tumor in the ventral abdominal wall after previous intraperitoneal injection with HEY human ovarian adenocarcinoma cells. The mouse was injected intraperitoneally with iron oxide nanoparticles (shown in dark) and an external magnet was placed next to the tumor for 2 h prior to magnetic resonance imaging (MRI) in order to drag the nanoparticles to the tumor. (Reprinted with permission from [11.39]. © 2006 Elsevier.)

11.2.2 Surface Functionalization of Nanoparticles

Various functional groups can be easily introduced onto the nanoparticle surface for mediating both the nanoparticles solubility and serving as a point of chemical attachment for biomolecules. Biofunctional ligands may be used which present a surface anchoring moiety to bind to the inorganic nanoparticle (for example, thiol) and an opposing hydrophilic end group (for example, hydroxyl, carboxyl) to achieve water compatibility (see [11.31]). Once the nanoparticle surface has been modified, biomolecules such as proteins, enzymes, antibodies, oligonucleotides can be linked to the nanoparticle following standard conjugation protocols [11.35, 11.42] (Fig. 11.11).

11.2.3 Examples for Labeling Biosystems by Nanoparticles

Here, a brief discussion of studying cells, deep tissue, DNA activity, proteins, and implementing immunoassays by making use of nanoparticle techniques (see [11.31, 11.34, 11.35] will be given.

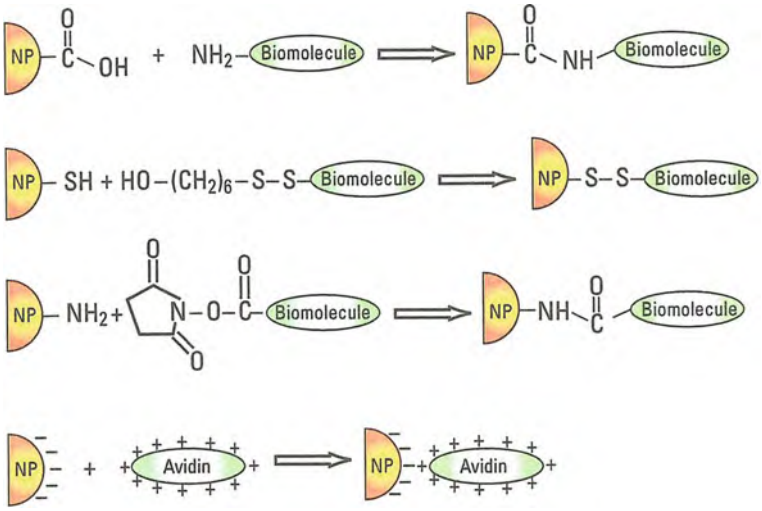

Fig. 11.11 Common bioconjugation protocols for the attachment of biomolecules onto the surface of silica nanoparticles. (Reprinted with permission from [11.43]. © 2006 American Chemical Society)

Cellular labeling by nanoparticles [11.31] has been used to study the cell nucleus containing the chromosomal DNA (Fig. 11.9), mitochondria providing the essential energy-delivery processes (Fig. 11.9), microtubules (Fig. 11.9), actin filaments (Fig. 11.9), etc. In addition, cellular membrane proteins and receptors such as serotonin transport proteins, prostate-specific membrane antigen, the breast cancer marker protein Her2, or the multidrug transporter P-glyco protein were investigated. These studies have been partially performed in live cells. The major hurdle of the labeling of live cells is the entry of the nanoparticles into the cell across the cellular membrane's lipid bilayer and into specific cellular compartments such as the nucleus. For this, a number of techniques are available (see [11.31]).

A combination of fluorescence detection of bioconjugated nanoparticles targeted to selective organelles in a cell, with Raman spectroscopy (see Sects. 1.7 and 7.6), which specifically can identify proteins and lipids by their characteristic vibration modes, has been demonstrated [11.44]. This combination allows for a quick scan of a cell by fluorescence microscopy to detect quantum dots targeted to specific sites in a cell and subsequently zoom in on regions of interest with Raman microscopy in order to perform intracellular chemical analysis. In Fig. 11.12a, Raman imaging of proteins and lipids combined with fluorescence microscopy of streptavidin-conjugated semiconductor nanoparticles (Fig. 11.12b) in murine RAW 264.7 macrophages (large cells which engulf and absorb, e.g., microorganisms in the bloodstream) is shown. Obviously the nanoparticles are mostly present in intracellular vesicles presumably due to non-specific internalization [11.44].

Apoptosis studies by means of semiconductor nanoparticles have been reported [11.45]. Apoptosis is the programmed or suicidal cell death (see [11.46]). It occurs in tissues for regulating cell numbers by counter balancing cell proliferation.

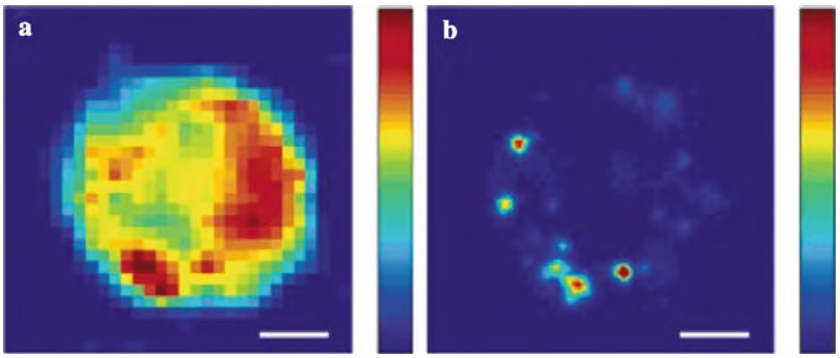

Fig. 11.12 Combined Raman and nanoparticle fluorescence microscopy in macrophages. (**a**) Raman spectral image constructed from the high-frequency region (2800–3050 cm^{-1}) of proteins and lipids. (**b**) Fluorescence image of semiconductor nanoparticles detected at ~600 nm. Scale bars, 3 μm. (Reprinted with permission from [11.44]. © 2007 American Chemical Society)

Dysfunction in apoptosis is therefore linked to disease states which are correlated either to a lack or to an excess of cell suicides. Understanding processes underlying apoptosis will help drug development and disease curing. Apoptosis involves a series of cellular changes in dependence of time. First, changes at the mitochondrion level occur. Then the cell shrinks with concomitant changes of the mechanical and electrical properties of the membrane, and a transfer of, e.g., phosphatidylserine groups (PS), which are normally located on the inner membrane, to the outer membrane. Finally, the nuclear membrane is disrupted.

Targeting PS moieties on the outer membrane of living cell, e.g., by the small protein annexin (35 kDa), is one of the main techniques to detect apoptotic cells. ZnS-coated CdSe nanoparticles functionalized with annexin V via streptavidin–biotin coupling can be used as an efficient fluorescent marker over all the apoptosis time period because of its bleaching resistance (see Fig. 11.13).

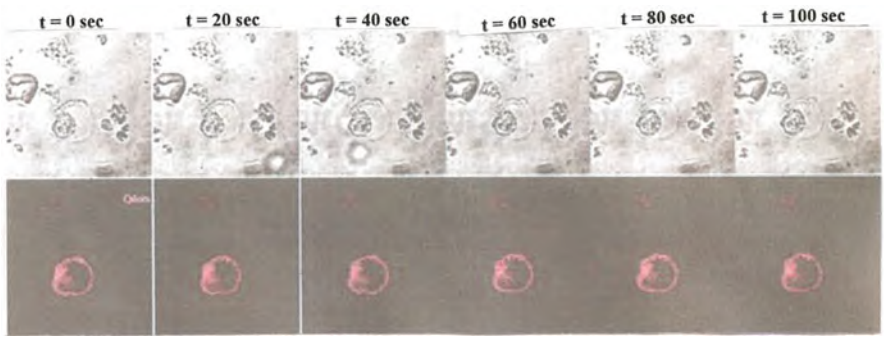

Fig. 11.13 Light microscope (*top row*) and nanoparticle fluorescence pictures (*bottom row*) of cells after treating with an apoptosis inducer. (Reprinted with permission from [11.45]. © 2006 American Chemical Society)

11.2.4 In Vivo and Deep Tissue Imaging

Injection of nanoparticles into cells can be performed by making use of carbon nanotubes as demonstrated by the injection of protein-coated CdSe/ZnS nanoparticles into live human cells with a subsequent measurement of the nanoparticles' diffusion coefficient [11.47]. The multiwall (MWNT) carbon nanotube is attached to the tip of an atomic force microscope (AFM) (Fig. 11.14a, b) and functionalized with a pyrene–biotin linker (Fig. 11.14d) to which the commercially available nanoparticle with its streptavidin conjugate can be attached by the strong non-covalent biotin–streptavidin bond (Fig. 11.14c). By the functionalized carbon nanotube the cell membrane can now be pierced with AFM precision without significant disruption because the membrane can readily heal by lipid diffusion without perturbation of the cytoskeleton (see [11.47]). In the reducing environment of the cytosol the disulfide S–S bond of the linker (Fig. 11.14d) is cleaved, liberating the attached nanoparticle–streptavidin–biotin cargo. In Fig. 11.15 cells before and after nanoparticle injection are shown with the nanoparticle fluorescence after injection. The diffusion coefficient D_{np} of the cytosolic nanoparticles can be measured by analyzing the mean displacement within the traveling time yielding $D_{np} = 3 \times 10^{-13} m^2/s$, ten times lower than in pure water. By this technique, a variety of molecules can be delivered with high spatial precision into live cells or organelles.

Semiconductor nanoparticles can be exploited to achieve somewhat deeper observation penetration in tissues than the available near-infrared dyes (see [11.31]). This was demonstrated by applying semiconductor nanoparticles (840–860 nm emission) to sentinel lymph-node mapping in cancer surgery of animals [11.48].

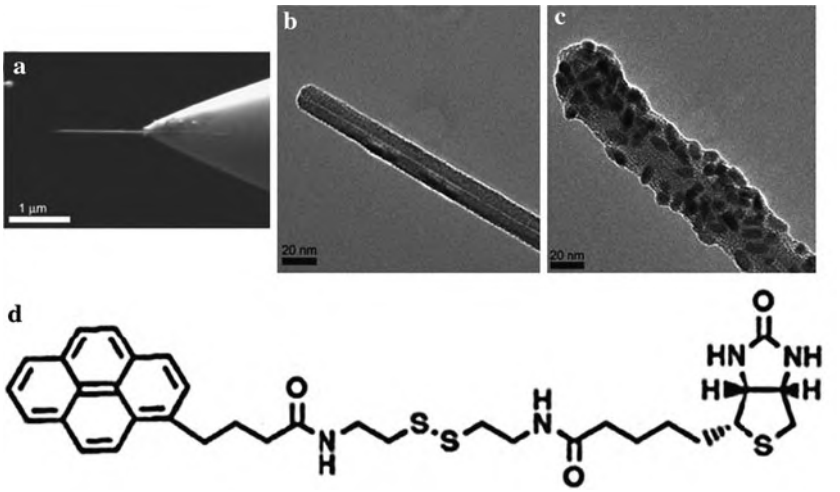

Fig. 11.14 (**a**) AFM image of a MWNT carbon nanotube attached to an AFMtip. (**b**) Tip region of (**a**). (**c**) TEM image of a MWNT-AFM tip coated with linker (**d**) and attached streptavidin-conjugated nanoparticles. (**d**) Pyrene–biotin linker with a disulfide S–S bond. (Reprinted with permission from [11.47]. © 2007 National Academy of Sciences USA)

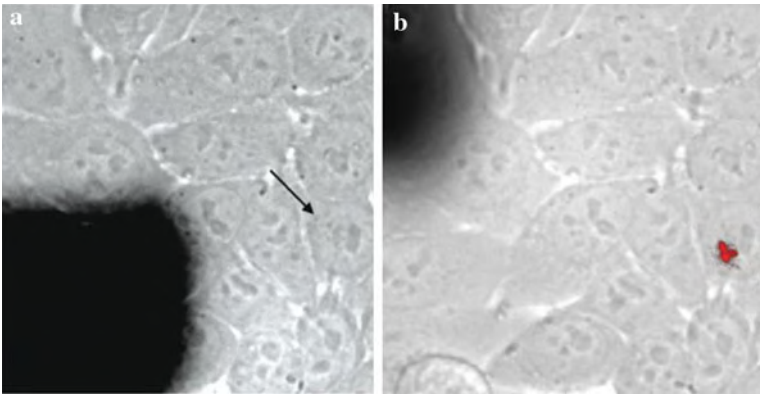

Fig. 11.15 Nanoinjection of nanoparticle streptavidin conjugates into a target human epithelial (HeLa) cell. Combined bright-field and fluorescence images of the cell before (**a**) and after (**b**) nanoinjection. The images are 70 × 70 $(\mu m)^2$. (Reprinted with permission from [11.47]. © 2007 National Academy of Sciences USA)

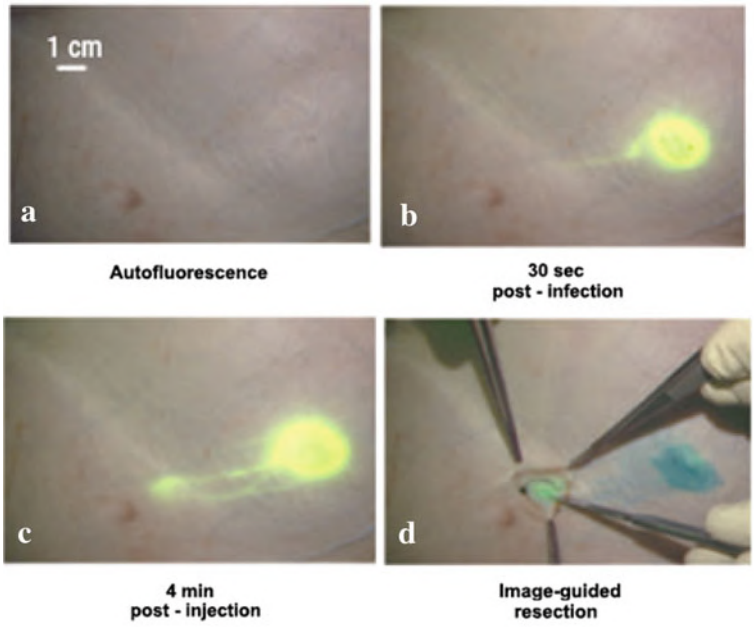

Fig. 11.16 Near infrared semiconductor nanoparticle imaging in vivo. Images of the surgical field in a pig injected intradermally with 400 pmol of nanoparticles in the right groin. Four time points are shown (**a**–**d**): before injection (autofluorescence), 30 s after injection, 4 min after injection, and during image-guided resection. Note the lymphatic vessel draining to the sentinel node from the injection site. (Reprinted with permission from [11.48]. © 2004 Nature Publishing Group)

Lymphatic vessels were clearly visualized 1 cm deep in tissue draining nanoparticle solutions into the sentinel nodes (Fig. 11.16). As an added bonus, the location of the nanoparticle accumulation in the nodes may be the most likely place for the pathologist to find metastatic cells. In a different approach, tumor cells were labeled with semiconductor nanoparticles, injected into mice, and then tracked with multiphoton microscopy as they invaded lung tissue [11.48], [11.49].

For deep tissue in vivo imaging by nanoparticles an alternative technique is available where the sensitivity can be greatly enhanced by suppression of the autofluorescence background of the tissue arising from external illumination [11.50]. This can be achieved by employing CdSe/ZnS nanoparticle QD 655 conjugates that luminesce (from red to near-infrared) by bioluminescence resonance energy transfer (BRET), in the absences of external illumination, when the nanoparticles are coupled to the bioluminescent protein *Renilla reniformis luciferase*, Luc8. This protein emits blue light at $\lambda = 480$ nm upon addition of its substrate coelenterazine which initiates by BRET the 655 nm emission of the nanoparticles [11.50]. These nanoparticle conjugates can be used to label cells and to monitor labeled cells in animals. For labeling cells the nanoparticles are additionally conjugated with a polycationic peptide (arginine 9-mer) to improve the cell uptake efficiency (QD655-Luc8-R9). In mice C6 glioma cells labeled with conjugated nanoparticles and injected via the tail vein can be optically detected in the lungs (Fig. 11.17).

The ability to track cells in vivo without continuously sacrificing animals represents a substantial improvement over current techniques.

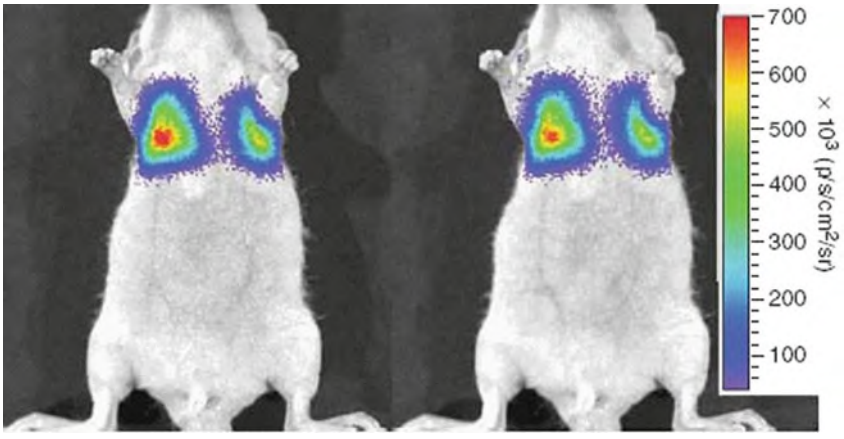

Fig. 11.17 Imaging C6 glioma cells labeled with QD655-Luc8-R9 nanoparticles in the lungs of mice after tail vein injection of the labeled cells. The bioluminescent protein Luc8 (see text) emits at $\lambda = 480$ nm. This emission initiates by bioluminescence resonance energy transfer (BRET) the emission of the QD655 nanoparticles at $\lambda = 655$ nm. The *left* photo was taken with a filter (575–650 nm), whereas the *right* photo was taken without filter, demonstrating that the Luc8 emission is largely absorbed in deep tissue. (Reprinted with permission from [11.50]. © 2006 Nature Publishing Group)

It should be pointed out here that there are open questions about the toxicity of inorganic nanoparticles containing Cd, Se, Zn, Te, Hg, and Pb [11.51]. However, lung and skin cells treated with CdSe/Zns nanoparticles embedded in SiO_2, which are able to cross the nuclear membrane [11.52], do not show signs of toxicity [11.53], neither do CdSe/ZnS nanoparticles coated with poly(ethylene glycol) (PEG) [11.54]. Yet, the fact that long-term in vivo studies have not found evidence of toxicity is promising but still not a blanket endorsement.

11.2.5 Nanoparticle-DNA Interaction

DNA transcription is an important biological process through which a DNA sequence is enzymatically copied by an RNA polymerase to produce a complementary RNA, enabling a transfer of genetic information required for protein synthesis. A number of small molecules have been used to bind specific DNA sequences and inhibit or activate DNA transcription (see [11.34]). Via cationic ligands with positively charged head groups, nanoparticles NPs can interact with the negatively charged DNA by electrostatic attraction. This process inhibits DNA transcription by T7 RNA polymerase (see Fig. 11.18). By the use of intracellular concentrations (0, 5–10 mmol dm^{-3}) of glutathione (GSH), the DNA transcription by the T7 polymerase is recovered (Fig. 11.18) due to a place exchange of the cationic NP residues with anionic GSH which diminishes the electrostatic affinity between the nanoparticles and the DNA backbone (Fig. 11.18). These studies show that the DNA transcription activity can be tuned by the intracellular GSH levels.

In addition to GSH-mediated DNA release, photochemical techniques can effectuate DNA release for transcription, in vitro and in cells, by converting a cationic nanoparticle ligand to an anionic ligand upon light irradiation (see Fig. 11.19).

Furthermore, recent studies show [11.55] that cationic photocleavable nanoparticles (NP-PC) can effectively carry DNA into the cell nuclei and that DNA is successfully unloaded from gold nanoparticles by photocleavage. Effective accumulation of DNA in the cell nucleus after dissociation from transporting vectors

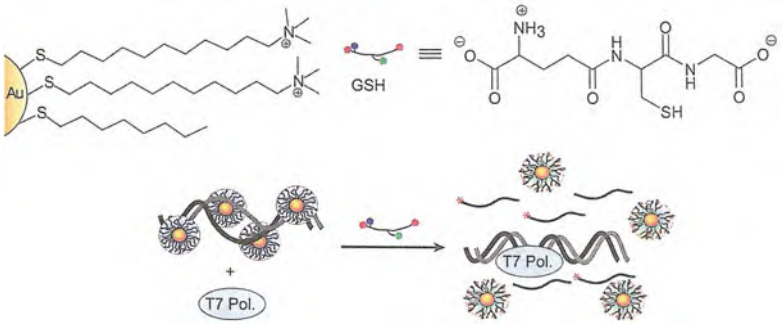

Fig. 11.18 Schematic depiction of the inhibition of the helical DNA molecules by functionalized Au nanoparticles and GSH-mediated reactivation of DNA transcription by T7 polymerase. (Reprinted with permission from [11.34]. © 2007 Elsevier)

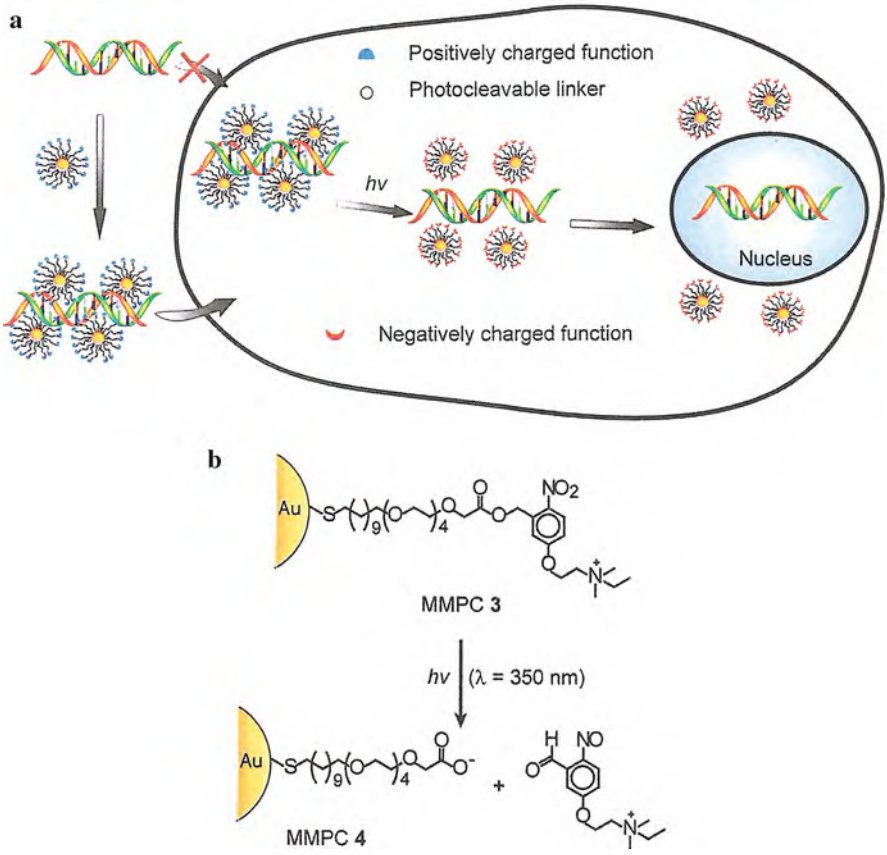

Fig. 11.19 (**a**) Schematic illustration of the release of DNA helices from the inhibited DNA–Au nanoparticle complex within the cell upon ultraviolet irradiation. (**b**) Schematic of light-induced transformation of a cationic ligand on a Au nanoparticle (MMPC3) to an anionic ligand (MMPC4). (Reprinted with permission from [11.34]. © 2007 Elsevier)

is an essential step in gene delivery, as gene expression takes place in the nucleus. Recent experiments [11.55] are briefly described in the following.

Gold nanoparticles quench conjugated organic fluorophores effectively through energy transfer (see [11.55]) and "light-up" again as the energy-transfer pathway is removed. Making use of that, fluorescein (FAM)-labeled 37-mer DNA (F-DNA), which bears the same sequence as that used in the T7 RNA polymerase assay, was used to detect DNA delivery and release in vivo. Mouse embryonic fibroblast cells were incubated with NP-PC–F-DNA complex and subsequently irradiated by UV light. The cell nucleus was stained with 4,6-diamidino-2-phenylindole (DAPI). The nuclear localization of the DNA is clearly shown (Fig. 11.20) because the fluorescence area of fluorescein-stained transferred DNA coincides with the DAPI-stained nucleus.

For gene delivery, i.e., transfer of DNA, into mammalian cells, bacteria have been used in a process called "bactofection" [11.56], where the cargo is carried

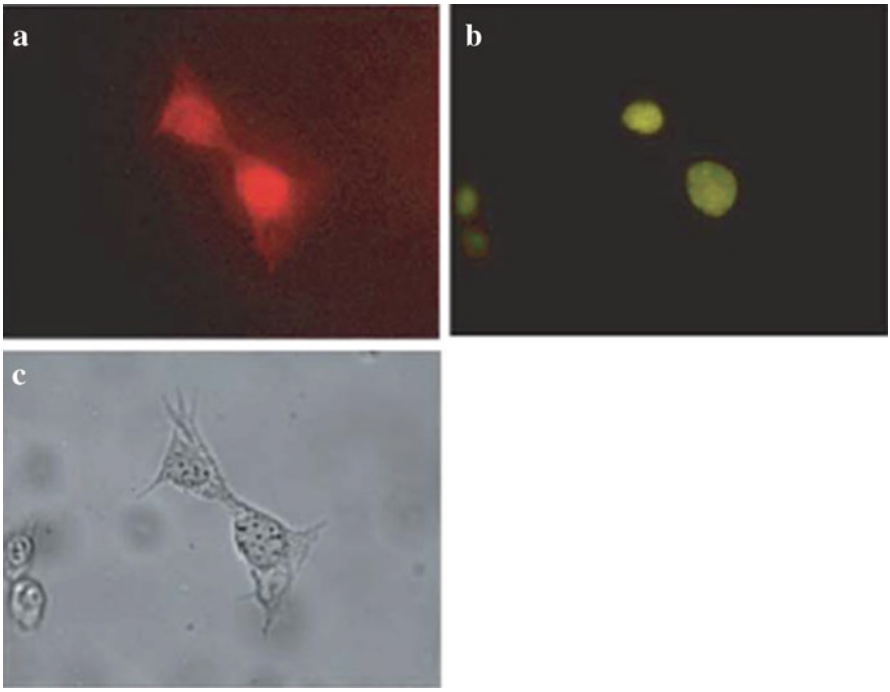

Fig. 11.20 Fluorescence and bright-field microscopy images of the nucleus of a mouse embryonic fibroblast cell after photo-triggered release of fluorescein-labeled DNA. (**a**) Spatial distribution of the fluorescein-labeled DNA which coincides with (**b**) the DAPI-labeled cell nucleus. This demonstrates that DNA can be successfully carried into a cell nucleus, for gene transfer, by a photocleavable nanoparticle NP-PC. (**c**) Bright-field image of the cell. (Reprinted with permission from [11.34]. © 2007 Elsevier)

inside the bacterium so that the bacteria have to be disrupted after penetration into the cell, e.g., by treatment with antibiotics. This can be circumvented when the gene or cargo is attached to the surface of the bacterium via a nanoparticle, an entity which is called a "microbot" [11.57]. This technique uses biotinylated monoclonal antibodies C11E9 against a surface protein, *N*-acetylmuramidase, on the bacterium *Listeria monocytogenes* to attach streptavidin-coated polystyrene nanoparticles onto the bacterial surface. Biotinylated green fluorescence protein (GFP) plasmid was then attached to the remaining streptavidin sites on the nanoparticles (Fig. 11.21a).

Fig. 11.21 Bacteria-mediated delivery of nanoparticles and DNA therapeutics. (**a**) Docking of bacteria with nanoparticles functionalized through biotinylated antibodies and surface-antigen interactions (microbots). Streptavidin-coated nanoparticles attached to the biotinylated bacterium surface can carry biotinylated plasmid DNA. (**b**) Delivery of intervention agents using microbots. (**c**) Scanning electron micrograph of a bacterium microbot; *arrows* show nanoparticles. (Reprinted with permission from [11.57]. © 2007 Nature Publishing Group)

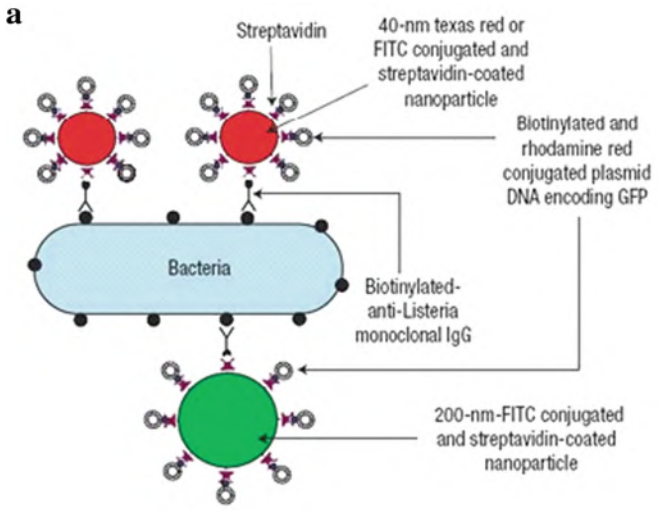
a
Streptavidin
40-nm texas red or FITC conjugated and streptavidin-coated nanoparticle
Biotinylated and rhodamine red conjugated plasmid DNA encoding GFP
Bacteria
Biotinylated-anti-Listeria monoclonal IgG
200-nm-FITC conjugated and streptavidin-coated nanoparticle

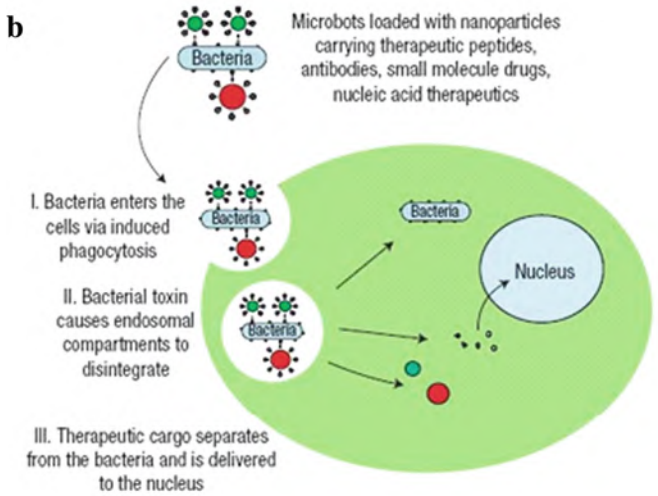
b
Bacteria
Microbots loaded with nanoparticles carrying therapeutic peptides, antibodies, small molecule drugs, nucleic acid therapeutics
I. Bacteria enters the cells via induced phagocytosis
Bacteria
Bacteria
Nucleus
II. Bacterial toxin causes endosomal compartments to disintegrate
Bacteria
III. Therapeutic cargo separates from the bacteria and is delivered to the nucleus

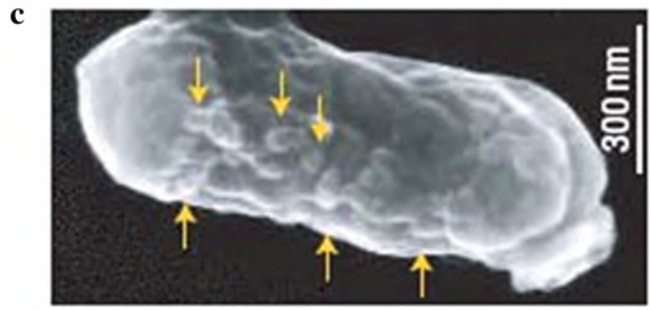
c
300 nm

This approach can be used to attach particles of various sizes or different entities onto *L. monocytogenes* to be delivered into eukaryotic cells (Fig. 11.21b). To confirm that the host cells express the desired plasmid-encoded antigens, the nuclei of several types of human cell lines were targeted to express the easily detected GFP. In addition, it was demonstrated by in vivo studies of mice that the microbots can be used to transfect entire organs [11.57]. The safety issues arising from the use of *L. monocytogenes* bacteria could be addressed by using bacteria that have already been approved for human use [11.58].

Enzymatic processes on DNA, such as telomerization, have been probed by employing semiconductor nanoparticles (CdSe/ZnS) [11.59]. The ZnS-coated CdSe nanoparticles were stabilized by mercaptopropionic acid modified with the thiolated oligonucleotide of about 25 nucleic acid units. The functionalized semiconductor nanoparticles were then incubated with a d NTP mixture that included the dye Texas-Red 14-d UTP (designated (**2**) in Fig. 11.22a) in the presence of telomerase. As telomerization proceeds, the characteristic emission of the dye at 610 nm

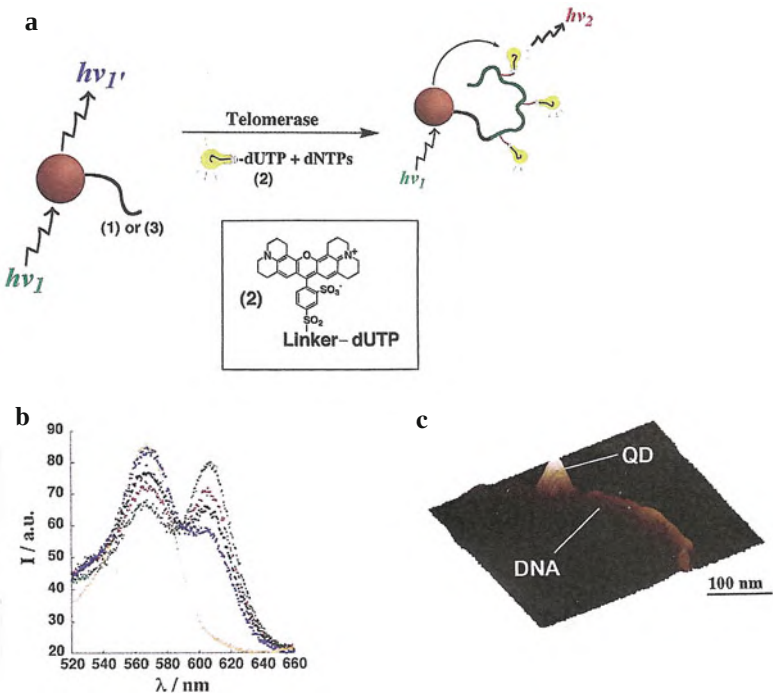

Fig. 11.22 (**a**) Schematic of telomerization on nucleic acid functionalized CdSe–ZnS nanoparticles with dye (**2**) incorporated. (**b**) Emission spectrum of the nanoparticle–DNA complex in dependence of the telomerization time: *blue*, before addition of telomerase; *black*, *red* and *green* after 10, 30, and 60 min of telomerization, respectively. (**c**) AFM image of a CdSe–ZnS nanoparticle after 60 min of telomerization on a mica surface. (Reprinted with permission from [11.59]. © 2003 American Chemical Society)

increases (Fig. 11.22b). As the emission of the ZnS-coated CdSe nanoparticles at $\lambda = 560$ nm coincides with the absorption band of the dye (**2**), the emission at $\lambda = 610$ nm observed upon telomerization (Fig. 11.22b) can be attributed to fluorescence resonance energy transfer (FRET) from the nanoparticles to the dye (**2**) molecules incorporated into the telomeric units by telomerase. By AFM imaging after incubation in the presence of telomerase, the nanoparticle together with the synthesized hinged DNA strand 300 nm long are visible, which corresponds to a telomerase-induced elongation of ca. 1000 base units in the telomeric DNA chain (Fig. 11.22c).

Molecular recognition in sandwich assays based on the hybridization of nucleic acid strands is widely used in disease diagnosis, drug development, and other biotechnology applications [11.35]. A sandwich-assay has been used for DNA detection based on silica nanoparticles [11.60] and working with three different DNA species (Fig. 11.23): capture DNA immobilized on a glass surface; a probe sequence attached to tetramethylrhodamine (TMR)-doped silica nanoparticles; and the unlabeled target DNA sequence which is complementary to both the capture and the probe sequences through different parts of its sequence. This scheme has also been introduced into a microarray platform and shows good correlation with the conventional single phycoerythrin labeling method with, however, greatly enhanced photo stability and detection sensitivity as well as a 20 times lower detection limit of 50 fM.

Gold nanostoves for fast DNA melting analysis. A DNA analysis faster than blood cultures can speed up the search of pathogens causing severe illnesses such as sepsis. But this requires a rapid DNA assay with the potential for mutant identification and multiplexing. Current DNA assays are based on thermal dehybridization or melting of the DNA duplex helix because the melting temperature is determined by the DNA base sequence. Currently the timescale for a melting analysis ranges

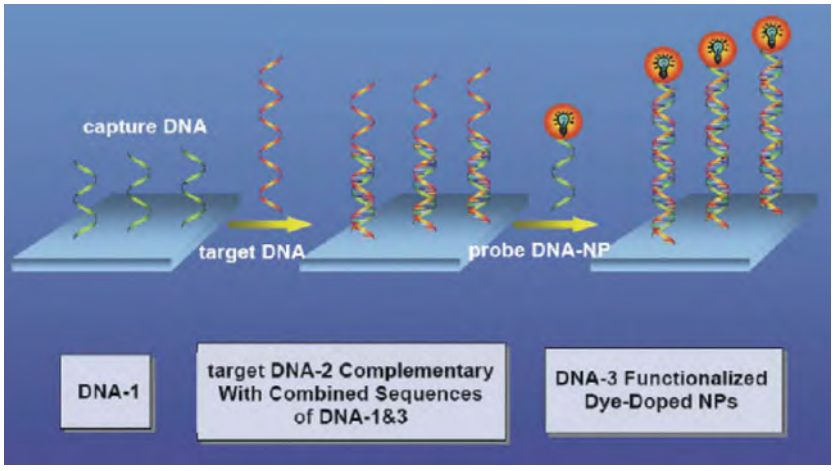

Fig. 11.23 Schematic of a sandwich DNA assay based on silica nanoparticles [11.35, 11.60]. (Reprinted with permission from [11.35]. © 2007 Elsevier)

from minutes to 1 h. [11.61]. However, DNA bound to 10 nm gold nanoparticles can be melt on a microsecond timescale upon laser irradiation due to plasmon absorption (see Sect. 7.6) in the gold nanoparticles [11.61]. A perfectly matching and a point-mutated DNA sequence can be clearly distinguished in less than a millisecond.

Gene expression profiling by means of high-throughput multiplexed screening is increasingly used as an indispensable tool for research, diagnosis, and drug screening. In all cells, the expression of individual genes (segments of a DNA sequence corresponding to, e.g., the expression of a single protein) is regulated. The cell adjusts the rate of transcription and translation of different genes independently, according to need. Making use of CdSe/ZnS nanoparticles on superparamagnetic microbeads, increased detection sensitivity, reduction of sample amount, improved profiling speed, etc., can be achieved. This has been demonstrated by investigating transforming growth factor-β1 (TGF- β1)-induced transcription changes in human bone marrow mesenchymal stem cells (MSCs) together with a comparative study by means of the Affymetrix high-throughput automations (HTA) platform [11.62] with a sensitivity of ∼20 zeptomoles of copies of target and of picograms of protein per milliliter. This nanoparticle profiling technique has the potential to impact genomics, proteomics, combinatorial chemistry, and other high-throughput screening assays [11.62].

11.2.6 Nanoparticle-Protein Interaction

Nanoparticles can regulate or study cellular processes such as protein–protein interaction [11.63] or enzyme activity (see [11.34]). In the following examples it will be discussed how the nanoparticle–protein interface can regulate enzymatic activity beyond simple inhibition, by introducing substrates with different electronic charges (see **15**, **16**, **17** in Fig. 11.24). The electrostatic repulsion between an anionic substrate **15** and the negatively charged monolayer on the nanoparticle (see Fig. 11.24) prevents the access of the substrate molecules to the active pocket of the surface-bound enzyme giving rise to an inhibition of the enzymatic activity. In contrast, with a cationic substrate **17** attracted by the monolayer no inhibition occurs. It may be mentioned, that the activity of the chymotrypsin (ChT)-catalyzed hydrolysis reaction can be followed spectroscopically by monitoring the formation of *p*-nitroaniline (pNA) [11.64].

Transition-metal complexes have been used to target surface-exposed histidines of proteins through coordinative interaction. Conjugation of transition-metal complexes on nanoparticles provides a possibility to create protein specific receptors (see [11.34]). Magnetic FePt nanoparticles (see **18** in Fig. 11.25a) with Ni-terminated nitrilotriacetic acid (NTA) can separate, transport, and anchor recombinant proteins engineered with six consecutive histidine residues (Fig. 11.25) Through metal chelation (formation of a heterocyclic ring containing a metal atom), these nanoparticles show a high affinity to histidine-tagged proteins

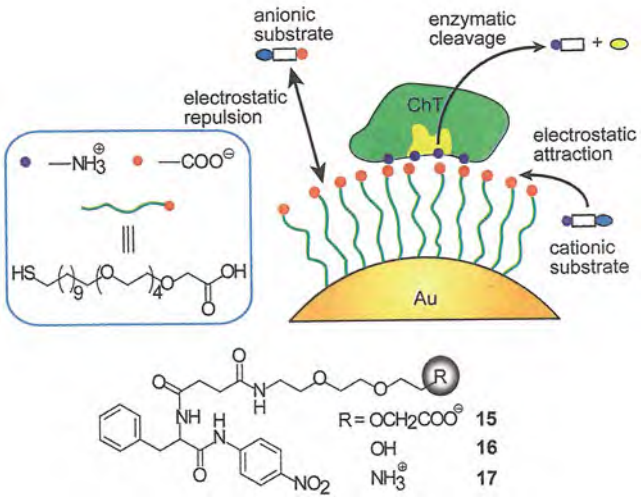

Fig. 11.24 At the interface between a Au nanoparticle with, e.g., TCOOH (alkanethioltetra [11.ethylene glycol] acetic acid) ligands and a chymotrypsin (ChT) enzyme protein, substrate molecules (see **15**, **16**, **17**) can be cleaved selectively. For the negatively charged substrate **15** the enzymatic cleavage is disfavored due to the repulsion of the substrate by the anionic, negatively charged nanoparticle ligands whereas the positively charged substrate **17** is attracted by the ligands yielding a high enzymatic activity [11.34, 11.64]. (Reprinted with permission from [11.34]. © 2007 Elsevier)

(histidine–amino acid, $C_6H_9N_3O_2$) yielding a high protein-binding capacity. Using these magnetic nanoparticles, pure proteins have been directly isolated from lysed cell mixtures through magnetic separation (see [11.34]). For other applications of magnetic nanoparticles see [11.65].

For nanoparticle–protein interaction, the idea of the "nanoparticle–protein corona" has been put forward [11.66] because a nanoparticle is always covered by proteins immediately upon contact with a physiological environment, with different residence times of proteins. In this sense, nanoparticles would be classified in terms of their biomolecule corona which mediates their interaction with cellular machinery and, e.g., can reconstruct lipids [11.67]. Both size and surface properties are found to play a role in determining the nanoparticle coronas on different particles of identical materials [11.68].

It has been shown that CdS quantum dots (QDs) alter the conformation of hemoglobin (Hb) with the sulfur of the cysteine residues directly bonding to the surface of the CdS QDs (see [11.66]). The stability of the model enzyme soybean peroxidase is enhanced when absorbed on C_{60} fullerenes whereas cerium oxide nanoparticles or poly(ethylene glycol) (PEG)-coated QDs enhance the transformation rate of amyloidogenic proteins to fibrils and then plaques, a process that is involved in serious pathological conditions as, e.g., Alzheimer's disease (see [11.66] and Sect. 12.7).

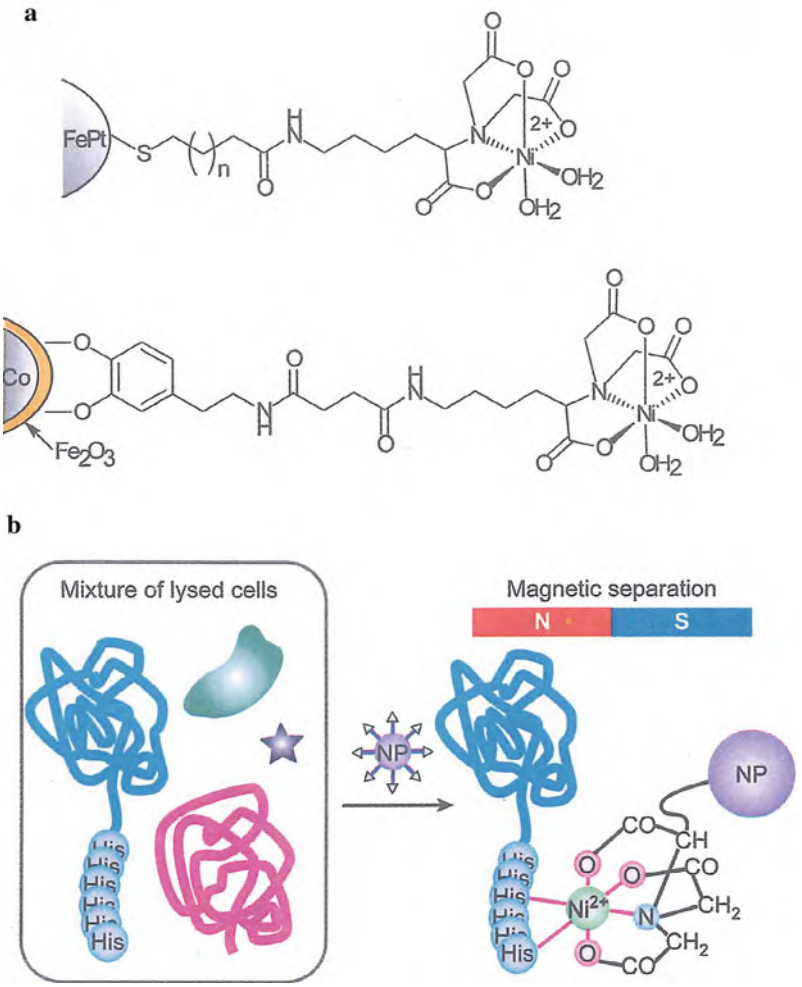

Fig. 11.25 (**a**) Structure of magnetic Fe–Pt nanoparticles modified with Ni-terminated nitrilotriacetic acid (NTA). (**b**) The surface-modified magnetic nanoparticles bind to histidine-tagged proteins in a cell lysate and then these proteins can be separated from the lysate by an external magnetic field. (Reprinted with permission from [11.34]. © 2007 Elsevier)

Immunoassays: In immunoassays for the detection of viral animal diseases, gold nanoparticles have been introduced [11.65, 11.69]. Efficient immunolabeling of *p*-glycoprotein (p-gp) overexpressed in the membrane MCF7r breast adenocarcinoma cells has been demonstrated making use of CdSe/ZnS nanoparticles conjugated with polyclonal antimouse antibodies (Abs; see Fig. 11.26).

Interfacing of nanowires with cells: Direct interconnection of cells with the external world by nanowires may yield new opportunities to probe and manipulate biological processes in the cell interior, across the membrane, and between

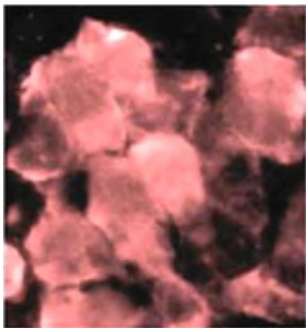

Fig. 11.26 Fluorescence image (20 × magnification) of MCF7r breast adenocarcinoma cells overexpressing p-glycoprotein which is stained by fluorescent CdSe/ZnS nanoparticles conjugated with polyclonal antimouse antibodies (Abs). Figure size 1.6 × 1.6 mm^2. (Reprinted with permission from [11.70]. © 2004 Elsevier)

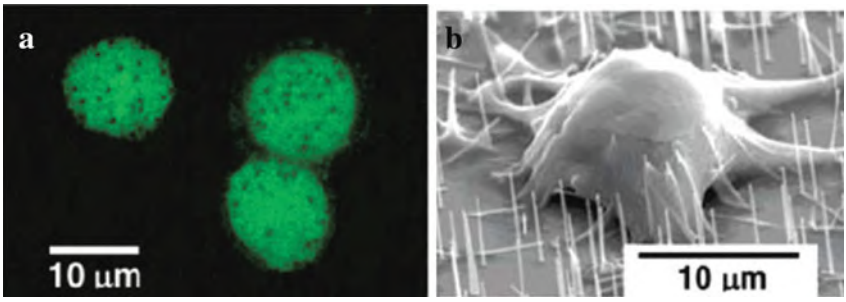

Fig. 11.27 (**a**) Confocal micrograph of mouse embryonic stem (mES) cells penetrated with the silicon nanowires appearing as *black* dots in the cells. (**b**) Scanning electron micrographs of an individual mES cell penetrated with Si nanowires. The diameter and the length of the nanowires are ∼90 nm and ∼6 µm, respectively. (Reprinted with permission from [11.71]. © 2007 American Chemical Society)

neighboring cells. Silicon nanowires have been implanted into mouse embryonic stem (mES) cells and human embryonic kidney (HEK 293T) cells during cell incubation with the cells surviving several days on the nanowire substrates (see Fig. 11.27). The Si nanowires with diameters of 30, 90, or 400 nm were grown by CVD techniques on a Si (111) substrate making use of Au nanoparticle catalysts [11.71].

The mouse embryonic stem (mES) cells were pierced by the Si nanowires during culturing to develop embryoid bodies (EBs) which were expressing green fluorescent protein (GFP) after 7 days of differentiation, demonstrating that the EBs had developed cardiac myocytes (muscle cells). In addition, gene delivery into the HEK 293T cells on a Si nanowire array was demonstrated by depositing and incubating a plasmid DNA construct containing GFP. After a day, some cells expressed GFP, indicating successful delivery and normal function of the exogenous gene [11.71].

11.2.7 Biodistribution of Nanoparticles

Although nanoparticles can be modified to avoid detection in the immune system by grafting biocompatible molecules to their surface, the properties of such particles in biological systems and their biodistribution and elimination are still poorly understood [11.72].

Gold–dendrimer nanocomposites in mice [11.73] were demonstrated to selectively accumulate in some organs by virtue of their size and/or charge alone (see Fig. 11.28). For the 5 nm particles, the positive particles persisted in the kidneys, whereas the negative and neutral particles remained in the liver and spleen. This may be explained by how the serum proteins (or opsonins) treat the particles. Opsonized particles recognized by macrophages in the liver (Kupffer cells) will end up in the liver and spleen, where the rate of opsonization can be controlled by surface charge.

When increasing the particle size to 22 nm, only low levels were seen in the kidney, and accumulation occurred in the lungs, liver, and spleen instead. None of the various nanoparticles used in the study appeared to readily cross the blood–brain barrier. The total excretion of the nanoparticles was found to be incomplete which

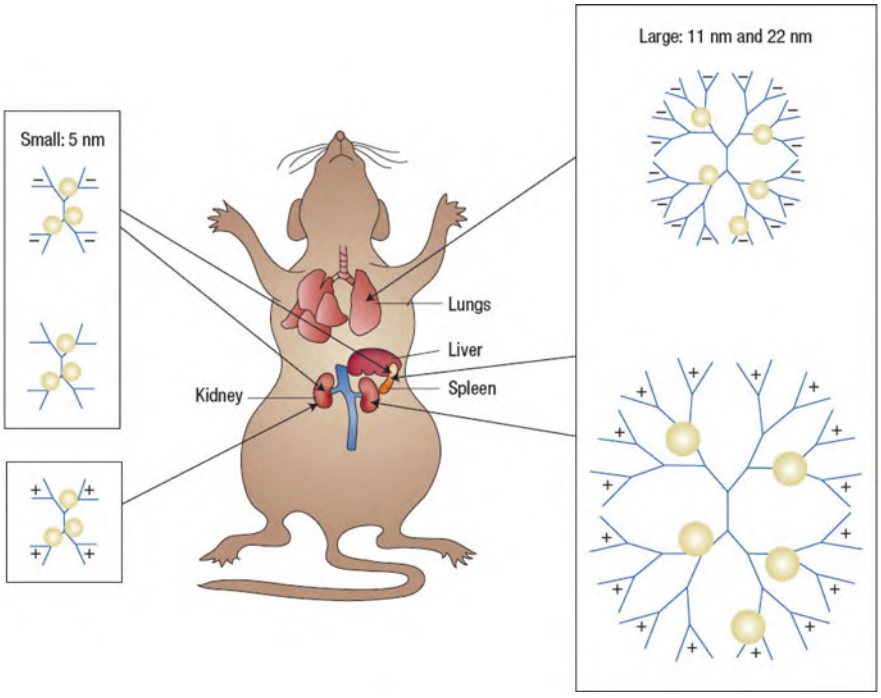

Fig. 11.28 Gold- dendrimer nanoparticles and their biodistribution in vivo. Dendrimers can be used as scaffolds for metals such as gold to attach to, enabling different nanoparticles with different diameters and surface charges (*left, right*) to be produced. The size and the charge of the nanoparticles influence their biodistribution in mice [11.72, 11.73]. (Reprinted with permission from [11.72]. © 2008 Elsevier)

suggests that they entered the peripheral tissues, which requires further investigation. This shows that size, charge, and probably the core of the nanoparticles are important considerations for pharmacokinetics when designing "targeted" systems.

11.3 Nanomechanics of DNA, Proteins, and Cells

Many basic features of DNA were elucidated during the half century following the discovery of the double helix. But only during the last years, researchers succeeded in measuring the mechanical properties of single DNA molecules (see [11.74]). These studies have illuminated the mechanisms of interactions between DNA and proteins and the forces created by DNA-dependent motors.

11.3.1 DNA Elasticity

DNA can in many contexts be described by the worm-like chain (WLC) model with the flexural persistence length A. The value of A ($\sim$50 nm for DNA in physiological buffer) defines the distance over which the direction of the DNA line persits. In this model the relationship between A and the bending rigidity κ of the polymer is given by $k_B TA = \kappa$. Thus, a polymer with a smaller bending rigidity tends to adopt a more compact random-coil structure with a low A value. This is reflected in the phenomenon of entropic elasticity which is responsible for the elastic properties at common polymeric materials such as rubber. Pulling the coiled molecule into a more extended chain is entropically unfavorable as there are fewer possible conformations at longer extensions. Tensions of the order of $k_B T/A$, i.e., $\sim$0.1 pN for double-stranded (ds) DNA or 5 pN for single-stranded (ss) DNA are required to extend the molecule significantly.

Force and extension measurements of single DNA molecules making use of optical traps and microscale beads (Fig. 11.29) provide a rigorous test of theories of entropic elasticity. Forces of $\sim$6 pN, within the range of forces exerted by characteristic molecular motors, stretch dsDNA to $\sim$95% of its contour length. The higher flexibility of ssDNA gives rise to a very compact conformation with an increased entropic force so that the extension per base pair is shorter than that of dsDNA, for forces smaller than 6 pN (Fig. 11.29). At higher forces, the situation is reversed because a single strand is not constrained to follow a helical path, so ssDNA becomes nearly twice as long as dsDNA [11.74].

11.3.2 From Elasticity to Enzymology

The different elastic properties of ssDNA and dsDNA have allowed researchers to observe replication of single DNA molecules (see [11.74]). In these studies, a molecule of ssDNA was stretched and a DNA polymerase was allowed to

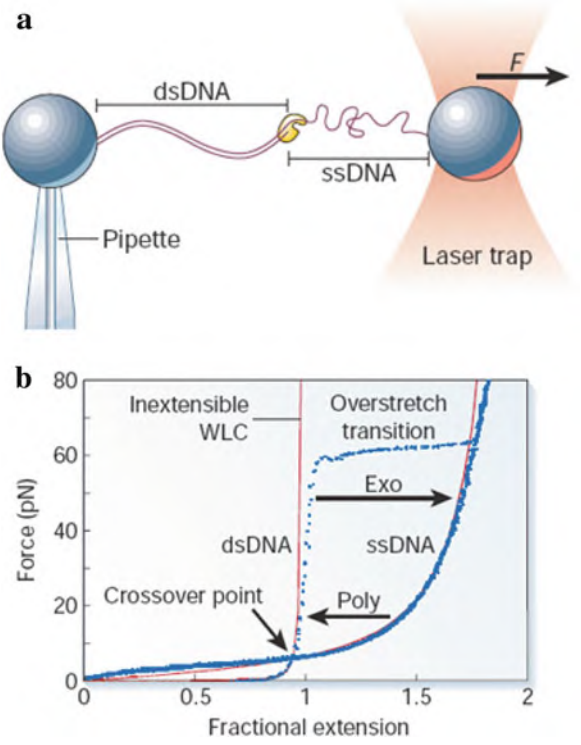

Fig. 11.29 (**a**) A DNA molecule is stretched between beads held in a micropipette and a force-measuring optical trap. The measured extension is the sum of contributions from the single-stranded DNA (ssDNA) and double-stranded DNA (dsDNA). (**b**) Force versus extension for ssDNA and dsDNA obtained with the instrumentation in (a). *Arrows* show changes in extension observed at constant tension during polymerization (Poly) or force-induced exonuclease (removal of nucleotide sections from the DNA) activity (Exo). (Reprinted with permission from [11.74]. © 2003 Nature Publishing Group.)

replicate the stretched molecule at given tension. As the ssDNA was converted into dsDNA by the polymerase, the replication process could be followed by monitoring the extension (below 6 pN) or contraction (above 6 pN) of the molecule (see Fig. 11.29).

The force-extension behavior of single supercoiled DNA molecules can further elucidate enzyme efficiency by performing elasticity measurements. By the rotation of a bead attached to a stretched DNA molecule, a torsional strain can be applied to this molecule (Fig. 11.30a) which finally gives rise to buckling and the formation of plectonemes (DNA units projecting out of the molecular axis) and reduces the apparent extension of the molecule. By the activity of the enzyme topoisomerase II, which is known to relax supercoils in eukaryotic cells [11.74], the extension of a single supercoiled DNA molecule is step-wise increased (Fig. 11.30b). The size of these steps corresponds to the removal of two DNA turns by cutting the molecule (Fig. 11.30c) so that the helix is passed through itself and finally resealed. It has been additionally shown in single-molecule studies that the topoisomerase IV enzyme has a chiral substrate specificity: it relaxes overwound DNA more efficiently than underwound DNA. This makes the enzyme relax the supercoils forming during replication while avoiding counterproductive relaxation in non-replicating DNA [11.74].

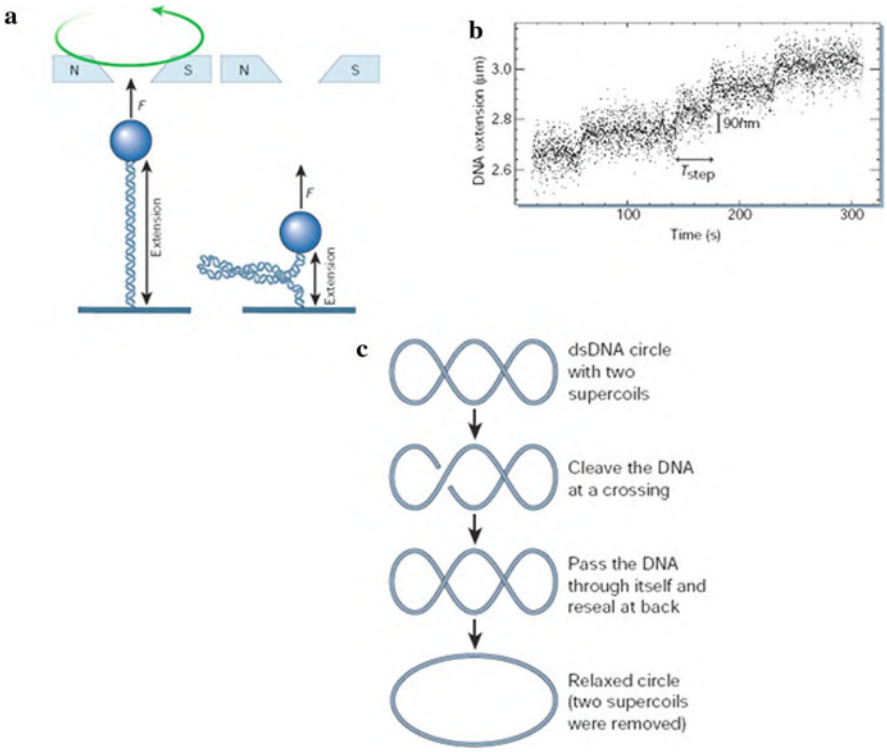

Fig. 11.30 The elastic behavior of supercoiled DNA molecules for single-molecule topoisomerase enzyme assays. (**a**) Molecules are stretched and twisted in magnetic tweezers until the DNA molecule buckles and forms plectonemes, shortening the apparent extension. (**b**) Under addition of topoisomerase II to plectonemed DNA molecules, 90 nm steps appear in the extension, corresponding to the removal of two turns as discussed by the model in (**c**). (**c**) Model of the topoisomerase II action. The enzyme cleaves both strands of the supercoiled DNA and passes the double helix through itself, leading to the removal of two turns. (Reprinted with permission from [11.74]. © 2003 Nature Publishing Group)

11.3.3 Unzipping of DNA

During replication the enzyme DNA helicase must generate force to unzip the parental DNA strands. In single-molecule studies the forces for mechanical separation were measured (see Fig. 11.31) for poly (dG-dC) DNA to $F_{G-C} = (20 \pm 3)$ pN and for poly (dA–dT) DNA to $F_{A-T} = (9 \pm 3)$ pN [11.75]. These forces can be ascribed to the difference in the stabilities of the triple hydrogen bonds of the guanine–cytosine base pair or the double hydrogen bond of the adenine–thymine base pair, respectively. By this type of experiments the helicase function might be studied directly [11.74].

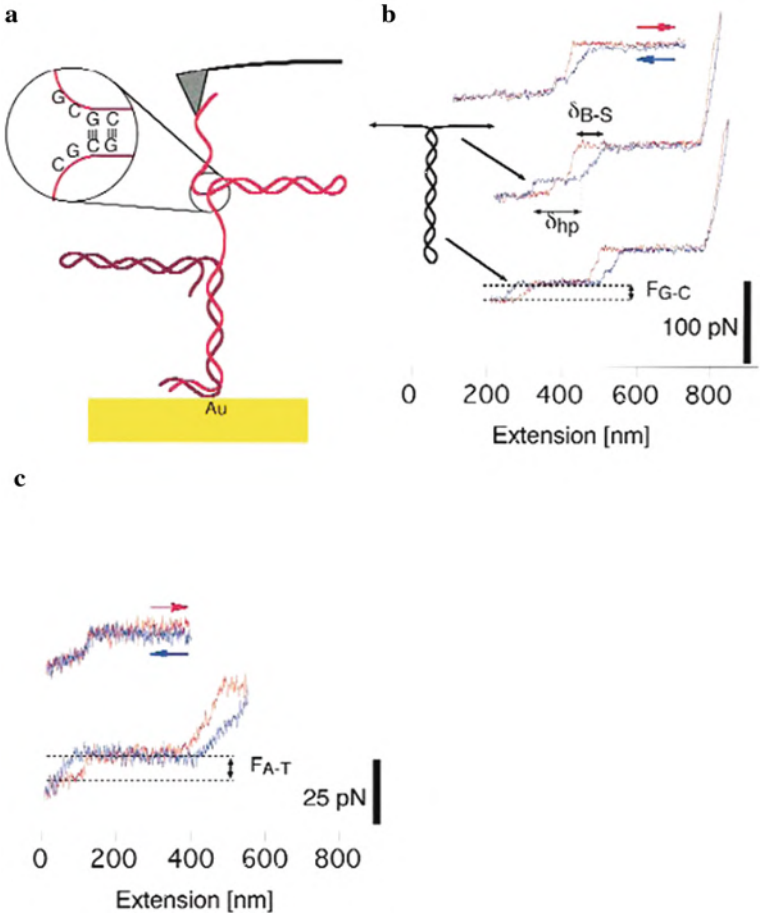

Fig. 11.31 (**a**) Measurement of the force between the base pairs of DNA. (**a**) Measuring principle in the atomic force microscope (AFM). (**b**) The steps in the stress–strain curve of a poly (dG–dC) DNA molecule with triple hydrogen bonds yield the binding force $F_{G-C} = 20$ pN (*bottom curve*). (**c**) For poly (dA–dT) DNA with double hydrogen bonds the binding force $F_{A-T} = 9$ pN is determined. (Reprinted with permission from [11.75]. © 1999 Nature Publishing Group)

11.3.4 Protein Mechanics

Proteins perform an array of tasks in living cells, from signal transduction to metabolic and catalytic functions, and mechanical support (see [11.6]). Proteins consist of 20 different amino acids (Fig. 11.32a) arranged in a specific polypeptide sequence (Fig. 11.32b). Hydrogen bonding leads to the formation of secondary structures, such as α-helices and β-sheets (Fig. 11.32c, d) which fold to globular domains due to short-range forces such as hydrophobic, electrostatic, van der

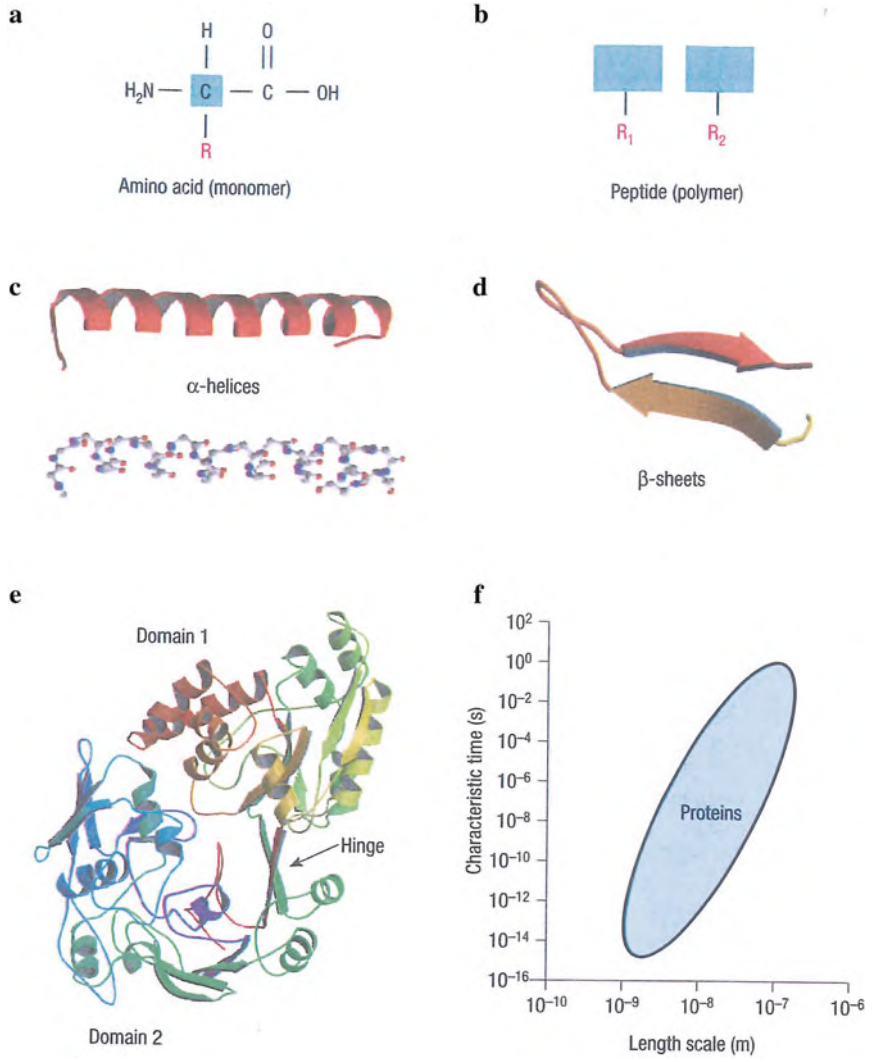

Fig. 11.32 Basic structural features, characteristic length, and timescales of proteins. (**a**) Protein structures are constructed from 20 different amino acids. A monomer of an amino acid with a side-chain labeled R. (**b**) A short peptide comprising two different amino acids yielding 20^2, or 400 possible sequences. (**c**) α-Helices and (**d**) β-sheets form proteins' secondary structure. (**e**) The 3D protein structures consist out of globular structures formed by the secondary structures. (**f**) The characteristic timescales for protein motion and deformation span from 1 s to 10^{-10} s. (Reprinted with permission from [11.6]. © 2003 Nature Publishing Group)

Waals, and hydrogen bonding (Fig. 11.32e) with size of 1–100 nm. Proteins in a cell undergo continuous motion and structural changes on 5 nm (domains) to 0.05 nm (single atom) scales over a wide range of timescales (10^{-15}–10^{0} s; Fig. 11.32f). Protein molecules can form domain hinge motion in cells with significant biological implications. The molecular motor myosin "moves" on an actin filament by generating hinge motion of its head, where as the rotation of the γ-submit of the F_1-ATPase might be driven by the hinge motion of the β-subunit (see [11.6]). Such as proteins can transform from a biologically active state to a denatured of

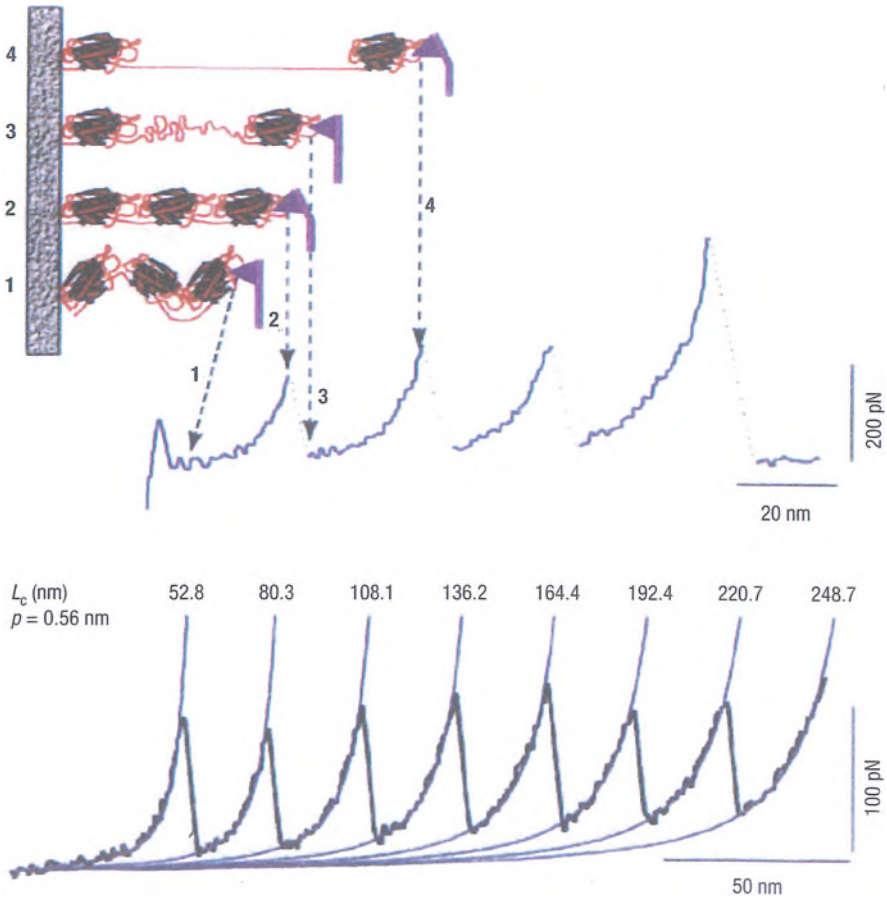

Fig. 11.33 Deformation and unfolding of a multidomain protein when stretched by an AFM. The sawtooth pattern corresponds to a sequential deformation and unfolding of individual domains. When the distance between the substrate and the cantilever increases (1–2) the force increases and the protein elongates. When a domain unfolds (3) the elongation of the protein reduces the force almost to zero. Further extension again stresses the cantilever (4). The consecutive domain deformation of the molecule (recombinant human tenascin C) obeys the worm-like chain (WLC) model with the persistence length fixed to 0.56 nm and the contour length L_0 for each peak adjusted as shown. (Reprinted with permission from [11.6]. © 2003 Nature Publishing Group)

inactive state in response to small changes in temperature or pH of the surroundings, the application of mechanical forces can lead to protein domain deformation and unfolding (Fig. 11.33). By these mechanical studies the force for, e.g., unfolding a protein domain can be measured specifically [11.76, 11.77].

11.4 Molecular Motors and Machines

Life implies movement. Motion in biology is a cascade of mechanical transduction processes, from the molecular scales of time and length upwards, which are powered by tiny protein machines known as molecular motors. Among the best known are motors that use sophisticated intramolecular amplification mechanisms to take nanometer steps along protein tracks in the cytoplasm. Three types of cytoplasmic motors are known (see [11.15, 11.78, 11.79]): myosins, which move on actin filaments, and kinesins, and dyneins, which use microtubules as tracks (see Fig. 11.34). In all three motor classes, ATP hydrolysis causes a conformational change in a globular motor domain that is amplified and translated into movement with the help of accessory structural motifs. These motors transport a wide variety of cargo, power cell locomotion, drive cell division and, when combined in large ensembles, allow organisms to move. Motor defects may lead to severe diseases or may even be lethal. The basic principles of these motors and of the rotational ATPase nanomachine synthesizing ATP will be presented below.

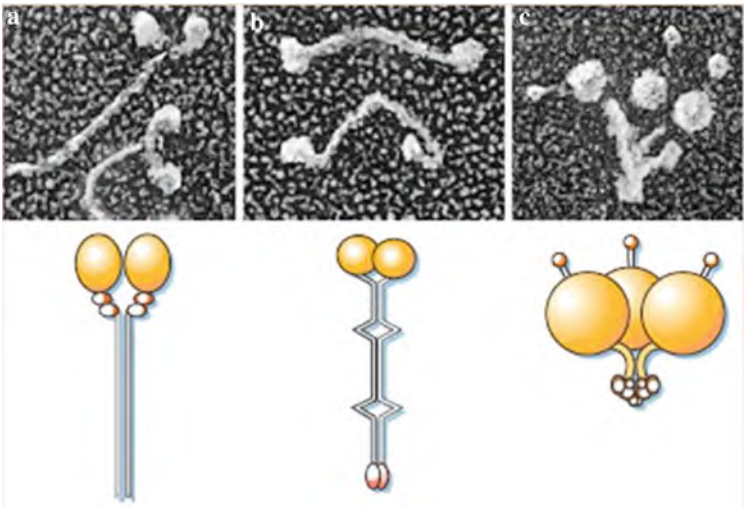

Fig. 11.34 Cytoskeletal motors. (**a**) Myosin II; (**b**) conventional kinesin; (**c**) ciliary dynein. *Top panel*: cryoelectron micrographs of rotary-shadowed single molecules. *Bottom panel*: schematic overviews. The diameter of the myosin II motor domains (*yellow*) is about 15 nm with the associated proteins (*brown*). Coiled-coil domains are represented by parallel *black lines*. (Reprinted with permission from [11.79]. © 2003 Nature Publishing Group)

11.4.1 Myosin

The myosins are a large family of molecular motors, where the human genome includes about 40 myosin genes.

Myosin V is an actin-based molecular motor that has a key function in organelle and messenger RNA (mRNA) transport, as well as in membrane trafficking. This motor was the first member of the myosin superfamily shown to be processive, meaning that a single motor protein can "walk" hand-over-hand along an actin filament for many steps before detaching. The active state is extended whereas the inactive state is compact (see [11.80]). Each myosin V molecule consists of two heads (see Fig. 11.35) that contain an amino-terminal motor domain followed by a lever-arm, a coiled-coil dimerization domain (S2), and a carboxy-terminal globular cargo-binding domain. After ATP hydrolysis (see [11.15]), the loss of the phosphate group from ATP leaves a space of approximately 0.5 nm, which is thought to cause a rearrangement of structural elements flanking the ATP-binding site. The rearrangement in this first level of amplification is coordinated with structural changes in the actin-binding site. The next level of amplification involves the communication of the initial conformational change in the active ATP site

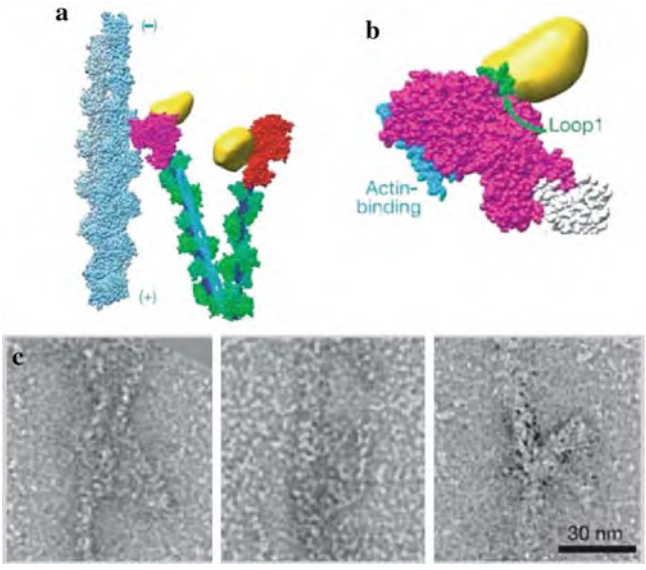

Fig. 11.35 Orientation of the myosin V inhibited structure on actin from *Spodoptera frugiperda* (Sf9) cells. (**a**) Only one myosin V head can be docked to the actin strand, rendered *light-blue* and *gray*. The unbound head extends up to the viewer. (**b**) Cargo-binding domain (*yellow*) on the motor domain (*magenta*) are rendered in a space-filling representation. The ATP-binding region and Loop1 are colored *green*. A decrease in the flexibility of Loop1 may decrease ADP release rates and the direct binding of the cargo binding domain to Loop 1 could stabilize its motion and decrease ADP release rates, thus accounting for the decreased ATPase activity of the folded monomer. (**c**) High-magnification electron micrographs of actin-bound myosin V molecules. (Reprinted with permission from [11.80]. © 2006 Nature Publishing Group)

to an α-helix mechanical amplifier which swings through an angle of up to 70°, presumably the ultimate cause for the working stroke and stepping of the motor molecule. It is proposed that the myosin V motor after cargo delivery returns to its starting position for rebinding cargo by an actin treadmilling and recycling process. Myosin V cargo delivery would then be akin to delivering a package by "running up the down escalator." Once the cargo has been delivered to the actin end, myosin V need only remain on the actin, which is facilitated by a conformation which inhibits ATP turnover but not actin binding. The treadmilling process on actin will eventually deliver myosin V to the other actin end where new cargo binding can unfold and activate the molecular motor.

Myosin II motor molecules are the constituents of the thick filaments of muscle. The α-helical coiled-coil myosin tails (see Fig. 11.34a) of the molecules form the backbone of the thick filament (see Fig. 11.36a), whereas the two heads of each molecule lie on the surface of the thick filament, where they can interact with the actin thin filament subunits (see [11.15]). Muscles relax when this interaction is blocked by molecular switches on either or both filaments. The structure of the relaxed myosin II thick filament of tarantula spider muscles has been studied by cryoelectron microscopy [11.81]. The repeating motif, occurring on the surface of the filament at axial intervals of 14.5 nm (Fig. 11.36a), represent a pair of myosin heads with a helical repeat of 43.5 nm. The filament backbone comprises 12 parallel strands, each ∼4 nm in diameter (and therefore containing more than one 2 nm diameter myosin tail), centered at a radius of ∼8 nm from the filament axis. This study shows intramolecular interactions between the two motor heads of the relaxed motor molecule (green and blue in Fig. 11.36b, c), between the motor heads and the thick filament backbone, and intermolecular interactions between the motor heads of adjacent molecules. These interactions may inhibit both the interaction of the relaxed myosin II motor molecules with the actin filaments and their ATPase activity. On activation of muscle, Ca^{2+} is released into the cytosol, increasing the thick filament activity by phosphorylation of the regulatory light chains (RLC in Fig. 11.36c). This breaks the bonds attaching the heads to each other and to the thick filament surface, such that they become mobile and disordered. They now can act independently of each other and are free to interact with the thin actin filament, leading to contraction.

Skeletal muscles and their rapid contraction enables vertebrates to run, walk, swim, or fly whereas involuntary movements such as heart pumping and gut peristalsis depend on the contraction of cardiac muscle and smooth muscles, respectively. All these forms of muscle contraction depend on the ATP-driven sliding of highly organized arrays of actin filaments against arrays of myosin II filaments (see [11.15]). The long thin muscle fibers consist of huge single cells where the bulk of the cytoplasm is made up of *myofibrils*, the basic contractile element with a diameter of ∼2 μm, which consists of tiny contractile units – called *sarcomeres*. Each sarcomere [11.15] is formed from thin actin filaments, thick myosin II filaments, and the spring-like titin proteins that give relaxed muscle its elasticity and which can unfold its immunoglobulin-like domains one by one as stress is applied. Muscle contraction can be activated by an incoming action potential which initiates Ca^{2+} flooding into the cytosol giving rise to the contraction of each sarcomere in the

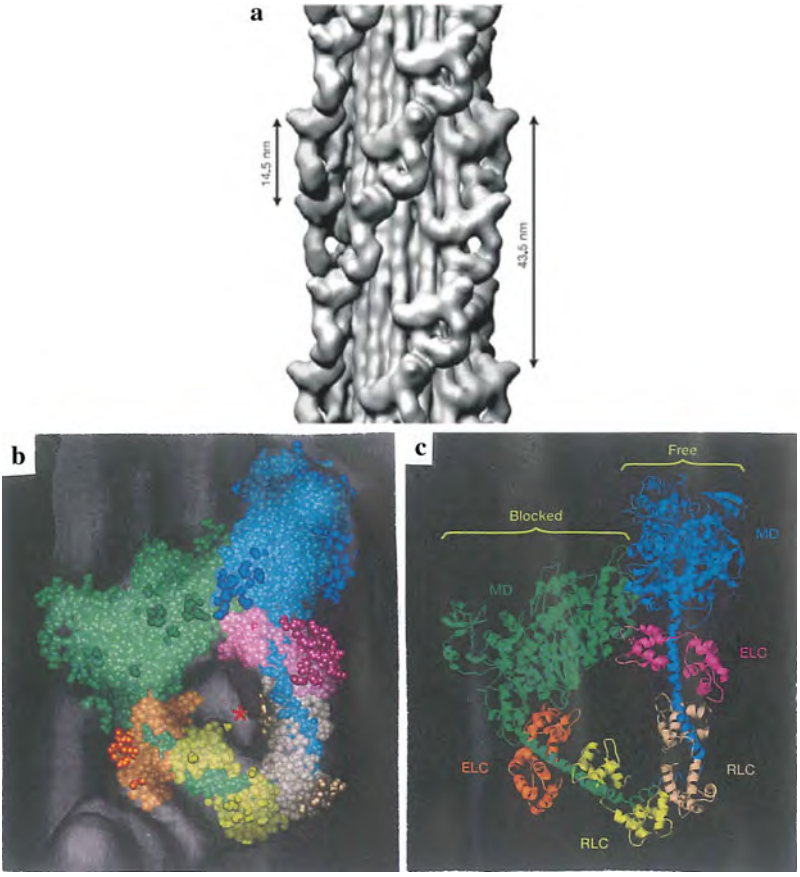

Fig. 11.36 Cryoelectron tomography of tarantula spider myosin II thick filaments. (**a**) Surface view of the 3D tomography reconstruction with the repeating motif, representing a pair of myosin heads with the shape of a tilted J. The filament backbone lying beneath the heads consists of subfilaments spaced ~4 nm apart and running parallel to the filament axis. (**b**) Best fit of the atomic structure of a relaxed pair of myosin II heads (space-filling model). (**c**) Ribbon presentation of the atomic structure from (**b**) showing the motor domains (MD), the essential light chains (ELC), and the regulatory light chains (RLC) of the blocked and the free heads, respectively. (Reprinted with permission from [11.81]. © 2005 Nature Publishing Group)

cell. Each myosin II thick filament has about 300 heads and each head cycles about five times/s in the course of rapid muscle contraction – sliding the myosin and the actin filament past one another at rates of up to 15 μm/s with a sarcomere length shortening by 10% in less than 20 milliseconds. Thus, muscle contraction consumes enormous amounts of ATP by two processes: filament sliding, driven by the ATPase of the myosin motor, and Ca^{2+} pumping, driven by the Ca^{2+} pump. The rapid synchronized shortening of the sarcomeres gives skeletal muscle the ability to contract rapidly for running or flying, and even for playing the piano [11.15].

11.4.2 Kinesin

Kinesin is a protein motor that ferries membrane-bound packages around cells. It can carry a packet of neurotransmitter from the human spine to the tip of a finger in about 2 days – a trip that would take a thousand years if left to simple diffusion [11.82]. Conventional kinesin is a two-headed motor (see Fig. 11.34) that moves along microtubules in the cytoskeletal scaffolding in 8 nm steps that match the repeat distance of the microtubule structure. There is fair insight into the molecular mechanisms underlying this process: Each step requires the hydrolysis of one molecule of adenosine triphosphate (ATP), the two kinesin heads move in a "hand-over-hand" fashion, and the movement stalls when the backward load exceeds ∼7 pN (see [11.82]). The head moves by unbinding in one hop within <50 μs [11.83]. By applying high loads to the kinesin it can be moved backwards, rather than simply being ripped from the microtubule. This reversal of moving is similar to that of a toy steam engine that can be made to run forward or backward by valve changes [11.82, 11.83].

Individual kinesin motors can be tracked in living cells by the imaging of conjugated single quantum dots [11.84]. Streptavidin-conjugated semiconductor quantum dots fluorescing at 655 nm were coupled to biotinylated conventional Drosophilae kinesins (QD-K). These QD-Ks were internalized into the cytoplasm of cultured mammalian HeLa cells (human epithelial cells) where the directed linear trajectories were observed in dependence of time (see Fig. 11.37) yielding a velocity of $v = 0.57 \pm 0.02$ μm/s similar to the in vitro motility [11.84].

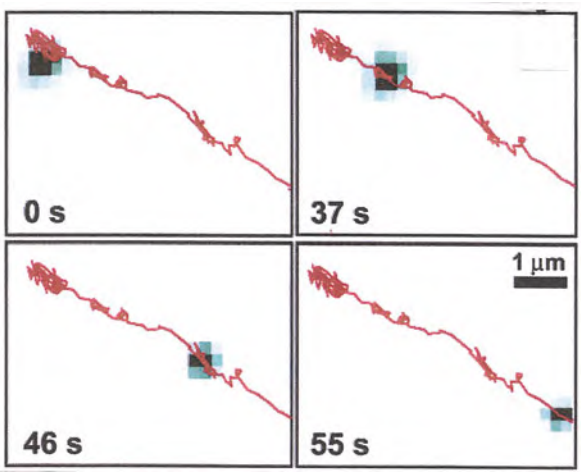

Fig. 11.37 Tracking of a single quantum dot – kinesin conjugate in a part of a human epithelial (HeLa) cell. (Reprinted with permission from [11.84]. © 2006 American Chemical Society)

Some details of the kinesin-1 walk or of the myosin V stepping have been elucidated by fluorescence resonance energy transfer (FRET) experiments [11.85] or by optical tweezer techniques [11.86], respectively.

11.4.3 Motor–Cargo Linkage and Regulation

Members of all three types of cytoskeletal motors are involved in organelle and vesicle transport. To understand these functions, one has to determine how motors link up to their cargoes and how transport is regulated [11.78]. In both processes, non-motor domains and associated proteins have a key role for a wide spectrum of attachment procedures (see Fig. 11.38). In some cell types, kinesin or dynein can latch onto their cargo via membrane proteins. In neurons, the kinesin light chains bind amyloid precursor protein (APP), a transmembrane protein of axonally transported vesicles. This link may be of medical significance as APP is the precursor of the amyloid plaques in patients with Alzheimer's disease (see Sect. 12.7). Impaired APP transport may well contribute to the development of the disease. The most wide-spread mode of association with cargo membrane proteins occurs via linker proteins (see Fig. 11.38a, b). Among the myosins, the motor–cargo linkage is characterized best. In pigment cells, the small GTPase Rab 27a and a Rab-binding protein, melanophilin, attach myosin V to melanosomes (see Fig. 11.38d and [11.15]).

From studies of motor–cargo association, the question of motor regulation in cellular transport arises. Transport activity can be regulated either by turning the motor on or off, or by inhibiting or promoting its association with cargo. In both mechanisms, phosphorylation plays a significant role [11.79].

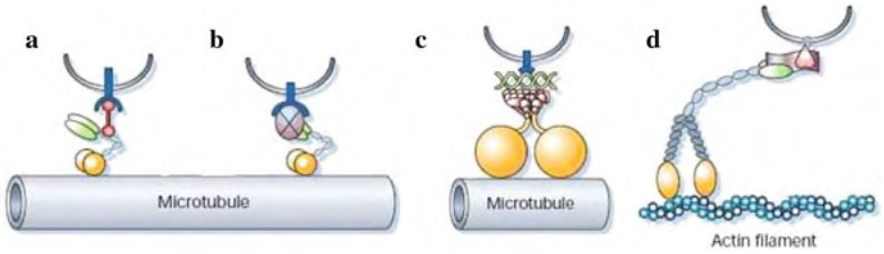

Fig. 11.38 Types of motor–cargo linkage. (**a**) Interaction between a transmembrane receptor and kinesin heavy chains mediated by a linker protein (red). (**b**) Interaction between a transmembrane receptor and kinesin light chains mediated by a linker complex (*purple*). (**c**) Interaction between cytoplasmic dynein and an integral membrane protein mediated by the dynactin complex (*red*) and spectrin (*green*). (**d**) Linkage of the tail domain of myosin V to membrane-anchored Rab 27a (*red*) via melanophilin (*purple*). (Reprinted with permission from [11.79]. © 2003 Nature Publishing Group)

11.4.4 Diseases

A number of molecular motors are involved in diseases such as, e.g., in myosin myopathies (myosin II), Griscelli syndrome (myosin V), hearing loss (myosin IIIa, myosin II, etc.), the photoreceptor degeneration (retinitis pigmentosa; cytoplasmic dynein), primary ciliary dyskinesia (axonemal dynein), polycystic kidney disease (dyneins and kinesins), Charcot–Marie tooth disease (Unc104 kinesin family), anthrax susceptibility (Unc104 kinesin family), or neurodegenerative diseases (kinesin, cytoplasmic dynein) [11.79].

11.4.5 ATP Synthase (ATPase)

ATPase, nature's smallest rotary motor, synthesizes ATP and, therefore, plays an important roll in energizing the cell and the whole organism. In 1997 P. D. Boyer and J. E. Walker were awarded the Nobel Prize in chemistry "... for their elucidation of the enzymatic mechanism underlying the synthesis of adenosine triphosphate (ATP)." This protein is a rotor with a diameter of ∼10 nm and a length of ∼25 nm with a shaft equipped with two parts – the enzymatic component F_1 in the cytoplasm and a hydrophobic F_0 component which is embedded in the membrane of the mitochondria, the power plants of the cell (see Fig. 11.39). The negatively charged F_0 section is a biological nanoturbine driven by a proton current from the exterior

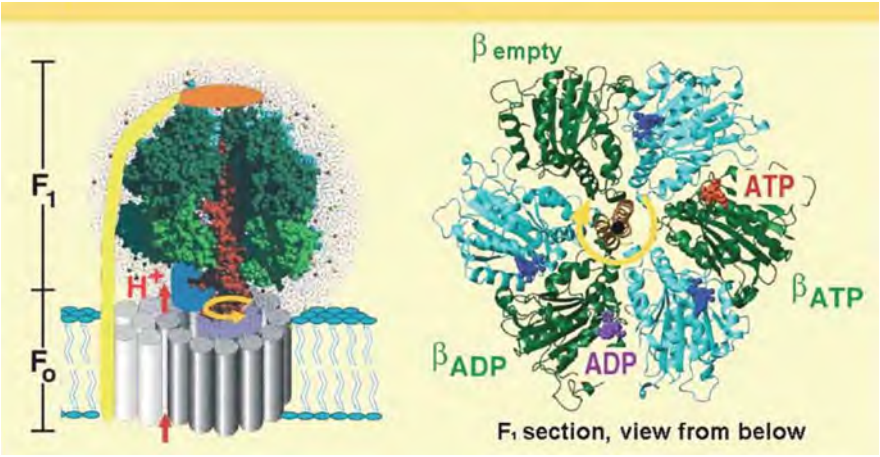

Fig. 11.39 Structure and functional principles of the ATPase enzyme. *Left panel:* a protein flux (*red arrows*) through the F_0 section gives rise to a rotation (*yellow arrow*) which is transferred by the shaft (*orange*) to the F_1 section where ATP synthesis occurs. *Right panel:* view of the F_1 section from below. In the course of the synthesis cycle one of the three β subunits is empty (*green*), one binds ADP and phosphate (*not shown*), and one contains the ATP reaction product. (Reprinted with permission from [11.87]. © 2006 Wiley-VCH)

to the interior of the cell (see [11.88]). The rotational motion of the ATPase motor has been demonstrated by mounting an actin filament on the F_1 section [11.89] from which a torque τ of $2\pi\tau = 3\Delta G$ can be derived where $\Delta G = 20\ k_B\ \tau$ is the energy difference between ATP and ADP. This indicates a high motor efficiency since three ATP molecules are consumed per one rotation.

Each cell contains some 100 ATPase molecules and as the human body contains some 10^{14} cells with each cell synthesizing 2×10^7 ATP molecules per hour the body produces about 70 kg of ATP daily or even a ton under high strain.

The F_0 component drives the rotation of the F_1 component with the three β subunits where ATP synthesis takes place (Fig. 11.39). One of the three β binding pockets of F_1 (see Fig. 11.39, right panel) is empty, one contains the starting molecule ADP, and one ATP as the synthesis product. The different binding strengths of the ADP and the ATP molecules in the different β pockets originate from the different conformations of these pockets which gives rise to ATP synthesis. The energy transferred by the rotating shaft initiates the release of the tightly bound ATP molecule from the pocket.

The atomic processes occurring during ATP synthesis in the enzymatic F_1 component when the ATPase shaft rotates have been studied by molecular dynamics computer simulation [11.87, 11.90] taking into account 200,000 atoms. In this "nanomechanical" process in the β subunits the tilting of the lower part of the subunit is transformed into a deformation of the ATP-binding pocket (Fig. 11.40). This

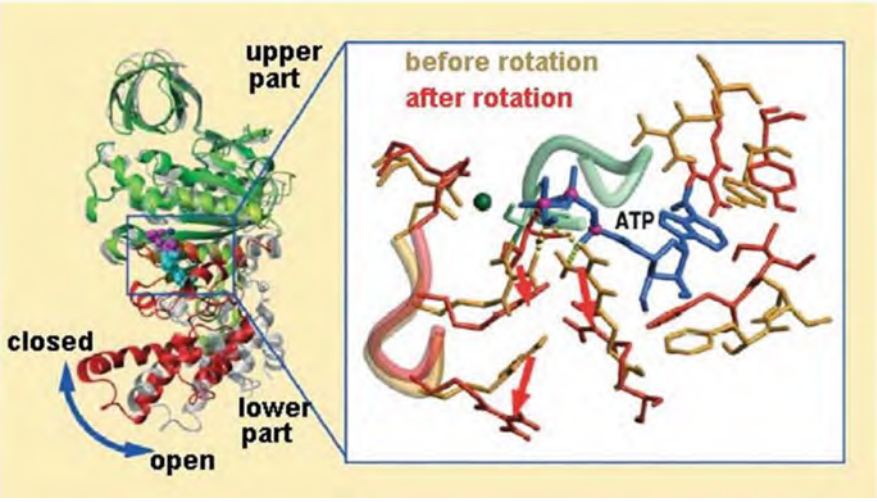

Fig. 11.40 Mechano-chemical energy conversion in the ATP-binding pocket of ATPase. *Left panel:* a tilt movement (*blue arrow*) of the lower part of the β subunit (*red* and *green*) originating from the shaft rotation is transferred to the ATP-binding pocket (*red arrows* in the *right panel*) giving rise to the release of the final ATP reaction product. *Right panel*: mechanically driven deformation of the binding pocket containing the ATP molecule (*blue*). (Reprinted with permission from [11.87]. © 2005 Wiley-VCH)

occurs by a sequence of structural changes where three positively charged amino acids (arginines) play a role. The movement withdraws them from the negatively charged ATP phosphate groups (see red arrows) which reduces the electrostatic attraction so that the ATP molecule can be released from the binding pocket. This behavior is similar to that of a combustion engine where the movements of the β subunits corresponds to the piston movement and the rotation of the molecular shaft to that of the crank shaft which synchronizes the mechano-chemical energy conversion. In fact, the ATPase motor has been mechanically forced by external electromagnets to rotate and generate chemical energy (ATP) [11.91].

11.5 Membrane Channels

Ion channels are nanometer-sized proteins with a seemingly simple task, but a highly sophisticated machinery – to allow the passive flow of ions across biological membranes. The dimensions of these channels are some 5 nm long and fractions of a nanometer wide. They must be highly selective for a particular type of ion, yet must also maintain high transport rates and be able to regulate ion flow by switching it on or off ("gating"). Ion channels are essential for important physiological processes such as sensory transduction, action-potential generation, and muscle contraction, to name just a few. When their function goes away, there can be serious consequences, including life-threatening disease (see [11.92]). In 1998 the first crystal structure of a bacterial potassium channel was revealed [11.93] with rapid progress hereafter, for which R. MacKinnon won a Nobel chemistry prize in 2003. Here, we will give an overview of the structures and dynamics of the K^+ and the Ca^{2+} channels, the Cl^- channel, the characteristics of the aquaporin water channel, which was discovered by P. Agre who shared the Nobel chemistry prize in 2003, and the main features of protein channels.

11.5.1 The K^+ Channel

Potassium (K^+) channels are important membrane-spanning proteins that catalyze the ionic movements required to generate electrical signals in nerve cells, where the K^+ concentration in the cell is about 30 times higher than outside. For structural studies of the K^+ channel proteins, clearly diffracting crystals are required. This could be helped by the use of a highly efficient system for expressing K^+ ion channels in bacteria [11.94] for large amounts of protein and by nibbling away the channel proteins' disorderly tops and tails – not essential to channel function – by means of enzymes [11.93]. The x-ray structure of the K^+ channel protein [11.93] revealed the molecular design of these channels (Fig. 11.41a) with a high selectivity and a rapid throughput that allows K^+ to pass at high rates, while the channel simultaneously acts as a concrete wall to the smaller Na^+ ion. This structure demonstrates the molecular specificity (Fig. 11.41b, c): a narrow, 1.2 nm long, [11.96] "selectivity

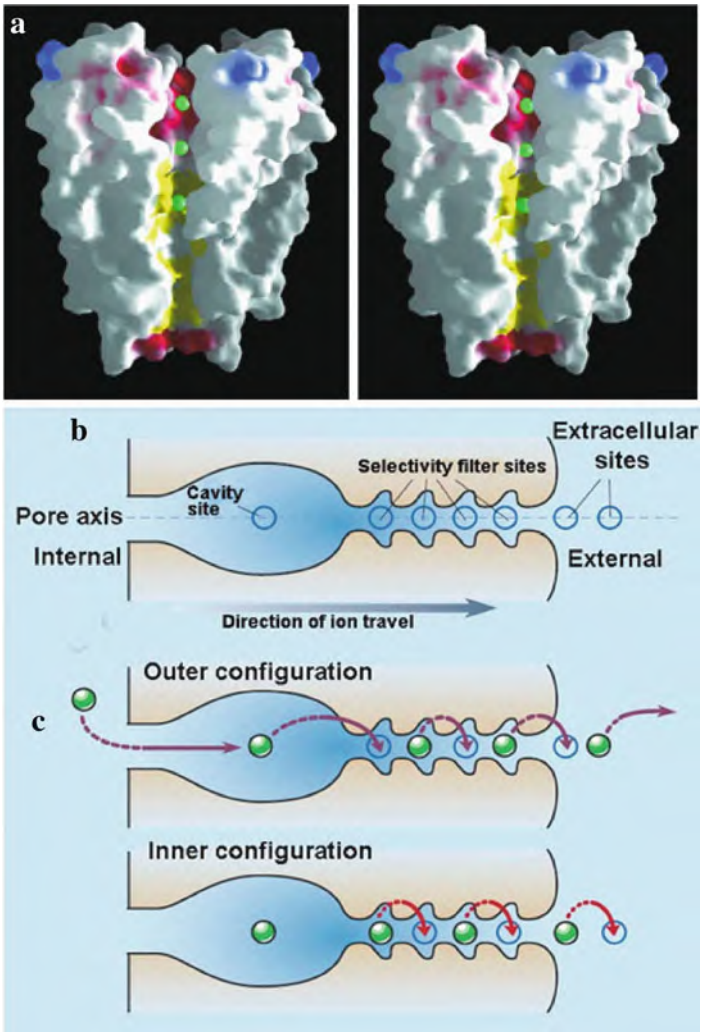

Fig. 11.41 Stereomolecular structure of the *Streptomyces lividans* bacterial K^+ channel and mechanism of the K^+ permeation. (**a**) A cutaway stereoview displaying the solvent-accessible surface of the tetrameric K^+ channel with the length of the selectivity filter (upper two *green* spheres) of ~1.2 nm, a total length of the channel of 4.5 nm, and the channel 1.0 nm wide in the middle of the channel. The surface coloration varies smoothly from blue in areas of calculated high positive charge through *white* to *red* in negatively charged regions. The *yellow* areas of the surface are colored according to carbon atoms of the hydrophobic side chains of protein residues in the inner vestibule. The *green* spheres represent K^+ ion positions in the conduction pathway [11.93]. (**b**) There are seven sites for K^+ ions along the channel axis: one in the cavity site, four in the selectivity filter, and two just beyond the external end of the channel. The cavity site is fully occupied, but (see **c**) only half of the remaining six are occupied at any one time. (**c**) The two main ion configurations (outer and inner) that are postulated to exist within the channel. *Purple arrows* indicate ion shifts that are linked directly to concerted ion entry into and exit from the pore with *red arrows* indicating K^+ shifts within the selectivity filter. Ion passage through the filter and extracellular sites occurs in a bucket-brigade fashion. (Reprinted with permission from [11.95]. © 2001 Nature Publishing Group)

filter" in the shape of an oxygen-lined electronegative tunnel in which dehydrated K^+ (but not Na^+) fits precisely. This structure rationalizes why a K^+ ion is so willing to leave the aqueous solution to enter the channel in a dehydrated form: the channel interior mimics the embrace of the water molecules in the hydration shell of the ion in solution. Subsequent experiments [11.97, 11.98] and simulations [11.99] showed how ions are coordinated in the filter; they reveal the K^+ ion transit from the channel into the aqueous solvent; and they indicate the character of water in the cation's inner hydration shell. In contrast to enzymes, channels process several substrate ions simultaneously in bucket-brigade fashion. The four filter sites (Fig. 11.41c) are not all occupied simultaneously, but a pair of K^+ ions separated by a single water molecule shifts in a concerted fashion between two configurations within the filter – inner and outer – occupying each about half the time (Fig. 11.41c). When the K^+ ion enters the channel from the solvent, it is coordinated in front by four carbonyls reaching outward from the channel, and behind by solvent; this is the "dehydration transition state" in which the ion sheds its water while entering the pore (see [11.95]). Simulations [11.99] predicted the K^+ ion right at the two sites where it is seen by x-rays. The K^+-binding configurations and the transition between them (Fig. 11.41c) are energetically similar, so that the entire conduction process is barrier-less and very rapid.

In addition to the channel structure, the hydration shell of the aqueous cation was determined in the channel's central cavity containing ~50 water molecules (see [11.95]) with the oxygens of eight water molecules packed against the K^+ ion at the corners of a twisted cube. This closely matches the arrangement of the K^+-coordinating oxygen in the selectivity filter which means that a flat energy landscape is traversed by the K^+ ions on their trip from one side of the membrane to the other.

Opening and closing mechanisms are necessary for most ion channels in addition to selectivity in order to respond by conformational changes to metabolic cues. From the structure of the Ca^{2+}-gated K^+ channel of the *Methanobacterium thermoautotrophicum* [11.100] in the closed and in the open K^+-channel versions [11.100, 11.101] a model for gating is offered (see [11.96]). At the interface of the channel with the cytoplasm inside the cell, protein bundles come together like an inverted tepee, with eight domains forming the RCK ("regulates conduction of K^+") gating ring which makes up the physical gate of the channel (see Fig. 11.42). This is just located beneath the membrane cavity and the selectivity filter. In the crystal structure, two Ca^{2+} ions are clearly positioned at clefts between two RCK domains. The Ca^{2+} binding presumably reshapes the clefts, expanding the diameter of the gating ring and exerting a force on the attached channel-lining helices that opens the channel (see Fig. 11.42b). In this way the bacterial channel proteins use the chemical Ca^{2+} binding energy to perform the mechanical work of gating.

11.5.2 The Ca^{2+} Channel

Communication between and within cells is essential for the development and survival of any complex organism. Cells converse with each other through neurotransmitters and hormones that impinge on the cell surface, generating further

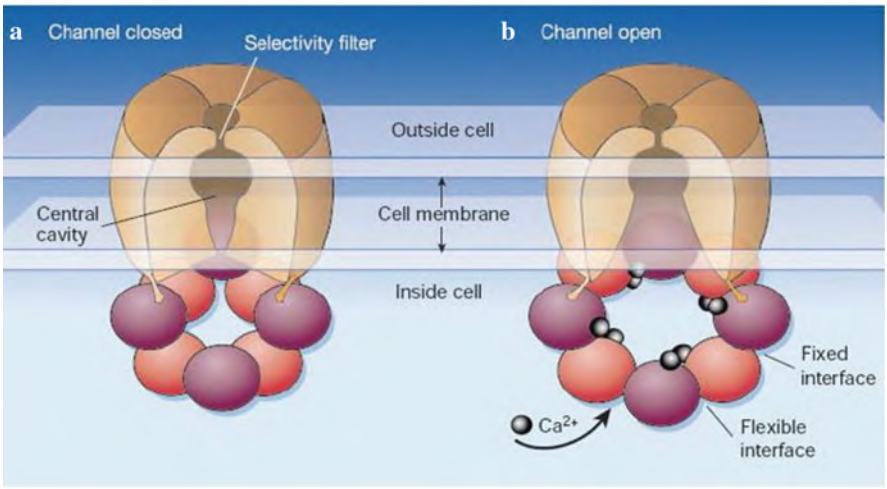

Fig. 11.42 Model for the gating and opening of a bacterial Ca^{2+} gated K^+ channel, based on structural studies [11.100, 11.101]. (**a**) Closed conformation, (**b**) open conformation. Three of the four subunits of the K^+ channel are shown in *brown*. The *purple* and *red* circles represent the eight RCK ("regulates conduction of K^+") domains, which, after binding Ca^{2+}, are thought to reorientate with respect to each other, causing changes in the pore (opening) in the center of the channel. (Reprinted with permission from [11.96]. © 2002 Nature Publishing Group)

signals (second messengers) within the cell which initiate appropriate responses. The most ubiquitous of the second messengers is the calcium ion. An essential component for the regulation of the intracellular Ca^{2+} concentration has been discovered by the forensic precision of molecular genetics [11.102, 11.104]. A sharp rise in intracellular Ca^{2+} concentration can stimulate neurotransmitter release, muscle contraction, cell metabolism, cell growth, or cell death. A primary route for Ca^{2+} influx is the CRAC (for Ca^{2+} release-activated channel) which is activated by a fall in Ca^{2+} within the endoplasmic reticulum. Despite their biological and clinical importance, very little about these channels, let alone their molecular composition, are known. Recently the protein Orai1 (encoded by the human gene *FLJ 14466*) has been identified as being fundamental to the activation of the Ca^{2+} influx channel [11.102, 11.103], although it is not yet clear whether this could be the elusive CRAC channel. The possible roles of Orai1 in the CRAC Ca^{2+} channel mechanism, either being the entire channel, an indispensable subunit of a multimeric channel complex, or a key component of the activation mechanism, are depicted in Fig. 11.43. It is not even clear, whether the CRAC complex is a channel through which ions would flow passively when it is open, or a transporter that uses energy to move ions across the membrane. In any case, the recent progress will improve the prospects for developing therapeutic agents aimed at combating the growing list of human diseases associated with aberrant store-operated calcium influx [11.105].

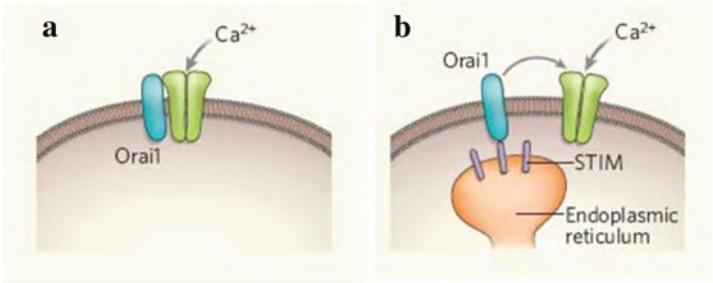

Fig. 11.43 Possible roles of the protein Orai1 in the Ca^{2+} release-activated channel (CRAC – Ca^{2+} release activated channel) mechanism for Ca^{2+} influx into the cell. The protein Orai1 is an important component of the CRAC mechanism. It could be the channel itself (not shown) or (**a**) a regulatory subunit of a multimeric CRAC channel complex or (**b**) an adapter protein coupling the depletion of the intracellular endoplasmic reticulum Ca^{2+} store to the opening of the CRAC channel. (Reprinted with permission from [11.104]. © 2006 Nature Publishing Group)

11.5.3 The Chloride (Cl^-) Channel

Some mammalian chloride channels (CLC) are found in the plasma cell membrane. Intracellular Cl^- channels may counterbalance electric current produced by proton pumps, and mutations of the Cl^- channel ClC-5, e.g., impair the transport of normally acidic vesicles in a kidney disease [11.106].

The crystal structure x-ray studies of bacterial CLC proteins allows peptide helices, amino acid side chains, and even the Cl^- ion within the channel to be identified (Fig. 11.44). The Cl^- channel is double-barreled – in contrast to the single-barreled K^+ channel (Fig. 11.44). It contains two proteins contracting each other with a broad interface formed by four helices from each protein and it is tilted rather than perpendicular to the membrane (Fig. 11.44b), both surrounded by protein helix dipoles of opposite charge. It may be mentioned here that the aquaporin water channels (see text below) are quadruple-barreled, where the physiological advantage having several pores is not clear [11.108]. Just above the chlorine binding site of the Cl^- channel (see Fig. 11.44b) there is located a negatively charged side chain of glutamate amino acid which is expected to hinder transport severely. It is speculated that this side chain acts as a gate [11.107], swinging out to open the channel. From the R helix (Fig. 11.44b) a carboxy-terminal end sticks out into the cell which is thought to transduce intracellular events into channel gating.

11.5.4 The Aquaporin Water Channel

Water channels span cell membranes in our kidneys, eyes, or sweat glands. Although water molecules can diffuse through cell membranes, in some parts of the body – notably the kidneys, which filter nearly 200 l of water a day – diffusion is too slow, suggesting a protein pore for water transport. The transport of water

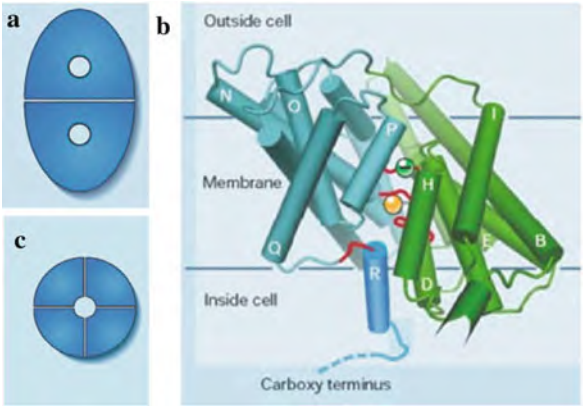

Fig. 11.44 Sketches of channels with different numbers of pores and x-ray structure of a bacterial chloride (Cl^-) channel. (**a**) Chloride channels are dimers, on which each subunit has its own pore. (**b**) Side view of the chloride channel structure derived from crystal x-ray diffraction [11.107, 11.108]. α-Helical structures are indicated by cylinders, colored in *green* and *cyan* to indicate the two repeat units. Regions involved in the formation of the ion-permeation pore are in *red*. A negative charge that might be involved in gating the channel is shown as a *green* sphere just above the site of the chloride ion (*yellow*). The amino terminus of the R helix (*bright blue*) contains a tyrosine amino acid, which helps to coordinate the Cl^- ion [11.107, 11.108]. (**c**) Cross-section of a tetrameric K^+ channel where a single pore is formed by four identical subunits. (Reprinted with permission from [11.108]. © 2002 Nature Publishing Group)

through a 28 kDa channel protein was demonstrated by experiments on genetically modified cells [11.109] and by fluorescence experiments on liposomes [11.110] conducting water 10–100 times faster when they contained this protein. By cryo-electron microscopy the structure of the water channel protein (aquaporin) could be determined (Fig. 11.45). This structure resembles a square cake with equal square quarters and in the center a vertical channel. This channel is highly selective. Because of the 0.3 nm width at its narrowest point, the channel is a mere 0.02 nm wider than the water molecule. Such a narrow opening explains why larger molecules cannot go through and protons are prevented from passing the channel by a particular mechanism [11.111]. Defects in aquaporins can cause a rare form of diabetes or brain aquaporins could play a role in dropsy. Thus the discovery and characterization of the aquaporin protein could answer many of these physiological problems (see [11.111]).

11.5.5 Protein Channels

Cellular proteins have to be transported – after synthesis in the cytosol – through phospholipid membranes to their final destinations, which might be intracellular compartments or, following secretion, outside the cell. The proteins are moved across the membranes through a protein channel which must change shape to

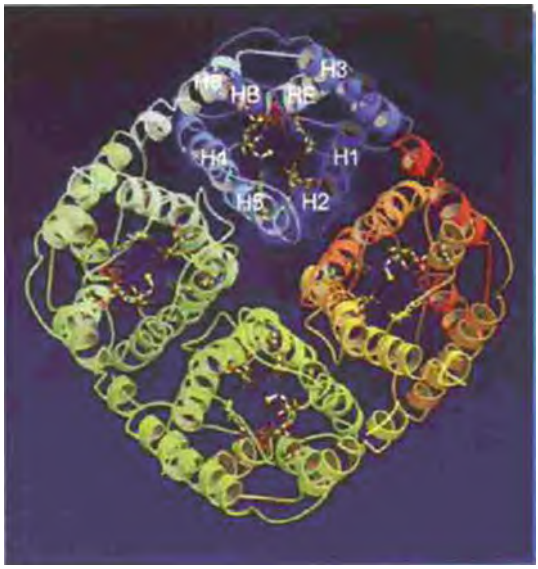

Fig. 11.45 Aquaporin-1 water channel in ribbon presentation, looking down the central channel. The eight α-helices that make up each of the tetramer's four subunits are designated H1-H8. (Reprinted with permission from [11.111]. © 2003 American Institute of Physics)

allow proteins to pass [11.112]. This translocation process has been shown to involve a heterotrimeric protein, or translocase according to biochemical, genetic, and biophysical studies (see [11.113]). The x-ray crystal structure of the translocase SecYEβ from the single-celled archaebacterium *Methanococcus jannaschii* provided an initial view of this channel [11.112]. Earlier studies had shown that newly made proteins ("preproteins") have an extension at one end, called signal peptide, directing them to different membrane-bounded compartments or channels [11.114, 11.115].

Ion channels have received attention because of their specificity, but the protein channel is more complex in that it must allow the passage of chemically and sterically varied substrates. So the pore of the channel seems likely to expand just enough to accommodate larger protein segments without compromising the integrity of the osmotic seal. According to the x-ray crystal structure studies [11.112] the channel's pore is located at the center of a single SecYEβ heterotrimer (Fig. 11.46). For the translocation of a secretory protein the following model is suggested (Fig. 11.46b). In the closed-state SecYEβ channel structure, the channel exit is initially plugged by a short α-helix (a canonical structural feature in proteins) which is moved out of the way during protein translocation. After the removal of this α-helix, the channel has a limiting constriction of 0.3 nm (Fig. 11.46a) lined by a ring of inflexible isoleucine amino acids. This suggests that the dynamic resizing of the channel must be mediated by diaphragm-like movements of the constituent transmembrane α-helices of the SecYEβ heterotrimer, rather than changes in side-chain conformation. In this model, the channel's dynamics are modulated directly by the signal peptide of the preprotein being transported.

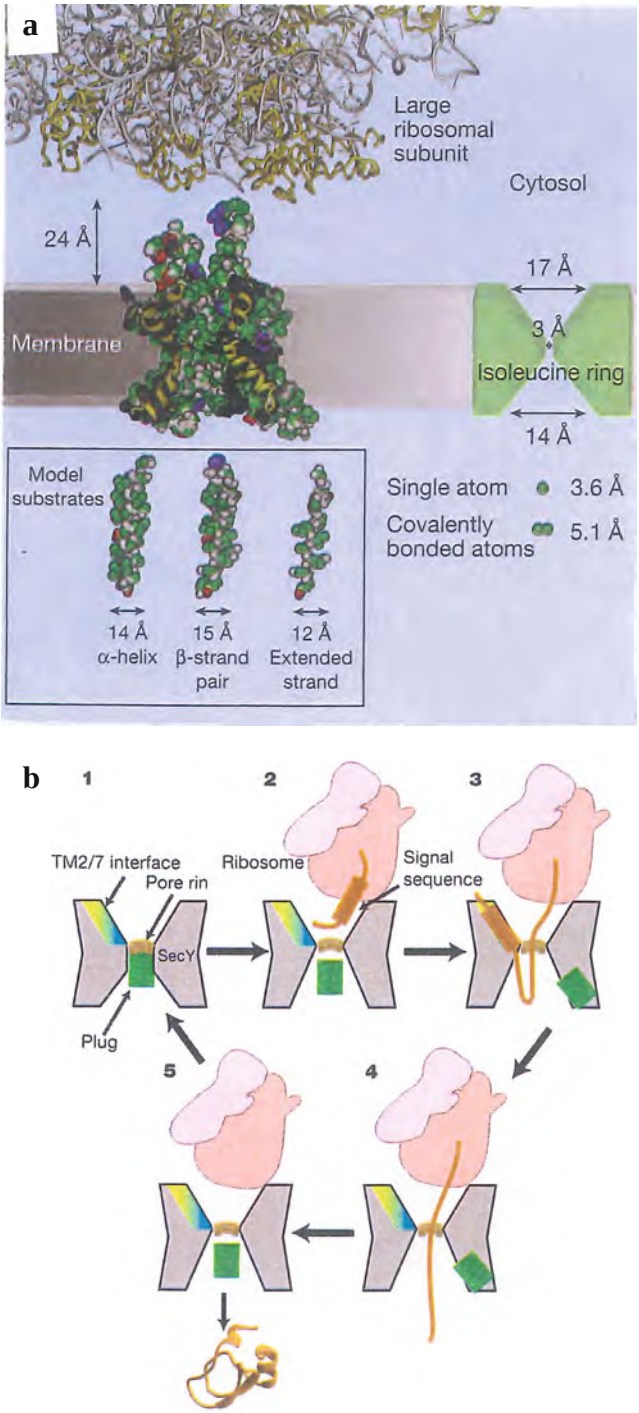
a
Large ribosomal subunit
Cytosol
24 Å
17 Å
3 Å
Isoleucine ring
14 Å
Membrane
Model substrates
14 Å α-helix
15 Å β-strand pair
12 Å Extended strand
Single atom 3.6 Å
Covalently bonded atoms 5.1 Å
b
1
2
3
TM2/7 interface
Pore rin
Ribosome
Signal sequence
SecY
Plug
5
4

11.5.6 Pentameric Ligand-Gated Ion Channels

This type of ion channels can mediate fast chemo-electrical transduction for cellular excitability through the opening of an intrinsic transmembrane ion channel (see [11.116]). The x-ray structure of the pentameric bacterial *Gloeobacter violaceus* ligand-gated ion channel (GLIC) [11.116, 11.117] is arranged as a funnel-shaped transmembrane pore widely open on the outer side (Fig. 11.47). On the inner side, a 0.5 nm constriction matches with rings of hydrophilic residues that are likely to contribute to the ionic selectivity (see [11.116]). The channel is selective for cations over anions with poor discrimination among monovalent cations (see [11.117]).

11.5.7 Nuclear Pores

Nuclear pore complexes (NPCs) reside in the nuclear envelope of eukaryotic cells and mediate the nucleocytoplasmic exchange of macromolecules. Traffic is regulated by mobile transport receptors that target their cargo to the central translocation channel, where phenylalanine–glycine-rich repeats serve as binding sites. Cryoelectron tomography has been used to study the structure of the nuclear pore in its functional environment, that is, in intact nuclei of the slime mold cell *Dictyostelium discoideum* [11.118] in the presence of a cargo molecule which was rendered visible by gold nanoparticles.

To map the route taken by the cargo in the nuclear pore (outer diameter, 135 nm), the position of gold-labeled fusion protein was imaged (see Fig. 11.48) consisting of a nuclear localization signal and two copies of green fluorescent protein (NLS-2xGFP).

Fig. 11.46 The SecYEβ protein channel for translocation of proteins and model for the different stages of translocation. (**a**) SecYEβ channel across a membrane shown at the same size scale as the neighboring large ribosomal subunit (Sect. 11.1). The α-helix (*yellow*) that can block the exit is moved into the proposed "open position." Hydrophobic amino acid side chains are in *green*, acid groups in *red*, basic groups in *blue*, and other groups in *gray*. In the large ribosomal subunit which synthesizes the proteins, the RNA is in *grey* and the protein backbone in *yellow* [11.113]. (**b**) Model for translocation of secretory proteins. (*1*) The channel is closed due to the plug blocking the pore. (*2*) A channel partner, e.g., a ribosome, binds. The closing plug may be destabilized. (*3*) The substrate inserts a loop into the channel with its signal sequence intercalated between the TM2b and TM7 subunits of SecYEβ channel and its mature region in the pore. The intercalation gives rise to a hinge motion of TM2b and TM7 and displacement of the plug to its open-state position. (*4*) The mature region of the polypeptide chain is then transported through the pore, and the signal sequence is cleaved. While the polypeptide chain is moving from an aqueous cytoplasmic cavity to an external one, the pore ring forms a seal around the chain, hindering the permeation of other molecules. (*5*) When the polypeptide has passed through, the plug returns to its closed-state position. (Reprinted with permission from [11.112]. © 2004 Nature Publishing Group)

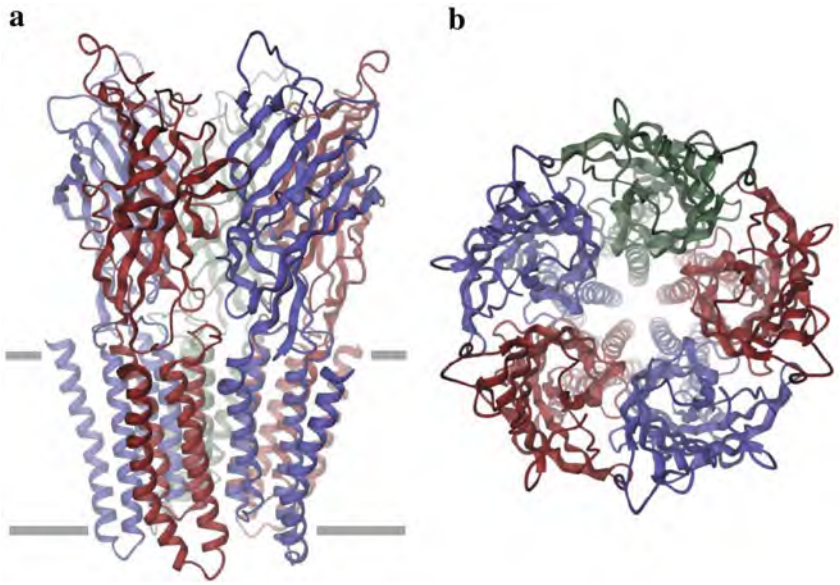

Fig. 11.47 (**a**) Ribbon presentation of the pentameric bacterial *Gloeobacter violaceus* ligand-gated ion channel (GLIC) viewed from within the membrane with the extracellular solution above. The approximate membrane boundaries are indicated. (**b**) Structure of the pentameric channel viewed from the extracellular side. (Reprinted with permission from [11.117]. © 2009 Nature Publishing Group)

11.6 Biomimetics

Biomimetics are technologies where designs for specific applications are inspired by the favorable properties of biological systems such as nanoscale efficiency, self-organization, and adoptability at relatively low cost. Some biomimetic designs for photonic energy conversion, sensing, signaling, molecular motion, materials, molecular motors, and artificial cells will be presented in the following.

11.6.1 Energy Conversion

The conversion of photonic to chemical energy is what powers nearly every ecosystem on earth. And yet this process not obviously warrants mimicry in solar energy research because the conversion efficiency of the chloroplast, a plant's light-harvesting organelle, is with ca. 9% far below that of commercial semiconductor solar cells with an efficiency up to 20%. But there may be aspects of photosynthesis that might be employed to create cheaper devices.

A biomimetic system for light energy conversion has been composed by making use of a light-harvesting porphyrin center sandwiched between an electron

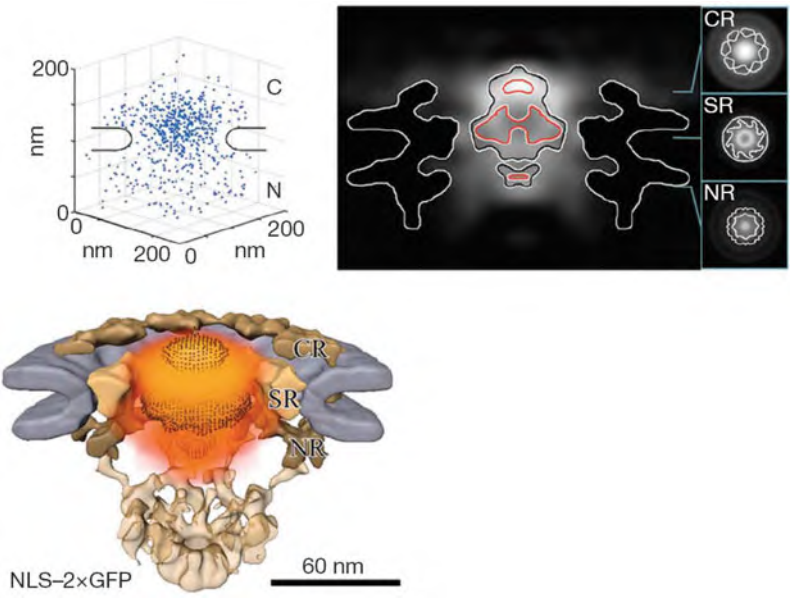

Fig. 11.48 Visualization of single molecules during nuclear import via a nuclear pore of the slime mold cell *Dictyostelium discoideum*. Gold-labeled classical import cargo consisting of a nuclear localization signal and two copies of *green* fluorescent protein (NLS-2xGFP). *Top left*: plot of the localization of (NLS-2xGFP) at the nuclear pore in the tomograms. Nuclear membranes are indicated on the sides. *Top right*: central slice along the nucleocytoplasmic axis of the 3D probability density map, superimposed into the structure of the nuclear pore complexes (NPCs). The three main electron-dense moieties of the central plug, in plane with the cytoplasmic (CR), spoke (SR), and nuclear rings (NR) of the pore, are indicated by *red* lines and are shown as cross-sections in the inset. *Bottom*: 3D probability distribution of NLS-2xGFP (*orange clouds*). (Reprinted with permission from [11.118]. © 2007 Nature Publishing Group)

donor and an electron acceptor (Fig. 11.49). Photon absorption by the porphyrin molecule causes charge separation, with a transfer of an electron from the donor to the acceptor group. The electron is then taken up by a shuttle molecule moving within the liposome wall. Once reduced, the shuttle transfers a proton from the outside to the inside of the liposome, so that the pH of the internal compartment decreases. So photon absorption induces the generation of a proton-motive force across the membrane, analogous to the situation in photosynthesis [11.119]. To utilize this electrochemical potential the enzyme ATP synthase has been incorporated in the liposome wall [11.120]. By the proton imbalance this molecule drives the conversion of the energy-poor ADP to the energy-rich ATP, the key "battery-molecule" of cellular metabolism. This process might also be used to generate the co-enzyme NADPH. In photosynthesis it is the photon-induced synthesis of ATP and NADPH that enables the production of sugars from CO_2. In these biomimetic photochemical devices, generation of these two molecules could in principle be used to power all kinds of enzymatic chemistry.

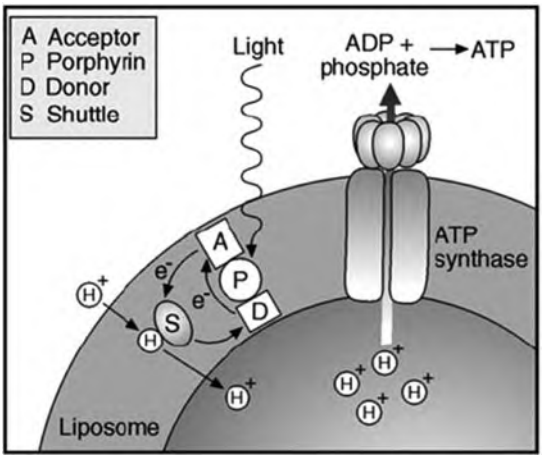

Fig. 11.49 Mimicking of photo synthesis in a liposome-based system. Three types of molecules embedded in the bilayer membrane allow photo-excited electrons to be transported across the membrane to acceptor species in the interior. This charge transport is accompanied by transmembrane flow of hydrogen ions giving rise to a pH decrease inside the compartment. This proton-motive force is than used to drive ATP synthesis by the membrane protein ATP synthase [11.119, 11.120]. (Reprinted with permission from [11.119]. © 2002 Nature Publishing Group)

11.6.2 Sensing

Nature has some of the most sensitive sensor devices known. The rod-type photoreceptors in the retina can register the absorption of a single photon, yielding some visibility even under starlight.

The olfactory system exemplifies a very common biological transduction mechanism, called the G-protein-coupled receptor signaling mechanism. When they bind to their substrates, receptor proteins embedded in a membrane activate a so-called G protein on the interior surface of the membrane (where the physics of the transduction underlying this activation still have to be disclosed [11.119]). This triggers a signaling route in which a subunit of the G protein activates adenylate cyclase that catalyzes the formation of cyclic adenosine monophosphate (cAMP). The cAMP triggers the opening of a sodium channel, setting up an action potential that leads to nerve signaling. An olfactory sensation cannot be identified with G-protein activation by any single kind of receptor. Rather, the information about the odorant is encoded in some distinctive pattern of receptor activity across the entire olfactory bulb [11.119].

Some artificial noses have derived inspiration from this mechanism by developing large arrays of relatively unspecific sensory elements combined with high-level computation for matching the resultant signal to a particular stimulus. On arrays of optical fibers, individual tips are coated with microscopic particles to which solvatochromic dyes are absorbed [11.121]. The fluorescence of each dye is sensitive to analyte molecules. The fluorescence from the laser-excited chromophores exposed

to the analyte is fed into a neural network trained to recognize the fingerprint of different molecular species. This principle mimics that of olfaction.

Molecular biosensors. Bacterial periplasmic binding proteins (pPBPs) [11.122], found in the bacterial periplasmic space, specifically bind a wide variety of small molecules and often perform large conformational changes as a result of this binding. This ligand-induced conformational change can be linked, e.g., to a fluorescence function to generate biosensors. Making use of this concept, biosensors specific for sugars, amino acids, anions, cations, and dipeptides [11.123], as well as for the explosive trinitrotoluene or for serotonin [11.124] have been developed.

11.6.3 Signaling

In engineering, signaling is conducted electronically or optically. However, electrical signals, e.g., in nerve cells travel by virtue of ion transport laterally in and out of the axon. Transmembrane ion transport is fundamental in cell biology and attempts to mimic it artificially started with supramolecular chemistry. Some early studies of molecular recognition by Lehn in the 1970s explored the use of crown ethers as mimics of cyclic peptide ionophores such as valinomycin, which bind cations selectively in their internal cavities.

One way to transport ions is to provide them with a polar channel – in cells, a protein pore embedded in the membrane with a lipophilic outer face and a hydrophilic inner face. Artificial mimics of ion channels are, e.g., peptide nanotubes – cyclic peptide molecules designed to stack into cylindrical channels [11.125] which induce transmembrane ion transport rates similar to those of natural ion-channel proteins such as gramicidin A [11.125] (see Sect. 11.5).

11.6.4 Molecular Motors

Generation of linear mechanical force and torque is wide spread in the cell. The power stroke of myosin molecular motors (see Sect. 11.4) is generated when the head undergoes a conformational change, ultimately powered by ATP hydrolysis. After kinking to pull the myosin filament along the actin thread, the head detaches and recovers its original conformation before attaching at a new location and repeating the cycle.

In synthetic DNA "machines," controlled rotational motion has been achieved by using conformational change of the double helix to develop torque [11.126] and in propeller-like molecules that can be rotated on a molecular axle in a specific direction by a sequence of chemical transformations [11.127].

There is a number of examples of the benefits from using natural systems to design at the nanoscale. The rotary motion of the membrane protein in ATP synthase has been used to drive a nanosized propeller (Fig. 11.50a). The ATP synthase enzyme, with a "spindle" that embeds in a lipid membrane and a head that fully

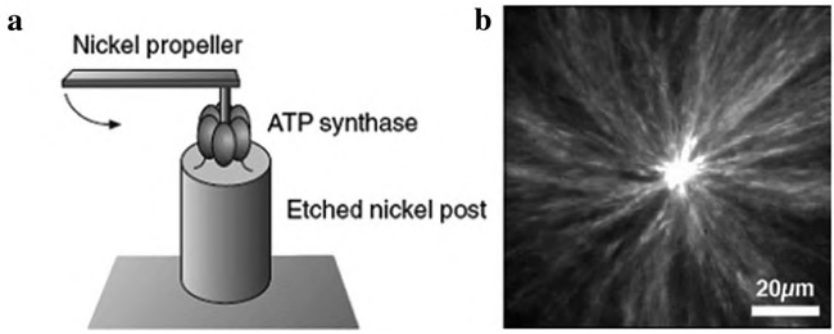

Fig. 11.50 (**a**) A molecular scale propeller representing a synthetic–natural hybrid: The enzyme ATP attached to a post is modified to allow the attachment of a nanoscale blade of nickel metal which rotates when it is energized by ATP [11.119, 11.128]. (**b**) The spontaneous organization of microtubules into aster-type formations as organized by synthetic molecular motors created by coupling four natural motor proteins [11.129]. (Reprinted with permission from [11.119]. © 2002 Nature Publishing Group)

rotates when it converts three ADP into three ATP molecules, has been connected with a micrometer nickel rod. Fuelled with ATP, the enzyme works "in reverse" to convert the ATP to ADP, rotating the blade by about five revolutions per second.

It has been furthermore shown [11.129] that the assembly of microtubules into the aster assembly, which forms before the development of the mitotic spindle prior to cell division, can be mimicked in vitro. First, an artificial molecular motor was synthesized by connecting four kinesin molecules. Kinesin binds the microtubules and moves along the filaments to finally arrange the microtubules into star-like bundles resembling asters (see Fig. 11.50b).

In a fusion of inorganic–organic nanotechnology molecular motors, gold-functionalized actin monomers were synthesized and polymerized to form conducting nanomeres. These gold nanomeres translocated across myosin-coated surfaces in the presence of ATP [11.130].

One of the smallest movable molecular units are mechanically interlocked molecules known as bistable rotaxanes **R1** (see [11.131–11.133]), where, e.g., a tetracationic cyclobis (paraquat-*p*-phenylene) ($CQPQT^{4+}$) ring component can be shifted on a linear rod section with the two units tetrathiafulvalene (TTF) and dioxynaphtalene (DNP) (Fig. 11.51). When **R1** is at its initial state, the TTF unit is encircled by the positively charged ring. Upon oxidation, the TTF unit becomes dicationic (TTF^{2+}) and causes electrostatic repulsion of the ring, so that the ring shuttles toward the DNP unit. Conversely, reduction of TTF^{2+} to TTF causes the **R1** to return to its starting state. The oxidation and reduction of bistable rotaxanes can be realized by applying an electric field, light, or a chemical stimulus.

Bistable rotaxanes are mechanically switchable in various solid-state environments and can be harnessed to perform larger-scale mechanical work (e.g., driving microcantilevers, rotating sub-millimeter-sized glass rods, and manipulating microliter droplets) [11.131].

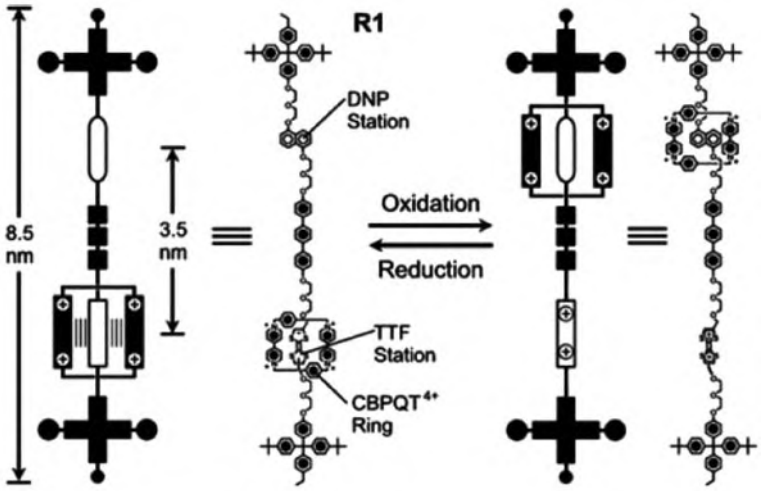

Fig. 11.51 Molecular structure and schematic representations of a redox-controllable bistable rotaxane **R1**. DNP is dioxynapthalene; TTF is tetrathiafulvalene; and $CBPQT^{4+}$ is cyclobis (paraquat-*p*-phenylene). (Reprinted with permission from [11.131]. © 2008 Materials Research Society)

11.6.5 Materials

The guiding principles that control the properties of natural materials at the nanoscale are regarded as an attractive target for biomimetic designs by materials scientist [11.119].

The combination of several desirable properties of materials is typically a matter of controlling structure and organization across a number of different length scales, i.e., natural materials display a hierarchical structure. The strength of bone exceeds that of a composite of organic collagen and inorganic hydroxyapatite materials; there is organization (Fig. 11.52a) at scales ranging from the primary structure of collagen helices, to the crystals along the fibrils at the 100 nm scale, to the osteon fibers at sub-millimeter scales, and to the centimeter porosity of the bulk substance. A hierarchical structure is also evident in wood, tendon, cartilage, or silk (Fig. 11.52b).

In functional tissues such as internal organs, the arrangement of cell types is complex and it is difficult to recognize what is essential for effective mimicry. The combination of, e.g., fibroblasts and hepatocytes in liver tissue is crucial for optimal function and must be understood in tissue engineering of an artificial liver [11.134].

In addition to hierarchy, a modular architecture plays a role in natural materials. The stepwise unfolding of the titin protein upon straining is due to a modular domain structure giving rise to a sawtooth-like stress–strain curve very different from a purely elastic filament [11.76]. A similar stress–strain curve has been measured for the polymeric filaments pulled out from the organic binder between the

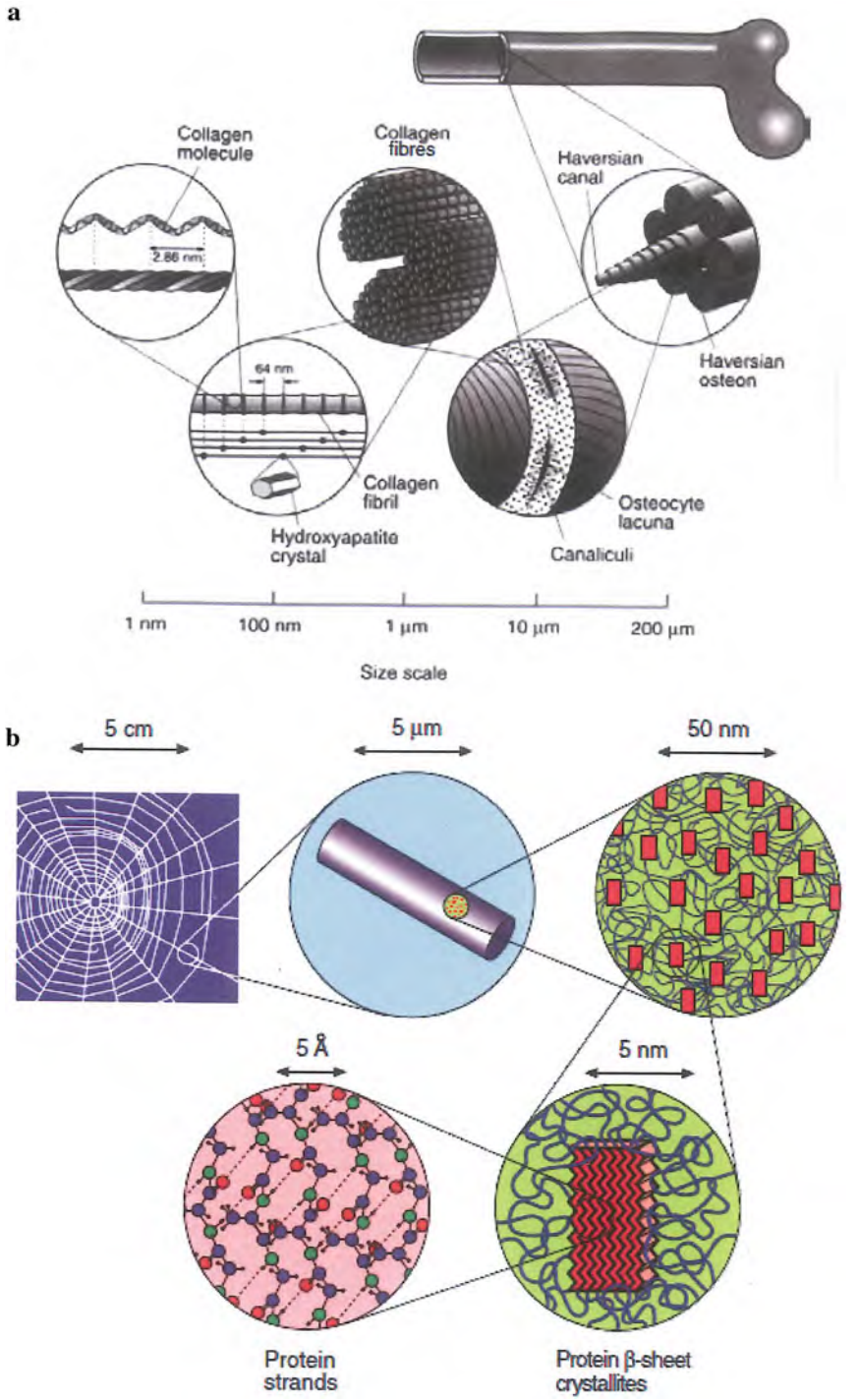

Fig. 11.52 The hierarchical structures of natural materials. (**a**) Bone; (**b**) silk. (Reprinted with permission from [11.119]. © 2002 Nature Publishing Group)

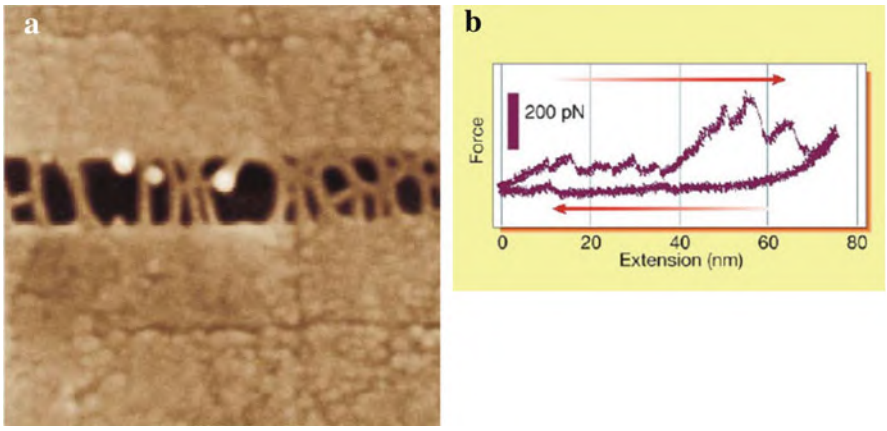

Fig. 11.53 The protein filaments pulled out of the organic layer between aragonite sheets (~400 nm thick) in nacre (**a**) extend in a stepwise manner (from ~30 to ~600 nm), as revealed by AFM force measurements (**b**). The sawtooth stress–strain curve signifies a greater work of fracture (area below the curve) than a stiff or elastic adhesive strand. (Reprinted with permission from [11.135]. © 1999 Nature Publishing Group)

aragonite plates of nacre as the plates are separated (see Fig. 11.53). Because the area under the curve, equal to the work of fracture, is greater in this case than for a stiff or elastic filament, this molecular extension behavior is characteristic for a highly tough adhesive. The layered structure of nacre lends itself obviously to mimetic synthesis since there is much experience available with the preparation of layered composites (see Sect. 6.9). The basic strengthening mechanism – crack deflection at weak interfaces – is well understood but questions remain about the evolution of the crystallites controlled by the organic matrix [11.119].

Protein self-assembly, protein–inorganic interfaces. Protein–protein self-assembly based on poly (EAK) (glutamine–alanine lysine) was employed to fabricate networks of filaments with diameters of 10–20 nm [11.136] which are unusually stable at extremes of temperature and pH. These peptides undergo a rapid conversion from β sheet to α helix above 70°C (see [11.122]).

Interfacing of protein and non-protein components can also be used for the design of new materials. The conjugation of peptides to carbon nanotubes has been explored for the development of vaccines, e.g., by conjugating the envelope protein of the foot-and-mouth virus to carbon nanotubes [11.137]. The peptide retained its structural integrity and its ability to be recognized by monoclonal and polyclonal antibodies.

Biomineralization [11.122, 11.138, 11.139, 11.140]. Making use of silica precipitating polycationic peptides, such as ply-LATHA-lysine (PLL), the morphology of the mineralized silica nanoparticles can be tailored from nanospheres to hexagonal silica platelets [11.141] whereas α-helical PLL results in the formation of 1.5 nm sized cylindrical pores in mineralized silica [11.142].

Peptide from the β amyloid protein was used to create nanotubes that were filled with silver [11.143]. The peptide was enzymatically digested, leaving silver nanowires. The M13 virus has been used to fabricate nanowires containing cobalt oxide, which have been assembled on polymer surfaces [11.144] and used to create electrodes for lithium ion batteries [11.145].

Hexapeptides with the ability of Ti binding and mineralization were fused to nanosized spherical ferritin protein units (see Fig. 11.54b) with development prospects for memories, solar batteries, or biosensors [11.146].

Mechanical properties of organic–inorganic composites. The mechanical properties of natural substances such as bone and sea shell are envied by materials scientists. To be strong, hard, and tough, a material must absorb a large amount of energy during mechanical deformation and also maintain high stiffness. In bone or shell this desirable combination of properties is made possible by one key attribute – a brick-and-mortar like structure, made up of strongly interacting, nanometer-sized building blocks (see Sect. 6.9). The "hard" bricks and the "soft" mortar are complementary in their response to stress and strain. The fabrication of

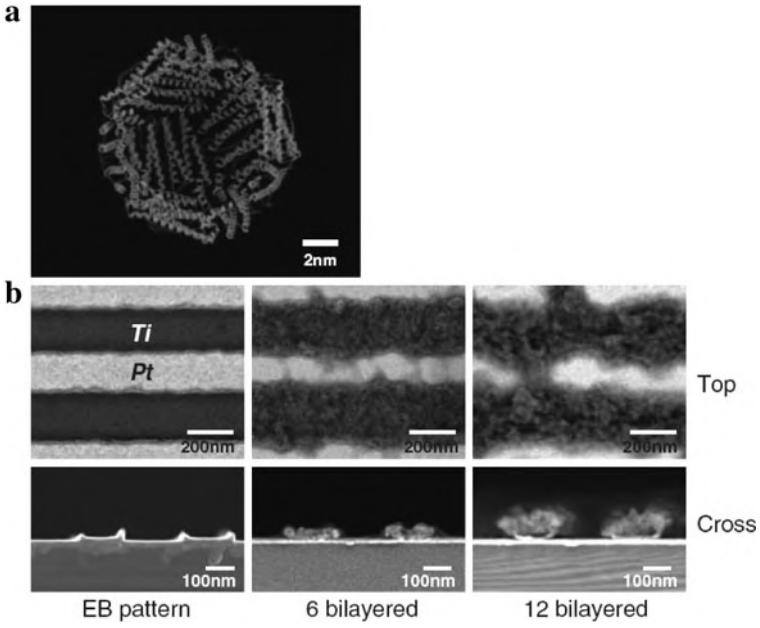

Fig. 11.54 (**a**) Ferritin, a protein tool for nanofabrication, is composed of 24 subunits with a cavity that is 8 nm in diameter. (**b**) *In aqua* assembly of 3D nanoarchitectures by biomimetic layering of hexapeptide–ferritin units for mineralization of metal oxide nanoparticles; top and cross-sectional scanning electron microscopy views the nanostructures after electron-beam (EB) pattering of Ti and Pt stripes, where the hexapeptide-ferritin units exclusively bind to the Ti substrate. (Reprinted with permission from [11.146]. © 2008 Materials Research Society)

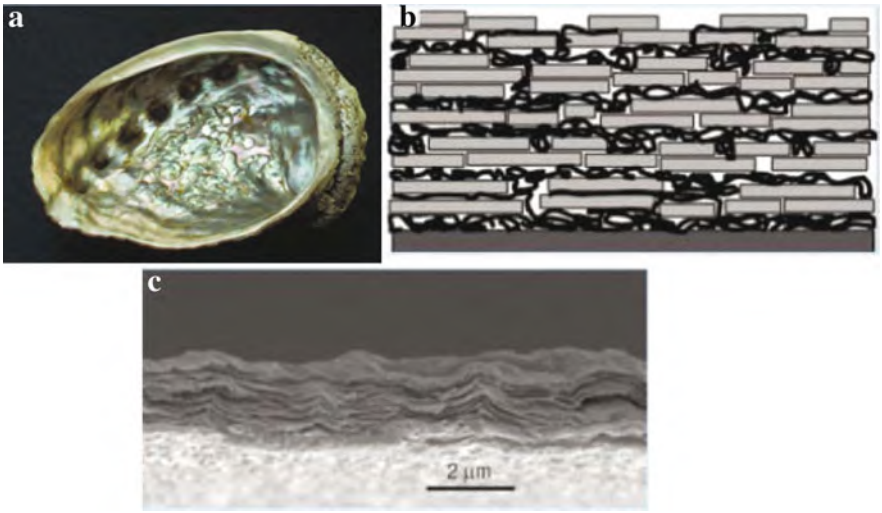

Fig. 11.55 The "brick-and-mortar" approach. (**a**) The natural strength, hardness, and toughness of bone and sea shell are due to their nanoscale-structure calcium carbonate bricks and mortar-like protein layers. (**b**) In a biomimetic approach, montmorillonite bricks (0.9 nm thick) are deposited layer by layer on a silicon wafer substrate, alternating with polymer chains of mortar. (**c**) Structures that are many layers deep can be built (here, 100 brick and polymer layers [11.147, 11.148]. (Reprinted with permission from [11.148]. © 2003 Nature Publishing Group)

such materials by biomimetic approaches has been achieved through the alternating sequential deposition of negatively charged nanometer-thick montmorillonite clay platelets (bricks) and a positively charged polymer (mortar) [11.147] so that the layers of the structure (Fig. 11.55c) electrostatically attract each other. The polymer chains are arranged in coils and folds, pinned by relatively weak electrostatic interactions.

As the material is deformed and the clay platelets begin to slide over each other, the polymer chains can rearrange through the breaking of "sacrificial" ionic bonds and concomitant unfolding of the coiled polymer chains. This process allows the material to absorb a lot of deformation energy so that the artificial layered structures have tensile strengths and stiffnesses that approach those of sea shell nacre [11.147].The application could be widespread, from synthetic engineering of biological hard tissue to thin-film protective coating.

Cell adhesion at nanostructured surfaces. An important issue of graft engineering is the topological study of cell interaction with surfaces (see [11.149] and Sect. 11.1). An early response of cells to nanotopography, compared with smooth surfaces of the same material, is to increase their complement of filopedia, which are cellular processes that anchor cells to surfaces at focal points. In general, the presence of nanoscale features increases cell attachment and proliferation, and ridges as thin as 70 nm guide cytoskeletal assembly.

The nanotopography and surface chemistry of a tissue engineered xenograft PepGen P-15^{TM}, which is porous bovine bone mineral coated with a synthetic peptide P-15 for improved cell attachment [11.150], was investigated by atomic force microscopy (AFM) and Fourier transform infrared spectroscopy (FTIR). FTIR was used to identify specific functional groups that are involved in the binding mechanism and to pick up changes in the peptide conformation as it attaches to OH groups on the surface of the hydroxyapatite bone material. Conformational changes include a decrease in the β strand proportion.

Viable bone cells adhere to carbon nanofiber scaffolds preferentially at smaller fiber diameters [11.151]. The attachment of human bladder cells on nanostructure titania wafers was found to occur favorably at hemispherical nanopillars compared to grooved surfaces [11.152].

11.6.6 Artificial Cells – Prospects for Biotechnology

Artificial cells designed for specific applications could combine properties of biological systems such as nanoscale efficiency, self-organization, and adaptability [11.153]. Individual components of such structures have been developed but the main challenge is to integrate them in functional microscopic compartments.

Creating *membrane boundaries* by the preparation of lipid bilayer vesicles (liposomes) is a mature field and these vesicles with sizes between 25 nm and 1 μm are used by the pharmaceutical industry as drug delivery agents (see [11.153, 11.156]). Transport across the cell walls of these vesicles via channels and pumps is necessary for exchanging nutrients, waste, regulatory molecules, and ions. *Synthetic channels* can be designed by mimicking natural ones. For example, the channel formed by M_2 protein fragments of the human influenza virus (Fig. 11.56a) folded into α helices conducts protons at high rates [11.154] presumably through a chain of properly aligned water molecules. Selectivity is provided by a gate of four histidine protein ($C_6H_9N_3O_2$) residues, one from each of the channel-forming helices which are sufficiently large to occlude the lumen. However, controlling the channel activity still remains a difficult task (see [11.153]).

The energy supply process to the liposome can be mimicked by the energy transduction process of living cells, in which light or chemical energy from the environment is converted to a transmembrane proton gradient for use in the production of ATP from ADP and phosphate (see [11.153]). The simplest and most robust artificial system for light-driven generation of ATP consists of the two membrane proteins bacteriorhodopsin, which works as a proton pump, and ATP synthase (ATPase), which couples the flow of protons through the enzyme to the phosphorylation of ADP (see [11.153]).

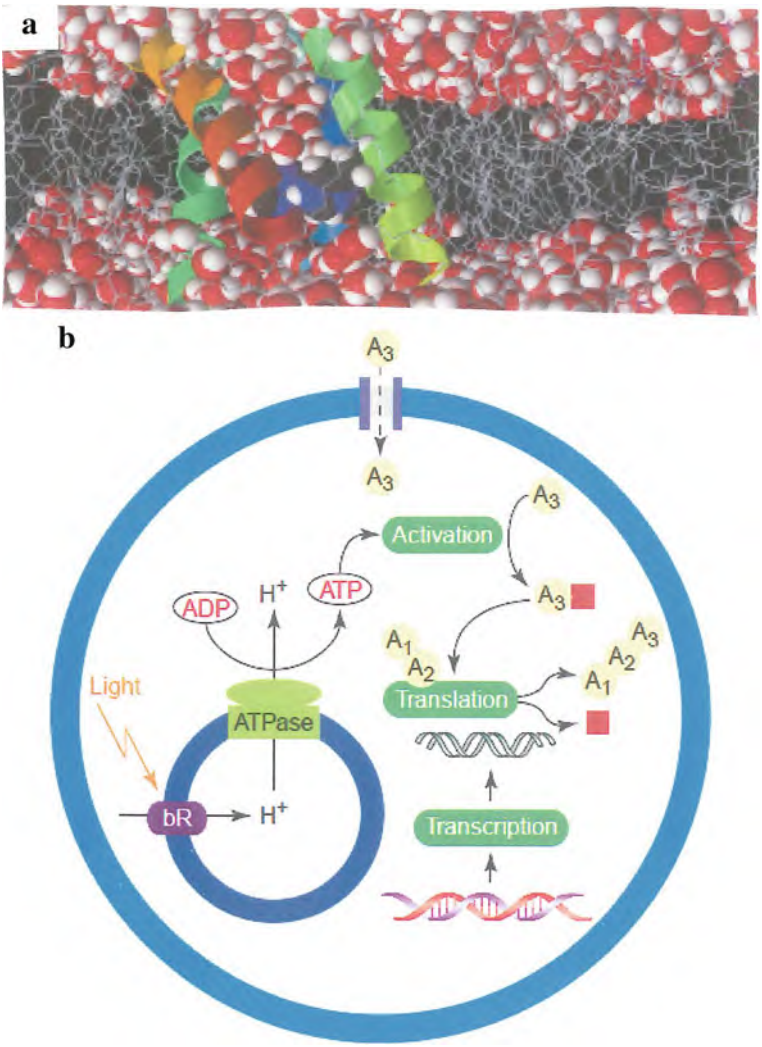

Fig. 11.56 (**a**) The M_2 protein proton channel in a hydrated phospholipid bilayer. The four α helices are represented in the ribbon model. The membrane-forming lipids are shown as wires and the oxygen or hydrogen atoms of water in *red* or *white* colors, respectively. The file of water molecules inside the channel is interrupted by histidine residues in the upper part of the channel. The structure of the channel was generated by molecular dynamics computer simulation. (**b**) A hypothetical cell-like structure. DNA is transcribed to RNA and translated to the protein with the aid of the encapsulated transcription and translation system. Amino acids for translation enter via the transmembrane channel and are activated (*red square*) by ATP (*top*). ATP is synthesized from ADP and phosphate by light-driven bacteriorhodopsin (bR) and ATP synthase (ATPase). (Reprinted with permission from [11.153]. © 2002 Elsevier)

Macromolecules inside the liposome are required for catalyzing the metabolic functions. One complex enzyme system that has been demonstrated to function after encapsulation in liposomes is the T7 RNA polymerase (see [11.153]) which uses all four nucleoside triphosphates to synthesize an RNA transcript from the DNA template. If the transcription from DNA to RNA and the translation process from RNA to a protein would be successful in a liposome it could be extended to encapsulate "mini-genomes" yielding products not obtainable from a single enzymatic reaction but requiring a metabolic pathway. A schematic of a cell-like structure equipped with these properties is shown in Fig. 11.56b.

Replication and ribozymes can be coupled in a minimal cell by incorporating into vesicles a replicating activity based on ribozymes, which are RNA molecules that possess catalytic activity and can, therefore, act as both catalysts and carriers of genetic information [11.155]. It has been demonstrated that an artificially evolved ribozyme can acts as RNA-dependent RNA polymerase [11.156]. This may show the way toward creating a true, ribosome-based, self-reproducing system, although there remain a number of technical hurdles [11.153].

Biotechnological applications for artificial cell-like structures are envisioned in pharmacology and medical diagnosis. A further approach of encapsulation are artificial blood cells [11.157] containing hemoglobin with increased oxygen affinity or the application of functionalized liposomes as biosensors (see [11.153]).

Remote control of cellular behavior with magnetic nanoparticles. Work in nanomagnetic actuation of cell functions has focused on targeting specific ion channels and cell membrane receptors in order to initiate controlled response by the cell [11.158]. By employing targeted iron oxide nanoparticles, specific ion channels on the surface of the cell membrane can be directly activated (see Fig. 11.57a) which requires less force (∼pN) than doing so through the deformation of the membrane or cytoskeleton. Nanomagnetic actuation has been used to promote membrane receptor clustering in RBL-2H3 mast cells [11.159] by targeting dinitrophenol–lysine conjugated 30-nm magnetic nanoparticles to cell surface IgE–FcεRI receptor complexes. By an electromagnetic microneedle generating a high field gradient over sub-micrometer-size areas (see [11.158]), cluster-mediated intracellular calcium signaling can be activated. This has potential use as a biosensor.

Experiments on magnetically activated TREK-1 channels implicate specific activation in the cartilage differentiation pathway (see [11.158]). For creating an ordered fibrin scaffold to support the adhesion and spreading of endothelial cells [11.160], thrombin-coated magnetic nanoparticles were positioned by a magnetic field in 2D arrays for the ordered growth of fibrin fibrils. To create layers of tissue, 10 nm magnetite nanoparticles within 150 nm liposomes attached to cells were seeded unto ultralow attachment plates with a magnet placed underneath. In the case of retinal pigment tissue [11.161], this prompted the cells to grow sheets up to 15 layers thick that were then easily detached by removing the magnet.

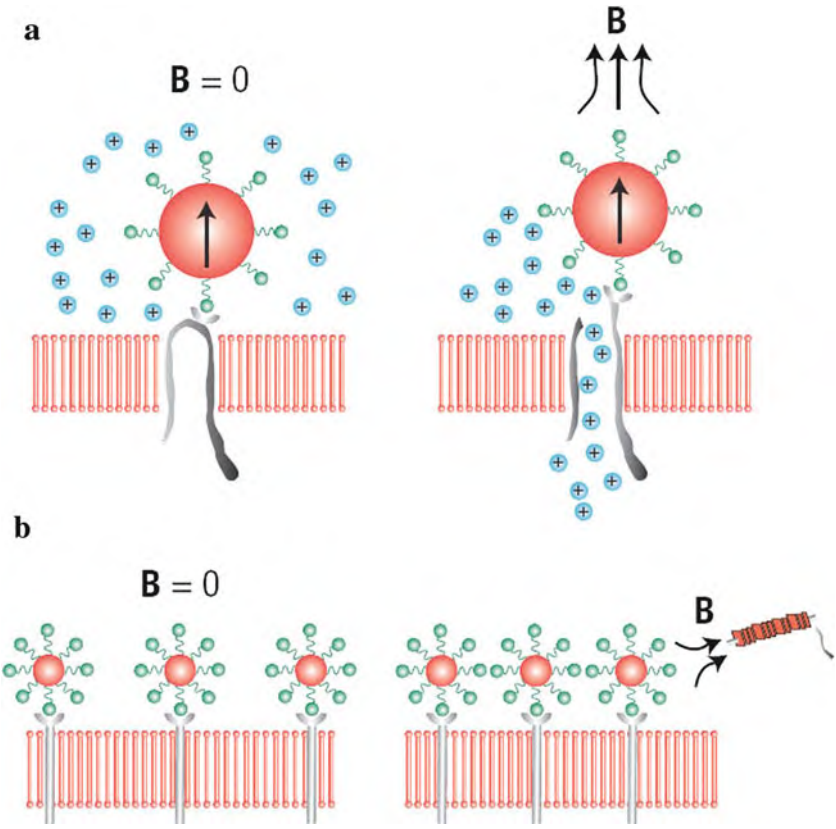

Fig. 11.57 Schematic representation of different types of nanomagnetic activation of cells. (**a**) Targeted ion-channel activation: magnetic nanoparticles (100 nm – 2.7 μm) are attached to an ion channel via an antibody (*left*) and, upon the application of a high-gradient magnetic field (*right*), the ion channel is forced to open. (**b**) Receptor clustering: magnetic nanoparticles (30 nm diameter) are bound to reception complexes. Without magnetic field (*left*), the receptors are spaced along the membrane surface. In a high-gradient magnetic field, the receptors are pulled toward the field source and initiate receptor clustering that can trigger intracellular signaling. (Reprinted with permission from [11.158]. © 2008 Nature Publishing Group)

11.7 Bone and Teeth

In vertebrate bone and teeth, a collagen matrix is reinforced by mineral nanoparticles. This composite structure yields high strength and toughness to these organic components.

11.7.1 Bone

Bone is a wet, natural hybrid nanocomposite [11.162]. Here, 2 nm hydroxyapatite sheets are embedded in 5 nm tropocollagen tuned to operate in a state of optimal energy dissipation [11.162].

Collagen is a structural protein (Fig. 11.58) containing predominantly the amino acids alanine, proline, and glycine. Macromolecular chains of collagen in the triple helix structure of tropocollagen, which are stabilized by hydrogen bonding between

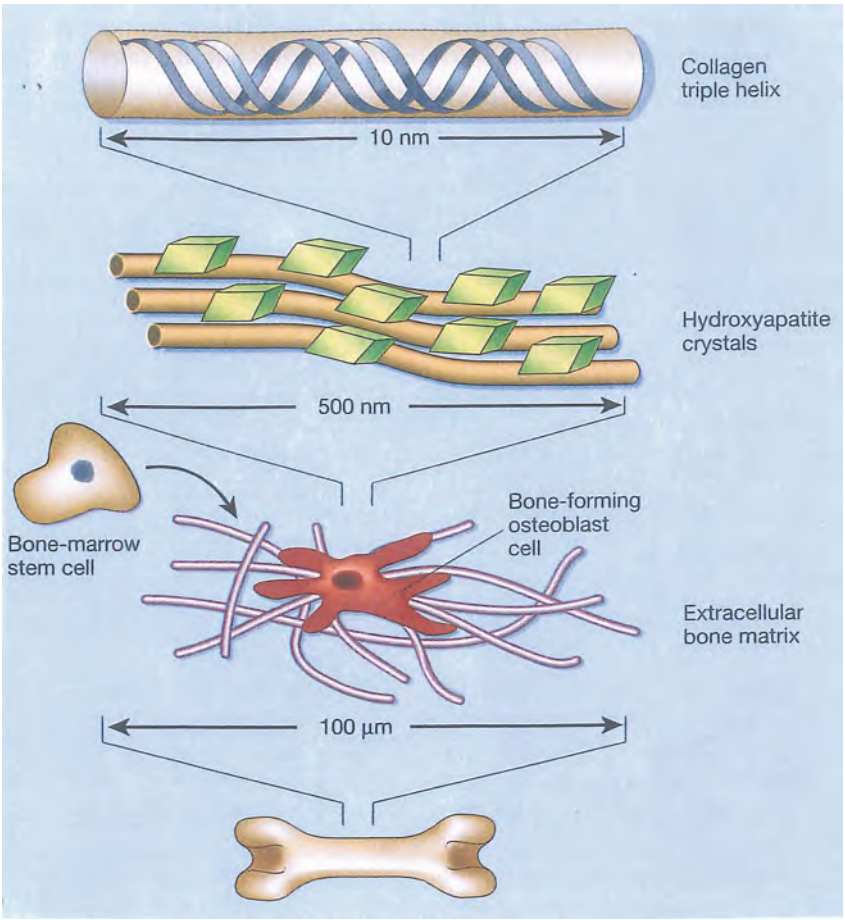

Fig. 11.58 Schematic presentation of the many scales of organization in natural bone. Collagen triple helices spontaneously form nanoscale bundles of protein as a template for the formation of hydroxyapatite nanocrystals. The collagen matrix is also recognized by bone-marrow stem cells which differentiate into bone-forming osteoblasts after signals from bone-specific proteins in the matrix. To duplicate the strength and the toughness of natural bone, researchers must design biomimetic materials that match these structural levels of organization from the nanoscale upwards [11.163]. (Reprinted with permission from [11.163]. © 2001 Nature Publishing Group)

the protein amide groups and by the additional water molecules (osteoid water) absorbed into the organic polymer. The pitch of the tropocollagen α-helix is about 10 nm and the diameter is ∼1.3 nm. The helical structure of tropocollagen stops the protein (polyamide) chains from folding and allows collagen to be oriented in bone, ligaments, and tendons. The Debye temperature is reported to be θ_D=420 K and the glass transition temperature T_g=300 K [11.162].

The hydroxyapatite $Ca_{10}(PO_4)_6(OH)_2$ nanoplatelets (Fig. 11.58) with approximate dimensions of 70×40×2.3 nm^3 are aligned along the tropocollagen fibrils with a ∼5 nm separation of the particles and a 38% mineral volume fraction in human bone. The elastic modulus of hydroxyapatite is with ∼110 GPa by two orders of magnitude higher than that of collagen which in its turn is responsible for the toughness of the bone.

Bones, as opposed to dentin and most mineralized tendons, often undergo internal remodeling. This process involves the excavating out of large tunnels by teams of specialized cells called osteoclasts. These tunnels are then refilled by osteoblasts, starting with the deposition of a thin layer of cement on the existing excavated surface, followed by layers of lamellar bone. The process stops when the tunnel is almost completely filled, leaving a narrow channel at the center – an osteon – that functions as a blood vessel. In fact, other even smaller capillary-like features (canaliculi) are also built into the structure. These canaliculi house the cells (osteocytes) that remain in the bone material itself and radiate out from the central blood vessel. Thus the structure of an osteon is basically onion-like with layers surrounding a central hole and contains many elongated pores [11.164].

Studies that aim at replicating the complex nanostructure of bone (see [11.163]) try to design self-assembling, synthetic substitutes for collagen, which can also act as templates for hydroxyapatite crystallization. It has been demonstrated that amphiphilic molecules – bearing a long hydrophobic alkyl group on one end and a hydrophilic peptide on the other end – spontaneously assemble into cylindrical structures that resemble collagen fibrils. More important, these cylinders guide the formation of hydroxyapatite crystallites with orientation and sizes similar to those in natural bone. It remains to be seen whether the nanoscale order in these materials translates into macroscale toughness in a prosthetic bone replacement (see [11.163]). In natural bone formation, for example, bone-specific proteins and possibly some types of collagen have peptide sequences that signal bone marrow stem cells to differentiate into bone-forming osteoblast cells (Fig. 11.58). The osteoblasts then supply the calcium required to form the nanocrystalline hydroxyapatite. The initial studies on replacing bone structures were obtained with molecules terminated by Arg-Gly-Asp (AGD), a peptide sequence known to be a general promoter of cell adhesion and growth (see [11.163]). For binding marrow cells and triggering osteoblast differentiation, other peptide sequences are necessary. But the presence of the sequences is not enough to promote osteoblast differentiation and bone formation. The technological goal of this research would be to replace solid bone grafts with an organic scaffold that would foster the growth of new, natural bone. However, this can be only achieved by communicating specific messages to bone-forming cells.

11.7.2 Tooth Structure and Restoration

A tooth is an organ, consisting of several types of tissues. The tooth is covered by dental enamel, the hardest mineral material of the organism. The main material of the tooth is the bone-like dentin, separated from the enamel by the dentin–enamel junction (DEJ) whereas the pulp contains blood vessels and nerves.

Enamel is a striking product of the biomineralization process being composed of 95–99% of dahlite (carbonated hydroxyapatite) mineral, differing from other biological apatites (e.g., bone or dentin) by the unusually long and spatially ordered mineral nanocrystals. In mature human enamel this crystallites are some 26 nm thick, 68 nm wide, and more than 1 mm long (see Fig. 11.59a). Unlike bone or dentin, dental enamel is not a collagen-based structure but originates as an extracellular protein matrix secreted into the premineralized dentin surface (DEJ) by specialized ameloblast cells within the inner enamel epithelium. Concomitant with the secretion of enamel gene products, the enamel matrix becomes progressively mineralized with the dahlite mineral phase.

The secreted protein matrix is dominated by the tissue-specific amelogenin proteins with sizes of 5–20 kDa, rich in the amino acids proline, glutamine, histidine, and leucine. The amelogenin undergoes a self-assembly aggregation initiated by the hydrophilic interaction of the carboxy-terminal regions of the molecule [11.167], leading to the formation of nanospheres, each of which comprising >100 monomers. It is suggested that these amelogenin nanospheres in a linear arrangement facilitate specific enamel crystallite growth and orientation (Fig. 11.59b). The numerous circular electron-lucent regions (20 nm in diameter) in the electron micrographs are ascribed to the amelogenin nanospheres, in sections of developing enamel, as beaded rows arranged in alignment with the initial

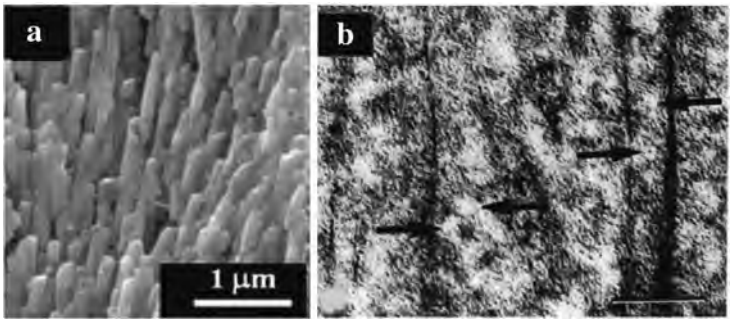

Fig. 11.59 The living tooth is an organ consisting of various types of tissue. The tooth is coated by a hard layer of enamel. The main part of the tooth is the dentin body. The interior pulp contains blood vessels and nerves [11.165]. (**a**) Scanning electron micrograph of human molar enamel, cut longitudinally [11.166]. (**b**) TEM image of mouse enamel matrix contrasted with uranyl acetate and lead citrate, early-stage enamel mineral crystallites (*dark lines*), and beaded rows of electron-lucent structures (*arrows*), comparable in size and properties to amelogenin nanospheres (*arrows*); bar, 50 nm [11.167]. (Reprinted with permission from [11.166] (**a**) and [11.167] (**b**). © 2006 Wiley-VCH (**a**) and © 1995 Elsevier (**b**))

mineral ribbons (Fig. 11.59b). By their linear aggregation, these nanospheres are active in defining the spatial ultrastructure of the enamel matrix with the oriented *c*-axis growth of the mineral crystallites and the organization of the crystallite spacing in order to suppress crystallite fusion [11.167].

Dentin is a calcified tissue somewhat similar to bone, where the collagen-rich organic matrix is reinforced by 3–10 nm thick (see [11.168]) calcium phosphate mineral nanoparticles, but unlike bone, dentin does not remodel once it is fully mineralized. As shown by x-ray diffraction and nanoindentation [11.168], dentin is a gradient material which is designed in such a way that the hardness and the elastic modulus are lowest close to the junction to the enamel, which is much stiffer and harder than dentin. As a consequence, the hardness and the elastic modulus are minimum close to the DEJ. In such a minimum, crack propagation is strongly inhibited and catastrophic failure of the tooth is prevented.

11.8 Photonic Bionanostructures – Colors of Butterflies and Beetles

Many insects (see Fig. 11.60a), birds, fishes, etc., exploit photonic nanostructures on their surfaces to make their color change with viewing angle (iridescence) and/or appear "metallic." These visual effects appear more pronounced than those produced by pigments and are used to attract the attention of potential mates or to startle predators [11.170]. Some antireflective surfaces are available to the eyes of,

Fig. 11.60 (**a**) The Buprestidae family of insects possesses many vividly colored members. The body of *Chrysochroa vittata* displays a *green* finish, which turns *blue* under large incidences. The ventral part (hidden) of the abdomen is *red* under normal incidence, but shifts to *green* under large angles [11.169]. (**b**) Scanning electron micrograph of an antireflective surface from the eye of a moth. Domains corresponding to individual cells are evident; scale bar, 1 μm [11.170]. (Reprinted with permission from [11.169] (**a**) and [11.170] (**b**). © 2006 American Physical Society (**a**) and © 2007 Nature Publishing Group (**b**))

e.g., moths or butterflies (Fig. 11.60b) to see in low-light conditions. These surfaces of nodules are arranged in a hexagonal array with a periodicity of 240 nm to introduce a gradual refractive index profile at an interface between chitin (a polysaccharide with a refractive index, n, of 1.54) and air ($n = 1$), and reduce reflectivity by a factor of about ten.

After the first photonic crystal in an animal was identified in 2001 [11.171], the scientific effort in this subject has accelerated, as discussed below.

11.8.1 Structures

Two structures have been identified to explain many of the interference color phenomena of butterflies and beetles [11.172]:

(1) Two-color phenomena are caused by a *multilayer structure* with alternating high and low refraction indices (see the blue *Morpho* butterfly in Fig. 11.61). These structures do not change the orientation of polarized light. Chitin is the dominant component in many of the layers, but proteins, melanin, lipids, etc., also contribute [11.172]. The multilayer stacks contain 10–20 bilayers with, e.g., thicker chitin layers (194 nm, $n = 1.56$) and thin layers of air (10 nm, $n = 1.0$). A simplified description for the dominant wave length λ for a multilayer reflector with two alternating layers is given by [11.169]

$$\lambda = \frac{2a\sqrt{\bar{n} - \sin^2\theta}}{m}$$

and for normal incidence $\lambda = 2a\bar{n}/m$, where a is the sum of the thicknesses of the two different layers, $\bar{n}$ the average refractive index, θ the angle from the multilayer normal, and m an integer. This well describes the observation that thicker layers result in longer reflected wavelengths and that grazing incidence gives rise to a blue shift of the reflected light. For an ideal multilayer stack with the refractive indices n_a and n_b and the number p of bilayers, the reflectivity (ratio of reflected and incident light intensity) is given by (see [11.172])

$$R^2 = \left[\left(1 - \left(\frac{n_a}{n_b}\right)^{2p}\right) \Big/ \left(1 + \left(\frac{n_a}{n_b}\right)^{2p}\right)\right]^2$$

demonstrating that R increases with the number p of bilayers and the ratio $n_b/n_a > 1$ of the refractive indices.

In Fig. 11.61 the blue iridescent wings of a *Morpho* butterfly are shown together with the structure of the scales that reflect the blue light. This structure can be mimicked by artificial layered structures (Fig. 11.61c).

(2) The observed color phenomena are explained by a twisted (helicoidal) multilayer chitin-rich structure. The chitin molecules are predominantly arranged

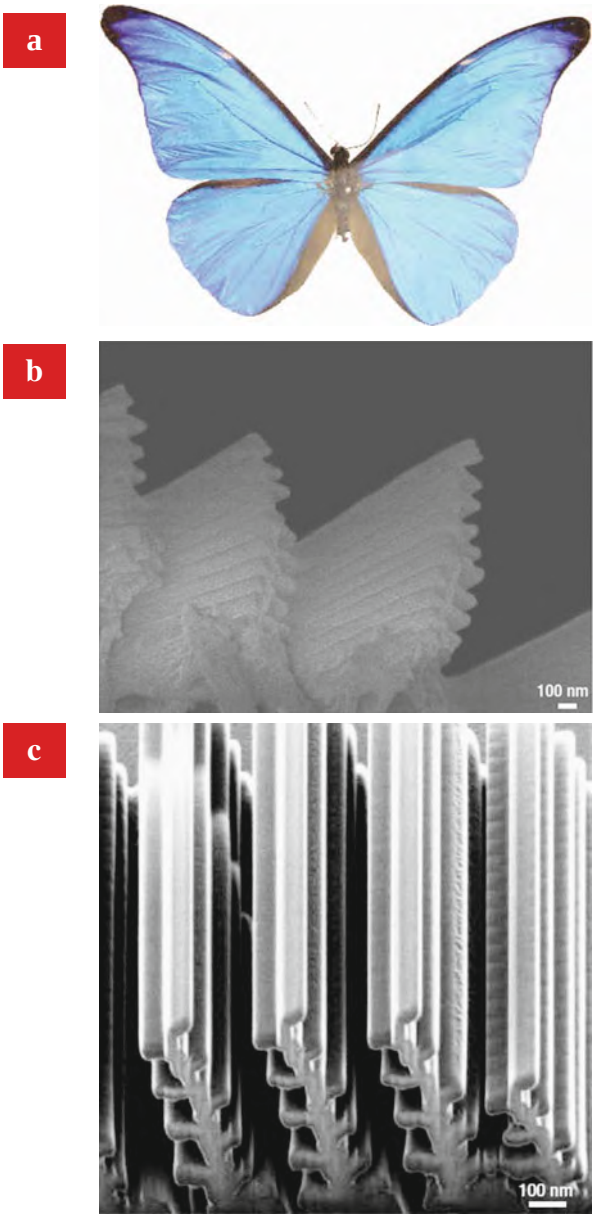

Fig. 11.61 The iridescent *blue* wings of a *Morpho* butterfly. (**a**) The nanoarchitecture gives the wings a distinctive iridescent *blue* color. (**b**) Scanning electron micrograph of the structure of the scales of the wing. (**c**) A mimic of the structure in (b), fabricated by focused ion beam chemical vapor deposition (FIB-CVD). Both structures give a wave length peak around 440 nm at an angle of about 30°, but the replica can cover areas only of micrometers. (Reprinted with permission from [11.173]. © 2005 Japanese Society of Applied Physics)

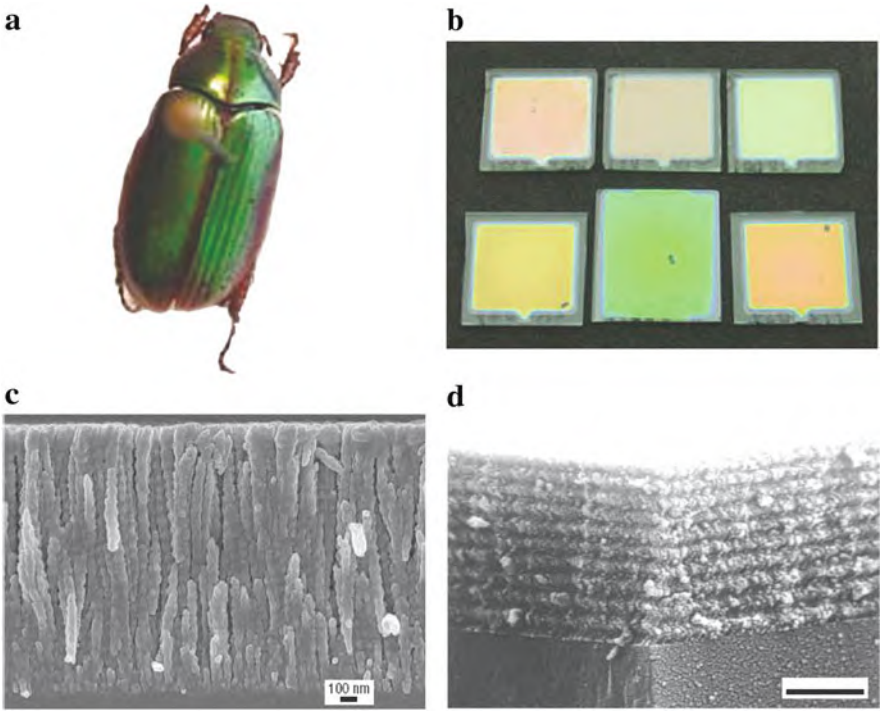

Fig. 11.62 Iridescent cuticle of a beetle and replica. (**a**) The Manuka (scarab) beetle exploits chiral films with a structure similar to a liquid crystal to make its cuticle iridescent. (**b**) Biomimetic replicas (each around 2 cm^2) made of titania exhibit different colors depending on the pitch of the film and the incidence angle of light. The circular polarization properties of the replica and of the beetle are also the same. (**c**) A scanning electron micrograph of the chiral reflector in the cuticle of the beetle and (**d**), the replica. Scale bar, 400 nm [11.174]. (Reprinted with permission from [11.170]. © 2007 Nature Publishing Group)

helically. Within each layer, the thread-like molecules lie parallel to each other (Fig. 11.62c), but the molecules of different layers show a twist (chirality) of thread orientation (director). A total rotation of the director of the layers through 360° is called the pitch. These structures – when birefringent – change the orientation of the polarization of light and are therefore referred to as optically active systems (see [11.172]).

When white light is incident on a surface of a helicoidal structure (parallel to the twist), selective reflection takes place. The wavelengths of the reflected maxima are varying with an angle v to the surface according to (see [11.170])

$$\lambda = 2Sn \sin v$$

with S the half-pitch. The highest reflectivity for a given color is obtained for an optical thickness (thickness times n) of a half-pitch equal to the wavelength. In a

chitinous material with a mean refractive index of about 1.53 and a half-pitch of 165 nm the structure will reflect blue green light with a wavelength of 505 nm (see [11.172]). The Manuka (scarab) (Fig. 11.62a) exploits chiral films to make its cuticle iridescent with a circular polarization. Biomimetic replicas made of TiO_2 (Fig. 11.62b, d) have different colors depending on the pitch of the film and the viewing angle.

11.8.2 Formation Processes of Photonic Bionanostructures

The material for the formation of scales or cuticle is made by epidermal cells with a size much larger than the nanostructures of the reflective multilayers. This suggests that the deposition pattern is defined by the presence of small organelles in the cell, such as mitochondria, microtubules, and microfibrils. For the formation of the helicoidal reflection layers, such as in the case of the Manuka beetle (Fig. 11.62c), the chitin molecules, initially in a liquid environment, self-assemble into a liquid crystal and become closer to each other during drying.

The same few designs for reflective nanomultilayers are found again and again within highly unrelated species, suggesting that the basic eukaryote cell contains an array of preexisting nanostructures that can be called upon in the manufacture of complex photonic nanostructures in any taxon (group of organisms). If the same molds, scaffolds, templates, or machineries are used each time, it is not surprising that the photonic devices show similarities. Equally, if similar physical processes are involved, such as molecular self-assembly, then similar nanoarchitectures could be expected to reoccur. The goal in the field of optical biomimetics, therefore, could be to replicate such nanomachinery that will self-assemble optical nanostructures with precision. DNA machines are already made by self-assembly [11.175], so this goal is not unrealistic [11.170].

11.9 Lotus Leaf Effect – Hydrophobicity and Self-Cleaning

A lotus leaf (*Nelumbo nucifera*) has been considered for centuries as a symbol of purity because of its self-cleaning nature (see Fig. 11.63a). This is due to a multi-lengthscale surface topology with hydrophobic micro- and nanostructures (Fig. 11.63b) giving rise to superhydrophobicity or water repellency [11.176–11.179].

Contact angle measurements of a droplet on a substrate are used for the determination of the wetting properties. In fact, two different angles are necessary to describe the wettability of a surface, the advancing and the receding angles, θ_A and θ_R, respectively. These angles can be measured when water is evaporated (θ_R) from or absorbed (θ_A) by a droplet. In the case of perfect hydrophobicity or superhydrophobicity ($\theta_A/\theta_R = 180°/180°$), the spherical drop touches the surface at a single point [11.179] and moves readily on the surface.

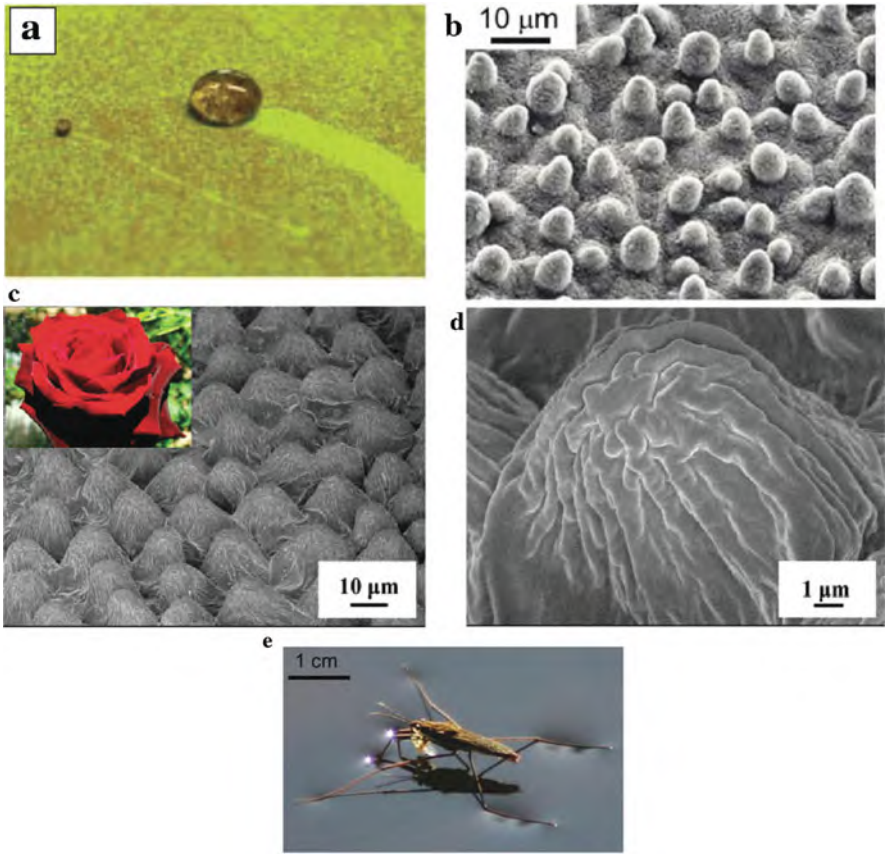

Fig. 11.63 Hydrophobicity as a prerequisite for the lotus effect, the rose petal effect, and the water strider. (**a**) Lotus effect. A water droplet collects dirt from the surface of a lotus leaf. (**b**) Close-up of a lotus leaf (*Nelumbo nucifera*), an example of a superhydrophobic plant surface which originates from the multilength-scale structuring by micrometer-sized bumps and nanoscale waxy hairs [11.178]. (**c**, **d**) Scanning electron micrograph (SEM) of the surface of a red rose petal showing a periodic array of micropapillae and nanofolds on each papilla top [11.180]. (**e**) Water strider (*Gerris remigis*) walking on the surface of a lake (see [11.178]). (Reprinted with permission from [11.178] (**a**) (**b**) (**e**) and [11.180] (**c**) (**d**). © 2008 Materials Research Society (**a**) (**b**) (**e**) and © 2008 American Chemical Society (**c**) (**d**))

In the lotus leaf the surface has hydrophobic hierarchical micro- and nanostructures (Fig. 11.63b) with a coexistence of micrometer-sized bumps and nanoscale waxy hairs [11.176, 11.178]. Similar hierarchical micro- and nanostructures are found on the surfaces of rose petals (Fig. 11.63c, d). Hydrophobicity permits water striders (*Gerris remigis*) with hierarchical micro–nanostructured legs to stroll effortlessly on water (Fig. 11.63e), where a single leg can hold up to 1.52 mN, which is 15 times the entire water strider's body weight [11.178].

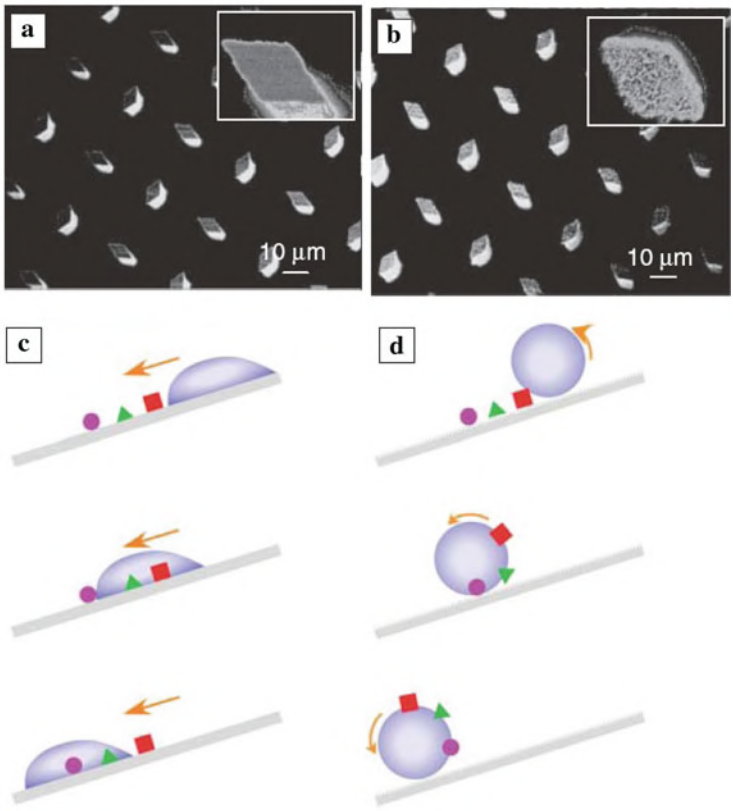

Fig. 11.64 (**a**, **b**) Model artificial lotus leafs. (**a**) Scanning electron micrograph (SEM) of a surface containing micrometer-sized posts with a smooth surface. (**b**) Post from (**a**) covered with nanosized methylsilicone fibrils (~40 nm in diameter) yielding superhydrophobic properties [11.179]. (**c**) Schematic representation of a flat hydrophilic surface where a water droplet just passes through strongly adhering dirt particles. (**d**) A different situation occurs on a topographically structured superhydrophobic substrate with weak adherence of dirt particles and spherical rolling droplets which pick up the dirt particles and hence clean the surface [11.178]. (Reprinted with permission from [11.179] (**a**) (**b**) and [11.178] (**c**) (**d**). © 2008 Materials Research Society)

In a model artificial lotus leaf (Fig. 11.64a, b) with micrometer smooth posts, water contact angles of $\theta_A/\theta_R = 176°/156°$ are measured (Fig. 11.64a), whereas with nanoscopic roughness on the posts (Fig. 11.64b) nearly perfect hydrophobicity $\theta_A/\theta_R => 176°/ > 176°$ is found. From this it is concluded that the nanohairs on the bumps of the lotus leaf substantially enhance hydrophobicity by increasing the local receding contact angle [11.179].

This superhydrophobic effect is the origin of self-cleaning [11.177]. As the spherical water droplets roll around easily on the leaf, they encounter debris and other particulates which minimally adhere to the surface with multiple length scales of roughness and therefore can be readily carried away by the traversing water droplet

(see Fig. 11.64d). The self-cleaning effect is unavailable on a hydrophilic surface with non-spherical water droplets (Fig. 11.64c).

11.10 Food Nanostructures

Milk, cereals, meat, etc., all these products are based on nanostructures such as gels, emulsions, foams, or combinations thereof [11.181]. Structural studies of foods can promote the understanding of the individual components and their effect on the overall microstructure of complex food products. Five out of ten of the world's largest food and beverage companies are investing in some form of this research [11.182]. Two studies on meat and milk proteins and an example from food packaging will be outlined in the following.

The protein forming the thick filaments in meat (muscle tissue) is myosin. The characteristics of myosin gel formation on the nanoscale (Fig. 11.65) are of importance for the structure of fabricated fish and meat products like surimi (minced fish) and sausages. Individual myosin molecules (Fig. 11.65a) associate

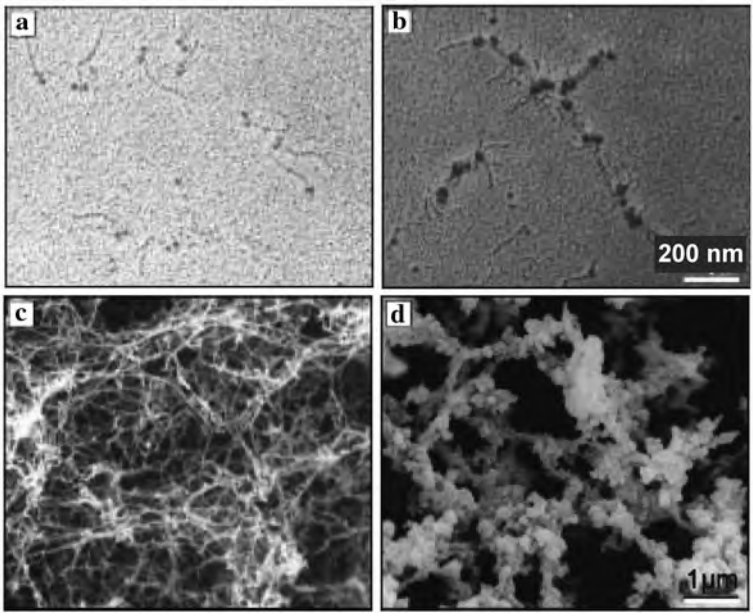

Fig. 11.65 Association and aggregation of myosin protein molecules to networks. (**a**) Transmission electron microscopy (TEM) of myosin molecules at pH 6.0 and 0.6 M KCl. (**b**) TEM of head-to-head interactions of myosin at pH 6 and 0.6 M KCl after heat treatment at 40°C. (**c**) Scanning electron microscopy (SEM) of a filamentous myosin gel at pH 5.5 and 0.25 M KCl after heat treatment at 60°C and (**d**) an aggregated myosin gel at pH 6.0 and 0.6 M KCl after heat treatment at 60°C. (Reprinted with permission from [11.181]. © 2000 Materials Research Society)

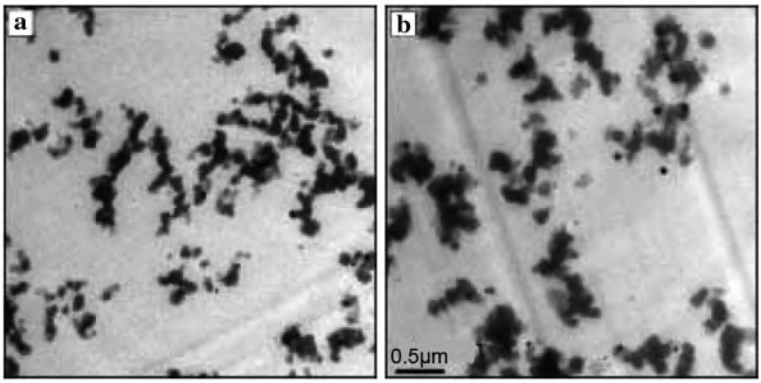

Fig. 11.66 Transmission electron micrographs (TEM) of 6% β-lactoglobulin gels at pH 5.4 (**a**) without and (**b**) with the addition of 0.06% monolaurin emulsifier. (Reprinted with permission from [11.181]. © 2000 Materials Research Society)

into different supramolecular assemblies (Fig. 11.65b), depending on the ionic strength. On heating of individual myosins, a filamentous network (Fig. 11.65c) and from the supramolecular assemblies and aggregated network (Fig. 11.65d) are formed.

Dairy products such as yoghurts and cheeses are based on a structure of protein gels in combination with the structure of emulsions, where emulsifiers are added to stabilize the fat. The effect of the emulsifier monolaurin on the gel formation of β-lactoglobulin, the most important gel-forming milk protein in whey, is a more open gel network with larger pores (Fig. 11.66b).

For food packaging materials polymers play an important role with an increasing demand to improve the barrier properties of the packaging materials concerning permeation of, e.g., water vapor or oxygen, in order to extend the shelf life of the packed foodstuff. Deposition of SiO_x barrier layer with a nanosized thickness of 100 or 30 nm on polyethyleneterephthalate (PET) or poly (propylene) (PP) foils, respectively, can reduce the oxygen permeability by up to a factor of 65 [11.183] (see also Sect. 6.9).

11.11 Cosmetics

Cosmetics are intended to improve the appearance of the skin, the hair, or the teeth. Today many cosmetic products aim at hydrating the skin, reducing or slowing the signs of aged skin, or protecting the skin against the multitude of daily aggressions that it encounters. As discussed below, nanoparticles, such as liposomes or nanosomes, may be used for the efficient transport of cosmetic ingredients into skin [11.185]. Ancient hair dyeing formulae have been found to be based on the formation of PbS (galena) nanocrystallites [11.188].

11.11.1 Skin Care

The emergence of deeper furrowing and wrinkling is related to a mechanical failure of the skin as shown by loss of tension and elasticity. The alteration of complexion is related to skin vasculature (see Fig. 11.67). The reduction in the water holding capacity of the outer layer of the epidermis, the stratum corneum (Fig. 11.67a, b), which only contains dead, strongly keratinized cells, also influences the general aspect of the skin.

Nanoparticles with sizes from 10 nm to a few hundred nanometers can be used as carriers for cosmetic components. Liposomes (Fig. 11.68b) can encapsulate water-soluble ingredients in their polar cavity and oil-soluble ingredients in their hydrophobic cavity. Liposomes have been used since the mid-1980s, when Christian Dior first introduced its Capture line to the market [11.185]. Nanotopes are formed

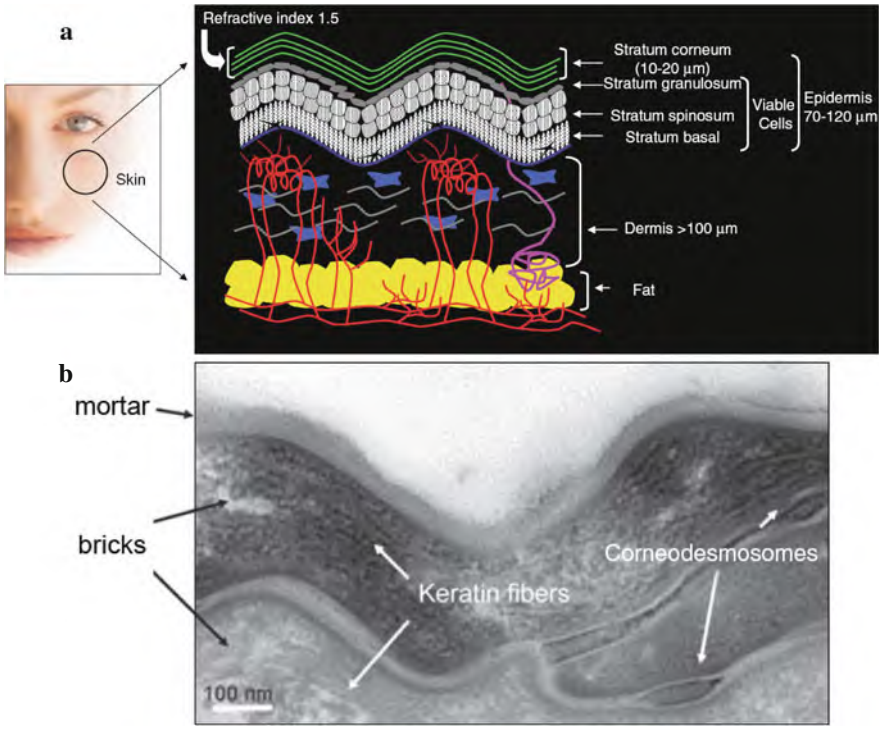

Fig. 11.67 (**a**) Skin appearance, texture, and mechanical strength depend on the structural organization of the layers of the skin (*right*). The stratum corneum, the outermost layer of the skin, is in contact with the environment. The epidermis comprises a layer of basal cells, the stratum spinosum, and the stratum granulosum. Under the epidermis is the dermis, which supports the skin's vasculature, nerves, hair follicles, and sebum-producing glands. (**b**) Transmission electron micrograph of the stratum corneum. Intercellular connections are via protein "rivets" called corneodesmosomes. Cells achieve rigidity and strength from a network of aligned keratin fiber bundles. (Reprinted with permission from [11.189]. © 2007 Materials Research Society)

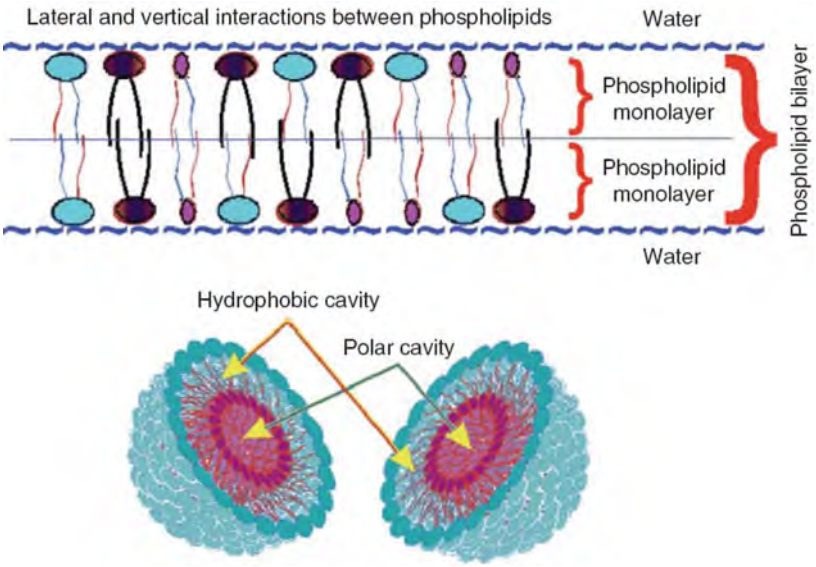

Fig. 11.68 Nanosized liposomes can encapsulate and transport water-soluble ingredients in their polar cavity and oil-soluble ingredients in their hydrophobic cavity. (Reprinted with permission from [11.185]. © 2007 Materials Research Society)

from a combination of lecithin, a phospholipid, and cosurfactants, which are aligned in an alternating arrangement. An example of a commercialized nanotechnology product is L'Oreal's Plenitude Revitalift, introduced in 1998, an antiwrinkle cream that uses a 200 nm technology (nanosomes to carry lipophilic material) to incorporate vitamin A into a polymer capsule to help deliver active ingredients to the skin's deeper layers [11.185]. The liposomes are able to bind to microorganisms responsible for skin disorders, sculp irritation, and underarm and foot odor, and hence can be used to selectively treat these disorders (see [11.184]).

While recognizing the value of these molecular-level advances, there is concern about the safety of nanotechnology for workers and consumers. Therefore, any new material now delivered to the market place must go through extensive testing to ensure that it is safe as recommended. This increase in safety requirements is due to increased regularity requirements, especially in the European Union where the REACH program (Registration, Evaluation, Authorization, and Restriction of Chemicals) requires cradle-to-grave documentation of all raw materials (see [11.185]).

For reducing the visibility of wrinkles, light diffusing pigments were developed from 1000 nm SiO_2 spheres coated with TiO_2 nanoparticles with a refractive index similar to that of the skin and Fe_2O_3 nanocrystals with a coloration resembling that of the skin. By this pigment the reflection of light out of a wrinkle is enhanced by factors of 4–10 compared to that from the skin [11.186].

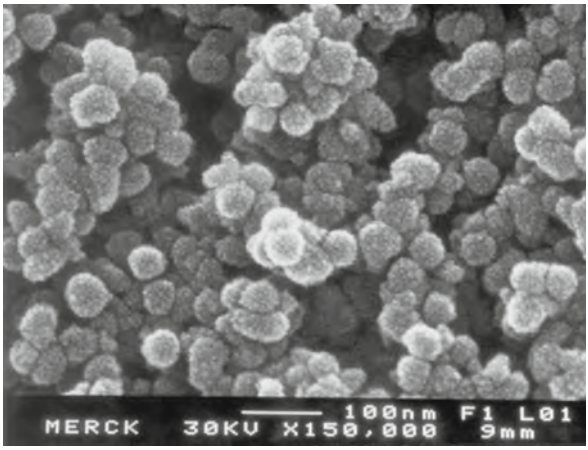

Fig. 11.69 Scanning electron microscopy of a sunscreen agent with SiO_2 spheres (20–50 nm) coated with TiO_2 particles smaller than 10 nm for optimum UV absorption. (Reprinted with permission from [11.186]. © 2001 Springer Verlag)

Efficient sun screen agents are produced making use of 20–50 nm SiO_2 spheres coated with TiO_2 nanoparticles smaller than 10 nm (Fig. 11.69). These agents are extremely good in UV absorption and they are invisible when applied to the skin because particles smaller than 60 nm practically do not scatter light.

11.11.2 Encapsulating a Fragrance in Nanocapsules

This is a method to avoid evaporation of volatile components at an early stage of usage and to increase shelf life of a product, offering a long-term usage for household purposes or as a fragrance in many cosmetic products or washing agents [11.187] (Fig. 11.70).

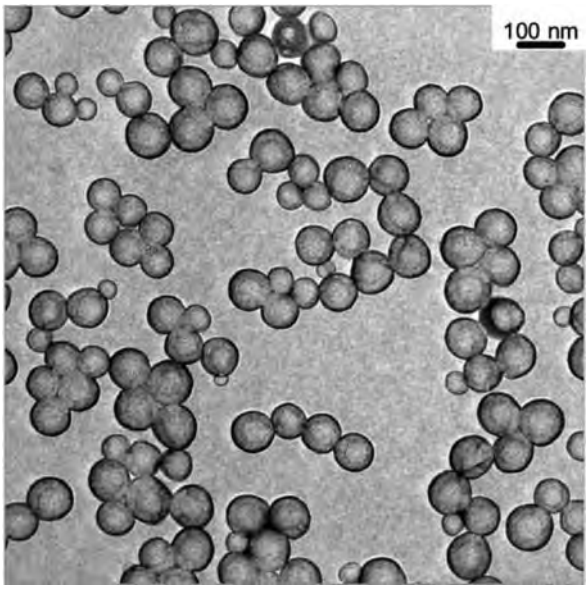

Fig. 11.70 Transmission electron micrograph (TEM) of poly (methyl metacrylate) (PMMA) nanocapsules for the hydrophobic fragrance 1,2-dimethyl-1-phenyl-butyramide (DMPBA). (Reprinted with permission from [11.187]. © 2009 Wiley-VCH)

11.11.3 PbS Nanocrystals in Ancient Hair Dyeing

A 2000-year-old recipe sold to this day as a remedy for graying hair is a mixture of lead oxide, PbO, and slaked lime, $Ca(OH)_2$, with a small amount of water [11.188]. The treatment of hair with this mixture (see Fig. 11.71a–c) gives rise to blackening due to the precipitation of 5 nm galena (PbS) crystallites as identified by x-ray scattering and by transmission electron microscopy (Fig. 11.71d, e). The progress of the crystallite precipitation starting from the hair surface was documented by scanning electron microscopy energy-dispersive x-ray emission (SEM-EDX) for the

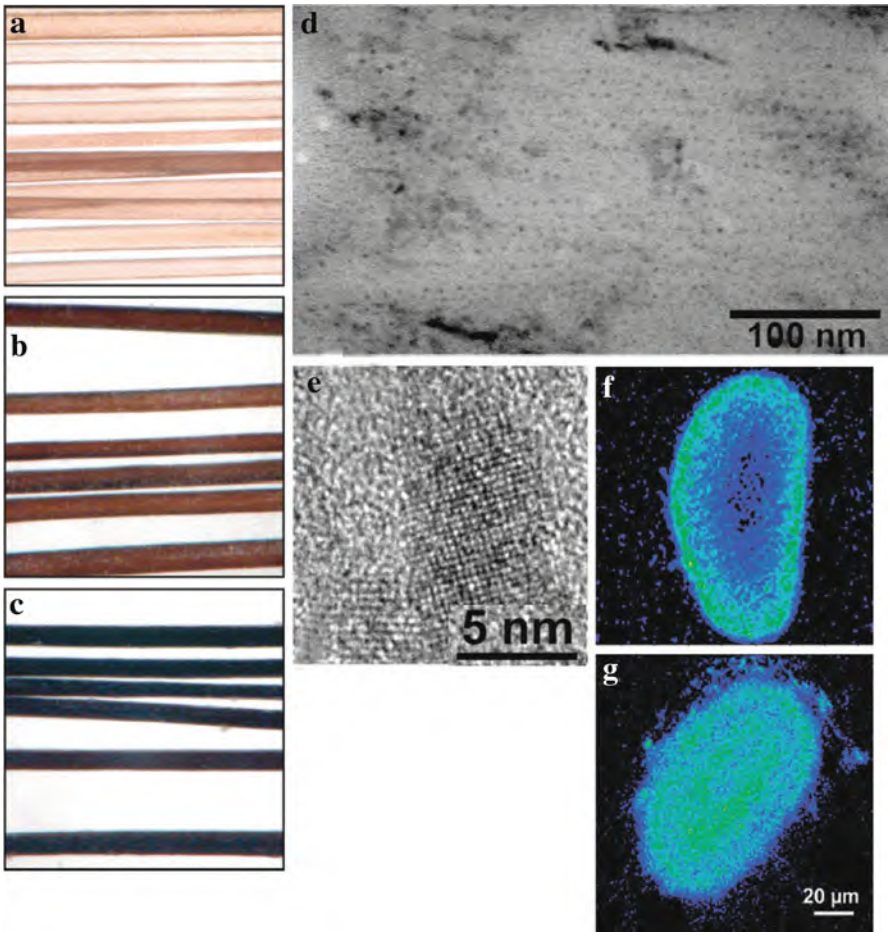

Fig. 11.71 Optical micrographs of hair (**a**–**c**; thickness = 10 µm), showing progressive blackening during treatment with $Ca(OH)_2$ and PbO in water (25°C, pH = 12.5). (**a**) Untreated, (**b**) and (**f**) after 6 h, (**c**) and (**g**) after 72 h. (**f**, **g**) Pb concentration as obtain from scanning electron microscopy energy-dispersive x-ray emission (SEM-EDX) with the Pb concentration increasing from *dark blue* to *green*). (**d**) High-resolution transmission electron micrograph (HRTEM) of a longitudinal section of a 3-day-treated hair. (**e**) HRTEM of a PbS nanocrystallite. (Reprinted with permission from [11.188]. © 2006 American Chemical Society)

quantification of Pb uptake (Fig. 11.71f, g). As deduced from the x-ray scattering results, the α-helical coiled structure of the hair keratin protein is preserved after the blackening reaction [11.188].

The PbS crystallites are formed by in-diffusion of Pb ions into the hair keratin structure where the sulfur for the formation of galena is provided by the natural amino acids, cystine and methionine [11.188]. The 5 nm sized PbS crystallites represent a kind of substitute of the natural black hair color which is due to the much larger 300 nm melanin pigment clusters within the colorless keratin-based cortex of the hair.

11.12 Summary

Nanoscience plays an important role in the investigation of biological phenomena because the size of inorganic nanoparticles as probes and the spatial resolution of nanotools match the sizes of macromolecular components (in the range of 2–200 nm) employed in living systems. The minimum size of a living system may have a diameter of 40–50 nm which is in the size range of a virus or of small biological structures. Cells in living organisms contain a system of nanoscale machines, molecular motors, and membrane channels. Nanoparticles can be employed for the bioanalysis of DNA and proteins and for the characterization of these species nanomechanical techniques may be used. Biomimetics are technologies inspired by the favorable properties of biological systems, such as nanoscale efficiency, self-organization, and adoptability at relatively low cost. Nanostructures are characteristic for bone, teeth, and for the photonic biostructures which yield colors to butterflies and beetles. Nanostructures, furthermore, enable the lotus leaf self-cleaning effect in plants and are typical for food and for cosmetic applications.

References

11.1 V.I. Maron et al., Nanobiology **2**, 189 (1993)
11.2 I. Prigogine, G. Nicolis, *Self-organization in non-equilibrium systems* (Wiley, New York, 1981)
11.3 M.D. Nussinov, V.I. Maron, J BIS **43**, 3 (1990)
11.4 S. Mitragotri, J. Laham, Nat. Mater. 8, 15 (2009)
11.5 G.M. Whitesides, Small **1** (2) 172 (2005)
11.6 G. Bao, S. Suresh, Nat. Mater. **2**, 715 (2003)
11.7 O. Medalia et al., Science **298**, 1209 (2002)
11.8 N. de Jonge et al., Proc. Natl. Acad. Sci. USA **106**, 2159 (2009)
11.9 B. Hein et al., Proc. Nat. Acad. Sci. USA **105**, 14271 (2008)
11.10 N. Ban et al., Science **209**, 902 (2000)
11.11 K. Madura, Nature **459**, 787 (2009)
11.12 M.M. Kozlov, Nature **447**, 387 (2007)
11.13 N. Toni et al., Nat. Neurosci. **10**, 727 (2007)
11.14 C. Eggeling et al., Nature **457**, 1159 (2009)

11.15 B. Alberts et al., *The Molecular Biology of the Cell* (Garland Science, New York, 2002)
11.16 B.J. Reynwar et al., Nature **447**, 461 (2007)
11.17 A. Bershadsky et al., Curr. Opin. Cell Biol. **18**, 472 (2006)
11.18 E. Sackmann, Phys. J. **5** (8/9), 28 (2006)
11.19 A.-S. Smith et al., Proc. Natl. Acad. Sci. USA **105**, 6906 (2008)
11.20 E. Sackmann, Phys. J. **3**, Nr. 2, 35 (2004)
11.21 T. Shemesh et al., Proc. Natl. Acad. Sci. USA **102**, 12383 (2005)
11.22 S. Suresh et al., Acta Biomaterialia **1**, 15 (2005)
11.23 J. Wood, Mater. Today, February 2005, p. 15
11.24 Y.K. Park et al., Proc. Natl. Acad. Sci. USA **105**, 13730 (2008)
11.25 H. Herrmann et al., Nat. Rev. Mol. Cell Biol. **8**, 562 (2007)
11.26 A. Vaziri, A. Gopinath, Nat. Mater. **7**, 15 (2008)
11.27 M. Ferrari, Nat. Nanotech. **3**, 131 (2008)
11.28 W. Jiang et al., Nat. Nanotech. **3**, 145 (2008)
11.29 M. Bruchez et al., Science **281**, 2013 (1998)
11.30 A.P. Alivisatos et al., Ann. Rev. Biomed. Eng. **7**, 55 (2005)
11.31 I.L. Medintz et al., Nat. Mater. **4**, 435 (2005)
11.32 X. Michalet et al., Science **307**, 538 (2005)
11.33 P. Gould, Nano Today **1**(4), 34 (2006)
11.34 C.C. You et al., Nano Today **2**, Nr. 3, 34 (2007)
11.35 J.L. Yan et al., Nano Today **2**, Nr. 3, 44 (2007)
11.36 K. Glynou et al., Anal. Chem. **75**, 4155 (2003)
11.37 J.-S. Oh et al., Clin. Vaccine Immunol. **13**, 520 (2006)
11.38 A. van Blaaderen, A. Vrij, Langmuir **8**, 2921 (1992)
11.39 P. Gould, Nano Today **1** (4), 34 (2006)
11.40 G.S. Baird et al., Proc. Natl. Acad. Sci. USA **97**, 11984 (2000)
11.41 X. Wu et al., Nat. Biotechnol. **21**, 41 (2003)
11.42 C.M. Niemeyer, *Bioconjugation Protocols: Strategies and Methods* (Humana Press, Totowa, NJ, 2004)
11.43 L. Wang, Anal. Chem. **78**, 646A (2006)
11.44 H.-J. van Manen, C. Otto, Nano Lett. **7** (6), 1631 (2007)
11.45 S. le Gac et al., Nano Lett. **6** (9), 1863 (2006)
11.46 D.R. Green, G.I. Evan, Cancer Cel. **1** (1), 19 (2002)
11.47 X. Chen et al., Proc Natl. Acad. Sci. **104**, 8218 (2007)
11.48 S. Kim et al., Nat. Biotechnol. **22**, 93 (2004)
11.49 E.B. Voura et al., Nat. Med. **10**, 993 (2004)
11.50 M.-K. So et al., Nat. Biotechnol. **24**, 339 (2006)
11.51 P.H. Hoet et al., J. Nanobiotechnol. **2**, 2 (2004)
11.52 F.Q. Chen, D. Gerion, Nano Lett. **4**, 1827 (2004)
11.53 C. Kirchner et al., Nano Lett. **5**, 331 (2005)
11.54 T.T. Zhang et al., Nano Lett. **6**, 800 (2006)
11.55 G. Han et al., Angew. Chem. Int. Edn. **45**, 3165 (2006)
11.56 G. Vassaux et al., J. Pathol. **208**, 290 (2006)
11.57 D. Akin et al., Nat. Nanotechn. **2**, 441 (2007)
11.58 G. Dietrich, Nat. Nanotechn. **2**, 441 (2007)
11.59 F. Patolsky et al., J. Am. Chem. Soc. **125**, 13918 (2003)
11.60 X. Zhao et al., J. Am. Chem. Soc. **125**, 11474 (2003)
11.61 J. Stehr et al., Nano Lett. **8**, 619 (2008)
11.62 P.S. Eastman et al., Nano Lett. **6**, 1059 (2006)
11.63 S.-P. Lin et al., Nano Today **4**, 235 (2009)
11.64 R. Hong et al., J. Am. Chem. Soc. **126**, 13572 (2004)
11.65 P. Gould, Mater. Today, February 2004, p. 36
11.66 I. Lynch, K.A. Dawson, Nano Today 3, Feb – Apr. 2008, p. 40

11.67 K.A. Dawson et al., Nat. Nanotechnol. **4**, 84 (2009)
11.68 M. Lundquist et al., Proc. Natl. Acad. Sci. USA **105**, 14265 (2008)
11.69 J.-S. Oh et al., Clin. Vaccine Immunol. **13**, 520 (2006)
11.70 A. Sukhanova et al., Anal. Biochem. **324**, 60 (2004)
11.71 W. Kim et al., J. Am. Chem. Soc. **129**, 7228 (2007)
11.72 R. Minchin, Nat. Nanotechnol. **3**, 12 (2008)
11.73 L. Balogh et al., Nanotechnol. Biol. Med. **3**, 281 (2007)
11.74 C. Bustamante et al., Nature **421**, 423 (2003)
11.75 M. Rief et al., Nat. Struct. Biol. **6**, 346 (1999)
11.76 M. Rief et al., Science **276**, 1109 (1997)
11.77 T.E. Fisher et al., Trends Biochem. Sci. **24**, 379 (1999)
11.78 M. Schliwa (ed.), *Molecular Motors* (VCH – Wiley, Weinheim, 2003)
11.79 M. Schliwa, G. Woehlke, Nature **422**, 759 (2003)
11.80 J. Liu et al., Nature **442**, 208 (2006)
11.81 J.L. Woodhead et al., Nature **436**, 1195 (2005)
11.82 J.E. Molloy, S. Schmitz, Nature **435**, 285 (2005)
11.83 N.J. Carter, R.A. Cross, Nature **435**, 308 (2005)
11.84 S. Courty et al., Nano Lett. **6** (7), 1491 (2006)
11.85 T. Mori et al., Nature **450**, 750 (2007)
11.86 G. Cappello et al., Proc. Natl. Acad. Sci. USA **104**, 15328 (2007)
11.87 B.L. de Groot et al., Phys. Unserer Zeit **37** (2), 73 (2006)
11.88 W. Junge et al., Nature **459**, 364 (2009)
11.89 H. Noji et al., Nature **386**, 299 (1997)
11.90 R.A. Böckmann, H. Grubmüller, Nat. Struct. Biol. **9**, 198 (2002); Biophys. J. **85**, 1482 (2003)
11.91 H. Itoh et al., Nature **427**, 465 (2004)
11.92 L. Anson, Nature **440**, 439 (2007)
11.93 D.A. Doyle et al., Science **280**, 69 (1998)
11.94 H. Schrempf et al., EMBO J. **14**, 5170 (1995)
11.95 Ch. Miller, Nature **414**, 23 (2001)
11.96 M. Schumacher, J.P. Adelmann, Nature **417**, 501 (2002)
11.97 H. Morais-Cabral et al., Nature **414**, 37 (2001)
11.98 Y. Zhou et al., Nature **414**, 43 (2001)
11.99 S. Bernèche, B. Roux, Nature **414**, 73 (2001)
11.100 Y. Jiang et al., Nature **417**, 515 (2002)
11.101 Y. Jiang et al., Nature **417**, 523 (2002)
11.102 S. Feske et al., Nature **441**, 179 (2006)
11.103 M. Vig et al., Science **312**, 1220 (2006)
11.104 A.B. Parekh, Nature **441**, 163 (2006)
11.105 A.B. Parekh, J.W. Putney, J. Physiol. Rev. **85**, 757 (2005)
11.106 N. Piwon et al., Nature **408**, 369 (2000)
11.107 R. Dutzler et al., Nature **415**, 287 (2002)
11.108 Th. J. Jentsch, Nature **415**, 276 (2002)
11.109 G.M. Preston et al., Science **256**, 385 (1992)
11.110 M.L. Zeidel et al., Biochemistry **31**, 7436 (1992)
11.111 C. Day, Phys. Today, December 2003, p. 27
11.112 B. van den Berg et al., Nature **427**, 36 (2004)
11.113 J. Benach, J.F. Hunt, Nature **427**, 24 (2004)
11.114 G. Blobel, B. Dobberstein, J. Cell Biol. **67**, 835 (1975)
11.115 G. Blobel, Proc. Natl. Acad. Sci. USA **77**, 1496 (1980)
11.116 N. Bocquet et al., Nature **457**, 111 (2009)
11.117 R.J. C. Hilf, R. Dutzer, Nature **457**, 115 (2009)
11.118 M. Beck et al., Nature **449**, 611 (2007)

11.119 P. Ball, Nanotechnol. **13**, R15 (2002)
11.120 G. Steniberg-Yfrach et al., Nature **385**, 239 (1997). **392**, 479 (1998)
11.121 T.A. Dickenson et al., Nature **382**, 697 (1996)
11.122 S. Banta et al., J. Nanosci. Nanotechnol. 7, 387 (2007)
11.123 R.M. de Lorimier et al., Protein Sci. **11**, 2655 (2002)
11.124 L.L. Looger et al., Nature **423**, 185 (2003)
11.125 M.R. Ghadiri et al., Nature **366**, 324 (1993); Nature **369**, 301 (1994)
11.126 C. Mao et al., Nature **397**, 144 (1999)
11.127 T.R. Kelly et al., Nature **401**, 150 (1999)
11.128 J.J. Schmidt, C.D. Montemagno, Drug Dis. Today **7**, 500 (2002)
11.129 F.J. Nédélec et al., Nature **389**, 305 (1997)
11.130 F. Patolsky et al., Nat. Mater. **3**, 692 (2004)
11.131 T.J. Huang, MRS Bull. **33**, 226 (2008)
11.132 C.-F. Lee et al., Nature **458**, 314 (2009)
11.133 Ph. Ball, Nat. Mater. **8**, 448 (2009)
11.134 P. Ball, Nature **391**, 128 (1998)
11.135 B.L. Smith et al., Nature **399**, 761 (1999)
11.136 S. Zhang et al., Proc. Natl. Acad. Sci. USA **90**, 3334 (1993); Biopolymer. **34**, 663 (1994)
11.137 D. Pantaroffo et al., J. Am. Chem. Soc. **125**, 6160 (2003)
11.138 S. Mann, *Biomineralization*, (Oxford University Press, Oxford, UK, 2001)
11.139 A. Navrotsky, Proc. Natl. Acad. Sci. USA **101**, 12096 (2004)
11.140 R.R. Naik, M.O. Stone, Mater. Today, September 2005, p. 18
11.141 M.M. Tomczak et al., J. Am. Chem. Soc. **127**, 12577 (2005)
11.142 K.M. Hawkins et al., J. Am. Chem. Soc. **126**, 9112 (2004)
11.143 M. Reches, E. Gazit, Science **300**, 625 (2003)
11.144 P.J. You et al., Nat. Mater **5**, 234 (2006)
11.145 K.T. Nam et al., Science **312**, 885 (2006)
11.146 K.-I. Sano, K. Shiba, MRS Bull. **33**, 524 (2008)
11.147 Z. Tang et al., Nat. Mater. **2**, 413 (2003)
11.148 M. Rubner, Nature **423**, 925 (2003)
11.149 J.R. Jones, Mater. Today **9** (12), December 2006, p. 34
11.150 B.B. Hole et al., J. Biomed. Mater. Res. **74A**, 712 (2005)
11.151 R.L. Price et al., J. Biomed. Mater. Res. **70A**, 129 (2004)
11.152 A.S. Andersson et al., Biomaterials **24**, 3427 (2003)
11.153 A. Pohorille, D. Deamer, Trends Biotechnol. **20**, Nr. 3, 123 (2002)
11.154 L.H. Pinto et al., Proc. Natl. Acad. Sci. USA **94**, 11301 (1997)
11.155 J.W. Szostak et al., Nature **409**, 387 (2001)
11.156 R.M. Fielding, D.D. Lasic, Exp. Opin. Therapeut. Patents **9**, 1679 (1999)
11.157 T.M.S. Chang, Trends Biotechnol. **17**, 61 (1999)
11.158 J. Dobson, Nat. Nanotech. **3**, 139 (2008)
11.159 R.J. Mannix et al., Nat. Nanotech. **3**, 36 (2008)
11.160 E. Alsberg et al., Tissue Eng. **12**, 3247 (2006)
11.161 A. Ho et al., Tissue Eng. **11**, 489 (2005)
11.162 D. Porter, F. Vollath, Nano Today **2**, 6 (2007)
11.163 T.A. Taton, Nature **412**, 491 (2001)
11.164 S. Weiner, H.D. Wagner, Annu. Rev. Mater. Sci. **28**, 271 (1998)
11.165 P.T. Sharpe, C.S. Young, Sci. Am., August 2005, p. 24
11.166 H.F. Chen et al., Adv. Mater. **18**, 1846 (2006)
11.167 A.G. Fincham et al., J. Struct. Biol. **115**, 50 (1995)
11.168 W. Tesch et al., Calcif. Tissue Int. **69**, 147 (2001)
11.169 J.P. Vigneron et al., Phys. Rev. **E73**, 041905 (2006)
11.170 A.R. Parker, H.E. Townley, Nat. Nanotechnol. **2**, 347 (2007)
11.171 A.R. Parker et al., Nature **409**, 36 (2001)

11.172 T. Lenau, M. Barfoed, Adv. Eng. Mater. **10** (4), 299 (2008)
11.173 K. Watanabe et al., Jpn. J. Appl. Phys. **44**, L48 (2005)
11.174 L. DeSilva et al., Electromagnetics **25**, 391 (2005)
11.175 J. Bath, A.J. Turberfield, Nat. Nanotech. **2**, 275 (2007)
11.176 C. Neinhuis, W. Barthlott, Ann. Botany **79**, 667 (1997)
11.177 J.P. Youngblood, N.R. Sottos, MRS Bull. **33**, 732 (2008)
11.178 J. Genzer, A. Marmur, MRS Bull. **33**, 742 (2008)
11.179 L.C. Gao et al., MRS Bull. **33**, 747 (2008)
11.180 L. Feng et al., Langmuir **24**, 4114 (2008)
11.181 A.-M. Hermansson et al., MRS Bull., December 2000, p. 30
11.182 www.eas.eu
11.183 J. Schneider et al., Plasma Process. Polym. **4**, S155 (2007)
11.184 P. Somasundaran et al., MRS Bull. **32**, 779 (2007)
11.185 S. Schnittger, M. Sinha, MRS Bull. **32**, 760 (2007)
11.186 R. Anselmann, J. Nanoparticle Res. **3**, 329 (2001)
11.187 S. Theisinger et al., Macromol. Chem. Phys. **210**, 411 (2009)
11.188 P. Walter et al., Nano Lett. **6**, 2215 (2006)
11.189 K. Subramanyan et al., MRS Bull. **32**, 770 (2007)

Chapter 12
Nanomedicine

12.1 Introduction

Applications of nanotechnology for diagnosis, treatment, monitoring, and control of biological systems have been referred to as "nanomedicine" by the US National Institute of Health (NIH) [12.1]. According to a Forward Report published by the European Science Foundation [12.2], nanomedicine aims at "ensuring the comprehensive monitoring, control, construction, repair, defense, and improvement of all human biological systems, working from the molecular level using engineering devices and nanostructures, ultimately to achieve medical benefit" [12.3]. Nanotechnology is positively impacting health care. Nanomedicine is an interdisciplinary approach because it requires the intersection of many disciplines including biology, chemistry, physics, chemical and mechanical engineering, materials science, and clinical medicine [12.4]. Nanoscale and biosystems research are merging with information technology and cognitive science, leading to completely new science and technology platforms such as those for genome pharmaceutics, biosystems on a chip, regenerative medicine, and neuroscience [12.5].

At the forefront of projects in nanomedicine is the research into the rational delivery and targeting of pharmaceutical, diagnostic, and therapeutic agents via intravenous and interstitial routes of administration [12.1]. These involve the identification of precise targets (cells and receptors) related to specific clinical conditions and choice of the appropriate nanocarriers to achieve the required responses while minimizing side effects. Since human illness begins and advances at the cellular level, recent breakthroughs and advances (see [12.1]) in understanding how materials like proteins or drug ingredients affect an individual cell can give researchers important insight into how the material might impact the entire human body [12.6].

The field of nanomedicine is currently in its early phase of sharp growth and may be a considerable number of years away from maturity [12.4]. A continuous impact of nanotechnology on health care is, however, expected at many levels including (1) detection of molecular changes in disease pathogenesis; (2) disease diagnosis and imaging; (3) targeted drug delivery and therapy; (4) multifunctional systems for combined diagnostic and therapeutic applications; (5) vehicles to report the in vivo efficacy of therapeutic agents, and (6) nanoscience basic research (see

H.-E. Schaefer, *Nanoscience*, DOI 10.1007/978-3-642-10559-3_12,

[12.4]). In addition, the unprecedented precision of nanotechnology for cellular and intracellular manipulation opens the field of nanosurgery [12.7]. Despite the great rash into nanomaterials, there certainly is a heightened awareness of the potential problems that exist [12.8]. For example, although NanoMedicine Summit 2008 presented a huge number of potential applications of nanotechnology to medicine (www.nanomedicinesummit.org/agenda.asp), we also note that there are serious concerns to be addressed [12.9].

Nanoparticles including colloidal gold, semiconductor quantum dots, iron oxide nanocrystals, or nanocrystalline bismuth sulfide with typical sizes of 1–20 nm or polymeric micelles, dendrimers, and liposomes ranging from a few to 250 nm are being studied for medical diagnosis and therapy. Some of them, such as iron oxide nanoparticles for contrast enhancement in magnetic resonance imaging (MRI) [12.10], liposomes conjugated with the anticancer agent doxorubicin (Doxil) [12.4], or albumin nanoparticles decorated with the anticancer drug paclitaxel (Abraxane) [12.11] have gained approval by the US Food and Drug Administration (FDA) and by regulatory bodies in other countries [12.10]. Gold and silver nanoparticles can absorb and scatter light from UV to near-infrared (NIR) wavelengths due to their size- and shape-dependent surface plasmon oscillations (see [12.12]). In semiconductor quantum dots, such as, e.g., CdSe, the fluorescence emission wavelength (UV to NIR) can be tuned due to the size-dependent spacing of the electron energy levels [12.13] yielding the potential to revolutionize cell, receptor, antigen, and enzyme imaging (see [12.1]). Iron oxide nanocrystals are of importance for MRI contrast enhancement, as they cause changes in the nuclear spin relaxation times of neighboring water molecules. By virtue of their small size and by functionalizing their surface with polymers and appropriate ligands, intravenously or subcutaneously administered nanoparticulate carriers can be targeted to specific cells, locations, or organs within the body where these agents can cure diseases, minimizing unwanted side effects. Some nanoparticles are designed with the focus on multifunctionality for simultaneous targeting, drug delivery, and sensing (see [12.1]).

Nanoparticles injected intravenously can be retained in the blood circulation for a longer period by appropriate surface manipulation. The particle escape from the vasculature is mainly restricted to sites where the capillaries have open fenestration, as in the sinus endothelium of the liver or when the integrity of the endothelial barrier is perturbed by inflammatory processes or by tumor growth which is the result of dysregulated angiogenesis. In the liver, the size of fenestrae in the sinus endothelium can be as large as 150 nm; in tumor capillaries they rarely exceed 300 nm. This escape of nanoparticles from the vasculature can be exploited to direct diagnostic and therapeutic entities to selected pathological vessels, particularly to those of cancer (see [12.1]). Furthermore, by appropriate targeting ligands conjugated to the nanoparticles, these can search for signature molecules expressed by the target, a process often referred to as active targeting.

Interstitial injection of nanoparticles, however, may be the preferred choice, particularly if the target is a specific lymph node (see [12.1]). After interstitial injection, many of the overlapping endothelial cells are separated and thus passage ways are

provided between the interstitium and the lymphatic lumen through which particles are conveyed to the node via the afferent lymph. The fate of interstitially injected nanoparticles is controlled by their size and surface characteristics. The size of the particles must be large enough to prevent their leakage into the blood capillaries; particles in the range of 30–100 nm satisfy this criterion, whereas particles larger than 100 nm move very slowly and are susceptible to clearance by interstitial macrophages. Very small particles (1–20 nm), particularly when they are long circulatory, can slowly extravasate from the vasculature into the interstitial spaces, from which they are transported to lymph nodes via lymphatic vessels (see [12.1]).

The convergence of nanoscale science with modern biology and medicine is a trend that is reflected in science policy decisions [12.5]. In the United States, the National Institute of Health (NIH) has sponsored approximately 20 Nanomedicine Development Centers [12.14], including the seven centers of Cancer Nanotechnology Excellence at the University of North Carolina, the University of California, San Diego, the Emory-Georgia Tech, Caltech, and Washington University, St. Louis, MO. [12.15]. The European Commission launched a European Technology Platform on nanomedicine, with the goal of defining a European Strategic Research Agenda with the following priority list: cardiovascular diseases, cancer, musculoskeletal disorders, neurodegenerative diseases and psychiatric conditions, diabetes and bacterial and viral infection diseases. The Commission will channel some 100€ million into nanomedicine projects annually under its Seventh Framework Programme for research (2007–2013). Meanwhile the European Group on Ethics has published an opinion on nanomedicine, specifying that safety concerns should be a priority in the development of new techniques and treatments [12.16].

A number of International Conferences focused to nanomedicine have been organized recently, such as, *Cancer Nanotech 2007*, Paris, France, *Investing in Medical Nanotechnologies*, London, UK, 2006, or *Euro Nano Medicine Conference*, Bled, Slowenia, 2009.

The market for many drugs is rapidly expanding due to nanotechnology and nanoscience approaches to particle design and formulation, which is the basis for a highly profitable niche within the industry, although some predicted benefits may be hyped [12.1]. In addition, a sharp increase over the past years in the number of patent applications in this area underscores the heightened level of interest in nanomedicine by both academia and industry investigators [12.4]. However, although an estimated 130 nanotech-based drugs and delivery systems are being developed worldwide [12.3], a number of outstanding issues related to toxicity and environmental impact of nanoscale materials will have to be resolved before regulatory agencies can approve further products (see [12.3, 12.17]).

This chapter will review the application of nanoscience and nanotechnology in medicine that will transform disease diagnosis, therapy, and prevention in the near future. This medical change will usher in the era of mature nanomedicine and will be instrumental in the eventual emergence of nanosurgery and nanoneurosurgery. Mature nanomedicine will involve the design and fabrication of molecular devices with anatomic precision and then using them in patients to establish and maintain health [12.14].

12.2 Diagnostic Imaging and Molecular Detection Techniques

Medical imaging systems that provide anatomical and physiological information are now in widespread clinical and preclinical use (see [12.18]). By contrast, systems that obtain molecular information are just emerging.

Medical imaging modalities include [12.19] the following:

(i) Magnetic resonance imaging (MRI). This is a phenomenon involving the transition between different energy levels of atomic nuclei under the action of a radiofrequency signal.
(ii) Computed tomography (CT). This technique uses x-rays to create with the aid of computers cross-section images of the body and three-dimensional images of areas of interest.
(iii) Ultrasound (US) imaging. This modality is based on the different passage rates of ultrasound through different types of tissues.
(iv) Positron emission tomography (PET). In this technique radioactive isotopes are used which emit positrons (antiparticles of electrons). The positron–electron annihilation radiation emerging from a particular site is employed for tomographic imaging.
(v) Emerging imaging modalities: Raman spectroscopy and photoacoustic tomography.
(vi) Biomolecular detection techniques to identify the expression and activity of specific molecules and of biological processes for medical diagnosis.

In the following, the recent advances in these diagnostic techniques provided by nanotechnology and molecular approaches will be concisely reviewed.

12.2.1 Magnetic Resonance Imaging (MRI)

Although magnetic resonance imaging (MRI) is one of the most powerful medical diagnosis tools, its temporal resolution and sensitivity performance can be significantly improved by utilizing magnetic nanoparticles [12.20, 12.21].

For MRI, ferrite iron oxide magnetite (Fe_3O_4) or maghemite (γ-Fe_2O_3) nanoparticles (Fig. 12.1) are used, with high saturation magnetizations of 92 $emug^{-1}$ or 78 $emug^{-1}$ at 300 K, respectively (see [12.21]). These nanoparticles are superparamagnetic, i.e., they are characterized by a large magnetic moment in an external magnetic field, but their magnetization is reduced to zero upon removal of the external field.

The effect of magnetic nanoparticles on MRI is the following: The external field induces a magnetization in the magnetic nanoparticles, they align and their magnetization gives rise to a stray field δM (Fig. 12.2) with a very high local magnetic field gradient. This induces dephasing of water proton spins and consequently shortening of the T_1 and T_2 relaxation times of the surrounding water molecules, resulting in a darkening of the local MR imaging (Fig. 12.2b).

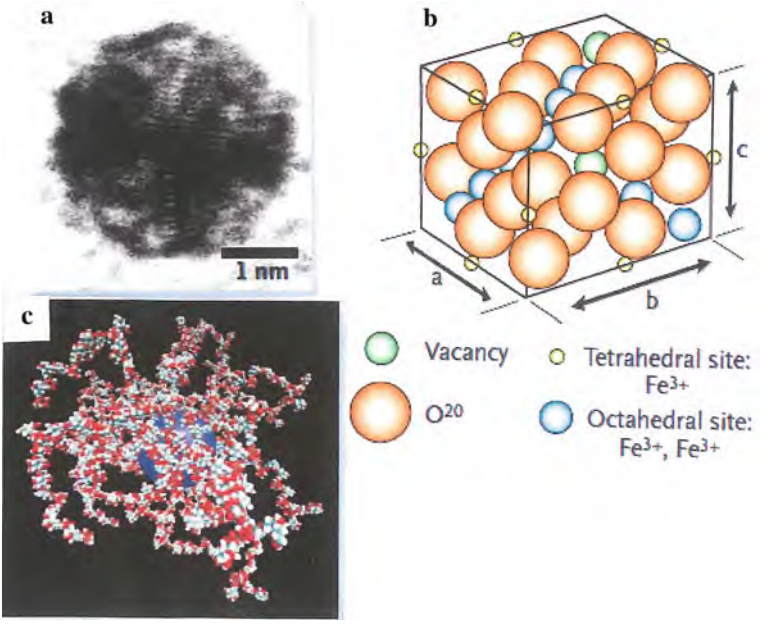

Fig. 12.1 Superparamagnetic iron oxide nanoparticles with a lymphotropic dextran coating. (**a**) Electron micrograph of a nanoparticle. (**b**) Crystal structure of the iron oxide nanoparticle. (**c**) Molecular model of the surface-bound 10 kDa dextrans with a mean size of 28 nm. (Reprinted with permission from [12.22]. © 2003 Massachusettes Medical Society)

For high-contrast magnetic resonance imaging (MRI), $MnFe_2O_4$ nanoparticles with a mixed spinel structure and a diameter of 12 nm have been developed, yielding higher relaxivities $R_2 = 1/T_2$ and therefore better contrast than Fe_3O_4 nanoparticles [12.23]. After conjugation with the cancer-targeting antibody Herceptin, which specifically binds to the HER2/neu marker overexpressed in breast and ovarian cancer, tumors as small as 50 mg could be detected in mice by MRI [12.23].

When magnetic nanocrystals are conjugated with biologically active materials (e.g., antibodies), the conjugates exhibit multifunctionality of both an MRI contrast enhancement and a selective biological recognition of target molecules. This conjugate can efficiently report on molecular and genetic events in target tissues [12.20]. Iron oxide nanocrystals of various sizes can be fabricated with narrow size distributions (Fig. 12.3) and modified by, e.g., 2,3-dimercaptosuccinic acid (DMSA) ligands for water solubility. When these modified nanocrystals are conjugated to the cancer-targeting antibody molecule, Herceptin (Fig. 12.3d), these conjugates can be effectively used for breast cancer diagnosis (see [12.20]). When used for in vivo detection of NiH3T6.7 cancer cells with Her 2/ neu overexpression, implanted in mice, these tumor sites could be imaged with high MRI contrast (Fig. 12.4). When unconjugated Fe_3O_4 control particles are injected into mice, no time-dependent changes in the color-mapped MRI signal (Fig. 12.4) and the T_2 value at the tumor

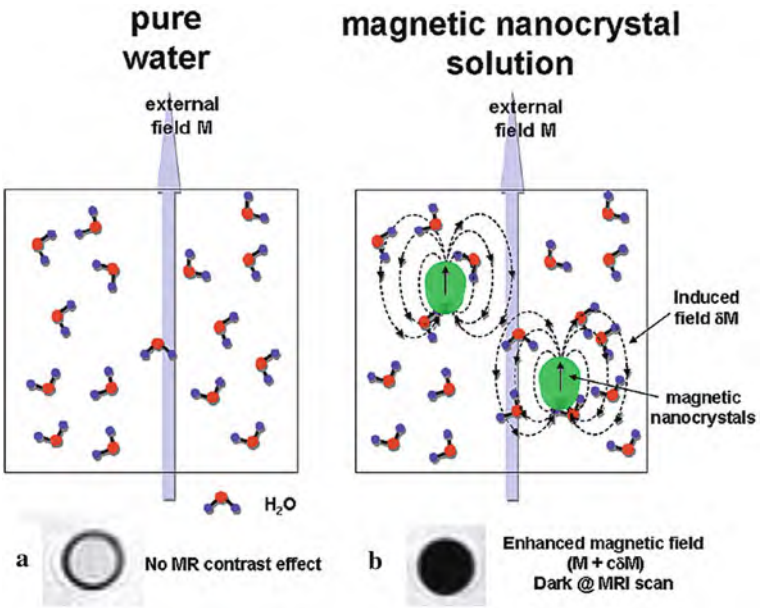

Fig. 12.2 Magnetic resonance imaging (MRI) contrast effect of magnetic nanocrystals. (Reprinted with permission from [12.20]. © 2006 Korean Chemical Society)

site are detected. In contrast, after injection of the Fe_3O_4–Herceptin conjugates, immediate color changes to blue are evident and a drop of the T_2 within 10 min is observed. This demonstrates that the Fe_3O_4–Herceptin conjugates successfully reach and bind to the target cancer cells for sensitive identification of tumors [12.20].

Most of the recent research of magnetic iron oxide nanoparticles for MRI contrast enhancement has concerned cellular imaging with imaging of in vivo macrophage activity showing that several clinical applications are possible: detection of liver metastases, metastatic lymph nodes, or inflammatory or degenerative diseases [12.21]. A few examples of nanoparticle MRI enhancement in brain cancer, breast cancer, myometrium and cervical tumors, prostate cancer lymph nodes, arthritis, infection, angiography, and atherosclerosis will be shown in the following.

Brain tumors. The determination of brain tumor margins both during the presurgical planning phase and during surgical resection has long been a challenging task in the therapy of brain tumor (see also Sect. 12.5) patients. Multimodal (magnetic and near-infrared fluorescent) nanoparticles have been explored recently in rats as a preoperative magnetic resonance imaging contrast agent in a 4.7T Bruker MRI tomography [12.24] and for intraoperative optical imaging of brain tumors [12.24]. The multimodal Cy5.5–CLIO nanoparticles consisted of dextran-coated iron oxide nanoparticles (CLIO) with the near-infrared fluorescent (NIRF) dye Cy5.5 attached to the coating.

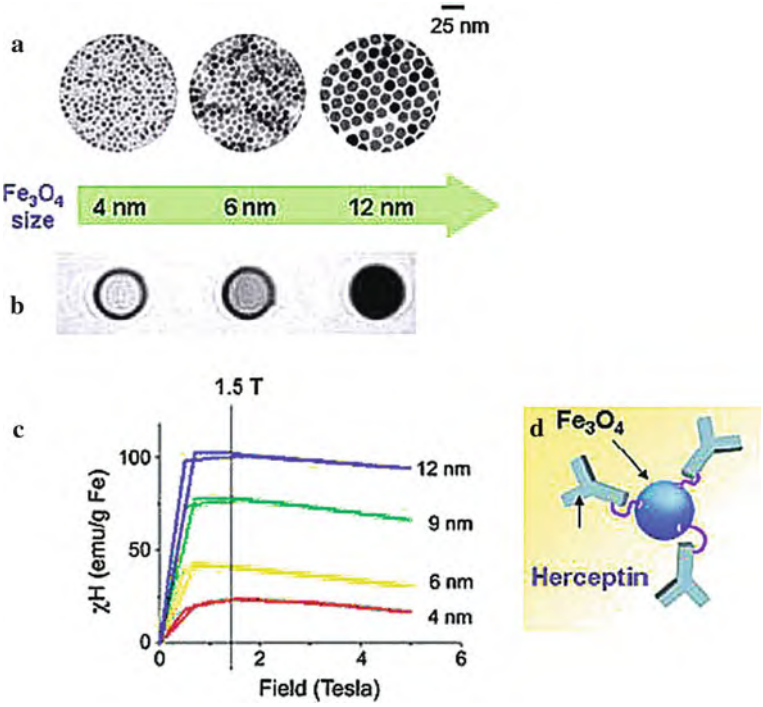

Fig. 12.3 Size-dependent properties of iron oxide (Fe_3O_4) nanocrystals and surface modification of the nanocrystals by Herceptin conjugates. (**a**) TEM imaging of Fe_3O_4 nanocrystals of various sizes. (**b**) Size-dependent T_2-weighted MR images of water soluble Fe_3O_4 nanocrystals. (**c**) Magnetization of the water soluble Fe_3O_4 nanocrystals. (**d**) Schematic representation of Fe_3O_4–Herceptin conjugates. (Reprinted with permission from [12.20]. © 2006 Korean Chemical Society)

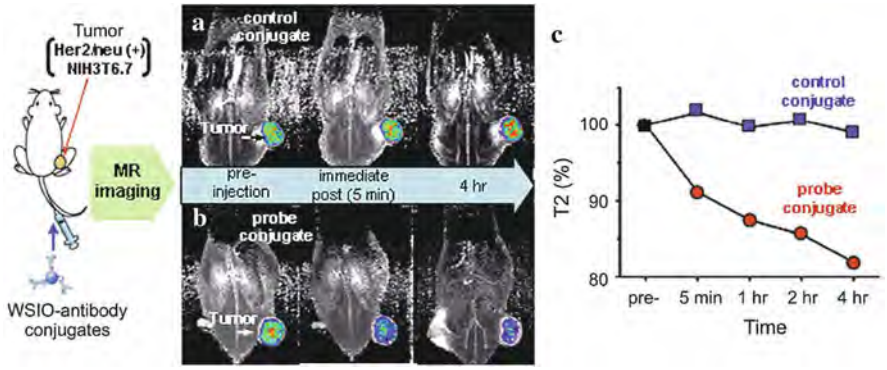

Fig. 12.4 In vivo MR detection of cancer implanted into a nude mouse. (**a**) Color maps of the T_2-weighted MR images of cancer cells (NiH3T6.7) at different times after injection of Fe_3O_4–antibody control conjugates into mice (preinjection; after 5 min, after 4 h) and (**b**) after injection of Fe_3O_4–Herceptin probe conjugates. (**c**) T_2 values of cancer cells in (**a**) and (**b**) samples versus time after injection of nanoparticles. (Reprinted with permission from [12.20]. © 2006 Korean Chemical Society)

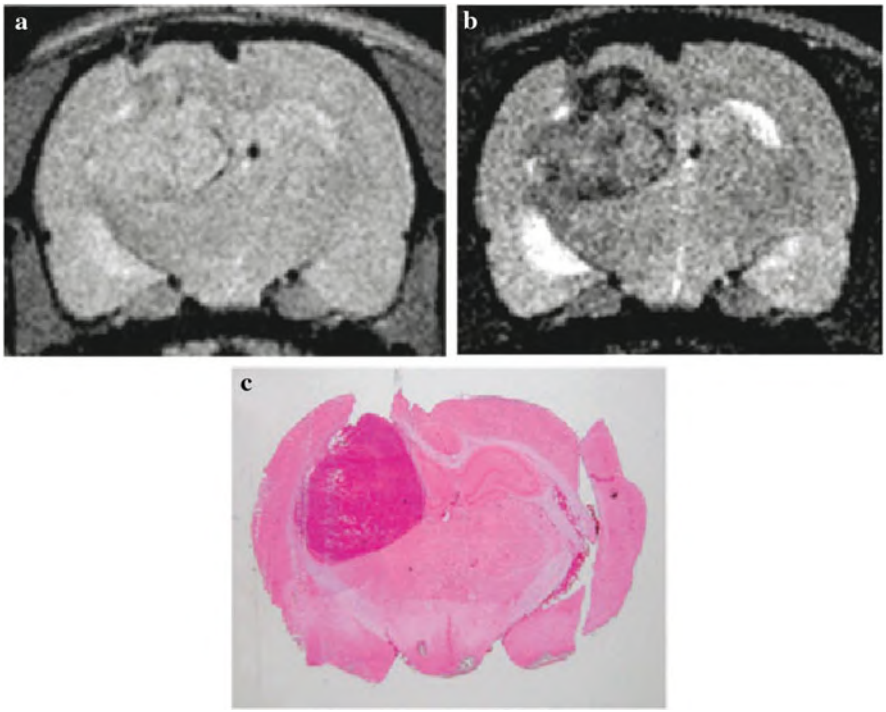

Fig. 12.5 Cy5.5-CLIO nanoparticles in a 9L rat glioblastoma (malignant cerebral tumor) as a preoperative MRI contrast agent. Proton density and T_2-weighted images are shown in **a** and **b**, respectively. Tumor uptake of iron oxide (CLIO) nanoparticles is evident in the T_2-weighted images (**b**) as regions of low-signal intensity (dark) whereas the tumor is isointense to the surrounding tissue using proton density images (**a**). (**c**) Hematoxylin and eosin (H&E) staining of a histological section corresponding to the MRI slices in A and B. (Reprinted with permission from [12.24]. © 2003 American Association of Cancer Research)

Figure 12.5 shows a representative example of a 9L rat glioblastoma by proton density-weighted MR imaging (Fig. 12.5a) and by T_2-weighted MR imaging after Cy5.5-CLIO administration (Fig. 12.5b). The hypointense tumor relative to the surrounding tissue on the T_2-weighted image (Fig. 12.5b) is indicative of nanoparticle accumulation, which causes a reduction of signal intensity with T_2-weighted spin echo pulse sequences. This contrast is not seen with conventional Gd chelates [12.24]. There is high congruency between signal reduction in MRI and the histological imaging by hematoxylin and eosin (H&E) staining (Fig. 12.5c). It can be shown that Cy5.5-CLIO nanoparticles can be used to delineate brain tumors precisely in a rat model intraoperative setting. In Fig. 12.6, a rat is shown by white light illumination after craniotomy and exposition of the tumor. In Fig. 12.6b the tumor is imaged by the green fluorescence protein (GFP) expressed by the tumor and in Fig. 12.6c by the Cy5.5 near-infrared fluorescence (NIRF) coinciding with the GFP image. The tumor delineations are furthermore confirmed by histological investigations making

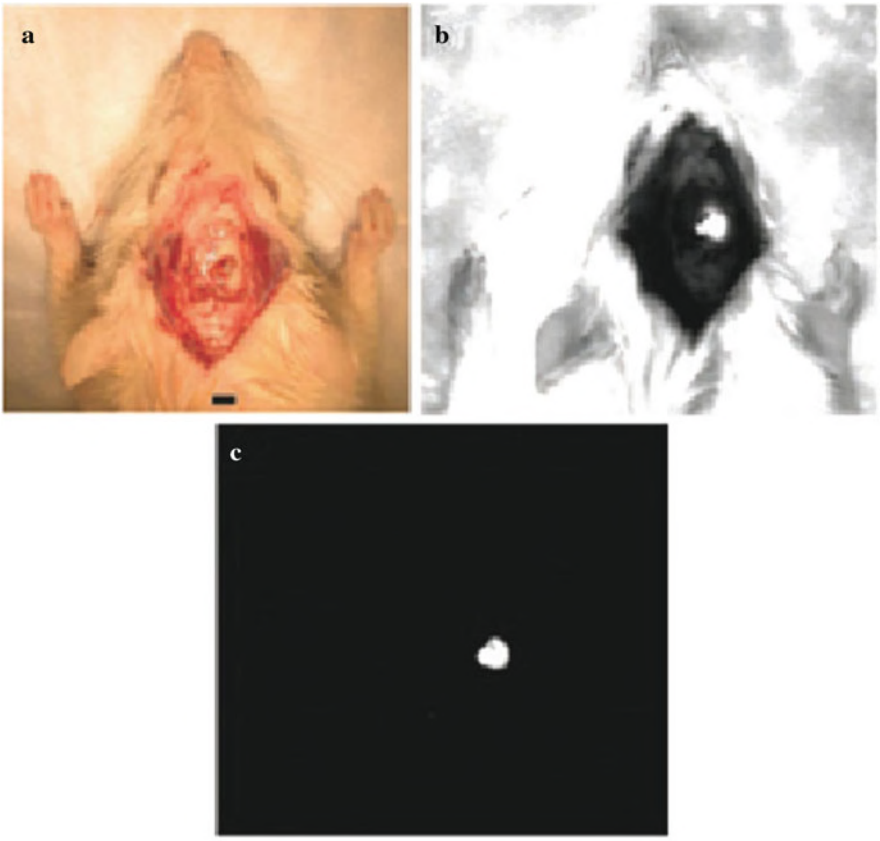

Fig. 12.6 Delineation of a GFP-expressing 9L glioma tumor (tumor in the supporting tissue of the brain) by optical imaging in an intraoperative setting. The brain tissue overlying the tumor was removed for optical imaging. (**a**) White-light imaging, (**b**) GFP imaging, and (**c**) Cy5.5 near-infrared fluorescence (NIRF) imaging. Scale bar: 5 mm. (Reprinted with permission from [12.24]. © 2003 American Association of Cancer Research)

use of H&E staining [12.24]. Thus, the combined NIRF optical and magnetic properties of Cy5.5–CLIO nanoparticles may allow neurosurgeons and radiologists to see the same probe in the same cells. This may increase the precision of surgical resection and improve the outlook for brain cancer patients.

Breast cancer lymphangiography. Breast cancer is the most common malignancy among women, resulting in approximately 45,000 deaths annually in the United States (see [12.25]). The presence of lymph node metastases has major prognostic implications in breast cancer patients, and it is the major criterion for adjuvant chemotherapy. The disease status of the sentinel lymph node (SLN) accurately reflects the status of the more distant lymph nodes. Therefore, the SLN metastasis diagnosis by non-invasive techniques such as MRI is of particular interest. By using polyamidoamine dendrimer G6 nanoparticles (9 nm in diameter; 240 kDa),

containing each 213 paramagnetic Gd ions, in lymphangiography, the metastatic foci of breast cancer-affected lymph nodes in mice could be revealed by the absence of MRI intensity [12.25]. This may be a powerful method for sentinel lymph node localization in human breast cancer [12.25]. It should be mentioned that there is a potential to detect even more and smaller lymph nodes by MRI in higher magnetic fields (3.0 T) compared to the situation in conventional fields (1.5 T) [12.26].

Myometrium and cervical carcinoma. Ultrasmall superparamagnetic iron oxide (USPIO) nanoparticles were used in order to study whether USPIO-enhanced T_2*-weighted gradient-echo (GRE) images might provide advantages on disease staging (T-staging) of uterine malignancies having surgery and histology as standards of reference [12.27]. A decrease of the signal intensity of myometrium carcinoma (Fig. 12.7a, b) and of cervical carcinoma patients (Fig. 12.7c, d) on T_2*-weighted

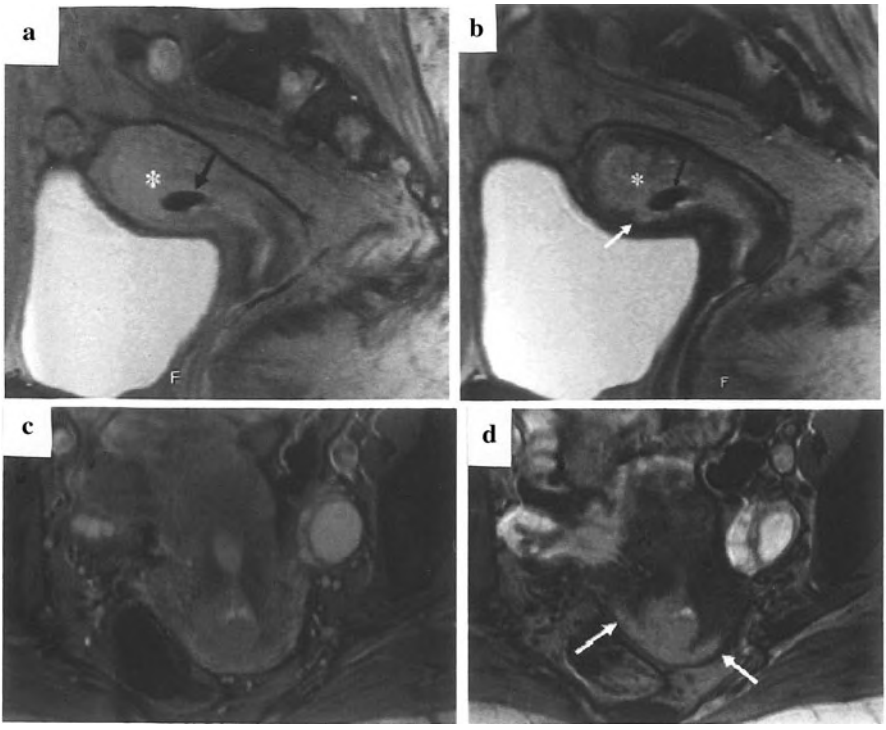

Fig. 12.7 (**a**, **b**): Patient with endometrial carcinoma (stage Ic according to the International Federation of Gynecology and Obstetrics-FIGO classification) and **c**, **d**: patient with cervical carcinoma (stage II FIGO). On the unenhanced T_2*-weighted graded echo (GRE) image (**a**) the tumor (asterisk) shows a superficial infiltration of myometrium; USPIO-enhanced MR (**b**) shows a focal area of deep infiltration of the myometrium (*white arrow*) with a calcification within the tumor (*black arrow*). On the unenhanced GRE T_2*-weighted image of a cervical carcinoma (**c**), the tumor appears as a slightly hyperintense mass confined within the cervical stroma; on the USPIO-enhanced MRI, the infiltration of the vaginal formix is well depicted (*arrows*). (Reprinted with permission from [12.27]. © 2004 Lippincott Williams & Wilkins)

GRE images after the intravenous administration of USPIO should be considered a constant and physiological finding that improves tumor conspicuity, allowing more accurate T-staging of neoplastic lesions [12.27].

Prostate cancer and lymph node metastases: In the United States more than 30,000 men died of prostate cancer in 2001 [12.22]. Therefore, the detection of occult lymph node metastases is greatly needed for identifying the disease. In conventional MRI, which is relatively insensitive for the detection of lymph node metastases, lymph nodes were classified as malignant if their diameter exceeded 8–10 mm (see [12.22]).

For the detection of metastases which have not caused an increase in the size of a lymph node (clinically occult disease), superparamagnetic iron oxide nanoparticles were used [12.22]. The intravenously injected nanoparticles are slowly extravasated from the vascular into the interstitial space, from which they are transported to lymph nodes via lymphatic vessels (Fig. 12.8a).

The sensitivity of the detection of lymph nodes with metastases in prostate cancer patients by MRI with lymphotropic superparamagnetic nanoparticles was 90.5% (see Fig. 12.8c) and is significantly higher than that of conventional MRI (sensitivity, 35.4%; see Fig. 12.8b). With MRI using superparamagnetic nanoparticles, metastases less than 2 mm in diameter can be detected. This is below the threshold of detection of any other imaging technique such as positron emission tomography (PET) where the limit of detection is 6–10 mm [12.28].

Arthritis: Rheumatic arthritis (RA) is the most common chronic inflammatory joint disease and a major cause for disability, morbidity, and premature mortality. The initial step in the management of RA is to establish the diagnosis as early as possible in order to prevent irreversible joint damage (see [12.29]). Clinically, RA can be difficult to diagnose in its early stage. Conventional x-rays only show secondary arthritic changes, e.g., bone erosions, late in the course of the disease. Conventional (unenhanced) MRI provides a superior soft-tissue contrast and a direct depiction of the synovium (a membrane in joint cavities secreting lubricating fluid), the initial site of the disease. The MRI contrast enhancement in the synovium by conventional gadopentetate dimeglumine (Gd-DTPA; 547 Da) is, however, limited. Ultrasmall superparamagnetic iron oxide particles (USPIO SHU555C) with a 3.5 nm iron oxide core and a carboxydextran coat (30 nm in diameter) may improve the specificity of MRI for the characterization of inflammation. These nanoparticles may identify inflammatory cell infiltration within the synovium, since they are phagocytosed by macrophages and subsequently cause a marked signal loss in inflammatory tissue on delayed postcontrast T_2-weighted MR images, 24 h postinjection.

USPIO SHU555C was shown [12.29] to cause in arthritis-induced knees of rats (Fig. 12.9) a substantial, progressive, and positive enhancement of the inflamed synovium on T_1-weighted gradient-echo (GE) images at 3 min postinjection slowly progressing over time and lasting for at least 2 h. USPIO SHU555C provides a higher difference between the patterns of arthritic and normal joints compared to standard Gd-DFPA because Gd-DFPA shows a higher enhancement in normal joints [12.29].

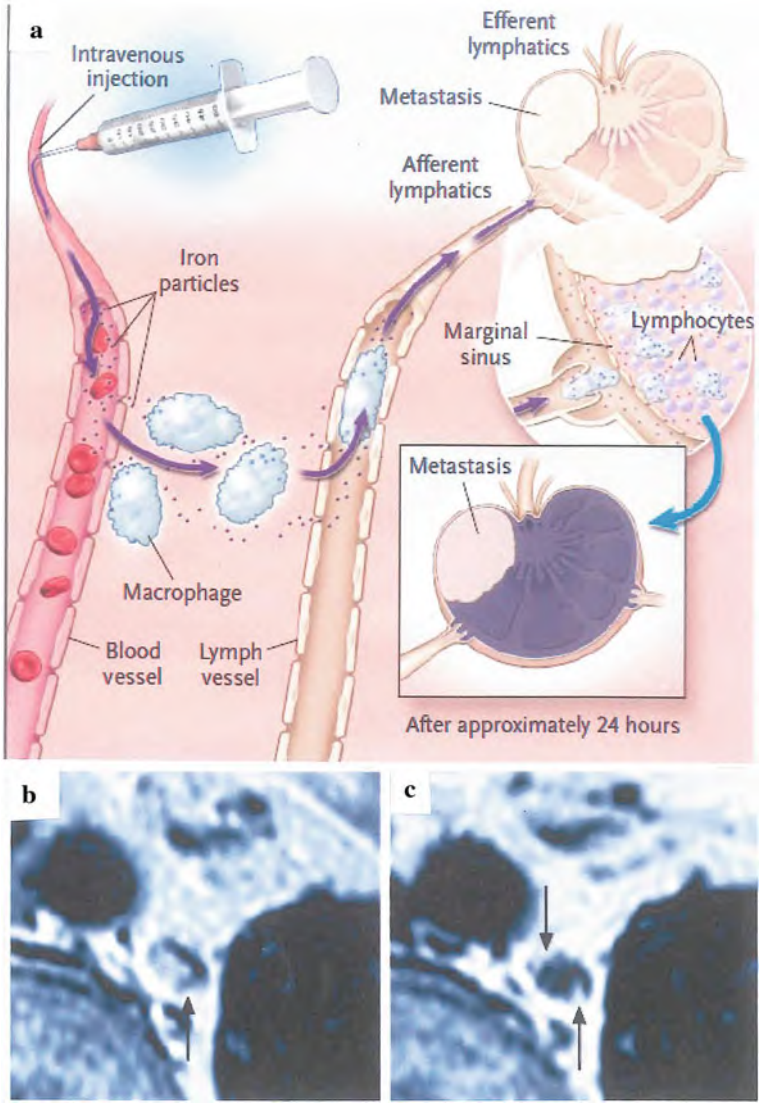

Fig. 12.8 (**a**) Systematically injected long-circulating nanoparticles gain access to the interstitium and are drained through lymphatic vessels. Disturbances in lymph flow or in model architecture caused by metastases lead to abnormal patterns of accumulation of lymphotropic superparamagnetic nanoparticles, which are detectable by MRI. (**b**) Conventional MRI shows high signal intensity in a retroperitoneal node with micrometastases (*arrow*). (**c**) MRI with lymphotropic superparamagnetic nanoparticles demonstrates two hyperintense foci (*arrows*) within the node, corresponding to 2 mm metastases. Corresponding histologic analysis confirms the presence of adenocarcinoma within the node. (Reprinted with permission from [12.22]. © 2003 Massachusetts Medical Society)

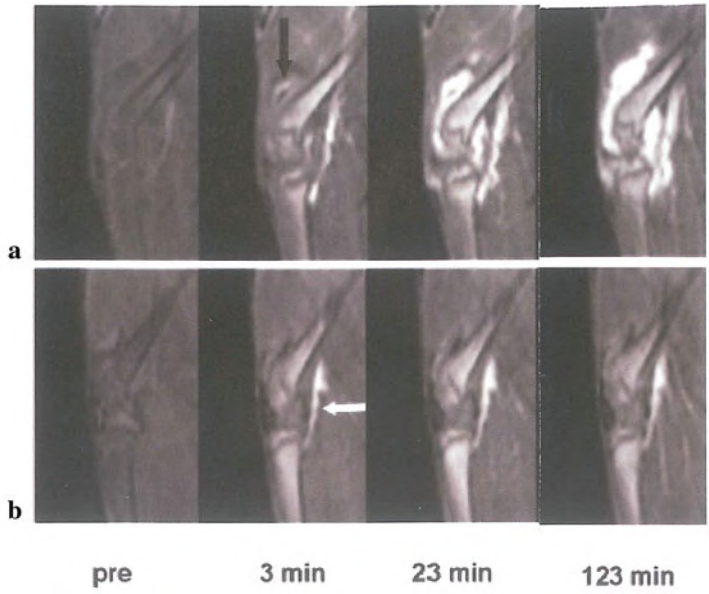

Fig. 12.9 Arthritic (**a**) and normal (**b**) knee joint of a rat on T_1-weighted MR images (magnetic field 2.0 T) before and at various times after injection of the USPIO SHU555C nanoparticles. Minor synovial enhancement can be seen as early as 3 min postinjection (*black arrow*) which increases over time and persists for at least 2 h. The popliteal artery is indicated by a *white arrow*. (Reprinted with permission from [12.29]. © 2006 Wiley Interscience)

Arthritis in its earliest stages can be detected by atomic force micrographs (AFM) of the thickening and reduction in elasticity of cartilage fibers [12.30], long before any outward signs appear.

Soft-tissue infection. The role of magnetic resonance imaging (MRI) for detection of macrophage (e.g., white blood cells) phagocytic activity is evolving. It has been shown [12.31] that bacterially induced soft-tissue abscesses in rats can be specifically detected after administration of superparamagnetic iron oxide nanoparticles (USPIO) by T_1-, T_2-, or T_2^*-weighted MR imaging (Fig. 12.10). The T_2^*-weighted MR images after USPIO administration show a slightly hyperintense oval center with according to histopathology, necrotic debris. The center is surrounded by an inner hypointense rim, a middle hyperintense ring, and an outer hypointense rim. According to histopathological examination (see [12.31]), the inner and the outer rims represent dense bands of accumulated macrophages within the wall of the tissue, which surrounds the liquified abscess center.

Atherosclerosis and MR angiography (MRA). The composition and stage of atherosclerotic plaques are clinically relevant because of the risk of ischemic events. Atherosclerosis is basically an inflammatory disease. Monocytes adhere to the vascular endothelium and accumulate in lesion-prone arterial sites. Adherent monocytes are subsequently enticed into the arterial intima where they differentiate into macrophages. This suggests that macrophages are a marker of unstable

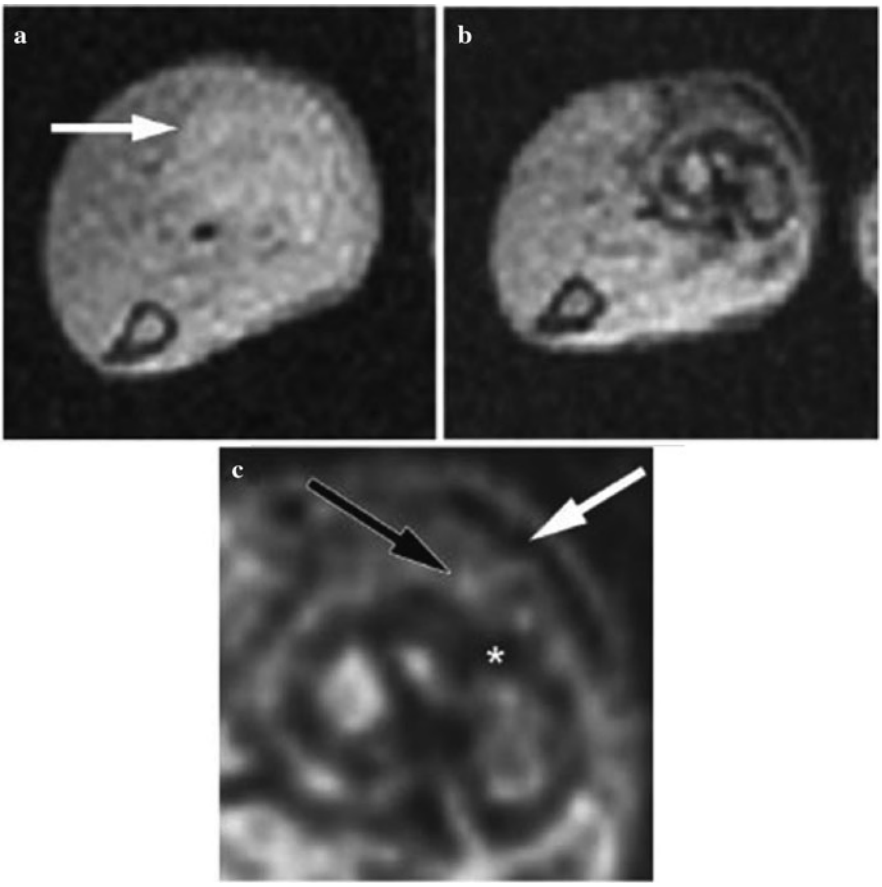

Fig. 12.10 Bacterially induced soft-tissue abscess in the calf of the left hind leg of a rat with high-dose USPIO administration. (**a**, **b**) T_2*-weighted MR images and (**c**) enlarged view of (**b**). (**a**) The image prior to USPIO administration shows a slight hyperintense signal bond (*arrow*) at the site of the tissue infection. (**b**) Image of the abscess 24 h after USPIO administration. (**c**) The enlarged view of (**b**) (original magnification 2.5×) shows three layers of the abscess wall; directly adjacent to the necrotic hyperintense center of the abscess is the hypointense layer (∗) followed by a hyperintense middle layer (*black arrow*) and a hypointense outer layer (*white arrow*). The hypointense wall layers correspond to higher accumulations of iron oxide-filled macrophages as shown by histologic examination. (Reprinted with permission from [12.31]. © 2005 Radiological Society of North America)

atherosclerotic plaques and that specific targeting of these cells may lead to the characterization of atheromatous plaques prone to rupture [12.21]. Animal studies have shown that superparamagnetic iron oxide nanoparticles induce a focal MRI signal intensity decrease in the aortic wall of atheromatous rabbits (see Fig. 12.11a, b). In coronary, pulmonary, or peripheral angiography, the use of superparamagnetic nanoparticles for MRI has been evaluated [12.21] with both arterial and venous contrast enhancement (see Fig. 12.11c).

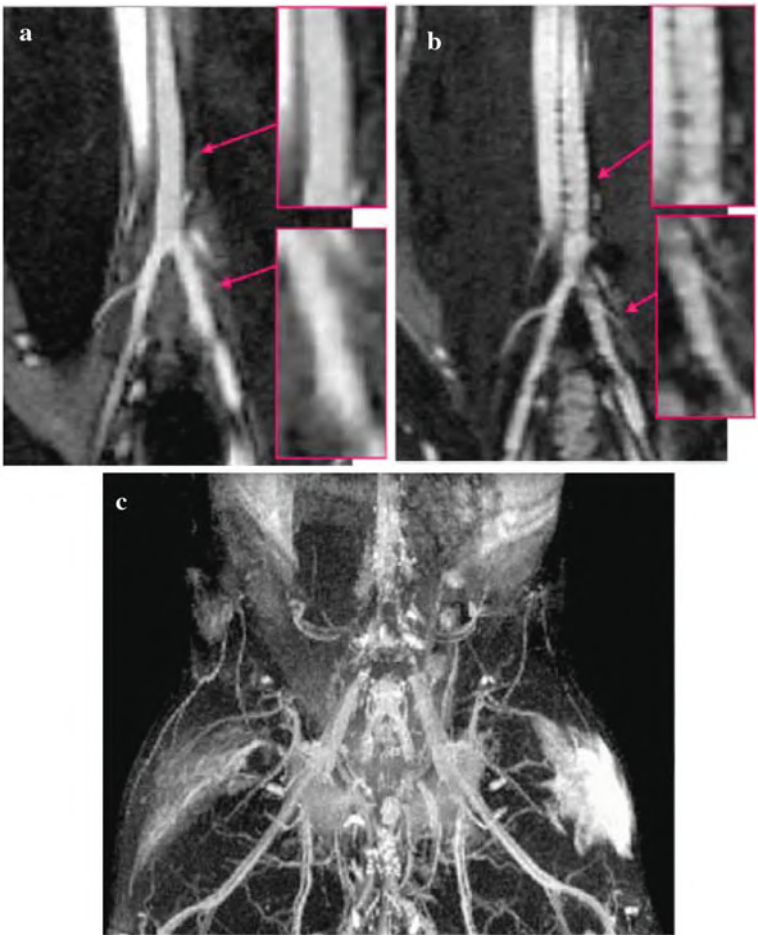

Fig. 12.11 (**a**, **b**) Atherosclerotic MRI in rabbits 5 days after injection of superparamagnetic nanoparticles. (**a**) Normal rabbit: bright blood due to the T_1 effect of the nanoparticles. (**b**) Atherosclerotic rabbit: note the dark signal in the vessel wall due to the macrophage uptake of the superparamagnetic nanoparticles in atherosclerotic lesions. (**c**) Angio-MR in a rabbit after injection of superparamagnetic nanoparticles. Even small arteries and veins are visible. (Reprinted with permission from [12.21]. © 2006 Elsevier)

A chip-based diagnostic magnetic resonance imaging (DMR) platform of tumor cells [12.18], using functionalized magnetic nanoparticles as sensors to amplify molecular interactions, can carry out highly sensitive and selective profiling of circulating cells (see Fig. 12.12). The number of circulating tumor cells (CTCs) is a sensitive biomarker for tumor progression and metastasis. Therefore, the quantification of CTCs is emerging as useful for diagnosing and "staging" cancer, for assessing response to treatment, and for evaluating whether there is residual disease [12.18].

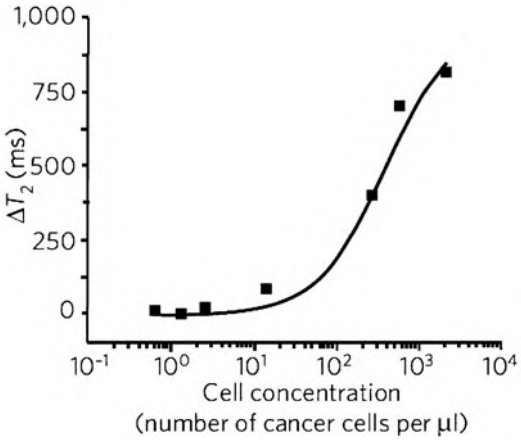

Fig. 12.12 Changes of chip-based diagnostic MRI (DMR; change in the time of magnetic relaxation, ΔT_2) of whole blood as a function of the concentration of cancer cells. (Reprinted with permission from [12.18]. © 2008 Nature Publishing Group)

12.2.2 CT Contrast Enhancement

For high-contrast x-ray computed tomography (CT), bismuth sulfide (Bi_2S_3) nanoplatelets (Fig. 12.13) coated with the biocompatible polymer polyvinylpyrrolidone (PVP) and with a hydrodynamic diameter of 30 nm are envisaged. The enhanced x-ray absorption of the coated Bi_2S_3 nanoparticles (five times higher than conventional iodine contrast agents) results in a clear delineation of the cardiac ventricles and all major arterial and venous structures (Fig. 12.14). CT imaging after intravenous administration confirms that the Bi_2S_3 nanoparticles had

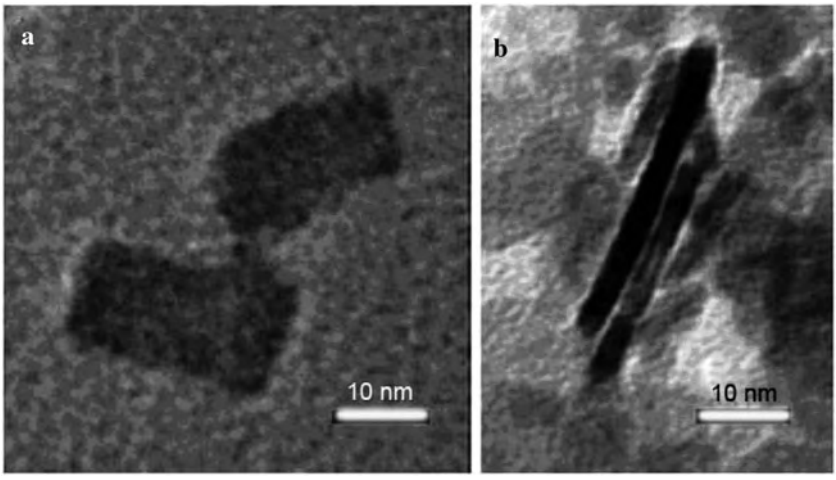

Fig. 12.13 Transmission electron micrograph (TEM) characterization of Bi_2S_3 nanoparticles. (Reprinted with permission from [12.32]. © 2006 Nature Publishing Group)

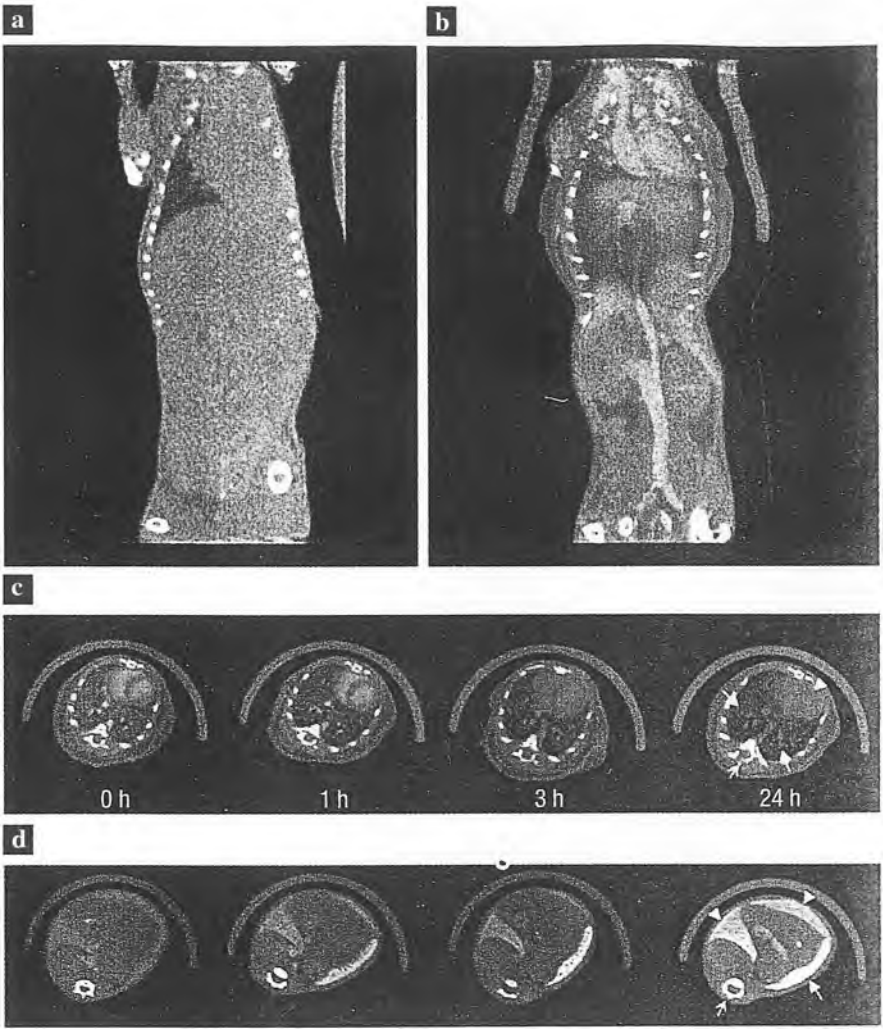

Fig. 12.14 In vivo imaging of vasculature (**a**, **b**). Coronal x-ray CT reconstruction of a live mouse before (**a**) and after (**b**) intravenous administration of polymer-coated Bi_2S_3 nanoparticles (BPNP), showing large vessels and the heart, and the organ delineation. The length of the reconstruction is 6.5 cm. (**c**, **d**) Serial CD scans of a live mouse following tail vein injection of BPNP suspension (0.228 M Bi). Series (**c**) shows transverse slices through the heart (*arrow head*), the lungs (*solid arrow*), and a vertebra (*open arrow*). Series (**d**) shows transverse slices including the liver (*arrow head*), the spleen (*solid arrow*), and a vertebral body (*open arrow*). The diameter of the mouse is 1.6 cm. (Reprinted with permission from [12.32]. © 2006 Nature Publishing Group)

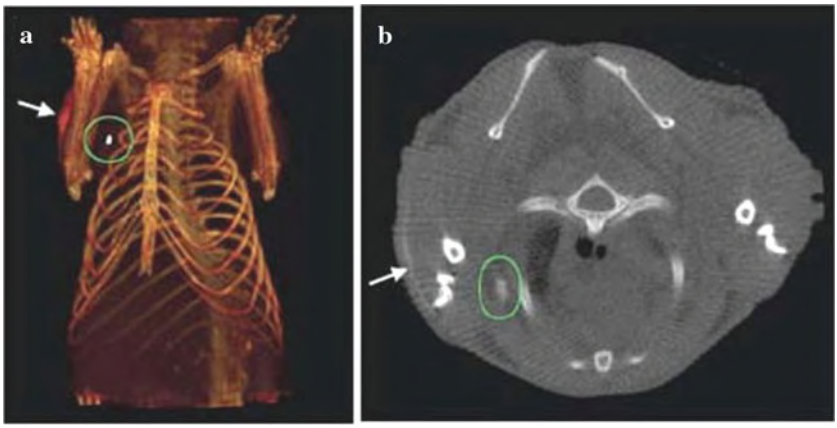

Fig. 12.15 Lymph node CT imaging of a mouse with the Bi_2S_3 nanoparticles imaging agent. (**a**) 3D volume rendering of the CT data set, 3.8 cm in length. (**b**) Transverse slice at the height of the lymph node in (**a**). The maximum diameter of the mouse is 1.8 cm. The position of the lymph node under the right shoulder is indicated by the *ovals*, and the injection site is shown by the *arrows*. Note the lack of contrast in the corresponding contra lateral (left shoulder) lymph node. (Reprinted with permission from [12.32]. © 2006 Nature Publishing Group)

distributed to organs containing phagocytic cells (liver, spleen, lymph nodes), reflecting uptake into macrophages, and hepatocytes so that this technique could be used for improved detection of hepatic metastases by CT. It further was investigated whether the Bi_2S_3 nanoparticles could be used for lymph node delivery to improve cancer staging. Lymph nodes in mice were clearly contrasted (Fig. 12.15). In toxicity studies [12.32], polymer-coated Bi_2S_3 nanoparticles showed to be at least one order of magnitude less toxic than free bismuth ions. When administered to human macrophage (U-937) cell lines, the coated Bi_2S_3 nanoparticles showed a toxicity profile similar to that of an iodinated agent in clinical use whereas for the hepatocyte (HepG2) cell line, the Bi_2S_3 nanoparticles showed a profile superior to that of the iodinated agent.

12.2.3 Contrast-Enhanced Ultrasound Techniques

Ultrasound (US) lymphography making use of contrast enhancement by nanobubble suspensions has been demonstrated by in vivo studies on dogs as an alternative to current sentinel lymph node detection methods [12.33]. Sentinel lymph nodes can be defined as the first nodes to receive lymphatic drainage from a neoplasm and are therefore at highest risk for regional metastasis through lymphatic spread. Regional lymphatic mapping together with selective lymph node biopsy has gained widespread acceptance as an alternative to radical axillary node dissection in

breast cancer patients due to proven staging accuracy [12.34], reduced perioperative patient anxiety, and lower postoperative morbidity when sentinel nodes are found to be negative for malignancy. When sentinel nodes are found to be free of metastases based on intraoperative section evaluation, the remainder of the lymphatic system is also considered free of metastases and surgery is limited to the excision of the primary tumor.

For the *US lymphography* investigations [12.33], ultrasound contrast formulations were used comprising nitrogen gas nanobubbles encapsulated within a bilayered shell composed of an outer layer of human serum albumin and an inner layer of biodegradable polymer. The contrast uptake in a lymph node following contrast injection is shown in Fig. 12.16. Whereas the lymph node is invisible before contrast administration, it is clearly visible 36 min following the injection of the contrast agent. This documents proof of principle for sentinel node detection using contrast-enhanced power Doppler ultrasound.

The specific mechanism by which the 740 nm nanobubble contrast agent enters the lymphatic system is not so clear. Leaky endothelial junction and fenestrations up to a few microns in width can provide an avenue for particle uptake (see [12.33]). Lymphatic ultrasound contrast enhancement, therefore, may be a compromise between the countervailing constraints for the nanobubble size of entry into the lymphatic system and ultrasound signal intensity.

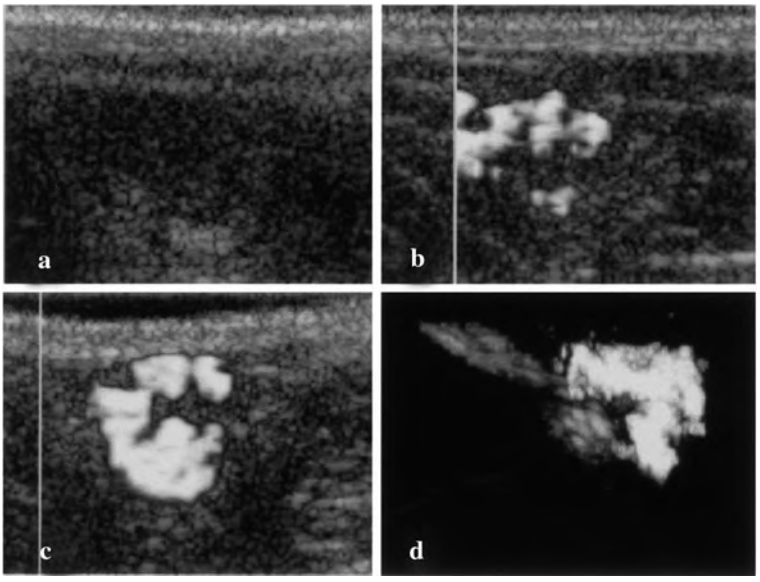

Fig. 12.16 Ultrasound images of a popliteal lymph node of a dog before contrast administration (**a**) and 5 min (**b**) and 36 min (**c**) following subcutaneous injection of a 740 nm nanobubble contrast agent. (**d**) A 3D rendering of the contrast-enhanced node seen in (**c**). (Reprinted with permission from [12.33]. © 2003 Lippincott Williams & Wilkins)

Hepatocellular carcinoma (HCC) is a liver cancer disease which accounts for about 400,000 deaths each year worldwide [12.35]. Image-guided percutaneous ablation therapy for HCC is most useful because of its minimal invasiveness, easy repeatability, and cost-effectiveness [12.36]. The recent development of ultrasound contrast agents gave rise to a significant improvement in the diagnostic potential of contrast-enhanced ultrasound (CEUS) in the detection of focal liver lesions. Due to this development CEUS has been stated to be complementary to contrast-enhanced computed tomography (CECT) and magnetic resonance imaging (CEMRI) for pre-treatment staging and assessment of lesion vascularity [12.37]. In Fig. 12.17 a nodule in the liver is imaged by conventional ultrasound and by CEUS making use of an aqueous suspension of phospholipid-stabilized sulfur hexafluoride (SF_6; Sono Vue®) as a contrast agent; these images are compared to a CECT study with iodinated contrast media. The sensitivity and accuracy of real-time CEUS in the detection of hepatocellular carcinoma vascularization are shown to have equal diagnostic efficacy as contrast-enhanced CT or MRI.

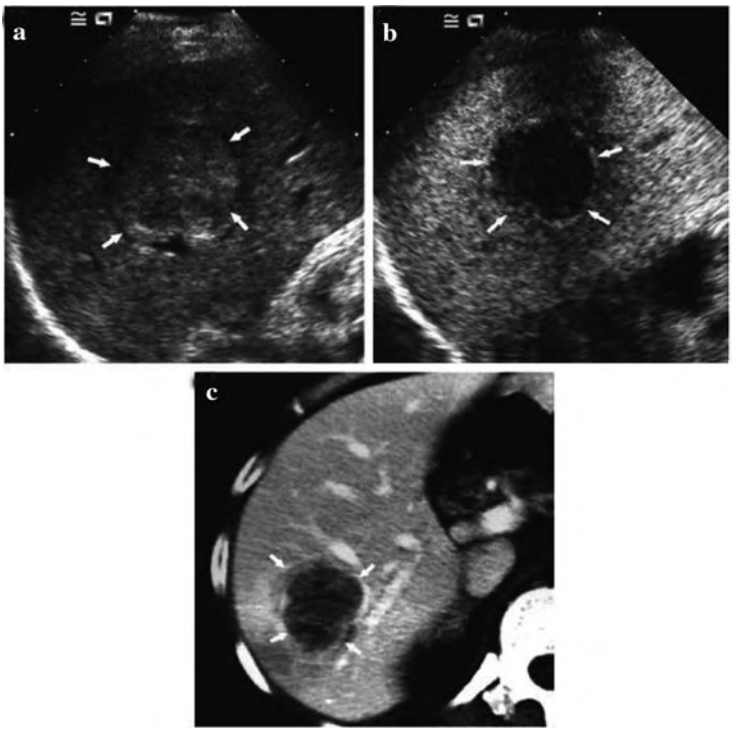

Fig. 12.17 Hepatocellular carcinoma (HCC) in a 46-year old woman. (**a**) Unenhanced ultrasound imaging shows an isoechoic nodule (diameter 4.1 cm) in the right lobe of the liver; (**b**) CEUS 170 s after contrast administration showing the HCC which is hypo-echoic with respect to the surrounding liver; (**c**) contrast-enhanced computed tomography where the nodule is hypo-enhanced with respect to the surrounding liver. (Reprinted with permission from [12.35]. © 2007 Elsevier)

12.2.4 Positron Emission Tomography (PET)

Positron emission tomography (PET) has emerged as a clinical corner stone in cancer staging and is one of the few molecular imaging technologies approved by the Food and Drug Administration (FDA) for imaging of breast cancer, colorectal cancer, esophageal carcinomas, head and neck cancer, lung cancers, melanoma, and lymphoma (see [12.38]). The most frequently used PET agent is [^{18}F] fluorodeoxyglucose (FDG), a glucose analog that is selectively taken up by cells [12.39]. The proton-rich ^{18}F nucleus (half-life 108.9 min) decays by emission of a positron which is annihilated with an electron in the surrounding tissue, emitting two γ-quanta. By detection of these γ-quanta, the accumulation of the ^{18}F agent in a tumor can be sensitively localized by non-invasive tomography techniques. FDG-PET imaging (Fig. 12.18) is a valuable clinical tool for predicting tumor response to therapy and patient survival [12.40] and was reported to be a more accurate predictor of response to neo-adjuvant chemotherapy than other clinical or histopathological criteria [12.41].

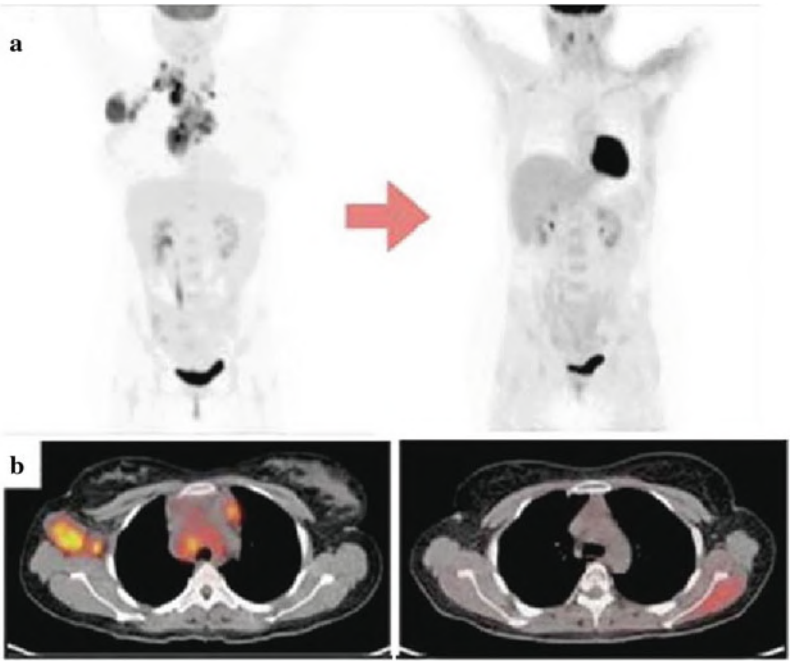

Fig. 12.18 Molecular [^{18}F] fluorodeoxyglucose positron emission tomography (FDG-PET) imaging used for monitoring of tumor patient response to therapy. (**a**) FDG-PET scan of a patient with a tumor of lymphoid tissue before (*left*) and after (*right*) treatment. (**b**) Corresponding axial PET-CT sections show a decrease in FDG activity (*yellow red*) in axilla and mediastinum after treatment. (Reprinted with permission from [12.38]. © 2006 AAAS)

Molecular imaging techniques, such as FDG-PET, may lower costs by reducing the number of patients eligible for a given treatment combination. In some settings, molecular imaging techniques may eliminate costly surgical procedures altogether. In preliminary studies, FDG-PET imaging has been shown to have a high benefit/cost ratio for cancer staging (see [12.38]).

Alzheimer's disease in its early stages can be diagnosed by PET which can be used for detecting neurodegenerative diseases that produce significant alterations in brain functions. Recent developments in small animal imaging provide PET images with a resolution of 1–2 mm [12.42]. By employing Gd-orthosilicate (GSO) [12.43] and lutetium oxyorthosilicate (LSO) [12.44] crystals as γ-detectors, resolutions of 3 mm have been obtained in the human brain. Even in patients with mild impairment, by the time the patient presents with symptoms of neurodegenerative dementia such as Alzheimer's disease, substantial alteration of cortical metabolic function generally has occurred. The associated decrease in glucose metabolism in certain brain areas are readily detectable on FDG-PET images (Fig. 12.19). The sensitivity and specificity for detecting Alzheimer's disease by PET were 92% and 71% as confirmed histopathologically. Even early Alzheimer's disease can be detected with PET due to regional cerebral metabolic changes with an accuracy exceeding 80% (see [12.45, 12.46]). Relative hypometabolism of the associative cortex can be accurately used to predict whether cognitive decline will occur at a rate faster (characteristic for Alzheimer's disease) than for normal aging (see [12.45]). There is also research underway for studying cerebrovascular diseases [12.47].

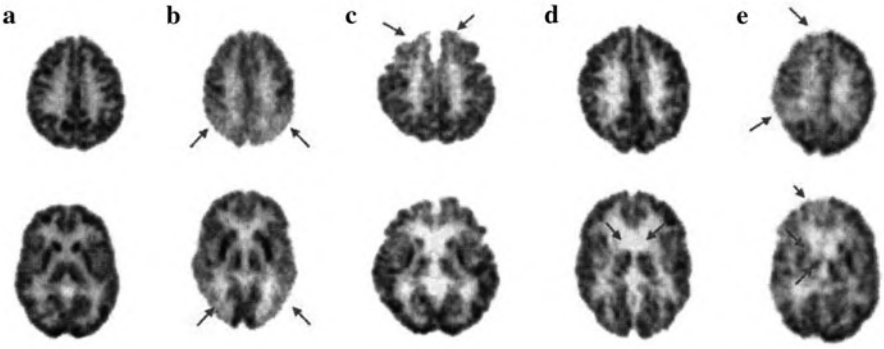

Fig. 12.19 Normal and abnormal patterns of [^{18}F] fluorodeoxyglucose (FDG) distribution. Positron emission tomography (PET) data are displayed with inverse *gray* scale, with darkness level of each pixel linearly related to radioactive counts per second. Planes are shown at high-(*top row*) and mid- (*bottom row*) transaxial levels for subjects with (**a**) a normal metabolic brain pattern, (**b**) posterior hypometabolism characteristic of early Alzheimer disease, (**c**) anterior hypometabolism characteristic for early frontal lobe dementia, (**d**) profound striatal hypometabolism characteristic of Huntington's disease, and (**e**) distributed foci of right-sided hypometabolism in cortical and subcortical structures, characteristic of multiple infarcts in tissue supplied by the right carotid artery. (Reprinted with permission from [12.45]. © 2005 Elsevier)

For the emerging field of molecular imaging, the combination of imaging approaches, i.e., simultaneous MR/PET imaging [12.48] or CT/PET fusion images [12.49] may be of future clinical interest.

12.2.5 Raman Spectroscopy Imaging

By this technique of inelastically scattered photons, highly specific analysis of molecular distributions, of pharmacokinetics, or of targeted drug delivery can be obtained. The sensitivity can be strongly enhanced by surface-enhanced Raman scattering (SERS) [12.50], which is a plasmonic effect (see Sects. 1.7 and 7.6) where molecules absorbed on a noble metal surface or on a nanoparticle experience a dramatic increase in the incident electromagnetic field, resulting in a high Raman intensity. SERS nanoparticles with a gold nanocore, a Raman-active molecular layer, and a silica coating (Biotags) are commercially available [12.51]. Single-walled carbon nanotubes (SWNTs) exhibit a strong Raman peak at 1593 cm^{-1} and do not use a metal surface enhancer. Near-infrared Raman excitation is ideal for penetration into biological tissue.

After injection of Biotag nanoparticles into living mice, an accumulation of the nanoparticles in the liver was observed (see Fig. 12.20a). When SWNTs were conjugated with arginine-glycine-aspartate (RGD) peptide for targeting them to an integrin-positive U87 MG tumor in living mice, a much higher SWNT concentration is demonstrated to be in the tumor by Raman scattering than without conjugation (see Fig. 12.20b).

12.2.6 Photoacoustic Tomography

This is a non-ionizing, non-invasive in vivo imaging technique (see [12.52]) where short 800 nm near-infrared (NIR) laser pulses for deep penetration (5 cm) into biological tissue induce a small temperature rise (< 5 mK) in the tissue due to absorption which causes thermoelastic expansion and the emission of photoacoustic waves. These signals can be detected by a transducer (see Fig. 12.21a) and stored in a computer for image reconstruction by a back-projection algorithm, yielding images with a spatial resolution of ~ 60 μm (see [12.52]). The injection of 50 nm gold nanocages with a strong 800 nm plasmon absorption (see Fig. 12.21b, c) into the circulatory system of a rat gives rise to a significantly enhanced contrast in the images of the rat's brain vasculature (see Fig. 12.22a–c).

12.2.7 Biomolecular Detection for Medical Diagnostics

Molecularly targeted agents are expected to broadly expand the capabilities of conventional anatomical imaging methods. Molecular detection will allow clinicians

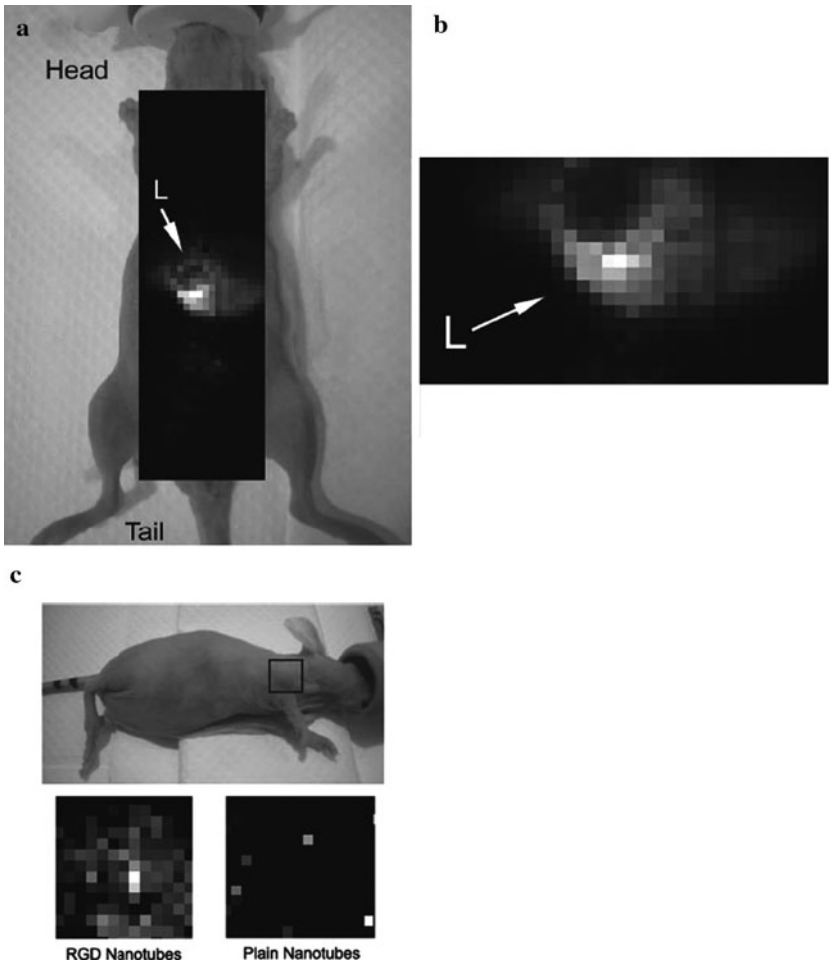

Fig. 12.20 (**a**) Whole-body raster-scan image (1 mm steps) of a nude mouse 2 h after tail vein injection of surface-enhanced Raman scattering (SERS) nanoparticles. The highest SERS concentration is accumulated in the liver (L; *arrow*). (**b**) Map of liver (0.75 mm steps), showing higher definition of the liver (*arrow*). (**c**) Accumulation of arginine-glycine-aspartate (RGD) peptide conjugated single-walled carbon nanotubes (SWNTs) within an integrin-positive U87 MG tumor model at 24 h after injection. Photograph of the mouse depicting the tumor area (*black square*) and corresponding Raman images at 24 h after SWNT injection by raster scan with 750 μm steps. Notice the accumulation of the RGD SWNTs in the tumor area as opposed to the unconjugated SWNTs (plain) that show little to no accumulation in the tumor. (Reprinted with permission from [12.51]. © 2008 National Academy of Sciences USA)

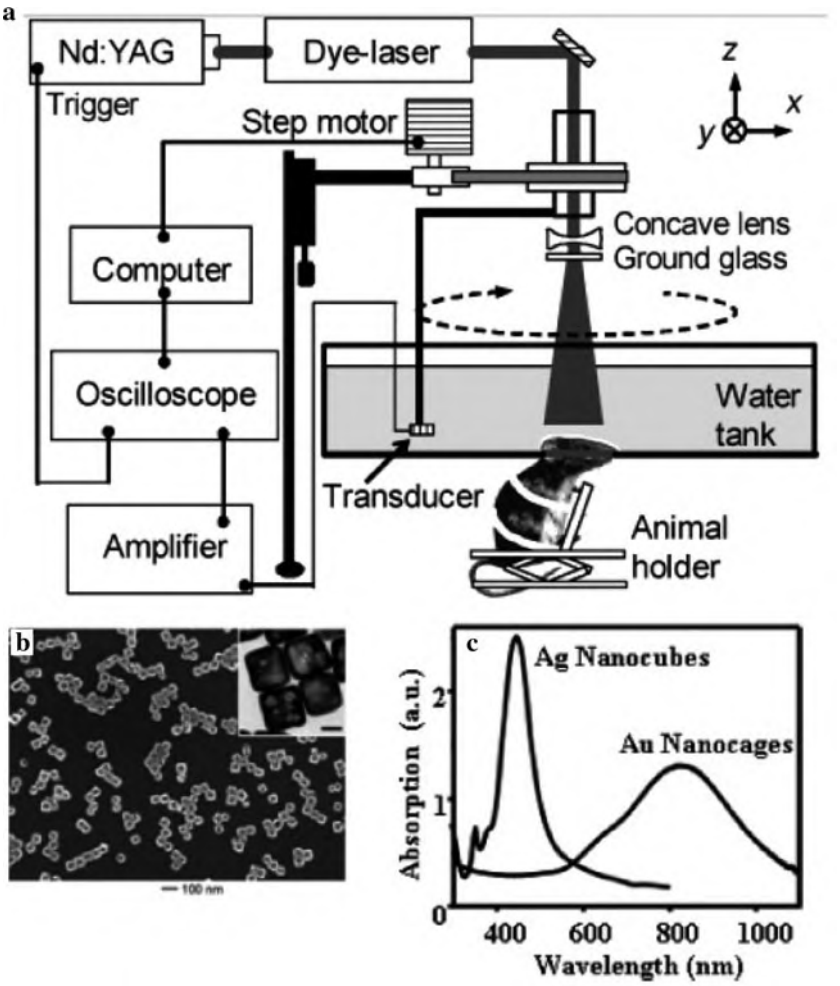

Fig. 12.21 (**a**) Schematic of the non-invasive photoacoustic tomography (PAT) of a rat brain in vivo for employing Au nanocages contrast agent and near-infrared (NIR) light [12.52]. (**b**) Scanning electron micrograph of Au nanocages prepared by a galvanic replacement reaction between Ag nanocubes and $HAuCl_4$ solution. The *inset* shows a transmission electron micrograph of Au nanocages, scale bar: 25 nm. (**c**) Absorption spectra of Ag nanocubes and Au nanocages. (Reprinted with permission from [12.53]. © 2007 American Chemical Society)

not only to see where a tumor is located in the body but also to visualize the expression and activity of specific molecules (e.g., DNA, RNA, or proteins [12.54]) and biological processes (e.g., apoptosis, angiogenesis, or metastasis) that influence, e.g., tumor behavior and response to therapy. The hope is that clinical molecular analysis will one day be used to detect physiological alterations due to a disease, such as cancer, when it is still at a curable stage, to adjust treatment protocols

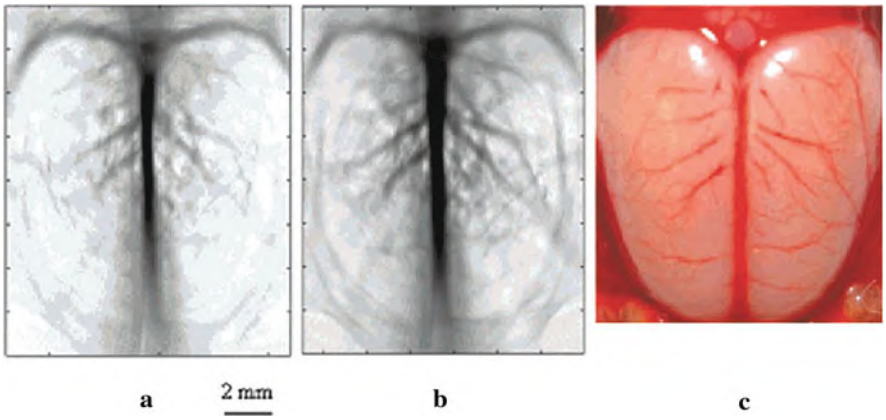

Fig. 12.22 Non-invasive photoacoustic tomograph of a rat's cerebral cortex (**a**) before the injection of Au nanocages and (**b**) about 2 h after the injection of Au nanocages. (**c**) An open-skull photograph of the rat's cerebral cortex. (Reprinted with permission from [12.53]. © 2007 American Chemical Society)

in real time, and to streamline the drug development process [12.38]. An example for a single molecule biomarker for a disease is the prostate-specific antigen (PSA) protein, which is elevated in men with prostate cancer, and researchers seek to find new biomarkers for various diseases. Therefore, characterizing the human plasma proteome is the main goal in proteomics, which is the research to understand the expression and function of proteins on a global level. The blood plasma not only contains the resident proteins but also immunoglobulins (antibodies in the immune response for binding the specific antigens), protein hormones, secreted proteins, foreign proteins, indicative of infection, and proteins from dying cells. Thus, the detailed understanding of the blood plasma proteome will make it possible to relate individual serum proteome profiles to the genome, environments, and lifestyles of individuals and, therefore, will reveal predisposition to, or onset of, disease [12.55].

For diagnostic technologies it is of relevance that the concentration range of the different proteins is of the order of 10^9, with serum albumin being most abundant (30–50 mg/ml) and low-level proteins such as interleukin-6 present at < 5 pg/ml. The focus of detection should be directed at the less abundant fraction of proteins in the blood plasma, as it is this fraction that best reflects tissue physiology and pathology, as these are the non-resident proteins that are either actively or passively released from tissue into the blood stream [12.55].

Primary examples for emerging nanotechnology approaches in biomolecular detection for medical diagnostics include nanostructured surfaces for the enhancement of proteomic analysis via mass spectrometry (MS), the bio-barcode method for the amplification of protein signatures via the use of a two-particle assay, nanowires as biologically gated transistors, and silicon cantilevers for the mechanical recognition of biomolecular ensembles [12.56] as reported in the following.

Nanostructured surfaces for proteomic analyses via mass spectrometry (MS). Mass spectrometry (MS) is currently the standard for protein expression profiling of biological fluids and tissues [12.56–12.58], with mounting evidence that matrix-assisted laser deposition/ionization time-of-flight (MALDI-TOF) MS can be employed for early detection of malignant diseases. It is hypothesized that the low–molecular-weight proteome (LMWP), comprising proteolytic fragments at extremely low concentrations, contains a wealth of information of diagnostic and prognostic utility. Nanoporous silicon oxide surfaces (Fig. 12.23a) are charged with a diluted human plasma sample to separate the low-molecular-weight (LMW) proteins/peptides from the less interesting high-molecular-weight (HMW) proteins. The LMW fraction is then analyzed in a MALDI-TOF experiment, yielding a mass spectrum (Fig. 12.23b) characteristic for peptide amounts down to the nanogram per milliliter range, which is roughly 400-fold more sensitive than conventional MS analysis. The technique can be improved by chemical and structural surface "tailoring" for a selective enrichment of specific protein/peptide classes. High-throughput MALDI-TOF MS of LMW-enriched plasma is a strategy to rapidly screen and profile a large number of samples, in the search of disease-related biomarkers. The limitations in sensitivity of protein-based molecular profiling due to the lack of PCR-like reactions (PCR – polymerase chain reaction) can be overcome by the bio-barcode assay (see below). The PCR technology allows for the duplication of portions of prospective targets and represents the ultimate in sensitivity but has significant drawbacks including complexity, sensitivity to contamination, cost, and lack of portability and major challenges with respect to multiplexing (detecting multiple targets in a single assay) [12.12].

The bio-barcode assay. This assay [12.56, 12.59] utilizes two types of particles for sample purification, detection, and amplification. The first is a microparticle with a recognition agent that in the case of nucleic acids is an oligonucleotide which is complementary to a statistically unique region of the target and, in the case of proteins, a monoclonal antibody. The second particle is a nanoparticle with a recognition agent that can sandwich the target with the microparticle (Fig. 12.24a). In addition, the nanoparticle carries hundreds of 15 – 20-mer oligonucleotides referred to as barcodes, allowing the user to pair a unique barcode with every conceivable recognition agent, since for a 20-mer there are 4^{20} unique combinations. Once the two particles have sandwiched the target, a magnetic field can be used to separate the complexed target from the sample solution. Release of the barcodes in a buffer is effected chemically (see [12.58]) and the barcodes can be identified with a high-sensitivity detection system, e.g., scanometrically (Fig. 12.24a). The scanometric method has provided the lowest limit of detection to date for both nucleic acid (high zeptomolar, 10^{-21} M) and protein targets (low attomolar, 10^{-18} M) (Fig. 12.24b). The good amplification of the technique is due to the high ratio of barcode to target recognition elements. In addition, it has high-sensitivity barcode sorting and sensing capabilities through the chip-based scanometric method. The barcode detection system allows one to detect nucleic acids close to the sensitivity of PCR without the need of complicated enzymatic processes. It may have, however, its most significant scientific and clinical impact in protein marker-based

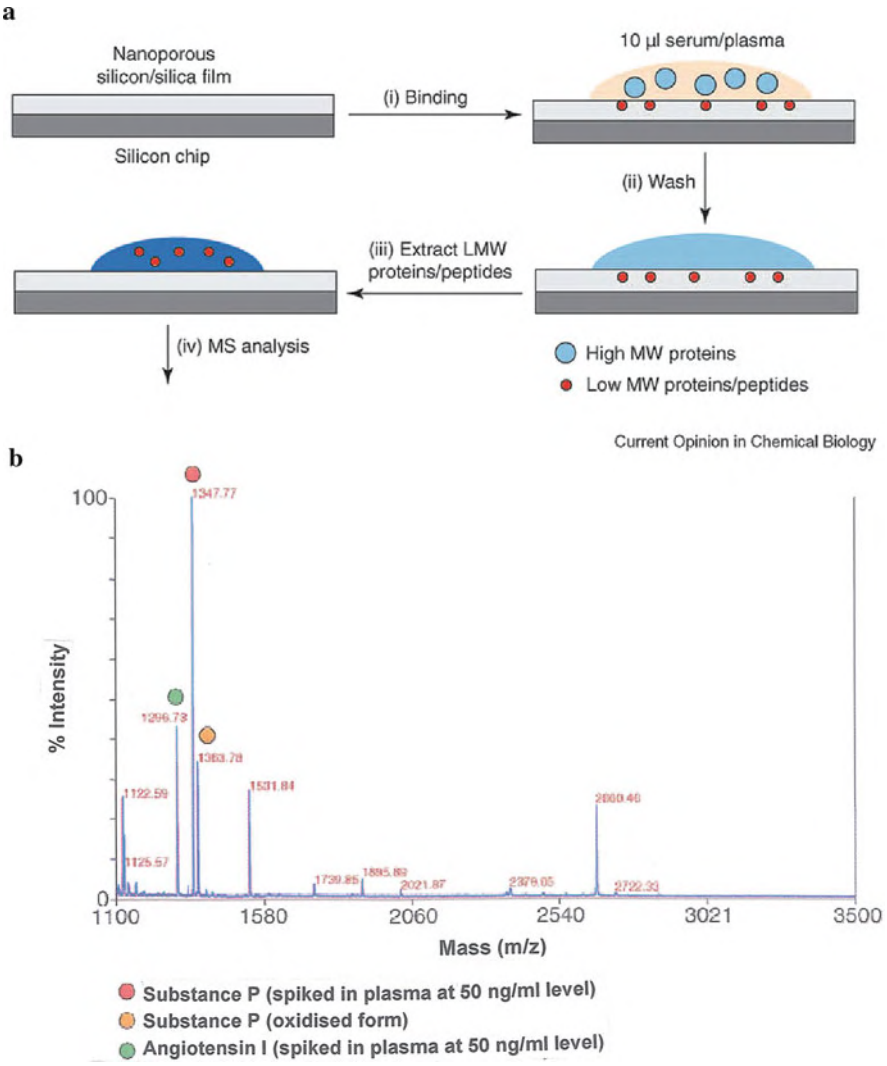

Fig. 12.23 (**a**) Procedure for low-molecular-weight (LMW) protein harvesting from plasma/serum with the capturing strategy on nanoporous surfaces. (i) Incubation of serum with nanoporous silica film; (ii) Washing of unbound substances; (iii) Release of LMW proteins by appropriate extraction solutions; (iv) MS analysis. (**b**) Mass spectrum of LMW peptides extracted by nanoporous harvesting of a 10 µl human plasma sample. Standard peptide substance P and angiotensin I were spiked into the plasma at a 50 ng/ml level. (Reprinted with permission from [12.56]. © 2006 Elsevier)

diagnostics because it is 10^6 times more sensitive than enzyme-linked immunosorbent (ELISA)-based technology. This offers (i) the ability to use new markers of low concentration for various types of diseases, (ii) the ability to use known markers via less invasive means, and (iii) the ability to use existing markers to sensitively

evaluate disease recurrence. An example is the use of the barcode assay to identify amyloid-derived diffusible ligands (ADDL, a marker initially linked to Alzheimer's disease in brain studies) in cerebral spinal fluid samples of Alzheimer patients [12.59]. This was the first time the ADDLs were identified in fluids outside the brain and, importantly, preliminary data showed a correlation between ADDL concentration and progression of the disease. Furthermore, the barcode assay is being evaluated for the early detection of the recurrence of prostate cancer after surgery because of its detection level much lower than in conventional tests (Fig. 12.24b). The barcode assay has also been used for serum-based prion detection in bovine spongiform encephalopathy (BSE; "mad cow disease").

Nanowires: label-free electronic sensors of genes and proteins. Semiconductor nanowire sensors operate on the basis that the change in chemical potential accompanying a target analyte binding event, such as DNA hybridization (the process whereby two complementary nucleic acid strands form a double helix), can act as a field-effect gate upon the nanowire, thereby changing its conductance. This is similar, in principle, to how a field-effect transistor operates. By superlattice nanowire pattern transfer (SNAP), large arrays of Si nanowires can be produced (Fig. 12.25a). Large-scale circuits can be constructed within very small (microfluidics) environments, thereby enabling measurements on large numbers of different genes and proteins from very small tissue samples, or even single cells [12.61]. The potential for both biological research and clinical applications is large. However, encoding the individual nanowires with single-stranded DNA (ssDNA) molecules or protein capture agents represents a serious challenge. Electrochemical methods have been applied to encode selected nanowires with proteins (see [12.56]). Data from Si nanowire sensors are shown in Fig. 12.25b which demonstrate the broad dynamic range (10^6) of sensing the nanowires can attain. Libraries containing up to 24 individual nanowire sensors have been constructed, and it should be possible to extend these libraries to 10^3- 10^5 elements [12.62] for rapid, high-throughput highly multiplexed biomolecular detection.

Cantilevers: nanomechanical detection of biological molecules: It has been demonstrated that molecular adsorption to nanomechanical systems results in measurable mechanical forces which offers an exciting opportunity for the development of highly sensitive, miniature, and label-free biological sensors [12.63–12.65]. For example, micron-sized silicon cantilever beams undergo bending due to surface stresses created by single-side molecular adsorption. The molecular mass loading gives also rise to a variation of the cantilever's resonance frequency. These variations can, e.g., be measured optically or piezoresistively. The cantilevers can be cost-effectively mass-manufactured. Selective chemical recognition of target molecules is achieved by affinity binding reactions, where the cantilever is coated with self-assembled monolayers, DNA probes, antibodies, or peptides. The mechanical stresses bending the cantilever originate from the changes of the free energy by specific binding of biomolecules. Non-specific interactions of biomolecules do not cause cantilever bending (see [12.56]).

DNA hybridization on a cantilever coated with thiol-modified ssDNA probes (20-mers) gives rise to a bending of the cantilever [12.66, 12.67] (Fig. 12.26). The

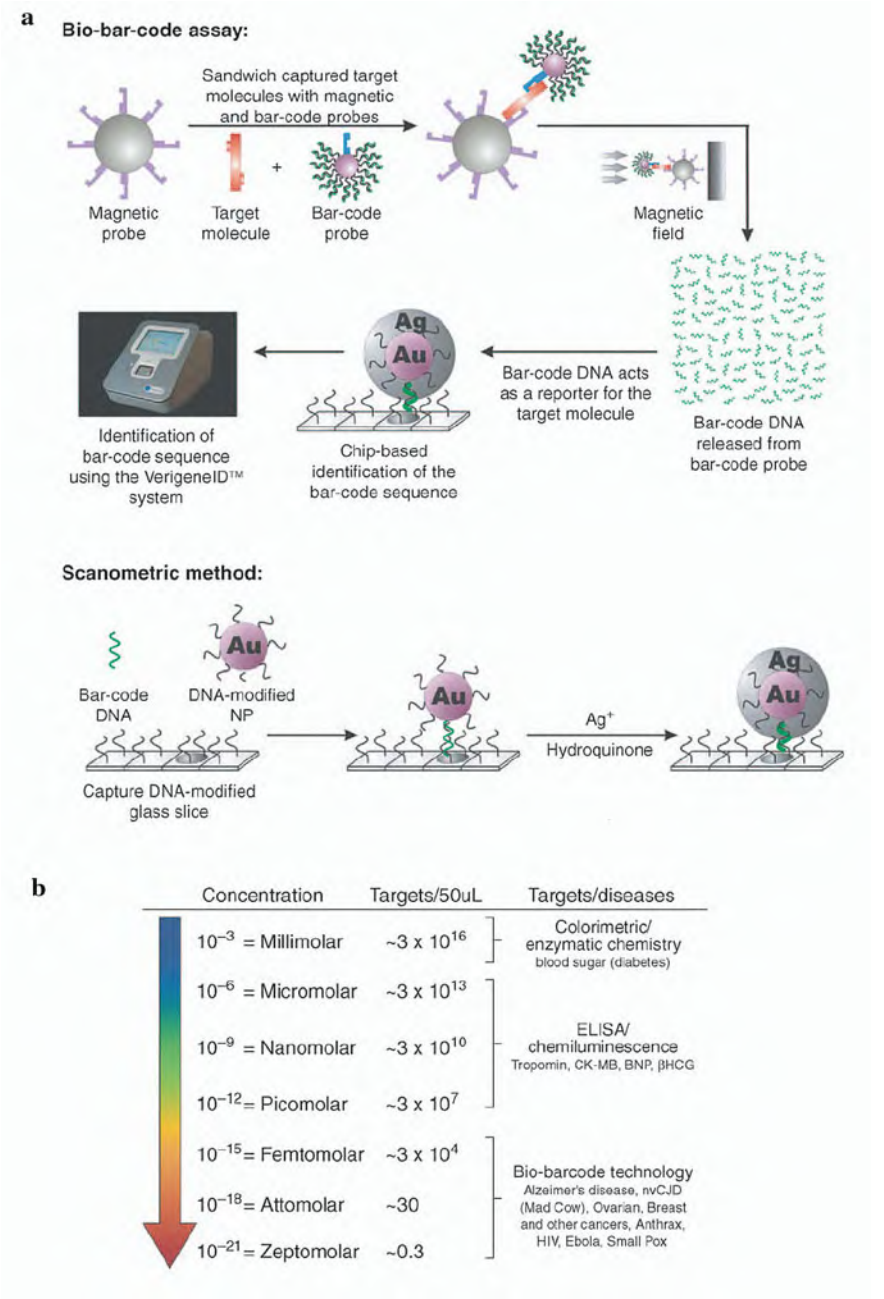

Fig. 12.24 (**a**) General bio-barcode assay scheme. A magnetic particle captures a target using either monoclonal antibodies (for proteins) or complementary oligonucleotides (for nucleic acids). Target-specific Au nanoparticles are conjugated to the target and account for target identification

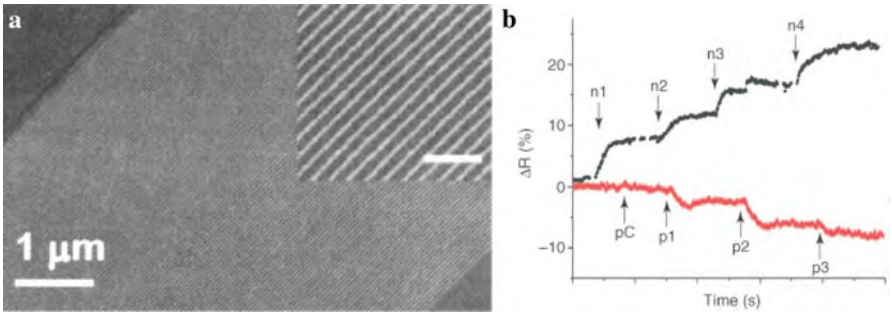

Fig. 12.25 (**a**) 128 12 nm wide Si wires. The *inset* reveals the structural fidelity of the nanowires at a higher resolution (scale bar, 150 nm) [12.60]. (**b**) Sensing results from n-type (*top*) and p-type Si nanowire sensors, demonstrating the sensitivity in the attomolar (10^{-18} M) range in buffer. The time axis is 0−600 s for n-type and 0–1400 s for p-type sensors. The nanowire sensing elements were coated with ssDNA, and oligonucleotides were flowed over the nanosensors using microfluidics. The various points indicated are n1 = 220 attoM cDNA; n2 = 22 femtoM cDNA; n3 = 2.2 picoM cDNA; n4 = 220 picoM cDNA; pC = 22 nanoM noncomplementary ssDNA; p1 = 220 attoM cDNA; p2 = 22 femtoM cDNA; p3 = 2.2 picoM cDNA. Both p- and n-type nanosensors exhibit sensitivity over a broad dynamic range, with the response scaling logarithmically with concentration. (Reprinted with permission from [12.56]. © 2006 Elsevier)

extent of cantilever bending varies as a function of the length of the complementary ssDNA. The cantilever deflection is attributed to a reduction in surface stress due to conformational changes caused by double-stranded DNA formation.

The detection of proteins depends on reproducible and robust immobilization techniques for antibodies. Antigens successfully detected on cantilevers include PSA, and the biowarfare agents ricin and tularemia [12.68, 12.69]. Upon exposure to antigens, the antibody-immobilized cantilevers undergo bending, with the bending amplitude proportional to concentration and time of exposure. Mechanical label-free detection, although in its early days, has the potential as a platform for sensitive multiplexed sensors for biomolecules [12.56]. Microcantilevers were introduced for detecting prostate-specific antigen (PSA) at clinically relevant concentrations [12.70] and for detecting BRCA1 gene mutations [12.71].

Molecular cancer diagnosis. Semiconductor nanoparticle (quantum dots – QD) probes allow sensitive imaging of cancer cells in living animals. The use of near-infrared-emitting QDs should improve both the tissue penetration depth and

Fig. 12.24 (continued) and amplification. The barcode oligonucleotides are released and detected using the scanometric method. The target can be DNA, RNA, or protein. The Verigene ID^{TM} is a commercial instrument (http://www.nanosphere-inc.com). (**b**) Biomolecule detection technology. The bio-barcode assay provides access to a target concentration range well below that of conventional enzyme-linked immunosorbent assays (ELISA). This ultrasensitivity provides the ability to utilize new, low-concentration markers for disease screening, or biodiagnostics. (Reprinted with permission from [12.56]. © 2006 Elsevier)

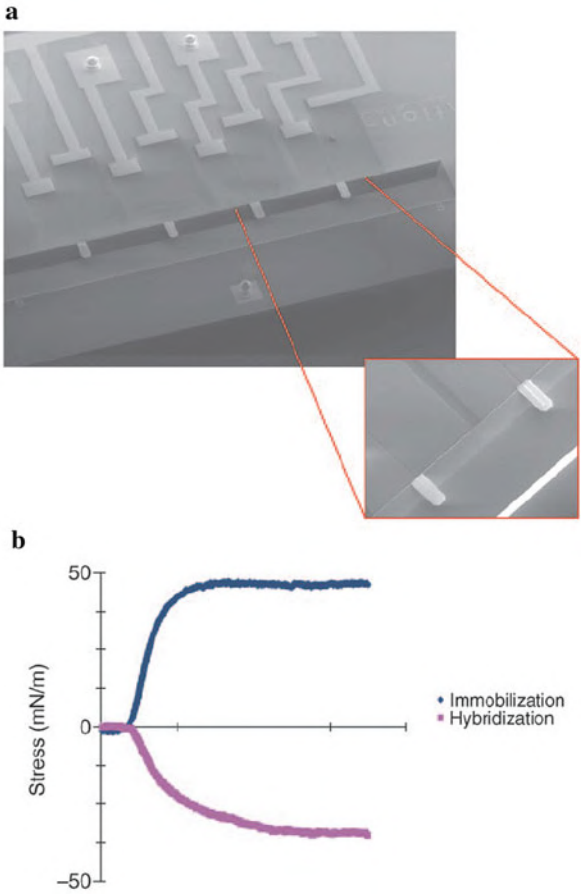

Fig. 12.26 Nanocantilevers for ssDNA detection. (**a**) An array of piezoresistive cantilevers in a fluidic well (Cantion Inc.).The cantilevers are 120 μm long and are separated by 470 μm. (**b**) Cantilever surface stress variation as a function of ssDNA probe (20-mer) immobilization and hybridization of fully complimentary 20-mers using a piezoresistive array. (Reprinted with permission from [12.56]. © 2006 Elsevier)

imaging sensitivity. Agents making use of QDs might be used for non-invasive diagnosis and treatment of cancer [12.72].

Bioconjugated QD probes have been developed for in vivo targeting and imaging of human prostate cancer cells growing in mice. This class of QD conjugates contains a triblock copolymer for in vivo protection, targeting ligands for tumor antigen recognition and multiple polyethylene glycol (PEG) molecules for improved biocompatibility and circulation [12.72]. The core–shell CdSe–ZnS QDs (2.5 nm radius) were covered with a 1 nm tri-*n*-octylphosphine oxide (TOPO) layer, a 2 nm thick polymer coating, and a 4–5 nm PEG antibody layer (Fig. 12.27a, b). Under in vivo conditions, QD probes can be delivered to tumors by both passive and active

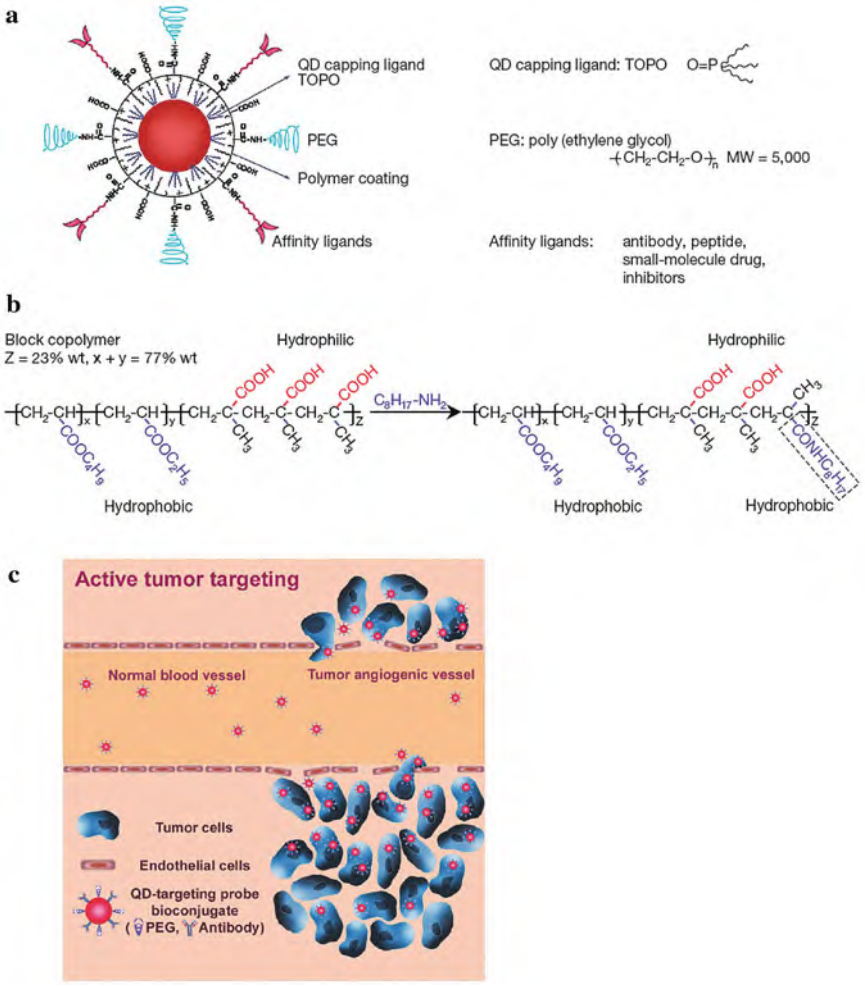

Fig. 12.27 Schematic of bioconjugated QDs for in vivo cancer targeting and imaging. (**a**) Structure of a multifunctional QD probe showing the capping ligand TOPO, an encapsulating copolymer layer, tumor-targeting ligands (peptides or antibodies), and PEG. (**b**) Chemical modification of a triblock copolymer with an 8-carbon side chain which interacts strongly with TOPO. (**c**) Permeation and retention of QD probes via leaky tumor vasculatures (passive targeting) and high-affinity binding of QD-antibody conjugates to tumor antigens (active targeting). (Reprinted with permission from [12.72]. © 2004 Nature Publishing Group)

targeting mechanisms (Fig. 12.27c). In the passive mode, nanometer-sized particles accumulate preferentially through an enhanced permeability and retention effect due to the hyperpermeabilization of the tumor-associated neovasculature and due to the lack of an effective lymphatic drainage system in the tumor. QD probes conjugated to a specific monoclonal antibody (Ab) exhibit a strong and specific binding to a

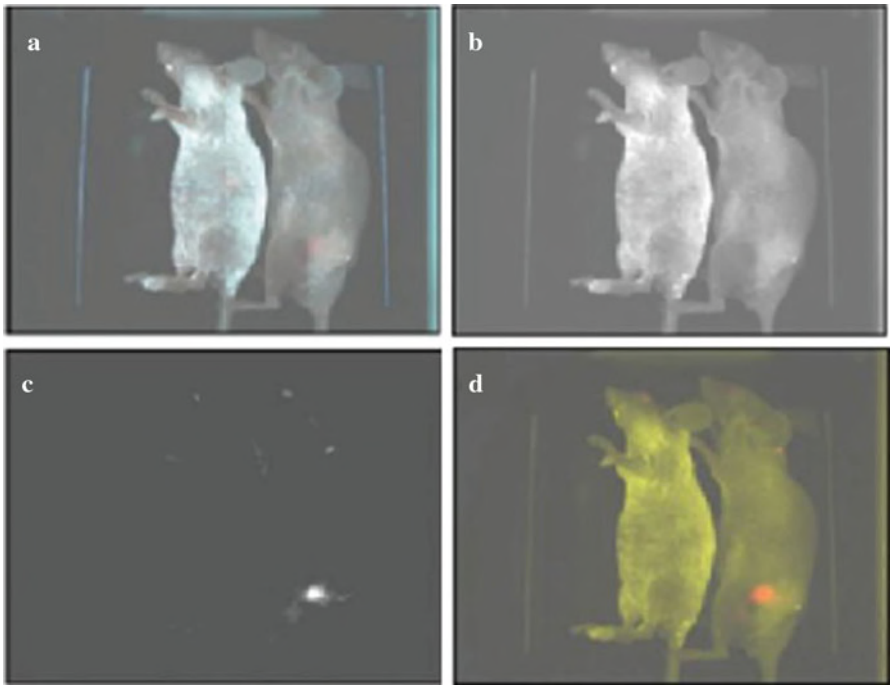

Fig. 12.28 Spectral imaging of QD-PSMA Ab conjugates in live mice harboring C4-2 human prostate tumor xenografts. Orange-red fluorescence signals indicate a prostate tumor growing in a live mouse (*right mouse*). Control studies using a healthy mouse (no tumor) and the same amount of QD injection showed no localized fluorescence signals (*left mouse*). (**a**) Original image; (**b**) unmixed autofluorescence image; (**c**) unmixed QD image; and (**d**) superimposed image. After in vivo imaging, histological and immunocytochemical examinations confirmed that the QD signals came from an underlying tumor. Note that QDs in deep organs such as liver and spleen were not detected because of the limited penetration depth of visible light. (Reprinted with permission from [12.72]. © 2004 Nature Publishing Group)

human prostate cancer cell line, C4-2, which is known to express prostate-specific membrane antigen (PSMA) on the cell surface.

Figure 12.28 depicts spectral imaging results obtained from QD-PSMA Ab probes injected into the tail vein of a tumor-bearing mouse (*right* mouse) and a control mouse (no tumor, *left* mouse). The original image (a) shows QD signals at one tumor site among an autofluorescence background of the mouse skin. Using spectral unmixing algorithms, the background signals (b) and the QD signals (c) were separated. The composite image (d) shows the tumor site in the whole animal.

The QD probes, which are highly stable in vivo, appear 10–20 times brighter than organic dyes. Due to the PEG shielding they circulate in blood for as long as 48–72 h. For deep tissue imaging (millimeters to centimeters) the use of far-red and near-infrared emitting QD in the spectral range 650–900 nm are required.

This wavelength provides a "clear" window for in vivo optical imaging because it is separated from the major absorption peaks of blood and water [12.73]. Based on tissue optical calculations it is estimated that near-infrared emitting QDs should improve the tumor imaging sensitivity to a detection limit of 10–100 cancer cells (see [12.72]). Semiconductor QDs of cadmium selenium telluride with fluorescence emission up to 850 nm have been developed [12.74].

In the absence of UV radiation, QDs with a stable polymer coating are essentially non-toxic to cells [12.72]. The polymer-protected QDs might be cleared from the body by slow filtration and excretion through the kidney.

Fluorescent nanoparticles could provide an early sign that apoptosis or programmed cell death is occurring as a result of anticancer therapy [12.75]. The fluorescent surface-enhanced Raman spectroscopic tagging material (F-SERS dots) are composed of silver nanoparticle-embedded silica spheres (diameter about 100 nm) with fluorescent organic dye and specific Raman labels for multiplex targeting, tracking, and imaging of cellular/molecular events in the living organism. The non-toxic F-SERS dots can monitor apoptosis through fluorescence signals as well as Raman signals in both cells and tissue with high selectivity [12.75].

Cholesterol sensor in blood based on Au nanowires in a microfluidic platform. Cholesterol and its fatty acids are important components of nerve and brain cells and are precursors of biological substances, such as bile acid and steroid hormones [12.76]. However, high cholesterol accumulation in blood serum is strongly correlated with coronary heart disease, arteriosclerosis, myocardial infarction, brain thrombosis, and hypertension (see [12.77]). Since, however, traditional cholesterol determination by non-enzymatic spectrophotometric techniques suffers from low specificity and high costs, convenient, rapid, sensitive, and cost-effective methods for the determination of cholesterol levels in blood are desirable.

Gold nanowires (175 nm in diameter; Fig. 12.29a) [12.77], based on a microfluidic platform (Fig. 12.29b), were covalently functionalized with thiol or carboxyl groups and further reacted with enzymes, such as cholesterol oxidase (COX) and cholesterol esterase (CE) for both monitoring the native and esterified cholesterol levels, which is important for the determination of the total cholesterol. The deposition of COX and CE globules from the blood on the gold nanowires is detected electrically (voltammetry) to concentrations up to 6 mM with an accuracy of $\pm$ 2% [12.77] and a good linear response between current and cholesterol level. The increased sensitivity of the gold wire assay compared with the sensitivity of a conventional 2D detector is due to the high surface of the nanowire. Ascorbic acid (2 μM), uric acid (10 μM), and glucose (20 μM) which are usually available in blood serum do not interfere with the cholesterol detection.

Vaccines. Nanoparticles have been studied as a vaccine platform by targeting lymph node residing dendritic cells via interstitial flow and activating these cells by in situ complement activation. The complement is a complex system of proteins found in normal blood serum that combines with antibodies to destroy, e.g., pathogenic bacteria. After intradermal injection of the nanoparticles into mice, interstitial flow transported small nanoparticles (25 nm) highly efficiently into lymphatic capillaries and their draining lymph nodes, whereas 100 nm particles were much

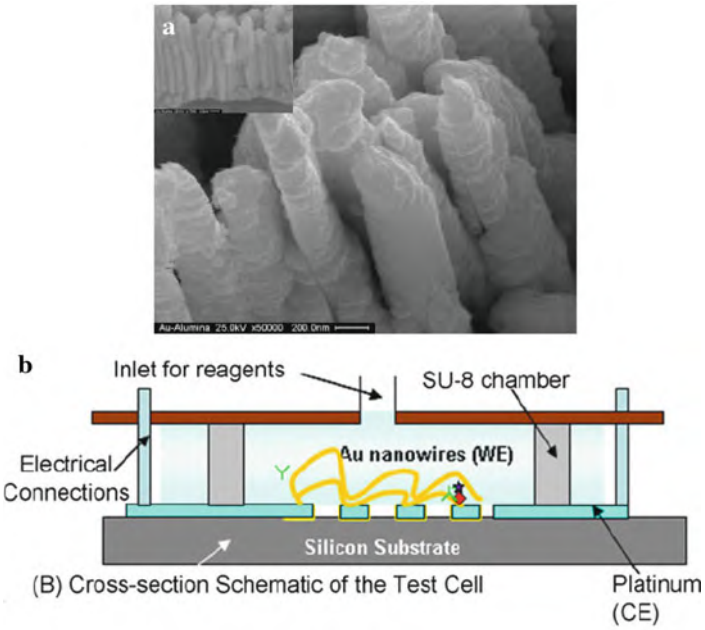

Fig. 12.29 (**a**) SEM images showing the top view and the cross-sectional view (*inset*) of the 175 nm Au nanowires; (**b**) Cross-sectional schematic of the test cell with nanowires aligned on the platinum "assembly lines" for dielectrophoresis. (Reprinted with permission from [12.77]. © 2007 Elsevier)

less efficient. The surface chemistry of these nanoparticles activated the complement cascade, generating a danger signal in situ and potently activating dendritic cells. Using nanoparticles conjugated to the model antigen ovalbumin in a strategy for vaccination, the generation of humoral and cellular immunity in mice was demonstrated in a size- and complement-dependent manner [12.78].

12.3 Nanoarrays and Nanofluidics for Diagnosis and Therapy

Microfluidic instrumentation can be applied to several diagnostic laboratory techniques, including blood chemistry, immunoassays, nucleic acid amplification test, biothreat detection [12.12], flow cytometry [12.79], and for biomarker-guided therapeutic targeting. Basic blood chemistry panels for analyzing enzymes, gases, electrolytes, lipids, thyroid indicators, and drugs consist of 12–20 tests and are routinely run on automated analyzers. Immunoassays allow quantification and monitoring of small molecules, large proteins, and even whole pathogens. Nucleic acid amplification tests, such as the polymerase chain reaction (PCR), can detect very small copy numbers of specific nucleic acid sequences. Test kits are commercially

available for tuberculosis, HIV, and sexually transmitted infections (STIs). Flow cytometry is the method of choice for counting cells with specific physical or chemical characteristics [12.79]. Microchips for drug delivery are microfabricated devices that incorporate micrometer-scale pumps, valves, and channels and allow controlled release of single or multiple drugs on demand [12.1, 12.80]. These devices are particularly useful for long-term treatment of conditions requiring pulsatile drug release after implantation in a patient.

12.3.1 Lab-on-a-Chip

The behavior of liquids changes when the volumes are reduced to below micro- or nanoliters. The corresponding micro- or nanofluidics govern the manipulation of small volumes of liquids of labs-on-a-chip which are being developed for medical, biological, and chemical application [12.81]. A lab-on-a-chip is a mini version of a chemical laboratory where chemical, biological, or medical analyses or diagnostic procedures should shrink to thumbnail size. The reason why chemical, biological, or medical procedures are scaled down to micro- and nanoliters is partly because small amounts of agents are cheaper and less toxic, but many materials are only available in small quantities as, for example, in the case of the determination of a genetic fingerprint which should be identified from a single hair or a tiny specimen of saliva. In addition, detection limits and times required for analyses are substantially reduced in the nanoliter regime.

In contrast to conventional hydrodynamics with large geometrical dimensions d, high flow velocities v, low viscosities η, and therefore high Reynolds numbers

$$Re = dv\rho/\eta,$$

where ρ is the mass density, the Reynolds numbers Re in nanofluidics are low due to small d, low v, and often enhanced η values. The transition from the macroscopic to the nanofluidic behavior is thought to occur at $Re = 1000$ [12.81]. In small tubes where the ratio of contact surface between fluid and tube wall and fluid volume is large, the interaction between fluid and tube wall (these adhesion forces may be of electrostatic nature) and the viscous forces dominates. In this situation, turbulence, appearing in macroscopic systems, is negligible, and laminar flow (Fig. 12.30a) prevails so that mixing of different fluid components is restricted to diffusive processes. The adhesion determines the wettability of a solid surface by a fluid which can be determined from the wetting angle of a drop on a surface (Fig. 12.30b). A wetting angle φ between 0° and 90° is characteristic for a wetting or hydrophilic interface, whereas $90° < \varphi < 180°$ characterizes a non-wetting or hydrophobic interface. Hydrophilicity can be employed for sucking a liquid into a narrow capillary which can be used for pumping a liquid.

Pumps are of particular importance for operating microfluidic chips. In addition to hydrophilicity, electrowetting (Fig. 12.30b) can be used for pumping because the

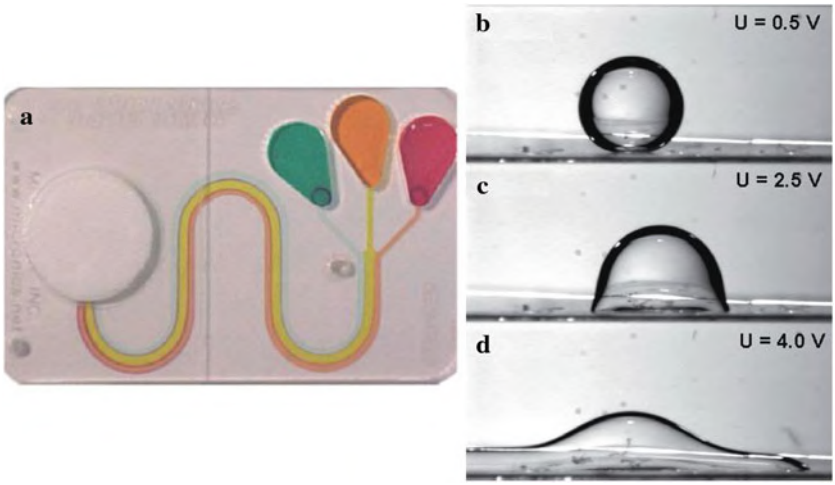

Fig. 12.30 (**a**) The lab-on-a-chip T-Sensor® Access™ LabCard by Micronics (credit card size) makes use of laminar flow for chemical analysis. (**b–d**) Water droplet in oil on an electrode substrate for deformation of the droplet by application of an electrical voltage. (Reprinted with permission from [12.81]. © 2007 Wiley-VCH)

adhesion forces between a capillary wall and a liquid are of electrostatic nature and, therefore, the wettability can be controlled by an electrical voltage. Furthermore, peristaltic pumps have been designed [12.82].

For mixing of nanofluids, the split-and-recombine technique can be used (Fig. 12.31a) where the nanofluid in a channel is separated into many smaller channels for diffusive mixing and then reunited in a larger channel. Furthermore, an alternating voltage for deformation of a droplet (Fig. 12.30b–d) or acoustic surface waves (Fig. 12.31b–c) can be applied for mixing nanofluids.

12.3.2 Microarrays and Nanoarrays

The use of miniaturized, chip-based, array detection methods, known as "*microarrays*," has been prevalent in many health-related research areas. This biomolecular assay allows for parallel processing of a variety of targets in a small area and a reduction in processing times. Such high-throughput detection systems have been most valuable in genomics and proteomics research [12.83, 12.84]. To fabricate such an array, nanoliter volumes of protein samples are delivered to a microscope slide in spots of approximately 200 μm in diameter and yielding 1600 spots per cm^2 [12.83] (Fig. 12.32a). Additional miniaturization and fabrication of nanoarrays would generate many orders of magnitude increase in multiplexed detection in the same area as a microarray. In addition, nanoarrays should allow for much smaller sample volumes and possibly lower detection limits. By dip-pen nanolithography

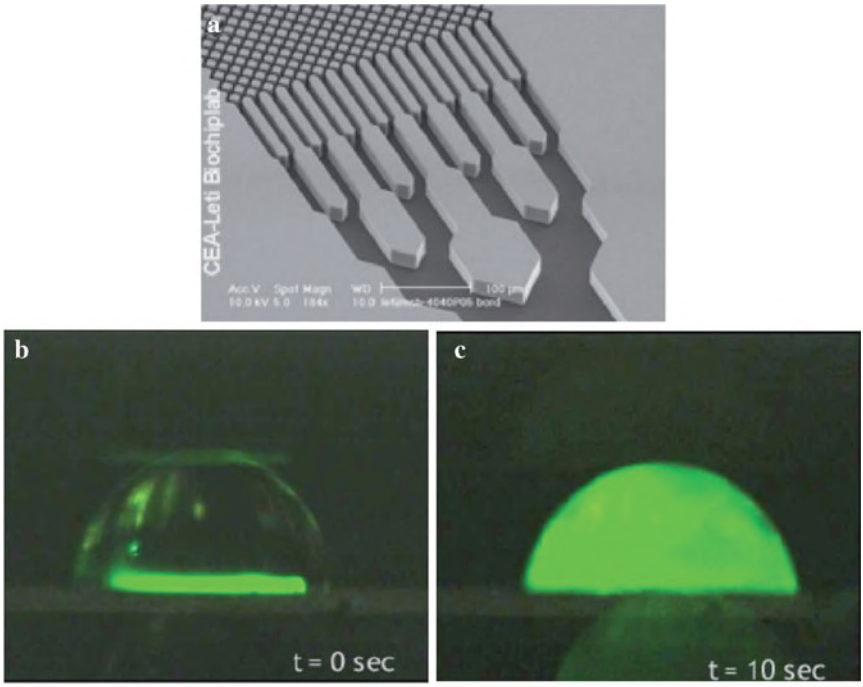

Fig. 12.31 (**a**) A microchannel can be sub-divided into smaller channels (split-and-recombine technique) for enhancing mixing by diffusion (scale bar, 100 μm). (**b**–**c**) In a 50 nl droplet acoustic surface waves can be employed for mixing the fluorescence dye (**b**) with the water (**c**). (Reprinted with permission from [12.81]. © 2007 Wiley-VCH)

(DPN; see Sect. 3.10), oligonucleotides and proteins can be patterned onto surfaces with a dot size as small as 15 nm. An array fabricated by DPN would result in 100,000,000 spots in the area of a single 200 × 200 μm spot in a conventional microarray (Fig. 12.32a). Using this technology, it is conceivable that some day the entire human genome could be screened for single-nucleotide polymorphism on a single chip [12.85] with an area of 2 × 2 cm^2 and a spot size of 150 nm [12.86]. By DPN, nanoarrays were generated with monoclonal antibodies against human immunodeficiency virus-1. Coupled to nanoparticle probes, these arrays demonstrated the detection of human immunodeficiency virus from samples of human plasma with a detection sensitivity that exceeded that of conventional ELISA (see Fig. 12.24) by more than 1000-fold [12.87].

12.3.3 Microfluidics and Nanofluidics

By multilayer elastomer microfluidics, integrating many pumps, valves, and channels within an easily fabricated microchip [12.61], multiple operations can be

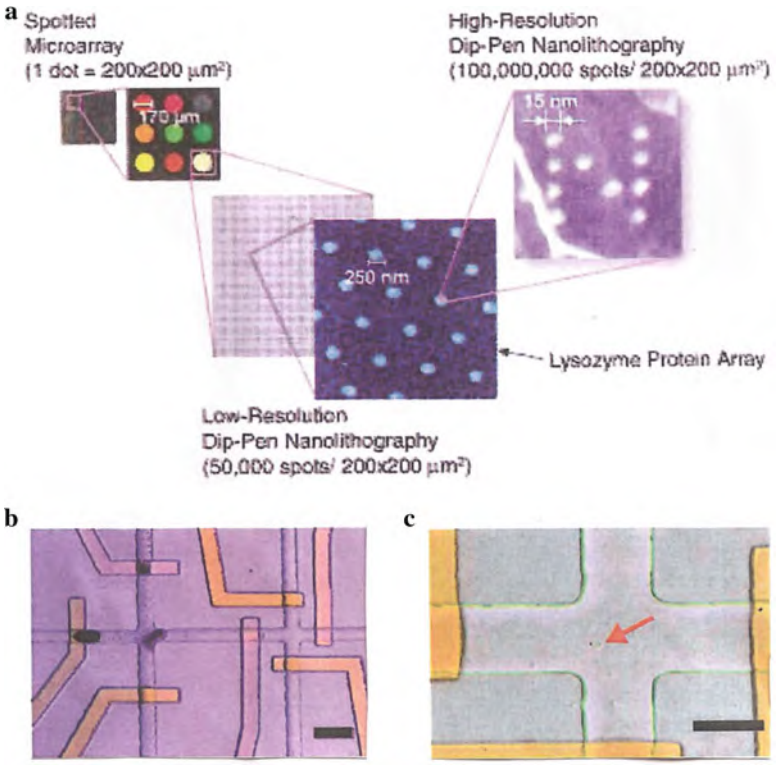

Fig. 12.32 (**a**) Conventional microarray versus a nanoarray fabricated by dip-pen nanolithography (DPN). In a microarray, spot sizes are typically 200 × 200 μm^2. Using low-resolution DPN, 50,000 250 nm spots can be generated in the same area. Remarkably, high-resolution dip-pen nanolithography (DPN) can generate 100,000,000 spots in the 200 × 200 μm^2 area [12.86]. (**b**, **c**) DNA purification microfluidic chip; (**b**) photograph of a portion of the chip showing multilayer elastomer microfluidic technology. The *orange-colored* regions are valves separating an empty chamber at the right from a region on the left, in which an affinity column for the target of interest is constructed (*dark regions*). (**c**) A single cell is loaded into a "cell chamber" before a lysis step. Scale bars, 100 μm [12.88]. (Reprinted with permission from [12.86] (**a**) and [12.88] (**b**) (**c**). © 2004 Wiley-VCH (**a**) and © 2004 Nature Publishing Group (**b**))

performed in parallel, such as cell sorting, DNA purification, and single-cell genetic profiling [12.88, 12.89]. This technology offers large-scale multiparameter analysis with several potential applications including single-cell dissection and analysis (e.g., from needle biopsies) and multiparameter disease detection from tissues and blood (Fig. 12.32b, c). Currently, integrated microfluidic systems that process only nanoliters of sample material are emerging that can be termed "*nanofluidic systems*" [12.90]. A microfluidic chip can demonstrate automated nucleic acid purification from small numbers of bacterial or mammalian cells including cell isolation, cell lysis, DNA or mRNA purification, and recovery, on a single microfluidic chip in nanoliter volumes without any pre- or postsample treatment. Measured amounts of

mRNAs were extracted from a single mammalian cell and recovered from the chip (Fig. 12.33). The achievement of extensive analysis on a single chip represents significant progress toward the realization of the "*lab-on-a-chip*," where a complete analysis system is fully integrated, automated, and portable [12.14].

Biological serum markers for the early detection of most cancers are not available. The markers that are in clinical use, such as the prostate-specific antigen (PSA) and carcinoembryonic antigen (CEA), are non-specific and have widely different baseline expressions in the population and, therefore, are for limited effectiveness for early detection. The goal of developing reliable early detection approaches from serum or non-invasive procedures remains of paramount importance [12.91]. The applicability of microcantilevers for the quantitation of PSA at clinically significant

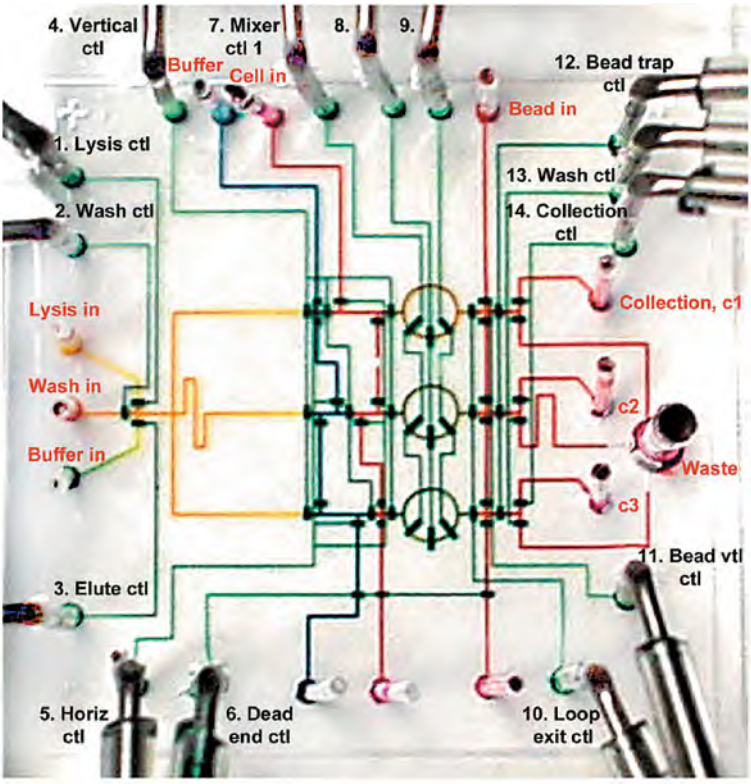

Fig. 12.33 Integrated nanoliter scale DNA processor chip with parallel architecture. The chip has two layers: the fluidic layer and the actuation layer. The actuation channels (100 μm wide) are filled with *green* food coloring and the fluidic channels with *yellow*, *blue*, and *red* food coloring, depending on their functionalities. A bacterial cell culture can enter through the "cell in" port (*upper left* corner) followed by various lysis and buffer solutions. Multiple parallel processes of DNA recovery from living bacterial cells are possible in three processors. The chip contains 26 access holes and 54 valves within 2×2 cm^2. (Reprinted with permission from [12.88]. © 2004 Nature Publishing Group)

concentrations has been demonstrated [12.70] and it is realistic to envision arrays of thousands of cantilevers constructed on individual centimeter-sized chips allowing the simultaneous reading of proteomic profiles or the entire proteome for high early-detection reliability. The many similarities that these protocols share with the fabrication of microelectronic components indicate that they will be suitable for production scale-up at low cost and with high reliability (see [12.92]).

12.3.4 Integration of Nanodevices in Medical Diagnostics

In addition to the functionalization of nanowires, nanotubes, or nanocantilevers, these devices can be fabricated in arrays, enabling multiple detection assays to be performed in parallel [12.93]. Moreover, these technologies can be combined with nanoparticle probes to increase sensitivity [12.94] and can be integrated with elastomer micro- and nanofluidics to create miniaturized and automated *microfluidics/nanotechnology platforms* [12.95] (Fig. 12.34). These types of platforms may emerge within the next few years with the ability to integrate multiple operations, such as cell sorting and serum purification, as well as the ability to detect and quantify 5–10 biomarkers from single cells or from very small sample fluid volumes [12.14, 12.61].

In a *magnetic lab-on-a-drop* "laboratory device" (Fig. 12.35), a single droplet of an aqueous suspension of antibody-coated superparamagnetic particles sealed in mineral oil can be moved, merged, mixed, and split by an external magnetic field. A 25 μL blood sample containing 30 human leukemia cells expressing a green fluorescent protein (CD15-bound GFP-transfected THP-1) was placed on the chip and anti-CD15-coated superparamagnetic nanoparticles bound to the target cells, which then could be extracted within a smaller droplet for 100-fold preconcentration. This droplet was purified and added to reagents for polymerase chain reaction (PCR). The magnetic droplet is finally moved clockwise (Fig. 12.35) through four different temperature zones while a fluorescence detector indicates the presence and quantity of the desired gene sequence within a total 17 min whereas bench-scale PCR typically takes hours [12.98].

12.3.5 Implanted Chips

A nanotechnology-enhanced objective for the near-term future is to realize delivery implants for the constant-rate release of a broad spectrum of agents. The constant-rate delivery of the hormonal agent leuprolide from an osmotic pump-powered implant is already in clinical use for the treatment of prostate cancer and exemplifies the potential benefits associated with controlled-release modalities: therapeutic advantages, reduction of side effects, regularity of dosing, localization of therapeutic action, and patient compliance. However, not many drugs can be delivered by osmotic pumps and time-variable drug delivery may be desirable. To address

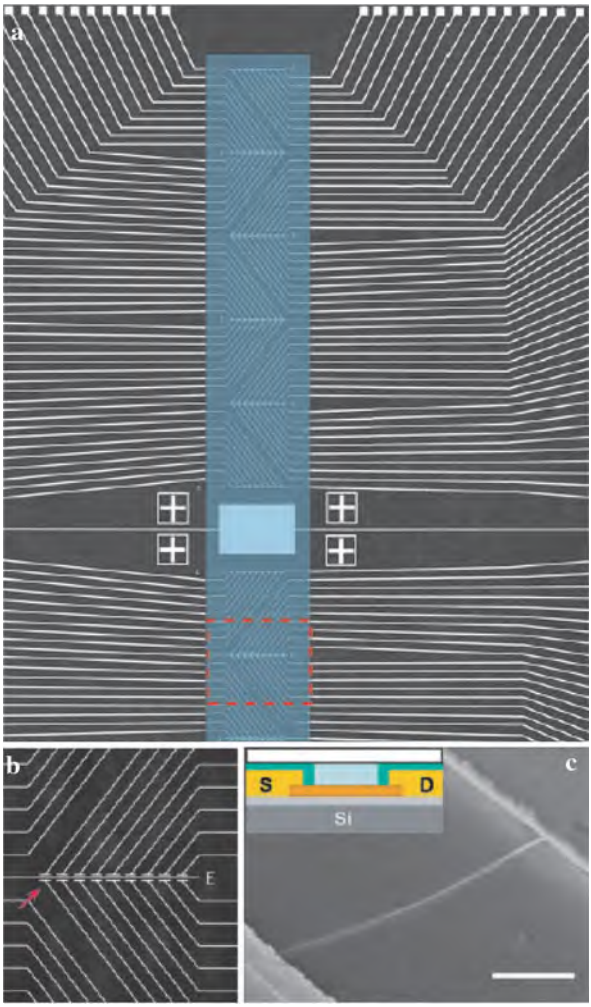

Fig. 12.34 Integrated platform: Nanowire-based biosensor incorporating nanoarray and microfluidic technology. (**a**) Portion of the device array with *white lines* corresponding to metal electrodes that connect to individual nanowire devices. The section colored in *blue* represents a microfluidic channel used to deliver sample material to the nanowire sensors and has a total size of 6 mm × 500 μm. (**b**) One row of nanowire devices from the *red* box in (**a**) with an image field of 500 × 400 μm^2. (**c**) Scanning electron micrograph of a single nanowire sensor device indicated by the *red arrow* in (**b**). The silicon nanowire stretches between the electrode contacts visible in the *upper right* and the *lower left* regions of the image (scale bar: 500 nm). *Inset*: schematic of a single device. The nanowire (*orange line*) is connected to source (S) and drain (D) gold electrodes that are insulated by a layer of silicon (*green*). The microfluidic channel is indicated (*blue*). (Reprinted with permission from [12.96]. © 2004 National Academy of Sciences USA)

Fig. 12.35 Surface-functionalized superparamagnetic particles emulsified in mineral oil turn a free-standing droplet into a flexible virtual laboratory with (sub)-microliter volumes. By using magnetic forces, rare acute monocytic leukemia cells are extracted from blood, preconcentrated, purified, lysed, and subjected to real-time polymerase chain reaction (PCR) in minutes. The PCR works like a clock work by rotating the drop over different temperature zones. (Reprinted with permission from [12.97]. © 2008 Elsevier)

these issues, silicon membranes with nanofabricated channels of well-controlled dimension (5–100 nm) were developed [12.99] for desired release rates for any drug. Based on the nanochannel technology [12.100], controllable systems are being developed for programmable, remotely controlled, and self-regulating implants.

12.4 Targeted Drug Delivery by Nanoparticles

An early approach to drug delivery was made by Paul Ehrlich (1854–1915; Nobel prize in medicine in 1908), who proposed that if an agent could selectively target a disease-causing organism, then a toxin for that organism could be delivered along with the agent of selectivity (see [12.101]). The potential of drug delivery systems nowadays, based on the use of nano- and microparticles, stems from significant advantages such as (i) the ability to target specific locations in the body; (ii) the reduction of the quantity of drug needed to attain a particular concentration in the target; and (iii) the reduction of the concentration of the drug at non-target sites, minimizing severe side effects. This is why the number of publications dealing with nanoparticles (NPs) for drug delivery applications grew exponentially (Fig. 12.36).

Nanoparticles can act at the tissular or cellular level. They can reach beyond the cytoplasmic membrane or beyond the nuclear membrane (i.e., transfection applications). Tumor targeting with NPs may use passive or active strategies. Passive targeting occurs as a result of extravasation at the disease site where the microvasculature is leaky, leading to the selective accumulation of NPs in tumor tissue, a

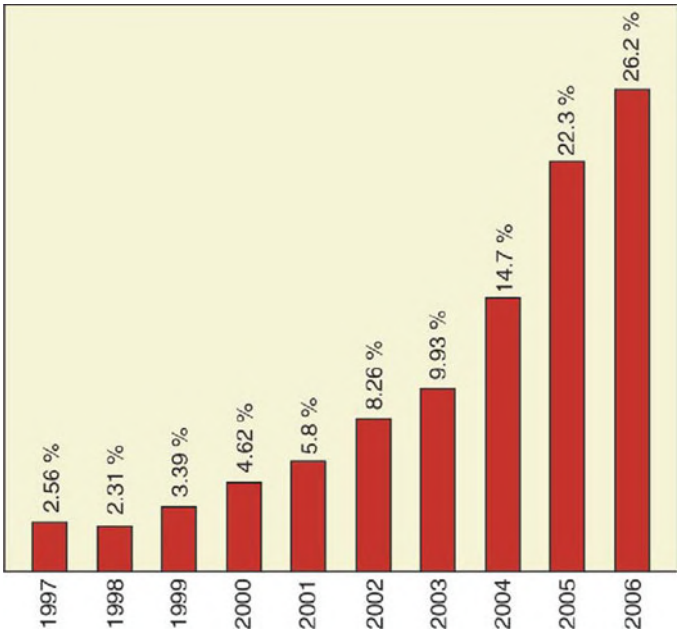

Fig. 12.36 Temporal evolution in the number of scientific papers published involving drug delivery using nanoparticles [12.101, 12.102]. (Reprinted with permission from [12.101]. © 2007 Elsevier)

phenomenon known as enhanced permeation and retention (EPR). The majority of solid tumors exhibit a vascular pore size between 380 nm and 780 nm, and NPs of this size can easily flow through the narrowest capillarities (5 μm wide). Active targeting is based on the exclusive expression of different epitopes (specific region of an antigenic molecule that binds to an antibody) or receptors in tumor cells or, alternatively, on overexpressed species such as low-molecular-weight ligands (folic acid, thiamine, sugars), peptides, proteins (transferrin, antibodies), polysaccharides, and DNA. [12.101].

New drug delivery systems with nanoparticles that can be targeted to specific cells or tissues are thought to be available by 2020 [12.103].

In the following we will discuss porous silica nanoparticles as drug carriers, gelatin nanoparticles for gene therapy, liposomes and micelles for drug delivery, and finally magnetic nanoparticles as vehicles for drugs.

12.4.1 Porous Silica Nanoparticles for Targeting Cancer Cells

Mesoporous silica nanoparticles (MSNs) show promise as novel drug delivery systems. They have been used as agents for administering the anticancer drug camptothecin (CPT) [12.104] or the protein cytochrome *c* [12.105] directly into

human cancer cells. Camptothecin induces cell death by poisoning DNA topoisomerase I, an enzyme capable of removing DNA supercoils [12.106]. Cytochrome *c* is a membrane-impermeable protein involved in apoptosis or controlled cell death, a mechanism that can fail in cancer cells. Fluorescent MSNs with a diameter of 130 nm and with a MCM-41-like structure (see Sect. 3.9) of 2 nm diameter channel pores (Fig. 12.37) were filled with CPT (a molecule 1.3 nm × 0.6 nm in size), one of the most promising cancer drugs of the 21st century (see [12.104]). Clinical application of CPT in humans has, however, not been achieved to date because of the poor water solubility of this drug. The MSNs can be used to overcome this insolubility problem.

A suspension of the CPT-loaded MSN was added to the human cancer cell lines PANC-1, AsPC-1, Capan-1 (pancreatic), MKN45 (gastric), and SW480 (colon) to determine if the nanoparticles were able to transport the hydrophobic CPT into the cancer cells. As shown in Fig. 12.37c, the cells that were treated with CPT-loaded MSNs showed strong blue fluorescence typical for CPT, while those that were treated in a control experiment with a suspension of CPT in phosphate-buffered

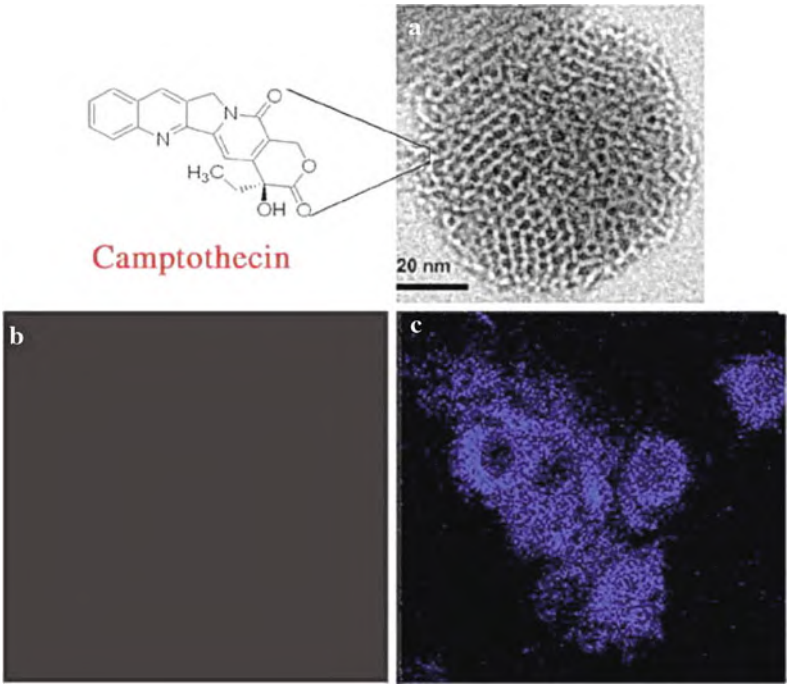

Fig. 12.37 (**a**) Transmission electron micrograph of a mesoporous silica nanoparticle (MSN). *Blue* fluorescence of camptothecin (**c**) after uptake of the camptothecin (CPT) loaded MSNs into the PANC-1 human pancreatic cancer cells after incubation for 3 h. No fluorescence was observed (**b**) within the cells that were incubated with a suspension of CPT in phosphate-buffered saline (PBS) solution. (Reprinted with permission from [12.104]. © 2007 Wiley-VCH)

saline (PBS) solution remained non-fluorescent (Fig. 12.37b). This observation indicates that the MSNs were able to transport and deliver CPT inside the cancer cell. CPT remained inside the nanoparticles during cell penetration and was then released in the hydrophobic regions of the cell compartments.

The cytotoxic effect of CPT-loaded MSNs leading to growth inhibition and cell death was demonstrated on pancreatic cell lines (PANC-1, ASPC-1, Capan-1), a colon cancer cell line (SW480), and a stomach cancer cell line (MKN45). By contrast, CPT suspended in phosphate-buffered saline (PBS) did not show any cytotoxicity to cancer cells [12.104]. These results show that mesoporous silica nanoparticles loaded with CPT can circumvent the problem of insolubility of cancer drugs in aqueous solutions in order to make use of their full efficiency.

Mesoporous silica nanoparticles can, furthermore, not only serve as vehicles for introducing membrane-impermeable proteins, such as the apoptosis-involved cytochrome *c*, into the cells, but they are also able to escape the endolysosomal entrapment so that the protein can be efficiently released into the cytoplasm [12.105]. In order to demonstrate this, cytochrome *c* was tagged with the green fluorescent dye fluorescein isothiocyanate (FITC), loaded into MSN, and efficiently introduced into the HeLa human cervical cancer cell cultures. In order to determine whether or not the cytochrome *c*-loaded MSNs could escape the endosomal entrapment, the endosomes were stained with the red fluorescent endosome marker FM4-64 (see [12.105]). In Fig. 12.38b, exclusively separate green and red dots are seen. This means that the MSNs loaded with cytochrome *c* can quantitatively escape the endosomes to efficiently deliver the drug in the cytoplasm. If the MSNs (green)

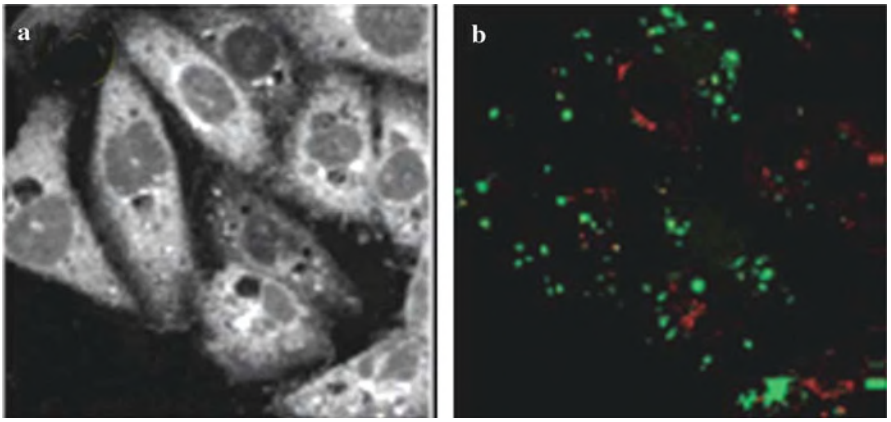

Fig. 12.38 Uptake of the mesoporous silica nanoparticles (MSNs), loaded with the dye fluorescein isothiocyanate (FITC) and the apoptosis-inducing protein cytochrome *c*, by HeLa human cervical cancer cells as observed by confocal fluorescence microscopy after incubation for 24 h. (**a**) Autofluorescence image of the cells. (**b**) Fluorescence images of the cytochrome *c* protein (*green*) and of the cellular endosomes (*red*). The separation of the *green* and *red* dots demonstrates that the protein is not entrapped in the endosomes but is delivered to the cytoplasm. (Reprinted with permission from [12.105]. © 2007 American Chemical Society)

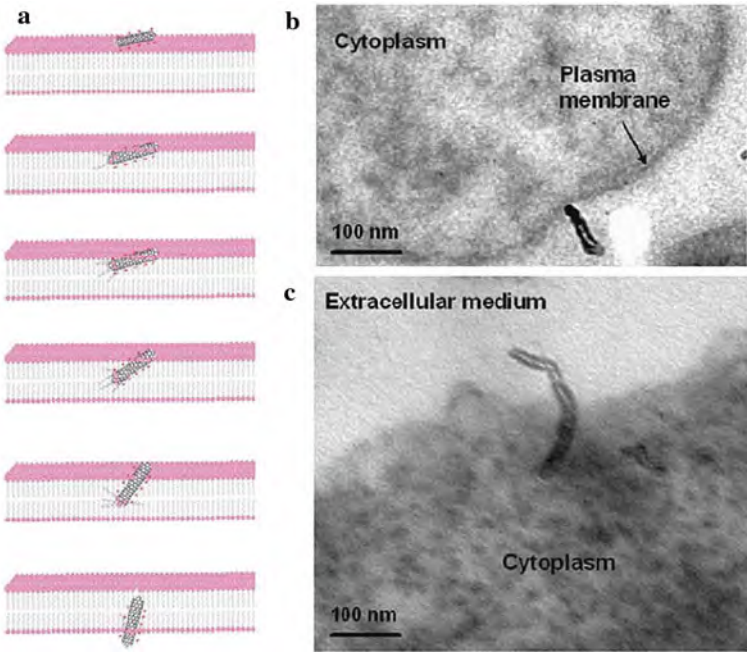

Fig. 12.39 Carbon nanotubes acting as nanoneedles. (**a**) Schematic of a CNT crossing the plasma membrane; (**b**) Transmission electron micrograph (TEM) of multiwalled carbon nanotubes functionalized with NH_3^+ (MWNT-NH_3^+) interacting with the plasma membrane of A549 cells; and (**c**) TEM of MWNT-NH_3^+ crossing the plasma membrane of HeLa cells. (Reprinted with permission from [12.107]. © 2007 Elsevier)

would be entrapped in the endosomes (red), this would result in yellow dots as a result of green-red superposition which is not observed [12.105].

Biocompatible functionalized carbon nanotubes can be internalized by a wide range of cell types (Fig. 12.39) and their high surface area can potentially act as a template for cargo molecules such as peptides, proteins, nucleic acids, and drugs. The application of carbon nanotubes includes vaccine delivery, gene delivery, cancer therapy, and HIV/AIDS therapy [12.107].

12.4.2 Gene Therapy and Drug Delivery for Cancer Treatment

If cancer can be detected early enough, statistics have shown that the burden of the disease is drastically reduced. The use of nanofunctional materials can significantly transform the way the disease is diagnosed, imaged, and treated [12.108, 12.109, 12.110]. Early detection of cancer can be achieved by using nanoparticles for magnetic resonance imaging (MRI) [12.111]. Normal, cancerous, and metastatic cells can be detected and differentiated by making use of nanoparticle sensor arrays [12.112].

Personalized cancer therapy will in the future require genetic testing to select the best treatment. The sequencing of the whole genome of a tumor (see[12.113]) that had spread from a patient's mouth to his lung demonstrated mutations in a tumor-suppressor gene called *PTEN*, and an abnormally high expression of a gene downstream of *PTEN*, called *RET* [12.114]. This explained why the patient had not responded to the drug erlotinib, to which patients with active *PTEN* respond better. Instead, the patient has been put on a drug called sunitinib, which inhibits the protein made by *RET*, and the patients cancer subsequently regressed (see [12.114]). The sequencing of a tumor genome cost US $1 million in 2008 but could drop to $50,000 per tumor in 2010 (see [12.114].)

Breast tumor xenografts treated by gene therapy [12.115]. Gene therapy strategies for solid tumors can be divided into methods that restore cellular growth control, confer drug sensitivity, induce antitumor immunity, or inhibit angiogenesis. The major difficulty in systemic gene therapy, however, is the need for safe and effective vector systems that can deliver the gene to the target tissue and cells and allow for the expression of the protein of interest. For anti-angiogenic gene therapy, the vascular endothelial growth factor (VEGF) is one of the most important regulators of tumor neovascularization and is overexpressed by most types of cancers (see [12.115]). The pro-angiogenic effects of VEGF can be suppressed by binding to the high-affinity tyrosine kinase receptors present on the endothelial cells. The soluble form sFlt-1 of the VEGF receptor can be used as a potent agent for anti-angiogenic gene therapy. The plasmid ps Flt-1/pc DNA3 contains the gene sequence encoding for the extracellular domain sFlt-1 of the VEFG receptor. When expressed in cells, the sFlt-1 plasmid results in the formation of soluble FMs-like tyrosine kinase receptor 1, a variant of the VEGF receptor. The expressed sFlt-1 has shown angiostatic activity by sequestering VEGF produced by tumor cells.

Successful use of adenoviral vectors (DNA-carrying viruses that cause conjunctivitis and upper respirator tract infections in humans) for sFlt-1-expressing plasma DNA delivery to tumor-bearing animals has been reported [12.116]. However, although viral vectors are efficient they have been plagued with serious toxicity concerns [12.117]. In contrast, it has been demonstrated that non-viral nanoparticles, such as gelatin nanoparticles, can safely and successfully transfect tumor mass in vivo.

Poly(ethylene glycol) (PEG)-modified thiolated gelatin nanoparticles (PEG-SHGel) were found to have the longest circulation time ($t_{1/2} > 15$ h) in plasma upon intravenous administration. The systemic delivery and the transfection potential of sFlt-1 expressing plasmid DNA in PEG-SHGel nanoparticles with a diameter of 320 nm has been examined in vitro in MDA-MB435 human breast adenocarcinoma cells and in vivo in human breast tumor bearing mice [12.115]. Anti-angiogenic efficacy studies (Fig. 12.40) indicate the capability of PEG-SHGel nanoparticles as vehicles for therapeutic gene delivery to human breast adenocarcinoma implanted in mice. In animals treated with PEG-SHGel nanoparticles loaded with DNA, the tumor volumes after 25 days were similar to those in the beginning of the studies, whereas the tumor volumes in untreated mice grew substantially. From the images of the excised tumors shown in Fig. 12.40, it is clear that the expressed sFlt-1 is

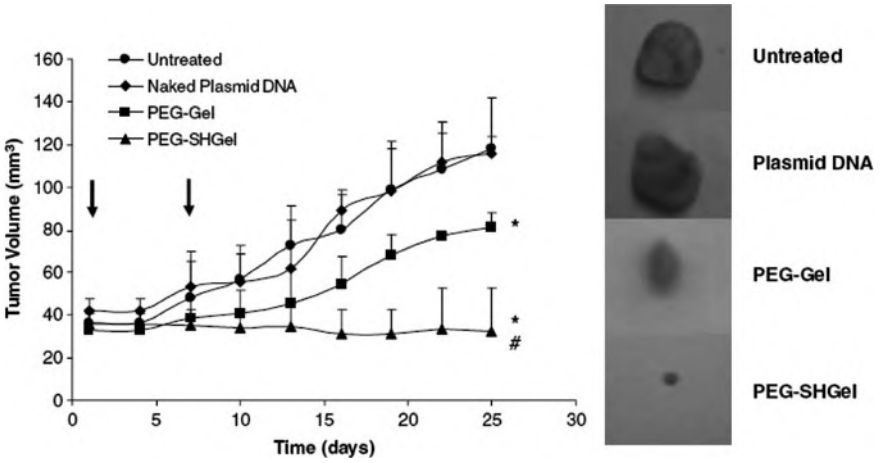

Fig. 12.40 In vivo antitumor efficacy study of expressed sFlt-1 in MDA-MB-435 human breast adenocarcinoma-bearing mice by tumor volume measurements. PEG-SHGel and PEG-Gel nanoparticles with sFlt-1 encoding plasmid DNA were administered intravenously to the mice. Untreated animals and those receiving naked plasmid DNA served as controls. After killing the mice 40 days posttherapy, the tumor masses from control and test animals were surgically excised showing the smallest tumor volume after PEG-SHGel treatment. (Reprinted with permission from [12.115]. © 2007 Nature Publishing Group)

effective in suppressing tumor growth in the MDA-MB-435 xenograft model. The nanoparticles with a diameter of 320 nm could be accumulated in the tumor mass by the enhanced permeability and retention (EPR) effect because the diameter is still smaller than the 400–600 nm vascular pore size [12.118], with additional accumulation only in the liver [12.115]. It, furthermore, should be emphasized that in the gelatin nanoparticles the plasmid DNA structure is maintained in the supercoiled state for efficient nuclear import. As the nuclear membrane pore diameter is <20 nm, supercoiled plasmid can penetrate the nucleus more effectively than a linear or open circular plasmid [12.115].

Oligonucleotide-modified gold nanoparticle complexes have been used as probes to control gene expression in cells [12.119].

Prostatic hyperplasia and prostate cancer has been studied in mice [12.120]. More than half of men in the United States over the age of 60 suffer from the effects of an enlarged prostate (benign prostatic hyperplasia – BPH). In addition, prostate cancer is the most common cancer diagnosed in the United States. Current prostate therapies are often accompanied by serious side effects that impact on the quality of life. Often these side effects result from the damage to healthy tissues in close proximity to the prostate. Thus, there is a need for an improved therapy that is more effective and safer than existing treatments.

In a gene therapy study [12.120], biodegradable C32 nanoparticles (poly(butane diol diacrylate co amino pentanol)) were used for delivering DNA which encodes a suicide gene that expresses the diphtheria toxin A chain (DT-A), a potent toxin that

arrests protein synthesis, resulting in cell death by apoptosis. In addition to delivering DNA to a specific site, a prostate-specific human PSA (prostate-specific antigen) promoter was used to regulate the gene DT-A expression. Extensive apoptosis was observed in prostate epithelial cells and prostate tumors, but not in the surrounding tissues, following local injection of C32 nanoparticles delivering PSA/DT-A DNA. This strategy may have applications in the treatment of BPH and prostate cancer.

Gross morphological abnormalities were observed in the ventral/lateral lobes of mice injected with C32-PSA/DT-A nanoparticles (Fig. 12.41a), while there was no evidence of an increased number of apoptotic smooth muscle cells and other stromal cells in the inter-acini (between the saclike dilatations of a compound gland) spaces. In contrast, only a few apoptotic cells were observed in prostates injected with phosphate buffer saline (PBS; Fig. 12.41b). Cell death in surrounding tissues and organs following intraprostatic injection of C32-PSA/DT-A nanoparticles did not appear to increase above the low normal levels. In mice injected with C32-PSA/DT-A nanoparticles no abnormalities were observed in the level

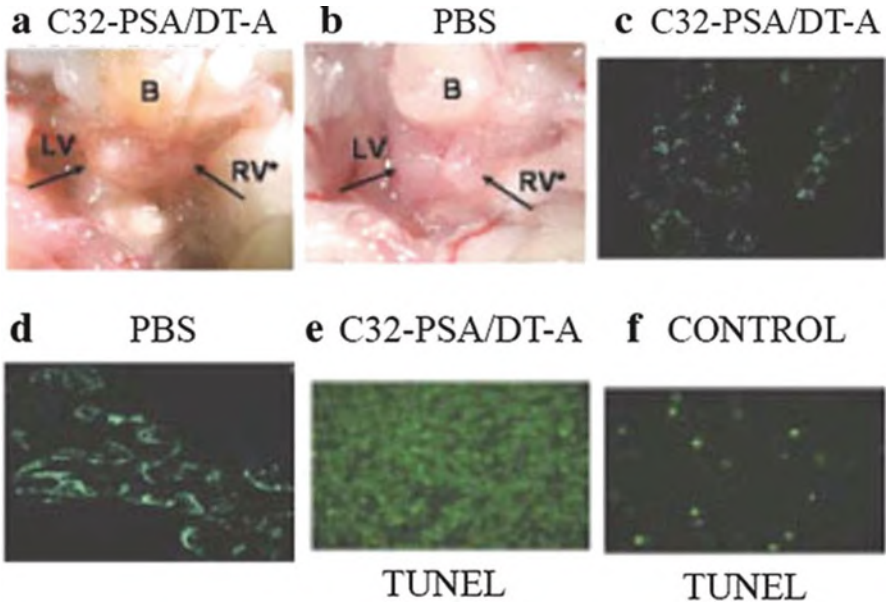

Fig. 12.41 (**a**, **b**) Morphological evidence for cell death following intraprostatic injection of (**a**) C32-PSA/DT-A nanoparticles (see text) and (**b**) phosphate-buffered saline (PBS) in mice. (**c**, **d**) Targeted death of luminal cells in the prostate following intraprostatic injection of C32-PSA/DT-A nanoparticles in mice. Basal cells (*blue* CFP fluorescence dye) have disappeared in the prostate epithelium after C32-PSA/DT-A injection (**c**) while they are visible after control PBS administration (**d**). (**e**, **f**) TUNEL (terminal deoxynucleotidyltransferase biotin–deoxyuridine triphosphate nick-end labeling) staining of sections of prostate tumors of mice following intratumoral injection of C32-PSA/DT-A nanoparticles. Upon TUNEL staining, apoptotic cells in the C32-PSA/DT-A treated tumor appear *green* (**e**) whereas after a control injection (**f**) no green apoptotic cells are visible. (Reprinted with permission from [12.120]. © 2007 Wiley Interscience)

of serum markers, liver function, or muscle damage. Likewise, no histological abnormalities were detected upon analysis of sections of organs, including bladder, testis, epididymis (tubular spermatic duct from a testicle), small intestine, large intestine, liver, spleen, pancreas, kidney, adrenal glands, lungs, thyroid, heart, skeletal muscle, skin, bone with marrow, and brain.

Experiments performed in order to explore the specificity, with which nanoparticle-delivered PSA/DT-A DNA kills basal or luminal prostate cells, demonstrate a reduction in green fluorescent protein (GFP) expression in PSA/DT-A injected prostate lobes of mice (Fig. 12.41c, d), reflecting the shutdown of protein synthesis in PSA-expressing luminal cells, resulting in their death.

The intratumor injection of C32-PSA/DT-A nanoparticles into transgenic mouse models that develop prostate tumors revealed that ~80% of the tumor cells at the site of injection had undergone apoptosis, as compared to < 5% of tumor cells in uninjected tumors (Fig. 12.41e, f). These results show that local injection of nanoparticle-delivered DT-A kills both normal prostate cells and prostate tumor cells. Locally administered nanoparticles with a transcriptionally regulated suicide gene payload may thus offer a distinct advantage over existing therapies for BPH and cancer that lack specificity and often damage neighboring tissue and cause unwanted side effects.

Nanoparticles (NPs) of poly(D, L-lactic-co-glycolic acid) (PLGA) – poly (ethylene glycol) (PEG) were conjugated with the prostate-specific membrane antigen (PSMA) targeting A10 2′-fluoropyrimidine RNA aptamers (Apt) and used as a vehicle to transport the platinum (IV) compound c, t, c-$[Pt(NH_3)_2(O_2CCH_2CH_2CH_2CH_2CH_3)_2Cl_2]$ (Fig. 12.42) to the prostate cancer cells. Within the cell, a lethal dose of the cancer drug cisplatin is released upon reduction of the platinum (IV) precursor. The effectiveness of PSMA targeted Pt-NP-Apt nanoparticles against the $PSMA^+$ LnCaP prostate cancer cells is approximately an order of magnitude greater than that of free cisplatin, because prostate cancer is resistant to chemotherapy with free cisplatin due to poor targeting [12.121].

Multifunctional nanoparticles with CdSe quantum dot (QD) cores and polymeric coatings were used for efficient short-interfering RNA (siRNA) delivery [12.122]. RNA interference is a powerful technology for sequence-specific suppression of

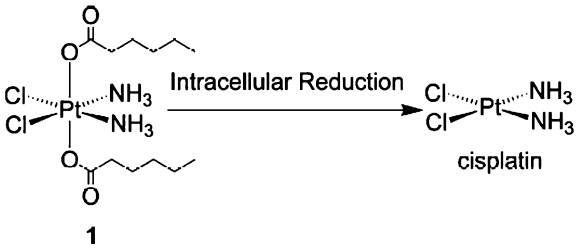

Fig. 12.42 Chemical structure of the hydrophobic platinum (IV) compound **1** and the chemistry by which the active drug, cisplatin, is released, after reduction in the cell. (Reprinted with permission from [12.121]. © 2008 National Academy of Sciences USA)

genes and has broad applications ranging from functional gene analysis to targeted therapy [12.122]. These QD–siRNA nanoparticles are simultaneously optical and electron microscopy probes and can be used for real-time tracking and localization of QDs during delivery and transfection. The results demonstrate improvement in gene silencing efficiency by 10–20-fold and simultaneous reduction in cellular toxicity by fivefold to sixfold, when compared directly with existing transfection agents for MDA-MB-231 cells [12.122]. For the delivery of siRNA (TERT) into tumor cells for silencing the TERT gene, which is critical for the development and growth of tumors, also carbon nanotubes have been used [12.123].

12.4.3 Liposomes and Micelles as Nanocarriers for Diagnosis and Drug Delivery

Pharmaceutical nanocarriers with an enhanced drug reservoir, such as liposomes (artificial nanoscopic vesicles, 70–200 nm in size, consisting of an aqueous core enclosed in phospholipid layers) or micelles (nanoscopic aggregation of molecules) can be equipped with a broad variety of useful properties, such as longevity in blood allowing for their accumulation in pathological areas; specific targeting to disease sites due to targeting ligands attached to the nanocarrier surface; enhanced intracellular penetration due to appropriate surface-attached cell-penetrating molecules; contrast properties due to carrier loading with contrast materials for in vivo visualization; stimuli sensitivity allowing for drug release from carriers under particular physiological conditions [12.19].

In vivo *longevity* is most frequently imparted to drug carriers, such as liposomes, by coating them with a protective layer of poly(ethylene glycol) or PEG, typically with a molecular weight from 1–20 kDa. The thus protected nanocarriers show a sharp increase in blood circulation time and a decrease in liver accumulation. The anticancer agent doxorubicin incorporated in PEG-liposomes has already demonstrated very good clinical results [12.124]. From a pharmacokinetic point of view, the association of drugs with nanocarriers has the pronounced effects of delayed drug absorption, spatially restricted drug biodistribution, decreased volume of drugs, etc.

Targeting vectors (antibodies, peptides, sugars, folates) can be attached to the nanocarriers for specific recognition of the surface characteristics of the target cells. Nanoparticles made of gelatin and human serum albumin were modified with the HER2 receptor-specific antibody trastuzumab (Herceptin®) via an avidin–biotin linkage [12.125]. These surface modified nanoparticles were efficiently endocytosed by HER2-overexpressing SK-BR-3 breast cancer cells (Fig. 12.43a). PEG-liposomes were targeted by peptides specific for integrins of tumor vasculature and, being loaded with the anti-cancer agent doxorubicin, demonstrated increased efficiency against C26 colon carcinoma in murine models [12.126].

Stimuli-sensitivity functions can be added to PEGylated pharmaceutical nanocarriers which allows for the detachment of the protecting polymer (PEG) chains under

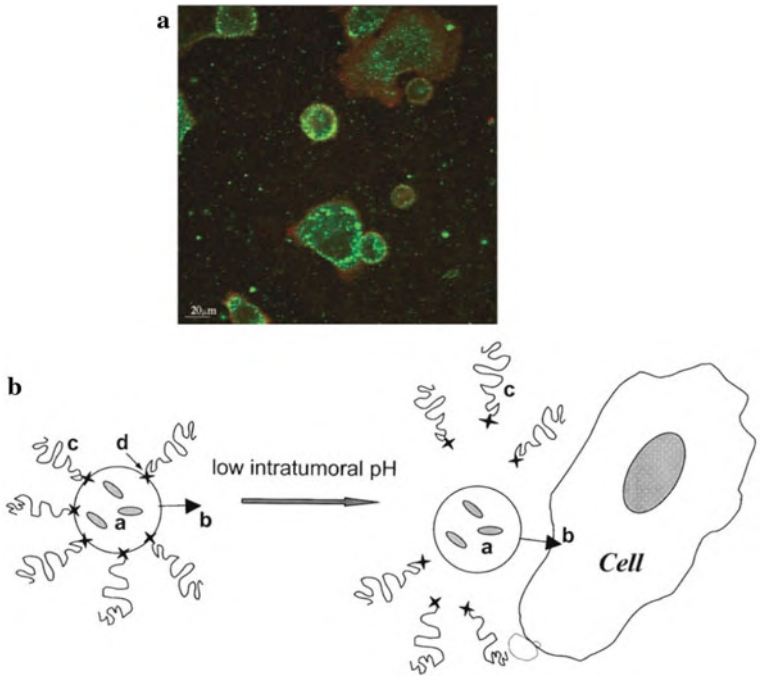

Fig. 12.43 (**a**) Cellular uptake and intracellular distribution of gelatin nanoparticles (*green*) modified with antibodies in SK-BR-3 breast cancer cells [12.125]. (**b**) Schematic representation of a "double-targeted" pharmaceutial nanocarrier (a – loaded drug; b – temporarily "hidden" function, e.g., cell-penetrating peptide; c – "shielding" polymeric coat providing longevity in the blood and preventing the hidden function from premature interaction with target cells; polymeric chains are attached to the carrier surface via d, which represent low pH degradable bonds) and its interaction with a tumor cell after the pH-dependent de-shielding of the hidden cell-penetrating function when already inside the tumor. (Reprinted with permission from [12.19]. © 2006 Elsevier)

the action of local stimuli in pathological areas, such as decreased pH value or increased temperature characteristic for inflamed or neoplastic areas. This detachment may be favorable for drug delivery. Labile linkage of PEG to a liposome can be based on diortho esters, double esters, vinyl esters (see [12.19]) that are quite stable at pH around 7.5 but are hydrolyzed rapidly at pH values of 6 and below, such as in tumors, infarcts, cell cytoplasm, or endosomes. By such a stimuli-sensitive technique a nanoparticular drug delivery system can be prepared capable to accumulate in the required organ or tissue, and then penetrate inside target cells delivering there its drug or DNA load (see Fig. 12.43b).

Functionalization for intracellular delivery may facilitate the therapeutic action of nanocarriers inside the cell unto the nucleus or other specific organelles, such as mitochondria. The delivery of DNA into somatic cells is the important step in gene therapy to supplement defective genes or provide additional biological functions (see [12.127]). Compared with viral vectors for gene therapy, synthetic cationic

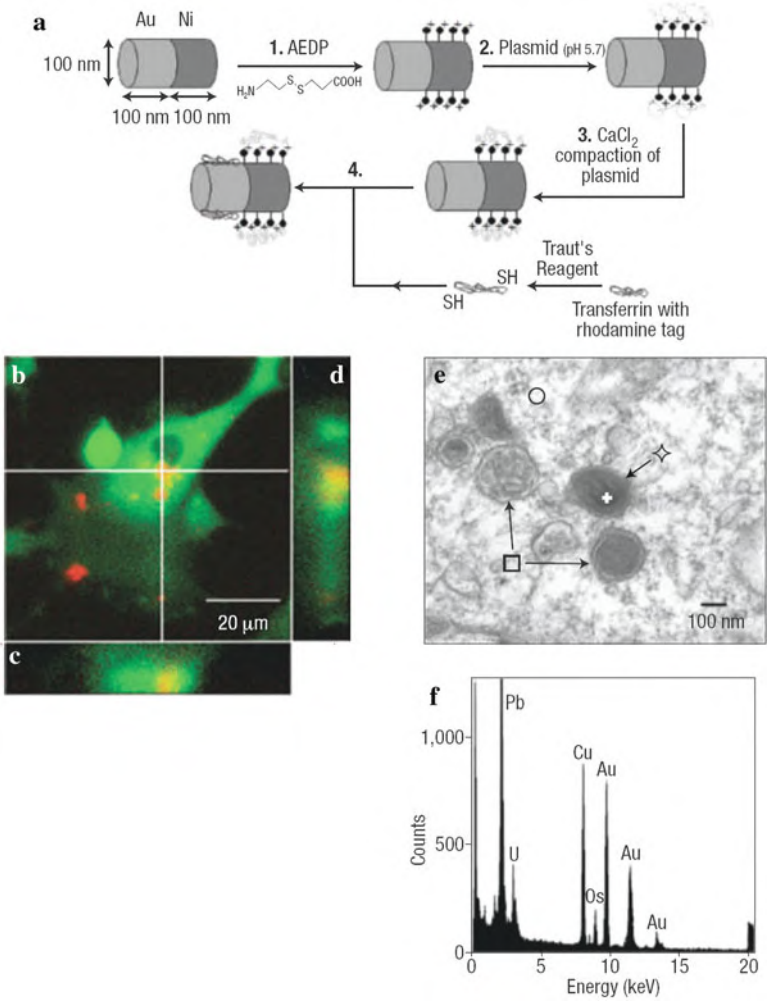

Fig. 12.44 Efficient DNA transfection by means of transferrin-conjugated Au/Ni nanorods. (**a**) Schematic representation of the spatially selective binding of DNA plasmids and transferrin to bimetallic nanorods. Illustration of the nanorod functionalization. *1.* Nanorods are incubated in the AEDP linker. The carboxylate end groups bind to the Ni segment. The cleavable disulfide linkage promotes DNA release within the reducing environment of the cell. *2.* Plasmids are bound by electrostatic interactions to the protonated amines on the Ni surface. *3.* $CaCl_2$ compacts the plasmids. *4.* Rhodamine-conjugated transferrin is selectively bound to the gold segment of the nanorod. (**b**) Laser scanning confocal microscopy images of transfected cells. Live HEK 293 cell with the *red* rhodamine (633 nm) fluorescence identifying the subcellular location of the nanorods while the *green* fluorescent GFP expression (543 nm) confirms the transfection. (**c**, **d**) Orthogonal sections confirm that the nanorods are within the cell. (**e**) TEM image showing the presence of the nanorods in one of the vesicles (✧); ○ denotes the cytoplasm of the cell and □ the empty vesicle. (**f**) TEM–EDX spot analysis (*white cross* on Fig. 12.44e) confirming that the nanorod is in the vesicle. The U, Pb, Cu, and Os are from grid and TEM sample preparation. (Reprinted with permission from reference. (Reprinted with permission from [12.127]. © 2003 Nature Publishing Group)

non-viral gene delivery systems reduce, e.g., the risk of cytotoxicity. In a recent approach for a non-viral gene delivery system in vitro and in vivo [12.127], bimetallic Au/Ni nanorods are used that can selectively bind DNA plasmid on the Ni section and a cell targeting protein, transferrin, on the Au section (Fig. 12.44a). Transferrin functionalization is favorably used because all metabolic cells take in iron through receptor-mediated endocytosis of the transferrin–iron complex. By means of a rhodamine tag on the transferrin, the intracellular distribution of the transfected DNA-conjugated nanorods can be observed.

In vitro transfection experiments on the human embryonic kidney (HEK 293) cell line show the green fluorescent protein (GFP) emission of the cells as a result of transfection (Fig. 12.44b). Superimposed is the red emission from the rhodamine conjugated together with the transferrin to the Au segments of the nanorods. Electron dispersive x-ray (EDX) analysis on the image of Fig. 12.44c shows the engulfment of the nanorods in a vesicle (Fig. 12.44c, d). This suggests that the transfection is due to DNA plasmids released or cleaved from the nanorods prior to nuclear entry. Nanorod-mediated DNA transfection making use of transferrin conjugation is substantially increased in comparison with naked DNA.

Increased anticancer activity of micelles loaded with the anticancer agent paclitaxel was achieved by coating the micelles with PEG-PE (PE-phospholipid) and Lipofectin® lipids (LL) [12.128] where Lipofectin® is a mixture of cationic lipids. The addition of LL facilitating the intracellular uptake and cytoplasmic release of paclitaxel-containing PEG-PE/LL micelle nanocarriers resulted in a substantially increased death of A2780 cancer cells (IC50 value $= 1.2\ \mu$M paclitaxel) compared to that under action of LL-free PEG-PE micelles with paclitaxel (IC50 $= 5.8\ \mu$M) or free paclitaxel [12.128].

12.4.4 Drug Delivery by Magnetic Nanoparticles

A drug can be bound to a magnetic nanoparticle, introduced in the body, and then concentrated in the target area by means of a magnetic field (using an internally implanted permanent magnet or an externally applied field). The main advantages of magnetic nanoparticles are that they can be (i) visualized (superparamagnetic NPs are used in MRI; see Sect. 12.2); (ii) guided by means of a magnetic field; and (iii) heated in a magnetic field to trigger drug release or to produce hyperthermia (see Sect. 12.6) of the tissue.

Superparamagnetic behavior of nanoparticles, which occurs for Fe-based NPs at sizes <25 nm, is needed in medical applications to avoid magnetic agglomeration and the possible embolization of capillary vessels (which could occur with ferromagnetic particles) once the magnetic field is removed. In superparamagnetic NPs without external magnetic field, the magnetization of each crystallite fluctuates, so that the magnetic moment of individual crystallites compensate for each other and the overall magnetic moment disappears. When an external field is

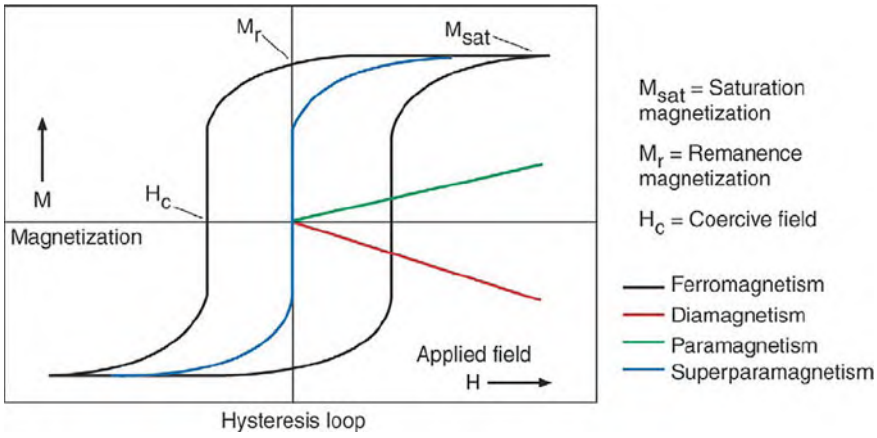

Fig. 12.45 Magnetization versus applied magnetic field (hysteresis loop) characteristic for ferromagnetic and superparamagnetic NPs. For comparison, para- and diamagnetic behaviors are also shown, as well as the values of remanence, M_r, and of coercive field, H_c. (Reprinted with permission from [12.101]. © 2007 Elsevier)

applied, the magnetic moment of entire crystallites aligns with the magnetic field (Fig. 12.45).

A wide variety of molecules has been loaded on nanoparticles, including cell-penetrating peptides for MRI applications [12.129], genes for transfection [12.130], anti-cancer agents [12.131], [12.132], and non-steroidal anti-inflammatory drugs [12.133]. Chemicell GmbH currently commercializes the anti-cancer agent Target MAG doxorubicin nanoparticles (50 nm) involving a multidomain magnetic core and a cross-linked starch matrix with terminal cations that can be reversibly exchanged by the positively charged doxorubicin [12.134]. These NPs loaded with mitoxantrone have already been used in animal models with successful results [12.135]. Other magnetic drug delivery systems, that have already been commercialized, are MagNaGel® [12.136] and FluidMag® (see [12.101]).

The main limitation of magnetic drug delivery relates to the availability of strong external magnetic fields for generating the magnetic field gradient to control the residence time of NPs in the desired area. Obviously the geometry of the magnetic field is extremely important for designing a magnetic targeting process. With respect to the high magnetic fields it may be mentioned here that human exposure to static magnetic fields up to 8 T has not shown any clinically relevant adverse physiological or neurocognitive effects [12.137], and human imaging at fields in excess of 10 T is now being planned (see [12.101]).

As a means to elude the limitations of an external magnetic field, internal magnets, e.g., permanent Nd–Fe–B magnets, can be located in the vicinity of the target by using minimally invasive surgery [12.138] together with simulation studies [12.139].

12.4.5 Nanoshells for Thermal Drug Delivery

Nanoshells for thermal drug delivery can be used in combination with an extracorporal low-power diode laser. Here, infrared absorbing gold nanoparticles can be integrated into a drug-entrapping polymeric hydrogel and, after interstitial implantation, drug release is initiated by a temperature increase (above the solution temperature of the polymer), induced with laser light at 800–1200 nm wavelengths, which is transmitted through tissue with little attenuation and no local damage [12.140].

12.4.6 Photodynamic Therapy

Photodynamic therapy, which is based on the use of photo-sensitive drugs, is another technique for tumor treatment [12.141]. Molecules called photosensitizers (e.g., 9,10-*bis*[4′-(4″-aminostyryl) styryl]anthracene – BDSA) are activated with light for fluorescence resonance energy transfer (FRET) to the energy acceptor (2-devinyl-2 (1-hexyloxyethyl) pyropheophorbide – HPPH) to promote the local formation of highly reactive species – such as singlet oxygen – to attack diseased tissue. Aggregates of fluorescent dye molecules BDSA and HPPH were shown to produce singlet oxygen in water dispersions upon 850 nm illumination as monitored by the oxidation of the disodium salt of 9,10-anthracenedipropionic acid (ADPA) [12.141]. In vitro studies show that the nanoparticles are taken up by HeLa (human cervix epitheloid carcinoma) cells (Fig. 12.46a) and give rise to cell necrosis due to singlet oxygen production by 850 nm illumination (Fig. 12.46e).

12.5 Brain Cancer Diagnosis and Therapy with Nanoplatforms

Brain cancer is a life-threatening disease in which a minority of patients survive (only 5% for glioma brain tumor after 5 years) and which accounts for at least 13,000 deaths in the United States annually [12.142]. Late diagnosis and limitations of conventional therapies, which may result from inefficient delivery of the therapeutic or contrast agents to brain tumors, due to the blood–brain barrier (BBB; see Sect. 12.7) and non-specificity of agents, are major reasons for this unsolved clinical problem. The nanoparticle-based delivery has emerged as a potential method to improve the efficacy of the existing detection and treatment armamentarium due to the non-toxicity and the “engineerability” of nanoparticles. The desirable properties such as high payload, controlled drug release profile, tumor-specific targeting, long blood circulation time, and the ability getting across the BBB can be achieved by the nanoparticle delivery system. Multifunctionality is another advantage which could integrate detection, treatment, and tracking of tumor response, leading to informed decisions about further treatment [12.142].

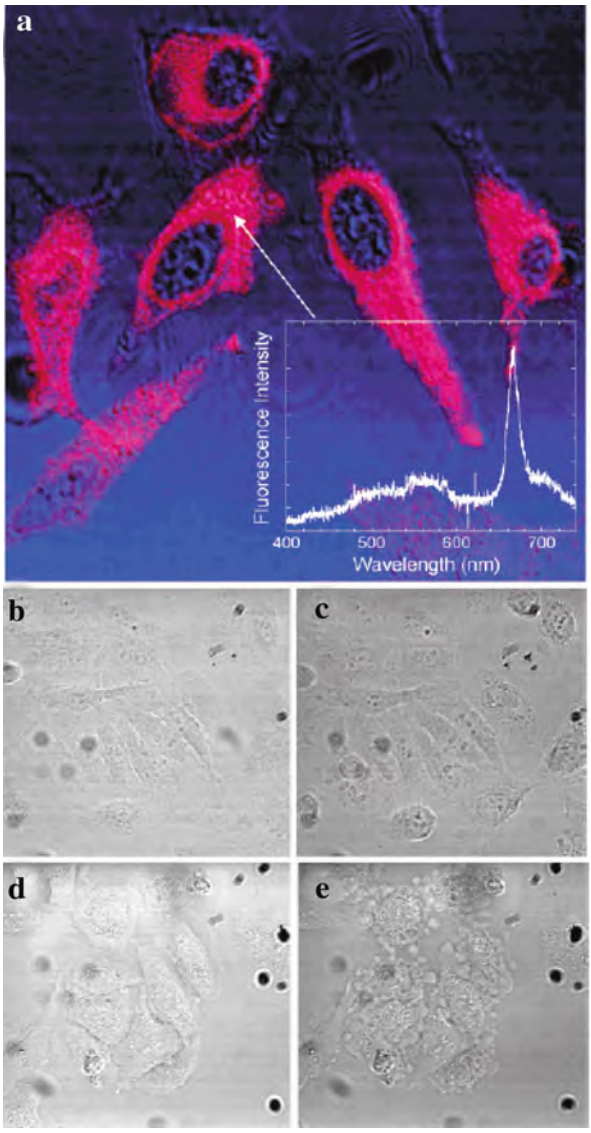

Fig. 12.46 (**a**) Transmission (*blue*) and 850 nm two-photon excited fluorescence (*red*) images of HeLa cells, stained with nanoparticles containing 1.1 wt% HPPH/20 wt% BDSA (see text). (**b**, **c**) Transmission images of HeLa cells treated overnight with nanoparticles containing 20 wt% BDSA and (**d**, **e**) 1.1 wt% HPPH and 20 wt% BDSA. *Left column* (**b**, **d**): before irradiation; *right column* (**c**, **e**): 15 min after 90 s of irradiation with femtosecond pulsed laser at 850 nm. (Reprinted with permission from [12.141]. © 2007 American Chemical Society)

12.5.1 General Comments

In the brain, the BBB cannot be overcome by other than passive diffusion (by which only small, lipid-soluble molecules can penetrate the brains), such as carrier/receptor-mediated influx or transcytosis (see [12.142]) for receiving essential metabolites such as glucose, aminoacids, and lipoproteins. These carrier/receptors can be used to deliver drugs to the central nervous system (CNS). It requires the discovery and development of receptor specific ligands, which can be attached directly to the drug of interest or the drug delivery system such as nanoparticles or liposomes. A "rule of thumb" suggests that nanoparticles less than 100 nm in diameter can enter cells, those with diameters below 40 nm can enter the cell nucleus and those that are smaller than 35 nm can pass through the blood–brain barrier and enter the brain [12.143]. In fact, some nanoparticles have been found to successfully cross the BBB. These nanoparticles are often coated with a surfactant (e.g., polysorbate) or are covalently linked to peptides. The exact mechanism of nanoparticle transport into the brain is not fully understood, but relies most likely on receptor-mediated endocytosis or passive leakage of nanoparticles across defects in the BBB [12.144]. Successful transport across an in vitro blood–brain barrier (BBB) has been shown for CdSe/CdS/ZnS quantum rods as targeted probes [12.145].

Several nanoparticle formulations have been clinically approved for MRI. Endorem® is approved for liver and spleen disease detection and Sinerem® (or Combinex®) is in phase III stage for the detection of metastatic disease in lymph nodes [12.142]. For cancer therapy, liposome-encapsulated formulations of doxorubicin were approved in 1995. A polymeric nanoparticle-based drug, albumin–paclitaxel was approved for breast cancer [12.146].

Nanoparticle sizes of 10–100 nm are believed to provide the best option because they are too large to undergo renal elimination and too small to be recognized by phagocytes (see [12.142]).

The amount of drugs such as Photofrin® for photodynamic therapy (PDT) or doxorubicin for cancer chemotherapy can be obtained by comparing the absorbance of the prepared nanoparticle sample solution with the calibration curve constructed from the mixture of free drug and blank nanoparticles of known concentration [12.142].

12.5.2 MRI Contrast Enhancement with Magnetic Nanoparticles

The magnetic resonance imaging (MRI) of the CNS is usually performed with short-lived gadolinium-based contrast agents, which gives rapid and transient imaging of brain and spinal permeability. Ultrasmall superparamagnetic iron oxide (USPIO) nanoparticles, with a 5–6 nm iron oxide core size surrounded by a dextran coating to give a 20–30 nm diameter, show also excellent potential for brain imaging. Unlike the pattern of enhancement with Gd chelate, which occurs immediately and decreases within hours, the contrast enhancement with USPIO occurs gradually, with a peak at 24–48 h after iron oxide administration [12.142].

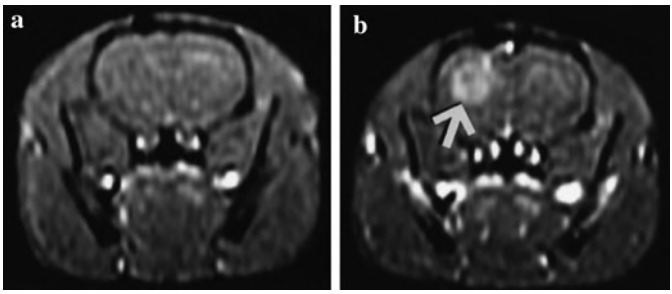

Fig. 12.47 Transverse gradient-echo magnetic resonance images (MRI) of a rat with 9L gliosarcoma tumor. The images were taken (**a**) before and (**b**) 24 h after intravenous administration of long-circulating dextran-coated iron oxide nanoparticles. After nanoparticle administration, the tumor (*arrow*) in the right hemisphere of the brain is enhanced because of nanoparticle accumulation and is clearly delineated against adjacent normal brain. Also note vascular enhancement. (Reprinted with permission from [12.147]. © 2000 Radiology Society of North America)

In vivo studies on rats bearing implanted 9L gliosarcoma or C6 glioma cells were performed after injection of dextran-coated iron oxide nanoparticles by MRI in a 1.5 T field with T_1-weighted and T_2-weighted imaging (Fig. 12.47). Accumulation of the nanoparticles in the brain, preferentially in the tumor periphery, was low (0.11% of the injected dose per gram of tumor tissue) but 10-fold higher than in the brain tissue adjacent to the tumor. The mechanism of MR enhancement by iron oxide nanoparticles appears to be leakage across the breached BBB, followed by intracellular trapping by reactive cells (e.g., astrocytes, macrophages) in and around the tumor, rather than by tumor cells [12.148].

Iron oxide nanoparticles tagged with the near-infrared fluorescent (NIRF) molecule Cy5.5 could by potentially used for both MRI and optical imaging in order to determine the brain tumor margins both during the presurgical planning phase (MRI) and during surgical resection (optical imaging) [12.149].

12.5.3 Nanoparticles for Chemotherapy

Chemotherapy of brain cancer has shown a poor outcome of most anti-cancer agents due to the low permeability through BBB. Nanoparticle delivery systems have emerged as promising brain cancer therapy tools due to the evidence for their ability to cross the BBB (see above), as discussed in the following.

Solid lipid nanoparticles (SLNs) loaded with the anticancer drugs paclitaxel or doxorubicin were studied. The SLNs with sizes below 100 nm to be loaded with paclitaxel were prepared from an emulsifying wax of an oil phase, water, and a surfactant [12.142]. The results of brain uptake in rats suggest that the paclitaxel uptake was significantly increased by the use of the nanoparticle delivery system. Another type of SLNs was loaded with the anti-cancer agent doxorubicin that inhibits DNA and RNA synthesis and cleaves DNA. Doxorubicin is a polar molecule that is not

known to be able to cross the BBB by normal intravenous injection. However, the doxorubicin concentration in liver, lung, or brain of rats was by a factor of 5–7 higher when the doxorubicin was administered in SLNs, compared to doxorubicin solution (see [12.142]).

Nanoparticles of poly(butylcyanoacrylate) (PBCA) were reported to achieve successful delivery of drugs to the brain by means of the surface-coated surfactant, polysorbate 80 (Tween®80). The favored transport of the polysorbate 80-coated particles has been suggested to be a receptor-mediated endocytosis by the brain endothelial cells. The studies on rats showed that the polysorbate 80-coated PBCA nanoparticles loaded with doxorubicine (DOX-NP/PS) produced a very high doxorubicin concentration in the brain whereas this concentration was below the detection limit in control preparation with unconjugated doxorubicin and doxorubicin-loaded uncoated PBCA nanoparticles. This suggests that polysorbate 80-coated PBCA nanoparticles could be an efficient delivery system for chemotherapy of brain cancer. The survival rates of rats, intracranially implanted with 101/8 glioblastoma in their brains and treated with DOX-NP/PS [12.150], showed a significant increase compared to control groups without treatment or with doxorubicin solution treatment. Biodistribution studies of PBCA nanoparticles showed highest concentrations in the brain after DOX-NP/PS treatment and significantly higher brain concentrations in rats 10 days after tumor implantation than in healthy rats. This demonstrates the selective delivery of appropriate nanoparticles to a tumor via the "leaky" tumor vasculature which is called the enhanced permeability and retention (EPR) effect (see [12.142]). The studies, in addition, indicate the therapeutic potential of DOX-NP/PS nanoparticles for the treatment of human glioblastoma.

12.5.4 Targeted Multifunctional Polyacrylamide (PAA) Nanoparticles for Photodynamic Therapy (PDT) and Magnetic Resonance Imaging (MRI)

It has been shown that the use of nanoparticles in PDT is a promising approach for killing tumor cells [12.151]. PDT for brain cancer treatment has been investigated using PAA nanoparticles [12.152]. Specifically, a targeted multifunctional nanoplatform [12.153, 12.154] combining PDT and MRI has been designed for synergistic cancer detection, diagnosis, and treatment (Fig. 12.48). The non-toxical PAA core particle carries the following components: (1) PDT agent Photofrin® which is a photosensitizer approved for clinical use in the United States; (2) MRI-detectable iron oxide nanoparticle contrast agent for good in vivo MRI efficacy; (3) vascular targeting ligand (e.g., F3 peptide). Systemic PDT, i.e., optical generation of singlet oxygen to attack diseased tissue, is particularly effective when it leads to complete ischemia of solid tumors through localization in the vascular space. Vascular targeting of a photosensitizer is required for irreversible damage of the tumor vascular system resulting in tumor necrosis [12.155]. The F3 peptide

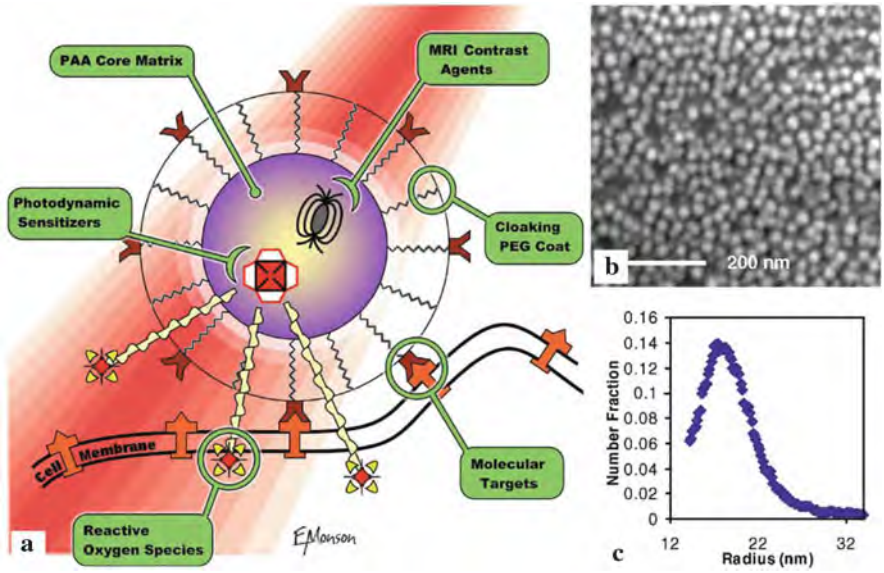

Fig. 12.48 Nanoparticle platform for magnetic resonance imaging (MRI) and photodynamic therapy (PDT) of brain cancers. (**a**) Schematic nanoplatform with photodynamic dye, MRI contrast enhancing agent, PEG cloaking, and molecular targeting. (**b**) SEM image of polyacrylamide (PAA) nanoparticles. (**c**) Nanoparticle size distribution derived from light scattering. (Reprinted with permission from [12.152]. © 2005 Elsevier)

is a 31-amino acid fragment of human high-mobility group protein 2 (HMGN2), which targets to and gets internalized into tumor endothelial cells and cancer cells through the nucleolin receptor [12.156]; (4) polyethylene glycol (PEG) providing longevity of the nanoparticle. The typical size of the PAA nanoparticle is 30–70 nm [12.142].

The in vivo PDT therapeutic activity of the targeted and untargeted nanoparticles containing Photofrin® was evaluated by diffusion MRI of rats bearing intracerebral 9L gliosarcoma tumors. Diffusion MRI relies upon the ability of MRI to quantify the diffusivity of water molecules in tissues and examines the changes of the apparent diffusion coefficients (ADC) within the tumor tissue [12.157]. The increase in tumor diffusion values corresponds to a loss of tumor cellularity within the region under study. The administration of F3-targeted Photofrin®-encapsulated nanoparticles resulted in the most significant increase in mean tumor ADC values, well correlated to the animals survival periods. Gliomas treated by Photofrin®-containing nanoparticles (Fig. 12.49b), followed by laser irradiation for PDT, produced massive regional necrosis, demonstrated by huge "bright" regions in the images, resulting in shrinkage of the tumor mass. The untreated 9L gliomas continued to grow over the life span of the animals (Fig. 12.49a). The mechanism of the efficient PDT activity appears to result from efficient targeting of the nanoparticles to the tumor vascular cells (see [12.142]).

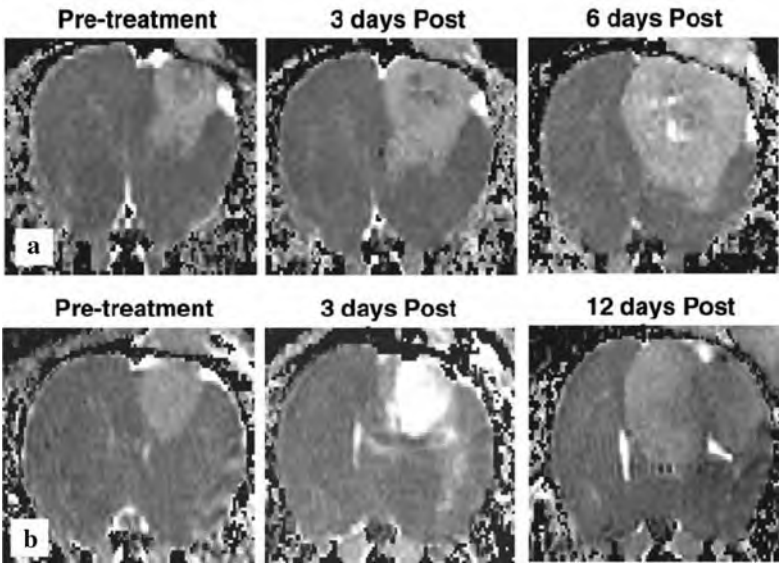

Fig. 12.49 Time series of water diffusivity maps by magnetic resonance imaging (MRI) images of a 9L glioma rat tumor after in vivo PDT: (**a**) untreated; (**b**) treated with laser light and Photofrin®-containing PAA nanoparticles. The images shown here are not diffusion-weighted images but rather computer-generated quantitative diffusion maps where the intensity of each pixel (voxel) is proportional to the diffusivity values. (Reprinted with permission from [12.152]. © 2005 Elsevier)

In future clinical application, total eradication of brain cancer by nanoparticle-based PDT may be possible at an early or intermediate stage and the detection could be made by the same multifunctional nanoparticle. The option of non-invasive direct illumination from outside the skull may need the development of a photosensitizer with a longer absorption wavelength than Photofrin®, for deeper photon penetration [12.142].

The nanomaterial is clearing at two different rates over a 90-day sampling interval, through a complex process of degradation and elimination of the nanoparticle constituents [12.142].

12.6 Hyperthermia Treatment of Tumors by Using Targeted Nanoparticles

The potential of hyperthermia and thermal ablation in cancer therapy has been well noted [12.158]. Temperatures between 42 and 46°C lead to inactivation of normal cellular processes, whereas above 46°C, extensive necrosis occurs [12.159]. The inability to safely induce a therapeutic response, because of difficulties in inducing selective tumor heating and facilitating heat dose determination, has limited its

widespread use in clinical therapy [12.159]. In the following the tumor treatment by heating of tumor-targeted nanoparticles by means of (i) an alternating magnetic field [12.159], by (ii) a radiofrequency field [12.160], or by (iii) near-infrared light [12.161, 12.162] will be discussed.

12.6.1 Alternating Magnetic Fields for Heating Magnetic Nanoparticles

Tumor cell immunotargeted magnetic nanoparticles can be heated to cytotoxic temperatures due to their response to an externally applied alternating magnetic field (AMF). For an in vivo study [12.159] of the therapy of a human breast cancer xenograft (HBT 3477) in mice, superparamagnetic iron oxide nanoparticles (Fig. 12.50a) were conjugated to human–mouse chimeric antibodies (ChL6 mAb) for tumor targeting. These antibodies react with a membrane glycoprotein highly expressed in human breast carcinomas and to the ^{111}In isotope (half-life 2.8 days) for pharmacokinetic and blood clearance studies. The iron oxide nanoparticles were coated with dextran and impregnated with poly(ethylene glycol) (PEG) (Fig. 12.50a). Pulsed alternating magnetic fields with an oscillation frequency of 153 kHz and an amplitude of ~0.1 T (see Fig. 12.50b) applied for 20 min (total heat dose 13–21 J/g tumor) to the mice subcutaneously injected with the conjugated nanoparticles (power absorption rate ~70 W/g) gave rise to a substantial tumor growth delay in response to the heat dose (Fig. 12.51a). In addition, electron microscopy showed normal appearance of the tumor cells after nanoprobe

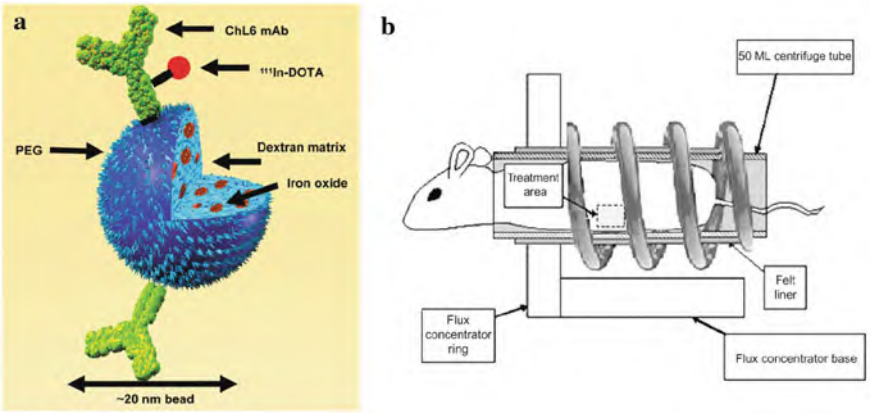

Fig. 12.50 (**a**) Schematic of a bioprobe for alternating magnetic field heating of tumors: ^{111}In-ChL6 conjugated to poly(ethylene glycol) (PEG) on iron oxide impregnated dextran 20 nm nanoparticles. (**b**) Coil for the delivery of the alternating magnetic field (AMF) to treat mice-bearing human xenograft tumors. AMF is focused in a 1 cm band in which the subcutaneous tumor located on the abdomen of the mouse was positioned. (Reprinted with permission from [12.159]. © 2007 Society of Nuclear Medicine)

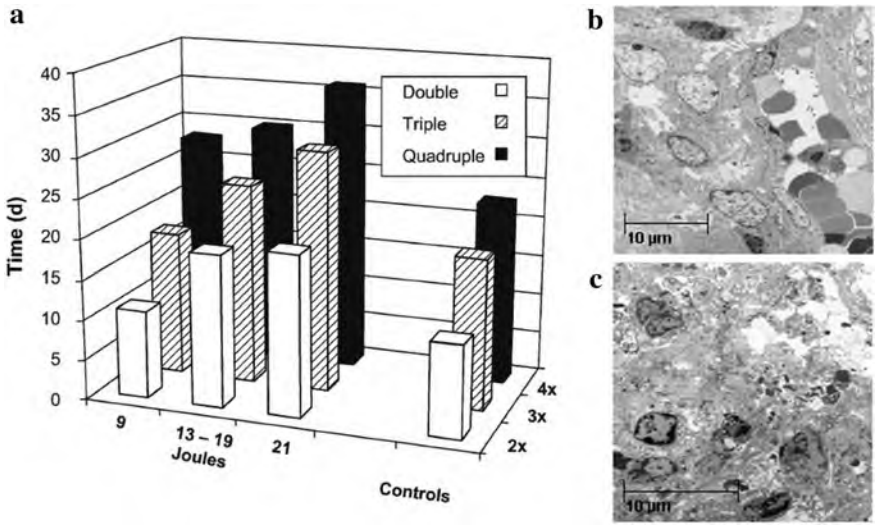

Fig. 12.51 (**a**) Relationship of tumor response to bioprobe AMF (alternating magnetic field) tumor-specific thermal therapy. The therapeutic response is reflected by the increased time to double, triple, or quadruple the tumor volume in mice with the tumor total heat dose (J) indicated, with a relationship between response and heat dose, compared with controls (tumor growth of AMF treatment alone, untreated control groups). (**b**, **c**) Electron micrographs of ultrathin osmium tetroxide-fixed epoxy-embedded HBT 3477 xenografts that had been excised from mice at time of sacrifice, 48 h after bioprobe injection, no AMF (**b**), and 48 h after AMF tumor-specific thermal therapy 18 J/g; (**c**). Viable tumor cells (**b**) contrast with evidence for cell necrosis at 48 h after AMF tumor-specific thermal therapy (**c**). (Reprinted with permission from [12.159]. © 2007 Society of Nuclear Medicine)

uptake prior to AMF treatment, however, progressive tumor cell necrosis after AMF treatment with no effect on the normal tissue [12.159].

In a first clinical application, interstitial hyperthermia employing 15 nm superparamagnetic ferrite nanoparticles with an aminosilane coating was applied for the treatment of prostate cancer [12.163] with guidance by computer tomography (CT) and transrectal ultrasound (TRUS) imaging. According to the individual anatomy of the prostate with a normal volume of 20 ml and the specific absorption rate (SAR) of the magnetic fluid (~ 0.3 W/g), the number and positions of magnetic fluid depots were calculated, while rectum and urethra were spared. The nanoparticle suspensions were injected transperineally into the prostate under ultrasound guidance (see Fig. 12.52a). For invasive thermometry, fiberoptic thermometry probes were positioned in the prostate, urethra, rectum, perineum, scrotum, and left ear, yielding in a 0.005–0.0063 T AC field maximum temperatures of 48.5°C in the prostate (thermoablative range; see Fig. 12.53), of 42.2°C in the urethra, and 42.1°C in the rectum. Selective uptake of nanoparticles into prostate cancer cells [12.164] offers the perspective of tumor cell selective hyperthermia. These first clinical results prompted a phase I study to evaluate the feasibility, toxicity, and quality of life during hyperthermia using magnetic nanoparticles in patients with local recurrence of

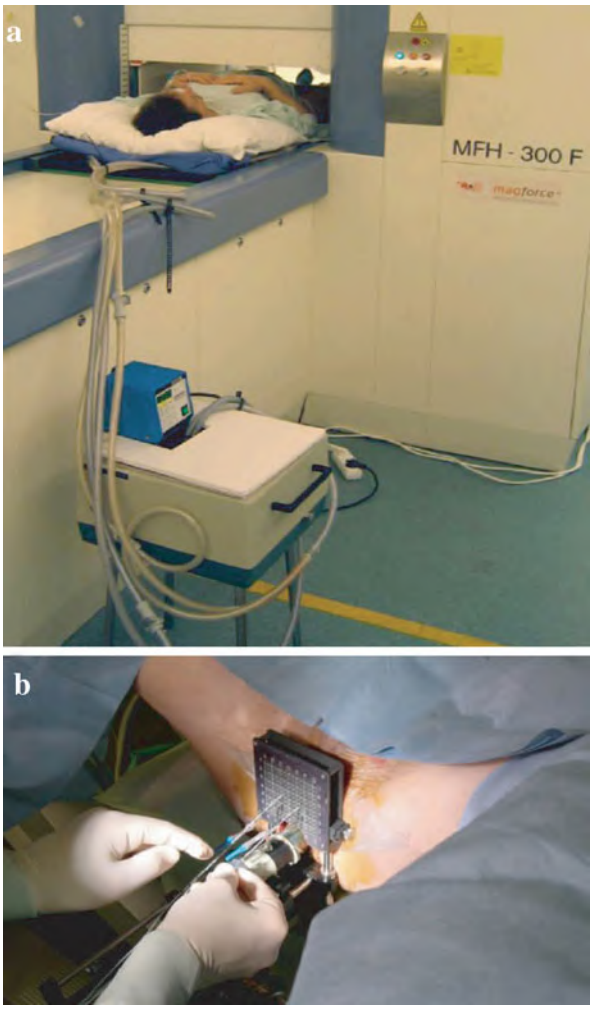

Fig. 12.52 (**a**) AC magnetic field applicator (MFH300F, MagForce® Nanotechnologies GmbH, Berlin). For cooling, hoses with circulating cold water are placed around the patients inner thigh, perineum, and the groin on both sides. An AC magnetic field with a frequency of 100 kHz and amplitudes of 0–0.023 T are used. Thermometers are positioned in the prostate, urethra, rectum, perineum, scrotum, and left ear. Hyperthermia is monitored online, so that the AC field amplitude can be kept constant or adjusted to a constant temperature in the tumor. (**b**) The administration of the nanoparticle suspension into the prostate is carried out transperineally with the patient in a lithotomy position. At the center, the template used for magnetic fluid injection as well as implantation of catheters to house the thermometry probes can be seen. (Reprinted with permission from [12.163]. © 2005 Taylor and Francis)

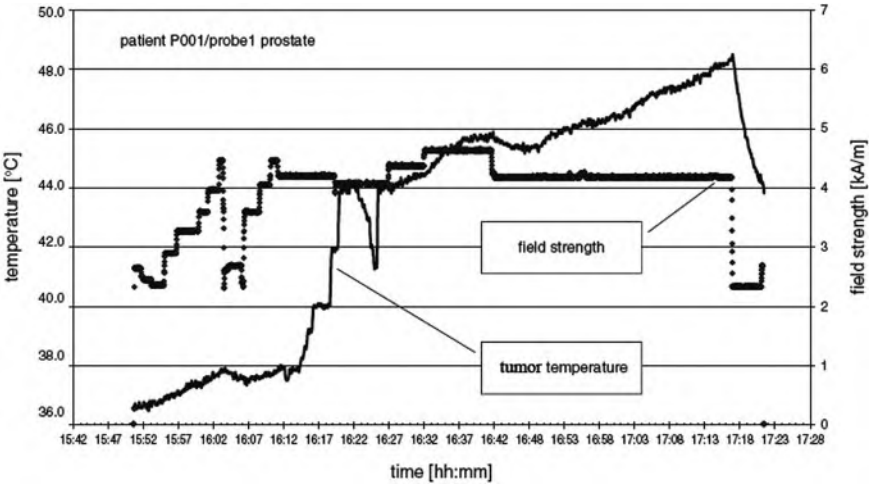

Fig. 12.53 Variation of the AC magnetic field strength and of the prostate temperature with time. (Reprinted with permission from [12.163]. © 2005 Taylor and Francis)

prostate cancer [12.163]. A clinical trial of magnetic field hyperthermia is performed with 69 patients [12.165].

12.6.2 Radiofrequency Heating of Carbon Nanotubes

Radiofrequency ablation (RFA) of malignant tumors [12.166] is currently an invasive treatment that requires the insertion of needle electrodes directly into the tumor to be treated; incomplete tumor destruction occurs in 5–40% of the treated lesion, with thermal necrosis in both malignant and normal tissues surrounding the needle electrode [12.160]. Conversely, it is known that the tissue penetration by radiofrequency (RF) fields is excellent. Thus, non-invasive RF treatment of malignant tumors at any site in the body should be possible if agents that convert RF energy into heat can be delivered to the malignant cells. In order to study this approach, direct intratumoral injection of single-walled carbon nanotubes (SWNTs) was performed followed by RF field treatment. This was tolerated well by rabbits bearing hepatic VX2 tumors which are particularly aggressive and resistant to standard cancer therapies [12.167]. At 48 h after RF treatment, all SWNT-treated tumors demonstrated complete necrosis, whereas control tumors treated with RF without SWNTs remained completely viable. Tumors that were injected with SWNTs but were not treated with RF were also viable. The remaining liver after histopathology section of the liver tumor and all other organs that were assayed had no evidence of thermal injury or other abnormalities [12.160] (Fig. 12.54).

The SWNTs, functionalized with Kentera [12.160], a polymer based on polyphenylene ethynylene for water solubility, were injected into an intrahepatic VX2 tumor (greatest dimension, 1.0–1.3 cm) with a subsequent treatment for 2 min

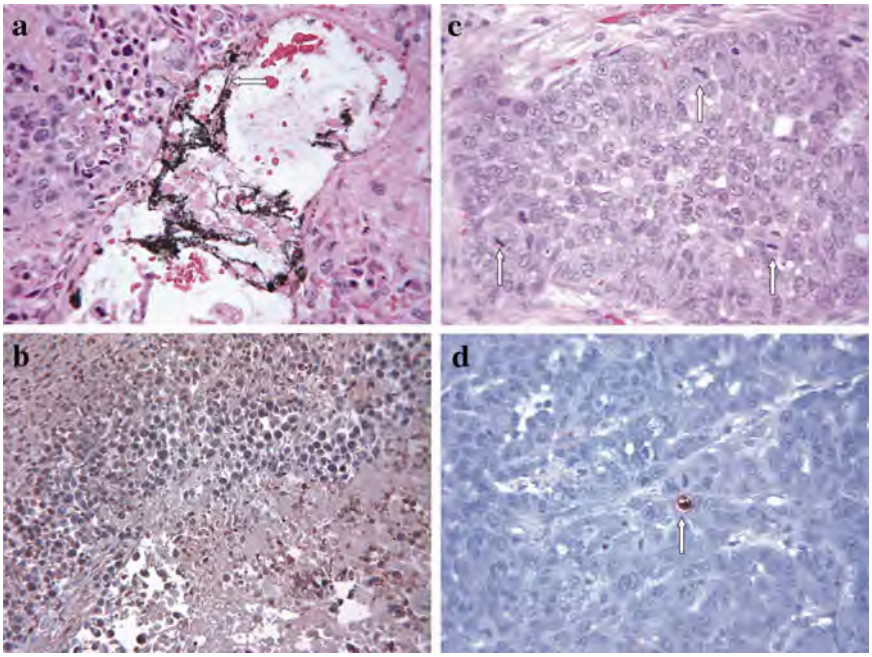

Fig. 12.54 (**a**, **b**) Photomicrographs of hepatic VX2 tumors from rabbits that received intratumoral injection of Kentera single-walled carbon nanotubes (SWNTs) followed by 2 min of radiofrequency (RF) field treatment. (**a**) Necrotic tumor cells, inflammatory cells, and black strands of SWNTs (*arrow*), standard hematoxylin and eosin staining – H&E; magnification ~ x400. (**b**) Characteristic *brown* staining observed with apoptotic and necrotic cells (stained with terminal deoxynucleotidyltransferase biotin–deoxyuridine triphosphate nick-end labeling – TUNEL; magnification ~ x250). (**c**) Hepatic VX2 tumors after intratumoral injection of Kentera polymer alone (no SWNTs) followed by RF treatment showing completely viable tumor cells with numerous mitotic bodies (*arrows*, standard H&E staining, magnification ~ x400). (**d**) Viable cells with only a rare *brown* apoptotic cell-TUNEL staining; magnification ~ x400).The rate of apoptosis in untreated VX2 tumors was 2–3%, and the control tumors treated with RF but no SWNTs had a similar 2–3% incidence of apoptotic cells. (Reprinted with permission from [12.160]. © 2007 Wiley Interscience)

in an RF field of 13.56 MHz for heating of the SWNTs. This frequency produces minimal heating of mammalian tissue [12.168]. The efficient RF heating of the SWNTs may be based on their resistive conductivity [12.169]. The development of cell-specific delivery and uptake of appropriately functionalized SWNTs is desirable for the future [12.160]. The absence of SWNT-related toxicity and no or minimal growth inhibition in three human cancer cell lines [12.160] is consistent with other reports [12.170, 12.171]. Nevertheless, for the assessment of the complete safety of SWNTs in animals or humans, long-term studies are required.

Treatments by heating carbon nanotubes inside cells by near-infrared laser light [12.172] are restricted to tissue depth of 2–3 cm. The specific power deposition in carbon nanotubes (75000 W/g) in RF fields exceeds that of iron oxide nanoparticles

in alternating magnetic fields (500 W/g) (see [12.160]), so that in the former case less nanomaterial is required for treatment.

12.6.3 Light-Induced Heating of Nanoshells

Light-induced heating of nanoshells has also been demonstrated for efficient destruction of tumors [12.161] where, in contrast to nanoparticle heating in a alternating magnetic field [12.159], lower quantities of nanoparticles are required. In metal nanoshells (Fig. 12.55), the plasmon resonance and the resulting optical absorption can be adjusted from near-UV to mid-infrared [12.162] for exploitation in photothermal ablation of cancer cells in vivo. The plasmon resonance and, therefore, the light-induced heating of silica nanoparticles (110 nm in diameter) with a 10 nm gold shell is maximum in the near-infrared (NIR) range (820 nm) where optical transmission through tissue is optimal, so that deep tissue treatment (~ 1 cm) is feasible. These nanoshells are far less susceptible to chemical/thermal denaturation and photobleaching effects than conventional NIR dyes and exhibit a 1 million times higher absorption cross section ($\sim 4 \times 10^{-14}$ m^2) than those dyes (see [12.161]). After injection of the nanoshells into a canine transmissible venereal

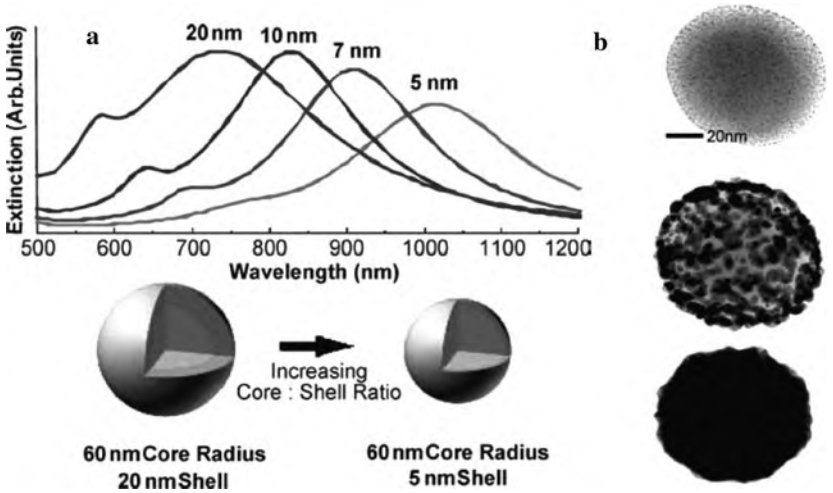

Fig. 12.55 Plasmon resonance of SiO_2–Au core–shell nanoparticles. (**a**) The optical tunability is demonstrated for nanoshells 5, 7, 10, and 20 nm thick on a 50 nm radius silica core. The plasmon resonance (extinction) of the particles red shifts with decreasing thickness of the Au shell. Nanoshells with resonances in the near infrared (NIR; 800–1200 nm) can be easily fabricated, with still greater tunability making use of multilayered structures. (**b**) Series of TEM images of gold colloids (*dark dots*) growing into a complete shell on a silica core structure. (Reprinted with permission from [12.162]. © 2003 National Academy of Sciences USA)

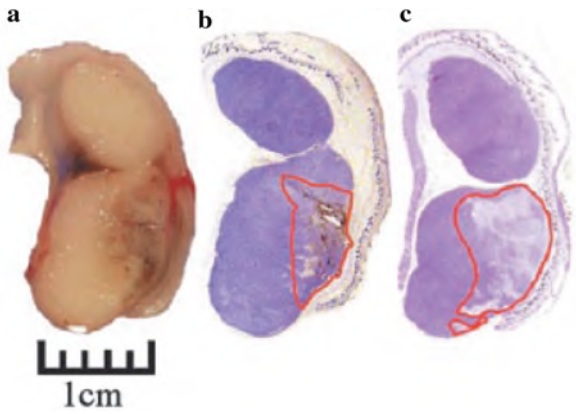

Fig. 12.56 (**a**) Gross pathology of a canine transmissible venereal tumor (TVT) in a mouse after nanoshell injection and NIR illumination reveals hemorrhaging. (**b**) Silver staining of the tissue section reveals the region of localized nanoshells (outlined in *red*). (**c**) Hematoxylin/eosin staining within the same plane clearly shows tissue damage within the area occupied by nanoshells. (Reprinted with permission from [12.161]. © 2003 National Academy of Sciences USA)

tumor (TVT) xenograft in a mouse, the tumor was exposed to external NIR light (820 nm, 20 W/cm^2, < 6 min) irradiation, giving rise to irreversible tissue damage (Fig. 12.56) due to radiation-induced temperature increase by ~37°C. This temperature increase was measured by magnetic resonance temperature imaging (MRTI) based on the temperature dependence of the proton resonance frequency shift [12.173]. The above laser dose is more than 10-fold less than that used in earlier studies examining indocyanine green dye [12.174]. Nanoshell-free control experiments with the same light irradiation saw average temperature increases of ~9°C leading not to tissue damage. The findings of the tumor tissue damage due to light absorbed in nanoshells correlate well with gross pathology (Fig. 12.56a), in which defined zones of edema were observed in the nanoshell-treated tumors in the region where MRTI suggested that there should be irreversible tissue damage. Histology also identified common markers of thermal damage in NIR/nanoshell-treated tumors (Fig. 12.56c). In addition, in regions of thermal damage, nanoshells were found by using a silver enhancement stain that amplifies the size of the nanoparticles for examination by optical microscopy (Fig. 12.56b). Due to the preferential accumulation of nanoshells in the tumor because of the enhanced permeability and retention effect [12.175], only the tumor regions within the tissue are destroyed, leaving surrounding tissue intact. Furthermore, nanoshells may be conjugated with antibodies targeting surface oncoproteins overexpressed within the tumor (see [12.161] and Fig. 12.57).

Tumor cells can also be selectively killed in vitro by specifically targeting them by single-walled carbon nanotubes which are heated by the absorption of near-infrared light [12.177].

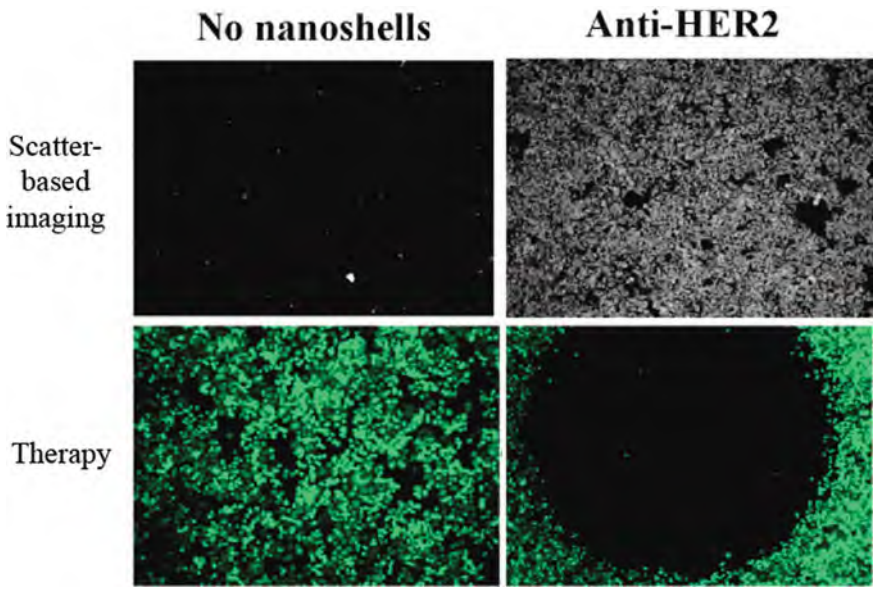

Fig. 12.57 Combined imaging and therapy of SKBr3 breast cancer cells using Au nanoshells targeted against HER2 expressed by the cancer cells. Scatter-based dark-field imaging of HER2 expression enabled by nanoshells conjugated to the cancer cells (*top row, right*). The cell viability is assessed via calcein staining (*bottom row*). Cytotoxicity (*dark spot*; *bottom row*, *right*) is observed only in cells heated by the Au nanoshells absorbing the near-infrared light of laser illumination compared to the control without nanoshells (*bottom row, left*). (Reprinted with permission from [12.176]. © 2005 American Chemical Society)

12.7 Nanoplatforms in Other Diseases and Medical Fields

12.7.1 Heart Diseases

Heart failure is a highly prevalent form of cardiovascular disease with ~ 300,000 deaths in 2004 in the United States and annual costs associated with diagnosis, monitoring, and therapy estimated to be >US $25 billion in the United States (see [12.178]). Clinical biomarkers are of particular importance for diagnosis and prognosis of heart diseases. A nanotechnique for detecting cardiac troponin I (cTnI) – a principal biochemical marker of acute myocardial infarction [12.179] – has been reported [12.180] in addition to conventional techniques developed earlier [12.181, 12.182].

In the heart, cTnI forms a protein complex with troponin T and troponin C. The troponin complex is broken up following myocardial damage, and the individual protein components are released into the bloodstream [12.183]. For the detection of cTnI, the electrode of an electrochemical immunoassay (voltammetry), which is a biosensor with antibodies as biological elements, is functionalized with the

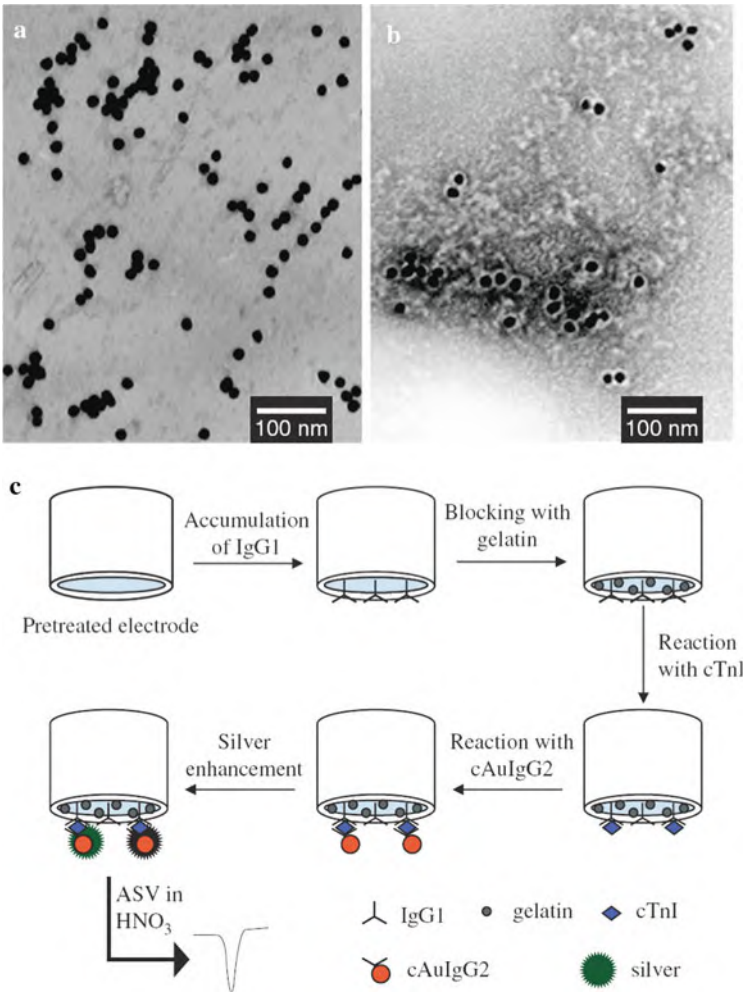

Fig. 12.58 TEM images of (**a**) unlabeled and (**b**) gold nanoparticles labeled with IgG2 detection antibodies. (**c**) Protocol format in the analytical procedure for the diagnosis of acute myocardial infarction by the detection of the cTnI biochemical marker via Au nanoparticles conjugated to IgG2 antibodies (cAuIgG2). (Reprinted with permission from [12.180]. © 2005 American Scientific Publishers)

capture antibody IgG1 for immunoreaction with the cTnI sample (Fig. 12.58c). After that, the reaction with gold nanoparticles labeled with the detection antibody IgG2 (cAuIgG2; Fig. 12.58a, b) is performed with final catalytic deposition of silver on the gold nanoparticles, yielding a peak in the anodic stripping voltammogram (ASV). The magnitude of this peak reflects the amount of cTnI in the serum with a detection limit of 0.8 ng/ml of cTnI. The cTnI concentrations determined by this nanotechnique fully coincide with the values obtained by enzyme-linked

immunoadsorbent assays (ELISA) [12.180]. This nanotechnique for the diagnosis of acute myocardial infarction may be important in the early phase of the disease where the symptoms are ambiguous, may shorten the assay time, and reduce costs by decreasing reagent consumption [12.180].

Using virus-derived nanoparticles, a highly sensitive and specific assay system for the specific marker troponin I of acute myocardial infarction (AMI) has been developed [12.184]. This assay can detect troponin levels that are 6–7 orders of magnitude lower than those detected by coventional enzyme-linked immunosorbent assays (ELISA).

12.7.2 Diabetes

Diabetes mellitus comprises a group of metabolic disorders characterized by high blood glucose resulting from reduced insulin secretion, decreased glucose utilization, or increased glucose production. At least 20 million people have diabetes in the United States (see [12.185]). Diabetes can lead to serious vascular complications, which include coronary heart disease, cerebrovascular disease, as well as peripheral vascular disease, and microvascular complications like diabetic retinopathy (DR), which makes diabetes the leading cause of new cases of blindness among adults (see [12.185]).

Oral delivery of insulin is not an effective diabetes therapy because of its susceptibility to enzymatic degradation in the gastrointestinal (GI) tract and low permeability across the intestinal epithelium [12.186, 12.187]. However, polymeric vesicles are thought to be potentially advanced candidates for the oral delivery of insulin as briefly discussed in the following [12.188]. Block copolymers comprising commercial Pluronic® F127 (PEO-PPO-PEO) and poly(lactic acid) (PLA) have been synthesized to PLAF 127-29 vesicles (molecular weight 29 kDa) with a radius of 56 nm (Fig. 12.59a, b) to be loaded with insulin. The nanoparticles within this size range exhibit a high circulation time in the human body and a good bioavailability. A biphasic in vitro insulin release behavior was found for the insulin-loaded PLAF 127-29 vesicles (Fig. 12.59c) due to diffusion control in the vesicles [12.188]. After in vivo oral administration of insulin-loaded PLAF 127-29 vesicles to mice, a minimum blood glucose concentration of 25% of the initial concentration was observed after 5 h and this concentration was maintained for at least an additional 18.5 h which is in contrast to the behavior of free oral insulin or subcutaneous insulin administration (Fig. 12.59d). There could be two reasons for the prolonged hypoglycemic effect (reduced glucose concentration in the blood) of insulin-loaded PLAF 127-29 vesicles. First, the insulin is protected from degradation by enzymes in the GI tract due to the PLAF 127-29 coating of the vesicles, so that the insulin load could reach the specific regions for favorable insulin absorption and nanoparticle uptake in the distal jejunum and in the ileum where abundant Peyer's patches exist (important in the immune surveillance of the intestinal lumen). Second, both the small size and the strong interaction of PEO blocks in the PLAF 127-29 block copolymer with the intestinal wall should be responsible for the delayed GI transit

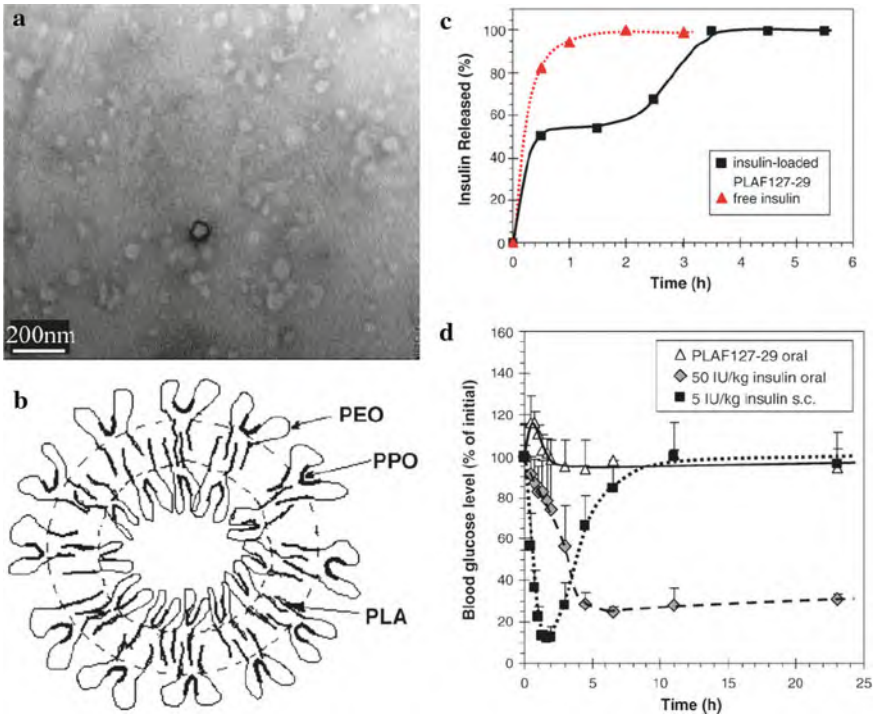

Fig. 12.59 (**a**) Transmission electron micrograph of PLAF 127-29 polymer vesicles (see text) and (**b**) possible microstructure. (**c**) The in vitro release behavior of insulin-loaded PLAF 127-29 vesicles in phosphate buffer saline. (**d**) Time dependence of the glucose level following oral administration of insulin-free PLAF 127-29 vesicles to control mice (PLAF 127-29 oral), insulin-loaded PLAF 127-29 vesicles (50 IU/kg), and subcutaneous injection of free insulin (5 IU/kg insulin s. c.). (Reprinted with permission from [12.188]. © 2007 Elsevier)

of the insulin – PLAF 127-29 vesicles, giving rise to the prolonged hypoglycemic effect. Therefore, the present nanoparticles may be promising carriers for oral insulin delivery [12.188].

12.7.3 Lung Therapy – Targeted Delivery of Magnetic Nanoparticles and Drug Delivery

Despite progress in optimizing aerosol delivery to the lung for the treatment of lung disorders such as asthma, cystic fibrosis, or lung cancer, targeted aerosol delivery to specific lung regions other than the airways or the lung periphery has not been achieved adequately to date [12.189]. However, it has been shown by simulation and experimentally in mice [12.190] that targeted delivery of aerosol droplets comprising superparamagnetic iron oxide nanoparticles can be achieved in combination with a target-directed magnetic field gradient. This may be useful

for treating localized lung disease, by targeting foci of bacterial infection or tumor nodules.

In simulative calculations of the magnetic field-gradient guided deposition of inhaled superparamagnetic iron oxide nanoparticles (SPIONs) in the lung, it turned out that the forces exerted by a field gradient (Fig. 12.60a) on a single 50 nm multidomain core SPION containing 5 nm single-domain magnetite nanoparticles would not be sufficient to efficiently guide the SPIONs [12.190]. In contrast, when a multitude of, e.g., 2930 SPIONs are assembled in an aqueous aerosol droplet, this is

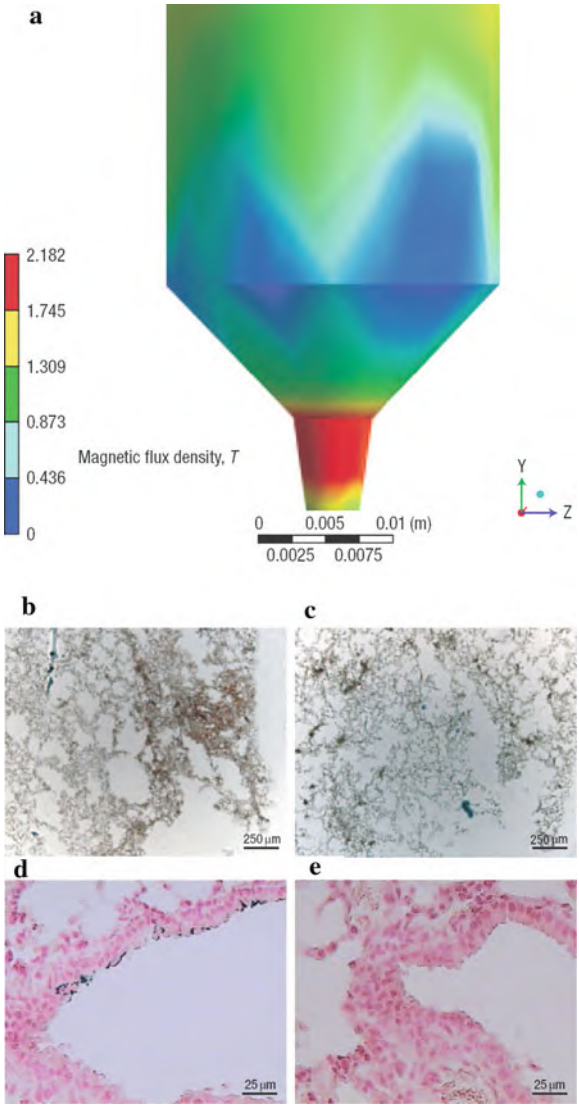

Fig. 12.60 (**a**) Iron–cobalt core tip surrounded by coil windings (not shown) for the generation of a high-gradient magnetic field for targeted delivery of superparamagnetic iron oxide nanoparticles (SPIONs). The magnetic flux density is shown in a multicolor representation. (**b**–**e**) Lung histology after inhalation of magnetic nanoparticles by a mouse with the magnetic tip (**a**) above the right lung lobe (**b**, **d**; left lung: **c**, **e**). The magnetic nanoparticles (*brown color*) accumulate in the focused area of a high magnetic field gradient in the right lung lobe (**b**, **d**) but not in the left lung tissue without a magnetic field (**c**, **e**). (**d**, **e**) Prussian *blue* staining of the SPIONs (**d**) and hematoxylin staining of the lung cells (**d**, **e**). (Reprinted with permission from [12.190]. © 2007 Nature Publishing Group)

predicted to result in aerosols guidable by technically feasible magnetic field gradients ($\nabla B > 100\ \mathrm{Tm}^{-1}$) in the proximity of a magnetic tip (Fig. 12.60a). In a simple model calculation, the SPION concentration deposited in a magnetized lung airway exceeded that in an airway without a magnetic field by a factor of 3.

In experiments on mice [12.190] it could be shown by histology that SPIONs were accumulated in an eightfold higher concentration in the right lung lobe exposed to a field gradient, compared with the left lobe in zero field (Fig. 12.60b, c). SPIONs could be identified on the magnetized surface of alveolar cells and on airway epithelial cells exposed to a magnetic field gradient (Fig. 12.60d, e). In order to demonstrate the potentials for drug delivery, plasmid DNA (pDNA) was formulated in the SPION aerosol droplets and a twofold higher dose of pDNA was detected in the magnetized right mouse lung than in the left lung without magnetic field. Several drugs can be administered simultaneously and other pharmaceutically relevant nanocarriers could be co-delivered with the SPIONs. It should be emphasized here that the biocompatibility and clinical feasibility of SPIONs has been proven by their years of clinical use as contrast agents in magnetic resonance imaging [12.191]. Scaling up of the magnetic field gradient to address the size of the human lung represents the major challenge, although high field-gradient electromagnets for use in magnetic drug targeting in pigs are already available [12.192, 12.193].

12.7.4 Alzheimer's Disease (AD)

The prevalence of most neurodegenerative disorders increases dramatically with advancing age. For example, Alzheimer's disease – the most prevalent of these disorders – affects ~ 15 million people worldwide today [12.194] and will give rise to financial, societal, and emotional cost staggering in the future. The disease is caused by plaques and tangles of protein in the brain. However, therapeutic strategies to probe the central nervous system (CNS) are limited by the blood–brain barrier (BBB). This barrier can be overcome by polymeric nanoparticles as drug carriers [12.195].

Senile plaques and neurofibrillary tangles were discovered by Alois Alzheimer [12.196] in the neocortex and hippocampus of a woman with memory deficits and a progressive loss of cognitive function. Neurodegeneration affects the cognition (learning, abstraction, judgement, etc.) and the memory with behavioral consequences such as aggression, depression, delusion, anger, and agitation (see [12.195]).

According to the amyloid cascade hypothesis (see [12.197]) Alzheimer's begins with the build up of amyloid-beta (A-beta), which is carved from the amyloid-beta precursor protein (APP). In a first step [12.197], the enzyme beta-secretase cuts APP outside the cellular membrane with the help of aspartic acids that make water molecules more reactive. Then the presenilin protein, a component of the gamma-secretase enzyme, cuts the remaining stump inside the membrane, releasing A-beta [12.197]. The reason why cells make A-beta is unclear, but current evidence suggests that the process is part of a signaling pathway (see [12.197]. In the aqueous

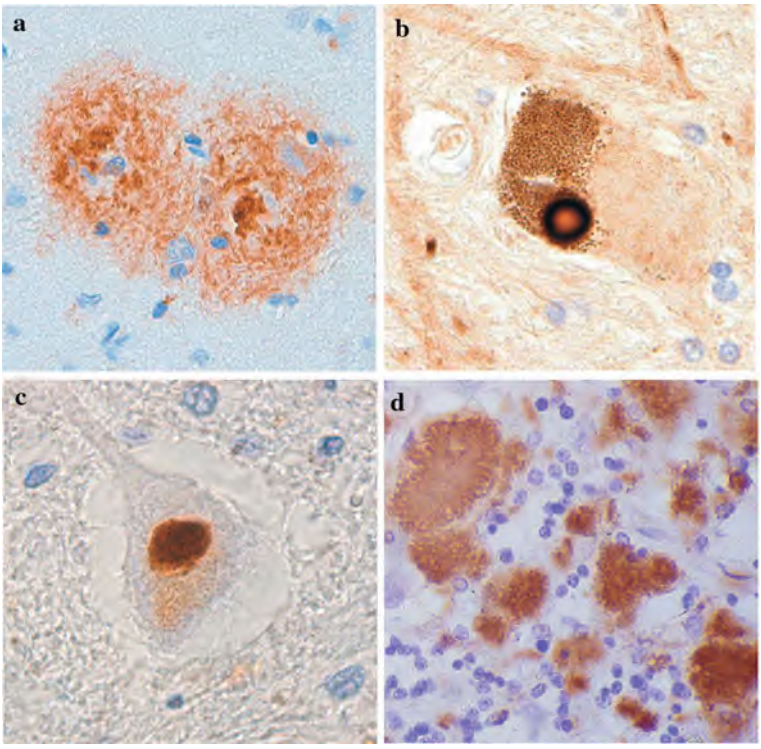

Fig. 12.61 Microscopy of protein aggregates in neurodegenerative diseases. (**a**) Senile plaques in neocortex of Alzheimer's disease. (**b**) Lewy body in substantia nigra of Parkinson disease. (**c**) Ubiquitinylated inclusion in spiral cord motor neuron in amyotrophic lateral sclerosis (ALS). (D) Protease-resistant prion protein (PrP) in cerebellum of Creutzfeldt–Jakob disease (CJD). (Reprinted with permission from [12.194]. © 2004 Nature Publishing Group)

environment between neurons, the A-beta peptides cling to one another, forming small soluble assemblies and long filaments ([12.197] and Fig. 12.61). Studies have shown that these assemblies and filaments can kill neurons cultured in Petri dishes and affect connections between neurons in mice (see [12.197]). It is not exactly understood how the A-beta assemblies and filaments kill neurons, but evidence suggests that aggregates of A-beta outside a neuron can initiate the alteration of the tau protein inside the cell and change the cellular activity of kinase enzymes that install phosphates into proteins. The affected kinases add too many phosphates to tau, which is connected to the intracellular microtubules, causing it to form twisted filaments. The altered tau proteins somehow kill the neuron, perhaps because they disrupt the microtubules that transport proteins and large molecules along axons and dendrites, and because the tau filaments and tangles clog the neuron's axons and dendrites. Thus, the formation of tau filaments is apparently a more general event leading to neuronal death, whereas A-beta is the specific initiator in Alzheimer's disease [12.197]. It is increasingly evident that aggregated disease proteins are not

simply neuropathological markers of neurodegenerative disorders but, instead, they almost certainly contribute to disease pathogenesis, thereby paving the way for the identification of rational therapeutic targets [12.194, 12.197]. But how amyloid contributes to the damage of Alzheimer's is not clear, and several anti-amyloid drugs have failed in phase III clinical trials [12.198].

The transition metals copper, iron, and zinc are implicated in the neurotoxicity of A-beta [12.195, 12.199]. A-beta Cu^{2+} catalyzes the generation of hydrogen peroxide (H_2O_2). The H_2O_2 permeates the cell membrane, and highly reactive hydroxyl radicals form, which disrupts the genetic material (DNA), and modify proteins and lipids. In addition, apoptosis is induced by the permeation of H_2O_2 throughout the cell membrane [12.200]. Zinc is redox-inert, and hence, inhibits the production of H_2O_2. Therefore, zinc's role in A-beta physiology is that of an antioxidant, but it is not concentrated enough in the brain to completely eliminate A-beta neurotoxicity (see [12.195]).

The strategies for fighting Alzheimer disease include to dissolve or clear toxic aggregrates of A-beta from the brain, to block the activity of beta-secretase, to reduce the cutting of APP by gamma-secretase, or to block the kinases that place an excessive amount of phosphates onto the tau protein (see [12.197]). However, the diagnostic and therapeutic strategies to probe the central nervous system (CNS) are limited by the restrictive tight junctions at the endothelial cells of the blood–brain barrier (BBB; see Sect. 12.5). The cerebral endothelial cells (ECs) are distinguished from the ECs of the periphery (Fig. 12.62a). For instance, the brain ECs have fewer endocytotic vessels than peripheral ECs, which limits the transcellular flux at the BBB. The occluded tight junctions, with a high electrical resistance, join ECs of the brain. Furthermore, cerebral ECs have more mitochondria than peripheral ECs, which drives the increased metabolic workload necessary to maintain ionic gradients across the BBB (see [12.195]).

To overcome the impositions of the BBB, nanoparticulate drug carrier technology is being developed. Polymeric nanoparticles are promising candidates in the diagnosis and therapy of AD because they are capable of opening tight junctions [12.201] crossing the BBB [12.202], because of their high drug-loading capacities, and because of their targeting toward the mutagenic proteins of Alzheimer's [12.203]. A successfully used nanoparticle (NP) for the in vivo administration of drugs targeted to the brain is the rapidly biodegradable polybutylcyanoacrylate (PBCA; see Fig. 12.62b), where one of the suggestions how PBCA-NP (20 nm) pass through the BBB is the phagocytosis or endocytosis by the endothelial cells (see [12.195]). Novel PBCA-NP have been fabricated with clioquinol (5-chloro-7-iodo-8-hydroxyquinoline, CQ; Fig. 12.62c) encapsulated within the polymeric matrix. CQ is known to solubilize the A-beta plaques in vitro and inhibits the A-beta accumulation in vivo [12.204]. The PBCA-CQ-NPs freely cross the BBB and upon in vivo intravenous administration in mice, the PBCA-CQ-NP have a greater brain uptake than the free drug alone, so that this delivery system can be used as a prototype in the treatment of AD [12.195]. The recent discoveries may indicate that the quest for ways to prevent and treat Alzheimer's will not be in vain [12.197].

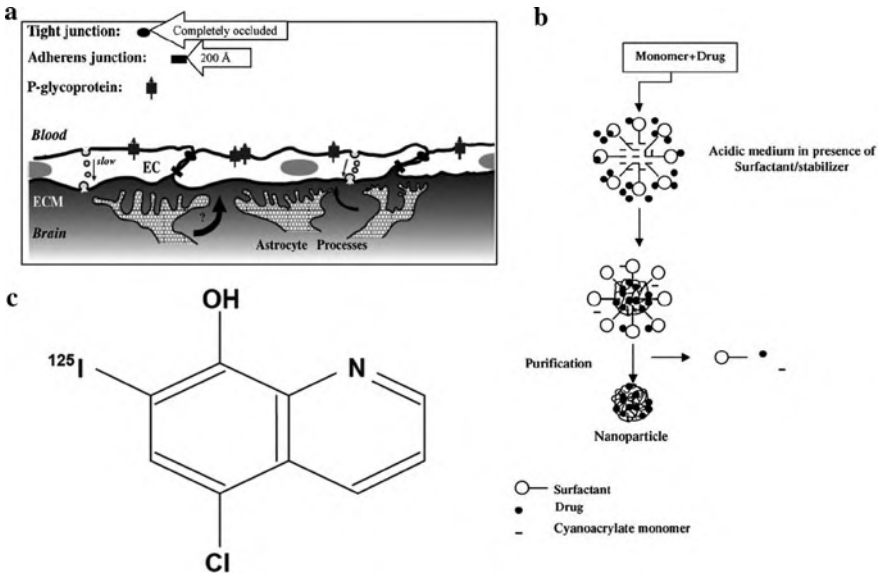

Fig. 12.62 (**a**) Features of the brain–blood barrier (BBB). The endothelial cells (EC) of BBB are coupled by tight junctions (TJ), that are completely occluded, and by adherens junctions (20 nm). The increased electrical resistance at the TJ strains paracellular movement of substances into the brain. Astrocytic processes (glial cells) in the extracellular matrix (ECM) envelope the capillaries and influence transport across the EC. Astrocytes do not participate in BBB because of the 20 nm gap between adjacent astrocytes. P-Glycoproteins (P-gp) on apical EC membranes let substances from the brain flow out into the bloodstream [12.195, 12.205]. (**b**) Emulsion polymerization of alkylcyanoacrylates [12.206]. (**c**) Structure of ^{125}I-clioquinol (CQ). The drug is radioiodinated for biodistribution studies [12.195]. (Reprinted with permission from [12.195]. © 2005 Elsevier)

Another strategy for Alzheimer therapy is to dissolve A-beta protein aggregates remotely in molecular surgery through the local heat delivered by metallic nanoparticles (NP) under gigahertz irradiation [12.207]. The 10 nm Au-NP, which are small enough to penetrate cell membranes, were linked to the peptide H-Cys-Leu-Pro-Phe-Phe-Asp/NH_2 (Cys-PEP). The sequence PEP selectively attaches to the A-beta aggregates, where it is believed that the peptides recognize a particular (hydrophobic) domain of the β-sheet structure of A-beta (i.e., amino acids 17–20 of the hydrophobic core of A-beta [12.208]). The Au-NP–Cys-PEP conjugates were incubated with A-beta solution where fibrils spontaneously start growing and form precipitates. In a 12 GHz weak microwave field (0.1 W), the Au-NP – Cys-PEP conjugates attached to the fibrils, absorbed the radiation and dissipated energy, causing disaggregation of the amyloid aggregates (Fig. 12.63). This effect is opposite to microscopic heating, where an increase in temperature results in an increased aggregation rate. Thus, attaching metallic Au-NP to a target and applying microwave fields allows a selective supply of energy to the system to remotely and non-invasively dissolve aggregates and deposits without past-irradiation reprecipitation,

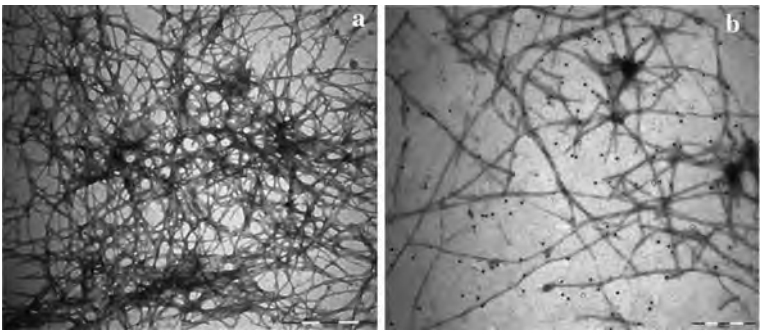

Fig. 12.63 (**a**) Electron microscopy of control A-beta alone incubated for 48 h and irradiated for 8 h (scale bar, 500 nm). (**b**) Au-NP–Cys-PEP + A-beta incubated for 48 h after 10 min of irradiation. Chopped fibrils and detached Au-NP can be seen (scale bar, 200 nm). (Reprinted with permission from [12.207]. © 2006 American Chemical Society)

which indicates that the in vitro amyloidogenic potential has been significantly decreased.

In the pursuit of diagnostic tools of AD, the analysis of cerebrospinal fluid (CSF) for potential biomarkers is of particular interest [12.209]. Several ELISA-based studies have shown that total tau protein and phosphorylated-tau protein (P-tau) levels are increased in Alzheimer's whereas the levels of A-beta with 42-amino acids (A-beta 42) are decreased in the CSF of patients at early stages of AD, compared to healthy controls (see [12.209]). However, these changes are not unique to AD and present tests diagnose only ~ 80% of AD correctly.

Nanoparticle-based assays can detect target protein levels many orders of magnitude lower than concentrations detected by ELISA (see Fig. 12.24 and Sect. 12.2). For a sensitive diagnosis of Alzheimer's disease the barcode assay for the detection of amyloid-derived ligands (ADDL), a marker oligomer linked to AD has been developed [12.79]. Furthermore, localized surface plasmon resonance (LSPR) on Ag nanoparticles has been utilized to monitor the interaction of ADDLs and specific anti-ADDL antibodies for the possible diagnosis of AD [12.210]. In the efforts to use NPs to detect, prevent, and treat protein misfolding diseases such as Alzheimer's [12.207, 12.211], it should be taken into account that uncoated NPs can promote fibrillation [12.212]. Indeed, designing coatings that limit or prevent protein adherence may prove to be of critical importance to safe application of NPs in medicine [12.213].

New treatment strategies for Alzheimer's could arise from the discovery [12.214] of interactions between beta-amyloid (A-beta), the toxic misfolded protein behind Alzheimer's, and prion protein (PrP), which itself forms aggregates in prion diseases like Creutzfeldt–Jakob disease (CJD). In this study [12.214], PrP has been identified as the surface protein needed for A-beta to disrupt functions of neurons. Screening for small molecules to block the interaction between A-beta and PrP could be straight forward for Alzheimer's therapy.

12.7.5 Ophthalmology

Human cataract lens cell membrane investigated at sub-nanometer resolution. Since human pathologies often originate from molecular disorder, imaging technologies with sub-nanometer resolution are required for the understanding of these pathologies. Malfunction of proteins in the eye lens gives rise to cataract, a disease leading to opacity of the lens, causing impairment of vision or blindness.

The lens of the eye has developed remarkable adaptions to ensure its transparency and to change its shape for focusing on different distances (accommodation). The lens is avascular, which minimizes light scattering. The cells are tightly packed with intercellular distances smaller than the wavelength of visible light. An internal microcirculation model that maintains a flow of water, ions, and metabolites can explain why cells located deep inside the lens are nourished (see [12.215]). In this microcirculation system, solutes flow in the extracellular space and flow through cell-to-cell channels back to the lens periphery. Two types of membrane proteins, aquaporin-0 (AQP0) and connexins (Cx), form the cell-to-cell junctions assuring metabolite transport, waste evacuation, water homeostasis, and intercellular adhesion. Six connexins form a connexon or half-channel and docking of two connexons from adjacent cells creates a cell-to-cell gap junction channel [12.216].

After cataract surgery from the eye of a 82-year-old male human, high-resolution atomic force microscopy (AFM) images (Fig. 12.64a, b) revealed only AQP0 in the AQP0 array borders, which is in contrast to healthy lens cell membranes where the arrays were edged by densely packed regions of connexons. In agreement with the AFM data, no molecules of the weight of connexon molecules could be detected by matrix-assisted laser desorption/ionization time-of-flight (MALDI-TOP) mass spectrometry [12.215]. Since the patient did not suffer from visual problems earlier, he must have disposed of connexons that were degraded with time and cataract formation has occurred by a progressive breakdown of the internal microcirculation system. Proteolytic degradation is considered as the most likely explanation for the absence of the connexons.

Based on these results, a model is suggested [12.215] for the molecular membrane protein organization in microdomains, in healthy and pathological cases (Fig. 12.64c–f). In the healthy lens membrane, connexons surround AQP0 arrays, control the size of the arrays, and assure together with the AQP0 arrays cell adhesion and the flow of water, ions, and metabolites. In the pathological case, when connexons are lacking, no metabolite or ion flow occurs, and an increased area of non-adhering membrane may result in lens opacification (Fig. 12.64d, f). The patient's cataract lens cells suffer from malnutrition, accumulation of waste products, diminished water flow, and inhomogeneously distributed cell adhesion over the cell surface. It is assumed that in the absence of connexons the internal microcirculation system of the lens collapses, resulting in the formation of cataract. The study shows the power of the AFM as a nanomedical imaging tool.

Cerium oxide nanoparticles to prevent retinal disorders. Retinal diseases that lead to partial or complete loss of vision cause misery for hundreds of millions of people throughout the world. Although the causes of these disorders are complex,

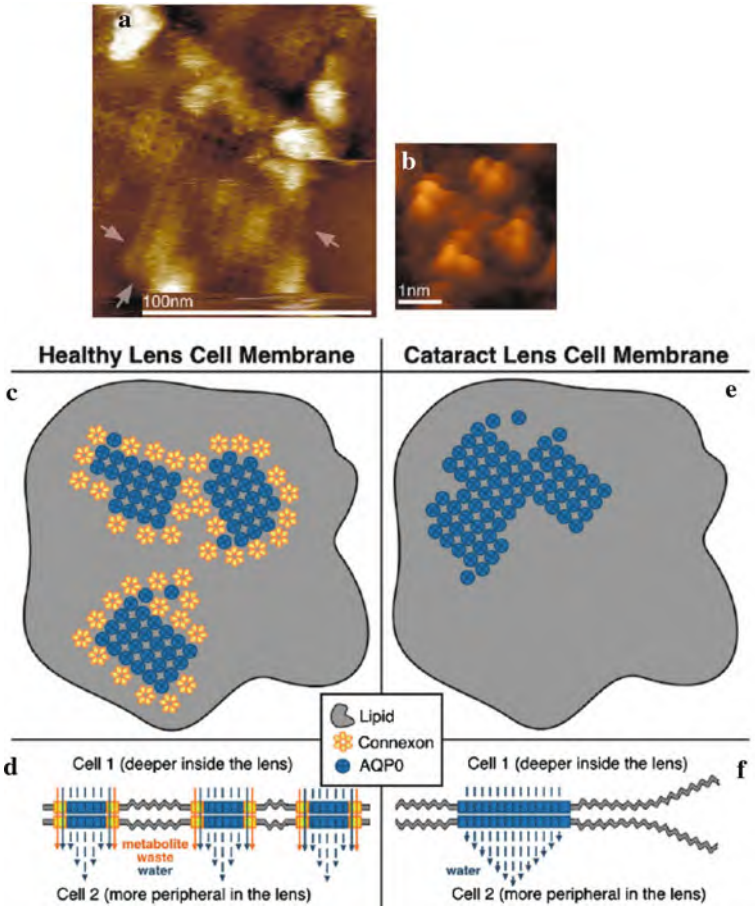

Fig. 12.64 High-resolution AFM images of aquaporin-0 (AQP0) junction arrays in the cataract lens cell membranes. (**a**) Medium-resolution topograph of AQP0 arrays. No connexons were found at the AQP0 microdomain edges (*arrows*). (**b**) Individual AQP0 in junctional conformation within the microdomain. (**c**) *Top view* at a healthy assembly with AQP0 square arrays edged by connexons [12.217]. (**d**) *Top view* of a pathological assembly in a senile cataract without connexons and larger AQP0 arrays. (**e**) *Side view* of a healthy assembly with water and metabolite transport and efficient cell adhesion where the non-adhering membrane areas are small. (**f**) *Side view* of a pathological assembly of a senile cataract. Fusion of AQP0 into large arrays favors the formation of large non-adhering membrane areas. According to the microcirculation model, the cell-to-cell flow of metabolites, waste (*orange arrows*), and water (*blue arrows*) is directional from the lens interior to the periphery [12.215]. (Reprinted with permission from [12.217] (**a**–**c**) and [12.215] (**d**–**f**).)

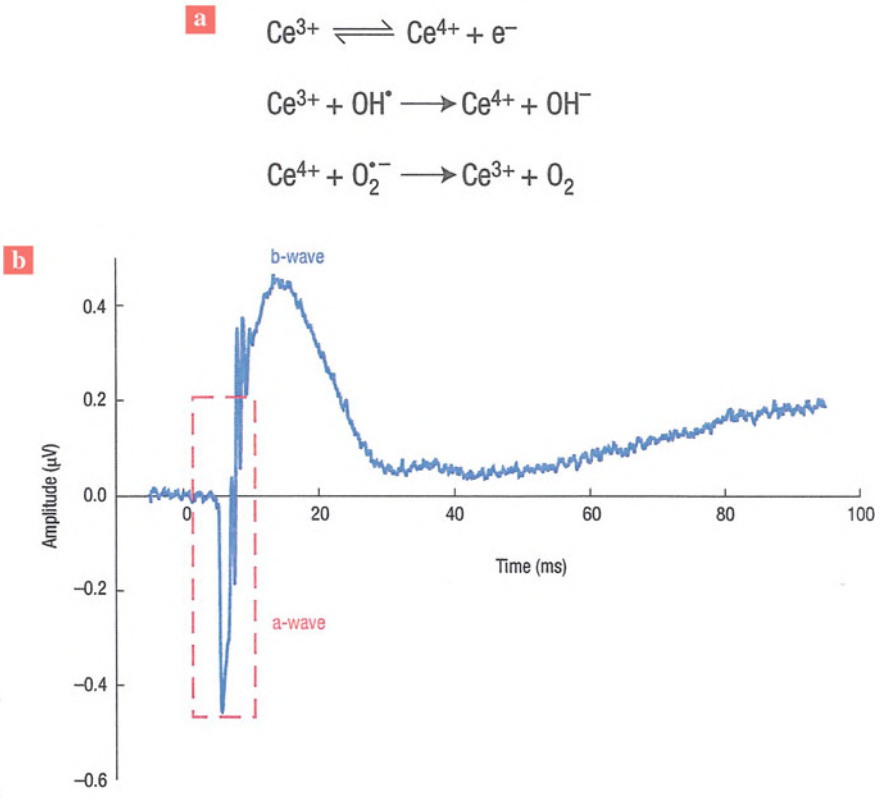

Fig. 12.65 (**a**) By switching between +3 and +4 valence states (*top*), nanoceria particles can reversibly scavenge free electrons from the reactive oxygen species (OH$^{\bullet}$ and $O_2^{\bullet -}$) to produce less harmful molecules (OH^- and O_2). This makes them attractive for treating diseases caused by reactive oxygen species. The $^{\bullet}$ symbol represents an unpaired electron which makes the molecule highly reactive. (**b**) A typical mammalian electrography wave forms in response to a flash of white light at $t = 0$. The "a-wave" (*red box*) indicates the initial part of the photoreceptor response, whereas the "b-wave" includes information about the response of the photoreceptor and other neural cells in the retina to light. (Reprinted with permission from [12.219]. © 2006 Nature Publishing Group)

oxygen radicals that damage the sensitive cells in the retina are thought to play a central role [12.218, 12.219]. Cerium oxide nanoparticles (nanoceria) can protect the retina from the "oxidative stress" caused by reactive oxygen species (Fig. 12.65). The rods and cones in our retina (Fig. 12.66) are specialized neurons that convert incoming light into a neurochemical signal. They are subjected to particularly high levels of oxidative stress, because, first, they are exposed to higher partial pressure of oxygen and possess a higher metabolic rate than other cell types. The high metabolic demands are met by the production of significant amounts of adenosine triphosphate (ATP) by the mitochondria in the cell which involves the reduction of oxygen to water, generating a small fraction of electrons which can form toxic

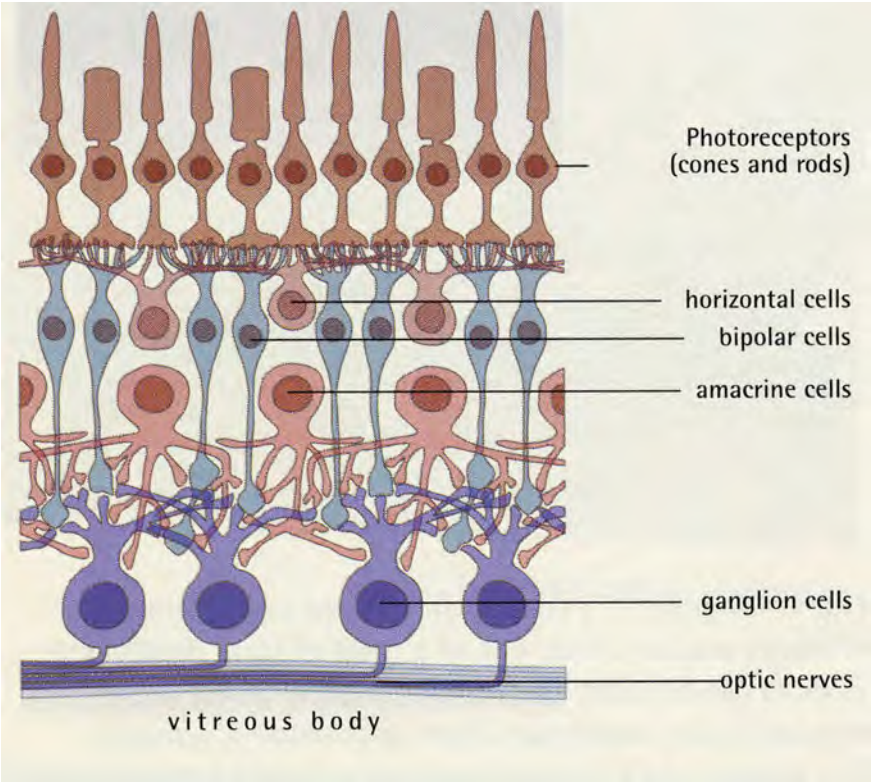

Fig. 12.66 Nerve cells and their connections with the retina. At the top there are the photoreceptors of which there are four types – rods for seeing in the dark and three types of cones with different color sensitivities. The receptors have a contact point (synapse) at their lower end with each of the two subsequent nerve cells, the bipolar and horizontal cells. The *lower part* shows complex contact points between bipolar, amacrine, and ganglion cells. Each ganglion cell sends a process to the brain in the optic nerve. (Reprinted with permission from [12.220]. © 2001 Max-Planck Society)

reactive molecules, known as superoxides, in the cell. Second, photons of visible light can produce highly reactive "singlet" oxygen species, and overproduction of the reactive species can overwhelm the natural defences to finally kill cells. Cerium, which can exist in both a +3 and a +4 state, can scavenge the free electrons from reactive oxygen species making them non-reactive (Fig. 12.65a).

Reducing the diameter of nanoceria to about 5 nm results in more oxygen vacancies (see [12.219]) which makes it even a better scavenger. When retinal cells are treated in vitro with hydrogen peroxide – a source of reactive oxygen molecules – and incubated with nanoceria, the nanoparticles protect the cells by preventing them from reactive molecules [12.218]. For in vivo studies nanoceria was injected into the eye vitreous body of albino rats which have retinas highly susceptible to photodamage. The retinas pretreated with nanoceria experienced

significantly less light-induced damage and cell death, compared with controls [12.218]. For studying the recovery from light-induced damage, the non-invasive test known as electroretinography exhibiting an "a-wave" and a "b-wave" was employed (Fig. 12.65b). The eyes pretreated with nanoceria showed ~ 80% of the a-wave and the b-wave amplitudes after light exposure compared to controls without light exposure, which is much higher than the ~ 23% after light exposure without nanoceria. Although it is unclear how the nanoceria protects the retina, it is speculated that the nanoparticles enter the photoreceptors because reactive oxygen species are naturally formed within these cells when exposed to light and only exist over a very short distance.

It has been demonstrated that a hybrid bionanodevice can be fabricated that links nerve cells and photovoltaic nanoparticle films where the properties of nanoparticles can be applied to light-stimulated nerve signaling devices, including the possibility of synthesizing a nanoparticle-based artificial retina [12.221].

Glaucoma drug conjugated to ceria nanoparticles. Many individuals suffer from the ocular disease glaucoma (see [12.222]). This condition describes a destruction of optic nerve cells and deterioration of eye sight as a result of increased intraocular pressure. The pressure is partially caused by the formation of carbon dioxide produced by the enzyme human carbonic anhydrase II (hCA II; Fig. 12.67a), a Zn^{2+} – containing metalloenzyme that catalyzes the reversible hydration of carbon dioxide to bicarbonate. Sulfonamide compounds, such as 4-carboxybenzene sulfonamide (CBS; Fig. 12.67b), have been shown to selectively inhibit hCA II which involves coordination of the sulfonamide group (as the anion) to the Zn atom in the active site of hCA II to form a complex. Since the ocular bioavailability of many drugs is significantly enhanced by binding to nanoparticles, the CBS drug has been

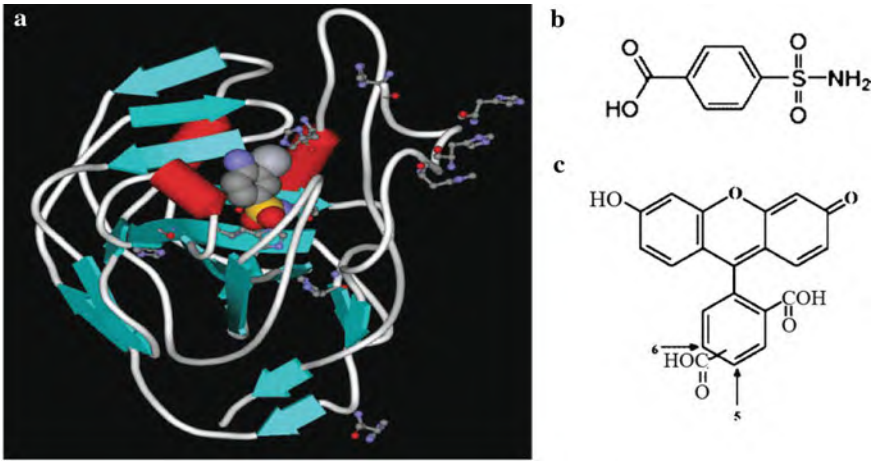

Fig. 12.67 (**a**) Cartoon diagram showing the structure of human carbonic anhydrase. (**b**) Molecular structure of carboxybenzene sulfonamide and (**c**) of carboxyfluorescein. (Reprinted with permission from [12.222]. © 2007 American Chemical Society)

conjugated to ~ 15 nm nanoceria using epichlorohydrin as an intermediate linkage, and carboxy fluorescein (Fig. 12.67c) as a conjugate for fluorescence imaging. The efficiency of the functionalized nanoparticles was tested by observing the effect of the nanoparticles on the rate of hCA II-catalyzed hydrolysis of 4-nitrophenyl acetate to form 4-nitrophenolate. The change in the spectroscopic data [12.222] with the concentration of functionalized nanoceria indicated the inhibiting effect. More studies will likely evolve into an inhibition of hCA II in living cells and an effective treatment of glaucoma.

12.7.6 Viral and Bacterial Diseases

HIV inhibitor saquinavir delivered into cells by nanoparticles. The human immunodeficiency virus (HIV) is a retrovirus which causes the widespread disease acquired immune deficiency syndrome (AIDS), a severe immunological disorder. The Nobel Prize in medicine 2008 has been awarded to F. Barre-Sinoussi and L. Montagnier for the discovery of the HIV virus. It is known that the HIV infects peripheral mononuclear phagocytic cells and the central nervous system in the early stages [12.223]. The phagocytic monocyte/macrophage cells (Mo/Mac) also act as shuttle for the viruses to go to other sites in the body and thrive there (see [12.224]). Saquinavir, the first HIV protease inhibitor to be marketed as Invirase® for the treatment of HIV, is a peptide derivative that inhibits HIV-1 and HIV-2 protease-mediated cleavage of the gag and pol polyproteins of the HIV genome, thus preventing the posttranslational processing required for virus maturation and spread [12.225]. However, the therapeutic use of anti-HIV protease inhibitors suffers from poor solubility and the oral bioavailability of a single dose of saquinavir is only 4% [12.225]. It has been shown [12.226] that at a concentration of 100 nM, free saquinavir was completely inactive in chronically HIV-infected Mo/Mac cells, but when bound to poly(hexylcyanoacrylate) nanoparticles, caused a 35% decrease in virus production.

It was hypothesized that the THP-1 human monocyte/macrophage (Mo/Mac) cell line derived from the blood of a 1-year-old boy with acute monocytic leukemia (see [12.224]) would endocytose a nanoparticulate formulation and provide optimal concentration of saquinavir in Mo/Mac cells as well as transport the drug to the central nervous system and other sites, which are potential reservoirs for HIV. The drug would be released at these sites and help in targeted and effective eradication of the viral load. Preliminary studies showed [12.224] that a poly(ethylene oxide)-modified poly(epsilon-caprolactone) (PEO-PCL) nanoparticulate system (Fig. 12.68a) with a particle size of 200 nm is an efficient delivery vehicle for the release of the saquinavir anti-HIV protease inhibitor and its intracellular delivery to the Mo/Mac cells (Fig. 12.68c). For optical detection of the PEO-PCL cell penetration, the hydrophobic fluorescent dye rhodamine 123 was encapsulated in the PEO-PCL nanoparticles (Fig. 12.68 c). Surface modification of PCL nanoparticles with PEO chains prevents aggregation and allows for efficient systemic delivery especially after intravenous administration [12.224]. For the

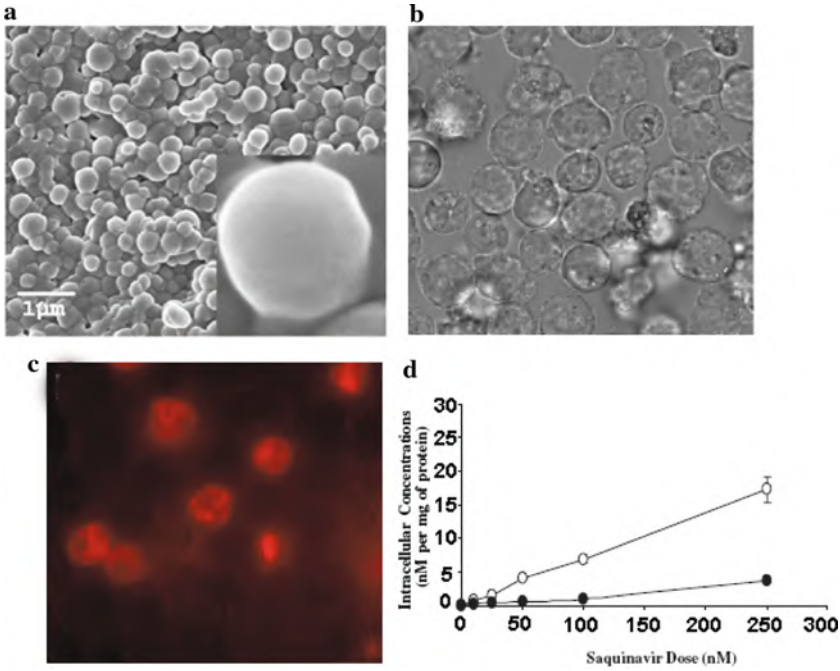

Fig. 12.68 Nanoparticles of PEO-PCL (poly(ethylene oxide))-modified poly(epsilon-caprolactone) for AIDS (acquired immunodeficiency syndrome) treatment. The PEO-PCL nanoparticles can be loaded with saquinavir, a HIV (human immunodeficiency virus) inhibitor for intracellular delivery of saquinavir to THP-1 human monocyte/macrophage (Mo/Mac) cells for AIDS treatment. (**a**) Scanning electron micrograph of PEO-PCL nanoparticles with the *inset* showing a nanoparticle at higher resolution. (**b**) Uptake of rhodamine 123 containing PEO-PCL nanoparticles by the THP-1 monocyte/macrophage cells incubated for 1 h at 37°C with bright-field (**b**) and corresponding fluorescent images (**c**). (**d**) Intracellular concentration of tritiated [^{3}H]-saquinavir as a function of dose administered to THP-1 monocyte/macrophage cells. The concentrations for [^{3}H]-saquinavir administered in PEO-PCL nanoparticles (○) are much higher than when administered in aqueous solution (●). (Reprinted with permission from [12.224]. © 2006 Springer Verlag)

determination of the drug concentration inside the cells, nanoparticles loaded with tritiated [^{3}H]-saquinavir were prepared [12.224], showing substantially increased drug uptake in the cells by nanoparticle formulations compared to aqueous drug solutions (Fig. 12.68d). It had been shown earlier that PEO-PCL nanoparticles can efficiently encapsulate hydrophobic drugs, such as tamoxifen and paclitaxel, and deliver them in tumor cells and in vivo, and that the by-products of PCL degradation are not acidic and do not cause any toxicity in vivo [12.227]. Further studies [12.224] show that efficient nanoparticle formulations can be developed for saquinavir to ensure better encapsulation and release of the drug. A significant

uptake of drug-loaded nanoparticles was also observed in the THP-1 cells of the monocyte/macrophage origin (Fig. 12.68d), which are known to shuttle the infected virions.

It has been demonstrated that 2 nm gold nanoparticles transform a weakly binding and biologically inactive small molecule into a multivalent conjugate that effectively inhibits HIV-1 fusion to human T cells [12.228], a principle type of white blood cell that has various roles in the immune system.

Viruses infect specific cells within host organisms, replicate, destroy the cells, and spread from cell to cell in infection cycles, thus causing disease (see [12.229]). These viral properties have inspired synthetic designs of various drug delivery vehicles. A synthetic nanosized polymer vehicle can mimic viral properties significantly. This virus-mimetic nanogel, loaded, e.g., with the model anticancer drug, doxorubicin, may prove valuable for treating diseases, such as tumors, with greater efficacy [12.229].

Antibacterial nanocomposites. Titanium dioxide (TiO_2) is an effective photocatalytic antimicrobial material when it is applied on an infected area of the human body or a contaminated area of the physical environment. However, it is difficult to remove from the treated surface. A removable, antimicrobial magnetic nanocomposite has been developed [12.230], consisting of a photocatalytic shell of anatase TiO_2 and a superparamagnetic core of nickel ferrite ($NiFe_2O_4$; Fig. 12.69a).

When TiO_2 nanoparticles in aqueous suspension are irradiated with UV light, free hydroxyl radicals ($OH^{\cdot}$) are generated that are highly toxic to microorganisms. This concept has been explored to investigate the inactivation of *Escherichia coli* bacteria with radiation dose in a culture medium in the presence of UV-irradiated TiO_2-coated $NiFe_2O_4$ nanoparticles (Fig. 12.69b). In the presence of the TiO_2-coated nanoparticles the concentration of *E. coli* bacteria is much faster reduced than with UV light alone. The TiO_2 photocatalytic shell provides the antimicrobial capability to inactivate bacteria and remove organic pollutants, while the $NiFe_2O_4$ magnetic core enables controlled delivery of the nanoparticles through a small magnetic field. This supports their application as removable antimicrobial photocatalyst nanoparticles.

Nano silver-titanium dioxide for enhanced hygiene. Mass Transit Railway (MTR), the corporation that runs Hong Kong subway, considered to invest on nanotechnology to enhance hygiene levels in MTR stations and trains. Nano silver-titanium dioxide coating (NSTDC, a non-toxic disinfectant) will be applied to surfaces that passengers commonly touch, including escalator handrails, the buttons on ticket issuing machines, as well as buttons and handrails in lifts, grab poles, and strap hangers in trains. Developed in Japan, NSTDC is certified to be effective in killing a wide range of bacteria and viruses, including the H1N1 influenza virus A. It is used in hospitals, offices, and homes in Japan. NSTDC's main component, TiO_2, has been approved for use in food by the United States Food and Drug Administration and under the Public Health and Municipal Service Ordinance in Hong Kong [12.231].

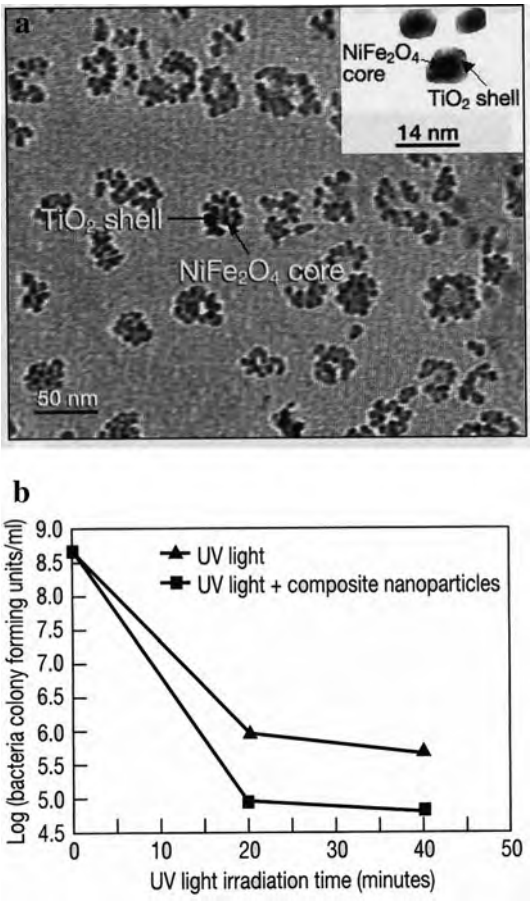

Fig. 12.69 (**a**) Transmission electron micrograph of TiO_2-coated $NiFe_2O_4$ nanoparticles, with a closer view in the *inset*. (**b**) *E. coli* bacterial inactivation response to TiO_2-coated $NiFe_2O_4$ nanoparticles as a function of UV irradiation time. The units of the *y*-axis represent the number of colonies of bacteria in 1 ml of solution. (Reprinted with permission from [12.230]. © 2006 Materials Research Society)

Single-walled carbon nanotubes (SWNTs) can kill bacteria like the common pathogen *E. coli* by severely damaging their cell walls [12.232]. It is projected that SWNTs could be used to create antimicrobial materials and surface coatings to improve hygiene, while their toxicity could be managed by embedding them to prevent their leaching into the environment.

12.8 Nanobiomaterials for Artificial Tissues

Nanotechnology can contribute to the development of biomaterials in medical fields including orthopedics, dentistry, cartilage treatment, vasculature, bladder therapy, central and peripheral nervous system therapy etc. [12.233]. In addition, first efforts to construct synthetic chromosomes have been undertaken [12.234]. The ultimate goal in tissue engineering [12.235] is to be able to draw stem cells to a scaffold in

vivo for controlled differentiation to the desired cell type to restore the functions of the diseased tissue [12.236].

12.8.1 Enhancement of Osteoblast Function by Carbon Nanotubes on Titanium Implants

The market for orthopedic implants is growing at a rapid rate due to the aging of our population. Each year, more than 600,000 joint replacements are performed in the United States alone with an estimated worldwide cost in excess of 3 billion dollars [12.237]. Orthopedic implants require the function of osteoblasts (see Sect. 11.7) to create new bone on their surface. Osteoblasts form the nanostructured organic matrix of the bone and produce proteins which play critical roles in the mineralization process. Critical in the design of successful implants is, therefore, the ability of implant materials to control protein adsorption and osteoblast adhesion after implantation. The degree to which proteins adsorb on implant surfaces depends on the chemistry, charge, wettability, and topography of the biomaterial (see [12.238]).

It has been shown [12.238] that osteoblasts closely interact with carbon nanotubes (CNT; Fig. 12.70c) which are grown on anodized Ti surfaces covered with

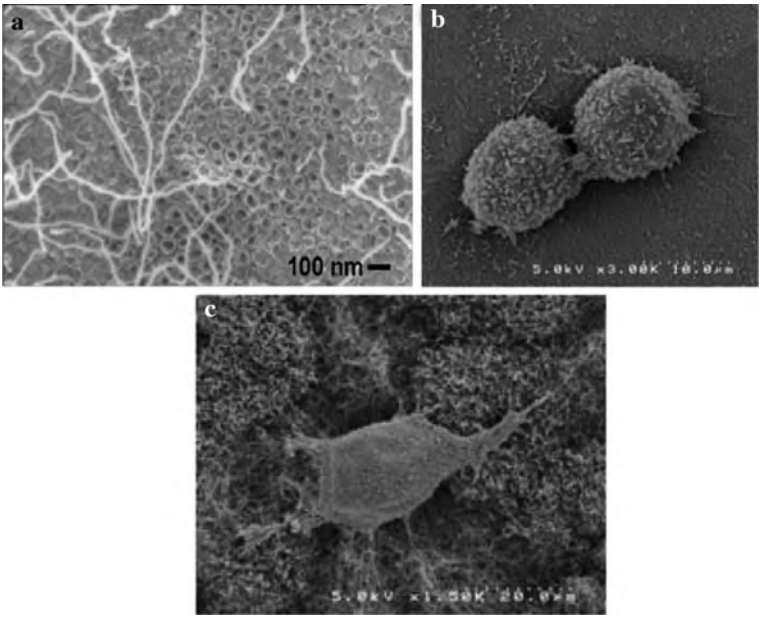

Fig. 12.70 (**a**) SEM micrograph of carbon nanotubes grown from the nanoholes of an anodized Ti surface with a Co catalyst. (**b**) Osteoblast adhesion after 4 h on anodized Ti (scale bar: 10 μm) and (**c**) on multiwalled carbon nanotubes grown out of a nanohole Ti surface (scale bar: 20 μm). (Reprinted with permission from [12.238]. © 2007 Institute of Physics)

50 nm holes (Fig. 12.70a) whereas less interaction of osteoblasts is observed with only anodized Ti surfaces (Fig. 12.70b). In addition, calcium deposition was found to be significantly higher when osteoblasts were cultured on CNTs grown from anodized Ti surfaces [12.238]. Surface-enhanced Raman scattering studies, furthermore, observed increased unfolding of vitronectin (a protein which mediates osteoblast function) and, thus, exposure of cell adhesive epitopes on nanoparticulate versus microparticulate materials [12.239, 12.237].

Composites of multiwalled carbon nanotubes (MWNTs) and hydroxyapatite on Ti 6Al4V medical alloys yield porous surfaces which are ideal for natural bone in-growth. Furthermore, cracks are effectively deflected by the MWNTs which contributes to an improvement of fracture toughness [12.240].

12.8.2 Nanostructured Bioceramics for Bone Restoration

Hydroxyapatite (HA), a calcium phosphate, is the ceramic constituent of bone, and the initial reason for its use as an implant material is that it forms direct bonds with living bone (see [12.241]). The adhesion and proliferation of osteoblast cells for bone growth are significantly higher on nanophase HA than on conventional HA [12.242] and are further increased on surfaces that contain $CaTiO_3$ [12.243].

Transplantation of osteogenic cells in a suitable matrix is another strategy for engineering bone tissue. 3D distribution and proliferation of cells within a porous scaffold are of clinical significance for the repair of large bony defects. In a 3D nanoporous HA scaffold, bone marrow stromal cells of rats were seeded in vitro. The cells adhered, proliferated, and differentiated well [12.244]. Likewise, bone scaffold material made of a nano-HA/collagen/polylactic acid (PLA) composite has been developed by biomimetic synthesis [12.245]. In an additional example, human osteoblast-like cells on a nanofluorapatite/collagen composite exhibited higher proliferation and differentiation rates than those on HA/collagen. These enhanced osteoblast cell responses were attributed to the fluorine release and the reduced dissolution rate [12.246]. Strong and bioactive composites have been developed by combining calcium phosphate ceramic (CPC) fillers with nanosized SiO_2 fused to whiskers in a resin matrix. The SiO_2 particles were fused to SiC whiskers to roughen the whisker surface for enhanced retention in the matrix. The mechanical properties of the non-cytotoxic CPC-whisker composites nearly matched those of cortical and trabecular bone [12.247]. Composites with needle-like HA crystals may be suitable for intraosseous implantation. These cements exhibit strengths matching those for cancellous bone and non-cytotoxicity qualifying for efficient bone repair surgery [12.248].

An optimum grain size of about 60 nm for osteoblast adhesion has been observed for Al_2O_3 [12.249], whereas the optimum particle size in the case of TiO_2 is about 45 nm. The following hydroxyapatite nanoparticles for treating bone defects are commercially available are Ostim® (Osartis GmbH, Germany); VITOSS® (Orthovita, Inc., USA); and NanOss™ (Angstrom Medica, USA) [12.250].

12.8.3 Fibrous Nanobiomaterials as Bone Tissue Engineering Scaffolds

Tissue engineering making use of nanoscale features to increase new bone synthesis is a potential alternative to current therapies. Nanofiber matrices have shown great promise as tissue engineering scaffolds for bone regeneration. The biomimetic environment of the nanofiber matrix (Fig. 12.71) affects cell–cell and cell–matrix interactions for favorable cell behavior. The advantages of a scaffold composed of ultrafine, continuous fibers are high porosity, variable pore size distribution, high surface-to-volume ratio, and importantly, morphological similarity to the natural extracellular matrix (ECM) [12.237]. In addition, both in vitro [12.251] and in vivo

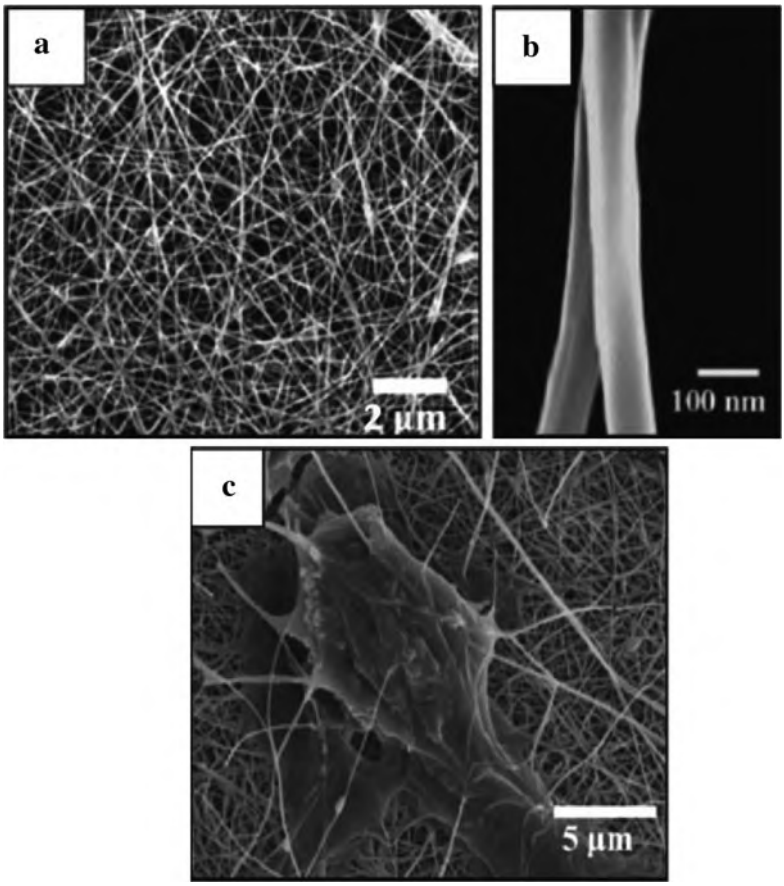

Fig. 12.71 Scanning electron micrographs of (**a**) electrospun nanofibrous mesh made of chitosan/(polyethylene oxide). (**b**) high magnification of the nanofibers shown in (**a**); and (**c**) osteoblast-like cells (MG 63) seeded on a nanofibrous mesh after 5 days culture. (Reprinted with permission from [12.253]. © 2005 Elsevier)

[12.252] results have shown that mesenchymal stem cells undergo osteogenic differentiation with the support of nanofibrous scaffolds with cell and type I collagen formation, and mineralization [12.252]. Human bone marrow stromal cells were found to adhere and proliferate well on a polymeric nanofiber scaffold. In fact, the cells were found to crosslink the nanofibers in the matrix and integrate with the surrounding fibers to form a 3D cellular network. Adherent osteoblast-like cells in electrospun (see Sect. 3.3) chitosan-based nanofibers are shown in Fig. 12.71c. Polymer nanofiber degradation generates space within a scaffold that facilitates cellular processes, such as proliferation and the deposition of newly synthesized ECM. Furthermore, reports indicate the feasibility of developing composite nanofibers by encapsulating nanohydroxyapatite particles within polyphosphazene nanofibers to develop scaffolds having better osteoconductivity and osteointegration [12.254].

The strategies used in bone research have also been applied to other musculoskeletal tissues. Nanofiber scaffolds have also been implemented in ligament and tendon reconstruction research [12.255], as well as in cartilage tissue engineering where nanophase titania has been used in biomaterial composites [12.256].

12.8.4 Tissue Engineering of Skin

In tissue engineering of skin there is much interest in producing scaffolds by electrospinning nanofibers for replacing the natural collagen skin scaffolds. This versatile method can produce 3D open porous structures that approximate the structure of collagenous dermis (see Fig. 12.72).

12.8.5 Angiogenesis

The formation of blood vessels (neovascularization or angiogenesis) has been identified as a problem for tissue-engineered constructs [12.257]. Angiogenesis can be substantially stimulated by self-assembled nanostructures of peptide amphiphile molecules on heparin, a complex organic acid (see Fig. 12.73). By this procedure, relatively rigid nanofibers are generated that can be loaded with vascular endothelial growth factor (VEGF), which when implanted in vivo gives rise to the stimulation of vascularization.

12.8.6 Promoting Neuron Adhesion and Growth

The stimulation of neuron adhesion and neurite outgrowth is of importance for the regeneration of both the peripheral and the central nervous system after injury or disease. It has been demonstrated (see [12.259]) that topographical features are of relevance for guiding axon growth and pathfinding. The preference of axons to grow on ridge edges rather than in grooves (see Fig. 12.74a) suggests that

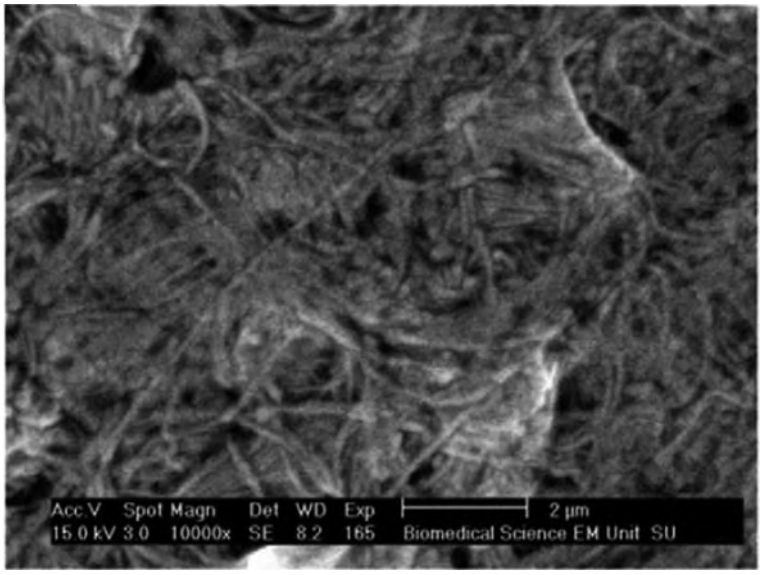

Fig. 12.72 A biodegradable electrospun scaffold. The scaffold fibers show good vascularization and penetration of granulation tissue. Scale bar: 2 µm. (Reprinted with permission from [12.257]. © 2008 Elsevier)

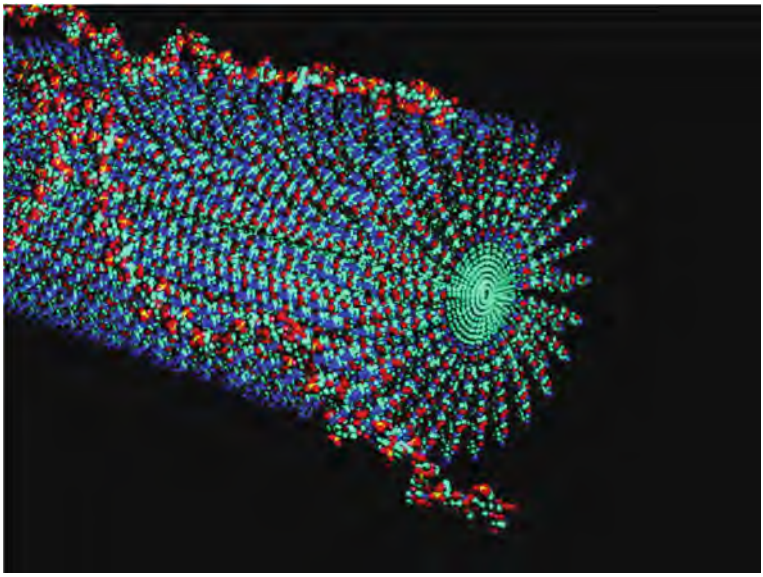

Fig. 12.73 Schematic of a heparin-nucleated nanofiber designed to promote the growth of blood vessels. The cylindrical nanostructure is formed by the aggregation of positively charged peptide amphiphile molecules, which have the capacity to bind to the negatively charged heparin chains and the poly-ion nucleates the fiber. (Reprinted with permission from [12.258]. © 2006 American Chemical Society)

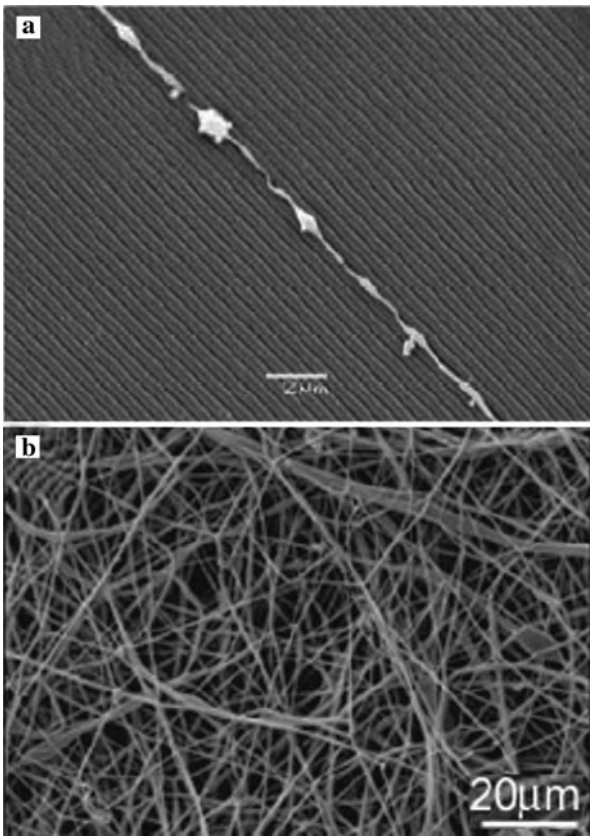

Fig. 12.74 (**a**) Scanning electron micrographs show that axons prefer to grow along the ridge edges and not in the grooves when the dimensions of the imprinted patterns are 100 nm in width and 500 nm pitch [12.262] ; (**b**) Scanning electron micrograph of random poly(ϵ-caprolactone) nanofibers produced by electrospinning. (Reprinted with permission from [12.259]. © 2008 Elsevier)

nanofeatures can be incorporated into tissue engineering design strategies to provide contact guidance for nerve regeneration. Creating a scaffold that mimics the in vivo 3D protein architecture of the extracellular matrix (ECM) ranging from 50 to 500 nm (see [12.259]) is pivotal for tissue regeneration as cell–matrix interactions are a vital component to cell survival, differentiation, and proliferation. Electrospun poly(ε-caprolactone) nanofibers, which are biodegradable and non-toxic (see [12.260]), have been shown to direct neural stem/progenitor cell (NSPC) differentiation into primarily oligodentrocytes (cells in brain supporting tissue) [12.261].

Peptide amphiphile (PA) molecules that self-assemble in vivo into supramolecular nanofibers were shown to promote axon elongation in a mouse model of spinal cord injury (SCI) [12.263].

12.8.7 Spinal Cord In Vitro Surrogate

Spinal cord injuries (SCI) give rise to paralysis. Central to the repair of these injuries is the need to regrow axonal bundles across the zone of damage which consists of

damaged and disrupted axonal processes, reactive glial and inflammatory cells, and developing glial scar tissue. The development of strategies for the regrowth of axons through a section of damaged spinal cord could benefit from the availability of an in vitro model in which the potential clinical utility of candidate techniques could be assessed. For this purpose, a spinal cord surrogate has been fabricated [12.264] from a composite of agarose gel as the parenchymal component and 8 μm thick glass fibers aligned along the surrogate axis to simulate the axonal bundles. This "artificial spinal column" (Fig. 12.75a) reproduces with its pores (pore size 10–100 nm) the characteristics of porous flow in the central nervous system (CNS; extracellular space in the tissue about 20 nm) and the anisotropic anatomical features of the spinal cord [12.264]. These properties are demonstrated when bromphenol blue dye is injected into the artificial spinal column with a spreading preferentially along paths aligned with the fibers (Fig. 12.75b–d). This is a consequence of a porous annulus (with the thickness of the diameter of a gel pore) around each fiber. The porous zones are formed because the polysaccharide gel molecules favor the formation of cross-links at junction zones removed from the fiber surface [12.264]. This surrogate structure may enable the preclinical evaluation of infusion strategies foreseen for drug and cell delivery into living spinal cord tissues. It also may serve

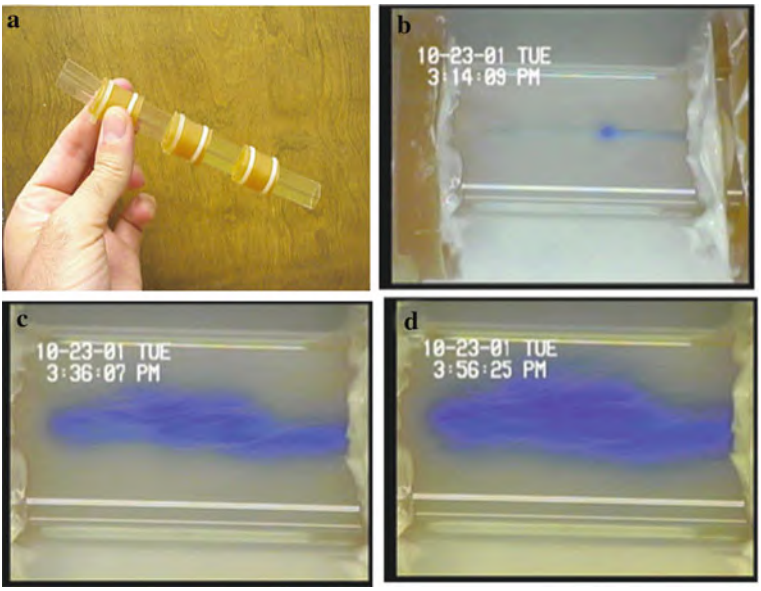

Fig. 12.75 (**a**) Mechanical structure of the "artificial spinal column" that serves as a glass container for the surrogate spinal cord. The hose junctions can allow for simulation of the effects of the intervertebral disks and facet joints. (**b–d**) Infusion of bromphenol blue dye into the spinal cord surrogate showing the volume of distribution at (**b**) 13 min, (**c**) 35 min, and (**d**) 55 min. The infusate is flowing preferentially along the fiber tracts within the gel. (Reprinted with permission from [12.264]. © 2002 Institute of Physics)

as a medium to study the regrowth of axons in order to model spinal cord tissue regeneration.

12.8.8 Efforts for Synthesizing Chromosomes

A synthetic chromosome has been constructed by a team of scientists assembled by Craig Venter and led by the Nobel laureate Hamilton Smith [12.234]. Using lab-made chemicals, the scientists have painstakingly stitched together a chromosome that is 381 genes long and contains 580,000 base pairs of genetic code. The DNA sequence is based on the bacterium *Mycoplasma genitalium* which the team pared down to the bare essentials needed to support life, removing a fifth of its genetic makeup. The wholly synthetically reconstructed chromosome was christened *Mycoplasma laboratorium*. It is then transplanted into a living bacterial cell and in the final stage of the process it is expected to take control of the cell and, in effect, become a new life form.

The new life form will depend on its ability to replicate itself and metabolize on the molecular machinery of the cell into which it has been injected, and in that sense it will not be a wholly synthetic life form. However, its DNA will be artificial, and it is the DNA that controls the cell and is credited with being the building block of life [12.234].

12.9 Nanosurgery – Present Efforts and Future Prospects

Incisions have become smaller, dissections have become more focused, and microsurgery performed under an operating microscope is now the norm. However, even current "microsurgery" is "macro" when compared with the dimensions that are relevant at the nanoscale level. Currently, several technical advances are leading to the manipulation of cellular and subcellular structures at the micrometer and nanometer scales [12.265].

12.9.1 Femtosecond Laser Surgery

By tightly focusing a femtosecond laser pulse, collateral damage to surrounding structures is negligible because the interaction of the laser pulse with the biological material occurs on a much shorter timescale than the heat transfer into the material [12.266]. This reduces the likelihood that the cell itself will be injured. In fact, spatial resolution in the nanometer range can be attained [12.267]. Femtosecond laser pulse energies between 1.2 and 1.7 nJ produce cuts as narrow as 200 nm. Figure 12.76 demonstrates the ablation of a single mitochondrion via precision targeting of the femtosecond laser. Additional studies have demonstrated that ablation of subcellular organelles can be accomplished in a live cell without compromising

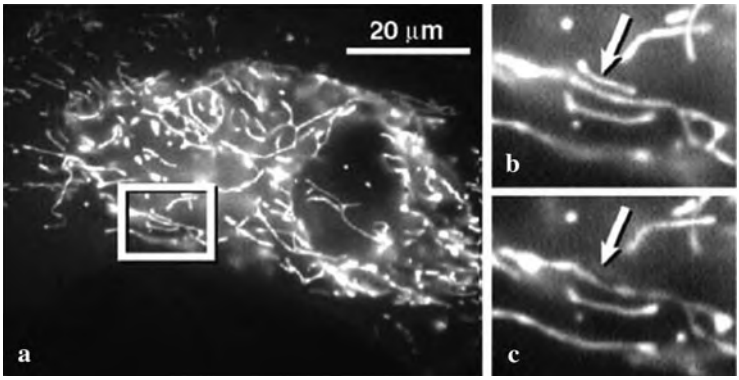

Fig. 12.76 Ablation of a single mitochondrion within a living cell. (**a**) Fluorescence image of multiple mitochondria. Target mitochondrion (*arrow*) before (**b**) and after (**c**) ablation with 2 nJ laser pulses, where the neighboring mitochondria are unaffected. (Reprinted with permission from [12.268]. © 2005 Tech Science Press)

cell viability [12.269]. These techniques have potential applications in intracellular surgery, including single chromosome dissection, non-invasive inactivation of specific genomic regions and individual chromosomes, and highly localized gene and molecular transfer. Femtosecond lasers have also been applied to gene therapy. A variety of mammalian cells could be directly transfected with DNA, without destroying the cellular structure by using femtosecond lasers to create a single, site-specific, localized perforation in the cell membrane through which DNA could enter (Fig. 12.77).

12.9.2 Sentinel Lymph Node Surgery Making Use of Quantum Dots

Sentinel lymph node mapping is a common procedure used to confirm the presence of cancer in a single "sentinel" lymph node (SNL) [12.265]. The current surgical procedures, using radioactive isotopes for lymph node mapping, are, however, inexact and result in more extensive lymph node dissection than is necessary. Near-infrared fluorescent quantum dots (10–20 nm) can be used to provide real-time image guidance for the dissection of SNL [12.271]. After injection of 400 pmol of quantum dots in a 35 kg pig the SNL position can be identified rapidly (see Chap. 11.2; Fig. 11.16).

12.9.3 Progress Toward Nanoneurosurgery

The study of neuronal regeneration is critical to the treatments for human neurological diseases. Surgical research has been directed at the neural circuit of

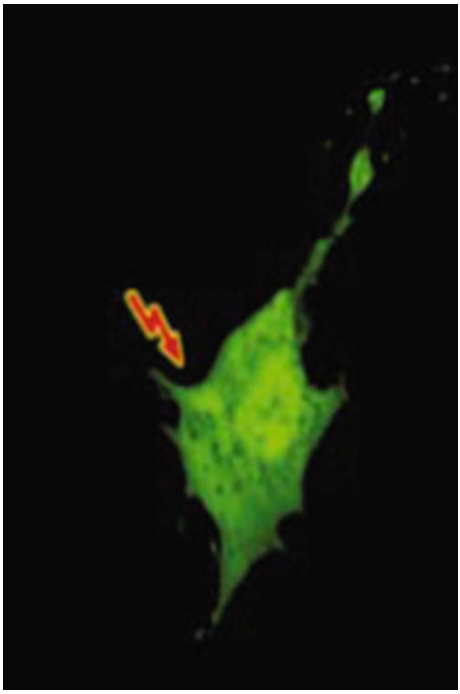

Fig. 12.77 Targeted transfection of Chinese hamster ovarian (CHO) cells with femtosecond lasers. The cell is suspended in a culture medium containing a plasmid DNA vector encoding enhanced *green* fluorescent protein (EGFP). A near-infrared laser pulse is focused precisely on the edge of the cell membrane (*arrow*) for single, site-specific, transient perforation of the cell membrane so that the transfection could occur. The expression of EGFP is clearly demonstrated throughout the cell. (Reprinted with permission from [12.270]. © 2002 Nature Publishing Group)

Caenorhabditis elegans nematode worms, that totals 302 neurons, for the ablation of entire neuronal cell bodies. But smaller structures, such as axons and dendrites, have not been targeted. To overcome this limitation, femtosecond laser dissection has been applied to *C. elegans*, where in a bundle of fluorescently labeled neurons the middle neuron was severed without the disruption of the neighboring neurons (Fig. 12.78a, b). For the study of the regeneration of motor neurons, laser surgery in *C. elegans* [12.272] and labeling with green fluorescent protein were employed. These neurons extend circumferential axons to form synapses with body muscles. When these axons were severed by laser pulses (Fig. 12.78c–f), both ends initially retracted, but the majority of the cut axons regrew toward their distal ends within 24 h and these regenerated axons were functional.

12.9.4 Future Directions in Neurosurgery

The visage of trillions of nanorobots streaming through our blood vessels (Fig. 12.79), intent on entering cells, performing nanosurgery on our very genes

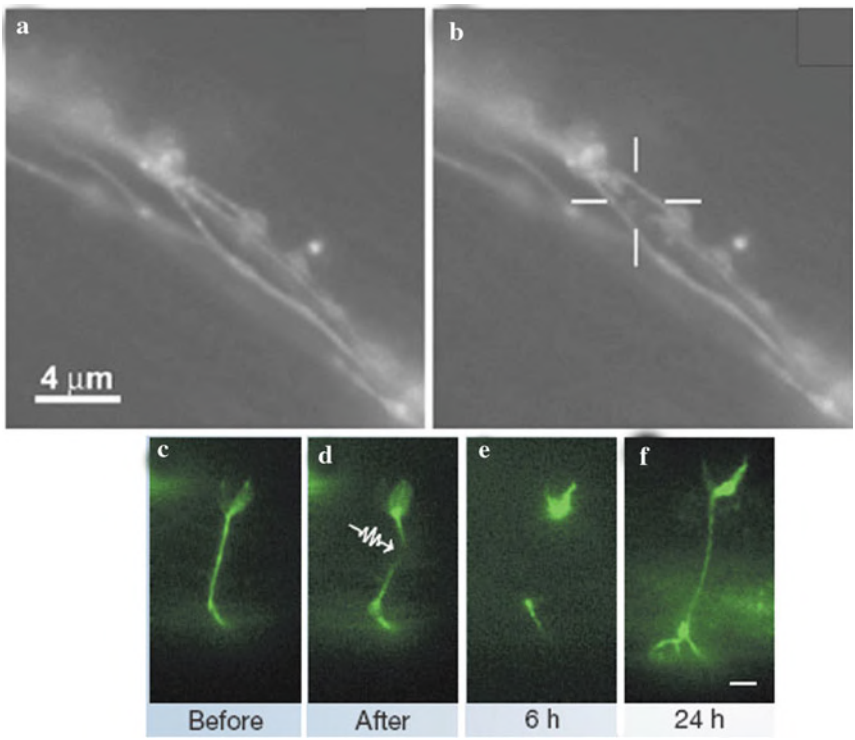

Fig. 12.78 (**a**, **b**) Femtosecond laser dissection of a single neuronal dendrite in a neuron bundle of *C. elegans* before (**a**) and after (**b**) dissection with a laser pulse of 3.6 nJ. The cross hairs in (**b**) indicate the region targeted by the laser. Note that the central dendrite is severed, whereas the outer two remain intact [12.267]. (**c**–**f**) Functional regeneration after laser axotomy. Fluorescent images of axons labeled with green fluorescent protein shown before, immediately after, and several hours after axotomy with femtosecond lasers. The axon has regenerated after 24 h. The *arrow* indicates the site of the axotomy. Scale bar: 5 µm [12.272]. (Reprinted with permission from [12.267] (**a**) (**b**) and [12.272] (**c**–**f**). © 2005 Elsevier (**a**) (**b**) and © 2004 Nature Publishing Group (**c**–**f**))

by means of femtosecond laser systems and optical tweezers, is still beyond the realm of possibility. However, current developments in nanotechnology are certain to become integrated into the delivery of medical and neurosurgical care in the near future [12.265]. Nanorobots are the stuff of science fiction. Yet, swimming microrobots propelled by artificial flagella bring that fantasy closer to reality [12.273].

There is a number of applications of nanotechnology that are in development today that could theoretically be integrated into surgical procedures to create highly advanced therapeutic modalities [12.265]. For example, intracranial tumor labeling with systemic injection of multimodal nanoparticles could improve intraoperative visualization of tumor margins. This would be particularly useful in glioma surgery, where tumor margins are frequently indistinct, and would greatly enhance the

Fig. 12.79 Nanorobots (nanobots). Artistic conception of a nanobot injecting a single red blood cell to obtain diagnostic information or implant therapeutic agents. (Reprinted with permission from [12.265]. © 2010 agentur-focus)

capabilities of image guidance systems. In addition, after open craniotomy, nanoparticulate suspensions of drug delivery systems or microchips/nanochips could be implanted within the resection cavity for slow release of antitumor agents to provide continuous prophylaxis against tumor recurrence. Another approach would be the implantation of drug delivery systems which could be activated in the presence of tumor antigens by integrated sensitive nanosensors. Intracranial pressure monitoring and cerebrospinal fluid shunting procedures will also be impacted by developments in nanotechnology. The incorporation of integrated nanotechnology platforms such as nanofluidic chips with nanowire sensors could theoretically improve shunt performance. In addition, bulky battery packs could be replaced with nanoscale hydrogen fuel cells derived, e.g., from nanotubes. Nanowire sensors could monitor the levels of neurotransmitters, thereby providing a means to regulate the amount of neural stimulation necessary to augment neurological function. Such devices could even be implanted into the brain or spinal cord after stroke or catastrophic spinal cord injury. Significant research effort is being devoted to the study of electrical interfacing between individual neurons and silicon microchips (Fig. 12.80) with the goal of developing "brain implants" that will enable restoration of neurological function [12.274]. A platform for single axon repair using combined microtechnology and electrokinetic axon manipulation has been developed [12.275]. Nanofiber polymer scaffolds that morphologically resemble collagen fibrils can be seeded with stem cells to generate cartilage and bone tissue in vivo, indicative of potential application in spinal surgery [12.251]. In fact, biomimetics and the development

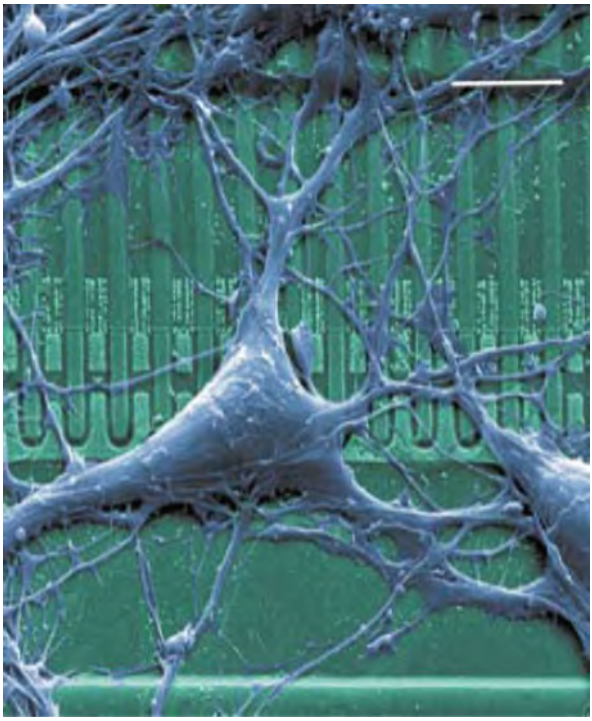

Fig. 12.80 Neuron–silicon interface. Colored electron micrograph of a cultured hippocampal neuron on a silicon chip with a silicon dioxide surface. An array of field-effect transistors is visible as *dark squares*. Scale bar: 10 μm. (Reprinted with permission from [12.274]. © 2002 Wiley-VCH)

of bioartificial organs will be impossible without the use of molecularly manipulated nanostructures, nanoelectronic interfacing, nanoscale drug delivery systems, etc. (see [12.265]).

A nanosurgery system based on a sub-nanosecond pulsed UV laser for the localized severing of biological polymers has been employed [12.276] to study the biophysical properties of the cytoskeleton by severing microtubules (MTs) and to test the models of the dynamic cytoskeleton behavior. The organized behavior of the cytoskeleton is fundamental for biological activities [12.277] involved in the generation of cell shape, polarity, movement, cell division, and intracellular transport. Defects in cytoskeletal functions have been implicated in vascular diseases, neuronal degeneration, and cancer (see [12.276]). The mechanism of severing likely involves nonlinear absorption of highly focused laser pulses which results in confined ionization and ultimately forms a plasma (see [12.276]).

12.10 Nanodentistry

Nanodentistry will make possible maintenance of comprehensive oral health by involving the use of nanomaterials, biotechnology (including tissue engineering), and ultimately nanorobotics [12.278]. Although the last point of this listing may be

highly speculative, dentistry will be strongly impacted by the current developments in nano- and biotechnologies as discussed with a few examples in the following.

12.10.1 Nanocomposites in Dental Restoration

Dental nanocomposites [12.279] of 75 nm silica particles (Fig. 12.81) treated in 3-methacryloxypropyltrimethoxysilane (MPTS) and dispersed in a resin used for conventional restorative composites (3 M ESPE Dental Products) exhibit mechanical properties equivalent to those of microhybrid composites [12.279]. The silane MPTS acts as a good coupling agent [12.280]. One end contains three methoxy sites that potentially etherify with hydroxyls on the hydrated surface of the silica nanoparticles to produce one to three possible ether bridges and chemically bond

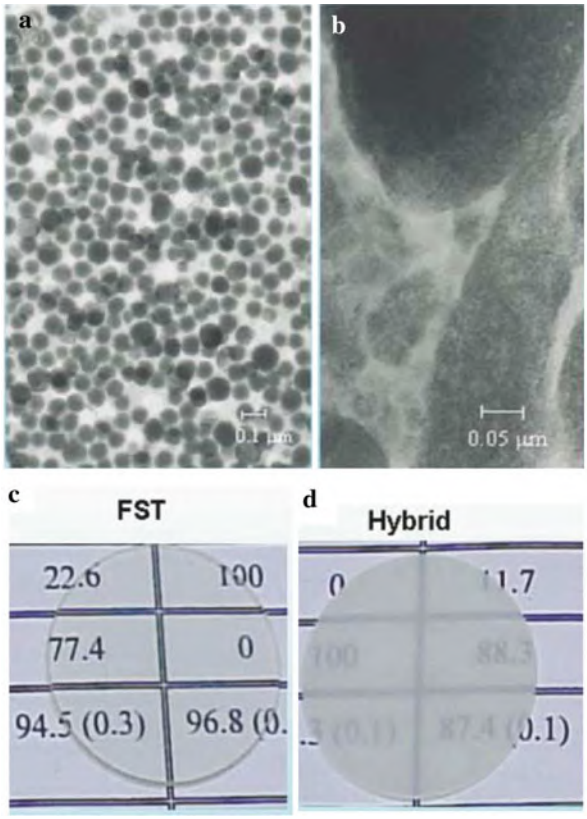

Fig. 12.81 Transmission electron micrographs and visual opacity of dental nanocomposites. (**a**) Composite with nanometric particles. (**b**) Conventional composite with a hybrid filler of micro- and nanoparticles. (**c**) Negligible visual opacity and full translucency of the nanocomposite. (**d**) Visual opacity of a composite with a hybrid filler of micro- and nanoparticles. (Reprinted with permission from [12.279]. © 2003 American Dental Association)

to that surface. The opposite end is a double-bond functional methacrylate, which becomes co-polymerized with the resin matrix to complete the chemical coupling. Yet, there is evidence of several problems in this hypothetical chain of events. The silane has a propensity to dimerize or trimerize creating methacrylate moieties that no longer can act as coupling agents, making coupling poor. Due to the nanoscale of these interactions, it has been impossible to date to measure the extent of actual chemical interaction along filler particles. Finally, when shrinkage does occur, it produces stresses at external interfaces with tooth structure and internal interfaces with filler particles. Shrinkage leads to porosity which may be concentrated at critical interfaces, having a great effect. If these shortcomings can be managed, there is a strong indication that the mechanical properties of today's composites could be substantially improved [12.280].

Nanocomposites display a much higher glossiness and a much higher gloss retention, measured after 500 tooth brush cycles, than conventional composites. This is due to the removal of particles of only nanosizes due to tooth brush abrasion. In addition, the nanocomposite shows a low visual opacity and high translucency (Fig. 12.81c, d) due to the reduced scattering of light with wavelengths much longer than the nanoparticle size. This allows the clinician to construct a wide range of shades and opacities and, thus, provide highly esthetic restoration in all posterior and anterior applications [12.279].

12.10.2 Nanoleakage of Adhesive Interfaces

The clinical performance of present day adhesives has significantly improved, allowing adhesive restoration with a high level of clinical success (see [12.281]). While the hermetic sealing between current bonding systems and the enamel of the tooth has been achieved, it is still a challenge to seal the resin–dentin interface due to the heterogeneous dentin structure and surface morphology. Bonding compromised by leakage is prone to degradation over time. Many adhesives show decreased bond strength as well as increased nanoleakage under long-term water storage [12.282]. Therefore, the sealing ability of an adhesive, providing long-term mechanical stability is of importance for the success of a resin restoration. The nanoleakage within the resin–dentin interface has been examined by studying silver penetration, from an external solution of silver salt with subsequent photodeveloping to metallic silver grains, via back-scattered electron imaging of field-emission scanning electron microscopy (FE-SEM) and energy-dispersive x-ray spectroscopy (EDS), making use of various adhesive resins. As demonstrated by negligible silver penetration (Fig. 12.82), nanoleakage can be suppressed by using a two-step self-etching adhesive (SE) or a one-bottle one-step self-etching adhesive (TB; Kuraray, Osaka, Japan; for compositions, see [12.281]). However, whereas the self-etch adhesive SE can bond strongly and stably both with the human enamel surface and with human dentin surface (see [12.281]), with regard to TB more studies concerning its bonding efficiency are necessary. Clinically, it is preferred that adhesive systems are hydrophilic during application, then become hydrophobic after application, and completely seal the restoration margins for a significant time.

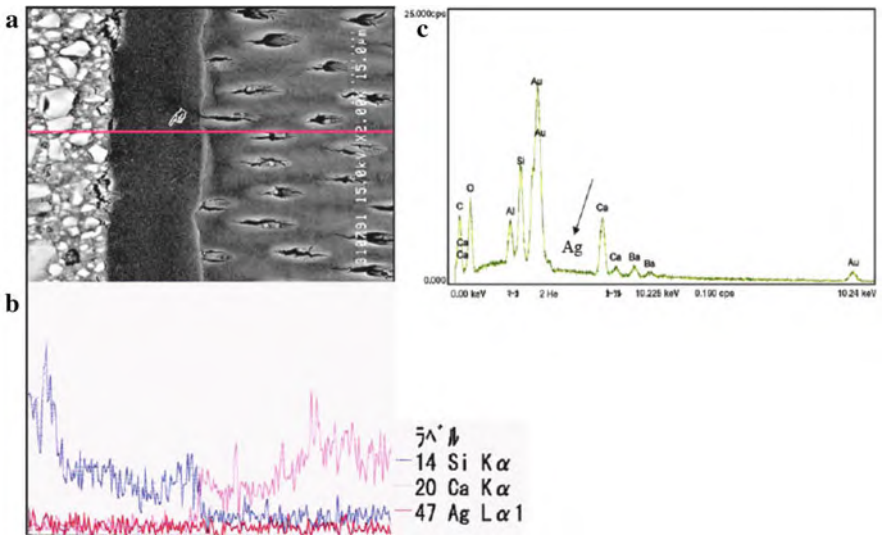

Fig. 12.82 (**a**) Energy-dispersive x-ray spectroscopy (EDS) of a package of composite (*left*), TB adhesive (*center*), and superficial dentin (*right*). No silver peak is visible in the energy spectra (*black arrow* in **c**). In subsequent line scan (**b**) along the *red line* (finger pointer in (**a**)) also no silver (*red curve*) and therefore no nanoleakage could be detected. (Reprinted with permission from [12.281]. © 2007 Elsevier)

12.10.3 Nanostructured Bioceramics for Maxillofacial Applications

Bioceramics in dentistry comprise inert, bioactive, resorbable, and composite systems. Nanophase bioceramics for clinical applications in maxillofacial surgery can be promising candidates for bone tissue engineering. Such applications may include replacement of lost teeth, filling of jaw defects or reconstruction of the mandible, and the temporomandibular joint [12.241].

Calciumphosphate ceramics (CPC; with hydroxyapatite $Ca_{10}(PO_4)_6(OH)_2$) have been used for dental implants, periodontal treatment, alveolar ridge augmentation, and maxillofacial surgery. Nanophase hydroxyapatite (HA) represents a promising class of maxillofacial implant formulations with improved osseointegrative properties, because the adhesion and proliferation of osteoblasts on nano-HA are significantly higher than on conventional HA. Nanoscale alumina (Al_2O_3) and titania (TiO_2) demonstrate similar properties. In particular, increased osteoblast function on Al_2O_3 nanofibers [12.283, 12.284] suggests that these ceramics may be ideal materials for next-generation maxillofacial reconstruction with increased efficacy (see [12.241]).

On novel nanocomposites consisting of a blend of polylactic acid (PLA) and carbon nanotubes, cell proliferation can be stimulated by electric currents through

the nanotubes, making this composite also a promising material for maxillofacial implants [12.285].

12.10.4 Release of Ca–PO_4 from Nanocomposites for Remineralization of Tooth Lesions and Inhibition of Caries

Secondary caries of the tooth-restoration margins is the most-frequent reason for replacement of restorations. Replacement dentistry accounts for 70% of all operative work and costs $5 billion/year in the United States (see [12.286]). Recent studies show that calcium (Ca) and phosphate (PO_4) ions can be released from composites to supersaturated levels for apatite precipitation and remineralization of tooth lesions in vitro [12.287]. For enhanced Ca and PO_4 release from a high-strength dental material, a composite of nanophase $CaHPO_4$ (DCPA), β-Si_3N_4 whiskers (length ~5 μm, diameter ~0.4 μm) fused with 40 nm SiO_2 particles, and a two-part chemically activated resin was synthesized [12.286]. At a mass fraction of the filler (DCPA + whiskers) of 75%, the flexural strength of 114 MPa was not much different from the 112 MPa of a hybrid control. The elastic modulus of the nanocomposite, 14.9 GPa, was higher than that of the control hybrid (11.7 GPa). The release of Ca and PO_4 ions from a 2 × 2 × 12 mm^3 composite specimen with 75% filler, in a 50 mL NaCl solution after 56 days was 0.65 mmol/L Ca and 2.29 mmol/L PO_4.

The elastic modulus of the composite with 75% filler is somehow lower than the 18 GPa of dentin, but higher than the 11.7 GPa of the commercial, stress-bearing, non-releasing composite control. The ion release properties of the present nanocomposite are superior to those of earlier microphase Ca–PO_4 composites with a release of 0.3–1.0 mmol/L of Ca and 0.1–0.7 mmol/L of PO_4 [12.287]. The nonlinear dependence of the ion release on the DCPA volume fraction (Fig. 12.83) may be

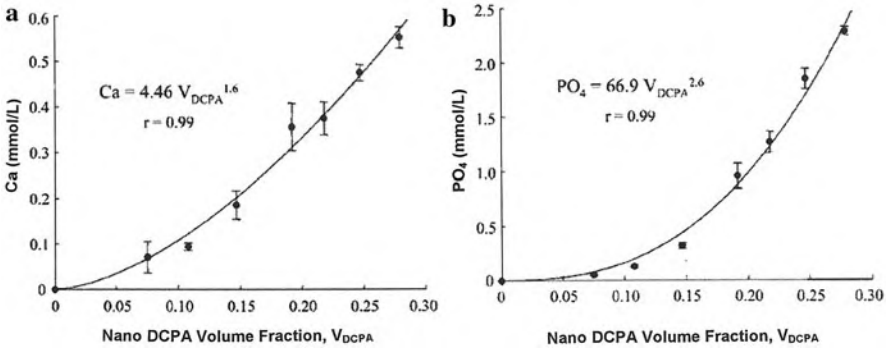

Fig. 12.83 Relationships between (**a**) Ca and (**b**) PO_4 release and nano-DCPA volume fraction V_{DCPA}. (Reprinted with permission from [12.286]. © 2007 SAGE)

due to a decrease of the resin polymerization conversion with increasing filler level and consequently an increased diffusion flow of water and ions through the resin.

Regarding the potential applications of the nano-DCPA-whisker composites with the combination of stress-bearing and caries-inhibiting capabilities, the composites with 30–50% fillers may be suitable for use as Ca–PO_4-releasing tooth cavity liners, adhesives, and pit-and-tissue sealants. Flowable DCPA-whisker composites with 50–60% filler may be used as crown cements and orthodontic bracket cements, and to repair defective margins. Composites with 70–75% fillers may be useful in stress-bearing and caries-inhibiting restorations [12.286].

12.10.5 Growing Replacement Bioteeth

Lost teeth are usually replaced with inert prosthetic versions. After age 50, an average of 12 teeth stand to have been lost. In theory, a natural tooth made from the patients own tissue and grown in its intended location would be the best replacement, although such bioengineered teeth have been little more than a dream. Recently, however, progress in understanding how teeth first develop has combined with advances in stem cell biology and tissue engineering to bring us close to the realization of biological replacement teeth. Moreover, teeth will serve as a crucial test of the feasibility of different tissue engineering techniques because mistakes with teeth would not be life threatening and could be corrected [12.288]. A good way to start learning how to build teeth, therefore, is to observe how nature does it.

Six weeks after conception, when a human embryo is less than an inch long, cells are already guiding the formation of its teeth (see [12.288]). Oral epithelial cells (which are destined to line oral cavities) send out the first instructions to mesenchymal cells (which will produce jawbone and soft tissue) to begin odontogenesis or tooth formation. A tooth bud is formed by the embryo's seventh week and a bell-shaped structure after 14 weeks [12.288]. Eventually, the epithelium will become the visible outer enamel of the tooth that erupts from the baby's gum line some 6–12 months after birth, and the mesenchymal cells will have formed the non-visible parts of the tooth, such as dentin, dental pulp, cementum, and periodontal ligament that attaches the tooth to the jawbone. The shape of a tooth will be determined by its position via the so-called homebox genes. The homebox gene called *Barx1*, for example, is switched on, or expressed, by mesenchymal cells in the positions where molar teeth will grow. Because the ability to predict and control tooth shape will be essential for the creation of engineered teeth, scientists can use genes such as *Barx 1* as predictive markers of future shape for teeth created in the lab [12.288].

Three milestones must be reached for the engineering of replacement biological teeth. Sources of cells that can form teeth and are easily obtained from patients themselves must be identified. These teeth must be able to develop in the adult jaw, producing roots. And the shape of the biological teeth must be predictable so that they match the patient's own teeth. Experiments for growing teeth from scratch are primarily performed with mouse cells [12.288]. For example, when stem

cells from adult bone marrow took the place of oral mesenchymal cell populations, the transplanted constructs produced structurally correct teeth, demonstrating that embryonic mesenchyme can be replaced with adult stem cells to generate new teeth. Efforts are continuing for seeking an effective population of substitute cells that could be derived from an adult source [12.288]. In addition, human somatic cells reprogrammed to induced pluripotent stem cells (iPS) [12.289, 290], that exhibit the essential characteristics of embryonic stem cells, could be envisaged to induce the appropriate initiating signals for odontogenesis.

The next experimental step was to see whether teeth could be formed within the mouth. For that, tooth buds from embryonic mice were transplanted into the diastema, the empty region between the molars and incisors, in the upper jaw of adult mice. Three weeks later, the teeth identified in the diastema had formed in the correct orientation, were of appropriate size for the mice, and were attached to underlying bone by soft connective tissue (see [12.288]).

A problem for the teeth generated by any of the tissue engineering methods was that they did not develop roots [12.287]. Efforts were, however, recently focused on stem cells found in the root apical papilla, tissue connected to the tip of the root that is responsible for the root's development [12.291]. These apical papilla cells, which can be considered as younger stem cells [12.291] than pulp cells, provide better tissue regeneration – leading to the formation of all root tissues as well as dentin and cementum, the support substances located in the crown and root, respectively. After the identification of stem cells for creating a new root, an incisor extracted from a miniature pig, which has a similar dental structure to humans, was replaced with stem cells from the extracted wisdom teeth of 18- to 20-year-old humans. Three months after loading the apical papilla stem cells into the incisor socket of the pig, a porcelain crown has been fitted over the mineralized roots and ligaments developing there. Six months after stem cell implantation, the tooth was believed to have a strength sufficient to withstand normal wear and tear [12.292].

12.11 Risk Assessment Strategies and Toxicity Considerations

At the nanoscale, material properties vary as a function of size, which not only enables new benefits but also may lead to unintended health and environmental risks [12.293]. The increased presence of nanomaterials in commercial products has resulted in a growing public debate on the toxicological and environmental effects of direct and indirect exposure to these materials. At present, these effects are not completely elucidated [12.294], but this topic is discussed by a number of agencies and workshops (see, e.g., [12.293, 12.295–12.305]). However, the ". . .overall federal government (USA) response to identifying and managing nanotechnology risks. . ." are described as ". . .slow, badly conceptualized, poorly directed, uncoordinated and undefended. . ." (see [12.306]). But a number of efforts have been initiated worldwide to investigate the toxicological effects of nanomaterials, including the program "Nanocare" of the German Federal Government [12.307]. Yet, the National

Research Council of the United States criticizes the recent federal nanotechnology plan for lacking risk research [12.308]. The report of the UK Royal Commission on Environmental Pollution (RCEP) [12.309] has concluded that the existing framework of regulation is sufficient and with adaptions should be capable of dealing with the use of nanomaterials.

The concern that nanotechnology will go out of control has been put forward by several futurists [12.310–12.312] and adopted gleefully by science fiction writers [12.313, 12.314]. It is the idea of small machines that can replicate themselves ("assemblers") and that escape the laboratory. Many scientists, however, see no way that such devices can exist and that this concern can be dismissed [12.315].

A most serious risk of nanotechnology may arise from the fast development of electronics, computers, and telecommunication – fast processors, ultradense memory, methods for searching data bases, ubiquitous sensors, electronic commerce, and banking – into most aspects of life, which is making it increasingly possible to collect, store, and sort enormous quantities of data about people [12.316].

The public perception of nanotechnology is currently studied [12.317, 12.318]. In studies aimed at determining how members of the public would react to balance information about nanotechnology risks and benefits, no evidence for the "familiarity hypothesis" has been reported that support for nanotechnology will grow as awareness of it expands [12.319]. Studies of the influence of religious beliefs on attitudes toward nanotechnology in the United States and Europe showed more positive attitudes about nanotechnology among less religious people [12.320].

In the present section, strategies will be described for environmental, health, and safety (EHS) research and how to gain information needed to enable sound risk assessment and risk management decision making [12.295] in order to guide commercial development [12.293, 12.298, 12.320]. Finally, the present state of specific toxicity studies on various types of nanoparticles [12.294, 12.321–12.323] will be outlined.

12.11.1 Risk Assessment and Biohazard Detection

Risk assessment and biohazard detection of nanomaterials has to comprise the following aspects [12.295]:

- nanomaterial characterization,
- standard terminology,
- standard reference nanomaterials,
- techniques for detecting nanomaterials in biological media,
- in vivo tests and correlation to in vitro tests
- in vitro test validation, and
- model development

Research needs are, furthermore, categorized within the following areas:

- metrology for risk measurement,
- assessment of bioavailability, and
- characterization of potential mobility of embedded nanomaterials

Within these aspects, information on nanoparticle translocation, agglomeration, and toxicity are of particular relevance. In addition, the adequacy of traditional toxicology tests should be scrutinized and cross-disciplinary communication is a prerequisite [12.298].

For *toxicology tests* cytotoxicity assays are utilized (see [12.321]). One simple cytotoxicity test involves visual inspection of cells with bright-field microscopy for changes in cellular or nuclear morphology. However, the majority of cytotoxicity assays used measure cell death via colorimetric methods. Neutral red is a dye that can cross the plasma membrane by diffusion. If the cell membrane is altered, the uptake of neutral red is decreased, allowing for discernment between live and dead cells. Trypan blue is only permeable to cells with compromised membranes; therefore, dead cells are stained blue while live cells remain colorless. The LIVE/DEAD viability test, which includes the two chemicals calcein acetoxymethyl and ethidium homodimer is another assay measuring the number of damaged cells. A third cytotoxicity assay used in several carbon nanoparticle studies (see [12.321]) is lactate dehydrogenase (LDH) release monitoring, where the amount of LDH released is proportional to the number of cells damaged or lysed. The most widely used test is the 3-(4,5 dimethylthiazol-2-yl)-2,5-diphenyl tetrazolium bromide (MTT) viability assay for mitochondria activity which prevails only in living cells.

12.11.2 Cytotoxicity Studies on Carbon, Metal, Metal Oxide, and Semiconductor-Based Nanoparticles

In general, cells can survive short-term exposure to low concentrations (< 10 μg/mL) of nanoparticles. However, at high doses, several groups have found cytotoxic effects (see [12.321]). As causes for the increase in cell death observed at higher concentrations, the generation of reactive oxygen species, and the influence of cell internalization of nanoparticles are common findings.

While much of the function of nanoparticles is due to their core structure, the surface coating defines much of their bioactivity [12.321]. Surface charge also plays a role in toxicity, with neutral surfaces being most biocompatible. Even if no cell damage or death may be apparent after nanoparticle exposure, changes in cellular function may result. Therefore, sub-lethal cellular changes should also be taken into account and tested for, e.g., by genomic and proteomic array tests to explore the cellular signaling alterations behind the toxicity. Furthermore, it should be pointed out that although nanoparticle-induced cytotoxicity has been reported by several

groups, it should be kept in mind that in vitro results can differ from what is found in vivo and are not necessarily clinically relevant [12.321].

In the following, a selection of studies of the toxicological impact of nanoparticles will be presented (see [12.294, 12.321, 12.322]).

Carbon and organic nanoparticles. Pristine C_{60} is considered to be fairly non-toxic (see [12.321]), whereas C_{60} derivatives are relatively non-toxic at low concentration (0.24 ppb) but more cytotoxic at the highest concentration [12.324].

Single-walled carbon nanotubes (SWNTs) have typically been labeled as having cytotoxic effects at high concentrations (see [12.321]). As illustrated in Fig. 12.84, cell death was highest in the cultures exposed to pristine SWNTs while functionalized SWNTs can yield high cell viability. It may be mentioned here that biodegradation of SWNTs through natural, enzymatic catalysis has been demonstrated recently [12.326].

Long fibers (>20 μm) of multiwalled carbon nanotubes (MWNTs) cause inflammation of the mesothelium of mice [12.327], the cell layer that covers the chest (pleural) peritoneal cavities, similar to asbestos, whereas the samples without long but short fibers did not induce inflammatory response. This short-term study [12.327] does not show whether the inflammatory response leads to mesothelioma (cancer).

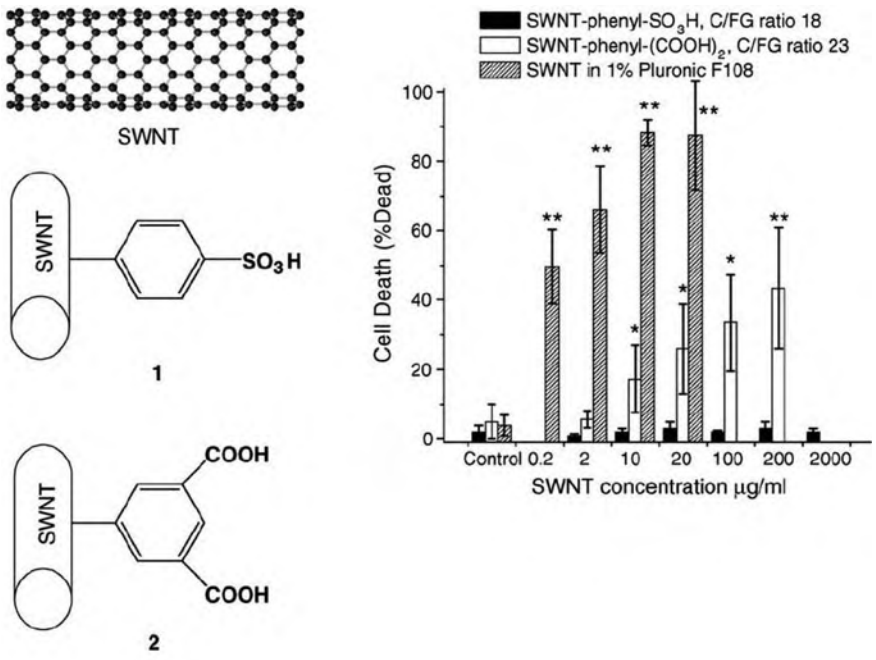

Fig. 12.84 Structure and human dermal fibroblast cytotoxicity data for single-walled carbon nanotubes (SWNTs) and derivatives [12.321, 12.325]. (Reprinted with permission from [12.335]. © 2006 Elsevier)

Cationic polyamidoamine dendrimer (PAMAM) nanoparticles, a class of nanomaterials that are being widely developed for clinical applications, can induce acute lung injury in vivo. Potential remedies are suggested [12.328].

Nanostructured metals. Au nanoparticles have great promise for bioimaging and therapy. Large nanoparticles (18 nm) with surface modifiers did not appear to be toxic at concentrations up to 250 μM [12.329]. In contrast, 1.4 nm Au nanoparticles stabilized by triphenylphosphine cause rapid cell death by necrosis [12.330] as shown by the IC_{50} values (the half-maximal inhibitory concentration – the concentration of an inhibitor that is required to achieve 50% target inhibition) in MTT assays.

Gold nanoshells, which are being developed for imaging contrast and photothermal therapeutic medical applications, show no physiological complications in mice [12.331].

Metal oxide nanoparticles. These types of nanoparticles are used in cosmetics and sunscreens (TiO_2, ZnO), dental fillers (SiO_2), or as contrast materials for magnetic resonance imaging (iron oxide, see Sect. 12.2). It should be pointed out, however, that TiO_2 absorbs about 70% of the incident UV radiation which leads for TiO_2 with anaphase structure (see [12.305]) in aqueous environments to the generation of hydroxyl radicals ($^{\circ}OH$). This may cause DNA strand breaks in human cells [12.332]. In other assessments (see [12.333]) TiO_2 and ZnO nanoparticles have been stated to be safe and non-toxic.

Whereas bare iron oxide nanoparticles at 250 μg/mL concentrations were shown to induce a loss in fibroblast viability [12.334], poly(ethylene glycol) (PEG)-coated iron oxide nanoparticles are found to be relatively non-toxic [12.335].

Charged nanoparticles can alter the local physical properties of lipid membranes, which could shed light on the interactions between living cells and nanomaterials [12.336].

Semiconductor nanoparticles. Since some of these nanoparticles or quantum dots (QDs) are composed of toxic elements including Cd, Se, Pb, and As, toxicity may be related to the release of free metal ions and the crucial factor, therefore, is stability. In mouse models, no toxicity was observed for ZnS-capped CdSe QDs coated with poly(ethylene glycol) (PEG) [12.337] where the ZnS shell is efficient in reducing the cytotoxicity of the CdSe QDs. In vitro cytotoxicity studies report findings similar to in vivo studies. Targeted CdSe/ZnS QDs can be internalized by HeLa cells and tracked in live cells for more than 10 days with no morphological signs of toxicity [12.338]. The QDs are internalized mainly within endosomes near the perinuclear region with no nuclear involvement (see [12.321]). It has been shown, however, that QDs can alter gene expression in human bone marrow mesenchymal stem cells [12.338], which can be reduced by PEG treatment of the QDs. Organic-coated CdSe/ZnS core–shell quantum dots, while safe to use at near-neutral pH, could be toxic under other conditions [12.339]. Small CdTe QDs were shown to penetrate the cell nucleus where they could cause damage to DNA and induce apoptosis or cell death. QD cytotoxicity is believed to be due to free-radical formation caused by the presence of free Cd^{2+} from the degradation of the QD core [12.321, 12.340].

At the current stage in nanoparticle safety research, it would be premature to conclude that nanoparticles are inherently dangerous. However, now that a basis has been established, future research should strive to address the deficiencies in current testing and exploit the findings to engineer improved nanoparticles ultimately, e.g., for clinical use [12.321].

12.12 Summary

Nanomedicine comprises the application of nanoscience for diagnosis, treatment, monitoring, and control of biological systems to achieve medical benefit. Nanotechnology is positively impacting health care. Nanoscale and biosystems research are merging with information technology and cognitive science, leading to completely new science and technology platforms such as those for genome pharmaceutic, biosystems on a chip, regenerative medicine, neuroscience. At the forefront of nanomedicine is the research into the delivery and targeting of diagnostic and therapeutic agents with the identification of precise targets and the choice of appropriate nanocarriers to achieve the required responses while minimizing side effects. An impact of nanotechnology on health care is expected by experts with full efficiency around 2020 at many levels including detection of molecular changes in disease pathogenesis, disease diagnosis and imaging, drug delivery and therapy, multifunctional systems for combined diagnosis and therapeutic application, vehicles to report the in vivo efficacy of therapeutic agents, and nanoscience basic research. The convergence of nanoscience with biology and medicine is reflected in science policy decisions, initiating the sponsoring of Nanomedicine Development Centers and the channeling of substantial amounts of money into nanomedicine projects. Some nanoparticles have already gained approval by the US Food and Drug Administration (FDA) but outstanding issues related to risk assessment strategies, toxicity considerations, and environmental impact of nanoscale materials have to be resolved before regulatory agencies can approve further pharmaceutical products.

References

12.1 S.M. Moghimi et al., FASEB J. **19**, 311 (2005)
12.2 http://www.esf.org/puplication/214/Nanomedicine.pdf
12.3 Editorial, Nat. Mater. **5**, 243 (2006)
12.4 O.C. Farokhzad, R. Langer, Adv. Drug Delivery Rev. **58**, 1456 (2006)
12.5 M.C. Roco, Curr. Opin. Biotechnol. **14**, 337 (2003)
12.6 C. Peng et al., Phys. Rev. **E75**, 041903 (2007)
12.7 N. Shen et al., Mech. Chem. Biosys. **2**, 17 (2005)
12.8 R.H. Austin, S.-F. Lim, Proc. Natl. Acad. Sci. USA **105**, 17217 (2008)
12.9 A.D. Maynard et al., Nature **444**, 267 (2006)
12.10 S.M. Moghimi, T. Kissel, Adv. Drug. Deliv. Rev. **58**, 1451 (2006)
12.11 M. Harris et al., J. Clin. Oncol. **23**, 7768 (2005)

12.12 N.L. Rosi, C.A. Mirkin, Chem. Rev. **105**, 1547 (2005)
12.13 P. Alivisatos, Nat. Biotechnol. **22**, 47 (2003)
12.14 S.P. Leary et al., Neurosurgery **58**, 805 (2006)
12.15 MRS Bulletin **30**, December 2005, p. 930
12.16 http://www.cordis.europa.eu/fetch?Caller=EN_NEWS&ACTION=D...
12.17 A.S. Barnard, Nat. Mater. **5**, 245 (2006)
12.18 R. Weissleder, M.J. Pittet, Nature **452**, 580 (2008)
12.19 V.P. Torchilin, Adv. Drug Deliv. Rev. **58**, 1532 (2006)
12.20 J.-W. Jun et al., Bull. Korean Chem. Soc. **27** (7), 961 (2006)
12.21 C. Corot et al., Adv. Drug Deliv. Rev. **58**, 1471 (2006)
12.22 M.G. Harisinghani et al., New Engl. J. Med. **348**, 2491 (2003)
12.23 J.-H. Lee et al., Nat. Med. **13**, 95 (2007)
12.24 M.F. Kircher et al., Cancer Res. **63**, 8122 (2003)
12.25 H. Kobayashi et al., J. Natl. Cancer Inst. **96**, 703 (2004)
12.26 R.A.M. Heesakkers et al., Radiolog. **239**, 481 (2006)
12.27 A. Laghi et al., Invest. Radiol. **39**, 666 (2004)
12.28 I.J. de Jong et al., Eur. Urol. **42**, 18 (2002)
12.29 G.H. Simon et al., J. Magn. Reson. Imaging **23**, 720 (2006)
12.30 M. Stolz et al., Nat. Nanotech. **4**, 186 (2009)
12.31 A.M. Lutz et al., Radiology **234**, 765 (2005)
12.32 O. Rabin et al., Nat. Mater. **5**, 118 (2006)
12.33 E.R. Wisner et al., Invest. Radiol. **38**, 358 (2003)
12.34 P. Schrenk et al., Eur. J. Surg. Oncol. **27**, 378 (2001)
12.35 M.D. Lu et al., Ultrasound Med. Biol. **33**, 1736 (2007)
12.36 W.Y. Lau et al., Ann. Surg. **237**, 171 (2003)
12.37 T. Albrecht et al., Ultraschall Med. **25**, 249 (2004)
12.38 R. Weissleder, Science **312**, 1168 (2006)
12.39 A. Quon, S.S. Gambhir, J. Clin. Oncol. **23**, 1664 (2005)
12.40 H.A. Wieder et al., J. Clin. Oncol. **22**, 900 (2004)
12.41 N. Avril et al., J. Clin. Oncol. **23**, 7445 (2005)
12.42 S. Surti et al., IEEE Trans. Nucl. Sci. **50**, 1357 (2003)
12.43 J.S. Karp et al., J. Nucl. Med. **44**, 1340 (2003)
12.44 S.I. Ziegler et al., J. Nucl. Med. **41**, 20 (2000)
12.45 D.H.S. Silverman, A. Alavi, Radiol. Clin. N. Am. **43**, 67 (2005)
12.46 D.H. S. Silverman, J. Nucl. Med. **45**, 594 (2004)
12.47 W.J. Powers, A.R. Zazulia, Neuroimaging Clin. N. Am. **13**, 741 (2003)
12.48 H.-P.W. Schlemmer et al., Radiolog. **248**, 1028 (2008)
12.49 F.A. Jaffer et al., Circulatio. **116**, 1052 (2007)
12.50 M. Fleischmann et al., Chem. Phys. Lett. **26**, 163 (1974)
12.51 S. Keren et al., Proc. Natl. Acad. Sci. USA **105**, 5844 (2008)
12.52 Y.W. Wang et al., Nano Lett. **4**, 1689 (2004)
12.53 X.M. Yang et al., Nano Lett. **7**, 3798 (2007)
12.54 B. Marte et al., Nature **452**, 547 (2008)
12.55 A.D. Weston, L. Hood, J. Proteome Res. **3**, 179 (2004)
12.56 M.M.-C. Cheng et al., Curr. Opin. Chem. Biol. **10**, 11 (2006)
12.57 M. Stoeckli et al., Nat. Med. **7**, 493 (2001)
12.58 S. Pan et al., Mol. Cell. Proteomics **4**, 182 (2005)
12.59 D.G. Georganopoulou et al., Proc. Nat. Acad. Sci. USA **102**, 2273 (2005)
12.60 R.A. Beckman et al., J. Appl. Phys. **96**, 5921 (2004)
12.61 L. Hood et al., Science **306**, 640 (2004)
12.62 R. Beckman et al., Science **310**, 465 (2005)
12.63 T. Thundat, A. Majumdar, *Sensors and Sensing in Biology and Engineering* (Springer, Berlin 2003)

12.64 C. Ziegler, Anal. Bioanal. Chem. **379**, 946 (2004)
12.65 R. Datar et al., MRS Bull. **34**, 449 (2009)
12.66 M. Alvarez et al., Langmuir **20**, 9663 (2004)
12.67 R. Mukhopadhyay et al., Langmuir **21**, 8400 (2005)
12.68 B.L. Weeks et al., Scanning **25**, 297 (2003)
12.69 H.F. Ji et al., Expert Rev. Mol. Diagnostics **47**, 859 (2004)
12.70 G. Wu et al., Nat. Biotechnol. **19**, 856 (2001)
12.71 H. Chen et al., Biomed. Microdevices **6**, 55 (2004)
12.72 X.H. Gao et al., Nat. Biotechnol. **22**, 969 (2004)
12.73 V. Ntzaichristos et al., Fur. Radiol. **13**, 195 (2003)
12.74 R.E. Bailey, S.M. Nie, J. Am. Chem. Soc. **125**, 7100 (2003)
12.75 K.N. Yu et al., Bioconjugate Chem. **18**, 1155 (2007)
12.76 P.L. Yeagle, *Biology of Cholesterol* (CRC Press, Boca Raton, 1988)
12.77 S. Avaramudhan et al., Biosen. Bioelectron. **22**, 2289 (2007)
12.78 S.T. Reddy et al., Nat. Biotechnol. **25**, 1159 (2007)
12.79 P. Yager et al., Nature **442**, 412 (2006)
12.80 A.C. R. Grayson et al., Nature Mater. **2**, 767 (2003)
12.81 T. Franke, A. Wixforth, Phys. Unserer Zeit 2/2007 (38), p. 88
12.82 M.A. Unger et al., Science **288**, 113 (2000)
12.83 G. MacBeath, S.L. Schreiber, Science **289**, 1760 (2000)
12.84 D.R. Walt, Science **287**, 451 (2000)
12.85 E.S. Lander, Nat. Genet. **21**, 3 (1999)
12.86 D.S. Ginger et al., Angew. Chem. Int. Edn. Engl. **43**, 30 (2004)
12.87 K.B. Lee et al., Nano Lett. **4**, 1869 (2004)
12.88 J.W. Hong et al., Nat. Biotechnol. **22**, 435 (2004)
12.89 T.H. Wang et al., J. Am. Chem. Soc. **127**, 5354 (2005)
12.90 J.W. Hong, S.R. Quake, Nat. Biotechnol. **21**, 1179 (2003)
12.91 P.R. Srinivas et al., Lab. Invest. **82**, 657 (2002)
12.92 M. Ferrari, Nat. Rev./Cance. **5**, 161 (2005)
12.93 R. McKendry et al., Proc. Natl. Acad. Sci. USA **99**, 9783 (2002)
12.94 M. Su et al., Appl. Phys. Lett. **82**, 3562 (2003)
12.95 R. Pantoja et al., Biosens. Bioelectron. **20**, 509 (2004)
12.96 F. Patolsky et al., Proc. Natl. Acad. Sci. USA **101**, 14017 (2004)
12.97 P. Gould, Materialstoday **11**, July – August 2008, p. 17
12.98 J. Pipper et al., Angew. Chem. Int. Edn. **47**, 3900 (2008)
12.99 T.A. Desai et al., Biomed. Microdevices **1**, 131 (1999)
12.100 P. Sinha et al., Nanotechnology **15**, S585 (2004)
12.101 M. Arruebo et al., Nanotoday **2**, June 2007, p. 24
12.102 ISI Web of Knowledge © The Thomson Corporation. Search terms: 'drug delivery' and 'nanoparticles'. Date of search: December 2006)
12.103 R. Langer et al., Nat. Mater. **8**, 444 (2009)
12.104 J. Lu et al., small. **3**, 1341 (2007)
12.105 I.I. Slowing et al., J. Am. Chem. Soc. **129**, 8845 (2007)
12.106 Y. Pommier, Nat. Rev. Cancer **6**, 789 (2006)
12.107 L. Lacerda et al., Nanotoday **2**, Dec. 2007, p. 38
12.108 L.A. Nagahara et al., MRS Bull. **34**, 406 (2009)
12.109 M.P. Melancon et al., MRS Bull. **34**, 415 (2009)
12.110 R.H. Liu et al., MRS Bull. **34**, 432 (2009)
12.111 W.B. Lin et al., MRS Bull. **34**, 441 (2009)
12.112 A. Bajaj et al, Proc. Nat. Acad. Sci. USA **106**, 10912 (2009)
12.113 M.R. Stratton et al., Nature **458**, 719 (2009)
12.114 E.C. Hayden, Nat. **458**, 131 (2009)

12.115 S. Kommareddy, M. Amiji, Cancer Gene Therap. **14**, 488 (2007)
12.116 G. Mahendra et al., Cancer Gene Ther. **12**, 26 (2005)
12.117 S. Lehrman, Nature **401**, 517 (1999)
12.118 F. Yuan et al., Cancer Res. **54**, 4564 (1994)
12.119 N.L. Rosi et al., Science **312**, 1027 (2006)
12.120 W.D. Peng et al., The Prostate **67**, 855 (2007)
12.121 S. Dhar et al., Proc. Natl. Acad. Sci. USA **105**, 17356 (2008)
12.122 M.V. Yezhelyev et al., J. Am. Chem. Soc., **130**, 9006 (2008)
12.123 Z. Zhang et al., Clin. Cancer Res. **12**, 4933 (2006)
12.124 P.G. Rose, Onclogist **10**, 205 (2005)
12.125 H. Wartlick et al., J. Drug Target **12**, 461 (2004)
12.126 R.M. Schiffelers et al., J. Control. Release **91**, 115 (2003)
12.127 A.K. Salem et al., Nat. Mater. **2**, 668 (2003)
12.128 J. Wang et al., J. Drug Target **13**, 73 (2005)
12.129 K.E. Bullock et al., Mol. Imaging **5**, 1 (2006)
12.130 U. Schillinger et al., J. Magn. Magn. Mater. **293**, 501 (2005)
12.131 M. Arruebo et al., Nanotechnology **17**, 4057 (2006)
12.132 J.Q. Zhang et al., Pharm. Res. **22**, 573 (2005)
12.133 P. Taepaiboon et al., Nanotechnology **17**, 2317 (2006)
12.134 U. Steinfeld et al., Int. J. Pharm. **311**, 229 (2006)
12.135 F. Wiekhorst et al., J. Nanosci. Nanotechnol. **6**, 3222 (2006)
12.136 C.J. Sunderland et al., Drug Develop. Res. **67**, 70 (2006)
12.137 D.W. Chakeres, F. Vocht, Prog. Biophys. Molec. Biol. **87**, 255 (2005)
12.138 A.J. Rosengart et al., J. Magn. Magn. Mater. **293**, 633 (2005)
12.139 O. Rotarin, N.J.C. Strachan, J. Magn. Magn. Mater. **293**, 639 (2005)
12.140 S.M. Moghimi, T. Kissel, Adv. Drug Deliv. Rev. **58**, 1451 (2006)
12.141 S.H. Kim et al., J. Am. Chem. Soc. **129**, 2669 (2007)
12.142 Y.-E.L. Koo et al., Adv. Drug Deliv. Rev. **58**, 1556 (2006)
12.143 K.A. Dawson et al., Nat. Nanotechnol. **4**, 84 (2009)
12.144 L.L. Maldoon et al., Neurosurgery **57**, 785 (2005)
12.145 G.X. Xu et al., Bioconjugate Chem. **19**, 1179 (2008)
12.146 http://www.medialnewstoday.com/medialnews.php?newsid=18716
12.147 A. Moore et al., Radiology **214**, 568 (2000)
12.148 E.A. Neuwelt et al., Neuropathol. Appl. Neurobiol. **30**, 456 (2004)
12.149 O. Veiseh et al., NanoLett. **5**, 1003 (2005)
12.150 S.C. Steiniger et al., Int. J. Cancer **109**, 756 (2004)
12.151 W. Tang et al., Photochem. Photobiol. **81**, 242 (2005)
12.152 R. Kopelman et al., J. Magn. Magn. Mater. **293**, 404 (2005)
12.153 W.H. Sub et al., Nanotoday **4**, 2 (2009)
12.154 T.-Y. Liu et al., Nanotoday **4**, 52 (2009)
12.155 K. Shimizu et al., Export Opin. Ther. Targets **9**, 63 (2005)
12.156 E. Ruoslathi et al., Curr. Pharm. Des. **11**, 3655 (2005)
12.157 D. Le Bihan et al., Radiology **161**, 401 (1986)
12.158 J. Overgard in J. Overgard, ed. *Hyperthermia Oncology* (Taylor and Francis, London, 1985)
12.159 S.J. DeNardo et al., J. Nucl. Med. **48**, 437 (2007)
12.160 C.J. Gannon et al., Cancer **110**, 2654 (2007)
12.161 L.R. Hirsch et al., Proc. Nat. Acad. Sci. USA **100**, 13549 (2003)
12.162 L.R. Hirsch et al., Ann. Biomed. Eng. **34**, 15 (2006)
12.163 M. Johannson et al., Int. J. Hyperthermia **21**, 637 (2005)
12.164 A. Jordan et al., J. Magn. Magn. Mater. **225**, 118 (2001)
12.165 K. Kupferschmidt, Stuttgarter Zeitung July 16, 2009
12.166 D. Haemmerich, P.F. Laeseke, Int. J. Hyperthermia **21**, 755 (2005)

12.167 P.F. Engstrom et al., in *Cancer Medicine*, vol. 7, eds. D.W. Kufe et al., (B.C. Dekker, Hamilton, Canada, 2006) p.1292
12.168 C.H. Durney et al., *Radiofrequency Radiation Dosimetry Handbook,* 4th edn. (Brooks AFB, Tex: U. S. Air Force School of Aerospace Medicine Press, 1986)
12.169 L.D. Landau, E.M. Lifshitz, *Electrodynamics of Continous Media* (Elsevier, Oxford, 2004)
12.170 H. Dumortier et al., NanoLett. **6**, 1522 (2006)
12.171 R. Singh et al., Proc. Natl. Acad. Sci. USA **103**, 3357 (2006)
12.172 N.W. Kam et al., Proc. Natl. Acad. Sci. **102**, 11600 (2005)
12.173 J.C. Hindman, J. Chem. Phys. **44**, 4582 (1966)
12.174 W.R. Chen et al., Cancer Lett. (Shannon, Irel.) **98**, 169 (1996)
12.175 H. Maeda, Adv. Enzyme Regul. **41**, 189 (2001)
12.176 C. Loo et al., NanoLett. **5**, 709 (2005)
12.177 P. Chakravarty et al., Proc. Natl. Acad. Sci. USA **105**, 8697 (2008)
12.178 A.M. Hawkridge et al., Proc. Natl. Acad. Sci. USA **102**, 17442 (2005)
12.179 G.S. Bodor et al., Clin. Chem. **38**, 2203 (1992)
12.180 H.S. Guo et al., J. Nanosci. Nanotechnol. **5**, 1240 (2005)
12.181 M. Wolf et al., Biosens. Bioelectron. **19**, 1193 (2004)
12.182 S.K. James et al., Int. J. Cardiol. **93**, 113 (2004)
12.183 M.C. Fishbein et al., Cardiovasc. Pathol. **12**, 65 (2003)
12.184 J.-S. Park et al., Nature Nanotech. **4**, 259 (2009)
12.185 T. Kim et al., Proteomics **7**, 4203 (2007)
12.186 M. Alonso-Sande et al., Macromolecules **39**, 4152 (2006)
12.187 A. Besheer et al., J. Control. Release **111**, 73 (2006)
12.188 X.Y. Xiong et al., J. Control. Release **120**, 11 (2007)
12.189 W.D. Bennett, Expert Opin. Drug Deliv. **2**, 763 (2005)
12.190 P. Dames et al., Nat. Nanotechnol. **2**, 495 (2007)
12.191 K. Saito et al., Magnet. Reson. Med. Sci. **4**, 151 (2005)
12.192 C. Alexiou et al., IEEE Trans. Appl. Superconduct. **16**, 1527 (2006)
12.193 B. Gleich et al., IEEE Trans. Nanotechnol. **6**, 164 (2007)
12.194 M.S. Forman et al., Nat. Med. **10**, 1055 (2004)
12.195 C. Roney et al., J. Control. Release **108**, 193 (2005)
12.196 A. Alzheimer, Allg. Z. Psychiatr. Psych. – Gerichtl. **64**, 146 (1907)
12.197 M.S. Wolfe, Sci. Am. May 2006, p. 61
12.198 J. Schnabel, Nature **459**, 310 (2009)
12.199 A. Finefrock et al., J. Am. Geriatr. Soc. **51**, 1143 (2003)
12.200 C. Opazo et al., J. Biol. Chem. **277**, 40302 (2002)
12.201 Z. Zhuang et al., J. Med. Chem. **44**, 1905 (2001)
12.202 Q. Smith, *A review of Blood Brain Barrier Transport Techniques* (Humana Press, Totowa, NJ, 2003)
12.203 C. Ritchie et al., Arch. Neurol. **60**, 1685 (2003)
12.204 X. Huang et al., Biochemistry **38**, 7609 (1999)
12.205 L.L. Rubin, J.M. Staddon, Annu. Rev. Neurosci. **22**,11 (1999)
12.206 K.S. Soppimath et al., J. Control. Rel. **70**, 1 (2001)
12.207 M.J. Kogan et al., NanoLett. **6**, 110 (2006)
12.208 C. Soto et al., Nat. Med. **4**, 822 (1998)
12.209 E.A. Fradinger, G. Bitan, Trends in Biotechnology **23**, 531 (2005)
12.210 A.J. Haes et al., J. Am. Chem. Soc. **127**, 2264 (2005)
12.211 X. Ji et al. Colloids Surf. B **50**, 104 (2006)
12.212 S. Linse et al., Proc. Natl. Acad. Sci. USA **104**, 8691 (2007)
12.213 V.L. Colvin, K.M. Kulinowski, Proc. Natl. Acad. Sci. USA **104**, 8679 (2007)
12.214 J. Laurén et al., Nature **457**, 1128 (2009)
12.215 N. Buzhynskyy et al., J. Mol. Biol. **374**, 162 (2007)

12.216 N.N. Kumar, N.B. Gilula, EMBO Reports **8** (1), 51 (1996)
12.217 N. Buzhynskyy et al., EMBO Rep. **8**, 51 (2007)
12.218 J. Chen et al., Nat. Nanotechn. **1**, 142 (2006)
12.219 G.A. Silva, Nat. Nanotechn. **1**, 92 (2006)
12.220 R. Oehler, Max-Planck-Research **4**, 38 (2001)
12.221 V.T. C. Pappas et al., Nanolett. **7**, 513 (2007)
12.222 S. Patil et al., J. Phys. Chem. **C111**, 8437 (2007)
12.223 M.T. Huisman et al., Mol. Pharmacol. **59**, 806 (2001)
12.224 L.K. Shah, M.M. Amiji, Pharm. Res. **23**, 2638 (2006)
12.225 S. Noble, D. Faulds, Drugs **52**, 93 (1996)
12.226 A. Bender et al., Int. Conf. AIDS **11**, 64 (1996)
12.227 D.B. Shenoy, M.M. Amiji, Int. J. Pharm. **293**, 261 (2005)
12.228 M.-C. Bowman et al., J. Am. Chem. Soc. **130**, 6896 (2008)
12.229 E.S. Lee et al., Angew. Chem. Int. Edn. **47**, 2418 (2008)
12.230 MRS Bull **31**, March 2006, p. 181
12.231 http://www.mtr.com.hk/eng/corporate/file_rep/PR-06-084-E.pdf
12.232 S.T. Kang et al., Langmuir **23**, 8670 (2007)
12.233 NSTI Nanotechnology Conference and Trade Show, Boston, USA, 2008; Biomaterials and Nanotechnology in Tissue Engineering
12.234 The Guardian, October 6, 2007
12.235 L.J. Zhang, T.J. Webster, Nanotoday **4**, 66 (2009)
12.236 J.Y. Ying, Nanotoday **4**, 1 (2009)
12.237 E.M. Christenson et al., J. Orthop. Res. **25**, 11 (2007)
12.238 S. Sirivisoot et al., Nanotechnology **18**, 365102 (2007)
12.239 T.J. Webster et al., Tissue Eng. **7**, 291 (2001)
12.240 C. Kaya et al., Adv. Eng. Mater. **10**, 131 (2008)
12.241 O. Adamopoulos and T. Papadopoulos, J. Mater. Sci.: Mater. Med. **18**, 1587 (2007)
12.242 T.J. Webster et al., J. Biomed. Mater. Res. **51**, 475 (2000)
12.243 T.J. Webster et al., J. Biomed. Mater. Res. **67A**, 975 (2003)
12.244 X. Mao et al., Tissue Cell **37**, 349 (2005)
12.245 S.S. Liao et al., J. Biomed. Mater. Res. Part B: Appl. Biomater. 69B, 158 (2004)
12.246 B.-H. Yoon et al., Biomaterials **26**, 2957 (2005)
12.247 H.H. K. Xu et al., Biomaterials **25**, 4615 (2004)
12.248 L.E. Carey et al., Biomaterials **26**, 5002 (2005)
12.249 T.J. Webster et al., Biomaterials **20**, 1221 (1999)
12.250 R. Saravana Kumar, R. Vijayalakshmi, Ind. J. Dent. Res. **17**, 62 (2006)
12.251 W.J. Li et al., Biomaterials **26**, 5158 (2005)
12.252 M. Shin et al., Tissue Eng. **10**, 33 (2004)
12.253 N. Bhattarai et al., Biomaterials **26**, 6176 (2005)
12.254 S. Bhattacharyya et al., MRS Symp. Proc. **845**, 91 (2005)
12.255 S. Sahoo et al., Tissue Eng. **12**, 91 (2006)
12.256 J.K. Savaiano, T.J. Webster, Biomaterials **25**, 1205 (2004)
12.257 S. MacNeil, Materialstoday **11**, May 2008, p. 26
12.258 K. Rajangam et al., Nano Lett. **6**, 2086 (2006)
12.259 L.M. Y. Yu et al., Materialstoday **11**, May 2008, p. 36
12.260 R.A. Hule, D.J. Pochan, MRS Bull. **32**, 354 (2007)
12.261 D.R. Nisbet et al., J. Biomater. Sci. Polym. Ed. **19**, 623 (2008)
12.262 F. Johansson et al., Biomaterials **27**, 1251 (2006)
12.263 V.M. Tysseling-Mattiace et al., J. Neurosci. **28**, 3814 (2008)
12.264 G.T. Gillies et al., Nanotechnology **13**, 587 (2002)
12.265 S.P. Leary et al., Neurosurgery **58**, 1009 (2006)
12.266 H.-E. Swoboda, Best Physik J., Sept. 2007, p. 12
12.267 I.Z. Maxwell et al., Med. Laser Appl. **20**, 193 (2005)

12.268 N. Shen et al., Mech. Chem. Biosys. **2**, 17 (2005)
12.269 U.K. Tirlapur, K. Konig, Plant J. **31**, 365 (2002)
12.270 U.K. Tirlapur, K. Konig, Nature **418**, 290 (2002)
12.271 S. Kim et al., Nat. Biotechnol. **22**, 93 (2004)
12.272 M.F. Yanik et al., Nature **432**, 822 (2004)
12.273 M. Sitti, Nature **458**, 1121 (2009)
12.274 P. Fromherz, Chem. Phys. Chem. **3**, 276 (2002)
12.275 D.W. Sretavan et al., Neurosurgery **57**, 635 (2005)
12.276 J. Colombelli et al., Traffic **6**, 1093 (2005)
12.277 B. Alberts et al., *Molecular Biology of the Cell* (Garland Science, New York, 2002)
12.278 R.A. Freitas, J. Amer. Dent. Assoc. **131**, 1559 (2000)
12.279 S.B. Mitra et al., J. Am. Dental Associat. **134**, 1384 (2003)
12.280 S.C. Bayne, J. Dental Educ., May 2005, p. 571
12.281 Y. Yuan et al., Dental Mater. **23**, 561 (2007)
12.282 M. Okuda et al., Oper. Dent. **27**, 289 (2002)
12.283 R.L. Price et al., J. Biomed. Mater. Res. **67A**, 1284 (2003)
12.284 T.J. Webster et al., Biomaterials **26**, 953 (2005)
12.285 R.L. Price et al., J. Biomed. Mater. Res. **70A**, 129 (2004)
12.286 H.H. K. Xu et al., J. Dent. Res. **86**, 378 (2007)
12.287 S.H. Dickens et al., Dent. Mater. **19**, 558 (2003)
12.288 P.T. Sharpe, C.S. Young, Sci. Am. August 2005, p. 24
12.289 J.Y. Yu et al., www.sciencemag.org/cgi/content/abstract/1151526
12.290 S. Yamanka et al., Cell **131**, 861 (2007)
12.291 N. Swaminathan, Sci. Am. News. December 26, 2006
12.292 W. Sonoyama et al., PLoS ONE, Dec. 2006
12.293 Environmental, Health, and Safety Research Needs for Engineered Nanoscale Materials, US National Nanotechnology Coordination Office (2006); www. Nano.gov
12.294 R. Brayner, Nanotoday **3**, 1–2, 48 (2008)
12.295 Towards Predicting Nano-Biointeractions: An International assessment of Nanotechnology, Health, and Safety Research, http://icon.rice.edu; see K. Rand, MRS Bull. **33**, 649 (2008)
12.296 J. Kling, Nat. Biotechnol. **10**, 1068 (2007)
12.297 Editorial, Nat. Nanotechnol. **3**, 697 (2008)
12.298 J.M. Balbus et al., Environ. Health Perspect. **115**, 1654 (2007)
12.299 Commission of the European Union, see Stuttgarter Nachrichten, June 17, 2008
12.300 *Legislation to Strengthen Nanotechnology Safety Research*, U. S. House of Representatives, Press Release June 5, 2008
12.301 http://www.oecd.org/env/nano-safety/
12.302 N. Pidgeon et al., Nat. Nanotech. **4**, 95 (2008)
12.303 A.D. Maynard et al., Nature **444**, 267 (2006)
12.304 R.H. Austin, S.F. Lim, Proc. Natl. Acad. Sci. USA **105**, 17217 (2008)
12.305 V. Murashov, J. Howard, Nature Nanotech. **4**, 467 (2009)
12.306 D. Goldston, Nature **450**, 1141 (2007)
12.307 www.fz-juelich.de/ptj/index.php?index=707
12.308 Nature **456**, 853 (2008)
12.309 M. Pitkethly, Materialstoday **12**, Jan-Feb 2009, p. 23; www.rcep.org.uk/novelmaterials.html
12.310 E. Drexler, *Engines of Creation: The Coming Era of Nanotechnology* (Anchor Press/Doubleday, Garden City, NY, 1986)
12.311 B. Joy, Wired 8.04, 37 (2000)
12.312 C. Phoenix, E. Drexler, Nanotechnology **15**, 869 (2004)
12.313 N. Stephenson, *The Diamond Age: Or, a Young Lady's Illustrated Primer* (Bantom Spectra, New York, 1995)

12.314 M. Crichton, *Prey* (Harper Collins Publ., New York, 2003)
12.315 G.M. Whitesides, Sci. Am. Sept. 2001, p. 70
12.316 P.S. Anton et al., The Global Technology Revolution: Bio/Nano/Materials Trends and their Synergies with Information Technology by 2015 (Rand, Santa Monica, 2001)
12.317 S.C. Currall, Nat. Nanotech. **4**, 79 (2009)
12.318 C. Toumey, Nat. Nanotech. **4**, 136 (2009)
12.319 D.M. Kahan et al., Nat. Nanotech. **4**, 87 (2008)
12.320 D.A. Scheufele et al., Nat. Nanotech. **4**, 91 (2008)
12.321 N. Lewinski et al., Smal. **4**, No. 1, 26 (2008)
12.322 C. Buzea et al., Biointerphases **2** (4), MR 17 (2007)
12.323 S. Tinkle (ed.) *Health and Environmental Impacts of Nanoscale Materials–Safety by Design* (MRS Proceedings Vol. 1103E, Warrendale, 2008)
12.324 C. Sayes et al., Nano Lett. **4**, 1881 (2004)
12.325 C. Sayes et al., Toxicol. Lett. **161**, 135 (2006)
12.326 B.L. Allen et al., Nano Lett. **8**, 3899 (2008)
12.327 C.A. Poland et al., Nat. Nanotechnol. **3**, 423 (2008)
12.328 C.G. Li et al., J. Mol. Cell. Biol. **1**, 37 (2009)
12.329 E. Connor et al., Small **1**, 325 (2005)
12.330 Y. Pan et al., Small **3**, 1941 (2007)
12.331 W.D. James et al., Radioanal. Nucl. Chem. **271**, 455 (2007)
12.332 R. Dunford et al., FEBS Lett. **418**, 87 (1997)
12.333 P. Somasundaran et al., MRS Bull. **32**, 779 (2007)
12.334 A.K. Gupta, S. Wells, IEEE Trans. Nanobio. **3**, 66 (2004)
12.335 W.W. Yu et al., Nanotechnology **17**, 4483 (2006)
12.336 B. Wang et al., Proc. Natl. Acad. Sci. USA **105**, 18171 (2008)
12.337 M. Akerman et al., Proc. Natl. Acad. Sci. (USA. **99**, 12617 (2002)
12.338 S.C. Hsieh et al., Biomaterials **27**, 1656 (2006)
12.339 S. Mahendra et al., Environ. Sci. Technol. **42**, 9424 (2008)
12.340 J. Lovric et al., Chem. Biol. **12**, 1227 (2005)

Name Index

Note: In the index the names of the first authors of those publications are given that are quoted in the bibliographies.

A
Abbé, E., 61–62
Adamopoulos, O., 706, 720
Ade, H., 49, 85, 87
Agbenyega, J., 522
Aharonov, Y., 218, 376
Aizenberg, J., 2
Ajayan, P. M., 139–140, 141
Aken, B. B., 412
Akerman, M., 727
Akin, D., 548, 550
Akinaga, H., 24
Akiyama, T., 331
Akopian, N., 327
Albert, F. J., 375
Alberts, B., 489, 532, 563–564, 565, 566, 568
Albrecht, M., 81
Albrecht, T., 634
Alexiou, C., 691
Algra, R. E., 114
Aliev, A. E., 306–307, 308
Alivisatos, A. P., 7, 180, 616
Allen, B. L., 726
Allenspach, R., 410–411
Allwood, D. A., 410
Alonso-Sande, M., 688
Alphenaar, B. W., 218
Alsberg, E., 592
Alvarez, M., 643
Alzheimer, A., 691
Andersen, E. S., 33
Anderson, P. W., 19
Andersson, A. S., 590
Ando, 209–210
Anker, J. N., 335, 338
Anselmann, R., 607
Anson, L., 571
Anton, P. S., 724
Anzenbacher, P., 498
Arimoto, Y., 446–447
Armatas, G. S., 150
Arndt, M., 259
Arnold, M. S., 240, 429
Arruebo, M., 658–659, 671
Arunachalam, V. S., 510–511
Asadi, K., 447
Ashcroft, N. W., 250
Attwood, D., 4, 88
Atwater, H. A., 331–332, 343–345
Atwood, J. L., 137
Atzmon, M., 132
Auslaender, O. M., 17
Austin, R. H., 616
Autumn, K., 323
Avaramudhan, S., 649–650
Aviram, A., 215
Avouris, P., 214–215, 220, 429
Avril, N., 635

B
Bachtold, A., 218, 429
Baek, I. G., 447–448
Baer, E., 132
Baibich, M. N., 20, 22
Bailey, R. E., 649
Baird, G. S., 539
Bajaj, A., 662
Baklanov, M. R., 472
Balashov, T., 374
Balasubramanian, G., 37
Balasubramanian, S., 500
Balbus, J. M., 724–725
Baldinozzi, G., 13
Balents, L., 214

H.-E. Schaefer, *Nanoscience*, DOI 10.1007/978-3-642-10559-3,

Ball, P., 259, 261, 319–320, 581–582, 584–587
Balogh, L., 556
Ban, N., 530–531
Banhart, F., 139–140, 256–257, 355
Banin, U., 170
Bansmann, J., 386–390
Banta, S., 583, 587
Bao, G., 529, 532
Bardeen, J., 52
Barnard, A. S., 120, 617
Barrett, C. R., 425, 427
Barth, J. V., 384, 481
Bartos, F. J., 436, 438
Bath, J., 601
Baud, S., 447–448
Bauer, C., 351
Baughman, R. H., 236
Baur, J., 294, 299–300
Bayne, S. C., 718–719
Béa, H., 415
Beck, J. S., 149
Beck, M., 579, 581
Becker, L., 1, 138, 254
Beckman, R., 643
Beckman, R. A., 645
Bedau, D., 412
Beecher, J. F., 299
Begstrup, G. E., 220
Bell, J. S., 327
Benach, J., 577
Bender, A., 701
Beng, M. F., 434
Bennett, W. D., 689
Bennewitz, R., 59
Benson, O., 328–329
Berber, S., 10
Berezinski, V. L., 201
Berger, C., 144
Berger, L., 410
Bernèche, S., 573
Bershadsky, A., 533
Besenbacher, F., 54, 502, 504–505, 507–509
Besheer, A., 688
Bethune, D. S., 254
Betzig, E., 64, 68
Bezryadin, A., 18–19
Bhattacharyya, S., 708
Bhattarai, N., 707
Biben, T., 348
Bichoutskaia, E., 436–437, 448–450
Biener, J., 310
Bierman, M. J., 116–117
Bimberg, D., 169, 330–331
Binasch, G., 20, 22
Binnig, G., 1, 49, 56, 59
Birringer, R., 267
Blackman, M., 8
Blakesley, J. C., 329
Blank, D. H. A., 202
Blencowe, M. P., 322
Blobel, G., 577
Blügel, S., 384
Bluhm, H., 502
Böckmann, R. A., 570
Bocquet, N., 579
Bode, M., 75, 370, 373–375, 401, 403–404
Bodker, F., 388
Bodor, G. S., 686
Boeckl, M., 27–28, 30–31
Boersch, H., 376
Bognitzki, M., 121
Bolte, M., 381
Bonderer, L. J., 296–297
Borchard-Tuch, C., 480
Borisov, B. F., 11–13
Borkent, B. M., 358
Bose, S., 19
Bosman, A. W., 482–483
Bottani, C. E., 12
Bottini, M., 178, 180, 254
Bourgeois, O., 3
Bouwmeester, D., 326–327
Bowman, M.-C., 703
Braginsky, V. B., 320
Branton, D., 152–154
Braunecker, B., 218–219
Brayner, R., 723–724, 726
Breaux, G. A., 12
Brechin, E. K., 483–484
Brenner, M. P., 358
Brezger, B., 259
Brinkmann, A., 199–200
Britz, D. A., 498
Bronikowski, M. J., 211
Brossmann, U., 305–306
Bruchez, M., 180, 537
Bruder, F.-K., 463–465
Brumfiel, G., 246
Brune, H., 28–29
Bruno, P., 388, 410
Budke, E., 271, 273
Bullock, K. E., 671
Bulusu, S., 258
Burg, T. P., 35–36, 315
Buschow, K. H. J., 399
Buseck, P. R., 254

Bustamante, C., 557–559
Butler, T. Z., 152
Butler, W. H., 441
Buzea, C., 726
Buzhynskyy, N., 696–697

C
Cacialli, F., 488–490
Cademartiri, L., 117–118, 120
Callen, E., 399
Cammarata, R. C., 99–100, 123, 128
Cantoro, M., 210–211
Cappello, G., 568
Carey, L. E., 706
Caroff, P., 114
Carter, N. J., 567
Casimir, H. B. G., 33
Casiraghi, C., 457, 461, 465
Castaño, F. J., 408
Castro Neto, A. H., 245, 248
Caviglia, A. D., 201
Celik-Aktas, A., 236–237
Cen, C., 200
Cerezo, A., 49, 89, 91, 93–94
Chacko, S., 11
Chadwick, A. V., 294
Chakeres, D. W., 671
Chakravarty, P., 685
Champion, Y., 273
Chan, E. P., 323
Chan, H. B., 33–35
Chan, K. C., 285
Chan, W. C. W., 180
Chan, Y. T., 331
Chang, A. M., 17
Chang, C. J., 41, 43
Chang, D. E., 343
Chang, L. L., 125
Chang, T. M. S., 592
Chao, W. L., 84, 86
Chapman, H. N., 49, 84–85, 87, 89, 90–91
Charlier, J.-C., 17
Checco, A., 349–350
Chen, F. Q., 546
Chen, H. F., 596
Chen, H. M., 505–506
Chen, H., 645
Chen, J., 132, 493, 698–700
Chen, P., 516, 518
Chen, W. R., 685
Chen, X., 543–544
Chen, Y., 333–334, 336, 340–341
Chen, Y. C., 245
Chen, Z.-H., 429
Cheng, J. P., 236
Cheng, M. M.-C., 640–643, 645–646
Cheng, W. L., 107–109
Chettiar, U. K., 184–186
Chiatti, O., 9
Chigashige, M., 132
Chin, P. W., 231
Chinnasamy, C. N., 106–107
Cho, Y., 447
Choucair, M., 144, 246
Chow, G. M., 101, 104
Christenson, E. M., 705–707
Chrzan, D. C., 268, 280, 282
Chiu, H.-Y., 244–245
Chu, Y.-H., 309
Chung, S.-Y., 520
Ciraci, F., 58
Cleland, A. N., 35, 315, 322
Clemente, G. B., 401
Coehoorn, R., 400
Coey, J. M. D., 401
Cohen, M., 99
Colin, S., 354
Colombelli, J., 717
Colvin, V. L., 695
Connor, E., 727
Corma, A., 145–146
Corot, C., 618, 620, 628–629
Coufal, H., 454–455, 462, 464
Courty, S., 567
Craighead, H. G., 315
Creton, C., 323
Crichton, M., 724
Cubukcu, E., 341
Cuevas, J. C., 194
Cumings, J., 449
Cuong Pham-Huu, 236
Curie, P., 316, 412
Currall, S. C., 724

D
Dai, H. J., 224–225, 227
Dalton, A. B., 221
Daltorio, K. A., 324–325
Dames, P., 689–690
Das Sarma, S., 198
Datar, R., 643
Datta, S., 24
Davies, H. A., 401
Davisson, C. J., 259
Dawson, K. A., 553, 674
Day, C., 576–577

de Gennes, P. G., 35, 349–350
de Greef, T. F. A., 483
de Groot, B. L., 569–570
de Heer, W. A., 231
de Jong, I. J., 625
de Jonge, N., 242, 529
de Lorimier, R. M., 583
de Smit, E., 509
Dearden, A. L., 483–484
Deb, B. M., 58
Dee, R. H., 455
Degen, C. L., 37–38, 315
Degen, C., 36
DeNardo, S. J., 678–680, 684
Derby, B., 184
Derlet, P. M., 284
Derycke, V., 429
Desai, T. A., 658
Deshpande, V. V., 214, 449
DeSilva, L., 600
Desirajou, G. S., 483, 487
Dhar, L., 425, 468–470
Dhar, S., 666
di Ventra, M., 4
Diat, O., 518–519
Dick, K. A., 114
Dickens, S. H., 721, 723
Dickenson, T. A., 582
Dieterich, F., 253
Dietl, T., 24–25
Dietrich, G., 550
Dietz, T., 100
Ding, L., 211
Dingle, R., 330
Dippel, M., 12
DiVincenzo, D. P., 181
Dobson, J., 592–593
Doctorov, C., 425
Doeff, M. M., 519
Dokter, A. M., 499–500
Dolling, G., 184–185
Donnert, G., 68–69
Döring, Th., 302–303
Douglas, S. M., 33
Doyle, D. A., 571–572
Dressaire, E., 358–359
Dresselhaus, M. S., 138, 159, 514
Drexler, E., 724
Drexler, K. E., 1, 6
Drings, H., 301, 306
Drösser, C., 426
Duan, X. F., 191–192
Duffy, J. A., 13
Dumortier, H., 683
Dunford, R., 727
Dürkop, T., 215, 243
Durney, C. H., 683
Dutzler, R., 575
Duwez, A.-S., 500–501
Dzyaloshinski, E., 373

E
Eastman, P. S., 552
Eckert, J., 290–291
Edel, J., 346
Edelstein, A. S., 12, 99–100, 267, 300
Ederer, C., 395
Eggeling, C., 529, 531
Eggert, S., 17
Eickenbusch, H., 253, 257
Eigler, D. M., 52
Einstein, A., 327
Eisert, J., 319
Eknici, K. L., 35
Eleftheriades, G. V., 185
Elemans, J. A. A. W., 498
Elghanian, R., 180
Elias, D. C., 252
El-Shall, M. S., 12, 555, 99–100
Enders, A., 384, 386, 388, 393, 395–396
Engel, B. N., 442
Engelhardt, U., 185
Engelkamp, H., 489–490
Engstrom, P. F., 682
Erb, R. M., 28, 31–32
Ertl, G., 502
Esaki, L., 123, 125
Eshelby, J. D., 117
Etaki, S., 322
Evans, D. J., 7
Evans, J., 502

F
Faivre, D., 418
Falsig, H., 503
Fan, H. J., 114, 236, 239
Faraday, M., 1
Farkas, D., 289–290
Farokhzad, O. C., 615–617
Fazio, A., 434–435
Fecht, H. J., 136
Fedutik, Y., 338, 340
Fedyk, R., 301
Feichtinger, D., 278
Feng, L., 602
Feng, X. D., 134
Feng, X. L., 316

Fennimore, A. M., 316, 318
Fernandez-Lopez, S., 482
Ferrari, A. C., 144
Ferrari, M., 536, 656
Ferrer, S., 502
Fert, A., 20–21
Feske, S., 574
Feynmann, R., 1
Fiederling, R., 25
Fielding, R. M., 590, 592
Figueiredo, R. B., 285
Fincham, A. G., 596
Finders, J., 431
Finefrock, A., 693
Fiorani, D., 365
Fischer, P., 383
Fishbein, M. C., 686
Fisher, M. E., 35
Fisher, T. E., 563
Fleischmann, M., 637
Fogler, M. M., 17
Fon, W. C., 315
Forman, M. S., 691–692
Först, C. J., 470
Fotheringham, E., 470
Fradinger, E. A., 695
Frandsen, C., 406
Franke, T., 651–653
Frauenfelder, H., 353
Freitag, M., 220
Freitas, P. P., 410
Freitas, R. A., 717
Frenken, J., 502
Frenken, J. W. M., 53
Fromherz, P., 716
Fukunaga, J., 400
Fung, R., 49, 85, 91–92

G

Gabor, D., 378
Gambardella, P., 118, 386, 388–390
Gannon, C. J., 679, 682–683
Gansen, E. J., 329
Gao, L. C., 601, 603
Gao, X. H., 646–649
Garcias, F., 357
García-Vidal, F. J., 65–66
Garvie, R., 13
Gass, M. H., 246–247
Gates, B. C., 502
Gatteschi, D., 412
Ge, J. P., 178, 180–181, 416–417
Ge, L. H., 324
Gearba, R. I., 489
Geim, A. K., 248, 251
Genzer, J., 602–603
Georganopoulou, D. G., 641, 643
Gerlich, S., 259
Getzlaff, M., 391
Ghadiri, M. R., 480, 482, 583
Gibot, P., 519–521
Giessibl, F. J., 50, 56
Gigan, S., 322
Gillan, E., 254
Gillies, G. T., 711
Ginger, D. S., 158, 653–654
Ginley, D., 513
Ginzburg, V. L., 357
Giordano, N., 18
Giorgio, S., 503
Giovambattista, N., 347
Girit, C. Ö., 247
Gleich, B., 691
Gleiter, H., 1, 267, 287
Glynou, K., 537
Goh, C., 513
Golas, M. M., 83
Goldberger, J., 236–237
Goldstein, A. N., 8
Goldston, D., 723
Goll, D., 400–401
Gonsalves, K., 103
Goodbrand, H. B., 483
Gould, P., 537, 540, 553–554, 658
Graf, M. J., 13
Graham, A. P., 240, 243–244
Granquist, C. G., 100
Grantham, S., 433
Grayson, A. C. R., 651
Greeley, J., 502
Green, D. R., 541
Greer, J. R., 280
Greiner, A., 235–236, 240
Gross, L., 61
Grünberg, P. A., 20–22, 461
Grunlan, J. C., 234
Grynkewich, G., 442–443
Gu, Q. F., 174
Guinier, A., 136
Guo, H. S., 686–688
Guo, T., 254
Guo, W., 358–359
Guo, X. J., 426, 428
Gupta, A. K., 727
Gutkin, M. Y., 272

H
Habas, S. E., 170
Hackermüller, L., 259, 261
Haddon, R. C., 253
Haemmerich, D., 682
Haes, A. J., 335–336, 695
Hafner, J. H., 239
Hahn, H., 267, 300–302
Haider, M., 76, 78, 616, 646–649
Halas, N. J., 332, 334, 335, 341
Haldane, F. D. M., 248
Hamann, H. F., 440, 465
Hammerer, K., 322
Han, D. S., 26
Han, G., 546–547
Han, Y., 149
Hanlon, T., 289
Hansen, M. F., 406
Hansma, P. K., 53, 624–625
Hanson, J. A., 353, 355
Hao, E., 334
Hara, T., 253
Hariharan, P. C., 468
Harisinghani, M. G., 619, 625–626
Harris, M., 616
Hartmann, U., 74–75, 366
Haruta, M., 503
Haruyama, J., 218
Hasegawa, H., 112–113
Hashi, C. K., 121
Hasnaoui, A., 278
Hatton, B. D., 472–473
Haubold, T., 270
Hawker, C. J., 159–161
Hawkins, K. M., 587
Hawkridge, A. M., 686
Hayashi, M., 410, 451–452
Hayden, E. C., 663
Hayden, O., 191–192
Hayward, J. J., 410
He, J. B., 351
He, Y., 493–494
Heber, J., 199–201
Heesakkers, R. A. M., 624
Heil, T., 431–433
Heilemann, M., 68, 645
Hein, B., 529–531
Heinrich, A. J., 54–55
Heinze, S., 75, 370
Heinzelmann, H., 63
Heiz, U., 502
Hell, S. W., 68
Hellmann, H., 58
Hellmig, J., 464
Helveg, S., 115–116, 210–211
Henzie, J., 335–336, 338
Hermansson, A. M., 5, 604–605
Herrmann, H., 536
Herron, N., 104
Hersam, M. C., 211
Hertel, T., 221
Herth, S., 400
Hertlein, C., 35
Herzer, G., 397–399
Herzing, A. A., 503
Heuer, A. H., 103
Hilf, R. J. C., 579–580
Himpsel, F. J., 111–112
Hindman, J. C., 685
Hines, M. A., 171
Hirahara, K., 233
Hirjibehedin, C. F., 401, 405
Hirsch, L. R., 679, 684–685
Hirth, J. P., 286
Ho, A., 592
Ho, M. K., 23
Hoet, P. H., 546
Hoffmann, A. J., 184
Hofmann, S., 210
Hofmeister, H., 12
Högele, A., 327
Hole, B. B., 590
Holt, J. K., 352
Hong, J. W., 654–655
Hong, R., 552–553
Hönlein, W., 212–214
Hono, K., 94, 398
Honolka, J., 386
Hood, L., 640, 643, 653, 656
Höppel, H. W., 289
Hopster, H., 365
Hornyak, G. L., 4
Hsieh, S. C., 727
Hu, Z. J., 447
Huang, B., 68, 72
Huang, H. C., 267, 279–280
Huang, T. J., 584–585
Huang, J. Y., 131, 222–223
Huang, S. M., 209
Huang, W. J., 172–173
Huang, X., 693
Huang, Y., 189
Huber, A. J., 49, 66–67
Hubert, A., 365, 371
Hubler, G. K., 124
Hudgens, S., 438, 441

Huffman, D. R., 138–139
Huisman, M. T., 701
Hule, R. A., 710
Hultman, L., 256
Hummer, G., 352
Hung, C.-Y., 410
Hunter, D. L., 294–295, 299
Hussain, F., 298
Hvolbaek, B., 502–504
Hyashi, M., 410

I
Ichimura, T., 40, 340
Ielmini, D., 439
Iijima, S., 137, 139, 141, 209
Ishii, H., 17–18
Ishikuro, H., 429
Itoh, H., 571

J
Jaffer, F. A., 637
Jagota, A., 323
Jain, J. K., 199
Jain, P. K., 344
James, S. K., 686
James, W. D., 727
Jang, W. W., 317, 319
Jansen, R., 139–140, 142
Jasti, R., 257–258
Javey, A., 215, 240
Jena, P., 510
Jensen, K., 244
Jentsch, Th. J., 575–576
Ji, H. F., 645
Ji, X., 695
Jia, C. L., 4, 78–79
Jia, X., 144
Jia, X. T., 249
Jiang, K., 241
Jiang, M. J., 132
Jiang, W., 536
Jiang, Y., 573–574
Jiao, L., 250
Jin, H. C., 334–335
Jin, R. C., 180
Johannson, M., 680–682
Johansson, F., 710
Jones, J. R., 589
Jones, R., 510
Jonker, B. T., 24
Joo, S. H., 506
Jordan, A., 680
Jorio, A., 213–214
Journet, C., 209
Joy, B., 6
Jun, J.-W., 619–621
Junge, W., 570

K
Kada, G., 61
Kaempgen, M., 522
Kahan, D. M., 724
Kaiser, U., 366, 369
Kako, S., 327
Kalsin, A. M., 110–111
Kam, N. W., 683
Kamiya, T., 200
Kane, C. L., 17
Kaneko, M., 466–467
Kang, B., 521
Kang, S. T., 704
Kanungo, M., 430
Karau, F., 495, 497
Károlyházy, F., 320
Karp, J. S., 636
Kato, Y., 446
Katsnelson, M. I., 143, 250–252
Kaur, I., 304
Kawata, S., 164
Kaya, C., 706
Keblinski, P., 271, 304
Kelley, B. T., 10
Kelly, K. L., 333–334, 336
Kelly, T. R., 583
Kemiktarak, U., 56
Kemp, M., 5
Keren, S., 637–638
Kerr, J., 365
Kerry, J., 6
Khairalla, S. A., 358
Khomskii, D., 416
Khvalkovskiy, A. V., 410
Kienberger, F., 62
Kikkawa, J. M., 26
Kikuchi, K., 253–254
Kilo, M., 306
Kim, B. N., 286
Kim, B. R., 473
Kim, C. W., 183–184
Kim, D.-H., 383
Kim, P., 10–11, 224, 227, 229
Kim, S., 543–545, 713
Kim, S. H., 672–673
Kim, T., 688
Kim, W., 555
Kim, W. K., 128
Kim, W. Y., 249

Kingon, A. I., 470
Kippenberg, T. J., 343
Kircher, M. F., 620, 622–623
Kirchner, C., 546
Kittel, C., 138, 384
Kläui, M., 409
Klein, A., 464
Klein, L. C., 103, 300
Kleinfeld, E. R., 123
Klimov, V. I., 331
Klitzing, K. v., 196–198
Kneller, E. F., 400
Knez, M., 128, 131
Knobel, M., 392
Knobel, R. G., 35
Knoll, M., 49, 76
Knöner, G., 300, 305
Kobayashi, H., 623–624
Koch, C. C., 267, 275
Kogan, M. J., 694–695
Kogelnik, H., 468
Kolesov, 333
Kommareddy, S., 663–664
Kondratyuk, P., 498
Koo, Y.-E. L., 672, 674–678
Kopelman, R., 676–678
Koppens, F. H. L., 181–183
Kortan, A. R., 104
Koshino, M., 230, 233
Kosterlitz, J. M., 201
Kötz, R., 521
Kouwenhoven, L. P., 14–16
Kozlov, M. M., 530, 533
Kraetschmer, W., 137
Krasheninnikov, A. V., 222
Krätschmer, W., 209
Krause, S., 375–376, 457
Kreibig, U., 180
Krenn, J. R., 340
Kronmüller, H., 370–374, 400
Kroto, H. W., 137, 209, 253
Kuester, K. H., 434
Kuiper, A. E. T., 463–464
Kumar, N. N., 696
Kumzerov, Yu. A., 12
Kuo, M.-L., 515–516
Kupferschmidt, K., 682

L

La Fontaine, B. M., 431, 433
Lacaita, A. L., 438
Lacerda, L., 662
Laghi, A., 624–625
Lahann, J., 522–524
LaHaye, M. D., 321
Lamber, R., 8, 12
Lambrecht, A., 33–34
Landau, L. D., 144, 683
Landauer, R., 194
Lander, E. S., 653
Lang, X. Y., 13, 396–397
Langer, R., 659
Larabell, C., 85, 87
Larson, M., 13
Lassagne, B., 244
Lau, W. Y., 634
Laughlin, R. B., 198
Laurén, J., 695
Le Bihan, D., 677
le Gac, S., 541–542
Le Gros, M., 85, 87
Leapman, R. D., 84
Leary, S. P., 617, 655–656, 712–713, 715–717
Ledentsov, N. N., 331
Lee, C.-F., 584
Lee, D., 401
Lee, E. S., 703
Lee, H. S., 324
Lee, I., 506
Lee, J.-H., 122–123, 230, 236, 241, 619
Lee, J. W., 146–147
Lee, K. B., 159–160, 653
Lee, K. G., 65–66, 334
Lee, S.-H., 437, 440
Lee, W., 147–148
Lefebre, J., 219
Lehmann, M., 378
Lehn, J.-M., 477–478, 482, 485–487, 493, 495
Lehrman, S., 663
Lenau, T., 598, 600–601
Lengeler, B., 85
Letellier, L., 235
Levy, P., 236, 239
Lewinski, N., 6, 725–728
Lewis, N. S., 510
Li, C., 132
Li, C. G., 6, 727
Li, D., 120
Li, H., 28, 33
Li, L., 183–184
Li, M., 315–317, 342
Li, T.-D., 347
Li, W. J., 707, 716
Li, W. Z., 141
Li, X.-W., 289
Li, Y., 186–191

Li, Z. Q., 249
Liao, F., 279
Liao, S. S., 706
Liao, X. Z., 272–273
Lie, Y. L., 242
Lieber, C. M., 331
Lin, S.-P., 552
Lin, W. B., 662
Lin, Y.-M., 250
Linden, S., 185
Linse, S., 695
Liu, H., 178, 180
Liu, J., 564
Liu, K. S., 349
Liu, N., 185, 187
Liu, R. H., 662
Liu, T. B., 483, 495, 497
Liu, T.-Y., 676
Liu, Z. P., 118–119
Livi, R., 11
Lobo, R. F., 141–142
Loew, L. M., 41, 594–595
Löffler, J., 270
Logginov, A. S., 416
Loidl, A., 412
Loo, C., 686
Looger, L. L., 583
López-Luke, T., 511–512
López-Urías, F., 389, 392–394
Lott, J. A., 331
Lounis, B., 326
Lounis, S., 401, 403
Lovric, J., 727
Low, D. M., 483–484, 500–502
Lu, J., 659–661
Lu, J. P., 217
Lu, L., 284
Lu, M. D., 634
Lu, W., 114
Lu, X. M., 118
Lucas, B. D., 158, 335–337
Lüer, L., 215
Lundquist, M., 542
Luo, Y. F., 284
Luttinger, J. M., 17
Lutz, A. M., 619–620
Lv, B. L., 105–107
Lynch, I., 553

M

Ma, Q., 304
Ma, X.-D., 117–118
MacBeath, G., 652
Macilwain, C., 5
Mackay, A. C., 100
MacNeil, S., 708–709
Madhavan, V., 56
Madubuonu, A., 300
Madura, K., 531
Maeda, H., 685
Mahdavi, A., 323–324
Mahendra, G., 663
Mahendra, S., 727
Maier, J., 300
Maier, S. A., 331
Mal, F., 479
Maldoon, L. L., 674
Mamin, H. J., 74, 315
Manai, G., 33
Mancini, S., 322
Manevitch, O. L., 294
Mann, S., 587
Mannhart, J., 127, 199–202, 412, 446, 443, 470–471
Mannini, M., 412–413, 452
Mannix, R. J., 592
Mao, C., 583
Mao, X., 706
Mao, Y. B., 236, 239
Marinescu, M., 400–402
Markl, H., 7
Markmann, J., 287
Markussen, T., 515
Maron, V. I., 527
Marshall, W., 319
Marte, B., 639
Martel, R., 215–216
Martin, C. R., 147–148
Martin, Y., 74
Maruyama, T. M., 309
Masmanides, S. C., 315
Matthews, G., 478
Matthey, D., 505
Mavrikakis, M., 502
Maxwell, I. Z., 712, 715
Maye, M. M., 171
Mayer, A. C., 512
Maynard, A. D., 616
Maze, J. R., 37
McCandlish, L. E., 103
McCann, E., 251
McCartney, M. R., 376
McEuen, P. L., 214–215
McFadden, S. X., 286–287
McFadyen, I. R., 454, 458–459
McGehee, M. D., 512

McKendry, R., 656
Medalia, O., 81, 529–530, 653–654
Medintz, I. L., 178, 537, 539–541, 543
Mehrer, H., 303
Meier, F., 384–385, 483
Meindl, J. D., 428
Meirom, R. A., 290
Melancon, M. P., 345, 662
Melechko, A. V., 231
Mermin, N. D., 144, 388
Mertig, M., 234
Meyer, J. C., 143–144, 245, 247
Meyer, R. R., 233
Michler, P., 325–327
Midgley, P. A., 49
Mikolajik, T., 447
Miller, Ch., 572–573
Milliron, D. J., 440, 511
Mills, C. A., 158
Milster, T. D., 467–468
Minchni, R., 556
Minor, A. M., 276–277
Minot, E. D., 218
Mirlin, A. D., 199
Misewich, A., 220
Mitra, S. B., 718–719
Mitragotri, S., 528, 532
Mittal, J., 346
Möbus, G., 81, 651–653
Moghimi, S. M., 615–617, 672
Moilanen, D. E., 353
Molegraaf, H. J. A., 397
Möllenstedt, G., 81
Molloy, J. E., 567
Momida, H., 366
Moniruzzaman, M., 297
Moore, A., 675
Moore, G. E., 3, 425
Moore, J. A., 7
Morais-Cabral, H., 573
Morgan, A. B., 299
Morgenstern, M., 385
Mori, T., 568
Moriya, R., 381
Mørup, S., 401, 403, 405–406
Mössinger, D., 257–258
Mott, N. F., 214, 269
Moulas, G., 386
Moya, J. S., 292
Mueggenburg, K. E., 107–108
Mukherjee, A. K., 285
Mukhopadhyay, R., 643
Müller, A., 478, 495–496
Muller, D. A., 80
Müller, E. W., 49, 91
Müller, S., 357
Munday, J. N., 34–35
Murashov, V., 723
Murphy, B., 340
Murphy, C. J., 132, 334, 341

N

Nagahara, L. A., 662
Naik, A., 315
Naik, A. K., 35
Naik, R. R., 587
Nairz, O., 259
Nakayama, Y., 331
Nalwa, H. S., 267
Nam, K. M., 105
Nam, K. T., 121–122, 588
Nan, C.-W., 412
Nanda, K. K., 8, 12
Narayan, O., 11
Nardelli, M. B., 221–222
Nath, M., 236
Navrotsky, A., 587
Nédélec, F. J., 584
Neel, L., 398
Neinhuis, C., 601–602
Nelayah, J., 333
Nellist, P. D., 80
Nelson, D. R., 144
Neuwelt, E. A., 675
Nian, Y. B., 448
Nielsch, K., 236
Niemeyer, C. M., 419, 540
Nisbet, D. R., 710
Nishide, D., 233
Nishiwaki, H., 464
Njoroge, W. K., 439
Noble, S., 701
Nogués, J., 370
Noji, H., 570
Nolting, F., 87
Norden, R. V., 138
Norris, D. J., 104–105
Novoselov, K. S., 137, 143, 209, 248–249, 251–252
Novotny, L., 333
Noy, A., 351–353
Nozaki, K., 331
Nozaki, T., 210
Ntzaichristos, V., 649
Nugent, K. A., 89
Nussinov, M. D., 527

O
Oepen, H. P., 365, 376, 379–380
Oestreich, M., 26
Oh, J.-S., 537, 554
Oh, S. H., 280–281, 346
Ohnishi, H., 193–194
Ohtomo, A., 199
Okazaki, T., 230
Okuda, M., 719
Okuda, T., 49, 54
Olson, T. Y., 336, 345
Opazo, C., 693
Oshima, Y., 236
Osten, H. J., 471
Otellini, P. S., 426
Ouyang, J. Y., 171
Ovchinnikov, I. V., 397
Overgard, J., 678
Overney, G., 220
Ovid'ko, I. A., 285, 287
Özer, M. M., 19–20
Ozin, G. A., 27–28

P
Padmanabhan, K. A., 287
Pan, S., 641
Pan, S. L., 334
Pan, Y., 727
Pantaroffo, D., 587
Pantoja, R., 656
Pappas, S. P., 483
Pappas, V. T. C., 700
Parekh, A. B., 574–575
Park, B.-E., 471
Park, G.-S., 448
Park, J.-S., 688
Park, S. J., 144
Park, W. J., 185
Park, Y. K., 536
Parker, A. R., 597, 600–601
Parkin, S. S. P., 410, 441, 443, 450, 452–453, 457
Pastor, G. M., 387
Patil, S., 700–701
Patla, I., 119–120
Patolsky, F., 190, 550, 584, 657
Pauzauskie, P. J., 191, 193
Peierls, R. E., 144
Pendry, J. B., 185, 345
Peng, B., 222
Peng, C., 615
Peng, H. B., 316–317
Peng, S., 105–107
Peng, W. D., 664–665
Penrose, R., 320
Person, B. N. J., 323
Pfleiderer, Ch., 375
Philipp, F., 76, 645
Phoenix, C., 724
Pietzsch, O., 371, 410
Pinard, M., 322
Pinto, L. H., 590
Pipper, J., 656
Pirovano, A., 438
Pitkethly, M., 724
Piwon, N., 575
Plombon, J. J., 240
Podsiadlo, P., 290, 294–296
Pohl, D. W., 49, 63, 615, 617
Pohorille, A., 590–592
Poland, C. A., 726
Pommier, Y., 660
Poole, C. P., 14, 17
Popov, A. G., 400
Portales, H., 172–173
Porter, D., 594–595
Poudel, B., 515
Powers, W. J., 636
Pradeep, T., 254
Pradhan, N., 119–120
Press, D., 183
Preston, G. M., 576
Price, R. L., 590, 720–721
Prigogine, I., 527
Prinz, G. A., 20
Prinzbach, H., 253
Prokes, S. M., 127
Psaltis, D., 315
Pugno, N. M., 324–325
Pushparaj, V. L., 519

Q
Qian, H. F., 104–105
Qiao, Y., 352
Qin, S. Y., 19
Qin, Y., 516–517
Qu, L. T., 325
Quadri, S. B., 13
Quon, A., 635

R
Rabin, O., 630–632
Radaelli, A., 441
Rae, A. I. M., 260
Rajangam, K., 709
Ramanathan, T., 299
Ranganathan, S., 270

Rao, A. M., 514
Rauscher, M., 348
Ray, S. S., 294, 299
Reches, M., 588
Reddick, R. C., 64
Reddy, S., 324
Reddy, S. T., 650
Reedijk, M. F., 499
Reichert, H., 13
Reiner, J. E., 235, 240
Remskar, M., 236, 238
Resnick, D., 405
Reynwar, B. J., 533
Reyren, N., 199, 201
Richter, H. J., 454, 456–458
Rief, M., 559–560, 563, 585
Rigney, D. A., 137
Ringler, M., 341
Rinzler, A. G., 426
Ristivojevic, Z., 17
Ritchie, C., 693
Rittweger, E., 69–70
Roberts, G. G., 123
Robertson, J., 210–211, 243–244, 236, 240, 243–245
Rochefort, A., 221
Roco, M. C., 1, 615, 617
Rodgers, P., 1
Rodrigues, J., 354
Rodríguez-Manzo, J. A., 219
Rohrer, H., 7
Rollmann, G., 172
Roney, C., 691, 693–694
Roorda, S., 133–134
Rose, P. G., 667
Rosengart, A. J., 671
Rosi, N. L., 616, 641, 650, 664
Rosi, N. R., 178
Rösner, H., 150–151
Ross, C., 123
Ross, F. M., 113–114
Rotarin, O., 671
Rothschild, M., 155–156
Roukes, M., 2
Rubin, L. L., 694
Rubner, M., 589
Ruderman, M. A., 384
Rugar, D., 315
Ruigrok, J. J. M., 457
Ruoslathi, E., 677
Rupprechter, G., 507
Rust, M. J., 49, 68–70
Rustom, A., 235–236, 240
Rytkönen, A., 8–9

S

Sackmann, E., 480, 533–534
Sahoo, S., 708
Saito, H., 24, 26, 331
Saito, K., 691
Saito, T., 401
Salaita, K., 154, 158–160
Salem, A. K., 668–670
Sander, M. S., 131
Sanderson, K., 308
Sandhu, A., 39
Sano, K.-I., 588
Sano, M., 230
Saravana Kumar, R., 706
Sargent, E. H., 170–171
Satishkumar, B. C., 231
Saurenbach, F., 60
Savaiano, J. K., 708
Sawa, A., 448–449
Sayes, C., 726
Schaefer, H.-E., 279, 271–272
Schattschneider, P., 376, 381–382
Scheer, E., 193–194
Scherzer, O., 76
Scheufele, D. A., 724
Schiffelers, R. M., 667
Schillinger, U., 671
Schimmel, T., 57
Schiøtz, J., 267, 275
Schlegel, C., 412
Schlemmer, H.-P. W., 637
Schlickum, U., 28–30
Schliesser, A., 319, 322
Schliwa, M., 563, 568–569
Schlom, D. G., 127–129, 412, 470–471
Schlosshauer, M., 320
Schmidt, J. J., 584
Schmidt, M., 11–13
Schmidt, R., 68, 70–71
Schmidt-Rohr, K., 519
Schnabel, J., 693
Schneider, C. M., 365
Schneider, J., 605
Schnittger, S., 605–607
Scholes, G. D., 169, 174, 176, 178
Schön, G., 18
Schönenberger, Ch., 214
Schrempf, H., 571
Schrenk, P., 633

Schrinner, M., 506
Schroer, C. G., 85, 89–90
Schultheiss, H., 408
Schultz, L., 400
Schumacher, M., 571, 573–574
Schur, R., 331
Schütz, G., 381–382
Schwab, K., 11
Schwab, K. C., 315, 319–322
Schwab, P., 26–27
Schwaiger, S., 186
Schwarz, A., 365–374
Schwarz, R. B., 137
Schwarz, U. D., 59
Scrosati, B., 520
Sealy, C., 149, 212, 296–297, 446, 452
Seebeck, T. J., 514
Seeman, N. C., 493
Seidel, J., 415
Seidman, D. N., 280
Sellmyer, D. J., 400
Selloni, A., 370
Seo, D., 132
Seo, J.-W., 248
Sessoli, R., 412
Shah, L. K., 701–702
Sharma, J., 28, 32–33
Sharpe, P. T., 596, 722–723
Shcherbakov, V. P., 418
Shelley, T., 7
Shen, J. L., 236, 239
Shen, N., 616, 713
Shenoy, D. B., 702
Shevchenko, E. V., 109–110
Shibata, N., 79, 172–174
Shik, A., 195–196
Shimizu, K., 676
Shin, M., 708
Shinohara, H., 253–254
Shiozawa, H., 499
Shluger, A., 60
Shvartsburg, A. A., 12
Shvets, G., 185
Siegel, R. W., 137, 267
Sigmon, G. E., 258
Silva, G. A., 698–699
Silverman, D. H. S., 636
Simon, G. H., 625, 627
Sindzingre, P., 357
Sing, M., 200
Singh, R., 683
Sinha, P., 658
Sirivisoot, S., 705–706
Sitti, M., 715
Slayter, G., 132
Slonczewski, J. C., 374
Slowing, I. I., 659–662
Smalley, R. E., 6
Smart, C., 137
Smith, A.-S., 533–534
Smith, B. W., 227, 230
Smith, B. L., 587
Smith, Q., 693
So, M.-K., 545
Solozhenko, V. L., 292
Somasundaran, P., 607, 727
Sommerlatte, J., 514
Sonoyama, W., 723
Soppimath, K. S., 694
Sørensen, M. R., 304
Soto, C., 694
Soukoulis, C. M., 185
Spaepen, F., 124, 127
Spaldin, N. A., 309
Spataru, C. D., 219
Sprengel, W., 305, 400
Sretavan, D. W., 716
Srinivas, P. R., 655
Staniland, S., 417–419
Stankovich, S., 137
Stankus, J. J., 121
Staudinger, H., 482
Steed, J. W., 493
Steele, G. A., 245
Stehr, J., 552
Steinfeld, U., 671
Steiniger, S. C., 676
Steniberg-Yfrach, G., 581–582
Stephenson, N., 724
Stern, N. P., 26
Stevenson, R. M., 327
Stewart, M. D., 158–159
Stier, D., 176
Stix, G., 1
Stoddart, J. F., 477
Stöhr, J., 381, 389
Stoll, H., 49, 85, 87, 381
Stolyarova, E., 246
Stolz, M., 627
Stone, A. J., 221
Störmer, H., 7
Stormer, H. L., 195–197, 199
Strano, M. S., 234
Stratton, M. R., 663
Strauf, S., 327
Su, M., 656

Sub, W. H., 676
Subramanyan, K., 606
Suenaga, K., 79, 230, 255
Suess, D., 456
Sugimoto, Y., 60–61
Sui, H. X., 83–84
Sui, Y. C., 235–236
Sukhanova, A., 555
Sun, J. L., 145–146
Sun, L., 224
Sun, S., 105–107
Sun, Y., 236
Sun, Y. G., 133, 180
Sunderland, C. J., 671
Suresh, S., 529, 532, 535–536, 560–562
Surti, S., 636
Suryanarayana, C., 283
Sutter, P. W., 353–356
Sutton, A. P., 268
Swaminathan, N., 723
Swoboda, H.-E., 712
Swygenhoven, H. V., 268, 271, 273, 275–276
Synge, E. H., 63
Szabó, D. V., 293
Szlufarska, I., 278–279
Szostak, J. W., 592
Szot, Z., 448
Szwacki, N. G., 258

T
Tabasztó, L., 249
Taepaiboon, P., 671
Taflove, A., 333
Takahara, J., 338
Takenobu, T., 230
Takesue, I., 218–219
Talbot, H. F., 259
Tammann, G., 150
Tanaka, H., 154
Tanaka, T., 164
Tang, C. B., 161
Tang, W., 676
Tang, Y., 172, 174
Tang, Y. H., 236–237
Tang, Z., 589
Tanimoto, H., 304
Tans, S. J., 215, 429
Tao, K., 384
Taton, T. A., 594–595
Taylor, R., 257
Terries, B. D., 457
Terrones, M., 114–116, 139, 144, 211, 231, 235, 245
Tersoff, J., 52–53, 370
Tesch, W., 597
Theisinger, S., 608
Thelander, C., 193
Thess, A., 141–142
Thibault, P., 85, 89
Thiele, E., 289
Thomas, I., 5
Thompson, S. E., 244
Thundat, T., 643
Tian, B. Z., 513
Tian, N., 505–506
Tian, Y., 324
Tien, C., 13
Tilke, A. T., 157, 428
Tillman, N., 123
Tinazli, A., 162–163
Tinkham, M., 14
Tinoco, J. C., 471
Tirlapur, U. K., 713–714
Toennies, J. P., 353, 357–358
Tomalia, D. A., 134
Tombari, E., 12
Tomczak, M. M., 587
Torchilin, V. P., 618, 667–668
Toumey, C., 724
Tour, J. M., 426
Tour, O., 41, 43
Tourillon, G., 236
Trafton, A., 283
Treacy, M. M. J., 221
Trinh, C., 434
Tritt, T. M., 511
Tsang, C., 23
Tsui, D. C., 198
Tsukagoshi, K., 218
Tsukazaki, A., 199, 201
Tu, K. N., 124, 126, 134
Tuccitto, N., 193
Tung, V. C., 144
Tyner, K. M., 40–42
Tysseling-Mattiace, V. M., 710

U
Ugarte, D., 138
Unger, M. A., 652
Unruh, K. M., 12
Urban, K. W., 76–80, 270, 300

V
Vaia, R. A., 294, 297–299
Vaida, S., 505
Valentine, J., 184–185, 187
Valiev, R. Z., 137, 282
van Benthem, K., 81

van Blaaderen, A., 258, 537
van de Craats, A. M., 489
van den Berg, B., 577, 579
van Dillen, T., 132–133
van Gorp, J. J., 489
van Heel, M., 81
van Manen, H.-J., 541–542
Varela, M., 80
Vassaux, G., 547
Vaz, C. A. F., 365, 408–409
Vaziri, A., 536
Vedmedenko, E. Y., 389
Veiseh, O., 675
Velikov, K. P., 258
Venema, L. C., 216–217
Vig, M., 574
Vigneron, J. P., 597–598
Villalpando-Paez, F., 245
Vinogradov, A., 288–290
Vitali, D., 322
Voit, J., 17
Vollath, D., 293
von Bergmann, K., 401, 407
Voura, E. B., 545

W
Wacker, R., 419–420
Wagner, G. M. J., 136
Wagner, H. D., 294, 297–299, 595
Wagner, R. W., 483
Wakai, H., 434–435
Wakayama, Y., 193
Wallace, P. R., 245
Walt, D. R., 652
Walter, P., 605, 609–610
Walther, A., 192
Wang, B., 727
Wang, C., 118
Wang, C. R., 255
Wang, G. M., 7–8
Wang, J., 670
Wang, K. L., 246, 397
Wang, L., 541
Wang, T. H., 654
Wang, X. R., 429–430
Wang, Y., 211
Wang, Y. W., 637, 639
Wang, Z. L., 134–135, 331
Warren, O. L., 276–277
Warren, S. C., 150–151
Wartlick, H., 667–668
Warusawithana, M. P., 200
Watanabe, K., 599
Watt, F., 157
Watton, S. P., 483
Webster, T. J., 704, 706, 708, 720
Wei, Y. Y., 197
Weidenkaff, A., 300
Weigand, M., 381
Weiner, S., 595
Weisheit, M., 310
Weismann, A., 55–56
Weissleder, R., 618, 629–630, 635–636, 640
Weissmüller, J., 270, 272, 274, 307–308
Weller, D., 390
Wełnic, W., 437–439, 441, 464
Wen, B. M., 186
Weston, A. D., 640
Westphal, V., 49, 68, 73
Weyland, M., 84
Whitby, M., 348
Whitby, R. L. D., 236, 238
White, R. L., 457
Whitesides, G. M., 4, 7, 27, 528, 724
Wieder, H. A., 635
Wiekhorst, F., 671
Wiesendanger, R., 49, 50–51, 53, 58, 64, 74–75, 365–369
Willets, K. A., 334
Wilson, L., 126
Wilson, N. R., 224
Wilson-Rae, I., 322
Winey, K. I., 294, 297, 299
Winkler, R., 23–26
Winklhofer, M., 418–419
Winterer, M., 300
Wise, W. D., 39
Wisner, E. R., 632–633
Withers, P. J., 84–86
Witkamp, B., 316–317
Wittingham, M. S., 519
Wolf, D., 268–270, 273–276
Wolf, M., 686
Wolf, S. A., 21, 441–442, 444, 577, 579
Wolfe, M. S., 691–693
Wong, S. S., 236, 239, 224–228
Wood, J., 3, 534
Woodhead, J. L., 434, 565–566
Wortmann, D., 370
Wu, G., 645, 656
Wu, R., 371
Wu, X., 539
Würschum, R., 102, 270–271, 300–301, 303–305, 399
Wuttig, M., 437–439, 441, 464
Wyckoff, R. W. G., 138

X
Xia, Y. N., 180, 332, 334
Xiao, T. D., 103
Xie, J. W., 120–121
Xie, L.-H., 434, 436
Xiong, X. Y., 688–689
Xiong, Y., 132
Xu, G. X., 674
Xu, H. H. K., 706, 721–722
Xu, X., 416

Y
Yablonovitch, E., 180
Yacaman, M. J., 100
Yager, P., 650–651, 695
Yamachika, R., 256
Yamamoto, T., 11
Yamanouchi, M., 410
Yan, J. L., 537, 540
Yang, A. H. J., 315, 343–344
Yang, D., 164
Yang, S. A., 412
Yang, X. M., 639–640
Yang, Y. T., 311
Yanik, M. F., 714–715
Yanson, A. I., 193–194
Yavari, A. R., 137
Yazdani, A., 194
Yeagle, P. L., 649
Yezhelyev, M. V., 666–667
Yildiz, I., 489, 491
Yin, G.-C., 85
Yin, L.-W., 258
Yin, Y. D., 134
Ying, J. Y., 705
Ynasa, S., 22–23
Yokoyama, M., 26
Yoon, B., 502
Yoon, B.-H., 706
Yoshida, C., 447
Yoshizawa, Y., 398
Yosida, K., 384
You, C. C., 546–548, 552–554
You, P. J., 588
Youngblood, J. P., 603
Yu, J. Y., 723
Yu, K. N., 649
Yu, L. M. Y., 708, 710
Yu, T. Y., 119
Yu, W. W., 726–727
Yuan, C. A., 473
Yuan, F., 664
Yuan, J., 523
Yuan, Y., 719–720
Yuan, Z. L., 327
Yuasa, S. J., 441
Yue, E. H., 184
Yulin, S., 201, 203–204
Yu-Ming, L., 514
Yurdumakan, B., 325

Z
Zaikin, A. D., 18
Zaric, S., 218
Zeidel, M. L., 576
Zenhausern, F., 65
Zgirski, M., 18
Zhai, J., 415
Zhang, D. Y., 245
Zhang, G. Y., 231
Zhang, J. Q., 671
Zhang, L. J., 704
Zhang, M., 221, 401
Zhang, S., 587
Zhang, W., 400
Zhang, X. Y., 401
Zhang, Y., 144, 240, 245, 250, 439, 468, 493
Zhang, Z., 667
Zhao, J., 256
Zhao, X., 210, 551
Zhao, Y.-H., 281–282
Zhao, Z. W., 520
Zheng, G. F., 188
Zheng, H., 414–415
Zheng, J. W., 32
Zheng, M., 212
Zhi, C. Y., 236–237
Zhong, D. Y., 230
Zhou, G. W., 134
Zhou, Y., 573
Zhu, J. J., 258
Zhu, J.-G., 22–23, 425, 441, 444–446, 460–461
Zhu, T., 279–281
Zhu, X. H., 471
Zhuang, L., 429
Zhuang, W. W., 447
Zhuang, Z., 693
Ziegler, S. I., 636
Zijlstra, P., 465
Ziman, J. M., 252
Zou, J. P., 236
Zuev, Y. M., 249
Žutić, 20
Zweck, J., 376–379
Zwolak, M., 152

Subject Index

A
Abbé limit, 337
Aberrant store-operated calcium influx, 574
Aberration corrected electron microscopy, 76–80
A-beta (amyloid-beta), 691–695
Ab initio calculations, 178, 280, 384, 389, 391, 502, 524
Abscess, 627–628
Acceleration in computation, 426
Acquired immune deficiency syndrome (AIDS), 701
Actin filaments, 480, 529, 539, 562–564, 565, 570
Action-potential generation, 571
Active targeting of drugs, 616, 647, 659
ADDL – Amyloid-derived ligands, 695
Adenosine triphosphate (ATP), 532, 567, 569
Adhesion force and pH variation, 226
Adhesive, sealing ability, 719
AFM (atomic forces microscopy), 56, 590, 627, 696–697
AFM in bionanotechnology, 61
Aharonov–Bohm effect, 81, 218
Alkoxides, 103, 120–121
Allende meteorite, 1, 254
ALS – Amyotrophic Lateral Sclerosis, 692
Alzheimer's disease (AD), 691–695
Alzheimer's therapy, 694, 695
Amelogenin nanospheres, 596
Amino acids, 560–561, 571, 579, 583, 591, 610
Amplifiers, 51, 169, 320, 331
Amyloid cascade hypothesis, 691
Amyloid-derived ligands (ADDL), 695
Angiogenesis, 616, 639, 663, 708
Angiography, 620, 623–624
Anodes, tin-based, 519
Anti-angiogenic gene therapy, 663
Antibacterial activity, 482
Antibacterial nanocomposites, 703
Antibodies, 189, 619, 640, 667–668, 685
Anticancer activity, increased, 670
Anticancer therapy, 649
Antiferromagnetic behavior, 401
Antiferromagnetic and complex magnetic nanostructures, 401–407
Antiferromagnetic domain walls, 403
Antiferromagnetic exchange, 484
Antiferromagnetic monatomic chains, 403
Antiferromagnetic nanoparticles, 403–406
Antiferromagnetic ordering, 369, 405
Antiferromagnetic structure, 75, 369–370, 373, 404
Antigens, 640, 645–648
Antioxidant, 693
Antireflection (AR) coating, 515
Antiwrinkle cream, 607
Apoptosis, 536, 639, 649, 661
Applications, aerospace, 299
Application of carbon nanotubes, 236–245
Application of nanocomposites, 294
Application of nanomaterials, clinical, 620, 643, 660, 678, 680, 720, 727
Application prospects of emerging solid state memory technologies, 436
Application prospects of plasmonics, 343–345
Applications, 415
Approval by the U.S. Food and Drug Administration (FDA), 616
Aquaporin-0 (AQP0), 696–697
Aquaporin water channels, 575–576
Aquaporin water-transporting channels, 352
Arthritis, 625, 627
Artificial blood cells, 592
Artificial cells, 580, 590–592
Artificial liver, 585
Artificial lotus leaf, 603

Artificial mimics of ion channels, 583
Artificial muscle, 308
Artificial nerves, 192
Artificial noses, 582
Artificial retina, 700
Artificial spinal column, 711
Artificial tissues by bionanomaterials, 704–712
Associative cortex, 636
Asters, 584
Astrophysical applications, 202
Atherosclerosis, 620, 627
Atomic diffusivity, activation energy, 269
Atomic force microscopy (AFM), 56–61, 590
Atomic force microscopy, contact mode, 57–58
Atomic force microscopy (AFM), non-contact, 59–60
Atomic layer deposition (ALD), 128–132
Atomic structure of nanocrystal surfaces, 172
Atom probes, 91–95
ATP, 581, 698
ATP hydrolysis, 563–564, 583
ATP synthase (ATPase), 569–571, 582–583, 590, 591
Attractive force, 34
Auger electron spectroscopy (AES), 124, 127, 304
Au nanocrystals, 502–505
Automobile parts, 299
Avalanche photodiode, 192

B

Back-projection algorithm, 637
Bacteriorhodopsin, 591
Bacterium, 531
Ballistic transport, 143
Band gap, 176
Barcode assay, 641, 695
Bardeen's transfer Hamiltonian, 51, 58
Batteries, 5, 477
Beetles, 597–601
Bell's inequalities, 183, 327
Berry phase, 251
Bio-barcode assay, 641
Biochip, 162
Biocompatibility, 186, 417, 646
Biodegradation of SWNTs, 726
Biodistribution of nanoparticles, 556–557
Biological nanotubes, 236
Biology on the nanoscale, 527–610
Bioluminescence resonance energy transfer (BRET), 545
Biomarker, 640, 686, 695
Biomimetics, 527, 580–593, 600–601
Biomineralization, 417, 587
Biomolecular detection techniques, 618
Bionanostructures, photonic, 597–601
Biophotonics, 527
Bio-quantum-wires, 121–122
Biosensors, 189, 583, 588, 592
Biosystems on a chip, 615
Biotin-modified nanotube, 228
Biowarfare agents ricin and tularaemia, 645
Bitter decoration technique, 365
Bladder therapy, 704
Blindness, 688, 696
Block copolymer lithography, 159–161
Block-copolymers, 149, 159
Blocking temperature, 386, 390
Blood-brain barrier, 656–657, 691, 693
Blood vessel regeneration, 121
Blue recording, 463–464
Blue-shift, 104, 178, 293, 300, 335–336, 353, 416, 598
Bluray disks (BDs), 462
Bonding to wet tissues, 324
Bone, 297, 527, 593–595
Bone replacement, 595
Bone restoration by nanostructured bioceramics, 706
Bone tissue scaffolds, polymeric nanofibers, 708
Bose-Einstein distribution, 320
Bottom-up assembly, 187
Bottom-up synthesis, 2, 99, 154
Bovine spongiform encephalopathy (BSE), 643
Brain cancer, 620, 623
Brain cancer diagnosis and therapy, 672–678
Brain thrombosis, 649
Brain tumors, 620–623
BRCA1 gene mutations, 645
Breast cancer, 619–620, 623–624, 633, 667–668, 679, 686
Breast cancer lymphangiography, 623
Breast tumor, 663
Brick-and-mortar like structure, 588–589
Brillouin light scattering, 408
Bubbles for tracking the trajectory of an individual electron, 359–360
Bubbles, nanopattering, 358–359
Burgers vector, 271, 285
Butterflies, 597–601

C

Ca^{2+} channel, 571, 573–575
Ca^{2+} concentration, intracellular, 574
Camptothecin, 659–660

Canaliculi, 595
Cancer, 616–617, 619–625
Cancer, early detection, 662
Cancer, neck, 635
Cancer targeting, 619, 647
Cancer therapy, 649, 662–663, 674–675, 678
Cancer therapy, personalized, 663
Canted spin configuration, 392
Cantilevers, 315–317, 640
Carbon molecular spoked wheel, 257–258
Carbon nanohoop, 257–258
Carbon nanostructures, 209–262, 307
Carbon nanostructures, other tubular, 227–230
Carbon nanotube cathodes, 519
Carbon-nanotube (CNT) – based data storage devices (NRAM), 448–450
Carbon nanotube electronics, 429
Carbon nanotube RAM (NRAM), 437
Carbon nanotubes, 236, 308, 682–684
Carbon nanotubes, filling and functionalizing, 230
Carbon nanotubes, multiwalled (MWNTs), 218, 308
Carbon nanotubes as nanoprobes, 224–227
Carbon nanotubes, optoelectronic properties, 219–220
Carbon nanotubes, outside functionalization, 234
Carbon nanotubes, radial breathing mode, 213
Carbon nanotubes, single-walled (SWNTs), 139–142, 638, 682
Carbon nanotubes, sorting, 211
Carbon nanotubes, structure, 212–214
Carbon nanotubes, thermal properties, 220
Carbon and organic nanoparticles in cytotoxicity studies, 726
Carbon peapod, 230
Carcerands, 478–479
Carcinoembryonic antigen (CEA), 655
Cardiac troponin I (cTnI), 686
Cargo-binding domain, 564
Cartilage, 627, 704
Cartilage tissue engineering, 708
Cartilage treatment, 704
Casimir forces, 33–35
Catalysis, 170, 484–485, 502–510
Catalysis, promoters for the MoS_2-based, 508
Catalysts, 300
Catalysts, in situ phase analysis, 509–510
Catalysts, MoS_2, 507–509
Catalysts, Pd, 506–507
Catalysts, Pt, 505–506
Catalyzing the metabolic functions, 592
Cavitands, 478
C. elegans nematode, 84, 714
Cell, 528
Cell adhesion, 533–534
Cell adhesion at nanostructured surfaces, 589
Cell division, 563, 584, 717
Cell line, 68, 632
Cell nanoimaging by 3D far-field optical microscopy, 70–72
Cell phones, 434
Cell sorting, 654, 656
Cell structure, 529–531
Cellular signaling alterations, 725
Central and peripheral nervous system therapy, 704
Ceramic/metal nanocomposites, 292–293
Ceramic particles, 102
Ceramics, 290
Cereals, 4, 604
Cerebral cortex, 640
Cerebrovascular disease, 636, 688
Cerium oxide nanoparticles to prevent retinal disorders, 553, 696–701
Cerro Paranal, 302
Cervical cancer cell cultures, 661
Cervical carcinoma, 624
Cervical tumors, 620
Chalcogenide semiconductor, 438
Channels through the cell membrane
  Aquaporin water channel, 352, 575–576
  Ca^{2+} channel, 571, 573–575
  Cl^{-} channel, 575–576
  K^{+} channel, 571
  Protein channels, 576–578
Charge quantization, 15
Cheeses, 605
Chemical identification of individual surface atoms by AFM, 60–61
Chemical reactions in confined space, 230
Chemical vapor deposition (CVD), 124, 183, 210, 229, 599
Chemical vapor synthesis, 300
Chemistry-driven actuation, 307, 310
Chemistry on the nanoscale, 477–524
Chemotherapy, 623, 635, 666, 674–676
Chignolin, 92
Chip-based diagnostic magnetic resonance imaging, 629
Chirality, 211, 248–250, 600
Chiral Kagomé lattice from molecular bricks, 29–30
Chiral magnetic order, 373
Chitin, 598

Chitosan-based nanofibers, 708
Chloride (Cl^-) channel, 575–576
Cholesterol, 649–650
Cholesterol sensor, 649
Christian Dior, 606
Chromatic aberration, 78, 238
Chromosome dissection, 713
Chromosomes, 529, 704, 712–713
Cilia, 83
Ciliary dyskinesia, 569
Circular dichroism electron microscopy, 376
Circulating tumor cells, 629
Cisplatin, 666
Clathrate, 497
Climbing robots, 324–325
Clinical application, 620, 643, 660, 678, 680, 720, 727
Clinically approved nanoparticle formulations, 674
Clinical medicine, 615
Clioquinol, 693–694
Clusters, 99–107, 383–399
CNT rings, 230
Coefficient of spherical aberration, 76
Coercivity, 396–400, 457, 466
Coherent x-rays, 89
Coiled CNTs, 230
Collagen, 585–587
Collagen formation, 708
Colon cancer cell line, 661
Colon carcinoma, 667
Colorectal cancer, 635
Colorful nanoparticles, 178–181
Combination of nanomechanics and nanophotonics, 315
Communication technology, 169, 315
Compact disks (CDs), 462
Complex magnetic structure, 407
Composite fermions, 199
Composite media, 456
Composites, 238–239, 290
Computed tomography (CT), 618
Computer tomography (CT) contrast enhancement, 630–637
Computer tomography – positron emission tomography (CT-PET) fusion images, 637
Concerns, 616–617, 663
Conduction through individual rows of atoms, 193–194
Connexins (Cx), 696
Connexon, 674, 696
Constant current imaging (CCI), 51–53
Constant-height imaging (CHI), 53–54
Contact angle, 348, 523, 603
Contrast enhancement in magnetic resonance imaging (MRI) by nanoparticles, 674–675
Conversion of mechanical energy into electricity, 516
Cooper pairs, 17–18, 218
Cosmetics, 361, 479, 527, 605–609
Costs, 299, 426, 511–512, 634, 649, 686–688, 721
Coulomb blockade, 14, 43
Coupled wave theory in holography, 468
CRAC, 574
Crack advance, 289–290
Crack deflection, 587
Cracks, 289–290, 706
Crack tip, 289–290
Creep resistance, 280
Creutzfeld-Jakob disease (CJD), 692, 695
'Critical' Casimir force, 35
Crown ether, 478, 489–490, 583
Cryoelectron microscopy, 61, 81–83, 494, 529, 565, 576
Cryoelectron tomography, 76, 83, 530, 566, 579
Cryoreactors, 357
Cryptands, 478
Cryptography, 69, 169, 315, 326–327
Crystallinity engineering, 174
CT contrast enhancement, 630–632
CT/PET fusion images, 637
Cuboctahedron, 100, 172, 504
Curie temperature T_C in dependence of size, dimensionality, and charging, 396–397
Current densities, 145, 194, 214, 243, 331, 410–411, 452, 488
Current-induced domain wall motion, 365, 410–412
Current-induced magnetic switching, 409
Current-induced spin torque, 444
Cuts as narrow as 200 nm, 712
Cyclodextrin, 479–480, 488
Cytochrome *c*, 659–661
Cytoplasm, 529
Cytosol, 529
Cytotoxic effect of CPT-loaded MSNs, 661
Cytotoxicity studies on carbon, metal, metaloxide, and semiconductor based nanoparticles, 725–728

D

Dahlite, 596
DAPI (4,6-diamidino-2-phenylindole), 547–548

Data storage densities, 461
2D-confinement of fluids, 346–351
De Broglie wave length, 169
Debye temperature, 595
Decahedron, 100, 494
Decoherence, 181, 259, 320–322
Decoherence time, 321
Deep penetration, 637
Deep tissue imaging, 543–546
Deep tissue treatment, 684
Defects and atomic dynamics in graphene, 247
Deformation of cells, 532–533
Delay time, 471
Demotools, 431
Density functional calculations, 357, 371
Density functional theory (DFT), 55, 115, 172, 210, 219, 258, 373, 403, 502, 504
Density of states, local (LDOS), 52
Dental nanocomposites, 718
Dentin, 297, 595
Dentistry, 704
Deoxyribonucleic acid (DNA), 3, 33, 485, 492
Detection of calcium at the nanometer scale, 41–43
Detection of DNA and proteins, lowest limits, 641
Detection limit, 649, 651–652, 687
Diabetes, 576, 688
Diagnosis, 537, 615, 645–646
Diagnostics by biomolecular detection, 637–650
Diagnostic imaging, 618–650
Diagnostic tools of AD, 695
Diamond, 137
Diblock copolymers, 146, 160–161
“Diffraction before destruction”, 91
Diffusion, 303–306
Diffusion-controlled deformation, 285
Diffusivity, 303–306
Digital cameras, 434, 441
Digital versatile disks (DVDs), 462–463
Digital video, 425
Dimensionality, 365
Dimensionality effects in nanomagnetism, 383–397
Diphtheria toxin A chain, 664–665
Dipole interaction, 391–392
Dip-pen nanolithography, 158–159, 652–653
Disaggregation of amyloid aggregates, 694
Discernment between live and dead cells, 725
Discrete dipole approximation (DDA) in plasmonics, 110, 333–334, 336
Disease detection, 654, 674
Disease-induced alterations, 534–536
Disease recurrence, 643
Diseases, 568–569
Disease staging (T-staging), 624
Dislocation nucleation, 276, 279, 284
Dislocations (string-like defects in the material), 283
Dislocation storage capability, 285
Dispersive x-ray emission, 609
Displacement sensing, 35
Disulfide linkage, 669
DNA, 152–154, 639, 643
DNA elasticity, 557
DNA entering of cells by perforation, 713
DNA hybridization, 643
DNA purification, 654
DNA strands, 529, 559
DNA, supercoiled, 558
DNA transcription, 546
DNA transfection by nanorods, 670
DNA unzipping, 559
Domain wall, antiferromagnetic, orientational, 404
Domain wall, antiferromagnetic, phase, 403
Domain wall, pinning potential, 412
Domain wall velocities, 410–411
Doping of magnetosomes, 418–419
Doping of nanocrystals, 104
Double emulsions, 354–355
Double quantum dots, 181–183
Double-stranded (ds) DNA, 557–558
Doxorubicin, 667, 671, 674–675, 703
2D quantum well, 195–196
DRAM (dynamic random access memory), 23
Dropsy, 576
Drug delivery, 537, 637, 651
Drug delivery by magnetic nanoparticles, 670–671
Drug delivergy by nanoshells, 672
Drug delivery, number of scientific papers, 659
Drug delivery vehicles, 703
Drug targeting, passive, 658
Dynamic processes in superparamagnetic particles, 371
Dynamic random access memory (DRAM), 436
Dynamic recovery, 285
Dynamics of nanoconfined water, 347
Dynamics of nanoscopic water in micelles, 353
Dynamics in water nanodroplets, 499–500
Dyneins, 563, 569
Dzyaloshinskii-Moriya interaction, 373

E
Early detection of cancer, 662
Easy magnetic axis, 390
Easy magnetization direction, 390
Eddy current losses, 399
Efficient destruction of tumors, 684
Efforts for synthesizing chromosomes, 712
Elasticity to enzymology, 557–559
Electrical conductivity, 514
Electric-field controlled magnetism, 308–310
Electric field enhancement, 334
Electrodeposition, 123
Electromagnetic microneedle, 592
Electron beam lithography, 157
Electron density of states D(E), 16–17
Electron dispersive x-ray (EDX) analysis, 670
Electron-energy-loss spectroscopy (EELS), 79–80, 333
Electron holography, 81–82, 376, 378–379
Electronic circuits, 201, 471
Electronic properties, 14–19, 214–219
Electronics, 215
Electronic structure of graphene, 248–250
Electron microscopy, 376–380, 409, 529
Electron microscopy, aberration correction, 76–80
Electron microscopy, chromatic aberration correction, 78, 238
Electron microscopy, circular dichroism, 376
Electron microscopy, cryoelectron microscopy, 61, 81–83, 494, 529, 565, 576
Electron microscopy, cryoelectron tomography, 76, 83, 530, 566, 579
Electron microscopy, energy filtered, 81
Electron microsocpy, exit plane wave function, 77
Electron microscopy, high-angle annular dark-field (HAADF), 170, 333
Electron microscopy, Lorentz, 376, 377, 402
Electron microscopy, nanotomography and holography, 81
Electron microscopy, negative spherical-aberration imaging, 77
Electron microscopy, scanning with polarization analysis (spin SEM), 379, 411
Electron microscopy, spherical aberration coefficient, 76
Electron microscopy, Z-contrast, 78
Electron singlet state in double quantum dots, 182
Electron spin resonance (ESR), 181–182
Electron spin resonance, single spin, 315
Electron states in dependence of size and dimensionality, 14–16
Electro-optical nanotraps for neutral atoms, 341
Electrospinning, 235
Electrospinning of nanofibers, 120–121, 708
Electrowetting, 651
ELISA (Enzyme-linked immunosorbent assays)-based studies, 695
Embedded-atom method (EAM) potential, 290
Emerging solid state computer memory technologies, 436–454
Emulsifiers, 605
Emulsions, 604
Emulsions, double, 354
Enamel, 596–597
Enamel matrix, ultrastructure, 597
Endocytosis, 533
Endohedral metallofullerenes, 254–255
Endoplasmic reticulum, 529–531, 574–575
Energy conversion, 580–581
Energy conversion by a piezoelectric-semiconductor process, 516
Energy dispersive x-ray emission, 609
Energy dispersive x-ray spectroscopy (EDS), 719–720
Energy-filtered transmission electron micrograph (EF-TEM), 81
Energy product, 400–401
Enhanced permeability and retention (EPR) effect, 647, 659, 664, 676, 685
Enhanced reactivity of low-coordinated Au atoms, 503
Enhanced transport rates, 315
Enhancement of both strength and ductility, 282–285
Enhancement of osteoblast function by carbon nanotubes on titanium implants, 705–706
Entangled-photon source, 325–329
Entropic elasticity, 557
Entry of the nanoparticles into the cell, 541
Environmental, health and safety (EHS) research, 724
Environmental nanotechnology, 522–524
Environmental protection, 477–524
Enzymatic processes on DNA, 550
Enzyme-linked immunosorbent assays (ELISA), 159, 420, 645, 688
Epidermis, 606
Equal-channel angular pressing, 285
Erlotinib, 663
Escape of nanoparticles from the vasculature, 616

Escherichia coli bacteria, 88, 703
Escherichia coli bacteria, inactivation, 703
Esophageal carcinomas, 635
Esthetic restoration, 719
Eukaryotic cells, 529, 550, 558
Eukaryotic flagella, 83
European Extremely Large Telescope (E-ELT), 302
European Synchrotron Radiation Facility (ESRF Grenoble, France), 89
European x-ray free-electron laser (XFEL), 89
EUV (extreme ultraviolet) irradiation, 432
EUV lithography, 157, 201, 302, 431–433
EUV mirror, Mo-Si, 433
EUV wafer scanner, 432
Exchange bias (EB) effect, 403
Exchange interaction, 397
Exciton, 174, 219, 326–327
Exciton binding energy, 176
Exciton Bohr radius, 176
Exciton exchange interaction, 178
Exit plane wave function, 77
Exocytosis, 533
Explosive trinitrotoluene, 583
Extended x-ray absorption fine structure (EXAFS), 127, 270
Extensions to hard disk magnetic recording, 456–457
Extinction behavior of nanoparticles and arrays, 335–336
Extreme ultraviolet (EUV) lithography, 431–433

F

Familiarity hypothesis, 724
Faraday effect, 365
Far-field nanooptical observation of synaptic vesicle movement, video-rate, 73
Far-field optical microscopy beyond the diffraction limit, 67–73
Far-field optical regime, 62–63
Fast transport of liquids and gases through carbon nanotubes, 351–353
Fatigue, 267, 288–290
Fatigue life, 288
FDA – U.S. Food and Drug Administration, 616
Femtosecond laser surgery, 712–713
Fermi wavelength of electrons, 3
Ferritin, 405, 537, 588
Ferroelectric hysteresis, 414
Ferroelectric polymers, 447
Ferroelectric random-access memory (FeRAM), 446–447
Ferromagnetic correlation length, 397
Ferromagnetic exchange length, 3
Ferromagnetic exchange stiffness, 397
Ferromagnetic interaction, 484
Ferromagnetic nanorings, 365, 407–410
Ferromagnetic nanowires, 388–393
$Fe_{73.5}Si_{13.5}B_9Nb_3Cu_1$ alloy, 94
Fibrin scaffold, 592
Fibrous nanobiomaterials as bone tissue engineering scaffolds, 707–708
Field effect displays (FEDs), 238
Field-effect transistors, 187, 429
Field-emission electron gun, 81
Figure of merit, 36, 514
Filling factor, 196–198, 200
Filling and functionalizing carbon nanotubes, 230
Filtration membrane, 161, 301–302
Finite-difference time domain (FDTD) in plasmonics, 333
Finite-size atomic clusters, 386–388
Fishnet topology of metamaterials, 185
Flame retardants, 299
FLASH x-ray facility, 89
Flash memory, 434–436
Flash memory devices, organic, 436
Flow stress, 285
Fluids, confinement, 346–351
Fluorescein, 547–548
Fluorescence resonance energy transfer (FRET), 551, 568
Fluorodeoxyglucose (FDG), 635–636
Fluorofullerene $C_{60}F_{48}$, 259, 261
Flux vortices in superconductors, 81
Fly height of the writing/reading head, 454, 461
Foams, 4, 604
Fock state, 322, 326
Food and Drug Administration (FDA), 303, 635
Food nanostructures, 604–605
Food packaging materials, 605
Foods, 299, 353, 604
Foreign proteins, 640
Fourier transform infrared (FTIR) spectroscopy, 481, 590
Fractional Quantum Hall Effect (FQHE), 195, 197–199
Fracture toughness, 278, 706
Fracture work, 587
Fragrance in nanocapsules, 608
Free-electron laser, 89
Freescale Comp., 441, 446

Fresnel zone plates, 85, 381
Frictional force microscopy, 59
Fuel cells, 301, 306
Fullerenes, 137–139, 209–262
Functionalization for intracellular delivery, 668
Fusion of nanophotonics and nanofluidics, 315
Future prospects of integrated circuits, 426

G
Galena (PbS) crystallites, 605
Gas leakage, 299
Gas phase chemical reaction, 99
Gas transport in CNTs, 353
Gate-controlled GaAs nanowires, 112
Gecko's toe, 323
Gels, 604–605
Gene delivery, 547, 663
Gene delivery to human breast adenocarcinoma, 663
Gene delivery, non-viral, 670
Gene expression, 664
Gene expression pathway, 529–531
Gene expression profiling, 552
Genes, 643
Gene silencing, 667
Gene therapy, 662–667
Gene therapy and drug delivery for cancer treatment, 662–667
Gene therapy study, 664–665
Genetic profiling, single cell, 654
Genome, 640, 653
Genome pharmaceutics, 615
Genomes project, 425
Genome of a tumor, 663
Genomics, 537, 652
GFP (green fluorescent protein), 548
Giant magnetoresistance (GMR), 19–26, 457
Giant proteins, 259
Glass transition temperature, 439
Glauber state, 326
Glaucoma drug conjugated to ceria nanoparticles, 700
Glial cell line-derived neurotrophic factor (GDNF), 121
Glioblastoma (malignant cerebral tumor), 622, 676
Gliosarcoma, 675, 677
Glossiness of dental nanocomposites, 719
GMR (giant magnetoresistance) read head, 458
Gold nanoparticles, 502–505, 546, 552, 687
Golgi apparatus, 81–83, 529–531, 533
Gradient material dentin, 597
Gradual refractive index, 598
Grain boundaries, 267–268
Grain boundary diffusivity, 269–270
Grain boundary dislocations, 286–287
Grain boundary migration, activation energy, 269
Grain boundary mobility, 269–270
Grain boundary sliding, 285–287
Grain growth, 300, 304
Grain rotation, 278, 285–286
Graphane, 252
Graphene bilayer, 251–252
Graphene devices, 252
Graphene nanoribbon, 144, 249, 429–430, 474
The graphene nanoribbon field effect transistor (GNRFET), 430
Graphene sheet, 144, 212, 222, 246–247, 299
Gravity, 174, 320, 348
Green fluorescent protein (GFP), 548, 555, 622–623, 656, 666, 669–670, 714
Griscelli syndrome, 569
Growth process of nanowires, 115–117
Guest-host container molecules, 479

H
HA/collagen/polylactic acid (PLA) composite, 706
Hematoxylin and eosin staining – H & E, 622, 683, 685–686, 690
Hagen-Poiseuille flow, 352
Hair dyeing, 605, 608–609
Half pitch, 155, 434
Hall-Petch behavior, inverse, 271, 275, 310
Hall-Petch relation, 136, 272–273, 275
Hard disk drive, 425, 452, 455, 457
Hard disk magnetic recording, 456–457
Hard disks, 425
Hard disks, optical, 462–470
Hardness, 597
Heart, 631
Heart diseases, 686–688
Heat of fusion, 11
Heisenberg model, 369, 405
HeLa cells (human epithelial cells), 567, 662, 672, 727
α-helical proteins, 565, 576, 587, 610
Helical motifs, 489
Helical vortices, 392
α-Helices, 560
Hepatocellular carcinoma, 634
HER2 marker protein, 541
HER2 receptor-specific antibody trastuzumab (Herceptin®), 667
Herceptin, 619–621

High-angle annular dark-field (HAADF) image, 80
High-angle annular dark-field (HAADF) scanning transmission electron micrograph (HAADF-STEM), 170, 333
High electrical current densities of a single strand of Au atoms, 194
High field-gradient electromagnets, 691
High-k dielectrics, 470–471
High-resolution transmission electron micrograph (HRTEM), 471, 610
HIV/AIDS therapy, 662
HIV inhibitor saquinavir delivered into cells by nanoparticles, 701–704
Hollow cages, 253–258
Hollow clusters, inorganic, 495–498
Hollow gold nanospheres, 336, 339
Hollow nanoparticles, 134
Hollow Pt nanospheres with nanochannels, 506
Holographic data storage, 468–470
Homebox gene called *Barx1*, 722
Human cancer-cell lines, 659–660, 683
Human cataract lens cell membrane, 696–701
Human exposure to static magnetic fields, 671
Human immunodeficiency virus–1 (HIV1), 159, 653
Huntington's disease, 636
Hydrodesulfurization (HDS), 507–509
Hydrodynamics at the nanoscale, limits, 351
Hydrogen storage, 5
Hydrogen storage and fuel cells, 516–519
Hydrophobic coating, 523
Hydrophobic hierarchical micro- and nanostructures, 602
Hydrophobicity, 601–603
Hydroxyapatite (HA), 594–596, 706–707
Hydroxyapatite (HA)/collagen/polylactic acid (PLA) composite, 706
Hydroxyapatite nanoparticles for treating bone defects, 706
Hygiene enhancement by nanoparticles, 703
Hypertension, 649
Hyperthermia treatment, 678–682
Hyperthermia treatment by heating of magnetic nanoparticles by means of an alternating magnetic field, 679–682
Hysteresis loop, 392–396, 398

I

IBM, 23, 123, 441, 454
IC_{50} values, 670, 727
Icosahedron, 100
Identification of tumors, 620
Identification (RFID) tags, 446
Imaging, 365–366, 618
Imaging of graphene, 246–248
Imaging, single biomolecule, 89–91
Immunoassays, 554, 650
Immunoglobulins, 640
Implanted chips, 656–658
Inactivation of specific genomic regions, 713
Incoherent interfaces, 173
Indentation simulation, 278
Infarction, 649, 686–688
Infarcts, 636, 668
Infection, 535, 617, 620, 627–628, 640, 651, 663, 690, 703
Influenza virus, 590, 703
Initial permeability, 397
Inks, 483
In-plane magnetic anisotropy, 395
Insulin-loaded PLAF vesicles, 688
Integral quantum Hall effect (IQHE), 196–198
Integrated circuits, 134, 234, 244, 426
Integration densities, 447
Integration of optical manipulation and nanofluidics, 342–343
Integrins, 531, 667
Intel, 3, 242, 244, 425–426, 471
Interconnects, 234, 240, 427, 471
Interdisciplinarity, 4
Interfaces, 3, 271
Interfaces, incoherent, 173
Interfaces, organic-inorganic, 294
Interfaces, temperature-dependent structural change, 270
Interfacing of nanowires with cells, 554
Interference color phenomena, 598
Interference pattern, 259–260
Interferon receptor, 162
Interlayer dielectric (ILD), 471–473
Intermolecular interactions, 500, 565
International Technology Roadmap for semiconductors (ITRS), 472
Intramolecular interactions, 565
Introduction, 1–43
Inverse Hall-Petch behavior, 271, 275, 310
Invisibility cloaks, 185, 360
Ion channels, 571
Ion channels, pentameric ligand-gated, 579
Iridescence, 597
Iron oxide (Fe_3O_4) nanocrystals, 620, 621
Island growth on substrates, 111
In vivo longevity of nanocarriers, 667

J
Japanese XFEL, 89
Jobs, 6
Junctions of carbon nanotubes, 229

K
K^+ membrane channel, 571
K^+ membrane channel, opening and closing mechanism, 573
Kerr effect, 365
Kidney disease, 569, 575
Kinesins, 563, 567–569, 584
Kirchhoff-Fresnel diffraction model, 260
Kirkendall effect, 174
Kupffer cells, 556

L
Labeling biosystems by nanoparticles, 540–542
Lab-on-a-Chip, 343, 651–652, 655
Landau levels, 196–197, 199, 250
Landau-Lifshitz-Gilbert equation, 410
Landau magnetic domain structure, 381
Langmuir-Blodgett, 123
Large carbon molecules, 253–258
Large Hadron Collider (LHC), 425
Large-scale curving of a membrane, 533
Laser ablation, 99, 124, 139, 471
Laser axotomy, 715
Laser cooling, 322
Laser deposition, 124, 414, 641
Laser dissection of a single neuronal dendrite, 715
Lasers, nanostructured, 191, 329
Laser surgery in *C. elegans*, 714
Lattice coherency, 173
Lattice parameter, 12–13
Layered oxide heterostructures, 127–128
Layer-by-layer (LBL) assembly, 294
Lenses, "perfect", 185
Lens-less coherent x-ray diffraction imaging, 89
Lens opacification, 696
Leukemia cells, 656, 658
Li^+ batteries, 245
$LiFePO_4$ cathodes for Li^+ ion batteries, 520–521
Ligament and tendon reconstruction, 708
Light conversion, 486–487
Light emitting diodes (LEDs), 24, 189–191, 243, 344
Light-induced heating of nanoshells, 684–686
Linac Coherent Light Source (LCLS), 89
Lipid nanoparticles, 675
Liposomes, 605–607
Liposomes and micelles as nanocarriers, 667–670
Lithium ion batteries, 519–522, 588
Lithography, 154–164, 431–433
Lithography demotools, 431
Lithography, extreme ultraviolet (EUV), 431–433
Lithography, liquid immersion, 156
Lithography, two-photon, 164
Lithography, UV, 154–155
Liver, 631–632, 648
Liver metastases, 620
Local spin density approximation (LSDA), 403
Logic circuits, 429
Logic gates, 187
L'Oreal, 607
Lorentz microscopy, 376–377, 402
Lotus effect, 348, 527, 602
Lotus leaf effect, 601–604
Low-k materials, 471–473
Low molecular weight ligands, 659
Low molecular weight proteome (LMWP), 641
Lungs, 631, 663
Lung therapy – targeted delivery of magnetic nanoparticles and drug delivery, 689–691
Luttinger liquid behavior of electrons, 17, 218–219
Lymph node, 623–625, 632–633
Lymph-node mapping, 543
Lymph node metastases, 623, 625
Lymphography, 632–633
Lymphoma, 635

M
Macrophages, 625
Magic numbers, 99–100
Magnetically sensitive scanning probe techniques, 365
Magnetically tunable photonic crystals, 416–417
Magnetic anisotropies, 308–309, 390
Magnetic anisotropy energy (MAE), 390, 395
Magnetic assembly of colloidal superstructures, 31–32
Magnetic circular dichroism studies by transmission electron microscopy, 380
Magnetic coercivities, 392
Magnetic dipole interaction, 391–392
Magnetic domain structure, 380
Magnetic domain-wall racetrack memory (RM), 450–453
Magnetic domain walls in nanowires, 391–392
Magnetic drug delivery systems, 671

Magnetic energy product, 400–401
Magnetic exchange bias (EB) effect, 403
Magnetic exchange energy, 410
Magnetic exchange force microscopy (MEx FM), 366–370
Magnetic exchange interaction, 367–369, 392, 406
Magnetic FePt nanoparticles, 552
Magnetic ferrite nanoparticles, 105
Magnetic films, 393–396
Magnetic flux quanta, 198–199, 371
Magnetic force microscopy (MFM), 74–75, 366–370
Magnetic hard disks, 454–461
Magnetic hysteresis (Fig. 8.37c) of purely molecular origin, 412
Magnetic hysteresis loops, 383
Magnetic imaging, 365–383
Magnetic imaging with atomic resolution, 374
Magnetic imaging, magnetic exchange force microscopy (MExFM), 366–370
Magnetic lab-on-a-drop, 656
Magnetic nanoparticles, 105, 592, 659
Magnetic nanoparticles, FePt, 552
Magnetic nanoparticles, ferrites, 105
Magnetic nanostructures, time-resolved imaging, 381
Magnetic properties, modification by electric fields, 307
Magnetic properties of single atoms, 384
Magnetic properties, size dependence, 386
Magnetic random access memory (MRAM), 23, 408
Magnetic resonance imaging (MRI), 36–37, 616
Magnetic scanning probe techniques, 74–76
Magnetic tunnel junctions, 22, 441, 443, 445
Magnetic tunneling junction (MTJ), MgO based, 461
Magnetite, 416
Magnetization behavior of Fe nanowires in carbon nanotubes, 392–393
Magnetization, onion state, 377, 408
Magnetization switching by means of SP-STM, 374
Magnetocrystalline anisotropy, 392, 398
Magnetocrystalline anisotropy energy, 384, 410
Magnetoelectric coupling, 414
Magneto-optical Kerr effect, 395
Magneto-optical recording, 466–467
Magnetoresistive random-access memory (MRAM), 441–446
Magnetoresistive random access memory (MRAM), switching, 438
Magnetosomes, 417
Magnetosomes for highly-sensitive biomarker detection, 419–420
Magnetostriction, 399
Magnetotactic bacteria, 417
Magnon excitation, 374
Magnons, 370
Malaria disease, 535
Manuka beetle, 600–601
Mapping vector fields, 65–66
Massless Dirac fermions, 143, 248–250
Mass saving, 299
Mass sensing, 35–36
Mass spectrometry (MS), 641
Materials, 596
Materials with bioinspired adhesion, 324
Mathematical techniques, novel, 425
Matrix-assisted laser deposition/ionization time-of-flight (MALDI-TOF) MS, 641
Matrix-assisted laser desorption/ionization time-of-flight (MALDI-TOP) mass spectrometry, 696
Maxillofacial application of nanobioceramics, 720–721
Maximum energy product, magnetic, 400
MCM-41 mesoporous silica, 149
Measuring techniques, nanoscale, 35–43
Meat, 4, 604
Mechanical alloying, 137
Mechanical properties, 184, 186, 588
Mechanical properties of carbon nanotubes, 220–222
Melanoma, 635
Melting of nanoparticles, 11–12
Melt viscosity, 483
Membrane boundaries, 590
Membrane channels, 527, 571–580
Membranes, 103
Memories for data storage, 425–474
Mesenchymal cells, 722
Mesenchymal stem cells, 121, 708
Messenger RNAs, 531
Metal chelation, 552
Metallofullerene Gd@C_{82} crystals in SWNTs, 230
Metal–organic chemical vapor deposition (MOCVD), 126
Metamaterials, 183–194, 345
Metastases, 533, 623, 632
Metastatic lymph nodes, 620
Metrology, 197

Micelles, 353–354
Microchips, 651
Microelectromechanical systems (MEMS), 315
Micromagnetic modeling, 409, 444
Microscopy, 49, 68
Microtubule doublets, 83
Microtubules, 529, 563, 601
Military supercomputers, 425
Milk, 4, 604
Mimicking of photo synthesis, 582
Mineralization, 705, 708
Mini-genomes, 592
Misfit dislocations, 126
Mitochondria, 81–83, 529, 542, 569, 601, 668, 693
Mitochondrion ablation, 712–713
Mitochondrion activity, 725
Mobilities, 215, 243, 248, 431
Molecular beam epitaxy (MBE), 112, 124
Molecular biology, 537
Molecular cancer diagnosis, 645
Molecular detection techniques, 618–650
Molecular dynamics (MD), 172, 221, 267–268, 536, 570
Molecular dynamics (MD) simulations, 267–268, 270–271, 279, 284, 297, 346, 591
Molecular magnets, 483
Molecular motors, 3, 527, 563–571, 580, 583–584
Molecular nanowires, 192, 487
Molecular recognition, 484–486
Molecular recognition in sandwich assays, 551
Molecular sieving, 145
Molecules in motion, 230
Monitoring of human biological systems, 615
Monocyte/macrophage cells (Mo/Mac), 701–702
Monte Carlo (MC) simulations, 392, 403
Montmorillonite (MTM) nanocomposites, 294, 589
Moore's law, 3, 153, 425, 471
Morpho butterfly, 598
MoS_2 nanocatalysts, 507–509
Mo–Si mirror for extreme ultraviolet (EUV) radiation, 433
Mössbauer spectroscopy, 405
Motor domain of a molecular motor, 563
Motorola, 441
Motor regulation, 568
Mott insulator, 214
MRI (magnetic resonance imaging) contrast enhancement with magnetic nanoparticles, 674–675
MR/PET imaging, 637
MTJ read head, 460
Multiferroic nanostructures, 365, 412–416
Multifunctionality of nanoparticles, 666, 672
Multilayered polymer composites, 132
Multilayered systems, 123–132
Multilayer-graded index profile, 515
Multilayer mirrors, 302, 431
Multilayer recording, 467–468
Multilayers, 195
Multilayers, metallic, 132
Multilayers, NiFe/CoFe/Cu/CoFe, 94
Multilayer structure, 598
Multiple multipole (MMP) techniques for local-field calculations in plasmonics, 333
Multiple operations of fluidic microchips, 653, 656
Multiplexed detection by nanoarrays, 652
Muscle, 565
Muscle contraction, 565
M13 virus, 121
Myometrium, 620, 624
Myosin myopathies, 569
Myosin protein molecules, 604
Myosins, 532, 564–566, 604–605

N

Nacre, 296, 587
Nacre of red abalone, 297
Nanoadhesion, 323–325
Nanoarrays, 650–658
Nanobell, 230
Nanobiomaterials for artificial tissues, 704–712
Nanobubbles, 315, 358–360, 632
Nanobubbles on surfaces, 358
Nanochannel technology, 658
Nanochemistry, 477–524
Nanocomposites, 290–300, 594, 718
Nanocomposites of carbon nanotubes, 297
Nanocomposites in dental restoration, 718–719
Nanocomposites, metallic, 290–291
Nanocomposites oxide/dye/polymer, 293–294
Nanocomposites, polymeric, 293–294
Nanocomposites for remineralization of tooth lesions, 721–722
Nanocrystalline ceramics, 102, 300–303
Nanocrystalline materials, 267–310
Nanocrystallite–glass ceramics, 301–303
Nanocrystallites, metals, 102, 172–174
Nanocrystals, 99–107, 169–205

Nanocrystals, semiconductors, 104, 174–178, 727
Nanodentistry, 717–723
Nanodevices in medical diagnostics, 656
Nanodroplets, 315, 353–358
Nanoelectromechanical switches, 316–319
Nanoelectromechanical systems (NEMS), 315–319
Nanofibers, electrospinning, 120
Nanofibers, poly (ε-caprolactone), 710
Nanofluidics, 315–361, 650–658
Nanofluidic systems, 654
Nanofluidics and optical manipulation, integration, 342–343
Nanofluidics, mixing, 652
Nanofocused hard x-ray beam, 89
Nanogenerator for energy conversion, 516
Nano-hedgehogs, 495
Nanohydroxyapatite, 708, 720
Nanoimprint lithography (NIL), 158–159
Nanoindentation, 276–279
Nanoindenter–TEM facility, 277
Nanolayers, 123–132, 169–205
Nanoleakage of adhesive interfaces in dentistry, 719
Nanoliters, 651
Nanomagnetism, 365–420
Nanomagnets in bacteria, 365, 417–420
Nanomagnets of SmCo and NdFeB alloys, 106
Nanomechanics, 315–361
Nanomechanics of DNA, proteins, 557–563
Nanomechanics and nanophotonics, combination, 315
Nanomedicine, 615–728
Nanometal–insulator composites, 147
Nanoneurosurgery, 617, 713
Nanoparticle-based assays, 695
Nanoparticle–DNA interaction, 546–552
Nanoparticle layer, 108
Nanoparticle–protein interaction, 552–557
Nanoparticles, 658
Nanoparticles and arrays, extinction behavior, 335–336
Nanoparticles for bioanalysis, 537–557
Nanoparticles for chemotherapy, 675–676
Nanoparticles, Fe and Co, 105
Nanoparticles, intracellular distribution, 668
Nanoparticles, metaloxides, 727
Nanoparticles, polymeric, 691
Nanoparticles shape control, 132–134
Nanoparticles, surface functionalization, 540
Nanoparticle superlattice sheets, 107–109
Nanopatterning of stable microbubbles, 358–359
Nanophotonics, 315–361
Nanophotonics and nanofluidcs, fusion, 315
Nanoporous anodic aluminum oxide, 147
Nanoporous hydroxyapatite (HA), 706
Nanoporous materials, 145–154
Nanoporous materials by self-assembly, 149
Nanoporous membranes, 147
Nanoporous metals, 150–152
Nanoporous semiconductors, 150
Nanoribbon, 246
Nanorobots, 714
Nanorod-mediated DNA transfection, 670
Nanoscale double emulsions, 354
Nanoscale measuring techniques, 35–43
Nanoscience research centers, 5
Nanoscopy, 49–95
Nanoshells, light-induced heating, 684–686
Nanoshells for thermal drug delivery, 672
Nano silver-titanium dioxide for enhanced hygiene, 703
Nanosized catalysts, 518
Nanosized FePt and FeCo alloys, 106
“Nanosized voltmeter”, 40–42
Nanosomes, 605
Nanostructured bioceramics for bone restoration, 706
Nanostructured bioceramics for maxillofacial applications, 720–721
Nanostructured hard magnets, 399–401
Nanostructured metals, 727
Nanostructures by ball milling, 136–137
Nanostructures with complex shapes, 134–135
Nanostructures, silicon, 512
Nanostructures in supercritical fluids, 163
Nanosurgery, 616, 712–717
Nanotechnology for computers, 425–474
Nanotechnology platforms, 656
Nano test tubes, 498–499
Nanotubes, 587
Nanotubes by the bacterium Shewanella, 122
Nanotubes from materials other than pure carbon, 235–236
Nanotubes, polymeric, 240
Nanotweezers, 224–229
Nanowire-based biosensor, 657
Nanowire growth, oriented attachment, 120
Nanowires, 169–205, 645, 649, 656–657
Nanowires in carbon nanotubes, 114
Nanowires, ligand control synthesis, 118
Nanowires, GaAs, gate-controlled, 112
Nanowires, metallic, 183–184

Nanowires and nanofibers, 111–123
Nanowires of pine-tree type, 116–117
Nanowires, semiconductors, 186–192
Nanowires, silver, 588
Nanowires, ultrathin, 117–120
Nantero Inc., 450
Navier–Stokes equations, 351
Near-edge x-ray absorption fine-structure (NEXAFS), 85
Near-field optical microscopy, 61–67
Near-field scanning interferometric apertureless microscopy, 64–65
Near-infrared (NIR) light, 639
Necrosis, 672, 676
Negative refraction, 186
Negative refractive index materials, 183
Nerve signaling, 582
Neuroblastoma, 68–69
Neurofilaments, 68–69
Neuron adhesion and growth, promotion, 708–710
Neuroscience, 615
Neutron scattering, 405
New life form, 712
NIH (National Institute of Health, U.S.A.), 615
Nitrogen-doped nanocrystalline TiO_2 films sensitized, 511
Nitrogen-vacancy center in diamond, 326
Nuclear magnetic resonance, 295
Nuclear magnetism, 218
Nuclear membranes, 581
Nuclear pores, 579–580
Nuclear spin relaxation, 315
Nucleus, cell, 529

O

Observatory mirror, 302
Odorant, 582
Olfactory system, 582
Oligonucleotides, 653
'Onion' magnetization state, 377, 408
Opening and closing mechanisms, 573
Ophthalmology, 696–701
Opsonins, 556
Optical absorption, 140
Optical hard disks, 462–470
Optically active biosystems, 600
Optical sideband cooling, 322
Optical transparency, 300
Optical traps for manipulation of nanowires, 191
Optical tweezers, 532
Optofluidic transport, 344
Orbital magnetic moment, 381, 386–388
Organic light emitting diodes (OLEDs), 243
Orthopedics, 705
Osteoblast function on Al_2O_3 nanofibers, 720
Osteoblast-like cells, 706
Osteoblasts, 594, 706
Osteocytes, 595
Osteogenic differentiation, 708
Osteoid water, 595
Osteon, 595
Oxygen permeability, 605
Oxygen radicals, 698
Oxygen vacancies, 699

P

Paclitaxel, 670, 674–675, 702
Pancreatic cell lines, 661
Parkinson disease, 692
Pauli exclusion principle, 359, 369, 392
PCR – polymerase chain reaction, 641
Peptides, 641
Peptides precipitating silica, 587
Perovskite, 414
Perpendicular recording, 458
Persistence length, 557
Pharmacokinetics, 557, 637, 679
Phase-change layer for optical hard disks, 464
Phase-change memory for data storage, 437–441
Phase I study of hyperthermia treatment, 680
Phase transitions, 13
Phase transitions induced by nanoconfinement of liquid water, 347
Phospholipid bilayer membrane, 531
Photoactivated localization microscopy, 68
Photobleaching of dyes, 537, 539
Photocatalysis of water, 5
Photoconductivity spectrum of a single carbon nanotube, 220
Photoelectron emission microscopy (PEEM), 87
Photoluminescence quantum yields of SWNTs, 220
Photon antibunching, 326
Photonic bionanostructures, 597–601
Photonic crystals, 180, 416–417
Photon sources, 325–328
Photovoltaics, 300, 510–513
Physical principles, 1–43
Piezoelectricity, 316
Piezoelectric properties, 186
Piezoelectric–semiconductor process, 516
Pilatus x-ray detector, 89

Pinning potential, 412
Pits on hard disks, 462
Pit-and-tissue sealants in dentistry, 722
Plasmon absorption, 637
Plasmon-controlled synthesis of metallic nanoparticles, 334–335
Plasmonic nanocavities, 337–338
Plasmonics, 331–345
Plasmon oscillations, 616
Plasmon resonance, 148, 180, 465, 684, 695
Plasmons, 174, 186
Plasticity, 267, 271–276
Plasticity and Hall–Petch behavior of nanocrystalline materials, 271–276
Plectonemes, 558–559
Point resolution in microscopy, 76
Polycarbonates for hard disks, 465
Polyethylene glycol (PEG), 646, 677
Poly (hexylcyanoacrylate) nanoparticles, 701
Polymerase chain reaction (PCR), 650, 656
Polymer-based solar cells, 512
Polymeric nanoparticles, 691
Polymer nanocomposites, 293–294
Polymer nanotubes, 240
Poly(methyl methacrylate) (PMMA), 299, 429
Polyyne $C_{10}H_2$ molecules, 233
Poly (ε-caprolactone) nanofibers, 710
Porosity, 301
Porous oranosilicas, periodic, 473
Porous silica nanoparticles for targeting cancer cells, 659–662
Porphyrin, 580–581
Positioning precision, 431
Positron annihilation (PA), 270
Positron emission tomography (PET), 618, 635–637
Positron lifetimes, 102, 301
Potassium channel, 571
Precipitates, 280
Precursor film, 349
Predisposition to, or onset of, disease, 640
Pre-messenger RNA, 83
Preproduction tool in lithography, 431
Probing superconductivity at the nanoscale, 39
Products, 5
Progress in electron microscopy, 76–84
Projection optics, 432–433
Prolonged hypoglycemic effect, 689
Promoters for the MoS_2-based HDS catalysis, 508
Promoting neuron adhesion and growth, 708–710
Prostate cancer, 189, 620, 625, 656, 680
Prostate specific antigen (PSA), 640, 645, 655
Proteasome, 531
Protein β-sheets, 560
Protein channels, 576–578
Protein hormones, 640
Protein–inorganic interfaces, 587
Protein mechanics, 560–563
Protein nanolithography, 162–163
Protein–protein interaction, 163
Proteins, 640, 653, 661
Proteins from dying cells, 640
Protein self-assembly, 587
Protein structures, 561
Protein unfolding, 563
Proteome, 640, 656
Proteomic analysis, 640
Proteomics, 537, 640, 652
Proton-beam writing, 157
Proton channel, 591
Ptychography, 89
PVBA (benzoic acid), 480

Q

Quantization of conductance, 113
Quantum-classical transition, 319
Quantum computing, 181–183, 315, 326
Quantum confinement, 14
Quantum cryptography, 326, 327
Quantum dot data storage devices, 183
Quantum dot lasers, 329–331
Quantum dot lasers, transparency current, 330
Quantum dots, 104, 616
Quantum dots, infrared, 170
Quantum electrodynamics, 143, 248
Quantum gates, 181
Quantum Hall effect, 195, 250–251
Quantum information technology, 328
Quantum phenomena, 315
Quantum physics, 259
Quantum tunneling of the magnetization, 384
Quantum wires, 111
Quasi-crystalline alloy, 290
Qubits, 181–183

R

Rabi oscillations, 181, 183
Race track memory (RM), 437
Radial breathing mode (RBM), 213
Radiation damage, 91
Radiation sources for EUV lithography, 431
Radiofrequency identification (RFID) tags, 446
Radiofrequency ablation (RFA) of malignant tumors, 682
Radiofrequency STM, 56

Radius of gyration, 294
Raman scattering, 173
Raman spectroscopy, 140, 541, 618
Raman spectroscopy imaging, 637
Raman spectroscopy on the nanometric scale, 40
Random anisotropy model, 397
RCK ('regulates conduction of K^+'), 573
REACH program of the European Union, 607
Reaction of single molecules, 500–502
Reactive milling, 137
Read back head, 457
Read heads, 454
Real time contrast-enhanced ultrasound imaging, 634
Receiver–transmitter nanoantenna pairs, 341
Recyclability, 299
Red abalone, 297
Red blood cells (RBCs), 534
Reflection high-energy electron diffraction (RHEED), 471
Regenerated axons, 714
Regeneration of both the peripheral and the central nervous system, 708
Regenerative medicine, 615
Regrowth of axons, 711
Remanence, 396
'Remanence enhancement', 399
Remote control of cellular behavior with magnetic nanoparticles, 592
Renewable energy, 477–524
Replicating the complex nanostructure of bone, 595
Repulsive long-range Casimir forces, 34
Resin–dentin interface, 719
Resist, 433
Resistance-area product RA, 442
Resistance RAM (ReRAM), 437
Resistance random access memories (ReRAMs), 447–448
Retina, 582, 696
Retinal pigment tissue, 592
Retinitis pigmentosa, 569
Reversible change of the GB radial distribution function, 270
Rewritable disks, 464
Reynolds numbers, 651
RHEED (reflection high-energy electron diffraction), 128, 471
Rhinovirus, 161
Rhodamine, 539, 701
Ribonucleic acid (RNA), 3
Ribosome-based self-reproducing system, 592
Ribosomes, 84, 529, 579
Ring oscillator, 429
Risk assessment and biohazard detection of nanomaterials, 724–725
Risk assessment strategies, 723–728
Risks, 7
RKKY-type (Ruderman–Kittel–Kasuya–Yosida) magnetic coupling, 21, 26, 370, 384, 459
RNA (ribo nucleic acid), 152, 529, 639
Roadmap, 432
Rose petal, 602
Rotational actuator, 316
Rotaxanes, 488–489, 584
Roughness, 127
Row-by-row growth, 111
Rutherford back scattering (RBS), 127, 304

S

Saliva, 651
Saquinavir, 701
Saturation magnetization, 395
Sausages, 604
Scales of organization, 594
Scaling down, 435
Scanning electron microscopy with polarization analysis (spin SEM), 379, 411
Scanning near-field optical microscopy (SNOM), 61–67
Scanning TEM (STEM), 76
Scanning tunneling microscopy (STM), 49–56
Scanning tunneling microscopy, constant current imaging, 51–53
Scanning tunneling microscopy, constant height imaging, 53–54
Scanning tunneling microscopy, operated at radiofrequencies, 56
Scanning tunneling microsocpy with spin polarization (SP-STM), 75–76, 370–376
Scanning tunneling microscopy, synchrotron radiation assisted, 54
Scratch/mar resistance, 299
Seagate Technology, 460
Sealing ability of an adhesive, 719
Sea urchin, 83
Secondary ion-mass spectrometry (SIMS), 304
Second-phase particles, 282
Secreted proteins, 640
Self-assembled monolayers (SAMs), 30–31
Self-assembled nanostructures, 708
Self-assembly, 27–33, 123, 596
Self-assembly of Fe nanoparticles, 29
Self-assembly of Ni nanoclusters, 28

Self-assembly via DNA or proteins, 33
Self-cleaning, 601–604
Self-organization, 489–493
Self-replicating nanoscale assemblers, 6
Self-reproducing system, 592
Sensing, 174, 582–583
Sensing range (10^6), 643, 645
Sensing of weak magnetic fields, 36–37
Sensors, 245, 300–301, 305
Sensors for biomolecules, 645
Sensors, nanowire-based, 657
Sensory transduction, 571
Sentinel lymph node (SLN), 623, 632
Sentinel lymph node surgery making use of quantum dots, 713
Separation of oil and water, 523
Severe plastic deformation, 287
SF3b splicing factor complex, 83
Shape anisotropy, 392
Shape control of nanoparticles, 132–134
Sharp Corporation, 447
β-Sheets, 560
Shift register, 450
Side effects, minimization, 658
Signaling, 580, 583
Signal peptide, 577
Silicon *p-n* junction, 81
Silk, 585
Single atom contacts, 193–194
Single-cell genetic profiling, 654
Single-electron transistors (SET), 321, 428
Single living cells, 534–536
Single molecule magnets, 365, 412, 452
Single molecule structure, 92
Single nanopores – potentials for DNA sequencing, 152–154
Single-photon source, 325–329
Single-photon detection, 328
Single-photon transistor, 343
Single-stranded (ss) DNA, 557
Singlet oxygen, 672
Single-walled carbon nanotubes (SWNTs), 139–142, 638, 682
Sintering, 300
Size dependence of magnetic properties, 386
Slip length of fluids, 348
Slot waveguide, 342
Softening of nanomaterials, 284
Soft-magnetic materials, 397–399
Solar batteries, 588
Solar cells, polymer based, 512
Solar energy – photovoltaics, 510–513
Solar energy – thermal conversion, 514–515
Sol–gel process, 103, 300
Solid immersion lens, 464
Sony Company, 446, 519
Sorting single-walled carbon nanotubes, 211
Spatulae on gecko toes, 323
Spiderman suit, 324–325
Spinal cord in vitro surrogate, 710–712
Spin canting, 405
Spinel, 414
Spin-flip scattering length, 218
Spin Hall effect, 26–27
Spin magnetic moment, 381, 386
Spin moment of Fe atoms, 387
Spin-polarized scanning tunneling microscopy (SP-STM), 75–76, 370–376
Spin torque effect, 375
Spin transistor, 23
Spintronic devices, 370
Spintronics, 20, 23–26
Spin valve, 21
Spin wave, 408
Spleen, 632, 648
Split-ring resonators, 185
Spontaneous polarization, 81
Spreading of liquids, 315, 346–351
Spreading velocity, 350
Sputtering, 99, 124
SRAM (static random access memory), 23
Stacking-fault energy, 272
Staging, 624–625
Standard quantum limit, 320
Static random access memory (SRAM), 425, 436
Stem cell biology, 722
Step assist, 298
Stimulated emission depletion (STED) optical microscopy, 68–70, 529–531
Stimuli-sensitivity functions, 667
Stochastic optical reconstruction microscopy, 68–70
Stomach cancer cell line, 661
Stone–Wales defect, 222
Storage densities, 461
Stranski–Krastanov growth, 111
Strength, 186, 267, 585, 589
Strength and ductility by second phase particles, 282
Strong plastic deformation, 136
Structural materials, 300
Structure of carbon nanotubes, 212–214
Sub-femtometer displacement sensing, 315
Sub-single-charge electrometry, 315
Substrate, 391

Sugars, 581
Sum rules for spin and orbital magnetic moments, 381
Sun screen agents, 608
Supercapacitors, 5, 519–522
Supercoiled DNA, 558
Superconducting interference device (SQUID), 322
Superconductivity, 17–19, 201, 218
Superconductivity at the nanoscale, 39
Superexchange, 369
Superfluid helium nanodroplets, 356–358
Superfluidity of pH_2 clusters, 358
Superhard materials, 292
Superheating and supercooling, 255–257
Superhydrophobicity, 601
Superhydrophobic surfaces, 348–349
Superlattices, 107–111
Superlattices of nanocrystals, 124
Superparamagnetic behavior of nanoparticles, 656, 670
Superparamagnetic blocking temperatures, 386
Superparamagnetic limit, 386, 456–457
Superplasticity, 267, 285–288, 300
Superposition of states, 259, 319
Supersonic expansion, 99
Supporting substrate, 384
Supramolecular chemistry, 477–524
Supramolecular DNA polyhedra, 493
Supramolecular materials, 480–484
Supramolecular polymers, 482
Supramolecular receptor–substrate interaction, 489
Surface atomic structures, 172
Surface atoms, chemical identification by AFM, 60–61
Surface-controlled actuation, 306–310
Surface energy, 8–9
Surface-enhanced fluorescence, 341
Surface-enhanced Raman scattering (SERS), 180, 341, 637, 706
Surface faceting, liquid state, 354
Surface functionalization of nanoparticles, 540
Surface-induced manipulation, 267
Surface nanobubbles, 358
Surfaces, 3
Surimi, 604
Survival, 676
Survival rates, 676
Switching, 438
Synaptic vesicle movement, far-field nanooptical observation, video-rate, 73
Synchrotron radiation assisted STM, 54
Synovium, 625
Synthesis, 99–165, 473
Synthesis by chemical routes, 101–104
Synthesis gas, 509
Synthesis of nanocrystals, 169–171
Synthesis of nanoparticles, plasmon controlled, 334–335
Synthetic membrane channels, 590

T

Tagging of biomedical targets by nanoparticles, 537
Talbot–Lau interferometry, 259
Tamoxifen, 702
Target-directed magnetic field gradient, 689
Targeted death of luminal cells, 665
Targeted drug delivery, 500–502, 637
Targeted drug delivery by nanoparticles, 658–672
Targeted multifunctional polyacrylamide (PAA) nanoparticles for photodynamic therapy (PDT) and magnetic resonance imaging (MRI), 676–678
Targeted nanoparticles, 678–686
Targeted therapy, 667
Targeting, 615, 637, 646
Targeting vectors, 667
Tau protein, 692, 695
Teeth, 593–597
Teleportation, 327
TEM nanotomography and holography, 81
Temperature-dependent structural change of interfaces, 270
Templating, 117
Tendon, 297, 585
Tensile strength, 296
Terahertz near-field nanoscopy, 66–67
TERT gene, 667
Tetrahedral amorphous carbon, 461
Tetraphenylporphyrin, 259
Therapy making use of nanoparticles, 537, 650
Therapy, photodynamic, 672
Thermal conductance, 9–11
Thermal conductivity, 514
Thermal evaporation, 99
Thermal expansion, 301–303
Thermal occupation factor of a quantum mechanical resonator, 320
Thermal properties of nanostructures, 7–13
Thermodynamics, violation of the second law, 7–8
Thermoelectric devices, 183
Thermoelectric power, 11

Thermogravimetric analysis (TGA), 140
Thermomagnetic recording, 466
Thermoplastics, 299
Thiophene, 508
Three-dimensional far-field optical nanoimaging of cells, 70–72
Three-dimensional superlattices of binary nanoparticles, 109
Tissue engineering, 585, 717
Tissue engineering of skin, 708
Titin protein, 585
TMA (trimesic acid (1, 3, 5-benzenetricarboxylic acid)), 480
Toggle MRAM, 446
"Toggle" switching, 441
Tomography, photoacoustic, 618, 637
Tooth, 596–597
Tooth formation, 722
Tooth replacement, bio, 722–723
Top-down synthesis, 2–3, 159
TOPO (tri-n-octylphosphine oxide), 646
Topoisomerase, 660
Topoisomerase II, 558
Toughness, 278, 290, 589, 593
Toxicity, 546, 632, 680, 702
Toxicity considerations, 723–728
Toxicology tests, 725
Transductance, 215
Transferrin, 669
Transistors, 187, 209, 239–240, 250, 321, 426–431
Translocase, 577
Translocation of a secretory protein, 577
Translucency, 719
Transmembrane ion transport, 583
Transmembrane protein receptors, 531
Transverse nuclear magnetic relaxation times (T2), 539
Triple helix, 492
Triple-junction migration, 285
Triplet state, 182
Tubular graphite cones, 229
Tumor cell necrosis, 680
Tumors, 636–637, 663, 678–686
Tumors, identification, 620
Tumor-targeting ligands (peptides or antibodies), 647
TUNEL (terminal deoxynucleotidyltransferase biotin-deoxyuridine triphosphate nick end labeling) staining, 665
Tungsten plugs, 87
Tunneling magnetoresistance (TMR), 21–23
Tunneling matrix element, 441
Tweezers, 532
Twin boundaries, 283
Twin deformation, 272
Twinning of crystals, 174
Twins, crystal, 273
Two-dimensional electron gases (2DEG) at oxide interfaces, 199–201
Two-slit interference experiment, 259

U

Ultrahigh data storage densities, 466
Ultrasound imaging, 358, 618
Ultrasound imaging techniques, 632–634
Ultrastrength nanomaterials, 279–282
Umklapp processes, 11
Unfolding a protein domain, 563
Unifying nanophotonics and nanomechanics, 342
Universal computer memory, 437
Unzipping of DNA, 559
UV optical lithography, 154–155

V

Vaccine delivery, 662
Vaccines, 587, 649
Valence, 193
Valinomycin, 583
Van der Waals forces, 323
Vapor–liquid–solid (VLS) growth of nanowires, 113–116
Vascular diseases, peripheral, 688
Vascular endothelial growth factor (VEGF), 708
Vascular targeting, 676
Vascular targeting ligand, 676
Vasculature, 631, 704
Venereal tumor, 685
Vertebral body, 631
Vesicle-like structures, 495
Vesicular membrane carriers, 530
Vias, 240
Viral and bacterial diseases, 701–704
Viral vectors, 663
Viruses, 189, 259
Vitamin A, 607
Vitronectin, 706
Vortex line in superfluidic He, 360
'Vortex' state of ferromagnetic rings, 408
Vortex structure in a permalloy film, 382
Vortices, magnetic and interaction with electrons in the fractional quantum Hall effect, 198

W
Water purification, 5
Water repellency, 601
Water strider, 602
Water transport in CNTs, 351–352
Water window, 87, 203
Waveguide, 342
Waveguide, slot, 342
Wave-particle duality, 209–262
Wear, 292–293
Wettability, 651
Wetting, 315, 346–351, 601
Wetting angle, 651
Whey, 605
Wood, 585
Work of fracture, 587
Worm-like chain (WLC) model, 557

X
X-ray beam, nanofocused, 89
X-ray diffraction microscopy (ptychography), scanning, 90
X-ray free electron lasers (XFEL), 89–91
X-ray magnetic circular dichroism (XMCD), 85, 87, 366, 381–383
X-ray microscopy, 84–91
X-ray microscopy, lens based, 85–87
X-ray microscopy, scanning transmission, 85
X-ray mirrors, 203
X-ray nanotomography, 87–88
X-ray photoelectron spectroscopy (XPS), 295, 502

Y
Yeast cell, 88
Yoghurts, 605
Young's modulus, 186, 276

Z
Zeolites, 145–149
Zeptogram-scale mass sensing, 315
Zeptoliter liquid alloy droplets, 354–356
Zeptonewtonscale force sensing, 315
Zernike phase contrast, 85